THIS DOCUMENT PROVIDED BY THE ABBOTT AEROSPACE
TECHNICAL LIBRARY
ABBOTTAEROSPACE.COM

AD-A253 603

AGARD-CP-507

(1)

AGARD-CP-507

AGARD

ADVISORY GROUP FOR AEROSPACE RESEARCH & DEVELOPMENT
7 RUE ANCELLE 92200 NEUILLY SUR SEINE FRANCE

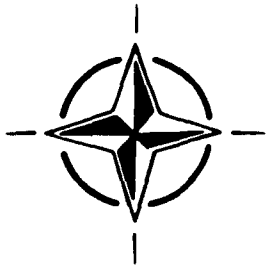
DTIC
ELECTE
JUN 4 1992
S D
C

AGARD CONFERENCE PROCEEDINGS 507

Transonic Unsteady Aerodynamics and Aeroelasticity

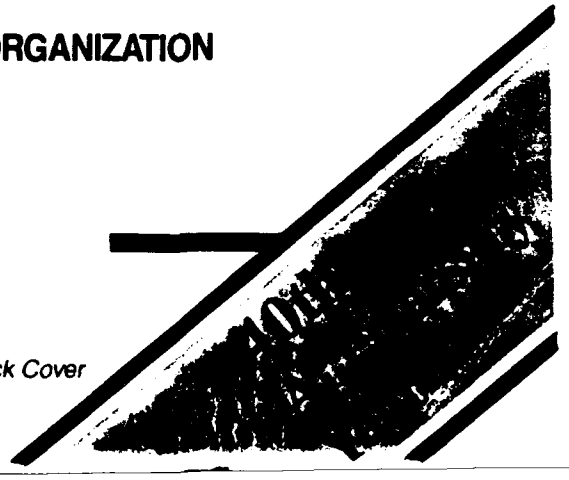
(L'Aérodynamique Instationnaire Transsonique et l'Aéroelasticité)

Papers presented at the 73rd Meeting of the AGARD Structures and Materials Panel, held in San Diego, California, United States from 7th—11th October 1991.



NORTH ATLANTIC TREATY ORGANIZATION

DISTRIBUTION STATEMENT A
Approved for public release;
Distribution Unlimited



Published March 1992

Distribution and Availability on Back Cover

THIS DOCUMENT PROVIDED BY THE ABBOTT AEROSPACE
TECHNICAL LIBRARY
ABBOTTAEROSPACE.COM

AGARD
ADVISORY GROUP FOR AEROSPACE RESEARCH & DEVELOPMENT
7 RUE ANCELLE 92200 NEUILLY SUR SEINE FRANCE

AGARD CONFERENCE PROCEEDINGS 507

Transonic Unsteady Aerodynamics and Aeroelasticity

(L'Aérodynamique Instationnaire Transsonique et l'Aéroelasticité)

Accession For
NTIS GRA&I
DTIC TAB
Unannounced
Justification
By
Distribution/
Availability Codes
Dist Avail and/or Special
A-1

Papers presented at the 73rd Meeting of the AGARD Structures and Materials Panel, held in San Diego, California, United States from 7th–11th October 1991.

North Atlantic Treaty Organization
Organisation du Traité de l'Atlantique Nord

Original contains color plates: All DTIC reproductions will be in black and white

92-14529

92 6 03 001

THIS DOCUMENT PROVIDED BY THE ABBOTT AEROSPACE
TECHNICAL LIBRARY
ABBOTTAEROSPACE.COM

The Mission of AGARD

According to its Charter, the mission of AGARD is to bring together the leading personalities of the NATO nations in the fields of science and technology relating to aerospace for the following purposes:

- Recommending effective ways for the member nations to use their research and development capabilities for the common benefit of the NATO community;
- Providing scientific and technical advice and assistance to the Military Committee in the field of aerospace research and development (with particular regard to its military application);
- Continuously stimulating advances in the aerospace sciences relevant to strengthening the common defence posture;
- Improving the co-operation among member nations in aerospace research and development;
- Exchange of scientific and technical information;
- Providing assistance to member nations for the purpose of increasing their scientific and technical potential;
- Rendering scientific and technical assistance, as requested, to other NATO bodies and to member nations in connection with research and development problems in the aerospace field.

The highest authority within AGARD is the National Delegates Board consisting of officially appointed senior representatives from each member nation. The mission of AGARD is carried out through the Panels which are composed of experts appointed by the National Delegates, the Consultant and Exchange Programme and the Aerospace Applications Studies Programme. The results of AGARD work are reported to the member nations and the NATO Authorities through the AGARD series of publications of which this is one.

Participation in AGARD activities is by invitation only and is normally limited to citizens of the NATO nations.

The content of this publication has been reproduced
directly from material supplied by AGARD or the authors.

Published March 1992

Copyright © AGARD 1992
All Rights Reserved

ISBN 92-835-0660-X

Printed by Specialised Printing Services Limited
40 Chigwell Lane, Loughton, Essex IG10 3TZ

THIS DOCUMENT PROVIDED BY THE ABBOTT AEROSPACE
TECHNICAL LIBRARY
ABBOTTAEROSPACE.COM

Abstract

This publication reports the papers presented to a Specialists' Meeting organized by the Structures and Materials Panel of AGARD and held at its Fall 1991 Meeting.

The Specialists' Meeting provided a forum for the exchange of experiences between the NATO nations with an aim to demonstrate and discuss the present state of knowledge in the field of transonic unsteady aerodynamics and aeroelasticity; to evaluate the various methods of calculation and to highlight straightforward engineering-level aeroelastic prediction techniques.

Abrégé

Cette publication rend compte des communications présentées lors de la réunion de spécialistes organisée par le Panel AGARD des Structures et Materiaux à l'automne 1991.

La réunion de spécialistes a servi de forum pour un échange d'expérience entre les pays membres de l'OTAN, afin de permettre la démonstration et la discussion de l'état de l'art dans le domaine de l'aérodynamique transsonique instationnaire et l'aéroélasticité, l'évaluation des différentes méthodes de calcul, et l'identification de techniques de prédiction aéroélastiques simples, susceptibles d'être mises en oeuvre au niveau industriel.

THIS DOCUMENT PROVIDED BY THE ABBOTT AEROSPACE
TECHNICAL LIBRARY
ABBOTTAEROSPACE.COM

Structures and Materials Panel

Chairman: Mr Samuel L. Venneri
Director, Materials & Structures
Division (Code RM)
Office of Aeronautics & Space Technology
NASA Hq
Washington DC 20546
United States

Deputy Chairman: Mr Roger Labourdette
Directeur Scientifique des Structures
ONERA
29 ave de la Division Leclerc
92320 Châtillon
France

SUB-COMMITTEE ON AEROELASTICITY

Chairman: Prof. Dr-Ing. H. Försching
Direktor der DLR Institut für Aeroelastik
Bunsenstrasse 10
3400 Göttingen
Germany

Members:

L. Chesta	IT
E.H. Dowell	US
G. Duvaut	FR
R. Freymann	LU
E. Fuente	SP
V. Giavotto	IT
J.J. Glaser	CA
J.J. Kacprzynski	CA
R. Labourdette	FR
G. Papakonstantinou	GR
N. Sandsmark	NO
P. Santini	IT
O. Sensburg	GE
A.F. Tovar de Lemos	PO
S.L. Venneri	US
R.J. Zwaan	NL

PANEL EXECUTIVE

Major William D. Lyle, CAF
(Acting SMP Executive)

Mail from Europe:
AGARD—OTAN
Attn: SMP Executive
7, rue Ancelle
92200 Neuilly-sur-Seine
France

Mail from US and Canada:
AGARD—NATO
Attn: SMP Executive
Unit 21551
APO AE 09777

Tel: 33 (1) 47 38 57 90 & 57 92
Telex: 610176 (France)
Telefax: 33 (1) 47 38 57 99

THIS DOCUMENT PROVIDED BY THE ABBOTT AEROSPACE
TECHNICAL LIBRARY
ABBOTTAEROSPACE.COM

Preface

The transonic flow regime is extremely critical for both static and dynamic aeroelastic problems in aircraft. Significant progress has been made in recent years to solve the inherently non-linear equations that describe the unsteady motions of lifting systems in transonic flow, which the availability of reliable and efficient computational methods has greatly enhanced the ability to predict the aeroelastic behaviour of modern aircraft operating under transonic flow conditions. Several computation techniques involving the full range of flow field approximation have been elaborated, and some of them are now available for practical use. However, it is necessary to evaluate all of these competing methods with regard to their applicability for economic and efficient engineering-type aeroelasticity predictions.

The AGARD-SMP Subcommittee on Aeroelasticity has continually monitored and stimulated the progress in unsteady transonic aerodynamics and aeroelasticity in the past decade by

- arranging a Specialists' Meeting on "Unsteady Airloads in Separated and Transonic Flow" in Spring 1977,
- forming a Working Group on "Standard Configurations for Aeroelastic Applications of Transonic Unsteady Aerodynamics" in Fall 1977 for the selection of standard airfoils and wings as a basis for the comparison of theoretical and experimental investigations,
- arranging another Specialists' Meeting on "Transonic Unsteady Aerodynamics and its Aeroelastic Applications" in Fall 1984, and
- organizing a workshop entitled "Future Research on Transonic Unsteady Aerodynamics and its Aeroelastic Applications" in Fall 1986, in order to discuss strategies for promoting engineering-level transonic aeroelastic predition techniques, to establish topics for further research work, and to reestablish new standard configurations for comparison of calculated and measured dynamic aeroelastic behaviour under high subsonic and transonic flow conditions.

This Specialists' Meeting was a continuation of the panel's effort to promote further progress in transonic unsteady aerodynamics and aeroelasticity. The aim of the meeting was to demonstrate and examine recent advances in transonic unsteady aerodynamics and aeroelasticity. The programme comprised parts on (1) Unsteady Transonic Computational Techniques, (2) Transonic Flutter, and (3) Experimental Investigations. In a concluding Round Table Discussion, the present state of the art was critically reviewed and topics and necessities for further research work were pointed out.

Hans Försching
Chairman,
SMP Subcommittee on Aeroelasticity

THIS DOCUMENT PROVIDED BY THE ABBOTT AEROSPACE
TECHNICAL LIBRARY
ABBOTTAEROSPACE.COM

Contents

	Page
Abstract/Abrégé	iii
Preface	iv
Structures and Materials Panel	v
	Reference
Technical Evaluation Report by J.W. Edwards	T
SESSION I – OVERVIEW	
Current Status of Computational Methods for Transonic Unsteady Aerodynamics and Aeroelastic Applications by J.W. Edwards and J.B. Malone	1
Unstructured-Grid Methods Development for Unsteady Aerodynamic and Aeroelastic Analyses by J.T. Batina, E.M. Lee, W.L. Kleb and R.D. Rausch	2
Paper 3 withdrawn	
Unsteady Aerodynamics and Aeroelasticity at the Flight Dynamics Directorate by M. Blair, L.J. Huttsell, W.A. Sotomayer and T.M. Harris	4
Recent Applications of Linear and Nonlinear Unsteady Aerodynamics for Aeroelastic Analysis by B. Winzell	5
SESSION II – UNSTEADY TRANSONIC COMPUTATIONAL TECHNIQUES I	
A Time-Linearization Approach forUnsteady Transonic Flows by Y.S. Wong, B.H.K. Lee and H.S. Murty	6
A Boundary Integral Formulation for Unsteady Transonic Potential Flow by U. Iemma, F. Mastroddi, L. Morino and M. Pecora	7
Comparison of Euler and Full Potential Methods for Unsteady Transonic Flow Calculations by R. Voss and W. Wegner	8
Computation of the Unsteady Transonic 2D Cascade Flow by an Euler Algorithm with Interactive Grid Generation by V. Carstens	9
Evaluation of an Unsteady Implicit Euler Code Against Two and Three-Dimensional Standard Configurations by A. Brenneis and A. Eberle	10
Unsteady Transonic Aerodynamics of Pointed Bodies of Revolution in Supersonic Freestream by P. García Fogeda and A. Sanz	11

THIS DOCUMENT PROVIDED BY THE ABBOTT AEROSPACE
TECHNICAL LIBRARY
ABBOTTAEROSPACE.COM

Reference

SESSION III – UNSTEADY TRANSONIC COMPUTATIONAL TECHNIQUES II

NLR Inviscid Transonic Unsteady Loads Prediction Methods in Aeroelasticity 12
by M.H.L. Hounjet

Computations of Unsteady Flows Around Airfoil Sections by Explicit and Implicit Methods Solving the Euler and Navier-Stokes Equations 13
by E.A. Gerteisen

***Computation of* Viscous Phenomena in Unsteady Transonic Flow** 14
by U.R. Müller, H. Henke and K. Dau

SESSION IV – TRANSONIC FLUTTER I

Transonic Aeroelastic Calculations in Both the Time and Frequency Domains 15
by M.J. Knott

Aeroelastic Calculations for Fighter Aircraft Using the Transonic Small Disturbance Equation 16
by D.M. Pitt and D.F. Fuglsang

Computation of Flutter Boundaries in the Time and Frequency Domain 17
by H. Zimmerman, S. Vogel, H. Henke and B. Schulze

SESSION V – TRANSONIC FLUTTER II

Analysis of Unsteady Aerodynamic and Flutter Characteristics of an Aeroelastic Model in Transonic Flow 18
by G. SenGupta, et al.

Couplage Direct Fluide Structure en Aéroélasticité Transsonique 19
par J.P. Grisval et J.L. Meurzec

Investigation of the Aeroelastic Stability of the AFW Wind-Tunnel Model Using CAP-TSD 20
by W.A. Silva and R.M. Bennett

Numerical Simulation of Shock-Stall Flutter of an Airfoil Using the Navier-Stokes Equations 21
by K. Isogai

Transonic Aeroelastic Computations in Wings Using Navier-Stokes Equations 22
by G.P. Guruswamy and S. Obayashi

Development of a Method to Predict Transonic Limit Cycle Oscillation Characteristics of Fighter Aircraft 23
by J.J. Meijer and A.M. Cunningham, Jr

SESSION VI – EXPERIMENTAL INVESTIGATIONS

***Transonic Wind Tunnel Investigation of Limit* Cycle Oscillations *on* Fighter Type Wings** 24
by A.M. Cunningham, Jr and R.G. den Boer

The Benchmark Aeroelastic Models Program – Description and Highlights of Initial Results 25
by R.M. Bennett, et al.

Further Investigation of the Effect of Model Cooling on Periodic Transonic Flow 26
by S. Raghunathan, F. Zarifi-Rad and D.G. Mabey

A Review of Scale Effects on Surfaces in Unsteady Motion 27
by D.G. Mabey

THIS DOCUMENT PROVIDED BY THE ABBOTT AEROSPACE
TECHNICAL LIBRARY
ABBOTTAEROSPACE.COM

TECHNICAL EVALUATION REPORT ON 1991 SPECIALISTS' MEETING ON "TRANSONIC UNSTEADY AERODYNAMICS AND AEROELASTICITY"

by
John W. Edwards
Unsteady Aerodynamics Branch
NASA Langley Research Center
Hampton, Virginia 23665 USA

SUMMARY

This paper presents a technical evaluation of the Specialists' Meeting on "Transonic Unsteady Aerodynamics and Aeroelasticity" held at the 73rd meeting of the AGARD Structures and Materials Panel on October 9-11 1991, in San Diego, California USA.

1. INTRODUCTION

The goals of the Specialists' Meeting were to demonstrate and discuss the present state of knowledge in the subject area, to evaluate the various methods of calculation, and to highlight straightforward engineering-level aeroelastic prediction techniques. Specific goals were:

- Application of the different techniques available for the prediction of motion-induced unsteady transonic airloads and their evaluation against the AGARD-SMP Standard Aeroelastic Configurations (see Appendix).
- Demonstration of transonic aeroelastic calculation techniques in both the time and frequency domains.
- Numerical solution of typical viscous-flow transonic aeroelastic flutter phenomena.
- Systematic experimental investigations with regard to Reynolds number, boundary layer and flow separation effects.
- Transonic aeroelastic interactions of wing/engine/external stores.

This Specialists' Meeting is the fourth in a series of SMP meetings on transonic unsteady aerodynamics and aeroelastic applications:

- 1977 - Unsteady Airloads in Separated and Transonic Flow, Lisbon, Portugal, AGARD CP-226.
- 1980 - Boundary Layer Effects on Unsteady Airloads, Aix-en-Provence, France, AGARD CP-296.
- 1984 - Transonic Unsteady Aerodynamics and its Aeroelastic Applications, Toulouse, France, AGARD CP-474.

The following meetings are also of note in this context due to their focus upon unsteady boundary layers, buffeting response at moderate angles, and vortex dominated flows at high angles:

- 1985 - Unsteady Aerodynamics - Fundamentals and Applications to Aircraft Dynamics, Goettingen, Germany, AGARD CP-386.
- 1990 - Aircraft Dynamic Loads due to Flow Separation, Sorrento, Italy, AGARD, CP-374.

The 1980 and 1990 conference proceedings contain evaluation reports while References 1, 2 and 3 contain evaluations of the 1977, 1984 and 1985 meetings. Table I summarizes the distribution of papers presented at these meetings and draws attention to the interaction between experimental studies and computational capabilities. Thus, throughout these meetings experimental studies covering most aspects of attached and separated flow, and low and high speed aeroelastic responses are found. Also, early work on unsteady pressure measurements for transonic attached flow conditions on oscillating models led to the AGARD Standard Aeroelastic Configurations documented in References 4, 5, and 6. Early computational capability for these conditions was evident at the 1977 meeting in the shock oscillation calculations of Magnus and Yoshihara (Ref 7) and Ballhaus and Goorjian (Ref 8). The maturation of these inviscid methods led to the preponderance of computational papers at the 1984 meeting.

Since 1984, three main thrusts in computational methods have been: aeroelastic applications; movement towards higher level fluid dynamic flow models; and the incorporation of viscous effects. At issue has been the determination of conditions when viscous effects are required for accurate predictions. A major thread which can be discerned in the papers reviewed is that this issue remains to be resolved for high speed incipiently separating flows which are critical for improved predictive capability for transonic flutter. A second major thread evident in the experimental papers from the 1990 meeting is the continued focus upon unsteady airloads due to flow separation; buffeting at moderate angles and vortex dominated flows at higher angles. Emerging computational capability for treating such flows is seen in several of the reviewed papers.

Computational Solution Nomenclature: Fluid dynamic flow models available for unsteady aerodynamic computation are illustrated in Figure 1. They include: the classical (LIN) small disturbance potential equation, the nonlinear potential equation (both Transonic Small Disturbance (TSD) and Full Potential (FPE)), the Euler equations (EE) and the Navier-Stokes equations (NS) (both Full (FNS) and Thin-Layer (TLNS) forms). All but the first of these are nonlinear partial differential field equation(s) (PDE) whose solutions for prescribed boundary conditions are sought. The inviscid potential and Euler equation(s) are nonlinear PDEs which may be augmented by simultaneously solving various forms of the viscous (-VISC) boundary layer equations in an interactive fashion, accounting for displacement thickness effects by modifying the boundary conditions for the inviscid flow. Other terms which will occur frequently include:

THIS DOCUMENT PROVIDED BY THE ABBOTT AEROSPACE
TECHNICAL LIBRARY
ABBOTTAEROSPACE.COM

Table I

SUMMARY OF UNSTEADY AERODYNAMICS AND AEROELASTICITY PAPERS PRESENTED AT AGARD MEETINGS

	Experimental	Semi-Empirical	Computational	Survey	Total
1977	10	1	5	2	18
1980	4	1	6	1	12
1984	2	1	11	2	16
1990	13	2	1		16
1991	4	1	19	2	26

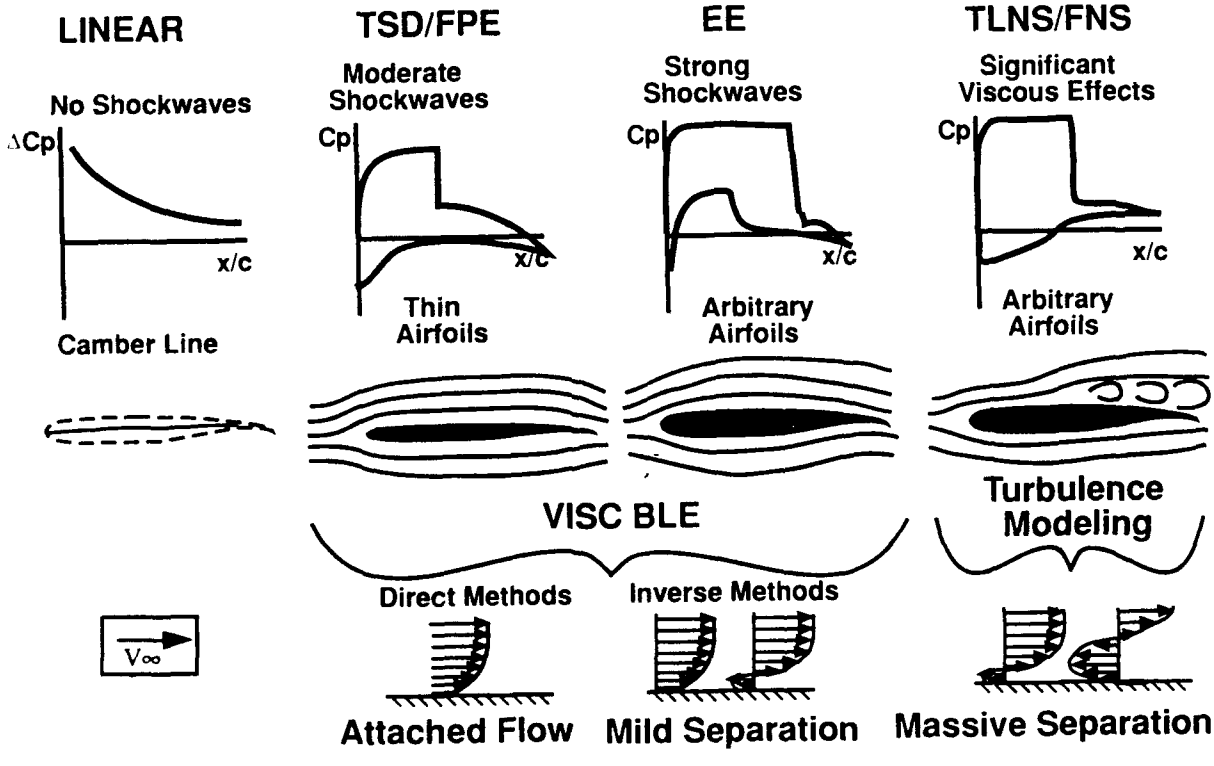


Figure 1. CFD Flow Modeling Levels

THIS DOCUMENT PROVIDED BY THE ABBOTT AEROSPACE
TECHNICAL LIBRARY
ABBOTTAEROSPACE.COM

Computational Fluid Dynamics (CFD); Computational Test case (CT); Approximate Factorization (AF) and Alternating Direction Implicit (ADI) solution algorithms; Aerodynamic Influence Coefficients (AICs) and Generalized Aerodynamic Forces (GAFs) used in aeroelastic analysis; and computational efficiency expressed in terms of microseconds per grid point per time step (μsec/gp/st). For this discussion, the following nomenclature will be used to describe the processes used to: manipulate the PDEs; obtain a computational solution; and produce an aeroelastic solution.

PDEs:

NL - fully nonlinear PDEs

TL - time-linearized (steady + small perturbation)

LIN - linearized PDE

Computational Solution:

TM - solution for "time-marching" coupled aero-structure transient response or prescribed modal motion

H - aero response to harmonic modal oscillation

HT - time domain TL solution

HF - frequency domain TL solution

P - aero response to shaped pulse modal motion

PF - frequency domain TL solution

PT - time domain TL solution

Aeroelastic Solution:

TM - time-domain: curve fits of transient responses yield frequency and damping

Pd - Pade curve fits of H or P results

EIG - frequency-domain: traditional eigenvalue solution using GAFs from H or P solutions (e.g. H/Pd/EIG)

Brief comments are given in section 2 on the individual papers in an attempt to give the reader a general indication of the content of the meeting. Section 3 summarizes the Round Table Discussion while Section 4 gives a discussion of the meeting and identifies areas where future research might be beneficial. Some conclusions and recommendations are given in section 5.

2. SYNOPSIS OF PAPERS

1. J. W. Edwards and J. B. Malone: "Current Status of Computational Methods for Transonic Unsteady Aerodynamics and Aeroelastic Applications"

This paper provides a survey of computational methods which have been applied for unsteady aerodynamic and aeroelastic predictions, focusing upon low-angle high speed flows and high-angle vortex-dominated flows. Computational challenges are discussed in terms of the complexity of the flow field: attached flows (Type I) and fully separated (Type III). Attention is drawn to an intermediate transitional state (Type II), where unsteady separating and reattaching flows are encountered in conjunction with minimum transonic flutter speeds. Computational resource issues are discussed and assessments given for accurate calculations of high-speed, low-angle conditions: TSD-VISC computations require about 400K gridpoints per surface and about one hour runtimes; TLNS computations require about 650K gridpoints per surface and 35-80 hour runtimes. The necessity of including viscous modeling is stressed.

The survey of applications lists numerous examples of unsteady aerodynamic applications. However, there are comparatively few examples of detailed aeroelastic applications, i.e. calculations of complete flutter boundaries compared with experiment or alternative calculations. Table II lists these cases, showing the prevalence of potential code applications (particularly TSD codes). Note that the total number of flutter points included in these detailed studies is only about 130 and that only three of the studies are from industry. Many more applications, particularly within industry, are needed to demonstrate a mature design and analysis capability for transonic flutter. It is pleasing to be able to note this issue being addressed in the papers presented at this meeting; particularly Papers 5, 6, 12, 15, 16, 17, and 20. Progress is noted for high-angle, vortex-dominated flow cases, particularly tail buffeting, although the computational expense of such cases will continue to be prohibitive.

2. J. T. Batina, E. M. Lee, W. L. Kleb, and R. D. Rausch: "Unstructured-Grid Methods Development for Unsteady Aerodynamic and Aeroelastic Analysis"

The current status of unstructured grid methods at NASA Langley Research Center is described. Both 2D and 3D EE codes using central difference explicit and upwind difference implicit flow solvers are described. The ability to easily model complicated geometries is stressed. A general mesh movement technique is described including capability of adaptive mesh refinement and coarsening. TM/P and TM/H calculations for the pitching/plunging NACA 0012 airfoil compare excellently with TM/H results from a structured grid EE code as did TM flutter results from the two codes. Wing rocking-like motions are shown for supersonic high angle conditions simulated using a conical flow EE code. 3D results include TM/H calculations for a complex fighter configuration at a supersonic speed, oscillating in an assumed flexible mode and the ONERA M6 wing, where steady pressures are in good agreement with experiment at M = 0.84. Efficiency gains from algorithm improvements and grid adaptation are beginning to make these unstructured grid methods competitive with structured grids.

3. Paper 3 was not presented.

4. M. Blair, L. Hutsell, W. Sotomayer and M. T. Harris: "Transonic Unsteady Aerodynamics and Aeroelasticity at the Flight Dynamics Directorate"

This paper gives an overview of in-house and contract efforts at the Flight Dynamics Directorate, USAF Wright Laboratory. Computational efforts with three CFD codes, a cooperative wind tunnel test of an F-16 wing/store model (described in more detail below under Paper 24), and plans for incorporating CFD results into a structural redesign case are described. The XTRAN3S, CAP-TSD and ENS3DAE codes are described. The first two are 3D TSD codes while the latter is a 3D NS code using the Beam-Warming Alternating-Direction Implicit (ADI) solution algorithm. The code uses the Baldwin-Lomax turbulence model and may be run in FNS, TLNS or EE modes. Steady NS results are shown for the full-span configuration F-15 and the F-5 wing. Wing pressures for a F-15 case compare well with experiment for M = 0.6 and α = 8.66 deg, as do pres-

THIS DOCUMENT PROVIDED BY THE ABBOTT AEROSPACE
TECHNICAL LIBRARY
ABBOTTAEROSPACE.COM

Table II

WING FLUTTER BOUNDARIES COMPUTED WITH CFD METHODS
(References from Edwards and Malone, Paper No. 1)

First Author	Wing/Model	Code	M	α, deg	# flutter pts.
Shieh [143]	Transport	Hybrid	0.70-0.85	0, 2	14
Guruswamy [69]	Rectangular	TSD	0.70-1.10		4
Mulak [112]	A310	TSD	0.78	-1.5, 0	6
Henke [71]	AMP	TSD-VISC	0.60-0.82		8
Borland [37]	A-6E	TSD	0.70-0.95		9
Cunningham [44]	445.6 Wing	TSD	0.34-1.14		12
Bennett [26]	445.6 Wing	TSD	0.40-1.00		8
Bennett [26]	Clipped delta	TSD	0.60-0.90		4
Gibbons [62]	70° delta	TSD	0.60-3.00		10
Silva [144]	AFW	TSD	0.50-1.10	0, 1.5	18
(Dassault) [13]	Falcons	TSD	0.80, 0.87		14
Hounjet [75]	Fighter	FPE time-lin.	0.90		9
Isogai [85, 87]	Transport	FPE	0.70-0.85		13
	Transport	FPE	0.70-1.10		4

sures for the F-5 case at M = 0.8 and α = 0 deg. A structural redesign effort is described involving an F-16 planform model loaded with stores. The goal is to use a transonic TSD code to produce (AICs) for use with the ASTROS aeroelastic analysis program (HT/Pd/EIG analysis).

5. B. Winzell: "Recent Applications of Linear and Non-Linear Unsteady Aerodynamics for Aeroelastic Analysis

Unsteady linear and FPE codes are used in this paper which emphasizes details of trailing edge and control surface pressures, viscous effects and flutter solutions. The AEREL linear program and a 3D FPE code using an AF solution algorithm with upwind density-biasing are described. Body-fitted C-H grids are used and a 2D-strip Nash-McDonald boundary layer method is available. TM/H results are given for the LANN wing for M = 0.62, 0.82 for six frequencies. The importance of including aeroelastic effects for this model is shown. Two PT/Pd/EIG flutter boundaries are given for an RAE flutter model: the first predicts a premature (0.03M) transonic dip and overall flutter speeds are too high. This latter effect is attributed to sensitivity in modeling the value of the pitch block inertia; the flutter boundary with the value halved shows proper alignment with experiment at lower speeds. The premature dip is discussed in relation to viscous effects. Single flutter points with the boundary layer model at a Mach number above the transonic dip show a proper trend of shifting the dip to higher Mach numbers. It is interesting to note that the viscous model used implies that the flow is attached on the "backside" of the flutter dip for these cases.

The final portions of the paper deal with the lack of accuracy in predictions of trailing-edge pressures due to control deflections. Comparisons of steady and unsteady AEREL and FPE TM/HT results with experiment are given for an unswept, low-speed wing/aileron/tab model, the F-5 wing/flap model at M = 0.80,0.95, and a cropped delta wing/flap model at M = 0.95. Modifications to the unsteady pressure and down-wash formulas to account for local velocity variation are suggested as possibilities for improving correlations. The discussion of these effects would benefit if shock-generated entropy/vorticity modifications were included. A final TM example for the cropped delta wing shows a 60% loss of control effectiveness due to static aeroelastic deformation.

6. Y. S. Wong, B. H. K. Lee and H. Murty: "A Time-Linearization Approach for Unsteady Transonic Flows"

Further details of the 3D TSD TL UST3D code are presented. The steady portion of the solution is obtained with a line relaxation solver using a Newton-like iterative algorithm. The unsteady portion is obtained from a time-domain semi-implicit ADI algorithm producing TL/HT AICs and TL/HT/EIG flutter solutions. Results include: steady pressures for the F/A-18 wing at M = 0.92; unsteady pressures for the F-5 wing at M = 0.80,0.95; unsteady airloads for the LANN wing for M = 0.82; and the ONERA M6 wing for M = 0.84. Unsteady results were obtained with 59K gridpoints. Workstation runtimes for three cycles of TL/HT motion are about 15 minutes. Comparison of pressure distributions for the oscillating ONERA M6 wing with CAP-TSD results indicates the limitation of time linearization

THIS DOCUMENT PROVIDED BY THE ABBOTT AEROSPACE
TECHNICAL LIBRARY
ABBOTTAEROSPACE.COM

methods for cases with moderate shock motions.

Flutter analyses of the AGARD 445.6 wing are presented for air and heavy gas test media and compared with results from linear theory, the CAP-TSD code (only the CAP-TSD LIN/TM results are given) and the ZONA51 supersonic harmonic gradient code. The TL/HT GAFs were computed for only one reduced frequency, k = 0.1, which corresponds to the flutter frequency only near the bottom of the transonic dip. The flutter boundary for the wing in a heavy gas also agrees reasonably well with the other data. The minimum flutter speed is well predicted at M = 0.96 followed by an abrupt premature rise at higher speeds. The flutter boundary for the wing in a heavy gas also agrees reasonably well with the other data, although the gradient of the boundary with Mach number is overpredicted. Modest differences in details of the boundaries may be attributed to: use of a single assumed reduced frequency; time-linearization; number of gridpoints used.

7. L. Morino, P. Santini, F. Mastroddi, U. Iemma and M. Pecora: "An Integral Formulation for Unsteady Transonic Potential Flows"

A boundary integral formulation is used to solve the 2D and 3D potential equation in a manner closely related to that of Morino and Tseng and extending applications to unsteady conditions. The resulting surface and volume integrals are discretized using a zeroth order formulation. Steady and unsteady results are shown for the NACA 0012, NACA 64A010 and RAE 2822 airfoils at transonic conditions. Typically, 30-40 elements are used along the chord, and 5 volume elements fore and aft of the chord and in the z-direction. Steady pressures are shown for a rectangular wing. The method shows promise but element refinement studies are needed before an assessment can be made.

8. R. Voss and W. Wegner: "Comparison of Euler and Full Potential Methods for Unsteady Transonic Flow Calculations"

A detailed comparison of inviscid results from EE, FPE, and TSD codes is given. Code-to-code comparisons are made with the exception of a comparison with LANN wing data.

- 2D EE/HT code: explicit solution algorithm with NRBC; four different upwinding procedures were implemented and showed no differences.

- 2D FPE/HT code: implicit line relaxation algorithm with mass-flux biased upwinding and Newton iteration. In the far-field, the flow is modeled by a potential vortex.

These two codes were used in a detailed study of the NACA 0012 and NLR 7301 airfoils. Identical C-type computational grids were used and rigid mesh rotation was used for oscillatory cases. Far-field boundaries were ten chordlengths from the airfoil. Amplitude and frequency variations are given. The results for the NACA 0012 airfoil show good agreement of unsteady pressures. Interestingly, the lift coefficient shows a nonlinear behavior at higher frequencies whereas the moment shows a strong nonlinear behavior at low frequency. While the details of the pressure distributions agree well, the integrated airloads show deviations large enough to cause concern for aeroelastic analysis. A possible explanation for the differences is the neglect of vorticity modeling in the FPE code (Figures 25 and 26 of Paper 12 show the effect of modeling vorticity with a FPE code to cause a shift in shock location of the order noted). For the lifting NLR 7301 airfoil, the agreement of the pressure distributions is not as good; differences are noted particularly in the vicinity of the multiple shocks calculated. Two possibilities for these differences are the entropy modeling of the FPE code (which assumes a single shock) and the extent of the computational grid. Reference 9 shows the significant effect of grid extent on steady EE solutions (on the order of 10% lift deficiency for lifting airfoils with 10 chordlength boundary location). No such grid extent study for unsteady flows has been published for any PDE.

- 3D FPE/HT code: same algorithm as the above 2D code, without shock generated entropy modeling; CH-grids with 108K gridpoints are used.

- 3D TSD/TL/HF PTRAN3 code: integral equation/finite difference solution algorithm; 25K gridpoints are used.

Computations with these two codes are given for a 30 deg swept wing with NACA 0012 section, oscillating about an unloaded condition at M = 0.82. The TL/HF approximation is in good agreement with the FPE/TM result for 0.25 deg pitching amplitude but differences become apparent for 1.0 deg. FPE/TM code steady and unsteady pressures are given for the LANN wing for CT 5 (M = 0.82). Comparison with experiment shows general agreement for the steady pressures. The unsteady results show differences in the "shock pulse" location and magnitude; however, the wing flexibility was not modeled.

9. V. Carstens: "Computation of the Unsteady Transonic 2D Cascade Flow by an Euler Algorithm with Interactive Grid Generation"

This paper presents results from a 2D EE code for cascase flow analysis. A flux-vector split upwind differencing method is used with a Beam-Warming implicit algorithm. Moving body-fitted H-grids are computed at each time step using the computed grid point speeds. Aeroelastic analysis of tuned blade rows requires gridding of up to eight blade channels for interblade phase angle increments of 45 degrees while a mistuned blade row case is treated using sixteen blade channels. Stability is inferred from computed aerodynamic damping of the oscillating blade row. Two tuned blade row standard configurations are studied: a turbine blade row for both subsonic and supersonic outflow Mach numbers; and a compressor blade row for subsonic and transonic flow cases. For the former blade row, results are encouraging for the subsonic outflow condition: stable and unstable regions of interblade phase angle are well predicted compared with experiment. Stability for the supersonic outflow condition is contrary to experiment, which may be due to the incorrect blade passage shock strength in the calculation. Comparison of the present method with published FPE/TL results for the compressor blade row show significant differences in the computed unsteady pressures and aerodynamic damping, leading to concern of the viability of TL methods for such cases. Finally, a simple model of a mistuned blade row gave results showing that average power coefficients remain positive for bending and pitching oscillations (indicating stable motion), in agreement with an alternative prediction.

10. A. Brenneis and A. Eberle: "Evaluation of an Unsteady Implicit Euler Code Against Two- and Three-Dimensional Standard Configurations"

Steady and unsteady EE/HT aerodynamic calculations are computed with the INFLEX2 (2D) AND INFLEX3 (3D) codes.

THIS DOCUMENT PROVIDED BY THE ABBOTT AEROSPACE
TECHNICAL LIBRARY
ABBOTTAEROSPACE.COM

The unfactored Euler equations are solved with a point Gauss-Seidel relaxation method using upwind differencing and a nonlinear Newton method. The principal feature of the algorithm is the characteristic flux extrapolation scheme based upon a local eigenvalue analysis. H- and H-H grids are used and an elliptic grid generation method, solved with point Gauss-Seidel iterations, provides the moving mesh at each time step. Extensive comparisons with the AGARD CTs are given for two airfoils and two wings.

NACA 64A010 airfoil: Unsteady pressures are compared with experiment for CT3, CT4, CT5, CT6, and CT7: agreement is very good to excellent. Time step and grid refinement studies are also discussed for this case. Algorithm efficiency is about 5 μsec/gp/st.

NLR 7301 Airfoil: For the design condition, CT8 (M = 0.721), agreement with experiment for the upper surface is poor due to the lack of viscous modeling; one subcritical case (CT2) with a boundary layer model included shows a good viscous correction for the steady pressures and no effect on the unsteady pressures. Similar agreement is shown for two oscillating flap cases for subcritical and transonic conditions.

LANN wing: CT2 (M = 0.77) and CT5 (M = 0.82) comparisons are shown from calculations with 140K gridpoints. Wing flexibility is not modeled. For the subcritical transonic case, CT2, favorable predictions of the forward shock location and unsteady pressures are given. For the design cruise case, CT5, suction peak levels are well predicted but the shock locations and unsteady shock pulses are too far aft, as is typical of inviscid calculations for this case.

NORA wing: Unsteady pressures for the strong transonic case CT6, M = 0.95, compare very favorably with experimental results from two wind tunnels.

11. P. Garcia-Fogeda and A. Sanz: "Unsteady Transonic Aerodynamics of Pointed Bodies of Revolution in Supersonic Freestream"

Small perturbation supersonic potential flow about pointed bodies of revolution is solved using time linearization as the sum of a steady thickness potential and an unsteady angle-of-attack potential. The method of characteristics is used to obtain solutions for arbitrary bodies of revolution oscillating in rigid or bending motions at any frequency. Applications are given for: steady pressures for 5 and 10 deg cones for $1 < M < 6$, and a parabolic ogive at M = 2; normal force coefficient, including unsteady loads due to pitching, for 5 and 10 deg cones for Mach numbers up to 12. Comparisons are made with linear, first order and exact solutions and show that the method agrees well with more exact methods. For Mach numbers near one there is not a substantial difference from first order theory, but nonlinear effects are shown to be important for large Mach numbers and thick bodies. Computational time is quite small, providing an attractive alternative analysis method for such geometries.

12. M. H. L. Hounjet: "NLR Inviscid Transonic Unsteady Loads Predicition Methods in Aeroelasticity"

An overview of unsteady inviscid methods developed at the NLR is given. Emphasis is on the use of a range of CFD methods, cross-checked against one another, in order to achieve efficient aeroelastic analysis with acceptable turn-around time on current workstations. Most of the examples are from the following TL methods: the 2D TSD FTRAN2 code, the 2D FPE FTRANC code, and the 3D FPE FTRAN3 code. The latter two codes employ mass-flux split upwinding, entropy corrections, multi-grid and Newton iteration with the solution on the coarsest grid being provided by an integral equation field panel method. AICs are obtained from a novel TL/HF/Pd procedure using positive real values of reduced frequency (simulating diverging motions). This eliminates the need for complex arithmetic yielding large savings in computational efficiency, and removes a frequency limitation.

- NLR 7301 airfoil, M = 0.7: steady pressures from FTRANC agree well with EE results

- Steady and unsteady pressures from FTRAN3 are compared with experiment for two fighter type wings at M = 0.9 and M = 0.6, 0.8, 0.9, 0.95 and for a rectangular supercritical wing at M = 0.7, 0.825. There is good agreement except for the higher Mach numbers where viscous effects are apparent.

- AGARD 445.6 wing: FTRAN3 TL/HF/Pd/EIG flutter boundary calculations at M = 0.6, 0.9, 0.96 show good agreement with experiment.

Time Marching methods reviewed include the 2D TSD-VISC ULTRAN-V code and the 2D FPE TULIPS code. The former includes an interacted quasi-steady integral boundary layer model capable of treating both attached and separated flows. The TULIPS code includes entropy and vorticity corrections and NRBC. Comparisons of steady pressures from TULIPS and an EE code for the NLR 7301 and NACA 0012 airfoils show the efficacy of the entropy and vorticity corrections. Also, for the oscillating NACA 0012 airfoil, good agreement is shown between results from TULIPS with entropy and vorticity corrections and an EE code, and between results from uncorrected TULIPS and inviscid ULTRAN-V. There is significant difference between the two sets of results, with and without entropy/vorticity effects, which should be carefully noted. A final comparison for the oscillating NACA 0012 airfoil with results from an inviscid EE code and the ULTRAN-V TSD code with viscous modeling shows that neither code satisfactorily predicts complete details of the experimental unsteady airloads for a case involving vortex shedding. While time linearized methods are shown to be fast, efficient aeroelastic analysis tools, the paper indicates that the direct time marching approach has been chosen as the basis for a complete aircraft aeroelastic analysis package.

13. E. A. Gerteisen: "Computations of Unsteady Flows Around Airfoil Sections by Explicit and Implicit Methods Solving the Euler and Navier/Stokes Equations"

A 2D FNS/EE code is described which uses an implicit LU-factorization algorithm with flux vector splitting. The Baldwin-Lomax turbulence model is used and moving meshes are treated using a network of tension/torsion springs. The example computations are:

- Steady, oblique shock wave/boundary layer interaction at M = 2. Results are in good agreement with experiment and other calculations.

- Karman vortex shedding about a cylinder for Re = 200, M = 0.1. The Strouhal number shedding frequency of 0.181 agrees well with experiment.

- NACA 64A006 airfoil with oscillating flap. Inviscid unsteady pressures for the Type A, B, and C shock motions

THIS DOCUMENT PROVIDED BY THE ABBOTT AEROSPACE
TECHNICAL LIBRARY
ABBOTTAEROSPACE.COM

at M = 0.822, 0.854, 0.875 agree well with the EE calculations of Magnus.

- A case of self-excited shock oscillation about a 14% circular arc airfoil is shown for M = 0.80. This is below the experimentally observed range of oscillations of about M = 0.83-0.87 and is attributed to lack of grid resolution and turbulence modeling. The oscillation frequency is not noted.

14. U. R. Muller, H. Henke and K. Dau: "Computation of Viscous Phenomena in Unsteady Transonic flow"

The validation of a 3D TSD-VISC code with a 2D strip interacted boundary layer model is described. The TSD code incorporates monotone differencing, entropy and vorticity corrections, NRBC, and an ADI algorithm. The unsteady integral boundary layer method for compressible turbulent flow is based upon a dissipation integral approach to better model separated flows. Strong interaction coupling is achieved via an implicit coupling with the inviscid flow during the final z-sweep of the ADI solution. For validation purposes, an unsteady 3D finite difference boundary layer code was also developed.

Three comparisons of viscous calculations with these two codes are given in order to validate the performance of the integral viscous method against the finite difference method: incompressible 2D flow in a wind tunnel with an oscillating freestream velocity; 3D low speed flow in an S-shaped duct exhibiting velocity profiles with "crossover" features; and a theoretical 3D compressible flow. Although none of these cases involve separated flow, the integral method reproduced the boundary layer displacement thicknesses very well.

Steady transonic cases indicating the viscous capability are given for the NLR 7301 airfoil, CT 11, M = 0.7; the RAE 2822 airfoil, case 9, M = 0.72; and the RA16SC1 airfoil with deflected spoiler, M = 0.727. Very good agreement with experimental pressures are shown for the first two cases, while general agreement with experiment and an alternative calculation is shown for the third case. Unsteady pressures for the NLR 7301 with oscillating flap, CT5, are in very good agreement with experiment.

The final example is for the transport wing model described in detail in Paper 17. Steady wing pressures are shown for M = 0.78. Comparison with steady and unsteady experimental pressures for η = 0.66 show very good agreement for the viscous calculations. The experimental data indicates the onset of trailing edge separation, whereas the computation appears to show attached flow.

15. M. J. Knott: "Transonic Aeroelastic Calculations in Both the Time and Frequency Domains"

The 3D TSD UTSP code is described and flutter boundaries for two wings are shown. The code employs monotone differencing, entropy corrections, and an ADI solution algorithm. A number of solution options are available: "non-linear harmonic" (TSD/HT), "linearized harmonic" (TSD/TL/HT), "linearized indicial" (TSD/TL/PT), and "coupled unsteady" (TSD/TM).

Comparison of calculations using 48K gridpoints with steady and unsteady pressures for the AGARD Taileron model at M = 0.95 do not agree well; the data indicates a rather strong viscous effect. A three mode flutter analysis (TSD/H/EIG) of the AGARD 445.6 wing shows good agreement with experiment for the minimum flutter speed at M = 0.96 and a favorable, though unconservative, agreement for the low supersonic conditions. However, the flutter speed at M = 0.68 is overpredicted by 33%.

A second flutter boundary calculation is given for a combat aircraft wing, showing a transonic dip at M = 0.9. Comparisons of three different computational procedures indicates a significant effect of loading and angle at attack. One comparison, at M = 0.9, gave the same flutter speed for TM and TL/HT/EIG solutions. Significantly, an early version of this code is in use on transport wing design projects.

16. D. M. Pitt and D. F. Fuglsang: "Aeroelastic Calculations for Fighter Aircraft Using the Transonic Small Disturbance Equations"

This paper presents further aeroelastic studies of the F-15 wing and the FA-18 wing with tip launcher and store using the 3D CAP-TSD code. Earlier studies included complex modeling (e.g. canard/wing/horizontal tail for the F-15 STOL demonstrator, and multiple control surfaces and wing twist for both wings) but a limited number of vibration modes were used. Subsequent linear analysis showed that the number of modes used was not sufficient to accurately model the transonic flutter mode, static deformation, or aileron reversal. This paper gives results for refined computations using 23 modes for the F-15 wing and 40 modes for the FA-18.

The CAP-TSD code allows modeling of multiple lifting surfaces and bodies and utilizes an AF solution algorithm with Newton iteration. Monotone differencing, NRBC, and entropy and vorticity corrections are employed. Gridsizes were 297K and 158K for the F-15 and FA-18 calculations.

Static deformation of the F-15 wing at M = 0.9 was computed using CAP-TSD with LIN/TM and NL/TM procedures and compared to a separate calculation using an EE/TM procedure. The wingtip deflections for the three approaches were 3.5, 7, and 9 inches, indicating that the nonlinear TSD model provides a good representation for analysis. Flutter boundaries for the wing were computed using doublet lattice, LIN/TM, and NL/TM procedures for M = 0.5 - 1.2. Flutter speeds from all three procedures agree at M = 0.5 and 1.2 and the maximum difference occurs at M = 0.9 where the nonlinear TSD result was 60 knots lower than linear theory.

Aileron reversal was calculated at M = 0.9 for the FA-18 using a NL/TM procedure. The tip missile fins were included in the analysis as four vertical and two horizontal lifting surfaces. The reversal dynamic pressure was 5.7 psi for the configuration with tip missile and 7.75 psi for the clean wing compared to 8.3 psi from flight test (clean wing). These are impressive results for realistic aeroelastic analysis situations and indicate that this level of nonlinear TSD method has matured for industrial applications.

17. H. Zimmerman, S. Vogel, H. Henke and B. Schulze: "Computation of Flutter Boundaries in Time and Frequency Domain"

This paper presents details of wind tunnel tests of sophisticated transport aircraft models conducted under the Aeroelastic

THIS DOCUMENT PROVIDED BY THE ABBOTT AEROSPACE
TECHNICAL LIBRARY
ABBOTTAEROSPACE.COM

Models Program, a cooperative effort of five European laboratories. Results from tests of a rigid pressure instrumented model and a flutter model of a modern transport are compared with flutter calculations from the 3D TSD-VISC code described in Paper 14. Sample unsteady pressures due to harmonic wing pitching at M = 0.78 show increasing higher harmonic content for increasing motion amplitude. The experimental flutter boundary shows a pronounced transonic dip with a minimum flutter pressure at M = 0.84.

A discussion of the procedures which may be used to incorporate nonlinear CFD methods into aeroelastic analysis is given: "TSP-Simulation" (NL/TM), "TSP-Harmonic" (NL/HT/EIG), and "Time Linearized TSP" (presumably a NL/PT/EIG procedure, wherein the pulse transform method, relying upon linearity and superposition, is used). A comparison of AICs for k = 0.2, 0.4, 0.6 shows good agreement between the harmonic and pulse methods. Six-mode flutter calculations using the three CFD methods are given for M = 0.6, 0.78, 0.80, 0.82. This is an important study, incorporating as it does some of the most complete modeling, both experimental and computational, of a flutter test which has been attempted. A most important detail is the inclusion of the interactive boundary layer model, which many see as a final modeling step in improved transonic flutter predictions. Thus it is curious that the calculated flutter boundary shows no significant deviation from that calculated with the pk-doublet lattice method. Also, if the experimental flutter points shown correspond to the simulation it appears that the computations predict a premature transonic dip on the order of 0.04 in Mach number. It will be most interesting to see what further analysis of this case yields.

18. G. SenGupta, C. J. Borland, F. T. Johnson, J. E. Bussoletti, D. P. Young, M. B. Bietrerman, P. A. Palotas and R. G. Melvin: "Analysis of Unsteady Aerodynamics and Flutter Characteristics of an Aeroelastic Model in Transonic Flow"

Extension of the 3D TRANAIR FPE code to treat unsteady problems is discussed. This is a TL/HF procedure based on a finite element discretization of the nonlinear integral equations. Steady and unsteady boundary conditions are developed for shock and slip surfaces. The solution is obtained on rectangular grids with automatic refinement used to treat geometry details and regions of large gradients. Solutions are obtained by means of Newton linearization and iteration.

Applications are given for three cases. Scattering of an acoustic plane wave by a sphere provides a good check with an exact solution. Unsteady pressures for a planform similar to the F-5 at M = 0.6 are in excellent agreement with experiment. For transonic conditions at M = 0.90, 0.95 steady pressures for the F-5 wing are somewhat overpredicted and the shock is too far aft for the higher Mach number. Unsteady pressures for these conditions agree reasonably well. This code is being used in conjunction with the ELFINI structural finite element code to perform flutter analysis.

19. J. P. Grisval and J. L. Mevrzec: "Couplage Direct Aerodynamique-Structure en Aeroelasticite Transsonique"

Application of the 3D TSD PPT3D code for aeroelastic analysis of a transport wing wind tunnel model is described. The ADI algorithm is solved by time marching to produce TSD/HT/EIG and TSD/TM flutter analyses. Issues involved in the use of CFD methods coupled with structural finite element models for static wing deformation calculations are discussed and illustrated by a calculation for the model at M = 0.82. A static wingtip deflection of 0.8m and wingtip twisting of 1.5 deg resulting in a 13% reduction in wing lift, is shown. Flutter calculations are given at M = 0.82 using 10 vibration modes and compared with a doublet lattice analysis. The HT/EIG flutter case agrees well with the linear analysis, showing a slight reduction in density at flutter. Analysis of subcritical TM transient responses using two postprocessing procedures were less successful. Curve-fitting of the wing coordinate response using Prony's method was difficult when more than 3-4 modes were involved and flutter is projected for a higher density than in the harmonic analysis. Curve-fitting the modal coordinate response using a Fourier transform method yields damped conditions and no projected flutter crossing for the densities covered.

20. W. A. Silva and R. M. Bennett: "Investigation of the Aeroelastic Stability of the AFW Wind-Tunnel Model Using CAP-TSD"

Detailed flutter analyses of the Active Flexible Wing model using the CAP-TSD code are described. This code has been described above in the notes on Paper 16. The paper discusses a sequence of modeling improvements which bring the calculated flutter results into better agreement with the experimental results. A half-span computational model was used for symmetric flutter analysis and a full-span model was used for antisymmetric flutter analysis. Both models consist of a fuselage (including an aft "coat-tail" region), the main wing(s) with four control surfaces per wing panel, and a wingtip ballast store(s). The symmetric case contained 424K gridpoints and ten vibration modes while the antisymmetric case contained 839K gridpoints and ten additional vibration modes. The modeling changes were: updated mode shapes and frequencies obtained from an improved structural finite element analysis; correction of an error in the definition of the surface slopes of the tip store model; and inclusion of entropy and vorticity corrections.

The original symmetric flutter boundary calculations, for M = 0.5-0.95, predicted a significant transonic dip near M = 0.93, well below the doublet lattice prediction. However, the drop in the predicted dynamic pressure at flutter, which was verified during testing, was excessive. The three improvements resulted in excellent agreement with experiment at transonic conditions. A good discussion of modeling requirements for treating antisymmetric flutter analyses with nonlinear CFD methods is given (symmetric modes are necessary to capture static wing twisting). An antisymmetric flutter calculation shown for M = 0.5 is unconservative compared with experiment, as is the corresponding symmetric flutter point. However, the relative levels of dynamic pressure at flutter are consistent with symmetric and antisymmetric doublet lattice predictions and with experiment. This discrepancy for subcritical Mach numbers is believed to be due to a modeling deficiency in the treatment of the tip store. Boundary conditions treat the store as a steady body of revolution but do not include unsteady terms needed to model its modal motion. Capability for including this effect is being added to the code. It will be interesting to see what effect viscous boundary layer modeling may have in light of the good agreement noted for the transonic dip.

THIS DOCUMENT PROVIDED BY THE ABBOTT AEROSPACE
TECHNICAL LIBRARY
ABBOTTAEROSPACE.COM

The effect of the entropy and vorticity corrections on the flutter boundary at the bottom of the transonic dip is significant. The ~20% change in the mimimum flutter dynamic pressure for this thin wing indicates that such modeling details are required for accurate aeroelastic analysis with codes based on the potential equation.

21. K. Isogai: "Numerical Simulation of Shock-Stall Flutter of an Airfoil Using the Navier-Stokes Equations"

An unusual flutter mechanism encountered during a test of a non-tailored, high aspect ratio, forward-swept wing is studied with a 2D strip, typical section analysis. The experimental flutter frequency was 13% below that of the first wing bending mode, strongly dependent upon α and it was conjectured that this was a case of shock-stall flutter. The simulation used a 2D NS/TM code employing a Yee-Harten total variation-diminishing scheme and a Baldwin-Lomax turbulence model. TM/H applications demonstrating typical results with this code are given for three airfoils. Steady pressures for the RAE 2822 airfoil at M = 0.725 agree very well with test data for a case close to separation. Unsteady pressures for the NACA 64A010 airfoil at M = 0.80 are in good agreement with experiment and grid convergence is studied. Dynamic stalling is calculated for the NACA 0012 airfoil at M = 0.3 and $\alpha = 9 + 6\sin(kt)$ deg with k = 0.068. The qualitative behavior of the experimental pitching moment is reproduced in the calculation. The NACA 64A010 airfoil at M = 0.79 and oscillating 1 deg. about 4 deg pitch angle exhibits severe shock-induced flow separation and computational results predict a stronger shock located aft of the experimental results.

To investigate the shock-stall behavior of the wing, typical section structural parameters are chosen to simulate the "wash-in" mode shape of the first bending mode of the forward swept wing. The airfoil shape is a natural laminar flow type supercritical section about 12% thick. The simulation, for M = 0.724 and wind-off pitch set at 2 deg., produced large diverging oscillations about a mean angle of about 3 deg. The frequency was about 15% below that of the first bending mode and flow field contours during the oscillation motion clearly show a shock-stall separation process. A key feature of these NS computations is the attention given to adequate grid density for accurate resolution of viscous effects. Values of y^+_1 (the scaled location of the first gridpoint) on the order of one are necessary in order to resolve the viscous sublayer.

22. G. P. Guruswamy and S. Obayashi: "Transonic Aeroelastic Computations on Wings Using Navier-Stokes Equations"

Calculations with the 3D TLNS ENSAERO code are given for the F-5 wing and a clipped-tip delta wing. Both cental and upwind differenced algorithms are available. The Baldwin-Lomax turbublence model is utilized, with the Degani-Schiff modification for vortex-dominated flows. Time marching solutions with coupled structural vibration modes are shown. C-H grids are used with exponential grid stretching to the far field boundaries. The minimum grid spacing in the normal direction is of the order $.0^{-5}$c and 128K gridpoints are used. Mesh motion is accomplished by shearing of the grid point locations in the ζ direction. Computational efficiency is on the order of 15-19 μsec/gp/st and the harmonic oscillation cases used 1440 and 3600 steps per cycle.

Steady and unsteady pressures are compared with experiment for the F-5 wing at M = 0.90 and Re= $12x10^6$. The agreement is good for the steady pressures. Fairly good agreement is shown for the unsteady pressures where the calculated shock pulse is 5-10% chord aft of experiment. Steady and unsteady pressures are also compared with experiment for a clipped tip delta wing model with a 6% thick circular arc profile. The model was oscillated in pitch about mean angles from 0 to about 5 deg. Leading-edge vortex flow develops between 3 and 4 deg at transonic speeds. Comparisons with experiment are given at M = 0.90 and Re = $17x10^6$ for mean angles of 3 and 4 deg. Suction peaks near the leading edge show the development of the vortex. The agreement for pressure levels and aft shock location are very good inboard, while agreement deteriorates towards the outboard station. Unsteady pressures for these two cases show corresponding agreement with experiment. This is an important comparison of computation with experiment, involving as it does vortex flow in conjunction with a transonic shockwave for an oscillating model.

Applications are also presented for both wings in which ramping motions in pitch angle are shown for rigid and flexible cases. Assumed structural vibration mode shapes are used and the impact of flexibility on section lift is demonstrated. There are no experimental results available for comparison with these cases.

23. J. J. Meijer and A. M. Cunningham, Jr.: "Development of a Method to Predict Transonic Limit Cycle Oscillation Characteristics of Fighter Aircraft"

Further applications of a semi-empirical Limit Cycle Oscillation (LCO) prediction method are given. Steady-state experimental surface pressure data are used to compute GAFs required to solve the structural equations in a TM fashion. The surface pressures are tabulated versus Mach number and steady angle-of-attack, and utilized during the transient response simulation in a quasi-steady fashion wherein the instantaneous, induced angle-of-attack is used to reference the pressures. Two configurations of a fighter aircraft which has experienced LCO in flight are studied: one with two pylons and missiles and a tip launcher per semispan; and a second with a different tip launcher. LCO is calculated for the first configuration, agreeing qualitatively with flight test. However, it is noted that oscillation amplitudes on the launcher were 2g in flight whereas the calculations show amplitudes of up to ±14g. Realistic values of structural damping for the second configuration show damped oscillations and no LCO, again confirming flight test experience.

A number of parameter variations are shown, demonstrating key dependencies of LCO upon structural damping, time step size, aerodynamic lag effects, and leading-edge flap setting. A number of important conclusions follow, including: shock-induced trailing-edge separation plays a dominant role in LCO; store configuration effects on LCO were qualitatively predicted in all cases using only the store mass effects in the vibration modes. One of the strongest effects on LCO was aerodynamic time lag which led to excessively large motions for moderate phase lags and to disappearance of LCO for modest phase leads. Thus a criteria for empirical selection of a proper amount of lag/lead would appear to be a critical item for further development of the method. Whether such a criteria will first emerge

THIS DOCUMENT PROVIDED BY THE ABBOTT AEROSPACE
TECHNICAL LIBRARY
ABBOTTAEROSPACE.COM

from further empirical testing, such as that described in Paper 24, or from computational calculations is one of the more interesting questions in this field.

24. A. M. Cunningham, Jr. and R. G. den Boer: "Transonic Wind Tunnel Invstigation of Limit Cycle Oscillations on Fighter Type Wings"

This paper describes recent cooperative tests conducted in the NLR High Speed Tunnel to investigate unsteady aerodynamic aspects of transonic LCO on fighter type aircraft. A sidewall mounted wing-body configuration with stores was tested for pitching oscillations at incidences up to 10 deg. Objectives were to understand the physics of such flows and to generate a data base for use in LCO calculations. Particular interest is in development of information on aerodynamic time lags involved with trailing-edge flow separation and aerodynamic damping for vibration modes typical of LCO. The model was tested for $0.9 < M < 0.975$ and preliminary data from pressure transducers, wing and tip launcher balance gages are shown. Variations of unsteady pressures and loads in the wing tip region were very sensitive and increased phase lags are noted for increasing frequency. This data set will be very important for comparison with calculations of unsteady transonic conditions involving shock-induced flow separation.

25. R. M. Bennett, C. E. Eckstrom, J. A. Rivera, B. E. Dansberry, M. G. Farmer and M. H. Durham: "Benchmark Aeroelastic Models Program-Description and Highlights of Initial Results"

The Benchmark Aeroelastic Models Program being conducted in the Transonic Dynamics Tunnel of NASA Langley Research Center is described. This is a multi-year program involving tests of generic models for: providing well documented data sets suitable for CFD code validation; understanding the physics of unsteady transonic flows; and providing data for empirical design. Approximately two tests per year will be conducted. The initial tests utilize rigid wings mounted on an apparatus allowing simple pitching and plunging motions. The first series of models have been designed and sample test results from the first model are described. The model has a NACA 0012 section and unsteady pressures, loads, flutter results and flow visualization are shown. The model has a conventional flutter boundary for $M = 0.3 - 0.92$ and a narrow region of unconventional flutter for $M = 0.88 - 0.92$ involving nearly pure plunging.

Tests of a flexible wing with an 18% circular arc section are also described. This model was fabricated to study the dynamic response of a flexible wing to transonic shock-induced separating flows. Over a narrow Mach range, $M = 0.76 - 0.80$, a buffeting-like response was observed in the first bending mode and an LCO response was evident in the 3rd bending-like mode. The reduced frequency of the LCO was near 0.5, which is typical of self-excited shock oscillations observed on rigid 2D airfoils with this section.

26. S. Raghunathan and F. Zarifi-Rad: "Investigations of the Effect of Model Cooling on Periodic Transonic Flow"

This paper describes tests of a 14% thick circular arc airfoil in which model cooling is employed with the aim of simulating higher Reynolds number flow. Laminar and turbulent boundary layer cases are studied at $Re = 0.9 \times 10^6$ and for $0.76 < M < 0.85$ where self-excited shock oscillations occur for this airfoil. For adiabatic wall temperatures, dynamic pressure transducer spectra show shock oscillation frequencies of $k = 0.5$ (laminar) and $k = 0.4$ (turbulent). With cooled walls, the laminar case showed increased gradients in the shock interaction region, decreases in the extent of the interaction region, and a decrease in the amplitude and frequency of the dominant fluctuations. Similar but smaller effects are noted for the turbulent case. All of these effects are thought to correspond with adiabatic flow at larger Reynolds numbers, thus providing an interesting alternative for studying Reynolds number effects.

27. D. G. Mabey: "A Review of Scale Effects on Surfaces in Unsteady Motion"

This review focuses upon subtleties involved in achieving proper similitude between test and full scale: namely, the interrelated requirements of matching Reynolds numbers (based upon a macroscopic length scale) and matching transition location. The subtlety results from the transition location being dependent not only upon the Reynolds number, but also upon e.g. microscopic surface roughness scales and freestream turbulence levels. For fully turbulent flows, the Reynolds number determines the thicknesses of attached and separated boundary layers, and conditions for separations. Three testing methods for addressing these effects are discussed and the author strongly recommends that unsteady tests should always be made with transition fixed.

Maps are presented of levels of scale effects for steady and unsteady measurements which is keyed to dynamic buffeting intensity criteria: onset (small separation), light, moderate, and heavy (fully separated flows). Thus, for steady measurements scale effects are noted to be very large for small separations between buffet onset and light buffeting, whereas small scale effects are noted for both attached and fully separated flows. In mild contrast, for unsteady measurements, scale effects are noted to be negligible for attached and fully separated flows, while they are most apparent between buffet onset and moderate buffeting levels. Hence, the necessity to pay careful attention to transition location when testing under the latter conditions. Many examples of airfoil and wing scale effects illustrating these points are reviewed. In order to account for such scale effects, it is recommended that computations be made for a range of Reynolds numbers. Finally, an appendix lists three suggested airfoil test cases for the prediction of scale effects in unsteady aerodynamics.

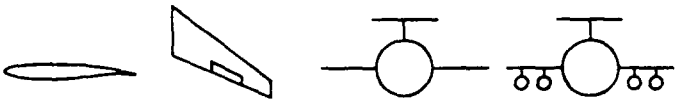
3. ROUND TABLE DISCUSSION

The meeting Chairman opened the discussion with Figure 2, giving an assessment of the present state of computational maturity for high-speed low angle aeroelastic analysis. A summary of comments made during the discussion is given below.

Comments from industry regarding the use of CFD methods in the aeroelastic design process:

- Linear methods (e.g. doublet lattice and kernel function methods) will remain workhorses in design, where hundreds of configurations must be screened for trends.

THIS DOCUMENT PROVIDED BY THE ABBOTT AEROSPACE
TECHNICAL LIBRARY
ABBOTTAEROSPACE.COM



TSD	✓	✓	✓	
FPE	✓	✓	?	
EE	✓	✓	?	
TSD/FPE/EE-VISC	✓	?		
NS	✓			

Figure 2. Configuration Modeling Capability for Aeroelastic Analysis

- There is a large amount of skepticism about the reliability of unsteady CFD methods for making structural design modifications, which may not be allayed until capability for treating entire configurations, including engine effects, is available. Care in not overselling capability is important.

- One researcher recommended continued attention to the lower level methods with interactive viscous modeling (e.g. TSD-VISC), in order to digest this capability for economical transonic dip prediction.

- A key aeroelastic analysis problem in design, which has received limited attention in CFD applications, is loads due to gusts. In addition, the problem of critical loading condition identification has also not yet been addressed.

- A problem with the use of CFD has been the level of expertise needed to properly utilize the methods. Particular issues mentioned were: grid dependent solutions, proper transition and turbulence modeling, and the lack of an experiential data base. The discussion highlighted a perception that the "data base" was rapidly expanding, and giving credibility to the methods.

Comment relating to interaction of computational/experimental methods:

- CFD is now being used for detailed investigation of aeroelastic problems seen in the wind tunnel. Another comment described an instance of the use of (steady) CFD to fine tune aeroelastic model design before going into the wind tunnel.

Comments relating to computational aereolasticity:

- A comment from an academician took issue with the developmental viewpoint expressed by Figure 2, stressing the need for basing new analysis approaches upon an understanding of physical phenomena. Attention was drawn to the fact that the "one really new thing" seen in the presentations, the LCO studied in Paper 23, was attacked using a semi-empirical method.

- It was noted that a speed up of about a factor of 60 is needed to make the aeroelastic codes practical. It was also noted that there may be too much pessimism in assaying the future rate of progress.

- One experimental researcher noted that the use of CFD methods (e.g. NS codes) to predict the buffet excitation on wings and airfoils was far from mature, notwithstanding elements of realism seen in isolated computations. It was noted that a challenge has been to predict the excitation associated with a simple unsteady bubble (i.e. a flow that is separating and reattaching). No such calculations were presented at this meeting (although some 2D computations of unsteady buffet-like shock-oscillations have been reported, see Ref 10).

- The question of using computational methods in conjunction with reduced flutter margins (e.g. from 20 percent to 15 percent) was raised. The level of discussion which followed would seem to indicate quite a bit more effort necessary to reach this level of confidence.

A summary comment was that a large amount of progress has been accomplished since the last SMP Specialists Meeting in 1984 and that the increasing rate of applications in this area should well justify another meeting in four or five years.

4. DISCUSSION

At the 1984 AGARD SMP meeting (AGARD-CP-374) two papers presented wing flutter calculations with viscous effects included. It is interesting to note that at the present meeting, only one paper, number 17, presented such calculations and thus it might appear that little has been accomplished. A detailed review of the presentations at the two meetings reveals quite the opposite conclusion; methods have matured and a large experiential data base in the use of computational aeroelasticity has been deposited. Whereas only two papers at the 1984 meeting presented 3D viscous results, six such papers have been reviewed herein. Experience has shown strengths and limitations of solution algorithms, algorithms have been augmented to allow treatment of more difficult cases, higher level algorithms continue to be developed, and treatment of much more complex geometries is becoming routine.

These advances have been demonstrated with applications primarily for attached or fully separated (vortex dominated) flow conditions. A lack of capability is seen for the most difficult and important cases where flow is separating and reattaching, and viscous effects are required. Conditions for these cases are illustrated in Figure 2 of Paper 1 (where it is termed Type II flow)

THIS DOCUMENT PROVIDED BY THE ABBOTT AEROSPACE
TECHNICAL LIBRARY
ABBOTTAEROSPACE.COM

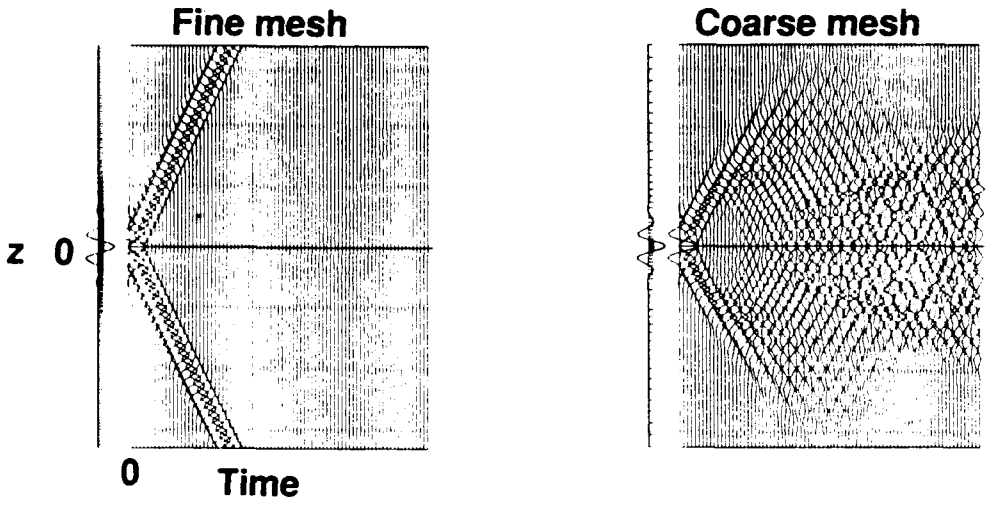


Figure 3. Effect of Gridpoint Distribution on Signal Propagation for the Wave Equation, NRBC (Bland[11]).

and Figure 4 of Paper 27 (flows between buffet onset and moderate buffeting). Key questions regarding transonic flutter are involved. How is the onset and development of unsteady flow separation related to minimum flutter speeds in the transonic dip region? For what conditions may transonic flutter boundaries be computed assuming attached flow (i.e. mild viscous effects)? What are the flow conditions on the backside of the dip region and for very low supersonic conditions? Answering these questions will occupy aeroelasticians for the immediate future. The critical element needed is a reliable and robust viscous analysis method for computing unsteady separating and reattaching flows. This capability has not yet matured for 3D wings.

Computational experience has by now provided guidelines on the proper use of CFD methods for computational aeroelasticity analysis. Grid extent, the number of gridpoints required, alternative gridding strategies, and the treatment of mesh movement for body-conforming grids have been studied. Table II of Paper 1 summarizes gridpoint requirements for converged computations using different flow modeling levels. About 250K gridpoints for inviscid computations and 650K gridpoints for TLNS computations are necessary per half-span lifting surface. Hybrid methods which restrict the domain requiring finite-difference gridding, such as field-panel integral equation methods, require fewer points.

The distribution of grid points for unsteady computations is a topic which deserves further consideration since it can lead to severe computational inaccuracy. Figure 3, from Bland (Ref 11), illustrates the problem of "internal reflections" caused by wave dispersion on coarse stretched meshes. The 1D wave equation model problem is studied with fine and coarse meshes. NRBC are employed and the fine mesh solution shows accurate propagation of the wave over the mesh and out of the computational boundary. The coarse mesh employs about 4 gridpoints per wavelength in the midfield and only 2 gridpoints per wavelength at the boundary. The rapid grid point stretching in the nearfield results in the wave energy being trapped within the computational domain by dispersive errors, while the NRBCs are ineffective in transmitting signals through the boundary for this case. Note that these internally relected signals return to the origin where they contaminate the solution. These effects are insidious, particularly for harmonic oscillation calculations, in that individual solutions appear smooth and well-behaved; the characteristic signature of erratic behavior is seen only when small parameter changes (e.g. frequency) are studied. Smooth variation of gridpoint distribution (particularly in the normal direction), which may be provided by polynomial stretching functions, is recommended. These effects are alleviated in 3D flows and have not been documented for calculations utilizing the higher-order EE or NS equations, although they might be anticipated, particularly for higher aspect ratio lifting surfaces.

Algorithm refinements which are advantageous or necessary for accurate transonic computations have also been developed: non-reflecting far-field boundary conditions, monotone differencing, upwind differencing, and entropy and vorticity corrections for potential codes. Similarly, steps needed to perform computational aeroelastic analysis are generally understood: time steps required for accuracy, number of steps per cycle for oscillatory motion, number of cycles to allow transients to decay, and the use of various excitation methods to provide GAFs. Post-processing of results to obtain stability boundaries relies upon two methods: traditional eigenvalue analysis using GAFs from some form of harmonic motion computation, and aeroelastic transient response curve fitting in the manner of Bennett and Desmarais (Ref 12).

To allow assessment of the accuracy and robustness of computational methods, it is mandatory to present results for a suitable range of a varied parameter (e.g. Mach number, reduced frequency, Reynolds number) and to compare with experiment or alternative computations. Regarding presentation of results, a general comment relates to the desirability of including integrated airloads along with such detailed computational results as pressure distributrions. Even though experimental data (e.g. integrated unsteady pressures) with which such airloads should be compared are fraught with issues (usually related to the coarse-

THIS DOCUMENT PROVIDED BY THE ABBOTT AEROSPACE
TECHNICAL LIBRARY
ABBOTTAEROSPACE.COM

Table III

WING FLUTTER BOUNDARIES COMPUTATIONS PRESENTED AT THE 1991 AGARD SPECIALIST'S MEETING

Paper No.	1st Author	Wing/Model	Code	M	#Flutter Pts.
5	Winzell	Transport Wing	FPE/TM	0.8-0.87	10
			FPE-VISC/TM		2
6	Wong	445.6 Wing	TSD/TL/HT/EIG	0.5-0.96	11
12	Hounjet	445.6 Wing	FPE/TL/HF/EIG	0.7-0.96	3
15	Knott	445.6 Wing	TSD/HT/EIG	0.7-1.14	5
		Fighter Wing	TSD/TL/HT/EIG	0.6-0.95	7
			TSD/TM	0.85, 0.90	2
16	Pitt	F-15 Wing	TSD/TM	0.5-1.2	7
			TSD/LIN/TM	0.5-1.2	7
17	Zimmerman	Transport Wing	TSD-VISC/TM	0.78-0.82	3
			TSD-VISC/HT/EIG	0.78-0.82	3
			TSD-VISC/PT/EIG	0.78-0.82	3
20	Silva	AFW	TSD/TM	0.5-0.95	19
23	Meijer	Fighter Aircraft	Semi-Empirical	0.92	Many LCO Pts.

ness of measured pressures), such comparisons need to be made in order to establish correct trends and ranges of validity of computational methods. This is particularly true for flutter calculations: conditions at which flow is transitioning may require modeling changes to maintain accuracy. Inspection of the detailed AICs can give important insight into the modal interactions involved.

In the following discussion, comments on selected aspects of the material presented are given. The comments are keyed to the paper number and first author.

Flutter Boundary Computations:

An impressive number of detailed flutter boundary analyses, including significant Mach number variations, were presented and are summarized in Table III. The semi-empirical LCO study of Paper 23 is included due to the number of parameter variations reported. The number of computational flutter points presented at this meeting, ~80, is more than half that of all previously published cases shown in Table II, ~130, indicating the increasing pace of applications. Particularly noteworthy is that four of the studies are from industry.

Papers 6, 12, and 15 add three additional flutter analyses for the AGARD 445.6 wing. For this model, linear methods provide good agreement with experiment up to M=0.90 and inviscid nonlinear effects are important at M=0.96. For the low supersonic test points, inviscid nonlinear analysis significantly overpredicts flutter speeds (figure 7 of Paper 15) whereas TSD/LIN/TM analysis (Ref 13) provides good agreement for these points. Further analysis of this model for $0.96 < M < 1.07$ is important in order to understand viscous modeling effects at such minimum transonic flutter speeds.

Complex Configurations:

The following papers treat significant configuration details;

- 2 Batina; EE; supersonic fighter with blended wing-body, canard, tail
- 4 Blair; FNS; F-15 wing, fuselage, horizontal and vertical tails
- 16 Pitt; TSD; F-15 wing, FA-18 wing, tip-launcher, missile, fins
- 20 Silva; TSD; AFW wing, fuselage, tip-store

The high number of modes needed for convergence, treatment of hingeline discontinuities, and the agreement between TSD and EE codes in the static wing deformation calculations presented in Paper 16 are impressive and indicative of a maturing design capability. This is also true of the attention to detail shown in the flutter computations for the complex model configuration of Paper 20.

Time Linearized Flow Modeling:

Interest in TL methods remains high since they are significantly less expensive than TM methods when their use is justified.

- 6 Wong; TSD; F-5, LANN, ONERA M6, and 445.6 wings
- 8 Voss; TSD; NACA 0012 wing and LANN wing
- 11 Garcia-Fogeda; TSD; cones, ogive bodies
- 12 Hounjet; TSD, FPE; NLR 7301 airfoil, Wing A, Wing B, RSW, 445.6 wing

THIS DOCUMENT PROVIDED BY THE ABBOTT AEROSPACE
TECHNICAL LIBRARY
ABBOTTAEROSPACE.COM

- 15 Knott; TSD; fighter aircraft wing
- 18 SenGupta; FPE; F-5 wing

The 445.6 wing flutter boundaries calculated using TL methods in Papers 6 and 12 agree favorably with experiment up to M = 0.96, although it should be noted that linear theory gives similarly good agreeement up to M = 0.90. An issue is the range of validity of the TL method. Figure 12 of Paper 8 gives results from TSD/TL/HF and FPE/HT codes for varying oscillation amplitude. Differences in agreement between the two codes can be seen for pressures in the shock pulse region and in the region ahead of the shock in going from 0.25 deg to 1.0 deg amplitude. It is acknowledged that TL methods may not be used for cases involving significant shock motions. Also, the issue of how to incorporate viscous effects, other than in a mean-steady "frozen" boundary layer sense, has not been addressed.

Code-to-Code Comparisons:

Comparisons between alternative computational methods should be a standard step in the certification of any new method, which should always be checked against older well calibrated methods for conditions at which both should produce similar results. This also protects against inappropriate use of "higher-order" methods. Of the flutter boundary calculations summarized in Table III, Papers 5, 6, 12, 15, 16, and 20 provide comparisons with linear theory and, in some cases, other computational results. Figures 5 and 6 of Paper 2 compare GAFs and aeroelastic transients showing excellent agreement between two EE codes, using structured and unstructured grid techniques.

Paper 5 shows many comparisons between linear and FPE methods of loads and pressures due to control deflection. Paper 16 gives very informative results of wing static deflection calculated with TSD/LIN/TM, TSD/TM, and EE/TM methods and a flutter boundary (figure 8) calculated with linear, TSD/LIN/TM, and TSD/TM methods. Note particularly the agreement in the latter comparison at M = 0.5. Unexplained differences in such flutter calculations at subcritical conditions can frequently be traced to deficiencies in modeling, such as inadequate number of gridpoints. Finally, Papers 8 and 12 give very interesting comparisons of FPE and EE unsteady aerodynamic results.

Viscous and Vortical Flow Modeling:

Seven papers treated viscous flow using either boundary layer models interacted with potential flow or NS methods;

- 5 Winzell; FPE-VISC; RAE wing flutter model
- 12 Hounjet; TSD-VISC; NACA 0012 airfoil
- 13 Gerteisen; FNS; 14% circular arc airfoil
- 14 Muller; TSD-VISC; 3 validation cases, transport wing
- 17 Zimmerman; TSD-VISC; transport wing flutter model
- 21 Isogai; NS; 2D section shock-stall flutter
- 22 Guruswamy; TLNS; F-5 and clipped-delta wings

The 2D strip interactive boundary layer method described in Papers 14 and 17 represents a significant step in viscous flow modeling for the flutter analysis of wings. Similar approaches (Refs. 10 and 14) have demonstrated the potential of such methods to treat separating and reattaching flows for airfoils. Paper 22 demonstrates new capability of treating unsteady vortex dominated flows and Paper 21 gives a very nice typical section analysis of shock-stall flutter of a wing.

Control Surface Effectiveness:

The following papers present results of modeling control surface aerodynamics:

- 5 Winzell; FPE; F-5, rectangular, cropped-delta wings
- 10 Brenneis; EE; NLR 7301 airfoil
- 13 Gerteisen; FNS; NACA 64A006 airfoil
- 14 Muller; TSD-VISC; RA16SC1 airfoil with spoiler
- 16 Pitt; TSD; FA-18 wing aileron reversal

Paper 16 is particularly noteworthy for the good agreement between computed and flight test aileron reversal speeds (note that an inviscid TSD method is used). On the other hand, Paper 5 describes well-known deficiencies of inviscid methods in predicting pressures on control surfaces.

Experimental Data Bases:

Five papers reviewed experimental programs focusing on transonic flutter for complex models and transonic flows involving Type II flow (unsteady separating and reattaching flow):

- 17 Zimmerman; Aeroelastic Models Program
- 20 Silva; Active Flexible Wing program
- 24 Cunningham; LCO on a fighter aircraft
- 25 Bennett; Benchmark Models Program
- 26 Raghunathan; Cooling effects on shock-induced oscillations

A common thrust of these programs is movement to more difficult flow conditions than those typified by the current SMP Aeroelastic Configurations. In short, cases are sought involving unsteady separation at transonic speeds and the selection of new Standard Aeroelastic Configurations for such conditions is called for. Mabey, in the Appendix of Paper 27, suggests 2D airfoil cases for periodic shock oscillations and unsteady separation bubbles. Unsteady pressure data from the oscillating rigid model reported in Paper 24 and from the flexible model reported in Reference 15 provide good computational test cases for 3D wings.

5. CONCLUSIONS AND RECOMMENDATIONS

Three conclusions may be drawn from this Specialists' Meeting:

1. Inviscid computational aeroelastic analysis has matured to the point where rather complete configuration details are being treated for cases of transonic flutter and aileron reversal, yielding improved predictions over linear theory.
2. Inclusion of unsteady viscous effects at the Navier-Stokes equations level is available, but is too expensive for routine aeroelastic analysis or design. Viscous-inviscid interactive boundary layer capability shows promise, but has not yet matured for lifting surface applications.
3. Experimental and computational efforts are focusing upon flow conditions which define the boundary of current analysis capability: situations in which the flow is near separation, or is alternately separating and reattaching.

The recommendations included in the technical reviews of the 1984, 1985, and 1990 AGARD meetings (References 2, 3, and Paper T in AGARD-CP-483) remain very relevant and should be reviewed. Several of these recommendations deserve repeating in the following list, along with several additions.

THIS DOCUMENT PROVIDED BY THE ABBOTT AEROSPACE
TECHNICAL LIBRARY
ABBOTTAEROSPACE.COM

1. Transition should be fixed in all sub-scale time-dependent experiments.
2. New AGARD Standard Aeroelastic Configurations and Computational Test cases for Type II flows should be established (unsteady separating and reattaching flows).
3. Complete the development of interactive viscous-inviscid methods for Type I and II flows.
4. Extensive computations are needed to establish the relative ranges of applicability of alternative flow modeling levels.
5. Determine the modeling requirements for accurate computations of aeroelastic response on the backside of transonic flutter "dip" boundaries and for very low supersonic conditions.
6. Establish levels of flow modeling necessary for accurate predictions of control surface effectiveness and hinge moments.
7. Establish levels of flow modeling necessary for accurate predictions of transonic Limit Cycle Oscillations.
8. In applications where unsteady viscous effects are simulated, care needs to be given to understanding effects of simulated Reynolds number, transition location, and turbulence model; particularly as these effects are under active study by the steady CFD community.
9. Applications should include computations with sufficient variation of controlling parameter(s) (e.g. Mach number, reduced frequency, Reynolds number) and comparisons with experiment or alternative computations in order to establish accuracy and robustness.

APPENDIX

The AGARD Standard Aeroelastic Configuration for Dynamic Response, documented in Reference 6, is a 45 degree swept wing flutter model tested in the Transonic Dynamics Tunnel at NASA Langley Research Center. A slight error in the tables of NASA TN D-1616, which is included as an appendix in Reference 6, has been pointed out by E. Lee of NASA Langley. The tables list the density, velocity, and dynamic pressure at the test conditions. However, the tabulated dynamic pressure is inconsistent with $1/2\ \rho V^2$. The error in most cases is 1-3% and within the ±2 psf accuracy quoted in TN D-1616 (with one exceptional point). It is suggested that ρ and V from the tables be used to compute dynamic pressures for use in aeroelastic analyses; this is consistent with the plots in the reference.

REFERENCES

1. Mykytow, W. J.; Laschka, B.; and Olsen, J. J.: Technical Evaluation Report of the Specialists' Meeting on Unsteady Airloads in Separated and Transonic Flow, AGARD-AR-108, April 1978.

2. Mykytow, W. J.: Transonic Unsteady Aerodynamics and its Aeroelastic Applications, AGARD-CP-374 Addendum I, June 1985.

3. Mabey, D. G. and Chambers, J. R.: Technical Evaluation Report on Unsteady Aerodynamics - Fundamentals and Applications to Aircraft Dynamics, AGARD-AR-222, January 1986.

4. Bland, S. R.: AGARD Two-Dimensional Aeroelastic Configurations, AGARD-AR-156, August 1979.

5. Bland, S. R.: AGARD Three-Dimensional Aeroelastic Configurations, AGARD-AR-167, March 1982.

6. Yates, E. C. Jr.: AGARD Standard Aeroelastic Configurations for Dynamics Response I - Wing 445.6, AGARD-R-765, July 1988.

7. Magnus, R. and Yoshihara, H.: The Transonic Oscillating Flap, AIAA Paper No. 76-327, July 1976.

8. Ballhaus, W. F. and Goorjian, P. M.: Implicit Finite-Difference Computations of Unsteady Transonic Flows about Airfoils. AIAA Jounal, Vol. 15, No. 12, December 1977, pp. 1728-1735.

9. Thomas, J. L. and Salas, M. D.: Far-Field Boundary Conditions for Transonic Lifting Solutions to the Euler Equations, AIAA Paper No. 85-0020, January 1989.

10. Girodroux-Lavigne, P.; and LeBalleur, J. C.: Time-Consistent Computation of Transonic Buffet Over Airfoils. 16th International Congress of the Aeronautical Sciences, Jerusalem, Israel, August 28–September 2, 1988.

11. Bland, S. R.: Personal Computer Study of Finite-Difference Methods for the Transonic Small Disturbance Equation. NASA TM 102582, December 1989.

12. Bennett, R. M. and Desmarais, R. N.: Curve Fitting of Aeroelastic Transient Response Data with Exponential Funcitons, NASA SP-415, pp. 43-58, May 1975.

13. Bennett, R. M.; Batina, J. T.; and Cunningham, H. J.: Wing Flutter Calculations with the CAP-TSD Unsteady Transonic Small Disturbance Program. AIAA Paper No. 88–2347, April 1988.

14. Houwink, R.: Computation of Unsteady Turbulent Boundary Layer Effects on Unsteady Flow About Airfoils. Presented at the 4th Symposium on Numerical and Physical Aspects of Aerodynamic Flows, Long Beach, CA., January 16–19, 1989 (also NLR TP 89003 U).

15. Eckstrom, C. V.; Seidel, D. A.; and Sandford, M. C.: Unsteady Pressure and Structural Response Measurements on an Elastic Supercritical Wing. Journal of Aircraft, Vol. 27, No. 1, January 1990.

THIS DOCUMENT PROVIDED BY THE ABBOTT AEROSPACE
TECHNICAL LIBRARY
ABBOTTAEROSPACE.COM

AD-P007 794

CURRENT STATUS OF COMPUTATIONAL METHODS FOR TRANSONIC UNSTEADY AERODYNAMICS AND AEROELASTIC APPLICATIONS

by
John W. Edwards
and
John B. Malone
NASA Langley Research Center
Hampton, Virginia 23665–5225 USA

Abstract

The current status of computational methods for unsteady aerodynamics and aeroelasticity is reviewed. The key features of challenging aeroelastic applications are discussed in terms of the flowfield state: low-angle high speed flows and high-angle vortex-dominated flows. The critical role played by viscous effects in determining aeroelastic stability for conditions of incipient flow separation is stressed. The need for a variety of flow modeling tools, from linear formulations to implementations of the Navier-Stokes equations, is emphasized. Estimates of computer run times for flutter calculations using several computational methods are given. Applications of these methods for unsteady aerodynamic and transonic flutter calculations for airfoils, wings and configurations are summarized. Finally, recommendations are made concerning future research directions.

1. Introduction

In the past decade there has been much activity in the development of computational methods for the calculation of unsteady aerodynamics about airfoils, wings and complete vehicle configurations. Two key areas of activity have been transonic aeroelasticity and lower speed, high-angle flight conditions. Advances have paralleled developments in steady Computational Fluid Dynamics (CFD) with a lag of approximately five years due to the additional requirement of time-accuracy. This paper presents a discussion of current aeroelasticity problem areas or challenges. The focus is primarily upon methods aimed at the study of nonlinear fluid dynamic flows, typically referred to as Computational Fluid Dynamics (CFD), although attention is also given to linear flow models.

Figure 1 (Edwards [53]) illustrates significant features which must be addressed in the use of computational aeroelasticity for flutter boundary prediction. In this figure, a typical flutter boundary curve, characterized by the flutter speed gradually dropping to a minimum in the transonic speed range followed by a rapid upward rise, is shown. The ability to predict this minimum, termed the transonic flutter dip, is of great importance in design, since the flutter boundary must be shown by a combination of analysis and flight test to be outside the flight envelope by a specified margin. For military aircraft, the margin in terms of equivalent airspeed is at least 15 percent. Subsonic linear unsteady aerodynamic theories have been reasonably successful in predicting this flutter boundary for Mach numbers up to 0.6–0.7 but linear theory is unable to account for the effects of aerodynamic shape and maneuvering condition upon unsteady airloads. At high Mach numbers linear analysis has been used with more or less success depending upon the severity of local transonic effects. The occurrence of flutter within the flight envelope of an aircraft usually leads to structural failure and loss of the vehicle, highlighting the necessity for careful validation of computational methods intended for use in this area. In addition, aircraft service life can be significantly degraded by unforeseen dynamic loadings, such as buffet, and predictive capability for such off-design point loadings must be well-understood before being utilized in structural design. These key differences in the utilization of steady and unsteady computational methods must be clearly understood.

This field received an initial impetus in the mid-1970's from three sources: Tijdeman's [152] experimental work on transonic unsteady pressure measurements, Magnus and Yoshihara's [108] demonstration of key transonic flow features for an airfoil with an oscillating flap and the introduction of an economical transonic finite-difference solution algorithm (LTRAN2) by Ballhaus and Goorjian [17]. Ballhaus [16] gives a survey of the field from this period. The AGARD Structures and Materials Panel Subcommittee on Aeroelasticity has selected experimental unsteady pressure data sets and defined two- and three-dimensional Standard Aeroelastic Configurations [30, 31] to provide reference computational test cases for the development and validation of improved computational methods.

Unsteady aerodynamics has been the theme of six recent conferences [8–12, 153] whose proceedings contain a wealth of information. Summary papers of the 1984 and 1985 AGARD conferences are given by Mykytow [114] and Mabey and Chambers [105]. The latter reference makes recommendations regarding computational and experimental methods for unsteady flow phenomena and draws particular attention to the need to pay careful attention to the nature of shock motions. The periodic oscillations about circular arc airfoils are recommended as benchmark computational cases for all time-dependent transonic viscous flow theories. Zwaan [167] surveys aeroelastic problems in transonic flow while Deiwert [46] reviews the numerical simulation of unsteady interactive flows. Reference [155] provides a collection of articles going into extensive detail for unsteady transonic aerodynamics. Mabey [106] gives a review of pertinent experimental research on time-dependent aerodynamics. Finally, Dowell [48] provides an overview of nonlinear aeroelasticity phenomena including structural as well as aerodynamic nonlinearities.

92-16032

THIS DOCUMENT PROVIDED BY THE ABBOTT AEROSPACE
TECHNICAL LIBRARY
ABBOTTAEROSPACE.COM

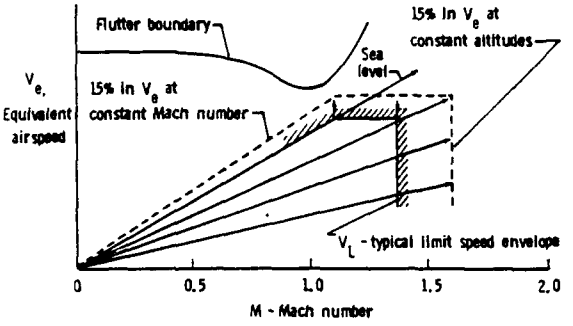


Figure 1 Graphical Representation of Minimum Required Flutter Margin for Military Aircraft [7].

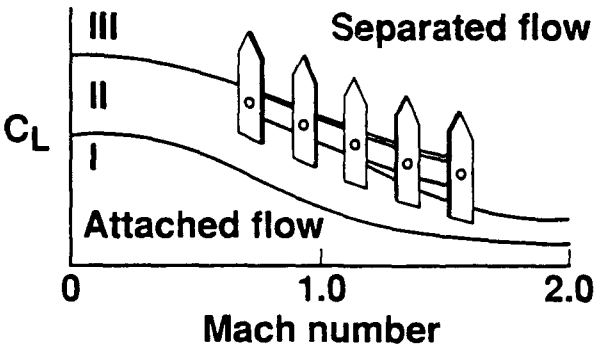


Figure 2 Characteristics of Attached and Separated Flow for Complete Aircraft (Edwards [53]).

Research in these areas requires the comparison of experimental and computational results with the goal of achieving accurate predictive capability. Edwards [52, 54] provides surveys of these efforts for the transonic flutter problem while Mabey[107] discusses the physical phenomena associated with unsteady transonic flow. Bobbitt's [36] review of the issues involved in obtaining accurate results from experiment and from computation is particularly noted. Regarding higher angle, vortex dominated flows, a trend of increasing interest by the aerodynamics community in unsteady flows is also noted. This is due to the inherent unsteadiness of such flows and to the ability of emerging CFD methods to simulate their details. Newsome and Kandil [117] discuss physical modeling issues involved in the computational prediction of vortex dominated flows and survey numerical results.

The remainder of this paper will review the current status of computational methods for unsteady aerodynamics and aeroelasticity. The key features of challenging aeroelastic applications are discussed in terms of the flowfield state: low-angle high speed flows and high-angle vortex-dominated flows. Next the computational methods and the basic fluid dynamic equations are introduced, followed by an assessment of the computer resources required for the unsteady aerodynamic computations. Then, the current state-of-the-art in CFD methods for transonic flows and vortex-dominated flows are each discussed, with emphasis in the progress achieved during the past half decade. Finally, an assessment of current capabilities and future research trends is offered.

2. Features of Low-Angle, High Speed Flows

The main features of steady transonic flow are described first in order to organize the discussion. With increasing Mach number and moderate angle-of-attack, the flow over the upper surface of an airfoil becomes critical between M_∞ = 0.4–0.7 with the first shocks forming at approximately 0.1 higher Mach number. Pearcy et al. [120] have classified several types of flow separation which may occur. For conventional airfoils the typical pattern involves the growth of a local separation bubble, induced by boundary layer separation at the shock foot, spreading rapidly to the trailing edge as Mach numbers increases. This condition is often accompanied by unsteady phenomena such as buffet and aileron buzz (Tijdeman [152]). The steep aft pressure gradients of modern airfoils can lead to an alternate pattern in which separation progresses from the trailing edge towards the shock. Tijdeman [152] notes that the flow conditions in the region between the onset of trailing edge separation and fully separated flow are very sensitive to Reynolds number and the location of transition from laminar to turbulent flow.

Figure 2 shows a diagram, from Edwards [53], of attached, mixed and separated flow regions for a complete aircraft at freestream Mach numbers between 0 and 2.0. In region I, the flow is predominantly attached. To obtain optimum performance and to avoid the drag penalty associated with flow separation, design cruise conditions for aircraft typically are located here near the boundary of region II.

As speed and/or angle of attack increase, a transition region of mixed flow (region II of fig. 2) is encountered. For rigid structures, this region is typified by the onset of localized regions of flow separation which may exhibit significant aerodynamic unsteadiness. For realistic flexible structures, the aeroelastic response of the structure interacts with the airflow to induce much more complicated situations. For instance, structural vibrations can cause the flow to alternately separate and reattach at flow conditions where a rigid structure would support attached flow. The associated high unsteady aerodynamic loading can interact with the structure to cause unusual aeroelastic phenomena which may restrict the vehicle flight envelope.

With further speed and/or angle of attack increases which may be encountered under maneuvering conditions, fully separated flow conditions emerge (region III of fig. 2). Leading-edge vortex flows and stalled wing flows are of this nature. At still higher angles, vortex bursting in the vicinity of the aircraft can cause severe buffeting. Within such regions the flow is highly unsteady and accurate computations will require careful attention to turbulence modeling. To emphasize the complexity which the aeroelastic response adds, the flow within the three regions of figure 2 will be referred to as Type I, II, and III respectively.

While the predictive methods for attached flows are reasonably well developed, the picket fence in figure 2 emphasizes the difficulty in predicting aeroelastic phenomena in the mixed and separated flow regions. It also symbolizes novel features that

THIS DOCUMENT PROVIDED BY THE ABBOTT AEROSPACE
TECHNICAL LIBRARY
ABBOTTAEROSPACE.COM

are being encountered in transonic flutter testing. Modern high performance aircraft are capable of maneuvering at transonic speeds, leading to a much enlarged parameter space that must be considered in flutter analysis and testing. Wing/store loading, fuselage interference, angle-of-attack, Reynolds number, wing shape, and wing sweep all must be considered, and the traditional flutter boundary parameterization of dynamic pressure at flutter versus Mach number may need to be augmented to adequately describe aeroelastic stability boundaries. For instance, flutter tests give some indication that these additional parameters affect the detailed aeroelastic stability condition near the flutter boundary. Thus, the pickets of the fence in figure 2 represent possible regions of low damping or instability that might be encountered.

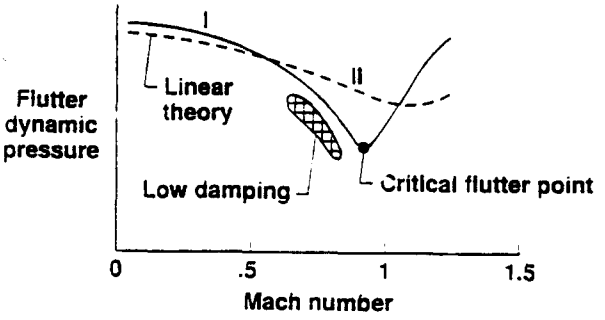


Figure 3 Features of Transonic Flutter (Edwards [53]).

3. Features of High-Angle, Vortex—Dominated Flows

Unsteady airloads due to flow separation are involved in a number of cases critical to the structural integrity of aircraft. As speed increases for moderate angles of attack, typical of maneuvering flight near trimmed flight conditions, local transonic flow effects are encountered which lead to separated flow over the aft portions of lifting surfaces. Minimum flutter speed indices are often encountered in this transonic region, in conjunction with the onset of separated flow. The ability to predict these minimums is obviously tied to the ability to treat such "local" separated flows on wings.

For slightly lower speeds where more aggressive maneuvering is possible, unsteady airloads due to flow separation over "remote" components (e.g. forebody and main wing panel) leads to issues of tail buffeting and structural fatigue of aircraft components. For these cases, as speed and/or angle of attack increase, smooth air flow over lifting surfaces breaks down in a variety of ways depending strongly upon the geometry. For lower sweep angles and blunt leading edges, flow separation may initiate near the trailing edge or near shocks and progress to completely separated and stalled conditions. For higher sweep angles and less blunt leading edges, leading edge flow separation bubbles foreshadow the development of leading edge vortex flows. At higher angles, unsteady and burst vortex flow in the vicinity of the wing and downstream lifting surfaces leads to strong unsteady airloads and buffeting. Flow conditions near the boundaries of these regions for the various flow phenomena can be sensitive to a number of conditions and an understanding of these effects is called for in order to avoid adverse aeroelastic effects such as stall flutter, buzz, and structural buffeting.

4. Computational Aeroelasticity Challenges

With figure 2 providing a framework within which typical flowfields encountered in aeroelasticity may be viewed, a number of current aeroelasticity problem areas are introduced in Table I and figures 3–7. Table I serves as a guide for discussing the current status in this area and the likely future trends. On the left are listed the key Challenges, most of which have been extensively commented on above. They are roughly graded in terms of increasing difficulty from top to bottom with the more difficult areas calling for more sophisticated flowfield modeling in order to achieve useful accuracies. Arrayed against these challenges are the Resource Issues impacting the economics of aeroelastic analysis, which are listed on the right. The choice of the appropriate level of CFD code to use, indeed the decision of whether to use a linear or nonlinear flow method, is dictated by the stage of design maturity, the required level of accuracy and computer resources available. The process of identifying critical loading conditions requires running large numbers of cases, almost always utilizing lower level methods. Critical cases, so identified, are then candidates for further analysis with higher level methods. It is interesting to query if this process can be relied upon to capture the actual critical loading cases.

Figure 3, from Edwards [53], indicates further features of high speed, low angle flutter. Dynamic pressure at flutter tends to decrease with increasing Mach number to a minimum "critical flutter point" value in the transonic speed range. At subsonic speeds where the flow can be assumed to be attached (Type I flow) at flutter, linear theory is reasonably accurate. As speed increases into the transonic region, the situation is complicated by the formation of shock waves and the onset of flow separation (Type II flow) and linear theory must be used with caution. The low damping region in the figure indicates the potential for nonclassical aeroelastic response and instabilities which may be encountered. Figures 4–6, illustrate several types of novel aeroelastic responses which have been encountered with the onset of Type II flows and which offer challenges for computational methods. Figure 4 (Edwards [53]) shows a region of nonclassical aeroelastic response observed on a high aspect ratio, flexible, supercritical wing (Seidel et al. [141]) where high dynamic response at nearly constant Mach number was encountered at dynamic pressures well below those for which flutter was predicted with linear theory. The motion is of the limit-amplitude type and the response is believed to be associated with flow separation and reattachment driving the wing motion in the first bending mode. Figure 5 (Edwards [53]) illustrates wing/store limited amplitude oscillations experienced by modern, high performance aircraft under various loading and maneuvering conditions at transonic Mach numbers. Such oscillations can result in limitations on vehicle performance. The conditions for which this type of response occurs appear to also be near the onset of Type II mixed flow. The response typically increases for maneuvering flight conditions. Dynamic vortex-structure interactions causing wing oscillations have been observed, figure 6 (Dobbs et al. [47]), on a bomber type aircraft for high wing sweep conditions during wind-up turn maneuvers. The flow involves the interaction of the wing vortex system with the wing first bending mode and occurs over a wide Mach number range at moderate angles of attack.

THIS DOCUMENT PROVIDED BY THE ABBOTT AEROSPACE
TECHNICAL LIBRARY
ABBOTTAEROSPACE.COM

For lower speed flight where higher angles are achieved, fully separated flows (Type III flows in fig. 2) are encountered which can range from diffuse vortical flow structures to concentrated vortices designed to enhance stability and control. Interaction of such forebody and wing vortex systems with aft vehicle components results in vortex-induced buffet loads. Figure 7 (Edwards [53]) shows typical operating conditions at which such empennage buffet may be encountered. Buffet of horizontal tails can occur at intermediate angles of attack and is a result of the vortex system propagating downstream and encountering the horizontal tail surface. As angle of attack increases, the location of vortex bursting moves upstream in the wake. Loss of lift is associated with the burst location reaching the vicinity of the aircraft, and vertical surfaces located in such regions can experience severe dynamic loads and structural fatigue.

These challenges, illustrated by figures 3–7, involve two types of unsteady flows. The first is the Type II flow (fig. 2) wherein the onset of flow separation at high speeds leads to critical flutter conditions and/or novel aeroelastic responses. The second involves fully separated Type III vortex-dominated flows at high angles. The search for the appropriate levels of sophistication in fluid dynamic modeling to adequately model these flows is the subject of this paper.

Table 1 COMPUTATIONAL AEROELASTICITY CHALLENGES AND RESOURCE ISSUES

Challenges	Resource Issues
Stability & Control divergence roll performance wing rock	Modeling Tradeoffs higher level CFD improved configuration detail
Gust Response	Design Maturity preliminary design final design critical loading conditions
Flutter Boundary Prediction 1-g maneuvering limit cycle oscillations	Computer Resources required level of accuracy cost per solution number of solutions
Control Effectiveness buzz hinge moment	
Buffet Response local: main wing panel remote: tail buffet	

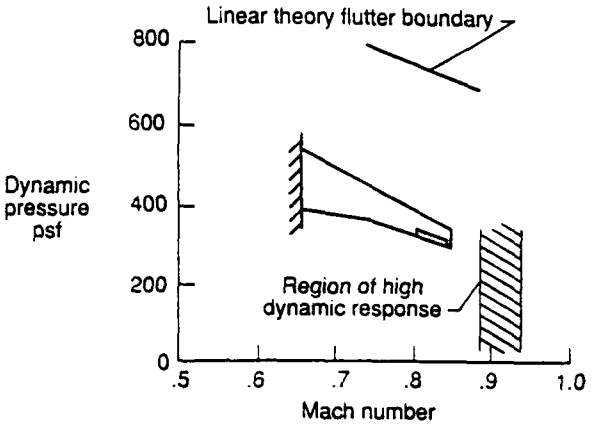


Figure 4 Region of High Dynamic Response Encountered During Test of a Flexible Supercritical Wing (Edwards [53]).

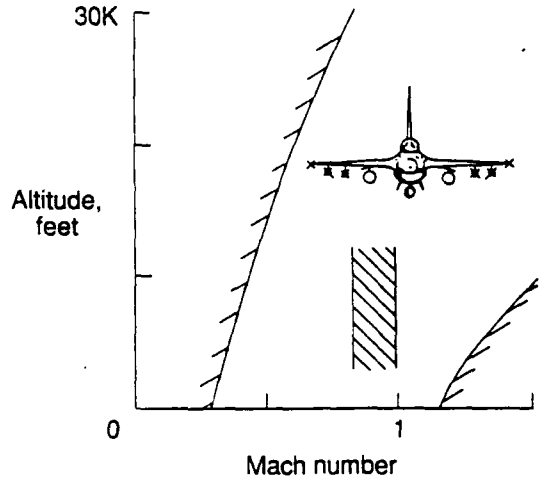


Figure 5 Region of Potential Limited-Amplitude Oscillations Due to Wing-Store Loading Effects (Edwards [53]).

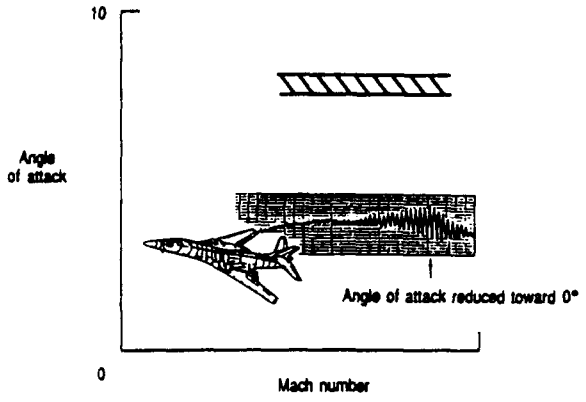


Figure 6 Vortex-Induced Wing Oscillations of a Bomber-Type Aircraft (Dobbs, Miller, and Stevenson [47]).

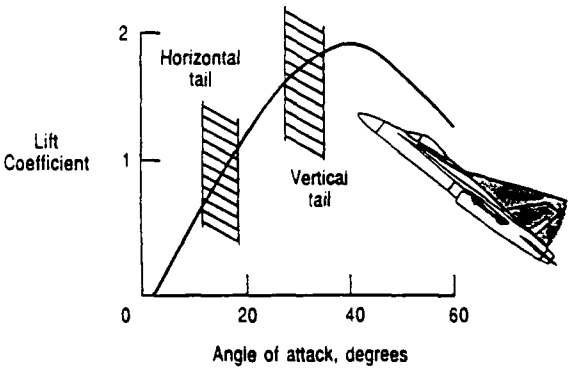


Figure 7 Regions of Vortex-Induced Buffet Loads (Edwards [53]).

THIS DOCUMENT PROVIDED BY THE ABBOTT AEROSPACE
TECHNICAL LIBRARY
ABBOTTAEROSPACE.COM

5. Computational Methods

A variety of fluid dynamic flow models is available to address unsteady aerodynamic computations. The choice of an appropriate method calls for assessment of the difficulty of the aerodynamic problem being addressed. Type I flows (fig. 1) include one of the most important aeroelastic analysis conditions, that of cruise at high dynamic-pressure. Classical linear aeroelastic analysis has been primarily focused upon this condition. The transition from Type I to Type II conditions can occur due to aircraft maneuvering, with little decrease in dynamic pressure. Thus, aeroelastic response and stability of aircraft operating in Type II flows can be quite important although they have only begun to be brought within the range of computational methods.

Fluid dynamic flow models available for unsteady aerodynamic computation include: the classical (linear) small disturbance potential equation, the nonlinear potential equation (both Transonic Small Disturbance (TSD) and Full Potential equation (FPE)), the Euler equations (EE) and the Navier-Stokes equations (both Full (FNS) and thin-layer (TLNS)).

Issues which have been central to unsteady CFD have been the choice of implicit versus explicit algorithms, the stability of alternative solution algorithms and the treatment of computational grids. Explicit schemes are simple to code and easily vectorizable but are limited in allowable time step by the stability limit imposed by the signal propagation time over the smallest grid cell. Faced with the requirement of maintaining time-accuracy throughout the entire field for aeroelastic computations, this easily leads to excessive computation times, especially for viscous flow calculations where a very fine mesh near the surface is required to resolve the boundary layer. The alternative implicit solution algorithms thus are currently favored for present-day computer architectures because of their relative stability and time-step characteristics. While no attempt will be made to present complete details of the various levels of flow models, the following sections highlight the key equations and relevant boundary conditions.

5.1 Navier-Stokes Equations

Anderson, Tannehill and Pletcher [2] provide a description of the three-dimensional Full Navier-Stokes equations. For engineering applications, the Reynolds-averaged form of the FNS equations are normally used as a basis for practical computational procedures. In a cartesian coordinate system, the FNS equations can be written as follows:

$$\frac{\partial}{\partial t}(Q)+\frac{\partial}{\partial x}(F-F_v)+\frac{\partial}{\partial y}(G-G_v)+\frac{\partial}{\partial z}(H-H_v)=0 \quad (1)$$

where the vector of independent, conserved variables is

$$Q=(\rho,\rho u,\rho v,\rho w,e)^T \quad (2)$$

and

$$F=\left(\rho u,\rho u^2+p,\rho uv,\rho uw,u(e+p)\right)^T \quad (3)$$

$$G=\left(\rho v,\rho uv,\rho v^2+p,\rho vw,v(e+p)\right)^T \quad (4)$$

$$H=\left(\rho w,\rho uw,\rho vw,\rho w^2+p,w(e+p)\right)^T \quad (5)$$

are the inviscid flux vectors. The viscous flux vectors, F_v, G_v and H_v are given in Ref. [2].

To facilitate solutions of the FNS equations on body-fitted computational grids, a curvilinear coordinate system is defined and eqs. (1) are converted using a generalized coordinate transformation of the type:

$$\xi=\xi(x,y,z,t),\quad \eta=\eta(x,y,z,t),\quad \varsigma=\varsigma(x,y,z,t),\quad \tau=t \quad (6)$$

into the following expressions:

$$\frac{\partial}{\partial t}\left(\hat{Q}\right)+\frac{\partial}{\partial \xi}\left(\hat{F}-\hat{F}_v\right)+\frac{\partial}{\partial \eta}\left(\hat{G}-\hat{G}_v\right)+\frac{\partial}{\partial \zeta}\left(\hat{H}-\hat{H}_v\right)=0 \quad (7)$$

where:

$$Q=\frac{1}{J}(\rho,\rho u,\rho v,\rho w,e)^T \quad (8)$$

$$F=\frac{1}{J}(\rho U,\rho Uu+\xi_x p,\rho Uv+\xi_y p,\rho Uw+\xi_z p,U(e+p)-\xi_t p)^T \quad (9)$$

$$G=\frac{1}{J}(\rho V,\rho Vu+\eta_x p,\rho Vv+\eta_y p,\rho Vw+\eta_z p,V(e+p)-\eta_t p)^T \quad (10)$$

$$H=\frac{1}{J}(\rho W,\rho Wu+\zeta_x p,\rho Wv+\zeta_y p,\rho Ww+\zeta_z p,W(e+p)-\zeta_t p)^T \quad (11)$$

Similar transformations are applied to the viscous flux vectors. Note that the transformation is time-dependent, allowing the grid to move to follow body motion and giving rise to grid motion terms such as ξ_t, η_t and ζ_t in eqs. (9) to (11). For viscous-flow aerodynamic computations, the solid-surface boundaries are modeled using the "no-slip" condition, together with adiabatic wall and zero normal pressure gradient conditions.

A modified form of the FNS equations, termed the thin-layer Navier-Stokes equations, has been found useful for applications where viscous effects in certain spatial directions are small enough to be neglected. For many aerodynamic flows of interest, the viscous terms normal to the body are of most importance, and the other viscous fluxes can be dropped. If the η–direction in eq. (7) is taken as the body normal direction, a TLNS form of eq. (7) is given by the expression:

$$\frac{\partial}{\partial t}\left(\hat{Q}\right)+\frac{\partial}{\partial \xi}\left(\hat{F}\right)+\frac{\partial}{\partial \eta}\left(\hat{G}-\hat{G}_v\right)+\frac{\partial}{\partial \zeta}\left(\hat{H}\right)=0 \quad (12)$$

For turbulent-flow calculations, turbulence modeling such as the algebraic eddy viscosity model of Baldwin and Lomax [15] is used. Rumsey and Anderson [134] are typical of applications using this thin-layer approximation to compute viscous-flow solutions for airfoils. Also, Thomas et al. [150] describe a three-dimensional implementation of the above equations in the CFL3D code.

5.2 Euler Equations

For aerodynamic flows in which viscous effects are expected to be negligible, the inviscid Euler equations can be derived from eq. (7) by dropping all three of the viscous flux vectors from the formulation. Then, $F_v=G_v=H_v=0$, and eq. (7) reduces to:

$$\frac{\partial}{\partial t}\left(\hat{Q}\right)+\frac{\partial}{\partial \xi}\left(\hat{F}\right)+\frac{\partial}{\partial \eta}\left(\hat{G}\right)+\frac{\partial}{\partial \zeta}\left(\hat{H}\right)=0 \quad (13)$$

THIS DOCUMENT PROVIDED BY THE ABBOTT AEROSPACE
TECHNICAL LIBRARY
ABBOTTAEROSPACE.COM

The boundary conditions appropriate to the Euler equations are the "slip" or "flow tangency" conditions. For these applications, only the velocity component normal to the body surface is set to zero. The flow streamlines are assumed to run parallel to the surface tangent at each point on the surface. Note that for situations where there is rotational flow, such as the regions behind strong or curved shock eaves, the Euler equations can propagate the vorticity downstream in a correct manner if an adequate number of grid points are used.

5.3 Full Potential Equation

The FPE is derived from the Euler equations by assuming that the flow is inviscid, isentropic and irrotational. A velocity potential can then be defined whose derivatives in the spatial directions recover the flow velocity components in the appropriate directions. The governing equations for this formulation are the continuity equation:

$$\rho_t + (\rho\Phi_x)_x + (\rho\Phi_y)_y + (\rho\Phi_z)_z = 0 \qquad (14)$$

and the isentropic energy equation:

$$\rho = \left[1 + \frac{\gamma-1}{2} M_\infty^2 \left(1 - 2\Phi_t - \Phi_x^2 - \Phi_y^2 - \Phi_z^2\right)\right]^{\frac{1}{\gamma-1}} \qquad (15)$$

As with the Euler equations, a generalized coordinate system is often used to solve the FPE and a flow-tangency boundary condition is enforced at the body surface. Sankar and Malone [136] describe such a FPE formulation in generalized coordinates.

5.4 Transonic Small Disturbance Potential Equation

The Transonic Small Disturbance Potential equation is derived from the inviscid Euler equations assuming that the flow is isentropic, irrotational and a small perturbation of a steady uniform flow, U, in the x direction. The TSD velocity potential function, ϕ, describes the perturbed velocity components u, v, w:

$$u = \frac{\partial\phi}{\partial x}, \qquad v = \frac{\partial\phi}{\partial y}, \qquad w = \frac{\partial\phi}{\partial z} \qquad (16)$$

where the total velocity in the x direction is U+u. Batina [20] and Batina et al. [21] give the modified TSD potential equation in conservation form as

$$\frac{\partial f_0}{\partial t} + \frac{\partial f_1}{\partial x} + \frac{\partial f_2}{\partial y} + \frac{\partial f_3}{\partial z} = 0 \qquad (17)$$

where

$$f_0 = -A\phi_t - B\phi_x \quad ; \quad f_2 = \phi_y + H\phi_x\phi_y$$
$$f_1 = E\phi_x + F\phi_x^2 + G\phi_y^2 \quad ; \quad f_3 = \phi_z \qquad (18)$$

The coefficients A-H are given by Batina [20]. The TSD equation (17) is distinguished from the higher equation level flow models in that, within the small disturbance assumption, the computational grid is not required to move with the body since boundary conditions are imposed at the mean plane, usually z = $0^\pm$. The wing flow tangency boundary condition is

$$\phi_z^\pm = f_x^\pm + f_t \qquad (19)$$

where $f^\pm$ (x,y,t) = 0 describes the upper and lower body surfaces. The trailing wake boundary conditions are

$$[\phi_x + \phi_t] = 0 \quad ; \quad [\phi_z] = 0 \qquad (20)$$

where [-] indicates that jump in the indicated quantity across the wake. The pressure coefficient may be computed using either linear or nonlinear forms of the Bernoulli equation. Batina et al. [21] describe this algorithm as implemented in the CAP-TSD code with a number of example calculations.

5.5 Viscous-Inviscid Interaction

Neither the potential equations nor the Euler equations described above incorporate viscous effects which can be important for high speeds and for lower speed at higher angles. It is possible to account for unsteady viscous effects by coupling a viscous boundary-layer model with an otherwise inviscid analysis. As commonly implemented, the inviscid outer flow solution provides the surface pressure distribution needed to solve the boundary layer equations. This yields the boundary-layer displacement thickness distribution which is used to modify the airfoil surface tangency boundary condition for the next iteration of the outer inviscid flow solution.

Guruswamy and Goorjian [65], Howlett and Bland [81], and Rizzetta [129] describe this method implemented in two-dimensional unsteady TSD codes. The effect of a viscous boundary layer for attached turbulent flow is modeled in a quasi-steady manner by means of the lag-entrainment equations of Green et al. [64]. In this integral method the displacement thickness δ^* is computed as a function of the boundary-layer momentum thickness θ and the shape factor H as

$$\delta^* = \theta \cdot H \qquad (21)$$

Given the velocity at the edge of the boundary layer (from the outer inviscid flow solution), the boundary layer equations may be integrated in a "direct" fashion to obtain δ^*. Coupling between the boundary-layer and the outer inviscid flow is through the boundary conditions on the airfoil and wake, eqs. (19) and (20), which are modified to

$$\phi_z^\pm = f_x^\pm + f_t + (\delta^*/c)_x^\pm \quad ; \quad [\phi_z] = [(\delta^*/c)_x] \qquad (22)$$

For cases of incipiently separating and separated flows the boundary layer equations become singular, requiring a reformulation of the equations in an "inverse" mode in which the edge velocity gradient is computed for a given displacement thickness (East et al. [49]). Consistency with the outer inviscid flow may be obtained via a "semi-inverse" relaxation coupling method (in which δ^* is updated based upon the error between inner and outer edge velocities) described by Carter [38] and also used by Fenno et al. [58]. For cases with large amounts of separated flow, particularly for unsteady flow, the semi-inverse method itself encounters stability problems (Edwards and Carter [50]). These cases have been more tractable via the "quasi-simultaneous" coupling method introduced by Veldman [158] and by Houwink and Veldman [79] and the "semi-implicit" coupling method of LeBalleur and Girodroux-Lavigne [98]. Both of these methods perform the viscous-inviscid coupling by developing, at each grid point, locally linear relations between the inner and outer flow variables. This enables simultaneous solution for the coupling variables which is usually accompanied by relaxation and iterations for convergence. The quasi-simultaneous method has been implemented using the low frequency LTRAN2–NLR TSD code and quasi-steady integral boundary layer equations. The semi-implicit method described in Ref. [98] achieves full time-consistency by coupling a time-accurate TSD code with a time-accurate integral boundary layer method.

THIS DOCUMENT PROVIDED BY THE ABBOTT AEROSPACE
TECHNICAL LIBRARY
ABBOTTAEROSPACE.COM

5.6 Time-Linearized Transonic Small Disturbance Equation

A second formulation of the Transonic Small Disturbance Potential equation is the time-linearized equation, which is derived by assuming that the unsteady flowfield can be treated as a small perturbation about the steady flow field solution. This theory assumes that shockwaves are neither created nor destroyed during the unsteady motion. .The steady flow potential is obtained from solutions to the steady-flow version of the TSD equation:

$$\left[1 - M_\infty^2 - (\gamma+1)M_\infty^2\phi_x^o\right]\phi_{xx}^o + \phi_{yy}^o + \phi_{zz}^o = 0 \qquad (23)$$

The unsteady potential, ϕ^1, is then computed from the unsteady TSD equation by solving the following equation:

$$-k^2M_\infty^2\phi_{tt}^1 - 2kM_\infty^2\phi_{xt}^1 + \left\{\left[1 - M_\infty^2 - (\gamma-1)M_\infty^2\phi_x^0\right]\phi_x^1\right\}_x + \phi_{yy}^1 + \phi_{zz}^1 = 0 \qquad (24)$$

Note that the steady potential ϕ^0, is required in the above equation. In practice, ϕ^0 can be obtained from other theoretical formulations or derived from experimental data. Hounjet [74] is representative of this approach to unsteady transonic flow modeling.

5.7 Computational Grid Effects

Grid generation for unsteady problems in which the body boundary moves, such as for an oscillating control surface or an aeroelastic deformation, raises new issues over those involved in steady flows. At the TSD equation level, wherein the boundary conditions are applied on a nonmoving, mean surface plane, stationary Cartesian grids have been used. For unsteady problems, care must be taken to ensure the fidelity of signals propagated through the stretched grids which are used. Seidel et al. [140] and Bland [34] give results for the TSD equation. A key effect of grid stretching is to modify the "dynamic impedance" of the mesh at internal grid points, leading to "internal reflections" of waves which may return to the vicinity of the modeled aircraft components and contaminate unsteady solutions. It is shown that this issue is typically more severe for exponentially stretched meshes, frequently used for steady calculations, than for meshes with less severe stretching in the near field. This effect is alleviated in three-dimensional flows. Bland [35] provides guidelines for generating grids and selecting time-step size for accurate unsteady computational characteristics. Finally, this effect has not been observed or documented for calculations utilizing the higher level Euler or Navier-Stokes equations.

For flow modeling equations higher than the TSD equation, the body-conforming grids used must be realigned with the moving body at each time step to maintain accuracy. Schemes for accomplishing this have been studied as well as the necessity of moving the grid at all. When body motions are small with perturbations mainly normal to the surface, imposing "transpiration" boundary conditions on the mean surface location may be an acceptable approximation (Sankar et al. [137]). Steger [147] formulated the TLNS equations including terms accounting for grid motion. Steger and Bailey [148] used simple shearing of the grid coordinate normal to the surface to allow the grid to follow aileron motions. Chyu and his coworkers [42, 43] used an interpolation scheme for defining grids at intermediate steps between the extremes of motion for oscillating airfoils and for fixed outer computational boundaries. Anderson et al. [3] present EE results for dynamically moving airfoils and wings in which the entire mesh is rotated to follow rigid airfoil and wing motions. For aeroelastic motions of flexible structures more general methods for dynamically moving the mesh are required. Guruswamy [67], Ide and Shankar [84], and Nakamichi [115] describe methods wherein the curvilinear coordinate normal to the surface is sheared based upon the instantaneous surface normal displacement as computed by the time-marching aeroelastic equations.

The above methods have all been implemented using structured grid meshes in which computed variables for neighboring grid points are stored in adjacent computer memory cells. Unstructured grids, which can be implemented with triangular grid cells in two-dimensions and as tetrahedral cells in three-dimensions, offer more flexibility in modeling complex geometries. Batina has developed a method for moving such body conforming meshes to maintain alignment during aeroelastic motions for airfoils [24] and complete configurations [23]. A network of springs is associated with the mesh in which the edge of each mesh cell is represented by a spring whose stiffness is related to the length of the edge. At each time step, the new location of the body boundary obtained from the aeroelastic equations of motion is used to solve for the new static equilibrium location of the nodes of the spring network. Robinson et al. [130] modified this grid motion technique for structured grids and give results of wing flutter calculations using an Euler code. Rausch et al. [124] further refined the method, treating spatial grid cell adaption (mesh enriching and coarsening procedures) on unstructured meshes.

6. Computational Aeroelasticity Resource Assessment

In this section, estimates of computer resources necessary to produce accurate, converged results are given. This is done prior to the discussion of the detailed applications in the following sections in order to provide a framework within which to assess what has been accomplished and where further work is necessary.

The measure which will be used for computational aeroelasticity resource requirements is the Computer Processing Unit (CPU) run time for a single steady or dynamic time-marching calculation. Typically, a steady calculation is required to establish an initial flowfield for subsequent dynamic calculations. Each dynamic calculation produces a time history of aeroelastic response from which stability or response measures, such as modal frequency and damping, may be derived. The CPU run time for a CFD calculation can be estimated from the relation

$$T_{cpu} = N_{cy}N_{st/cy}N_{gp}\tau \qquad (25)$$

relating computer CPU run time, T_{cpu}, to the number of computational steps, N_{st}; the number of cycles of oscillation for a given frequency, N_{cy}; the number of steps per cycle (required for accuracy or stability), $N_{st/cy}$; the number of grid points, N_{gp}; and the algorithm speed, τ.

The algorithm speed, τ, is a common measure of the speed of an algorithm given in microseconds per grid point per time step (μsec/gp/st). Values used for this parameter herein assume machine speeds typical of a Cray 2 class supercomputer: 250 million floating point operations per second. Lower values of τ are associated with less complex algorithms, such as explicit methods, while more complex algorithms yield larger values. However, the higher level algorithms (e. g. implicit, upwind-biased, etc.) allow larger time steps and are generally favored

THIS DOCUMENT PROVIDED BY THE ABBOTT AEROSPACE
TECHNICAL LIBRARY
ABBOTTAEROSPACE.COM

Table II COMPUTATIONAL RESOURCE ESTIMATES FOR HIGH SPEED, LOW ANGLE CONDITIONS

Single half-span wing; up to "locally separating" flow

$$T_{cpu} = N_{cy} N_{st/cy} N_{gp} \tau$$

		TSD	TSD-VISC	Euler	TLNS
Algorithm speed, μsec/gp/st	τ	3.0	6.2	60	65
Number of steps					
Steady state	N_{st}	1000	1000	1000	5000
Dynamic	N_{cy}	3-7	3-7	3-7	3-7
	$N_{st/cy}$	100-300	100-300	300	1000
Number of grid pts	N_{gp}	200 K	400 K	240 K	650 K
Run time, hrs	T_{cpu}				
Steady		0.2	0.7	4.0	59*
Dynamic		0.05	0.2-1.4	3.6-8.4	35-82*

*Assumes uniform global time step; no zonal decomposition

for calculations requiring time-accuracy. For a TSD code, values are in the range of 3–10 μsec/gp/st while Navier-Stokes codes call for values ranging from 10–100 μsec/gp/st. A value of 65 will be used below for the Navier-Stokes code resource estimates. This is representative of the speed for a three-dimensional implicit, upwind-biased code.

Table II presents computational resource estimates for a single steady or unsteady (aeroelastic) response calculation for a high speed, low-angle problem. This implies that attached or only mildly separated flows are to be treated. The estimates are for a single half-span wing panel which is typically utilized when symmetry may be assumed. The four classes of CFD codes listed are: inviscid TSD, TSD with interacted boundary layer model (TSD-VISC), Euler equations, and Thin-Layer Navier-Stokes equations. The number of steps for steady and dynamic response calculations are typical of those reported in the literature. The number of grid points have been selected based upon published grid convergence studies: see Anderson and Batina [4] for TSD and EE results and Vatsa and Wedan [157] for Euler and Navier-Stokes results. The second and fourth columns giving estimates including viscous modeling are the most interesting as this level of flow modeling is required in order to achieve desired levels of improvement over well developed linear unsteady aerodynamic methods. The estimates range from approximately one hour per case for the TSD-VISC capability to over 50 hours for codes based on the TLNS equations. Treatment of full-span configurations would double these estimates and increased geometric complexity, such as additional lifting panels and bodies which would be called for in complete configuration modeling, would also increase these estimates. Each additional component modeled (tail, fuselage, etc.) would cost roughly the amounts given in the Table for the single wing. This last cost factor is due to the nature of grid point densities used, wherein the large majority of grid points are clustered near the body surfaces with the grid density coarsening quickly away from surfaces. It is noted that the TLNS estimate is likely to be conservative in that a uniform global time step (limited by small grid cells in boundary layers) is assumed. A number of straightforward modeling changes could lead to more economical methods with no loss of accuracy.

Higher-angle vortex-dominated flows call for significantly more complicated flow modeling: flow separation over the forebody/wing must be accurately predicted; vortex formation and the convection of vorticity over significant distances without loss of accuracy are involved. Perhaps the most difficult computational aeroelasticity challenge is vertical tail buffeting wherein vortical flow from the region of the forebody/wing is convected downstream, possibly encountering vortex bursting, and impacts on the flexible tail structure. CFD computations of these features are beginning to emerge and are reviewed below. Edwards [55, 56] assesses the computer resource requirements for such calculations along the lines given above. The flowfield is assumed decomposed into three regions: an inner viscous region adjacent to bodies and lifting surfaces, a nearfield region encompassing the vehicle and the vortical flow region above it and an outer inviscid, irrotational region. Assuming these three regions to be modeled using TLNS, Euler and potential equations respectively leads to the following rough computer resource estimate for a tail buffeting calculation:

$$T_{cpu} = N_{cy} N_{st/cy} \frac{f_{max}}{f_{min}} \tau \left[196{,}000\, N_{bod} + \frac{V_{II} N_{gp/wl}^3 f_{max}^3}{U_\infty^3} + 50{,}000 \right] \tag{26}$$

The frequency bandwidth of interest is specified by f_{min} and f_{max}, N_{bod} is the number of lifting surfaces and bodies wetted by viscous flow, V_{II} is the volume of the nearfield vortical flow region and $N_{gp/wl}$ is the number of grid points per spatial wavelength assumed necessary for accurate vortical flow calculations. The sample estimate given by Edwards indicates run times on the order of 1000 hours for such a calculation. Use of an Euler code for a similar calculation leads to reduced estimates on the order of 100 hour run times. However, issues related to the use of inviscid Euler codes for this type of calculation indicate caution in their use [55].

7. Low-Angle, High-Speed Flow Applications

This section will discuss applications of CFD methods for flows which are generally at lower angles and high speeds. First, the available experimental databases needed for validation of CFD codes are described. Then, recent applications of

THIS DOCUMENT PROVIDED BY THE ABBOTT AEROSPACE
TECHNICAL LIBRARY
ABBOTTAEROSPACE.COM

CFD methods for unsteady transonic aerodynamic analysis are presented, followed by a survey of aeroelastic applications for flutter prediction. Finally, the status of complete aircraft configuration modeling is illustrated through cited examples found in the current literature.

7.1 Experimental Data Bases for CFD Code Validation

The AGARD Structures and Materials Panel Subcommittee on Aeroelasticity has selected experimental unsteady pressure data sets as Standard Configurations to provide reference computational test cases for CFD code validation. Data from essentially rigid models oscillating in selected degrees of freedom is available for six airfoils (Bland [30]) and five wings (Bland [31]). Reference [11] contains many comparisons with these data sets. Edwards and Thomas [52] survey calculations for these and other cases, providing tables of example applications. Detailed comparisons of calculations with these experimental data sets can be found in Angelini et al. [5], Houwink [77], Bland and Seidel [32], and Howlett and Bland [81].

The major intended use of unsteady aerodynamic calculations is for prediction of aeroelastic response of aircraft and, more specifically, flutter. There have been numerous published calculations of two degree-of-freedom airfoil studies which are devoid of experimental data comparisons since realistic 2-D flutter models are very difficult to fabricate. On the other hand, there are only a small number of published 3-D flutter calculations which are compared with experimental results. An important reason for this is the detail and effort required to perform a valid flutter analysis of a flutter model. Vibration mode shapes and masses must be accurately calculated or measured and surface coordinates measured.

In many instances, experimental flutter data obtained for actual or proposed flight vehicles are considered proprietary by individual private organizations, and consequently, are not in the public domain. However, Yates [166] describes an AGARD standard aeroelastic flutter model consisting of a 45 degree sweptback wing for which extensive flutter test results are available. Also, NASA Langley Research Center has recently begun a multi-year experimental program to generate extensive flutter and unsteady aerodynamic data suitable for aeroelastic CFD code validation applications. This research activity, known as the Benchmark Models program, is outlined in Bennett et al. [27]. Rivera et al. [126] describe the first flutter and unsteady pressure measurement model test completed as part of this ambitious test program.

7.2 Unsteady Aerodynamic Applications

7.2.1 Linear Aerodynamic Methods. Although the major focus of this survey is on computational methods for nonlinear unsteady flows, it is prudent to be aware of the capabilities of linear methods for two reasons. First, economy of effort demands that proof be offered that supposedly more accurate methods do indeed make a difference. Secondly, new methods should always be checked against older well calibrated methods for conditions at which both should produce similar results, thus protecting against inappropriate use of "higher-order" methods.

For subsonic lifting surfaces, the standard linear methods are the doublet-lattice method (e.g. Rodden et al. [131] and the kernal function method (e.g. Rowe and Cunningham [133]). Recent developments of unsteady supersonic aerodynamic theories have been the potential gradient method of Hounjet [76] and the harmonic gradient method of Chen and Liu [40, 41]. These references contain numerous examples of aeroelastic applications.

These linear aerodynamic methods have been highly refined and calibrated with aeroelastic model test data. Coupled with powerful finite element structural dynamic analysis programs, they are used at all stages of design. Two notable analysis codes, NASTRAN and Elfini, are described by Johnson and Reymond [89] and Petiau and Brun [121].

Liu et al. [104] describe extensions to an unsteady aerodynamics panel method to permit more accurate modeling of wing/fuselage configurations for subsonic flow field conditions. Improvements to the technique used to implement unsteady boundary conditions on the body surfaces, the addition of an embedded singularity to simulate the aft flow separation in the body wake region, and the use of constant-pressure wing panels (as opposed to doublet lattice panels) are discussed in the paper. Results are presented for wing-tail, body-alone, and wing/body configurations.

7.2.2 Nonlinear Aerodynamic Methods. Much effort has been directed towards predicting unsteady transonic aerodynamic flows using the transonic small disturbance equation. The XTRAN3S TSD code has been extended to allow treatment of wing-tail (Batina [18]) and wing-fuselage (Batina [19] and Guruswamy and Goorjian [70]) configurations. Batina [20] has adapted an approximate factorization (AF) solution algorithm based upon the work of Shankar et al. [142] to the TSD potential equation. The AF algorithm is implemented in a computer code termed CAP-TSD (Computational Aeroelasticity Program – Transonic Small Disturbance) developed at NASA Langley Research Center (Batina et al. [21]). The code permits the aeroelastic analysis of complete aircraft through the modeling of multiple lifting surfaces and bodies. Results are presented for five configurations illustrating this capability. Steady and unsteady pressures for the F-16C aircraft modeled by four lifting surfaces and two bodies are presented and agreement with experimental steady pressures is considered good. The grid used for these calculations contained 324,000 points. The calculations required 0.88 CPU seconds per time step or 2.7 microseconds per grid point per time step on the CDC VPS-32 computer. Thirteen million words of memory was required. Pitt et al. [123] give flutter analyses obtained with the XTRAN3S code and the CAP-TSD code. Both codes were used for the wing-alone analysis of the F-15 and F/A-18 aircraft. The latter code was used to study canard/wing/tail and wing/launcher/tip missile configurations. There is a general lack of unsteady experimental data for complex configurations with which to validate such computations.

Rodman, Nixon and Huttsell [132] describe modifications to the XTRAN3S code to permit the use of experimental steady-flow pressure data in the unsteady flow solution of the TSD equation. The TSD equation is split into a steady and an unsteady component. Experimental surface pressure data are used to define a "strained-coordinate" system, which is then used to solve the perturbation equation for the unsteady flowfield potential. The method is limited to those situations in which shockwaves are preserved throughout the unsteady motion. Test cases are presented for both 2D and 3D configurations (NACA

THIS DOCUMENT PROVIDED BY THE ABBOTT AEROSPACE
TECHNICAL LIBRARY
ABBOTTAEROSPACE.COM

64A006, NLR 2302, airfoils and the F-5 wing).

Angelini, et al. [5] report on a large number of unsteady transonic-flow computations performed using five different CFD methods. The computational procedures include a 1) 2D TSD code, 2) a 2D coupled TSD code/boundary-layer method for unseparated turbulent flows, 3) a 2D coupled TSD/boundary-layer code for unseparated and separated laminar and turbulent flows, 4) a 2D Euler code for inviscid flows, and 5) a 3D TSD code for inviscid flows. Computed results are presented for several AGARD standard airfoil configurations and a rectangular wing model. Some comparisons are made with available experimental data.

Sotomayer, Sankar, and Malone [146] provide a comparison of computed results for the F-5 wing using three different numerical procedures. Results are presented for a transonic small disturbance code (XTRAN3S), a full potential code (USIPWING), and an Euler code (GTEUL-3D). Steady and unsteady-flow results are compared with experimental data for several Mach numbers (M_∞ = .8, .9, .95, .99 and 1.35). Sotomayer and Borland [145] describe an application of the XTRAN3S code to the prediction of unsteady wing airloads arising from oscillating control surfaces. The boundary conditions used to simulate unsteady control surface motions are outlined. Numerical results for the F-5 wing with a deflected and oscillating trailing-edge flap are presented for a range of transonic Mach numbers. Comparisons are also made with existing experimental data for this wing.

A number of investigators have also used the FPE as a basis for developing unsteady transonic flow solution procedures. Isogai [86] describes a procedure to solve the quasi-linear form using a finite difference procedure on a stretched Cartesian mesh. A quasi-conservative form of Jameson's rotated differencing scheme is used to capture shock waves. Since the grid used in this method is not boundary conforming, interpolation formulas are used to project values of the surface boundary conditions to appropriate computational grid points near the actual body surface. A semi-implicit solution procedure is used to advance the resulting equations in time. Computed results and experimental data are presented for the ONERA M6 wing (steady flow) and the NORA wing (steady and unsteady flow).

Sankar and Malone [136] describe two different procedures (SUNTANS and USIPWING) used to solve 2D and 3D problems, respectively. These methods differ in the manner in which surface motion is prescribed. In the SUNTANS code [109] the computational grid deforms with time to permit an exact implementation of numerical boundary conditions at the instantaneous airfoil surface. In the USIPWING code [135], a surface transpiration technique is used to simulate small unsteady motions of the wing surface. Reference [136] presents 2D and 3D computed results compared to experimental data for a number of airfoil and wing geometries.

Additional 2D FPE methods are presented by Schippers [138] and Whitlow [163]. Schippers describes the mathematical formulation and numerical implementation found in the NLR TULIPS code. The TULIPS code solves the 2D full-potential equation in strong-conservation form. The FPE is solved on a body-fitted grid, using a second order time-integration procedure, together with flux-splitting techniques. The resulting finite-difference equations are integrated in time using the implicit method of fractional-steps. The algorithm is demonstrated for unsteady transonic flows about the NACA 64A010 airfoil and an airfoil of the ONERA M6 wing. Whitlow describes modifications to a 2D Full Potential equation solution procedure which simulate nonisentropic flow effects arising from strong transonic shockwaves. A nonisentropic formulation is used to modify the density upwind biasing incorporated in the original FPE code. Calculated results are presented for several airfoil shapes.

The important effects of control surface effectiveness and hinge moments are studied in Bharadvaj [29] and Ominsky and Ide [119]. Both studies involve full potential equation codes and the former includes the effect of a 2-D quasi-steady boundary layer model to calculate pressures due to oscillatory control surfaces on a high aspect-ratio supercritical wing. The latter reference studies multiple surface control of a free-to-roll model for simultaneous flutter suppression and roll control.

Damodaran [45], Whitfield et al. [162], Chaderjian and Guruswamy [39], and Nakamichi [115] provide four examples of the use of structured-grid Euler/Navier-Stokes solvers for unsteady aerodynamic applications. Damodaran describes an application of Jameson's explicit Runge-Kutta time-stepping scheme to the solution of the 2D Euler equations for unsteady transonic flows about oscillating airfoil configurations. Nonreflecting far-field boundary conditions are used to help reduce non-physical wave reflections at the outer boundary of the computational grid. Numerical results are presented for the NACA 64A010 and the NACA 0012 airfoils. Additional calculations are presented for an airfoil experiencing axial oscillations (simulating a helicopter-rotor environment) and for the transient aerodynamic response of an airfoil due to angle of attack change. For the latter case, comparisons are made with classical linear aerodynamic theory. In Ref. [162], the authors describe a solution procedure for the 3D Euler equations in transonic flow. Dynamic multi-blocked grids are used to model complex aircraft configurations. The Euler equations are cast in strong conservative form and solved using an implicit, approximately factored scheme. Computational results are presented for a wing with store and a wing/counter-rotating prop-fan configuration. Limited comparisons with experimental data are provided for the wing/store configuration. Reference [39] describes a computational procedure for the thin-layer Navier-Stokes equations. The method can be used to model complex configurations via the multi-block technique for grid-generation. An implicit approximate-factorization diagonal algorithm is used to integrate the fluid dynamics equations. The method is considered first-order accurate in time. Computational results are presented for a low-aspect-ratio rectangular wing. Both steady-flow and unsteady-flow calculations are compared, and one case is presented for which the wing grid is split into an inner and an outer region in order to demonstrate the time accuracy of the method. Finally, Nakamichi presents comparisons of TLNS code results for the NORA wing, one of the AGARD Standard Configurations. A moving grid capability is employed, allowing the computational grid to follow the harmonically pitching wing motion.

Batina [23] has developed an Euler code based upon an unstructured grid with very general configuration modeling capability. Results are given for a supersonic fighter configuration with canard/fuselage/cranked delta-wing/tail/flow-through nacelle components modeled. Calculations are given for the complete vehicle oscillating in an aeroelastic mode and utilizing the moving mesh technique described above. Such unstruc-

THIS DOCUMENT PROVIDED BY THE ABBOTT AEROSPACE
TECHNICAL LIBRARY
ABBOTTAEROSPACE.COM

tured grid methods involve more complex programming than structured grid methods. Efficiency can be regained by algorithm improvements such as the temporal-adaptive algorithm described by Kleb et al. [93] which may relax the stringent requirement of using a global time-step dictated by the size of the smallest grid cells. See also Angelini and Soize [6] for a two-dimensional small perturbation treatment of body-fitted unstructured grids for unsteady calculations.

Mortchelewicz and Sens [111] also describe a solution procedure for the 3D Euler equations using unstructured grids. An explicit-implicit two phase integration scheme is used to solve the discretized equations on a mesh of tetrahedral cells. Surface transpiration is used to simulate motion of the solid surfaces for unsteady computations. Sample computations are presented for a wing-body configuration and compared to experimental data. The experimentally measured wing deformation is included in the computational mesh to account for static aeroelastic effects.

7.2.3 Hybrid Aerodynamic Methods. A number of hybrid computational schemes have been developed which combine features of different aerodynamic theories. Liu and Kuo [102, 103] describe a Transonic Equivalent Strip (TES) method for computing unsteady transonic flow about three-dimensional wing configurations. The method uses 2D steady-flow pressure distributions to determine an "equivalent" airfoil shape obtained by an automated airfoil design procedure. This insures that the mean-flow transonic effects are matched closely. Then the equivalent shape is used to compute 2D unsteady transonic-flow using a nonlinear method, such as the LTRAN2 TSD code. Finally, the 2D unsteady transonic airloads are applied at each span station of the wing, using phase-lag modifications obtained from a 3D linear wave theory. Computed unsteady pressure distributions are given for several wing configurations, including wings with oscillating control surfaces.

Hounjet [74] describes a hybrid field-panel/finite-difference procedure (FTRAN3) which combines features of both linear and nonlinear methods. The field panel procedure is used to compute a proper radiating boundary condition on the outer boundary of the grid used for the finite-difference method. This permits the grid extent to be reduced in size, resulting in a decrease in computational effort overall. Hounjet implements a multigrid technique to further improve convergence of the finite-difference method.

Voss [160] describes other hybrid schemes. An unsteady field panel method (PTRAN3) for solving the time linearized 3D Transonic Small Disturbance equation is described. The wing and wake surfaces are modeled with unsteady dipole distributions, while the region near the wing surface, where compressibility effects are greatest, is modeled using volume sources. Voss also describes a combined field-panel/finite-difference procedure.

Zimmerman and Vogel [169] describe a time-linearized method for solving the transonic small perturbation equation (LIN TSP). Comparisons are made for the unsteady transonic airloads computed using several different methods, including LIN TSP, TSP and doublet lattice. Some calculations are made using both a steady and a quasi-steady boundary layer. The paper also investigates the behavior of higher order harmonics of the computed airloads, and concludes that for small amplitude motions the higher-order harmonics can be neglected.

Steiginga and Houwink [149] describe an engineering type method (Q3D) which couples 2D linear theory, 2D nonlinear theory and 3D linear theory, in order to predict unsteady transonic airloads on transport-type aircraft wings. In this method, 2D scaling matrices are first obtained by forming a ratio of unsteady 2D nonlinear to 2D linear AICs, where each nonlinear AIC is computed for a representative airfoil section of the 3D wing. The resulting scaling matrices are used to modify 3D AICs obtained from a doublet lattice analysis.

Finally, Reisenthal and Nixon [125] have supplemented the TSD equation with a transport equation for streamwise vorticity and a vector potential equation to predict vortex effects over missile configurations. Results for a complete missile configuration at subsonic, transonic, and supersonic speeds are encouraging.

7.3 Aeroelastic Applications

A restricted selection of the many publications of 2–D-potential flow flutter calculations includes Isogai [85], Edwards et al. [51], Bland and Edwards [33], Berry et al. [28], and Zimmerman [169]. References [33] and [51] document the somewhat surprising "locally linear" nature of transonic potential flows. That is, about the steady mean flow condition which is a nonlinear function of Mach number and angle-of-attack, unsteady perturbation airloads behave very linearly for reasonable airfoil motions. Reference [51] included the static twisting of the airfoil due to the steady pitching moment into the flutter problem and demonstrated a marked effect upon flutter boundaries, particularly for the supercritical MBB-A3 airfoil. Reference [28] documented the utility of s-plane Pade curve fits of transonic airloads (which rely on the concepts of linearity and superposition) for aeroelastic analysis. Viscous effects are shown to generally result in larger values of flutter speed since transonic effects are alleviated by the boundary layer. Zimmerman [170] describes the application of several unsteady aerodynamic theories to the prediction of transonic flutter instabilities for a 2D airfoil profile. Flutter predictions are made using TSP theory, linearized TSP, TSP with quasi-unsteady boundary-layer and doublet lattice. Both frequency domain and time-marching methods are used in these flutter predictions.

Wu et al. [164] describe the use of a compressible-flow, FNS code for the prediction of unsteady airloads and flutter of 2D airfoil sections. Unsteady flow results are shown for harmonically oscillating NACA 0006 and NACA 0012 airfoils. Time marching aeroelastic solutions are given for the NACA 0012 airfoil showing stall flutter for several different Mach numbers and Reynolds numbers.

At the NLR, a number of unsteady aerodynamic computational procedures have been developed for use in transonic flutter prediction (Hounjet [74] and Steiginga and Houwink [149]). Zwann [168] describes an investigation into the accuracy of several of these methods for predicting flutter of a transport-type wing model. The methods examined include doublet lattice with quasi-steady corrections, the Q3D quasi 3D method and the FTRAN3 hybrid field-panel/finite-difference procedure. Corrected doublet lattice results are shown to display a flutter dip, probably due to the use of available experimental sectional airloads data. The flutter dip computed is, however, unconservative. The correlations of flutter speed versus Mach num-

THIS DOCUMENT PROVIDED BY THE ABBOTT AEROSPACE
TECHNICAL LIBRARY
ABBOTTAEROSPACE.COM

ber reported for the Q3D code are slightly conservative, but in good agreement with test results over a range of Mach numbers, and up to a point where the flow begins to separate. Several FTRAN3 predicted flutter points compared closely to the Q3D results. Hounjet and Meijer [75] give additional applications of the time linearized FTRAN3 code to flutter calculations for a fighter configuration with stores.

Other time-linearized finite-difference methods for solving the unsteady transonic flow about harmonically oscillating wings are described by Weatherill and Ehlers [161] and Shieh, Schoen, and Fung [143]. In Reference [161] the transonic small disturbance equation is split into a steady and an unsteady flow component, and the unsteady portion is solved using an out-of-core LU decomposition procedure (OPTRAN3). Sample flutter analysis results are presented for a flexible rectangular-wing. Reference [143] describes an implicit finite-difference procedure for solving the 3D full-potential equation for small unsteady perturbations of the body surface. The potential function is split into steady and unsteady components. The steady component can be obtained from a number of sources, such as higher order fluid dynamic equations (e.g. Euler, Navier-Stokes) or experimental data. Corrections are applied for nonisentropic effects, and the body motion is enforced using surface transpiration on a static grid conforming to the mean position of the solid surfaces (ZUNAS code). Computed results are given for unsteady oscillations of a NACA 0012 airfoil and for flutter boundaries of a 3D transport-type wing.

Comparisons of calculated and experimental flutter boundaries for wings have been given by Guruswamy and Goorjian [66], Isogai [87], Isogai and Suetsugu [88] and Myers et al. [113]. Isogai [85] studied the supercritical wing of Farmer et al. [57] using a nonconservative full potential code and an interacted boundary layer model. The trend of the transonic flutter dip is very nicely predicted although the dip occurs about 0.08 low in Mach number. The premature flutter dip and the subsequent premature rise of the calculated boundary at higher speeds is of concern. Myers [113] also shows such a premature rise in the boundary. Finally, Isogai [87] shows flutter comparisons for a different supercritical transport wing which agree nicely with the experimental flutter dip.

Cunningham et al. [44] describe TSD code flutter calculations for the AGARD Standard Aeroelastic flutter model configuration [166]. This is a 45° sweptback wing with a taper ratio of 0.66. Experimental and computed flutter boundaries are given for Mach numbers from 0.338 to 1.14. For this 4 percent thick wing, transonic effects are delayed to high subsonic Mach numbers and linear theory results from both CAP-TSD and a kernel function program are in very good agreement with experiment up to $M_\infty = 0.98$. Nonlinear CAP-TSD subsonic flutter calculations agree better with experiment than the linear theory, particularly for the change in slope of the flutter boundary near $M_\infty = 0.95$. Robinson et al. [130] have also performed flutter calculations for this wing using an Euler code. The moving mesh scheme described above was modified for use with a structured grid algorithm and the flutter boundary prediction was in good agreement with the TSD code and experiment.

Borland and Nagaraja [37] describe extensions to the XTRAN3S code to permit aerodynamic modeling of wing-pylon-stores and wing-fuselage configurations as well as the addition of supersonic analysis capability, non-reflecting boundary conditions and a Fourier analysis option for unsteady surface pressures. A number of applications of the code are presented for steady- and unsteady-flow aerodynamics and static/dynamic aeroelastic solutions. The configurations studied included an A-6 fighter configuration with stores, and a transport wing/fuselage configuration with winglet.

Mulak, Meurzec and Angelini [112] describe a finite-difference procedure to solve the 3D unsteady transonic small disturbance equation. The method solves a discretized form of the equation using an ADI splitting technique. Unsteady generalized airforces are computed for a number of normal modes for a swept, high-aspect-ratio transport-type wing. Some comparisons are made for steady and unsteady surface pressures and test data at a transonic Mach number. Flutter calculations are performed using different wing twist distributions corresponding to jig and flight condition shapes. A comparison is also presented for flutter calculations using both the doublet lattice and the TSD method.

Wong and Lee [165] describe a numerical procedure to compute unsteady transonic flow about 3D isolated-wing configurations (UST3D code). The procedure solves the transonic small disturbance equation, split into a nonlinear steady component, and a linear unsteady component. The steady part of the equation is solved with an implicit Newton-iteration scheme, used in conjunction with a preconditioned gradient type procedure. The unsteady part is solved with a semi-implicit technique which is explicit in the stream direction and implicit in the cross-flow planes. A nonreflecting far-field boundary condition is applied at the outer boundaries of the Cartesian mesh. Computed results are given for a fighter wing. Real and imaginary components of lifting pressure are given for a Mach number of 0.9 and $k = 0.45$. Aeroelastic results are compared with doublet lattice computations for unsteady pressures and a sample flutter calculation is presented.

Five additional applications of TSD codes to wing flutter calculations are described in Ref. [13], Bennett and Batina [26], Gibbons et al. [62], Silva and Bennett [144], and Guruswamy and Goorjian [69]. Reference [13] describes an implicit finite-difference procedure (ΔTRANS code) for solving the 3D transonic small disturbance equations on a Cartesian mesh. Aeroelastic calculations are made for the Falcon 900 wing at transonic Mach numbers, both with and without the incorporation of static aeroelastic deformations. Comparisons are also made with a doublet lattice method at a subsonic Mach number of 0.8. Bennett and Batina [26] present flutter calculations for a three percent thick clipped tip delta wing with a leading edge sweep angle of 50.5 degrees. The Mach range covered was 0.6–0.9. At the lower Mach numbers the results were in excellent agreement with linear theory, while there was a 6 percent reduction in flutter speed from linear theory at $M_\infty = 0.907$, bringing the results into better agreement with experiment. Gibbons studied a 70 degree swept delta wing for Mach numbers ranging from 0.6 to 3.0. The calculated flutter speeds are in very good agreement with experiment at transonic speeds. At supersonic speeds, the trend of the flutter boundary with Mach number agrees well with experiment. Silva and Bennett [144] show transonic flutter boundary predictions for a complex wind tunnel model. The blended wing-fuselage and tip ballast store were modeled. Significant improvement in predicted flutter points over those calculated with linear theory are shown for high transonic Mach

THIS DOCUMENT PROVIDED BY THE ABBOTT AEROSPACE
TECHNICAL LIBRARY
ABBOTTAEROSPACE.COM

number experimental points. Finally, Guruswamy and Goorjian [69] give flutter boundary calculations for a rectangular wing which agree well with experiment including a low supersonic condition.

Several investigators have studied airfoil and wing limit-cycle-oscillations (LCO) using both CFD-based and empirically-based computational methods. Bendiksen and Kousen [25] and Kousen and Bendiksen [94, 95] studied nonlinear aeroelastic dynamic response of an airfoil section using a CFD method based on the Euler equations. The Euler procedure is a finite-volume scheme solved using an explicit five-step Runge-Kutta algorithm. A two-degree-of-freedom structural dynamics model was solved iteratively along with the fluid dynamic equations to predict the dynamic response of the airfoil section. Aeroelastic stability was studied for NACA 0006 and NACA 64A010 airfoil sections over a range of Mach numbers. Limit cycle oscillations were found to occur at transonic speeds as a bifurcation phenomenon. A divergence/flutter interaction [94] was identified for which the airfoil dynamically approaches a static equilibrium offset at non-zero angles-of-attack.

Kousen and Bendiksen [95] also examined the effects of torsional spring free-play on the flutter response of 2D airfoil sections restrained by a two-degree-of-freedom elastic system (pitch and plunge). For the 2D case, the incorporation of free-play in the torsional spring lowers the stability boundary for conventional flutter. A bifurcation phenomenon is shown to exist above the maximum reduced velocity for flutter. Above these values, a limit-cycle behavior is exhibited by the airfoil/spring system. This 2D analysis method was applied to the flutter behavior of a well known typical section model of sweptback wing bending and torsion modes. It is shown that the dual-mode instability calculated for this model corresponds to a region, or pocket, of limit-cycle behavior. Finally, the effects of reduced airfoil thickness were examined and shown to be destabilizing, leading to limit-cycle behavior at lower Mach numbers than for a thicker airfoil section.

Meijer and Zwann [110] describe a semi-empirical computational method for the prediction of LCO occurring on fighter-type aircraft (see figure 5). Steady-state experimental surface pressure data are used to compute generalized airforces required to solve the structural dynamic equations of motion for a vehicle. The surface pressures are tabulated versus Mach number and steady angle-of-attack and utilized during the transient response simulation in a quasi-steady fashion wherein the instantaneous, induced angle of attack is used to reference the pressures. Both rigid and elastic mode shapes are used in the computations. Sample calculations of dynamic structural responses were made for two vehicle configurations, an isolated wing and a wing-with-missile configuration. Limit-cycle oscillations were found only for the clean-wing configuration, where the computed frequency and mean angle-of-attack data compared well with flight test results. For the flight conditions were LCO was observed, single-degree-of-freedom predictions using single mode shapes failed to show indications of LCO behavior. The authors state that LCO may not be associated with single degree-of-freedom systems, but rather with multiple-degree-of-freedom systems where modal coupling takes place, in a manner similar to the classical flutter mechanism.

The suppression of flutter instabilities by active controls has been demonstrated using CFD methods by Ominsky and Ide [119] and Guruswamy [68]. Ominsky and Ide use a Full Potential equation CFD method to evaluate aeroservoelastic control laws for flutter suppression. A test case for a swept wing is created by first determining a flutter condition to be controlled. A single trailing edge flap is deflected with time using a simple open loop multi-parameter control law. The parameters of flap amplitude of oscillation frequency and phase lag are studied to determine their effects on flutter response and a second-order control law is used in a closed loop manner to control the identified flutter instability. Guruswamy summarizes efforts at NASA-Ames to develop CFD methods for aeroelastic applications. Applications of the ATRAN3S code (TSD) and the TNS code (Euler/Navier-Stokes) are given. These include unsteady aerodynamic results, flutter analyses and flutter suppression demonstrations. Some comparisons with experimental data are given.

Schuster et al. [139] have developed a FNS code using zonal grid generation techniques to enable aeroelastic analysis of complete vehicles. Static aeroelastic calculations are presented for a fighter aircraft at a high wing-loading transonic condition. Calculated twisting of the aeroelastically tailored wing/fuselage configuration compares favorably with experiment.

Obayashi and Guruswamy [118] describe applications of the ENSAERO code to compute unsteady aerodynamics of a delta wing in oscillatory and ramp motions. The ENSAERO code is an Euler/Navier-Stokes method which includes a structural dynamics model to account for wing flexibility. The method solves the thin-layer Navier-Stokes equations and incorporates an algebraic turbulence model. Comparisons of theory and experimental data are presented for a number of steady flow and unsteady flow (pitching-oscillations) conditions. Computational results are also presented for a delta-wing undergoing an unsteady ramp motion (pitch). The computed results indicate a vortex breakdown condition occurring for a ramp motion which reaches a maximum amplitude of 10 degrees angle-of-attack.

Vinh et al. [159] present an interesting augmentation to the aeroelastic response capability of such codes. In addition to the structural dynamic equations of motion normally used for aeroelastic analysis, two additional degrees of freedom modeling the rigid aircraft short period mode were implemented along with an automatic trimming capability. This allows the interaction of the elastic modes upon vehicle stability and control to be calculated in a straightforward manner.

7.4 Viscous-Inviscid Interaction Applications

The transonic aeroelastic stability illustrations shown in figures 3–5 all involve strong viscous effects which inviscid analyses cannot predict. In order to achieve desired improved accuracy in predictive methods for such cases, an accounting of the effect of the viscous boundary layer is mandatory. Flows which must be treated include those with thickening boundary layers, incipient separation, shock-induced and trailing-edge separation, and alternately separating and reattaching flows. The computational resource estimates given in Table II indicate the severe cost incurred oy going to higher level CFD flow models and lead to the desirability of achieving the maximum possible viscous flow analysis capability with lower level CFD methods coupled with interacted viscous boundary layer models. Due to the importance of this issue for aeroelastic analysis, this section focuses on such applic ions. Interacted boundary layer methods have been developed for unsteady applications using

THIS DOCUMENT PROVIDED BY THE ABBOTT AEROSPACE
TECHNICAL LIBRARY
ABBOTTAEROSPACE.COM

direct solution for attached flows and indirect solution for separated flows. Calculations using TSD, full potential, and Euler equation codes have been extensively reported.

Examples of viscous flow effects for attached 2–D flows (direct solution method) are given by Guruswamy and Goorjian [65], Howlett [80, 81], and Houwink [77, 78]. All of these references use an integral boundary layer model coupled to a TSD inviscid method and calculations for the AGARD Standard Configurations are given (NACA 64A010, NACA 64A006, MBB-A3, NLR 7301, and NACA 0012 airfoils). Pirzadeh and Whitfield [122] report a 3–D direct viscous solution coupled to the Euler equations and give results for the NACA 64A010 airfoil and the ONERA M6 wing.

Unsteady results using the quasi-simultaneous method coupled to TSD solvers are reported by Houwink and Veldman [79] for 2–D cases and by Henke et al. [71] for 3–D cases. Houwink gives separated flow results for an oscillating supercritical airfoil and for an airfoil with a deflected spoiler. Henke gives details of a similar viscous coupling method implemented in a stripwise fashion in a 3–D TSD code and including aeroelastic computations. Comparisons with measured unsteady pressure from a modern transport wing model with a supercritical airfoil are shown and flutter calculations using the interacted viscous-TSD code are compared with doublet lattice calculations.

The most elaborate viscous interaction calculations of unsteady separated 2–D flows have been published by LeBalleur and his coworkers [98, 99]. An unsteady deflect integral boundary layer model is coupled to a TSD solver using the alternating-direction implicit solution method which enables an incorporation of the strong interaction of the viscous influence during the final z-sweep. The semi-implicit solution procedure involves a relaxation solution of a viscous influence function to force convergence of the viscous and inviscid solutions at each time step. Reference [99] gives unsteady shock-induced separation results for an oscillating NACA 64A010 airfoil, self-induced shock oscillations for a circular arc airfoil, and a supercritical airfoil with an oscillating spoiler. Giroudrouux–Lavigne and LeBalleur [63] further explore the self-excited shock oscillations, giving examples for the RA16 SC1 supercritical airfoil and the NACA 0012 airfoil. The shock oscillation conditions are shown to coincide with experimentally observed buffet onset boundaries. It is interesting to note similar calculations of buffet onset boundaries reported by Hirose and Miwa [72]. Experimental buffet boundaries for the NACA 0012 and KORN 75–06–12 airfoils are compared with calculations from a 2–D TNS code. As in the above viscous-inviscid interaction results, self-excited oscillating shocks are observed for conditions in good agreement with the experimental buffet boundaries.

In summary, viscous interaction methods are capable of treating important transonic effects when coupled with lower level CFD methods. Impressive results have been published for 2–D flows. Similar capability for 3–D flows involving shock-induced separating and reattaching flows remains a most important research topic.

7.5 Complete Aircraft Configurations

This section will survey the most ambitious CFD modeling of complete aircraft in order to indicate the levels of details and the level of effort such studies involve. All of the cases covered are for steady conditions; thus they can serve as a baseline for estimating resources which would be required for unsteady analyses. It is not surprising that the most detailed aircraft geometry modeling has been applied for cases at low angles of attack, near design conditions, where the flow is attached or mildly separated. These conditions are most important in design and the codes can be expected to perform at their best due to good flow quality (steady, attached, thin shear-layers, etc.). Thus, indications of the accuracy of results here will help to assess the readiness of the codes for the more demanding transonic flutter and low-speed, high-angle buffet conditions. Table III summarizes a number of CFD applications for such cases. All of these studies used the TLNS equations and all implemented simple turbulence models. All used convergence acceleration devices (local time-stepping, multigrid, etc.) which yield accurate results only for converged, steady flows. Except for Flores and Chaderjian [59], all made use of assumed symmetry in the flow to reduce by half the grid size (only one-half aircraft model analyzed). Finally, the codes used in these studies were generally second-order accurate in space and first-order accurate in time. Fujii and Obayashi [61] and Huband et al. [83] give results for complete aircraft models at transonic speeds while Thomas et al. [151] studies a detailed forebody/strake model at low speed and high angle. The latter is included due to its complex surface modeling. Vadyak and Schuster [156] give results for a sharp-edged generic fighter wing-body configuration at high angles. Kwon and Sankar [97] and Rizk and Gee [128] give results of buffet flowfield calculations about two high performance fighter configurations at high angles. These last three cases of high angle vortex-dominated flows will be discussed in the next section.

Fujii and Obayashi [61] modeled the W-18 transport configuration as a wing-fuselage and made calculations for three angles-of-attack. The overall surface pressures compared fairly well with experiment except in the outboard wing region where elastic deformations were not accounted for. Their numerical algorithm allowed the calculations with 700K grid points to be obtained in 5–6 cpu hours. Flores and Chaderjian's [59] study of the F-16A aircraft is one of the most ambitious applications to date. They modeled the wing, fuselage, tail, inlet, inlet-diverter, and the exhaust nozzle using 27 grid zones for the half-airplane. The flow-through inlet was modeled including power effects. Comparisons with experimental pressures indicated that the wing leading-edge expansion was not adequately resolved and the wing shock location was off by 12% chord. Doubling the grid size to one million points allowed the calculation of the full-span aircraft at five degrees sideslip angle. This also doubled the runtime to 50 hours. With regard to buffet calculations, it is interesting to note that the vertical tail tip vortex for this condition dissipated within one tip chordlength due to numerical dissipation (due of grid stretching downstream of the tip). Huband et al. [83] studied the same F-16A (the inlet is faired over) for a low supersonic Mach number. Their fine grid solution (1,241K grid points) occupied 59 million words of memory and required 40 hours of runtime. They obtained favorable agreement with experimental surface pressures but the wing leading-edge suction peaks were not correctly predicted due to lack of numerical resolution.

THIS DOCUMENT PROVIDED BY THE ABBOTT AEROSPACE
TECHNICAL LIBRARY
ABBOTTAEROSPACE.COM

TABLE III — CFD APPLICATIONS TO COMPLEX AIRCRAFT GEOMETRIES

Ref.	Configuration	M	α, deg.	Re, 10^6	N_{st}	N_{gp}	τ, μsec	T_{cpu}, hrs
Fujii[61]	W-18	0.82	2, 4, 6	1.67	3000+	700K	9.5	5-6
Flores[59]	F-16A w/inlet	0.9	6	4.5	5000	500K	36+	25
Huband[83]	F-16A w/o inlet	1.2	6	12.75	40,000+	1,241K	30+	40
Thomas[151]	F/A-18 forebody & LEX	0.3	30	0.74 WT 10.0 FLT		300K		
Vadjak[156]	generic wing/body	0.3	10,21*, 23,25	1.25	1,200	101K		
Kwon[97]	F-15 wing/body/inlet	0.15	20*			224K		
Rizk[128]	F-18 aircraft	0.243	30*	11.0	4,100			55

*Unsteady vortex flows

TABLE IV — CFD CALCULATIONS FOR HIGHLY-SWEPT WINGS AT HIGH ANGLES OF ATTACK

Ref.	Configuration	Λ, deg.	α, deg.	Re, 10^6	M_∞	N_{gp},K	N_{st}	τ,μsec	T_{cpu},hrs
Hitzel[73]	cropped delta, s,e	65	10,20,24,28* 10-28,24*, 28*10	1.25	0.4 0.85 1.20	270, 540			
Hsu[82]	delta, r	60	12(20)	1.3	0	712	700(1000)	52	7 (10)+
Hsu[82]	double-delta, r	80-60	12(20)	0.01, 1.3, 100	0	955	700(1000)	52	10 (14)+
Hsu[82]	cropped, double-delta, r,	80-40	12(20)	1.3	0	1021	700(1000)	52	10 (14)+
Hsu[82]	double-delta, r	80-60	6,12,15,20, 25,30,35*, 40*	1.3	0	859	500(1000)	52	6 (12)+
Fujii[60]	double-delta, r	80-60	6,12,(30*,35*)	1.3	0.3	850	1000(5000)	20	5 (25)+
Thomas[150]	delta, s	75	0-40, 20.5,40*	0.95	0.3	545	400	40	2.5
Krist[96]	delta, s	75	20.5	0.5	0.3	350(1000)			
Agarwal[1]	delta, s	70	(20, 25, 30, 35, 40)*	1.0	0.3		1-2000		3

e-Euler code s-sharp leading-edge r-round leading-edge *-vortex burst/unsteady calculations +-estimated

THIS DOCUMENT PROVIDED BY THE ABBOTT AEROSPACE
TECHNICAL LIBRARY
ABBOTTAEROSPACE.COM

8. High-Angle Vortex-Dominated Flow Applications

Computational studies are beginning to delineate the required levels of effort to produce accurate computations for separated, vortex-dominated flows. In this section attention will be given to a brief assessment of the state-of-the-art in computing vortical flows using CFD methods, followed by a discussion of recent research efforts in two specialized categories, wing rock and vortex buffet.

8.1 Status of CFD Prediction Methods for Vortical Flows

Edwards [56] provides a detailed study of current research and applications into the use of CFD methods for the prediction of separated, vortical flows over airfoils, wings and bodies. Table IV lists a selection of these applications relevant to computational aeroelasticity at high angles. All except Hitzel [73] represent applications of the TLNS equation, while Hitzel utilizes the Euler equations. The major conclusions of this study are repeated here for completeness.

Calculations of stable vortex-dominated flows about simplified highly swept wing geometries at low speeds are available. Early Euler equation results gave encouragement to their use for such flows, but recent detailed studies point to issues regarding their accuracy and convergence for realistic geometries. The thin-layer Navier-Stokes equations, both laminar and turbulent are being used. The results capture key features of the flowfield such as primary and secondary vortices and surface pressure details. Indications that vortex breakdown is being simulated have been published. However, all cases surveyed indicated the need for further grid refinement in order to achieve quantitative agreement with experiment. Currently, grid sizes of 250,000 to 10^6 grid points are being used for half airplane modeling leading to CPU runtimes of 2–25 hours. These grids are typical of those developed for attached shear flows with the highest grid density near the body. This leads to inadequate density in off-the-body regions where concentrated vortices are located and mesh enrichment methods are being developed to address this problem. A fundamental problem is the lack of any turbulence model designed for dynamic free shear layers.

Agrawal et al. [1] provide an interesting numerical study of this issue of off-the-surface turbulence modeling. Calculations for a sharp-edged delta wing from an Euler code, a laminar TNS code and a turbulent TNS code show vortex bursting at locations in general agreement with experiment. It is noted that the solutions are based on meshes that are not usually considered fine enough for resolving flowfields in primary vortex regions.

8.2 Rolling Oscillations and Wing Rock

Several studies have been published of unsteady airloads on rolling delta wings at high incidences. The dynamics of the leading-edge vortices which form at such conditions are one of the driving forces which can lead to wing-rock; a limited amplitude rolling oscillation which limits aircraft performance. Computations have been reported for low speed flows and for supersonic flows simulated via a conical flow assumption. Nayfeh et al. [116] use an unsteady vortex-lattice method to predict low-speed experimental wing-rock conditions.

Kandil and his coauthors have studied unsteady vortex-dominated flow about delta wings using the conical flow assumption of supersonic flow. Reference [90] gives compressible Navier-Stokes results for rolling oscillations while Ref. [91] gives results for oscillating leading-edge flaps. Lee and Batina [101], again making use of the conical flow assumption, couple an unstructured grid Euler code with a wing rolling equation of motion to make calculations of supersonic wing-rocking motions. In a later work, Lee and Batina [100] demonstrated that this supersonic wing-rock phenomenon can be controlled with the use of oscillating, leading-edge flaps, activated by a simple control-law. More recently, Kandil and Salman [92] used an Euler conical flow solution procedure to study the control of wing-rock using leading edge flaps, together with a nonlinear control law.

8.3 Buffet Flowfield Calculations

Current and future military fighters are called upon to perform high angle maneuvers at elevated loading conditions and are experiencing structural fatigue problems due to dynamic buffet loads on aft components of the empennage, in particular the vertical tail(s). This has led to a desire for improved prediction methods for such flows, which emerging CFD methods might be expected to fulfill. Key flow modeling issues involve: i) unsteady flow separation for moderately swept, rounded leading-edge wings, ii) grid densities necessary for accurate calculation of vorticity convected over significant distances, iii) dynamic turbulence modeling for free shear layers, iv) detailed modeling necessary for accurate calculations of vortex instabilities, and v) vortex flows about wings at high subsonic speeds.

Three cases of the computation of buffet flowfields are given as the last three entries in Table III. All are for quite complex configuration models of high performance fighter aircraft and it has been noted above that this type of computation is the most demanding for aeroelastic applications. Vadyak and Schuster [156] made calculations for a generic fighter configuration consisting of a sharp-edged strake/wing/fuselage. Low speed wind tunnel LDV flowfield data was available and crossflow velocity comparisons for α = 21 deg. appear to be good. A bubble-type reverse flow region, indicating breakdown, is observed at approximately x/L = 0.9. These comparisons for this high angle, vortex flow case are very noteworthy, particularly due to the complex geometry tested. However, the computational results, obtained with a grid of 101,000 points, cannot be regarded as converged.

Kwon and Sankar [97] give calculations for a half-span wing/body/inlet model of the F-15 aircraft. The FNS equations are solved using a hybrid time differencing scheme suitable for implementation on virtual memory machines. On a grid consisting of 224,000 points, calculations of unsteady, buffet-like flowfields are given for M_∞ = 0.15 and α = 20°. The unsteadiness is shown to consist primarily of a low frequency of about 5 Hz. (full scale aircraft) and a high frequency ranging from 29–34 Hz. The higher frequency content compares favorably with low speed wind tunnel tests for the complete aircraft (Triplett [154]) even with the relatively coarse grid used.

The final entry in Table III, that of Rizk and Gee [128], gives results for a complex configuration model of the half-span F-18 aircraft. An overset zonal grid scheme consisting of ten grids was used to model the forebody, fuselage, LEX,

THIS DOCUMENT PROVIDED BY THE ABBOTT AEROSPACE
TECHNICAL LIBRARY
ABBOTTAEROSPACE.COM

faired-over inlet, wing, deflected leading-edge flaps, vertical and horizontal tails and an idealized boundary layer diverter vent. TLNS results are given for M_∞ = 0.243 and α = 30.3°. The solution required about 8 million words of memory and took about 55 hours of CPU time for 5,100 steps. Bursting of the LEX vortex in the vicinity observed in flight tests is shown. Unsteady loads on the vertical tail show a dominant frequency of 15–20 Hz. Other higher frequencies are evident but are not well resolved. Triplett [154] gives test results indicating that the principal modal buffeting response frequencies of this aircraft are 15 Hz. and 45 Hz. Earlier calculations [127] indicate that finer meshes (e.g. about 2 million grid points) will be needed to accurately predict such features as the location of vortex bursting.

The buffeting response of launch vehicles is a critical issue in their performance. Up to the present, wind tunnel studies have largely been relied upon for the prediction of such airloads. Azevedo [14] presents novel TLNS results of buffeting response calculations for a hammerhead payload configuration.

In summary, ambitious applications of CFD to complicated aircraft geometries are being performed. Available studies are very encouraging in the overall agreement with experiment. Important areas are also being highlighted where additional grid resolution is needed to achieve local accuracy in such important features as suction peaks and shock locations. Computer runtimes for these cases are in the range of 5–55 hours (half-airplane). It is probable that accurate buffet calculations will require capability such as this forebody and wing flows in order to generate accurate "starting" conditions for the convecting vortex flows. It is also probable that similar capability will be required to calculate the buffeting response of the tail to the oncoming buffet flow. Indeed, this is likely to be a more difficult problem than the calculation of the "starting" wing flow due to the turbulent nature of the local flow at the tail.

9. Discussion and Future Trends

The proceeding sections have surveyed a segment of the large efforts that have been spent on computational unsteady aerodynamics suitable for aeroelastic applications of fixed wing aircraft. These efforts can be divided into five general categories: i) development and demonstration of unsteady aerodynamic methods, ii) rigorous calibration and validation of these unsteady methods, iii) development and demonstration of aeroelastic analysis procedures, iv) rigorous calibration and validation of these aeroelastic procedures, and v) application of the resulting aeroelastic methods in the design or modification of actual or proposed flight vehicle configurations. Although nearly a decade and a half has passed since the earliest pioneering demonstrations of CFD applied to aeroelastic analyses, considerable efforts are still needed to reach a state where the aircraft industry, as a whole, accepts and routinely utilizes CFD for category v. activities. By far, the largest number of references cited herein fall within category i., and to a lesser extent, category iii. Also, to a large extent, the authorship of these cited references seems to indicate that a large segment of this research is currently occurring in universities and government sponsored research laboratories. Although there are some notable exceptions to this trend, many more industrial applications of aeroelastic CFD methods are needed and desirable. The following comments are offered regarding the current status and future trends of computational methods to meet the challenges listed in Table I and illustrated in figures 3–7:

1. Stability and control estimates, including aeroelastic effects, are being treated with linear methods which are well suited for design conditions well removed from flow separation boundaries where viscous effects are important. Initial demonstrations of the unified treatment of complete vehicle dynamics (rigid body and aeroelastic) using CFD methods are available.

2. Gust response analyses are currently conducted using linear aerodynamic methods. While CFD codes capable of treating complete configurations (necessary for gust response analysis) are available, there have been no reported attempts of such calculations other than isolated vortex-airfoil interactions.

3. A number of studies of flutter boundary calculations with CFD codes have been cited. Many more cases are needed in order to establish the required level of flow modeling detail which will provide accurate and useful results. It is not yet established for what conditions nonlinear flow modeling results differ sufficiently from linear results to justify their use. Also, the tradeoffs between the computational expense of the various levels of flow modeling (e.g. TSD-viscous vs. TLNS) and improved accuracy of results have not yet been established. A few cases have shown significant improvement over linear theory for small, but critical, ranges of transonic Mach numbers.

4. Prediction of these critical minimum transonic flutter speeds and nonclassical aeroelastic response phenomena, such as control surface buzz and aeroelastic limit cycle oscillations, certainly will require, at the very least, reliable, robust interacted boundary layer models capable of handling some amount of flow separation and reattachment. This capability is not yet mature for wings or more complete configuration modeling. This is also the case for the important design issues relating to aerodynamic control surfaces: control effectiveness and control hinge moments.

5. Cases of tail buffeting and structural fatigue being encountered by operational aircraft have focused attention upon this area. The achievements in the ability to compute vortex-dominated flows are truly impressive and initial calculations of buffet-like flows appear to contain elements (frequency content, etc.) of realism. However, studies of the accuracy and convergence of such calculations in terms of grid density, sensitivity to initial conditions, repeatability, etc. are necessary. Two interesting questions regarding such flowfield simulations are:

   a. if the flowfield simulations are repeatable, can the flow modeling contain adequate fluid dynamic modeling to ensure accurate buffet flows calculations?
   b. if the flowfield simulations are very sensitive to initial conditions or are not repeatable, what measures are to be used in establishing the required number of cases and computational record lengths to ensure solution convergence?

THIS DOCUMENT PROVIDED BY THE ABBOTT AEROSPACE
TECHNICAL LIBRARY
ABBOTTAEROSPACE.COM

Regarding future trends in computational aeroelasticity the following comments are offered:

1. Robust interactive boundary layer methods coupled with all levels of inviscid codes will mature and be applied to aeroelastic stability and response calculations for high-speed, low angle conditions. The resulting improved accuracy in key areas such as transonic flutter prediction will be of great value.

2. Studies will delineate conditions best suited for the use of CFD methods. A hierarchy of the problem areas, keyed to the complexity of the flow problem being studied (e.g. Types I, II, or III flows), will be established and will be addressed by a suite of tools drawn from the alternative levels of CFD flow modeling.

3. Unstructured and hybrid grid methods will mature, leading to computations of quite detailed configuration complexity. The increased expense of unstructured grid methods (due to more complex coding) will be offset by the anticipated payoffs of the approach: fewer grid points required for comparable accuracy along with the complex geometry modeling capability. Continued improvements in algorithm efficiency will be seen for all gridding approaches; block-structured, zonal and hybrid grid schemes will also be used in the search for robust, economical and user-friendly geometry modeling capability.

4. Improvements in conventional computer architectures will not achieve the orders of magnitude speedup needed to make the most complex aeroelastic computations, such as tail buffeting, routine. Massively parallel processing architectures may eventually provide relief, but not in the near future.

5. The need for experimental data bases specialized for the validation of computational methods for interesting aeroelastic flows is being addressed by NASA's Benchmark Models Program and the European Aeroelastic Models Program. Tests directed at unsteady off-the-surface flow measurements will continue to press the limits of instrumentation technology.

6. A final comment relates to differing uses of computational methods in the fields of aircraft performance analysis and aeroelastic analysis. The former application may be broadly typified as dealing with well-behaved, stable flows exemplified by performance and design studies where steady CFD methods are currently being utilized heavily. The latter application typically must deal with flows on the edge of flow breakdown (i.e. structural dynamic instabilities in the presence of dynamic flows and flows transitioning between states) where safety-of-flight is of paramount concern. Attention by the user-communities to the appropriately different standards to be applied to the validation or calibration of CFD methods in these two areas is required.

In conclusion, it is anticipated that unsteady CFD methods will emerge to be routinely used for aeroelastically challenging problems.

10. References

1. Agrawal, S.; Barnett, R. M.; and Robinson, B. A.: Investigation of Vortex Breakdown on a Delta Wing Using Euler and Navier-Stokes Equations, 67th AGARD Fluid Dynamics Panel Symposium on Vortex Flow Aerodynamic, Scheveningen, Netherlands, October 1–4, 1990.

2. Anderson, D. A.; Tannehill, J. C.; and Pletcher, R. H.: Computational Fluid Mechanics and Heat Transfer, McGraw-Hill Book Company, 1984.

3. Anderson, W. K.; Thomas, J. L.; and Rumsey, C. L.: Extension and Applications of Flux-Vector Splitting to Unsteady Calculations on Dynamic Meshes, AIAA Paper No. 87–1152, June, 1987.

4. Anderson, W. K.; and Batina, J. T.: Accurate Solutions, Parameter Studies, and Comparison for the Euler and Potential Flow Equations, Paper No. 15, AGARD 62nd Meeting of the Fluid Dynamics Panel Symposium on Validation of Computational Fluid Dynamics, AGARD CP 437, Vol. 1, Lisbon, Portugal, May 2–5, 1989.

5. Angelini, J. J.; Girodroux-Lavigne, P.; Grisval, J. P.; Le Balleur, J. C.; Mulak, P.; and Sides, J.: Unsteady Transonic Flow Computations for AGARD Two Dimensional and Three Dimensional Aeroelastic Configurations, ESA-TT-1020; December, 1986.

6. Angelini, J. J.; and Soize, C.: New Approach to Small Transonic Perturbations Finite Element Numerical Solving Method, *Parts I and II. La Recherche Aerospatiale (English* edition), No. 1989–2, 1989, pp. 1–41.

7. Anon: Military Specification; Airplane Strength and Rigidity; Flutter, Divergence, and Other Aeroelastic Instabilities. MIL-A-008870A (USAF), March 1971.

8. Anon: Unsteady Aerodynamics. AGARD-CP-227, 1978.

9. Anon: Boundary Layer Effects on Unsteady Airloads. AGARD-CP-296, 1981.

10. Anon: Unsteady Aerodynamics-Fundamentals and Applications to Aircraft Dynamics. AGARD-CP-386, 1985.

11. Anon: Transonic Unsteady Aerodynamics and its Aeroelastic Applications. AGARD-CP-374, 1985.

12. Anon: Aircraft Dynamic Loads Due to Flow Separation. AGARD-CP 483, September 1990.

13. Anon: Rapport de Synthese: Aeroelasticite Instationnaire Transsonique 6 EME Phase Configuration Aile du Falcon 900, Avions Marcel Dassault-Brequet Aviation, Document PBM.MI/YC-DTM-6233/88, Merignac, 7 October 1988.

14. Azevedo, J. L. F: Transonic Aeroelastic Analysis of Launch Vehicle Configurations. Ph.D. Dissertation, Department of Aeronautics and Astronautics, Stanford University, February 1988 (Also NASA CR 4186, October 1988).

15. Baldwin, B.; and Lomax, H.: Thin Layer Approximation and Algebraic Model for Separated Turbulent Flows, AIAA

THIS DOCUMENT PROVIDED BY THE ABBOTT AEROSPACE
TECHNICAL LIBRARY
ABBOTTAEROSPACE.COM

Paper No. 78–257, 1978.

16. Ballhaus, W. F.: Some Recent Progress in Transonic Flow Computations. VKI Lecture Series: Computational Fluid Dynamics, von Karman Institute for Fluid Dynamics, Rhode-St-Genese, Belgium, March 1976.

17. Ballhaus, W. F.; and Goorjian, P. M.: Implicit Finite-Difference Computations of Unsteady Transonic Flows about Airfoils. AIAA Journal, Vol. 15, No. 12, December 1977, pp. 1728–1735.

18. Batina, J. T.: Unsteady Transonic Flow Calculations for Interfering Lifting Surface Configurations. Journal of Aircraft, Vol. 23, No. 5, May 1986, pp. 422–430. (Also NASA TM-86432, May 1985.)

19. Batina, J. T.: Unsteady Transonic Flow Calculations for Wing-Fuselage Configurations. Journal of Aircraft, Vol 23, No. 12, December 1986, pp. 897–903.

20. Batina, J. T.: An Efficient Algorithm for Solution of the Unsteady Transonic Small-Disturbance Equation. Journal of Aircraft, Vol 25, No. 7, July 1988, pp. 598–605. (Also NASA TM 89014, December 1986.)

21. Batina, J. T.; Seidel, D. A.; Bland, S. R.; and Bennett, R. M.: Unsteady Transonic Flow Calculations for Realistic Aircraft Configurations. Journal of Aircraft, Vol. 26, No. 2, February 1989, pp. 131–139. (Also NASA TM-89120, March 1987.)

22. Batina, J. T.: Unsteady Euler Airfoil Solutions Using Unstructured *Dynamic Meshes.* AIAA Journal, Vol. 28, No. 8, August 1990, pp. 1381–1388.

23. Batina, J. T.: Unsteady Euler Algorithm with Unstructured Dynamic Mesh for Complex-Aircraft Aeroelastic Analysis. AIAA Journal, Vol. 29, No. 3, March 1991, pp. 327–333.

24. Batina, J. T.: Unsteady Euler Airfoil Solutions Using Unstructured Dynamic Meshes. AIAA Journal, Vol. 28, No. 8, August 1990, pp. 1381–1388.

25. Bendiksen, O. O.; and Kousen, K. A.: Transonic Flutter Analysis Using the Euler Equations, AIAA Paper No. 87–0911, April, 1987.

26. Bennett, R. M.; and Batina, J. T.: Application of the CAP-TSD Unsteady Transonic Small Disturbance Program to Wing Flutter. Paper No. 89–003 in Proceedings of European Forum on Aeroelasticity and Structural Dynamics, DGLR Bericht 89–01, Aachen, FRG, April 17–19, 1989, pp. 25–34.

27. Bennett, R. M.; Eckstrom, C. V.; Rivera, J. A., Jr.; Dansberry, B. E.; Farmer, M. G.; and Durham, M. H.: Benchmark Aeroelastic Models Program – Description and Highlights from Initial Results. Paper No. 25, AGARD Specialists Meeting on Transonic Unsteady Aerodynamics and Aeroelasticity, San Diego, CA, October 9–11, 1991.

28. Berry, H. M.; Batina, J. T.; and Yang, T. Y.: Viscous Effects on Transonic Airfoil Stability and Response. Journal of Aircraft, Vol. 23, No. 5, May 1986, pp. 361–369.

29. Bharadvaj, B. K.: Computation of Steady and Unsteady Control Surface Loads in Transonic Flow. AIAA Paper No. 90–0935, April 1990.

30. Bland, S. R.: AGARD Two-Dimensional Aeroelastic Configurations. AGARD-AR-156, 1979.

31. Bland, S. R.: AGARD Three-Dimensional Aeroelastic Configurations. AGARD-AR-167, 1982.

32. Bland, S. R.; and Seidel, D. A.: Calculation of Unsteady Aerodynamics for Four AGARD Standard Aeroelastic Configurations, NASA TM 85817, May 1984.

33. Bland, S. R.; and Edwards, J. W.: Airfoil Shape and Thickness Effects on Transonic Airloads and Flutter. Journal of Aircraft, Vol. 21, No. 3, March 1984, pp. 209–217.

34. Bland, S. R.: Personal Computer Study of Finite-Difference Methods for the Transonic Small Disturbance Equation. Proceedings of the Third International Congress of Fluid Mechanics, Cairo, Egypt, January 2–4, 1990, Vol. II, pp. 527–543. (also NASA TM 102582, December 1989).

35. Bland, S. R.: Suggestions for CAP-TSD Mesh and Time-Step Input Parameters, NASA TM 104083, June 1991.

36. Bobbitt, P. J.: The Pros and Cons of Code Validation. AIAA Paper No. 88–2535. June 1988.

37. Borland, C. J.; and Nagaraja, K. S.: Applications and Improvements of XTRAN3S. WRDC-TR-89–3051, November 1989.

38. Carter, J. E.: A New-Boundary-Layer Interaction Technique for Separated Flows. AIAA Paper No. 79–1450, July 1979.

39. Chaderjian, N. M.; and Guruswamy, G. P.: Unsteady Transonic Navier-Stokes Computations for an Oscillating Wing Using Single and Multiple Zones, AIAA Paper No. 90–0313, January 1990.

40. Chen, P. C.; and Liu, D. D.: Unsteady Supersonic Computations of Arbitrary Wing-Body Configurations Including External Stores. Journal of Aircraft, Vol. 27, No. 2, February 1990, pp. 108–116.

41. Chen, P. C.; Liu, D. D.; James, D. K.; and Potozky, A. S.: Further Studies of Harmonic Gradient Method for Supersonic Aeroelastic Applications. Paper No. 89–068 in Proceedings of European Forum on Aeroelasticity and Structural Dynamics, DGLR-Bericht 89–01, Aachen, FRG, April 1989, pp. 605–620.

42. Chyu, W. J.; Davis, S. S.; and Chang, K. S.: Calculation of Unsteady Transonic Flow Over an Airfoil. AIAA Journal, Vol. 19, No. 6, June 1981, pp. 684–690.

43. Chyu, W. J.; and Davis, S. S.: Numerical Studies of Unsteady Transonic Flow Over an Oscillating Airfoil. Paper No. 3 in AGARD CP-374, Transonic Unsteady Aerodynamics and its Aeroelastic Application, January 1985.

44. Cunningham, H. J.; Batina, J. T.; and Bennett, R. M.: Modern Wing Flutter Analysis by Computational Fluid Dynamics Methods. ASME Paper No. 87–WA/Aero-9, ASME

THIS DOCUMENT PROVIDED BY THE ABBOTT AEROSPACE
TECHNICAL LIBRARY
ABBOTTAEROSPACE.COM

Winter Annual Meeting, Boston, Massachusetts, December 13–18, 1987.

45. Damodaran, M.: Finite Volume Computation on Unsteady Inviscid Rotational Transonic Flows Past Airfoils in Rigid Body Motion, AIAA Paper 88–0006, January, 1988.

46. Deiwert, G. S.: Finite-Difference Simulation of Unsteady Interactive Flows. In Computational Methods in Viscous Flow, ed. by Habashi, W. G.; Pineridge Press, 1984, pp. 281–308.

47. Dobbs, S. K.; Miller, G. D.; and Stevenson, J. R.: Self-Induced Oscillation Wind Tunnel Test of a Variable Sweep Wing. AIAA Paper No. 85–0739, April 1985.

48. Dowell, E. H.: Nonlinear Aeroelasticity. AIAA Paper No. 90–1031, April 1990.

49. East, L. F.; Smith, P. D.; and Merryman, P. J.: Prediction of the Development of Separated Turbulent Boundary-Layers by the Lag-Entrainment Method. RAE-TR-77046, March 1977.

50. Edwards, D. E.; and Carter, J. E.: A Quasi-Simultaneous Finite Difference Approach for Strongly Interacting Flow. Third Symposium on Numerical and Physical Aspects of Aerodynamic Flows, Long Beach, California, January 21–24, 1985.

51. Edwards, J. W.; Bennett, R. M.; Whitlow, W., Jr.; and Seidel, D. A.: Time-Marching Transonic Flutter Solutions Including Angle-of-Attack Effects. Journal of Aircraft, Vol. 20, No. 11, November 1983, pp. 899–906.

52. Edwards, J. W.; and Thomas, J. L.: Computational Methods for Unsteady Transonic Flow. Chapter 5 in Unsteady Transonic Aerodynamics, Ed. by D. Nixon, Vol. 120 of AIAA Progress in Astronautical and Aerodynamics, 1989, pp. 211–261. (Also AIAA Paper No. 87–0107).

53. Edwards, J. W.: Computational Aeroelasticity Challenges and Resources. In Transonic Unsteady Aerodynamics and Aeroelasticity, NASA CP 3022, 1989, Part 2, pp. 631–637.

54. Edwards, J. W.: Unsteady Aerodynamics: Physical Issues and Numerical Predictions. In Proceedings of the Third International Congress of Fluid Mechanics, Cairo, Egypt, January 2–4, 1990, Vol. I, pp. 99–115.

55. Edwards, J. W.: Assessment of Computational Prediction of Tail Buffeting. NASA TM 101613, January 1990.

56. Edwards, J. W.: Unsteady Airloads Due to Separated Flow on Airfoils and Wings. Paper No. 16 in AGARD-CP-483, Aircraft Dynamic Loads Due to Flow Separation, Sorrento, Italy, April 1990.

57. Farmer, M. G.; Hanson, P. W.; and Wynne, E. C.: Comparison of Supercritical and Conventional Wing Flutter Characteristics. NASA TM X-72837, May 1976.

58. Fenno, C. C., Jr.; Newman, P. A.; and Hassan, H. A.: Unsteady Viscous-Inviscid Interaction Procedures for Transonic Airfoils Using Cartesian Grids. Journal of Aircraft, Vol. 26, No. 8., August 1989, pp. 723–730.

59. Flores, J.; and Chaderjian, N. M.: The Numerical Simulation of Transonic Separated Flow About the Complete F-16A. AIAA Paper No. 88–2506, June 1988.

60. Fujii, K.; and Schiff, L. B.: Numerical Simulation of Vortical Flows Over a Strake-Delta Wing. AIAA Paper No. 87–1229, June 1987.

61. Fujii, K.; and Obayashi, S.: Navier-Stokes Simulations of Transonic Flows over a Wing-Fuselage Combination. AIAA Journal, Vol. 25, No. 12, December 1987, pp. 1587–1596.

62. Gibbons, M. D.; Soistmann, D. L.; and Bennett, R. M.: Flutter Analysis of Highly Swept Delta Wings by Conventional Methods. NASA TM 101530, November 1988.

63. Girodroux-Lavigne, P.; and LeBalleur, J. C.: Time-Consistent Computation of Transonic Buffet Over Airfoils. 16th International Congress of the Aeronautical Sciences, Jerusalem, Israel, August 28–September 2, 1988.

64. Green, J. E.; Weeks, D. J.; and Brooman, J. W. F.: Prediction of Turbulent Boundary-Layers and Wakes in Compressible Flow by a Lag-Entrainment Method. RAE-TR-722311, January 1973.

65. Guruswamy, G. P.; and Goorjian, P. M.: Effects of Viscosity on Transonic-Aerodynamic and Aeroelastic Characteristics of Oscillating Airfoils. Journal of Aircraft, Vol. 21, No. 9, September 1984, pp. 700–707.

66. Goorjian, P. M.; and Guruswamy, G. P.: Unsteady Transonic Aerodynamic and Aeroelastic Calculations About Airfoils and Wings. Paper No. 5 in Transonic Unsteady Aerodynamics and its Aeroelastic Applications, AGARD CP-374, January 1985.

67. Guruswamy, G. P.: Time-Accurate Unsteady Aerodynamic and Aeroelastic Calculations of Wings Using Euler Equations. AIAA Paper No. 88–2281, April 1988.

68. Guruswamy, G. P.: Interaction of Fluids and Structures for Aircraft Applications, Computers and Structures, Vol. 30, No. 1/2, 1988, pp. 1–13.

69. Guruswamy, G. P.; and Goorjian, P. M.: Unsteady Transonic Aerodynamics and Aeroelastic Calculations at Low-Supersonic Freestreams. Journal of Aircraft, Vol. 25, No. 10, October 1988, pp. 955–961.

70. Guruswamy, G. P.; and Goorjian, P. M.: Unsteady Transonic Flow Simulation on a Full-Span-Wing Body Configuration. AIAA Journal, Vol. 26, No. 12, December 1988, pp. 1450–1456.

71. Henke, H.; Muller, U. R.; and Schultze, B.: A Viscous Inviscid Interaction Method for Use in Transonic Flutter Analysis, International Forum on Aeroelasticity and Structural Dynamics 1991, Aachen, Germany, June 3–6, 1991.

72. Hirose, N.; and Miwa, H.: Computational and Experimental Research on Buffet Phenomena of Transonic Airfoils, NAL TR 996T, 1988.

THIS DOCUMENT PROVIDED BY THE ABBOTT AEROSPACE
TECHNICAL LIBRARY
ABBOTTAEROSPACE.COM

73. Hitzel, S. M.: Wing Vortex-Flows Up Into Vortex-Breakdown. AIAA Paper No. 88–2518, June 1988.

74. Hounjet, M. H. L.: A Hybrid Field Panel/Finite Difference Method for 3–D Potential Unsteady Transonic Flow Calculations. AIAA Paper No. 83–1690, July, 1983.

75. Hounjet, M. H. L.; and Meijer, J. J.: Application of Time-Linearized Methods to Oscillating Wings in Transonic Flow and Flutter, Paper No. 11 in AGARD CP-374, Transonic Unsteady Aerodynamics and its Aeroelastic Applications, Toulouse, France, September, 1984.

76. Hounjet, M. H. L.: Calculation of Unsteady Subsonic and Supersonic Flow About Oscillating Wings and Bodies by New Panel Methods, Paper No. 89–009 in European Forum on Aeroelasticity and Structural Dynamics, DGLR-Bericht 89–01, Aachen, FRG, April 1989, pp. 85–104.

77. Houwink, R.: Unsteady Transonic Flow Computations, National Aerospace Laboratory NLR, Memorandum AE-83–004 U, 1983.

78. Houwink, R.: Unsteady Viscous Transonic Flow Computations Using the LTRAN2–NLR Code Coupled with Green's Lag-Entrainment Method. Numerical and Physical Aspects of Aerodynamic Flows II, Chapter 15, ed. by T. Cebeci, Springer, New York, 1984.

79. Houwink, R.; and Veldman, A. E. P.: Steady and Unsteady Separated Flow Computations for Transonic Airfoils. AIAA Paper No. 84–1618, June 1984.

80. Howlett, J. T.: Efficient Self-Consistent Viscous-Inviscid Solutions for Unsteady Transonic Flow, Journal of Aircraft, Vol. 24, No. 11, November 1987, pp. 737–744.

81. Howlett, J. T.; and Bland, S. R.: Calculation of Viscous Effects on Transonic Flow For Oscillating Airfoils and Comparisons with Experiment. NASA TP-2731, September 1987.

82. Hsu, C.-H.; and Liu, C. H.: Upwind Navier-Stokes Solutions for Leading-Edge Vortex Flows, AIAA Paper No. 89–0265. January 1989.

83. Huband, G. W.; Rizzetta, D. P.; and Shang, J. J. S.: The Numerical Simulation of the Navier-Stokes Equations for an F-16 Configuration. AIAA Paper No. 88–2507, June 1988.

84. Ide, H.; and Shankar, V. J.: Unsteady Full Potential Aeroelastic Computations for Flexible Configurations. AIAA Paper No. 87–1238, June 1987.

85. Isogai, K.: Numerical Study of Transonic Flutter of a Two-Dimensional Airfoil. NAL Report TR-716T, July 1980.

86. Isogai, K.: Calculation of Unsteady Transonic Potential Flow Over Oscillating Three-Dimensional Wings, NAL TR-706T, March 1982.

87. Isogai, K.: The Development of Unsteady Transonic 3–D Full Potential Code and Its Aeroelastic Applications. Paper No. 17 in Transonic Unsteady Aerodynamics and Its Aeroelastic Applications, AGARD CP-374, January 1985.

88. Isogai, K.; and Suetsugu, K.: Numerical Simulation of Transonic Flutter of a Supercritical Wing, NAL Report TR-726T, August 1982.

89. Johnson, E. H.; and Reymond, M. A.: Multidisciplinary Aeroelastic Analysis and Design Using MSC/NASTRAN, AIAA Paper No. 91–1097, April 1991.

90. Kandil, O. A.; and Chuang, J. A.: Unsteady Navier-Stokes Computations Past Oscillating Delta Wing at High Incidence, AIAA Paper No. 89–0081, January 1989.

91. Kandil, O. A.; and Salman, A. A.: Unsteady Vortex-Dominated Flow Around Wings with Oscillating Leading-Edge Flaps, AIAA Paper No. 91–0435, January 1991.

92. Kandil, O. A.; and Salman, A. A.: Effects of Leading Edge Flap Frequency on Unsteady Flow Around Delta Wings, AIAA Paper No. 91–1796, June 1991.

93. Kleb, W.; Batina, J. T.; and Williams, M.: Temporal-Adaptive Euler/Navier-Stokes Algorithm Unsteady Aerodynamic Analysis of Airfoils Using Unstructured Dynamic Meshes. AIAA Paper No. 90–1650, June 1990.

94. Kousen, K. A.; and Bendiksen, O. O.: Nonlinear Aspects of the Transonic Aeroelasticity Stability Problem, AIAA Paper No. 88–2306, April 1988.

95. Kousen, K. A.; and Bendiksen, O. O.: Limit Cycle Phenomena in Computational Transonic Aeroelasticity, AIAA Paper No. 89–1185, April 1989.

96. Krist, S. L.; Thomas, J. L.; Sellers, W. L., III; and Kjelgaard, S. O.: An Embedded Grid Formulation Applied to a Delta Wing. AIAA Paper No. 90–4029, January 1990.

97. Kwon, O. J.; and Sankar, L. N.: Viscous Flow Simulation of Fighter Aircraft, AIAA Paper No. 91–0278, January 1991.

98. LeBalleur, J. C.; and Girodroux-Lavigne, P.: A Semi-Implicit and Unsteady Numerical Method of Viscous-Inviscid Interaction for Transonic Separated Flow. La Recherche Aerospatiale, 1984–1, English and French editions (1984), pp. 15–37.

99. LeBalleur, J. C.; and Girodroux-Lavigne, P.: A Viscous-Inviscid Interaction Method for Computing Unsteady Transonic Separation. Proc. 3rd Symposium on Numerical and Physical Aspects of Aerodynamic Flows, ed. by T. Cebici, Springer-Verlag, 1986, pp. 5–49. (Also ONERA TP 1985–5, 1985).

100. Lee, E. M.; and Batina, J. T.: Conical Euler Simulation and Active Suppression of Delta Wing Rocking Motion, Presented at the High-Angle-of-Attack Technology Conference, NASA Langley Research Center, Hampton, Virginia, October 30–November 1, 1990, Also NASA TM 102683, October 1990.

101. Lee, E. M.; and Batina, J. T.: Unsteady Euler Methodology for Unsteady Vortical Flows About Rolling Delta Wings, AIAA Paper No. 91–0730, January 1991.

THIS DOCUMENT PROVIDED BY THE ABBOTT AEROSPACE
TECHNICAL LIBRARY
ABBOTTAEROSPACE.COM

102. Liu, D. D.; Kao, Y. F.; and Fung, K.-Y.: Transonic Equivalent Strip Method for Aeroelastic Applications, Proceedings of the 2nd International Symposium on Aeroelasticity and Structural Dynamics, 1985, pp. 17–32.

103. Liu, D. D.; Kao, Y. F.; and Fung, K.-Y.: An Efficient Method for Computing Unsteady Transonic Aerodynamics of Swept Wings with Control Surfaces, AIAA Paper No. 85–4058, October, 1985.

104. Liu, D. D.; Lee, H. W.; and Chen, P. C.: Unsteady Subsonic Aerodynamics for Bodies and Wings with External Stores Including Wake Effect, Paper 91–060, International Forum on Aeroelasticity and Structural Dynamics, Aachen, FRG, June 3–5, 1991.

105. Mabey, D. G.; and Chambers, J. R.: Unsteady Aerodynamics – Fundamentals and Applications to Aircraft Dynamics, AGARD-AR-222, 1986.

106. Mabey, D. G.: A Review of Some Recent Research on Time-Dependent Aerodynamics. Aeronautical Journal, February, 1984, pp. 23–37.

107. Mabey, D. G.: Physical Phenomena Associated with Unsteady Transonic Flows, Chapter 1 in Unsteady Transonic Aerodynamics, ed. by D. Nixon, Vol. 120 of AIAA Progress in Astronautical and Aeronautics, 1989, pp. 1–55.

108. Magnus, R.; and Yoshihara, H.: The Transonic Oscillating Flap, AIAA Paper No. 76–327, July 1976.

109. Malone, J. B.; and Sankar, L. N.: Numerical Simulation of Two-Dimensional Unsteady Transonic Flows Using the Full Potential Equation. AIAA Journal, Vol. 22, No. 8, August 1984, pp. 1035–1041.

110. Meijer, J. J.; and Zwann, R. J.: Investigation of a Semi-Empirical Method to Predict Limit Cycle Oscillations of Modern Fighter Aircraft, AGARD CP-483, April, 1990.

111. Mortchelewitez, G. D.; and Sans, A. S.: Solution of 3D Euler Equations with Unstructured Meshes for Aeroelasticity Problems, Paper 91–066, International Forum on Aeroelasticity and Structural Dynamics, Aachen, FRG, June 3–5, 1991

112. Mulak, P.; Meurzec, J. L.; and Angelini, J. J.: Extension and Use of Numerical Procedure for the Three Dimensional Unsteady Transonic Flows, Proceedings of the 2nd International Symposium on Aeroelasticity and Structural Dynamics, 1985, pp. 62–70.

113. Myers, M. R.; Guruswamy, P.; and Goorjian, P. M.: Flutter Analysis of a Transport Wing Using XTRAN3S, AIAA Paper No. 83–0922, 1983.

114. Mykytow, W. J.: Transonic Unsteady Aerodynamics and its Aeroelastic Applications, AGARD-CP-374, Addendum 1, June 1985.

115. Nakamichi, J.: Calculations of Unsteady Navier-Stokes Equations Around an Oscillatory 3–D Wing Using Moving Grid System, AIAA Paper No. 87–1158, June 1987.

116. Nayfeh, A. H.; Elzebda, J. M.; and Mook, D. T.: Analytical Study of the Subsonic Wing-Rock Phenomenon for Slender Delta Wings. Journal of Aircraft, Vol. 26, No. 9, September 1989, pp. 805–809.

117. Newsome, R. W.; and Kandil, O. A.: Vortical Flow Aerodynamics – Physical Aspects and Numerical Simulation, AIAA Paper No. 87–0205, January 1987.

118. Obayashi, S.; and Guruswamy, G. P.: Unsteady Shock-Vortex Interaction on a Flexible Delta Wing, AIAA Paper No. 91–1109, April 1991.

119. Ominsky, D.; and Ide, H.: An Effective Flutter Control Method Using Fast, Accurate CFD codes, AIAA Paper No. 89–3468, August 1989.

120. Pearcy, H. H.; Haines, A. B.; and Osborne, J.: The Interaction Between Local Effects at the Shock and Real Separation, Paper No. 11 in Transonic Aerodynamics, AGARD-CP No. 356, 1968.

121. Petiau, C.; and Brun, S.: Tendances Actuelles De L'Analyse Aeroelastique Des Avions Militaires, Paper No. 2 in Static Aeroelastic Effects on High Performance Aircraft, AGARD-CP-403, 1986.

122. Pirzadeh, S.; and Whitfield, D. L.: Three-Dimensional Unsteady Transonic Viscous-Inviscid Interaction Using the Euler and Boundary-Layer Equation, AIAA Paper No. 88–2578, June 1988.

123. Pitt, D. M.; Fuglsang, D. F.; and Drouin, D. V.: Applications of XTRAN3S and CAP-TSD to Fighter Aircraft, AIAA Paper No. 90–1035, April 1990.

124. Rausch, R. D.; Batina, J. T.; and Yang, H. T. Y.: Spatial Adaption Procedures on Unstructured Meshes for Accurate Unsteady Aerodynamic Flow Computation, AIAA Paper No. 91–1106, April 1991.

125. Reisenthel, P. H.; and Nixon, D.: Prediction of Unsteady Separated Transonic Flow Around Missile Configurations, AIAA Paper No. 91–0601, January 1991.

126. Rivera, J. A., Jr.; Dansberry, B. E.; Farmer, M. G.; Eckstrom, C. V.; Seidel, D. A.; and Bennett, R. M.: Experimental Flutter Boundaries with Unsteady Pressure Distributions for the NACA 0012 Benchmark Model, AIAA Paper No. 91–1010, April 1991.

127. Rizk, Y. M.; Schiff, L. B.; and Gee, K.: Numerical Simulation of the Viscous Flow Around a Simplified F/A-18 at High Angles of Attack, AIAA Paper No. 90–2999, August 1990.

128. Rizk, Y. M.; and Gee, K.: Numerical Prediction of the Unsteady Flowfield Around the F-18 Aircraft at Large Incidence, AIAA Paper No. 91–0020, January 1991.

129. Rizzetta, D. P.: Procedures for the Computation of Unsteady Transonic Flows Including Viscous Effects, NASA CR 166249, January 1982.

THIS DOCUMENT PROVIDED BY THE ABBOTT AEROSPACE
TECHNICAL LIBRARY
ABBOTTAEROSPACE.COM

130. Robinson, B. A.; Batina, J. T.; and Yang, H. T. Y.: Aeroelastic Analysis of Wings Using the Euler Equations with a Deforming Mesh, AIAA Paper No. 90–1032, April 1990.

131. Rodden, W. P.; Giesing, J. P.; and Kalman, T. P.: New Developments and Applications of the Subsonic Doublet-Lattice Method for Nonplanar Configurations, Paper No. 4 in the Symposium on Unsteady Aerodynamics for Aeroelastic Analyses of Interfering Surfaces, AGARD CP-80–71, Part 2, 1971.

132. Rodman, L. C.; Nixon, D.; and Huttsell, L. J.: Modifications to Transonic Flow Codes for Unsteady Perturbations Around an Experimental Mean. Journal of Aircraft, Vol. 26, No. 8, August 1989, pp. 765–771.

133. Rowe, W. S.; and Cunningham, H. J.: On the Convergence of Unsteady Generalized Aerodynamic Forces. Journal of Aircraft, Vol. 21, No. 6, June 1984, pp. 420–427.

134. Rumsey, C. L.; and Anderson, W. K.: Some Numerical and Physical Aspects of Unsteady Navier-Stokes Computations Over Airfoils Using Dynamic Meshes, AIAA Paper No. 88–0329, January 1988.

135. Sankar, L. M.; Malone, J. B.; and Tassa, Y.: An Implicit Conservative Algorithm for Steady and Unsteady Transonic Potential Flows, AIAA Paper No. 81–1016, June 1981.

136. Sankar, L. M.; and Malone, J. B.: A Numerical Solution Procedure for Steady and Unsteady Transonic Potential Flows. Advances in Computational Transonics, Recent Advancements in Numerical Methods in Fluids, Vol. IV, W. G. Habashi, Editor; Pineridge Press, 1985.

137. Sankar, L. M.; Ruo, S. Y.; and Malone, J. B.: Application of Surface Transpiration in Computational Aerodynamics. AIAA Paper No. 86–0511, January 1986.

138. Schippers, J.: Numerical Integration of the Unsteady Full-Potential Equation with Applications of Transonic Flow about a 2D Airfoil, NLR MP 84022 U, 1984.

139. Schuster, D. M.; Vadyak, J.; and Atta, E.: Static Aeroelastic Analysis of Fighter Aircraft Using a Three-Dimensional Navier-Stokes Algorithm. Journal of Aircraft, Vol. 27, No. 9, September 1990, pp. 820–825.

140. Seidel, D. A.; Bennett, R. M.; and Whitlow, W., Jr.: An Exploratory Study of Finite Difference Grids for Transonic Unsteady Aerodynamics, AIAA Paper No. 83–0503, January 1983.

141. Seidel, D. A.; Sandford, M. C.; and Eckstrom, C. V.: Measured Unsteady Transonic Aerodynamic Characteristics of an Elastic Supercritical Wing. Journal of Aircraft, Vol. 24, No. 4, April 1987, pp. 225–230.

142. Shankar, V.; Ide, H.; Gorski, J.; and Osher, S.: A Fast Time-Accurate Unsteady Full-Potential Scheme, AIAA Paper No. 85–1512, July 1985.

143. Shieh, T. H.; Schoen, J. G.; and Fung, K.-Y.: Techniques for Accurate, Efficient Computation of Unsteady Transonic Flow, AIAA Paper No. 91–0597, January 1991.

144. Silva, W. A.; and Bennett, R. M.: Using Transonic Small Disturbance Theory for Predicting the Aeroelastic Stability of a Flexible Wind-Tunnel Model, AIAA Paper No. 90–1033, April 1990. (Also NASA TM 102617, March 1990.).

145. Sotomayer, W. A.; and Borland, C. J.: Numerical Computation of Unsteady Transonic Flow About Wings with Flaps, AIAA Paper No. 85–1712, July 1985.

146. Sotomayer, W. A.; and Sankar, L. N.; and Malone, J. B.: A Comparison of Numerical Algorithms for Unsteady Transonic Flow. Computer Methods in Applied Mechanics and Engineering, Vol. 64, 1987, pp. 237–265.

147. Steger, J. L.: Implicit Finite-Difference Simulation of Flow about Arbitrary Two-Dimensional Geometries. AIAA Journal, Vol. 16, No. 7, July 1978, pp. 679–686.

148. Steger, J. L.; and Bailey, H. E.: Calculation of Transonic Aileron Buzz. AIAA Journal, Vol. 18, No. 3, March 1980, pp. 249–255.

149. Steiginga, A.; and Houwink, R.: Correlation of Experimental and Quasi-3D Theoretical Airloads on the Oscillating LANN Supercritical Wing Model, AFWAL-TR-83–3050, December 1982.

150. Thomas, J. L.; Taylor, S. L.; and Anderson, W. K.: Navier-Stokes Computations of Vortical Flows Over Low Aspect Ratio Wings, AIAA Paper No. 87–0207, January 1987.

151. Thomas, J. L.; Walters, R. W.; Reu, T.; Ghaffari, F; Weston, R. P.; and Luckring, J. M.: A Patched-Grid Algorithm for Complex Configurations Directed Towards the F/A-18 Aircraft, AIAA Paper No. 89–0121, January 1989.

152. Tijdeman, J.: Investigations of the Transonic Flow Around Oscillating Airfoils, National Aerospace Laboratory NLR, The Netherlands, NLR TR 77090U, 1978.

153. Transonic Unsteady Aerodynamics and Aeroelasticity. Proceedings from a conference at NASA Langley Research Center, May 20–22, 1987, NASA CP 3022, 1989, 2 Parts.

154. Triplett, W. E.: Pressure Measurements on Twin Vertical Tails in Buffeting Flow, AFWAL-TR-82–3015, Volume I, April 1982.

155. Unsteady Transonic Aerodynamics. ed. by Nixon, D.; Volume 120 in AIAA Progress in Astronautics and Aeronautics, 1989.

156. Vadyak, J.; and Schuster, D. M.: Navier-Stokes Simulation of Burst Vortex-Flowfields for Fighter Aircraft at High Incidence, AIAA Paper No. 89–2190, July 31–August 2, 1989.

157. Vatsa, V. N.; and Wedan, B. W.: Development of an Efficient Multigrid Code for a 3–D Navier-Stokes Equations, AIAA 89–1791, June 1989.

THIS DOCUMENT PROVIDED BY THE ABBOTT AEROSPACE
TECHNICAL LIBRARY
ABBOTTAEROSPACE.COM

158. Veldman, A. E. P.: New Quasi-Simultaneous Method to Calculate Interacting Boundary Layers. AIAA Journal, Vol. 19, No. 1, January 1981, pp. 79–85.

159. Vinh, L. S.; Edwards, J. E.; Seidel, D. A.; and Batina, J. T.: Transonic Stability and Control of Aircraft Using CFD Methods, AIAA Paper No. 88–4374, August 1988.

160. Voss, R.: Calculation of Unsteady Transonic Flow About Oscillating Wings by a Field Panel Method, Proceedings of the 3rd GAMMS Seminar, January, 1987, pp. 232–242.

161. Weatherill, W. H.; and Ehlers, F. E.: Development and Application of a Program to Calculate Transonic Flow Around an Oscillating Three-Dimensional Wing Using Finite Difference Procedures, NASA CR 181744, February 1989.

162. Whitfield, D. L.; Janus, J. M.; and Arabshahi, A.: Unsteady Euler Solutions on Dynamic Blocked Grids for Complex Configurations, AGARD CP-464, May 1989.

163. Whitlow, W., Jr.: Application of a Nonisentropic Full Potential Method to AGARD Standard Airfoils, AIAA Paper No. 88–0710, January 1988.

164. Wu, J. C.; Kaza, K. R. V.; and Sankar, L. N.: A Technique for the Prediction of Airfoil Flutter Characteristics in Separated Flow, AIAA Paper No. 87–0910, 1987.

165. Wong, Y. S.; and Lee, B. H. K.: Development of a Three Dimensional Unsteady Transonic Aerodynamics Computer Code for Flutter Analysis, Paper No. ICAS-90–1.1.4, September 1990.

166. Yates, E. C., Jr.: AGARD Standard Aeroelastic Configurations for Dynamic Response I-Wing 445.6, AGARD-R-765, July 1988.

167. Zwann, R. J.: Aeroelastic Problems of Wings in Transonic Flow, VKI Lecture Series on Unsteady Airloads and Aeroelastic Problems in Separated and Transonic Flow, Rhodes-Saint-Genese, Belgium, March 1981. (Also NLR MP 81005U).

168. Zwann, R. J.: Verification of Calculation Methods for Unsteady Airloads in the Prediction of Transonic Flow, NLR MP 84014 U, May 1984.

169. Zimmerman, H.; and Vogel, S.: Applications of Transonic Unsteady Methods for Calculation of Flutter Airloads, Proceedings of the 2nd International Symposium on Aeroelasticity and Structural Dynamics, 1985, pp. 47–61.

170. Zimmerman, H.: Comparison Between 2D Transonic Flutter Calculations in the Time and Frequency Domain, AGARD Report No. 749, October 1986.

171. Zimmerman, N. H.; Ferman, M. A.; and Yurkovich, R. N.: Prediction of Tail Buffet Loads for Design Application, AIAA Paper No. 89–1378, April 1989.

THIS DOCUMENT PROVIDED BY THE ABBOTT AEROSPACE
TECHNICAL LIBRARY
ABBOTTAEROSPACE.COM

AD-P007 795

UNSTRUCTURED-GRID METHODS DEVELOPMENT FOR UNSTEADY AERODYNAMIC AND AEROELASTIC ANALYSES

John T. Batina
Elizabeth M. Lee
William L. Kleb
NASA Langley Research Center
Hampton, Virginia 23665-5225 USA

and

Russ D. Rausch
Purdue University
West Lafayette, Indiana 47907 USA

92-16033

Summary

The current status of unstructured-grid methods development in the Unsteady Aerodynamics Branch at NASA Langley Research Center is described. These methods are being developed for unsteady aerodynamic and aeroelastic analyses. The paper first highlights the flow solvers that have been developed for the solution of the unsteady Euler equations and then gives selected results which demonstrate various features of the capability. The results demonstrate two- and three-dimensional applications for both steady and unsteady flows. Comparisons are also made with solutions obtained using a structured grid code and with experimental data to determine the accuracy of the unstructured grid methodology. These comparisons show good agreement which thus verifies the accuracy.

Introduction

Considerable progress has been made over the past two decades on developing computational fluid dynamics (CFD) methods for aerodynamic analysis.[1,2] Recent work in CFD has focused primarily on developing algorithms for the solution of the Euler and Navier-Stokes equations. For unsteady aerodynamic and aeroelastic analysis, these methods generally require that the mesh move to conform to the instantaneous position of the moving or deforming body under consideration. Many of the methods that are currently being developed assume that the mesh moves rigidly or that the mesh shears as the body deforms. These assumptions consequently limit the applicability of the procedures to rigid-body motions or small-amplitude deformations. Furthermore, these methods of solution typically assume that the computational grid has an underlying geometrical structure. As an alternative, algorithms have been developed recently which make use of unstructured grids.[3-19] In two dimensions these grids are typically made up of triangles and in three dimensions they consist of an assemblage of tetrahedra.

The unstructured grid methods have several distinct advantages over structured grid methods which make them attractive for unsteady aerodynamic and aeroelastic analyses. For example, the primary advantage of the unstructured grid methodology is the ability to easily model very complicated three-dimensional geometries such as the F/A-18 aircraft shown in Fig. 1.[9] The aircraft was modeled by including the wings with leading edge extension, horizontal and vertical tails, as well as the canopy and the fuselage. The modeling also includes engine inlets and nozzles to simulate engine power effects. With a structured grid, it is extremely difficult to achieve this level of geometrical complexity. A second advantage is that the methodology allows for a general way to move the mesh to treat realistic motions and structural deformations of complete aircraft configurations. An example of the deforming surface grid for a transport-type configuration undergoing a complete-vehicle bending motion is depicted in Fig. 2. The deforming grid capability does not involve any assumptions which limit applications to small deformations, such as the simple grid shearings done in some structured grid codes. A third advantage is that it enables in a natural way for adaptive mesh refinement to predict more accurately the physics for the flow. For example, shown in Fig. 3 is a conical vortex-dominated flow solution for a flat plate delta wing at a supersonic freestream Mach number.[13] The solution was obtained by adapting the original coarse mesh three times to the instantaneous flow. The final result is a highly accurate solution of the Euler equations, produced by using an order of magnitude fewer grid points than if a globally fine mesh was used. Similar to spatial adaption, temporal adaption may also be employed with unstructured grids for unsteady problems to resolve more accurately and efficiently the physics of the flow in time.[18] Temporal adaption can be thought of as time-accurate local time-stepping where smaller time steps are used in grid cells where the temporal gradients are large and larger time steps are used in cells where the gradients are small. Time accuracy is maintained by bringing all grid cells to the same time level as determined by the largest step size in the problem.

The purpose of the paper is to describe the current status of unstructured-grid methods development within the Unsteady Aerodynamics Branch at NASA Langley Research Center.[10-19] The paper first highlights the flow solvers that have been developed for solution of the time-dependent Euler equations and then gives selected results which demonstrate various features of the capability. The flow solvers that are described are either of the central-difference-type with explicit artificial dissipation or of the upwind-type which are naturally dissipative. Both implicit and explicit temporal discretizations are discussed for the time-integration of the governing fluid flow equations. Details on the spatial and temporal adaption procedures are also

THIS DOCUMENT PROVIDED BY THE ABBOTT AEROSPACE
TECHNICAL LIBRARY
ABBOTTAEROSPACE.COM

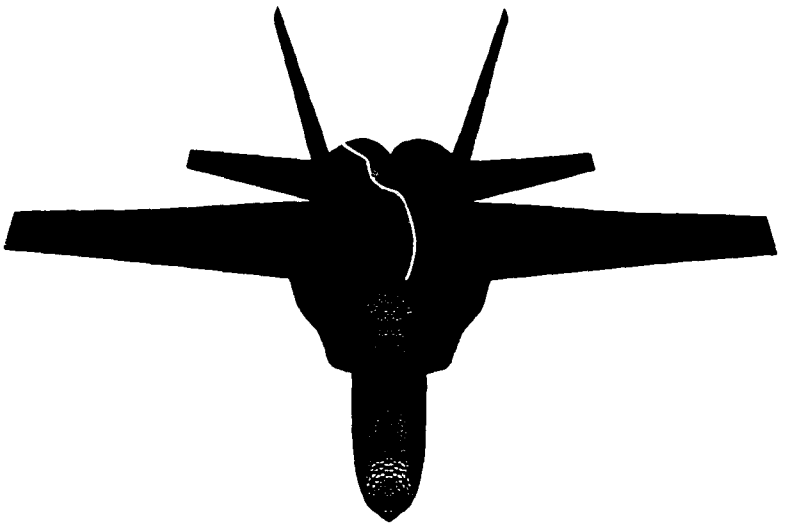


Fig. 1 Unstructured surface grid for F/A-18 fighter configuration.

given. The selected results that are presented demonstrate two- and three-dimensional applications for both steady and unsteady flows. Comparisons are also made with solutions obtained using a structured grid code and with experimental data to determine the accuracy of the unstructured grid methodology.

Central-Difference-Type Flow Solver

The unsteady Euler equations in integral form are solved using a finite-volume algorithm that was developed for use on unstructured grids of triangles in 2D or tetrahedra in 3D.[10–14] The algorithm reduces conceptually to central differencing on a rectangular mesh and thus is referred to as a central-difference-type flow solver. With this solver, artificial dissipation is added explicitly to prevent oscillations near shock waves and to damp high-frequency uncoupled error modes. Specifically, an adaptive blend of harmonic and biharmonic operators is used, corresponding to second and fourth difference dissipation, respectively. The biharmonic operator provides a background dissipation to damp high frequency errors and the harmonic operator prevents oscillations near shock waves.

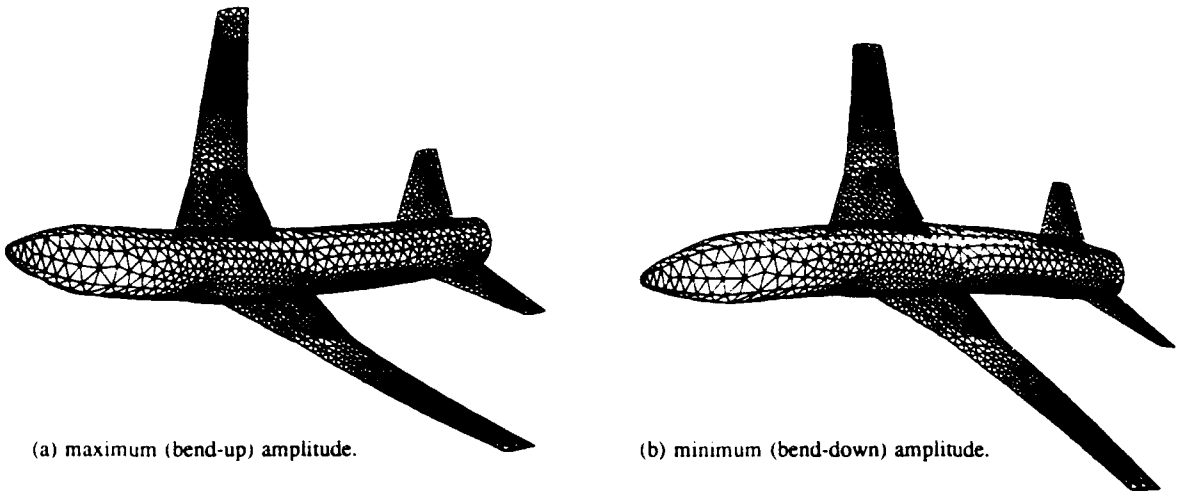
The Euler equations are integrated in time using a standard, explicit, four-stage, Runge-Kutta time-stepping scheme. In this scheme the convective operator is evaluated at each stage and, for computational efficiency, the dissipative operator is evaluated only at the first stage. The scheme is second-order-accurate in time and includes the necessary terms to account for changes in cell volumes due to a moving or deforming mesh. Furthermore, this explicit-scheme has a step size that is limited by the Courant-Friedricks-Lewy (CFL) condition corresponding to a CFL number of $2\sqrt{2}$. To accelerate convergence to steady-state, the CFL number may be increased by averaging implicitly the residual with values at neighboring grid points. These implicit equations are solved approximately using several Jacobi iterations. Convergence to steady-state is further accelerated using enthalpy damping and local time stepping. The local time stepping uses the maximum allowable step size at each grid point as determined by a local stability analysis. For unsteady applications, however, a global time step is usually used because of the time-accuracy requirement. The maximum allowable global time step may be increased to a value that is larger than that dictated by the CFL condition by using a time accurate version of the residual smoothing. Alternatively, temporal adaption may be used which involves a spatially varying time step, as described in a subsequent section.

Upwind-Type Flow Solver

The unsteady Euler equations may be solved alternatively by using upwind differencing and either flux-vector or flux-difference splitting similar to upwind schemes developed for use on structured meshes.[10, 15–19] The present unstructured grid algorithm is thus referred to as an upwind-type flow solver. The spatial discretization of this solver involves a so-called flux-split approach based on either the flux-vector splitting of van Leer[20] or the flux-difference splitting of Roe.[21] These flux-split discretizations account for the local wave-propagation characteristics of the flow and they capture shock waves sharply with at most one grid point within the shock structure. A further advantage is that these discretizations are naturally dissipative and consequently do not require additional artificial dissipation terms or the adjustment of free parameters to control the dissipation.

The Euler equations are integrated in time using either an explicit Runge-Kutta method (described in the previous section) or an implicit time-integration scheme involving a Gauss-Seidel relaxation procedure.[15] The procedure is implemented by reordering the elements that make up the unstructured mesh from upstream to downstream. The solution is obtained by sweeping two times through the mesh as dictated by stability considerations. The first sweep is performed in the direction from upstream to downstream and the second sweep is from downstream to upstream. For purely supersonic flows the second sweep is unnecessary. This relaxation scheme is unconditionally stable and thus allows the selection of the step size based on temporal accuracy of the problem being considered, rather than on the numerical stability of the algorithm. Consequently, very large time steps may be used for rapid convergence to steady state, and an appropriate step size may be selected for unsteady cases, independent of numerical stability issues.

THIS DOCUMENT PROVIDED BY THE ABBOTT AEROSPACE
TECHNICAL LIBRARY
ABBOTTAEROSPACE.COM



(a) maximum (bend-up) amplitude.

(b) minimum (bend-down) amplitude.

Fig. 2 Surface grid for the Pathfinder I configuration which illustrates how the mesh moves for an assumed complete-vehicle bending mode.

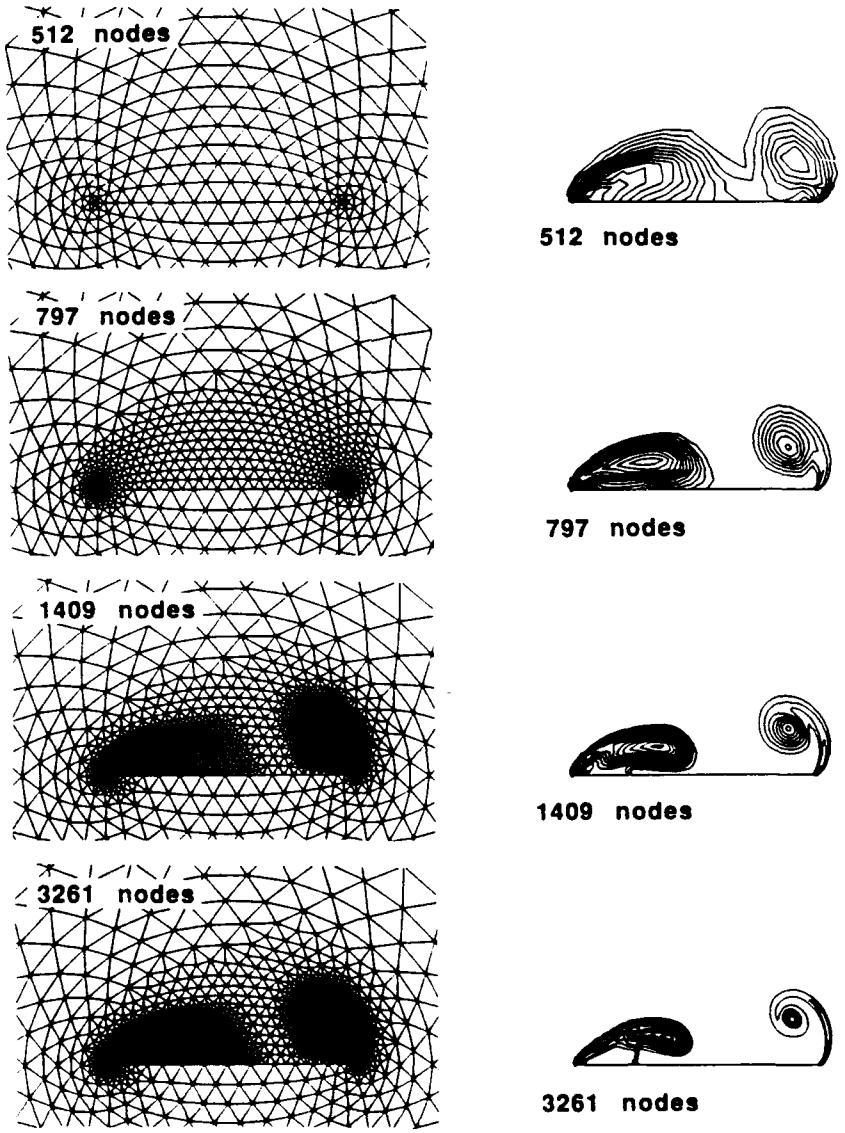


Fig. 3 Effects of adaptive mesh refinement on the total pressure loss contours for a 75° swept flat-plate delta wing computed using the conical Euler equations at $M_\infty = 1.4$, $\alpha = 20°$, and $\beta = 10°$.

THIS DOCUMENT PROVIDED BY THE ABBOTT AEROSPACE
TECHNICAL LIBRARY
ABBOTTAEROSPACE.COM

Spatial Adaption Procedure

Spatial adaption is employed with the unstructured grid flow solvers to enrich the mesh locally in regions of high spatial flow gradients to resolve more accurately and efficiently the physics of the flow.[13] Equally attractive are coarsening techniques that remove elements from regions where relatively small changes in the flow variables occur. Both enrichment and coarsening procedures are currently being developed.[19] However, only the enrichment procedure is described herein. The enrichment procedure uses an indicator to determine if an element in the mesh is to be refined or subdivided into smaller elements. Typically, the absolute change in density along an edge is used as an indicator for flows with shock waves and total pressure loss is used for flows with vortices. More recently a refinement indicator based on the material derivative of density[19] has been shown to be a superior indicator for unsteady flows. In general, the refinement indicator is compared with a preset tolerance to determine whether a given element should be refined. If the tolerance is exceeded, a new node is created at the midpoint of the edge and the element is divided. Each time the mesh is refined, an element may be divided in one of several different ways. The coordinates of the new node are determined by averaging the coordinates of the endpoints that make up the bisected edge. Special care must be taken, however, when an edge that is to be divided lies on a boundary of the grid, since the midpoint of the edge does not generally lie on the boundary. In this case, the location of the new node is determined generally by using a spline of the boundary coordinates.

Temporal Adaption Procedure

Temporal adaption is employed with the unstructured grid flow solvers, similar to spatial adaption, to resolve more accurately and efficiently the physics of the flow in time.[18] Temporal adaption can be thought of as time-accurate local time-stepping. Local time-stepping is typically used in a non-time-accurate manner to accelerate the convergence of the governing fluid flow equations to steady-state. Since only steady-state is desired, it does not matter that every point in the flow is at a different time. This, of course, is not the case for a time-accurate problem, since each point in the flow for such a calculation must be on the same temporal level to maintain time-accuracy. The problem is that if all of the grid cells are marched at the same time step with an explicit time-marching scheme, the most restrictive time step must be used in order to maintain numerical stability. Temporal adaption is a method to march each cell at its own time step, although ultimately the flow variables in all cells reach the same point in time. Temporal adaption can be viewed as similar to spatial adaption in that small time steps should be taken only in localized areas governed by the flow physics and not in the entire flow field. Typically, small grid cells are integrated with small time steps and large grid cells are integrated with large time steps. All of the cells reach the same time level $n + 1$ to maintain time-accuracy by using local time steps that are multiples of one another. The solution is integrated in a special sequence so that all values necessary for the calculations at an intermediate level are available at the proper times. For a particular cell to be integrated from time level n to time level $n + 1$, for example, the solution must also be known at its neighboring cells at time level n. If the value needed for the integration is unknown at a particular temporal node, it is determined from a linear interpolation between two known values.

Deforming Mesh Algorithm

For problems where the aircraft moves or deforms, the mesh must move so that it continuously conforms to the instantaneous shape or position of the vehicle. This is accomplished by using a spring network to model the original mesh such that each edge of the triangle or tetrahedron is represented by a spring.[12] The spring stiffness for a given edge is taken to be inversely proportional to the length of the edge. Grid points on the outer boundary of the mesh are held fixed and the instantaneous locations of the points on the inner boundary (aircraft) are given by the prescribed surface motion. At each time step, the static equilibrium equations in the x, y, and z directions, which result from a summation of forces, are solved iteratively at each interior node of the grid for the displacements. This is accomplished by using a predictor-corrector procedure, which first predicts the displacements of the nodes by extrapolation from grids at previous time levels and then corrects these displacements using several Jacobi iterations of the static equilibrium equations. The predictor-corrector procedure has been found to be more efficient than simply performing Jacobi iterations because far fewer iterations are required to achieve acceptable convergence. In practice it has been found that only one or two iterations are sufficient to accurately move the mesh.

Results and Discussion

Selected results from the unstructured-grid methods of Refs. 10–19 are presented for two- and three-dimensional geometries for both steady and unsteady flows. Comparisons are made with solutions obtained using a structured grid code and with experimental data to determine the accuracy of the methodology.

Two-Dimensional Euler Results

To assess the two-dimensional central-difference-type Euler flow solver, calculations were performed for the NACA 0012 airfoil.[11] These results were obtained using the unstructured grid shown in Fig. 4. The grid has 3300 nodes, 6466 triangles, and extends 20 chordlengths from the airfoil with a circular outer boundary. Also there are 110 points that lie on the airfoil surface. Generalized aerodynamic forces for the NACA 0012 airfoil oscillating in either plunge or pitch-about-the quarter-chord

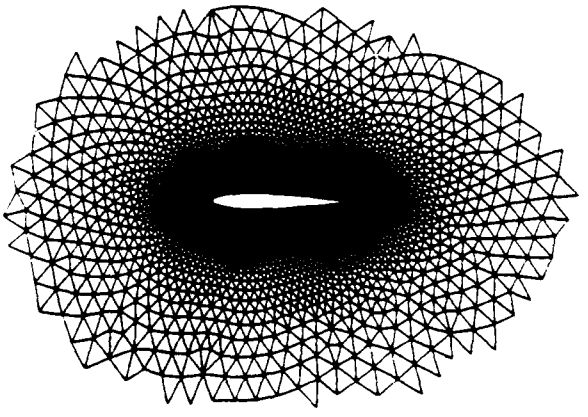
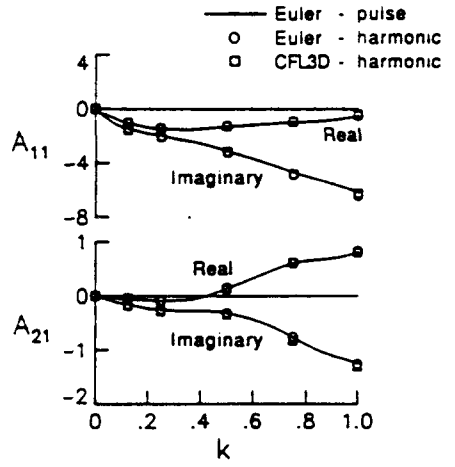
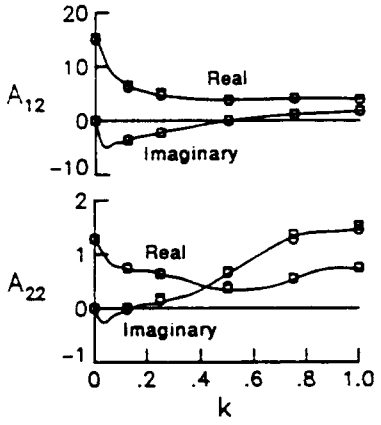


Fig. 4 Partial view of unstructured grid of triangles about the NACA 0012 airfoil.

THIS DOCUMENT PROVIDED BY THE ABBOTT AEROSPACE
TECHNICAL LIBRARY
ABBOTTAEROSPACE.COM



(a) due to plunge.



(b) due to pitch.

Fig. 5 Comparisons of generalized aerodynamic forces computed using CFL3D and the unstructured-grid central-difference-type Euler flow solver for the NACA 0012 airfoil at $M_\infty = 0.8$ and $\alpha_o = 0°$.

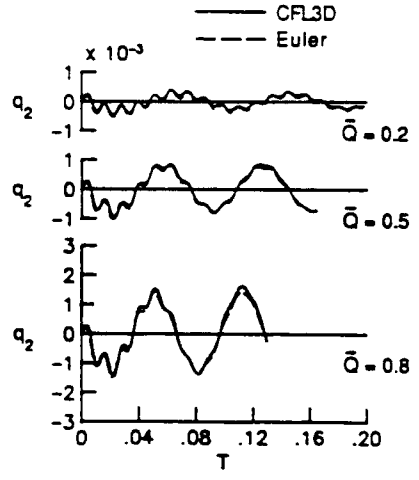
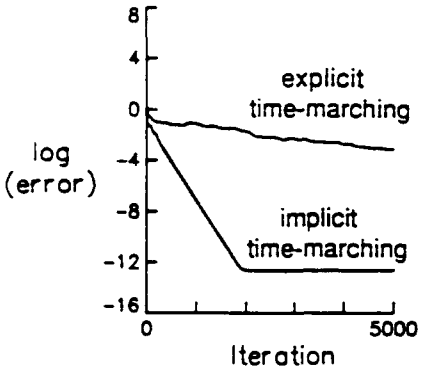
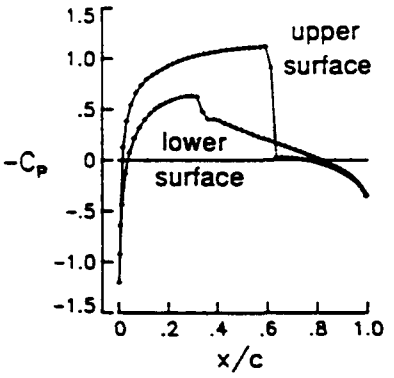


Fig. 6 Comparisons of generalized displacements computed using CFL3D and the unstructured-grid central-difference-type Euler flow solver for the NACA 0012 airfoil at $M_\infty = 0.8$ and $\alpha_o = 0°$.



(a) convergence histories.



(b) steady pressure distribution.

Fig. 7 Comparisons of steady-state results for the NACA 0012 airfoil at $M_\infty = 0.8$ and $\alpha_o = 1.25°$ computed using the upwind-type Euler flow solver with flux-vector splitting.

are shown in Fig. 5. For this case the freestream Mach number was $M_\infty = 0.8$ and the angle of attack was $\alpha_o = 0°$. Comparisons are given among results obtained using the so-called pulse transfer-function analysis, the harmonic analysis, and a harmonic analysis performed using a structured grid Navier-Stokes code (CFL3D) run in an Euler mode. The three sets of results agree well with one another, for both plunge and pitch motions, thus verifying the accuracy of the unstructured grid method.

Aeroelastic results were also obtained for the NACA 0012 airfoil with two degrees-of-freedom (pitch and plunge) at M_∞= 0.8 and $\alpha_o = 0°$.[11] Comparisons of second mode generalized displacements (q_2) are shown in Fig. 6 for three values of nondimensional dynamic pressure ($\bar{Q}$) that bracket the flutter point. The generalized displacements agree well with the structured grid (CFL3D) solution which verifies the unstructured grid methodology for aeroelastic analysis. The flutter speed for this case, determined by interpolation of the dominant damping of these generalized displacements, also agrees to within 2% of the CFL3D value.

THIS DOCUMENT PROVIDED BY THE ABBOTT AEROSPACE
TECHNICAL LIBRARY
ABBOTTAEROSPACE.COM

To test the more-recently-developed upwind-type Euler flow solver, steady flow results were obtained for the NACA 0012 airfoil at $M_\infty = 0.8$ and $\alpha_o = 1.25°$, using both implicit and explicit time-marching.[15] The explicit time-marching results were obtained using a CFL number of 2.5 and the implicit time-marching results were obtained using a CFL number of 100,000. A comparison of the convergence histories is shown in Fig. 7(a) and the resulting steady pressure distribution is shown in Fig. 7(b). The "error" in the solution was taken to be the L_2–norm of the density residual. As shown, the explicit solution is very slow to converge whereas the implicit solution is converged to four orders of magnitude in only approximately 500 steps. Also, the pressure distributions indicate that there is only one grid point within the shock structure, on either the upper or lower surface of the airfoil, due to the sharp shock capturing ability of the flux splitting. Converged steady solutions are thus obtained with the implicit algorithm with an order of magnitude less CPU time than the explicit algorithm, and the shock waves are more sharply captured with the flux-split spatial discretization than the central-difference-type discretization. These improvements in accuracy and efficiency are also realized for unsteady applications.

Conical Euler Results

Calculations were performed using the conical Euler version of the central-difference-type flow solver to investigate unsteady vortex-dominated flows about highly-swept delta wings.[14] This code includes the additional analysis of the free-to-roll case by the inclusion of the rigid-body equation of motion for simultaneous time integration with the governing flow equations. Results were obtained for a 75° swept delta wing at a freestream Mach number of 1.2 and an angle of attack of 30°. A partial view of the grid which was used is shown in Fig. 8. The grid, which has a total of 4226 nodes and 8299 elements, indicates that the wing has thickness and sharp leading edges.

Figure 9 shows the free-to-roll response of the wing which was initiated by using an initial angular velocity. In this calculation, for simplicity, the mesh was moved to conform to the instantaneous position of the wing by rotating rigidly according to the wing roll angle, rather than by using the deforming mesh algorithm. The results indicate that initially the oscillatory response diverges for small values of roll angle. As the angle increases to around 35°, the rate of divergence decreases due to stabilizing aerodynamics, and finally, the response reaches a maximum amplitude of motion at $\phi = 38°$ corresponding to a limit cycle. These results are similar in nature to those obtained by Arena and Nelson[22] in a low-speed experimental investigation of wing rock. The wing-rock time history from Ref. 22, shown in Fig. 10, was obtained for an 80° swept delta wing at 30° angle of attack. Although the case considered in Fig. 9 is different from that of Ref. 22 (the data from Ref. 22 are for low speed flows whereas the conical Euler code is limited to supersonic freestream applications), the similarity between the two sets of results in Figs. 9 and 10 is noteworthy and gives credibility to the present calculations.

Three-Dimensional Euler Results

Unsteady flow results were obtained for a supersonic fighter configuration that was oscillating in a complete-vehicle bending mode to demonstrate a three-dimensional application of the central-difference-type Euler solver.[12] The results were obtained using a grid which has 13,832 nodes and 70,125 tetrahedra. The surface triangulation of the aircraft is shown in Fig. 11(a) and the bending mode shape (exaggerated by a factor of five) is shown in Fig. 11(b). Instantaneous pressure distributions on the surface of the vehicle at the maximum (bend-up) and minimum (bend-down) amplitudes of oscillation are shown in Fig. 12. For this case the freestream Mach number was 2.0, the reduced frequency (based on wing tip semi-chord) was 0.1, and two angles of attack of 0 and 12 degrees were considered. The results of Fig. 12 show the effects of angle of attack on unsteady pressures, and clearly demonstrate that the unstructured grid methodology can treat complex aircraft configurations undergoing structural deformation.

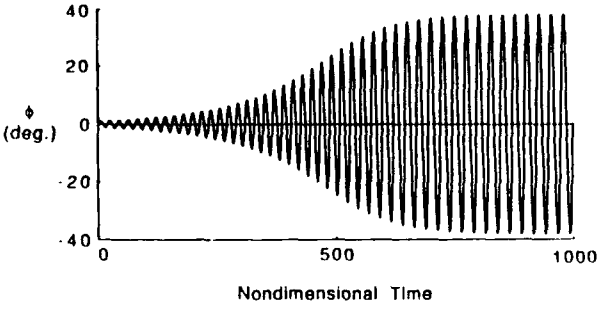


Fig. 9 Free-to-roll time history for a 75° swept delta wing at $M_\infty = 1.2$ and $\alpha = 30°$.

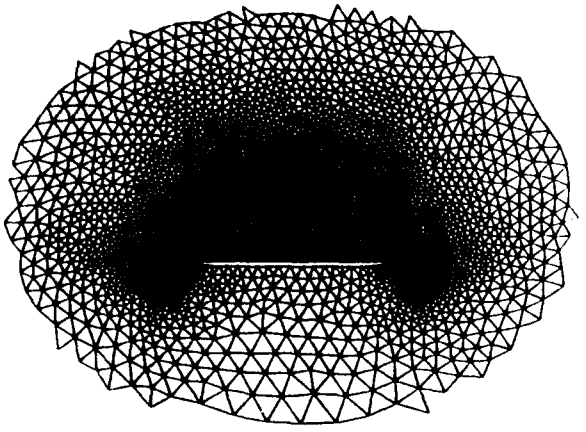


Fig. 8 Partial view of unstructured grid about a 75° swept delta wing.

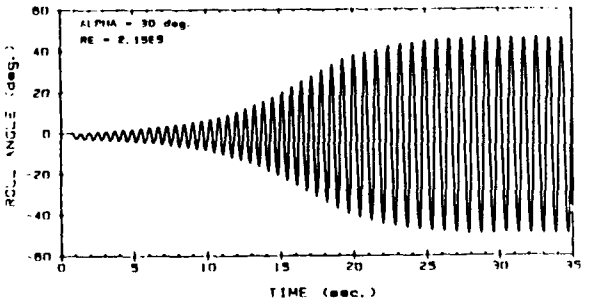
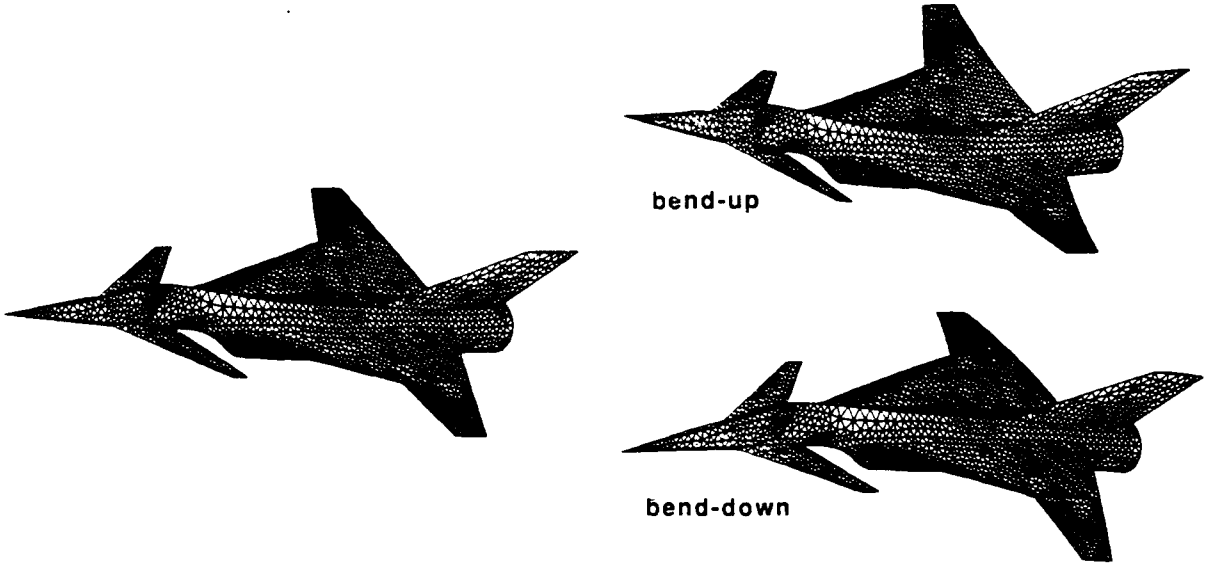


Fig. 10 Wing-rock time history for an 80° swept delta wing at 30° angle of attack (Ref. 22, reprinted with permission from Professor Robert C. Nelson, Notre Dame University).

THIS DOCUMENT PROVIDED BY THE ABBOTT AEROSPACE
TECHNICAL LIBRARY
ABBOTTAEROSPACE.COM

To test the more-recently-developed upwind-type Euler flow solver, calculations were performed for the ONERA-M6 wing.[16] The M6 wing has a leading edge sweep angle of 30°, an aspect ratio of 3.8, and a taper ratio of 0.562. The airfoil section of the wing is the ONERA "D" airfoil which is a 10% maximum thickness-to-chord ratio conventional section. The results were obtained using a grid which has 42,410 nodes and 231,507 tetrahedra. Results were obtained for the M6 wing at a freestream Mach number of 0.84 and 3.06° angle of attack. These conditions were chosen for comparison with the experimental pressure data of Ref. 23 as shown in Fig. 13. The results indicate that there is a weak supersonic-to-supersonic



(a) original surface grid. (b) assumed bending mode.

Fig. 11 Surface grid for the Langley supersonic fighter configuration.

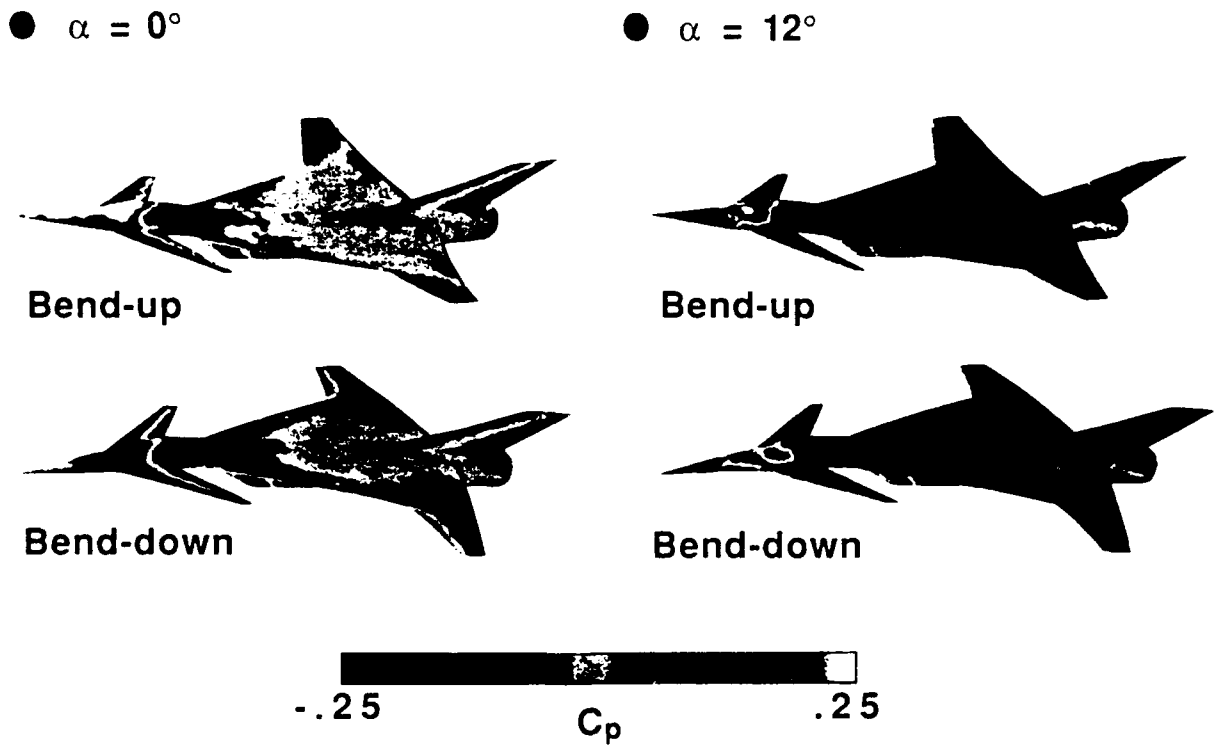


Fig. 12 Effects of angle of attack on the instantaneous pressure coefficient contours on the Langley fighter configuration at the maximum (bend-up) and minimum (bend-down) amplitudes of deformation computed using the central-difference-type Euler flow solver at M_∞ = 2.0 and k = 0.1.

THIS DOCUMENT PROVIDED BY THE ABBOTT AEROSPACE
TECHNICAL LIBRARY
ABBOTTAEROSPACE.COM

shock wave in the inboard region, forward toward the leading-edge. The primary, supersonic-to-subsonic shock which occurs in the midchord region coalesces with the first shock in the outboard direction toward the wing tip. Near the tip, the two shocks merge to form a single, strong, supersonic-to-subsonic shock wave. The Euler results are in fairly good agreement with the experimental pressure data, especially in predicting the strength and location of the shock waves, which tends to verify the upwind-type algorithm. The shocks are sharply captured with only one grid point within the shock structure, due to the flux splitting.

Spatial Adaption Results

To demonstrate the spatial adaption procedures, results are obtained for the NACA 0012 airfoil pitching harmonically about the quarter chord.[19] The freestream Mach number was 0.755 and the mean angle of attack was 0.016°. The pitching amplitude was 2.51° and the reduced frequency (based on semi-chord) was 0.0814. Figure 14 shows the instantaneous adapted meshes and Fig. 15 shows the corresponding instantaneous density contour lines ($\Delta\rho$ = 0.02). The instantaneous meshes and density contour lines during the third cycle of motion were plotted at eight points in time. In each plot, the instantaneous pitch angle $\alpha(\tau)$ and the instantaneous angular position $k\tau$ in the cycle are noted. The instantaneous meshes (Fig. 14) clearly indicate the enrichment in regions near the shock waves and near the stagnation points. They also show coarsened regions where previously enriched regions have relatively small flow gradients. The density contours during the cycle (Fig. 15) demonstrate the ability of the spatial adaption procedures to produce sharp transient shock waves.

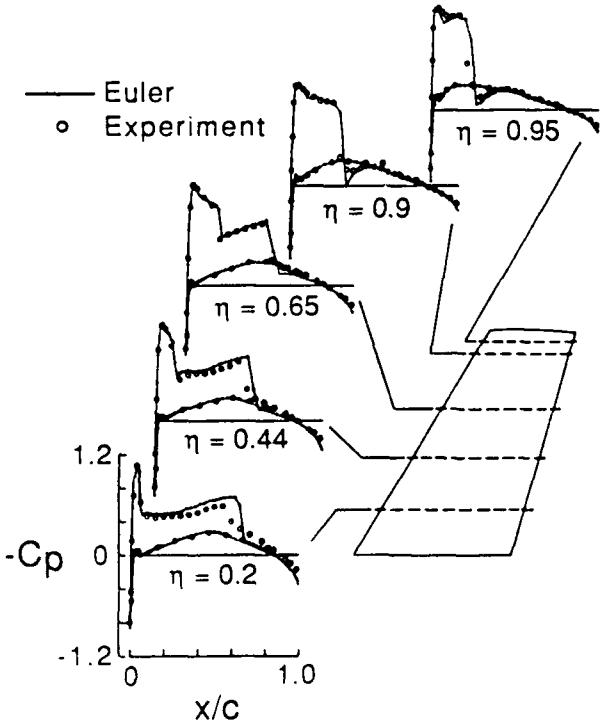


Fig. 13 Comparisons of steady pressure distributions for the ONERA M6 wing computed using the upwind-type Euler flow solver with flux-vector splitting at M_∞ = 0.84 and α_o = 3.06°.

Temporal Adaption Results

To demonstrate the efficiency of temporal adaption over global time-stepping for unsteady problems, results were obtained for the same NACA 0012 pitching airfoil case of the previous section.[18] Figure 16 shows calculated results obtained using temporal adaption and global time-stepping as well as comparisons with the experimental pressure data of Ref. 24. In each pressure plot the instantaneous pitch angle $\alpha(\tau)$ and the angular position in the cycle $k\tau$ are noted. During the first part of the cycle there is a shock wave on the upper surface of the airfoil, and the flow over the lower surface is predominately subcritical. During the latter part of the cycle the flow about the upper surface is subcritical, and a shock forms along the lower surface. The pressure distributions indicate that the shock position oscillates over approximately 25% of the chord along each surface, and in general, that the two sets of calculated results compare well with each other. This good agreement verifies the time-accuracy of the solution computed using temporal adaption, which was obtained at one-fourth of the CPU time that the global time-stepping solution required. Both sets of calculated results also agree well with the experimental data.

Concluding Remarks

The current status of unstructured-grid methods development in the Unsteady Aerodynamics Branch at NASA Langley Research Center was described. These methods are being developed for unsteady aerodynamic and aeroelastic analyses. The paper highlighted the flow solvers that have been developed for the solution of the unsteady Euler equations and gave selected results which demonstrated various features of the capability. The results demonstrated two- and three-dimensional applications for both steady and unsteady flows. Comparisons of two-dimensional steady and unsteady results were made with solutions obtained using a structured grid code and with experimental data to determine the accuracy of the two dimensional flow solvers. Comparisons of three-dimensional steady results were also made with experimental data to determine the accuracy of the three-dimensional flow solver. These comparisons showed good agreement which thus verifies the accuracy of the unstructured grid methods.

Acknowledgements

The authors acknowledge Ken Morgan of the University College of Swansea, UK, and Jaime Peraire of the Imperial College of Science, Technology, and Medicine, London, UK, for providing meshes for the F/A-18 and Langley fighters, and for providing the two-dimensional grid generation program that was used to generate meshes for the delta wing cross section and the NACA 0012 airfoil. The authors also acknowledge Rainald Lohner, George Washington University, Washington, D. C., and Paresh Parikh, ViGYAN Research Associates, Hampton, Virginia, for providing meshes for the Pathfinder I configuration and M6 wing, and for providing the two-dimensional grid generation program that was used to generate meshes for the NACA 0012 airfoil.

References

1. Jameson, A.: "Successes and Challenges in Computational Aerodynamics," AIAA Paper No. 87-1184, January 1987.

THIS DOCUMENT PROVIDED BY THE ABBOTT AEROSPACE
TECHNICAL LIBRARY
ABBOTTAEROSPACE.COM

2. Edwards, J. W.; and Thomas, J. L.: "Computational Methods for Unsteady Transonic Flows," AIAA Paper No. 87–0107, January 1987.

3. Jameson, A.; and Mavriplis, D. J.: "Finite Volume Solution of the Two-Dimensional Euler Equations on a Regular Triangular Mesh," AIAA Journal, vol. 24, April 1986, pp. 611–618.

4. Mavriplis, D. J.: "Multigrid Solution of the Two-Dimensional Euler Equations on Unstructured Triangular Meshes," AIAA Journal, vol. 26, July 1988, pp. 824–831.

5. Jameson, A.; Baker, T. J.; and Weatherill, N. P.: "Calculation of Inviscid Transonic Flow Over a Complete Aircraft," AIAA Paper No. 86–0103, January 1986.

6. Morgan, K.; and Peraire, J.: "Finite Element Methods for Compressible Flow," Von Karman Institute for Fluid Dynamics Lecture Series 1987–04, Computational Fluid Dynamics, March 2–6, 1987.

7. Lohner, R.: "Finite Elements in CFD: What Lies Ahead," International Journal of Numerical Methods in Engineering, vol. 24, 1987, pp. 1741–1756.

8. Morgan, K.; Peraire, J.; Thareja, R. R.; and Stewart, J. R.: "An Adaptive Finite Element Scheme for the Euler and

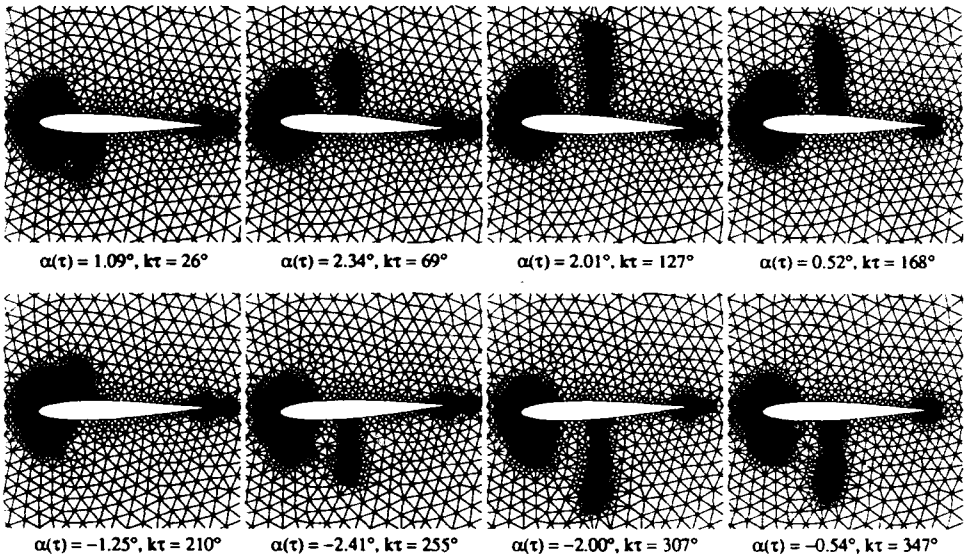


Fig. 14 Instantaneous meshes produced by the spatial adaption procedure for the NACA 0012 airfoil pitching harmonically at $M_\infty = 0.755$, $\alpha_o = 0.016°$, $\alpha_1 = 2.51°$, and k = 0.0814.

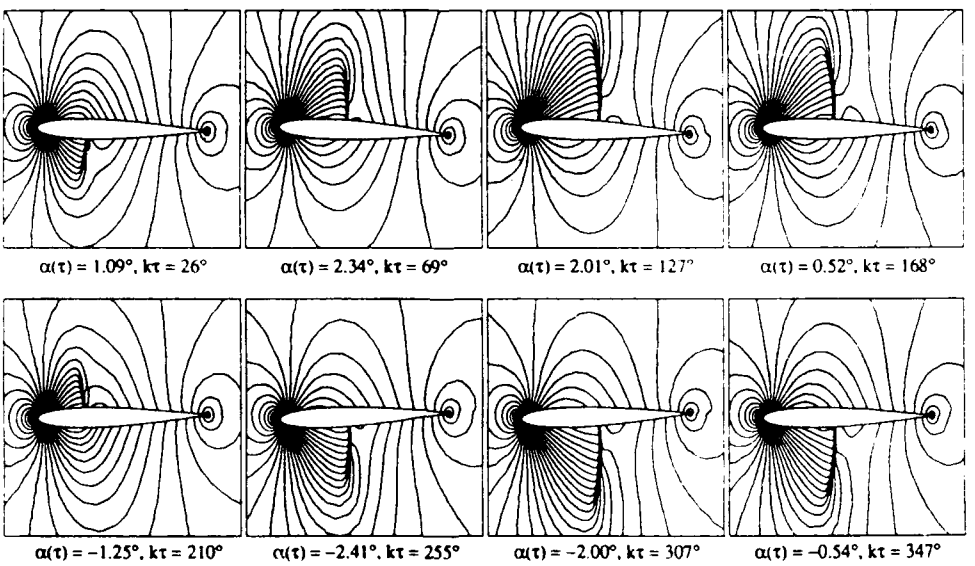


Fig. 15 Instantaneous contour lines ($\Delta\rho = 0.02$) from the spatially adapted solution for the NACA 0012 airfoil pitching harmonically at $M_\infty = 0.755$, $\alpha_o = 0.016°$, $\alpha_1 = 2.51°$, and k = 0.0814.

THIS DOCUMENT PROVIDED BY THE ABBOTT AEROSPACE
TECHNICAL LIBRARY
ABBOTTAEROSPACE.COM

Navier-Stokes Equations," AIAA Paper No. 87–1172, 1987.

9. Peraire, J.; Peiro, J.; Formaggia, L.; and Morgan, K.: "Finite Element Euler Computations in Three Dimensions," AIAA Paper No. 88–0032, January 1988.

10. Batina, J. T.: "Unsteady Euler Airfoil Solutions Using Unstructured Dynamic Meshes," AIAA Paper No. 89–0115, January 1989.

11. Rausch, R. D.; Batina, J. T.; and Yang, H. T. Y.: "Euler Flutter Analysis of Airfoils Using Unstructured Dynamic Meshes," AIAA Paper No. 89–1384, April 1989.

12. Batina, J. T.: "Unsteady Euler Algorithm with Unstructured Dynamic Mesh for Complex-Aircraft Aeroelastic Analysis," AIAA Paper No. 89–1189, April 1989.

13. Batina, J. T.: "Vortex-Dominated Conical-Flow Computations Using Unstructured Adaptively-Refined Meshes," AIAA Paper No. 89–1816, June 1989.

14. Lee, E. M.; and Batina, J. T.: "Conical Euler Solution for a Highly-Swept Delta Wing Undergoing Wing-Rock Motion," NASA TM 102609, March 1990.

15. Batina, J. T.: "Implicit Flux-Split Euler Schemes for Unsteady Aerodynamic Analysis Involving Unstructured Dynamic Meshes," AIAA Paper No. 90–0936, April 1990.

16. Batina, J. T.: "Accuracy of an Unstructured-Grid Upwind-Euler Algorithm for the ONERA M6 Wing," presented at the Accuracy of Unstructured Grid Techniques Workshop, NASA Langley Research Center, Hampton, Virginia, January 16–17, 1990.

17. Batina, J. T.: "Three-Dimensional Flux-Split Euler Schemes Involving Unstructured Dynamic Meshes," AIAA Paper No. 90–1649, June 1990.

18. Kleb, W. L.; Batina, J. T.; and Williams, M. H.: "Temporal Adaptive Euler/Navier-Stokes Algorithm for Unsteady Aerodynamic Analysis of Airfoils Using Unstructured Dynamic Meshes," AIAA Paper No. 90–1650, June 1990.

19. Rausch, R. D.; Batina, J. T.; and Yang, H. T. Y.: "Spatial Adaption Procedures on Unstructured Meshes for Accurate Unsteady Aerodynamic Flow Computation," AIAA Paper No. 91–1106, April 1991.

20. Van Leer, B.: "Flux-Vector Splitting for the Euler Equations," Lecture Notes in Physics, vol. 170, 1982, pp. 507–512.

21. Roe, P. L.: "Approximate Riemann Solvers, Parameter Vectors, and Difference Schemes," Journal of Computational Physics, vol. 43, 1981, pp. 357–372.

22. Arena, A. S.; and Nelson, R. C.: "The Effect of Asymmetric Vortex Wake Characteristics on a Slender Delta Wing Undergoing Wing Rock Motion," AIAA Paper No. 89–3348, August 1989.

23. Schmitt, V.; and Charpin, F.: "Pressure Distribution on the ONERA M6 Wing at Transonic Mach Numbers," Appendix B1 in AGARD-AR-138, Experimental Data Base for Computer Program Assessment, May 1979.

24. Landon, R. H.: "NACA 0012. Oscillating and Transient Pitching," Data Set 3 in AGARD-R-702, Compendium of Unsteady Aerodynamic Measurements, August 1982.

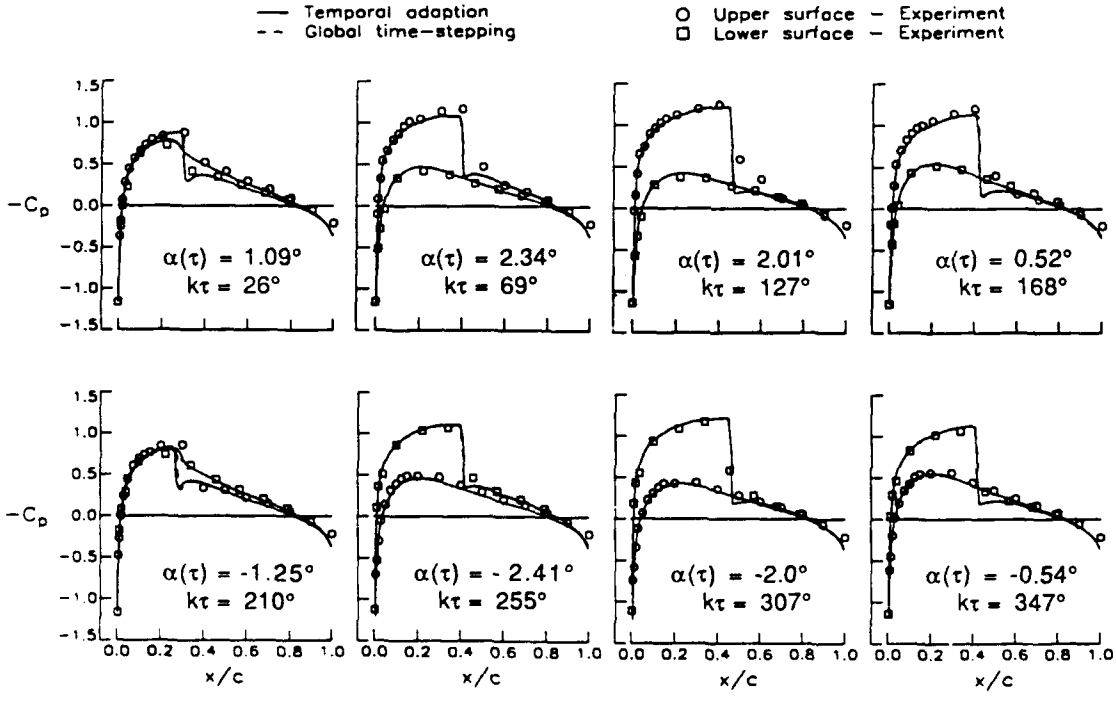


Fig. 16 Comparison of instantaneous pressure distributions for the NACA 0012 airfoil pitching harmonically at $M_\infty = 0.755$, $\alpha_o = 0.016°$, $\alpha_1 = 2.51°$, and $k = 0.0814$ computed using the upwind-type Euler flow solver with flux-vector splitting.

THIS DOCUMENT PROVIDED BY THE ABBOTT AEROSPACE
TECHNICAL LIBRARY
ABBOTTAEROSPACE.COM

AD-P007 796

UNSTEADY AERODYNAMICS FOR AEROELASTICITY AT THE FLIGHT DYNAMICS DIRECTORATE

M. Blair
L. J. Huttsell
W. A. Sotomayer
T. M. Harris

Aeroelasticity Group
Structures Division
Flight Dynamics Directorate
USAF Wright Laboratory
Wright-Patterson AFB, Ohio
45433-6553
United States

SUMMARY

This paper presents an overview of the recent in-house and contractual efforts in the area of transonic unsteady aerodynamics for aeroelasticity at the Flight Dynamics Directorate of the USAF Wright Laboratory. Three major topics are addressed. The first topic, analytical unsteady aerodynamics, involves the application of both transonic small disturbance and Euler/Navier-Stokes codes to fighter-type aircraft. Aeroelastic calculations made with these codes are compared with test results. The second topic involves a description of unsteady pressure testing in the NLR tunnel in The Netherlands. Finally, the plan for incorporating transonic unsteady aerodynamics into structural redesign is presented.

LIST OF SYMBOLS

C	local chord
CP	pressure coefficient
E, F, G	Eulerian flux matrices
E_v, F_v, G_v	viscous flux vectors
J	Jacobian of transformation from (x, y, z) space to (ξ, η, ζ) space
k	nondimensional time scaling
M	Mach number
Q	solution vector
u, v, w	cartesian velocity components
α	angle of attack
γ	ratio of specific heats
η	fractional semispan
μ	viscosity at temperature T
μ_0	viscosity at reference temperature T_0
ξ, η, ζ	curvilinear coordinates
Φ	perturbation potential

1 INTRODUCTION

The charter of the Aeroelasticity Group of the Flight Dynamics Directorate, USAF Wright Laboratory, is to develop the technology required to predict aeroelastic behavior and prevent aeroelastic instabilities on USAF flight vehicles. In so doing, the group advances the state of the art through both contracted and in-house research in such fields as unsteady aerodynamics, flutter prediction, aeroelastic design methods, and aeroservoelastic analysis.

Possession of accurate, reliable unsteady aerodynamic information is fundamental to achieving advanced aeroelastic design and analysis techniques. High speed flight is accompanied by the presence of complex flow phenomena that must be considered. Among these are the effects of moving shock waves, shock/boundary layer interaction, vortices, and separated flow. The following sections describe the work which is ongoing, both sponsored on contract and through in-house manpower, in the area of unsteady aerodynamic research. The first topic, analytical unsteady aerodynamics, involves various applications of both transonic small disturbance and Euler/Navier-Stokes codes to fighter-type configurations. Aeroelastic calculations made with these codes are compared with test results. The second topic involves a description of testing in the NLR tunnel in The Netherlands, in which the Aeroelasticity Group has helped to sponsor the measurement of unsteady pressure data on a rigid, pitching F-16 wing/store model. Finally, the plan for incorporating transonic unsteady aerodynamics into structural redesign is presented.

2 DESCRIPTION OF ANALYTICAL METHODS

The following paragraphs describe the three non-linear aerodynamic methods and one linear structural optimization method currently being employed.

92-16034

THIS DOCUMENT PROVIDED BY THE ABBOTT AEROSPACE
TECHNICAL LIBRARY
ABBOTTAEROSPACE.COM

XTRAN3S and CAP-TSD

The XTRAN3S [Ref 1] and CAP-TSD [Ref 2] codes solve the time-accurate Transonic Small Disturbance (TSD) equations using finite-difference techniques. The TSD equation is given as

$$\begin{aligned} & M^2\left(k^2\Phi_{tt} + 2k\Phi_{xt}\right)_t \\ & = \left[\left(1 - M^2\right)\Phi_x + F\Phi_x^2 + G\Phi_y^2\right]_x \\ & \quad + \left(\Phi_y + H\Phi_x\Phi_y\right)_y + \left(\Phi_z\right)_z \end{aligned} \tag{1}$$

Depending upon the assumptions used in deriving the TSD equation, several choices are available for the coefficients F, G, and H. The NASA/Ames coefficients are defined as:

$$F = -\frac{1}{2}(\gamma + 1)M^2 \tag{2a}$$

$$G = \frac{1}{2}(\gamma - 3)M^2 \tag{2b}$$

$$H = -(\gamma - 1)M^2 \tag{2c}$$

The surface boundary condition for the TSD equation is flow tangency at the wing surface and is satisfied on the mean chord plane instead of on the actual upper and lower surface. For unsteady flow the boundary condition on the wing surface is

$$\Phi_z^{\pm} = f_x^{\pm} + kf_t \tag{3}$$

where $f^{\pm}$ is the nondimensional description of the local airfoil surface ordinates, with + denoting the upper surface and - denoting the lower surface.

The TSD equation is transformed so that a swept-tapered wing can be analyzed by using a finite-difference mesh that is aligned with the leading and trailing edge of the wing. The XTRAN3S code solves the transformed TSD equation using a time-accurate Alternating Direction Implicit (ADI) finite difference scheme. The CAP-TSD code uses a time-accurate Approximate Factorization (AF) algorithm to solve the TSD equations. The aeroelastic solution procedure implemented within both XTRAN3S and CAP-TSD computer codes integrates the TSD Equation (1) in a time-accurate manner in conjunction with the linear structural equations of motion.

ENS3DAE

Until recently, aerodynamic calculations for transonic flow could only be made with numerical methods based on potential theory. This is sufficient for some regions of transonic flow, but not for situations involving vortices or separated flow. Hence, a need exists to numerically compute three dimensional unsteady transonic flows with viscous effects.

Computer program ENS3DAE (Euler/Navier Stokes 3 Dimensional AEroelastic) was developed by Lockheed under an Air Force contract [Ref 3]. As the name implies, the program is based on a numerical solution of the Euler or Navier-Stokes three-dimensional equations coupled with a set of linear structural dynamic equations.

For unsteady, compressible flow, the Navier-Stokes equations are expressible in conservation law form, in curvilinear coordinates, as:

$$Q_t + E_\xi + F_\eta + G_\zeta = \left(\tilde{E}_v\right)_\xi + \left(\tilde{F}_v\right)_\eta + \left(\tilde{G}_v\right)_\zeta \tag{4}$$

where:

$$Q = J^{-1}\begin{Bmatrix}\rho\\ \rho u\\ \rho v\\ \rho w\\ e\end{Bmatrix}, \; E = J^{-1}\begin{Bmatrix}\rho U\\ \rho uU+\xi_x p\\ \rho vU+\xi_y p\\ \rho wU+\xi_z p\\ U(e+p)-\xi_t p\end{Bmatrix}, \tag{5}$$

$$F = J^{-1}\begin{Bmatrix}\rho V\\ \rho uV+\eta_x p\\ \rho vV+\eta_y p\\ \rho wV+\eta_z p\\ V(e+p)-\eta_t p\end{Bmatrix}, \; G = J^{-1}\begin{Bmatrix}\rho W\\ \rho uW+\zeta_x p\\ \rho vW+\zeta_y p\\ \rho wW+\zeta_z p\\ W(e+p)-\zeta_t p\end{Bmatrix}.$$

and contravariant velocity vectors are given by:

$$\begin{aligned} U &= \xi_t + \xi_x u + \xi_y v + \xi_z w \\ V &= \eta_t + \eta_x u + \eta_y v + \eta_z w \\ W &= \zeta_t + \zeta_x u + \zeta_y v + \zeta_z w \end{aligned} \tag{6}$$

The viscous flux terms appearing in (4) are:

$$\begin{aligned} \tilde{E}_v &= J^{-1}(\xi_x E_v + \xi_y F_v + \xi_z G_v) \\ \tilde{F}_v &= J^{-1}(\eta_x E_v + \eta_y F_v + \eta_z G_v) \\ \tilde{G}_v &= J^{-1}(\zeta_x E_v + \zeta_y F_v + \zeta_z G_v) \end{aligned} \tag{7}$$

ENS3DAE solves either the Reynolds-averaged Navier-Stokes equations or the thin-shear-layer Navier-Stokes equations. By setting the right hand side of (4) to zero, numerical solution of the Euler equations is obtained. Equation (4) is solved numerically using a Beam-Warming type of algorithm [Refs 4-6]. This algorithm uses an ADI time accurate solution scheme [Ref 4]. A general coordinate transformation of the form

$$\begin{aligned} \tau &= t \\ \xi &= \xi(x,y,z,t) \\ \eta &= \eta(x,y,z,t) \\ \zeta &= \zeta(x,y,z,t) \end{aligned} \tag{8}$$

is applied to the numerically generated grid. This allows the non-uniformity in physical space to be replaced by a uniform-

THIS DOCUMENT PROVIDED BY THE ABBOTT AEROSPACE
TECHNICAL LIBRARY
ABBOTTAEROSPACE.COM

ly spaced mesh in computational space. This, in turn, allows the ADI solution to be efficiently accomplished as a sequence of spatial sweeps on the computational mesh.

Numerical solution of the Navier-Stokes equations requires that viscous effects be accounted for. The kinematic viscosity of most gases, including air, increases considerably as the temperature is increased [Refs 7 and 8]. For the case of air, it is possible to use an interpolation formula based on D. M. Sutherland's theory of viscosity. This can be written as

$$\frac{\mu}{\mu_0} = \left(\frac{T}{T_0}\right)^{\frac{3}{2}} \frac{T_0 + S_1}{T + S_1} \qquad (9)$$

where μ_0 is the viscosity at the reference temperature T_0 and S_1 is a constant which is 198.6°R for air. Laminar thermal conductivity is determined using μ and the laminar Prandtl number Pr.

For turbulent viscous flow, viscosity is computed using the Baldwin-Lomax turbulence model in which viscosity is based on the two layer formulation described in Reference 9.

Grids are generated by a program known as CAMP (Complete Aircraft Mesh Program) [Ref 3]. CAMP uses a zonal H-grid topology to model aircraft configurations composed of combinations of wing, fuselage, canard, horizontal and vertical tail surfaces. CAMP makes use of a combination of two- and three-dimensional algebraic, parabolic, and elliptic grid generation techniques to define grid point spacing. For the wing, a 2-D scheme is used to generate a streamwise grid section. These sections are then stacked spanwise to develop a 3-D grid. For the wing block the grid is generated by first defining the surface geometry. These surfaces are defined by reading airfoil section geometry at a number of defining stations, splitting the sections and distributing points streamwise at each section. The functions used to distribute points are the hyperbolic sine and tangent functions [Ref 10]. After boundary conditions have been defined at each spanwise grid section, the grid generation scheme from Reference 11 is used to generate the field grids.

Initially, ENS3DAE was tested and applied by the contractor to generic wing-body vehicles and to models of fighter aircraft [Ref 3]. Reference 3 also presents numerical computations for a generic wing-body configuration developed by Lockheed. Comparisons between test results and computations were favorable for the steady state cases considered.

ASTROS

For structural analysis and optimization, computer program ASTROS is employed. ASTROS (Automated STRuctural Optimization System) [Ref 12] is a multidisciplinary software system that can be used in the preliminary design of aerospace structures. The Flight Dynamics Directorate contracted with Northrop Corporation and Universal Analytics to provide the aerospace community with a proven structural design capability. The structural members of aerospace designs can be rapidly sized with multiple boundary conditions and constraints including structural stress limits and minimum flutter speed limits. All the structural and aerodynamic models are based on linear theory.

3 APPLICATIONS AND RESULTS

Application of ENS3DAE to F-15

Twin tailed fighter aircraft operating at high angles of attack can encounter severe oscillations of the vertical tails. Vortices impinge on the surfaces, and the accompanying pressure fluctuations cause the oscillations. The result is poor performance and structural fatigue problems.

The original ENS3DAE code was capable of performing analysis only on a single, centerline-mounted vertical tail. Under contract, Georgia Tech Research Institute extended the capabilities of the code to model twin tail configurations. A full configuration F-15 model with faired over engine inlets was used as a check case.

The surface grid generated for an Euler analysis is shown in Figure 1. This grid contained five zones with a total of 376,832 grid points. For the Navier-Stokes test case, a grid which clustered points near the wing and tail surfaces was necessary to capture the boundary layer near the surface. This grid had a total of 435,712 points. These grids were somewhat coarse so that the execution time remained relatively low, but were still detailed enough to compute surface conditions for this configuration.

One of the validation cases was performed for a Mach number of 0.6 and an angle of attack of 8.66°. The Navier-Stokes computation at 1000 iterations is shown in the following figures. Figure 2 shows the computed steady wing surface pressures and test data at two wing stations (η =.429 and .696). The correlation is shown to be very good. Figure 3 shows the computed pressure on the vertical tail at 40 and 80 percent span. In this case, no test data was available for comparison.

Application of ENS3DAE to F-5 Wing

To independently test the applicability of ENS3DAE to wings typical of fighter configurations, in-house numerical experiments were undertaken. As a test case a model of the F-5 wing, as pictured in Figure 4, was selected. This model was wind tunnel tested previously by NLR of the Netherlands [Ref 13]. The F-5 wing was selected because of the excellent data base which now exists for steady and unsteady flow for M = .6 to M = 1.35. These data are in the form of steady and unsteady pressure coefficients on the upper and lower wing surfaces. Also, sectional and total lift and moment coefficients are available. In the ENS3DAE analysis, an elliptic grid scheme was used with 92 grid points in the streamwise direction and 32 grid points in both the spanwise and vertical directions. The

THIS DOCUMENT PROVIDED BY THE ABBOTT AEROSPACE
TECHNICAL LIBRARY
ABBOTTAEROSPACE.COM

grid contained two zones with 94,208 points in each zone.

Steady state pressure computations for M = .80, α = 0° are shown in Figure 5 for 1200 time steps. The time history for the L-2 residual indicated virtually no change for the last 300 iterations. Hence, the steady state result was considered as having converged. Comparisons with NLR test data are shown for wing sections 2,4, and 7.

In general, numerical computations from ENS3DAE showed favorable agreement with experimental results. It should be noted that for the steady state results that there are perceptible differences between test results and theory on the inner portion of the wing. In the wind tunnel tests conducted by NLR it is to be noted that the model was attached directly to the wall of the tunnel. This, very likely, resulted in wall boundary layer effects. In general the numerical computations did agree favorably with test data.

Starting with the converged steady state result, unsteady numerical computations are now being made. Unsteady numerical computations are being performed for rigid wing oscillation about the 50% root chord at 20 Hz about a mean angle of attack of 0° with a pitch amplitude of 0.108°. These computations will be compared with the NLR test data.

Aeroelastic Analysis

The dynamic aeroelastic option of the ENS3DAE code is currently being run and evaluated. A 45° swept wing model [Ref 14] was selected as a check case. A sketch of this model is shown in Figure 6. A Mach number of 0.797 was chosen from the available test data.

First the XTRAN3S code was applied to this check case. Steady state aerodynamic calculations were performed and used as a starting solution for the static aeroelastic analyses. The static aeroelastic results were then used as a starting solution for the flutter calculations. Three vibration modes were used in these analyses. The dynamic aeroelastic solution produced three transient responses. These responses were curve fit using a series of damped sine waves to extract frequency and damping. A typical time history is shown in Figure 7 for a dynamic pressure of 1.2 psi. The experimental dynamic pressure at flutter was 1.34 psi, and the XTRAN3S prediction was 1.30.

The static aeroelastic capability of ENS3DAE has been demonstrated and documented in Reference 15 for an aeroelastically tailored wing configuration. For the 45° swept wing, the steady pressure and static aeroelastic deflection were computed and compared with XTRAN3S results, since no test data was available. For this essentially linear case, the XTRAN3S and ENS3DAE comparison was very good. The dynamic aeroelastic calculations are underway.

4 UNSTEADY PRESSURE TESTS

Fighter aircraft with high maneuverability can encounter a transonic nonlinear flutter known as Limit Cycle Oscillations (LCO). The LCO is a limited amplitude self-sustaining oscillation produced by structural/aerodynamic interaction. As part of an on-going investigation of LCO, unsteady pressure tests will be performed on an F-16 wing/store model and a straked delta wing model. This effort is partially funded by the Flight Dynamics Directorate. The testing will be performed at the National Aerospace Laboratory (NLR) in the Netherlands.

Figure 8 shows a sketch of the F-16 wing model with stores. The model will be oscillated in pitch at several different frequencies and amplitudes. Various configurations of this model will be tested over a Mach range of 0.90 to 0.96 and angles of attack of 0° to 10°. Unsteady pressure measurements will be made at 87 locations. Force and moment data will also be measured on the main wing and at the store attachments.

A simple straked delta wing (Figure 9) will be tested to study transonic unsteady vortex flow. The model will be oscillated in pitch at several different frequencies and amplitudes. The unsteady pressure distribution will be measured at Mach numbers of 0.3, 0.6, and 0.9. The Mach 0.3 test is planned to correlate with available full-span model tests data [Ref 16].

5 UNSTEADY AERODYNAMICS FOR STRUCTURAL REDESIGN

If flutter is to be a design problem, it will often be encountered at transonic speeds. Unfortunately, transonic aerodynamic calculations require significant computer resources. It is important to establish an approach to incorporate unsteady transonic aerodynamic effects in the structural redesign process and then to make the procedure more cost effective.

While many of the ingredients are in place in the Aeroelasticity Group, this design process has yet to be demonstrated. The biggest lesson learned is that CFD codes are not easy to implement and are even more difficult to modify. We do not maintain an in-house CFD code with resident authors; this creates a major difficulty. The progress achieved with the transonic redesign process is presented here.

The developers of ASTROS are interested in showing that linearized transonic aerodynamics (based on small perturbations about a steady state mean) can also be used in place of the linear unsteady aerodynamic software which is resident within the code. A test case was based on an F-16 planform taken from the open literature. The wing has no twist and a constant representative fighter airfoil. This model, as shown in Figure 10, is referred to here as the FDFD (Flight Dynamics Fighter Derivative). The FDFD wing structure is totally original with ten spars and three ribs. The fuselage is assumed rigid and is assigned a weight of 16,000 lbs. The aluminum wing structure was designed to withstand a 9.0g symmetric pullup. This resulted in a full

THIS DOCUMENT PROVIDED BY THE ABBOTT AEROSPACE
TECHNICAL LIBRARY
ABBOTTAEROSPACE.COM

span wing with structure weight of 502 lbs and a flexible to rigid ratio of 3.90/ 4.05 in lift curve slope.

Subsequent analyses were restricted to the anti-symmetric deformations. The wing design, with no additional weight, was flutter free. One may induce a flutter problem with the addition of weight due to fasteners, fuel, actuators and non-load-carrying members (eg. control surfaces). For this study, store flutter is of particular concern. Two stores were simultaneously placed on the wing. The stores selected for this study are a 2250 lb store on the rib near the midspan and a 400 lb store on the next rib outboard. The first three modes of free vibration are 0.0 Hz (rigid roll), 5.63 Hz (torsion) and 9.08 Hz (first bending). These two flexible modes are shown in Figures 11 and 12.

A flutter analysis was performed at Mach 0.85 with the ASTROS program. ASTROS uses subsonic doublet lattice theory to model lifting surface aerodynamics and uses the PK method for flutter identification. Flutter occurred at a velocity of 1136 ft/ sec at sea level density. Under standard conditions, this represents a 20% flutter margin. The flutter frequency is 4.53 Hz and the flutter mode is predominantly rigid roll and wing torsion. This is consistent with the root locus diagram, shown in Figure 13, in which the torsion mode loci go unstable independent of the other flexible modes.

The design challenge is to use a transonic aerodynamic model to resize the structure. The first step is to recreate the linear flutter phenomenon with non-linear transonic codes. The next step is to identify the critical transonic flutter problem in terms of Mach number, dynamic pressure, and angle of attack. With the flutter problem identified, the transonic redesign process can begin. At this point, the assumption is made that the unsteady transonic generalized forces can be usefully linearized in order to make use of the ASTROS design capability.

The unsteady generalized forces are perturbations superimposed on the steady state loads. For a linear aerodynamic system, one can develop a matrix of linear aerodynamic transfer functions which relate generalized motion input to generalized force output. Consistent with linear aerodynamic theory, any one transfer function can be

expressed as

$$G(s) = \sum_{i=1}^{m} \frac{A_i}{s+a_i} \qquad (a_i \neq 0) \qquad (10)$$

The input (generalized deformation) is in the form

$$f(t) = \begin{cases} 0 & t < 0 \\ \frac{A}{2}\left[1-\cos\left(\frac{\pi t}{a}\right)\right] & 0 < t < a \\ A & t > a \end{cases} \qquad (11)$$

A time domain expression for the assumed output (generalized force) can now be derived. The values of a_i are selected and the least squares method is used to obtain the best fit of the aerodynamic (CFD) response in terms of the assumed output function.

This matrix of transfer functions can be evaluated for specific values of frequency ($s=i\omega$) in order to obtain a set of harmonic aerodynamic influence coefficients, consistent with what the ASTROS computer code uses in its flutter calculations. The ASTROS code can now be used to develop a new minimum weight design which meets the minimum flutter speed requirement. Of course, if the redesigned vehicle is significantly different from the original design, the steady state condition may also be different. If this is the case, a new set of transonic aerodynamic transfer functions would be obtained for the new steady state conditions and an additional design iteration would be performed.

The CAP-TSD code [Ref 2] was chosen for an in-house analysis of the FDFD wing/body. This code favors versatility over user-friendliness. Therefore, by necessity, some effort was expended in developing an interactive preprocessor for the CAP-TSD code. The graphical output is shown in Figure 14. The graphics are generated using HOOPS software for 3-D modelling.

6 CONCLUDING REMARKS

The Aeroelasticity Group is actively involved in advancing the state of knowledge in the field of unsteady aerodynamics for aeroelastic analysis and design. Program ENS3DAE continues to be run and evaluated. The Aeroelasticity Group has recently awarded a contract to include fuselage flexibilities in the program and plans to extend the aeroelastic analysis capability of ENS3DAE to whole aircraft configurations. Also, the first test in the series of NLR unsteady pressure measurements was recently completed. Results are presented in Reference 17. The straked delta wing tests are scheduled for the spring of 1992. Supplementary efforts are underway to model the FDFD flutter problem and to obtain aerodynamic transfer functions for transonic redesign. Dr P. Guruswamy is currently working with ENSAERO, a code similar to ENS3DAE, at NASA Ames Research Center. Ms Anne Stephenson of the University of Dayton will start to work with ENSAERO soon, applying this program to transonic redesign.

In other, related, areas, the Aeroelasticity Group is supporting the design of hypersonic vehicles by designing and wind tunnel testing both transonic lifting surface models and panel flutter models. Work also continues in panel flutter analysis methods (on contract) and in aeroservoelastic analysis and aeroelastic optimization methods (in-house). Along with general improvements to the ENS3DAE code, future plans include applying ENS3DAE to the high angle of attack vertical tail buffet problem, making use of data to be measured in

THIS DOCUMENT PROVIDED BY THE ABBOTT AEROSPACE
TECHNICAL LIBRARY
ABBOTTAEROSPACE.COM

the NASA Ames Research Center's full-scale F-18 wind tunnel tests.

7 REFERENCES

1. Borland, C. J., Rizzeta, D. P., Thorne R. G., and Yeagley, L. R., "Transonic Unsteady Aerodynamics for Aeroelastic Applications", AFWAL-TR-80-3107, June 1982.

2. Batina, J. T., Seidel, D. A., Bland, S. R,. and Bennett, R. M., "Unsteady Transonic Flow Calculations for Realistic Aircraft Configurations", AIAA Paper No. 87-0850, 28th Structures, Structural Dynamics, and Materials Conference, Monterey CA, April 1987.

3. Schuster, D. M., Vadyak, J., and Atta, E. J., "Flight Loads Prediction Methods for Fighter Aircraft", WRDC-TR-89-3104, November 1989.

4. Beam, R. M. and Warming, R. F., "An Implicit Factored Scheme for the Compressible Navier-Stokes Equations", AIAA Journal, Volume 16, April 1978, pp 393-402.

5. Pulliam, T. H. and Steger, J. L., "Implicit Finite-Difference Simulations of Three-Dimensional Compressible Flow", AIAA Journal, Volume 18, February 1980.

6. Jameson, A., Schmidt, W. E., and Turkel, E., "Numerical Solutions of the Euler Equations by Finite Volume Methods Using Runge-Kutta Time-Stepping Techniques", AIAA Paper No. 81-1259, 22nd AIAA Fluid Dynamics Conference, Honolulu HI, June 1981.

7. Roache, P. J., Computational Fluid Dynamics, Hermosa Publishers, Albuquerque, New Mexico, 1976.

8. Schlichting, H., Boundary Layer Theory, McGraw-Hill Book Company, New York.

9. Baldwin, B. S., and Lomax, H., "Thin Layer Approximation and Algebraic Model for Separated Turbulent Flows", AIAA Paper No. 78-257, 16th Aerospace Sciences Conference, Pasadena, CA, January 1978.

10. Thompson, J. F., Warsi, Z. U., and Mastin, C. W., Numerical Grid Generation Foundations and Applications, North Holland Publishing Company, 1985.

11. Noack, R. W. and Anderson, D. A., "Solution Adaptive Grid Generation Using Parabolic Partial Differential Equations", AIAA Paper 88-0315, 26th Aerospace Sciences Conference, Reno NV, January 1988.

12. Neil, D. J., Johnson, E. H., and Canfield, R., "ASTROS - A Multidisciplinary Automated Structural Design Tool", Journal of Aircraft, Volume 27, December 1990.

13. Tijdeman, H., et.al., "Transonic Wind Tunnel Tests on an Oscillatory Wing with External Store", AFFDL-TR-78-194, Parts I and II, December 1978.

14. Maier, H. G. and King, S. R., "Transonic Flutter Model Tests, Part I: 45 Degree Swept Wings", WADC-TR-56-214, Part I, September 1957.

15. Schuster, D. M., Vadyak, J., and Atta, E., "Static Aeroelastic Analysis of Fighter Aircraft Using a Three-Dimensional Navier-Stokes Algorithm", Journal of Aircraft, Volume 27, Number 9, September 1990.

16. Boer, R. G. den, Dogger, C. S. G., Geurts, E. G. M., Persoon, A. J., Retel, A. P., and Zwaan, R. J., "Unsteady Low-Speed Wind Tunnel Test of a Straked Delta Wing Oscillating in Pitch", AFWAL-TR-87-3098, April 1988.

17. Cunningham, A. M. and Boer, R. G. den, "Transonic Wind Tunnel Investigations of Limit Cycle Oscillations on Fighter Type Wings", to be presented at the AGARD Specialists Meeting on Transonic Unsteady Aerodynamics and Aeroelasticity, San Diego CA, October 1991.

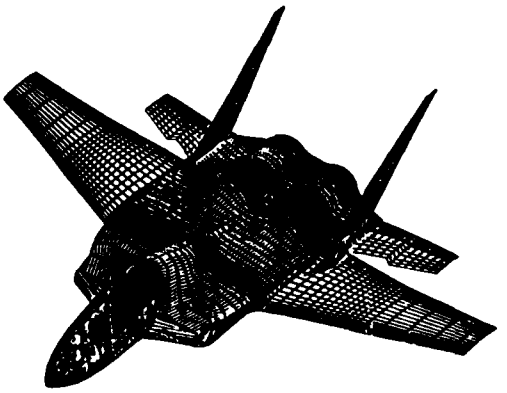


Figure 1. F-15 Euler Surface Grid

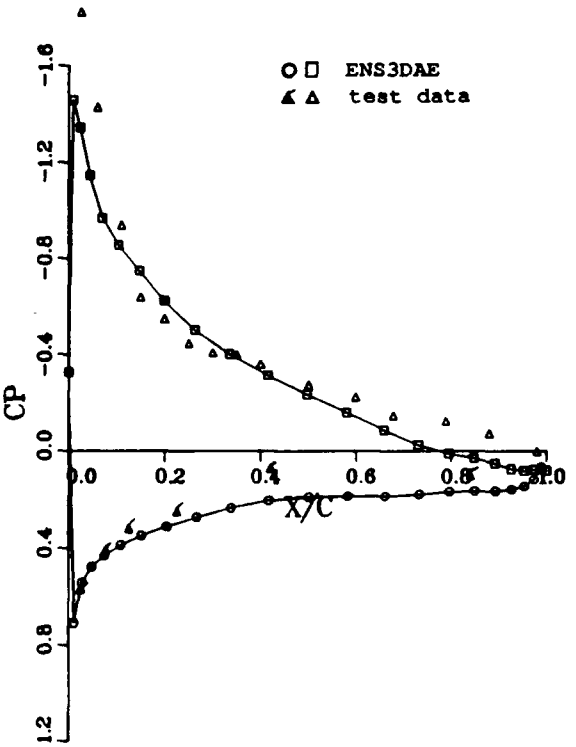


Figure 2a. Steady Pressure Distribution on F-15 Wing (M = 0.6 and α = 8.66°), 42.9% Span

THIS DOCUMENT PROVIDED BY THE ABBOTT AEROSPACE
TECHNICAL LIBRARY
ABBOTTAEROSPACE.COM

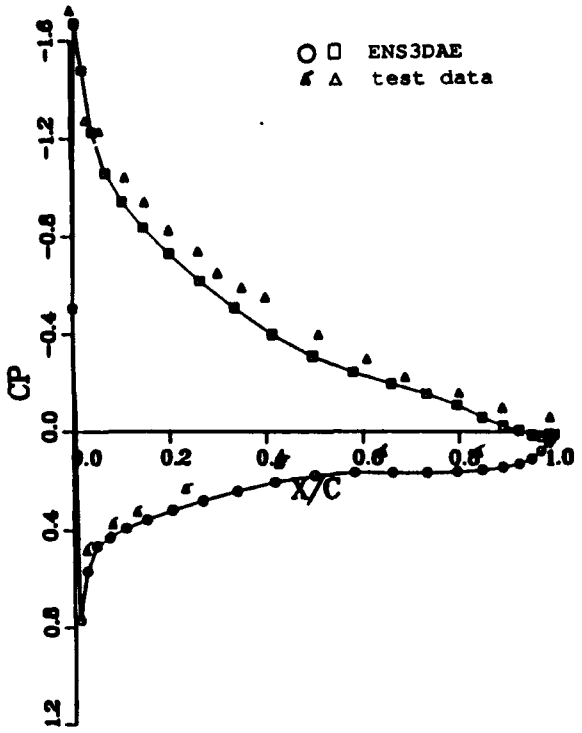


Figure 2b. Steady Pressure Distribution on F-15 Wing (M = 0.6 and α = 8.66°), 69.6% Span

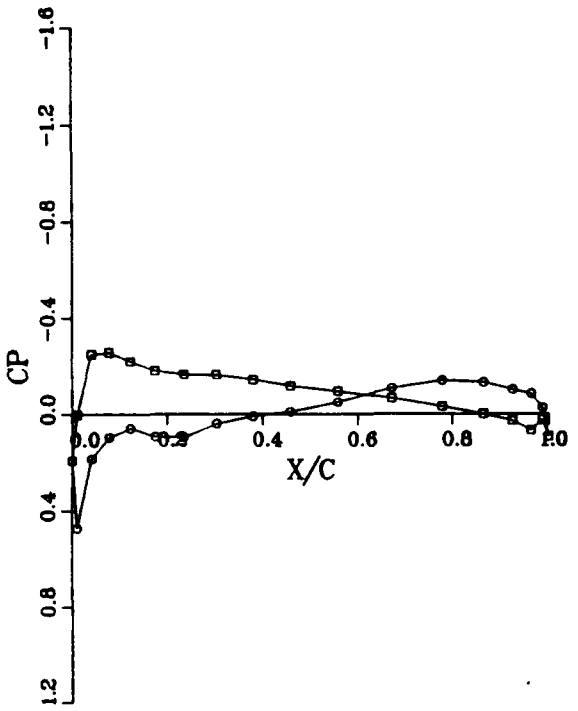


Figure 3b. Steady Pressure Distribution on F-15 Vertical Tail (M = 0.6, α = 8.66°), 80% Span

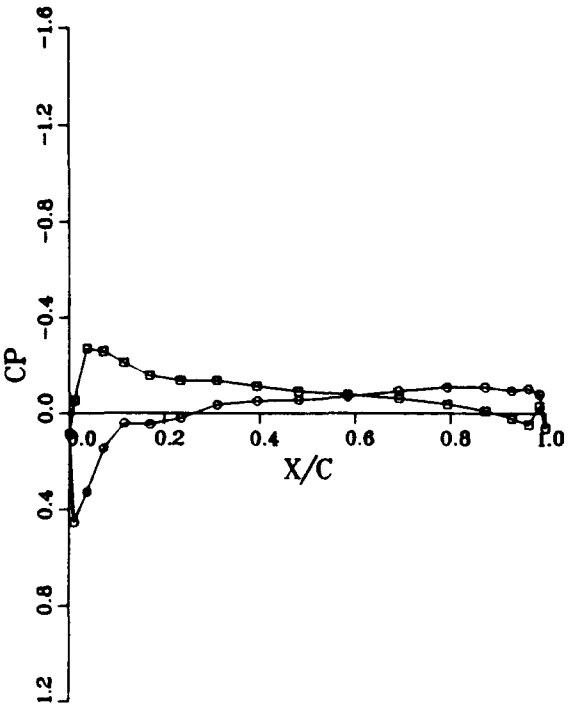


Figure 3a. Steady Pressure Distribution on F-15 Vertical Tail (M = 0.6, α = 8.66°), 40% Span

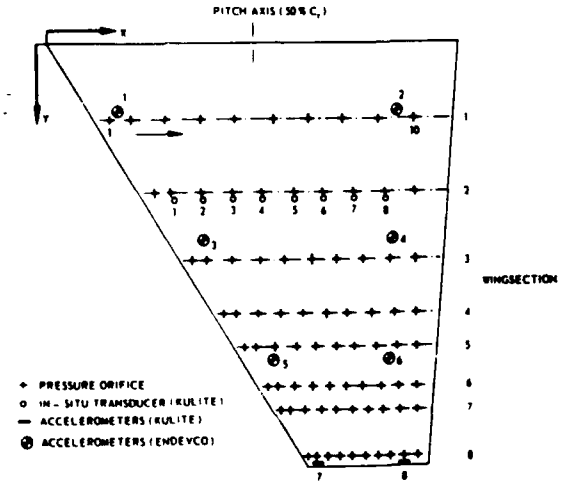


Figure 4. General Layout of F-5 Wing

THIS DOCUMENT PROVIDED BY THE ABBOTT AEROSPACE
TECHNICAL LIBRARY
ABBOTTAEROSPACE.COM

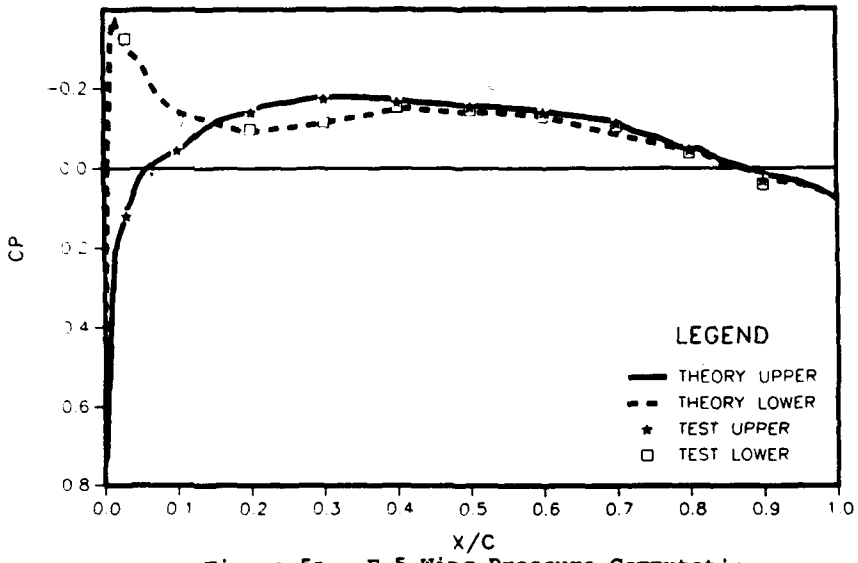


Figure 5a. F-5 Wing Pressure Computations, M = .80, Section 2, α = 0°

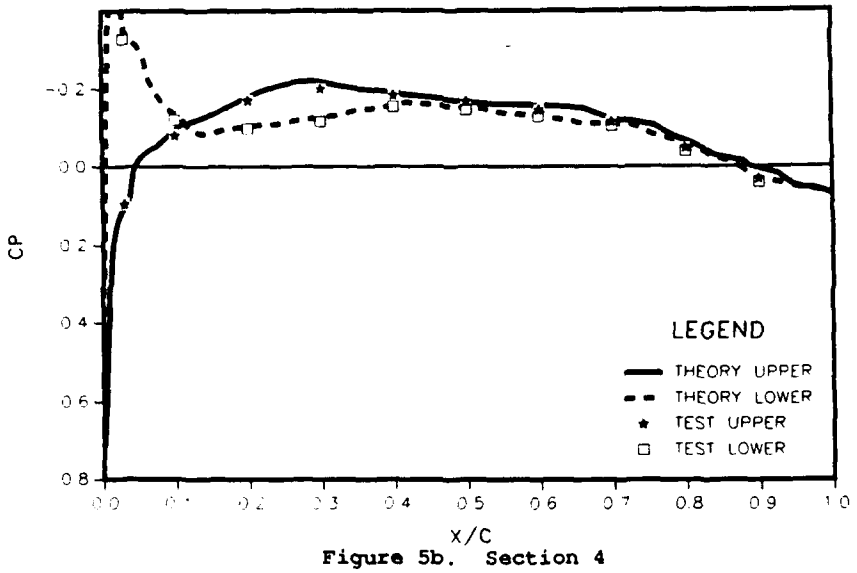


Figure 5b. Section 4

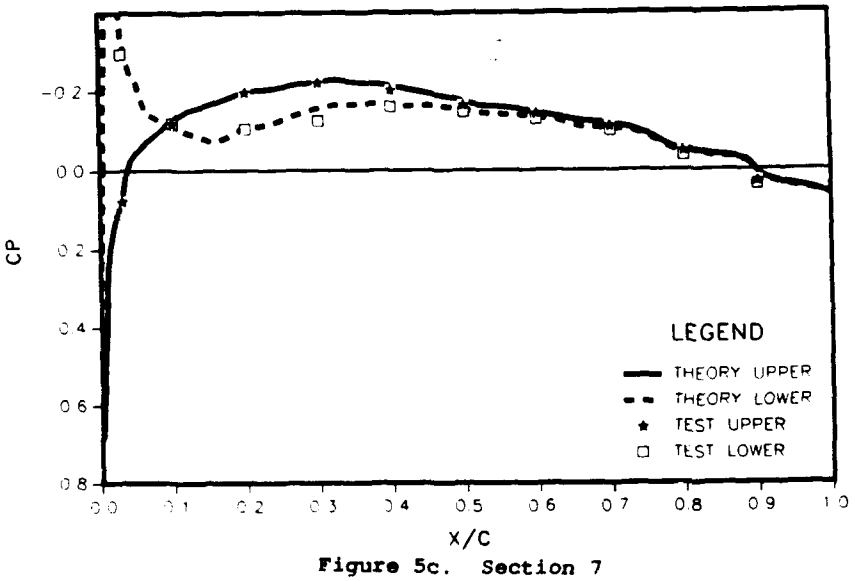


Figure 5c. Section 7

THIS DOCUMENT PROVIDED BY THE ABBOTT AEROSPACE
TECHNICAL LIBRARY
ABBOTTAEROSPACE.COM

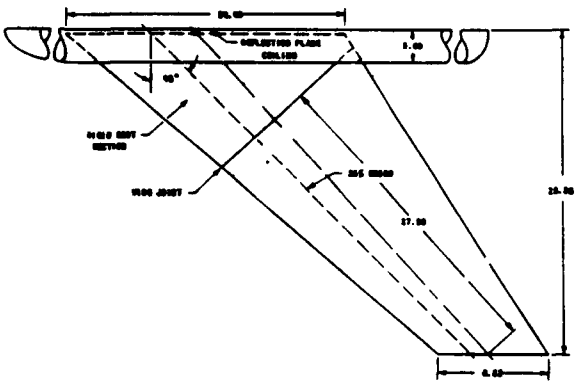


Figure 6. Planform View of 45° Swept Wing Model

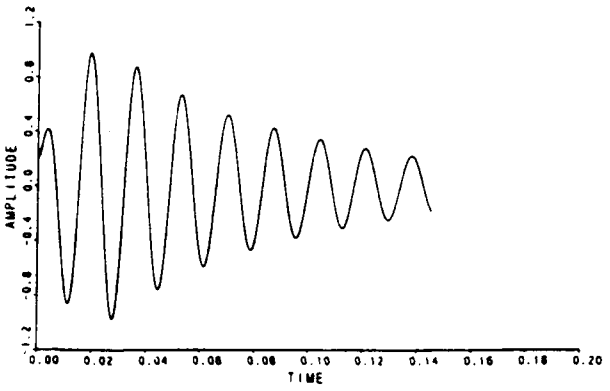


Figure 7. Time History for Mode 1 at a Dynamic Pressure of 1.2 psi

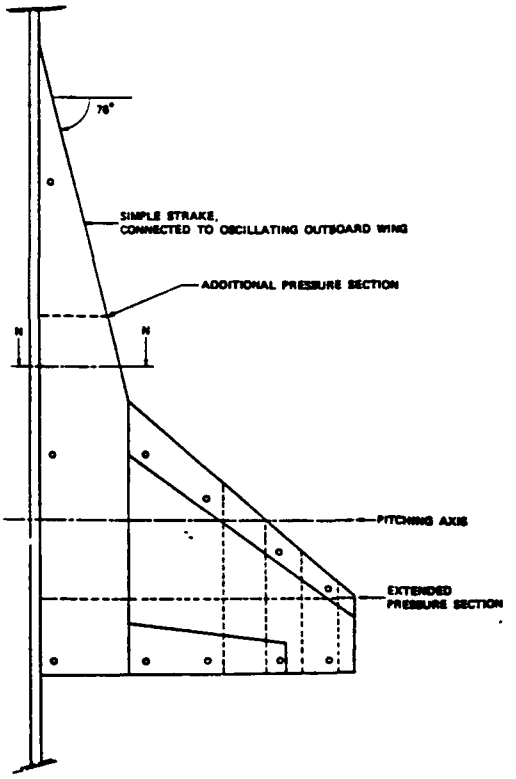


Figure 9. Straked Wing Configuration

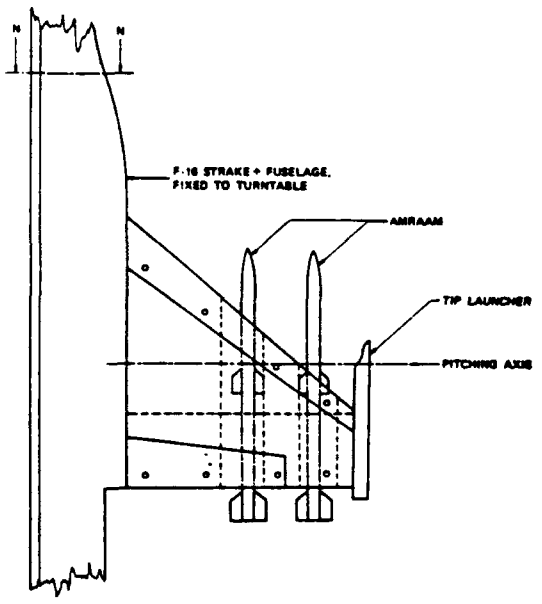


Figure 8. F-16 Wing/Store Configuration

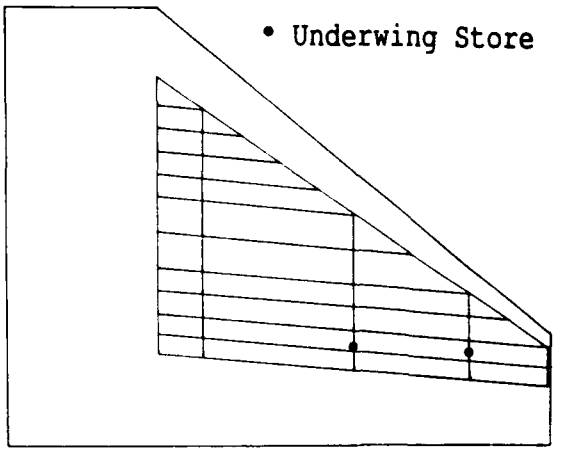


Figure 10. Flight Dynamics Fighter Derivative Structure

THIS DOCUMENT PROVIDED BY THE ABBOTT AEROSPACE
TECHNICAL LIBRARY
ABBOTTAEROSPACE.COM

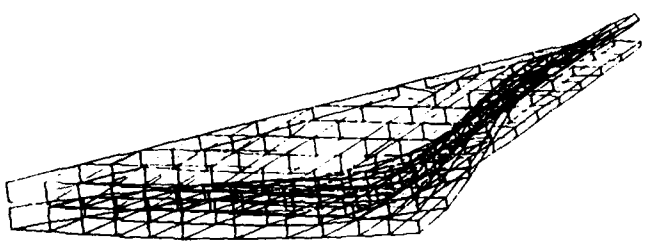


Figure 11. FDFD Torsion Mode (5.63 Hz)

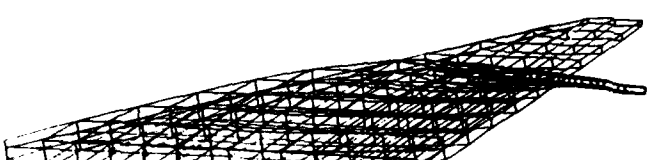


Figure 12. FDFD Bending Mode (9.08 Hz)

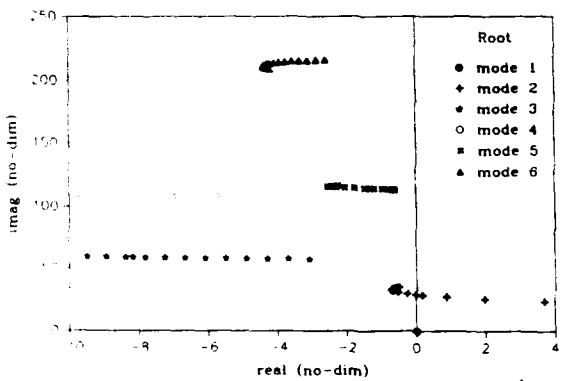


Figure 13. FDFD Velocity Root Locus

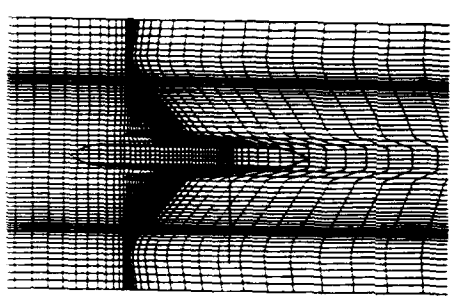


Figure 14. FDFD Computational Grid for CAP-TSD

THIS DOCUMENT PROVIDED BY THE ABBOTT AEROSPACE
TECHNICAL LIBRARY
ABBOTTAEROSPACE.COM

AD-P007 797

Recent Applications of Linear and Nonlinear Unsteady Aerodynamics for Aeroelastic Analysis.

Bengt Winzell

Department of Aeroelasticity
Saab Aircraft Division
S-58188 Linköping
Sweden

92-16035

SUMMARY

Results of unsteady linear and full potential theory are used for analysis of wings and aircraft configurations. In particular the details of unsteady pressure distributions at the trailing edge are investigated aiming at better representation of control surface hinge moments. The importance of viscous effects are observed and a comparison between potential theory and Navier–Stokes predictions is made.

INTRODUCTION

Unsteady aerodynamic forces, applied in the engineering design of aircraft, are still mainly computed by linear potential theory. This is usually not a limitation, since for subsonic speed such methods are satisfactory, and in many cases other requirements on the structure make margins to flutter large enough to admit extrapolation in the transonic region. In particular, several Saab aircraft have been successfully analyzed by the dependable and computationally efficient AEREL linear aerodynamics package, developed by Valter Stark[1]. It also appears that integrated quantities like lifting force or pitching moment are much less sensitive to the transonics than the detailed pressure distribution.

We will discuss a few cases where the nonlinearity plays a role and where the aeroelastic properties are considerably different when using a theory that accounts for the transonic effects. One case is the appearance of a transonic dip, or rather a strong recovery of flutter speed after a minimum at a certain Mach number. This is a phenomenon that can not be predicted by the standard methods, based on linear theory, which dominate the design work in the aerospace industry. However, to take advantage of the rising flutter speed, it must be possible to find the proper location on the Mach number axis for the minimum flutter speed in order to make a safe prediction. We will demonstrate the difficulties we have encountered in that respect, showing the importance of not only the shock position but also viscous effects.

Another area of great importance concerns the prediction of aerodynamic forces due to control surface deflections, quasi-steady and unsteady. It appears that unsteady pressure distributions, obtained by solving the linear equation that results when perturbing a constant velocity free stream, are too large at the trailing edge. This is of course because of the viscous environment here, but already the fact that the linear theory assumes a constant velocity instead of the true mean flow velocity that is reduced at the leading trailing edges renders the computed hinge moments over estimated. We will discuss means of correcting this. We will also demonstrate how well an analysis with an unsteady full potential solver[2], coupled with a simple integral boundary layer theory, can reproduce measured pressure distributions due to control surface deflection on the F5 wing, in particular at the trailing edge.

In passing we will also discuss the possibility to obtain more realistic results with Navier–Stokes computations.

UNSTEADY AERODYNAMICS METHODS AT SAAB

The unsteady aerodynamics for design at Saab are almost exclusively computed by the linear ADE method of Stark. It has been considerably extended to treat full configuration aircraft and includes many options for correcting the linear, inviscid method. In the last few years the present author has also developed and applied a method based on the unsteady full potential equation, which should be valid in the transonic regime. We will here briefly discuss the properties of the methods.

Our methods for Euler's and Navier–Stokes' equations are only for explicit time stepping and are considered impractical for engineering time accurate application at present.

The linear ADE method in AEREL.

The basic unsteady aerodynamics for aircraft design and certification at Saab is the AEREL program package by Stark[1]. The aircraft is modeled as a configuration of thin plates and the unsteady part of the flow is considered to be a small perturbation of a con-

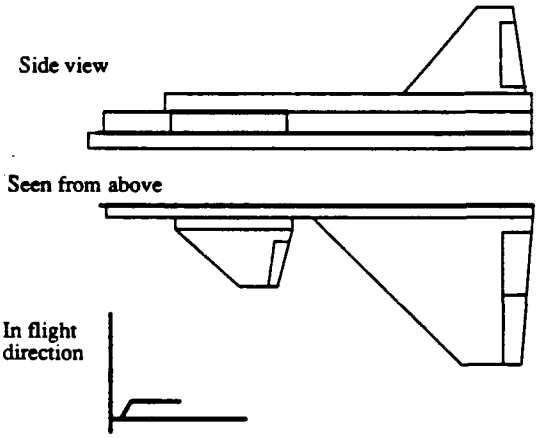


Fig 1: Geometric modelling for AEREL analysis

stant velocity flow field, having a time dependent potential ϕ, satisfying the linear wave equation

$$M^2\left(\frac{\partial}{\partial t}+\frac{\partial}{\partial x}\right)^2\phi=\frac{\partial^2\phi}{\partial x^2}+\frac{\partial^2\phi}{\partial y^2}+\frac{\partial^2\phi}{\partial z^2} \qquad (1)$$

with boundary conditions for the down wash in terms of the mode shape. The equation is transformed to the Fourier plane and there

THIS DOCUMENT PROVIDED BY THE ABBOTT AEROSPACE
TECHNICAL LIBRARY
ABBOTTAEROSPACE.COM

Stark uses the advanced potential to obtain an integral identity which is discretized into the Advanced Doublet Element method ADE (Ref 1) leaving us with a large equations system to be solved for the potential jump across the surface elements. The most expensive part of the computation is the establishment of the elements in the influence matrix corresponding to the integral identity. This matrix is the same for all mode shapes and depends only on the geometry, the Mach number, the frequency and the particular element partitioning. Hence, the linear method is very cost effective in producing full aerodynamic matrices, using a vectorizable factorization for the solution of the equations system. Moreover, the influence matrix can be saved on an external file to be used subsequently in a series of computations, admitting quick and extensive sensitivity analysis. In this way we can easily study effects of changes in control surface dimension and mass balancing, failure cases, new stores etc.

In most practical implications, the accuracy of the method is acceptable. Prior to extensive aeroelastic analysis we compare generalized air forces at zero frequency with available data for the corresponding aerodynamic derivatives in the Aero Data Book for the Aircraft. Figure 2 shows a typical comparison. To get those results we constructed the thin surfaces model according to simple rules, based on experience and slender body theory. It is often possible to further improve the comparison by adjusting the geometry a little bit.

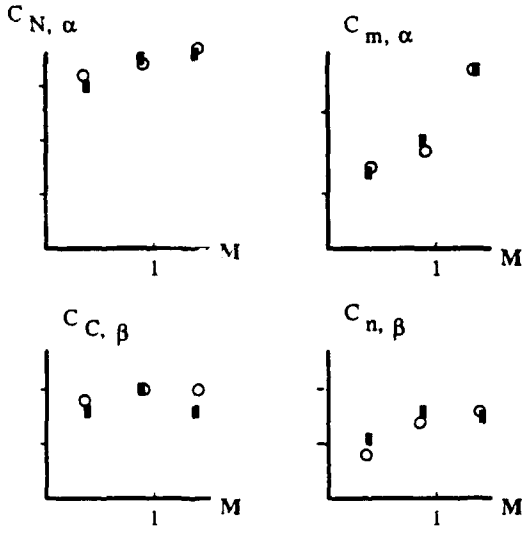


Fig 2a: Comparison of zero frequency generalized aerodynamic forces from AEREL (▮) and Aero Data (o) for an aircraft configuration.

We find acceptable to good agreement (Fig 2a) for quantities like lifting force or pitching moment due to angle of attack, and side force or yawing moment due to side slip. For loads due to control surface motion, like lifting force and pitching moment due to elevator deflection or yawing and rolling moment due to aileron deflection, we get a substantial over prediction (Fig 2b) using the theory without corrections. We will return to the reason and possible remedy for these discrepancies below.

Full potential method for wing configuration.

In order to account for transonic phenomena, we have developed a computer program that solves the unsteady full potential equation in body fitted, CH topology grids, around general three–dimensional wings[2]. The method closely follows the published details of Shankar[3] and Sankar, Ruo and Malone[4]. The equation for the velocity potential ϕ now reads

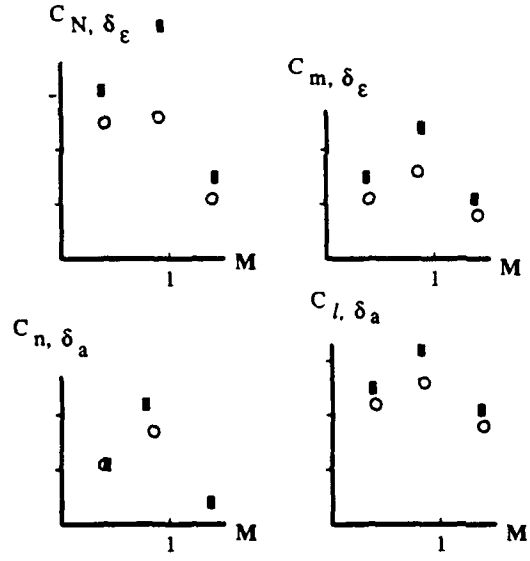


Fig 2b: Comparison of zero frequency generalized aerodynamic forces from AEREL (▮) and Aero Data (o) for an aircraft configuration. Derivatives with respect to control surface angles.

$$\frac{\partial \rho}{\partial t} + \operatorname{div}(\rho \operatorname{grad} \phi) = 0 \qquad (2)$$

where the density ρ is given by

$$\rho = \rho_\infty \left(1 + \frac{\gamma-1}{2} M_\infty^2 \left(1 - 2\frac{\partial \phi}{\partial t} - |\nabla \phi|^2\right)\right)^{\frac{1}{\gamma-1}} \qquad (3)$$

Here the full non–linearity (under the assumption of potential, isentropic flow) is retained, and by a proper upwind technique, shocks appear and move according to the conservative scheme.

The pressure is computed by a formula similar to how ρ is defined in (3), but with another exponent. For very small perturbations ψ of the mean potential ϕ we get the corresponding pressure coefficient increment

$$\Delta C_p^{FP} = -\frac{\partial \psi}{\partial t} - \nabla\phi \cdot \nabla\psi \qquad (4a)$$

which can be compared with the corresponding expression in the linear case, where the mean (non–dimensional) velocity is unity in the downstream direction:

$$\Delta C_p^{Lin} = -\frac{\partial \psi}{\partial t} - \frac{\partial \psi}{\partial x} \qquad (4b)$$

We will come back to the difference between these two expressions.

It is a well known fact, that the full potential equation, accounting for thickness and flow discontinuities, produces unphysical results unless it also simulates the viscous flow phenomena. We have included a strip–wise correction for the displacement thickness using the two–dimensional Nash–Macdonald[5] formulation as it is included in the Bauer–Garabedian–Jameson–Korn method[6].

THIS DOCUMENT PROVIDED BY THE ABBOTT AEROSPACE
TECHNICAL LIBRARY
ABBOTTAEROSPACE.COM

The full potential code is written such that it simultaneously computes displacement thickness from the viscous routine, elastic deformation for the structural dynamics equations (formulated in generalized coordinates using eigen modes) and the next time step potential for the flow.

RESULTS

We will now present several examples of computations on validation configurations and discuss the impact of the findings on the engineering application. We first will demonstrate, that when comparing with experiments, it is very important to take into account all features of the experiment. In this case the wing which will be analyzed turned out to be weak enough to have an eigen frequency in the range of tested frequencies of the pitching oscillation.

The LANN wing at M=0.62 and M=0.82.

The LANN wing model was tested by NLR[7,8]. The configuration is an example of a modern transport wing, having a 12% thick supercritical profile, an aspect ratio of 8 and a taper ratio of 0.4. The 25% chord axis was swept back by 25 degrees. The wing model was oscillated about an axis through 62% root chord at frequencies up to 72 Hz (in steps of 12 Hz). A ground vibration test revealed a first modal frequency of about 30 Hz. However, during the test, the true motion (which, due to the elastic character of the model, was not a pure pitching one) was recorded and is included in the documentation.

Figure 3 shows the unsteady lift coefficient as a function of frequency at M=0.62. This is a subsonic case. Hence we would expect that the two theories would both reproduce the experiment. Apparently the two theories (line and open circles) agree, the full potential real parts being only a little bit larger than those from the linear method.

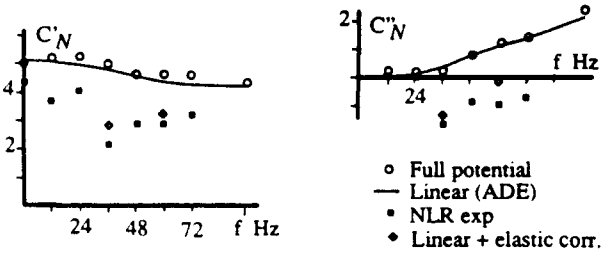


Fig 3: Real (left) and imaginary (right) part of the unsteady lift force coefficient of the LANN wing at M = 0.62 and α = 0.6 degrees.

However, the differences to the experiment (black boxes) are very large. The efficiency of the linear ADE method made it possible to compute the lifting force for a series of other mode shapes, close to the elastic ones described in Ref 7. At two frequencies, f = 36 Hz and f = 60 Hz, a combination of these was determined such that it as closely as possible represented the measured motion of the model. Then it was possible to compute better estimates of the unsteady lift coefficient (work completed by Mr M Rönn while a Masters of Science student at Linköping University). The new estimates are included as shaded diamonds, and show much better agreement with the experiment.

This shows the sensitivity of aerodynamics to elastic effects. Next we will look at the similar situation at M=0.82, a transonic case with large regions of supersonic flow over the wing. This is Fig 4. Here we find that the discrepancy between the two theories has grown considerably, the inviscid full potential real part of the lifting force being much higher for low frequencies. The differences between the linear theory result and the experiment is again large due to the elasticity of the wing, not admitting a pure pitch oscillation with the intended amplitude at any frequency. However, the corrected values obtained using the measured deformations are in reasonable agreement with the experiment. Note that the full potential results, reacting strongly to thickness without any other means to correct for the boundary layer, would not be as good even if they were corrected for elasticity. We have therefore included the full potential estimate at f=24 Hz, obtained with activated Nash–Macdonald viscous correction. This brings the full potential result close to the linear one.

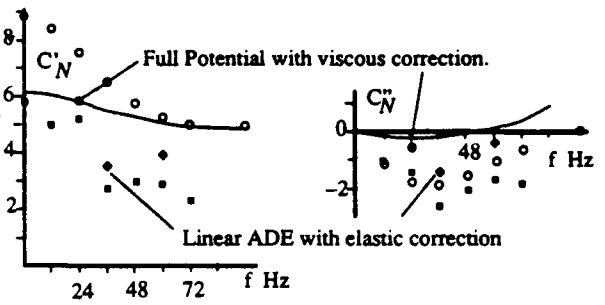


Fig 4: Real (left) and imaginary (right) part of the unsteady lift force coefficient of the LANN wing at M = 0.82 and α = 0.6 degrees.

The conclusion of the LANN comparison seems to be that, a *non–linear inviscid method on a thick wing does not improve the unsteady aerodynamics prediction*. It is also necessary, when comparing experiments and theory, to *account for elastic effects*. Hence the recording of the motion during the test is an important piece of data to add to the documentation. We have shown, that using such information, it is possible to compare theoretical computations and measurements, even in cases where the intended oscillation is distorted by elastic effects.

The appearance of a transonic dip.

In Ref 9, Garner, Payne and Baldock present an experiment, performed in the RAE 8 ft x 8 ft wind tunnel at Bedford, UK, and an impressing analysis of computational predictions. The model, which was subjected to flutter test in the Mach number range from M=0.75 to M=0.9 is again of a transport wing type, having a large aspect ratio, modest taper ratio and a swept back planform. It had a symmetric section profile, constant along the span, with transonic effects beginning to appear at about M=0.8. In Ref 9, measured vacuum frequencies of the first eigen modes were given, and there also were presented diagrams from which the mode shapes could be recovered. However, the modal masses are absent, and the mounting of the model on a root pitch block, which was not entirely rigid, requires more information in order for a good numerical simulation to be possible.

TABLE 1

Mode shapes in the test of Ref 9.

Fundamental bending	36.8 Hz
First overtone bending	113.4 Hz
Second overtone bending	260.0 Hz
Fundamental torsion	326.5 Hz
Third overtone bending	406.5 Hz

Thanks to Angus Kittney and Timothy Openshaw of British Aerospace, Commercial Aircraft, Airlines Division, we have received a full set of mass, frequency and shape for a root block

THIS DOCUMENT PROVIDED BY THE ABBOTT AEROSPACE
TECHNICAL LIBRARY
ABBOTTAEROSPACE.COM

oscillation, the fundamental and two first overtone bendings and the fundamental torsion, computed by a finite element structural dynamics method. The data seems to closely reproduce the measurements in Ref 9.

As demonstrated in Ref 9, flutter occurs in a coupling of the fundamental bending and fundamental torsion in spite of the fact, that the quotient of vacuum frequencies of these modes is as large as 9. Fig 5 shows the flutter speed as a function of Mach number.

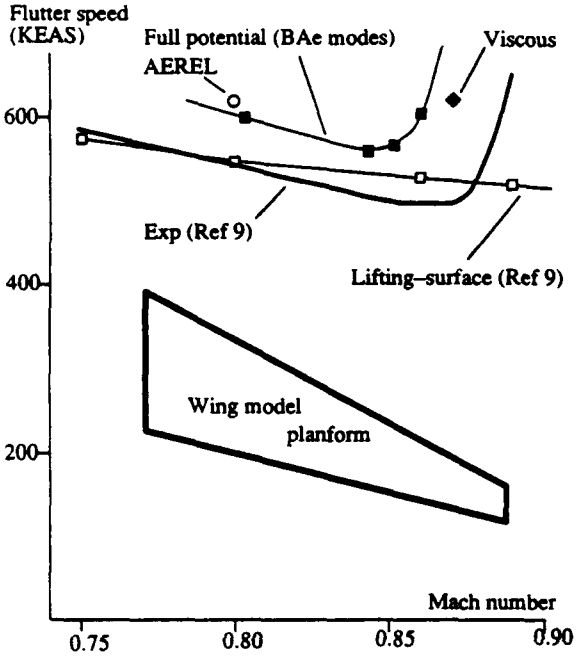


Fig 5: Flutter speed of the wind tunnel flutter model tested in RAE 8 ft x 8 ft tunnel. (Ref 9)

Both the test and the present computation show the occurrence of a minimum in flutter speed at a certain Mach number and a strong and sudden recovery for higher Mach numbers. This is in contrast to the linear method (here represented by the data in Ref 9, using Davies' lifting surface theory). On the other hand, the Mach number, at which the flutter speed increases to very high values again, is quite different in the full potential computation and the test: there is a shift in Mach number of about 0.03, and since the theory *predicts recovery at too small a Mach number*, in addition to delivering *too high flutter speeds* in the whole Mach number range, the prediction is *non–conservative*.

The Saab full potential method can be run with simultaneous solution of the Nash–Macdonald turbulent boundary layer method. This is done strip–wise, which should be reasonable at least for the inboard sections. However, the flutter instability probably is more related to outboard flow conditions, and therefore the simple viscous correction used here must be considered rather approximate. Nevertheless, the trend of shifting the minimum towards higher Mach number is clearly demonstrated in Fig 5. Similarly, Fig 6 shows the effect of boundary layer on the motion of center of pressure for the torsional motion of the wing (compare the discussion of Baldock in Ref 9):

We have chosen the Ref 9 linear values to indicate that the results of Garner, Payne and Baldock were actually closer to the experiment than the ones we get here. The corresponding line of AER-

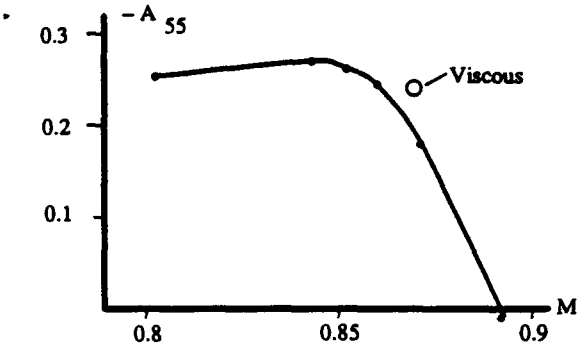


Fig 6: Aerodynamic torsional stiffness due to torsion for the flutter model.

EL would be closer to the full potential result as is indicated by the single point included in Fig 5 at M=0.8.

The appearance of the *minimum in flutter speed and the error in its position are transonic phenomena* and *depend* strongly *on the boundary layer*. The over–prediction of flutter speed must be due to something else. At M=0.8, the transonic effects are small, and our experience from other flutter investigations is that the linear theory gives much closer agreement with experiment than we see here. One might contemplate the role of the pitch block mode and the very modelling of the wing. In the tunnel, the model was fixed to a rather large mass (the root pitch block), but with low frequency, about half the frequency of the fundamental wing bending. Moreover, the wing was attached to a cylinder, shielding the pitch block. The fairing is not aerodynamically modeled in our analy-

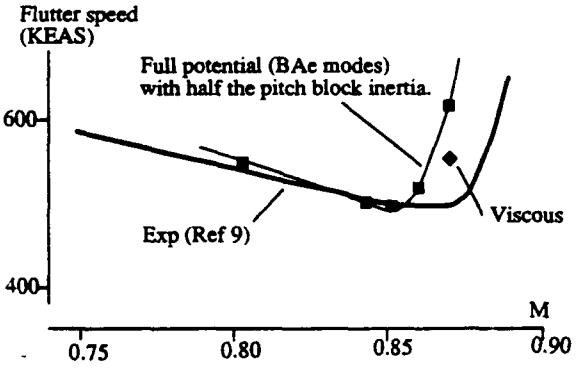


Fig 7: Sensitivity of the flutter speed to the modelling of root pitch block. Predictions made using only half the nominal pitch block inertia.

sis, but the pitch block was considered in the BAe structural analysis. In Fig 7 we demonstrate the sensitivity of the result to the pitch block inertia. We have also studied the effect of small variations of the modal frequencies of the wing and found that the flutter speed curve moves significantly when changing from the finite element analysis values to those of the experiment although this is a very small change of stiffness. We did observe a considerable error in the prediction of flutter frequency, as a matter of fact of the order 10–15% using the full potential aerodynamics in the inviscid cases. We believe that the *center of pressure increment is too strongly affected by the thickness in the full potential analysis*.

Before leaving this validation case we would like to make a comment on the computation of unsteady full potential generalized

THIS DOCUMENT PROVIDED BY THE ABBOTT AEROSPACE
TECHNICAL LIBRARY
ABBOTTAEROSPACE.COM

aerodynamics forces. The solver works in the time domain. We thus have several options to compute flutter speed. One is to introduce the structural dynamics equations of motion in Lagrangian formulation and couple the flow solver to the solution of these differential equations in time. Such an option is included in the program and will be demonstrated in an other example below. Another is to assume small amplitude motion and that the difference between the steady and unsteady part is small enough to admit time linearization. Then we have two ways to establish aerodynamic transfer functions for the use within a classical flutter analysis program. We can impose a harmonic oscillation of one mode shape and one frequency at a time, and run the program until the response becomes harmonic. This is usually extremely expensive. The other way is to excite one mode shape at a time with a pulse, the Fourier transform of which is non–zero for a large enough interval of frequencies. Recording the instantaneous aerodynamic forces at each time step, the aerodynamic transfer function is obtained as the quotient of the Fourier transforms of the response and the exciting pulse. When there are only a few mode shapes to account for, the pulse method for computing the transfer function is least expensive and has been used here. We demonstrate in Fig 8 the evolution of the unsteady part of the

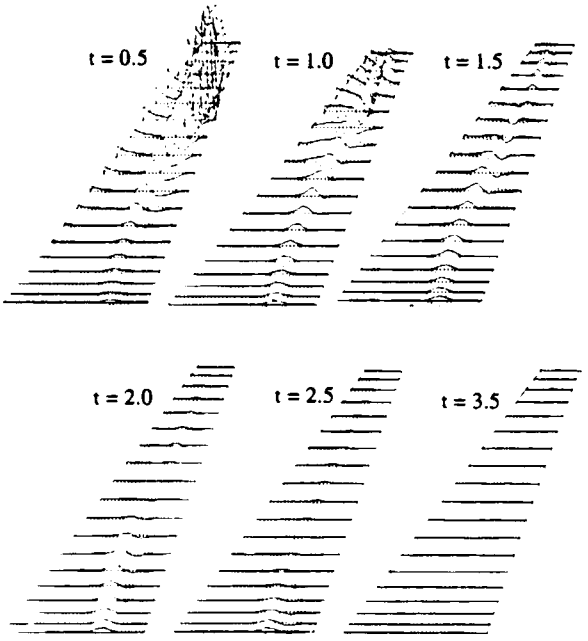


Fig 8: The time evolution of the unsteady pressure increment due to a pulse excitation of the torsional mode. M=0.86.

pressure distribution. The pulse excitation takes the form $\Delta z = q(t)\, h(x,y)$ where

$$q(t) = q_o\,(1 - \cos(2\pi t/t_o)) \quad \text{for } t \le t_o \text{ and}$$
$$q(t) = 0 \quad \text{for } t > t_o.$$

The duration of the "1–cos" pulse, t_o, was chosen such that during that time the wing travels 5.16 mean chords. The time labelling in Fig 8 is in units of t_o.

Unsteady and quasi–steady pressure distributions due to control surface deflection, in particular at the trailing edge.

As already mentioned above, it is much harder to get good accuracy for control surface aerodynamics than for loads due to translation, pitch, yaw or roll. For rigid control surfaces one often can correct the computed air loads on the basis of wind tunnel measurements. However, this is not so easy for complicated eigen modes of an aircraft, where the mode shape is partly a control surface rotation, but also to a large extent an elastic deflection of the control surface and the other parts of the structure. Control surfaces with an aerodynamic balance are also hard to treat by correction factors.

We will now present comparison with experiments and means of improving the computational accuracy for the pressure distribution at the trailing edge in an attempt to eventually find engineering tools of handling the aerodynamics of elevators and ailerons with tabs and aerodynamic balance. I turns out, that it is not easy to find good experimental data for steady, quasi–steady and unsteady pressure distribution at the rear end of a wing. However, in Ref 10 Wenzinger presents a low speed test, carried out in the 30's in the N.A.C.A. 7 ft x 10 ft wind tunnel. The wing had a part

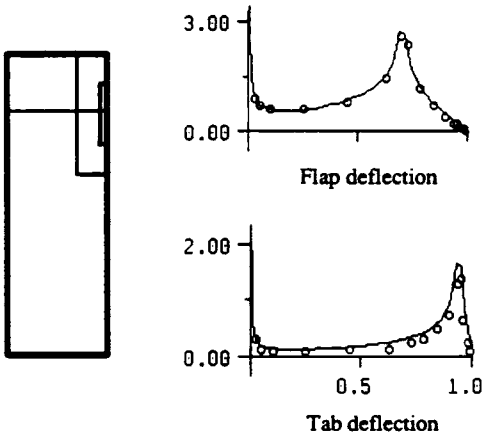


Fig 9: Three–dimensional full potential computation (lines) compared with measurements (symbols) on the Wenzinger wing with rudder and tab in low speed (Ref 10). Quasi–steady pressure increment.

span flap, occupying the outer 40% of the semispan, 30% deep chord–wise, and a tab of 20% semispan length, centered at the rear of the flap. The tab is only 6% of the chord.

In Fig 9 we compare the measured data with an application of the full potential solver. We present quasi–steady pressure distributions due to deflection of the tab and the flap. The agreement

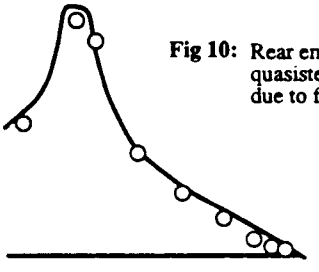


Fig 10: Rear end close up view of quasisteady pressure increment due to flap deflection in Fig9.

looks very good, but a closer look at the trailing edge reveals some of the difficulties with predictions of this kind: The quality of the computed tab hinge moment coefficient due to flap deflection, for instance, is directly related to *the accuracy of the pressure distribution in the last* 4%, say, *of the chord* and *here the comparison is poor* (Fig 10). This is probably an effect of the boundary layer at the trailing edge. We also realize that, even a

THIS DOCUMENT PROVIDED BY THE ABBOTT AEROSPACE
TECHNICAL LIBRARY
ABBOTTAEROSPACE.COM

fine resolution of the wing with many grids point, only leaves a few of them on tab, occupying only 6% of the chord.

We have used the same configuration of the Wenzinger wing to assess the *three–dimensionality of the flap and tab aerodynamics*.

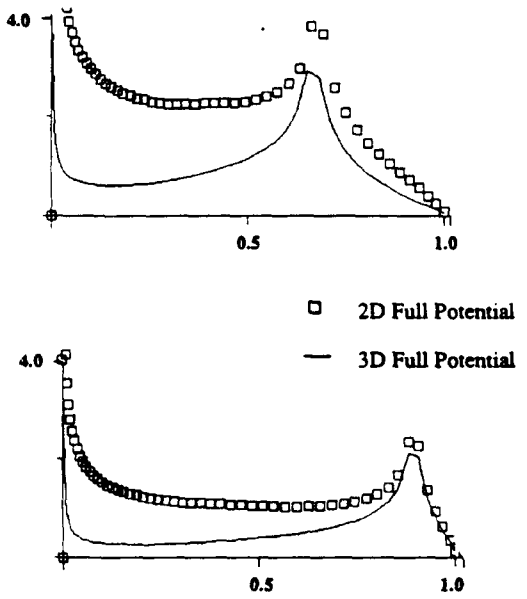


Fig 11: The three–dimensionality of the control surface aerodynamics for flap and tab deflection.

Fig 11 shows the comparison in one section over the flap and tab for the pressure distribution, computed by the two– or three–dimensional full potential. Obviously the difference *is large*, except on the tab due to tab deflection.

Since the bulk of computations on a complete aircraft will be done by means of linear theory for many years yet, it is important to observe differences between the linear method, the full potential method and experiments at the trailing edge. Fig 12 shows the

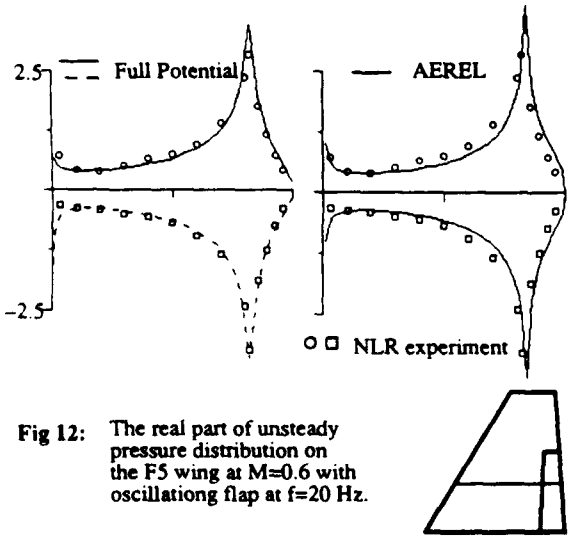


Fig 12: The real part of unsteady pressure distribution on the F5 wing at M=0.6 with oscillationg flap at f=20 Hz.

real part unsteady pressure distribution on the F5 wing (Ref 11) in the 34% section. The driving motion is a 20 Hz flap oscillation.

There is a small asymmetry because the wing is unsymmetrical in its profile. However, we conclude that both theories give a fair agreement with the experiments. However, there is a difference in the way that they represent the trailing edge pressure. The linear method overestimates the singularity at the edge. This time we cannot blame the boundary layer, since the full potential method is closer and a run of the full potential method with viscous correction showed very small influence of a turbulent boundary layer.

Instead we have looked a little bit closer at the definition of unsteady pressure in equations 4a and 4b. The linear method assumes a constant velocity field all over the chord. This is not generally true. A better formula would be

$$\Delta C_p^{\text{Lin_modified}} = -\frac{\partial \Psi}{\partial t} - U_{loc}\frac{\partial \Psi}{\partial x} \qquad (4c)$$

where U_{loc} is the local mean velocity which is not constant. In particular it is less than the free stream velocity at the trailing and leading edges. Similarly, the mode shape boundary condition reads

$$\frac{\partial \Psi}{\partial z} = \frac{\partial h}{\partial t} + \frac{\partial h}{\partial x} \qquad (5a)$$

but should more realistically be

$$\frac{\partial \Psi}{\partial z} = \frac{\partial h}{\partial t} + U_{loc}\frac{\partial h}{\partial x} \qquad (5b)$$

Just to introduce this into the linear method is not correct, since there should be a similar introduction of non–constant coefficients in the wave equation (1). However, for the F5 analysis in Fig 12 we have adapted formulas (4c) and (5b) to assess the *sensitivity of the trailing edge incremental pressures to the local mean velocity*. We assumed that $U_{loc} = U_\infty$ except in the last 18% of the chord (over the flap) where it is linearly reduced to 0.9 U_∞ at the trailing edge. This is of course a rather random choice and is made only to see if there is an effect of such a modification.

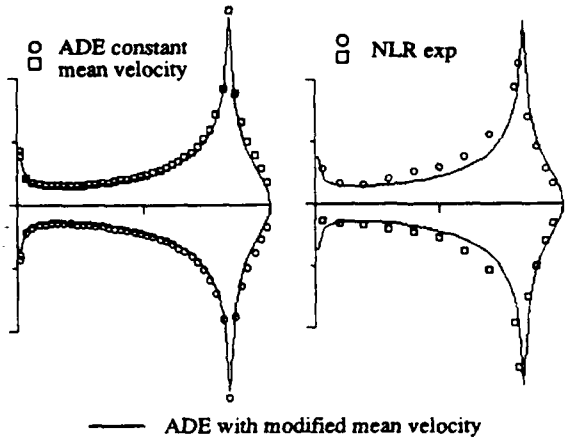


Fig 13: The effect of modifying the mean flow velocity in the linear method. Test case as in Fig 14.

Fig 13 demonstrates how the reduction of mean local velocity improves the trailing edge distribution. The message of the left hand diagram is that there is an effect of the mean velocity variation. Furthermore, it shows, that the pressure ahead of the hinge has changed too. This is due to the fact that we have introduced the local velocity variation also in the down–wash, admitting global perturbation. The change in pressure ahead of the hinge line is in

THIS DOCUMENT PROVIDED BY THE ABBOTT AEROSPACE
TECHNICAL LIBRARY
ABBOTTAEROSPACE.COM

the wrong direction, however, and this could be explained by the fact that U_{loc} is actually greater than U_∞ in this region while we have kept it at unity there.

The right hand diagram of Fig 13 should be compared with the right hand diagram of Fig 12 to see how much better the new distribution fits the experiment. We conclude that *working with the formulas for unsteady pressure and* possibly *down–wash* opens a way to *improve* linear methods predicting *control surface aerodynamics*.

The following discussion points in another direction. We will make a comparison with a Navier–Stokes method in a low speed application. A section of the Saab 340 fin with rudder and tab was taken as the profile for a 2–D viscous computation of the quasi–steady pressure increment due to a 2 degree deflection of the rudder, here considered without aerodynamic balance. The author

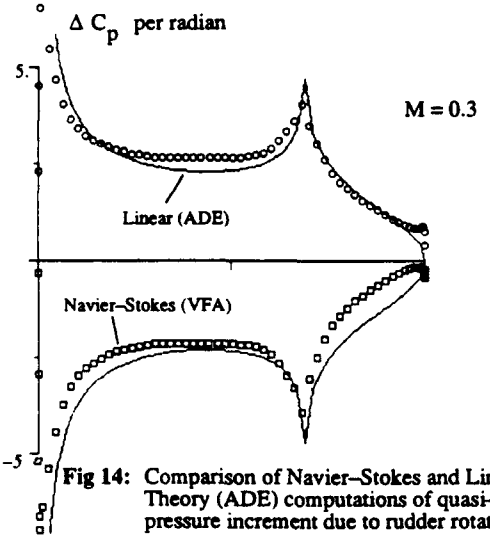


Fig 14: Comparison of Navier–Stokes and Linear Theory (ADE) computations of quasi–steady pressure increment due to rudder rotation.

owes the present Navier–Stokes results to Dr G Sidén of Volvo Flygmotor (VFA) who applied his mixed finite element and Beam–Warming unsteady viscous aerodynamics solver.

In Fig 14 we see the FVA viscous quasi–steady pressure increments due to a deflection of the rudder of two degrees compared with the corresponding linear theory result, and in Fig 15 there is a similar comparison with a full potential computation, including Nash–Macdonald turbulent boundary layer correction. The surprising result is that the Navier–Stokes computation reproduced the *fat* pressure increment distribution at the trailing edge rather than the *reduction* that is predicted by Nash–Macdonald plus full potential analysis. Since we generally believe that we are over–estimating the pressure increment due to control surface deflection by the classical methods, we had expected the Navier–Stokes computation to show a reduction too. The grid used in the Navier–Stokes computation was fine also at the rear end of the profile and modeled a non–sharp trailing edge with a small radius.

In the F5 case we observed that the test gave a *lower* pressure jump across the aft region of the wing than predicted by the potential theories. It remains to understand why the Navier–Stokes computation gives another answer for the 2–D profile.

Transonic unsteady pressure distributions due to flap oscillation on the F5 wing.

We now turn to high subsonic and transonic comparison on the F5 wing with flap. We will look at the results for M=0.8, in which

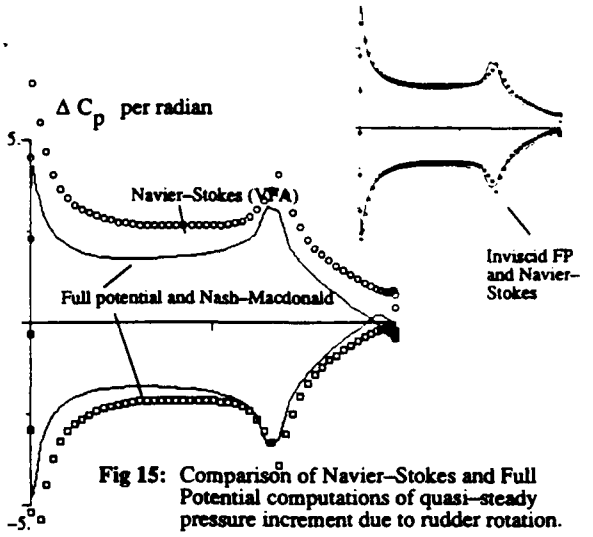


Fig 15: Comparison of Navier–Stokes and Full Potential computations of quasi–steady pressure increment due to rudder rotation.

case the linear aerodynamics still provides point–wise pressure distribution close to the experiments. At M=0.8 there were no de-

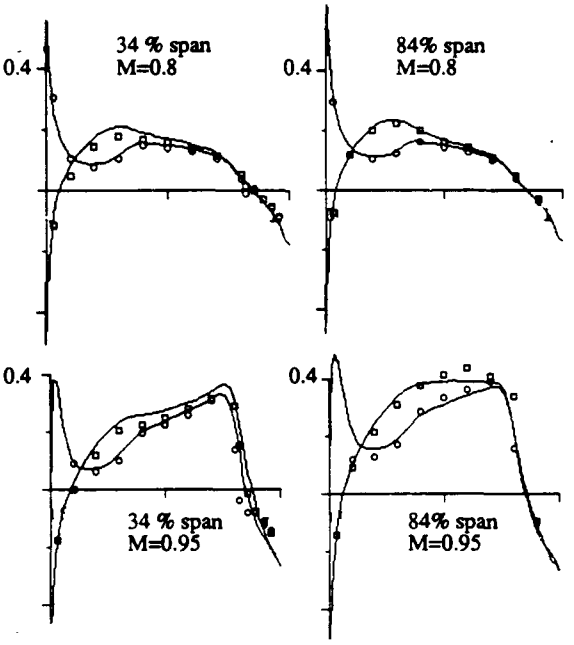


Fig 16: Steady pressure distribution comparison at an and an outboard section for M=0.8 and M=0.95 with zero angle of attack.
NLR experiments as symbols.

tection of supersonic flow in the test. However, the full potential method actually encounters a very thin zone of transonic flow just below the leading edge (see the high peaks for lower side pressures in Fig 16). We will discuss the implication of that zone on the unsteady pressure increments.

For M=0.9 we have a transonic situation, but with very weak shocks. We will show very good agreement between theory and measurements. When we get to M=0.95, however, the transonic flow is more aggressive to the flow solver, in the sense that we could not get a fine grid converged inviscid solution even to the steady state problem. Thus we will only present results in which the viscous correction method is active. According to the strip–

THIS DOCUMENT PROVIDED BY THE ABBOTT AEROSPACE
TECHNICAL LIBRARY
ABBOTTAEROSPACE.COM

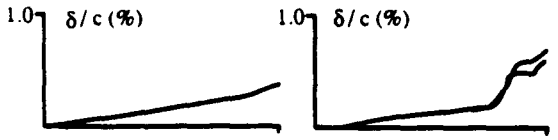


Fig 17: Displacement thickness in the midspan section of the F5 wing model for M=0.6 (left) and M=0.95 (right). Both upper and lower sides included.

wise Nash–Macdonald prediction (see Fig 17) of displacement thickness it is not very thick, less than a percent of the chord, but there is a strong interaction between the shock and the boundary layer. One should also doubt the realism in using the strip–wise integral method for the viscous effects on this small aspect ratio and tapered F5 wing.

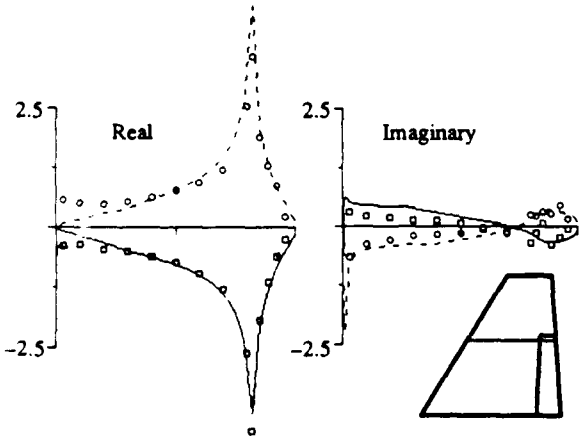


Fig 18: Unsteady pressure distribution on the F5 wing for M=0.8 and $\alpha = 0$.
Comparison of full potential computation (lines) and NLR experiment (symbols) for an oscillation of the flap with 40 Hz.

Consider Fig 18. There we have plotted the unsteady incremental pressure distribution in a section, at 51% semispan, i.e. almost at the end of the flap. There are some obvious differences between computed pressures and measured ones. The trailing edge agreement is less than in the M=0.6 case, and we also observe a striking difference in the leading edge pressures. This could possibly be an effect of the beginning supersonic region in the leading edge area. This idea is supported by Fig 19 in which we have plotted the full potential results for M=0.8 against the NLR measurements at M=0.85. The combination of Figures 18 and 19 would suggest that the M=0.8 results would be a better prediction of the true flow case at a Mach number slightly above M=0.8. This would again demonstrate the observation that in isentropic potential methods, Mach number effects come too early.

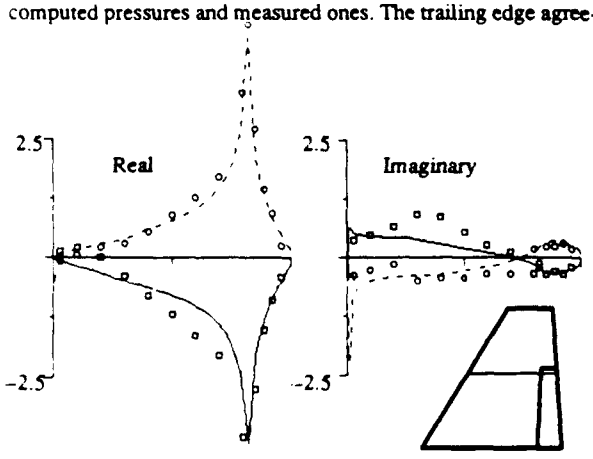


Fig 19: Unsteady pressure distribution on the F5 wing. Comparison of full potential computation (lines) at M=0.8 with NLR experiments (symbols) at M=0.85. The flap oscillates with f=40 Hz.

Note that the discrepancies in pressure differences over the flap as they appear in Fig 18 would result in up to 50% error of the hinge moment coefficients! However, the corresponding comparison of the linear aerodynamics in Fig 20 is much worse for the hinge moment, but better in the vicinity of the leading edge.

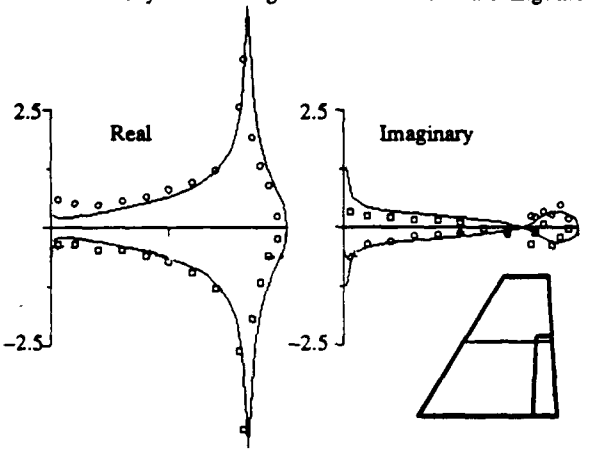


Fig 20: Unsteady pressure distribution on the F5 wing for M=0.8 and $\alpha = 0$.
Comparison of linear ADE computations (lines) and NLR experiment (symbols) for an oscillation of the flap with 40 Hz.

The 40 Hz flap oscillation in the M=0.95 case is presented in Fig 21. Here we have simultaneously included full potential and linear method results. The reason for this is to show that the linear theory still shows great relevance to the physical behavior and would give decent estimates of lifting force and rolling moment. It is not obvious and probably not true that the full potential results would be more accurate for these generalized forces. However, the transonic theory correctly acknowledges the fact that in the supersonic region there is no up stream propagation of disturbances from the flap. This is not so in the linear, subsonic theory, and hence we would expect errors in pitching moment. The comparison between experiments and computations is worse on the upper side than on the lower one in the full potential data. This indicates some problem with the shock motion in the M=0.95 case.

Finally we will show a comparison of full potential computations and NLR measurements for the M=0.9 case. Fig 22 shows a good agreement between theory and computations, at least for the in–phase component. Note the appearance of a moving shock wave at a location ahead of the flap hinge line. In the M=0.95 case, there also is a moving shock. However, it is located very close to the hinge line, and therefore the discontinuities due to the shock are shielded by the hinge line discontinuity itself in Fig 21.

The conclusions of the flap aerodynamics investigation, using F5 test data, is that in general the *full potential method better reproduces the trailing edge effects* than does the linear theory. On the other hand, still the discrepancies at the rear end of the flap are

THIS DOCUMENT PROVIDED BY THE ABBOTT AEROSPACE
TECHNICAL LIBRARY
ABBOTTAEROSPACE.COM

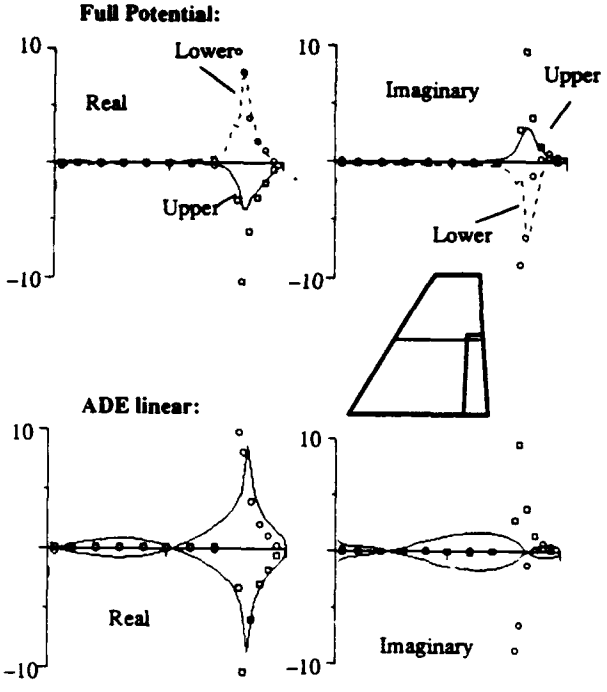


Fig 21: Unsteady pressure distribution on the F5 wing for M=0.95 and α=0. Comparison of computational methods (lines) and NLR experiments (symbols) for flap oscillation at 40 Hz.

large enough to render hinge moments off by perhaps 50% in many cases. Hence we do *not* see the full potential method as *a solution of the control surface problem*, but learning from the numerical experiment, introducing a non–constant local mean velocity in the linear method pressure formula, we think there will be a way to *adapt the cost effective ADE method to better control surface accuracy*.

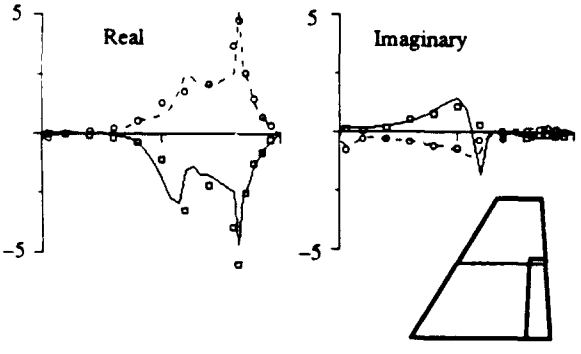


Fig 22: Unsteady pressure distribution on the F5 wing for M=0.9 and α = 0. Comparison of full potential computation (lines) and NLR experiment (symbols) for an oscillation of the flap with 20 Hz.

Aeroelastic coupling.

Since the boundary conditions for the aerodynamics mathematical problem is contained in the geometric shape of the wing, and this shape in its turn is determined by its state of elastic deflections, it is quite natural to solve the structural dynamics equations of motion and the flow equation simultaneously. This is a way to handle general response analysis, like flutter stability, divergence, limit cycle oscillations etc. In case of flutter stability of wings around a configuration in which the small perturbation assumption is valid, it is more efficient, however, to first compute aerodynamic transfer functions and then consider the flutter or response problem in a linear control theory approach. This enables quick sensitivity analysis and parametric studies like mass balancing just to name a few. Here we will give an example in which the coupling seems to be efficient. The example will be static aeroelastic deflection, estimating the loss of control surface effectiveness due to elasticity.

The equations of motion for a system with N elastic degrees of freedom is

$$m_k(\ddot{q}_k + 2\,d_k\,\omega_k\,\dot{q}_k + \omega_k^2) + Q\,A_k(q_1, \ldots, q_N) = 0 \quad (6)$$

where the m_k:s are modal inertias, the q_k:s are the Lagrangian generalized coordinates (functions of time) for the elastic deflections, the d_k:s are structural damping rates, the ω_k:s are eigen (circular) frequencies, Q is the dynamic pressure and the A_k:s are the generalized aerodynamic forces at the current time, depending on all the generalized coordinates and their current history. The A_k:s are obtained from integration at each time instance of the current pressure distribution, computed by the flow solver. Hence the aeroelastic coupling is to perform integration of (6) in each time step of the flow solver. Since the full potential method we have developed works with internal Newton iterations (see Refs 4 and 2), time accuracy can be retained by solving (6) too in an implicit fashion. However, we will not consider the time accurate procedure here.

When computing for static deflection, the true time evolution is not interesting, and we have put the damping rates equal to unity, since that gives an aperiodic damping of all modes. Therefore we see quick convergence to the steady state. Fig 23 shows how the

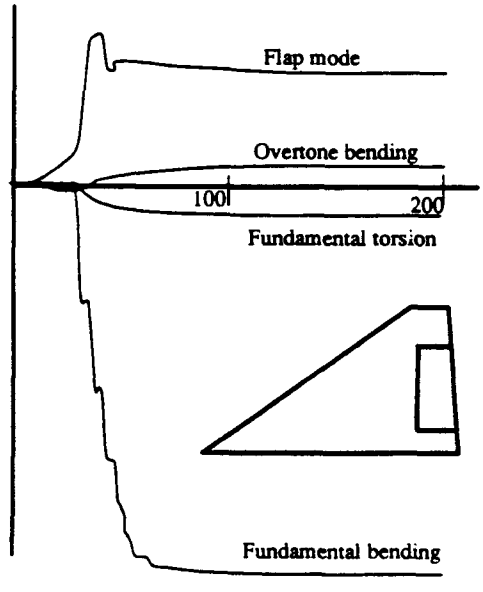


Fig 23: The convergence of static aeroelastic deflections on a Saab cropped delta wing with intended one degree flap deflection.

four modes considered on a cropped delta wing elastic model

THIS DOCUMENT PROVIDED BY THE ABBOTT AEROSPACE
TECHNICAL LIBRARY
ABBOTTAEROSPACE.COM

with trailing edge control surface converges in about 100 iterations, and this is the same time it takes for the flow solver to converge in this case of a Mach number of 0.9. The flap was given a one degree deflection, and then the coupled full potential unsteady aerodynamics code and the modal equations of motions were run for 200 time steps. The four elastic modes considered were

Fundamental bending
Fundamental torsion
Control surface mode (essentially deflection (actuator etc))
Overtone bending.

The quotient of the overtone bending frequency to that of the fundamental bending is about 4. Therefore a more accurate analysis should have included a few more eigen modes in the static deflection case. However, we believe that the set of mode shapes was enough to demonstrate the principle of aeroelastic coupling. We obtained the following loss of control surface effectiveness due to elastic effects:

TABLE 2

Loss in percent of rigid case coefficient for the control surface deflection at M=0.9.

Lifting force	63 % loss
Pitching moment about root mid chord	58 % loss
Bending moment	66% loss
Hinge moment	55% loss.

We find that there is *an overall tendency of losing 3/5 of the forces on the rigid wing and flap when accounting for the fact that the model was elastic*. Although no test data is available that verify the numbers, they are of the right order of magnitude.

CONCLUSIONS

Validation of computer codes for unsteady aerodynamics to be used in the design of aircraft must account for irregularities in the test and for major physical phenomena. We have given examples of how to correct for such things.

Control surface deflections cause perturbations of the pressure distribution that are sensible to viscous boundary layers. Not many good pressure measurements have been carried out that reach the trailing edge zone, which is important for the estimation of flap and tab hinge moments. An important task for further development is to find means of updating the fast and robust basic linear tools in industry to better model control surface aerodynamics. For this we need theoretical and physical understanding of the flow and unsteady flow perturbations in this region, and we need test results that are detailed enough.

A direct coupling of aerodynamics and structure in a non–linear fashion may be valid in the future, but with the quality of practical methods of today, the coupling procedure seems to be of highest value for static aeroelastic analysis. It is always important, however, to account for boundary layers and other effects that strongly influence the transonic nature of the flow.

ACKNOWLEDGEMENT

The investigations and the methods development discussed in this paper have been carried out in close collaboration with Dr Valter Stark at Saab. Much less had been accomplished without his vast experience and never failing problem solving ability.

This work has been carried out at Saab–Scania, Saab Aircraft Division, partly on a contract with Swedish Defence Administration. The reception of the NLR test data for the LANN and F5 wing is gratefully acknowledge as is the willingness of BAe to let us use their structural dynamics data on the RAE flutter model. Thanks are also due to Dr G Sidén of Volvo Flygmotor for providing Navier–Stokes results in a 2–D application.

REFERENCES

1 Stark, V. J. E., "The AEREL flutter prediction system", ICAS–90–1.2.3

2 Winzell, B., "Applications of the unsteady full potential equation for wings", *Proc European Forum on Aero–elasticity and Structural Dynamics*, 1989, pp. 65–83.

3 Shankar, V. & Ide, H., "Treatment of steady and unsteady flows using a fast, time–accurate full potential scheme", AIAA Paper 85–4060.

4 Sankar, L. N., Ruo, S. Y. & Malone, J. B., "Application of of surface transpiration in computational aerodynamics", AIAA Paper 86–0511.

5 Nash, J. F. & Macdonald, A. G. J., "The calculation of momentum thickness in a turbulent boundary layer at Mach numbers up to unity", *Aeronautical Research Council C. P.* No. 963, London, 1967.

6 Bauer, F., Garabedian, P., Korn, D. and Jameson, A., "Supercritical wing sections II", *Lecture Notes in Economics and Mathematical Systems* No 108, Springer, 1975.

7 Horsten, J. J., den Boer, R. G. & Zwaan, R. J., "Unsteady transonic pressure measurements on a semispan wind tunnel model of a transport–type supercritical wing (LANN model)", AFWAL–TR–83–3039, PARTs I and II, 1983.

8 Steiginga, A. & Houwink, R., "Correlation of experimental and quasi–3D theoretical airloads on the oscillating LANN supercritical wing model", AFWAL–TR–83–3050, 1983.

9 Garner, H. C., Payne, B. W. & Baldock, J. C. A., "Experimental flutter at high subsonic speeds and its theoretical prediction, taking into account wing thickness and Reynolds number", Paper 7 in *AGARD Conference Proceedings No 296: Boundary Layer Effects on Unsteady Airloads*. 51st AGARD SMP meeting in Aix–en–Provence, France, 1980.

10 Wenzinger, C.J., "Pressure distribution over an airfoil section with a flap and tab", *NACA Report* No 574, 1935.

11 Persoon, A. J., Roos, R. and Schippers, P., "Transonic and Low Supersonic Wind–tunnel Tests on a Wing with Inboard Control Surface", AFWAL–TR–80–3146, 1980.

THIS DOCUMENT PROVIDED BY THE ABBOTT AEROSPACE
TECHNICAL LIBRARY
ABBOTTAEROSPACE.COM

92-16036

AD-P007 798

A TIME-LINEARIZATION APPROACH FOR UNSTEADY TRANSONIC FLOWS

Y.S. Wong
Department of Mathematics, University of Alberta, Edmonton, Canada.

B.H.K. Lee
Institute for Aerospace Research, National Research Council, Ottawa, Canada.

H.S. Murty
Department of Mechanical Engineering, University of Ottawa, Ottawa, Canada.

SUMMARY

In this paper, development of a time-linearization approach for solving the unsteady transonic small disturbance equation is described in UST3D simulation code (UnSteady Transonic code for a 3D isolated wing). The accuracy of the method was examined by comparing the unsteady pressure distributions with those obtained from XTRAN3S code and experiments carried out at NLR on the F-5 wing at subsonic and transonic speeds. Some comparisons were also made for thicker wings (ONERA M6 and LANN) to show the deficiencies of the method. Using the UST3D code, flutter analysis was carried out on the AGARD 445.6 wing. The flutter boundaries were compared with experimental results and those from CAP-TSD code.

LIST OF SYMBOLS

b_s	semichord at wing root
c	chord length
C_L	lift coefficient
C_M	moment coefficient
C_Z	sectional normal force
ΔC_P	difference between lower and upper surface pressure coefficient
κ	reduced frequency based on chord
κ_b	reduced frequency based on semichord
M_∞	free-stream Mach number
s	total span
U	free-stream velocity
μ	wing mass to air mass ratio
γ	ratio of specific heats
ω	flutter frequency
ω_α	natural circular frequency of wing in first uncoupled torsion mode
α	angle of attack
ϕ	disturbance velocity potential
ϕ^s	steady component of ϕ
ϕ^u	unsteady component of ϕ
x_{le}	location of the wing leading edge in x-direction
x_{te}	location of the wing trailing edge in x-direction
y_{tip}	location of the wing tip in y-direction
$\tilde{\delta}_x$	forward difference operator to first derivative
δ_x	central difference operator to first derivative
δ_{xx}	central difference operator to second derivative
D_x	type-dependent upwing difference operator to first derivative

1. INTRODUCTION

Over the past decade, there has been considerable progress and promise in the development of numerical simulation techniques for unsteady transonic flow calculations. This activity was motivated by the need to supplement the expensive and time-consuming wind tunnel investigations and flight tests with inexpensive, fast and efficient computer simulation programs to accurately predict flutter boundaries and many other important aeroelastic phenomena in the transonic regime.

Although the basic fluid motion in unsteady aerodynamics is governed by the Navier-Stokes (NS) equation, numerical simulations of the complete NS equation for general three-dimensional flow problems are not yet sufficiently developed for flutter applications. Computational methods in three-dimensional unsteady transonic flows concentrate mainly on the transonic small disturbance (TSD) equation (Refs. 1-3) or full potential (FP) equation (Ref. 4). The major advantage of the simpler model using TSD or FP approach over those based on Euler and NS formulation is the large reduction in computational cost requirements.

At the 17th Congress of the International Council of the Aeronautical Sciences, a time-linearization approach for solving the transonic small disturbance equation was described by the first two authors (Ref. 1). It was demonstrated that the technique could be used with confidence for computations of three-dimensional unsteady transonic flows over an isolated thin wing. This paper fills in some of the details omitted from Ref. 1 and describes an improved version of the UST3D program. Also, comparisons of numerical results with other computer simulation codes and wind tunnel experiments are given to assess the accuracy of UST3D code.

In Section 2, the time-linearization approach for the transonic small disturbance equation is described. Numerical methods based on finite-difference approximations to the TSD equation are presented in Section 3. Computational results for a number of wing geometries and comparisons with other computer codes and experimental data are given in Section 4. In Section 5, the UST3D code is used with the Institute for Aerospace Research (IAR) flutter analysis computer program to determine flutter boundaries for the AGARD 445.6 wing. Correlations with experiments and with computed results from CAP-TSD (Ref. 3) are presented.

THIS DOCUMENT PROVIDED BY THE ABBOTT AEROSPACE
TECHNICAL LIBRARY
ABBOTTAEROSPACE.COM

2. A TIME-LINEARIZATION APPROACH FOR TSD EQUATION

The governing equation for three-dimensional unsteady transonic flows based on the TSD formulation is given by:

$$\frac{\partial f_0}{\partial t}+\frac{\partial f_1}{\partial x}+\frac{\partial f_2}{\partial y}+\frac{\partial f_3}{\partial z}=0 \tag{1}$$

where

$$f_0=-A\phi_t-B\phi_x$$

$$f_1=-E\phi_x-F\phi_x^2+G\phi_y^2$$

$$f_2=\phi_y+H\phi_x\phi_y$$

$$f_3=\phi_z$$

The coefficients A, B, E, F, G, and H are defined as:

$$A=M_\infty^2\kappa^2$$

$$B=2M_\infty^2\kappa$$

$$E=1-M_\infty^2$$

$$F=-\frac{1}{2}(\gamma+1)M_\infty^2$$

$$G=\frac{1}{2}(\gamma-3)M_\infty^2$$

and

$$H=-(\gamma-1)M_\infty^2$$

Equation (1) is the modified TSD equation. In the standard TSD equation, the coefficients for H and G are set to zero. In the present formulation, these additional crossflow terms $\phi_x\phi_{xy}$ and $\phi_x\phi_{yy}$ are retained in order to permit a better resolution of shock waves with large sweep angles.

Assuming the wing surface is located at $z=0$, where

$$z=g^{\pm}(x,y,t)$$

Then the wing surface boundary condition can be defined as

$$\phi_z=g_x^{\pm}+\kappa g_t^{\pm} \tag{2}$$

on $z=0$, $x_{le}\le x\le x_{te}$, $y\le y_{tip}$.

Two computational techniques could be used for solving the TSD equation (1): one based on a time-integration method, and the other using a time-linearization approach. Well-known examples of a time-integration technique are the XTRAN3S and CAP-TSD (Refs 2,3). In this paper, we consider a time-linearization approach, in which the solution of the TSD equation (1) is separated into its (non-linear) steady ϕ^s and (linear) unsteady ϕ^u components. This approach had been investigated by Weatherill and Ehlers (Ref. 5). Let ε be a parameter related to the amplitude of oscillation and which is assumed to be small, Weatherill and Ehlers considered the solution of the TSD equation of the form

$$\phi(x,y,z,t)=\phi^s(x,y,z)+\varepsilon\hat{\phi}^u(x,y,z)e^{i\omega t}$$

$$\varepsilon<<1 \tag{3}$$

It can be shown that $\hat{\phi}^u$ satisfied a linear partial differential equation (which is independent of time) with variable coefficients.

In this paper, we consider a time-linearization approach, in which the velocity potential is expressed in a more general form

$$\phi(x,y,z,t)=\phi^s(x,y,z)+\varepsilon\phi^u(x,y,z,t)$$

$$\varepsilon<<1 \tag{4}$$

The steady component ϕ^s satisfies a nonlinear partial differential equation

$$\frac{\partial f_1^s}{\partial x}+\frac{\partial f_2^s}{\partial y}+\frac{\partial f_3^s}{\partial z}=0$$

or,

$$C^s\phi_{xx}^s+G^s\phi_{xy}^s+E^s\phi_{yy}^s+\phi_{zz}^s=0 \tag{5}$$

where

$$C^s=(1-M_\infty^2)-(\gamma+1)M_\infty^2\phi_x^s$$

$$G^s=-2M_\infty^2\phi_y^s$$

$$E^s=1-(\gamma-1)M_\infty^2\phi_x^s$$

The unsteady component ϕ^u satisfies a linear time-dependent partial differential equation

$$A^u\phi_{tt}^u+B^u\phi_{xt}^u=C^u\phi_{xx}^u+D^u\phi_x^u+E^u\phi_{yy}^u+F^u\phi_y^u+G^u\phi_{xy}^u+\phi_{zz}^u \tag{6}$$

where

$$A^u=M_\infty^2\kappa^2$$

$$B^u=2M_\infty^2\kappa$$

$$C^u=(1-M_\infty^2)-(\gamma+1)M_\infty^2\phi_x^s$$

$$D^u=-(\gamma+1)M_\infty^2\phi_{xx}^s-(\gamma-1)M_\infty^2\phi_{yy}^s$$

$$E^u=1-(\gamma-1)M_\infty^2\phi_x^s$$

$$F^u=-2M_\infty^2\phi_{xy}^s$$

$$G^u=-2M_\infty^2\phi_y^s$$

Notice that the coefficients in Eq. (6) are computed from the solution of the steady velocity potential ϕ^s.

Following a time-linearization procedure, one can assume that

$$g=g^s+\varepsilon g^u \qquad \varepsilon<<1$$

Therefore, the wing surface boundary condition given in Eq. (2) becomes

$$\phi_z^s=g_x^s \tag{7}$$

and

THIS DOCUMENT PROVIDED BY THE ABBOTT AEROSPACE
TECHNICAL LIBRARY
ABBOTTAEROSPACE.COM

$$\phi_z^u = g_x^u + \kappa g_t^u \tag{8}$$

The wing surface boundary condition for the steady TSD equation is defined in Eq. (7), it includes the effects of thickness and mean angle of attack. Equation (8), on the other hand, represents a wing of vanishing thickness undergoing an unsteady motion with zero mean angle of attack.

The far-field boundary conditions for the steady TSD equation (5) are given as follows:

Far upstream: $\phi^s = 0$

Far downstream: $\phi_{xx}^s + \phi_{zz}^s = 0$

Far above and below: $\phi^s = 0$

Far spanwise: $\phi^s = 0$

For the plan of symmetry: $\phi_y^s = 0$ and $\phi_{xy}^s = 0$

These boundary conditions have also been employed by Boppe (Ref. 6) for solving the steady TSD equation applied to an isolated wing.

For the unsteady TSD equation (6), non-reflecting boundary conditions developed by Jiang and Wong (Ref. 7) are imposed on the outer computational boundaries. The boundary conditions are derived from the theory of wave propagation, and it can be shown that these conditions are perfectly absorbing for wave packets propagating at certain group velocities. The application of the non-reflecting boundary conditions allows wave solution travelling in one directly only. Consequently, the solution of the unsteady TSD equation is permitted to propagate through the artificial computational boundaries as if there are no boundaries presented. The major advantage in the application of non-reflecting boundary conditions is to provide more accurate numerical simulations for the unsteady TSD equation (6) because the effect of the non-physical reflections due to a finite computational domain is reduced. The first-order non-reflecting boundary conditions for Eq. (6) are derived using the approach presented in Ref. [7], and they can be expressed as:

Far upstream and downstream:

$$\alpha\phi_t^u + \beta\phi_x^u + \gamma\phi_y^u = 0$$

where

$$\alpha = \sqrt{\frac{B^2}{4} + AC} - \frac{B}{2} + \left(\frac{1}{\upsilon} - 1\right)\frac{AC}{\sqrt{\frac{B^2}{4} + AC}}$$

$$\beta = A\left[\left(1 - \frac{1}{\upsilon}\right)\frac{B}{2\sqrt{\frac{B^2}{4} + AC}} - 1\right]$$

$$\gamma = \frac{AG}{2\upsilon\sqrt{\frac{B^2}{4} + AC}} \qquad -1 \le \upsilon < 0$$

for far upstream and

$$\alpha = \sqrt{\frac{B^2}{4} + AC} + \frac{B}{2} + \left(\frac{1}{\upsilon} - 1\right)\frac{AC}{\sqrt{\frac{B^2}{4} + AC}}$$

$$\beta = A\left[\left(1 - \frac{1}{\upsilon}\right)\frac{B}{2\sqrt{\frac{B^2}{4} + AC}} + 1\right]$$

$$\gamma = \frac{AG}{2\upsilon\sqrt{\frac{B^2}{4} + AC}} \qquad -1 \le \upsilon < 0$$

for far downstream.

Far above and below:

$$\upsilon\sqrt{A}\phi_t^u + \frac{B\upsilon}{2\sqrt{A}}\phi_x^u + \phi_z^u = 0$$

where $0 < \upsilon \le 1$ for above and $-1 \le \upsilon < 0$ for below.

Far Spanwise:

$$\upsilon\sqrt{AC}\phi_t^u + \frac{1}{2}\left(G + \upsilon\sqrt{\frac{E}{A}}B\right)\phi_x^u + E\phi_y^u = 0$$

where $0 < \upsilon \le 1$.

For the plane of symmetry:

$$\phi_y^u = 0$$

The coefficients A, B, C, E, and G are defined in the unsteady TSD equation (6), which are calculated locally at the computational boundaries. The parameter υ can be chosen to improve the absorptivity of the non-reflecting boundary conditions, and they are taken to be υ=1 or υ=-1 in our computations.

3. COMPUTATIONAL PROCEDURES

In this section, computational techniques based on finite-difference approximations for solving the TSD equation are presented. Recall that the steady and unsteady TSD equations (5) and (6) are effectively uncoupled because of the conditions given in Eqs. (7) and (8). In section 3.1, computational grid systems are described, and the solution procedures for the steady and unsteady TSD equations are then presented in sections 3.2 and 3.3. The superscripts s and u will be omitted in the discussion given in sections 3.2 and 3.3.

3.1 Computational Grid Systems

The computational space and grid systems employed here are the same as that adopted by Boppe (Ref. 6). The grid systems consist of two levels.

In the first level grid, the computational space is divided by a Cartesian grid, in which the original (x, y, z) coordinates are mapped into the new (ξ, η, ζ) coordinates. A stretching transformation is then applied so that the physical

THIS DOCUMENT PROVIDED BY THE ABBOTT AEROSPACE
TECHNICAL LIBRARY
ABBOTTAEROSPACE.COM

boundaries corresponding to infinity becomes a finite computational domain in the ξ, η, ζ region. Hence

Physical Space	Computational Space
$-\infty \le x \le \infty$	$-4.167 \le \xi \le 4.167$
$0 \le y \le \infty$	$0 \le \eta \le 1$
$-\infty \le z \le \infty$	$-1 \le \zeta \le 1$

For a typical calculation, there are 72 computational cells (i.e., 73 grid points) in the x-direction, in which at least 48 cells are used to cover the wing planform. In the y-direction, the total number of grid points is 26 with 18 of which being in the wing span. There are 31 grid points in the z-direction, and the wing mean plane is located at z=0 (i.e. 15 grid points above and below the wing). In the first level grid the total number of grid points is $73 \times 26 \times 31$ (i.e. 58838).

The second level grid is considered to be a fine grid system, in which the wing grid is evenly spaced in both the x- and z- directions. The second level grid boundaries are positioned at 20% local chord distance in front of the leading edge and 10% behind the trailing edge. In the z-direction, the grid is constructed in such a way that 30% of the wing chord above the wing plane and 10% below. The number of grid points in the x-, y- and z- direction is 127 (in which 100 grid points are place along the wing chord), 19 and 31, respectively.

The steady TSD equation (5) can be computed either using the first level grid alone or a combination of first and second level grids. The solution of the unsteady TSD equation (6), however, is always obtained using only the first level grid. The steady state results needed to solve the unsteady flow are sometimes obtained using a second level grid. In that case, solution of the unsteady equation uses interpolated steady results from second to first level grid.

3.2 Procedure for Steady TSD Equation

The steady TSD equation (5) is nonlinear and of mixed elliptic-hyperbolic type. The type of the equation is determined by

$$D = G^2 - 4CE$$

where the coefficients G, C, and E are defined in Eq. (5). The steady TSD equation is of elliptic type (i.e. for subsonic region) if $D < 0$, and of hyperbolic type (i.e., for supersonic region) if $D > 0$.

A finite-difference approximation is used to discretize Eq. (5), and the Murman-Cole type-dependent difference scheme (Ref. 8) is used for the ϕ_{xx} term, that is

$$\phi_{xx} = \frac{\phi_{i+1,j,k} - 2\phi_{i,j,k} + \phi_{i-1,j,k}}{\Delta x^2}$$

if the grid point (i, j, k) is in subsonic region (i.e. $D < 0$), and

$$\phi_{xx} = \frac{\phi_{i,j,k} - 2\phi_{i-1,j,k} + \phi_{i-2,j,k}}{\Delta x^2}$$

if the grid point (i, j, k) is in supersonic region (i.e. $D > 0$).

Central differencing is used for all other derivatives regardless of the local flow velocity, that is,

$$\phi_x = \frac{\phi_{i+1,j,k} - 2\phi_{i-1,j,k}}{2\Delta x}$$

$$\phi_y = \frac{\phi_{i,j+1,k} - \phi_{i,j-1,k}}{2\Delta y}$$

$$\phi_{yy} = \frac{\phi_{i,j+1,k} - 2\phi_{i,j,k} + \phi_{i,j-1,k}}{\Delta y^2}$$

$$\phi_{zz} = \frac{\phi_{i,j,k+1} - 2\phi_{i,j,k} + \phi_{i,j,k-1}}{\Delta z^2}$$

$$\phi_{xy} = \frac{\Phi}{4\Delta x \Delta y}$$

where

$$\Phi = \phi_{i-1,j-1,k} - \phi_{i-1,j+1,k} - \phi_{i+1,j-1,k} + \phi_{i+1,j+1,k}$$

By the application of the finite-difference approximations, the solutions of equation (5) is then transformed to the solutions of a large system of difference equations,

$$L(\phi) = 0 \tag{9}$$

where ϕ is a vector with elements $\phi_{i,j,k}$ corresponding to the potential at the grid point (i, j, k). Since Eq. (5) is nonlinear, the resulting system of difference equation is also nonlinear.

3.2.1 *Newton-like iterative algorithm*

A Newton-like iterative scheme, which was first proposed by Wong (Ref. 9) for the two-dimensional nonlinear transonic full potential equation, is applied for the solution of Eq. (9) The iterative procedure is described as follows:

Let $\phi^{(0)}$ be an initial approximation for the potential vector, then for n=0, 1, 2, ...,

$$\left.\begin{array}{l} \text{step 1, compute the residual vector} \\ \quad r^{(n)} = L(\phi^{(n)}) \\ \text{step 2, solve the linear system} \\ \quad M_n \delta\phi^{(n)} = -r^{(n)} \\ \text{step 3, update the potential vector} \\ \quad \phi^{(n+1)} = \phi^{(n)} + \delta\phi^{(n)} \end{array}\right\} \tag{10}$$

where n is an iteration number, $\delta\phi^{(n)}$ is the correction vector and M_n is a matrix operator varying from iteration to iteration. The iterative process is repeated until the residual norm $\| r^{(n)} \|$ is less then ε.

In the above formulation, the convergence of the iterative scheme depends upon the linear operator M_n. For example, a simple choice for $M_n = I$ (the identity matrix) or $M_n = D$ (a diagonal matrix) can only be used if the entire flow field is subsonic. For transonic flow problems, it is well-known that the successive line over-relaxation method (SLOR) provides a stable solution. For the SLOR method, M_n corresponds to a tridiagonal matrix. This method, however, could be inefficient because it requires a relaxation

THIS DOCUMENT PROVIDED BY THE ABBOTT AEROSPACE
TECHNICAL LIBRARY
ABBOTTAEROSPACE.COM

parameter which is usually difficult to determine a priori for practical problems. Notice that, if the parameter is incorrectly chosen, it will result in a slow convergence or even divergence. In this paper, a fully implicit scheme is developed. It not only provides a faster convergence rate than the SLOR method, but it also does not require any parameter.

The operator M_n is chosen to be an approximation to the linearized transonic operator. Suppose, at the nth iteration, the coefficients C, E, and G is Eq. (5) have been calculated from the value of the potential at the $(n\text{-}1)$-th iteration. The result of the application of a finite-difference approximation to Eq. (5) then leads to a 12-point formula, where

$$\begin{aligned}(L\phi)_{i,j,k} &= \mathrm{AC}_{i,j,k}\,\phi_{i,j,k} + \mathrm{AW}_{i,j,k}\,\phi_{i-1,j,k} \\ &\quad + \mathrm{AWW}_{i,j,k}\,\phi_{i-2,j,k} + \mathrm{AE}_{i,j,k}\,\phi_{i+1,j,k} \\ &\quad + \mathrm{AN}_{i,j,k}\,\phi_{i,j+1,k} + \mathrm{AS}_{i,j,k}\,\phi_{i,j-1,k} \\ &\quad + \mathrm{AO}_{i,j,k}\,\phi_{i,j,k+1} + \mathrm{AI}_{i,j,k}\,\phi_{i,j,k-1} \\ &\quad + \mathrm{NW}_{i,j,k}\,\phi_{i-1,j+1,k} + \mathrm{NE}_{i,j,k}\,\phi_{i+1,j+1,k} \\ &\quad + \mathrm{SW}_{i,j,k}\,\phi_{i-1,j-1,k} + \mathrm{SE}_{i,j,k}\,\phi_{i+1,j-1,k} \end{aligned} \tag{11}$$

Notice that the coefficient AWW_{ijk} is equal to zero if the grid point (i, j, k) is in the subsonic region. Moreover, the coefficients NW_{ijk}, NE_{ijk}, SW_{ijk} and SE_{ijk} are due to the cross-term $G\phi_{xy}$ in Eq. (5), and their values are usually smaller than other coefficients for the transonic small-disturbance formulation. In the present work, the operator M_n is chosen by setting the coefficients AWW_{ijk}, NW_{ijk}, NE_{ijk}, SW_{ijk} and SE_{ijk} to zero. Hence, M_n corresponds to a seven-point formula:

$$\begin{aligned}(M_n\phi)_{i,j,k} &= \mathrm{AC}_{i,j,k}\,\phi_{i,j,k} + \mathrm{AW}_{i,j,k}\,\phi_{i-1,j,k} \\ &\quad + \mathrm{AE}_{i,j,k}\,\phi_{i+1,j,k} \\ &\quad + \mathrm{AN}_{i,j,k}\,\phi_{i,j+1,k} \\ &\quad + \mathrm{AS}_{i,j,k}\,\phi_{i,j-1,k} \\ &\quad + \mathrm{AO}_{i,j,k}\,\phi_{i,j,k+1} \\ &\quad + \mathrm{AI}_{i,j,k}\,\phi_{i,j,k-1} \end{aligned} \tag{12}$$

3.2.2 *Preconditioned minimal residual algorithm*

The main computational work in the Newton-like iterative procedure given in (10) is in step 2 for the solution of the correction vector,

$$M\,\delta\phi = \tag{13}$$

where M is a large sparse matrix consisting of seven non-zero diagonals. For simplicity, the subscript and superscript n are omitted. It is important to have an efficient solution technique for Eq. (13), since the large system of equations has to be solved for each step in the Newton-like procedure. A direct method is not possible because it requires a large amount of storage and arithmetic operations. In this paper an iterative scheme base on a minimal residual algorithm is applied. Moreover, the algorithm is used in conjunction with a preconditioning technique in order to yield a rapid rate of convergence.

The purpose of using a preconditioning technique is to accelerate the convergence rate of an iterative process. Suppose C is a nonsingular matrix, Eq. (13) can be written as

$$MC^{-1}C\,\delta\phi = -r \tag{14}$$

where C is generally known as a preconditioning matrix, and Eq. (14) is called the preconditioned system for Eq. (13). If the operator C is chosen so that C^{-1} is a good approximation to M^{-1}, the condition number of MC^{-1} would be much smaller than that for M itself. Since the rate of convergence for an iterative method depends upon the condition number of the linear system, solving the preconditioned system (14) could yield a faster convergence rate than that of the original system (13). A detailed account of the construction for the C matrix will be discussed shortly.

The preconditioned minimal residual algorithm is given as follows.

Let $\delta\phi^{(0)}$ be an initial guess correction vector, compute the initial residual vector for the system,

$$p^{(0)} = -r - M\,\delta\phi^{(0)}$$

and solve the preconditioning system,

$$Cz^{(0)} = p^{(0)}$$

Then for $k = 0,1,2,\ldots,\bar{k}$, do:

step 1, compute the parameter:

$$\alpha_k = \frac{(p^{(k)}, Mz^{(k)})}{(Mz^{(k)}, Mz^{(k)})}$$

step 2, update the new correction vector:

$$\delta\phi^{(k+1)} = \delta\phi^{(k)} + \alpha_k z^{(k)}$$

step3, update the new residual vector:

$$p^{(k+1)} = p^{(k)} - \alpha_k Mz^{(k)}$$

step 4, solve the preconditioning matrix for $z^{(k+1)}$:

$$Cz^{(k+1)} = p^{(k+1)}$$

(15)

In step 1, (x, y) denotes the usual inner product, i.e. $(x, y) = x^{\mathrm{T}}y$. Notice that, if $C = I$ (the identity matrix), then $z^{(k)} = p^{(k)}$ for all k and the method becomes the basic minimal residual algorithm with no preconditioning.

The main computational work per iteration in the preconditioned minimal residual algorithm is one matrix by vector multiplication for Mz, and solving the preconditioning system for $Cz = p$.

The iterative procedure for the solution of the transonic flow equation thus consists of outer and inner iterations: the outer is based on a Newton-like algorithm for solving the nonlinear TSD equation (5), and in the inner iteration, a preconditioned minimal residual technique is applied to find the solution for the linear system(10). Since we are interested in the overall convergence for the nonlinear problem (i.e. Eq. 5), it may not be necessary to solve the linear system in Eq. (13) to excessive accuracy for each Newton-like iteration. In the present implementation, only an approximate solution is sought for the linear system. Hence, a small fixed number of iterations (such as $\bar{k} = 4$) is

THIS DOCUMENT PROVIDED BY THE ABBOTT AEROSPACE
TECHNICAL LIBRARY
ABBOTTAEROSPACE.COM

sufficient in the preconditioned minimal residual algorithm (15).

The preconditioning matrix C plays an important role in the convergence rate of the minimal-residual algorithm. For an effective preconditioning, the matrix C should have the following two properties:

(1) C should be chosen so that C^{-1} is a good approximation to M^{-1} in some sense. Consequently, the condition number of MC^{-1} is much smaller than that of M itself.

(2) The preconditioning step $Cz = p$ or $z = C^{-1}p$ should be easily computed; otherwise, the preconditioning step will not be efficient.

A popular preconditioning algorithm which satisfy the conditions mentioned above is an incomplete LU factorization preconditioning. In this approach, the preconditioning operator C is taken to be an approximation to the matrix M, and it is also a product of sparse triangular matrices:

$$C = LU = M + E \tag{16}$$

where L and U are sparse lower and upper triangular matrices. The nonzero elements of L and U appear in the same locations as those in the matrix M, where

$$(L\phi)_{i,j,k} = D_{i,j,k}\phi_{i,j,k} + A_{i,j,k}\phi_{i,j,k-1} + C_{i,j,k}\phi_{i-1,j,k} + B_{i,j,k}\phi_{i,j-1,k}$$

and

$$(U\phi)_{i,j,k} = \phi_{i,j,k} + E_{i,j,k}\phi_{i+1,j,k} + F_{i,j,k}\phi_{i,j+1,k} + G_{i,j,k}\phi_{i,j,k+1}$$

The matrix E in eq. (16) is known as the error matrix which measures how good the approximation between C and M is. Since L and U are constructed so that their nonzero diagonals are in the same locations as those in the lower and upper triangular part of M, this approach is generally referred to as an incomplete LU factorization preconditioning (Refs.10, 11).

The coefficients of L and U are computed from the coefficients of M according to the relations:

$$\begin{aligned}
A_{i,j,k} &= \mathrm{AI}_{i,j,k} \\
B_{i,j,k} &= \mathrm{AS}_{i,j,k} \\
C_{i,j,k} &= \mathrm{AW}_{i,j,k} \\
D_{i,j,k} &= 1 + \alpha(\mathrm{AC}_{i,j,k} + \mathrm{AWW}_{i,j,k}) \\
&\quad - A_{i,j,k}G_{i,j,k-1} - C_{i,j,k}E_{i-1,j,k} \\
&\quad - B_{i,j,k}F_{i,j-1,k} \\
&\quad - A_{i,j,k}(E_{i,j,k-1} + F_{i,j,k-1}) \\
&\quad - B_{i,j,k}(E_{i,j-1,k} + G_{i,j-1,k}) \\
&\quad - C_{i,j,k}(F_{i-1,j,k} + G_{i-1,j,k}) \\
E_{i,j,k} &= \mathrm{AE}_{i,j,k} / D_{i,j,k} \\
F_{i,j,k} &= \mathrm{AN}_{i,j,k} / D_{i,j,k} \\
G_{i,j,k} &= \mathrm{AO}_{i,j,k} / D_{i,j,k}
\end{aligned} \tag{17}$$

A small value α is added to the main diagonal elements of M to ensure the stability of the iterative scheme. However, the convergence rate is not sensitive to α and $\alpha = 0.05$ is used in our computer implementation. Notice that $\mathrm{AWW}_{i,j,k}=0$ if the point (i, j, k) is in the subsonic region, and $\mathrm{AWW}_{i,j,k} \neq 0$ if it is in the supersonic region. However, if $\mathrm{AWW}_{i,j,k} \neq 0$, then the sign of $\mathrm{AWW}_{i,j,k}$ is the same as that for the $\mathrm{AC}_{i,j,k}$. Consequently, adding the coefficient $\mathrm{AWW}_{i,j,k}$ to the $\mathrm{AC}_{i,j,k}$ will improve the stability of the scheme.

Since $C = LU$, the preconditioning step

$$Cz = p$$

can be computed efficiently via solving a forward substitution

$$Ls = p$$

and then a back substitution

$$Uz = s$$

3.3 Procedures for Unsteady TSD Equation

Upon solving the steady TSD equation, the coefficients of the unsteady TSD equation (6) can then be calculated. Eq. (6) is a linear hyperbolic partial differential equations, and two computational algorithms (one based on a semi-implicit scheme and the other a fully implicit scheme) have been investigated.

3.3.1 *Semi-implicit ADI (SADI) scheme*

The SADI scheme described in this section is similar to the ADI algorithm employed by Borland and Rizzetta (Ref. 12) for solving the unsteady TSD equation. In the present algorithm, Eq. (6) is finite differenced in which the x-direction is treated explicitly while the y- and z-directions are discretizated by an ADI type method.

The SADI scheme is used to advance the solution ϕ from the time level n to n+1 until some prescribed time is reached. At a particular time level, the value of ϕ is updated from n to n+1 on each successive y-z plane marching from upstream to downstream. The solutions on the first and the last plane are obtained via the applications of the upstream and downstream boundary conditions. On each subsequent y-z plane, the following two sweeps of the SADI algorithm are performed.

y-sweep:

$$B\bar{\delta}_x\frac{\tilde{\phi}-\phi^n}{\Delta t} = CD_x\bar{\delta}_x\phi^n + D\delta_x\phi^n + \tfrac{1}{2}E\delta_{yy}(\phi^n+\tilde{\phi}) + F\delta_y\phi^n + \tfrac{1}{2}G\bar{\delta}_xD_y(\phi^n+\tilde{\phi}) + \delta_{zz}\phi^n \tag{18}$$

and

z-sweep:

$$A\frac{\phi^{n+1}-2\phi^n+\phi^{n-1}}{(\Delta t)^2} + B\bar{\delta}_x\frac{\phi^{n+1}-\tilde{\phi}}{\Delta t} = \tfrac{1}{2}\delta_{zz}(\phi^{n+1}-\phi^n) \tag{19}$$

In Eq. (18), $\tilde{\phi}$ denotes the intermediate potential. The coefficients A, B, C, D, E, F, and G are defined in the

THIS DOCUMENT PROVIDED BY THE ABBOTT AEROSPACE
TECHNICAL LIBRARY
ABBOTTAEROSPACE.COM

unsteady TSD equation (6), and the difference operators are given by:

$$\bar{\delta}_x \phi_{i,j,k} = \frac{\phi_{i,j,k} - \phi_{i-1,j,k}}{x_i - x_{i-1}}$$

$$\bar{\delta}_y \phi_{i,j,k} = \frac{\phi_{i,j,k} - \phi_{i,j-1,k}}{y_i - y_{i-1}}$$

$$\bar{\delta}_z \phi_{i,j,k} = \frac{\phi_{i,j,k} - \phi_{i,j,k-1}}{z_i - z_{i-1}}$$

$$\delta_x \phi_{i,j,k} = \frac{1}{2}(\bar{\delta}_x \phi_{i+1,j,k} + \bar{\delta}_x \phi_{i,j,k})$$

$$\delta_y \phi_{i,j,k} = \frac{1}{2}(\bar{\delta}_y \phi_{i,j+1,k} + \bar{\delta}_y \phi_{i,j,k})$$

$$\delta_{yy} \phi_{i,j,k} = \frac{2}{y_{j+1} - y_{j-1}}(\bar{\delta}_y \phi_{i,j+1,k} + \bar{\delta}_y \phi_{i,j,k})$$

$$\delta_{zz} \phi_{i,j,k} = \frac{2}{z_{k+1} - z_{k-1}}(\bar{\delta}_z \phi_{i,j,k+1} + \bar{\delta}_z \phi_{i,j,k})$$

$$D_x \phi_{i,j,k} = \begin{cases} \dfrac{\phi_{i,j,k} - \phi_{i-1,j,k}}{x_i - x_{i-1}} & \text{if } C < 0 \\ \dfrac{\phi_{i+1,j,k} - \phi_{i,j,k}}{x_{i+1} - x_i} & \text{if } C \geq 0 \end{cases}$$

and

$$D_y \phi_{i,j,k} = \begin{cases} \dfrac{\phi_{i,j,k} - \phi_{i,j-1,k}}{y_j - y_{j-1}} & \text{if } G < 0 \\ \dfrac{\phi_{i,j+1,k} - \phi_{i,j,k}}{y_{j+1} - y_j} & \text{if } G \geq 0 \end{cases}$$

It should be pointed out that the two sweeps of the SADI algorithm given in Eqs. (18) and (19) are computed via solving the following two sets of tridiagonal matrix equations.

The resulting system of equations in the y-sweep Eq. (18) can be expressed as:

$$a_j^y \tilde{\phi}_{j-1} + b_j^y \tilde{\phi}_j + c_j^y \tilde{\phi}_{j-1} = d_j^y$$

$$j=2, 3, \ldots, J_{max-1} \qquad (20)$$

for each fixed value of z. After solving the intermediate value $\tilde{\phi}$ from Eq. (20), the solution ϕ^{n+1} can be computed from the z-sweep in which Eq. (19) leads to the tridiagonal system.

$$a_k^z \phi_{k-1}^{n+1} + b_k^z \phi_k^{n+1} + c_k^z \phi_{k+1}^{n+1} = d_k^z$$

$$k=1, 2, \ldots, K_{max} \qquad (21)$$

In the SADI algorithm, the size of the time-step is limited by the Courant-Friedrichs-Lewy (CFL) condition (Ref. 13). The CFL condition must be satisfied in order to ensure for numerical stability. The allowable time-step can be computed via

$$\Delta t \leq \frac{B}{\max C} \Delta x \qquad (22)$$

where the coefficients B and C are defined in Eq. (6). It has been observed that a larger time-step Δt could be used for most practical applications while numerical stability is maintained.

3.3.2 *Fully Implicit scheme*

Let θ be a parameter such that $0 < \theta \leq 1$, and consider the following numerical algorithm for Eq. (6):

$$A\frac{\phi_{i,j,k}^{n+1} - 2\phi_{i,j,k}^{n} + \phi_{i,j,k}^{n-1}}{(\Delta t)^2} + B\bar{\delta}_x \frac{\phi_{i,j,k}^{n+1} - \phi_{i,j,k}^{n}}{\Delta t}$$

$$= \theta\left[C\phi_{xx}^{n+1} + E\phi_{yy}^{n+1} + G\phi_{xy}^{n+1} + \phi_{zz}^{n+1}\right]$$

$$+(1-\theta)\left[C\phi_{xx}^{n} + E\phi_{yy}^{n} + G\phi_{xy}^{n} + \phi_{zz}^{n}\right] + D\phi_x^n + F\phi_y^n \qquad (23)$$

Eq. (23) can be rewritten as

$$A\phi_{i,j,k}^{n+1} + B\Delta t\bar{\delta}_x \phi_{i,j,k}^{n+1}$$

$$-(\Delta t)^2\theta\left[C\phi_{xx}^{n+1} + E\phi_{yy}^{n+1} + G\phi_{xy}^{n+1} + \phi_{zz}^{n+1}\right]$$

$$= 2A\phi_{i,j,k}^{n} + B\Delta t\bar{\delta}_x \phi_{i,j,k}^{n}$$

$$+(\Delta t)^2(1-\theta)\left[C\phi_{xx}^{n} + E\phi_{yy}^{n} + G\phi_{xy}^{n} + \phi_{zz}^{n}\right]$$

$$+(\Delta t)^2(D\phi_x^n + F\phi_y^n) - A\phi_{i,j,k}^{n-1} \qquad (24)$$

Notice that when ϕ_{xx}, ϕ_{yy}, ϕ_{zz}, ϕ_{xy}, ϕ_x, and ϕ_y are expressed in the standard finite-difference notations, Eq. (24) leads to a large and sparse system of linear equations

$$M\phi^{n+1} = f(\phi^n, \phi^{n-1}). \qquad (25)$$

The structure of the matrix operator M is similar to the finite difference operator for the steady TSD equation $\mathcal{L}$ given in (11), and it consists of 12 non-zero diagonals. Hence, the solution ϕ^{n+1} at a given time-step is obtained by solving the large matrix Eq. (25). The preconditioned minimal residual algorithm, which has been discussed in Section 3.2 for the solution of steady TSD equation, can also be applied here. Notice that when θ=0, Eq. (24) becomes an explicit scheme. For practical computations, $\theta = \frac{1}{2}$ (which corresponds to a Crank-Nicolson type method) is suggested. Even though the CFL condition is no longer required for the fully implicit scheme, the time-step should

THIS DOCUMENT PROVIDED BY THE ABBOTT AEROSPACE
TECHNICAL LIBRARY
ABBOTTAEROSPACE.COM

not be chosen too large because of the accuracy consideration.

4. COMPUTATIONAL RESULTS

The semi-implicit ADI algorithm and the fully implicit scheme described in the previous section are implemented into UST3D and UST3DF computer simulation codes. Both codes perform a time-linearization approach to solve a three-dimensional transonic small-disturbance equation. As expected, numerical results obtained from the UST3D and UST3DF codes are essentially the same. A smaller time-step is needed for the semi-implicit scheme. The SADI algorithm is generally preferred because the fully implicit scheme is very time consuming due to the requirement of solving a large system of matrix at each time-level. Numerical results reported in this paper will be obtained from the UST3D code.

4.1 Steady Transonic Flows

As discussed previously, the solution of the steady TSD equation (5) can be computed using either one level grid (73 × 26 × 31) alone or a combination of two level grid systems (73 × 26 × 31 and 127 × 19 × 31). Experience indicates that one level grid is usually sufficient for fighter type wings with thin airfoil sections. The application of two level grids, however, provides more accurate numerical solutions for thicker wings.

Figure 1 and 2 compare results obtained using the Newton-like iterative scheme with the classical successive line over-relaxation (SLOR) method. Unlike the Newton-like algorithm, the residual vector is usually not calculated in the SLOR method. Consequently, the convergence test to the steady TSD equation will be examined via considering the development of the supersonic points in the flowfield and the circulations at each semispan station. In figure 1, the supersonic points versus number of iterations have been plotted for the F/A-18 wing at M_∞ = 0.92. The corresponding circulations at 66% and 87% semispan stations versus number of iterations have been shown in figure 2. As can be seen, the Newton-like algorithm provides a very rapid rate of convergence. The superiority of the present method is also clearly demonstrated in Tables 1 and 2.

Table 1. Number of iterations required to attain 90%, 95%, 99% of the supersonic points for F/A-18 wing at M_∞ = 0.92, α=0°

	90%	95%	99%
Newton-like	14	18	32
SLOR	119	168	295

Table 2. Number of iterations required to attain 90%, 95%, 99% of the circulation at 66% semispan station for F/A-18 wing at M_∞ = 0.92, α=0°

	90%	95%	99%
Newton-like	15	22	36
SLOR	148	230	450

A significant speed-up in convergence rate is achieved by applying the Newton-like iteration algorithm used in conjunction with an incomplete LU factorization preconditioning. Rapid rates of convergences have also been achieved when the present algorithm is tested for the F5 wing, ONERA M6 wing and the LANN wing.

4.2 Unsteady Transonic Flows

To verify the accuracy of the time-linearization approach for unsteady transonic flows, the UST3D code is tested for the F5 wing, the LANN wing and the ONERA M6 wing. These wing models are selected because of the availability of results from other existing computer simulation programs. Experimental data are also available for the F5 wing and the LANN wing.

4.2.1 *F5 Wing*

The F5 wing is a fighter type model which has an aspect ratio of 2.98, a taper ratio of 0.31, and a leading-edge sweep angle of 31.92°. A variety of computational methods such as XTRAN3S (Ref. 2), ATRAN3S (Ref. 14), ENSAERO (Ref. 15) are available to compare with the NLR experimental unsteady pressure distribution data provided by Tijdeman et al. (Ref. 16).

For the computational results reported in this section, the F5 wing is undergoing a pitching motion about an axis located at the 50% root chord and the pitching axis is normal to the wing root. The frequency of oscillation is set to be 40 Hz.

Figure 3 displays the real and imaginary unsteady pressure distributions at 50% semispan station for the F5 wing at M_∞ = 0.95. Figures 3a, 3b, and 3c illustrate the numerical results after one, two and three cycle computations using the UST3D code with 250 time-step per cycle. These results are also compared with NLR experimental data. Figure 3d shows the results after five cycle of computations using the UST3D with 500 time-step per cycle. It is interesting to note that even after one cycle of computation, the UST3D code already provides a good representation of the unsteady pressure distributions. It is recommended that three cycle of computations will be sufficient for most practical calculations. The total computing time for the UST3D code applied to the F5 wing at M_∞ = 0.95 using 250 time-step per cycle with three cycle of computations is about 15 minutes on IBM RISC 6000/320H workstation.

Figure 4 displays the unsteady pressure distributions for the F5 wing at M_∞ = 0.80. The UST3D results are compared with those obtained from XTRAN3S (Ref. 2) and NLR experiments (Ref. 16). The corresponding results for M_∞ = 0.95 are shown in Figure 5. As illustrated in Figure 4 for the case of M_∞ = 0.80 in which the flow field is subsonic, both the real and imaginary parts of the unsteady pressure distributions of the UST3D code compare well with those obtained using XTRAN3S code and NLR experiment. At M_∞ = 0.95, unsteady pressure distributions computed by the UST3D code provide a better agreement to the NLR experiment than those obtained by XTRAN3S code. In particular, unlike the XTRAN3S results, good agreement is observed for the imaginary parts for all semispan stations. The real parts also compare well except those near the wing tip.

4.2.2 *LANN Wing*

The LANN wing is a transport-type model with supercritical airfoil sections, which has been selected as one of the AGARD three-dimensional standard aeroelastic configurations for comparison of transonic flow computations (Ref. 17). Extensive experimental results on the unsteady pressure measurements for the LANN wing

THIS DOCUMENT PROVIDED BY THE ABBOTT AEROSPACE
TECHNICAL LIBRARY
ABBOTTAEROSPACE.COM

were reported in Ref. 18. The test conditions for the present study were made for a Mach number M_∞=0.82, a mean angle of attack α=0.6°, a pitching amplitude $\Delta\alpha$=0.25° at a reduced frequency κ=0.2046. Unsteady sectional airloads presented in this section are defined as follows:

$$C_z = C_z' + iC_z'' \tag{26}$$

for the normal force, and

$$C_M = C_M' + iC_M'' \tag{27}$$

for the moment coefficient (pitching about 1/4 chord and positive nose down).

The unsteady spanwise normal force distributions and the moment coefficient distributions are shown in figures 6 and 7, respectively. The UST3D results are compared with the experimental data as well as other published computational results including XTRAN3S, a quasi-three-dimensional (Q-3-D) method, and subsonic three-dimensional code (Ref. 19). Agreements for both real and imaginary parts of the UST3D results for the unsteady sectional airloads are generally good.

4.2.3 *ONERA M6 Wing*

The ONERA M6 wing has an aspect ratio of 3.8, a taper ratio of 0.562 and a leading edge swept angle of 30°. The airfoil section is a 10% maximum thickness-to-chord ratio conventional section known as the ONERA "D" airfoil. The test conditions were made for a Mach number M_∞=0.84, a mean angle of attack α=3.06°, a pitching amplitude $\Delta\alpha$=1° at a reduced frequency κ=0.1. The wing was undergoing a pitching motion about an axis located at the 25% root chord and the pitching axis is normal to the wing root.

Experimental data for the unsteady pressure distributions is not available. However, computational results using the modified CAP-TSD algorithm were reported by Batina (Ref. 20). Figure 8 compares the instantaneous pressure distributions computed by the UST3D code with those based on the CAP-TSD algorithm. The unsteady pressure distributions corresponding to both maximum (α=4.06°) and minimum (α=2.06°) pitch angles during the third cycle of computations are displayed in Figure 8. The agreement between the UST3D and CAP-TSD methods is generally reasonable, but larger shock motions were reported by the CAP-TSD algorithm. The UST3D code is developed based on a time-linearization approach, and hence cannot predict large amplitude shock oscillations accurately.

5. APPLICATIONS IN FLUTTER ANALYSIS

The AGARD standard configuration for aeroelastic analysis (Ref. 21) was used as a test case in this paper. Experimental flutter boundaries and structural properties of these wings are well documented. Comparisons were also made with results from CAP-TSD (Ref. 3) and subsonic doublet lattice solutions (N5KA).

5.1 Flutter Analysis Procedure

The menu-driven Institute for Aerospace Research (IAR) flutter analysis program first determines structural mode shapes and frequencies using NASTRAN and then carries out the aerodynamic calculations. Three flutter analysis methods (p-k, p, and V-g) are available. Figure 9 shows the basic elements of the flutter analysis procedure.

An aerodynamics pre-processor checks the input data and generates the input date file for the Mach number range. If the range specified is subsonic, the doublet lattice program is used, otherwise the input data is generated for the supersonic harmonic gradient program (ZONA51). The option of using the transonic aerodynamics code UST3D is specified in the initial input and the program prepares the appropriate input data files. The initial preprocessor also generates mode shapes and graphics for the geometric and aerodynamic panel models. The aerodynamics program determines the generalized forces for each of the user selected modes. Subsequently the flutter analysis program uses the generalized forces data to calculate the flutter trend for each mode. These trends are accurately tracked for the flutter method selected by the user. Flutter crossings for specified damping values are determined and printed out. In addition, frequency and damping variation plots can be generated to assist in the determination of flutter trends for each of the modes.

5.2 AGARD 445.6 Wing Test Case

This series of wings were tested in the NASA Langley Research Center Transonic Dynamics Tunnel. They have been chosen by AGARD-SMP as standard aeroelastic configurations for comparisons of calculated and measured aeroelastic response. These wings have a quarter chord sweep angle of 45° and a NACA 65A004 airfoil section.

In order to obtain wind tunnel flutter test data for a range of density conditions, some of the wings have holes drilled through in order to reduce the stiffness. For the purpose of comparison of results from IAR flutter analysis code, the weakened wing denoted as model 3 (WEAK3) in Ref. 21 was chosen for the test case.

The five natural vibration modes of WEAK3 used in the present flutter analysis are: first bending (9.60 Hz), first torsion (38.10 Hz), second bending (50.70 Hz) and second torsion (98.50 Hz) and a mode at 118.11 Hz corresponding probably to the third torsion mode.

The ΔC_p distributions with chord at span location Y/S = 0.85 for the first four modes at M_∞ = 0.9 and κ_b = 0.1 are shown in Figure 10 for the WEAK3 wing. Good agreement was obtained between linear theory and UST3D for this thin wing. Figure 11 shows the C_L and C_M distributions with span. These results show good agreement in loads determined by linear theory and UST3D.

Flutter analysis using the p method was carried out for the WEAK3 wing. In this case the frequency chosen for the aerodynamic calculations was κ_b = 0.1. Plots of the flutter speed index $\frac{U}{b_r\omega_\alpha\sqrt{\mu}}$ and nondimensional flutter frequency $\frac{\omega}{\omega_\alpha}$ as function of freestream Mach number are shown in Figure 12a and 12b. These figures show the characteristic transonic dip near M_∞=1. Also included in these figures are the results from CAP-TSD code. Flutter calculations at supersonic Mach numbers were carried out using the aerodynamics computed by the supersonic harmonic gradient code (ZONA51). Good agreement was obtained between the UST3D results, doublet lattice method and CAP-TSD. Comparisons between computed and experimental results for the AGARD WEAK3 wing in Freon are given in Figure 13a and 13b. The agreement between IAR, CAP-TSD and experimental results is fairly good. Figure 14 shows the frequency and damping trend with speed for the case of M_∞ = 0.9 and κ_b = 0.1.

THIS DOCUMENT PROVIDED BY THE ABBOTT AEROSPACE
TECHNICAL LIBRARY
ABBOTTAEROSPACE.COM

5.3 Conclusions

For thin wings the aerodynamic results from UST3D compared favourably with linear doublet lattice theory, CAP-TSD, as well as experimental data. The accuracy of the method suffered for thick wings.

Comparisons of results from IAR flutter analysis using UST3D were carried out for the AGARD standard aeroelastic configuration WEAK3.. Good correlations with experimental data were obtained.

ACKNOWLEDGEMENT

This research was support by the Department of National Defence of Canada. The work of Y.S.W. was also supported in part by the Natural Sciences and Engineering Research Council of Canada.

REFERENCE

1. Wong, Y.S. and Lee, B.H.K., Development of a three dimensional unsteady transonic aerodynamics computer code for flutter analysis. Proceeding of the 17th Congress of the International Council of the Aeronautical Sciences, ICAS-90-1.1.4, pp.19-29 (1990).

2. Guruswamy, G.P. and Goorjian, P.M., An efficient coordinate transformation technique for unsteady, transonic aerodynamic analysis of low aspect-ratio wing, AIAA paper 84-0872 (1984).

3. Bennett, R.M., Batina, J.T. and Cunningham, H.J., Wing flutter calculations with the CAP-TSP unsteady transonic small disturbance program, J. Aircraft, Vol. 26, No. 9, pp. 876-882 (1989).

4. Isogai, K., The development of unsteady 3-D full potential code and its aeroelastic applications, AGARD-CP-374, (1985).

5. Ehlers, F.E. and Weatherill, W.H., A harmonic analysis method for unsteady transonic flow and its application to the flutter of airfoils, NASA CR-3537 (1982).

6. Boppe, C.W., Transonic flow field analysis for wing-fuselage configurations, NASA CR-3243 (1980).

7. Jiang, H. and Wong, Y.S., Absorbing boundary conditions for second-order hyperbolic equations, J. of Computational Physics, Vol. 88, No. 1, pp. 205-231 (1990).

8. Murman, E.M. and Cole, J.D. , Calculation of plane steady transonic flows, AIAA J., Vol. 9, pp. 114-121 (1971).

9. Wong, Y.S., Newton-like minimal residual method applied to transonic flow calculations, AIAA J., Vol. 23, No. 4, pp. 515-521 (1985).

10. Meijerink, J.A. and van der Vorst, H.A., An iterative solution method for linear systems of which the coefficient matrix is a symmetric M-matrix, Math. Comp., Vol. 31, pp. 148-162 (1977).

11. Wong, Y.S., Preconditioned gradient type methods applied to nonsymmetric linear systems, Intern. J. Computer Math. Vol. 23, pp. 141-165 (1988).

12. Borland, C.J. and Rizzetta, D.P., Nonlinear transonic flutter analysis, AIAA J., Vol. 20, No. 11, pp. 1606-1615 (1982).

13. Sod. G.A., Numerical Methods in Fluid Dynamics. Cambridge University Press, 1985.

14. Guruswamy, G.P., Goorjian, P.M. and Merritt, F.J., ATRAN3S: an unsteady transonic code for clear wings, NASA TM-86783 (1985).

15. Guruswamy, G.P., Navier-Stokes computations on swept-tapered wings, including flexibility, AIAA paper 90-1152, (1990).

16. Tijdeman, J. et al., Transonic wind tunnel tests on an oscillating wing with external stores; Part II–the clean wing, AFFDL-TR-78-194 (1979).

17. Bland, S.R., AGARD 3-D aeroelastic configurations, AGARD AR-167, (1982).

18. Horsten, J.J., Boer, R.G. den. and Zwaan, R.J., Unsteady transonic pressure measurements on a semi-span wind-tunnel model of a transport-type supercritical wing (LANN models, NLR TR 82069U, Parts I and II, (1982).

19. Ruo, S.Y., Malone, J.B., Horsten, J.J. and Houwink, R., Steady and unsteady transonic airloads on a supercritical wing, J. Aircraft, Vol. 22, No. 1, pp. 28-36 (1985).

20. Batina, J.T., Unsteady transonic algorithm improvements for realistic aircraft applications, AIAA paper 88-0105 (1988).

21. Yates Jr. E.C., AGARD standard aeroelastic configurations for dynamic response I-Wing 445.5, AGARD R-765, 1988.

THIS DOCUMENT PROVIDED BY THE ABBOTT AEROSPACE
TECHNICAL LIBRARY
ABBOTTAEROSPACE.COM

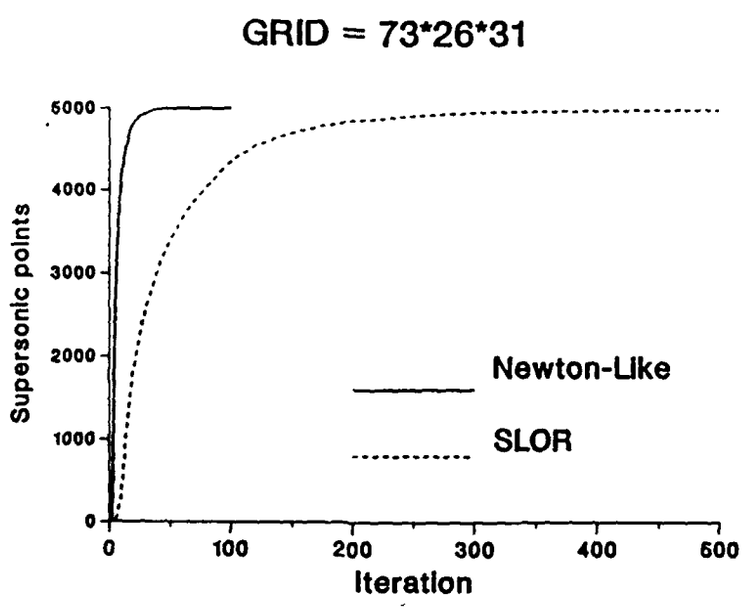


Figure 1. Comparison of supersonic points for Newton-like and SLOR methods. F/A-18 Wing, $M_\infty = 0.92$, $\alpha = 0.0^\circ$.

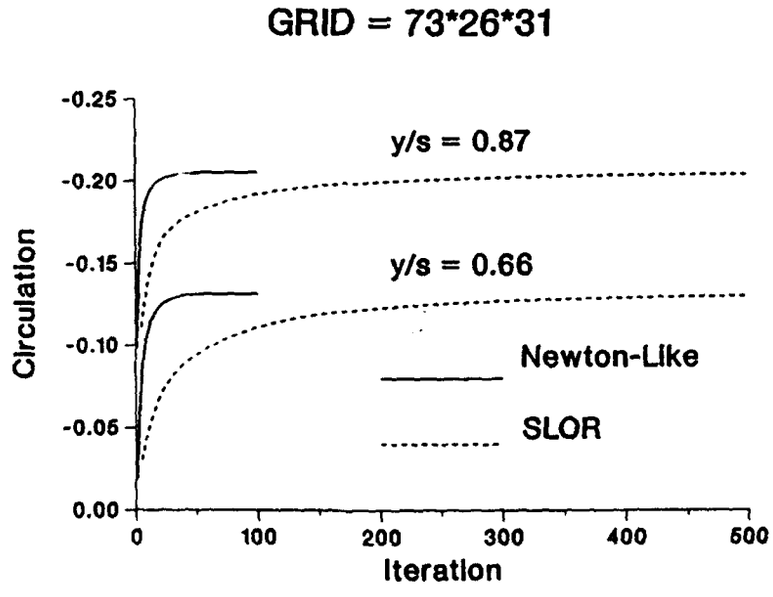


Figure 2. Comparison of circulations at 66% and 87% semispan stations for Newton-like and SLOR methods.
F/A-18 Wing, $M_\infty = 0.92$, $\alpha = 0.0^\circ$.

THIS DOCUMENT PROVIDED BY THE ABBOTT AEROSPACE
TECHNICAL LIBRARY
ABBOTTAEROSPACE.COM

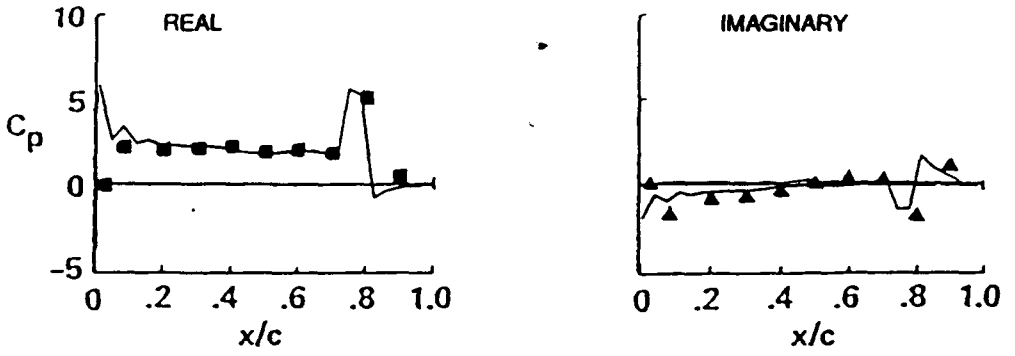


Fig. 3d UST3D after 5 cycle computations with 500 time-step/cycle.

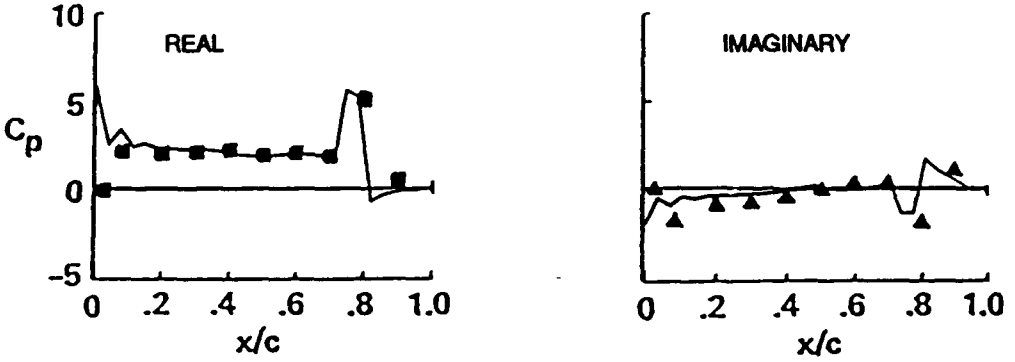


Fig. 3c UST3D after 3 cycle computations with 250 time-step/cycle.

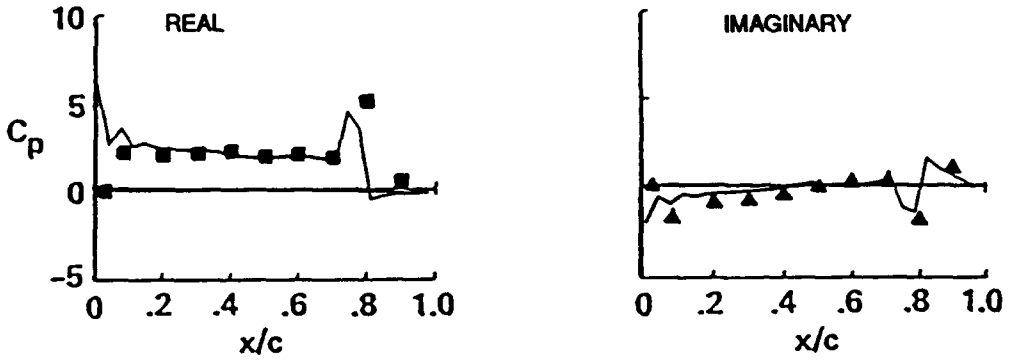


Fig. 3b UST3D after 2 cycle computations with 250 time-step/cycle.

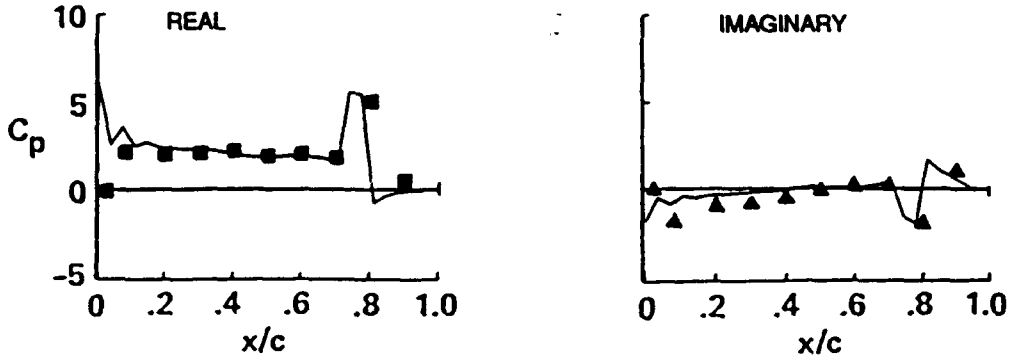


Fig. 3a UST3D after 1 cycle computations with 250 time-step/cycle.

Figure 3. Comparison of unsteady pressure distributions at 50% semispan station for UST3D(———) and NLR experiment (■ , ▲).
F5 Wing, M_∞=0.95, $\alpha = 0.0^\circ$, $\kappa = 0.528$.

THIS DOCUMENT PROVIDED BY THE ABBOTT AEROSPACE
TECHNICAL LIBRARY
ABBOTTAEROSPACE.COM

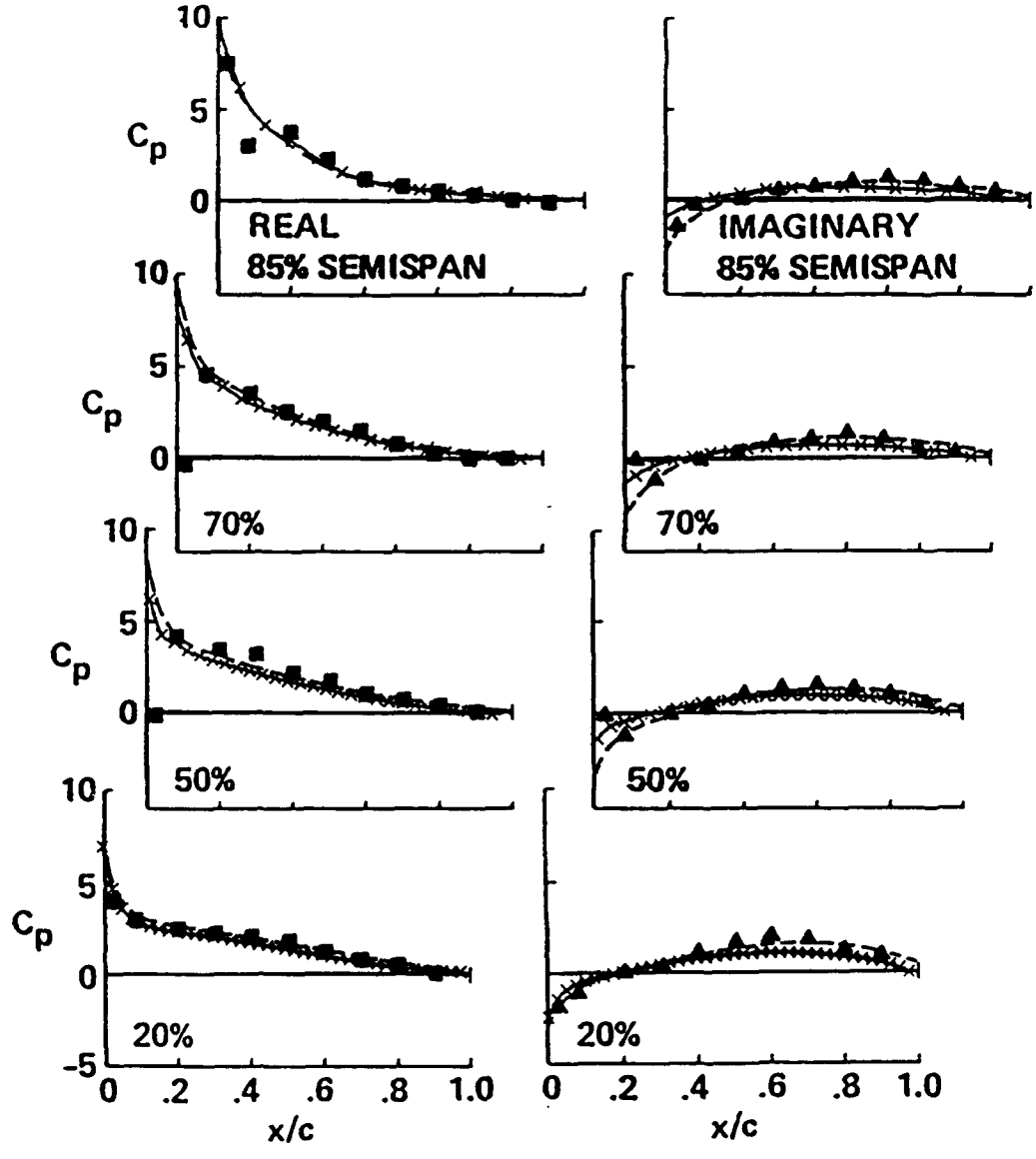


Figure 4. Comparison of unsteady pressure distributions between UST3D (-×-×-×-), XTRAN3S (- - - -) and NLR experiment (■ , ▲).
F5 Wing, M_∞=0.80, α=0.0°, κ = 0.614.

THIS DOCUMENT PROVIDED BY THE ABBOTT AEROSPACE
TECHNICAL LIBRARY
ABBOTTAEROSPACE.COM

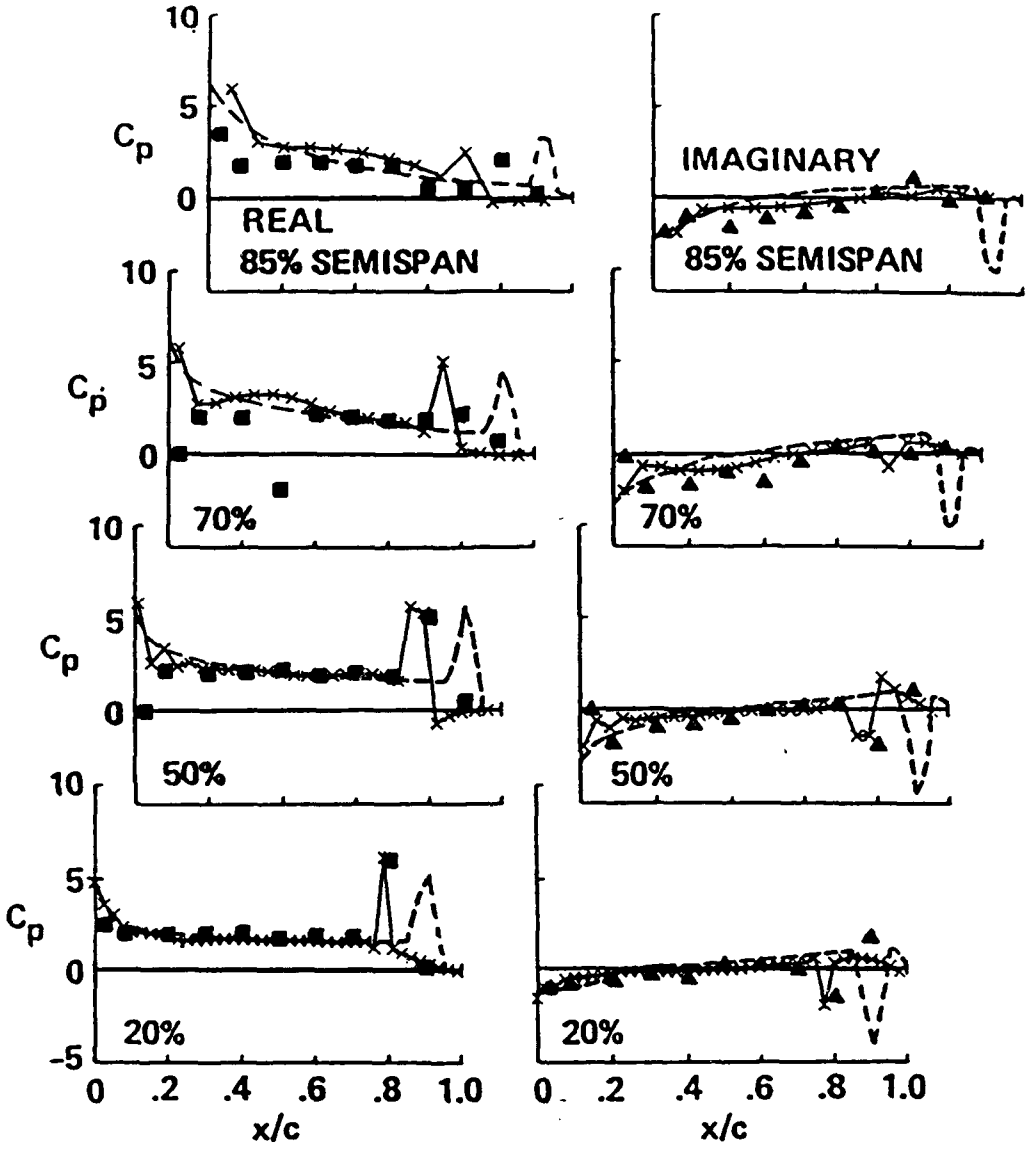
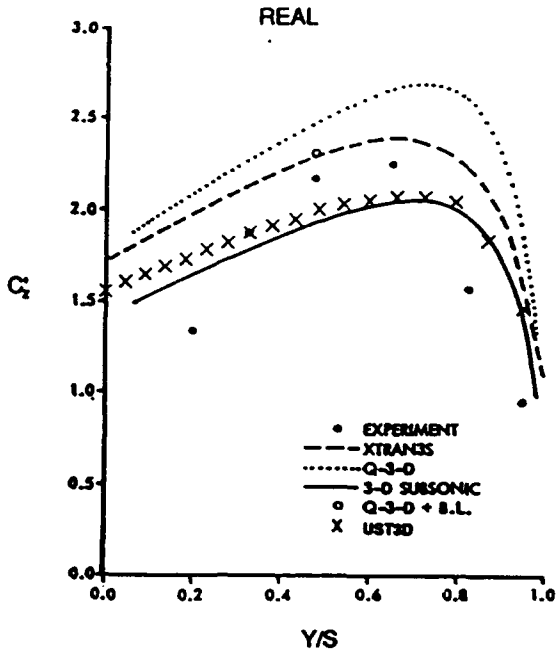
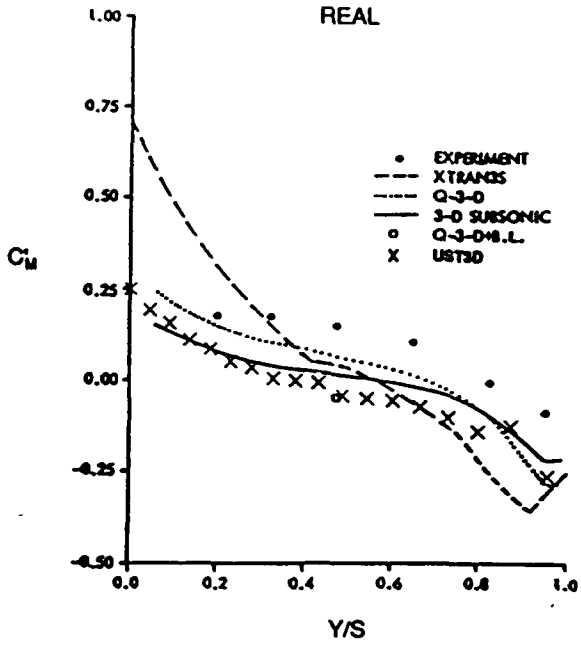
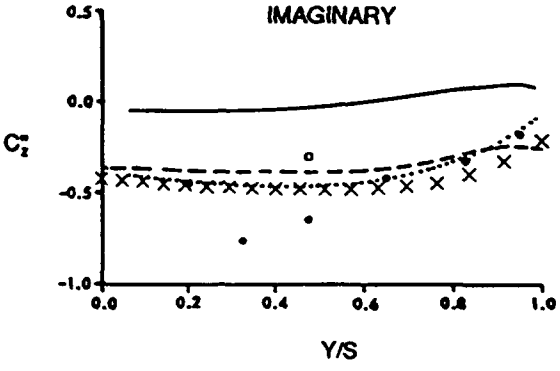


Figure 5. Comparison of unsteady pressure distributions between UST3D (-×-×-×-), XTRAN3S (- - - -) and NLR experiment (■ , ▲).
F5 Wing, M_∞=0.95, α=0.0°, κ = 0.528.

THIS DOCUMENT PROVIDED BY THE ABBOTT AEROSPACE
TECHNICAL LIBRARY
ABBOTTAEROSPACE.COM







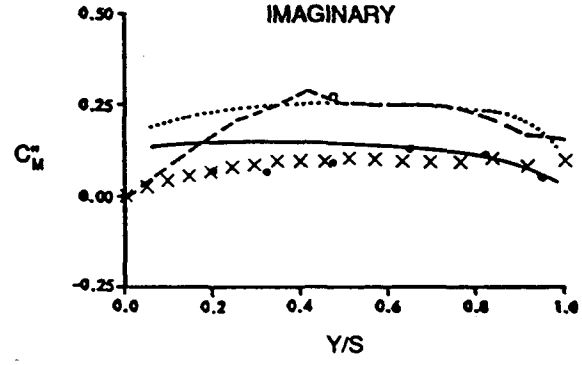


Figure 6. Comparison of unsteady spanwise normal force distributions.
LANN Wing, M_∞=0.82, α=0.6°, κ= 0.2046.

Figure 7. Comparison of unsteady spanwise moment coefficient distributions.
LANN Wing, M_∞=0.82, α=0.6°, κ= 0.2046.

THIS DOCUMENT PROVIDED BY THE ABBOTT AEROSPACE
TECHNICAL LIBRARY
ABBOTTAEROSPACE.COM

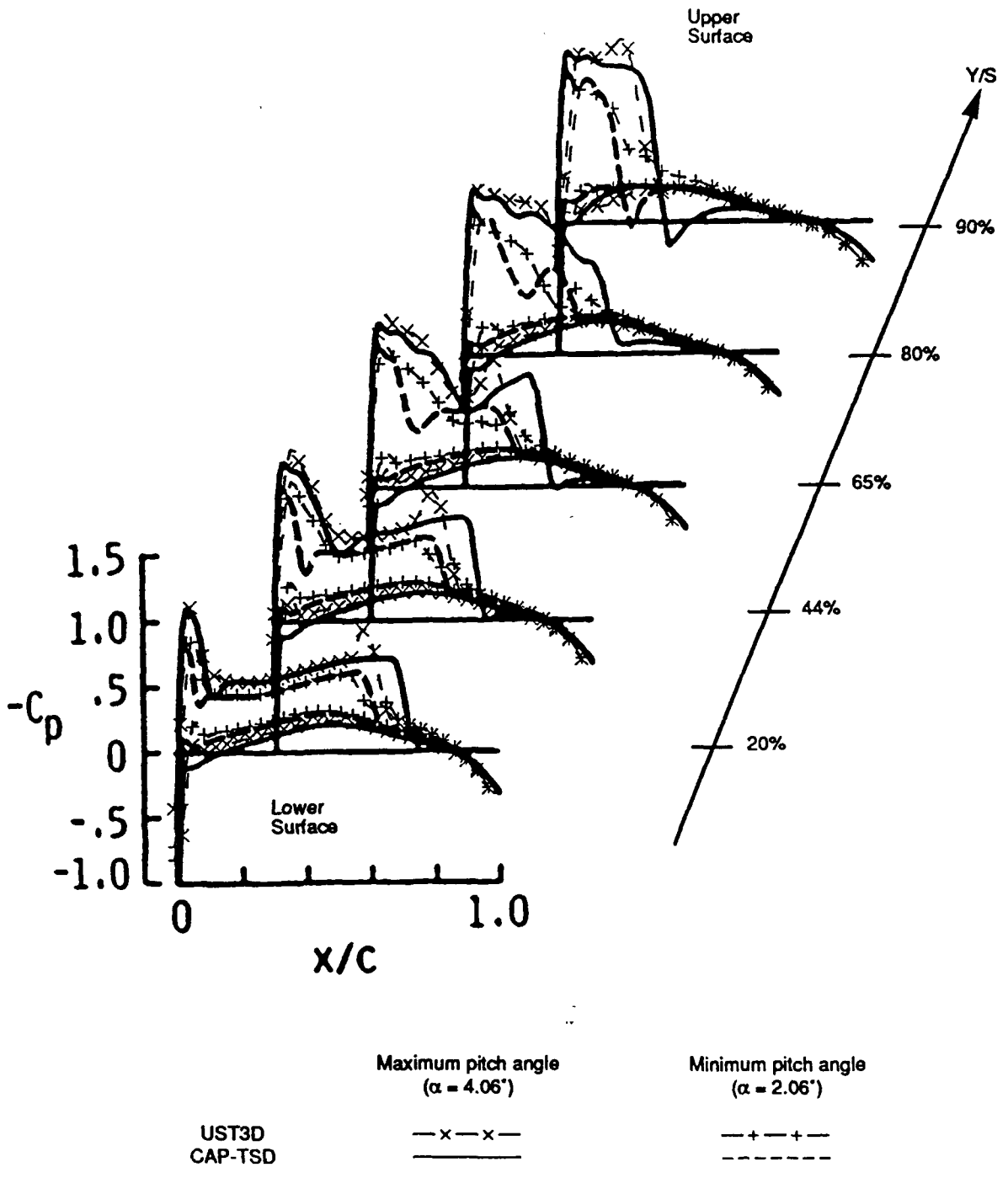


Figure 8. Comparison of instantaneous pressure distributions during the third cycle of pitching between UST3D and CAP-TSD.
ONERA M6 Wing, M_∞=0.84, α=3.06°, κ = 0.1.

THIS DOCUMENT PROVIDED BY THE ABBOTT AEROSPACE
TECHNICAL LIBRARY
ABBOTTAEROSPACE.COM

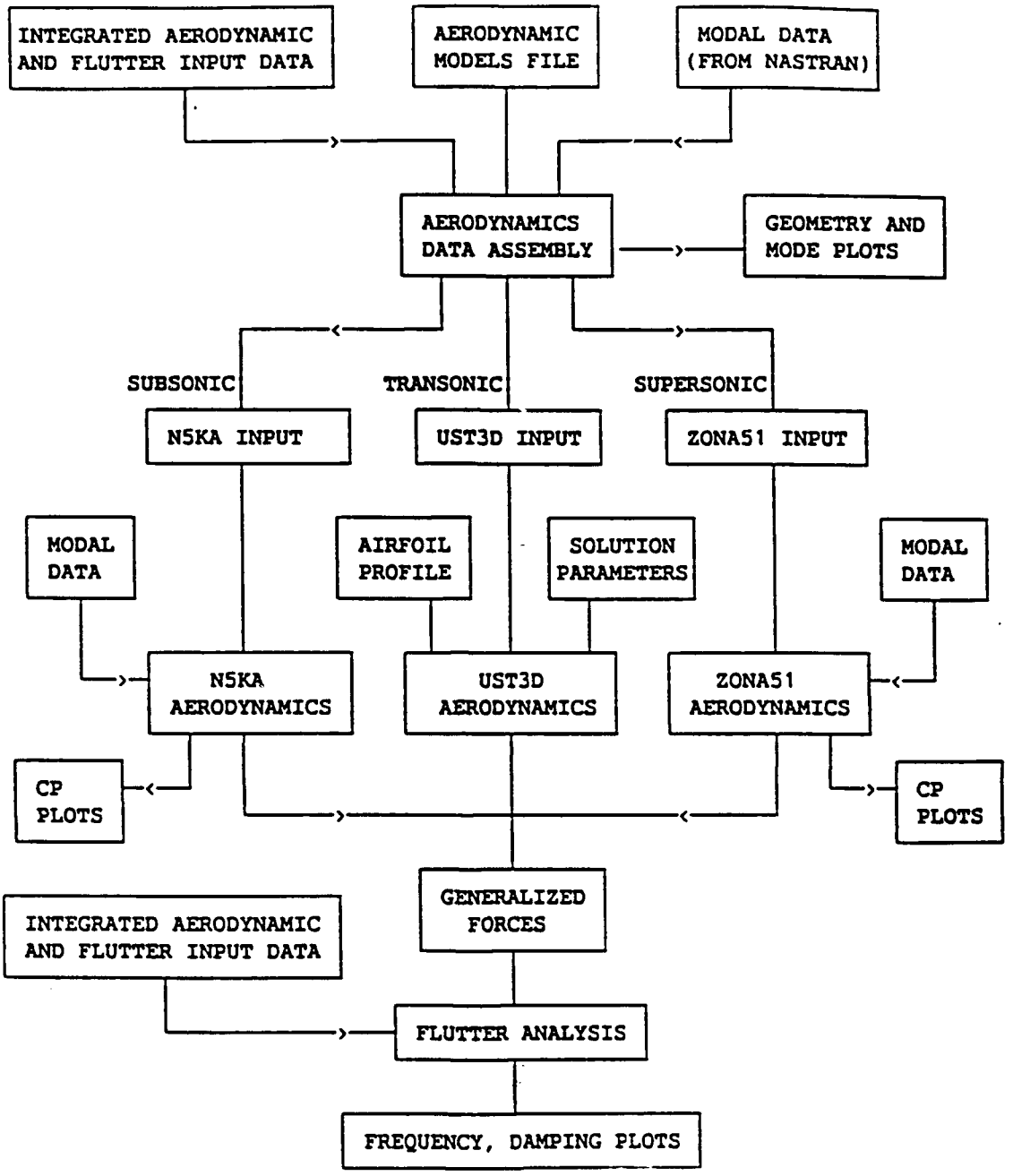


Figure 9. Overview of flutter analysis procedure.

THIS DOCUMENT PROVIDED BY THE ABBOTT AEROSPACE
TECHNICAL LIBRARY
ABBOTTAEROSPACE.COM

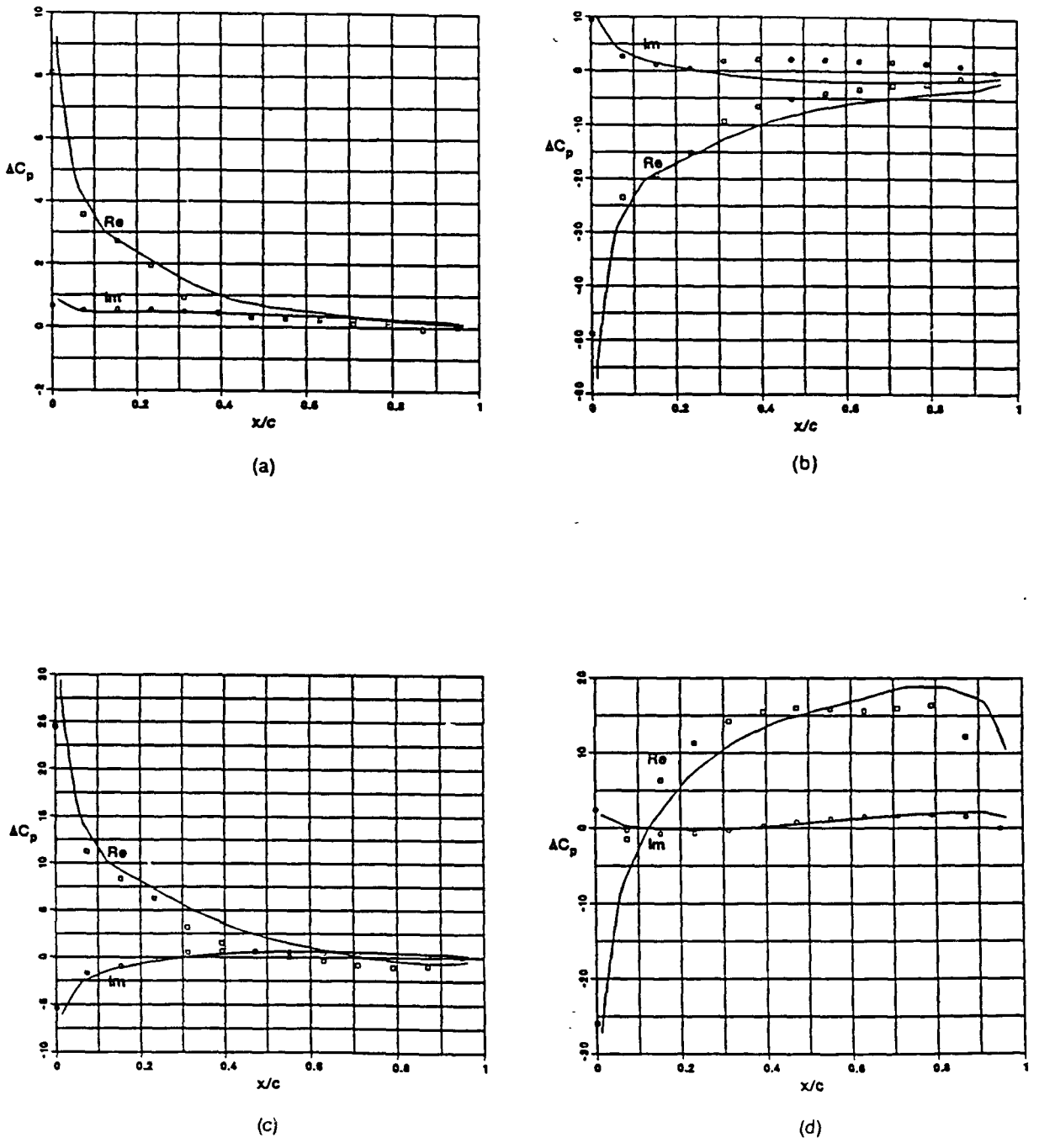
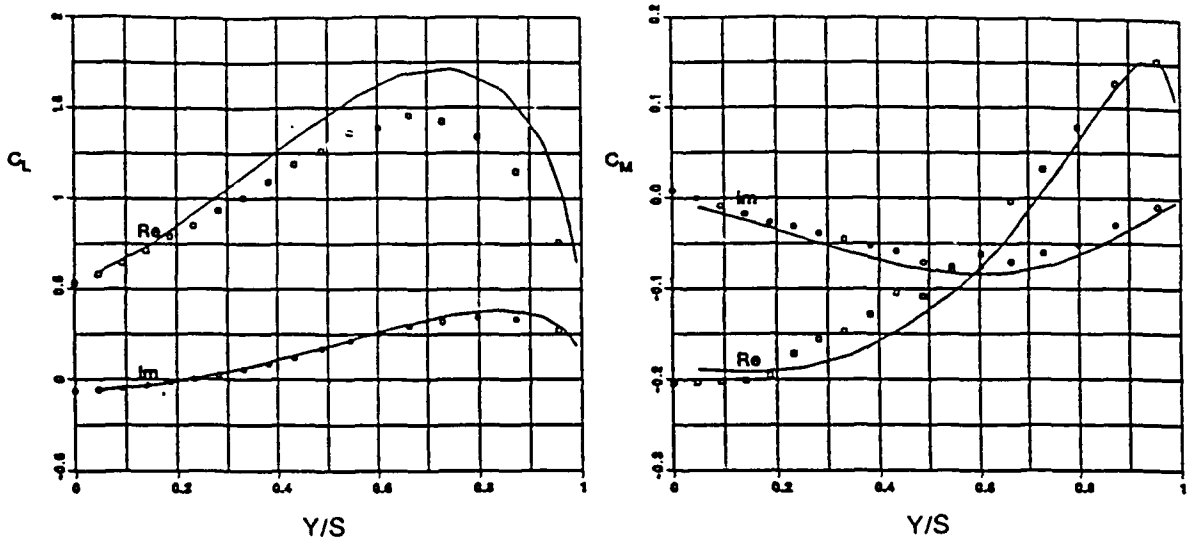
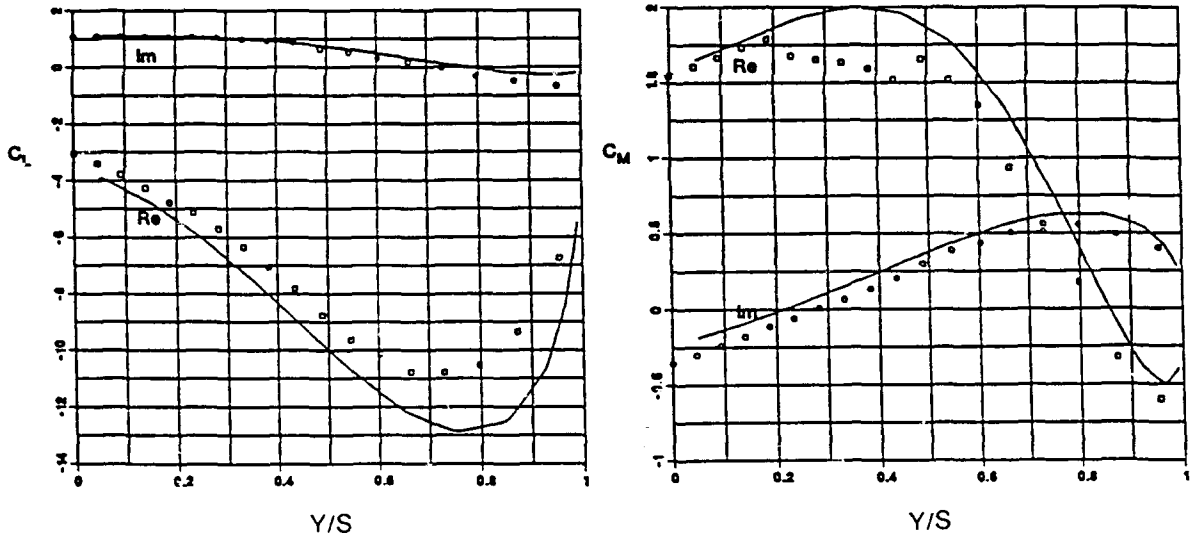


Figure 10. ΔC_p versus chord for the AGARD 445.6 Wing at $M_\infty = 0.9$, $\kappa_b = 0.1$ for (a) mode 1 (b) mode 2 (c) mode 3 (d) mode 4, at spanwise location Y/S = 0.85

THIS DOCUMENT PROVIDED BY THE ABBOTT AEROSPACE
TECHNICAL LIBRARY
ABBOTTAEROSPACE.COM



(a)



(b)

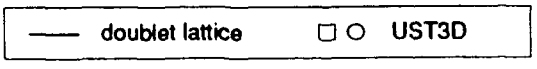
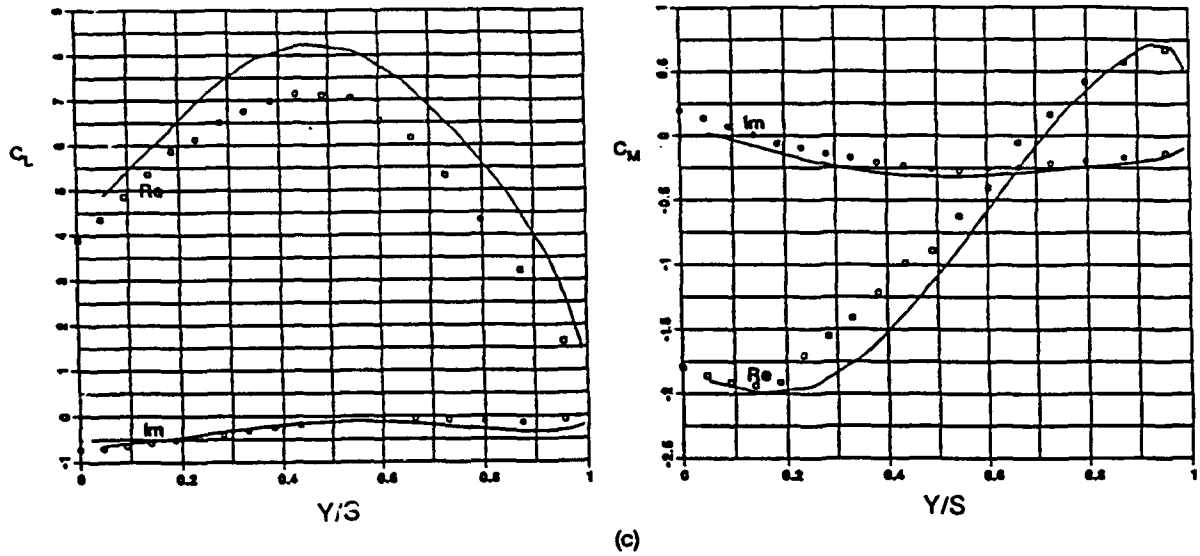
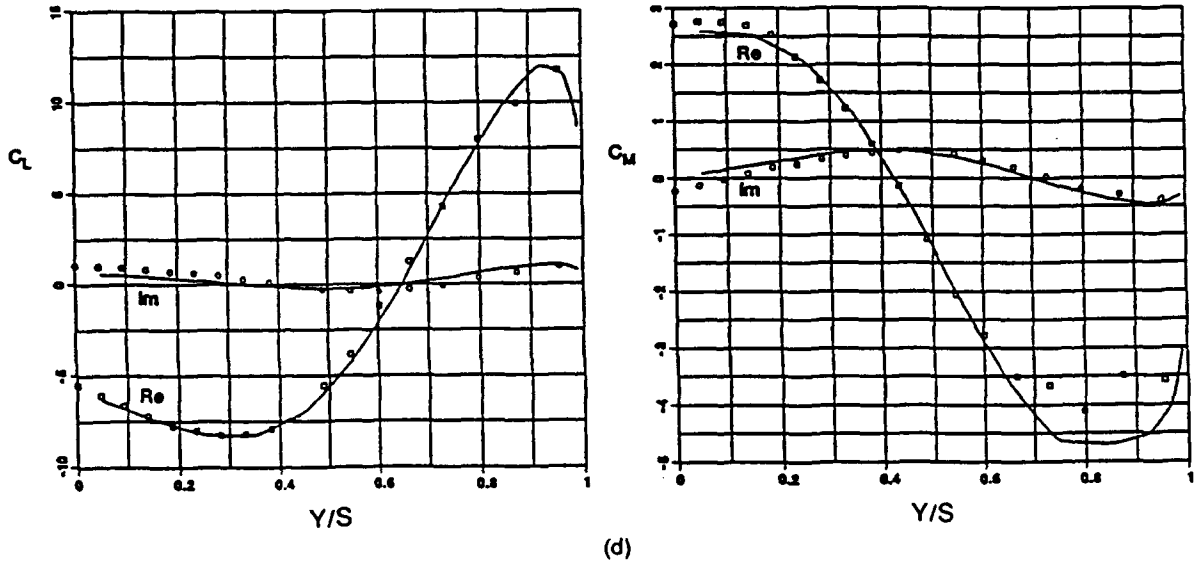


Figure 11. C_L and C_M versus span location for the AGARD 445.6 Wing at $M_\infty = 0.9$, $\kappa_b = 0.1$ for (a) mode 1 (b) mode 2

THIS DOCUMENT PROVIDED BY THE ABBOTT AEROSPACE
TECHNICAL LIBRARY
ABBOTTAEROSPACE.COM



(c)



(d)

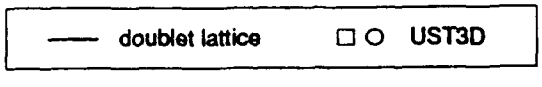


Figure 11. (cont'd) C_L and C_M versus span location for the AGARD 445.6 Wing at $M_\infty = 0.9$, $\kappa_b = 0.1$ for (c) mode 3 (d) mode 4

THIS DOCUMENT PROVIDED BY THE ABBOTT AEROSPACE
TECHNICAL LIBRARY
ABBOTTAEROSPACE.COM

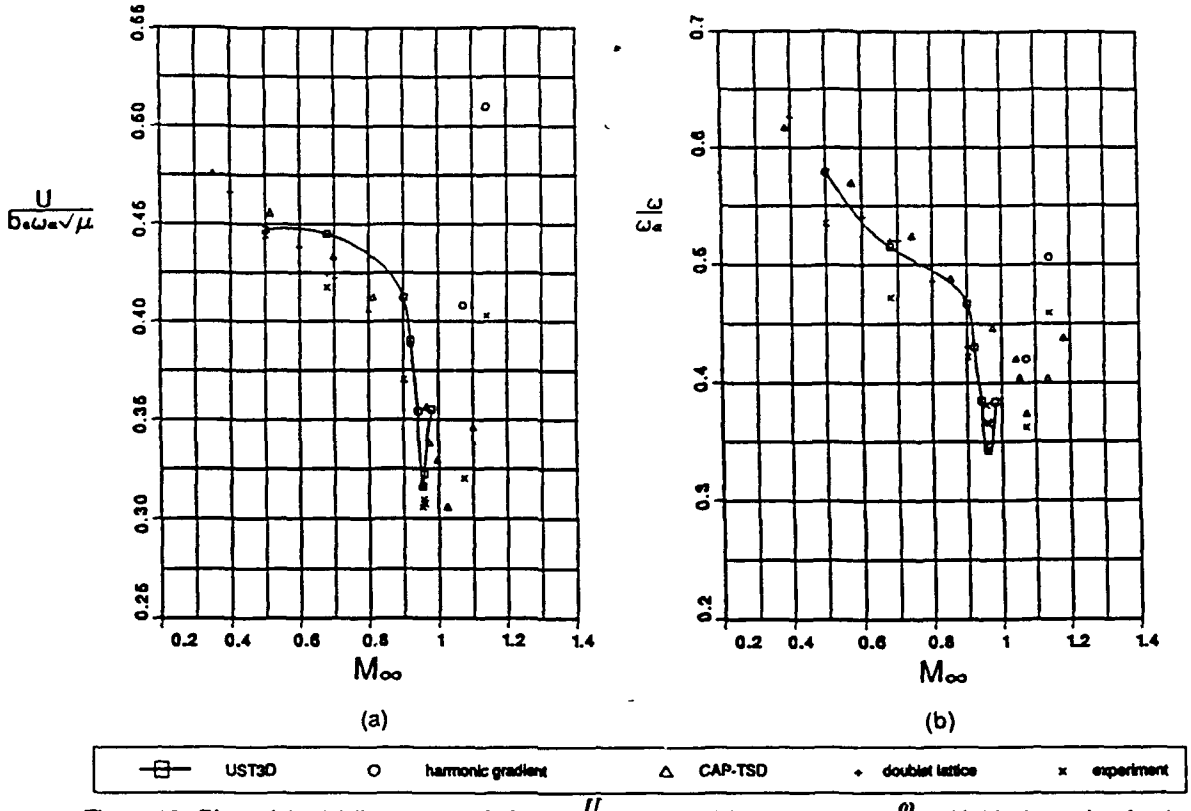


Figure 12. Plots of the (a) flutter speed index $\frac{U}{b_s \omega_\alpha \sqrt{\mu}}$ and (b) frequency ratio $\frac{\omega}{\omega_\alpha}$ with Mach number for the AGARD 445.6 WEAK3 wing in air.

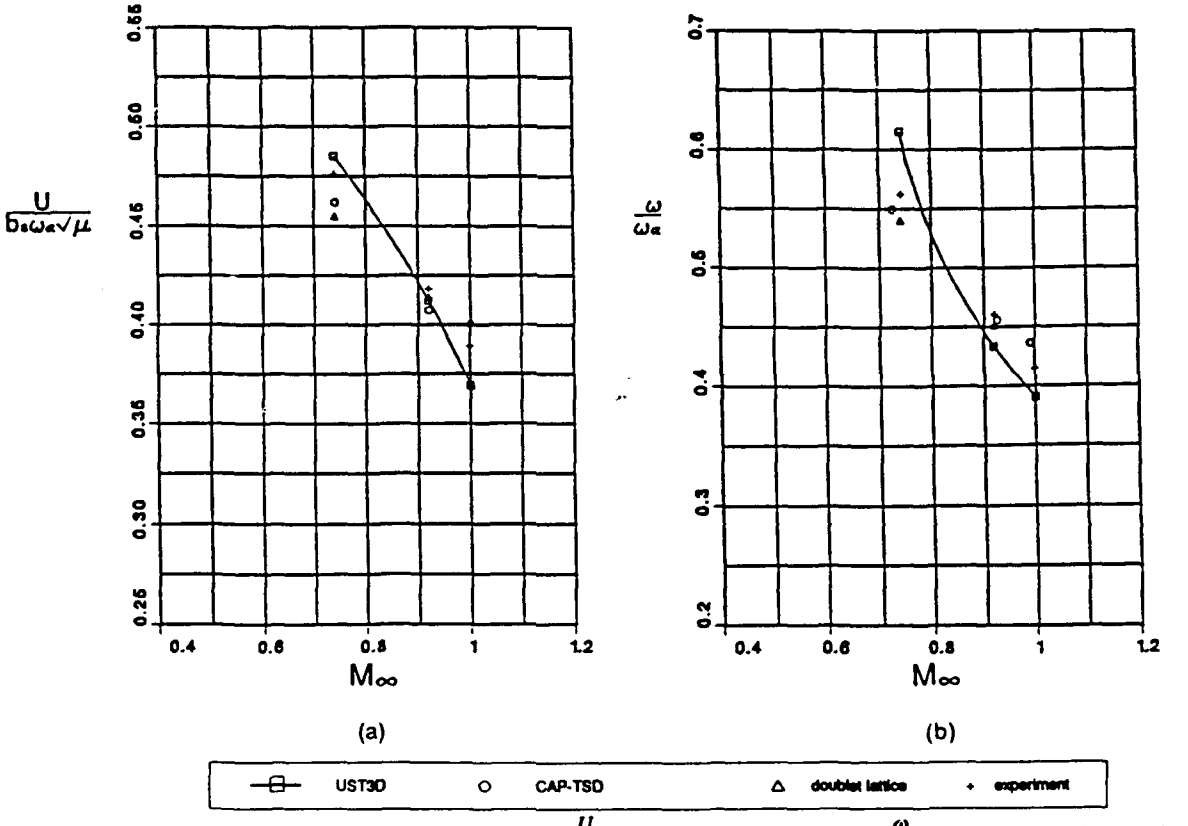


Figure 13. Plots of the (a) flutter speed index $\frac{U}{b_s \omega_\alpha \sqrt{\mu}}$ and (b) frequency ratio $\frac{\omega}{\omega_\alpha}$ with Mach number for the AGARD 445.6 wing in Freon.

THIS DOCUMENT PROVIDED BY THE ABBOTT AEROSPACE
TECHNICAL LIBRARY
ABBOTTAEROSPACE.COM

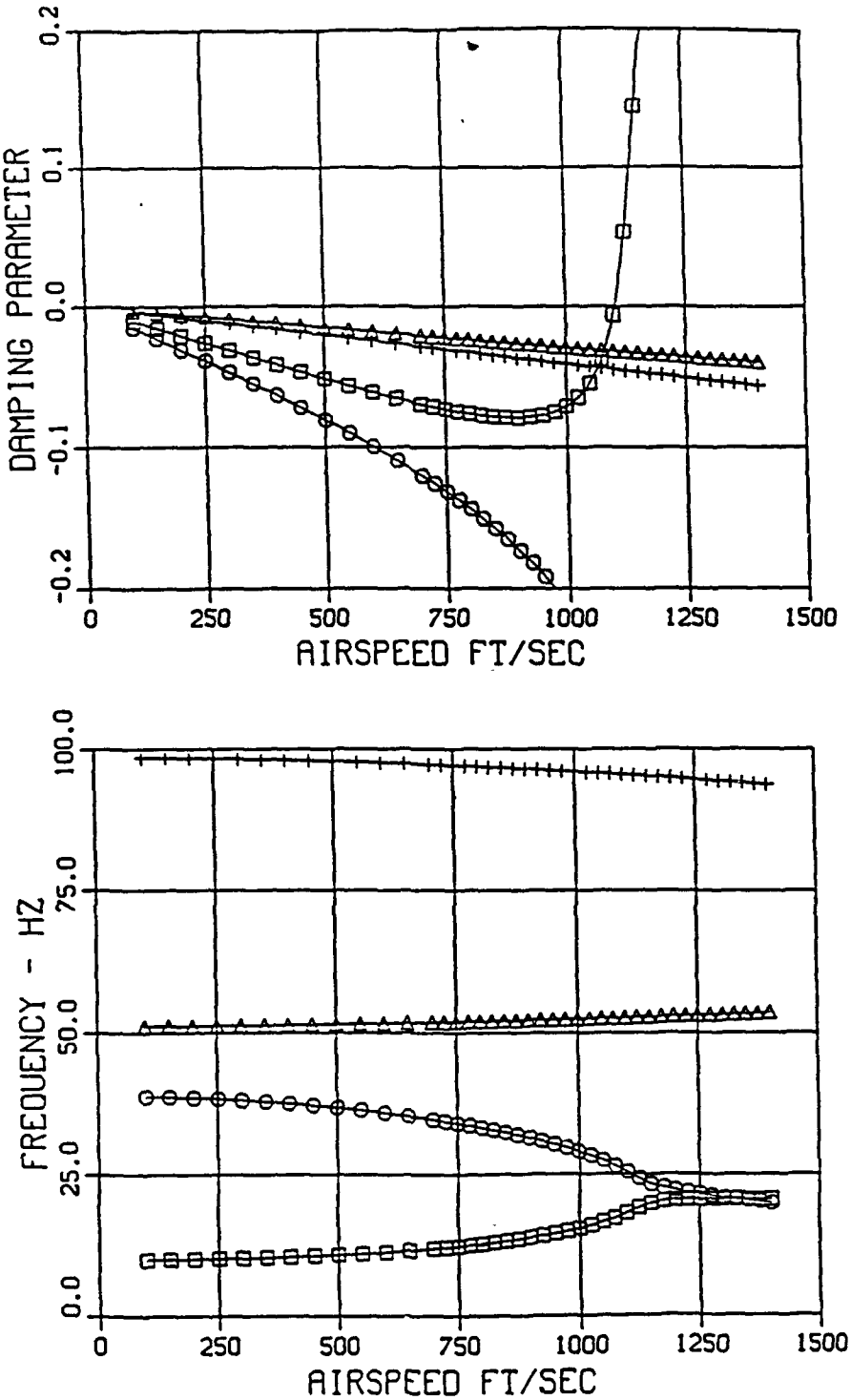


Figure 14. Damping and frequency versus airspeed for the AGARD 445.6 Wing (WEAK3) in air using the p method at κ_b = 0.1 and UST3D aerodynamics.

THIS DOCUMENT PROVIDED BY THE ABBOTT AEROSPACE
TECHNICAL LIBRARY
ABBOTTAEROSPACE.COM

AD-P007 799

A BOUNDARY INTEGRAL FORMULATION FOR UNSTEADY TRANSONIC POTENTIAL FLOWS

by

U. Iemma, F. Mastroddi, L. Morino
University of Rome "La Sapienza"
Via Eudossiana 16
00184 Rome
Italy

M. Pecora
ALENIA SpA-GAT, DITN/AFAN
Viale dell'Aeronautica
80038 Pomigliano d'Arco
Italy

92-16037

Summary

A boundary integral formulation for the analysis of unsteady potential transonic flows around airplanes is presented. The formulation is applied to steady and unsteady two-dimensional and three-dimensional configurations under the small-perturbation assumption. The results are compared with existing numerical and/or experimental results, and demonstrate that the algorithm is capable of capturing shocks. However, the location predicted appears to be ahead of that predicted by conservative finite-difference schemes; nonetheless, considering the preliminary nature of this work, the agreement obtained is quite satisfactory.

List of symbols

a	speed of sound
AR	wing aspect-ratio
b	non-linear term (see Eq. 1)
$\hat{b}$	non-linear term (see Eq. 1)
B_{kj}, C_{kj}, D_{kj}	body coefficients (see Eq. 14)
c	chord length
C_p	pressure coefficient
F_{kn}, G_{kn}	wake coefficients (see Eq. 14)
E	domain function (see Eq. 9)
G	fundamental solution (see Eq. 6)
$\mathbf{H}_{kq}$, $\hat{\mathbf{H}}_{kq}$, $\hat{H}_{kq}$	volume coefficients (see Eq. 14)
k	reduced frequency, $\omega c/2U_\infty$
h	enthalphy
i, j, k	base vectors
M_∞	Mach number
$\mathbf{n}$	unit normal
N	number of elements
N_1, N_2, N_3,...	discretization parameters
p	pressure
r	$\|\mathbf{x} - \mathbf{x}_*\|$
$\mathbf{v}$	fluid velocity
$\mathbf{x}$	location vector
$\mathcal{V}$	fluid volume
$\mathcal{S}$	surface
U_∞	undisturbed air speed
α	angle of attack
γ	specific heat ratio
δ	Dirac delta function
θ	compressibility time delay
ρ	air density
σ	non-linear term (see Eq. 1)
τ	dimensionless time, $tU_\infty 2/c$
ϕ	velocity potential
χ	$\mathbf{v}_B \cdot \mathbf{n}$
ψ	$\omega t = k\tau$
ω	angular frequency

Subscripts

B	body
BW	body-wake
F	field
W	wake
0	quantity in Prandtl-Glauert space
1	upper side of wake
2	lower side of wake
$*$	collocation point

Special symbols

$[\,]^\theta$	evaluation at time $t = t_* - \theta$
$\Delta(...)$	discontinuity across the wake
D_W/Dt	substantial derivative on wake
d_B/dt	$\partial/\partial t + U_\infty \partial/\partial x$

1. Introduction

The objective of this work is to present recent developments on a boundary-integral-equation method for the analysis of non-linear potential aerodynamic flows around airplanes. The formulation is given in terms of the velocity potential, for which an explicit treatment of the wake is required, and is based on

THIS DOCUMENT PROVIDED BY THE ABBOTT AEROSPACE
TECHNICAL LIBRARY
ABBOTTAEROSPACE.COM

the 'direct velocity-potential formulation' introduced by Morino (1974). An extensive review of the field of boundary-integral-equation methods (also known as boundary-element methods) for potential aerodynamics is beyond the scope of this paper; detailed reviews of the field are available, for instance, in several papers collected in Morino (1985) and in a review paper by Morino and Tseng (1990). In the following we present a brief literature review of the development of boundary-integral-equation methods for transonic potential aerodynamics of airplanes, with emphasis on the direct method for unsteady flows, which is the basis of this paper.

Probably the first successful attempt to use an integral-equation approach for transonic-flow analysis may be credited to Oswatisch (1950) for his work on two-dimensional steady-state flows. Two-dimensional steady transonic flows are considered by Spreiter and Alksne (1955), Crown (1968), Norstrud (1973), and Piers and Slooff (1979). Steady and unsteady two-dimensional, and steady-state three-dimensional flows are considered by Nixon (1974, 1978). Tseng and Morino (1982) extended the direct formulation of Morino (1974) to non-linear flows. Closely related is the formulation proposed by Gear (1987). In addition, Kandil and Yates (1985) presented an alternative formulation for full-potential flows based on the Helmholtz decomposition, where both linear and non-linear terms in the expression for the compressibility are treated as field sources. A similar approach is employed by Sinclair (1986, 1988) for two-dimensional and three-dimensional flows, respectively. An extension of the formulation to bodies in arbitrary motion (in particular, helicopter rotors in hover and forward flight) is presented in Morino and Tseng (1990); however, their transonic applications are limited to fixed-wing problems. Nonetheless, the generality of this approach stimulated a renewed interest in this methodology.

In this paper we present some preliminary results which were obtained using a formulation based on the work of Morino and Tseng (1990). The governing equations for compressible non-linear potential flows are presented in Section 2. The integral formulation is treated in Section 3, whereas its space and time discretizations are dealt with in Section 4. Numerical results are presented in Section 5.

2. Transonic Potential Flows

For the sake of completeness we outline the derivation of the equation for the velocity potential and the related boundary conditions; the presentation follows closely that of Morino and Tseng (1990) to which the reader is referred for details.

The basis for this work are the equations for potential isentropic compressible flows: the expression for the velocity, $\mathbf{v} = \nabla\phi$, the continuity equation in conservative form, $\partial\rho/\partial t + \nabla\cdot(\rho\mathbf{v}) = 0$, Bernoulli's theorem in an air frame of reference, $\partial\phi/\partial t + \frac{1}{2}v^2 + h = h_\infty$ (where h is the enthalpy), and the isentropic law, $p\rho^\gamma = const.$ In addition, we need the relations $h = \gamma p/(\gamma-1)\rho$ and $a^2 = \gamma p/\rho$. Combining the above equations yields

$$\nabla^2\phi - \frac{1}{a_\infty^2}\frac{\partial^2\phi}{\partial t^2} = \sigma = \nabla\cdot\mathbf{b} + \frac{\partial\hat{b}}{\partial t} \qquad (1)$$

where $a_\infty^2 = \gamma p_\infty/\rho_\infty$ is the undisturbed speed of sound, whereas σ denotes the non-linear terms, which, for full-potential flows, are given by

$$\mathbf{b} = \left(1 - \frac{\rho}{\rho_\infty}\right)\nabla\phi \qquad \hat{b} = -\frac{\rho}{\rho_\infty} - \frac{1}{a_\infty^2}\dot{\phi} \qquad (2)$$

(where $\rho/\rho_\infty = [1-(\gamma-1)(\dot{\phi}+v^2/2)/a_\infty^2]^{1/(\gamma-1)}$), whereas, for small-perturbation flows,

$$\mathbf{b} = \frac{(\gamma+1)}{2}\frac{U_\infty}{a_\infty^2}\left(\frac{\partial\phi}{\partial x}\right)^2\mathbf{i} \qquad \hat{b} = 0 \qquad (3)$$

(where $\mathbf{i}$ is the unit vector in x-direction).

In order to complete the differential formulation we need boundary conditions. The surface S_B of the body (a wing, in the results presented here) is typically assumed to be impermeable; hence, the boundary condition on a point of S_B is $\mathbf{n}\cdot(\mathbf{v}-\mathbf{v}_B) = 0$, where $\mathbf{v}_B$ is the velocity of the point on the surface of the body S_B. In the air frame of reference, the boundary condition at infinity is given by $\mathbf{v} = \mathbf{0}$. In terms of the velocity potential, we have, respectively, $\partial\phi/\partial n = \chi$ (where $\chi = \mathbf{v}_B\cdot\mathbf{n}$) and $\phi = 0$. Next, consider the wake boundary condition for potential compressible flows. Starting from the two wake conditions (no-penetration, $\mathbf{v}\cdot\mathbf{n} = \mathbf{v}_W\cdot\mathbf{n}$, and no pressure discontinuity, $\Delta p = 0$) one obtains (see Morino and Tseng, 1990) the conditions $\Delta(\partial\phi/\partial n) = 0$ and

$$\frac{D_W(\Delta\phi)}{Dt} = 0 \qquad (4)$$

with $D_W/Dt = \partial/\partial t + \mathbf{v}_W\cdot\nabla$, where the velocity of a wake point $\mathbf{x}_W$ is given by $\mathbf{v}_W = \frac{1}{2}(\mathbf{v}_1+\mathbf{v}_2)$, with 1 and 2 denoting the two sides of the wake. Note that D_W/Dt is the substantial wake derivative (*i.e.*, the time derivative following $\mathbf{x}_W$). Hence, the above equation implies that $\Delta\phi$ remains constant following $\mathbf{x}_W$, and equal to the value it had when $\mathbf{x}_W$ left the trailing edge. The value of $\Delta\phi$ at the trailing edge is obtained by using the Joukowski hypothesis that no vortex filament exists at the trailing edge; this implies that the value of $\Delta\phi$ on the wake and the

THIS DOCUMENT PROVIDED BY THE ABBOTT AEROSPACE
TECHNICAL LIBRARY
ABBOTTAEROSPACE.COM

value of $\Delta\phi$ on the body are equal at the trailing-edge.

Note that no conditions are required on the shock, as they are automatically included in the integral formulation presented here (see Morino and Tseng, 1982). This is due to the fact that these conditions are obtained from Eq. 1 by interpreting the derivatives within the framework of generalized functions. In particular, for the steady case one obtains $\Delta\phi = 0$ and $\Delta(\partial\phi/\partial n_0) = \Delta \mathbf{b}_0 \cdot \mathbf{n}_0$, where $\mathbf{b}_0$ arises from the conservative form of the non-linear term (see the next Section) and $\mathbf{n}_0$ is the normal derivative on the shock surface in the Prandtl-Glauert space.

3. Transonic Integral Formulation

In this section we present the integral formulation for airplanes in transonic flows. Typically, in this case, even for unsteady problems, the motion of the surface of the aircraft consists of small perturbation with respect to a frame of reference (body frame of reference) that travels with velocity $\mathbf{v}_B = -U_\infty \mathbf{i}$ with respect to the air frame of reference. Therefore, it is convenient to formulate the problem in the body frame of reference. For simplicity, we assume that the motion of the surface of the aircraft in this frame of reference is infinitesimal (although such a restriction is not required, see Morino and Tseng, 1990).

The differential equation for the velocity potential expressed in the body frame of reference is given by

$$\nabla^2\phi - \frac{1}{a_\infty^2}\frac{d_B^2\phi}{dt^2} = \sigma \qquad \mathbf{x} \in \mathcal{V} \qquad (5)$$

where $d_B/dt = \partial/\partial t + U_\infty \partial/\partial x$ denotes the total derivative following a point fixed to the body frame of reference, whereas $\mathcal{V}$ denotes the fluid volume with the exception of an arbitrary thin layer that includes the wake. In addition to the boundary condition we need initial conditions: we assume that the fluid is initially at rest, so that $\dot\phi(\mathbf{x},0) = \phi(\mathbf{x},0) = 0$.

The fundamental solution, G, is obtained by solving the adjoint problem, *i.e.*, the differential equation

$$\nabla^2 G - \frac{1}{a_\infty^2}\frac{d_B^2\phi}{dt^2}G = \delta(\mathbf{x}-\mathbf{x}_*)\delta(t-t_*) \qquad (6)$$

(where δ denotes the Dirac delta function) with "initial" conditions $\dot G(\mathbf{x},\infty) = G(\mathbf{x},\infty) = 0$ and boundary condition at infinity $G(\infty,t) = 0$.

If $M_\infty < 1$, G is given by (Morino, 1974)

$$G(\mathbf{x},\mathbf{x}_*;t,t_*) = \frac{-1}{4\pi r_\beta}\delta(t-t_*+\theta) \qquad (7)$$

with $\theta(\mathbf{x},\mathbf{x}_*) = [r_\beta + M_\infty(x-x_*)]/a_\infty\beta^2$ and $r_\beta(\mathbf{x},\mathbf{x}_*) = \sqrt{(x-x_*)^2+\beta^2[(y-y_*)^2+(z-z_*)^2}$, where $M_\infty = U_\infty/a_\infty$ and $\beta = \sqrt{1-M_\infty^2}$.

Multiplying Eq. 5 by G, Eq. 6 by ϕ, subtracting, integrating in time and over the volume $\mathcal{V}$, applying Gauss' theorem, and using the boundary condition at infinity and the initial conditions on ϕ and G, one obtains:

$$E_*\phi_* = \int_0^\infty \iiint_{\mathcal{V}} G\,\sigma\, d\mathcal{V}\, dt + \int_0^\infty \oiint_{S_{BW}} \left[\left(G\frac{\partial\phi}{\partial n} - \phi\frac{\partial G}{\partial n}\right) - \frac{U_\infty}{a_\infty^2}\left(G\frac{d_B\phi}{dt} - \phi\frac{d_B\phi}{dt}\right) n_x\right] dS\, dt \qquad (8)$$

where $\phi_* = \phi(\mathbf{x}_*,t_*)$, S_{BW} is the boundary of $\mathcal{V}$ (*i.e.*, a surface that surrounds body and wake), and E_* is a domain function defined as $E_* = 1$ if $\mathbf{x}_*$ is inside S_B, $E_* = 0$ if $\mathbf{x}_*$ is outside S_B. Combining with Eq. 7 one obtains

$$E_*\phi_* = \iiint_{\mathcal{V}} [\sigma]^\theta \hat G\, d\mathcal{V} + \oiint_{S_{BW}} \left[\hat G\frac{\partial\phi}{\partial\hat n} - \phi\frac{\partial\hat G}{\partial\hat n} + \hat G\dot\phi\frac{\partial\hat\theta}{\partial\hat n}\right]^\theta dS \qquad (9)$$

where $(\,)\dot{}$ denotes time differentiation and $[...]^\theta$ denotes evaluation at the retarded time $t = t_* - \theta$, whereas $\hat G = -1/4\pi r_\beta$,

$$\frac{\partial}{\partial\hat n} = (1-M_\infty^2)\, n_x\frac{\partial}{\partial x} + n_y\frac{\partial}{\partial y} + n_z\frac{\partial}{\partial z} \qquad (10)$$

and $\hat\theta(\mathbf{x},\mathbf{x}_*) = [r_\beta - M_\infty(x-x_*)]/a_\infty\beta^2$.

If $\mathbf{x}_*$ is in $\mathcal{V}$, Eq. 9 is an integral representation for $\phi(\mathbf{x}_*,t_*)$ in terms of ϕ, $\partial\phi/\partial\hat n$, and $\dot\phi$ on S_{BW}. If $\mathbf{x}_*$ is on S_{BW}, Eq. 9 represents a compatibility condition between ϕ, $\partial\phi/\partial\hat n$, and $\dot\phi$ for any function ϕ satisfying Eq. 5.

Next, introducing the Prandtl-Glauert variables, $x_0 = x/\sqrt{1-M_\infty^2}$, $y_0 = y$, $z_0 = z$, and isolating the contribution of the wake, one obtains

$$E_*\phi_* = \iiint_{\mathcal{V}_0} [\sigma]^{\theta_0} G_0\, d\mathcal{V}_0 + \oiint_{S_{B_0}} \left[\frac{\partial\phi}{\partial n_0}G_0 - \phi\frac{\partial G_0}{\partial n_0} + \dot\phi G_0\frac{\partial\hat\theta_0}{\partial n_0}\right]^{\theta_0} dS_0 - \iint_{S_{W_0}} \left[\Delta\phi\frac{\partial G_0}{\partial n_0} - \Delta\dot\phi G_0\frac{\partial\hat\theta_0}{\partial n_0}\right]^{\theta_0} dS_0 \qquad (11)$$

where $G_0 = -1/4\pi r_0$, $r_0 = r_\beta/\beta = \|\mathbf{x}_0 - \mathbf{x}_{0*}\|$, $\theta_0 = [r_0 + M_\infty(x_0 - x_{0*})]/a_\infty\beta$, and $\hat\theta_0 = [r_0 - M_\infty(x_0 - x_{0*})]/a_\infty\beta$, whereas $\partial/\partial n_0$ denotes the normal derivative in the Prandtl-Glauert space.

THIS DOCUMENT PROVIDED BY THE ABBOTT AEROSPACE
TECHNICAL LIBRARY
ABBOTTAEROSPACE.COM

In the following, an integration by parts is performed in order to avoid second-order derivatives of the velocity potential for the evaluation of the non-linear term. Note that the non-linear term σ (see Eq. 2) can be written as $\sigma = \nabla_0 \cdot \mathbf{b}_0 + \partial\hat{b}/\partial t$, where ∇_0 is the nabla operator in the Prandtl-Glauert space and $\mathbf{b}_0$ has components $b_x/\beta, b_y, b_z$. Using

$$\nabla_0 \cdot [\mathbf{b}_0]^{\theta_0} = [\nabla_0 \cdot \mathbf{b}_0]^{\theta_0} - \left[\frac{\partial \mathbf{b}_0}{\partial t}\right]^{\theta_0} \cdot \nabla_0 \theta_0 \quad (12)$$

and Gauss' theorem one obtains

$$\begin{aligned} \iiint_{\mathcal{V}_0} [\sigma]^{\theta_0} G_0 d\mathcal{V}_0 &= -\oiint_{S_{B_0}} [\mathbf{n}_0 \cdot \mathbf{b}_0]^{\theta_0} G_0 dS_0 \\ &+ \iiint_{\mathcal{V}_0} \left[\frac{\partial \hat{b}}{\partial t} + \frac{\partial \mathbf{b}_0}{\partial t} \cdot \nabla_0 \theta_0\right]^{\theta_0} G_0 d\mathcal{V}_0 \\ &- \iiint_{\mathcal{V}_0} [\mathbf{b}_0]^{\theta_0} \cdot \nabla_0 G_0 d\mathcal{V}_0 \end{aligned} \quad (13)$$

4. Discretization

In order to solve the problem, the integral formulation presented above must be discretised. A zeroth-order formulation is used in the actual computations for all the results presented and is briefly outlined here. Let us divide the surface of the body into N_B elements S_j, that of the wake into N_W elements S_n[1] and the fluid volume in N_F volume elements $\mathcal{V}_q$. Using the collocation method (*i.e.*, satisfying the equation at N_B collocation points), and setting the collocation points at the centers of the elements, one obtains

$$\begin{aligned} E_k \phi_k(t) &= \sum_j^{N_B} B_{kj} [\tilde{\chi}_j]^{\theta_{0_{kj}}} \\ &+ \sum_j^{N_B} C_{kj} [\phi_j]^{\theta_{0_{kj}}} + \sum_j^{N_B} D_{kj} [\dot{\phi}_j]^{\theta_{0_{kj}}} \\ &+ \sum_n^{N_W} F_{kn} [\Delta\phi_n]^{\theta_{0_{kn}}} + \sum_n^{N_W} G_{kn} [\Delta\dot{\phi}_n]^{\theta_{0_{kn}}} \\ &+ \sum_q^{N_F} \mathbf{H}_{kq} \cdot [\mathbf{b}_{0_q}]^{\theta_{0_{kq}}} + \sum_q^{N_F} \hat{\mathbf{H}}_{kq} \cdot [\dot{\mathbf{b}}_{0_q}]^{\theta_{0_{kq}}} \\ &+ \sum_q^{N_F} \hat{H}_{kq} [\dot{\hat{b}}_q]^{\theta_{0_{kq}}} \end{aligned} \quad (14)$$

where $[...]^{\theta_{0_{kj}}}$ denotes evaluation at the retarded time $t - \theta_{kj}$, whereas (see Eq. 2)

$$\tilde{\chi} = \chi - \mathbf{n}_0 \cdot \mathbf{b}_0 \quad (15)$$

[1] In particular, hyperboloidal quadrilateral elements are used for all the results presented here (see Morino and Tseng, 1990).

Note that, in the case of full-potential flows, $\tilde{\chi} = \mathbf{v}_B \cdot \mathbf{n}_0 \rho/\rho_\infty$.

In addition, $\Delta\phi$ is obtained from the above mentioned wake and trailing-edge conditions: these imply that $\Delta\phi$ remains constant following a wake point and is equal to the value that it had when it left the trailing edge. Furthermore, the coefficients B_{kj} are defined as

$$B_{kj} = \iint_{S_j} G_{0_k} dS \quad (16)$$

where $G_{0_k} = G_0|_{\mathbf{x}_0 = \mathbf{x}_k}$. Also,

$$C_{kj} = \iint_{S_j} \frac{\partial G_{0_k}}{\partial n_0} dS, \quad D_{kj} = \iint_{S_j} G_{0_k} \frac{\partial \hat{\theta}_{0_k}}{\partial n_0} dS \quad (17)$$

Similar definitions hold for F_{kn} and G_{kn}. Finally,

$$\mathbf{H}_{kq} = -\iiint_{\mathcal{V}_q} \nabla_0 G_{0_k} d\mathcal{V} \quad (18)$$

$$\hat{\mathbf{H}}_{kq} = \iiint_{\mathcal{V}_q} G_{0_k} \nabla_0 \theta_{0_k} d\mathcal{V} \quad (19)$$

$$\hat{H}_{kq} = \iiint_{\mathcal{V}_q} G_{0_k} d\mathcal{V} \quad (20)$$

Note that we have assumed that S_B and S_W are rigidly connected with the body frame; hence all the coefficients are time independent.

At each time step, χ_k are known from the boundary conditions, $\Delta\phi_n$ are known from the preceding time steps, and Eq. 14 may be used to evaluate ϕ_k: the time discretization is accomplished by a first-order finite-element procedure. Note that $\mathbf{b}_0$, $\dot{\mathbf{b}}_0$ and $\dot{\hat{b}}$ at the current time step are unknown because of their non-linear expression in the unknown ϕ; hence, they are obtained, at each time step, through a predictor-corrector procedure.

5. Numerical results

In this section we present some results obtained using the above formulation, for the limited case of transonic small perturbation flows (T.S.P.). Additional approximations are used. For instance, the wake is assumed to be parallel to the x-axis; also, the next to the last term in Eq. 14 is neglected (low-frequency approximation). In addition, the derivative $\partial\phi/\partial x$ in the expression for $\mathbf{b}$ (Eq. 3) is evaluated as follows: first we compute the values of ϕ at the centers of the field elements, then the derivatives are approximated by central finite differences in the subsonic region and by backward finite differences in the supersonic region. Finally, it should be noted that even the two-dimensional results are obtained using

THIS DOCUMENT PROVIDED BY THE ABBOTT AEROSPACE
TECHNICAL LIBRARY
ABBOTTAEROSPACE.COM

the three-dimensional formulation; for steady-state flows this is accomplished by considering an infinite wing (with one infinite element in the y-direction), whereas for unsteady flows, we consider a finite number of uniformly-spaced elements in the y-direction, each with its own time delay (for all the results presented here, $N_2 = 18$ on half wing, with $\Delta y = .8c$).

The following parameters are used for the geometric discretization: N_1 is the number of wing elements in the chordwise direction, N_2 is the number of wing elements in the spanwise direction, N_w is the number of wake elements in the flow direction, N_3 is the number of field elements in the z-direction, N_f is the number of field elements in the x-direction in front of the wing, N_a is the number of field elements in the x-direction aft the wing, and N_s is the number of field elements in the y-direction on the side of the wing. Note that stretching is used in order to have small elements at the leading and trailing edge (Figs. 1-2).

Consider, first, results for two-dimensional steady problems (Figs. 3-8). Figure 3 depicts the distribution of the potential, ϕ, along the chord for a NACA 0012 airfoil at zero angle of attack, for $M_\infty = 0.85$. The parameters used for the geometry discretization are: $N_1 = 25$, $N_w = 1$, $N_3 = N_a = N_f = 5$. The dots represent the results, whereas the dashed line is an interpolation curve obtained by using two splines: one in the portion ahead of the shock and one in the portion behind the shock. Note that the change in slope is quite sharp (indicating that the shock is not smoothed by the numerical scheme) and that two curves may be extrapolated to obtain the location of the shock. Next, consider the pressure distribution, which is shown in Fig. 4. The dots are obtained using algorithm A (central finite differences, in contrast to the evaluation of b, performed as stated above). The dashed line is obtained with algorithm B (*i.e.*, directly from the splines), with a vertical line located at the abscissa of intersection of the two splines[2]. Our results are compared in the same figure with those of Renzoni and Pagano (1991) (continuous line); these were obtained using a conservative finite-difference T.S.P. code.

Next, consider the numerical results for a NACA 64A010 airfoil with incidence $\alpha = -0.21°$ and $M_\infty = 0.796$ ($N_1 = 35$, $N_w = 20$, $N_3 = N_a = N_f = 5$). These are presented in Figure 5, which depicts the pressure distribution along the chord (dots). They are compared with those of Renzoni and Pagano (1991) obtained by using a T.S.P. conservative finite-differences code (continuous line). The same airfoil (with the same discretization parameters) is considered in the results presented in Figure 6, which depicts the pressure distribution for $\alpha = 1°$ and increasing Mach number (*i.e.*, $M_\infty = .75, .77, .79, .80$). The pressure distribution on the same airfoil with $M_\infty = 0.8$ and $\alpha = 0°$ ($N_1 = 35$, $N_w = 20$, $N_3 = N_a = N_f = 7$) is compared in Fig. 7 with experimental results of King and Johnson (1980) and numerical results of Brenneis and Eberle (1991) obtained with an Euler implicit code (with a mesh 88×48).

Figures 8 and 9 present two results on an NLR 7301 airfoil, a modern supercritical airfoil designed to be shock-free at $M_\infty = 0.721$ and $\alpha = -0.19°$ (this steady-state case corresponds to the unsteady test cases CT6-CT9 of Bland, 1979). The pressure distribution for the above flow condition (obtained with $N_1 = 40$, $N_w = 20$, $N_3 = N_a = N_f = 7$) is shown in Fig. 8 and compared with the experimental results from AGARD R-702 (Anon., 1982) and with numerical results of Brenneis and Eberle (1991) obtained with an Euler implicit code (mesh used: 108×74). The pressure distribution on the same airfoil (with the same discretization, $M_\infty = 0.7$, and $\alpha = 2°$) is shown in Fig. 9. This steady-state case corresponds to the cases CT3-CT5 of Bland, 1979. Our results are compared with the T.S.P. solution presented by Müller, Henke, and Dau (1991); in the same figure we present other results by Müller, Henke, and Dau (1991), *i.e.*, a viscous-inviscid-interaction results and an Euler solution, as well as the experimental results from AGARD-R-702 (Anon., 1982).

Next, consider results for two-dimensional unsteady flows (Figs. 10-14). Figures 10 and 11 depict the upper and lower pressure distribution on a conventional NACA 0012 airfoil, at $M_\infty = 0.755$, pitching about quarter-chord with $\alpha(\tau) = \alpha_m + \alpha_0 \sin(k\tau)$ (where $\alpha_m = 0.02°$, $\alpha_0 = 2.51°$, $k = \omega c/2U_\infty = 0.081$) for a complete cycle of oscillation ($N_1 = 32$, $N_w = 20$, $N_3 = N_f = N_a = 5$). This case of "type-B" shock (Tijdeman and Seebass, 1980) is CT5 of Bland (1979) and describes typical conditions for helicopter applications. These results are compared in Figs. 12 and 13 (for $\alpha = 2.0°$ and $\alpha = -2.4°$, respectively) with the experimental results from AGARD R-702 (Anon., 1982) and with the numerical results obtained by Renzoni and Pagano (1991) with a full potential non-conservative formulation. Finally, hysteresis cycle in the $C_\ell - \alpha$ plane for the same case is presented in Fig. 14 and is compared with the results (dotted line) obtained by Goorjian and Guruswamy (1985).

Next, consider three-dimensional steady-state results. The case of a rectangular wing (having $AR = 4$, NACA 64A010 airfoil cross section, and zero angle of

[2] We acknowledge that the "spline procedure" used to evaluate the pressure procedure is quite "ad hoc", and therefore it is not used in the following results. However, it was presented in order to emphasize that sharp shocks may be extracted from the values of the potential.

THIS DOCUMENT PROVIDED BY THE ABBOTT AEROSPACE
TECHNICAL LIBRARY
ABBOTTAEROSPACE.COM

attack) is considered in Figs. 15 and 16, for $M_\infty = 0.85$; this is one of the flow conditions suggested by Bland (1982). The discretisation parameters used are $N_1 = 18$, $N_2 = 8$, $N_3 = N_a = N_f = N_s = 4$. Figure 15 presents the complete three-dimensional pressure distribution, whereas Fig. 16 depicts the 60% semi-span station distribution which is compared with that of Goorjian and Guruswamy (1985).

Finally, three-dimensional unsteady problems are considered in Figures 17-21 which deal with the case of a rectangular wing oscillating in pitch around quarter chord, with $\alpha(\tau) = \alpha_m + \alpha_0 \sin(k\tau)$ (where $\alpha_m = \alpha_0 = 1°$ and $k = 0.0785$). The aspect ratio is $\mathcal{AR} = 8.0$, the section is a biconvex airfoil with a 6% thickness, and $M_\infty = 0.857$. The discretisation parameters used are $N_1 = 18$, $N_2 = 8$, $N_w = 20$, $N_3 = N_a = N_f = N_s = 4$. The pressure distributions over the half wing are shown in Figs. 17-20 for $\psi = k\tau = -3°$, 105°, 213°, 285°, respectively (the lines shown correspond to $y/c = .468$, 1.34, 2.09, 2.71, 3.21, 3.59, 3.84, 3.96). The pressure distribution at the root station for $\psi = 105°$ (dotted line) is presented in Fig. 21 and compared to that obtained by Steger and Caradonna (1980, continuous line).

6. Comments

A boundary integral equation method for steady and unsteady transonic flows has been presented. In order to assess the formulation, two- and three-dimensional, steady and unsteady results have been obtained. It may be noted that, for all the results presented, the shock intensity and its position have a behaviors similar to those observed in finite-difference non-conservative methods, *i.e.*, the shock is weaker and its location is more up-wind than in the case of conservative finite-difference schemes. The reason for this behavior is not clear at this point. It is likely that it is due to convergence (the results have been obtained on an workstation IBM RISC System/6000, Model 320, with 16 Mbyte RAM, a thorough study of convergence is now underway on a larger machine). However, it is also possible that the numerical discretisation used makes the scheme non-conservative. Additional work on this issue appers to be highly desirable: to this aim, different schemes for evaluating the non-linear are being considered.

Additional activities now under way include an extension of the numerical algorithm to helicopter rotors in hover and an extension of the code to full-potential flows, as well as aeroelastic applications.

7. References

Anon., (1982): "Compendium of Unsteady Aerodynamic Measurements," AGARD-R-702.

Bland, S. R., (1979): "AGARD Two Dimensional Aeroelastic Configurations," AGARD A-R No. 156.

Bland, S. R., (1982): "AGARD Three Dimensional Aeroelastic Configurations," AGARD A-R No. 167.

Brenneis, A., Eberle, A., (1991): "Evaluation of an Unsteady Implicit Euler Code Against Two and Three-Dimensional Standard Configurations," Paper No. 10, presented at the AGARD Specialists' Meeting on Transonic Unsteady Aerodynamics and Aeroelasticity, San Diego, CA.

Bridgeman, J. O., Steger, J. L., and Caradonna, F. X., (1982): "A Conservative Finite-Difference Algorithm for the Unsteady Transonic Potential Equation in Generalized Coordinates," AIAA Paper 82-1388.

Crown, J. C., (1968): "Calculation of Transonic Flow over Thick Airfoils by Integral Methods," AIAA Journal, Vol. 6, pp. 413-423.

Gear, J. A., (1987): "Three-Dimensional Unsteady Transonic Flow: An Integral Equation Formulation," Computational Mechanics, No. 2, pp. 268-270.

Goorjian, P. M., Guruswamy, G. P., (1985): "Unsteady Transonic Aerodynamic and Aeroelastic Calculation about Airfoils and Wing," in Transonic Unsteady Aerodynamics and its Aeroelastic Applications, AGARD CP-374.

Kandil, O. A., and Yates, E. C., Jr., (1985): "Computation of Transonic Vortex Flows Past Delta Wings – Integral Equation Approach," AIAA Paper No. 85-1582.

King, L. S., Johnson, D. E., (1980): "Calculations of Transonic Flow About an Airfoil in a Wind Tunnel," AIAA Paper 80-1366.

Morino, L., (1974): "A General Theory of Unsteady Compressible Potential Aerodynamics," NASA CR-2464.

Morino, L., (editor), (1985): Computational Methods in Potential Aerodynamics, Computational Mechanics Publications, Southampton, UK.

Morino, L., and Tseng, K., (1990): "A General Theory of Unsteady Compressible Potential Flows with Applications to Aeroplanes and Rotors," Eds.: P. K. Banerjee and L. Morino, Developments in Boundary

THIS DOCUMENT PROVIDED BY THE ABBOTT AEROSPACE
TECHNICAL LIBRARY
ABBOTTAEROSPACE.COM

Element Methods, Volume 6: Nonlinear Problems of Fluid Dynamics, Elsevier Applied Science Publishers, Barking, UK.

Müller, U., R., Henke, H., Dau, K., (1991): "Computation of Viscous Phenomena in Unsteady Transonic Flow," Paper No. 14, presented at the AGARD Specialists' Meeting on Transonic Unsteady Aerodynamics and Aeroelasticity, San Diego, CA.

Nixon, D., (1974): "Transonic Flow Around Symmetric Aerofoils at Zero Incidence," Journal of Aircraft, Vol. 11, pp. 122-124.

Nixon, D., (1978): "Calculation of Unsteady Transonic Flows Using the Integral Equation Method," AIAA Journal, Vol. 16, No. 9, pp. 976-983.

Norstrud, H., (1973): "High Speed Flow past Wings," NASA CR-2246.

Oswatitsch, K., (1950): "Die Geschwindigkeitsverteilung ab Symmetrische Profilen beim auftreten lokaler Uberschallgebiete," Acta Physica Austriaca, Vol. 4, pp. 228-271.

Piers, W. J., and Slooff, J. W., (1979): "Calculation of Transonic Flow by Means of a Shock-Capturing Field Panel Method," AIAA Paper 79-1459.

Renzoni, P. G., and Pagano, A., (1991): private communication.

Sinclair, P. M., (1986): "An Exact Integral (Field Panel) Method for the Calculation of Two-Dimensional Transonic Potential Flow around Complex Configurations," Aeronautical Journal, Paper No. 1394, pp. 227-236.

Sinclair, P. M., (1988): "A Three-Dimensional Field Integral Method for the Calculation of Transonic Flow on Complex Configurations – Theory and Preliminary Results," Aeronautical Journal, Paper No. 1482, pp. 235-241.

Spreiter, J. R., and Alksne, A. Y., (1955): "Theoretical Prediction of Pressure Distribution on Non-Lifting Airfoils at High Subsonic Speeds," NACA Rept. 1217.

Steger, J. L., and Caradonna, F. X., (1980): "A Conservative Implicit Finite Difference Scheme for the Unsteady Transonic Full Potential Equation," AIAA Paper 80-1368.

Tijdeman, H., and Seebass, R., (1980): "Transonic Flow Past Oscillating Airfoils," Annual Review of Fluid Mechanics, Vol. 12, pp. 181-222.

Tseng, K., and Morino, L., (1982): "Nonlinear Green's Function Method for Unsteady Transonic Flows," Ed.: D. Nixon, Transonic Aerodynamics, Progress in Aeronautics and Astronautics, Vol. 81, American Institute of Aeronautics and Astronautics, New York, NY, USA.

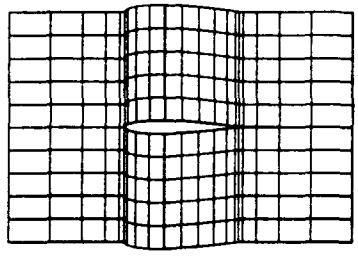


Figure 1: body, wake and volume discretization; cross-view.

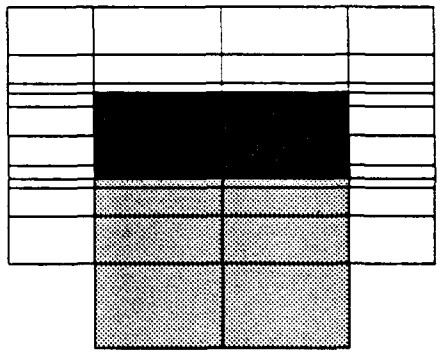


Figure 2: body, wake and volume discretization; top view.

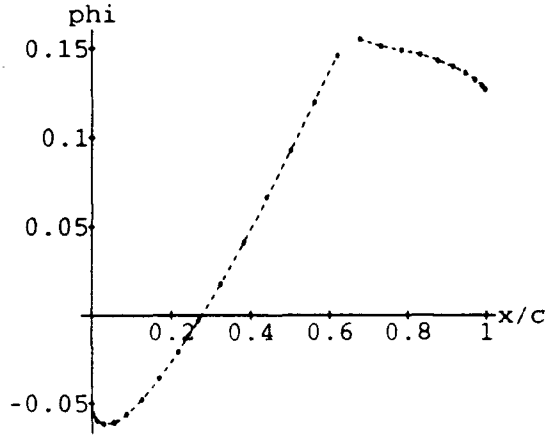


Figure 3: velocity potential distribution on a NACA 0012 airfoil with $M_\infty = 0.85$ and $\alpha = 0°$ (dots) with interpolation (dashed line).

THIS DOCUMENT PROVIDED BY THE ABBOTT AEROSPACE
TECHNICAL LIBRARY
ABBOTTAEROSPACE.COM

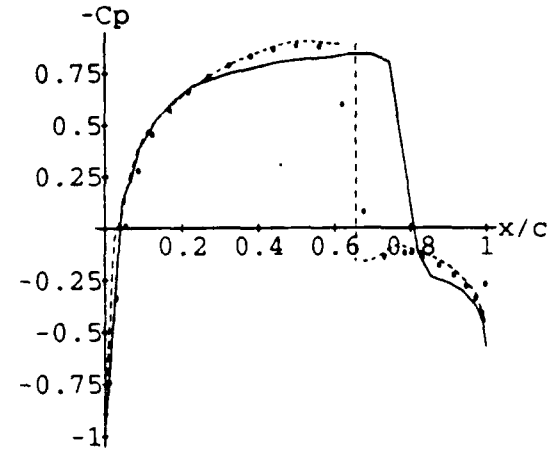


Figure 4: pressure distribution corresponding to the velocity potential of Fig. 3: algorithm A (dots), algorithm B (dashed line), and numerical results obtained by a finite-difference T.S.P. code (continuous line, Renzoni, Pagano, 1991).

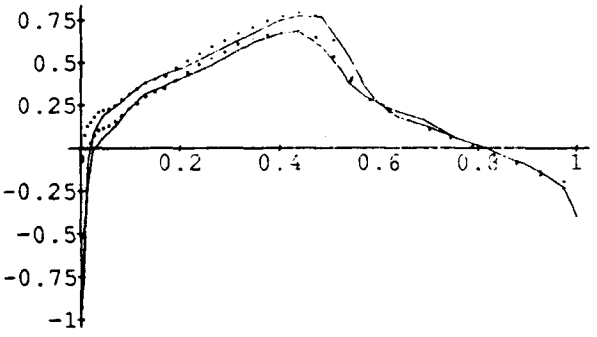


Figure 5: pressure distribution on a NACA 64A010 airfoil with $M_\infty = 0.796$ and $\alpha = -0.210°$ (dotted line) compared with results obtained by using a finite-difference T.S.P. model (continuous line, Renzoni, Pagano, 1991).

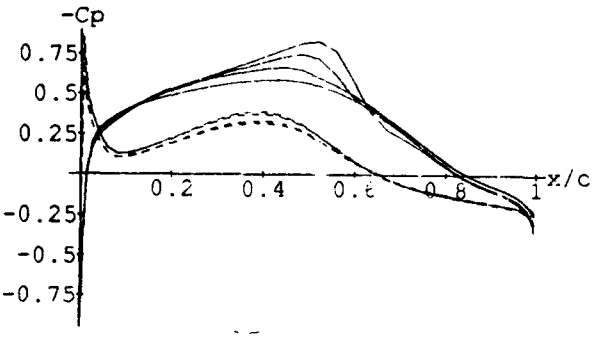


Figure 6: pressure distributions on a NACA 64A010 airfoil at $M_\infty = 0.75, 0.77, 0.79, 0.80$, and $\alpha = 1°$.

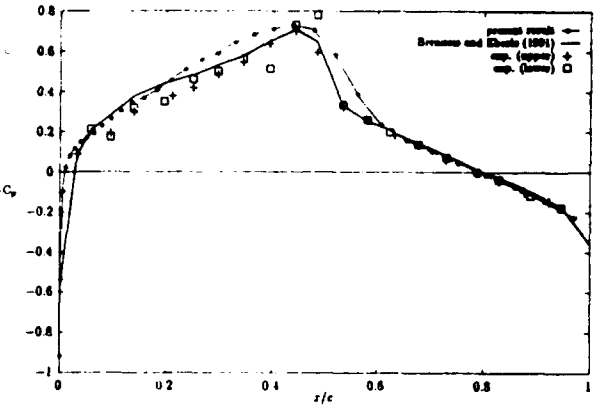


Figure 7: pressure distribution on a NACA 64A010 airfoil with $M_\infty = 0.8$ and zero angle of attack compared with an Euler solution (Brenneis and Eberle, 1991) and experimental results (King and Johnson, 1980).

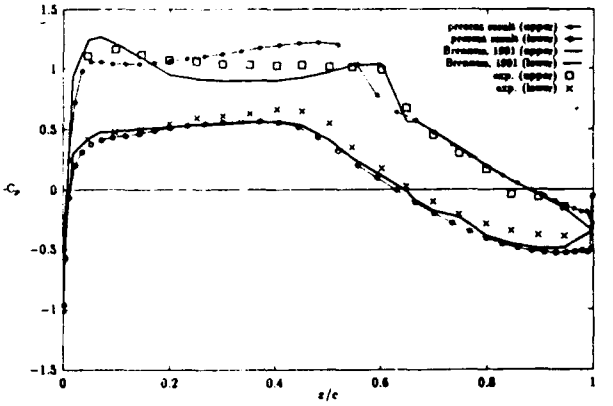


Figure 8: pressure distribution on a NLR 7301 airfoil with $\alpha = -0.19$ and $M_\infty = 0.721$ compared with an Euler solution (Brenneis and Eberle, 1991) and experimental results (AGARD R-702, 1982).

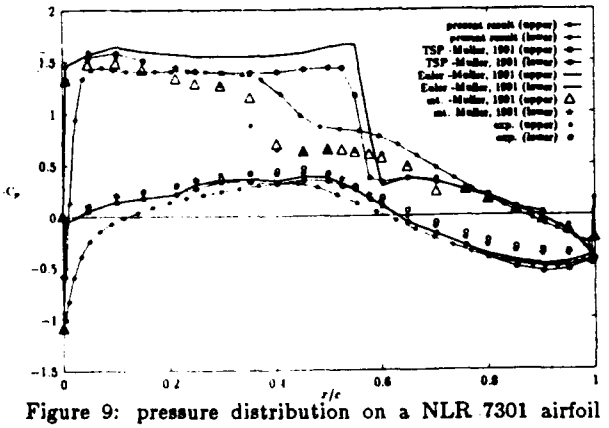


Figure 9: pressure distribution on a NLR 7301 airfoil with $\alpha = 2$ and $M_\infty = 0.7$ compared with an Euler solution, with a finite-difference T.S.P. solution, with an interactive T.S.P. solution (Müller, Henke and Dau, 1991), and with experimental results (AGARD R-702).

THIS DOCUMENT PROVIDED BY THE ABBOTT AEROSPACE
TECHNICAL LIBRARY
ABBOTTAEROSPACE.COM

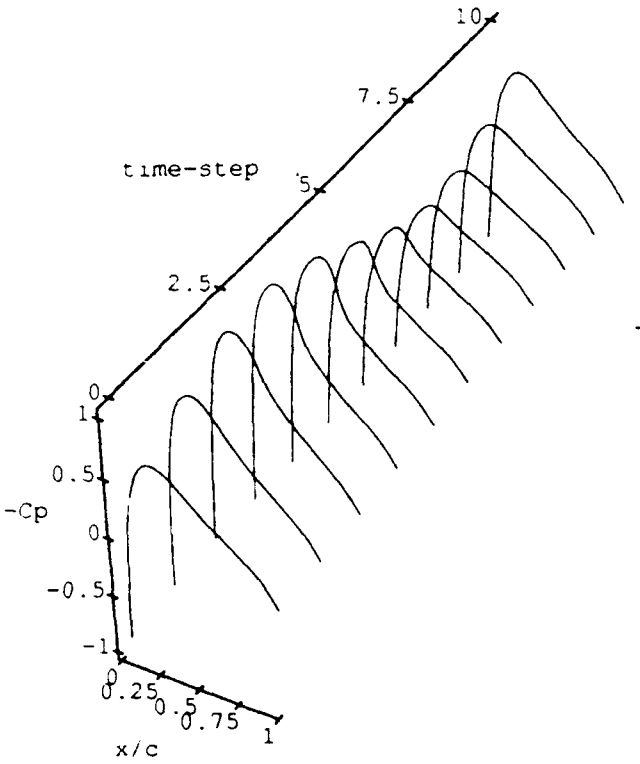


Figure 10: upper pressure distribution in a cycle of time on a NACA 0012 oscillating in pitch at a quarter-chord with $M_\infty = 0.755$, $\alpha_m = 0.02^0$, $\alpha_0 = 2.51^0$, $k = \omega c/2U_\infty = 0.081$.

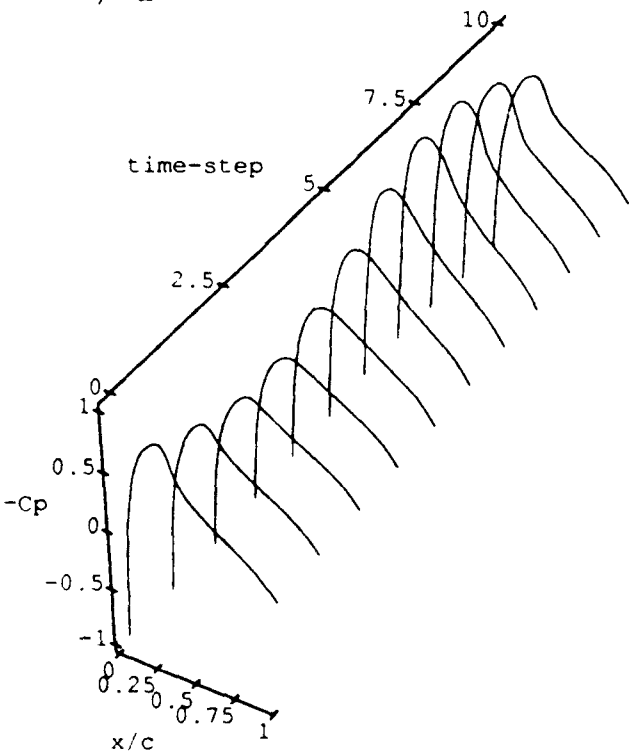


Figure 11: lower pressure distribution in a cycle of time on a NACA 0012 oscillating in pitch at a quarter-chord with $M_\infty = 0.755$, $\alpha_m = 0.02^0$, $\alpha_0 = 2.51^0$, $k = \omega c/2U_\infty = 0.081$.

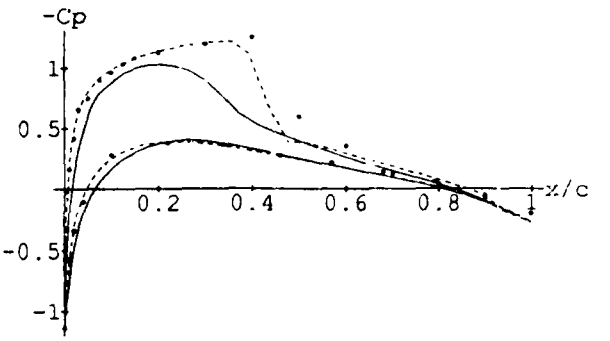


Figure 12: upper and lower pressure distribution in the case of Figs. 10-11 at $\alpha = 2.0^0$ (continuous line) compared with experimental results obtained by Lambourne (1982, dotted line) and numerical results obtained by Renzoni and Pagano (1991, dashed line).

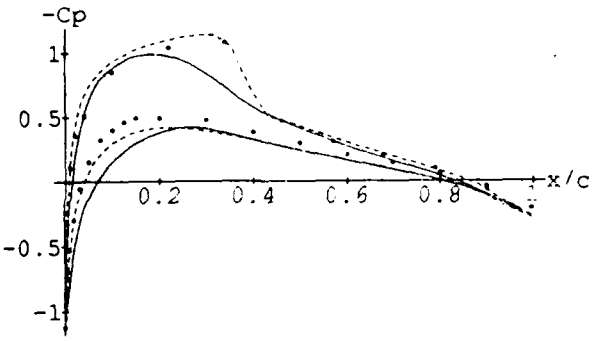


Figure 13: upper and lower pressure distribution in the case of Figs. 10-11 at $\alpha = -2.4^0$ (continuous line) compared with experimental results obtained by Lambourne (1982, dotted line) and numerical results obtained by Renzoni and Pagano (1991, dashed line).

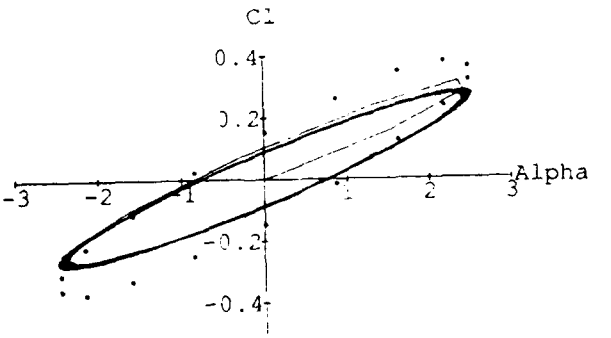


Figure 14: C_ℓ vs α for the case of Figs. 10-11 (continuous line) compared with the results of Goorjian and Guruswamy (1985, dotted line).

THIS DOCUMENT PROVIDED BY THE ABBOTT AEROSPACE
TECHNICAL LIBRARY
ABBOTTAEROSPACE.COM

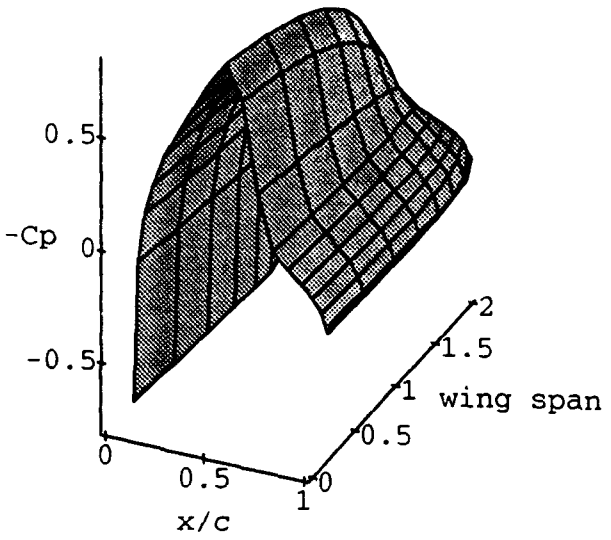


Figure 15: pressure distribution on a rectangular wing with $\mathcal{AR} = 4$ at $M_\infty = 0.85$, zero angle of attack and NACA 64A010 airfoil section.

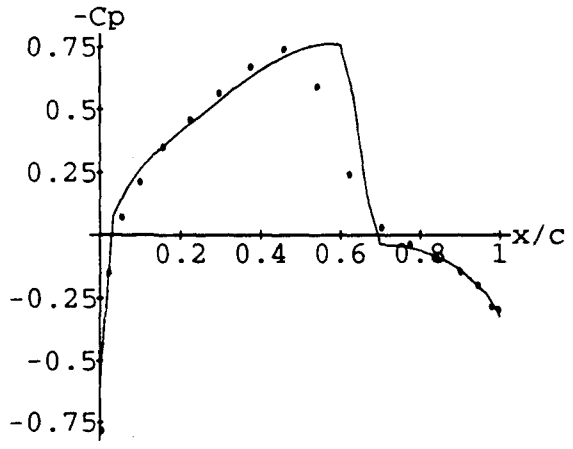


Figure 16: pressure distribution at 60% span section (dotted line) for the case of Fig. 15 compared with the results of Goorjian and Guruswamy (1985, continuous).

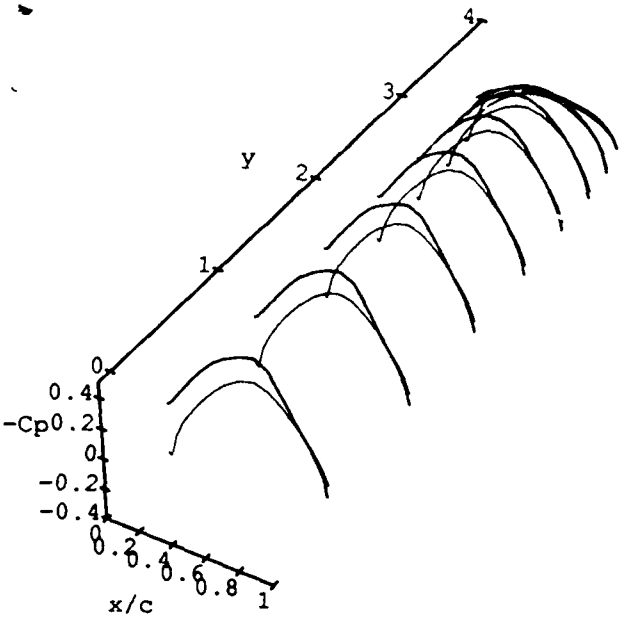


Figure 17: upper and lower pressure distribution on a half-span rectangular wing with $\mathcal{AR} = 8$ at $M_\infty = 0.857$ oscillating in pitch at the quarter chord with $\alpha(\tau) = 1° + 1° \sin(k\tau)$: $\psi = k\tau = -3°$.

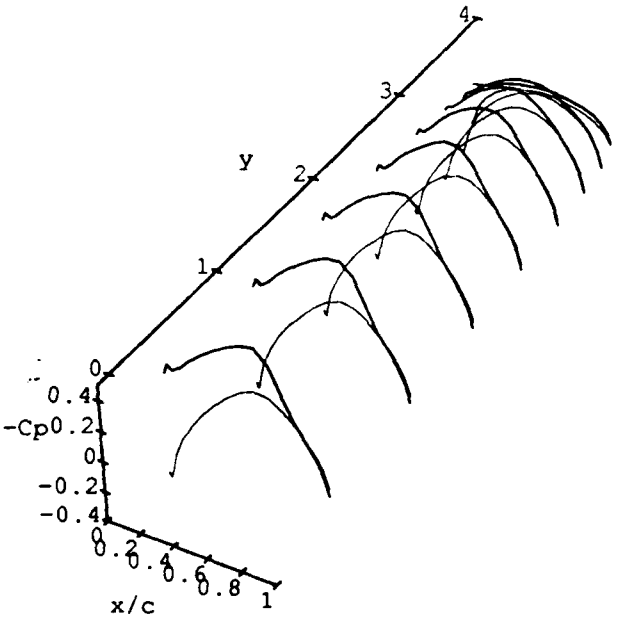


Figure 18: the same case of Fig. 17 at the time station $\psi = 105°$.

THIS DOCUMENT PROVIDED BY THE ABBOTT AEROSPACE
TECHNICAL LIBRARY
ABBOTTAEROSPACE.COM

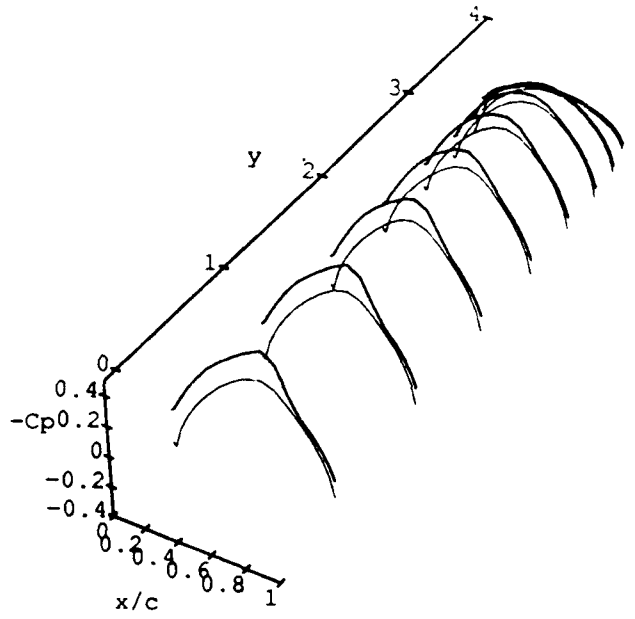


Figure 19: the same case of Fig. 17 at the time station $\psi = 213°$.

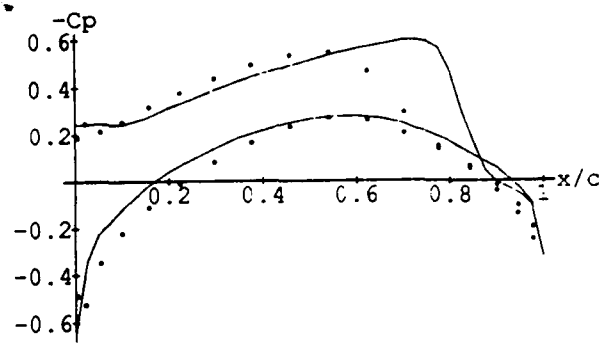


Figure 21: pressure distribution at the root section when $\psi = 105°$ (dotted line) for the case of Fig. 17 compared with the results of Steger and Caradonna (1980, continuous line).

Acknowledgements

This work was partially supported by CIRA grant no. 90.3014.VE.046 to the University of Rome "La Sapienza". The authors wish to thank Dr. P. G. Renzoni and A. Pagano of CIRA for supplying the finite-difference data used for comparison.

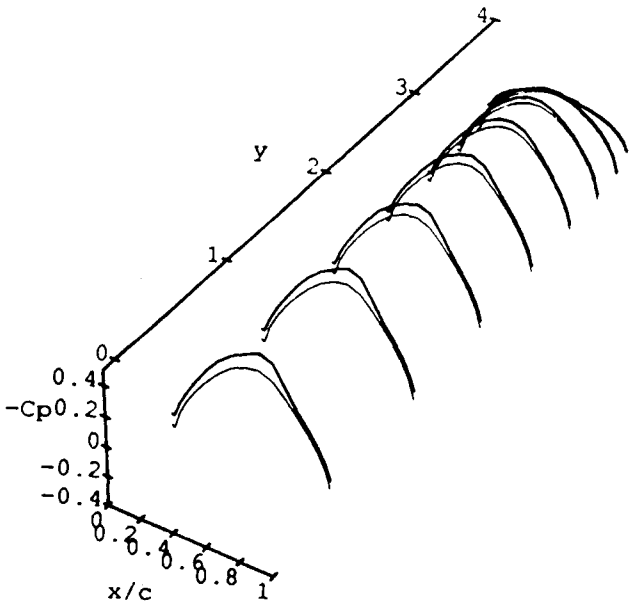


Figure 20: the same case of Fig. 17 at the time station $\psi = 285°$.

THIS DOCUMENT PROVIDED BY THE ABBOTT AEROSPACE
TECHNICAL LIBRARY
ABBOTTAEROSPACE.COM

AD-P007 800

COMPARISON OF EULER AND FULL POTENTIAL METHODS FOR UNSTEADY TRANSONIC FLOW CALCULATIONS

Dr. rer.nat. R. Voß and W. Wegner
Deutsche Forschungsanstalt für Luft- und Raumfahrt (DLR)
Institute of Aeroelasticity
Bunsenstrasse 10
3400 Göttingen
Germany

92-16038

SUMMARY

This paper presents the results of unsteady transonic flow calculation methods developed at the DLR Institute of Aeroelasticity for oscillating airfoils and wings. 2D Euler and Full Potential calculations in the nonlinear regime with pronounced shock dynamics at the conventional NACA0012 and the supercritical NLR7301 airfoil show that the unsteady pressure distributions agree well, whereas the unsteady lift and moment curves are not always in good agreement.

3D results are obtained with a 3D Full Potential code and a 3D time linearized TSD method for a swept NACA0012 wing and for the LANN wing, an AGARD standard test wing, both oscillating with small amplitudes. The agreement of the unsteady first harmonics of pressure distribution indicates that the time linearized approach may be sufficient for low amplitudes. For higher amplitudes, however, the appearance of pronounced higher harmonics (even for a wing with a conventional airfoil section) indicates strong nonlinear behavior combined with complicated shock motions.

1. INTRODUCTION

Progress in theoretical aeroelastic investigation depends strongly on the improvement of computational methods for unsteady flows. Flutter predictions in the design stage of new airplanes demand the variation of several geometrical, structural dynamics, and flow parameters and thus a huge number of single unsteady flow calculations. In order to reduce the corresponding computational effort for predicting motion-induced unsteady airloads, the application of different aerodynamic models with different grades of physical simplifications, depending on the complexity of the flow, seems to be very important. The computer times for different methods may vary by several orders of magnitude. The investigations of this paper are restricted to inviscid flow models.

Methods for compressible unsteady inviscid flow calculations in order of ascending completeness of the flow modeling and of computational effort are based on: linear compressible potential theory (methods like doublet lattice), time linearized equations, Transonic Small Disturbance (TSD), Full Potential (FP), and Euler equation.

Linear potential methods apply surface panel techniques at very low computer costs, but they are restricted to pure sub- and supersonic flows. Time linearized methods are able to treat unsteady transonic flows, if the unsteady airloads induced by harmonic motions of the lifting system can be approximated as small harmonic perturbations of a steady or mean basic flow, an assumption often valid in flutter investigations. These methods apply, for instance, field panel techniques in the frequency domain. They already need significantly more computer time than surface panel techniques, but still offer the advantages of linearity and inherent time accuracy. The mean flow determines just the coefficients of the linear equations and may be taken from nonlinear steady flow calculations or from experiment.

If it is no longer possible to distinguish between a basic mean flow and a linear small unsteady perturbation flow, for instance in cases of shock waves moving nonharmonically and with large amplitudes, methods based on nonlinear equations have to be applied. These CFD methods mostly use Finite Difference, Finite Volume or Finite Element techniques.

While the very common and far developed TSD methods, the simplest of this class, may be applied for thin wings, the treatment of thick wings and bodies demands methods based on the FP and Euler equations. The latter ones additionally afford *boundary fitted grids.*

Among these, the FP methods are not able to treat flows with too strong shocks and complicated vortex dynamics. Thus, Euler methods have to be applied, yielding a complete model for inviscid flows.

Although many computer codes have been developed in the past, especially for two-dimensional flow, their reliability is still an existing problem. Some reasons for these uncertainties are, for example, the choice of the abovementioned different flow equations (linearized or nonlinear, TSD or FP or Euler), the treatment of the time dependence (time accuracy), the capability of capturing shocks automatically (conservative or nonconservative methods).
For this reason, different codes have to be validated carefully both against experimental results and against one another, in order to test their reliabilty and to define their regions of applicability within a complete flutter investigation.

In Ref. [1], unsteady Euler and Full Potential results were compared for the NACA0012 airfoil. These investigations are extended, and as a next step, results of four different computer codes for unsteady transonic flow calculations developed at the DLR Institute of Aeroelasticity - namely a 2D Euler, a 2D Full Potential, a 3D Full Potential and a 3D time linearized TSD code - are compared. 2D Euler and FP results are compared for the conventional NACA0012 and the supercritical NLR7301 airfoil oscillating in a strongly nonlinear flow regime, i.e. with pronounced shock waves and large amplitudes for the NACA0012 and about the very sensitive design condition of the NLR7301, respectively. The influences of unsteady flow parameters (reduced frequency and amplitude) on flow field details like shock dynamics, on lift and moment coefficients, and on the agreement between both codes is studied. In order to avoid two

THIS DOCUMENT PROVIDED BY THE ABBOTT AEROSPACE
TECHNICAL LIBRARY
ABBOTTAEROSPACE.COM

possible sources of discrepancies, both codes used the same computational grids and both took special care of time accuracy by applying an explicit version of the Euler code and a special Newton Iteration technique in the implicit FP code. The comparison between 3D Full Potential and 3D time linearized codes is carried out for a swept wing with NACA0012 wing sections and for the supercritical LANN wing, but only at moderate and low amplitudes, where the time linearized approach is reasonable.

2. EULER ALGORITHM

The fundamental equations of inviscid gas dynamics arise from the three basic physical principles: conservation of mass, momentum, and energy. Procedures in gas dynamics can be treated as approximately adiabatic and neglecting gravitational forces. With regard to a spatial control volume V_0, the integral representations follow, which by means of elementary transformations may be cast into the conservation form

$$\int_{V_0} [Q_t + F_x + G_y + H_z] \, d V_0 = 0 \qquad (1)$$

with the so-called conservative variables

$$Q = \begin{bmatrix} \rho \\ \rho u \\ \rho v \\ \rho w \\ \rho e_{tot} \end{bmatrix}, \quad e_{tot} = e + \frac{1}{2}\left[u^2 + v^2 + w^2\right] \qquad (2)$$

and the fluxes

$$F = \begin{bmatrix} \rho u \\ \rho u^2 + p \\ \rho uv \\ \rho uw \\ [\rho e_{tot} + p]u \end{bmatrix}, \quad G = \begin{bmatrix} \rho v \\ \rho vu \\ \rho v^2 + p \\ \rho vw \\ [\rho e_{tot} + p]v \end{bmatrix}, \quad H = \begin{bmatrix} \rho w \\ \rho wu \\ \rho wv \\ \rho w^2 + p \\ [\rho e_{tot} + p]w \end{bmatrix} . \qquad (3)$$

ρ, p, and e denote density, pressure, and energy, and u, v, w the velocity components. The application of the corresponding differential form is permissible, because the conservative form fulfills the Rankine-Hugoniot shock relation.

The equations of state of the calorically and thermically ideal gases yield the further necessary relation

$$p = [\gamma - 1]\, \rho e \ . \qquad (4)$$

γ denotes the ratio of specific heats.

The numerical solution model for the discrete field point x_i, y_j, z_k is determined principally by the conservative discretization

$$Q^{n+1}_{i,j,k} = Q^n_{i,j,k} - \frac{\Delta t}{\Delta x}\left[F_{i+\frac{1}{2},j,k} - F_{i-\frac{1}{2},j,k}\right] - \frac{\Delta t}{\Delta y}\left[G_{i,j+\frac{1}{2},k} - G_{i,j-\frac{1}{2},k}\right] - \frac{\Delta t}{\Delta z}\left[H_{i,j,k+\frac{1}{2}} - H_{i,j,k-\frac{1}{2}}\right] , \qquad (5)$$

which satisfies the integral form of the conservation theorems for every grid cell $\Delta x\, \Delta y\, \Delta z$. The fluxes on the cell surfaces depend on the local left and right-side variables, respectively:

$$F_{i+\frac{1}{2},j,k} = F\left(Q_{i+\frac{1}{2},L}\ ,\ Q_{i+\frac{1}{2},R}\right)_{j,k} \ . \qquad (6)$$

The relationships of the left and right-side variables correspond with the wave propagation of disturbances (upwind procedure). Their directions of propagation correspond to the positive and negative eigenvalues of the Jacobian matrix $A = \partial F/\partial Q$ at the position $x_{i+1/2}$, y_j, z_k. The functional relation of the left and right-side cell boundary values in x-direction is decoupled from those in the y and z-direction, which means that the multidimensional wave propagation is numerically treated as a sequence of one-dimensional propagation phenomena.

Usual upwind procedures are, for example:

- the Flux Vector Splitting from B. van Leer [2],
- the approximate Riemann Solver from A. Harten, P.D. Lax and B. van Leer [3],
- the approximate Riemann Solver from P.L. Roe [4], and
- the complete Riemann Solver from W. Wegner [5].

All of these procedures were tested. Their results showed no differences in the unsteady pressure distributions regarding the two-dimensional configurations presented here.

The second order is expressed in the extrapolation of the left and right-side cell boundary variables, corresponding to MUSCL (Monotonic Upstream Scheme for Conservation Laws) of B. van Leer [6].

Transformation of the basic Euler equations to a boundary fitted moving coordinate system is a linear mapping which does not alter the principle of the one-dimensional Riemann Solver. Introducing a known time dependent coordinate transformation

$$\begin{array}{l} x = x(\xi, \eta, \zeta, \tau) \\ y = y(\xi, \eta, \zeta, \tau) \\ z = z(\xi, \eta, \zeta, \tau) \\ t = \tau \end{array} \quad \Leftrightarrow \quad \begin{array}{l} \xi = \xi(x, y, z, t) \\ \eta = \eta(x, y, z, t) \\ \zeta = \zeta(x, y, z, t) \\ \tau = t \end{array} \ , \qquad (7)$$

the Euler equations are given in the new system in conservative form by

$$\hat{Q}_\tau + \hat{F}_\xi + \hat{G}_\eta + \hat{H}_\zeta = 0 \ . \qquad (8)$$

In the following equations, the subscripts ξ, η, ζ, and τ denote derivatives with respect to the boundary fitted coordinates. J is the Jacobian of the coordinate transformation

$$J = \frac{\partial(\xi, \eta, \zeta)}{\partial(x, y, z)} \qquad (9)$$

and corresponds physically to the inverse cell area.

The transformed flux vectors may be cast into the form

$$\hat{Q} = Q / J$$

THIS DOCUMENT PROVIDED BY THE ABBOTT AEROSPACE
TECHNICAL LIBRARY
ABBOTTAEROSPACE.COM

$$\hat{F} = \frac{1}{J}\begin{bmatrix} \rho U \\ \rho u U + p\xi_x \\ \rho v U + p\xi_y \\ \rho w U + p\xi_z \\ [\rho e_{tot} + p]U - p\xi_t \end{bmatrix}$$

$$\hat{G} = \frac{1}{J}\begin{bmatrix} \rho V \\ \rho u V + p\eta_x \\ \rho v V + p\eta_y \\ \rho w V + p\eta_z \\ [\rho e_{tot} + p]V - p\eta_t \end{bmatrix} \qquad (10)$$

$$\hat{H} = \frac{1}{J}\begin{bmatrix} \rho W \\ \rho u W + p\zeta_x \\ \rho v W + p\zeta_y \\ \rho w W + p\zeta_z \\ [\rho e_{tot} + p]W - p\zeta_t \end{bmatrix}$$

with the contravariant velocity components

$$\begin{aligned} U &= \xi_t + \xi_x u + \xi_y v + \xi_z w \ , \\ V &= \eta_t + \eta_x u + \eta_y v + \eta_z w \ , \qquad (11) \\ W &= \zeta_t + \zeta_x u + \zeta_y v + \zeta_z w \ . \end{aligned}$$

It is possible to rewrite $\hat{F}$, $\hat{G}$ and $\hat{H}$ as a product of local transformation matrices T_1, T_2 and T_3 and modified flux vectors $\bar{F}$, $\bar{G}$ and $\bar{H}$, which formally equal the corresponding cartesian flux vectors, but contain transformed co- and contravariant velocities instead of cartesian velocities:

$$\hat{F} = T_1\bar{F}, \quad \hat{G} = T_2\bar{G}, \quad \hat{H} = T_3\bar{H} \ . \qquad (12)$$

T_1, T_2 and T_3 only depend on metric terms and are given, for example, by W.K. Anderson et al [7]. Thus, the upwind procedure of the transformed Euler equations agree with the cartesian ones.

Multidimensional flow problems require boundary conditions for the body contour and the outer boundary.

The inviscid kinematic flow condition on the body contour demands that relative to the specified body motion

$$V_k^T = [x_\tau, y_\tau, z_\tau] \ , \qquad (13)$$

the normal relative velocity components disappear:

$$[V - V_k]N = 0, \quad N = \text{grad}\,\zeta \ . \qquad (14)$$

The other flow variables on the contour are extrapolated out of the field. For the pressure p, the normal momentum equation that contains the effect of the curved coordinates is applied.

The final extension of the computing area leads to the fact that the propagation of disturbances at the far field grid cells has not faded out, which is taken into account with the implementation of non-reflecting boundary conditions. Nevertheless, for the presented results, influence of far field boundaries has proven negligible.

3. FULL POTENTIAL ALGORITHM

3.1 Basics

The Full Potential equation in conservative form is obtained from the Euler equations by simplifying assumptions about entropy and vorticity. The flow is assumed to be homentropic (even downstream of shock waves), and thus the isentropic relation is valid:

$$\frac{p}{p_\infty} = \left(\frac{\rho}{\rho_\infty}\right)^\gamma \ . \qquad (15)$$

Additionally, the flow is assumed to be irrotational outside of the wake, and hence a velocity potential Φ exists. The wake geometry has to be prescribed as the surface of shed vorticity downstream of the wing.

$$\vec{v} = \text{grad}\,\Phi \qquad (16)$$

Thus, the essential restrictions of potential theory in comparison with Euler theory are:

- Inability to treat strong shock waves (esp. curved shocks), causing entropy rises and producing vorticity. These effects have to be specially modelled and incorporated into potential theory.
- A prescribed path of vorticity transport.

The basic equations of Full Potential theory, derived from the Euler equations using the above assumptions, are then the continuity equation

$$\left(\frac{\rho}{J}\right)_\tau + \left(\frac{\rho U}{J}\right)_\xi + \left(\frac{\rho V}{J}\right)_\eta + \left(\frac{\rho W}{J}\right)_\zeta = 0 \qquad (17)$$

and the Bernoulli equation

$$\frac{\rho}{\rho_\infty} = \left[1 - \frac{\gamma - 1}{2} M_\infty^2 \left(2\Phi_t + q^2 - 1\right)\right]^{\frac{1}{\gamma - 1}} \ , \qquad (18)$$

where the magnitude q of flow velocity is defined by

$$q^2 = (U - \xi_t)\Phi_\xi + (V - \eta_t)\Phi_\eta + (W - \zeta_t)\Phi_\zeta \ . \qquad (19)$$

The contravariant velocity components now read:

$$\begin{aligned} U &= \xi_\tau + a_{11}\Phi_\xi + a_{12}\Phi_\eta + a_{13}\Phi_\zeta \\ V &= \eta_\tau + a_{12}\Phi_\xi + a_{22}\Phi_\eta + a_{23}\Phi_\zeta \qquad (20) \\ W &= \zeta_\tau + a_{13}\Phi_\xi + a_{23}\Phi_\eta + a_{33}\Phi_\zeta \ . \end{aligned}$$

The appearing metric coefficients are defined by

$$\begin{aligned} a_{11} &= \xi_x^2 + \xi_y^2 + \xi_z^2 & a_{12} &= \xi_x\eta_x + \xi_y\eta_y + \xi_z\eta_z \\ a_{22} &= \eta_x^2 + \eta_y^2 + \eta_z^2 & a_{33} &= \zeta_x^2 + \zeta_y^2 + \zeta_z^2 \qquad (21) \\ a_{13} &= \xi_x\zeta_x + \xi_y\zeta_y + \xi_z\zeta_z & a_{23} &= \eta_x\zeta_x + \eta_y\zeta_y + \eta_z\zeta_z \ . \end{aligned}$$

Density ρ and fluxes ρU, ρV, ρW are nonlinear functions of the velocity potential, given by (18) and (19). Following the ideas of Ref. [8], the unsteady Full Potential equation is solved by a Newton Iteration procedure in order to obtain time accurate solutions, i.e.

$$R(\Phi) \equiv \left(\frac{\rho}{J}\right)_\tau + F_\xi + G_\eta + H_\zeta = 0 \qquad (22)$$

(with $F = \rho U/J$, $G = \rho V/J$, $H = \rho W/J$) has to be fulfilled for each time step τ_n by a solution Φ^n.

A new solution Φ^{n+1} for the next time step τ_{n+1} is then obtained by the following iterative process:

1. Generation of an initial solution Φ_0 by extrapolation from Φ^n and Φ^{n-1}.
2. Iteration cycle for $i = 0, \ldots, I - 1$
   $R(\Phi_i) + R_\Phi\,|_{\Phi = \Phi_i} \cdot (\Phi_{i+1} - \Phi_i) = 0.$

THIS DOCUMENT PROVIDED BY THE ABBOTT AEROSPACE
TECHNICAL LIBRARY
ABBOTTAEROSPACE.COM

The residual of the unsteady equation $R(\Phi_l)$ is driven below a given error bound, and Φ_l is accepted as the solution for the new time

$$\Phi^{n+1} = \Phi_l \quad . \tag{23}$$

The numerical solution applies an implicit finite difference scheme with second order time and second order central space discretization:

$$\left(\frac{\rho}{J}\right)^{n+1} - \left(\frac{\rho}{J}\right)^{n} + \Delta\tau(F_\xi + G_\eta + H_\zeta)^{n+1/2} = 0. \tag{24}$$

The necessary upwinding in order to form compression shocks and to exclude expansion shocks is introduced into the scheme by a mass flux balanced biasing of the density in upwind direction for the supersonic flow regions, see Ref. [9]. The density ρ is replaced by an upwind density $\tilde{\rho}$:

$$\tilde{\rho} = \rho - \frac{1}{q}\left(\frac{U}{Q}\Delta\xi\overleftarrow{\partial}_\xi + \frac{V}{Q}\Delta\eta\overleftarrow{\partial}_\eta + \frac{W}{Q}\Delta\zeta\overleftarrow{\partial}_\zeta\right)(\rho q)^- \tag{25}$$

$$\text{with} \qquad Q = \sqrt{U^2 + V^2 + W^2} \tag{26}$$

$$\text{and} \quad (\rho q)^- = \begin{bmatrix} \rho q - \rho^* q^* \\ 0 \end{bmatrix}, \quad \text{if} \begin{bmatrix} q > q^* \\ q \le q^* \end{bmatrix}. \tag{27}$$

$\overleftarrow{\partial}$ denotes finite differencing in upwind direction, and $\rho^* q^*$ denotes the sonic value of mass flux, given by

$$(q^*)^2 = \frac{2}{(\gamma+1)M_\infty^2} \cdot \left(1 - (\gamma-1)M_\infty^2\left(\Phi_\tau + \xi_t\Phi_\xi + \eta_t\Phi_\eta + \zeta_t\Phi_\zeta - \frac{1}{2}\right)\right) \tag{28}$$

$$\text{and} \qquad \rho^* = (q^* M_\infty)^{\frac{2}{\gamma-1}} \quad . \tag{29}$$

For unsteady flow, $\rho^* q^*$ is not a constant.

Calculation of the iteration matrix R_Φ in (25) demands several derivative expressions, such as ρ_Φ, $\tilde{\rho}_\Phi$, U_Φ, V_Φ, W_Φ. As the accuracy of R_Φ is important only for the convergence behavior but not for the final result of the Newton Iteration, $\tilde{\rho}_\Phi$ was replaced by ρ_Φ in order to decrease the complexity of the bandwidth of the matrix structure of R_Φ. This did not significantly decrease the convergence speed. (Even if ρ_Φ is totally neglected in the derivatives of the mass flux terms ρU, ρV, ρW, the Newton Iteration is still fast.) Each Newton Iteration demands the solution of the following linear system for the correction vector $\varphi = (\Phi_{l+1} - \Phi_l)$:

$$\begin{aligned} R_\Phi \varphi = \Big[& -\beta(I + \Delta\tau U\partial_\xi + \Delta\tau V\partial_\eta + \Delta\tau W\partial_\zeta) + \\ & + \frac{1}{2}\partial_\xi(\alpha_{11}\partial_\xi + \alpha_{12}\partial_\eta + \alpha_{13}\partial_\zeta - \Delta\tau\beta UI) + \\ & + \frac{1}{2}\partial_\eta(\alpha_{12}\partial_\xi + \alpha_{22}\partial_\eta + \alpha_{23}\partial_\zeta - \Delta\tau\beta VI) + \\ & + \frac{1}{2}\partial_\zeta(\alpha_{13}\partial_\xi + \alpha_{23}\partial_\eta + \alpha_{33}\partial_\zeta - \Delta\tau\beta WI) \Big] \varphi = \\ & = -R(\Phi) \end{aligned} \tag{30}$$

$$\text{with} \qquad \beta := \frac{\rho}{J^{n+1} a^2 \Delta\tau^2}$$

$$\text{and} \qquad \alpha_{ij} := \frac{\rho}{J^{n+1}}\left(a_{ij} - \frac{U_i U_j}{a^2}\right),$$

$U_1 = U$, $U_2 = V$, $U_3 = W$, I = identity, ∂_ξ, ∂_η, ∂_ζ denote central difference operators, and all appearing flow field variables are obtained from the intermediate solution $\Phi = \Phi_l$ of the last Newton Iteration.

(30) may be solved by Approximate Factorization (AF) as in Ref. [8], but in the present code line relaxation was preferred in order to avoid factorization errors of the AF procedure and because of an easier implementation of boundary conditions.

(30) is approximately solved by a few line relaxations for all three space coordinates before the next Newton Iteration step is started. The error bounds to be reached before finishing one time step iteration were defined to be 10^{-6} and 10^{-4} for the average and maximum values of the residual, respectively. The number of necessary Newton Iterations per time step varies between 4 and 10, depending on the magnitude of the flow field changes within this time interval.

3.2 Boundary Conditions

On the wing surface, the contravariant velocity component V has to vanish: $V = 0$. Along the prescribed wake surface, which coincides with a grid surface (in the present study, the branch cut of the applied C-grid), the vorticity transport equation is fulfilled and no flux across this line is allowed, which yields

$$\Gamma_\tau + \langle U \rangle \Gamma_\xi = 0 \quad . \tag{31}$$

Here, Γ denotes the potential jump across the wake cut and $\langle U \rangle$ is the mean value of U between upper and lower surfaces of the wake. At the trailing edge, the condition of equal pressure values for upper (u) and lower (ℓ) trailing edge grid points is applied (Kutta condition).

$$\left[2\Phi_t + q^2 - 1\right]_\ell^u = 0 \quad . \tag{32}$$

In the far field, the flow is modelled by a potential vortex whose strength is determined by the current potential jump Γ across the downstream end of the wake cut.

3.3 Entropy Correction in the Full Potential Algorithm

The restriction of potential theory to cases with only moderate shocks can be alleviated by modelling the effects of entropy jump ΔS across a shock. For normal shocks,

$$\frac{\Delta S}{C_V} = \ell n\left(\frac{2\gamma M_n^2 - (\gamma-1)}{\gamma+1}\right) - \gamma\ell n\left(\frac{(\gamma+1)M_n^2}{2 + (\gamma-1)M_n^2}\right) \tag{33}$$

with M_n as the Mach number just upstream of the normal shock. The nonisentropic relation between pressure and density reads

$$\frac{\bar{p}}{p_\infty} = \left(\frac{\bar{\rho}}{\rho_\infty}\right)^\gamma e^{\Delta S/C_V} \quad , \tag{34}$$

where bars denote nonisentropic values.

Using (34) instead of (15) in the momentum equation yields a modified Bernoulli equation:

THIS DOCUMENT PROVIDED BY THE ABBOTT AEROSPACE
TECHNICAL LIBRARY
ABBOTTAEROSPACE.COM

$$\frac{\bar{\rho}}{\rho_\infty} = \Sigma\left[e^{\frac{\Delta S}{\gamma C_V}} - \frac{\gamma-1}{2} M_\infty^2 (2\Phi_t + q^2 - 1)\right]^{\frac{1}{\gamma-1}} \quad (35)$$

$$\frac{\bar{\rho}}{\rho_\infty} \approx \Sigma \cdot \frac{\rho}{\rho_\infty} \quad , \quad (36)$$

$$\text{with} \quad \Sigma := e^{-\Delta S/((\gamma-1)C_V)} \quad .$$

Using this relation in the continuity equation yields

$$\left(\frac{\rho}{J}\right)_\tau + \left(\rho\frac{U}{J}\right)_\xi + \left(\rho\frac{V}{J}\right)_\eta + \left(\rho\frac{W}{J}\right)_\zeta - \\ - \frac{\rho}{J(\gamma-1)C_V}\frac{d}{dt}(\Delta S) = 0 \quad . \quad (37)$$

As the total time derivative of entropy vanishes everywhere except for at shocks, the equation remains unchanged except at shock points, where ρ has to be replaced by $\bar{\rho}$ in the potential algorithm.

In the general case of different entropy jumps on the upper and lower wing surface, caused by different shock strengths, the Kutta condition also has to be modified. A nonisentropic Kutta condition then reads

$$\left[\Sigma\left(1 - \frac{\gamma-1}{2} M_\infty^2 (2\Phi_t + q^2 - 1)\right)\right]_\ell^u = 0 \quad . \quad (38)$$

In the special case of steady flow this yields

$$q_u - q_\ell = \frac{1-\sigma}{q_u + q_\ell}\left(\frac{2-(\gamma-1)M_\infty^2}{(\gamma-1)M_\infty^2} - q_\ell^2\right) \quad , \quad (39)$$

$$\text{with} \quad \sigma := (\Sigma_\ell / \Sigma_u)^{\frac{\gamma-1}{\gamma}} \quad . \quad (40)$$

If the shocks on the upper and lower side are equal or of negligible strength (isentropic flow), $\sigma = 1$ and $q_u = q_\ell$. The shock strengths are different for a lifting wing flow, thus $\Delta S_u > \Delta S_\ell$, which yields $\sigma > 1$ and thus $q_u < q_\ell$. **Fig. 1** sketches these two cases. The flow angle off the trailing edge depends on the different entropy increases. The second case shows a decambering effect (and thus a lift reduction) in comparison to the case with isentropic or equal shock condition.

Precise implementation of these entropy corrections demands that both the shock speed and the shock orientation be taken into account to obtain the correct value of M_n, and that ΔS is convected downstream with the actual flow velocity to obtain the correct value of σ at the trailing edge. This is complicated for 3D flows with geometrically complex shock surfaces. Therefore, the entropy correction was only implemented for 2D cases.

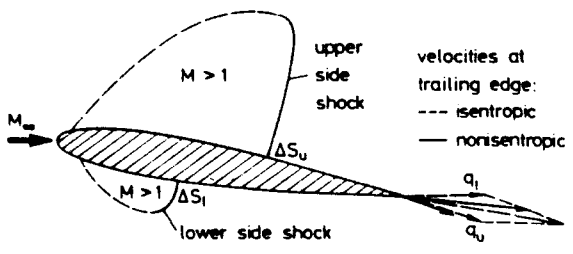


Fig. 1. Influence of entropy correction at the trailing edge

4. THE TIME LINEARIZED POTENTIAL METHOD

In industrial flutter calculations, it is often still convenient to use unsteady airloads from harmonic wing oscillations of small amplitudes. Thus, the unsteady flow may be treated as a superposition of a mean flow and a small unsteady harmonic perturbation flow, applying the following approach for the velocity potential:

$$\Phi(x, y, z, \tau) = \Phi^0(x, y, z) + \mathrm{Re}\left(\Phi^1(x, y, z)e^{i\omega^*\tau}\right) \quad (41)$$

$$\text{with} \quad |\Phi^0| >> |\Phi^1| >> \text{higher harmonics.} \quad (42)$$

Neglecting contributions of higher order in the perturbation values, the flow problem is split into a steady and an unsteady part. The former may be solved by steady nonlinear flow solvers, the latter is governed by a time linearized unsteady potential equation for the unsteady complex valued potential function Φ^1, which reads for the TSD potential:

$$\left(1 - K\Phi_{\bar{x}}^0\right)\Phi_{\bar{x}\bar{x}}^1 + \Phi_{\bar{y}\bar{y}}^1 + \Phi_{\bar{z}\bar{z}}^1 - \\ - \left(2i\varepsilon + K\Phi_{\bar{x}\bar{x}}^0\right)\Phi_{\bar{x}}^1 + \omega^*\varepsilon\Phi^1 = 0 \quad (43)$$

$$\text{with} \quad K = \frac{(\gamma+1)M_\infty^2}{\beta^2} \quad , \quad \varepsilon = \frac{\omega^* M_\infty^2}{\beta^2} \quad , \quad (44)$$

$\beta^2 = (1 - M_\infty^2)$ and $\bar{x} = x$, $\bar{y} = \beta y$, $\bar{z} = \beta z$.

Boundary conditions are to be fulfilled at the wing surface, as well as for the potential jump across the wake surface downstream of the trailing edge. Both surfaces are projected onto the $z = 0$ plane, which is compatible with the TSD approach. The boundary conditions read:

$$\Phi_z^1 = h_{1x} + i\omega^* h_1 \quad \text{(at wing)}, \quad h_1 = \text{amplitude} \\ \left[\Phi_x^1\right] + i\omega^*\left[\Phi^1\right] = 0 \quad \text{(across the wake)} \quad . \quad (45)$$

Equation (43) is linear but coupled to the mean flow Φ^0 by the spacewise varying coefficients, which may be strongly nonuniform, especially for flows with embedded supersonic regions and shocks. The coefficient of the first term in equation (43) changes sign when mean flow conditions change from subsonic to supersonic, yielding a mixed elliptic/hyperbolic character. By introducing a reduced potential function φ

$$\varphi = \Phi^1 \cdot e^{-i\varepsilon x} \quad , \quad (46)$$

equation (43) is transformed into a nonhomogeneous Helmholtz equation:

$$L(\varphi) = \varphi_{\bar{x}\bar{x}} + \varphi_{\bar{y}\bar{y}} + \varphi_{\bar{z}\bar{z}} + \lambda^2\varphi = S \quad (47)$$

$$\text{with} \quad S = \sigma_x + i\varepsilon\sigma \\ \lambda = \omega^* M_\infty / \beta^2 \quad (48) \\ \sigma = K\Phi_x^0(\varphi_x + i\varepsilon\varphi) \quad .$$

The magnitude of the right-hand side S is determined mainly by $K\Phi_x^0 \approx \Phi_x^0/\Phi_x^{0*}$, i.e. the deviation of the mean disturbance velocity from the corresponding critical value and thus the size of local Mach numbers of the mean flow.

Equation (47) shows a correspondence between unsteady linearized transonic flow problems and acoustic wave propagation in a nonhomogeneous moving fluid, which was investigated in detail in Ref. [10]. The pure Helm-

THIS DOCUMENT PROVIDED BY THE ABBOTT AEROSPACE
TECHNICAL LIBRARY
ABBOTTAEROSPACE.COM

holtz operator L describes propagation of disturbances in a compressible uniform subsonic flow with velocity u_∞, while the right-hand side S accounts for nonuniform compressibility effects introduced by the transonic mean flow. While disturbance energy propagates on rectilinear *rays in uniform flow*, the ray paths in a highly nonuniform transonic flow field show a strong curvature, deviation, and focusing effects, see **Fig. 2**. The time linearized flow problem is solved by a code called PTRAN3, which applies a combined Integral Equation/Finite Difference method for the solution of (43) and (47), respectively. Details are described in Refs. [11] and [12].

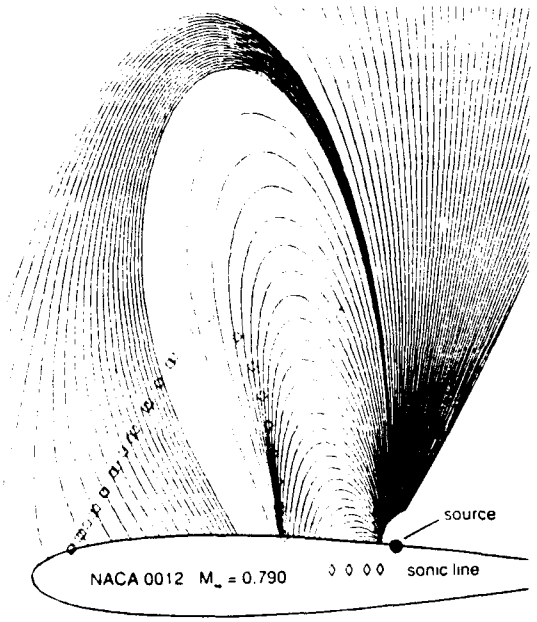


Fig. 2. Acoustic rays in a transonic flow field

5. PRESENTATION AND DISCUSSION OF 2D RESULTS

5.1 Grid Generation

The presented results were calculated on a boundary fitted coordinate system, obtained by a method presented in Ref. [13], which is an elliptic grid generation code with the ability to control the line spacing and intersection angles of the grid at physical boundaries (here the wing and wake surface) and at the far field boundary. C-type grids were chosen because they offer the possibility of clustering mesh points towards the branch cut in order to guarantee a better resolution of the unsteady wake. In the Full Potential code, the branch cut equals the wake location. The branch cut location is prescribed as a boundary condition of the grid generation code. In order to facilitate the implementation of wall boundary conditions, orthogonality of the grid lines was introduced on the airfoil surface, on the far field boundary, and also on the branch cut, thus avoiding strong mesh distortions. Additionally, the line spacing between the first and second grid lines on the airfoil and the branch cut were prescribed to be 0.5 % chord length everywhere. Since the present study only deals with rigid body oscillations, unsteady calculations were done on grids, keeping fixed to the moving airfoils.

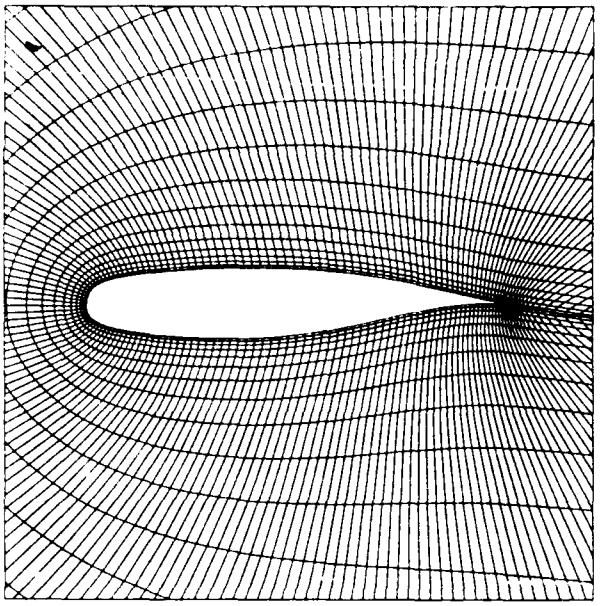


Fig. 3. Grid for NLR7301 calculations

Both Euler and Full Potential calculations used identical grids. The NACA0012 grid had 205 x 42 grid points, while the NLR7301 grid had 225 x 32. **Fig. 3** shows the inner region of the NLR grid. Far field boundaries were 10 chord lengths away from the airfoil.

5.2 NACA0012 Results

The NACA0012 airfoil was investigated at flow conditions of an AGARD standard test case with Mach number $M_\infty = 0.755$ and mean incidence $\alpha = 0.02°$ undergoing pitching oscillations about the quarter chord axis with 2.51° amplitude. **Fig. 4** shows calculated unsteady pressure distributions at three different reduced frequencies $\omega^* = 0.1$, 0.5 and 1.0. The agreement between Euler and Full Potential results is good. There are only small discrepancies in the shock region. Generally, the Euler results need only one grid spacing for shock resolution, due to the upwinding procedure, while Full Potential needs two grids. The special shock dynamics at higher frequencies should be mentioned: the shock profiles get steeper during upstream motion and stay flat during downstream motion of the shock. At reduced frequency $\omega^* = 1.0$, a pronounced shock is formed only at the farthest downstream position just before it starts moving upstream again. These details are captured by Euler and Full Potential models with good agreement. The strong nonlinearity of the creation and disappearance of shock waves during one oscillation cycle is also reflected in the unsteady lift and moment coefficients in **Fig. 5**. Deviation of these curves from elliptic shape indicate nonlinearities. It is well-known that in cases of small amplitudes unsteady transonic airloads approach linear behavior with increasing frequency. In the present case, amplitude is big and nonlinear behavior appears for all five reduced frequencies, more pronounced for higher frequencies in the lift coefficient while very strong for low frequencies in the moment coefficient. Moment coefficients seem to be much more sensitive, because they are much more influenced by shock motions than lift.

THIS DOCUMENT PROVIDED BY THE ABBOTT AEROSPACE
TECHNICAL LIBRARY
ABBOTTAEROSPACE.COM

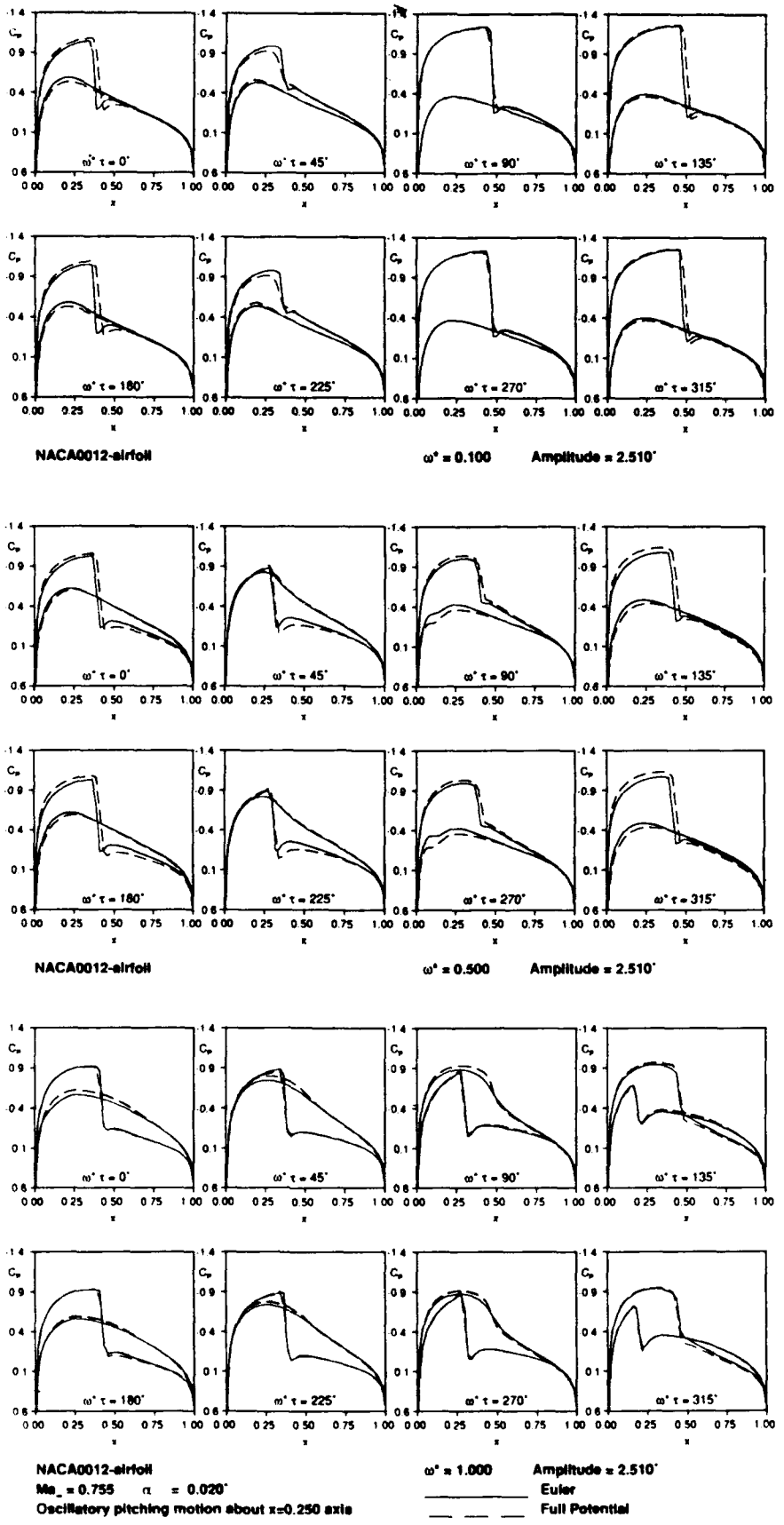


Fig. 4. Frequency dependence of unsteady pressure at the NACA0012

THIS DOCUMENT PROVIDED BY THE ABBOTT AEROSPACE
TECHNICAL LIBRARY
ABBOTTAEROSPACE.COM

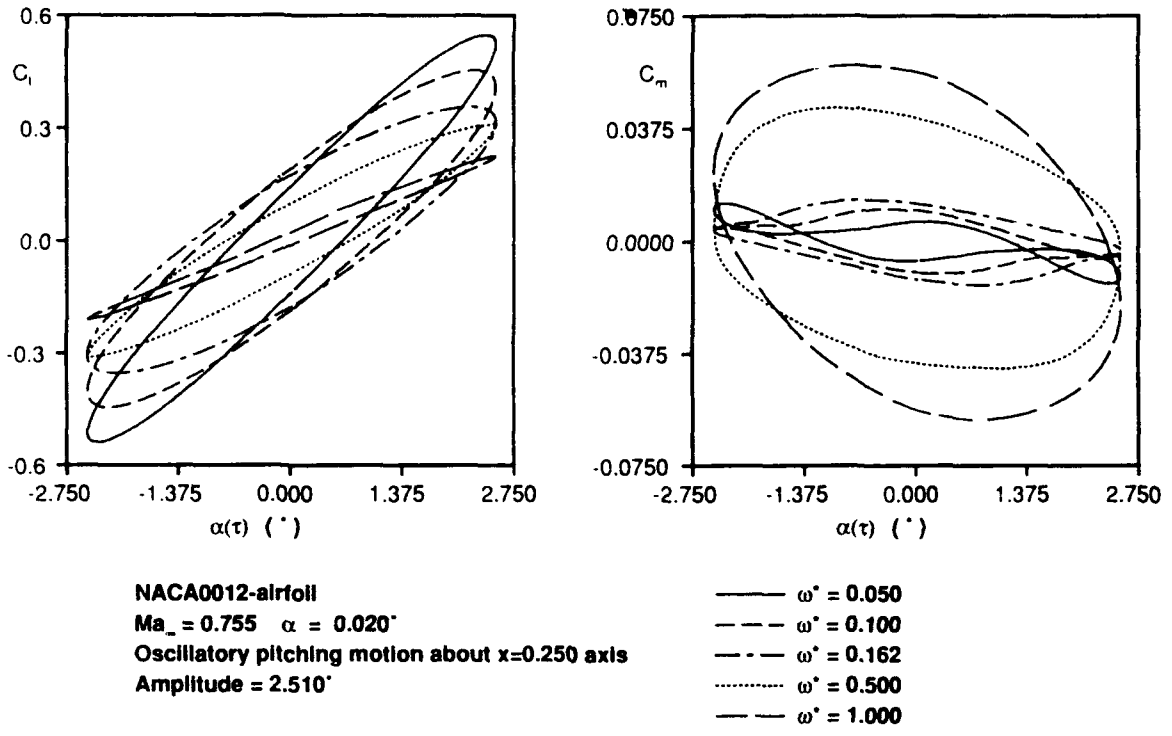


Fig. 5. Frequency dependence of unsteady lift and moment at the NACA0012

Comparisons between Euler and Full Potential results for lift and moment coefficients show more pronounced discrepancies than the unsteady pressure distributions. **Fig. 6** shows the time histories of calculations, starting with the steady flow solution until periodic behavior is achieved. It is apparent that high frequency Potential calculations need more cycles than Euler before reaching periodicity. The direct comparison in **Fig. 7** shows generally bigger lift and moment amplitudes and a bigger phase shift (reflected in the width of the loops) predicted by Potential theory. Similar tendencies have also been observed in comparisons between Euler and TSD results (see Ref. [14]).

5.3 NLR7301 Results

While strong linearities for the oscillation of the conventional NACA0012 airfoil were achieved by large amplitudes, the supercritical NLR7301 airfoil may be expected to show nonlinear behavior due to its sensitivity to small disturbances of shape and therefore also at moderate amplitudes. The nominal design condition was $M_\infty = 0.721$ and $\alpha = -0.19°$, and pitching oscillations aobut the 40 % chord axis were investigated. **Fig. 8** shows unsteady pressure distributions for three different reduced frequencies and a fixed amplitude, while the amplitudes are changed in **Fig. 9**. The agreement between Euler and Full Potential results is good on the lower surface and in the rear portion of the airfoil.

On the upper surface, the agreement is sometimes not satisfactory upstream of the main shock. Like for the NACA0012, the shock resolution of the Euler method is better, and especially weak and downstream moving shocks are smoothed by Potential theory. In general, the flow details are in agreement, note especially the double-shock system at the high frequencies $\omega^* = 0.500$ and 1.00 for phase angle $\omega^*\tau = 315°$. The disagreement is growing with both increasing frequency and increasing amplitude. For the reduced frequency $\omega^* = 1.00$, no convergent behavior of the moment coefficient was achieved by the Full Potential calculation. **Fig. 10** shows the corresponding unsteady lift and moment coefficient curves. Like for the NACA0012, Potential theory predicts higher amplitudes and phase shifts.

One reason for the discrepancies appearing between Euler and Potential results may be the insufficient model of entropy correction. The present entropy model in the Full Potential Code only treats a single normal shock. Furthermore, modeling the vorticity production at shocks could improve the agreement of results. The difference between Euler and Potential Theory in treating the wake, i.e. fixing the path of vorticity to the branch cut, may be another source of discrepancy, especially for the highly sensitive NLR airfoil.

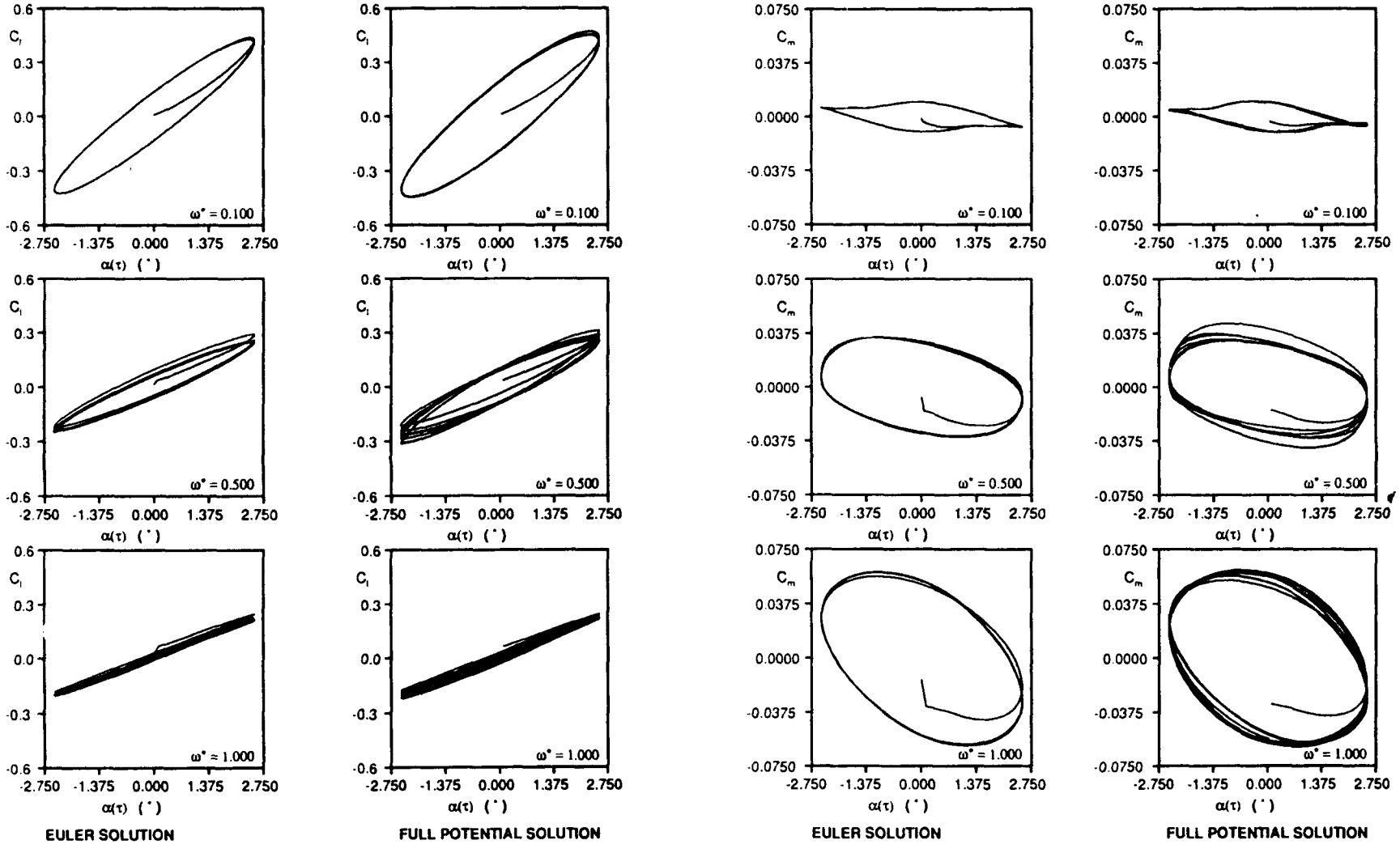


Fig. 6. Time histories of calculated unsteady lift and moment coefficients

THIS DOCUMENT PROVIDED BY THE ABBOTT AEROSPACE TECHNICAL LIBRARY ABBOTTAEROSPACE.COM

THIS DOCUMENT PROVIDED BY THE · ABBOTT AEROSPACE
TECHNICAL LIBRARY
ABBOTTAEROSPACE.COM

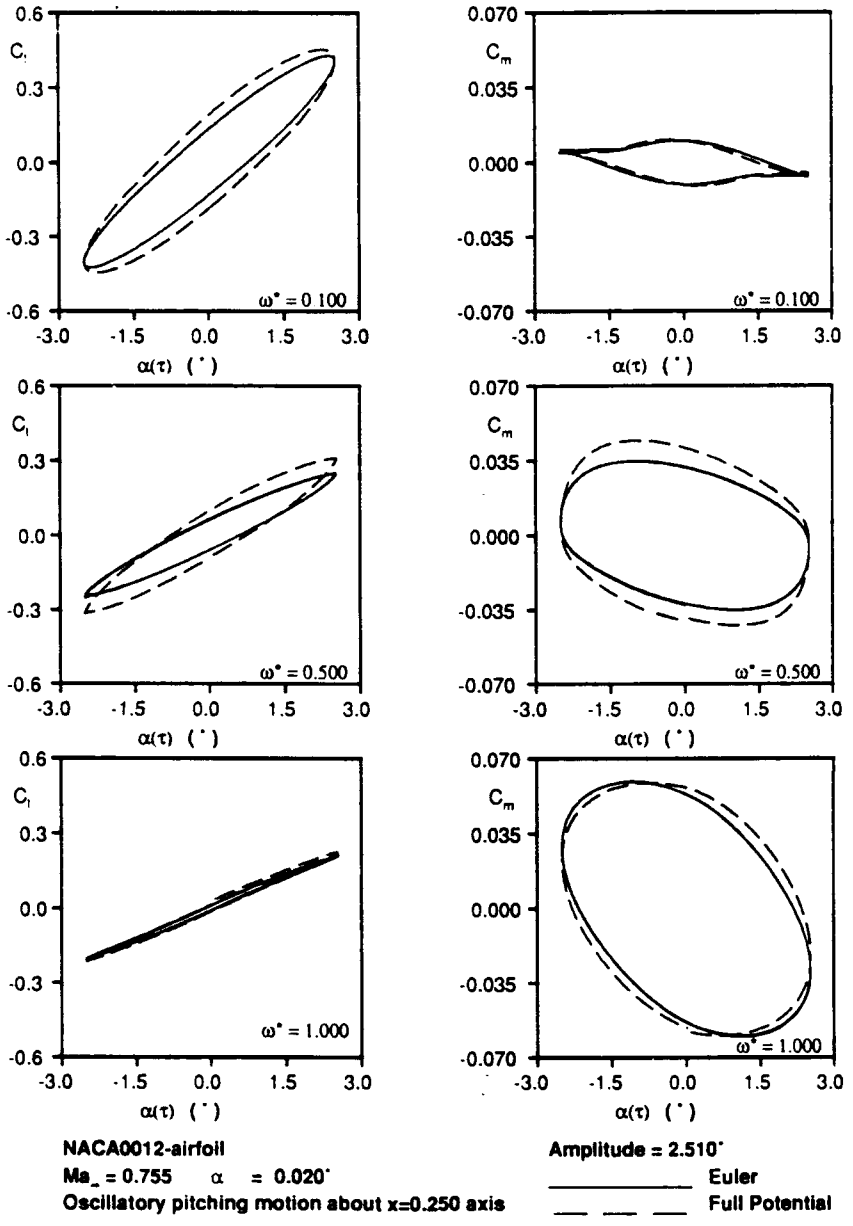


Fig. 7. Comparison of calculated unsteady lift and moment coefficients

THIS DOCUMENT PROVIDED BY THE ABBOTT AEROSPACE
TECHNICAL LIBRARY
ABBOTTAEROSPACE.COM

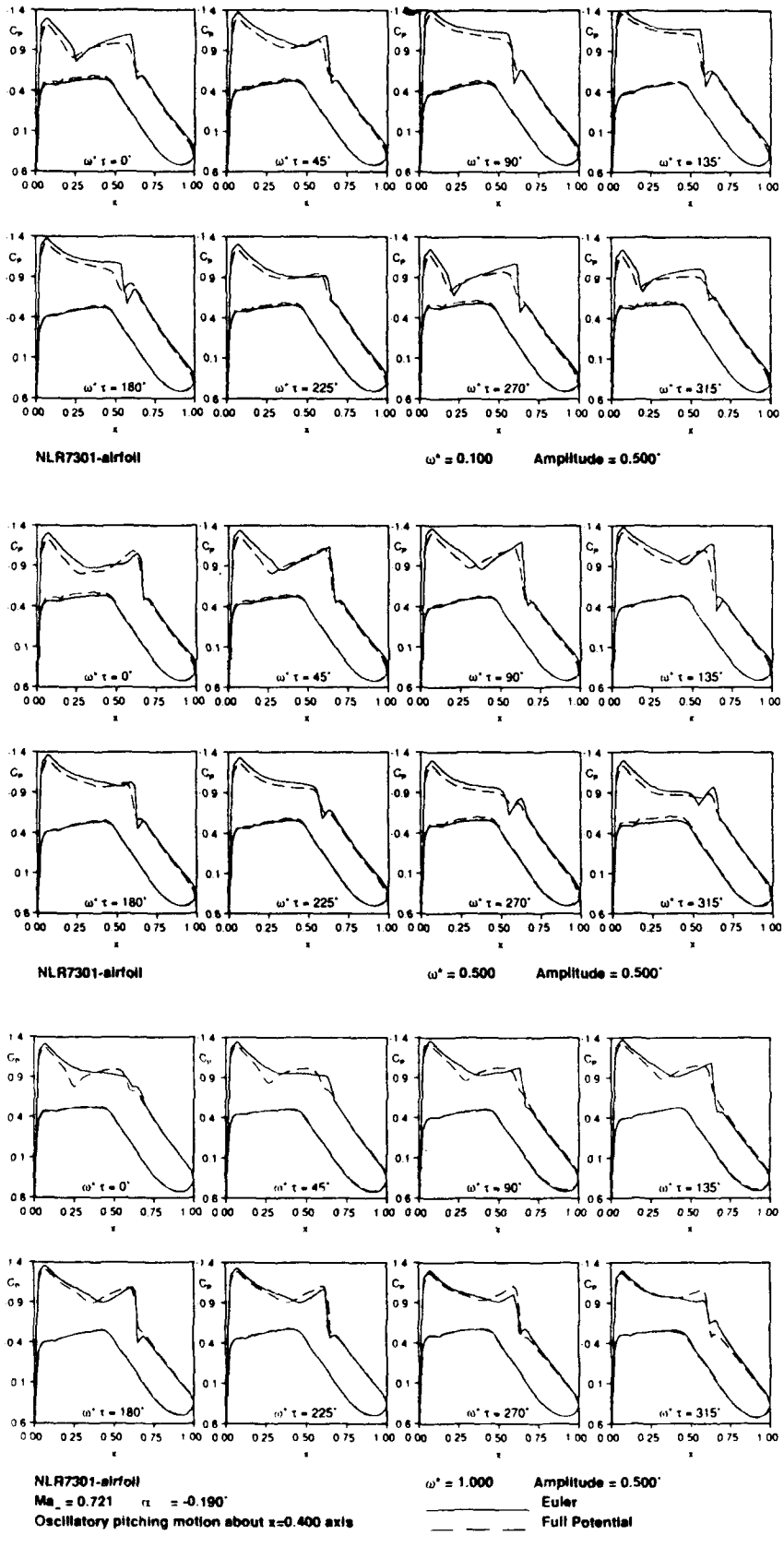


Fig. 8. Frequency dependence of unsteady pressure at the NLR7301

THIS DOCUMENT PROVIDED BY THE ABBOTT AEROSPACE
TECHNICAL LIBRARY
ABBOTTAEROSPACE.COM

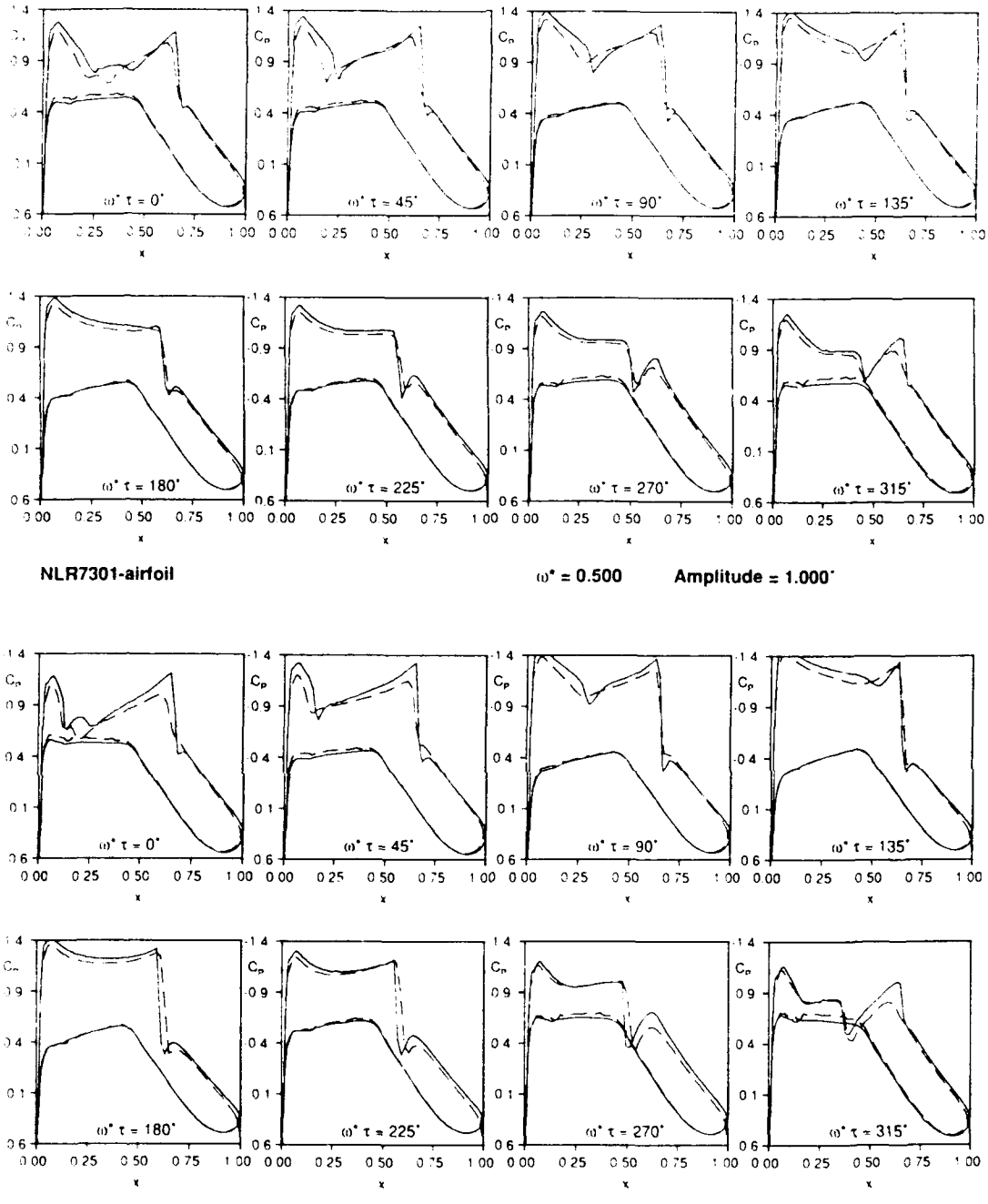


Fig. 9. Amplitude dependence of unsteady pressure at the NLR7301

THIS DOCUMENT PROVIDED BY THE ABBOTT AEROSPACE
TECHNICAL LIBRARY
ABBOTTAEROSPACE.COM

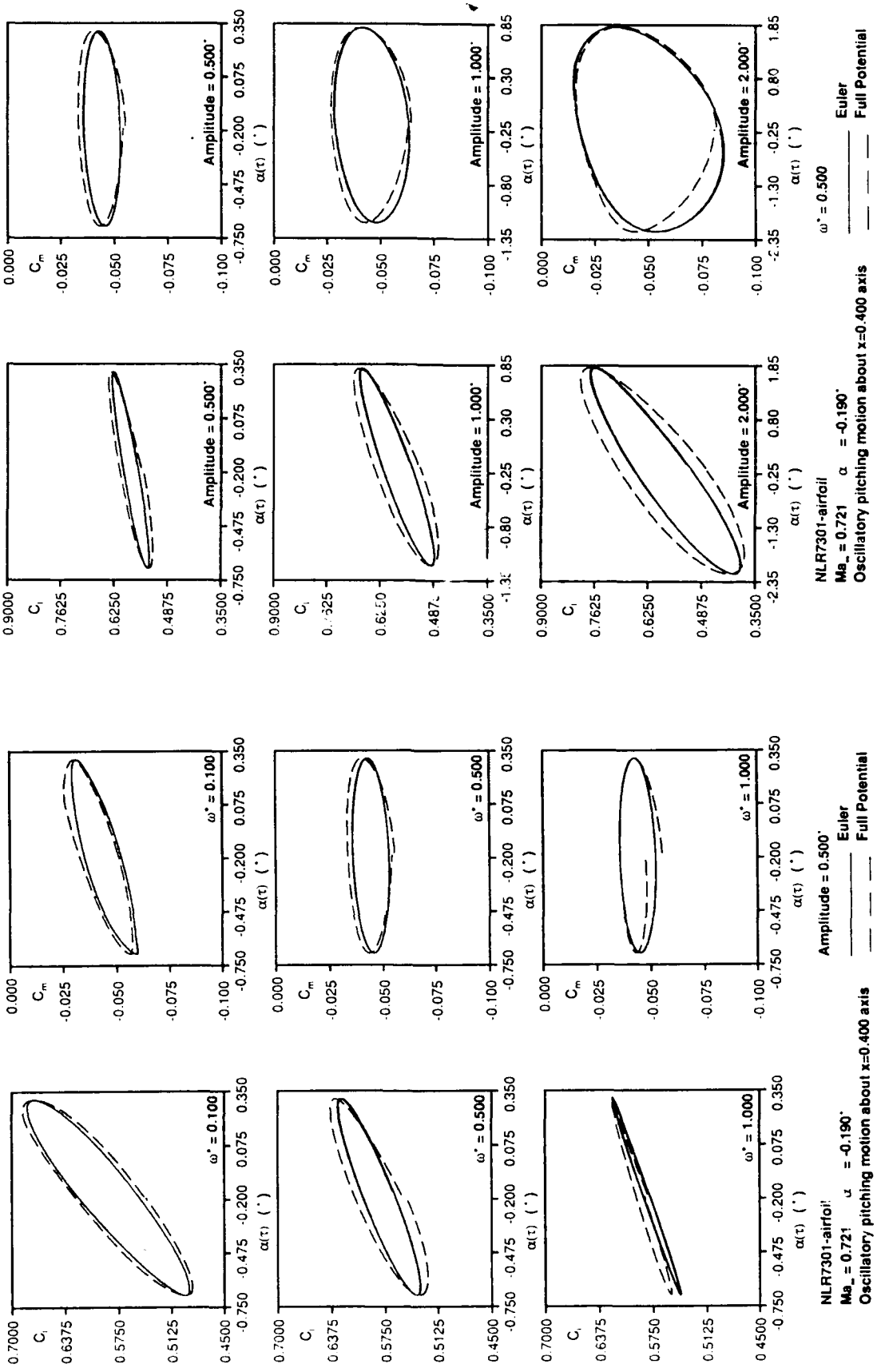


Fig. 10. Comparison of calculated unsteady lift and moment coefficients

THIS DOCUMENT PROVIDED BY THE ABBOTT AEROSPACE
TECHNICAL LIBRARY
ABBOTTAEROSPACE.COM

6. PRESENTATION AND DISCUSSION OF 3D RESULTS

Unsteady transonic flow calculations for oscillating wings were carried out with the 3D Full Potential code and the 3D time linearized method. The harmonic perturbation approach of the time linear code makes comparisons meaningful only for small amplitude oscillations, where nonlinear effects may be slight and only small amplitude harmonic shock oscillations appear.

Full Potential calculations were done on a CH-type grid, with 129 x 28 x 30 points in ξ-, η- and ζ-direction, 97 x 20 points being on the wing surface. **Fig. 11** shows the grid on the wing and wake surface and the symmetry plane. The calculated mean flow field was used as an input for the time linearized method, interpolating it to the sheared Cartesian grid of the PTRAN3 code, which is comprised of approximately 25000 grid points. **Fig. 12** shows real and imaginary parts of the first component of unsteady pressure distributions for a 30° swept wing with symmetrical NACA0012 airfoil sections oscillating in pitch about the 60 % axis with 1° and 0.25° amplitude about 0° incidence position, both obtained by the 3D Full Potential code. The corresponding time linear results are in good agreement with both nonlinear calculations. These are only slightly different from one another in the region that is traversed by the shock. Note that values at the upper and lower wing surface have just the opposite sign and that both are plotted. For this example, time linear theory is a good approximation, because higher harmonic components are not significant.

This becomes quite different if the frequency value is increased by a factor of five. **Fig. 13** shows the unsteady time dependent pressure distributions on the upper wing surface from the Full Potential code. Here, the appearing shock motions are strongly nonlinear, and significant higher harmonic components of pressure appear. Note the different kinds of shock motions at different span positions of the wing. A shock remains at the outboard position during the whole oscillation cycle. In the mid-span region, shocks disappear during part of the cycle. In the inner parts (near the symmetry plane) of the wing, shocks are moving in upstream direction and vanishing near the leading edge in the form of a pressure wave and are simultaneously built up again in the rear part of the wing near the leading edge. This indicates the appearance of the three shock motion types A, B and C of Tijdeman (see Ref. [15]). In such cases, of course, linear theories can not be applied, although wing geometry is simple (not supercritical) and amplitude is moderate.

Finally, **Fig. 14** shows results for the supercritical LANN wing for the AGARD test case CT 5. The steady flow field shows two shocks at the inboard part of the wing, and there is one shock at the outer span positions. The steady input for the time linearized code was provided from the Full Potential code. Comparisons with experimental results from Ref. [16] show only a general agreement. The double shock system at the inner part of the wing is reflected in the unsteady first harmonic pressures by two pressure pulses. Most of the discrepancies between theory and experiment are certainly due to viscous effects and are already apparent in the steady flow.

7. CONCLUSION

Comparisons of different codes for unsteady transonic flow calculations about oscillating wings and airfoils have been carried out. All codes, i.e. the explicit 2D Euler, implicit 2D and 3D Full Potential (including Newton Iteration) and 3D time linearized TSD, are time accurate.

The 2D Euler and Full Potential calculations used identical moving boundary fitted grids. Thus, discrepancies could only be due to the different physical modelling, i.e. entropy and vorticity. Agreements are partly very good, even for cases of pronounced nonlinear effects, such as severe shock motions. Appearing discrepancies, especially in lift and moment coefficients, are caused by insufficient modelling of entropy and vorticity in the Full Potential code. Here, improvements seem to be necessary in order to make the Full Potential code a reliable tool for strong nonlinear flow calculations.

The 3D Full Potential and time linearized calculations by definition had identical mean flow fields. Comparison of their unsteady results shows that the time linearized approach is justified only for very low amplitudes, even if wing geometry is relatively simple.

Much more detailed and systematic work in unsteady transonic inviscid code validation is necessary (including time linearized, nonlinear TSD, FP and Euler methods) before the ranges of applicability of different methods become sure, especially for applications in flutter investigation.

8. REFERENCES

[1] Voß, R. and Carstens, V., "Computation of Unsteady Transonic Flows Around Oscillating Airfoils Using Full Potential and Euler Equations", in "Proc. of the European Forum on Aeroelasticity and Structural Dynamics", DGLR, April 1989, Report 89-01, pp. 51-64.

[2] van Leer, B., "Flux Vector Splitting for the Euler Equations", ICASE Report 82-30, 1982.

[3] Harten, A., Lax, P.D. and van Leer, B., "On Upstream Differencing and Godunov-Type Schemes for Hyperbolic Conservation Laws", SIAM Review, 25, 1983, pp. 35-61.

[4] Roe, P.L., "Approximate Riemann Solvers, Parameter Vectors and Difference Schemes", J. Comput. Phys., 43, 1981, pp. 357-372.

[5] Wegner, W., "Riemannlösung der gasdynamischen Grundgleichungen", Dissertation, Tech. Univ. München, 1991.

[6] van Leer, B., "Towards the Ultimate Conservative Difference Scheme V. A Second Order Sequel to Godunov's Method", J. Comput. Phys., 32, 1979, pp. 101-136.

[7] Anderson, W.K., Thomas, J.L. and van Leer, B., "A Comparison of Finite Volume Flux Vector Splittings for the Euler Equations", AIAA Paper 85-0122, 1985.

[8] Shankar, V., Ide, H., Gorski, J. and Osher, S., "A Fast Time-Accurate Unsteady Full Potential Scheme", AIAA Journal, 25, 2, 1987, pp. 230-238.

THIS DOCUMENT PROVIDED BY THE ABBOTT AEROSPACE
TECHNICAL LIBRARY
ABBOTTAEROSPACE.COM

[9] Hafez, M.M., Osher, S. and Whitlow, Jr., W., "Improved Finite Difference Schemes for Transonic Potential Calculations", AIAA Paper 84-0092, Reno, Nevada, USA, 1984.

[10] Voß, R., "Über die Ausbreitung akustischer Störungen in transsonischen Strömungsfeldern von Tragflügeln", Dissertation, Univ. of Göttingen, 1988, DFVLR-FB 88-13.

[11] Voß, R., "Calculation of 3D Unsteady Transonic Potential Flows by a Field Panel Method", in "Proc. of the 2nd Internat'l Symposium on Aeroelasticity and Structural Dynamics", DGLR, 1985, Report 85-02.

[12] Voß, R., "Calculation of Unsteady Transonic Flow About Oscillating Wings by a Field Panel Method", in "Notes on Numerical Fluid Mechanics", 21, Ballmann et al, Eds., Vieweg, 1987, pp. 232-242.

[13] Carstens, V., "Two-Dimensional Elliptic Grid Generation for Airfoils and Cascades", DFVLR-FB 88-52, 1988.

[14] Anderson, W.K. and Batina, J.T., "Accurate Solutions, Parameters Studies, and Comparisons for the Euler and Potential Flow Equations", Validation of Computational Fluid Dynamics, AGARD CP-437, 1, 1988, Paper No. 14, pp. 14-1 - 14-16.

[15] Tijdeman, H., "Investigations of the Transonic Flow Around Oscillating Airfoils", NLR TR 77090, 1977.

[16] Zwaan, R.J., "LANN Wing, Pitching Oscillation, Compendium of Unsteady Aerodynamic Measurements", AGARD Report No. 702, Addendum No. 1, 1985.

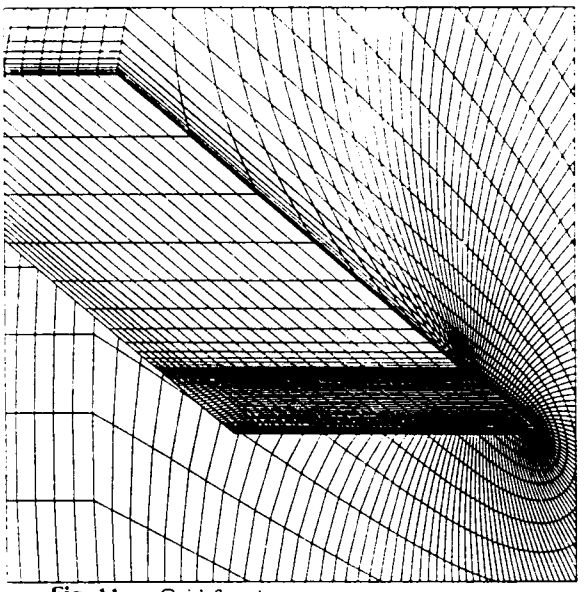


Fig. 11. Grid for the swept wing calculations

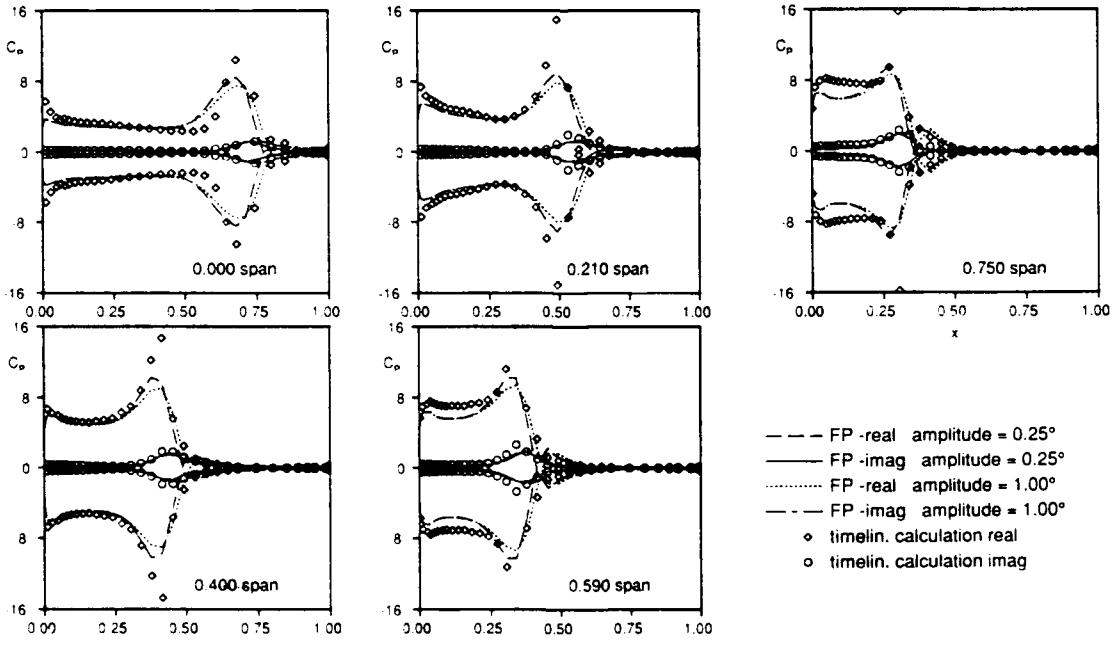
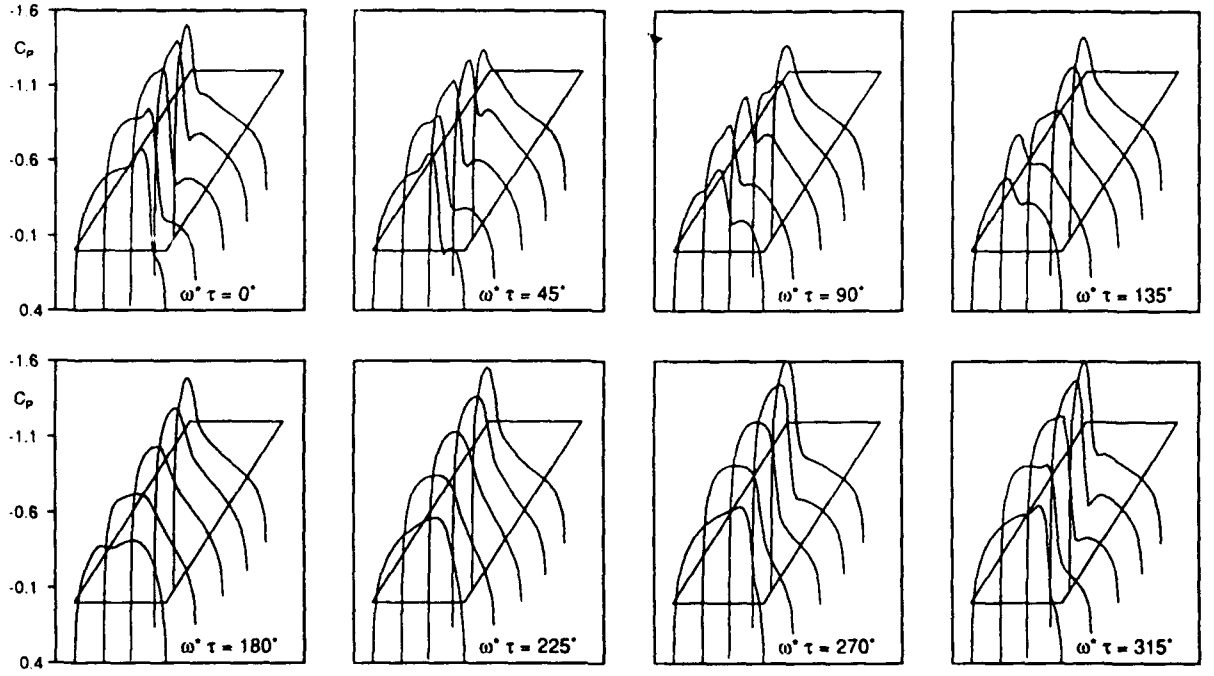


Fig. 12. Unsteady first harmonic of pressure distributions on the NACA0012 swept wing

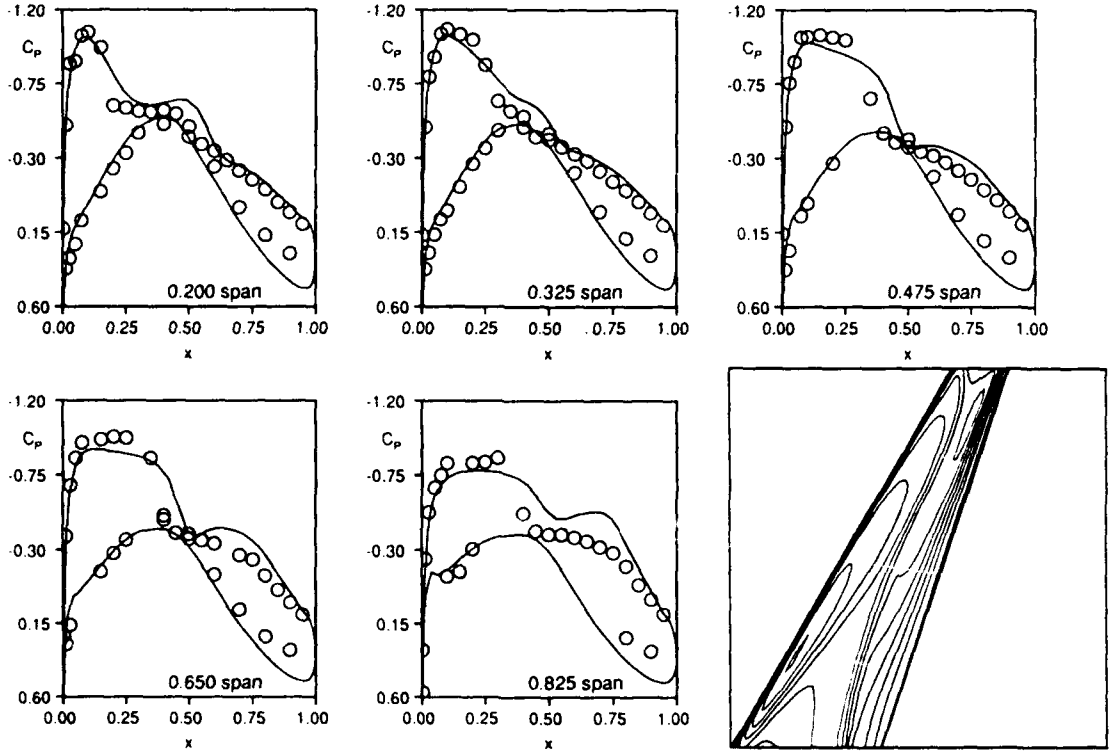
NACA0012 - 30° swept wing $Ma_\infty = 0.850$ $\alpha = 0.$
pitching oscillation about 0.600 root chord $\omega = 0.100$

THIS DOCUMENT PROVIDED BY THE ABBOTT AEROSPACE
TECHNICAL LIBRARY
ABBOTTAEROSPACE.COM



NACA0012 - 30° - swept wing AR=2.0 **ω* = 0.500** **Amplitude = 1.000°**
Ma_∞ = 0.850 **α = 0.000°**
Oscillatory pitching motion about x=0.600 axis **Unsteady Full Potential Calculation**

Fig. 13. Unsteady nonlinear pressure distribution at the NACA0012 swept wing



steady LANN WING **Ma_∞ = 0.820** **α = 0.600°**
Isobars on upper wing surface Δc_p = 0.100

Experiment
Full Potential calculation

THIS DOCUMENT PROVIDED BY THE ABBOTT AEROSPACE
TECHNICAL LIBRARY
ABBOTTAEROSPACE.COM

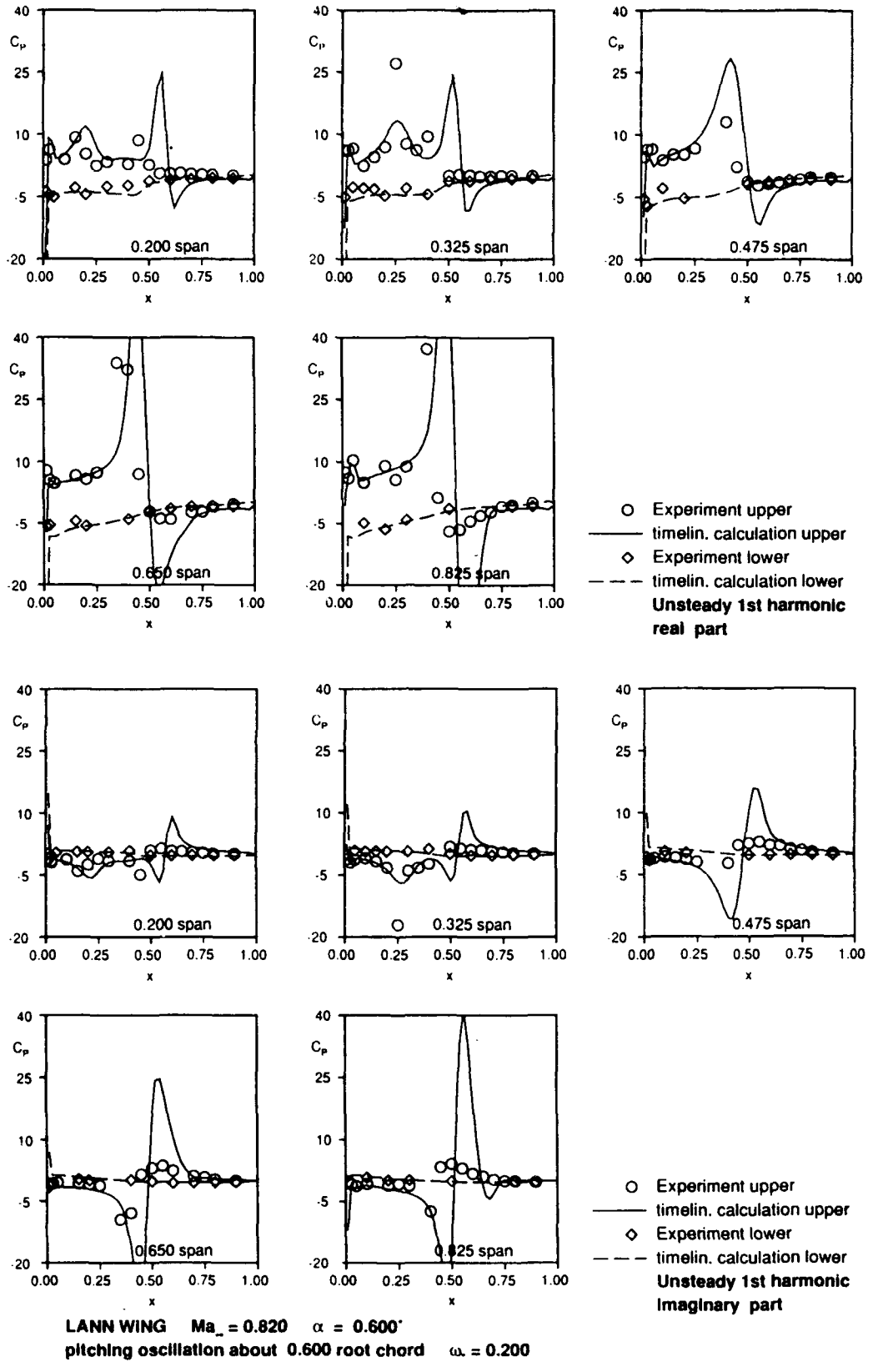


Fig. 14. Unsteady first harmonics of pressure distribution at the LANN wing

THIS DOCUMENT PROVIDED BY THE ABBOTT AEROSPACE
TECHNICAL LIBRARY
ABBOTTAEROSPACE.COM

AD-P007 801

COMPUTATION OF THE UNSTEADY TRANSONIC 2D CASCADE FLOW BY AN EULER ALGORITHM WITH INTERACTIVE GRID GENERATION

Dr. rer.nat. V. Carstens
Deutsche Forschungsanstalt für Luft- und Raumfahrt (DLR)
Institute of Aeroelasticity
Bunsenstrasse 10
3400 Göttingen
Germany

92-16039

SUMMARY

This paper presents the numerical results of a code for computing the unsteady transonic flow in a 2D cascade of harmonically oscillating blades. The calculation of the flow field is based on an Euler code using flux vector splitting. After a description of the basic equations and the special numerical techniques applied in the code, results are presented for the first harmonics of pressure, lift and moment coefficients.

For the present investigations, two basic oscillation modes were chosen: tuned modes where all blades perform oscillations with the same frequency, same amplitude and a constant interblade phase angle, and mistuned modes, where all blades are oscillating with the same amplitude, but with varying frequency from one blade to another. The computed results refer to two standard configurations given by the IUTAM "Workshop on Aeroelasticity in Turbomachine Cascades", one of which is a subsonic-transonic turbine cascade, and the other is a subsonic-transonic compressor cascade. In the case of tuned bending modes, the theoretical results are compared with the experimental data from the turbine standard configuration.

Special attention is directed to the occurrence of aerodynamic instability in the oscillating cascade. It can be shown that the interblade phase angles, at which the above-mentioned experimental test case shows unstable behavior, are generally well-reproduced by the computational results.

1. INTRODUCTION

The numerical prediction of unsteady aerodynamic lift and moment coefficients for oscillating cascades in the transonic regime is still an urgent problem. Although great progress has been made in the past and many codes, especially for two-dimensional flow, are now available, the reliability of these codes is still an existing problem. The reason for this uncertainty is the variety of factors hidden in the calculation of an unsteady transonic flow configuration.

Some of these factors are often interdependent, e.g. the choice of flow equations (full or linearized equations), the treatment of the time dependence, the capability of capturing shocks automatically (conservative or nonconservative methods), or the possibility of including viscous effects (inviscid or viscous flow calculation).

Through a literature survey it becomes evident that theoretical research has progressed steadily over the past three decades. Whitehead [1] studied the unsteady flow of an incompressible fluid through a cascade of vibrating flat plates, where the mean flow was deflected by the cascade. Atassi [2] also assumed incompressible flow and developed a model using conformal mapping, whereby arbitrary shape of the blades and steady loading can be admitted. Similar to Atassi's work, the author has contributed a publication based on the solution of integral equations [3].

Further progress has been made by taking into account compressibility effects. The simplest way to achieve this is to solve the acoustic approximation of the inviscid flow equations for the unsteady problem. Typical representations of this manner of treating the problem are the papers of Smith [4], who analyzed vibrating flat plate cascades in subsonic flow, and Verdon and Caspar [5], who developed a fairly comprehensive analysis for the case of unsteady subsonic flow in a vibrating cascade with mean flow deflection.

In the last years, increasing efforts were made to extend the flow calculations to the transonic regime. The methods used can roughly be divided into two types: methods which linearize the unsteady flow equations about the mean flow, assuming that the unsteadiness in the flow is small, and methods for solving the full equations. Linearized methods were presented, e.g. by Verdon and Caspar [6] (linearized Potential equation) and Hall and Crawley [7] (linearized Euler equations). Their advantage lies in the short computation time needed to calculate the unsteady flow, but undoubtedly their greatest disadvantage is that they are not able to correctly predict complicated shock structures and shock displacements. In order to check the validity of linearized codes and to obtain a better insight into the dynamics of unsteady transonic cascade flow, time-marching methods for solving the non-linearized Euler equations have been developed. The publications of Kau [8] and Gerolymos [9] should be mentioned as two examples of such. Kau investigated the unsteady flow through turbine as well as compressor cascades, while Gerolymos calculated the unsteady loads in a single compressor cascade where the blades were vibrating in so-called tuned and mistuned modes. A final mention should be made of the work of Rai [10], who computed the transonic flow through a complete rotor-stator configuration with a Navier-Stokes code.

The present Euler code, written in conservative form, makes use of flux vector splitting. This technique, in which the flux vectors are decomposed into positive and negative contributions such that the corresponding Jacobian matrices have either positive or negative eigenva-

THIS DOCUMENT PROVIDED BY THE ABBOTT AEROSPACE
TECHNICAL LIBRARY
ABBOTTAEROSPACE.COM

lues, more or less simulates the method of characteristics. Performing the spatial differences of the split flux vectors with backward and forward differences, respectively, the arising algorithm belongs to the class of upwind methods and has the advantage of being naturally dissipative. The special type of decomposition used in the present algorithm is van Leer splitting [11], the excellent shock capturing properties of which have already been elaborated in the paper of Anderson, Thomas and van Leer [12].

For the sake of simplicity, the present investigations are restricted to harmonic rigid body motions of the blades, i.e. to heaving and pitching oscillations. In order to show the different aerodynamic behavior of the cascade due to special selected modes of the blade row, two basic oscillation modes have been chosen: tuned modes where all blades perform oscillations with the same frequency, same amplitude and a constant interblade phase angle, and mistuned modes where the blades are oscillating with the same amplitude but varying frequency from one blade to another.

Computational results are presented for two standard configurations of the IUTAM "Workshop on Aeroelasticity in Turbomachine Cascades", namely a turbine cascade where experimental data are available for tuned bending modes and a compressor cascade designed solely for theoretical investigations.

2. EULER ALGORITHM

2.1 Flux Vector Splitting in Cartesian Coordinates

The two-dimensional Euler equations for an ideal gas expressed in Cartesian coordinates and conservative form are

$$\frac{\partial Q}{\partial t} + \frac{\partial F}{\partial x} + \frac{\partial G}{\partial y} = 0 \qquad (1)$$

where

$$Q = \rho \begin{bmatrix} 1 \\ u \\ v \\ E \end{bmatrix}, \; F = \rho \begin{bmatrix} u \\ u^2 + \frac{a^2}{\kappa} \\ u\,v \\ u\,H \end{bmatrix}, \; G = \rho \begin{bmatrix} v \\ u\,v \\ v^2 + \frac{a^2}{\kappa} \\ v\,H \end{bmatrix} \qquad (2)$$

with the specific total energy

$$E = \frac{a^2}{\kappa(\kappa - 1)} + \frac{1}{2}(u^2 + v^2) \qquad (3)$$

where

$$\kappa = \frac{c_p}{c_v} \quad \text{, ratio of specific heats}$$

and the specific total enthalpy

$$H = \frac{a^2}{\kappa - 1} + \frac{1}{2}(u^2 + v^2) \; . \qquad (4)$$

The dependent primitive variables ρ, u, v and a are the density, the Cartesian velocities, and the local speed of sound, respectively.

In a flux vector splitting algorithm, the flux vectors are decomposed into positive and negative contributions $F = F^+ + F^-$ and $G = G^+ + G^-$ such that the Jacobian matrices $\partial F^+/\partial Q$, $\partial G^+/\partial Q$ have only positive and $\partial F^-/\partial Q$, $\partial G^-/\partial Q$ have only negative eigenvalues. According to the artificial characteristic directions of signal transport, introduced by the split flux vectors, the calculation of the spatial derivatives of F^+, G^+ and F^-, G^- has to be performed with backward and forward difference operators, respectively. This upwind method yields a robust algorithm with excellent shock capturing properties.

In the splitting suggested by van Leer [11], $F^\pm$ and $G^\pm$ are given in terms of the local one-dimensional Mach numbers $M_x = u/a$ and $M_y = v/a$, respectively. The decomposition of F runs as follows:

Subsonic flow $|M_x| \le 1$

$$F^\pm = \begin{bmatrix} \pm\frac{\rho a}{4}(1 \pm M_x)^2 \\ \frac{a}{\kappa}[(\kappa - 1)M_x \pm 2]\,f_1^\pm \\ v\,f_1^\pm \\ \frac{\kappa^2}{2(\kappa^2 - 1)}\frac{(f_2^\pm)^2}{f_1^\pm} + \frac{v^2}{2}f_1^\pm \end{bmatrix} , \qquad (5)$$

Supersonic flow $|M_x| \ge 1$

$$F^+ = F \; , \; F^- = 0 \quad \text{for} \quad M_x \ge +1$$

$$F^+ = 0 \; , \; F^- = F \quad \text{for} \quad M_x \le -1 \; ,$$

and the decomposition of G is obtained by:

Subsonic flow $|M_y| \le 1$

$$G^\pm = \begin{bmatrix} \pm\frac{\rho a}{4}(1 \pm M_y)^2 \\ u\,g_1^\pm \\ \frac{a}{\kappa}[(\kappa - 1)M_y \pm 2]\,g_1^\pm \\ \frac{\kappa^2}{2(\kappa^2 - 1)}\frac{(g_3^\pm)^2}{g_1^\pm} + \frac{u^2}{2}g_1^\pm \end{bmatrix} , \qquad (6)$$

Supersonic flow $|M_y| \ge 1$

$$G^+ = G \; , \; G^- = 0 \quad \text{for} \quad M_y \ge +1$$

$$G^+ = 0 \; , \; G^- = G \quad \text{for} \quad M_y \le -1 \; .$$

2.2 Flux Vector Splitting in Boundary-Fitted Coordinates

Introducing a boundary-fitted moving coordinate system

$$\begin{array}{l} x = x(\xi, \eta, \tau) \\ y = y(\xi, \eta, \tau) \\ t = \tau \end{array} \quad \Leftrightarrow \quad \begin{array}{l} \xi = \xi(x, y, t) \\ \eta = \eta(x, y, t) \\ \tau = t \end{array} \; , \qquad (7)$$

the Euler equations are given in the new coordinate system in conservative form by

$$\frac{\partial \hat{Q}}{\partial \tau} + \frac{\partial \hat{F}}{\partial \xi} + \frac{\partial \hat{G}}{\partial \eta} = 0 \qquad (8)$$

with the transformed vectors

$$\begin{aligned} \hat{Q} &= J\,Q \\ \hat{F} &= (-y_\eta x_\tau + x_\eta y_\tau)\,Q + y_\eta F - x_\eta G \\ \hat{G} &= (-x_\xi y_\tau + y_\xi x_\tau)\,Q - y_\xi F + x_\xi G \; . \end{aligned} \qquad (9)$$

where it is assumed that the left-hand side of (7) is given. In (9) and in the following equations, the subscripts ξ, η

THIS DOCUMENT PROVIDED BY THE ABBOTT AEROSPACE
TECHNICAL LIBRARY
ABBOTTAEROSPACE.COM

and τ denote the derivatives of the physical coordinates with respect to the boundary-fitted coordinates. $J = x_\xi y_\eta - x_\eta y_\xi$, the Jacobian of the transformation, physically corresponds to the cell area.

Correct splitting of the transformed flux vectors is obtained by the following procedure:

Anderson et al [12] have shown that it is possible to rewrite $\hat{F}$ and $\hat{G}$ as the product of a local deformation matrix and a modified flux vector, which is formally equal to the corresponding Cartesian flux vector, but contains transformed instead of Cartesian velocities. The resulting formulas are

$$\begin{aligned} \hat{F}(\hat{Q}) &= \sqrt{x_\eta^2 + y_\eta^2}\; T_F\, \bar{F}(\bar{Q}) \\ \hat{G}(\hat{Q}) &= \sqrt{x_\xi^2 + y_\xi^2}\; T_G\, \bar{G}(\bar{Q}) \end{aligned} \tag{10}$$

where

$$\bar{Q} = \rho \begin{bmatrix} 1 \\ \bar{u} \\ \bar{v} \\ \bar{E} \end{bmatrix}, \bar{F} = \rho \begin{bmatrix} \bar{u} \\ \bar{u}^2 + \dfrac{a^2}{\kappa} \\ \bar{u}\,\bar{v} \\ \bar{u}\,\bar{H} \end{bmatrix}, \bar{G} = \rho \begin{bmatrix} \bar{v} \\ \bar{u}\,\bar{v} \\ \bar{v}^2 + \dfrac{a^2}{\kappa} \\ \bar{v}\,\bar{H} \end{bmatrix} \tag{11}$$

with the transformed velocities

$$\begin{aligned} \bar{u} &= \hat{y}_\eta (u - x_\tau) - \hat{x}_\eta (v - y_\tau) \\ \bar{v} &= \hat{x}_\eta (u - x_\tau) + \hat{y}_\eta (v - y_\tau) \end{aligned} \quad \text{in } \bar{F} \tag{12}$$

$$\begin{aligned} \bar{u} &= \hat{x}_\xi (u - x_\tau) + \hat{y}_\xi (v - y_\tau) \\ \bar{v} &= -\hat{y}_\xi (u - x_\tau) + \hat{x}_\xi (v - y_\tau) \end{aligned} \quad \text{in } \bar{G} \,. \tag{13}$$

The terms $\hat{x}_\eta$, $\hat{y}_\eta$, $\hat{x}_\xi$ and $\hat{y}_\xi$ are normalized, i.e. $\hat{x}_\eta^2 + \hat{y}_\eta^2 = 1$ etc., the modified total energy $\bar{E}$ and enthalpy $\bar{H}$ are given by (3) and (4), respectively, with the corresponding velocities $\bar{u}$ and $\bar{v}$ instead of u and v. The deformation matrix T_F is given by

$$T_F = \begin{bmatrix} 1 & 0 & 0 & 0 \\ x_\tau & \hat{y}_\eta & \hat{x}_\eta & 0 \\ y_\tau & -\hat{x}_\eta & \hat{y}_\eta & 0 \\ \dfrac{x_\tau^2 + y_\tau^2}{2} & \hat{y}_\eta x_\tau - \hat{x}_\eta y_\tau & \hat{x}_\eta x_\tau + \hat{y}_\eta y_\tau & 1 \end{bmatrix} \tag{14}$$

and T_G is obtained by replacing $\hat{y}_\eta$ and $\hat{x}_\eta$ in (14) with $\hat{x}_\xi$ and $-\hat{y}_\xi$. The splitting of the transformed flux vectors can now be performed according to (10)

$$\begin{aligned} \hat{F}^\pm &= \sqrt{x_\eta^2 + y_\eta^2}\; T_F\, \bar{F}^\pm \\ \hat{G}^\pm &= \sqrt{x_\xi^2 + y_\xi^2}\; T_G\, \bar{G}^\pm \end{aligned} \tag{15}$$

where $\bar{F}^\pm$ and $\bar{G}^\pm$ are calculated in the same fashion as the Cartesian split flux vectors, but now in terms of the Mach numbers $M_\xi = \bar{u}/a$ and $M_\eta = \bar{v}/a$ with $\bar{u}$ from (12) and $\bar{v}$ from (13).

The correctness of the splitting is demonstrated by forming the Jacobian matrices from (15). Elementary mathematical operations yield

$$\begin{aligned} \frac{\partial \hat{F}^\pm}{\partial \hat{Q}} &= \frac{\sqrt{x_\eta^2 + y_\eta^2}}{J}\, T_F\, \frac{\partial \bar{F}^\pm}{\partial \bar{Q}}\, T_F^{-1} \\ \frac{\partial \hat{G}^\pm}{\partial \hat{Q}} &= \frac{\sqrt{x_\xi^2 + y_\xi^2}}{J}\, T_G\, \frac{\partial \bar{G}^\pm}{\partial \bar{Q}}\, T_G^{-1} \,. \end{aligned} \tag{16}$$

i.e. the matrices on the left and right-hand sides of (16) are diagonally similar except for a positive factor. Consequently, the eigenvalues of the left-hand side matrices remain positive or negative depending on the sign of the eigenvalues of the right-hand side matrices.

2.3 Solution Algorithm

After flux splitting, the Euler equations in boundary-fitted coordinates are given by

$$\frac{\partial \hat{Q}}{\partial \tau} + \frac{\partial \hat{F}^+}{\partial \xi} + \frac{\partial \hat{F}^-}{\partial \xi} + \frac{\partial \hat{G}^+}{\partial \eta} + \frac{\partial \hat{G}^-}{\partial \eta} = 0 \,. \tag{17}$$

The method of solution is the approximately factored Beam-Warming implicit algorithm [15] given in delta form with first-order time accuracy by

$$\begin{aligned} &\left[1 + \Delta\tau \left(\delta_\xi^- \frac{\partial \hat{F}^+}{\partial \hat{Q}} + \delta_\xi^+ \frac{\partial \hat{F}^-}{\partial \hat{Q}} \right) \right] \cdot \\ &\cdot \left[1 + \Delta\tau \left(\delta_\eta^- \frac{\partial \hat{G}^+}{\partial \hat{Q}} + \delta_\eta^+ \frac{\partial \hat{G}^-}{\partial \hat{Q}} \right) \right] \Delta \hat{Q} = \\ &= -\Delta\tau \left[\delta_\xi^- \hat{F}^+ + \delta_\xi^+ \hat{F}^- + \delta_\eta^- \hat{G}^+ + \delta_\eta^+ \hat{G}^- \right] \,. \end{aligned} \tag{18}$$

The numerical scheme is written in a cell-centered finite volume formulation, where the spatial derivatives are approximated by so-called MUSCL-type differencing (MUSCL = Monotic Upstream centered Scheme for Conservation Laws) [16], i.e. they are generated indirectly by extrapolating the Cartesian solution vector with backward or forward formulas. The split-flux differencing in the ξ-direction, for example, is written as

$$\delta_\xi^\mp = \frac{1}{\Delta\xi} \left[\begin{matrix} \hat{F}^\pm \left(Q^\mp_{j+\frac{1}{2},k}, M_{j+\frac{1}{2},k} \right) - \\ \hat{F}^\pm \left(Q^\mp_{j-\frac{1}{2},k}, M_{j-\frac{1}{2},k} \right) \end{matrix} \right] \,. \tag{19}$$

The terms M represent all geometric terms involved in the transformation to boundary-fitted coordinates and have to be calculated at the cell interfaces (see Figure 1). The extrapolated values of the solution vector Q are determined by the formulas

$$\begin{aligned} Q^-_{j+\frac{1}{2},k} &= Q_{j,k} + f_{j,k} \left(Q_{j,k} - Q_{j-1,k} \right) \\ Q^+_{j+\frac{1}{2},k} &= Q_{j+1,k} + f_{j+1,k} \left(Q_{j+1,k} - Q_{j+2,k} \right) \end{aligned} \tag{20}$$

with the control factors

$$\begin{aligned} f_{j,k} &= 0 \qquad \text{for first order accuracy} \\ f_{j,k} &= \frac{1}{2} \qquad \text{for second order accuracy} \,. \end{aligned} \tag{21}$$

THIS DOCUMENT PROVIDED BY THE ABBOTT AEROSPACE
TECHNICAL LIBRARY
ABBOTTAEROSPACE.COM

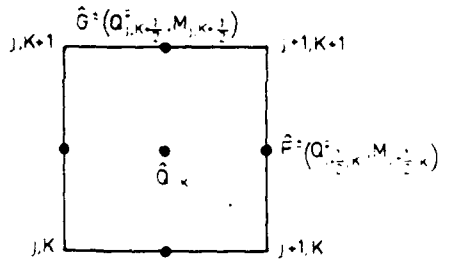


Fig. 1. Calculation of solution and flux vectors by the MUSCL Scheme

Further investigation of the flux splitting technique described above shows that differencing (19) together with (20) is the only way to avoid undesired discretization errors in a boundary-fitted coordinate system.

The left-hand side of (18) requires the calculation of the split Jacobian matrices. Their values at the point (j,k) are easily determined with the aid of equation (16). Using first-order upwind differencing on the left-hand side of equation (18), a procedure which does not reduce the accuracy in space and time, we obtain a block-tridiagonal structure for the implicit equations. Since upwind spatial differencing is used, no artificial dissipation is required.

2.4 *Boundary Conditions*

The steady or unsteady flow calculation for a cascade demands the implementation of different boundary conditions which determine the solution. These boundary conditions are: the kinematic flow condition (vanishing normal velocity at the blade's surfaces), inlet and outlet boundary conditions (either prescribed flow values for steady flow or nonreflecting boundary conditions for unsteady flow at the in- and outlet boundary of the computational grid), and periodic boundary conditions on certain parts of the outer boundaries of the computational domain (prescribed periodicity of the flow due to the geometric repeat condition of the cascade).

On the blade's surface, the normal relative velocity is set to zero

$$(\vec{v} - \vec{v}_k) \cdot \vec{n} = 0 \qquad \text{with } \vec{v}_k = [\,x_\tau, y_\tau\,]_{\text{wall}} \tag{22}$$

where $\vec{v}$, $\vec{v}_k$ and $\vec{n}$ are the Cartesian velocity vector, the prescribed kinematic velocity vector of the blade's surface, and the normal vector on the body, respectively. The pressure is determined from the normal momentum equation [17], which runs in Cartesian form as follows

$$\rho \left\{ \left[\frac{\partial \vec{n}}{\partial t} + (\vec{v}\,\text{grad})\,\vec{n} \right] \cdot \left[\vec{v} - \vec{v}_k \right] - \left[\frac{\partial \vec{v}_k}{\partial t} + (\vec{v}\,\text{grad})\,\vec{v}_k \right] \cdot \vec{n} \right\} = \text{grad}\, p \cdot \vec{n}\,. \tag{23}$$

Assuming the blade's surface is identical with a η = const.-line, the transformation of (23) into a boundary-fitted coordinate system yields

$$(x_\xi^2 + y_\xi^2)\,\frac{\partial p}{\partial \eta} = (x_\xi x_\eta + y_\xi y_\eta)\,\frac{\partial p}{\partial \xi} \cdot \rho\, J \left\{ \frac{\bar{u}^2}{(x_\xi^2 + y_\xi^2)} (y_\xi x_{\xi\xi} - x_\xi y_{\xi\xi}) + y_\xi x_{\tau\tau} - x_\xi y_{\tau\tau} + \frac{2\,\bar{u}}{\sqrt{x_\xi^2 + y_\xi^2}} (y_\xi x_{\xi\tau} - x_\xi y_{\xi\tau}) \right\} \tag{24}$$

with the tangential relative velocity $\bar{u}$ from equation (13).

The density ρ and the tangential relative velocity $\bar{u}$ at the body's surface, both needed to compute the normal pressure derivative, are calculated by extrapolation from the interior field. If the grid lines are orthogonal at the body, the first term on the right-hand side of (24) vanishes, and hence the pressure at the body can be determined directly by (24) without the solution of a linear system of equations.

The implementation of inlet and outlet boundary conditions is closely related to the theory of characteristics. Casting the Euler equations into their characteristic form, a new set of so-called characteristic variables is created, representing the propagation of entropy, vorticity and pressure waves along the characteristic surfaces that are determined by the eigenvalues of a linear combination of the Jacobian matrices $\partial\hat{F}/\partial\hat{Q}$ and $\partial\hat{G}/\partial\hat{Q}$. Selecting special directions on the characteristic surfaces to integrate the flow equations at a boundary, these directions may either point away from or toward the computational domain, indicating that outgoing or incoming waves are to be treated. Since the outgoing waves are determined completely by the interior field solution, the replacement of the incoming waves by appropriate physical conditions makes it possible to compute the flow boundary values in characteristic form. However, the calculation of a "genuine" characteristic solution at the regarded boundaries implies the integration of the characteristic equations along the characteristic cone and always leads to a large-scale scheme. An important contribution to simplify this problem has been made by Chakravarthy [18], who used a quasi-one-dimensional approach.

Supposing the in- and outlet boundaries are ξ = const.-lines (typical for an H-grid), a cut through the characteristic cone in ξ-direction causes all characteristics to fall into the ξ-τ-plane. Regarding the wave transport in this plane only and treating the flux along the boundaries as source term, the eigenvalues and left eigenvectors of $\partial\hat{F}/\partial\hat{Q}$ are the ones that determine the direction of wave transport and the characteristic variables. The characteristic transformation of the Euler equations with the restrictions mentioned above leads to

$$\vec{\sigma}_i \frac{\partial \hat{Q}}{\partial \tau} + \lambda_i \vec{\sigma}_i \frac{\partial \hat{Q}}{\partial \xi} + \vec{\sigma}_i \frac{\partial \hat{G}}{\partial \eta} = 0\,; \quad i = 1, \ldots, 4$$

or

$$\frac{\partial r_i}{\partial \tau} + \lambda_i \frac{\partial r_i}{\partial \xi} + \vec{\sigma}_i \frac{\partial \hat{G}}{\partial \eta} = 0 \tag{25}$$

with

$\partial r_i = \vec{\sigma}_i\, \partial \hat{Q}$ = characteristic variables

λ_i = eigenvalue of $\partial \hat{F} / \partial \hat{Q}$

$\vec{\sigma}_i$ = corresponding left eigenvector.

THIS DOCUMENT PROVIDED BY THE ABBOTT AEROSPACE
TECHNICAL LIBRARY
ABBOTTAEROSPACE.COM

The incoming waves which are to be replaced by appropriate physical boundary conditions are identified by positive λ_i if the positive ξ-direction points from the boundary to the interior field, or by negative λ_i if the positive ξ-direction points from the interior field to the boundary.

If the in- and outlet boundary conditions are given as

$$B_i(\hat{Q}) = 0\,;\quad i = 1, \ldots, p\,;\quad p \le 4\,,$$

i.e. after differencing with respect to time

$$\frac{\partial B_i}{\partial \hat{Q}}\,\frac{\partial \hat{Q}}{\partial \tau} = 0\,. \tag{26}$$

the system of equations to be solved is

$$\begin{aligned} &\vec{\sigma}_i\,\frac{\partial \hat{Q}}{\partial \tau} + \lambda_i\,\vec{\sigma}_i\,\frac{\partial \hat{Q}}{\partial \xi} + \vec{\sigma}_i\,\frac{\partial \hat{G}}{\partial \eta} = 0\,; \\ &\qquad i = 1, \ldots, 4 - p \\ &\frac{\partial B_i}{\partial \hat{Q}}\,\frac{\partial \hat{Q}}{\partial \tau} = 0\,; \\ &\qquad i = 4 - p + 1, \ldots, 4\,. \end{aligned} \tag{27}$$

Fixed boundary conditions (prescription of any flow quantity such as velocity, pressure, enthalpy, etc.) are then given by

$$\frac{\partial B_i}{\partial \hat{Q}} = f_i \tag{28}$$

and nonreflecting boundary conditions (suppression of incoming waves) by

$$\frac{\partial r_i}{\partial \tau} = 0 \Leftrightarrow \frac{\partial B_i}{\partial \hat{Q}} = \vec{\sigma}_i\,. \tag{29}$$

Rewriting (27) in the form

$$D_1\,\frac{\partial \hat{Q}}{\partial \tau} + D_2\left[\,\frac{\partial \hat{F}}{\partial \xi} + \frac{\partial \hat{G}}{\partial \eta}\,\right] = 0$$

with the matrices

$$D_1 = \begin{bmatrix} \vec{\sigma}_1 \\ \vdots \\ \vec{\sigma}_{4-p} \\ \partial B_{4-p+1}/\partial \hat{Q} \\ \vdots \\ (\partial B_4/\partial \hat{Q}) \end{bmatrix};\quad D_2 = \begin{bmatrix} \vec{\sigma}_1 \\ \vdots \\ \vec{\sigma}_{4-p} \\ 0 \\ \vdots \\ 0 \end{bmatrix} \tag{30}$$

we finally obtain

$$\begin{aligned} &\frac{\partial \hat{Q}}{\partial \tau} = D\left[\,\frac{\partial \hat{F}}{\partial \xi} + \frac{\partial \hat{G}}{\partial \eta}\,\right] \\ &D = D_1^{-1}\,D_2\,. \end{aligned} \tag{31}$$

(31) is the system of modified Euler equations valid on the in- and outlet boundaries, differing from (8) in the multiplication of the flux terms with an influence matrix D effecting the implementation of boundary conditions. What remains is the application of periodic boundary conditions. Since their implementation strongly depends on the computational grid used and the prescribed oscillation mode of the cascade, the next chapter will discuss this.

3. GRID GENERATION

The grid generation needed to compute the solution of the Euler algorithm in a boundary-fitted coordinate system is obtained by a method presented by the author [19]. The procedure used is an elliptic grid generation code based on the solution of two coupled Poisson equations. A basic feature of the present method is the possibility to control the line spacing and intersection angle of the grid lines at the physical boundaries, in this case, for example, at the blade's surface and at the channel boundaries.

The type of grid used for the cascade flow calculation is a line-periodic H-grid, i.e. each grid point on the lower channel boundary has its counterpart on the upper channel boundary in the direction of the cascade axis (see Figure 2). Although this type of grid is characterized by rapidly changing metrics near the stagnation point and rather skewed grid meshes near the trailing edge of the blade, its advantage is that an implicit code is easily introduced on the grid and the periodic boundary conditions can be imposed in an implicit manner by a simple re-entry condition.

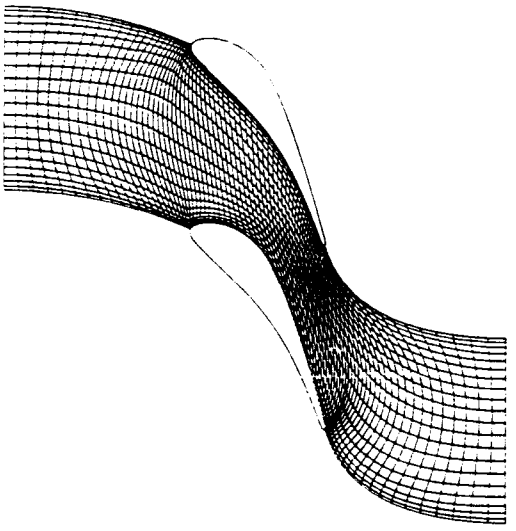


Fig. 2. H-grid for flow calculation

The grid point displacement must be carefully organized due to the motion of the blades. For an arbitrarily chosen oscillation mode, no coordinate system exists in which all blades are at rest. Hence, in contrast to a single oscillating airfoil, no simple rigid body motion can be imposed on the grid points. The total grid has to be deformed steadily to enable it to conform to the new position of the vibrating blades after each time step. In order to accomplish this requirement, a special interactive grid generation procedure was developed. A new grid is calculated after each time step, regarding the old grid as the initial solution and the new position of the blades as changed boundary conditions. This method requires only one or

THIS DOCUMENT PROVIDED BY THE ABBOTT AEROSPACE
TECHNICAL LIBRARY
ABBOTTAEROSPACE.COM

two iterations for the new grid and enables the code to take into account every possible oscillation mode of the cascade. It can even be used for a direct aeroelastic analysis where the flow field and the elastomechanic vibrations of the blades are calculated simultaneously. The grid point speeds $\dot{x}_i$ and $\dot{y}_i$, needed to update the transformed flux vectors and the Jacobian matrices for every time step, are computed by backward time differences.

The number of blade channels in which the flow has to be computed depends on the oscillation mode of the cascade. Tuned modes (same amplitude and constant interblade phase angle) always result in a pitchwise spatially periodic flow, where the spatial periodic length is determined by the interblade phase angle. For example, if an interblade phase angle of $\pm 180°$ is prescribed, the flow values are repeated every time when proceeding two blade pitches along the cascade axis. Hence, two blade channels are sufficient for computation (see Figure 3). Analogously, the flow has to be calculated in four blade channels for a phase angle of $\pm 90°$ and so on. It should be mentioned that it is also possible to restrict the flow computation to only one blade channel for this type of motion (see Kau [8] and Gerolymos [9]). The spatial periodicity condition is then not imposed instantaneously as in the present method, but with a time lag corresponding to the interblade phase angle. Although this technique has the special merits of a reduced computational domain, its disadvantage is that the flow values on the periodic channel boundaries have to be stored in space and time (storage problems) and that many cycles of motion must be computed to drive the solution to periodic convergence in time (slow convergence).

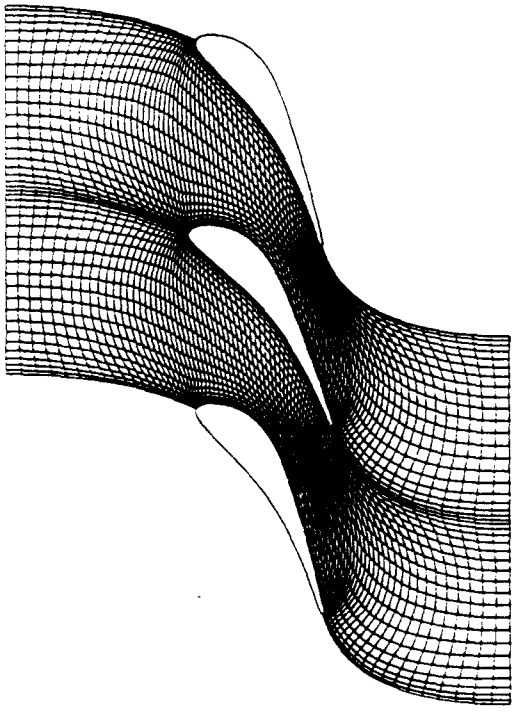


Fig. 3. Moving H-grid for tuned pitching oscillations with an interblade phase angle of 180°

In contrast to the tuned modes (often called "traveling wave modes"), mistuned modes with a varying frequency from blade to blade do not effect any spatial periodic behavior of the flow quantities in pitchwise direction. Consequently, the computational domain has to include the complete cascade, which may consist of twenty blades or more.

4. PRESENTATION AND DISCUSSION OF RESULTS

Results for unsteady cascade flow were calculated for the two standard configurations no. 4 and no. 10 of the IUTAM "Workshop on Aeroelasticity in Turbomachine Cascades". The geometrical data of these subsonic-transonic cascade configurations are listed in Figure 4 and Figure 5, respectively.

Experimental data are available for the turbine standard configuration no. 4 and refer to nine selected aeroelastic test cases [13,14], where unsteady pressure distributions were measured for different outlet Mach numbers and interblade phase angles. These cases treated tuned bending vibrations with a vibration frequency of 150 Hz and a vibration direction, which is depicted in Figure 4. From the nine measured test cases, six were selected for comparison of experimental and theoretical results. The test cases were: $Ma_2 = 0.76,\ 1.19;\ \Theta = -90°$ and $Ma_2 = 0.90,\ \Theta = 0°, \pm 90°, 180°$. The interblade phase angle Θ in this turbine configuration is defined such that it is positive if the phase of the lower blade in Figure 4 advances to the phase of the upper blade, i.e. a positive Θ causes a traveling wave running upwards, whereas a negative Θ produces a traveling wave running downwards along the cascade axis.

The second cascade configuration treated here (standard configuration no. 10) is a compressor-type cascade, which was proposed by Verdon [20] in order to investigate the unsteady aerodynamic response to a vibrating cascade of cambered airfoils in transonic flow. The compressor blades are constructed by superimposing a NACA 0006 profile on a circular arc camber line with a height of 5 %. Two different inlet operating conditions for steady flow were considered, namely $Ma_1 = 0.70$, $\beta_1 = 55°$ and $Ma_2 = 0.80$, $\beta_1 = 58°$ (see Figure 5). In the first case, the steady flow through the cascade is entirely subsonic, whereas the second case leads to a transonic flow through the cascade with a normal shock occurring on the blade's suction side at approximately 25 % of the chord length. The proposed harmonic blade motion is either a heaving motion perpendicular to the chord or a pitching motion around the midpoint of the camber line.

In contrast to standard configuration no. 4, the interblade phase angle is defined such that it is positive if the phase of the upper blade in Figure 5 advances to the phase of the lower blade.

First of all, the computed results for steady flow must be validated, because they are the starting point for the unsteady flow calculations. The steady pressure coefficient for both standard configurations is defined with respect to the inlet-values of total and static pressure

$$(c_p)_s = \frac{p - p_1}{p_{t_1} - p_1} \qquad (32)$$

p_1 = static inlet pressure

p_{t_1} = total inlet pressure .

THIS DOCUMENT PROVIDED BY THE ABBOTT AEROSPACE
TECHNICAL LIBRARY
ABBOTTAEROSPACE.COM

Figure 6 shows the comparison between experimental and theoretical results of standard configuration no. 4 for the two subsonic outflow Mach numbers 0.76 and 0.90, at which the theoretical data predict the experimental results quite well. The corresponding values for the supersonic outflow Mach number 1.19 are depicted in Figure 7. This case is characterized by the occurrence of two shock waves, one emanating from the suction side and the other from the pressure side of the blade's trailing edge (see Schlieren pictures in Böles and Fransson's publication [13]). The shock wave that impinges on the suction side of the neighboring profile is not predicted by the theory if the computation is performed with a normal grid (e.g. 85 x 23 grid points, see upper picture in Figure 7). Even the flow computation with a very fine solution-adaptive grid does not lead to sufficient agreement with the measured pressure (see lower picture in Figure 7). The shock position is predicted correctly, but not the shock strength. Hence, the theoretical and experimental pressure distributions differ from each other for the aft portion of the blade's suction side. Evidently, this discrepancy in the case of steady supersonic outflow, which demands further investigation, also causes significant differences in the unsteady flow values which strongly depend on the steady flow quantities.

The steady pressure distribution for the transonic flow through standard configuration no. 10 is given in Figure 8, where the result of the present Euler code is compared with the Full Potential solution of Verdon [20]. Small differences in the shock position and the shock strength are noticeable, but the overall agreement of both results is satisfactory.

The calculation of the unsteady flow quantities for tuned modes has always been performed with the same technique: at rest in the computed steady flow, the blades are started with the prescribed oscillation mode. The calculation is stopped when good periodic convergence of the unsteady lift or moment coefficient is achieved, i.e. when the peak values of these quantities for two successive periods of blade motion do not differ from each other more than 0.1 %. Since the reduced frequencies

$$\omega^* = \frac{2\pi f \cdot L}{V_2} \text{ for the turbine configuration}$$

$$\omega^* = \frac{2\pi f \cdot L}{V_1} \text{ for the compressor configuration} \qquad (33)$$

L = chord length of the blade

V_1 = cascade inlet velocity

V_2 = cascade outlet velocity

in all test cases used have a relatively low value $\omega^* < 0.35$, three or four cycles of blade motion were enough to drive the solution to the desired convergence. Applying a Fourier analysis to the time-dependent pressure, lift and moment coefficients for the last calculated period, the first harmonics of these quantities were obtained and can be compared with the corresponding measured values. Denoting the dimensionless amplitude of a harmonic blade oscillation with A, the unsteady pressure coefficient is then defined as the complex number

$$(c_p)_{us} = \frac{\tilde{p}\, e^{i\varphi}}{A\,(p_{t_1} - p_1)} \qquad (34)$$

$\tilde{p}$ = pressure amplitude

φ = phase angle between pressure and blade motion.

Figures 9 and 10 show the comparison between the computed and measured unsteady pressure distributions for the outflow Mach number $Ma_2 = 0.90$ and the two interblade phase angles $\Theta = 180°$ and $\Theta = -90°$, respectively. The results of the first harmonics are presented in a module-phase diagram. Although a certain overprediction of the suction peak near the leading edge is observed in the theoretical results, good agreement with the experimental data is obtained for the phase lead or lag of the unsteady pressure with respect to the blade motion. The integrated values of the unsteady pressure, the lift coefficient for bending, and the moment coefficient for pitching motion can be decomposed into two parts: the in-phase and the out-of-phase part, where the latter (the so-called "aerodynamic damping") determines the aerodynamic stability of the cascade. Figure 11 shows the aerodynamic damping as function of the interblade phase angle for the outflow Mach number $Ma_2 = 0.90$. For this test case, experimental data are available in steps of $\Delta\Theta = 90°$, whereas the numerical results were computed in steps of $\Delta\Theta = 45°$.

Figure 11 demonstrates the strong influence of the interblade phase angle on the aerodynamic stability of tuned bending modes. Here we can observe a high amount of aerodynamic damping for phase angles in the domain of $+90°$ and a significant excitation for Θ-values in the area of $-90°$. Although the absolute values of the computed results are different from the experimental ones, the transition from damping to excitation is in agreement with the theory. A further insight into the stability behavior of the cascade is obtained by the damping-outlet Mach number diagram in Figure 12, where the experimental and theoretical results for the worst case of damping ($\Theta = -90°$) are depicted. Experiment and theory agree well for subsonic outflow, indicating an unstable behavior of the cascade, but not for supersonic outflow ($Ma_2 = 1.19$). Here, the experimental data express a stable oscillation, whereas the theoretical results predict an unstable motion of the blades. When the corresponding pressure distribution (see Figure 13) is studied, the reason for this discrepancy becomes clear. The absence of the blade passage shock wave in the theoretical results leads to a rather smooth pressure distribution without any significant phase shift of pressure at the shock position. Hence, the computed aerodynamic damping cannot reproduce the response to this shock wave, which seems to have a stabilizing effect on the blade motion.

Furthermore, results were computed for tuned pitching oscillations around the midpoint of the blade's skeleton line. As the most interesting result, the aerodynamic damping as function of the interblade phase angle is depicted in Figure 14. In contrast to bending modes, an excitation takes place for Θ-values near $+90°$, while the largest damping is observed in the area of $\Theta = -90°$.

Tuned pitching oscillations were also investigated for standard configuration no. 10 (Verdon's compressor cascade). The computed results presented refer to the case of transonic flow ($Ma_1 = 0.80$; $\beta_1 = 58°$) with a reduced frequency $\omega^* = 0.25$. Figures 15 and 16 depict the comparison between the present Euler method and Verdon's linearized potential solver [20]. Figure 15 shows the module-phase diagram of the unsteady pressure coefficient for an interblade phase angle of 0°. Significant differences between the two CFD methods just mentioned are observed in the pressure modules in the region of the mean shock position and in the pressure phases especially on the suction side. As expected, the aerodynamic damping coefficients resulting from both methods are also different. Figure 16 shows the damping coefficients

THIS DOCUMENT PROVIDED BY THE ABBOTT AEROSPACE
TECHNICAL LIBRARY
ABBOTTAEROSPACE.COM

as functions of the interblade phase angle in steps of 45°. Although both methods predict an overall stable pitching motion, the amount of damping is evidently different for most of the eight interblade phase angles.

Since the results of both codes agree fairly well for steady flow (see Figure 8), these discrepancies must be due to a different treatment of the unsteady flow problem. Obviously, the occurrence of a shock and its oscillatory motion combined with a periodic change of shock strength strongly influence the module and phase of the moment coefficient. The question arises whether a linearized code is able to handle this problem satisfactorily. On the other hand, in order to improve the accuracy of the present method, the Euler code has to be supplied with a time-dependent shock-adapting grid to investigate the physical effects of the shock movement in detail.

Finally, mistuned modes were investigated in order to take into account the fact that the blades of a real turbomachine always possess eigenfrequencies that are slightly different from one another. However, this frequency mistuning poses a nearly unsolvable problem for the theory if one tries to compute pressure, lift and moment coefficients for an arbitrary mistuned mode in the time domain. The reasons for this are that the spatial periodicity of the cascade flow is lost, i.e. one has to calculate the flow values in the total blade row, and that one must extend the computation as long as time periodicity of the flow values is achieved, which often makes it necessary to calculate flow for 100 or more cycles of blade motion.

In order to circumvent this problem, a simple and somewhat artificial configuration was investigated, still yielding a good insight into the aerodynamic effect of mistuning. The treated case is a blade row consisting of 16 blades which are alternately mistuned, i.e. the blades 1, 3, etc. are vibrating with the frequency f_0, while the other blades 2, 4, etc. perform oscillations with the frequency $f_1 = f_0 (1.0 + 0.1)$ which is 10 % higher than f_0. All the blades vibrate with the same amplitude. This choice of frequency mistuning is characterized by a beat frequency of $f_b = 0.1 \times f_0$, i.e. time periodicity of the flow values is expected after ten cycles of motion for the blades 1, 3, etc. and eleven cycles for the blades 2, 4, etc. The computations were performed with standard configuration no. 4 for subsonic outflow ($Ma_2 = 0.90$).

The aerodynamic behavior of the cascade with respect to stability is determined by the following procedure: after each finished cycle of blade motion, the mean aerodynamic power coefficients for this cycle are updated for blades 1 and 2 (all other blades are aerodynamically identical with either blade 1 or blade 2). Performing this procedure over the beat period $T_b = 1 / f_b$, the mean value of all power coefficients gives rise to damping or excitation. Figures 17 and 18 show the results for bending and pitching motions. In both diagrams, the aerodynamic power coefficients of blades 1 and 2 are depicted as functions of the reduced time period T / T_0, where T_0 refers to blade 1. Both figures demonstrate that within the beat period T_b energy is partly received from and partly released to the flow. The important result, however, is that the average power coefficients of blades 1 and 2 remain positive for bending as well as for pitching vibrations, indicating a stable oscillation of the total blade row. This stabilizing effect of frequency mistuning has already been predicted by Bloemhof [21], although his investigations were restricted to linear aerodynamic theory.

5. SUMMARY AND CONCLUSIONS

A method that computes the two-dimensional unsteady flow through a cascade of oscillating blades has been presented here. The time-dependent Euler equations in conservative form are solved by an implicit algorithm using van Leer's flux vector splitting. A special feature of the present method is the use of an interactive grid generation which enables the code to treat every possible oscillation mode of the cascade.

In order to demonstrate the dependence of the aerodynamic stability on the selected cascade modes, tuned harmonic modes as well as frequency mistuned modes were investigated. Results were computed for two standard configurations of the "IUTAM Workshop on Aeroelasticity in Turbomachine Cascades", namely a turbine cascade (st. conf. no. 4) and a compressor cascade (st. conf. no. 10).

The comparison between the experimental data of the turbine configuration no. 4 and the corresponding theoretical values is encouraging in the case of subsonic outflow. The measured regions of stable and unstable interblade phase angles are predicted well by the computed results. In the case of supersonic outflow, there remains an unexplained discrepancy between experiment and theory concerning the aerodynamic stability of the motion. The question to be answered is whether this deviation is due to the incorrect prediciton of the blade passage shock strength or due to a fundamental difference between a 3D experiment (the experiments were performed in an annular cascade) and a 2D theory.

Furthermore, a comparison between the predicted values of the present Euler code and a linearized potential method [20] were performed for the compressor standard configuration no. 10, where tuned pitching oscillations in transonic flow were investigated. Significant differences were observed between the two CFD methods concerning the pressure and the aerodynamic damping coefficients. The question arises whether a linearized method is able to correctly predict the effect of a moving shock with respect to the aerodynamic stability. In addition, an improved shock-adaptive grid generation in the present Euler code and further comparisons with the results from other Euler methods could help clarify the discrepancies mentioned above.

In order to demonstrate the aerodynamic behavior of a frequency mistuned cascade, a special alternately mistuned turbine configuration was investigated. The important result for the chosen configuration is that the average power coefficients of the blades remain positive for bending oscillations as well as for pitching oscillations, indicating a stable motion of the blade row.

6. REFERENCES

[1] Whitehead, D.S., "Bending Flutter of Installed Cascade Blades at Finite Deflection", Aeronautical Research Council Reports and Memoranda, No. 3386, 1965.

[2] Atassi, H. and Goldstein, M.E., "Unsteady Aerodynamic Forces Acting on Loaded Two-Dimensional Blades in Non-Uniform Incompressible Flows", in "Revue Francaise de Mécanique", IUTAM Symposium sur Aeroélasticité dans les Turbomachines, Paris, 1976.

THIS DOCUMENT PROVIDED BY THE ABBOTT AEROSPACE
TECHNICAL LIBRARY
ABBOTTAEROSPACE.COM

[3] Carstens, V., "Theoretical Flutter Investigations on a Plane Cascade in Incompressible Flow", IUTAM Symposium for Unsteady Aerodynamics of Turbomachines and Propellers, Cambridge, U.K., 1984.

[4] Smith, S.N., "Discrete Frequency Sound Generation in Axial Flow Turbomachines", Aeronautical Research Council, Reports and Memoranda, No. 3709, 1972.

[5] Verdon, J.M. and Caspar, J.K., "Subsonic Flow Past an Oscillating Cascade with Finite Mean Flow Deflection", AIAA, 18, 1980, pp. 540-548.

[6] Verdon, J.M. and Caspar, J.K., "A Linear Aerodynamic Analysis for Unsteady Transonic Cascades", NASA-CR, 3833, 1984.

[7] Hall, K.C. and Crawley, E.F., "Calculation of Unsteady Flows in Turbomachinery Using the Linearized Euler Equations", AIAA, 27, 1989, pp. 777-787.

[8] Kau, H.P., "Berechnung der zweidimensionalen, instationären Durchströmung axialer Turbomaschinengitter mit einem expliziten Zeitschrittverfahren (Calculation of the Two-Dimensional Unsteady Flow Through Axial Turbomachine Cascades with an Explicit Time-Marching Method)", Doctoral Thesis, Rheinisch-Westfälische Technische Hochschule Aachen, 1989.

[9] Gerolymos, G.A., "Numerical Integration of the Blade-to-Blade Surface Euler Equations in Vibrating Cascades", AIAA, 26, 1988, pp. 1483-1492.

[10] Rai, M.M., "Navier-Stokes Simulations of Rotor-Stator Interaction Using Patched and Overlaid Grids", AIAA Paper 85-1519, 1985.

[11] van Leer, B., "Flux Vector Splitting for the Euler Equations", ICASE Report No. 82-30, 1982.

[12] Anderson, W.K., Thomas, L.L. and van Leer, B., "A Comparison of Finite Volume Flux Vector Splittings for the Euler Equations", AIAA Paper 85-0122, 1985.

[13] Böles, A. and Fransson, T.H., "Aeroelasticity in Turbomachines - Comparison of Theoretical and Experimental Results", Communication du Laboratoire de Thermique Appliquée et de Turbomachines, 13, EPFL Lausanne, 1986.

[14] Böles, A. and Fransson, T.H., "Aeroelasticity in Turbomachines - Appendix A5: All Experimental and Theoretical Results for the 9 Standard Configurations", Communication du Laboratoire de Thermique Appliquée et de Turbomachines, 13, EPFL Lausanne, 1986.

[15] Beam, R.M. and Warming, R.F., "An Implicit Finite-Difference Algorithm for Hyperbolic Systems in Conservation-Law Form", Journ. Comp. Phys., 22, 1976, pp. 87-110.

[16] van Leer, B., "Towards the Ultimate Conservative Difference Scheme V. A Second-Order Sequel to Godunov's Method", Journ. Comp. Phys., 32, 1979, pp. 101-136.

[17] Rizzi, A., "Numerical Implementation of Solid-Body Boundary Conditions for the Euler Equations", ZAMM, 58, 1978, pp. 301-304.

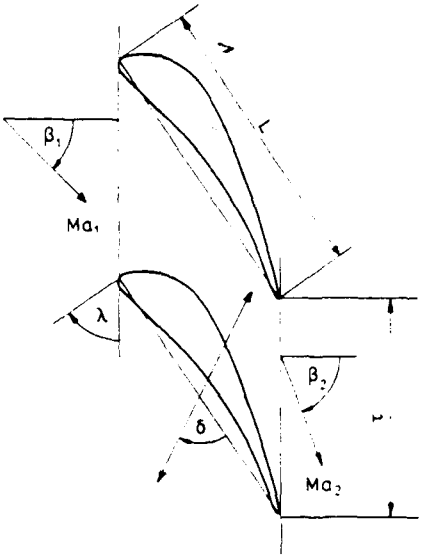
[18] Chakravarthy, S.R., "Euler Equations - Implicit Schemes and Boundary Conditions", AIAA Paper 82-0228, 1982.

[19] Carstens, V., "Two-Dimensional Elliptic Grid Generation for Airfoils and Cascades", DLR-FB 88-52, 1988.

[20] Verdon, J.M. and Usab, W., "Advances in the Numerical Analysis of Linearized Unsteady Cascade Flows", AFWAL TR 88-2055.

[21] Bloemhof, H., "Flutter of Blade Rows with Mistuning and Structural Coupling", Communication du Laboratoire de Thermique Appliquée et de Turbomachines 14, EPFL Lausanne, 1988.

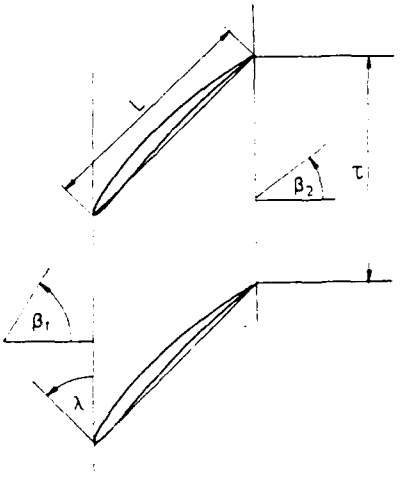
THIS DOCUMENT PROVIDED BY THE ABBOTT AEROSPACE
TECHNICAL LIBRARY
ABBOTTAEROSPACE.COM



chord length	L = 0.0744m	direction of
pitch chord ratio	τ/L = 0.76	bending against
stagger angle	λ = 56.6°	chord δ = 60.4°

nominal values : $\beta_1 = 45°$, $\beta_2 = 72.4°$
$Ma_1 = 0.28$, $Ma_2 = 0.90$

Fig. 4. Cascade geometry of the fourth standard configuration of the IUTAM "Workshop on Aeroelasticity in Turbomachine Cascades"



pitch chord ratio τ/L = 1.0	stagger angle λ = 45°
in–and outlet valves	1.) $Ma_1 = 0.70$, $Ma_2 = 0.45$
for steady flow :	$\beta_1 = 55.0°$, $\beta_2 = 40.2°$
	2.) $Ma_1 = 0.80$, $Ma_2 = 0.43$
	$\beta_1 = 58.0°$, $\beta_2 = 40.3°$

Fig. 5. Cascade geometry of the tenth standard configuration of the IUTAM "Workshop on Aeroelasticity in Turbomachine Cascades"

THIS DOCUMENT PROVIDED BY THE ABBOTT AEROSPACE
TECHNICAL LIBRARY
ABBOTTAEROSPACE.COM

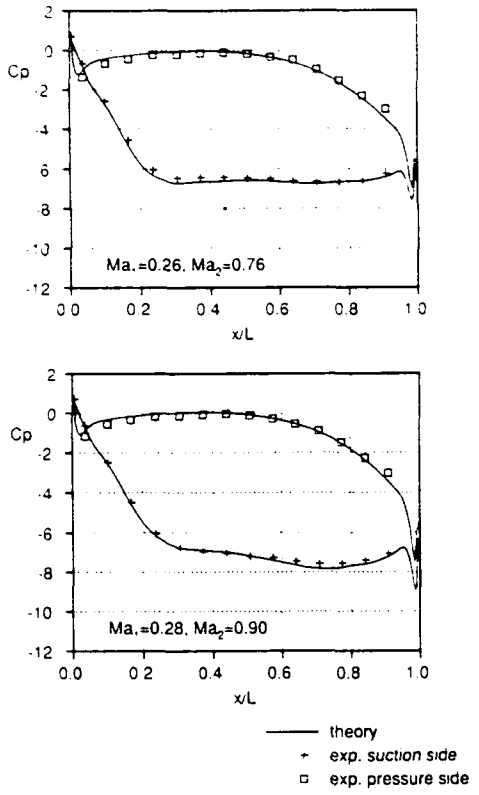


Fig. 6. Theoretical and experimental steady pressure distributions for subsonic outflow, st. conf. no. 4

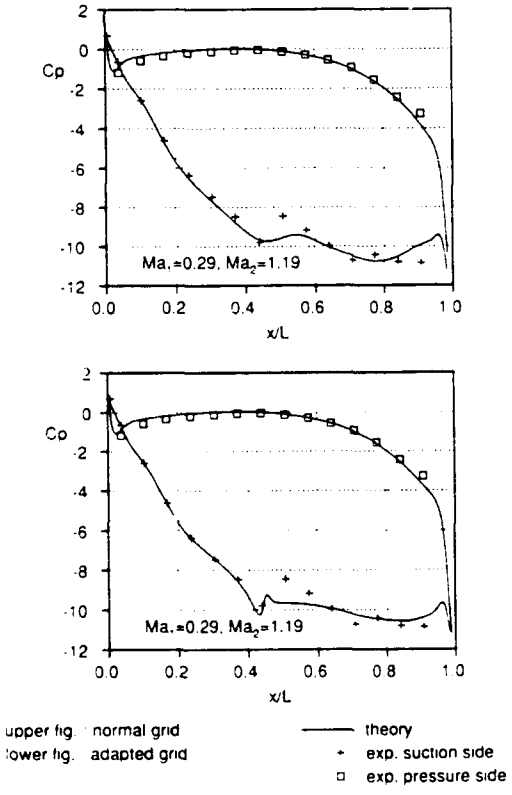


Fig. 7. Theoretical and experimental steady pressure distribution for supersonic outflow, st. conf. no. 4

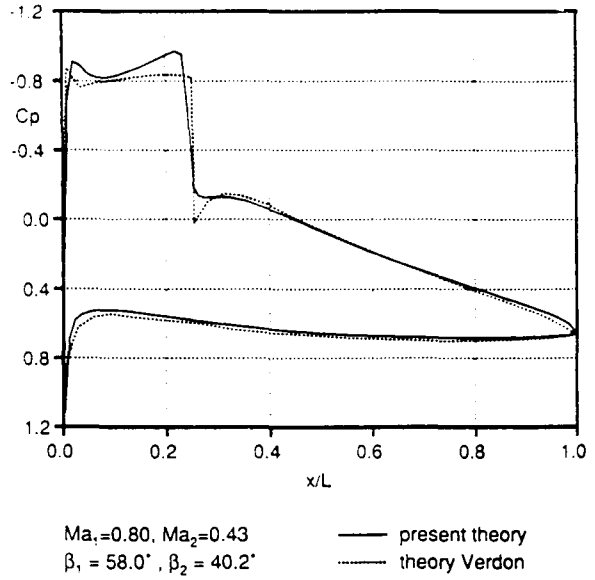


Fig. 8. Theoretical steady pressure distribution for transonic flow, st. conf. no. 10

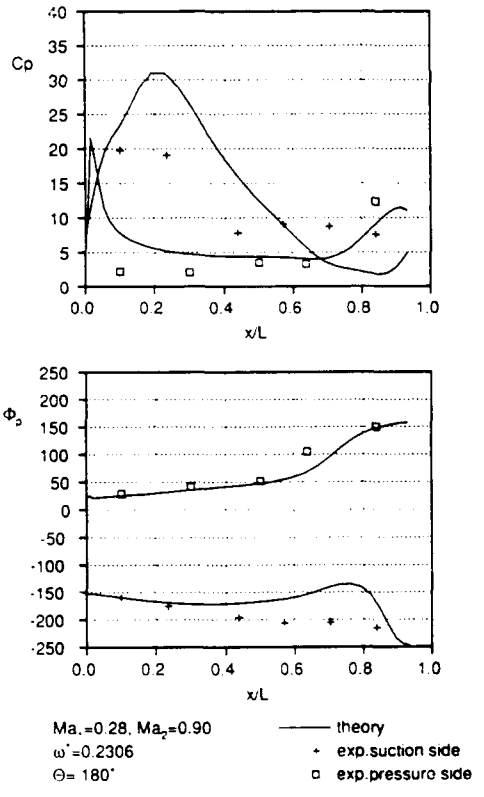


Fig. 9. Theoretical and experimental unsteady pressure distribution for subsonic outflow, heaving motion with $\Theta = 180°$, st. conf. no. 4

THIS DOCUMENT PROVIDED BY THE ABBOTT AEROSPACE
TECHNICAL LIBRARY
ABBOTTAEROSPACE.COM

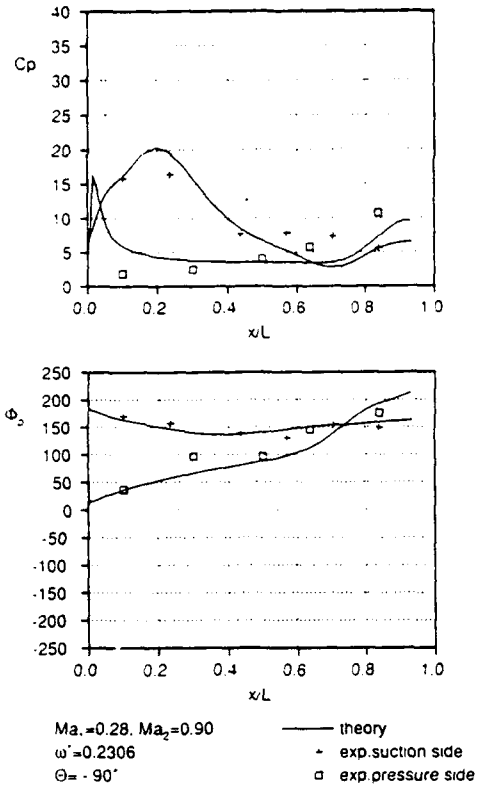


Fig. 10. Theoretical and experimental unsteady pressure distribution for subsonic outflow, heaving motion with $\Theta = -90°$, st. conf. no. 4

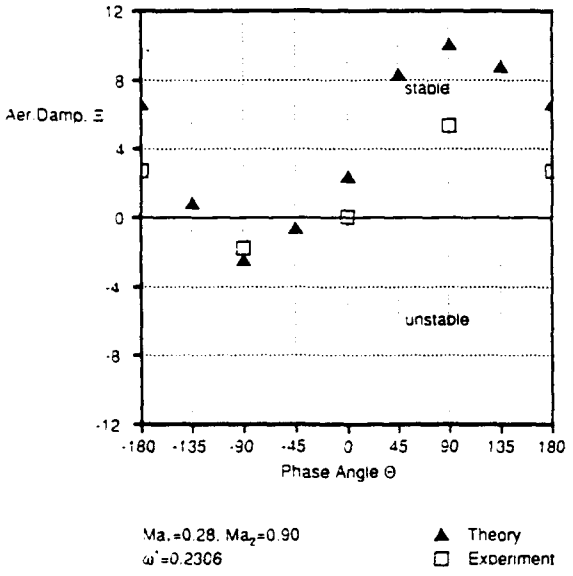


Fig. 11. Aerodynamic damping versus interblade phase angle, theory and experiment, heaving motion, st. conf. no. 4

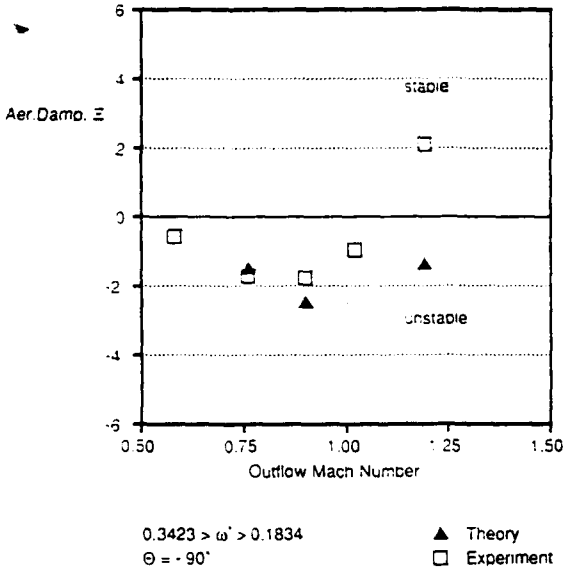


Fig. 12. Aerodynamic damping versus outlet Mach number, theory and experiment, heaving motion, st. conf. no. 4

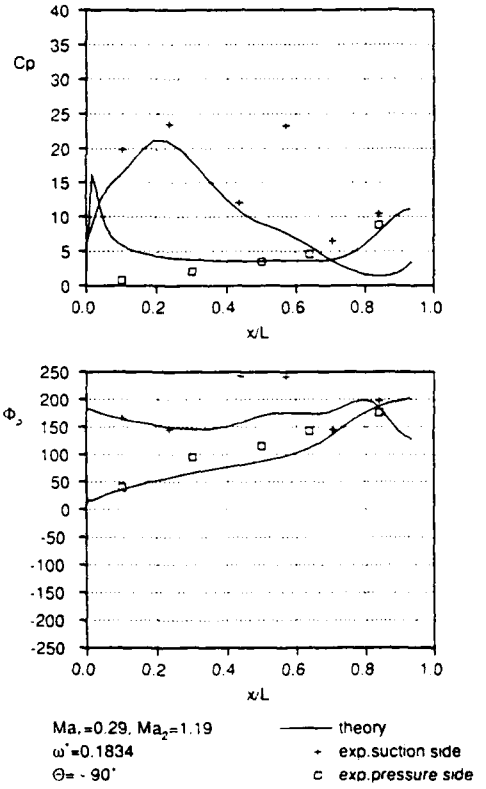


Fig. 13. Theoretical and experimental unsteady pressure distribution for supersonic outflow, heaving motion with $\Theta = -90°$, st. conf. no. 4

THIS DOCUMENT PROVIDED BY THE ABBOTT AEROSPACE
TECHNICAL LIBRARY
ABBOTTAEROSPACE.COM

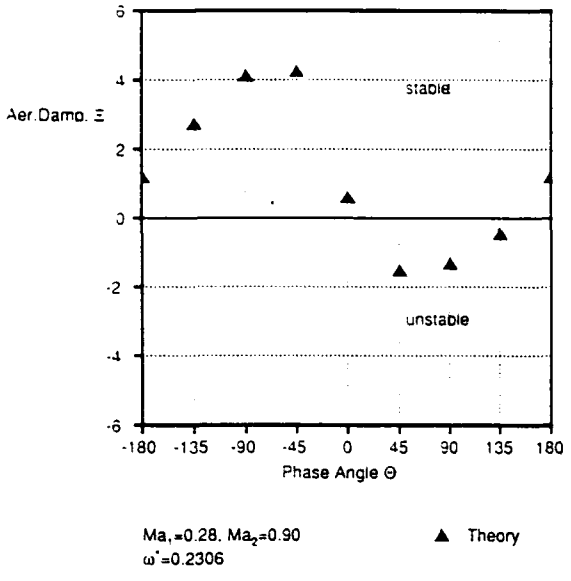


Fig. 14. Aerodynamic damping versus interblade phase angle, theory, pitching motion, st. conf. no. 4

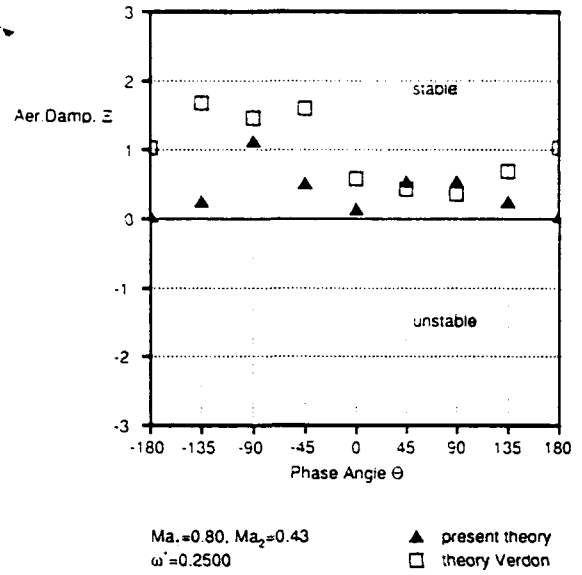


Fig. 16. Aerodynamic damping versus interblade phase, theory, pitching motion, st. conf. no. 10

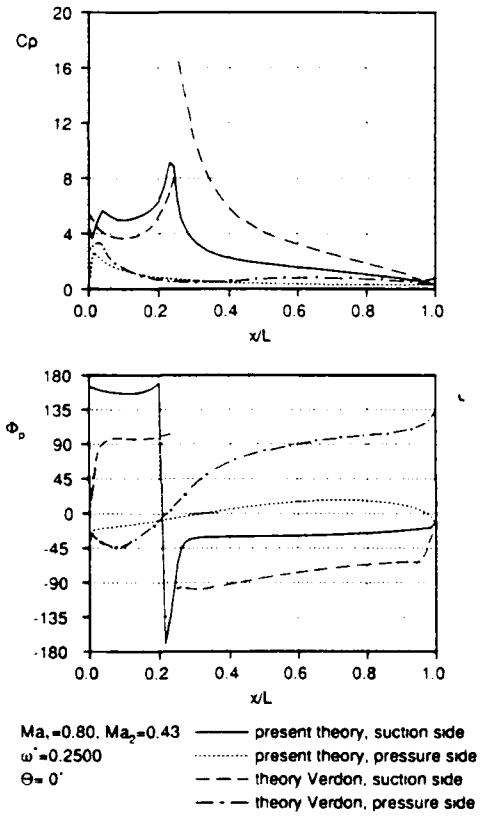


Fig. 15. Theoretical unsteady pressure distribution for transonic flow, pitching motion with $\Theta = 0°$, st. conf. no. 10

THIS DOCUMENT PROVIDED BY THE ABBOTT AEROSPACE
TECHNICAL LIBRARY
ABBOTTAEROSPACE.COM

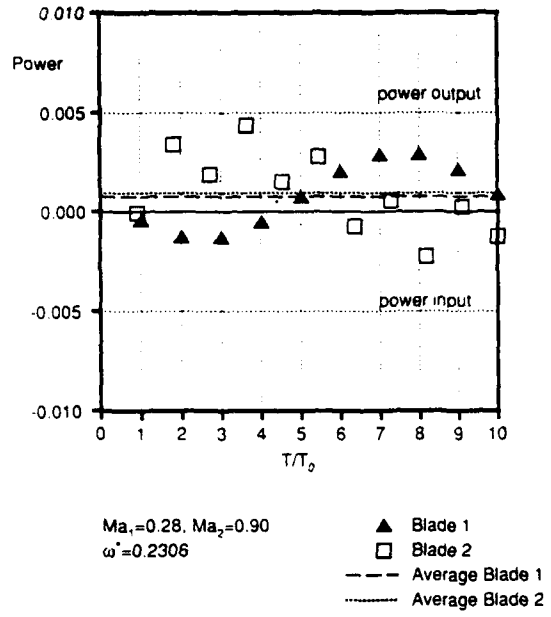


Fig. 17. Aerodynamic power of mistuned modes, theory, heaving motion, st. conf. no. 4

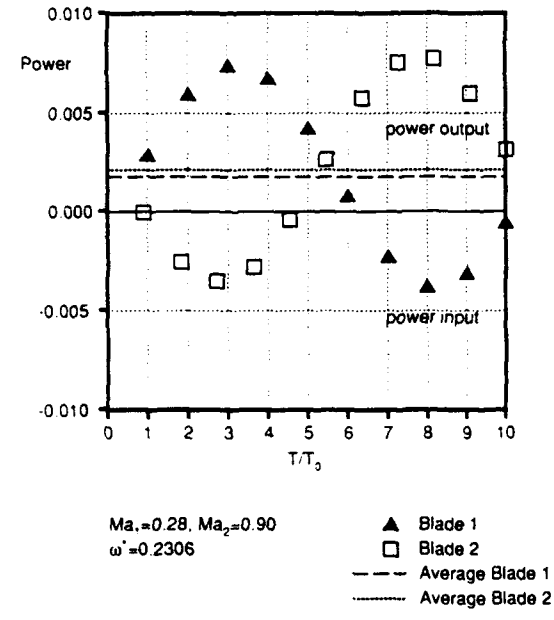


Fig. 18. Aerodynamic power of mistuned modes, theory, *pitching motion*, st. conf. no. 4

THIS DOCUMENT PROVIDED BY THE ABBOTT AEROSPACE
TECHNICAL LIBRARY
ABBOTTAEROSPACE.COM

AD-P007 802

EVALUATION OF AN UNSTEADY IMPLICIT EULER CODE AGAINST TWO AND THREE-DIMENSIONAL STANDARD CONFIGURATIONS

A. Brenneis
A. Eberle

Military Aircraft Division
Messerschmitt-Bölkow-Blohm GmbH
FE211, P.O.Box 80 11 60
D-8000 München 80
Germany

92-16040

SUMMARY

The numerical solution of the unsteady Euler equations in conservative form for time-accurate problems using a relaxation method is considered. The unfactored implicit equations are solved by applying a nonlinear Newton method. Relaxation is performed with a point Gauss-Seidel algorithm ensuring a high degree of vectorization by employing the so-called checkerboard scheme. The fundamental feature of the Euler solver is a characteristic variable splitting scheme (Godunov-type averaging procedure, linear locally one-dimensional Riemann solver) based on an eigenvalue analysis for the calculation of the fluxes. Singular behavior of the coefficient matrix is evaded by a simple matrix conditioning needing only few operations. Numerical results are presented for two and three-dimensional standard AGARD configurations. The airfoils and wings at sub- and transonic flows perform harmonically pitching oscillations or trailing-edge flap oscillations. Comparisons with experiments show good agreement except in regions where viscous effects are evident.

LIST OF SYMBOLS

A,B,C	= Jacobians of the fluxes E, F and G
CFL	= Courant-Friedrichs-Lewy number
c	= airfoil chord
c_{AC}	= mean aerodynamic chord
c_p	= pressure coefficient
c_r	= wing-root chord
CT	= Computational Test Case
E,F,G	= fluxes
e	= total energy per volume
Im( )	= imaginary part of ( )
J	= Jacobian of the inverse mapping
k	= reduced frequency
M	= Mach number
N	= number of time steps
p	= static pressure
Re( )	= real part of ( )
t, τ	= nondimensional time
U_∞	= freestream velocity
u,v,w	= velocity components in streamwise, normal and cross-stream directions, respectively
x,y,z	= nondimensional Cartesian coordinates in streamwise, spanwise and vertical directions, respectively
$\dot{x},\dot{y},\dot{z}$	= velocity components of the moving cell
$\alpha(t)$	= instantaneous angle of attack
α_0	= mean value of the angle of attack
α_1	= pitch oscillation amplitude
$,\alpha_1$	= nondimensionalized by α_1, per radian
γ	= ratio of specific heats
$\delta(t)$	= instantaneous angle of flap deflection
δ_1	= flap amplitude
$,\delta_1$	= nondimensionalized by δ_1, per radian
$\Delta t, \Delta\tau$	= time step
Δt/cycle	= number of time steps per cycle
$\Delta Mag(c_p^1)$	= magnitude of lifting pressure coefficient
$\Delta\phi(c_p^1)$	= phase between lifting pressure and wing pitch angle, deg (positive for pressure leading motion
λ	= eigenvalue
ρ	= density
ϕ	= conservative solution vector
ξ,η,ζ	= transformed nondimensional coordinates in x, y and z directions, respectively
ω	= underrelaxation factor, angular frequency

Subscripts

m	= mean value
max	= maximum
i,j,k	= cell index

Superscripts

n	= time index
μ	= nonlinear iteration state
ν	= Gauss-Seidel subiteration count
1	= first component of the Fourier analysis

1. INTRODUCTION

Transonic flow around oscillating airfoils and wings is characterized by the presence of subsonic and supersonic flow regions and moving shock waves of varying strength. To describe the inviscid transonic flow correctly the Euler equations must be solved. The assumptions and simplifications made in the potential equation restrict the codes based on them to flows with weak and moderately strong shocks (nonlinear potential equation) and to thin airfoils with small oscillation amplitudes (transonic small-perturbation method). As the Rankine-Hugoniot relations cannot be fulfilled by a full potential equation solver in conservative form, the shock position is predicted too far downstream. The nonconservative form, giving a better shock location, suffers from the drawback of false shock wave motion. The modifications of the conservative full potential equations, e.g., nonisentropic potential formulations or entropy corrections, to overcome the lack of uniqueness [1-3] is only a remedy to approximate the inviscid flow. Additionally, nowadays existing implicit unsteady Euler methods are as fast as full potential unsteady flow solvers since the latter require many iterations because of the circulation phase lag.

The first generation of unsteady Euler solver were based on explicit schemes [4-9]. In order to overcome the limitation of the global time step which is necessary to treat time-accurate unsteady prob-

THIS DOCUMENT PROVIDED BY THE ABBOTT AEROSPACE
TECHNICAL LIBRARY
ABBOTTAEROSPACE.COM

lems, and thus to reduce the large CPU times, implicit approximate-factorization (AF) schemes [10-12] and hybrid schemes [13] were introduced. However the optimal convergence of the approximate-factorization scheme in two-dimensional applications is obtained at a value of the time step that is not known a priori. It can be found by trial and error only and varies from problem to problem, although it usually corresponds to a CFL number of the order of 10 only. Additionally, in three dimensions the stability restrictions are stronger and reduce the maximum CFL number considerably. Therefore the saving of computational time in the AF scheme versus the explicit scheme is reduced further through extension from two to three dimensions.

Because of these drawbacks an implicit relaxation method solving the unfactored Euler equations was employed [14,15]. This unsteady solver INFLEX is based on the well proven steady Euler code EUFLEX [16] using characteristic flux extrapolation. The advantages of this iterative scheme, applicable to steady and time-accurate unsteady flows, are that it is unconditionally stable in a linear stability analysis both in two and three dimensions, the CFL number can be arbitrarily high and the maximum damping occurs at large time steps. Hence it is less sensitive to the choice of time step than the AF method. Furthermore, the algorithm used with its high degree of vectorization is optimally suited to supercomputers.

The present paper gives a short description of the Euler code developed in [14]. Applications of the two and three-dimensional versions INFLEX2 and INFLEX3 were made onto several AGARD standard configurations (conventional NACA 64A010 airfoil [17], supercritical NLR 7301 airfoil [18], high and low-aspect ratio wings [18,19]) and compared with measurements. The objective was to evaluate the accuracy, efficiency and range of applicability of the code and to get necessary knowledge for further developments.

2. GOVERNING EQUATIONS

The conservation law vector form of the three-dimensional, dimensionless unsteady Euler equations in curvilinear coordinates

$$\xi=\xi(x,y,z,t),\ \eta=\eta(x,y,z,t),\ \zeta=\zeta(x,y,z,t),\ \tau=t \qquad (1)$$

with the Cartesian velocity components u, v, w can be written as

$$\frac{\partial \phi}{\partial \tau}+\frac{\partial E}{\partial \xi}+\frac{\partial F}{\partial \eta}+\frac{\partial G}{\partial \zeta}=0. \qquad (2)$$

$\phi=J(\rho,\rho u,\rho v,\rho w,e)^T$ is the solution vector and

$$E = J(\tilde{E}\xi_x+\tilde{F}\xi_y+\tilde{G}\xi_z),$$

$$F = J(\tilde{E}\eta_x+\tilde{F}\eta_y+\tilde{G}\eta_z),$$

$$G = J(\tilde{E}\zeta_x+\tilde{F}\zeta_y+\tilde{G}\zeta_z), \qquad (3)$$

are the fluxes normal to the faces ξ=const., η=const. and ζ=const.

$$J=x_\xi(y_\eta z_\zeta-y_\zeta z_\eta)+x_\eta(y_\zeta z_\xi-y_\xi z_\zeta)+x_\zeta(y_\xi z_\eta-y_\eta z_\xi) \qquad (4)$$

is the Jacobian of the inverse mapping, representing the volume of the cell, and the quantities such as ξ_x, ξ_y etc. are the metrics of transformation related to the x,y,z-coordinate system through relationships, e.g.,

$$\xi_x=\frac{y_\eta z_\zeta-y_\zeta z_\eta}{J}, \qquad \xi_y=\frac{x_\zeta z_\eta-x_\eta z_\zeta}{J}. \qquad (5)$$

$\dot{x}$, $\dot{y}$ and $\dot{z}$ in the Cartesian fluxes

$$\tilde{E}=\begin{bmatrix}\rho(u-\dot{x})\\ \rho u(u-\dot{x})+p\\ \rho v(u-\dot{x})\\ \rho w(u-\dot{x})\\ e(u-\dot{x})+pu\end{bmatrix}, \qquad \tilde{F}=\begin{bmatrix}\rho(v-\dot{y})\\ \rho u(v-\dot{y})\\ \rho v(v-\dot{y})+p\\ \rho w(v-\dot{y})\\ e(v-\dot{y})+pv\end{bmatrix},$$

$$\tilde{G}=\begin{bmatrix}\rho(w-\dot{z})\\ \rho u(w-\dot{z})\\ \rho v(w-\dot{z})\\ \rho w(w-\dot{z})+p\\ e(w-\dot{z})+pw\end{bmatrix} \qquad (6)$$

are the velocity components of the moving cell, ρ is the density, p the pressure, and the total energy per unit volume for a perfect gas is

$$e=\frac{p}{\gamma-1}+\frac{1}{2}\rho(u^2+v^2+w^2). \qquad (7)$$

3. NUMERICAL METHOD

The time consistency which is required for the treatment of time-accurate unsteady problems means that the unsteady evolution must be computed with a uniform time step over the whole computational domain. This global time step is defined as

$$\Delta t \le \Delta t_{max}=\min_{i,j,k}\left(\frac{J\cdot CFL}{\lambda_{max}}\right)_{i,j,k}, \qquad (8)$$

where λ_{max} is the maximum eigenvalue of the cell i,j,k. Due to the restriction of the CFL number for explicit methods this can lead to an enormous number of time steps

$$N=\frac{T}{\Delta t}, \qquad (9)$$

dependent on the smallest cell in the computational domain (T is a characteristic time interval, e.g., period of oscillation or relaxation time).

In order to reduce the number of time steps per cycle and thus the overall computational time an implicit procedure, which allows time steps with CFL>>1, is applied to solve equation (2). The first order in the time-discretized implicit form of (2) reads

$$\frac{\phi^{n+1}-\phi^n}{\Delta\tau}+E_\xi^{n+1}+F_\eta^{n+1}+G_\zeta^{n+1}=0. \qquad (10)$$

Because of its nonlinearity this equation is not directly solvable for the dependent variable ϕ^{n+1}. Therefore a sequence of approximations denoted by ϕ^ν such that

$$\lim_{\nu\to\infty}\phi^\nu \to \phi^{n+1} \qquad (11)$$

is constructed.

Linearizing the fluxes

THIS DOCUMENT PROVIDED BY THE ABBOTT AEROSPACE
TECHNICAL LIBRARY
ABBOTTAEROSPACE.COM

$$E^{\mu+1} = E^{\mu} + \frac{\partial E^{\mu}}{\partial \phi}\,\Delta\phi^{\mu+1} + O(\Delta\tau^2) + \ldots,$$

$$F^{\mu+1} = F^{\mu} + \frac{\partial F^{\mu}}{\partial \phi}\,\Delta\phi^{\mu+1} + O(\Delta\tau^2) + \ldots, \qquad (12)$$

$$G^{\mu+1} = G^{\mu} + \frac{\partial G^{\mu}}{\partial \phi}\,\Delta\phi^{\mu+1} + O(\Delta\tau^2) + \ldots$$

around the iteration state μ, a nonlinear Newton method [20] can easily be yielded:

$$\frac{\Delta\phi^{\mu+1}}{\Delta\tau} + (A^{\mu}\cdot\Delta\phi^{\mu+1})_{\xi} + (B^{\mu}\cdot\Delta\phi^{\mu+1})_{\eta} + (C^{\mu}\cdot\Delta\phi^{\mu+1})_{\zeta} =$$

$$-\left[\frac{\phi^{\mu}-\phi^{n}}{\Delta\tau} + E_{\xi} + F_{\eta} + G_{\zeta}\right] = \mathrm{RHS}. \qquad (13)$$

The flux differences E_{ξ}, F_{η} and G_{ζ} are approximated via a third-order characteristic flux extrapolation scheme, using sensor functions to detect shocks, where the scheme reduces to first-order accuracy [16]. The principal feature of the characteristic flux extrapolation scheme is a Godunov-type averaging procedure based on an eigenvalue analysis of the Euler equations by means of which the fluxes are evaluated at the finite-volume face (linear locally one-dimensional Riemann solver) which separates constant sets of flow variables on either side. All nonlinear terms at time level μ are collected together in the quantity RHS (right-hand side). On the left-hand side (LHS) upwind differencing of order one or two is used. The solution vector $\Delta\phi^{\mu+1}$ from equation (13) leads to the update

$$\phi^{\mu+1} = \phi^{\mu} + \Delta\phi^{\mu+1}. \qquad (14)$$

Converging $\Delta\phi$ to zero on the LHS of equation (13), the implicit formulation of equation (10) with $\mu \rightarrow n+1$ remains on the RHS. A^{μ}, B^{μ} and C^{μ} are the true Jacobians of the fluxes E^{μ}, F^{μ} and G^{μ} at the nonlinear iteration state μ.

Because the numerical solution of the Newton method in two or more dimensions is too time-consuming and the application of an approximate-factorization scheme in three dimensions leads to tremendous time-step restrictions, a relaxation technique is used to solve the unfactored implicit Euler equations. The discretized form of equation (13) for a point Gauss-Seidel (GS) iteration reads

$$\left[\frac{I}{\Delta\tau} + \mathrm{DIAG}^{\mu}_{i,j,k}\right]\cdot\Delta\phi^{\mu+1,\nu+1}_{i,j,k} = \omega\cdot\mathrm{RHS}^{\mu}_{i,j,k} + \mathrm{ODIAG}_{i,j,k}, \qquad (15)$$

where $\mathrm{DIAG}^{\mu}_{i,j,k}$ is a 5*5 matrix containing the sum of the eigenvalue splitted Jacobians connected with $\Delta\phi_{i,j,k}$ and $\mathrm{ODIAG}_{i,j,k}$ consists of the complementary eigenvalue splitted Jacobians and the $\Delta\phi$'s of the neighboring points, [14,15].

ν indicates the GS-subiteration count and I is the identity matrix. The underrelaxation factor ω compensates for errors of different spatial orders of accuracy on RHS and LHS, thus ensuring convergence. During the ν-iterations DIAG^{μ} and RHS^{μ} rest at the level μ, whereas ODIAG is evaluated using the latest available values of $\Delta\phi$. By applying the so-called checkerboard scheme, in which points are divided into black and white ones, a high degree of vectorization is achieved.

In order to avoid singular behavior of the coefficient matrix $\overline{\mathrm{LHS}}$ (expression in the brackets of equation (15)) which causes sudden breakdowns of computer runs without any indications of divergence, the equation system (15) is modified, [14, 15]. Multiplying matrix $\overline{\mathrm{LHS}}$ by the transformation matrix M from the right, yields a new coefficient matrix, the diagonal elements of which cannot be zero. After solving the modified system, the solution vector must be substituted back. Because of the sparse nature of matrix M, which converts the conservative variables to the nonconservative ones, this matrix conditioning requires only a few operations.

4. BOUNDARY CONDITIONS

Due to the artificial boundaries of the computational domain and the physical condition at the solid body surface, two different types of boundary conditions have to be implemented into the code.

At the farfield boundaries formally all flow quantities are prescribed. The sign of the eigenvalues at the cell faces forming the farfield boundary is used to automatically select the proper characteristic variables from the data offered. This guarantees correct wave absorbtion at the farfield boundaries.

For inviscid flows the surface tangency condition dictates that the contravariant velocity is zero at the solid body surface. Depending on the structure of the grid used, either U, V or W given by

$$U = \rho(u-\dot{x})\xi_x + \rho(v-\dot{y})\xi_y + \rho(w-\dot{z})\xi_z,$$

$$V = \rho(u-\dot{x})\eta_x + \rho(v-\dot{y})\eta_y + \rho(w-\dot{z})\eta_z,$$

$$W = \rho(u-\dot{x})\zeta_x + \rho(v-\dot{y})\zeta_y + \rho(w-\dot{z})\zeta_z \qquad (16)$$

must be zero. This condition is also called the no-through flow condition, since the normal flux across the finite body element moved with $\dot{x}$, $\dot{y}$ and $\dot{z}$ vanishes.

5. GRID GENERATION

All calculations reported here were done on H-type (2D) and H-H type (3D) grids with fixed farfield boundaries. The meshes were generated using the higher-order elliptic grid-generation systems developed by Schwarz [21] which solve Poisson equations. Due to the inherent smoothness in solving elliptic systems and the fact that boundary slope discontinuities are not propagated into the field, solutions of elliptic systems are a convenient method for constructing boundary-fitted coordinate systems.

In order to completely specify the geometry of the first two grid cells adjacent to the boundary, a sixth-order system

$$\nabla^6 x^i = 0 \quad (i=1,2,3) \qquad (17)$$

is employed. This partial differential equation of the order six is implemented as three systems of second-order equations (Poisson and Laplace equations). These linear algebraic equations in the physical domain are discretized by central differences and solved with point Gauss-Seidel iterations. The resulting grid points $(x,y,z)_{i,j,k}$ and the source terms are stored. After each time step in the flowfield computation the wing surface is moved and the mesh is deformed, rearranged by one to two grid iterations. The checkerboard scheme is used to speed up the generation procedure as in the Euler solver.

This Document Provided by the Abbott Aerospace
TECHNICAL LIBRARY
ABBOTTAEROSPACE.COM

6. RESULTS

Applications of the two and three-dimensional codes (INFLEX2 and INFLEX3) were made onto AGARD standard configurations [22,23]

- NACA 64A010 airfoil,
- NLR 7301 airfoil,
- LANN wing,
- NORA wing

and were compared with measurements [24,25]. The configurations performed pitching oscillations with a harmonically varying angle of attack

$$\alpha(t) = \alpha_0 + Re(\alpha_1 \cdot e^{i\omega t}) = \alpha_0 + \alpha_1 \cdot \cos(\omega t) \qquad (18)$$

about an axis normal to the root chord except for the NORA wing which oscillates about a sweptback axis. Additionally, computations were done on the NLR 7301 airfoil with a harmonically rotating trailing-edge flap:

$$\delta(t) = Re(\delta_1 \cdot e^{i\omega t}) = \delta_1 \cdot \cos(\omega t). \qquad (19)$$

The reduced frequency, which is the important similarity parameter for flows with unsteady boundary conditions, is defined as

$$k = \frac{\omega \cdot c}{2U_\infty} . \qquad (20)$$

U_∞ is the freestream velocity and c either the chord length of the airfoil, the wing root c_r, or the mean aerodynamic chord length c_{AC}, and may not be confused with the velocity of sound. The surface pressure coefficient $c_{p(x/c,t)}$ is decomposed by Fourier analysis into the mean value of the local surface pressure coefficient $c_{p_m(x/c)}$ and the n-th complex component (real or in-phase and imaginary or out-of-phase parts) of the locally unsteady pressure coefficient per radian:

$$c_{p(x/c,t)} = c_{p_m(x/c)} + \sum_{n=1}^{\infty} Re\left((c^n_{p,\alpha_1(x/c)}) \cdot \alpha_1 e^{in\omega t} \right). \qquad (21)$$

All computations were carried out on the SIEMENS VP200 vector computer and were started with parallel flow. As the wave propagation is inversely proportional to the frequency and as the reduced frequency was low in most of the test cases examined, two to three cycles were required during which the transients died out and a periodic solution was obtained.

NACA 64A010

The conventional NACA 64A010 airfoil performed oscillations about the one-quarter point at a Mach number of 0.8. The reduced frequency varied between 0.01 and 0.303 with a mean value of the angle of attack α_0=0 deg and a pitch oscillation amplitude of α_1=1 deg. The airfoil geometry was taken from [26]. The grid used with 88 points in x and 48 points in z direction is shown in Fig. 1.

The comparison of the calculated mean pressure distribution with the experimental data is displayed in Fig. 2. The numerical and experimental results agree very well except in the region upstream of the shock. The overexpansion of the pressure may be attributed to wind-tunnel wall interferences. Calculations by King and Johnson [27] done with the experimentally measured wall-pressure boundary condition indicate that the discrepancies are due to blockage effects.

The components of the first harmonic analysis for six different reduced frequencies are shown in Fig. 3. The imaginary part increases as the real part decreases with increasing reduced frequency (especially upstream of the shock wave). For the limiting case k→0 (quasisteady), the out-of-phase component must disappear due to the vanishing dynamic effects. The reason for the minor change to the complex components aft of the shock wave is explained by the nature of the pressure response. In front of the shock the pressure response is sinusoidal, whereas it is nearly constant behind it, Fig. 4. The comparison of the local pressure coefficients with measurement and numerical results from Chyu and Davis [28] displays that for this conventional airfoil and flow condition viscous effects are small. Viscous effects are apparent in the shock region: Due to the lack of them a) the pressure rises abruptly when the shock moves upstream and b) the peak in the computational result during pressure recovery is caused by Zierep singularities. However, the hysteresis, the rapid pressure rise and the following pressure recovery due to the different velocity of wave propagation upstream and downstream is reproduced well.

The resulting pressure distribution (CT6: k=0.202) on the upper surface for the third cycle is plotted in Fig. 5. The shock-wave excursion and the increase and decrease of the shock strength can be seen very well. The shock wave reaches its maximum strength and its most downstream position with a phase shift to the angle of attack.

As the CPU time depends primarily on the number of time steps per cycle, computations were done to show the influence of CFL variations on the result, Fig. 6. The c_p-distribution with 25 Δt/cycle (CFL=3200) is shifted horizontally (to the left) with respect to the one with 200 Δt/cycle (CFL=400). This leads to an increase in the real part and a decrease in the imaginary part of the harmonic analysis. The reason for simulating a lower frequency by a higher CFL number is the dispersion error, induced by the truncation errors of the odd derivative terms. The investigations in [14] showed that 50 to 100 time steps per cycle are adequate to obtain a good result. The best quality with respect to the explicit one is obtained with 200 Δt/cycle. In order to get a first estimation only 25 Δt/cycle are sufficient. The computational efforts for various Δt/cycle and of the explicit solution are listed in Tab. 1. It can be seen that considerable CPU-time saving is possible by reducing time steps per cycle without loss of accuracy.

Detailed investigations in [14,15] showed that there is no influence of grid refinement on the accuracy of the unsteady pressures. However, emphasis should be placed on fine discretization at the leading edge and in the shock-wave region for good reproduction of the curvature and the suction peak and not to smooth out the shock by numerical viscosity.

NLR 7301

This airfoil represents the category of modern supercritical airfoils, which are characterized by a blunt nose, a high thickness ratio (t/c=16.5%) and an extended supercritical flow region. It was designed for shock-free flow at M=0.721 and α_0 = -0.19 deg by Boerstoel [29]. The airfoil geometry was taken from [22] and the results were compared with the experimental data set 4 from [24]. The computational mesh used, Fig. 7, has 108 points in x and 74 points in z direction. Each surface is covered by 50 nodes.

Pitching Oscillation

The pitching axis is located at 40 percent of the

THIS DOCUMENT PROVIDED BY THE ABBOTT AEROSPACE
TECHNICAL LIBRARY
ABBOTTAEROSPACE.COM

chord. The calculated mean pressure and the first harmonic analysis for the design condition (CT8: M=0.721, k=0.181, α_0=-0.19 deg, α_1=0.5 deg) are compared with measurement in Fig. 8. On the upper surface the computed c_{p_m} shows two weak shocks at about x/c=0.25 and x/c=0.6 in contrast to the measurement plateau. The real and imaginary parts on the lower surface are predicted well, whereas on the upper surface agreement is poor. Only the qualitative behavior is reproduced.

The local pressure coefficients on the upper surface, Fig. 9, display the following behavior: pure sinusoidal, but with a phase shift with respect to the angle of attack in the most upstream locations on the airfoil (points A, B and C), severe harmonic distortion in the supersonic region and minimal response downstream of the shock. Only the pressure distribution of points H and I, lying in the shock region, are showing the same feature as the ones of the NACA 64A010 airfoil: rapid pressure rise and following pressure recovery.

The sensitivity of the flow to changes in free-stream Mach number, incidence and location of transition strip (dashed-dotted line in Fig. 8) is discussed in [30]. The influence of the boundary layer on the c_p-distribution is demonstrated in Fig. 10 for the subcritical flow (CT2: M=0.5, k=0.262, α_0=0.4 deg, α_1=0.5 deg) by coupling the Euler solution with a first-order boundary-layer solution [31]. The boundary layer causes an increase of pressure on the upper and a decrease on the lower surface. The calculated c_{p_m} with the boundary layer correlates much better than without it. No differences were noticed in the real and imaginary parts at this low free-stream Mach number. However, when shocks appear, the situation changes dramatically: Due to the downshift position of the shock in c_{p_m} and the overprediction of the shock strength, the peak in the unsteady components is overpredicted and shifted rearwards, too. Two different effects are responsible for the discrepancies between inviscid and viscous flow: First, shock-boundary layer interactions which reduce the pressure rise and shift the shock location upstream with respect to the inviscid flow. The viscous displacement ramp converts the normal shock of an inviscid flow to an oblique shock yielding a reduced pressure rise. Secondly, the differing displacement thickness on upper and lower surface decambers the airfoil, changes the geometry (chord to thickness ratio, incidence), and displaces the shock. Investigations with respect to changes in geometry are reported in [14] (results and comparison with the NASA Ames model).

Oscillating Flap

The hinge point of the trailing-edge flap is located at x/c=0.75. Evaluations were made for the test cases
- CT10: M=0.500, k=0.098, α_0=0.4 deg, δ_1=1.0 deg and
- CT12: M=0.721, k=0.067, α_0=-0.19 deg, δ_1=1.0 deg.

The comparison of the calculated mean pressure distribution with the measured one for the subsonic case CT10, Fig. 11, shows both on the upper and lower surface discrepancies in level. The results obtained with the geometry of the wind-tunnel model and with the corresponding flow conditions are plotted in order to demonstrate that slight changes of the geometry and flow condition cause considerably variations in the c_p-distribution (dotted and chain-dotted lines). The unsteady pressure distribution, expressed as real and imaginary parts are not affected by this variation of parameters. The correlation with the experimental data is very good.

The situation is quite different for the supercritical design case CT12. Both the c_{p_m} and the in-phase and out-of-phase components are influenced severely. Additional to the shock-boundary layer interaction and the effect of decambering of the airfoil, already observed and discussed for the harmonically pitching NLR 7301 airfoil another effect of viscosity appears: The reduction of the effective flap angle by the boundary layer. Due to Magnus and Yoshihara [32] this is the main reason for the large deviations between the numerical and experimental results.

LANN Wing

This wing, tested at the NASA Langley Research Center is a typical transport-type wing with a high aspect ratio, leading- and trailing-edge sweep and supercritical airfoils. The planform with the location of the six spanwise sections for the pressure evaluation and the surface mesh is shown in Fig. 13. The wing tip is formed by connecting the lower and upper surface with semi-circular arcs. The pitching axis is located at 62.1 percent of the root chord from the wing apex. Rigid body motion was assumed. The computation was performed on a grid with 80*38*46 points and with 100 Δt/cycle.

The results presented here refer to the
- subcritical transonic test case CT2: M=0.77, k_{Ac}=0.080 and to the
- design cruise condition CT5: M=0.82, k_{Ac}=0.076.

α_0 and α_1 were 0.6 deg and 0.25 deg, respectively, in both test cases.

The comparison between the computed mean surface pressure distribution and the experimental one is favorable at all span stations, Fig. 14. The suction peak at the leading edge is reproduced exactly. Only a slight underprediction of the upper-surface pressure downstream of the shock is observed. Discrepancies in the recompression area on the lower surface towards the trailing edge are due to viscous effects changing the airfoil geometry. The in-phase and out-of-phase components are predicted accurately, both on the lower and on the upper surface, Fig. 15 and Fig. 16. Computation and measurement give values of the same order of magnitude in the shock region ($Re(-c_p{}^1, \alpha_1)$=-66.93 at x/c=0.15 at the fractional section η=0.65 on the upper surface is not plotted).

The mean pressure distribution (Fig. 17), the real (Fig. 18) and the imaginary parts (Fig. 19) are in good agreement with experimental data on the lower surface. On the upper surface the leading-edge suction peak of the mean pressure distribution is represented exactly at all fractional sections. Due to the shift of the shock location aft of the measured shock position and the overprediction of the shock strength, indicating that noticeable viscous effects are present in the real flow, the peaks in the in-phase and out-of-phase components are shifted downwards and overpredicted, too. With the exception of this, the unsteady pressures are reproduced well by INFLEX3.

NORA Wing

The NORA wing shown in Fig. 20 is characterized by a small aspect ratio, a large leading-edge sweep, and a high taper ratio. The computational model differs somewhat from the experimental one: The wind-tunnel model has a round sharped wing tip and the analytical model a cropped streamwise tip

THIS DOCUMENT PROVIDED BY THE ABBOTT AEROSPACE
TECHNICAL LIBRARY
ABBOTTAEROSPACE.COM

[24]. The airfoil geometry is based on the symmetric NACA 63006 profile with a modified thickness ratio of about 5 percent and a small updroop near the nose [23]. Rigid body motion was assumed about a 35 deg sweptback axis intersecting the root chord at x/c_r=0.526. The angular displacement is measured in a streamwise plane parallel to the plane y=0. The calculation of the transonic test case (M=0.95, k_r=0.27, α_0=0.0 deg, α_1=0.5 deg) was performed on a grid with 106*54*58 points and a CFL number equivalent to 100 Δt/cycle. The numerical results were compared with measurements from the NLR High Speed Tunnel (HST) and from the ONERA Modane (S2) tunnel. In both tunnels the experiments were carried out using the same techniques with the same instrumentation. Hence discrepancies are due to tunnel interference, the character of the tunnel flow and consistency of the parameter settings.

Although there exist no experimental data for the mean pressure distribution the numerical result on six span stations is included, Fig. 21. The suction peak with the following recompression at the leading edge on the upper surface is due to the updroop nose. The tendency observed in the local Mach number distribution in [24] that the shock is moving upstream stepping towards the wing tip is reproduced.

The comparison between the computed real and imaginary parts of the harmonic analysis and the experimental ones is favorable at both span stations examined, Fig. 22 and Fig. 23. The suction peak of the real part at the leading edge of the upper surface is represented exactly. The fluctuations of the measured data, especially upstream of the shock, may be attributed to irregularities of the wing surface geometry, because they occur in both measurements. The computation predicts a shock position located slightly upstream of the experimental ones. This shift is probably due to the sensitivity of the pressure distribution to small variations of Mach number, Fig. 24 and Fig. 25.

7. CONCLUSIONS

A relaxation method solving the unfactored implicit Euler equations was applied to compute time-accurate unsteady transonic flows about two and three-dimensional AGARD standard configurations with conventional and supercritical airfoils. The airfoil and wings performed harmonic pitching oscillations and flap oscillations. Relaxation is performed with a point Gauss-Seidel technique with the so-called checkerboard scheme ensuring a high degree of vectorization.

Investigations with respect to grid refinement and variation of CFL number showed that there is no influence of grid refinement on the accuracy of the unsteady pressures. 50 to 100 time steps per cycle are sufficient. The numerical results showed good agreement with experimental data in cases where viscous effects are negligible (leading-edge region, conventional airfoils). However, the results on supercritical airfoils demonstrated that viscous effects should be taken into account for this type of airfoil. Due to the absence of viscosity in the numerical procedure the shock strength is overpredicted and the location of the shock aft of the experimental shock position. Three-dimensional effects were simulated very well.

The advantages of this iterative scheme, applicable to steady and time-accurate unsteady flows, are that it reduces considerably the computational times with respect to explicit codes and that it is unconditionally stable in a linear stability analysis both in two and three dimensions. The CFL number can be arbitrarily high and the maximum damping occurs at large time steps. The acceleration factor is maintained by extension from two to three dimensions. This fact is one of the great advantages of the relaxation method employed.

REFERENCES

[1] Klopfer, G.H., Nixon, D., "Nonisentropic Potential Formulation for Transonic Flows," AIAA Paper 83-0375, January 1983.

[2] Hafez, M.M., Lovell, D., "Entropy and Vorticity Correction for Transonic Flows," AIAA Paper 83-1926, July 1983.

[3] Whitlow, W.,Jr., Hafez, M.M., Osher, S.J., "An Entropy Correction Method for Unsteady Full Potential Flows with Strong Shocks," AIAA Paper 86-1768-CP, June 1986.

[4] Magnus, R.J., Yoshihara, H., "Unsteady Transonic Flows over an Airfoil," AIAA Journal, Vol. 13, No. 12, Dec. 1975, pp. 1622-1628.

[5] Jameson, A., Venkatakrishnan, V., "Transonic Flows about Oscillating Airfoils Using the Euler Equations," AIAA Paper 85-1514, 1985.

[6] Smith, G.E., Whitlow, W.Jr., Hassan, H.A., "Unsteady Transonic Flows past Airfoils Using the Euler Equations," AIAA Paper 86-1764-CP, June 1986.

[7] Deslandes, R., "Eine Explizite Methode zur Lösung der Eulergleichungen Angewandt auf Instationäre Ebene Strömungen," MBB/LKE121/S/PUB/257, 1986.

[8] Belk, D.M., Janus, J.M., Whitfield, D.L., "Three-Dimensional Unsteady Euler Equations Solutions on Dynamic Grids," AIAA Paper 85-1704, July 1985.

[9] Jameson, A., Schmidt, W., Turkel, E., "Numerical Solutions of the Euler Equations by Finite Volume Methods Using Runge-Kutta Time-Stepping Schemes," AIAA Paper 81-1259, June 1981.

[10] Steger, J.L., "Implicit Finite-Difference Simulation of Flow about Arbitrary Two-Dimensional Geometries," AIAA Journal, Vol. 16, No. 7, July 1978, pp. 679-686.

[11] Chyu, W.J., Davis, S.S., Chang, K.S., "Calculation of Unsteady Transonic Flow over an Airfoil," AIAA Journal, Vol. 19, No. 6, June 1981, pp. 684-690.

[12] Chyu, W.J., Davis, S.S., "Numerical Studies of Unsteady Transonic Flow over an Oscillating Airfoil," In AGARD CP-374: "Transonic Unsteady Aerodynamics and Its Aeroelastic Applications," Paper No. 3, Jan. 1985.

[13] Sankar, N.L., Wake, B.E., Lekoudis, S.G., "Solution of the Unsteady Euler Equations for Fixed and Rotor Wing Configurations," Journal of Aircraft, Vol. 23, No. 4, April 1986, pp. 283-289.

[14] Brenneis, A., "Berechnung Instationärer Zwei- und Dreidimensionaler Strömungen um Tragflügel Mittels eines Impliziten Relaxationsverfahrens zur Lösung der Eulergleichungen," Doctoral Thesis, UniBw München, FORTSCHRITT-BERICHT VDI 7/165, Düsseldorf, 1989.

[15] Brenneis, A., Eberle, A., "Application of an Implicit Relaxation Method Solving the Euler Equations for Time-Accurate Unsteady Problems," Journal of Fluids Engineering, Vol. 112, Dec. 1990, pp. 510-520.

[16] Eberle, A., "3D Euler Calculations Using Characteristic Flux Extrapolation," AIAA Paper 85-0119, 1985.

[17] Brenneis, A., Eberle, A., "Unsteady Transonic Flows past Airfoils Using a Fast Implicit Godunov-Type Euler Solver," Proceedings of the 7th GAMM Conference on Num. Meth. in

THIS DOCUMENT PROVIDED BY THE ABBOTT AEROSPACE
TECHNICAL LIBRARY
ABBOTTAEROSPACE.COM

Fluid Mechanics (ed.: Deville, M.), Notes on Numerical Fluid Mechanics, Vol. 20, Vieweg, Braunschweig-Wiesbaden, 1988, pp. 37-47.

[18] Brenneis, A., Eberle, A., "Unsteady Transonic Flows past Airfoils and Wings Using a Fast Implicit Godunov-Type Euler Solver," 16th Congress of the International Council of the Aeronautical Sciences. August 28 to September 2, 1988, Jerusalem/Israel.

[19] Schmatz, M.A., Brenneis, A., Eberle, A., "Verification of an Implicit Relaxation Method for Steady and Unsteady Viscous and Inviscid Flow Problems," In AGARD-CP-437: "Validation of Computational Fluid Dynamics", 2nd to 5th May, 1988, Lisbon/Portugal.

[20] Chakravarthy, S.R., "Relaxation Methods for Unfactored Implicit Upwind Schemes," AIAA Paper 84-0165, 1984.

[21] Schwarz, W., "Elliptic Grid Generation System for Three-Dimensional Configurations Using Poisson Equations," Numerical Grid Generation in Computational Fluid Dynamics, 1st. ed., Pineridge Press, 1986, pp. 341-352.

[22] Bland, S.R., "AGARD Two-Dimensional Aeroelastic Configurations", AGARD-AR-156.

[23] Bland, S.R., "AGARD Three-Dimensional Aeroelastic Configurations", AGARD-AR-167.

[24] "Compendium of Unsteady Aerodynamic Measurements," AGARD-R-702, August 1982.

[25] Zwaan, R.J., "LANN Wing. Pitching Oscillation," Data Set 9, AGARD-R-702, Compendium of Unsteady Aerodynamic Measurements, Addendum No. 1, 1982.

[26] Abbott, I.H., von Doenhoff, A.E., "Theory of Wing Sections," Dover Publications Inc., New York, 1958.

[27] King, L.S., Johnson, D.A., "Calculations of Transonic Flow About an Airfoil in a Wind Tunnel," AIAA Paper 80-1366, 1980.

[28] Chyu, W.J., Davis, S.S., " Numerical Studies of Unsteady Transonic Flows over an Oscillating Airfoil," In AGARD CP-374: "Transonic Unsteady Aerodynamics and its Aeroelastic Applications", Paper No. 3, 1985.

[29] Boerstoel, J.W., van Egmond, J.A., "Design of Shock Free, Basic Aerofoils for a Supercritical Wing,", NLR TR 75059 C, 1975.

[30] Tijdeman, H., "Investigations of the Transonic Flow around Oscillating Airfoils," NLR TR 77090 U, 1977.

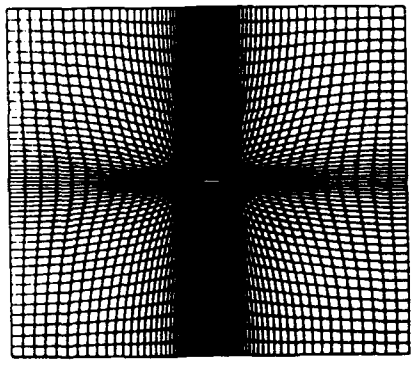
[31] Monnoyer, F., "SOB2D, a FORTRAN Program for the Calculation of Two-Dimensional Boundary Layers," MBB-LKE122-AERO-MT-780, 1987.

[32] Magnus, R.J., Yoshihara, H., "Calculation of the Transonic Oscillating Flap with 'Viscous' Displacement Effects," AIAA Paper 76-0327, July 1976.

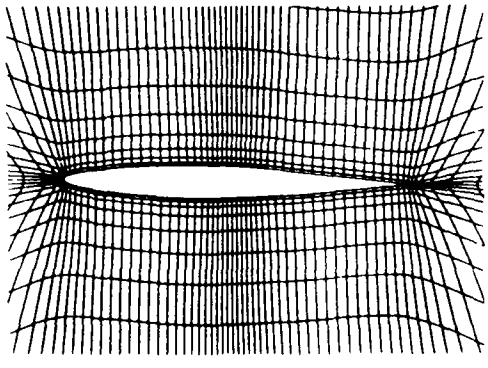
Tab. 1 Comparison of the CPU times of the explicit and implicit algorithm for the NACA 64A010, CT6

	explicit[1]	implicit			
CFL	0.4	400	800	1600	3200
Δt/cycle	17580	200	100	50	25
CPU [min/cycle] (SIEMENS VP200)	20.6	3.9	2.1	1.46	0.8

[1] The explicit algorithm was applied to a modified mesh with the wake cells being discarded. This causes an acceleration of the explicit code by a factor of ten.



a) overall view



b) partial view

Fig. 1 Computational mesh for the NACA 64A010 airfoil (88*48 points)

THIS DOCUMENT PROVIDED BY THE ABBOTT AEROSPACE
TECHNICAL LIBRARY
ABBOTTAEROSPACE.COM

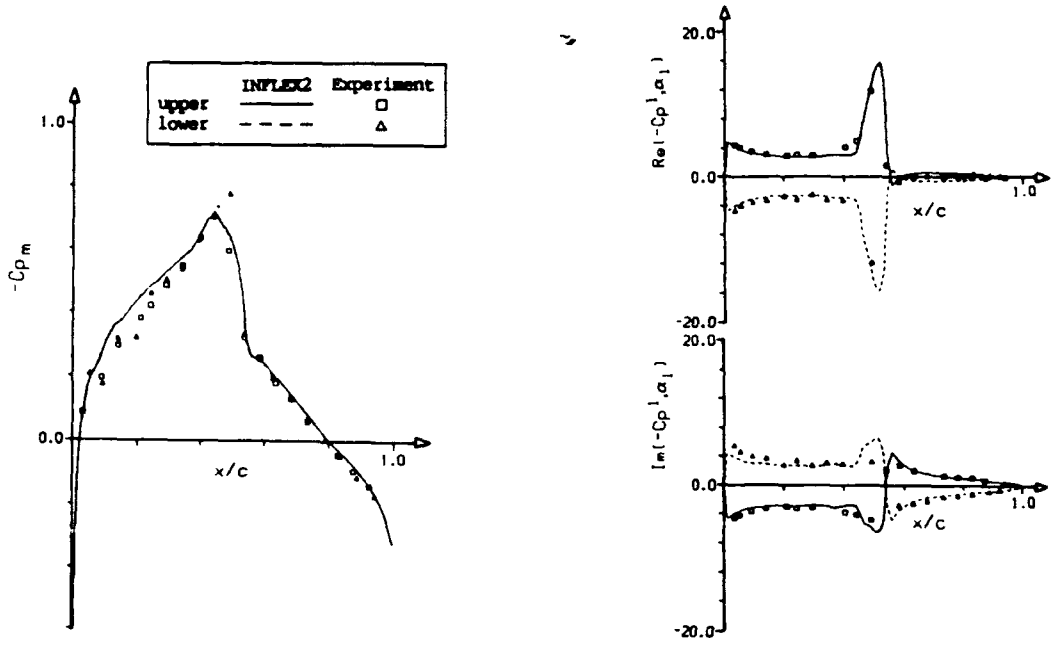


Fig. 2 Comparison of the measured and calculated mean and unsteady pressure distribution over the NACA 64A010, CT6: M=0.8, k=0.202, α_0=0.0 deg, α_1=1.0 deg

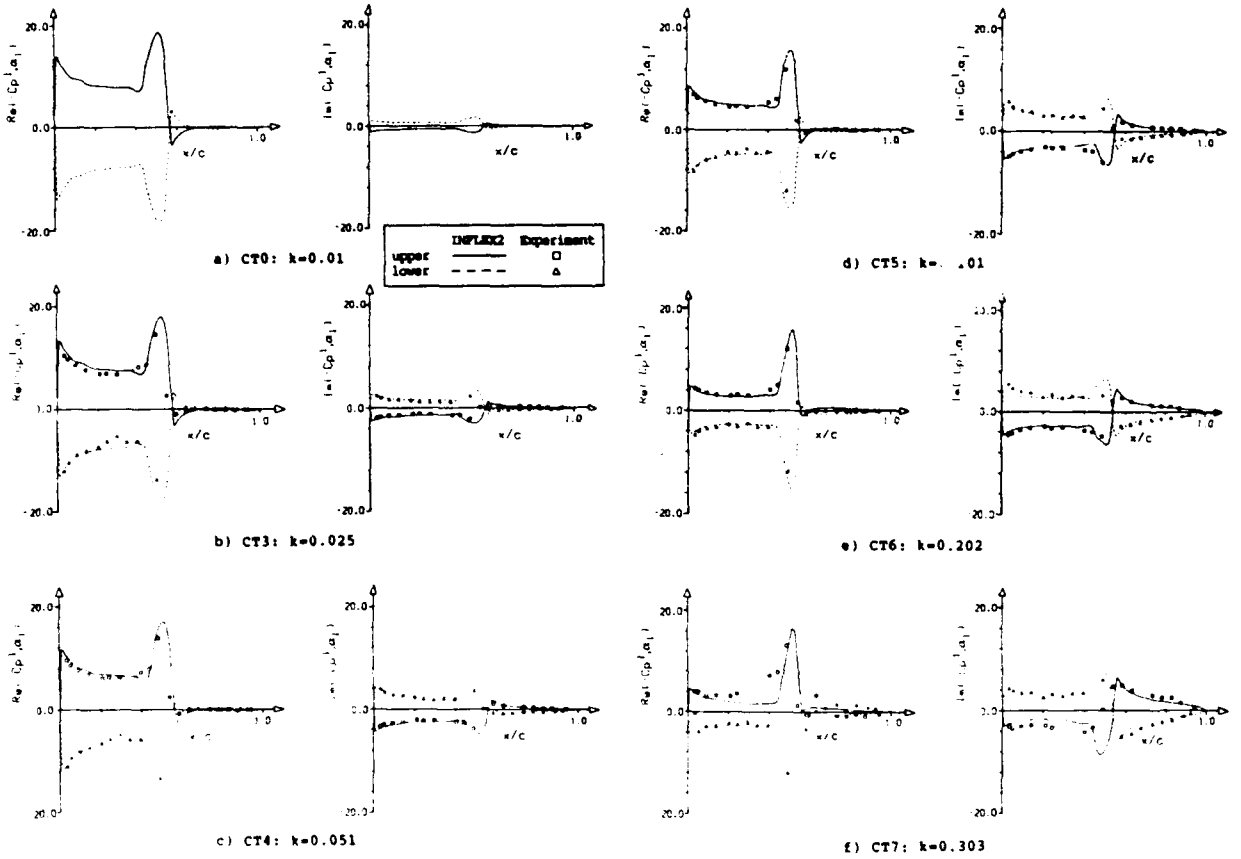


Fig. 3 Comparison of the unsteady pressure distribution for the NACA 64A010. M=0.8, α_0=0.0 deg, α_1=1.0 deg

THIS DOCUMENT PROVIDED BY THE ABBOTT AEROSPACE
TECHNICAL LIBRARY
ABBOTTAEROSPACE.COM

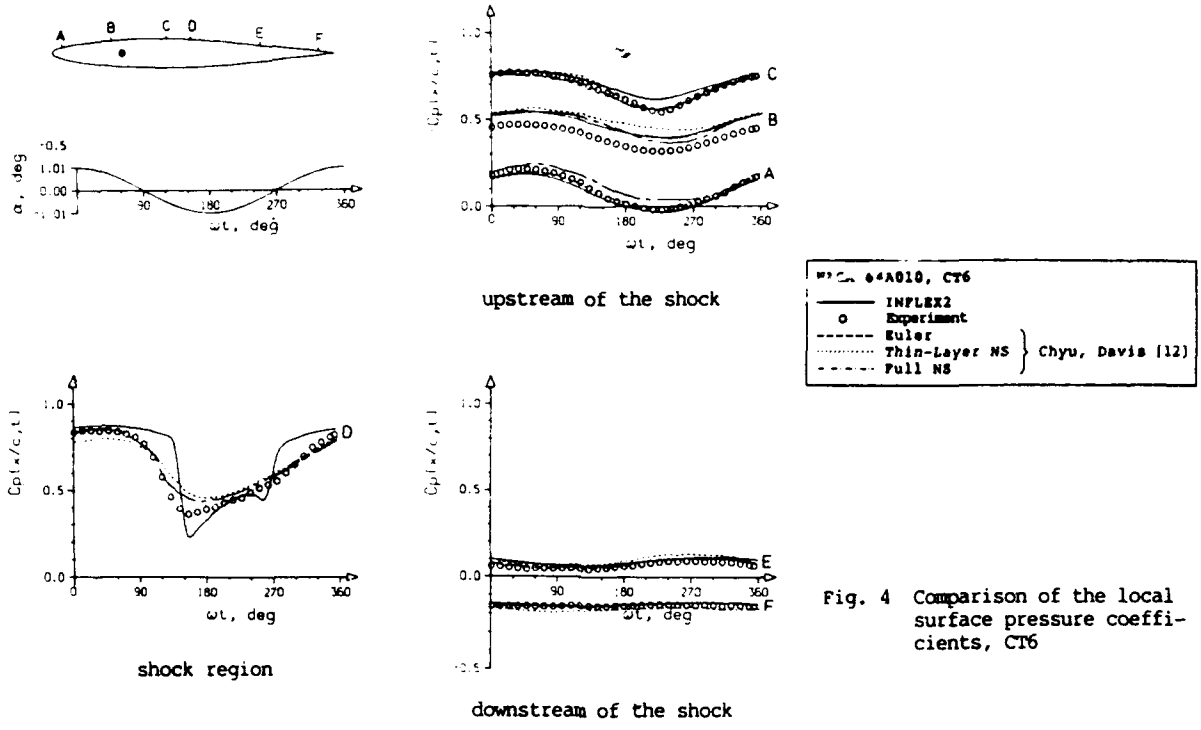


Fig. 4 Comparison of the local surface pressure coefficients, CT6

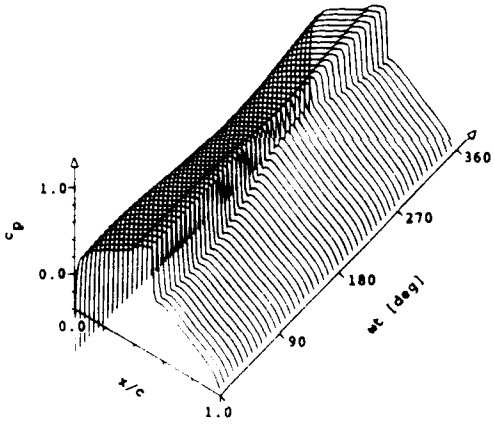


Fig. 5 Time history of the upper-surface pressure coefficients for the third cycle, NACA 64A010, CT6: M=0.8, k=0.202, α_0=0.0 deg, α_1=1.0 deg

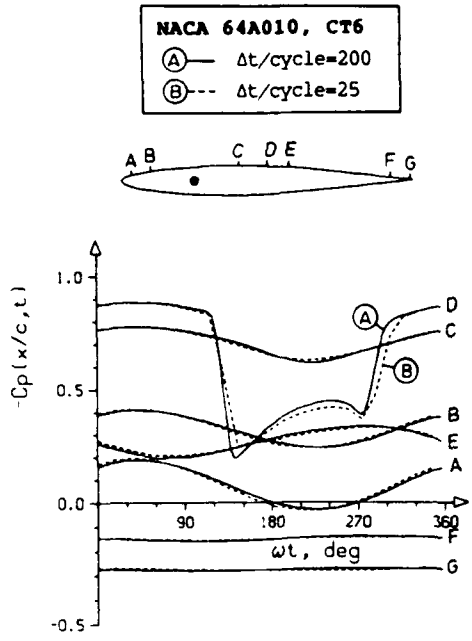


Fig. 6 Comparison of the local pressure coefficients on the upper surface at various CFL numbers, CT6

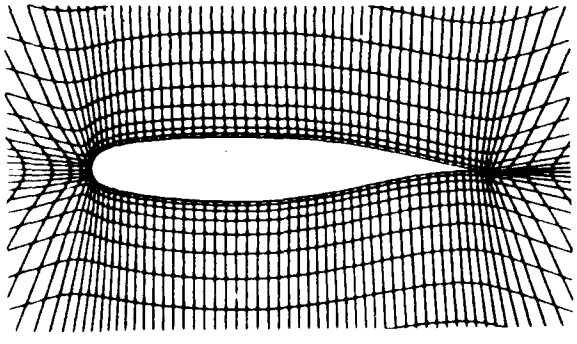


Fig. 7 Partial view of the computational mesh for the NLR 7301 airfoil (108*74 points)

THIS DOCUMENT PROVIDED BY THE ABBOTT AEROSPACE
TECHNICAL LIBRARY
ABBOTTAEROSPACE.COM

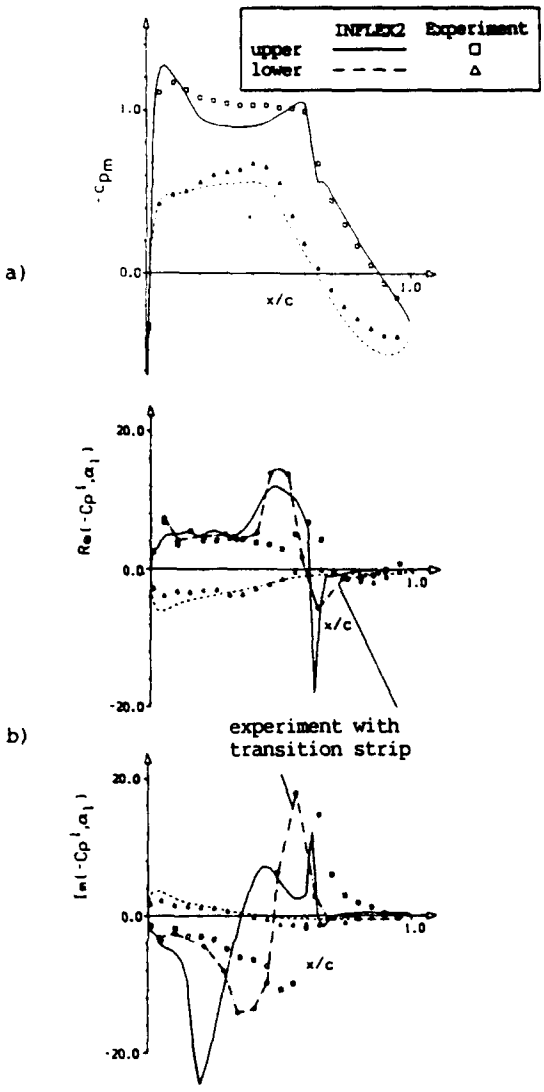


Fig. 8 Comparison of the measured and calculated mean (a) and unsteady pressure (b) distribution over the NLR 7301. M=0.721, k=0.181, α_0=-0.19 deg, α_1=0.5 deg

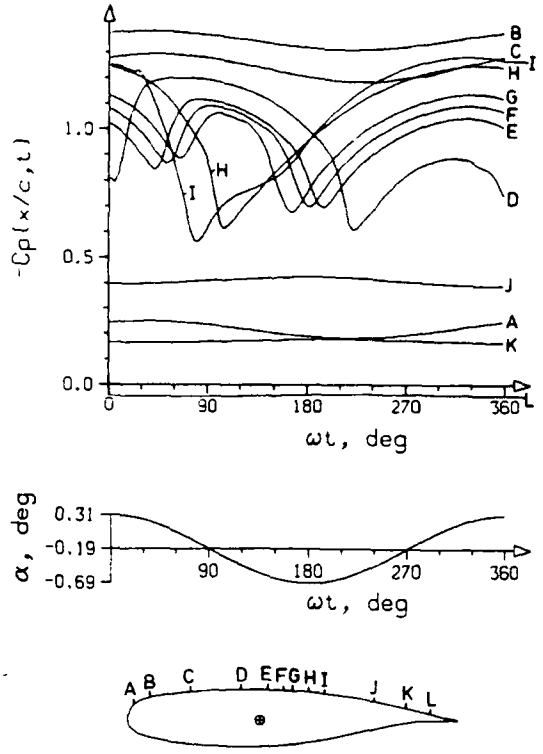
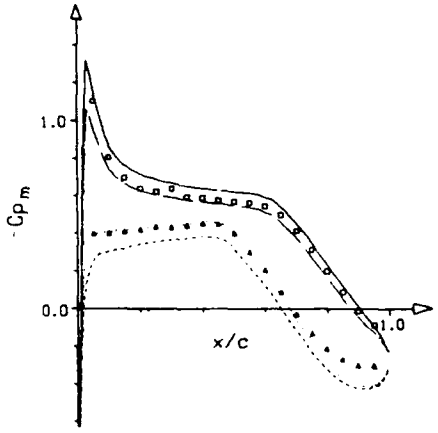
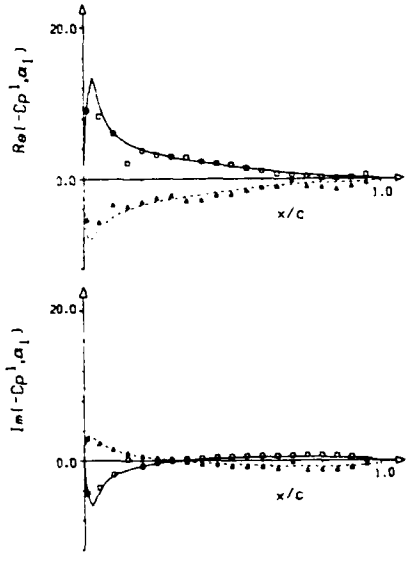


Fig. 9 Local surface pressure coefficients on the NLR 7301 airfoil, CT8





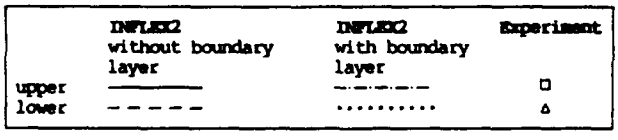


Fig. 10 Comparison of the mean and unsteady pressure distribution with and without boundary layer over the NLR 7301. M=0.5, α_0=0.4 deg, α_1=0.5, k=0.262

THIS DOCUMENT PROVIDED BY THE ABBOTT AEROSPACE
TECHNICAL LIBRARY
ABBOTTAEROSPACE.COM

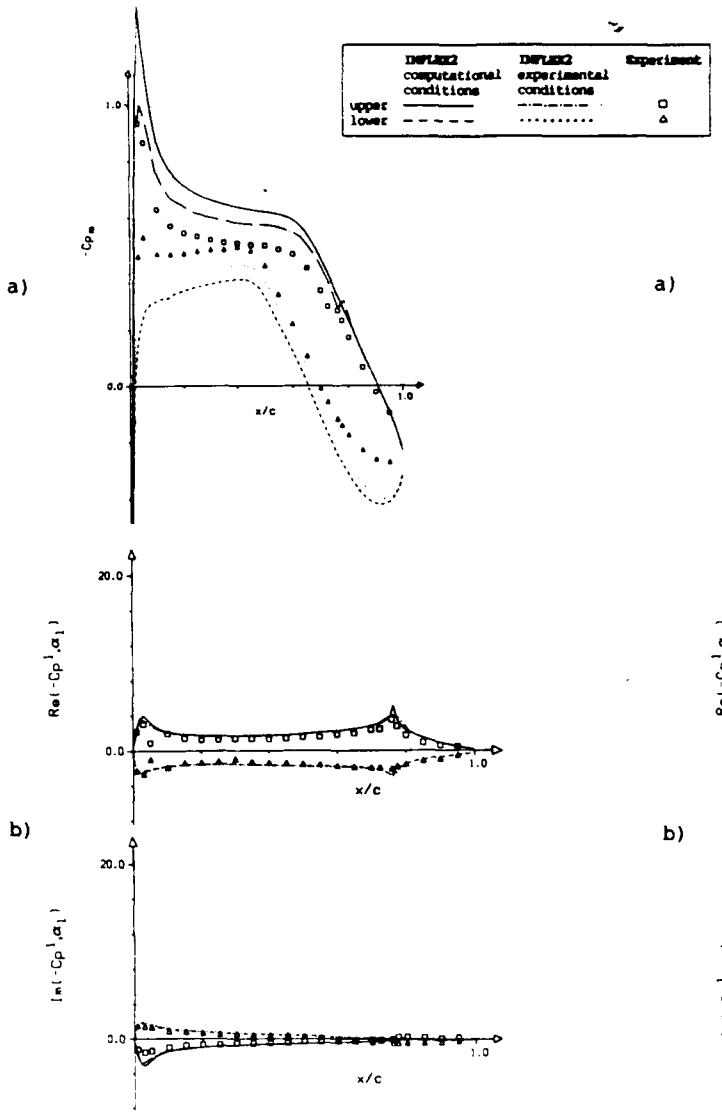


Fig. 11 Comparison of the measured and calculated mean (a) and unsteady pressure (b) distribution over the NLR 7301 airfoil with oscillating flap. CT10: M=0.5, k=0.098, α_0=0.4 deg, δ_1=1.0 deg

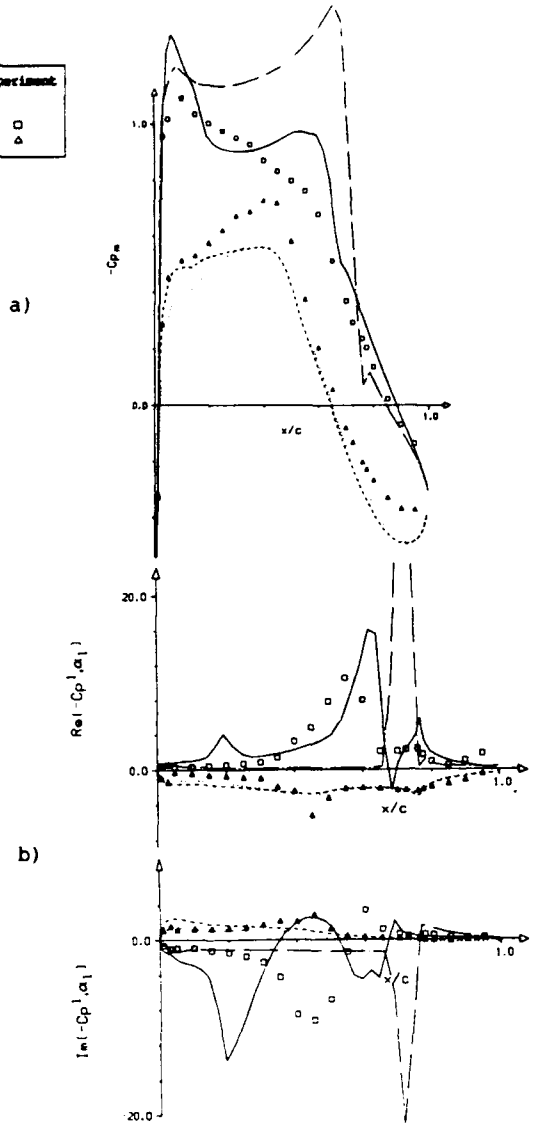


Fig. 12 Comparison of the measured and calculated mean (a) and unsteady pressure (b) distribution over the NLR 7301 airfoil with oscillating flap. CT12: M=0.7, k=0.067, α_0=-0.19 deg, δ_1=1.0 deg

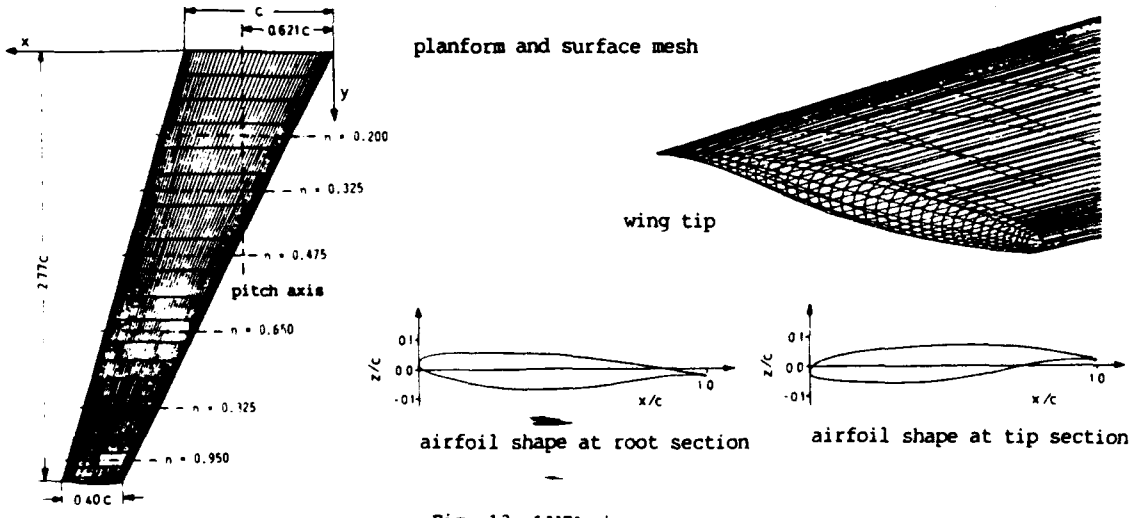


Fig. 13 LANN wing

THIS DOCUMENT PROVIDED BY THE ABBOTT AEROSPACE
TECHNICAL LIBRARY
ABBOTTAEROSPACE.COM

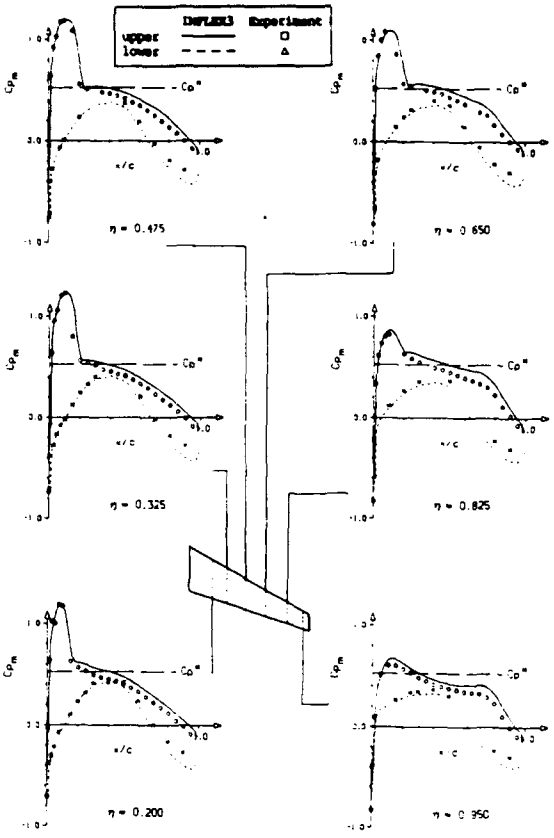


Fig. 14 Spanwise comparison of the mean pressure distribution over the LANN wing, CT2

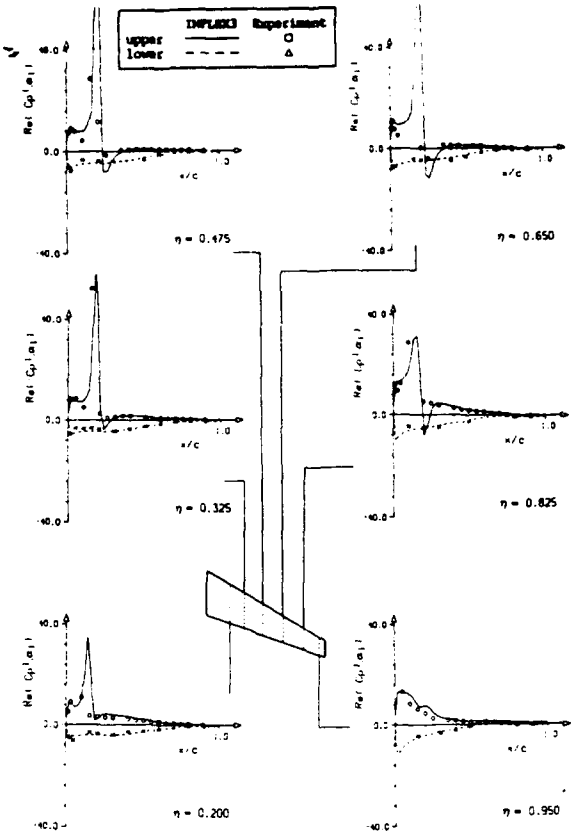


Fig. 15 Spanwise comparison of the in-phase component on the LANN wing, CT2

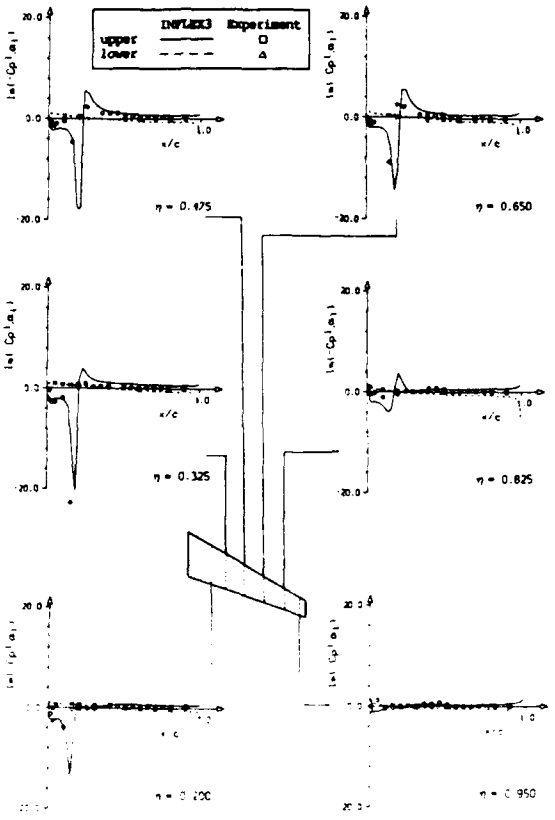


Fig. 16 Spanwise comparison of the out-of-phase component on the LANN wing, CT2

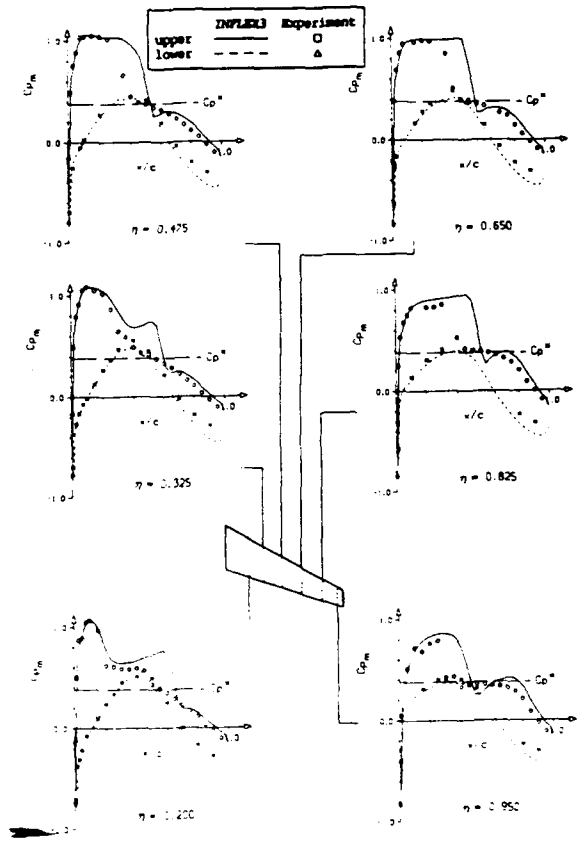


Fig. 17 Spanwise comparison of the mean pressure distribution over the LANN wing, CT5

THIS DOCUMENT PROVIDED BY THE ABBOTT AEROSPACE
TECHNICAL LIBRARY
ABBOTTAEROSPACE.COM

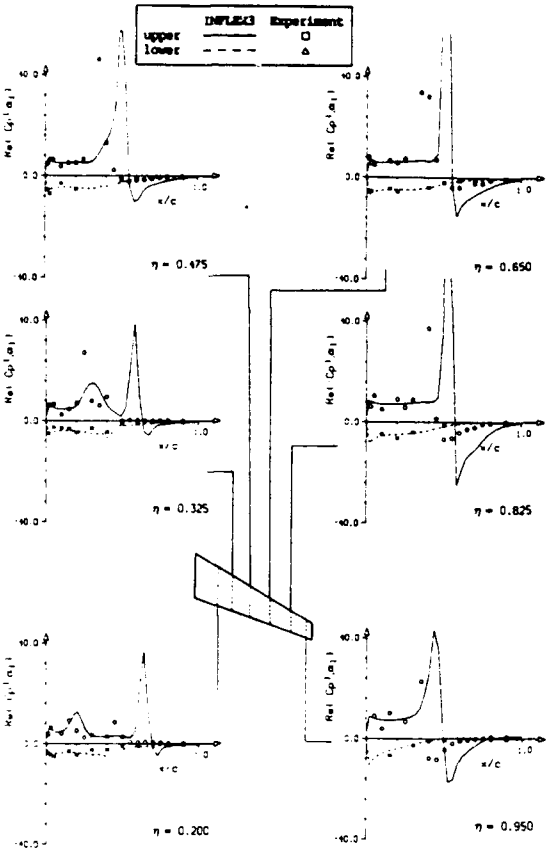


Fig. 18 Spanwise comparison of the in-phase component on the LANN wing, CT5

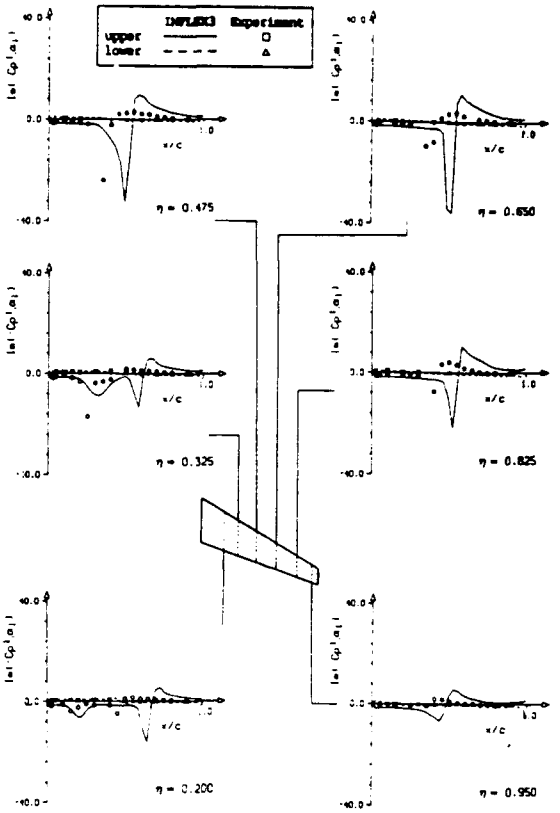


Fig. 19 Spanwise comparison of the out-of-phase component on the LANN wing, CT5

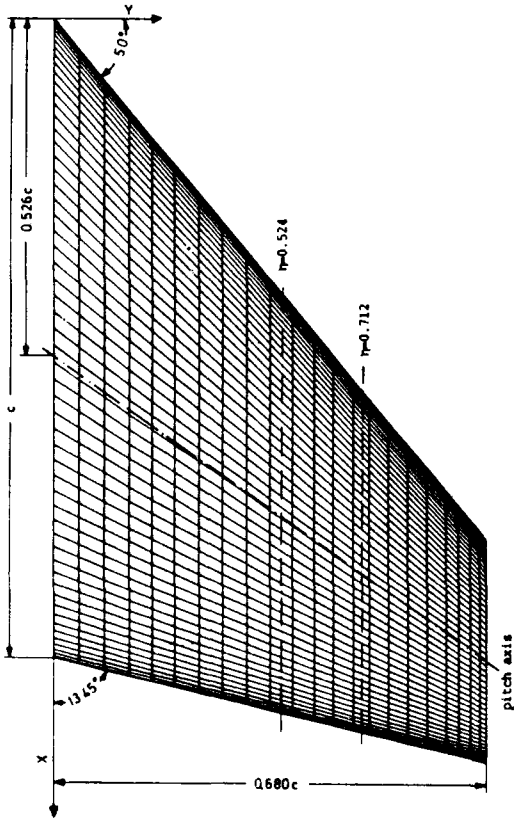


Fig. 20 NORA wing

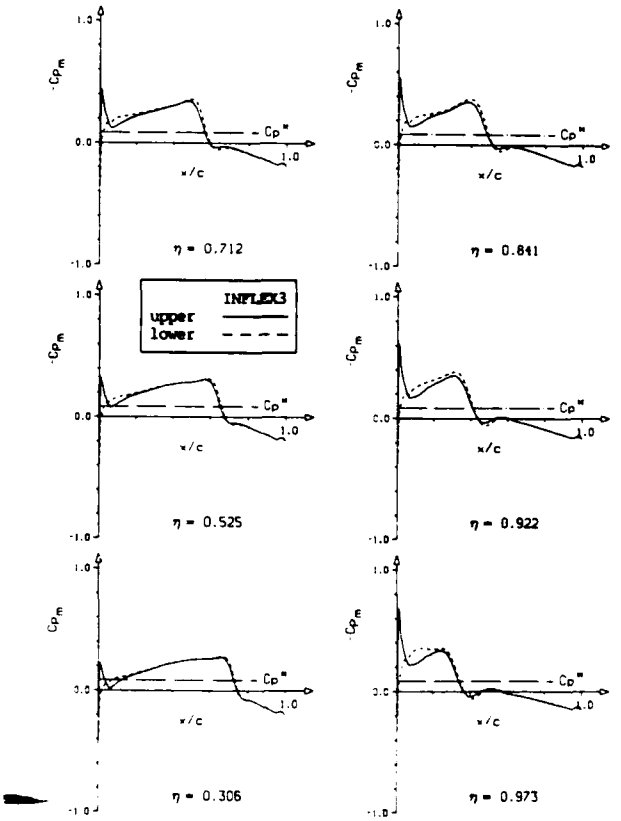


Fig. 21 Calculated mean pressure distribution over the NORA wing. CT6: M=0.95, k_r=0.27, α_0=0.0 deg, α_1=0.5 deg

THIS DOCUMENT PROVIDED BY THE ABBOTT AEROSPACE
TECHNICAL LIBRARY
ABBOTTAEROSPACE.COM

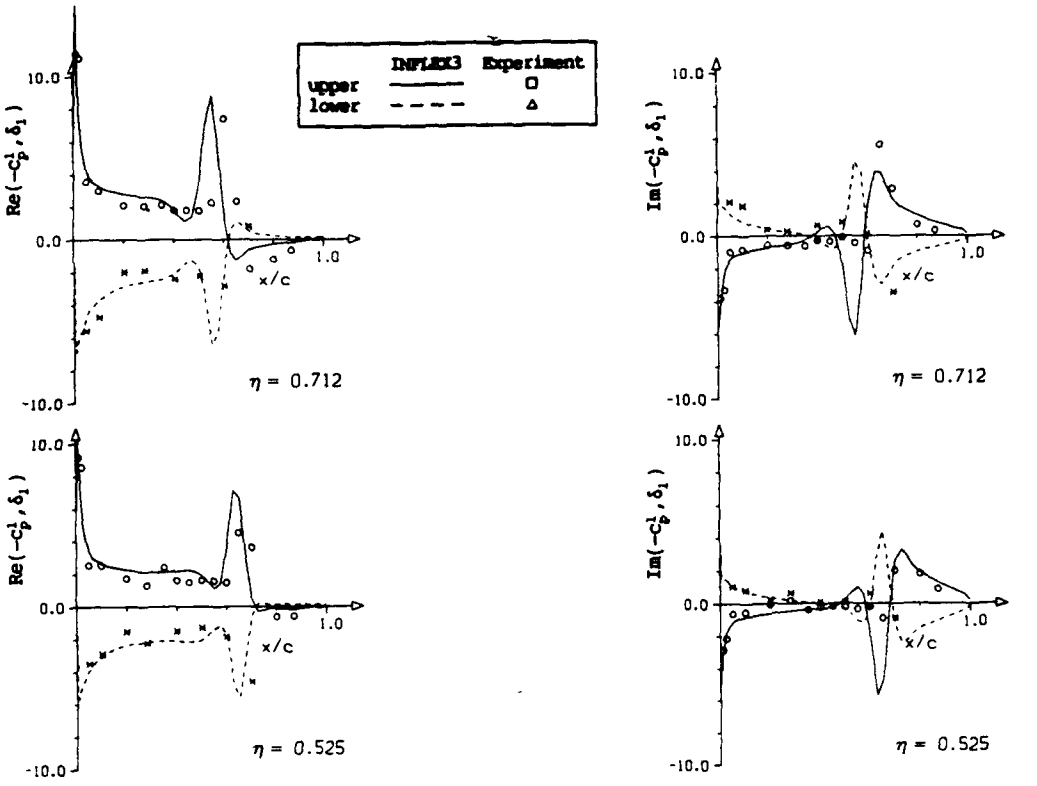


Fig. 22 Spanwise comparison of the measured (HST) and calculated in-phase and out-of-phase components on the NORA wing. CT6: M=0.95, k_r=0.27, α_0=0.0 deg, α_1=0.5 deg

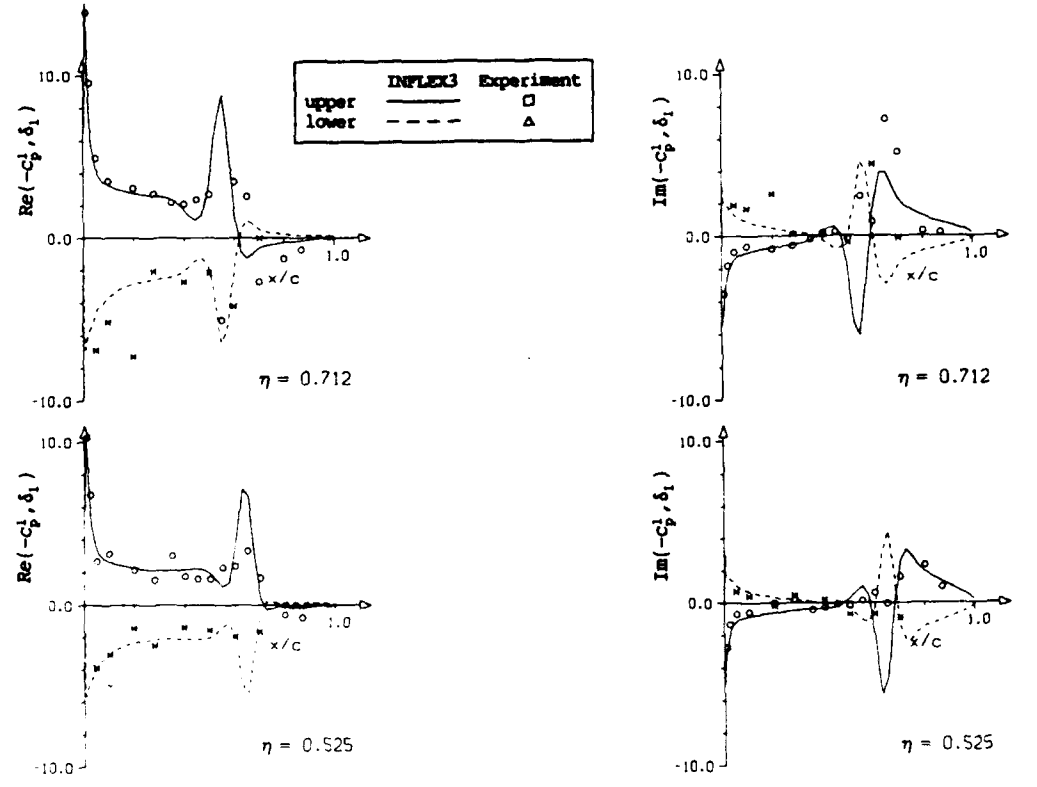


Fig. 23 Spanwise comparison of the measured (S2) and calculated in-phase and out-of-phase components on the NORA wing. CT6: M=0.95, k_r=0.27, α_0=0.0 deg, α_1=0.5 deg

THIS DOCUMENT PROVIDED BY THE ABBOTT AEROSPACE
TECHNICAL LIBRARY
ABBOTTAEROSPACE.COM

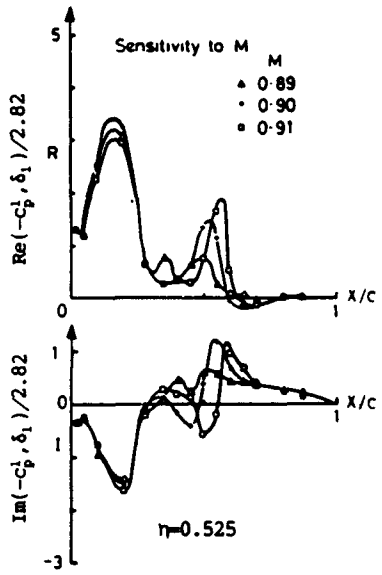


Fig. 24 Sensitivity of the unsteady pressures to small changes of Mach number, [24]. M=0.9, α_0=4.0 deg, α_1=0.5 deg, k=0.28

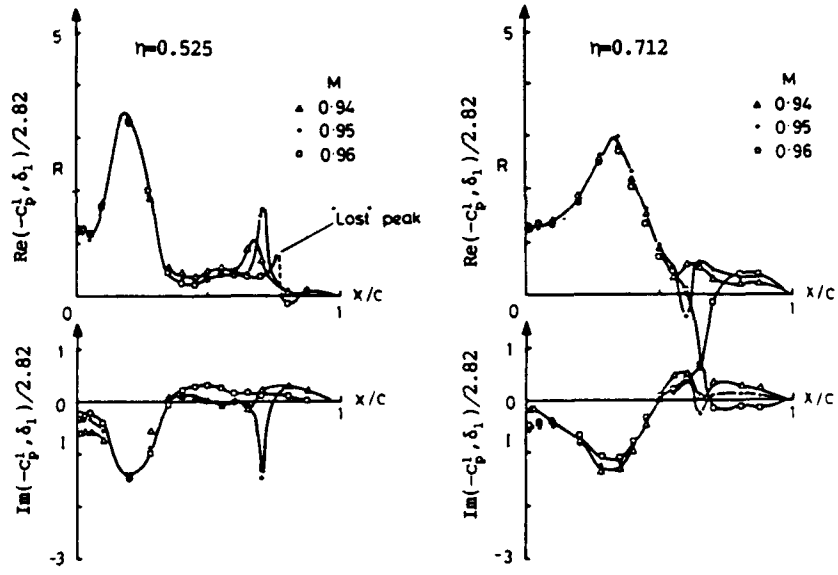


Fig. 25 Sensitivity of the unsteady pressures to small changes of Mach number, [24]. M=0.95, α_0=4.75 deg, α_1=0.5 deg, k=0.28

THIS DOCUMENT PROVIDED BY THE ABBOTT AEROSPACE
TECHNICAL LIBRARY
ABBOTTAEROSPACE.COM

AD-P007 803

Unsteady Transonic Aerodynamics of Pointed Bodies of Revolution in Supersonic Freestream

P. García Fogeda
A. Sanz
E.T.S.I. Aeronáuticos
U.P. de Madrid
28040 Madrid
Spain

92-16041

1. SUMMARY

A method to determine the aerodynamic forces acting on oscillating pointed bodies of revolution in transonic-supersonic flight has been developed. The nonlinear equation for the mean-flow perturbation potential and the time linearized equation for the cross-flow perturbation potential are both of hyperbolic type, for the Mach number range of interest, and have been solved by the method of characteristics. The method is valid for arbitrary frequencies of oscillation and can be applied for rigid or flexible body motions. Results are presented for the stability force coefficients, unsteady pressure distributions and shock deformations for various body shapes and Mach numbers.

2. INTRODUCTION

During the last two decades it has been observed that the nonlinear aeroelastic effects are very important for the design of aerospace vehicles. One of these effects with more interest to the industry, and that has not yet been fully investigated by the scientific community, is the determination of the dynamic loads on the vehicle during its transonic/low-supersonic regime of flight. It is in this regime where the dynamic loads are maximum and where the nonlinear effects due to the body thickness may be also very important.

In the past, the determination of the static and dynamic loads, for bodies of revolution in supersonic flight, has been investigated namely within the limitation of the linear theory. Thus, Kármán and Moore (Ref. 1) used the method of singularities to estimate the wave drag, Tsien (Ref. 2) used the same method to determine the static stability force coefficients, Platzer and Sherer (Ref. 3) used the linearized method of characteristics to obtain the dynamic stability force coefficients and García-Fogeda and Liu (Ref. 4) employed the method of singularities to determine the flutter boundaries for flexible bodies of revolution. For cones, some works that include the nonlinear effects have been developed. Thus, Taylor and Maccoll (Ref. 5) solved the Euler equations for supersonic flight around cones at zero angle of attack, and Kopal (Ref. 6), Brong (Ref. 7) and Hsu (Ref. 8) determined the static and dynamic force coefficients for this same geometry.

The objective of the present investigation is to develop a method that, including the nonlinear effects, is valid for arbitrary bodies of revolution oscillating in rigid or bending oscillations at any frequency.

To simplify the problem the following hypotheses are made: the vehicle is a slender pointed body of revolution that oscillates harmonically and with a shock wave that all the time remains attached to the body apex. The flight conditions and body shape are such that guarantee the existence of a velocity potential and the validity of the transonic small disturbance theory.

The resulting equations are nonlinear for the steady case and linear with variable coefficients for the unsteady but of hyperbolic type, within the Mach number range investigated, in both cases. In most of the cases of engineering interest the errors due to the use of these hypotheses are small except if the amplitude of oscillation is large or if the flow separation is present. The formulation of the problem is completed with the boundary conditions, tangential flow on the body surface and the Rankine-Hugoniot conditions on the shock wave, however the position and deformation of the shock are part of the solution.

The method of characteristics that we apply to solve the steady and unsteady flow equations is just an extension to bodies of revolution of the work done by Chadwick (Ref. 9) for airfoils and cascades. In this reference it has been shown that the method is efficient in computational time and produce exact results when compared with other theories.

The results presented in terms of the static and dynamic force coefficients, shock deformation and unsteady pressure coefficient for different body geometries show to be in good agreement with other theories in the Mach number range of interest.

In what follows all the variables have been adimensioned

THIS DOCUMENT PROVIDED BY THE ABBOTT AEROSPACE
TECHNICAL LIBRARY
ABBOTTAEROSPACE.COM

taking as reference length L, that of the body, and as velocity U_∞, that of the free stream.

3. PROBLEM FORMULATION

The small perturbation equation that describes the unsteady transonic flow around a pointed body of revolution is given in cylindrical coordinates [Landahl (Ref. 10)] by

$$\left[M_\infty^2 - 1 + (\gamma+1)M_\infty^2\Phi_x\right]\Phi_{xx} - \Phi_{rr} - \frac{1}{r}\Phi_r - \frac{1}{r^2}\Phi_{\theta\theta} = -M_\infty^2\Phi_{tt} - 2M_\infty^2\Phi_{xt} \qquad (1)$$

Following Revell (Ref. 11) a coordinate system attached to the body will be used. In this system the boundary condition staying that at any instant the flow particles are tangent to the body surface is given by

$$\nabla\Phi\cdot\nabla S = 0 \quad \text{at} \quad S(x,r,\sigma,t) = 0 \qquad (2)$$

where $S(x,r,\sigma,t)$ is the body surface. For small rigid body oscillations the body surface can be expressed as

$$S(x,r,\sigma,t) \equiv r - R(x) + \delta(t)\left(x - x_g\right)\cos\sigma \qquad (3)$$

where $R(x)$ is the body radius at x, x_g the center of oscillation and $\delta(t)$ the instantaneous oscillation amplitude.

The problem formulation is completed by imposing the boundary conditions at the shock wave. With the assumptions made here these conditions are the conservation of mass and momentum across the shock wave better known as the Rankine-Hugoniot conditions for isentropic flows.

After substitution of equation (3) into equation (2) terms of two different orders of magnitude appear, ones are stationary and of order of the body thickness and the others are unsteady and of order of the amplitude of oscillation. Then the velocity potential can be written as the sum of a steady thickness potential $\phi_o(x,r)$ and an unsteady angle-of-attack potential, $\phi_1(x,r)\cos\sigma$

$$\Phi(x,r,\theta,t) = \phi_o(x,r) + \delta(t)\phi_1(x,r)\cos\sigma \qquad (4)$$

Then, the problem can be split into one for the steady flow and another for the unsteady flow. The steady flow problem is given by the following differential equation and boundary conditions on the body surface and on the shock wave,

$$\left[M_\infty^2 - 1 + (\gamma+1)M_\infty^2\phi_{ox}\right]\phi_{oxx} - \phi_{orr} - \frac{1}{r}\phi_{or} = 0 \qquad (5.a)$$

$$\phi_{or} - R'(x)\phi_{ox} = R'(x) \quad \text{at} \quad r = R(x) \qquad (5.b)$$

$$\phi_{or} = -\tan\theta\,\phi_{ox} \quad \text{at} \quad r = x\tan\theta \qquad (5.c)$$

$$\phi_{ox} = \frac{2}{(\gamma+1)M_\infty^2}\left(1 - M_\infty^2\,\mathrm{sen}^2\theta\right) \quad \text{at} \quad r = x\tan\theta \qquad (5.d)$$

where θ is the local shock wave angle. The unsteady angle-of-attack flow problem is given by the following equations and boundary conditions

$$\left[M_\infty^2 - 1 + (\gamma+1)M_\infty^2\phi_{ox}\right]\phi_{1xx} - \phi_{1rr} - \frac{1}{r}\phi_{1r} + \frac{1}{r^2}\phi_1 = M_\infty^2k^2\phi_1 - 2ikM_\infty^2\phi_{1x} - (\gamma+1)M_\infty^2\phi_{1x}\phi_{oxx} \qquad (6.a)$$

$$\phi_{1r} - R'(x)\phi_{1x} = -1 - ik\left(x - x_g\right) \quad \text{at} \quad r = R(x) \qquad (6.b)$$

$$\phi_{1x} = a_1\frac{dh}{dr} + ia_2h \quad \text{at} \quad r = x\tan\theta \qquad (6.c)$$

$$\phi_{1r} = b_1\frac{dh}{dr} + ib_2h \quad \text{at} \quad r = x\tan\theta \qquad (6.d)$$

where it has been assumed harmonic motion for the oscillation, $\delta(t) = \delta_o e^{ikt}$, where k is the reduced frequency defined as $k = \omega L/U_\infty$, a_1, a_2, b_1 and b_2 are constants which depend only of the local shock wave angle, θ, and can be found in Ref. 9, and $h(r)$ is the shock deformation due to the body oscillation and it is part of the solution to the problem. It can be observed that in equation (6.a) only linear terms in δ_o have been considered. Landahl (Ref. 10) has shown for two dimensional airfoils that while the consideration of the nonlinear terms is essential for the study of steady transonic flow problems, for unsteady flow the main features of the transonic flow are transmited through the terms $(\gamma+1)M_\infty^2\phi_{ox}\phi_{1xx}$ and $(\gamma+1)M_\infty^2\phi_{oxx}\phi_{1x}$ to the unsteady flow. Therefore, it is not necessary to solve the nonlinear equation for the unsteady potential ϕ_1.

The exact isentropic pressure coefficient is expanded to yield the mean-flow and unsteady flow pressure coefficients,

$$C_p(x,r,\theta,t) = C_{p_o}(x,r) + \delta_o e^{ikt}C_{p1}(x,r)\cos\theta \qquad (7)$$

where

$$C_{p_o}(x,r) = \frac{2}{\gamma M_\infty^2}\left(S_o^\gamma - 1\right) \qquad (8.a)$$

$$C_{p1}(x,r) = -2S_o\left\{(1+\phi_{ox})\phi_{1x} + \phi_{or}(1+\phi_{1r}) + ik\left[\phi_1 + (x - x_g)\phi_{or} - R(x)\phi_{ox}\right]\right\} \qquad (8.b)$$

and

THIS DOCUMENT PROVIDED BY THE ABBOTT AEROSPACE
TECHNICAL LIBRARY
ABBOTTAEROSPACE.COM

$$S_o = \left[1 - \frac{\gamma - 1}{2} M_\infty^2 \left(2\phi_{ox} + \phi_{ox}^2 + \phi_{or}^2\right)\right]^{\frac{1}{\gamma - 1}}$$

Once the pressure coefficients C_{p_o} and C_{p_1} are known the static and dynamic force coefficients can be obtained by integration along the body surface.

4. METHOD OF SOLUTION

Equations (5.a) and (6.a) are of hyperbolic type for the Mach numbers of interest and both have the same characteristic lines. The difference between them is that while equation (5.a) is nonlinear and the characteristic lines are part of the solution, equation (6.a) is linear with variable coefficients and the characteristic lines are known once the steady-flow problem has been solved. Therefore we must solve first the steady flow problem.

5. STEADY FLOW SOLUTION

The equation for the α and β characteristics is

$$\left(\frac{\partial r}{\partial x}\right) = \pm \lambda^{1/2} \tag{9}$$

where $\lambda = M_\infty^2 - 1 + M_\infty^2(\gamma + 1)\phi_{ox}$, the positive sign is along the β characteristic and the negative one along the α characteristic (see Fig. 1).

Along each of these characteristics the variables $u_o = \phi_{ox}$ and $v_o = \phi_{or}$ change accordingly to the following compatibility relations

$$-\lambda^{1/2} u_{o\alpha} r + (v_o r)_\alpha = 0 \tag{10.a}$$

along the β characteristic, and

$$\lambda^{1/2} u_{o\beta} r + (v_o r)_\beta = 0 \tag{10.b}$$

along the α characteristic. The subindex α, β in equations (10.a) and (10.b) means derivatives of the variables with respect to α or β.

The procedure to solve the steady flow is as follows: starting from the body surface and by assuming the values of λ along the α characteristic the mesh point positions on the flow field are obtained by integration of equation (9). To determine the point on the shock wave, and thus the shock wave position, the shock wave angle is assumed to be the average between the free stream Mach wave and the local Mach wave angles. Of course these locations of the mesh points are not correct because of the assumed values of λ. After the first assumed mesh points have been computed for one α characteristic, we proceed to compute the flow field velocities starting at the shock point and moving towards the body surface along the α characteristic. For the point at the shock, u_o and v_o are determined from the two shock conditions. The rest of the points along the α characteristic are determined by using both compatibility relations (equations (10.a) and (10.b)) along the α characteristic and along the intersecting β characteristic with the point considered. Finally, when the body surface is reached the flow properties on it are determined from the tangency condition and from the compatibility relation along the α characteristic. At this state a convergency criterion is established to verify if the assumed values of λ to compute the slopes of the characteristics and the computed ones are less than a tolerance, if this is not true, the mesh points along the α characteristic are determined again using the last computed values of u_o to determine the new values of λ. The process is repeated until the new computed values of λ are less than the tolerance. Usually five to ten iterations are needed, depending on the Mach number. Then, we move to a new point along the body surface and generate a new set of mesh points along an α characteristic repeating the same procedure as the one described above. We keep marching in this way along the body surface until the end of the body is reached.

From the solution of the steady flow the velocities u_o, v_o in the whole flow field and the shock position are known. From these results the stationary pressure coefficient on the body surface can be computed.

6. UNSTEADY FLOW SOLUTION

Once the steady flow problem has been solved and that the mesh point locations are known we can proceed to solve the unsteady flow. There is, however, one important observation which is that since the shock deformation $h(r)$ is part of the solution it is necessary to make an additional hipothesis in order to start the solution. The assumption that in the region between 0 to x_1 (see Fig. 1) the flow properties are equal to the values computed by the slender body theory is made. Also, we observe that all the β characteristics passing through the shock mesh points intersect the body surface in this small region. Then, the shock deformation $h(r)$ and the u_1 and v_1 velocities just behind the shock wave can be determined first in the following way. The values of the velocities u_1 and v_1 in the body apex are given by

$$v_1 = -1 - ik\left(x - x_g\right) \tag{11.a}$$

$$u_1 = -2R'(x)v_1 + ikR(x) \tag{11.b}$$

where equations (11.a) and (11.b) come from applying the unsteady tangency condition and the slender body theory at the body apex.

Now the values of the velocities u_1 and v_1 in the shock points and the deformation of the shock wave $h(r)$ are determined from the two shock conditions, equations (6.c) and (6.d), and from the compatibility condition along the β characteristic, going from the body surface of the interval between 0 to x_1 to the shock point, and that is given by

THIS DOCUMENT PROVIDED BY THE ABBOTT AEROSPACE
TECHNICAL LIBRARY
ABBOTTAEROSPACE.COM

$$\sqrt{\lambda}\,du_1 - dv_1 - \left[\frac{v_1}{r} - \frac{1}{r^2}\phi_1 - 2ikM_\infty^2 u_1 + M_\infty^2 k^2 \phi_1 - M_\infty^2(\gamma+1)u_1 u_{ox}\right]dr = 0 \qquad (12)$$

Once the shock deformation and the values of u_1 and v_1 at the shock are known, the procedure to obtain the flow properties at the rest of the points is as follows: starting from a shock point, and moving along an α characteristic toward the body surface, the flow field properties are determined from the compatibility relation along the α characteristic

$$\sqrt{\lambda}\,du_1 + dv_1 + \left[\frac{v_1}{r} - \frac{1}{r^2}\phi_1 - 2ikM_\infty^2 u_1 + M_\infty^2 k^2 \phi_1 - M_\infty^2(\gamma+1)u_1 u_{ox}\right]dr = 0 \qquad (13)$$

and equation (12) along the β characteristic intersecting the mesh point considered. When the body surface is reached, equation (12) is replaced by equation (6.b) and the velocities u_1 and v_1 on the body surface are obtained. The procedure is repeated along all the mesh points and the whole flow field properties are determined. Note that since the equations in this case are linear there is no need to iterate in the unsteady flow problem, the computation time is then kept rather small.

7. RESULTS AND DISCUSSION

To verify the present method, numerical examples are presented in terms of steady and unsteady pressures, stability derivatives and shock deformations for various body shapes.

Figures 2 and 3 present the steady pressure coefficient for a 5° cone and a 10° cone versus Mach number. For the 5° cone, it can be observed that almost no difference exists between the present method, the linear theory and the exact solution by Taylor and Maccoll. For the 10° cone, although there is not jet a big difference between the linear theory and the Taylor and Maccoll solution it can be observed that the present method, for the low Mach numbers, lies very close to the exact solution.

In figure 4 the steady pressure coefficient along the body surface is presented for a parabolic ogive at Mach number of 2. It can be observed that the present method is in very good agreement with the exact method of characteristics showing an important improvement with respect to the linear theory.

In figures 5 and 6 comparisons of the normal force coefficient between the present method, Kopal's exact solution (Ref. 6) and the first order theory (Ref. 2) are presented for a 5°and a 10° cone versus Mach number. In these figures it is seen that while the contribution of the nonlinear terms is very important for high Mach numbers it is not so important for Mach numbers close to one.

In figure 7 the dynamic normal force coefficient versus Mach number for a 10° cone pitching with respect to the apex is presented. As happened for the static case the main contribution of the nonlinear terms occurs for high Mach numbers.

In figure 8 the dynamic moment coefficient versus Mach number for a 10% thick parabolic ogive pitching at $x_g = 0.4$ is compared to the linearized method of characteristics (Ref. 3) and to the slender body theory (Ref. 12). Again as in the previous figures the main differences between the linear and nonlinear method occurs at high Mach numbers.

In figure 9, the real and imaginary pressure coefficient along the body surface is compared to the first order theory (Ref. 4) for a 10° cone. The body oscillates with respect to the apex at the reduced frequencies of .5 and 1.0 and at a Mach number of 1.3. In this figure, it can be observed that the main difference between the linear and the nonlinear methods occurs in the real part of the pressure coefficient and also that, although some oscillation of the pressure coefficient of the present method occurs along the body surface, they are not so large as it happens in the two dimensional case for airfoils (Ref. 9).

The real part and the imaginary part of the shock deformation for the oscillating cone of figure 9 are presented in figure 10. It is important to note that while the in-phase shock deformation decreases with increasing frequency the out-of-phase increases. Also it can be noted that while for k = 0.5 the in-phase shock deformation is almost a straight line, for k = 1.0 there is an important curvature towards the freestream.

In figure 11 the real and imaginary part of the pressure coefficient along the body surface for a 5% thick parabolic ogive is presented. The body is pitching about the apex at the reduced frequency of k = 1.0 and at the Mach number of 1.2. Again in this case it can be observed that slight oscillations appear in the present nonlinear method mainly in the in-phase pressure coefficient.

8. CONCLUSIONS

The method of characteristics has been applied to solve the nonlinear-small-disturbance transonic flow equation for bodies of revolution at zero angle of attack and to the linearized transonic-unsteady-flow equation for bodies oscillating at arbitrary frequencies.

From the results presented the following conclusions can be drawn:

- Although some oscillations have been observed in the pressure coefficient for low Mach numbers, they are not so large as for the airfoil cases where large oscillations occur in this transonic flow regime.

THIS DOCUMENT PROVIDED BY THE ABBOTT AEROSPACE
TECHNICAL LIBRARY
ABBOTTAEROSPACE.COM

- The computed forces with the present method are in good agreement with other more exact methods. However, for the Mach numbers close to one there is not a substantial difference between the present method and the first order theory.

- For large Mach numbers and thick bodies there is an important contribution of the nonlinear terms to the unsteady forces.

The computational time is small. For the cases presented as many as 50 points along the body surface were used to generate the grid taking only a few seconds to obtain the complete solution.

Acknowledgment
This work is supported by the Universidad Politécnica de Madrid.

References

1. Von Kármán, T. and Moore, N.B., "The Resistance of Slender Bodies", Trans. ASME, *54*, 1932, pp 303-310.
2. Tsien, Hsue-Shen, "Supersonic Flow over and Inclined body of Revolution", J. Aeronautical Sciences, *5*, 12, December 1938, pp 480-483.
3. Platzer, M.F. and Sherer, A.D., "Dynamic Stability Analysis of Bodies of Revolution in Supersonic Flow", J. Spacecraft and Rockets, *5*, 7, July 1968, pp 833-837.
4. García-Fogeda, P. and Liu, D.D., "Analysis of Unsteady Aerodynamics for Elastic Bodies in Supersonic Flow", J. Aircraft, *24*, 12, December 1987, pp 833-840.
5. Taylor, G.I. and Maccoll, J.W., "The Air Pressure on a Cone at High Speeds", Proceedings of the Royal Society, *139*, 1933, pp 278-311.
6. Kopal, Z., "Tables of Supersonic Flow Around Cones", M.I.T. Technical Report No. 1, 1947.
7. Brong, E.A., "The Flow Field about a Right Circular Cone in Unsteady Flight", AIAA Paper 65-398, 1965.
8. Hsu, P.T., "A Fortran Computer Code for the Calculation of Unsteady Supersonic Field by the Method of Perturbation", M.I.T. Report 67-3, 1967.
9. Chadwick, W.R., "Unsteady Supersonic Cascade Theory Including Nonlinear Thickness Effects", Ph.D. Thesis, Naval Postgraduate School, Monterey, California, USA, 1975.
10. Landahl, M. "Unsteady Transonic Flow", Pergamon Press, London, 1961.
11. Revell, J.D., "Second-Order Theory for Unsteady Supersonic Flow Past Slender, Pointed Bodies of Revolution", Journal of the Aerospace Sciences, *27*, 10, October 1960, pp 730-740.
12. Miles, J.W., "On Non-Steady Motion of Slender Bodies", Aeronautical Quarterly, *11*, November 1950, pp 183-194.

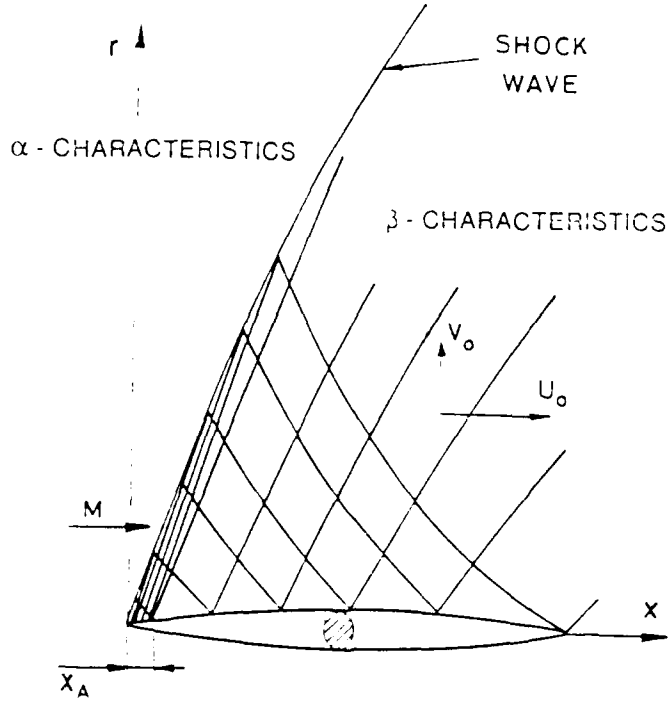


Fig. 1. Characteristics mesh.

THIS DOCUMENT PROVIDED BY THE ABBOTT AEROSPACE
TECHNICAL LIBRARY
ABBOTTAEROSPACE.COM

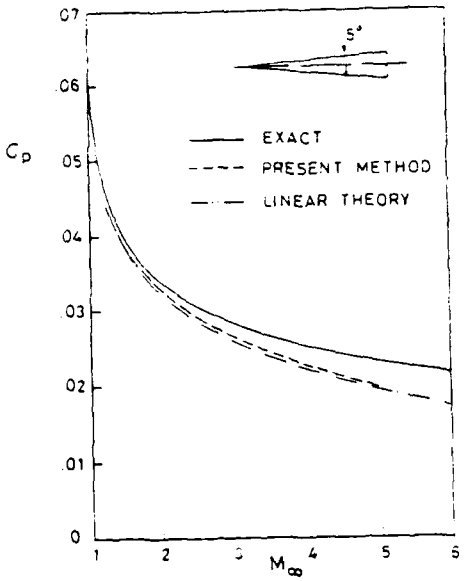


Fig. 2. Steady pressure coefficient for a 5° cone versus Mach number.

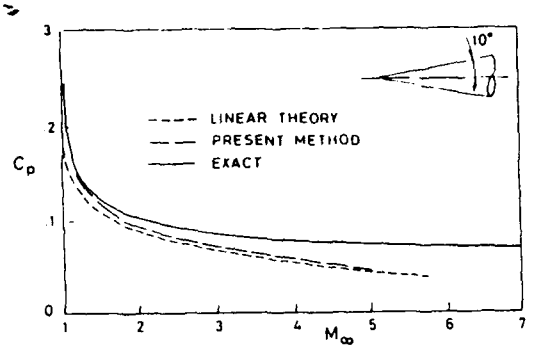


Fig. 3. Steady pressure coefficient for a 10° cone versus Mach number.

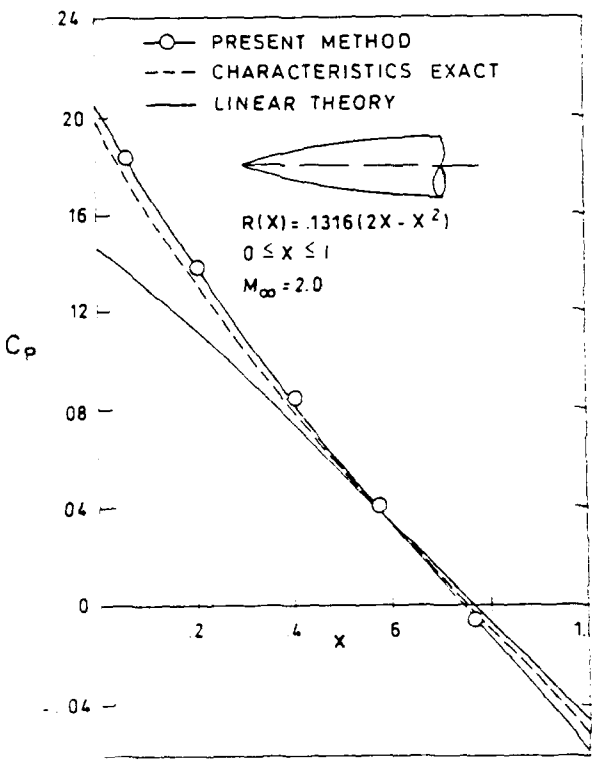


Fig. 4. Steady pressure distribution along the body surface for a parabolic ogive at Mach number 2.0.

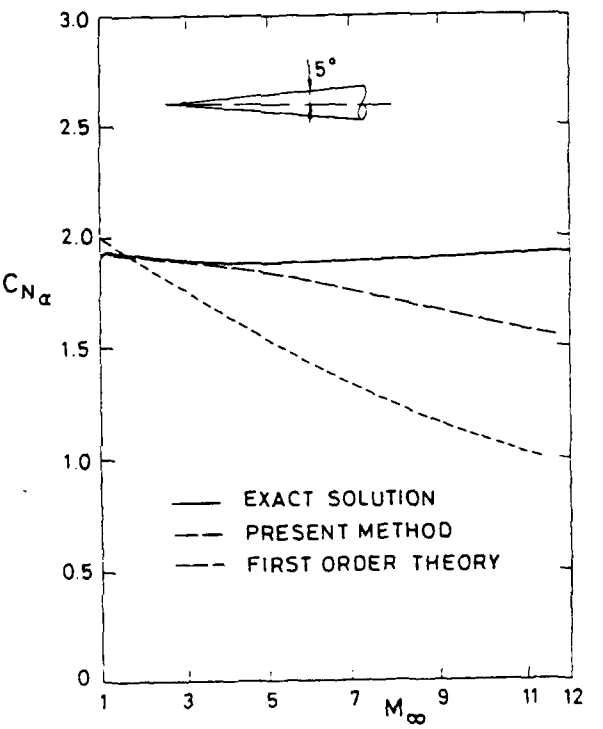


Fig. 5. In-phase normal force coefficient for a 5° cone versus Mach number.

THIS DOCUMENT PROVIDED BY THE ABBOTT AEROSPACE
TECHNICAL LIBRARY
ABBOTTAEROSPACE.COM

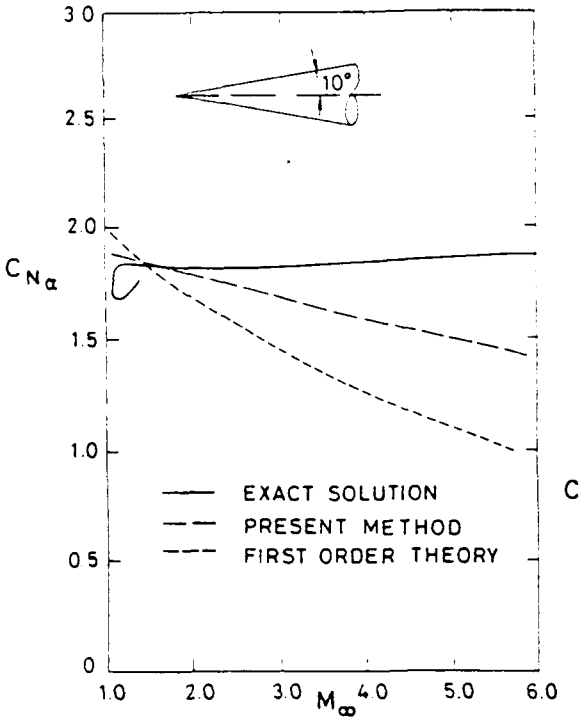


Fig. 6. In-phase normal force coefficient for a 10° cone versus Mach number.

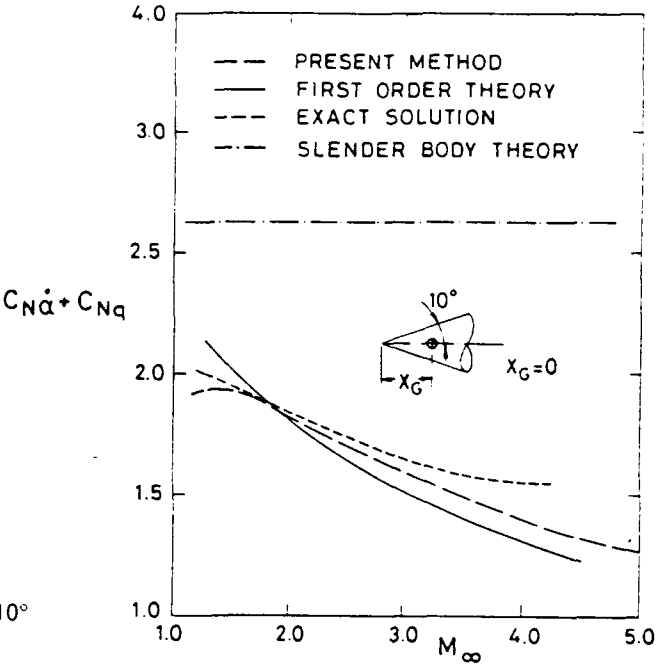


Fig. 7. Out-of-phase normal force coefficient for a 10° cone pitching at the apex versus Mach number.

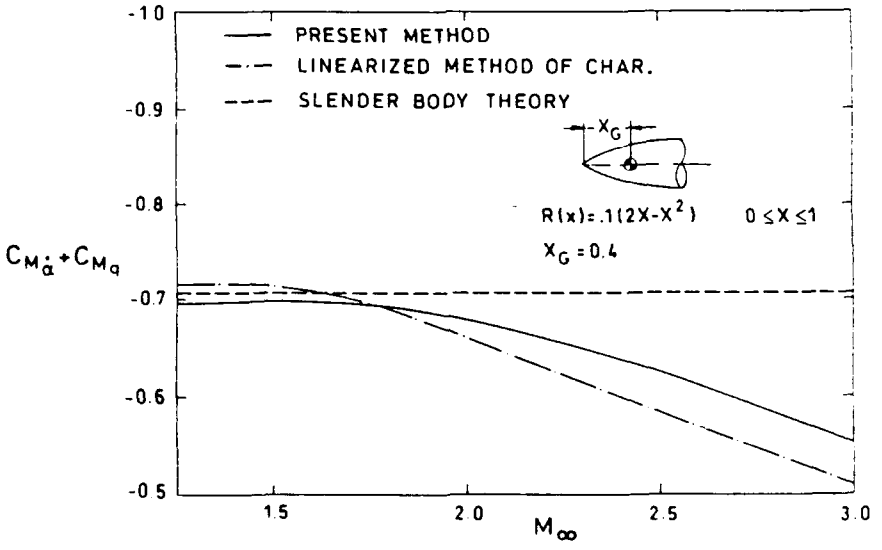
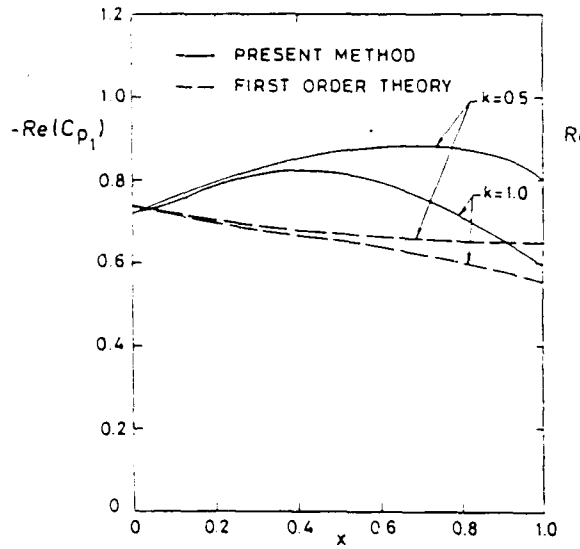
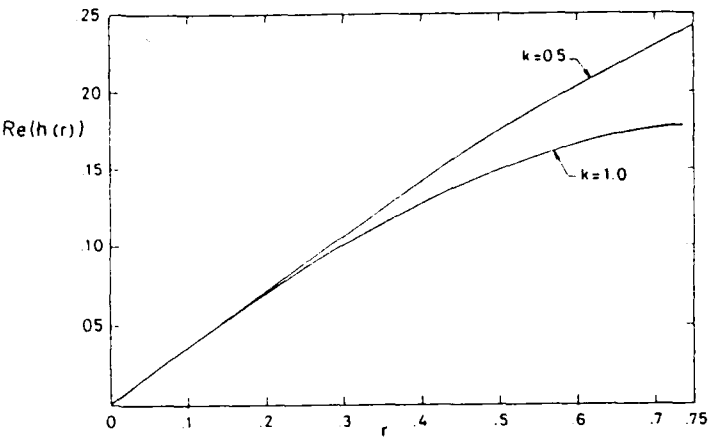


Fig. 8. Out-of-phase moment coefficient for a 10% thick parabolic ogive pitching at x_g = 0.4 versus Mach number.

THIS DOCUMENT PROVIDED BY THE ABBOTT AEROSPACE
TECHNICAL LIBRARY
ABBOTTAEROSPACE.COM





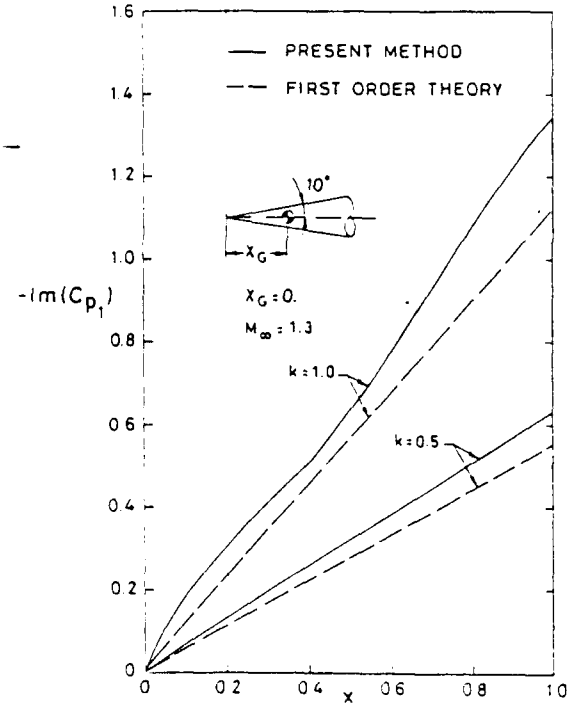


Fig. 9. Unsteady pressure coefficient along the body surface for a 10° cone pitching at the apex at Mach number of 1.3 and reduced frequencies of .5 and 1.0.

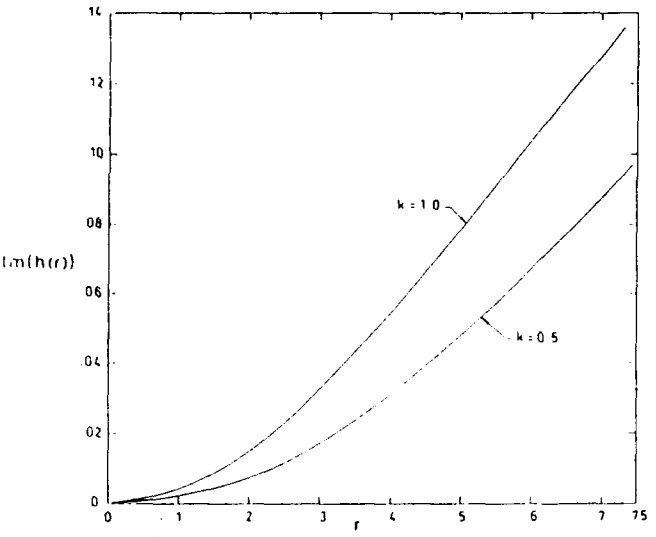


Fig. 10. Shock deformation for a 10° cone pitching at the apex at Mach number of 1.3 and reduced frequencies of .5 and 1.0.

THIS DOCUMENT PROVIDED BY THE ABBOTT AEROSPACE
TECHNICAL LIBRARY
ABBOTTAEROSPACE.COM

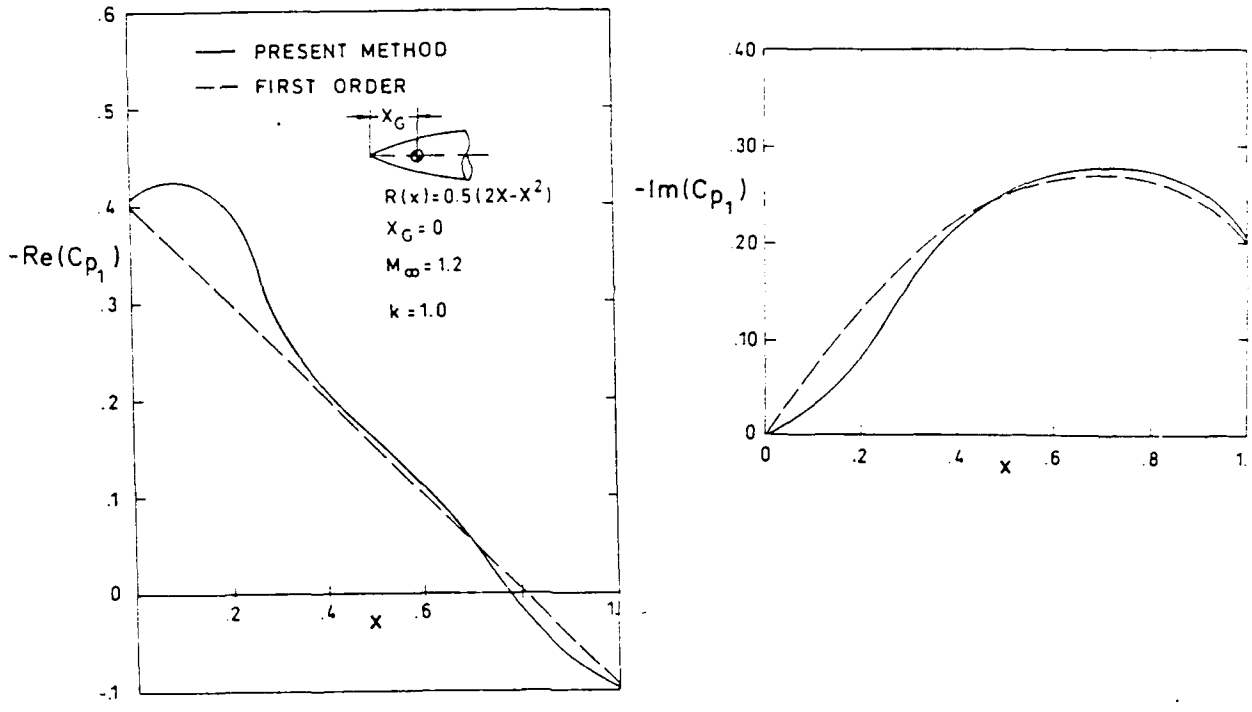


Fig. 11. Unsteady pressure coefficient for a 5% thick parabolic ogive pitching at the apex at Mach number of 1.2 and reduced frequency of 1.0.

THIS DOCUMENT PROVIDED BY THE ABBOTT AEROSPACE
TECHNICAL LIBRARY
ABBOTTAEROSPACE.COM

AD-P007 804

NLR inviscid transonic unsteady loads prediction methods in aeroelasticity

M.H.L. Hounjet

National Aerospace Laboratory (NLR)
Anthony Fokkerweg 2
1059 CM Amsterdam
The Netherlands

92-16042

Abstract

An overview is presented of unsteady inviscid calculation methods developed at NLR, which are primarily based on the full potential equation for the prediction of airloads on oscillating structures in transonic flow.

Attention is given to experience with entropy / vorticity corrections and a procedure which removes the frequency barrier associated with time-linearized modelings. This procedure has a favorable effect on computer cost such that transonic flutter boundaries can be obtained in acceptable turn-around times on current workstations.

A method for the transonic aeroelastic analysis of complete aircraft which is currently in the stage of development will be introduced and attention is given to its grid generation procedure.

The methods are demonstrated by showing results of unsteady loads and pressure coefficients applications in 2-D and 3-D transonic flow and of an aeroelastic application to a 3-D AGARD standard aeroelastic case in transonic flow.

1 Introduction

In the development of many modern airplanes aeroelastic analysis is required in the transonic speed range. This implies the development of computer methods to determine the unsteady transonic flow about realistic aircraft configurations. At NLR, research has been performed since the late seventies on two type of approaches:

time-linearized approach , which assumes that the unsteady disturbances are small relative to a fixed steady state solution, and the

time-integration approach , which fully simulates the development of unsteady flow with time.

Both techniques have pros and cons:

- The first approach can be applied as long as the unsteady disturbances are small and non-linear unsteady effects can be neglected. When this condition is locally violated, for example at the nose of an airfoil or in the shock trajectory, the approach is valid as long as the corresponding flow regions are small. Therefore the range of applicability is restricted to aereoelastic applications with small shock excursions resulting in classical flutter. As a consequence strongly non-linear problems such as Limit Cycle Oscillations cannot be treated. The second method has no severe formal restrictions.

- The second approach has potential for the embedding of viscous and vorticity effects. Due to the nature of these effects implementation in time-linearized unsteady methods seems to be less appropriate.

- In an aeroelastic application the first procedure requires the usual structural pre-processing and the well-known aerodynamic processing (i.e. generation of aerodynamic stiffness and damping (generalized forces) matrices) with an additional dependence on the angle of attack parameter as compared to subsonic and supersonic applications . Thereafter the flutter trajectory is obtained by any classical flutter method. The first approach has a lower threshold as the efficient utilization of the second approach requires a careful procedure to detect the flutter boundaries by direct simulation while also postprocessing is required to detect which structural or aerodynamic component is primarily responsible for the flutter boundary which is important in pre-design studies.

- The first approach is in general computationally more efficient than the second approach since the fastest existing iteration methods for solving linear systems can be used and also the results are depending on fewer parameters (no time step and observation time parameters). The 3-D routine application of the second method is not realistic without the computing power of recent supercomputers.

Apart from the aforementioned advantages or disadvantages which may motivate the development of a particular method the development and or availability of both type of methods offers additional possibilities:

THIS DOCUMENT PROVIDED BY THE ABBOTT AEROSPACE
TECHNICAL LIBRARY
ABBOTTAEROSPACE.COM

- The time to develop a method can be reduced since it is possible to compare calculated results very closely.
- The influence of numerical errors in each of the methods can be investigated.
- The applicability range of each of the methods can be complemented by the other.

NLR has made significant contributions with respect to the time-linearized approach during the development of 2-D and 3-D time-linearized methods:

- It has been shown that the effect of the moving shock wave is implicitly captured in the loads [1]. No need exists to do anything special in case of shock waves with respect to the pressure integration.
- The restriction that time-linearization is only valid for very small shock motions has been relaxed [2, 3] by utilizing an approximation of the *mean* steady flow field instead of the steady flow field at the mean position. The approximation is defined as the average of steady potentials determined at several different positions (phases) during the motion.
- The frequency limitation has been practically removed by introducing a procedure[4, 5] which renders data for harmonic oscillations from data for diverging motions. At the same time a more than 50% computer cost reduction is achieved.
- The development of the 2-D small disturbance method FTRAN2 [6],the 2-D full potential method FTRANC [3] and the 3-D full potential method FTRAN3 [7].

NLR contributions with respect to the second approach for two-dimensional flows include:

- The extension of the applicability in the frequency domain of the well-known LTRAN2 code from very low to moderate reduced frequencies [8].
- The embedding of viscous effects including a strong interaction modeling of separated flow resulting in the ULTRAN-V code [9].
- The development of the full potential method TULIPS [10].

At present research is performed aiming at the development of a complete time integration 3-D aeroelastic simulation method in which the unsteady aerodynamics are governed by the full potential equation with embedding of viscosity,entropy and vorticity corrections. The validation of this method is expected to be enhanced by the availability of the time-linearized 3-D FTRAN3 method.

The paper presents the past development and status of the abovementioned subjects and shows relevant results.

2 Aerodynamic Analysis

This section summarizes the well-known equations governing the unsteady potential flow around wings.

2.1 Unsteady full potential equations

The potential flow is considered about wings in a flow with free-stream velocity U in the direction of the x -axis. Assuming that the disturbances created by the wing are irrotational except for areas occupied by wing and wakes a velocity potential Φ can be introduced which satisfies the nonlinear equation:

$$\rho_t + \frac{\delta}{\delta x}(\rho\Phi_x) + \frac{\delta}{\delta y}(\rho\Phi_y) + \frac{\delta}{\delta z}(\rho\Phi_z) = 0\,, \qquad (1)$$

where the density ρ satisfies the unsteady Bernoulli equation:

$$\rho = \left(1 + \frac{\gamma-1}{2}M_\infty^2(1 - \Phi_x^2 - \Phi_y^2 - \Phi_z^2 - 2\Phi_t)\right)^{\frac{1}{\gamma-1}}. \qquad (2)$$

In the above equations M_∞ is the free-stream Mach number. The variables are made dimensionless using reference length l, speed U and freestream density ρ_∞. γ is the ratio of specific heats.

At the wing boundary the condition for tangential flow are applied:

$$(\vec{q} - \vec{q}_b).\vec{n} = 0, \qquad (3)$$

where $\vec{q}$ is the fluid velocity $\vec{q} = \nabla\Phi$ and $\vec{q}_b$ is the velocity of the body surface.

Across the wakes which emanate from sharp trailing edges no pressure differences are allowed:

$$\Delta C_p = 0\,. \qquad (4)$$

At a sharp trailing edge in subsonic flow a smooth transition to the zero pressure jump condition in the wake is required (Kutta condition). The pressure coefficient is given by the expression:

$$C_p = \frac{2(\rho^\gamma - 1)}{\gamma M_\infty^2}. \qquad (5)$$

Finally in calculations the unbounded physical space around a wing must be truncated at some finite distance. Therefore radiation conditions have to be applied which simulate that disturbances propagate outwards from the wing to infinity.

2.2 Time-linearized formulations

In the time-linearized methods for an unsteady exponentially time varying motion he^{st}, the assumption is made that the potential can be split up into a mean steady component ϕ and an unsteady time varying component φe^{st}:

$$\Phi = \phi + \varphi e^{st}. \qquad (6)$$

THIS DOCUMENT PROVIDED BY THE ABBOTT AEROSPACE
TECHNICAL LIBRARY
ABBOTTAEROSPACE.COM

Here $s = g + ik$ in which g is the divergence rate and k the reduced frequency $k = \frac{\omega l}{V}$, ω being the frequency of oscillation. h is the component of the displacement of the wing in normal direction.

It is usual to define ϕ by the steady potential at the mean position and substitution of (6) into (1) leads to :

$$\frac{\delta}{\delta x}(\rho^0\phi_x) + \frac{\delta}{\delta y}(\rho^0\phi_y) + \frac{\delta}{\delta z}(\rho^0\phi_z) = 0, \tag{7}$$

where

$$\rho^0 = \left(1 + \frac{\gamma-1}{2}M_\infty^2(1 - \phi_x^2 - \phi_y^2 - \phi_z^2)\right)^{\frac{1}{\gamma-1}} \tag{8}$$

and

$$\frac{\delta}{\delta x}(\rho^0\varphi_x + \rho^1\phi_x) + \frac{\delta}{\delta y}(\rho^0\varphi_y + \rho^1\phi_y) + \frac{\delta}{\delta z}(\rho^0\varphi_z + \rho^1\phi_z) + s\rho^1 = 0, \tag{9}$$

where

$$\rho^1 = -\rho^0\frac{s\varphi + \phi_x\varphi_x + \phi_y\varphi_y + \phi_z\varphi_z}{a^{0^2}} \tag{10}$$

and a^0 is the mean speed of sound:

$$a^0 = \sqrt{\frac{1}{M_\infty^2} + \frac{\gamma-1}{2}(1 - \phi_x^2 - \phi_y^2 - \phi_z^2)}. \tag{11}$$

At the wing boundary the conditions for tangential flow are applied:

$$\phi_N = 0 \tag{12}$$

and

$$\varphi_N = \phi_x h_x + \phi_y h_y + \phi_z h_z + sh, \tag{13}$$

where the suffix N means differentiation along the outward pointing normal direction at the wing surface. The conditions for no pressure differences in the wakes are:

$$\Delta C_p^0 = \Delta C_p^1 = 0\,. \tag{14}$$

The mean and unsteady components of the pressure coefficients are given by the expressions:

$$C_p^0 = \frac{2(\rho^{0^\gamma} - 1)}{\gamma M_\infty^2} \tag{15}$$

and

$$C_p^1 = -2\rho^0(\phi_x\varphi_x + \phi_y\varphi_y + \phi_z\varphi_z + s\varphi)\,. \tag{16}$$

Also radiation conditions have to be applied which simulate that disturbances propagate outwards from the wing to infinity.

The choice of the steady potential at the mean position for the mean steady potential suffices if the non-linear effects are small and /or are restricted to small areas. This is sufficient when the resulting data is used to determine flutter boundaries. In case the data is meant to be used for other applications (such as comparing with experimental data) and non-linear effects become very important the aforementioned choice may not be appropriate anymore and one should use a mean steady potential defined as an average of steady potentials determined at several different positions (phases) during the motion. For more details see [3].

3 Time-linearized methods

3.1 Overview

This section presents the time-linearized unsteady full potential methods FTRANC and FTRAN3 which are in use at NLR. FTRANC described in [3] solves the 2-D steady and time-linearized unsteady flow about thick blunt-nosed airfoils using a C-type grid and is attractive because of its low computational cost (10-40 CPU seconds on a 6 Mflop workstation for a steady application and 5-20 CPU seconds for an unsteady application (one frequency, one vibration mode) on a 90x13 grid) . The FTRAN3 code has been introduced in reference [7] and applies to 3-D wings using an H-H type grid. It is the only 3-D transonic unsteady method available at NLR and its computational cost times are about 100-400 CPU seconds for a steady application and 25-100 CPU seconds for an unsteady application (one frequency, one vibration mode) on a 34x8x20 grid on a 6 Mflop workstation. Transonic flutter boundaries can be estimated in acceptable turn-around times on the workstation.

Both methods are based on the same computational model:

1. A free stream consistent fully conservative finite volume discretization of the full potential flow governed by the equations (7, 8,12) and (9, 10,13). Mass-flux splitting according to Engquist-Osher or Godunov is used to maintain stability in supersonic flow regions.

2. Entropy corrections as explained in [11] are embedded to enable a better prediction of shock wave positions.

3. Newton iteration procedure for solving the steady flow. The Newton iteration is very fast for cases with weak to moderately strong shock waves in which case 3-5 iterations are sufficient. Incase of strong shock waves the iteration is hampered by the restricted displacement of shock waves being approximately limited to one grid-cell per iteration. As a consequence potential jumps are formed at the incorrect shock position which detoriate the convergence. The formation of the potential jumps is diminished by introducing a non constant sonic flux in the mass-flux splitting which depends not only on M_∞ but also on the artificial time-like Newton iteration index. By this time-like damping is added in supersonic zones especially at sonic conditions. When this time-like

THIS DOCUMENT PROVIDED BY THE ABBOTT AEROSPACE
TECHNICAL LIBRARY
ABBOTTAEROSPACE.COM

damping is added the Newton procedure performs well in case of strong shocks. The formulations of the time-dependent sonic flux were taken from [10].

4. Multi-grid iteration for solving the unsteady flow and each linear stage of the Newton process

5. The minimization of the size of the grid by using an integral equation (field panel) discretization method on the coarsest grid generating appropriate outflow conditions on the fine grid. This is done assuming that outside the grid the linearized unsteady flow equation is satisfied:

$$(1-M_\infty^2)\varphi_{xx}+\varphi_{yy}+\varphi_{zz} -2sM_\infty^2\varphi_x-s^2M_\infty^2\varphi=0\,. \quad (17)$$

By the integral equation method the outflow conditions are prescribed:

$$\phi(x,y,z)=\iiint m(u,v,w)E(x-u,y-v,z-w)dudvdw\,, \quad (18)$$

where E is the elementary solution of equation (17):

$$E(x,y,z)=-\frac{e^{\frac{sM(Mx-R)}{1-M^2}}}{4\pi R}. \quad (19)$$

Here $R=\sqrt{x^2+(1-M^2)(y^2+z^2)}$ and m is the source strength which is equal to the left hand side of the uniform equation (17).

Eq. (18) is discretized on a coarse grid using potential data of the finest grid for the evaluation of the source strength m . Therefore the fine grid solution determines the outflow boundary conditions.

6. Formulations for real positive values of s (the divergence rate) which reduces the computational cost in various aspects:

   - All calculations can be performed with real quantities, reducing the computational work by a factor as high as four by eliminating complex floating point operations in evaluating the aerodynamic influence coefficients and in solving the aerodynamic equations.
   - A factor of 2 reduction in memory requirements.
   - The convergence of the multi-grid iteration solver improves with increasing divergence rate. No stability limit with respect to Mach number and frequency shows up.

3.2 Efficient use of time-linearized methods and removal of frequency limit

The applicability of time-linearized methods derived specifically for purely harmonic motions is strongly reduced in frequency range due to stability problems of the applied iterative solvers and/or the requirement with respect to the minimum grid sizes . In reference [4] a simple procedure has been developed to obtain the unsteady aerodynamic forces for all types of motion, applying data for purely exponentially diverging motions. This procedure offers the advantages mentioned in item 6 of the previous section. The procedure is based on the following steps:

1. Obtain aerodynamic data for a purely exponentially diverging motion with the time function e^{st} where s is positive and real.
2. Make a polynomial fit through those data.
3. Assume that the fit is valid throughout the complex s plane and render data for harmonic motions by simple evaluation of the fit for complex s.

For active control studies and in modern flutter calculation methods an algebraic description of the aerodynamic forces is required which is usually obtained by generating a Laplace transformable fit through complex aerodynamic data corresponding to harmonic motions. It is much easier, however, to generate the polynomial fit through the real data for diverging motions, for all information is contained in the real data!

3.3 Time-linearized examples

3.3.1 Overview

Results of applications to two-dimensional airfoils made with the FTRANC method have already been published in [3, 5]. Results of applications to three-dimensional wings made with the FTRAN3 method were published in [2, 12, 13, 14, 5]. The applicability of the afore mentioned methods to steady and unsteady transonic potential flow problems is demonstrated in the next sections for the 2-D NLR7301 airfoil and for fighter type wings, a rectangular supercritical wing and a 3-D AGARD standard aeroelastic case. In all the examples the steady potential at the mean position is used as approximation of the mean steady potential. It should be noted that prior to time-linearized computations, the steady flow fields are computed using fully nonlinear flow solvers.

3.3.2 2-D NLR7301 airfoil

This section shows results for the NLR7301 airfoil. For the geometry one is referred to [15]. An example of a steady FTRANC application is shown in figures 1 and 2 demonstrating the use of the entropy correction.

THIS DOCUMENT PROVIDED BY THE ABBOTT AEROSPACE
TECHNICAL LIBRARY
ABBOTTAEROSPACE.COM

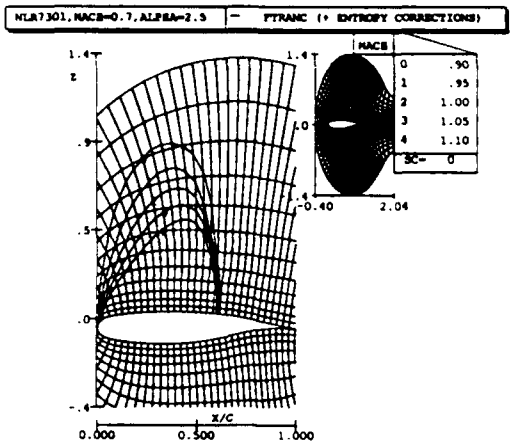


Figure 1: Isomach contours for NLR7301 airfoil at $M_\infty = 0.700, \alpha = 2.5$ deg

Figure 1 shows the grid applied to the NLR7301 airfoil together with the isomach contour distribution for M_∞=0.7 and α=2.5 deg. The grid was generated by the hyperbolic grid generator described in [16]. The outer edge of the computational grid is only a few chords away from the airfoil and about 100 field panels were used to control the outflow conditions.

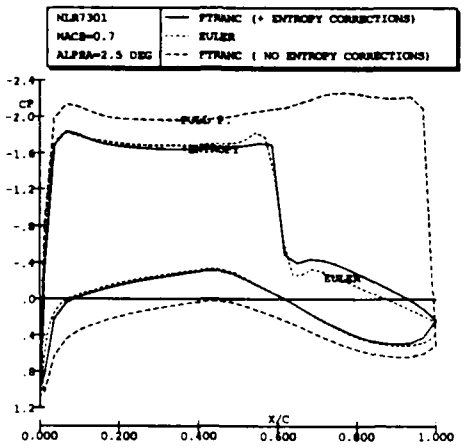


Figure 2: Pressure distribution on the NLR7301 airfoil at $M_\infty = 0.700, \alpha = 2.5$ deg

In figure 2 the steady pressure distributions calculated with FTRANC using the entropy correction modeling are compared with data from an Euler method [17] and with data obtained by applying FTRANC without entropy correction modeling for M_∞=0.7 and α=2.5 deg. At this highly transonic condition the FTRANC method without entropy correction predicts a strong shock at the trailing edge of the airfoil. Due to a large extension of the supersonic zone the result is probably affected by a to small grid extent. The FTRANC data including entropy corrections compare fairly well with the results of the Euler method regarding shock position and pressure distributions. Downstream of the shock the differences are larger which might be explained from the fact that no vorticity correction was utilized in the FTRANC method.

The procedure of obtaining unsteady loads for oscillatory motions from applications to diverging motions is demonstrated for the NLR7301 airfoil. Figures 3 to 6 compare results of the unsteady lift coefficient versus frequency due to a pitching motion about 0.40 chord at the supercritical flow condition M_∞=0.721 and α=-0.19 deg (inviscid shock-free design condition). Two types of results are shown: direct results calculated for diverging and harmonic motions and indirect results obtained by fitting the diverging data by Padé polynomials.

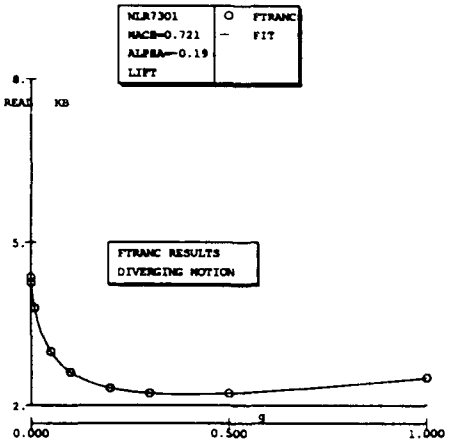


Figure 3: Unsteady lift coefficient of an exponentially diverging, pitching NLR7301 airfoil at supercritical design condition $M_\infty = 0.721, \alpha = -0.19$ deg

The results depicted in figure 3, decrease and subsequently increase monotonously with increasing g and exhibit a large gradient at divergence rates approaching zero. In the calculations it turned out that the higher the divergence rate, the faster the convergence.

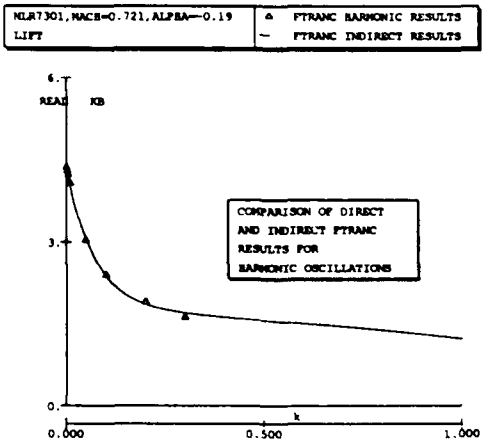


Figure 4: Real part of unsteady lift coefficient of a harmonically pitching NLR7301 airfoil at supercritical design condition $M_\infty = 0.721, \alpha = -0.19$ deg

Figures 4 to 6 compare harmonic results of the direct calculation in which results could only be ob-

THIS DOCUMENT PROVIDED BY THE ABBOTT AEROSPACE
TECHNICAL LIBRARY
ABBOTTAEROSPACE.COM

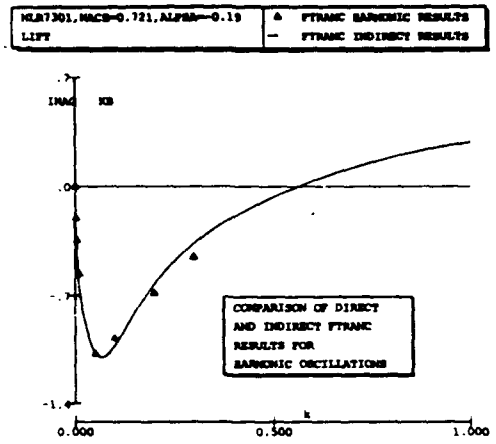


Figure 5: Imaginary part of unsteady lift coefficient of a harmonically pitching NLR7301 airfoil at supercritical design condition $M_\infty = 0.721, \alpha = -0.19$ deg

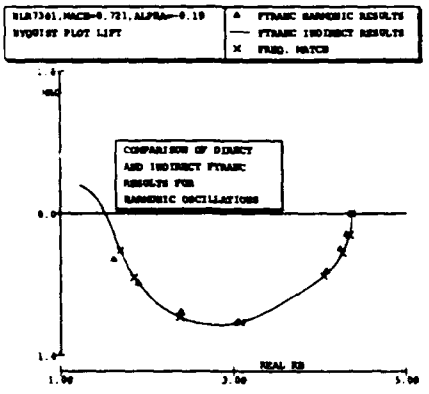


Figure 6: Nyquist plot of unsteady lift coefficient of a harmonically pitching NLR7301 airfoil at supercritical design condition $M_\infty = 0.721, \alpha = -0.19$ deg

trained up to k=0.3 with indirect data. It was not possible to obtain direct solutions for higher frequencies on the current grid due to the break down of the iteration procedure. A satisfactory agreement exists between the results in the whole frequency range for which the comparison can be made.

3.3.3 Fighter-type wing,A

The applicability of FTRAN3 in static aeroelastic analysis is demonstrated for a modern fighter type configuration in transonic flow at $M_\infty = 0.9$ and $\alpha = 6$ deg. Inviscid calculations have been performed with FTRAN3 for the clean wing with entropy correction modeling and without entropy correction modeling, and with XFLO22 [18] using the cross-wind concept for modeling the fuselage effects. The FTRAN3 computations were performed on a medium mesh of 9x24x20 points which is supposed to be adequate for generating loads distributions for static aeroelastic analysis.

Figure 7 show the calculated (right) and experimental (left) [19] isobar contour distribution at the upper

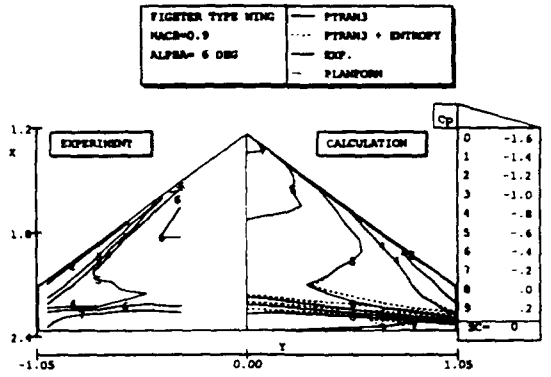


Figure 7: Comparison of experimental and calculated isobar contours at upper part of fighter type wing at $M_\infty = 0.9, \alpha = 6$ deg

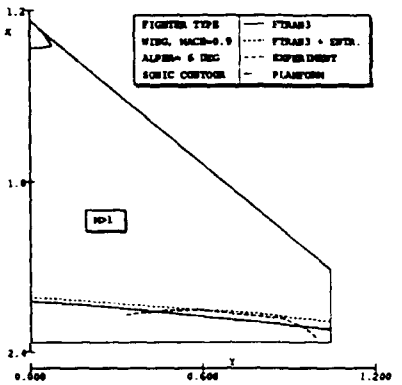


Figure 8: Comparison of experimental and calculated sonic contours at upper part of fighter type wing at $M_\infty = 0.9, \alpha = 6$ deg

wing surface. Figure 8 shows the shock position and figure 9 compares pressure coefficients at selected stations . The predicted and experimental distributions exhibit a similar flow structure. The entropy corrections predict the shock wave more upstream and closer to the experiment over the main wing part. At the lower side a good agreement is obtained between the calculated and experimental pressure data except for the trailing edge region. The non-conservative XFLO22 data show a weaker and less downstream located shock as compared with the FTRAN3 data and the experiment. Downstream of the shock the prediction by the codes are in disagreement with the experimental data probably due to the neglect of viscous effects. At the leading edge region the XFLO22 data show a very good agreement with the experimental data while the FTRAN3 data are too low due to less resolution and the fact that the code cannot model effects of bodies. Between the leading edge region and the location of the shock the FTRAN3 data and especially the one with entropy correction show the better comparison with the experimental data.

THIS DOCUMENT PROVIDED BY THE ABBOTT AEROSPACE
TECHNICAL LIBRARY
ABBOTTAEROSPACE.COM

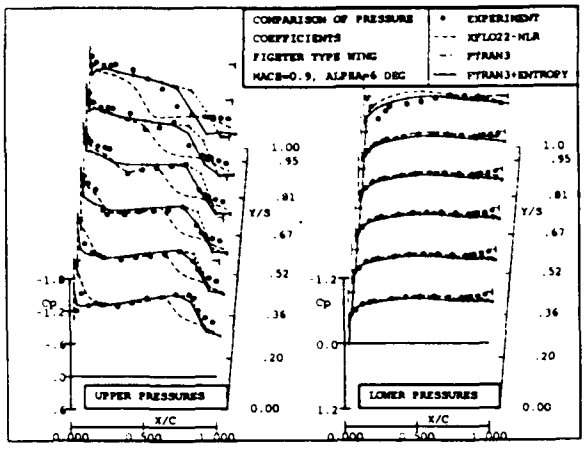


Figure 9: Comparison of experimental and calculated distributions of steady pressure coefficients at $M_\infty = 0.9, \alpha = 6$ deg

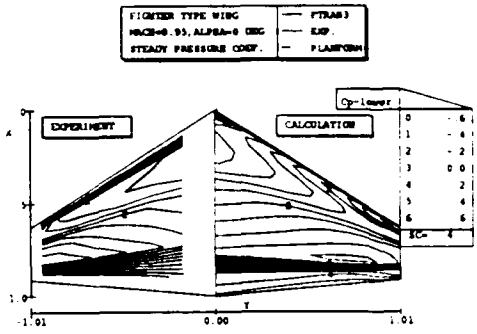


Figure 12: Comparison of experimental and calculated isobar contours at lower part of fighter type wing at $M_\infty = 0.95, \alpha = 0$ deg

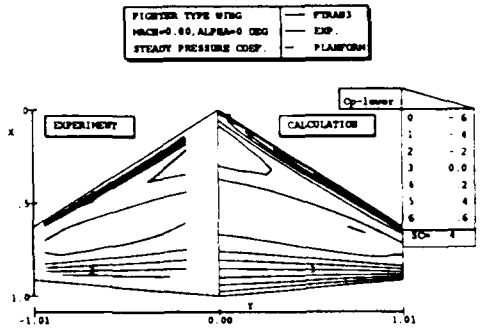


Figure 10: Comparison of experimental and calculated isobar contours at lower part of fighter type wing at $M_\infty = 0.8, \alpha = 0$ deg

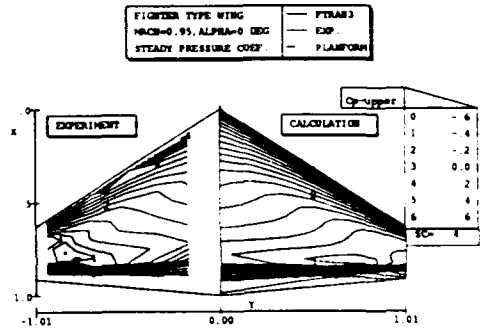


Figure 13: Comparison of experimental and calculated isobar contours at upper part of fighter type wing at $M_\infty = 0.95, \alpha = 0$ deg

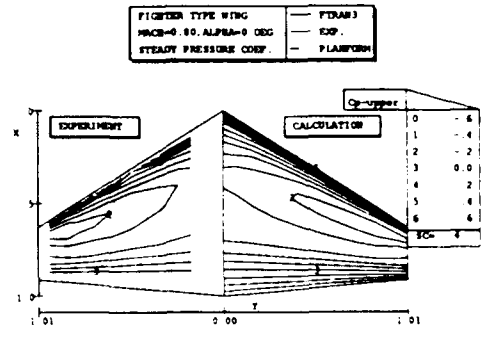


Figure 11: Comparison of experimental and calculated isobar contours at upper part of fighter type wing at $M_\infty = 0.8, \alpha = 0$ deg

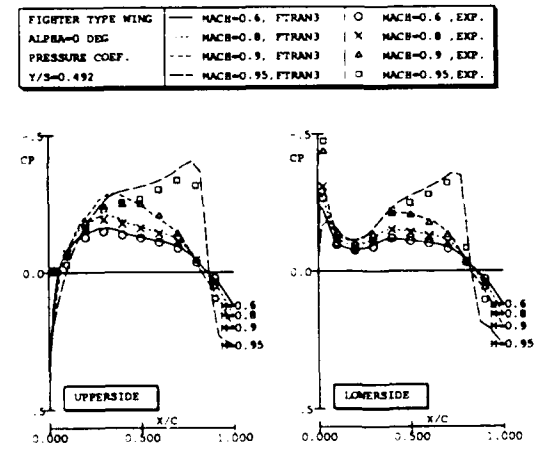


Figure 14: Comparison of experimental and calculated steady pressure coefficients on fighter type wing

THIS DOCUMENT PROVIDED BY THE ABBOTT AEROSPACE
TECHNICAL LIBRARY
ABBOTTAEROSPACE.COM

3.3.4 Fighter-type wing,B

The applicability of the FTRAN3 code is further demonstrated by comparing calculated data with experimental data of the NLR wind tunnel test described in Ref.[20] for the clean wing of a fighter type configuration. The vibration mode is pitch about the root midchord. The frequency is 20 Hz and four flow conditions are considered: $M_\infty = 0.6, 0.8, 0.9, 0.95$ at $\alpha = 0$ deg. The computations were made on a mesh of 12x34x26 points.

Figures 10 to 13 show the calculated (right) and experimental (left) isobar contour distributions at the upper and lower wing surfaces for $M_\infty = 0.8$ and 0.95. The calculations show similar patterns as observed in the experiment.

Figure 14 compares the calculated and experimental steady pressure coefficients at the span station $y/s = 0.492$ for all flow conditions. At the subsonic conditions the pressure level is predicted quite well. At the transonic conditions the pressure level is underpredicted at the upperside in the supersonic zone and at the lowerside at the nose. The latter is attributed to the resolution of the mesh which seems to be too coarse.

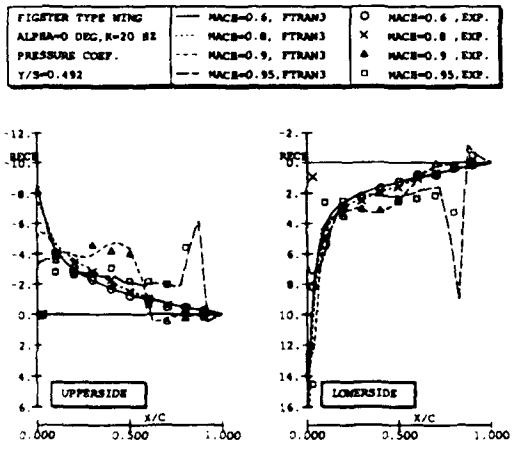


Figure 15: Comparison of real part of experimental and calculated first-harmonic pressure coefficients on fighter type wing

Unsteady pressure coefficients are compared in figures 15 and 16 at the span station $y/s = 0.492$ for all flow conditions. Except for peak values a fairly good agreement is shown. In the subsonic cases the agreement is slightly better. The only major discrepancy shows up in the trajectory of the shock wave and in the imaginary part at $M_\infty = 0.95$ (fig.16) where the predicted and measured peaks have opposite signs. It should be noted that the pressure orifices in the experiment are relatively widely spaced and do not allow a concise recording of the shockwave motion.

3.3.5 Supercritical rectangular wing

Furthermore results of FTRAN3 calculations are presented concerning a supercritical wing with a rectangular planform of aspect-ratio 4, oscillating in pitch about an axis located at 0.46 chord. The geometric properties were taken from Ref.[21] and a comparison is made with experimental data from Ref.[22]. Steady computations were performed at $M_\infty = 0.7, 0.825$ and $\alpha = 2$ deg. For each of the two conditions one unsteady computation has been made at a reduced frequency of $k = 0.15$.

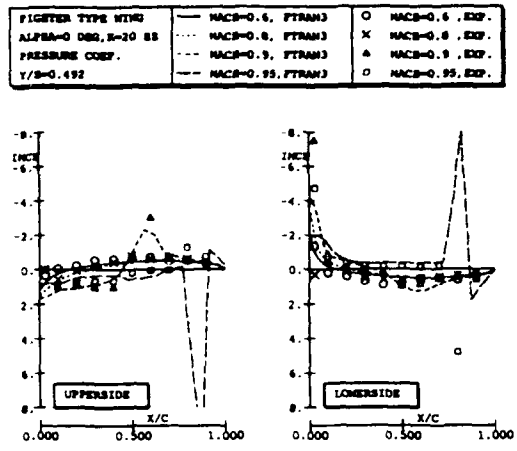


Figure 16: Comparison of imaginary part of experimental and calculated first-harmonic pressure coefficients on fighter type wing

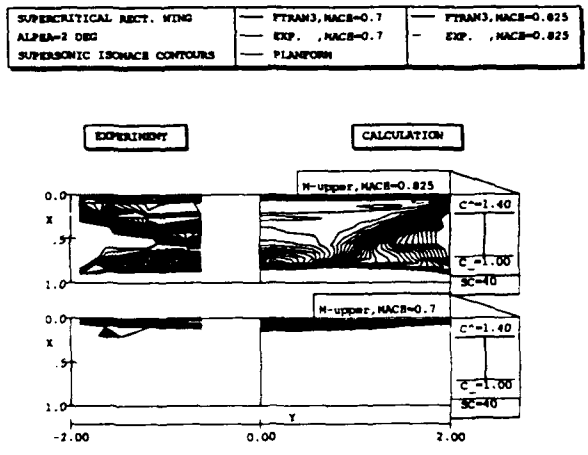


Figure 17: Comparison of supersonic contours at upper part of supercritical rectangular wing at $M_\infty = 0.7 - 0.825, \alpha = 0$ deg

Figure 17 shows the calculated (right) and experimental (left) supersonic contour distributions at the upper wing surface for $M_\infty = 0.7$ and 0.825. At the lower Mach number the location and size of the relatively small supersonic region seems to be fairly well predicted except for the rather unusual shape of the experimental data. This is probably associated with an excessive value at one experimental data point, discussed below. At the higher Mach number the location and size of the relatively large supersonic region seems to be fairly well predicted except for the size of the embedded subsonic region which penetrates much

THIS DOCUMENT PROVIDED BY THE ABBOTT AEROSPACE
TECHNICAL LIBRARY
ABBOTTAEROSPACE.COM

further from the tip in the experiment. This is probably caused by viscous effects. The irregularities which can be notified in some regions in the experimental data raise some doubt about the experimental accuracy at some data points.

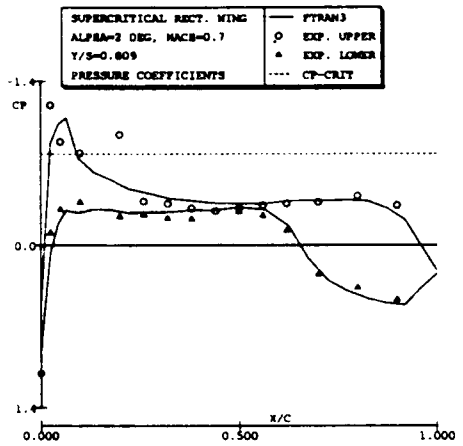


Figure 18: Comparison of experimental and calculated steady pressure coefficients on supercritical rectangular wing at $M_\infty = 0.7$ and $\alpha = 2$ deg

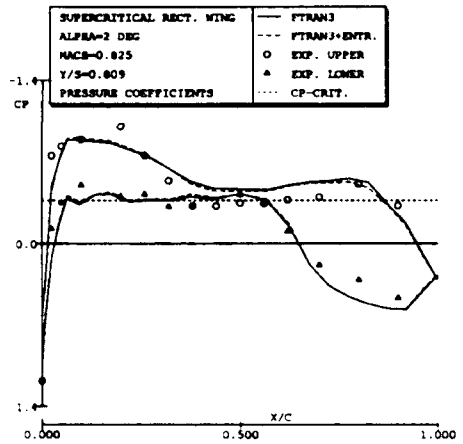


Figure 19: Comparison of experimental and calculated steady pressure coefficients on supercritical rectangular wing at $M_\infty = 0.825$ and $\alpha = 2$ deg

Figures 18 and 19 compares the calculated and experimental steady pressure coefficients at the span station $y/s = 0.809$ for all flow conditions. At the lower Mach number the calculated pressures at upper and lower side match fairly well with almost all the experimental data points, except for one point at about 20% where the experimental value is implausible. At the higher Mach number the calculated pressures at the lower side match fairly well with the experimental data points, except for the trailing edge region. This probably may partly be attributed to the neglect of viscous effects. At the upper side the calculated data overestimate the magnitude between the quarter and three-quarter point and show one large supersonic region. The experimental data show two supersonic regions with a relatively large subsonic zone in between. Also a calculated result is shown using the entropy correction modeling, which for this case has a limited effect.

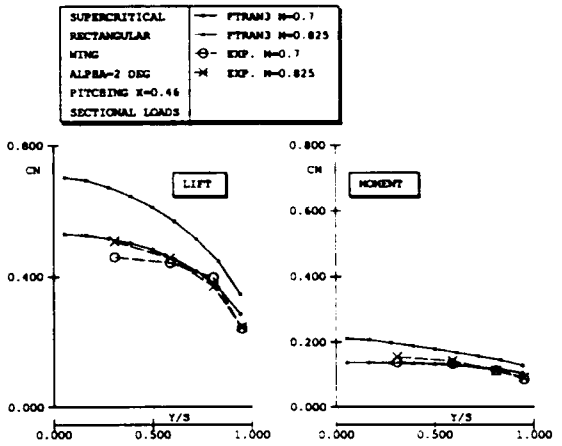


Figure 20: Comparison of experimental and calculated steady spanwise normal load and pitching moment about the quarter-chord coefficients on supercritical rectangular wing

Figure 20 compares the calculated and experimental steady sectional loads coefficients for both flow conditions. The transonic data at $M_\infty = 0.7$ agrees fairly well (especially the moment coefficient) while at the higher Mach number the agreement is poor. The experiment does not show the increasing trend of the FTRAN3 data with increasing Mach number. This, again, probably may partly be attributed to the neglect of viscous effects.

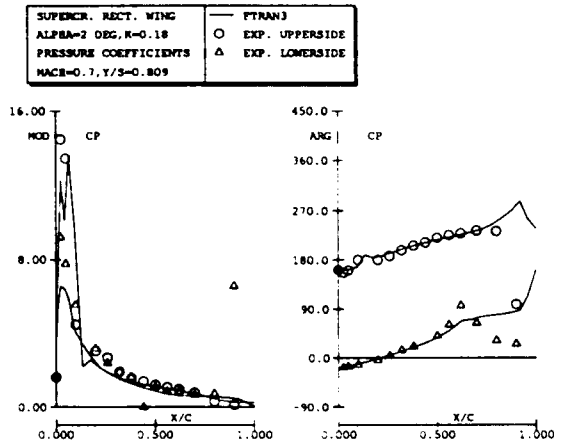


Figure 21: Comparison of experimental and calculated first-harmonic pressure coefficients on supercritical rectangular wing at $M_\infty = 0.7$ and $\alpha = 2$ deg

Figures 21 to 22 compare the calculated and experimental unsteady pressure coefficients at the span station $y/s = 0.809$ for both flow conditions. At the lower Mach number a reasonable agreement is obtained (especially the magnitude) except for the questionable experimental value at the trailing edge and in the last

THIS DOCUMENT PROVIDED BY THE ABBOTT AEROSPACE
TECHNICAL LIBRARY
ABBOTTAEROSPACE.COM

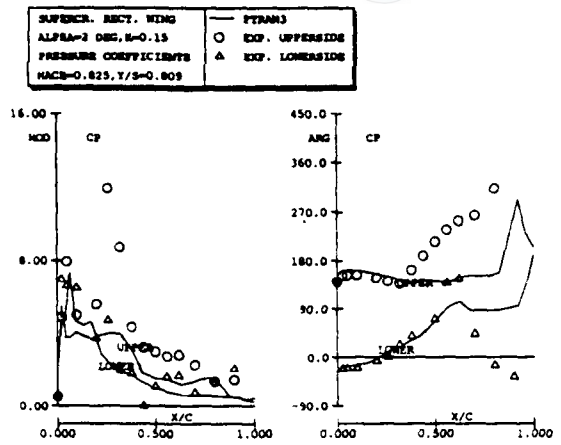


Figure 22: Comparison of experimental and calculated first-harmonic pressure coefficients on supercritical rectangular wing at $M_\infty = 0.825$ and $\alpha = 2$ deg

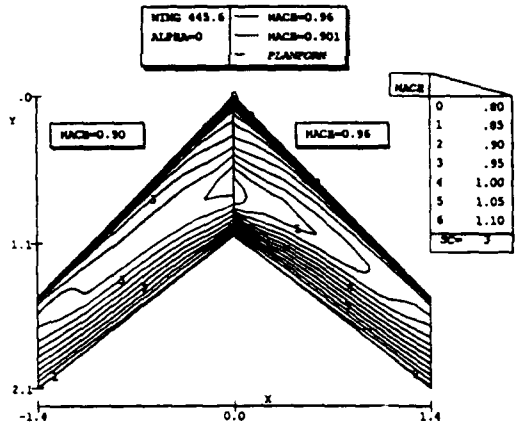


Figure 23: Isomach contours for NACA wing 445.6 at conditions, $M_\infty = 0.901$ (left) and 0.96 (right), $\alpha = 0.0$ deg at wing surface

quarter chord where the experiment shows a different trend in the phase. At $M_\infty = 0.825$ the agreement is disappointing. Only in the first quarter chord the phase shows a reasonable agreement and the magnitude of the lower surface. The experimental data show the effect of a moving shock wave at 30% chord which is totally absent in the calculated data. The discrepancies are mainly due to the fact that the calculated steady flow field differs to much , in particular near the shock waves from the measured steady data.

In view of the strong pressure gradients on upper and lower surface, and of the large discrepancies between the experimental data and the inviscid results, it is suspected that flow separation occurs at both upper and lower surfaces. Also, there is some doubt about the reliability of some experimental steady and unsteady pressure values, as shown in figs. 18 and 21. Therefore it is concluded that the current test case is not suitable for validation of an inviscid method. For a meaningful validation, for this test case viscous effects should be taken into account.

3.3.6 3-D AGARD standard aeroelastic wing

As a final FTRAN3 example results are included of an aeroelastic investigation which was conducted for the 3-D AGARD standard aeroelastic configuration in subsonic,transonic and supersonic flow. This configuration is described in [23]. Model "weakened no. 3" was selected. The calculations were performed with the GUL panel method [24] using a 10x15 panel discretization and the FTRAN3 method using a 34x8x20 grid (20x6 on wing upper and lower side) for 6 vibration modes and for 10 reduced frequencies up to $s = 1$.

Figure 23 show the isomach contour distribution at the wing surface at M_∞=0.901(lower part) and 0.96(upper part) at $\alpha = 0$ deg. No supersonic zone occurs at M_∞=0.901 while at M_∞=0.96 the supersonic zone extends almost to the trailing edge over a large part of the wing surface so it can be expected that the flutter boundary will deviate more from the results obtained with subsonic theory. The generalized aerodynamic forces were obtained by using the procedure of rendering data for harmonic oscillations from applications of the GUL and FTRAN3 method to diverging motions. It has been checked by comparison with direct calculations of the methods that the current procedure is equally accurate. The flutter calculations were made by the pk-method.

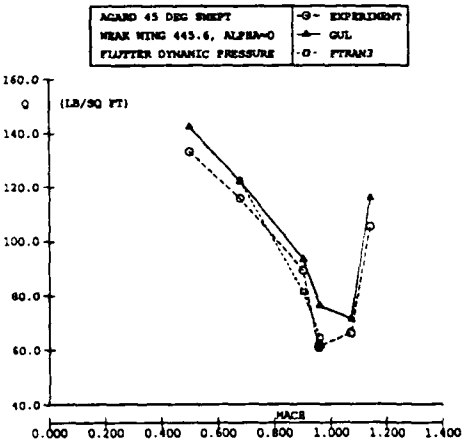


Figure 24: Comparison of calculated and measured flutter boundaries NACA wing 445.6

The flutter results are compared with experimental data in figure 24. In the whole Mach range the fully linear GUL results overestimate the flutter boundaries as compared to the experiment. The FTRAN3 result at M_∞=0.678 agree with the GUL result while in the transonic region a transonic dip is predicted. No FTRAN3 results were obtained for $M_\infty \geq 1.0$ because the method is not applicable in supersonic flow.

THIS DOCUMENT PROVIDED BY THE ABBOTT AEROSPACE
TECHNICAL LIBRARY
ABBOTTAEROSPACE.COM

4 Time-integration methods

4.1 Overview

This section presents the 2-D time-integration methods ULTRAN-V and TULIPS which are in use at NLR and shows results. A 3-D unsteady full potential method has recently been developed which forms the main part of the AESIM method which is described in section 5.

The ULTRAN-V method is described in [9] and is based on the following computational model:

- Unsteady transonic small perturbation theory.
- Integral methods for the steady laminar and unsteady turbulent boundary layer and wake.
- Efficient simultaneous strong-interaction coupling procedure for attached as well as separated flows.

The ULTRAN-V method is a result of extensive modifications during the last decade starting from the NASA-Ames code LTRAN2 and has proved its applicability for a wide range of flow conditions, thereby exceeding the formal limits of the underlying computational model. The computer costs are 25-100 CPU seconds on a 6 Mflop workstation for a 79x59 grid.

The TULIPS method is described in [10] and is based on the following computational model:

1. A free stream consistent fully conservative finite volume discretization of the full potential flow governed by the equations (1, 2,3) on a boundary conforming C-type grid. Mass-flux splitting is employed to maintain stability in supersonic fow regions.
2. Entropy corrections are embedded to enable a better prediction of shock wave position together with vorticity corrections obtained through the Clebsch formulation [25].
3. The minimization of the grid extent by using absorbing boundary conditions.

The TULIPS method has primarily been developed to establish and/or complement the range of applicability of the ULTRAN-V method. The computer costs are 300-1200 CPU seconds on a 6 Mflop workstation for a 104x24 grid.

4.2 2-D inviscid examples of time - integration

Results of applications to two-dimensional airfoils made with the TULIPS method without entropy and vorticity correction have already been published in [3]. In this section results of the TULIPS full potential method, including entropy and vorticity modeling, will be show for the NLR7301 airfoil and NACA0012 airfoil. The geometries were taken from [15].

The applicability of the ULTRAN-V method has been investigated for a wide range of conditions, including low speed high angle of attack conditions and transonic flow, both with massive flow separation (e.g.[26, 27, 28, 29]. Here unsteady results will be show for the NACA0012 airfoil.

An example of steady TULIPS applications is shown in figure 25 for the NLR7301 airfoil and in figure 26 for the NACA0012 airfoil demonstrating the use of entropy and vorticity corrections.

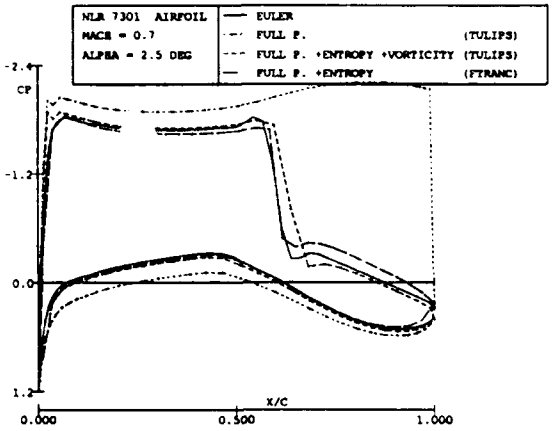


Figure 25: Pressure distribution on NLR7301 at $M_\infty = 0.700, \alpha = 2.5$

In figure 25 calculated steady pressure distributions including entropy and vorticity corrections at M_∞=0.7 and α=2.5 deg. are compared with data from an Euler method [17] ,with data obtained by applying TULIPS without entropy and vorticity corrections and with data from FTRANC with entropy correction. At this severe condition the TULIPS method without entropy and vorticity corrections predicts a strong shock at the trailing edge of the airfoil. The TULIPS data including entropy and vorticity corrections are in good agreement with the results of the Euler method regarding shock position and pressure distributions. Downstream of the shock the differences between the TULIPS and Euler data are very small compared to the differences between the FTRANC and Euler data which can be explained from the fact that the vorticity correction is absent in the FTRANC method.

In figure 26 calculated steady pressure distributions including entropy and vorticity corrections at M_∞=0.8 and α=1.25 deg. are compared with data from an Euler method [17] ,with data obtained by applying FTRANC without entropy and vorticity corrections and with data from FTRANC with entropy correction. At this severe condition the FTRANC method without entropy and vorticity corrections predicts a strong shock at the trailing edge of the airfoil. The TULIPS data including entropy and vorticity corrections are in excellent agreement with the results of the Euler method regarding shock position and pressure distributions. The FTRANC data including en-

THIS DOCUMENT PROVIDED BY THE ABBOTT AEROSPACE
TECHNICAL LIBRARY
ABBOTTAEROSPACE.COM

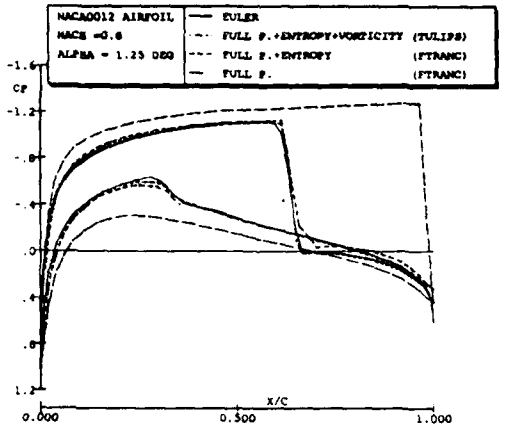


Figure 26: Pressure distribution on NACA0012 at $M_\infty = 0.800, \alpha = 1.25$

tropy corrections are in fairly good agreement with the results of the Euler method. A part of the somewhat larger differences are due to the coarser grid used in the FTRANC applications. Downstream of the shock the differences between the TULIPS and Euler data are nihil compared to the larger difference between the FTRANC and Euler data which is due to the lacking of vorticity corrections in the FTRANC method.

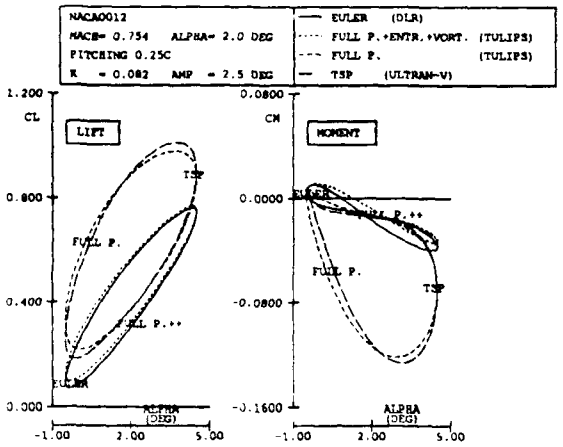


Figure 27: Comparison of calculated lift and moment about the quarter-chord coefficients during oscillatory pitching motion on NACA0012

An example of inviscid unsteady ULTRAN-V and TULIPS applications is shown in figure 27 for an oscillatory pitching motion of the NACA0012 at transonic conditions ($M_\infty = 0.754$,mean angle of attack $\alpha_m = 2$ deg, amplitude $\Delta\alpha = 2.5$ deg and reduced frequency based on semi-chord $k = 0.082$). Figure 27 shows a comparison of lift and moment coefficients from inviscid calculations. Results of TULIPS with and without entropy and vorticity corrections are compared with results of ULTRAN-V and with unsteady results of an Euler method presented in Ref.[30]. The agreement between the transonic small disturbance results and the full potential results is very good and exceeds the expectation of the small disturbance computational model. The good agreement between the entropy and vorticity corrected full potential results and the Euler results leads to the expectation that the corrected full potential modeling is very close to an Euler modeling,except for vorticity dominated flows. The importance of modeling viscous effects for this case is demonstrated in section 6.

5 Aeroelastic 3-D simulation method

The need of the aircraft industry requires the development of an efficient and cost effective method for aeroelastic analysis in transonic flow. Such a method is under development at NLR on the basis of direct simulation of unsteady transonic flow about a flexible aircraft. This requires the simultaneous solution of the equations of unsteady aerodynamics and equations of a flexible aircraft. The feasibility of the development of such a direct coupled aeroelastic simulation method has been demonstrated by comparable developments at Rockwell [31] and at NASA-Langley [32]. Such a development is not realistic without the computing power of supercomputers of the second generation such as NLR's NEC SX-3 supercomputer. The performance of the NEC SX-3 is such that the method is expected to be cost effective. Computation times in the order of 15 minutes CPU-time for a complete aircraft are required. The alternative based on the time-linearized modeling has not been considered because of the limitations in applicability mentioned in the introduction. The method is based on the following concepts:

- OH- Mono-block grid to reduce the computation time, the development time and to ease usage for the 'non-gridexpert' aeroelastic specialists. Current sophisticated alternatives as the multi-block methods and unstructured grid methods are rejected because of various drawbacks: 1) multi-block methods are not easy to use for 'non-grid experts' and 2) multi- block and unstructured grids increase the computation time and the development time considerably. The consequence of some limitations in accuracy of the mono-block grid approach to more complex configurations is considered as more acceptable for aeroelastic applications than for steady aircraft design. Research [16] was performed on methods which generate grids in a more natural way by an evolutionary process starting at the boundaries of the configuration and constructing the grid according to an inflation analogy. This research has resulted in a grid generator [33] which essence is based on the hyperbolic grid generation method of Ref.[34] extended by an integral method for direction and growth control in concave areas where the standard hyperbolic grid generator fails thereby reducing the effort to generate grids of acceptable

THIS DOCUMENT PROVIDED BY THE ABBOTT AEROSPACE
TECHNICAL LIBRARY
ABBOTTAEROSPACE.COM

quality in particular about concave areas such as airfoil noses and wing-fuselage junctions. The grid generator requires a mono-block surface description of the complete aircraft with embedded upwind slits and downwind slits (wake surfaces). A geometry preprocessor has been developed which generates the surface grid by assembling the separate airframe components provided by the user and by constructing the slits. Also the structural data is interpolated to the surface grid.

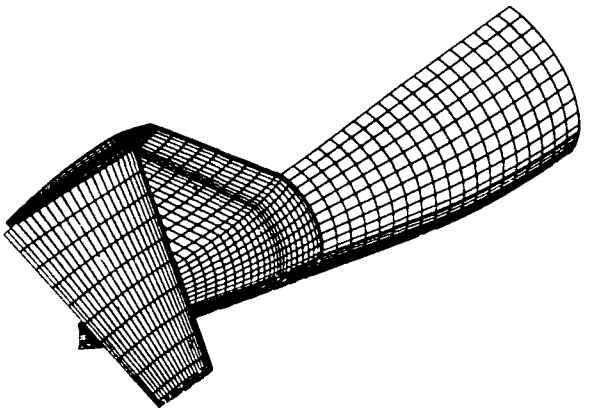


Figure 28: Input surface grid for preprocessor for a T-tail-fuselage combination

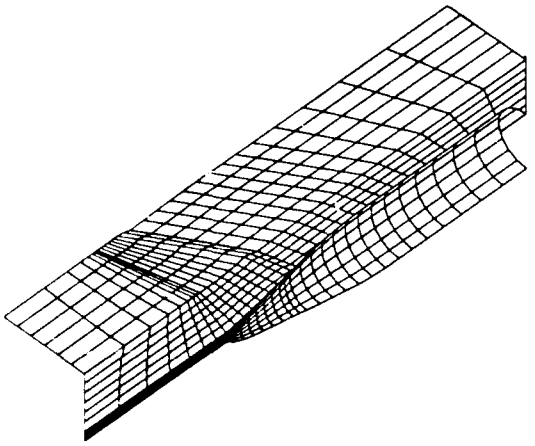


Figure 29: Surface grid with upwind and downwind slits for a T-tail-fuselage combination

An example of an application with the geometry preprocessor to a T-tail-fuselage is depicted in figure 28 to 29. Figure 28 shows the input surface grid which is input to the geometry preprocessor of which the result, i.e. a surface grid distribution with upwind and downwind slits, is shown in figure 29.

Examples of applying subsequently the grid generator are shown in figures 30-31. The tail surfaces have sweep angles which is reflected by the curvature of the grid planes. The example shows

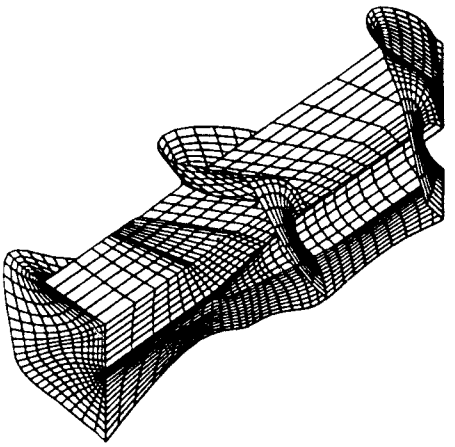


Figure 30: 3-D Grid part about a T-tail-fuselage combination

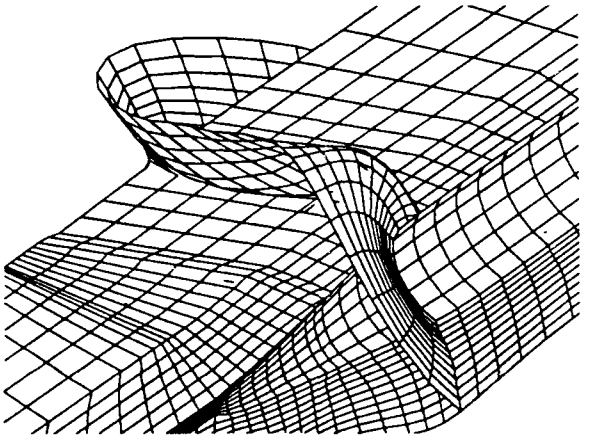


Figure 31: Close-up at middle part of figure 30

that the present grid generator method is able to generate OH type grids around fairly complex shapes with concavities in a small turn-around time.

- In a first phase the unsteady aerodynamic flow is modeled in the time domain by the unsteady full potential equation, taking into account entropy and vorticity corrections. In a second phase, implementation of a correction for viscous effects is foreseen. The model is mainly motivated by operational requirements with respect to computational costs and computational times. The choice of this model instead of an alternative modeling by the unsteady transonic small disturbance theory or the unsteady Euler equations is based on the following considerations:

  1. The leading edge flow about wings equipped with rather thick and blunt-nosed airfoils and the occurring oblique shock waves cannot be modeled with sufficient accuracy by transonic small disturbance theory. Hence, this theory is less suitable for the calculations of unsteady airloads on those wings.

THIS DOCUMENT PROVIDED BY THE ABBOTT AEROSPACE
TECHNICAL LIBRARY
ABBOTTAEROSPACE.COM

2. The best set of equations to model inviscid transonic flow about general aircraft configurations are beyond doubt the Euler equations. However, for the simulation of unsteady flow about complete aircraft configurations the solution of these equations is still to expensive in terms of computer time on the current generation of supercomputers.

3. The full potential equation is restricted to flows with weak shock waves. When it is applied to flows with strong shock waves ,results are obtained where shock waves are too strong and located too far aft in comparison with results obtained with the Euler method. This is mainly due to neglecting effects of shock generated entropy end vorticity. Effects of shock generated entropy and vorticity can be approximately embedded in potential flow formulation as has been shown in the 2-D examples while retaining its cost efficiency in comparison with the Euler equations and obtaining results for flows with strong shock waves which are in good agreement with Euler calculations.

- Dynamic structural behavior of the aircraft is based on the generalized modal deflection approach.

- Unsteady aerodynamics and dynamic structural behavior are solved simultaneously in the time domain.

At present the grid generation work is completed, the aerodynamic solver, based on the full potential equation, is running for several 2 and 3-D testcases. It is expected that a complete pilot system is soon available. Thereafter the entropy,vorticity and viscosity correction modelings will be embedded.

6 Viscous effects

The comparisons made in the previous sections with data calculated by inviscid methods and with experimental data have show the need for modeling viscous effects especially at higher angle of attack and for thick wings. The improvements by adding viscous modeling is demonstrated in this section.

An example of an unsteady viscous ULTRAN-V application is shown in figure 32 for an oscillatory pitching motion of the NACA0012 at transonic conditions ($M_\infty = 0.754, Re_\infty = 5.710^6$,mean angle of attack $\alpha_m = 2$ deg, amplitude $\Delta\alpha = 2.5$ deg and reduced frequency based on semi-chord $k = 0.082$). Figure 32 shows a comparison of lift and moment coefficients from inviscid and viscous calculations. Viscous results of ULTRAN-V are compared with experimental results [35] and with results of the Euler method presented in Ref. [30].. The agreement between the viscous transonic small disturbance results

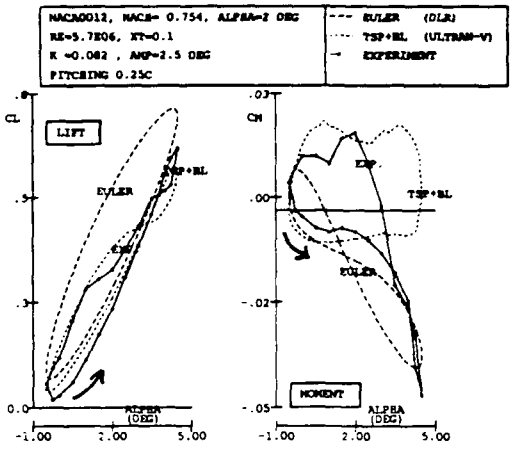


Figure 32: Comparison of calculated and experimental lift and moment about the quarter-chord coefficients during oscillatory pitching motion on NACA0012

and the experimental results is fairly good with respect to the lift coefficient. The large difference between the ULTRAN-V data for the moment coefficient near maximum incidence might be explained probably to the influence of vortex shedding from the leading edge which is absent in the ULTRAN-V method. The Euler results match with the experiment only near the minimum incidence and in the part of the motion with increasing incidence.

7 Concluding remarks

The unsteady inviscid calculation methods which are used at NLR for the prediction of airloads on oscillating structures in transonic flow are described and results of their applications are presented.

From the applications it is concluded:

- Provided that viscous effects are weak unsteady loads in transonic unsteady flow for oscillatory motions can be obtained by time-linearized methods with satisfactory accuracy up to high frequencies using the approach of rendering data for oscillatory motions from data due to diverging motions. The computer cost can be reduced by more than 50%. The solution method is robust, has no stability problems and converge faster with increasing divergence rate. The moderate computer cost makes it possible to perform aeroelastic analysis in transonic flow in acceptable turn-around time on current workstations. Therefore in routine aeroelastic calculations the time-linearized method is an attractive alternative.

- In case of wings equipped with thin airfoils (e.g. fighter-type wings) calculated time-linearized and experimental data correlate reasonably well.

- The straightforward time-linearized application to the supercritical wing with a rectangular planform has shown reasonable to poor correlations.

THIS DOCUMENT PROVIDED BY THE ABBOTT AEROSPACE
TECHNICAL LIBRARY
ABBOTTAEROSPACE.COM

The poor correlations can probably be explained largely by the neglect of strong viscous effects encountered in the experimental results. This leads to differences in the initial steady state flow fields and even more in the corresponding experimental and theoretical unsteady pressure distributions. Therefore it is advised in case of thick wings to pay attention in matching the steady experimental data (e.g. by correcting the angle of attack) and to include some modeling of viscous effects in the inviscid method.

- By adding entropy and vorticity corrections to the unsteady full potential model results are obtained which closely match results of models based on the unsteady Euler equations.
- The modified hyperbolic grid generator will ease usage of unsteady transonic simulations methods by reducing the effort to generate OH grids around transport type aircraft.
- Experience with 2-D coupled viscous-inviscid calculations indicate that this might be a good basis for accounting for viscous effects in 3-D methods.

8 Acknowledgement

This investigation was carried out partly under contract with the Netherlands Agency for Aerospace Programs(NIVR),contract number 01904N and partly under contract with the Royal Dutch Airforce RNLAF. Special thanks are due to Fokker Aircraft B.V. for providing the input data of the T-tail example. Also the author would like to thank Mr. R.Houwink,Mr. H. Schippers and Mr. J. Westland for their contributions.

References

[1] M. H. L. Hounjet .*Transonic Panel Method to determine loads on oscillating airfoils with shocks*, AIAA Journal, Vol. 19, No. 5, May 1981, pp 559-566

[2] M. H. L. Hounjet and J. J. Meijer.*Application of time-linearized methods to oscillating wings in transonic flow and flutter*, AGARD-CP-374,pp 11.1-11.16,October 1984.

[3] H. Schippers and M.H.L. Hounjet .*Two complementary approaches to transonic potential flow about oscillating airfoils*, Journal of Aircraft, Vol. 25 , No.5, May 1988, pp 395-398.

[4] M. H. L. Hounjet .*Application of diverging motions to calculate loads for oscillating motions*, AIAA Journal, Vol. 24, No. 10, October 1986, pp 1723-1725 also as *How to make your aerodynamics in flutter calculations cheaper*, NLR MP 85056 U, August 1985.

[5] M. H. L. Hounjet and B. J. G. Eussen.*Beyond the frequency limit of time-linearized methods*, NLR TP91216 U, June 1991.

[6] M. H. L. Hounjet *A field panel method for the calculation of inviscid transonic flow about thin oscillating airfoils with shocks*, NLR MP81043 U, September 1981.

[7] M. H. L. Hounjet .*A field Panel/finite difference method for potential unsteady transonic flow*, AIAA Journal, Vol.23, No. 4, April 1985, pp 537-545.

[8] R. Houwink and J. van der Vooren.*Improved version of LTRAN2 for unsteady transonic flow computations*, AIAA Journal, Vol. 8, pp 1008-1010, 1980.

[9] R. Houwink .*Unsteady Strong Viscous/Inviscid Interaction modeling in the ULTRAN-V code*, NLR CR 91025 L, May 1991.

[10] H. Schippers .*TULIPS: A method to calculate transonic potential flow about oscillating airfoils*, NLR TR 88193,December 1988

[11] W. Jr. Whitlow, M. M. Hafez and S. J. Osher .*An entropy correction method for unsteady full potential flows with strong shocks*, Journal of fluids and structures, 1987, No. 1, pp 401-414.

[12] M. H. L. Hounjet , J Th. van der Kolk and J.J. Meijer .*Application of NLR's calculation methods to transonic flow about oscillating wings*, Journal of Aircraft, Vol.22, No. 12, December 1985, pp 1034-1042.

[13] M. H. L. Hounjet .*FTRAN3S and FTRAN3: Methods to calculate steady and time linearized unsteady transonic flows about wings*, NLR TR 87020 L, Januari 1987.

[14] M. H. L. Hounjet .*Unsteady transonic flow computations for a rectangular supercritical wing*, NLR TR 87024 L, Februari 1987.

[15] S. R. Bland .*AGARD 2-D aeroelastic configurations*, AGARD, AR-156,1979.

[16] M. H. L. Hounjet. *Hyperbolic grid generation with BEM source terms*,NLR TP 90334 U ,October 1990 also in Proceedings IABEM-90,Springer Verlag

[17] H. Schippers .*Private communications*, 1990.

[18] J. van der Vooren, J. Th. van der Kolk an J.W. Slooff.*A system for the numerical simulation of sub-, and transonic flow about wing-body configurations*, AIAA-82-0935, June 1982

[19] Anonymous. *Edited pressure data and integrated loads from AFTI/F-16 pressure test, TF-549, Volume 14, Wing pressure coefficients* ,General Dynamics Report 20PR071,April,1989

THIS DOCUMENT PROVIDED BY THE ABBOTT AEROSPACE
TECHNICAL LIBRARY
ABBOTTAEROSPACE.COM

[20] H. Tijdeman et al *Transonic wind-tunnel tests on an oscillating wing with external store*, NLR TR78106 U, Pt. II, September 1978.

[21] R.H. Rickets et al. *Geometric and structural properties of a rectangular supercritical wing oscillating in pitch for measurements of unsteady transonic pressure distributions*, NASA TM 85673, November 1983

[22] R.H. Rickets et al. *Subsonic and transonic unsteady and steady pressure measurements on a rectangular supercritical wing oscillated in pitch*, NASA TM 85765, August 1984

[23] E. C. Yates Jr. *.Agard standard aeroelastic configurations for dynamic reponse, I-wing 445.6*, AGARD report No.765,July 1988.

[24] M. H. L. Hounjet *.Calculation of unsteady subsonic and supersonic flow about oscillating wings and bodies by new panel methods*, NLR TP89119 U, April 1989.

[25] J. Westland *.Clebsch variable model for unsteady transonic flow: Applications to 2-D airfoils*, NLR TP 91387L, October 1991.

[26] R. Houwink *.Results of a new version of the LTRAN2-NLR code (LTRANV) for unsteady viscous transonic flow computations*, NLR TR 81078 U, 1981.

[27] R. Houwink and A.E.P. Veldman *.Steady and unsteady separated flow computations for transonic airfoils*, NLR MP 84028 U, 1984.

[28] R. Houwink , J.A. van Egmond and P.A. van Gelder *.Computation of viscous aerodynamic characteristics of 2-D airfoils for helicopter applications*, NLR MP 88052 U, 1988.

[29] R. Houwink *.Computation of unsteady turbulent boundary layer effects on unsteady flow about airfoils*, NLR TP 89003 L, 1989.

[30] G. Polz *.Current european rotorcraft research activities on development of advanced CFD methods for the design of rotor blades (BRITE/EURAM 'DACRO' Project)* in Proceedings 17th European Rotorcraft Forum,pp 39.1-39.10

[31] H. Ide and V. J. Shankar *.Unsteady full potential aeroelastic computations for flexible configurations*, AIAA Paper No. 87-1238, June 1987

[32] J. T. Batina, D. A. Seidel, S. R. Bland and R. M. Bennnett. *Unsteady transonic flow calculations for realistic aircraft configurations*, Journal of aircraft, Vol. 26,No. 2, Februari 1989, pp 131-139.

[33] M. H. L. Hounjet *.Hyperbolic grid generation control by panel methods*, NLR TP 91061 U , June1991

[34] J.L. Steger et al. *Generation of three dimensional body-fitted coordinates using hyperbolic partial differential equations*,NASA TM 86753,June,1985

[35] M.E. Wood *.Results of oscillatory pitch and ramp tests on the NACA0012 blade section*, Aircraft Research Associated Limited,ARA Memo No.220

THIS DOCUMENT PROVIDED BY THE ABBOTT AEROSPACE
TECHNICAL LIBRARY
ABBOTTAEROSPACE.COM

AD-P007 805

Computations of Unsteady Flows around Airfoil Sections by Explicit and Implicit Methods Solving the Euler and Navier-Stokes Equations

by
Edgar A. Gerteisen
Numerical Fluid Mechanics
Dornier Luftfahrt GmbH, P.O.Box 1303
7990 Friedrichshafen 1, F.R.G

92-16043

1. SUMMARY

An Euler/Navier-Stokes solution algorithm is presented for unsteady aerodynamic analysis of flows around airfoil sections. Several numerical methods have been involved in the flow solver; beginning with an explicit Runge-Kutta time-stepping scheme it is outlined that for practical handling of many proplems the implicit integration schemes are strongly recommended due to their extended stability margin. Two methodological closely connected moving mesh algorithms have been implemented, concerning the mesh adaption for improved accuracy with a minimal number of mesh points, and the body conforming mesh movement which is completely general and can treat realistic configurations.

A description is given of the latest version of the developed implicit solving algorithm which can be used as a direct method but also includes an option for iterating the unsteady residual to enhance the time accuracy. The included moving mesh methods for solution adapting and body conforming the grid are summarized. Numerical simulations of steady and unsteady well known flow phenomena, comprising a shock / boundary layer interaction, a flow about a cylinder, an airfoil with oscillating flap and a circular arc airfoil, substantiate the above mentioned topics.

2. INTRODUCTION

For the analysis of flutter problems and of self-induced oscillations as wing buffeting and inlet buzz the behaviour of unsteady flow is of extraordinary interest. Especially within the transonic flow regime nonlinear effects in the flow field can occur which demand nonlinear computational methods. The proper treatment of inviscid flow discontinuities like shocks, slip lines etc. require at least the numerical solution of the Euler equations, whereas in addition strong viscous-inviscid interaction phenomena have to be modeled by the complete Navier Stokes (NS) equations.

Very frequently, also for steady state solutions of the Euler- and NS-equations, time marching solution methods are applied which in principle can also be used for time-accurate computations. Various implicit and explicit time integration schemes were proposed in the past; both approaches being quite competitive for steady state computations if the explicit schemes are combined by appropriate convergence acceleration techniques. However, for time-accurate computations the use of explicit integration methods becomes questionable because most of the convergence acceleration techniques can not be applied and it turns out that the necessary stability conditions of these methods impose a far too restrictive bound on the time step allowed. This problem becomes more obvious if flow problems are considered where in some regions of the flow field discretizations with very small mesh sizes are required. Although many unsteady flow problems are characterized physically by small frequencies concerning changes in the flow field, the stability conditions of explicit methods which are essentially proportional to the cell lengths require very small time steps dictated by the smallest mesh cells in the solution domain. Therefore purely explicit methods can only be applied efficiently in time-accurate computations if the characteristic features of the actual physical problem and the numerical discretization are balanced in some sense.

It is outlined that implicit methods are strongly recommended if the viscous, transonic phenomena such as control surface buzz, wing torsional buzz or buffeting should be attacked efficiently. A description is given of the current method which consists of a LU-factorization method, where the unsteady residual can be iterated within each individual time-step and which also includes the coupling with efficient moving mesh algorithms for simultaneously generating solution adapted and body conforming grids. The calculated examples, which are the well known Hakkinen test case of an oblique shock wave interacting with a flat plate boundary layer, the unsteady flow about a cylinder exhibiting a von Karman vortex street, an airfoil with oscillating flap where different type of shock motions occur observed by Tijdeman and the experimentally well examined 14% circular arc airfoil, demonstrate the capabilities of the method. Further steps towards an engineering-type application tool are discussed in the conclusions

3. GOVERNING EQUATIONS

Within the continuum limit, the motion of a compressible fluid is governed by the Navier Stokes equations. This set of equations can be derived from the principles of classical mechanics and thermodynamics in an integral form by applying the conservation law of mass, momentum and energy to a control volume Ω with the control surface $\partial\Omega$ (Ref 1). Let $\rho, \vec{v}, \varepsilon$ be respectively the density, the velocity vector and the total absolute enthalpy per unit mass, then the system to solve can be written, neglecting the body forces, as:

$$\frac{d}{dt}\int_{\Omega}\rho d\Omega + \int_{\partial\Omega}\rho\vec{v}\cdot\vec{n}\,d(\partial\Omega) = 0$$

THIS DOCUMENT PROVIDED BY THE ABBOTT AEROSPACE
TECHNICAL LIBRARY
ABBOTTAEROSPACE.COM

$$\frac{d}{dt}\int_{\Omega}\rho\vec{v}\,d\Omega+\int_{\partial\Omega}\rho\vec{v}(\vec{v}\cdot\vec{n})d(\partial\Omega)+\int_{\partial\Omega}p\cdot\vec{n}\,d(\partial\Omega)-\int_{\partial\Omega}\bar{\sigma}\cdot\vec{n}\,d(\partial\Omega)=0$$

$$\frac{d}{dt}\int_{\Omega}\rho\varepsilon d\Omega+\int_{\partial\Omega}\rho\varepsilon(\vec{v}\cdot\vec{n})d(\partial\Omega)+\int_{\partial\Omega}p(\vec{v}\cdot\vec{n})d(\partial\Omega)-\int_{\partial\Omega}\vec{v}(\bar{\sigma}\cdot\vec{n})d(\partial\Omega)+\int_{\partial\Omega}\vec{q}\cdot\vec{n}\,d(\partial\Omega)=0 \quad .$$

(2.1)

In order to close this system it is necessary to establish relationships between the thermodynamic variables as well as to relate the transport properties to the thermodynamic variables. The pressure is related to the conservative variables by the equation of state for a thermally and calorically perfect gas

$$\rho\varepsilon=\frac{1}{2}\rho\left(\vec{v}\cdot\vec{v}\right)+\frac{1}{\kappa-1}p \quad .$$

In the case of a *Newtonian fluid* the stress tensor $\bar{\sigma}$ depends linearly with the rates of strain and (neglecting the bulk viscosity) the general deformation law becomes

$$\bar{\sigma}=\mu\left[\left(\nabla\cdot\vec{v}^{T}\right)+\left(\nabla\cdot\vec{v}^{T}\right)^{T}-\frac{2}{3}\left(\nabla\cdot\vec{v}\right)I\right] \quad .$$

Assuming Fourier's law for heat transfer the heat flux vector can be expressed as

$$\vec{q}=-k\cdot\nabla T \quad ,$$

and normally it is convenient to apply Sutherland's assumption that the molecular viscosity is a function of the temperature alone:

$$\mu=\frac{1.462\cdot10^{-6}\cdot T^{3/2}}{T+110.3}$$

Because the ratio (c_p/Pr) is approximately constant for most gases the coefficient of thermal conductivity k can be determined by the relation

$$k=\frac{c_p\mu}{Pr}$$

once μ is known.

While it is generally accepted that the presented NS-equations are in principle capable of describing the behaviour of all kind of flows, at high Reynolds numbers the onset of turbulence makes it impracticable to solve them. The main problem is that time and space scales of the turbulent motion are so small that the number of grid points and the small time step size puts the computational time required outside the realm of present computers. Therefore the most common used approach to overcome this difficulty is to use the statistical averaging procedure, called Reynolds averaging. The thereby appearing turbulent shear stresses are usually related to the rate of mean strain through a scalar turbulent or "eddy" viscosity following a suggestion of Boussinesq. In this work the, in engineering calculations, widespread Baldwin/Lomax model is used to determine the eddies within the flow field.

Another approach to the NS-equation is a reduced set of equation which is valid only in the inviscid portion of the flow field, the Euler equations. These are obtained by dropping both the viscous terms and the heat transfer terms from the complete set. Because of less computational effort this approach is strongly recommended when viscous effects can be neglected but strong and complicated shock structures appear.

4. NUMERICAL METHOD

4.1 Discretization

The computational domain is subdivided into finite volumes and following this concept the semi-discrete form of the conservation law (3.1) is recovered to

$$\frac{d}{dt}\left(\Omega_{ij}U_{ij}\right)+F_{ij}-D_{ij}=0 \quad . \qquad (4.1)$$

where F_{ij} represents the flux integrals (Euler- and NS-fluxes) including the grid speed terms which is mentioned as ideal method to use with moving grid schemes for unsteady flows or with schemes in which the grid evolves with the solution at each time step; U_{ij} denotes the vector of conservative variables, Ω_{ij} the finite volume, and D_{ij} the numerical diffusion operators for each cell. By defining the space discretization the system of partial integro differential equations has been transformed into a system of ordinary differential equations in time direction.

Allowing some time variation of the cell, an appropriate discretization can be written by a first order approximation with respect to the volume:

$$\frac{U_{ij}^{n+1}-U_{ij}^{n}}{\Delta t}+\bar{R}_{ij}(U)=0 \qquad (4.2)$$

where

$$\bar{R}_{ij}=\frac{1}{\Omega_{ij}^{n+1}}\left(\frac{\Omega^{n+1}-\Omega^{n}}{\Delta t}t+F_{ij}-D_{ij}\right)$$

This form directly represents a defect equation for the steady state solution with $\bar{R}$ representing the residual. For time accurate computations a one step method has to be used or the definition of the residual has to be modified.

Several numerical methods have been implemented as driving algorithms to solve this system of nonlinear equations. An explicit one step multi-stage scheme (Ref 2) has been carried out considering a time-accurate multigrid formulation (Ref 3) as well as an implicit residual averaging procedure to overcome the limitations in time step size. Unfortunately both modifications could increase the time step size only by about one decade, whereas for the practical handling of many problems the stability margin should extend to several decades ($10^3 < CFL < 10^5$) (Ref 4) which so far can be achieved only by implicit integration schemes.

For that reason the Beam-Warming- Steger- method (Ref 5) was implemented in the ADI-formulation and some selected examples have been calculated. Further

THIS DOCUMENT PROVIDED BY THE ABBOTT AEROSPACE
TECHNICAL LIBRARY
ABBOTTAEROSPACE.COM

development steps have been done in order to improve the implicit formulation, i.e. the factorization has been changed to LU which extends the linear stability range to three space dimensions. The latter version of the implicit solving algorithm will be described in more detail.

4.2 Numerical Algorithm

4.2.1 Implicit Time Step Iteration

In order to apply a LU-factorization, the implicit operator must be split into forward and backward differences. The resulting scheme should be centralized in the point (i,n + 1/2) to insure second order accuracy (Ref 6) with respect to a Crank-Nicholson step. Therefore the appropriate splitting for the explicit terms will be into corresponding backward/forward differences. Commonly the implicit algorithms are written in delta formulation which garanties that an iterated steady state solution will be independent of the step size in time. Following this concept the space/time discretization is expressed as

$$f(U^n, U^{n+1}) = \frac{\Omega^{n+1}}{\Delta t}\Delta U + \frac{(\Omega^{n+1} - \Omega^n)U^n}{\Delta t}$$

$$+ \Theta(\delta^+ \Delta F^* + \delta^- \Delta F^*) + \frac{1}{2}(\delta^+ + \delta^-)F^n = 0 \quad , \qquad (4.3)$$

where (n) and (n + 1) denote the time levels and the Δ symbol the difference of quantities of these levels, and Θ denotes the weighted average taken from the old and new time levels, i.e. for $\Theta = 0$ we get the implicit Euler algorithm, for $\Theta = 1/2$ the implicit Crank-Nicholson scheme and for all other $0 < \Theta \leq 1$ some more or less stable combination of both. The symbols δ^+ and δ^- represent the forward and backward differences and the sum $1/2(\delta^+ + \delta^-)$ is equal to the symmetric difference operator δ. The basis of solving this equation is to linearize the changes in the flux vectors using Taylor-series expansions in time (Ref 7) which is given by

$$\Delta F = F^{n+1} - F^n = F(U^n + \Delta U) - F(U^n)$$

$$= F(U^n) + A(U^n)\Delta U - F(U^n) = A(U^n)\Delta U$$

where $A(U^n) = \partial \Delta F / \partial \Delta U$ symbolizes the Jacobian matrices of the flux vector; therby it is convenient to drop the cross derivatives by computing the viscous flux Jacobians.

With equation (4.3) the solution ΔU^* of the considered time step is expressed as a zero point of the nonlinear unsteady residual function $f(U^n, U^{n+1}) = 0$ which can be iterated for example by a first order Newton-Raphson method. Developing this algorithm, we assume some given first approximation $\Delta U^{(0)}$ (here the upper index means the iteration number), write a truncated Taylor series at this point

$$f(\Delta U^*) = 0$$

$$\cong f(\Delta U^{(0)}) + Df(\Delta U^{(0)})(\Delta U^* - \Delta U^{(0)}),$$

and with some remodeling an iteration process can be defined by

$$Df(\Delta U^{(\nu-1)})(\Delta U^{(\nu)} - \Delta U^{(\nu-1)}) = -f(\Delta U^{(\nu-1)}) \quad ,$$

which delivers a contracting functional mapping within some radii around the solution point.

4.2.2 Splitting of Jacobians

The one sided, implicit, spatial differences are represented by the Jacobian matrices and the choosen splitting has to provide diagonally dominant implicit factors for each matrix inversion in every mesh cell to insure a stable algorithm.

In the present method the splitting by components corrsponding to the flux vector splitting (Ref 8) is used for the Euler Jacobians, although it needs some more computational time to determine the split matrices. Especially concerning the included mesh velocities, which are expressed more straightforward, this splitting incorporates a better representation of the physics as for example the maximum eigenvalue splitting (Ref 9) and has, furthermore, some remarkable properties by applying the method in time marching manner. During the evaluation of different splittings and testing of the method by calculating the shock boundary layer interaction on a flat plate, it was detected that the method with splitting by components delivers a faster convergence (fig.2, fig.3) with respect to the time step. Difficulties of this splitting with respect to solution quality in the case of transonic calculations have been reported (Ref 8) due to unsteady first order derivatives of the splitted eigenvalues at the sonic point. Also in the present implementation, it has been found that this unsteadyness holds responsibility for severe stiffness problems by advancing with large time step size. In order to circumvent them, some derivation of Steger's eigenvalue modification has been introduced.

Concerning the viscous flux Jacobians, it is convenient to drop the cross derivatives; the subsequently remaining second derivatives are approximated by appropriate second differences which can be split and recombined by two one sided differences. For strongly viscous flows and detached shear layers it may be neccessary to calculate the cross terms which in principle can be introduced in the time iterative procedure. Simultaneously, the temporal accuracy may be enhanced by temporal averaging of the Jacobians.

4.2.3 LU - Factorization

The linearized implicit operator (4.3) produces a large, block banded matrix system which requests large storage and operational count for its solution. The most common way of dealing with this problem is to perform an approximate factorization. In contrast to a central differenced alternate direction approach (ADI) of the operator, methods based on LU decomposition have the benefit of being stable in all dimensions, while ADI, at least in theory, is unstable for scalar hyperbolic equations in three dimensions. Although it was shown by Pulliam and Steger (Ref 10) that conditional stability can be achieved by adding some artificial dissipation for ADI type schemes, the advantage of LU with respect to significantly less storage requirements and a less computational time wa-

THIS DOCUMENT PROVIDED BY THE ABBOTT AEROSPACE
TECHNICAL LIBRARY
ABBOTTAEROSPACE.COM

sting solving algorithm due to the triangular structure still remains.

With the backward-forward approach in (4.3) the factorization process is quite straightforward. Presenting the implicit part of the equation in symbolic form it can be written as

$$Df = \frac{\Omega^{n+1}}{\Delta t} + \Theta\left(\delta^{-}A^{+} + \delta^{+}A^{-}\right) \quad .$$

By splitting this into its parts

$$Df = \left[\frac{\Omega^{n+1}}{\Delta t} + \Theta\delta^{-}A^{+}\right]\frac{\Delta t}{\Omega^{n+1}}\left[\frac{\Omega^{n+1}}{\Delta t} + \Theta\delta^{+}A^{-}\right]$$

$$= \frac{\Omega^{n+1}}{\Delta t} + \Theta\left(\delta^{-}A^{+} + \delta^{+}A^{-}\right) + \Theta^{2}\cdot\frac{\Delta t}{\Omega^{n+1}}\cdot\delta^{-}A^{+}\cdot\delta^{+}A^{-}$$

$$= Df_{L}\cdot\frac{\Delta t}{\Omega^{n+1}}\,Df_{U} \quad ,$$

the solving process can be performed in two sweeps throughout the field

$$Df_{L}\,\Delta Y = Rhs$$

$$Df_{U}\Delta U = \frac{\Omega^{n+1}}{\Delta t}\,\Delta Y \quad ,$$

for two dimensions as well as for three dimensions. The decomposition into these factors produces some factorization error which degrades the algorithm to first order accuracy and grows remarkably with larger time step sizes. The described solving process is first order accurate, and therefore, in contrast to i.e. a Gauss-Seidel iteration, it can be used as a direct method to solve the nonlinear algebraic system of equations, though it is recommended to use the time iteration in order to maintain second order accuracy.

4.3. Computational Grids

4.3.1 Adaptive Grid

The following concept of grid generation and adaption relates closely to the work done by Nakahashi and Deiwert (Ref 11). The grid itself is considered as an organized set of points formed by the intersection of lines of a boundary conforming coordinate system. They state that an optimal grid is ideally one in which the numerical solution error (which results from discretization and is usually reflected by the residuals) is uniformly distributed over all grid points. Since this error is not known a priori the grid has to be adapted in time. In the above mentioned publication, the point distribution is specified by desired maximum and minimum grid spacings and by a model consisting of tension springs for controlling distance and torsion springs for controlling inclination of mesh lines. The spring constants themselves are defined by a driving function which represents the flowfield or some geometry definition so that the grid can be clustered, for example near shock waves concerning solution adaption or near the leading edge concerning geometric resolution, without resulting in an extremely coarse mesh. The model results in a line by line space marching solution procedure which can be implemented very efficiently.

This method can be used as a parabolic like mesh generation algorithm if some geometric parameters alone, i.e. curvature, are used as driving functions. For adapting shock waves in the transonic regime the density was proposed (Ref 11) as a reference flow property. Another reasonable sensor may be curvature of pressure which is commonly used for blending second and fourth order differences in numerical dissipation operators for preventing oscillations. The adaption of grid points in a boundary layer or in a shear layer was proposed by referencing the transverse gradient of the streamwise momentum component.

Both the accuracy and the rate of convergence can be improved by using solution adapted grids and also significantly less mesh points are sufficient for a comparable solution in a nonadapted grid.

4.3.2 Body Conforming Grids

With respect to aeroelastic applicability, a boundary fitted dynamic computational mesh-algorithm should be capable to conform continuously to the instantaneous position of the airfoil, its motions and deformations. Similar to the concept of Nakahashi and Deiwert, the mesh is modelled as a spring network (Ref 12), where each edge of each cell represents a linear spring in the original mesh corresponding to the steady state aeroelastic configuration. The spring stiffness for a given edge i,j is specified to be inversely proportional to the length of the edge as

$$k_{ij} = 1/\left[(x_j - x_i)^2 + (y_j - y_i)^2\right]^{1/2} \quad .$$

At each time step, the points located on the surface boundary are prescribed while the points on the outer boundary are held fixed, and the static equilibrium equations in the x an y directions are solved iteratively at each interior node i of the grid for the displacements δx_i, δy_i. This solution is accomplished by using a predictor-corrector procedure, which first predicts the displacement by extrapolation from grids at previous time levels and then corrects these by several Jacobi iterations. Due to the predictor step it has been found that only one or two iterations are sufficient to accurately move the mesh.

The described method can be seen as a derivation of the variational principle developped by Brackbill and Saltzmann (Ref 13), the spring constants representing the weight distribution function, where the very fast and efficient process to solve the elliptic like system results from close attraction points due to a good approximation of the first prediction. The algorithm is completely general and can treat realistic configurations in two- and three dimensions, in structured (Ref 12) as well as unstructured (Ref 14) meshes. Therefore it seems to be the most comprising method for future applications with respect to complete aircraft aeroelastic computations.

THIS DOCUMENT PROVIDED BY THE ABBOTT AEROSPACE
TECHNICAL LIBRARY
ABBOTTAEROSPACE.COM

5. RESULTS

5.1 Shock / Boundary Layer Interaction

As first numerical test a steady viscous/inviscid interaction problem is considered (fig. 1). An oblique shock wave interacting with a laminar flat plate boundary layer is chosen corresponding to the well known Hakkinen test case (Ref 15). Taking into account the quite coarse mesh resolution the results obtained by the implicit method compare quite well with the other numerical schemes of fig. 1.

Some basic features of the eigenvalue splitting and the residual iteration on the time step have been evaluated on the basis of this example. The residual reduction over the iteration step of the two regarded schemes is compared in fig.2 and fig.3. The factorization error of the ADI-factorization is realized to grow so much that for large time step sizes (CFL = 100,200,400) the iteration process will not converge anymore. Therefore the LU-factorization promises much more robustness for large CFL-numbers, and it is also recognized that the eigenvalue splitting by components is preferable for relaxation procedures regarding the total number of time steps needed to reach the converged solution. The results of time step iteration, depicted in fig.4, give some interesting functional behaviour for the residual of the case with only one iteration. The convergence with respect to the time step is remarkably better and the total CPU-time needed to reach the fifth decade delivers some breakeven point. Performing more than one residual iteration gives still some better convergence characteristic but the waste of CPU-time rises considerably. It has also to be emphasized that these investigations have only been done for study reasons and that the explicit method of (Ref 2) including all convergence acceleration technique will keep its justification for steady state calculations.

5.2 Flow About a Cylinder

In order to test the metrics in the implicit terms and to validate the time-accuracy of the unsteady implicit scheme, a simulation of the low Re-number flow around a infinitely long cylinder has been considered. The experiments show, that with a Reynolds (Re) number in the order of $Re \cong 5$ the initial potential flow merges into a detached one, where the bubble length grows linearly up to a Re-number of fifty. Aside this point the flow property changes totally from steady to unsteady characteristic and a double row of alternating vortices is observed behind the cylinder, the upper row turning clockwise and the lower row turning counterclockwise. This so-called *von Karman vortex street* occurs in laminar flow for the Re-number range of $40 < Re < 5000$, disappears then and rearises in high Re-numbers turbulent flow (Ref 16).

For the Re-number at which the calculation has been performed, the viscous zone is not exhibited by a very thin boundary layer, which enables to resolve the near wall area in a very coarse mesh (fig. 5). Therefore the numerical problem turns out to be in no sense stiff which results in a time resolution with CFL number of ten. The simulation has been started with a potential solution which developped a growing separation bubble (fig. 6) and finally merged into the vortex street. In the experiment the vortices are visualized by streak lines, just as well they can be illustrated by entropie contours (fig. 5) which are simple to calculate from the solution vector. It can be seen clearly how the entropy is generated at the viscous dominated contour and convectively transported into the field. Caused by the physics as well as by the very coarse mesh, the vortices dissolve after ten diameters. However, the obtained Strouhal number $S = (nD^2)/(\nu Re) = 0.181$, where n represents the frequency, D the diameter of the cylinder and ν the kinematic viscosity, is in good agreement (fig. 7) with the experiment.

5.3 Airfoil with Oscillating Flap

The formation and movement of shocks is a fundamental problem of time-dependent transonic aerodynamics which is adressed in a careful study (Ref 17) by Tijdeman. In his classic experiments with attached flow on a NACA 64A006 airfoil at zero incidence with oscillating trailing edge flap he observed and explained different types of shock motion. For the defined type A shock motion at a Mach number, $M = 0.9$, a small oscillatory motion of amplitude $x_0 = 0.05c$, where c represents the chord length, causes an oscillatory variation of shock strength. For the type B shock motion observed at a lower Mach number, $M = 0.875$, the corresponding steady shock is located farther upstream and the shock moves with a much larger oscillatory variation, and even it disappears by moving downstream. The type C shock motion observed at a Mach number, $M = 0.85$, is represented by the flow where the steady shock is close to the extreme upstream position of the shock in the sonic range pressure distribution. Herein the shock wave moves upstream while increasing, leaves the airfoil from the leading edge and propagates into the oncoming flow as a (weak) free shock wave. Also the shock wave disappears and reforms during a part of the cycle.

The illustrated shock movement problem has been calculated by using the explicit one step multistage integration scheme of (Ref 2) taking also advantage of the residual averaging procedure to enlarge the stability region. According to the method proposed in (Ref 3) as time-accurate multigrid implementation, dramatic phase errors occured which are related to the advancement with the time step in the coarse meshes; as a consequence, it can be stated that a time-accurate multigrid algorithm should be in a formulation which enables to iterate some defined unsteady residuals. Such a formulation has been tried by Jameson (Ref 18). He reported the need of an intolerable number of iterations if the CFL number is growing very large. In the present calculation one degree of the period has had to be simulated by about ten to hundred time steps considering the limited allowable time step size. Therefore, already this Euler simulation turned out to be numerically quite stiff, although the mesh resolution in the near wall region can be chosen very coarse compared to a corresponding Navier-Stokes mesh which has to resolve the viscous boundary layer. The present results (fig. 8) are in good agreement with calculations reported by Magnus (Ref 19), though both exhibit a growing discrepancy to the measurement from shock type C, over type B to type A.

THIS DOCUMENT PROVIDED BY THE ABBOTT AEROSPACE
TECHNICAL LIBRARY
ABBOTTAEROSPACE.COM

Consequently the test case of type A motion has been re examined in detail with the developed LU-factorization by a Navier-Stokes simulation. The adapted steady state solution of a Euler calculation is seen in (fig.9) in form of pressure contours with the underlayed mesh, the corresponding cp-curve (fig.10) depicts an excellent shock resolution. Unfortunately the solution adaption is not yet robust enough to present reliable results with dynamically adapted grids during the simulation of shock movement. The result of the mentioned Navier-Stokes simulation is compared with the Euler solution and the measurement in (fig.11), where the shift of the phase angle is caused by the ambiguousity of the arctan-functional behaviour. A sequence of the recalculated unsteady cycles is exhibited in (fig.12).

5.4 Circular Arc Airfoil

As a self-induced unsteady transonic viscous flow problem which also is of great interest in aeroelasticity, a buffeting case has been examined. Shock motions of type A and B have been observed (Ref 19-20) on the considered 14% thick biconvex circular arc airfoil. Instead of an oscillation of a control surface, the oscillatory pressure behind the shock is provided by the periodic oscillation of a separated shear layer and the wake. The Reynolds - Mach number domain with fixed transition, where periodic shock oscillation occur (Ref 20), is shown in (fig.13). In another interesting experiment of (Ref 20) with free transition it has been found that for a defined range which is connected directly with the transition point the unsteadyness disappears completely. It seems that the transition modes dominate the flow and suppress the unsteady shock movement. The present calculation with a Re / Mach number combination slightly outside the reported unsteady domain (fig.14) already produced type A motion (fig.15). Reasons for the observed discrepancies are probably a non-sufficient shock resolution and the non-adequate description of turbulence quantities in the separated flow region by the algebraic turbulence model applied. Unfortunately, due to limited time constraints, it was not possible to perform a recalculation with the newly implemented mesh adaption facility and time iteration algorithm which should deliver more credible results.

6. CONCLUSIONS

An Euler-Navier-Stokes solver was introduced which is designed for two dimensional steady and unsteady flow analysis including two mesh movement algorithms which allow first to adapt the grid and second to conform the grid to moving control surfaces. It was outlined that, because of the recommended and desired fine shock and shear layer resolution which makes the numerical problem very stiff, it is necessary to use implicit methods for integrating time-accurate solutions of the nonlinear equations especially if the viscous, transonic phenomena such as control surface buzz, wing torsional buzz or buffeting should be attacked efficiently.

In order to demonstrate the capabilities of the present method and to substantiate the above mentioned remarks some selected examples of steady and unsteady flow calculations were presented. Thereby, the adequate modelling of all interesting physical phenomena like turbulence and transition will be a main topic for future research.

The method is very promising for future development steps, which should include an extension to three spatial dimensions and also a direct coupling to the aeroelastic equations of motion (Ref 21-22) considering the nonlinearity of the problem to deal with. One problem, however, arises in extending the method to treat more complicated geometries in three dimensions, i.e. a complete aircraft configuration, because of the difficulty to generate an appropriate structured grid. An alternative approach will be the use of unstructured or coupled structured - unstructured meshes.

Unfortunately, it is beyond the scope to use such a three dimensional Navier-Stokes method as a engineering-type application tool for aeroelastic studies because of the computational time required even on present supercomputer systems, although, "we are on the threshhold of a new era in computer architecture" (Ref 23). The most exciting and promising technology for future computational systems is best expressed with the magic word "Massively Parallel Processing" in the sense of distributed concurrent systems. A comprehensive survey of the topics concerning foundations, parallel software and parallel hardware is given in (Ref 23). A typical approach for grid problems is to subdivide the total computational domain into subdomains where each subdomain corresponds to a processor node of the system. The mentioned domain splitting produces internal boundaries over which some communication processes have to be performed. This synchronization is recently realized by language extensions which are available with implemented library routines resulting in a quasi standardization. Though, the computation power of today's parallel machines is limited because of less sophisticated node processors and lack of available memory. Nevertheless, the computational model can be developed and likely rather soon, hopefully earlier, concurrent computing system should be available where each node should be based on the most advanced local parallel technologies concerning RISC processors and VECTOR facilities.

7. ACKNOWLEDGEMENTS

The author would like to thank his collegues at Dornier who contributed with helpful discussions to the successful completition of this work, especially H.Rieger who provided much support by developing the implicit algorithms. Also the work of K.Grunert is acknowledged, implementing the algorithms for dynamically adapting and body-conforming the grid as a M.S. thesis at Technical University of Munich staying at Dornier for some months.

8. REFERENCES

1. Dale A. Anderson, John C. Tannehill, Richard H. Pletcher "Computational Fluid Mechanics and Heat Transfer", McGraw-Hill Book Company, 1984 (ISBN 0-07-050328-1), pp181-257

2. A. Jameson, Transonic Flow Calculations, Princeton University Report, MAE 1651, 1984, included in

THIS DOCUMENT PROVIDED BY THE ABBOTT AEROSPACE
TECHNICAL LIBRARY
ABBOTTAEROSPACE.COM

Lecture Notes in Mathematics, 1127, edited by F.Brezzi, Springer Verlag, 1985, pp.156-242

3. Dennis C. Jesperson, A Time-Accurate Multiple-Grid Algorithm, AIAA Paper No.85-1493, AIAA 7th Computational Fluid Dynamics Conference, Cincinnati Jyly 15-17, 1985

4. Christopher L. Rumsey, W. Kyle Anderson, Parametric Study of Grid Size, Time Step, and Turbulence Modelling on Navier-Stokes Computations over Airfoils, AGARD 62nd Meeting of the Fluid Dynamics Panel Symposium on Validation of Computational Fluid Dynamics, Paper No. 5, May2-5, 1988, Lisbon, Portugal

5. R.M. Beam and R.F. Warming, An Implicit Factored Scheme for the Compressible Navier-Stokes Equations, AIAA Journal, Vol.16, No.4, 1978

6. Vallorie Peridier and J. David A. Walker, An Algorithm for Unsteady Flows With Strong Convection, NASA Technical Memorandum 100828, ICOMP-88-5

7. J. L. Steger, Implicit Finite Difference Simulation of Flow About Arbitrary Geometries with Application to Airfoils, AIAA Paper 77-665, AIAA 10th Fluid&Plasmadynamics Conference, 1977

8. Joseph L. Steger, A Preliminary Study of Relaxation Methods for Inviscid Conservative Gasdynamics Equations Using Flux Splitting, NASA Contractor Report 3415, Contract NAS1-15852, March 1981

9. Jameson A. and Turkel E., Implicit Schemes and LU-Decomposition, Math.Comp., Vol.37, 1981, pp 385-397

10. T. H. Pulliam and J. L. Steger, Recent Improvements in Efficiency, Accuracy and Convergence for Implicit Approximate Factorization Algorithms, AIAA-85-0360, 1985

11. K. Nakahashi and G. S. Deiwert, Self-Adaptive Grid Method with Application to Airfoil Flow, AIAA Journal, 25, 4, April 1987, pp.513-520

12. Brian A. Robinson, John T. Batina, Henry T. Y. Yang, Aeroelastic Analysis of Wings Using the Euler Equations with a Deforming Mesh, AIAA-90-1032-CP

13. Dale A. Anderson, John C. Tannehill, Richard H. Pletcher "Computational Fluid Mechanics and Heat Transfer", McGraw-Hill Book Company, 1984 (ISBN 0-07-050328-1), pp532-548

14. John T. Batina, Unsteady Euler Algorithm with Unstructured Dynamic Mesh for Complex-Aircraft Aeroelastic Analysis, AIAA 89-1189-CP

15. W. Haase, B. Wagner, A. Jameson, Development of a Navier-Stokes Method based on a Finite-Volume Technique for the Unsteady Euler Equations, Vieweg, Notes on Numerical Fluid Mechanics Volume 7

16. M. Van Dyke, An Album of Fluid Motion, The Parabolic Press, Stanford, California, 1982

17. H. Tijdeman, Investigations of the Transonic Flow Around Oscillating Airfoils, NLR TR 77090 U

18. A. Jameson, private communication, October 1990

19. John B. McDevitt, Lionel L. Levy Jr. and George S. Deiwert, Transonic Flow about a Thick Circular-Arc Airfoil, AIAA Journal, Vol.14, No.5, 1976, pp.606-613

20. D.G. Mabey, B.L. Welsh, B.E. Cripps, Periodic Flows on a Rigid 14 % Thick Biconvex Wing at Transonic Speeds, Technical Report 81059, Royal Aircraft Establishment

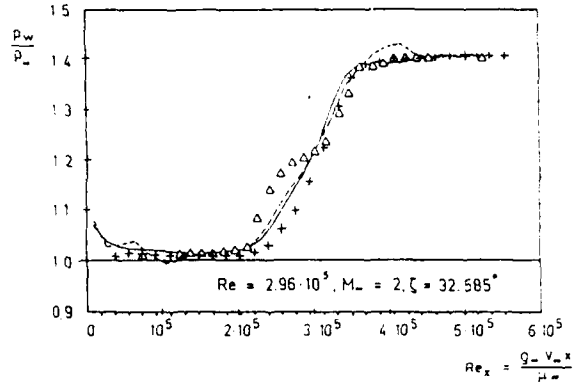
21. H. Ide, Unsteady Full Potential Aeroelastic Computations for Flexible Configurations, AIAA-87-1238, AIAA 19th Fluid Dynamics, Plasma Dynamics and Lasers Conference

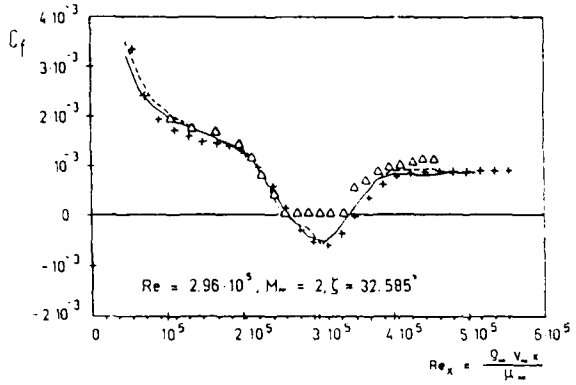
22. Russ D. Rausch, John T. Batina, Henry T.Y. Yang, Euler Flutter Analysis of Airfoils Using Unstructured Dynamic Meshes, AIAA-89-1384-CP

23. George S. Almasi, Allan Gottlieb, "Highly Parallel Computing", The Benjamin Cummings Publishing Company, Inc., (ISBN 0-8053-0177-1)

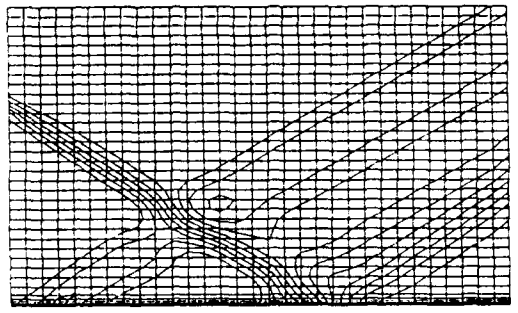
THIS DOCUMENT PROVIDED BY THE ABBOTT AEROSPACE
TECHNICAL LIBRARY
ABBOTTAEROSPACE.COM

9. FIGURES

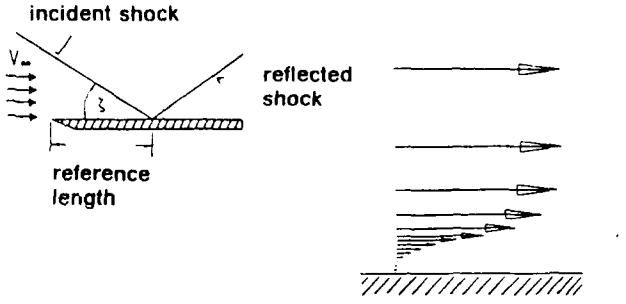




MacCormack explicit-implicit
Runge-Kutta multistage-scheme
△ Experiment of Hakkinen
\+ present results

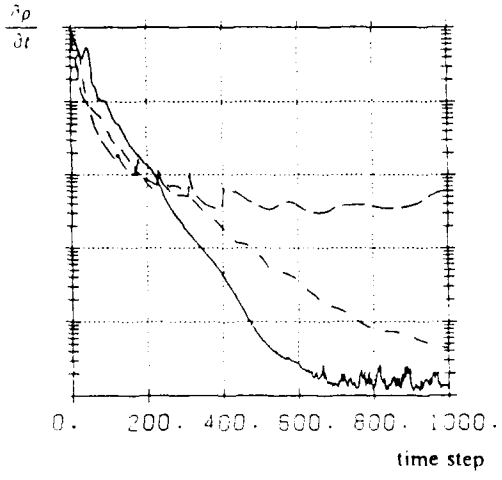


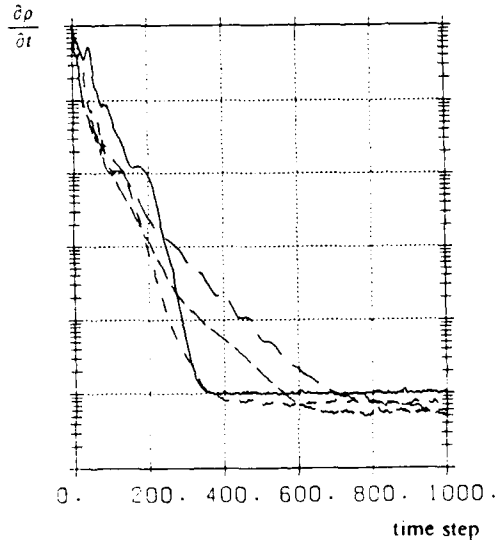
computational mesh within pressure contour lines



resolution of boundary layer in the environment of separation bubble

fig. 1: Oblique shock wave interacting with a laminar boundary layer





CFL = 100
CFL = 200
CFL = 400 , LU eigenvalue splitting by components
CFL = 400 , LU eigenvalue splitting by maximum eigenvalue

fig. 2: residual function, ADI - factorization

fig. 3: residual function, LU - factorization

THIS DOCUMENT PROVIDED BY THE ABBOTT AEROSPACE
TECHNICAL LIBRARY
ABBOTTAEROSPACE.COM

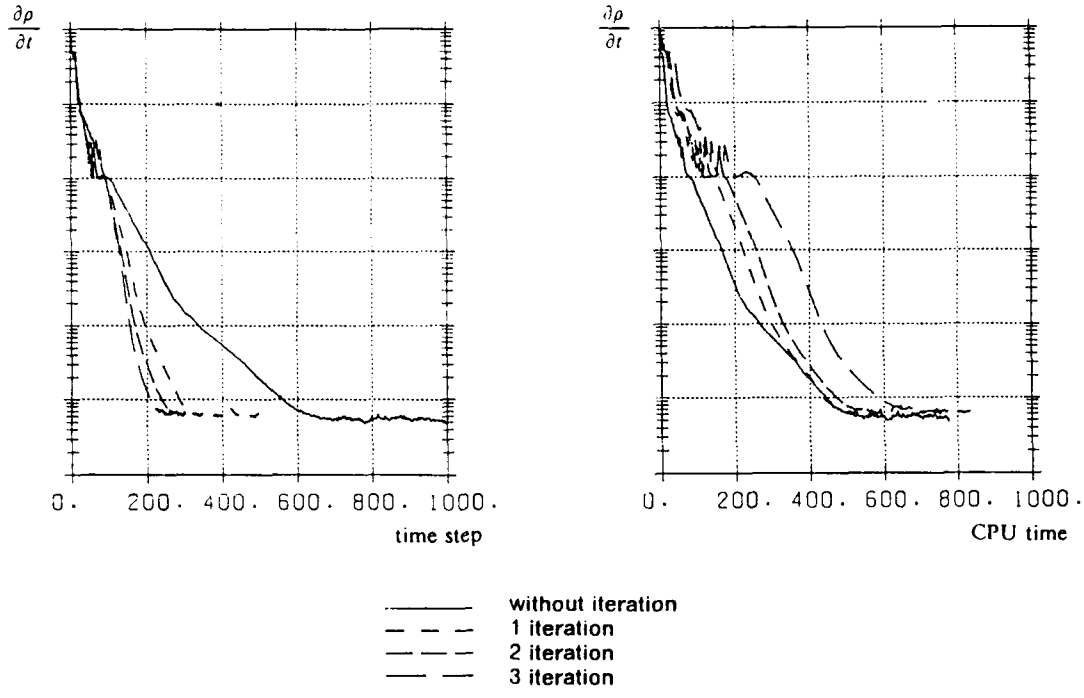


fig. 4: residual function, influence of time step iteration

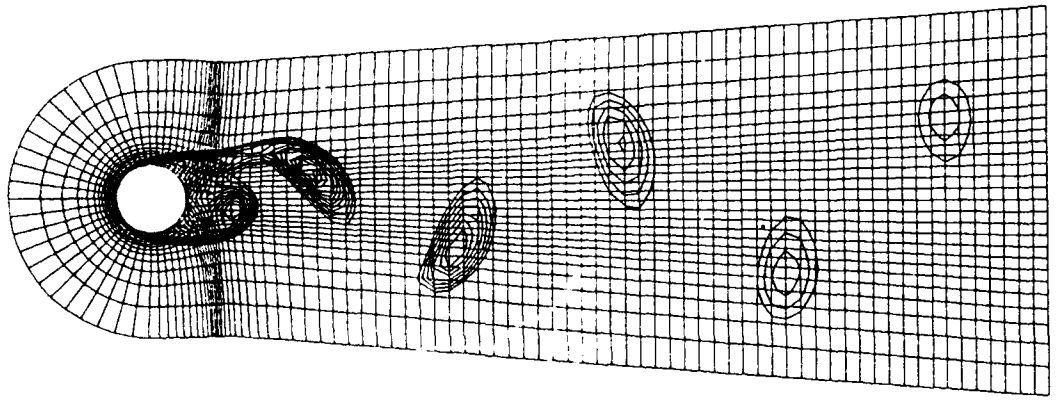


fig. 5: flow about a cylinder. Re = 200. M = 0.1. part of computational mesh within entropy contour lines

THIS DOCUMENT PROVIDED BY THE ABBOTT AEROSPACE
TECHNICAL LIBRARY
ABBOTTAEROSPACE.COM

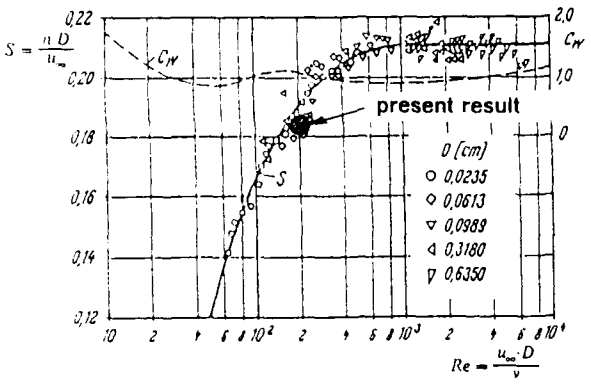


fig. 7: Strouhal / Re number dependency for the flow about a cylinder

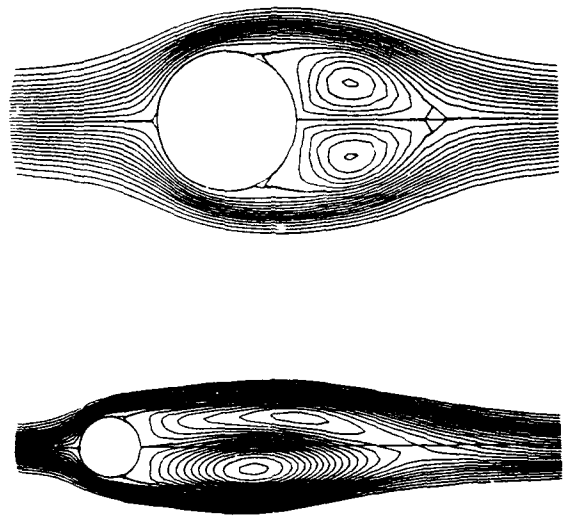


fig. 6: developement of asymetric separation bubble

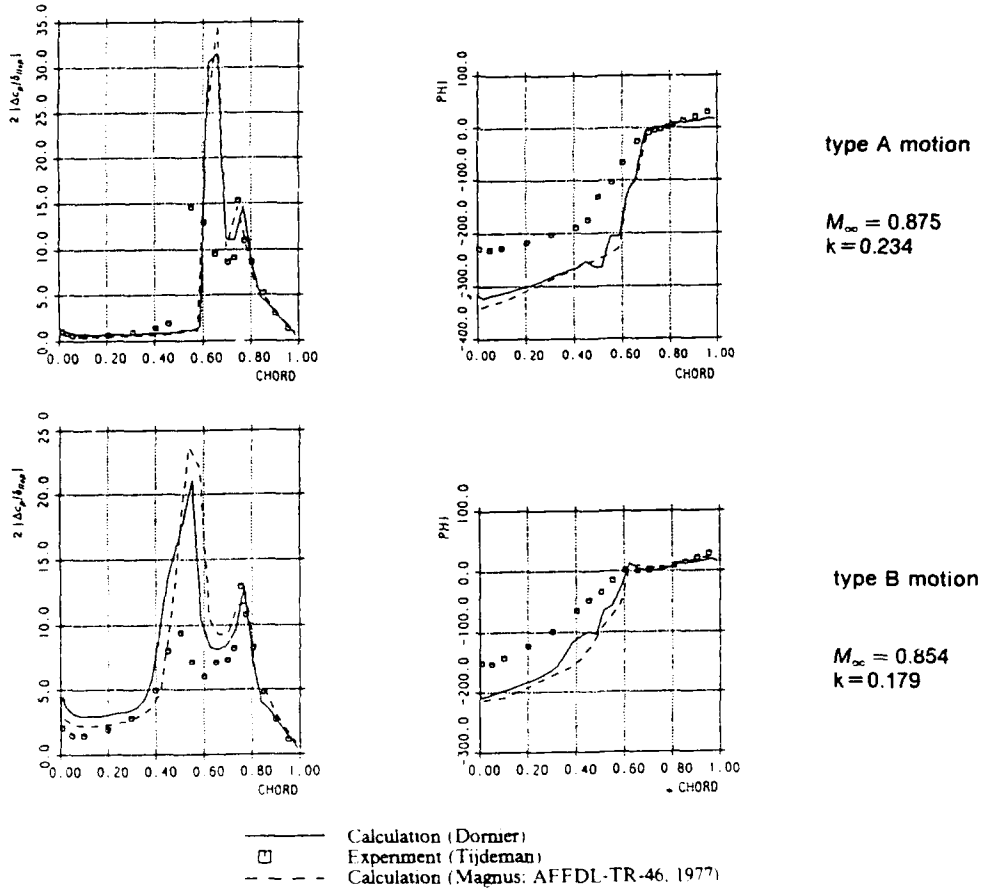


fig. 8 a,b: magnitude and phase angle of the first harmonic for the NACA006 airfoil with moving flap. amplitude $\delta_{Flap} = 1°$ (k = reduced frequency)

THIS DOCUMENT PROVIDED BY THE ABBOTT AEROSPACE
TECHNICAL LIBRARY
ABBOTTAEROSPACE.COM

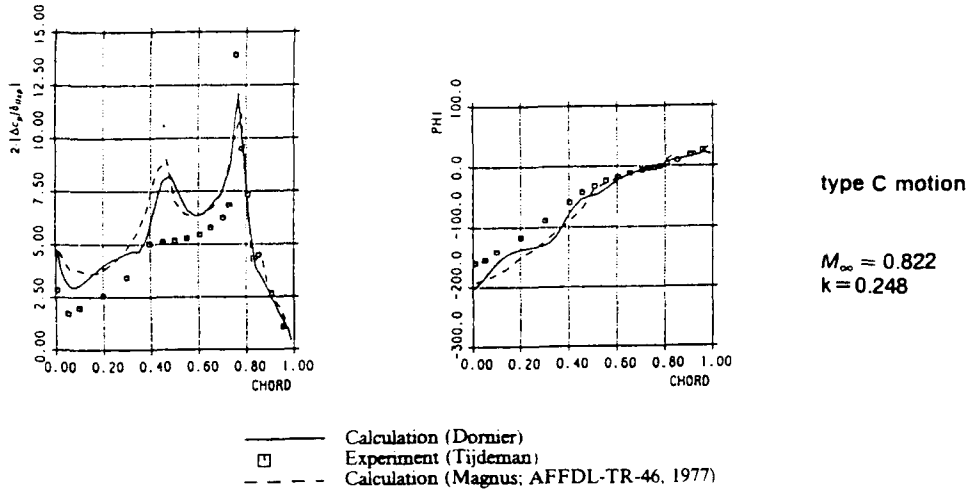


fig. 8 c: magnitude and phase angle of the first harmonic for the NACA006 airfoil with moving flap, amplitude $\dot{o}_{Flap} = 1.5°$ (k = reduced frequency)

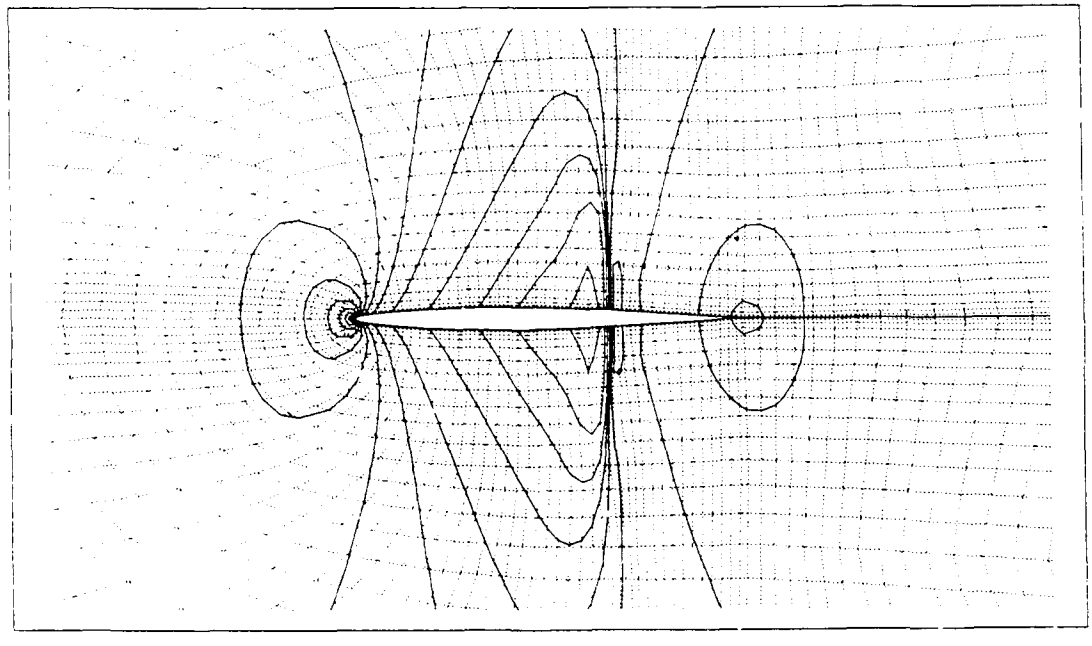


fig. 9: adapted steady state solution with pressure contour lines, NACA006, M = 0.875

THIS DOCUMENT PROVIDED BY THE ABBOTT AEROSPACE
TECHNICAL LIBRARY
ABBOTTAEROSPACE.COM

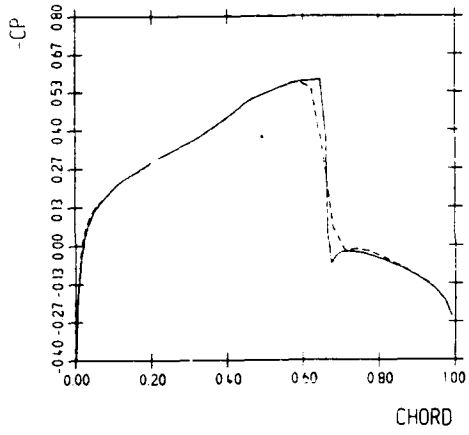
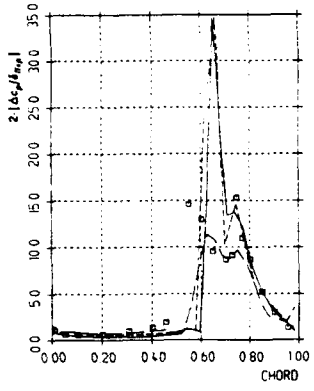
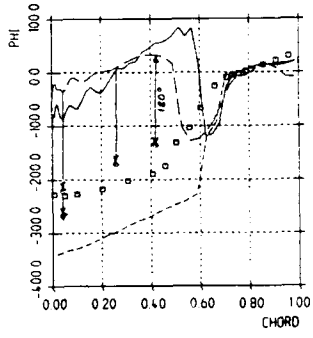


fig. 10: functional behaveour of cp for adapted and nonadapted mesh

NACA006, M = 0.875

——— adapted
- - - - - nonadapted





type A motion

$M_\infty = 0.875$
k = 0.234

——— present result (Euler calculation)
— — present result (Navier-Stokes calculation)
□ Experiment (Tijdeman)
- - - - Calculation (Magnus; AFFDL-TR-46, 1977)

fig. 11: magnitude and phase angle of the first harmonic for the NACA006 airfoil with moving flap, amplitude $\delta_{Flap} = 1°$ (k = reduced frequency)

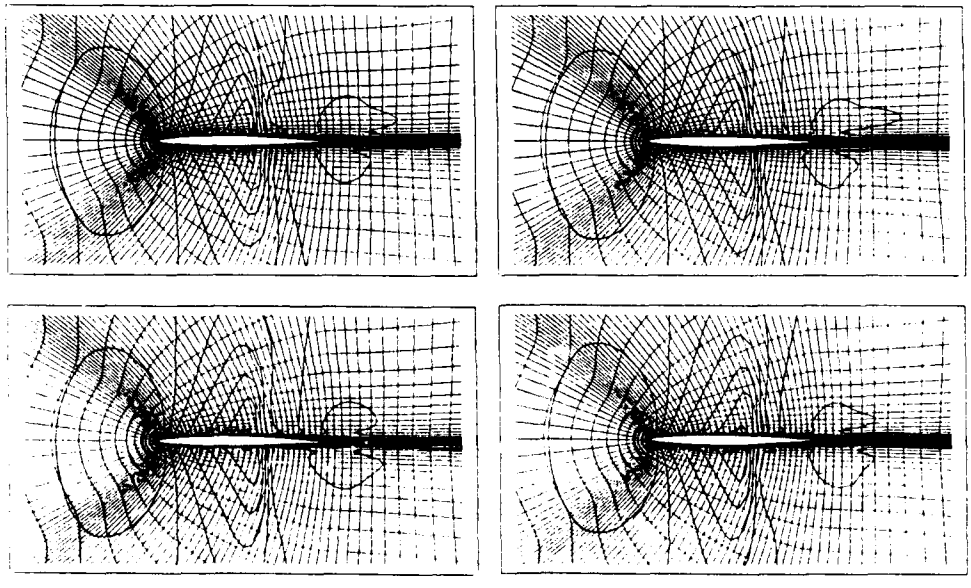


fig. 12: sequence of unsteady type A shock motion, Navier-Stokes simulation, NACA006 airfoil with moving flap, $M = 0.875$, amplitude $\delta_{Flap} = 1°$, reduced frequency $k = 0.234$

THIS DOCUMENT PROVIDED BY THE ABBOTT AEROSPACE
TECHNICAL LIBRARY
ABBOTTAEROSPACE.COM

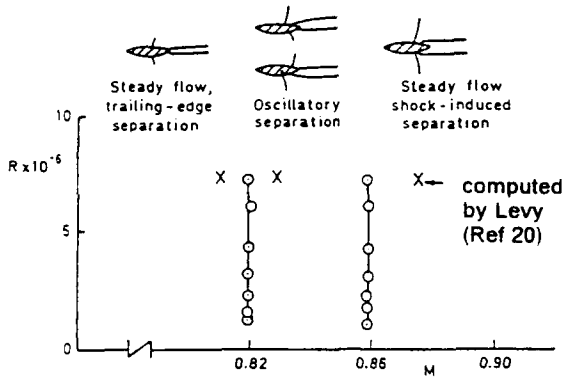


fig. 13: Reynolds/Mach number domain of periodic shock motion (fixed transition) for a 14% circular arc airfoil

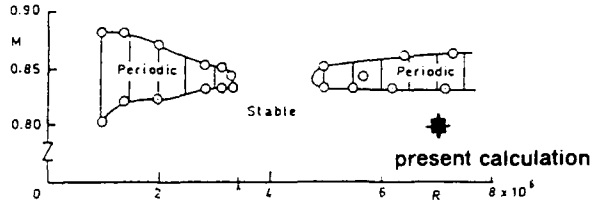


fig. 14: Reynolds/Mach number domain of periodic shock motion (free transition) for a 14% circular arc airfoil

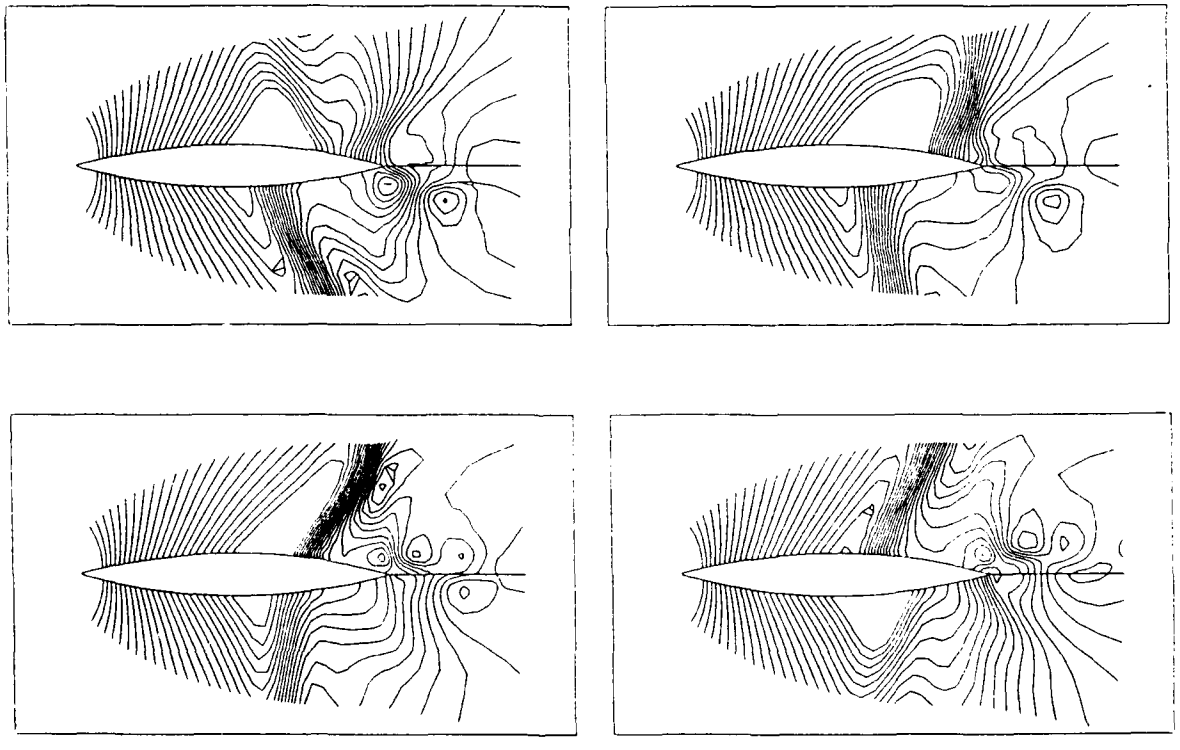


fig. 15: sequence of self-induced type A shock motion. Navier-Stokes simulation of the flow about a 14% circular arc airfoil. test parameters depicted in fig. 14

THIS DOCUMENT PROVIDED BY THE ABBOTT AEROSPACE
TECHNICAL LIBRARY
ABBOTTAEROSPACE.COM

AD-P007 806

COMPUTATION OF VISCOUS PHENOMENA IN UNSTEADY TRANSONIC FLOW

U.R. Müller
H. Henke
K. Dau

Deutsche Airbus GmbH
Dept. Aeroelastics
Hünefeldstr. 1-5
D-2800 Bremen 1, FRG

92-16044

Summary

Progress in the development towards a 3D viscous-inviscid strong interaction method for computing unsteady transonic wing flow is reported. In the current version, an ADI-technique for solving the 3D unsteady Transonic Small Perturbation Equation (TSP) has been extended by incorporating an unsteady 2D integral boundary layer method and then simultaneously solving the viscous and inviscid flow equations in a stripwise fashion. Here attention is focussed on the viscous part of the method, and a 3D boundary layer version is introduced. Detailed calculations of 2D unsteady and 3D incompressible/ compressible turbulent boundary layers were performed by the integral methods and also by a finite-difference solver, and the results are compared to experimental data. The strong-interaction technique is validated by comparison with experimental pressure distributions on several airfoils and a wing for various transonic Mach numbers. For steady and and unsteady flows, the computed influence of viscous displacement on the pressure distribution is demonstrated in contrast to purely inviscid calculations.

1 Introduction

The computational methods that are used to predict unsteady transonic airloads on airfoils and wings play a significant role in determining the accuracy of the methods used to analyse the aeroelastic behaviour of modern transport aircraft (Ref 1). For this reason, research on finite-difference computer algorithms for transonic flows is actively being pursued on various levels, with the most advanced methods solving the Navier-Stokes equations, and the more standard application-type techniques solving the potential equation.

Particular attention is most often given to the transonic flow region for two major reasons: The first one is to develop and exploit new supercritical wing technologies, and the second one is that in this speed range a critical minimum occurs in the variation of flutter speed with Mach number, known as the "transonic dip". Recognizing the computational cost of most of the elaborate methods, particularly that of Navier-Stokes solvers, the main thrust in the development of computational tools for unsteady transonic flow is still being directed towards the simpler potential flow methods.

In the case of moderate to strong shock-boundary-layer interaction, possibly leading to separation, viscous displacement becomes important and needs to be included into the potential flow solver. Provided there is a suitable interaction approach for coupling the viscous and inviscid flow regions, interaction computations turn out to be very efficient and sufficiently accurate for aeroelastic analyses. Such an approach has the lowest level of sophistication needed to treat problems such as time-dependent severe shock-boundary-layer interaction and unsteady shock oscillation.

The present paper reports on a recent step in the development of a 3D unsteady transonic interaction method with particular emphasis on the viscous part. The actual version (Ref 2) comprises a 3D unsteady TSP method (Ref 3), with a stripwise inclusion of a 2D unsteady integral method for compressible boundary layers. Currently, a corresponding 3D method is being incorporated into the TSP method. Both the 2D and the 3D integral boundary layer methods are validated by comparing the results of test calculations with those of finite-difference calculations, and with experimental data. The field method employs either an algebraic mixing length turbulence model or a low-Reynolds-number k-ε transport equation model. Examples for 2D unsteady and 3D compressible flows are discussed. In transonic steady and unsteady flows, the influence of the viscous displacement on airfoils and wings is demonstrated by comparing pressure distributions that were computed interactively with those from inviscid flow calculations. The examples chosen for comparison were the AGARD aeroelastic reference cases, and the AMP ("Aeroelastic Model Program") wing. The paper concludes with a review of current and prospective unsteady aerodynamic applications of the interaction computations.

THIS DOCUMENT PROVIDED BY THE ABBOTT AEROSPACE
TECHNICAL LIBRARY
ABBOTTAEROSPACE.COM

2 Computational Methods

In this section, the computational methods for 3D unsteady compressible flow used in the present paper will be described briefly, i.e.

- a finite-difference field boundary layer method,
- an integral boundary layer method,
- a TSP (transonic small perturbation) method for potential flow,
- and a 3D unsteady transonic interaction method currently being developed.

2.1 Unsteady field boundary layer method

The boundary-layer equations for three-dimensional compressible unsteady flow are

$$\frac{D\rho}{Dt} + \rho\left(\frac{\partial U}{\partial x} + \frac{\partial V}{\partial y} + \frac{\partial W}{\partial z}\right) = 0 \qquad (1)$$

$$\rho\frac{DU}{Dt} = -\frac{\partial p}{\partial x} + \frac{\partial}{\partial z}\left(\mu\frac{\partial U}{\partial z}\right) - \frac{\partial}{\partial z}(\rho u'w') \qquad (2)$$

$$\rho\frac{DV}{Dt} = -\frac{\partial p}{\partial y} + \frac{\partial}{\partial z}\left(\mu\frac{\partial V}{\partial z}\right) - \frac{\partial}{\partial z}(\rho v'w') \qquad (3)$$

$$\rho\frac{DT}{Dt} = (\kappa-1)M^2\left(\rho\frac{Dp}{Dt} + \frac{\partial}{\partial z}\left(\frac{\mu}{Pr}\frac{\partial T}{\partial z} - \rho w'T'\right) + (\kappa-1)M^2\left(\mu\left(\left(\frac{\partial U}{\partial z}\right)^2 + \left(\frac{\partial V}{\partial z}\right)^2\right) - \rho u'w'\frac{\partial U}{\partial z} - \rho v'w'\frac{\partial V}{\partial z}\right)\right) \qquad (4)$$

All variables are nondimensionalised by freestream values, and the normal coordinate is stretched by the square root of the Reynolds number. The Cartesian coordinates x-y-z are transformed into curvilinear, non-orthogonal ξ_1-ξ_2-ξ_3 ones. The in-plane coordinates ξ_1 and ξ_2 are defined as follows : ξ_2 is parallel to y, ξ_1 is defined by means of the limiting streamlines defining the lateral extent of the Raetz domain of influence. The direction of ξ_1 on the lateral boundaries is given by the directions of the limiting streamlines, at interior grid points the direction is linearly interpolated in ξ_2- direction between the boundary values. The z-axis is perpendicular to the other coordinates. The metric coefficients are constant in the normal direction. The ξ_3- coordinate is scaled by a prescribed, estimated development of the boundary-layer thickness, thereby virtually eliminating the need to increase the number of grid points due to boundary-layer thickening.

Two closure assumptions were employed, a mixing length model and a version of the low-Reynolds-number k-ε model of Ref 4 admitting integration down to the wall rather than using a wall function approach. The original method was extended for use in three-dimensional flows; for the present computation, isotropic eddy viscosities were used. The turbulent transport of energy was closed by means of a turbulent Prandtl number Pr_t=0.9.

In a Cartesian frame of reference, the mixing length model is defined by

$$-\rho u'w' = \mu_t\,\partial U/\partial z$$

$$-\rho v'w' = \mu_t\,\partial V/\partial z$$

$$\mu_t = \rho\, l^2\, F^2\, \partial U/\partial z$$

$$l = \delta\, K \tanh(\kappa z/K/\delta)$$

$$F = 1-\exp(-z^+/26)$$

$$\kappa = 0.41,\ K = 0.009, \qquad (5)$$

and the k-ε model by

$$\rho\frac{Dk}{Dt} = \frac{\partial}{\partial z}\left\{\left(\mu+\frac{\mu_t}{\sigma_k}\right)\frac{\partial k}{\partial z}\right\} + \mu_t\left\{\left(\frac{\partial U}{\partial z}\right)^2 + \left(\frac{\partial V}{\partial z}\right)^2\right\} - \rho\varepsilon - \rho D$$

$$\rho\frac{D\varepsilon}{Dt} = \frac{\partial}{\partial z}\left\{\left(\mu+\frac{\mu_t}{\sigma_\varepsilon}\right)\frac{\partial \varepsilon}{\partial z}\right\} - c_{\varepsilon 2}\,\rho\, f_\varepsilon\frac{\varepsilon^2}{k} + \rho E + c_{\varepsilon 1}\,\rho\,\frac{\varepsilon}{k}\,\mu_t\left\{\left(\frac{\partial U}{\partial z}\right)^2 + \left(\frac{\partial V}{\partial z}\right)^2\right\}$$

$$c_\mu = 0.09 \quad ; \quad c_{\varepsilon 1} = 1.35 \quad ; \quad c_{\varepsilon 2} = 1.8$$

$$\sigma_k = 1.0 \quad ; \quad \sigma_\varepsilon = 1.3$$

$$\mu_t = \rho\, c_\mu\, f_\mu\frac{k^2}{\varepsilon},$$

$$f_\mu = 1 - \exp(-c_3\, z^+), \quad c_3 = 0.0115$$

$$f_\varepsilon = 1 - \frac{\kappa}{c_{\varepsilon 2}}\exp\left\{-\left(\frac{k^2}{6\nu\varepsilon}\right)^2\right\}$$

$$D = \frac{2\nu k}{z^2}, \quad E = \frac{2\nu\varepsilon}{z^2}\exp(-c_4\, z^+) \qquad (6)$$

$$c_4 = 0.5$$

The conservation equations for mass and momentum as well as the turbulence transport equations for kinetic energy and its dissipation rate were discretised by a three-dimensional version of the Laasonen scheme yielding a numerical accuracy of

THIS DOCUMENT PROVIDED BY THE ABBOTT AEROSPACE
TECHNICAL LIBRARY
ABBOTTAEROSPACE.COM

$O(\Delta\xi_1, \Delta\xi_2, \Delta\xi_3^2)$. At every grid point, the CFL condition was accounted for by upwind differencing. The difference equations are Newton-linearised and solved simultaneously by a method for inverting block tridiagonal matrices (Ref 5). This coupled solution procedure reduces the computer time required by a decoupled method to about one third.

2.2 Unsteady integral boundary layer method

The integral boundary layer method used here is capable of treating a boundary layer that is three-dimensional, compressible, unsteady and turbulent. It includes the dissipation integral rather than the entrainment closure assumption which makes it applicable, with a suitably chosen velocity profile family, to attached as well as separated flow regions. The method is based on the momentum and energy conservation equations integrated over the boundary layer thickness, yielding the following equations (summation over repeated indices implied):

By conservation of momentum ($i = 1,2$)

$$k(\partial D_i/\partial t - u_i \partial R/\partial t) + \partial T_{ik}/\partial x_k + D_k \partial u_i/\partial x_k = 0.5\rho q^2 c_{fi} \qquad (7)$$

By conservation of energy

$$0.5k\partial(T_{kk} + u_k D_k)/\partial t - 0.5kq^2\partial R/\partial t - kD_{uk}\partial u_k/\partial t + 0.5\partial F_k/\partial x_k + (u_k D_i - u_i D_{uk})\partial u_k/\partial x_i = 0.5\rho q^3 c_d \qquad (8)$$

where

- $D_i = \rho q \delta_i$ = mass-flow defect vector
- $T_{ik} = \rho q^2 \theta_{ik}$ = momentum-flow defect matrix
- $R = \rho q \theta_c$ = term due to compressible unsteady flow
- $D_{uk} = \rho q \delta_{uk}$ = volume-flow defect vector
- $E_{ik} = \rho q^3 \varepsilon_{ik}$ = energy-flow defect matrix
- $F_k = E_{1k} + E_{2k}$

Following Ref 6, the method employs the 2-D relationships developed in Ref 7 of the general form

$$H_{ij} = H_{ij}(H,M) \qquad c_f = C_f(H,M,Re\theta) \qquad c_d = C_d(H,M,Re\theta) \qquad (9)$$

for the 3-D streamwise closure. The cross-flow closure relationships are based on a relation between U and V in the outer boundary-layer velocity profile, with

$$V/q = A*(1-U/q) \qquad (10)$$

where U and V are the velocity components parallel and normal respectively to the edge velocity vector, and q is its magnitude.

By applying the closure relationships to the conservation equations the numerous boundary layer lengths and shape factors were reduced to the three unknowns H, δ_1, and δ_2, in contrast to the approach (Ref 6), which reduces the boundary layer variables to the three unknowns H, δ_1, and A. It was felt that this choice of variables is more amenable to the coupling procedure between the external and boundary layer flows, and also makes the algorithm formally independent of the choice of cross-stream closure.

As in the case of the finite-difference method, all partial derivatives with respect to x_1 and x_2 were transformed into derivatives with respect to ξ_1 and ξ_2. Secondly, all boundary layer variables were transformed into streamwise and cross-flow components by means of a local rotation, since the closure relationships are defined in a streamwise coordinate system.

The three equations so obtained may be written in the form

$$A_{ij}*\partial p_j/\partial t + B_{ijk}*\partial p_j/\partial \xi_k = R_i, \qquad i = 1,2,3 \quad j = 1,2,3 \quad k = 1,2 \qquad (11)$$

with $p_1 = H$, $p_2 = \delta_1$, $p_3 = \delta_2$,

and $A_{ij} = f(H,\delta_1,\delta_2)$, $B_{ijk} = f(H,\delta_1,\delta_2)$, $R_i = f(H,\delta_1,\delta_2,Re\theta_{11})$,

and where the p_j's are defined in the streamwise coordinate system. The right-hand sides R_i furthermore contain all partial derivatives of the local edge velocity.

If the velocity field at the outer edge of the boundary layer is given, the right-hand sides of the equations are known, and the system of equations may be solved for the three unknowns. This approach is commonly known as the direct method of solution. The numerical solution of the three equations proceeds in ξ_1-marching fashion. The ξ_2-derivatives are defined on the preceding line ξ_1 = constant, where all quantities are known, and are transferred to the right-hand side of the equations. Instead of solving for the derivatives themselves, the ξ_1- and time derivatives were replaced by difference quotients from the current and preceding ξ_1- and time-levels yielding a system of three equations

$$C_{ij} * p_j = Q_i \qquad (12)$$

THIS DOCUMENT PROVIDED BY THE ABBOTT AEROSPACE
TECHNICAL LIBRARY
ABBOTTAEROSPACE.COM

2.3 Unsteady Transonic Small Perturbation potential method

The computer program for the potential outer flow is a development of the Transonic Small Perturbation ONERA code of Ref 3 . The basic equations were modified according to Ref 8 to become, in conservative form,

$$\frac{\partial f_0}{\partial t} + \frac{\partial f_1}{\partial x} + \frac{\partial f_2}{\partial y} + \frac{\partial f_3}{\partial z} = 0 \qquad (13)$$

with the fluxes defined by

$$f_0=-A\phi_t-B\phi_x,\ f_1=E\phi_x+F\phi_x^2+G\phi_y^2,$$

$$f_2=\phi_y+H\phi_x\phi_y,\ f_3=\phi_z \qquad (14)$$

In the literature, various forms of the coefficients F, G, and H have been proposed, depending on the underlying assumptions in the derivation of Eq.(13). In this paper, the following coefficients of the potential equation are used:

$$\begin{aligned} A&=k^2M^2 & F&=-.5*(3+(\chi-2)M^2)M^2 \\ B&=2kM^2 & G&=-M^2/2 \\ E&=1-M^2 & H&=-M^2 \end{aligned} \qquad (15)$$

For F=G=H=0, the linear unsteady small perturbation potential equation is obtained. The boundary conditions on the upper and lower wing surface are given by the flow tangency condition

$$\phi_z^{\pm} = h_x+kh_t \quad \text{for} \quad 0\leq x/c\leq 1 \qquad (16)$$

where h=h(x,y,t) describes the wing geometry. The boundary conditions in the wake are given by the jump conditions across the wake streamline

$$\begin{aligned} [\phi_z]&=0 \\ [\phi_x+k\phi_t]&=0 \end{aligned} \quad \text{for } x/c>1 \qquad (17)$$

It is convenient to transform the Cartesian coordinates of Eq. (13) such that the wing planform is mapped into a rectangular computational domain.

The numerical method for solving the TSP equation is the Alternating Direction Implicit (ADI) method. The additional cross derivatives, which were introduced to modify the TSP equation, have not yet been implemented fully implicitly, and therefore might impose some limitations on the maximum computational time step. Special attention was given to the numerical treatment of sonic and shock points. The operator of Ref 9 was introduced, which fulfills the entropy condition, and achieves stable and monotone solutions in transonic flow regions. The entropy and vorticity production at the shock is incorporated into the algorithm by a procedure described in Ref 10.

The lateral extent of the computational domain was about ten times the wing root chord in each direction. Nonreflective boundary conditions (Ref 11) were used at the outer boundaries. For the present computation, a grid with 92x24x36 points in the x-, y-, and z-direction was used. For accurately capturing the unsteady shocks, a number of 50 grid points on the wing was required for the x-direction. The specific computational time per grid point and time step was about $3.6*10^{-5}$ sec on an IBM 3090 computer. The computer time increased by 10% approximately, when the viscous-inviscid interaction mode was applied. For unsteady flow calculations, typically 256 time steps for one period of oscillation were used, for a reduced frequency of k=0.6. For lower reduced frequencies, the number of time steps per period had to been increased. The initial flow transients were minimized by computing four cycles of oscillation, and then analysing the last one.

2.4 Viscous-inviscid interaction

In principle most viscous-inviscid interaction methods consist of modifying the boundary conditions of the outer flow by the introduction of a transpiration velocity w_{BL} to account for the displacement effect of the boundary layer.

$$\rho w_{BL} = \partial(\rho u\delta_k)/\partial x_k + \partial(\rho\theta_c)/\partial t \qquad (18)$$

This results in a new boundary condition at the solid wall and at the wake given by

$$\begin{aligned} w=\phi_z &= \partial h/\partial x+k\partial h/\partial t+w_{BL} \quad \text{for} \quad 0\leq x/c\leq 1 \\ [\phi_z] &= [d\delta_1/dx] \quad \text{for} \quad x/c>1 \end{aligned} \qquad (19)$$

The semi-inverse method for coupling boundary layer and potential flow is widely used for treating weak to moderate interaction. It performs successive inviscid and viscous computations iteratively with boundary conditions being prescribed explicitly. In the case of strong interaction, however, this method does not always yield converged solutions.

In order to overcome this problem, a different approach is used in Ref 12 and 13, involving the simultaneous solution of the governing equations for inviscid and viscous flow. At each point on the wing or the wake the equations for the z-sweep of the potential code are augmented by an equation supplied by the boundary layer calculation, relating the outer flow to the variable w_{BL}. The augmented system of equations is now capable of being solved for both the outer flow values and the boundary layer transpiration velocity simultaneously. This computationally strong interaction approach reflects the close physical interdependence of viscous and inviscid flow regions.

The implicit coupling scheme has been developed and tested in our previous airfoil computations (Ref 14). In principle the extension of this procedure to 3D wing flow is straightforward. But in practice it requires not only considerable rearrangement of the inviscid algorithm, but also an appropriately modeled boundary layer solver. As mentioned above, we are about to complete a corresponding 3D viscous method in the near future, which to the best of our

THIS DOCUMENT PROVIDED BY THE ABBOTT AEROSPACE
TECHNICAL LIBRARY
ABBOTTAEROSPACE.COM

knowledge is the first one to use this approach. For the present the viscous-inviscid interaction computations are tested by means of the 2D boundary layer method.

The essence of the implicit coupling scheme is to derive appropriate formulations for both the viscous and the inviscid flow solvers at the interface. After reducing the tridiagonal matrix of the z-sweep to triangular form in the potential solver the equation at the wing surface becomes

$$\phi_{xx} = \partial U/\partial x = C_1 + C_2 * w_{BL} \qquad (20)$$

with C_1 and C_2 being known coefficients. Secondly, the boundary layer equations, in conjunction with the boundary condition at the wing can be similarly reduced to the form

$$\partial U/\partial x = C_3 + C_4 * w_{BL} \qquad (21)$$

Equations (20) and (21) provide the means of solving for both variables U and w_{BL} simultaneously. The velocity field does not need to be prescribed as a boundary condition for the boundary-layer equations but is evaluated for the elliptic problem, thereby avoiding the Goldstein singularity at the separation point, as an inverse solution technique also does.

For the upper and lower part of the wake, one equation each for the potential and the boundary layer flows yields four equations with the six unknowns ϕ, δ_{1x}, and ϕ_z for each side. The set of equations is closed by the condition of zero jump of the normal velocities and pressure across the wake streamline.

The present interactive method was enhanced by an option to ensure time-accuracy coupling. This is achieved by following Ref 13 and repeating the z-sweeps at a given time instant. Successive solutions increase the time consistency, and thus allows for upstream propagation of pressure waves. In the present computer code, the additional iteration within one time step may optionally be activated, but in the computed examples discussed below this was not significant.

The stripwise coupling of the 2-D boundary layer with the 3-D outer flow was used to furnish some of the results discussed below. Coupling the 3-D boundary layer with the outer flow is a straightforward extension of the two-dimensional procedure. For simplification we assume that the flow external to the boundary layer is a potential flow. Replacing the velocity components by difference quotients in ϕ, we acquire a fourth unknown, ϕ, in the boundary layer equations, yielding

$$C_{ij} * p_j + C_{i4} * \phi = S_i; \qquad i = 1,2,3 \qquad (22)$$

Equation (18) for the transpiration velocity w_{BL} due to the change in the contour of the solid surface constitutes the fourth equation. As in the two-dimensional method this system of equations is augmented by an equation derived entirely from the z-sweep of the TSP-code similar to Eq.(20)

$$\phi + a * w_{BL} = c \qquad (23)$$

completing a system of five equations with the five unknowns H, δ_1, δ_2, ϕ, and w_{BL}. With this formulation the coupling between the boundary-layer flow and the outer flow can be accomplished not only in the simultaneous mode but also in the direct mode. Sample calculations are described in the following section.

3 Subsonic Boundary-Layer Computations

The aim of preliminary subsonic boundary-layer computations was to validate the performance of the integral method by comparing it to that of a finite-difference field method. Both in turn were compared to experimental data sets of two-dimensional unsteady and three-dimensional steady incompressible flows, while a theoretical test case was chosen in the case of three-dimensional compressible flow.

3.1 Unsteady incompressible two-dimensional flow

The first case concerns the unsteady turbulent boundary layer in a wind tunnel (Ref 15) where the flow was made unsteady by choking a downstream throat with a sinusoidally oscillating wedge, thus producing a high-quality sinusoidal variation of the free stream, see Fig 1. The edge Mach number oscillation amplitude and phase were calculated by the method of Ref 15, and yielded results that very closely reproduced those of Fig 2; the freestream Mach number was 0.142, and the Reynolds number was $3.25*10^6$. At the positions x=0.6, 1.12 and 1.58 m, hot-wire measurements of phase-averaged mean velocities and some components of the Reynolds stress tensor had been carried out. The computations were run at external frequencies of f=7, 15, 21 and 29.4 Hz, so that the unsteady boundary-layer behaviour could be examined at constant reduced frequencies of $\bar{\omega}=\omega x/\bar{U}_e$= 0.97, 2.18, 2.99 and 4.16. With the external flow being prescribed by

$$U_e = \bar{U}_e + \Delta U_e \sin (\omega t + \varphi_{ue}) \qquad (24)$$

the local velocity oscillation within the boundary layer was analysed by extracting its first harmonic

$$U = \bar{U} + \Delta U \sin (\omega t + \varphi_u) \qquad (25)$$

The finite-difference computations, obtained with the mixing length model, are compared with the experimental data in Fig 3. The amplitudes of oscillation are normalised by the external value, and the

THIS DOCUMENT PROVIDED BY THE ABBOTT AEROSPACE
TECHNICAL LIBRARY
ABBOTTAEROSPACE.COM

normal coordinate is nondimensionalised by the steady boundary-layer thickness. The experimental data show the tendency to correlate with reduced frequency, and so do the computations. The measured maximum overshoot of about 0.15 is underestimated in the prediction by a maximum value of 0.06, but the general boundary layer behaviour is simulated well. With increasing $\bar{\omega}$, the inner-layer flow becomes more and more involved in the unsteadiness, since with decreasing external time scales the unsteady vortical mixing layer between inner and outer layers is shifted toward smaller time scales, i.e. towards the wall (Ref 16). Also, the overshoot in ΔU first increases with increasing $\bar{\omega}$ and then begins to decrease. This waviness in terms of reduced frequency has already been found in the experiments of Ref 17 and in our corresponding but unpublished comparison calculations. The period, however, is approximately $\bar{\omega}=5$, which range of reduced frequencies is not covered by the experiment in question.

The results for the phase of the velocity oscillations are shown in Fig 4. The calculations generally yield a monotonically increasing phase-lead relative to the external flow, yielding a maximum value of about 12° at the wall. With increasing $\bar{\omega}$, a phase lag develops at the boundary-layer edge, which however is smaller than 2.5°, and thus about half the value of the experiment.

Complementary test calculations by means of the k-ε turbulence model yielded some markedly different features. While the velocity overshoot still increased for $\bar{\omega}=4$, and reached a level of ten percent, Fig 5, the phase developed a lag at this reduced frequency of about two degrees in the outer layer, and produced the relative near-wall maximum of about nine degrees, like the experimental data. Evidently, the local equilibrium assumption implied by the algebraic model does not yield quite as detailed results as the transport equation model does. Therefore we plan further investigations to analyse the unsteady behaviour of the Reynolds shear stresses, which has been shown in the computations of Ref 18 to react differently from that calculated by the mixing length model.

Since the finite-difference method simulated the unsteady turbulent boundary layer behaviour fairly well, it provided a suitable means to check the performance of our industrial integral technique. At the measuring station farthest downstream, the integral momentum budget of both computations was evaluated for one cycle, and compared with each other in Fig 6. Shown are the unsteady, inertia, pressure and skin friction terms. For f=21 Hz, a noticeable effect due to higher harmonics develops in the unsteady term due to the phase difference of the displacement thickness relative to the external excitation. The oscillation of the inertia term is larger in the integral boundary computation than in the field mixing length calculation because of a larger amplitude of oscillation of the displacement thickness.

3.2 Three-dimensional incompressible flow

The ERCOFTAC experimental investigation of a three-dimensional turbulent boundary layer was initiated within a joint European effort and is conducted at Lausanne (Ref 19). It aims to provide detailed mean flow and turbulence measurements in order to guide the development of computational methods and suitable turbulence models.

The experiment was carried out in a low speed wind tunnel with a test section of about 1m in width and height and 8m in length. The S-shaped configuration, Fig 7, was chosen in order to skew the initially two-dimensional flow in one direction first and then skew it back again, thus producing crossover profiles in the downstream part. Figure 7 shows some computational grid lines within the Raetz domain of influence, and also the measuring stations for the range x>3m.

In general, the results of a "blind case" workshop (Ref 19) showed reasonable agreement between the experimental data and each computational method or turbulence model, respectively. In our current work, the calculations of Ref 20 were repeated by the same finite-difference method; the k-ε model was employed and the external boundary conditions were derived from the unsmoothed pressure measurements, Fig 8.

Sample results are given in Fig 9 for the measuring station at x=5.255m and y=1.3m. The mean velocity profile in the external streamline direction is somewhat overpredicted due to a slight mismatch of the local edge values, while the cross flow profile exhibits a crossover behaviour: the low-energy near-wall flow has already changed its direction according to the external boundary conditions, in contrast to the flow direction in the outer layer. The Reynolds shear stress in streamwise direction is computed within the experimental error band, also the computation of the cross flow shear stress agrees acceptably well with the data and reveals much closer agreement than in any of our previous computations (Ref 21). In the figure, the near-wall asymptotes $\tau_i=\tau_{wi}+\partial p/\partial x_i * z$ are included and show that the adverse pressure gradients drive the inner-layer maxima away from the wall. Unfortunately, the measured skin friction coefficient is too large by about fifty percent.

THIS DOCUMENT PROVIDED BY THE ABBOTT AEROSPACE
TECHNICAL LIBRARY
ABBOTTAEROSPACE.COM

In the next step of the present investigation, our three-dimensional integral boundary-layer method was checked against the results of the finite-difference computation and the experimental data. In the region of small cross flow, both computations were successful in simulating the data. In the fully developed three-dimensional flow, the displacement thicknesses as well as the corresponding momentum thicknesses were evaluated from the measured streamwise and cross flow velocity profiles, and are shown in Fig 10. At the cross section x=4.7m, the field method underpredicts the data by ten percent at most, while the integral technique reveals an underprediction up to thirty percent, approximately. Correspondingly, the integral method showed some deficiencies in the computed flow properties at the wall; in particular, the skin friction coefficient was computed too low at too large a skewing angle of the wall streamline. The discrepancies can be attributed to the rather crude closure assumptions taken from Ref 6 , which are limited by a simplified cross flow velocity profile, a corresponding relation for the wall streamline direction and also by a two-dimensional version of the dissipation integral rather than a three-dimensional one. Any further improvement of the closure relations should be started at these weaknesses.

3.3 Three-dimensional compressible flow

Because of the lack of experimental boundary layer data in compressible three-dimensional flow, a theoretical test was chosen for comparing the integral method to the finite-difference one. A pressure distribution similar to that of the Lausanne experiment was prescribed in the form

$$c_p = A*x + B*\sin(\pi*2*(x-x_0)/(x_m-x_0))*(y-y_1)$$

with x_0=1m, x_m=2m and y_1=0.5m. In order to avoid separation, the test was run at Ma=0.7 with A=0 and B=-0.4. For the cross sections x=1.25m and 1.75m, the computed displacement thicknesses of the streamwise and cross flow velocity profiles as well as the corresponding momentum thicknesses are shown in Fig 11 and 12. At x=1.25m, both computations agree well with each other, both showing an increase of displacement thickness in the adverse pressure gradient region at the concave side of the flow. At the next station, this region has been shifted to the opposite side. The integral method overestimates the viscous displacement, and also the near-wall results deviate somewhat from the other computation.

Despite the above mentioned problem areas, which are amenable to improvements in the turbulent closure assumptions, the integral method works fast and is sufficiently accurate for moderately three-dimensional flows subject to pressure gradients of varying sign.

4 Transonic Viscous-Inviscid Interaction Calculations

4.1 Steady/unsteady airfoil flow

Computations of steady and unsteady transonic viscous-inviscid interactions were performed for the harmonically oscillating NLR 7301 supercritical airfoil, and compared with the data compiled in Ref 22 for the AGARD aeroelastic reference airfoils. Also, the steady flow about the RAE 2822 was computed. In Fig 13, the experimental, and two theoretical inviscid and interactive steady pressure distributions for the AGARD computational test case CT 11 with M =.7, α=2.°, and Re =2.1*10^6 are compared with each other. Both the Euler and the purely inviscid TSP solutions yield substantially overestimated shock strengths, followed by a pronounced reexpansion. The most striking influence of the boundary layer is to shift the shock upstream from the inviscid position, i.e. from 60 to 35 percent of chord. The computation with boundary layer agrees fairly well with the measurements and shows a reduction of Δc_p due to the effective viscous decambering of the airfoil.

The experimental data collected in Ref 23 for the RAE 2822 airfoil include test cases of varying complexity. One of the more difficult tests is "case 9" with M=.73, α=3.19°, and Re =6.5*10^6. The interactive computation yields a good agreement with the measured pressure distribution, Fig 14, except for a somewhat larger shock strength, which however has also been predicted by most other computations published in the literature. The distribution of the displacement thickness, Fig 15, reproduces the measured ramp at the shock location, while the skin friction coefficient reveals a dip. At the trailing edge, the computed displacement thickness underestimates the measurement, but increases to more than one percent of chord.

As a final sample calculation for steady severe viscous-inviscid interaction producing boundary layer separation, the flow about the supercritical RA16SC1 research airfoil with deflected spoiler was chosen. This test case has already been calculated in Ref 24, for instance, for the conditions M=0.727, α=0°, Re=4.2*10^6, and a spoiler with the hinge line at 0.56 chord, a depth of 0.15 chord and an angle of deflection of δ=10°. The computations assume no slip of the external flow at the spoiler trailing edge. As a consequence the boundary layer momentum thickness remains unchanged, while the displacement thickness exhibits a jump, and so does the shape factor H. Fig 16 compares the pressure distributions computed with and without spoiler deflection. In the undisturbed case, a fairly small lift and

THIS DOCUMENT PROVIDED BY THE ABBOTT AEROSPACE
TECHNICAL LIBRARY
ABBOTTAEROSPACE.COM

rear loading, compared to the previous examples, is revealed. With the spoiler deflected the pressure distribution changes markedly. Severe decambering of the airfoil produces a supersonic flow region on the lower side, while the pressure is larger on the upper side. General agreement with the calculations of Ref 24 is obtained. The pressure level in the separated trailing edge region is somewhat overestimated, but further improvements appear possible by modifying the wake boundary conditions.

In our previous computation (Ref 14) we compared the computed and measured unsteady pressure distributions for the pitch motion of the NLR 7301 airfoil (CT5) about 0.4 chord with M =.7, α=2.5°, α_0=.55°, Re =2.1*10^6, k=0.384. The reduced frequency is based on airfoil chord. Another example is the case with flap motion of the same airfoil. The first harmonic of the unsteady pressure distributions is evaluated for the upper side of the profile from the fourth cycle of oscillation, Fig 17. The test case CT11 was measured for the reduced frequency of k=.142 and a rather large amplitude of δ_0=0.97°. As shown in our previous calculations, the magnitude and also the sign of the real part are sensitive to the reduced frequency. The present computation was run at smaller time steps than the previous one, and is compared with the measurements in the figure. On the upper side, the results reveal a reasonable reproduction of the peaks of both the real and the imaginary parts of the unsteady pressures. Also the width of shock oscillation is simulated well, and so is the phase jump behind the shock.

The hinge-line singularity at 0.75 chord in the real part is also predicted well. The computed real and imaginary parts of the unsteady pressure distribution for the lower side behave typically subsonic, with their magnitudes being considerably smaller than on the other side.

A more detailed look at the time-dependent behaviour of the displacement thickness at a number of selected locations on the NLR profile (Fig 18) shows a typically harmonic variation outside the shock region . The foot of the shock, however, is followed by a slight reexpansion, and both produce a second harmonic in the oscillation. This type of non-linear behavior caused some concern about the influence of higher harmonics on the flutter behaviour and the flutter speed predicted by more standard methods. To check this point a time-accurate flutter simulation was performed, and the results are discussed in Ref 25 .

4.2 Steady/unsteady wing flow

The recently developed 3D interaction method was extensively tested, and validated by comparing it with experimental data. The main emphasis of the present wing calculations is focussed on comparisons with the experimental data of the recent Aeroelastic Model Program (AMP), in which transonic experiments were performed in considerable detail and comprehensiveness (Ref 26). They are therefore excellently suited for comparisons with the results of computations.

In a first test series, steady and unsteady pressure distributions were measured at about three hundred pressure taps along with the static and dynamic deformation of the wing. In a second test, a geometrically similar wing was used for flutter measurements. The AMP used a 1/25 scaled wing-body half-model of a modern transonic aircraft wing with supercritical profiles. The model had a span of 1.16 meter, a reference sweep angle of 30°, an aspect ratio of 9.3, and a taper ratio of 0.29. The airfoil thickness at the wing root was 15%, and at the wing tip nearly 12%. The wing was twisted from about 5° at the root to about -3° at the tip. For further details, the reader is referred to the reference. For steady and unsteady flows, the advantages of the new interactive method over the purely inviscid one will be shown.

Transonic flow about the AMP wing was computed for Ma=0.78, α=2.84° and Re= 3*10^6, which case served for detailed comparisons with the experiment. The measured static deformation was taken into account within the boundary conditions on the wing. A survey of computed pressure distributions is illustrated in Fig 19, which shows the purely inviscid and the interactive pressure distributions on the wing for a few selected cross sections.

At the root, the sectional pressure distributions are close to subsonic conditions with fairly weak shocks, if any, while further down the span a distinct shock front builds up. The figure gives a first impression of the influence of the viscous displacement, which noticeable changes shock position and strength. Rather severe shocks were obtained in the range between 40 and 80 percent half-span, for which region a detailed pressure distribution is displayed in Fig 20 for the section at y/s=0.66, showing that the interactive solution agrees fairly well with the measured data. Comparison with the inviscid results reveals an upstream shift of the shock position of 10 to 15 percent chord due to the boundary layer displacement. Also, both the shock strength and the expansion behind the shock are reduced substantially. As in the previous two-dimensional results, both computation methods overestimate the experimental pressures on the rear part of the wing. The rear loading, however, is clearly decreased because of the decambering effect of boundary layer flow on the trailing edge. The effect arises because the boundary layer thickness on the upper surface is greater than the one

THIS DOCUMENT PROVIDED BY THE ABBOTT AEROSPACE
TECHNICAL LIBRARY
ABBOTTAEROSPACE.COM

on the lower surface where a negative pressure actually decreases the boundary layer thickness.

Next, unsteady pressure distributions were computed by means of the TSP method for the AMP wing executing the pitch oscillations measured in the wind tunnel, with the frequencies and the amplitude being $k=0.614$, $f=60$ Hz and $\alpha_0=0.223^0$ at the root. In Fig 21, the real and imaginary parts of the first harmonic of the unsteady pressure on the upper surface are displayed for the section $y/s=0.66$. Both the inviscid and the interactive results reflect the shock position and strength of the steady solution, and therefore the interactive solution for the unsteady pressures also agrees better with the experiment in magnitude and phase angle than the inviscid solution. On the lower surface, the unsteady pressures are typically subsonic.

In summary, the viscous-inviscid TSP method was found to agree well with the experiment and the results of other transonic computational methods. It is expected to fully develop its capability to deal with severe viscous effects, when the reduced frequency or the Mach number increase.

5 Current and Prospective Applications

Although the interactive method outlined and validated above is applicable to a variety of engineering problems in the aerospace industry, up to now we have used it mostly to calculate the unsteady airloads that are used in the calculation of the transonic flutter speed of aircraft.

An example of a flutter calculation where the present interaction method was used is described in Ref 2. The generalized airloads were calculated there as the time-varying response to a sinusoidally oscillating wing, and were then transformed by Fourier analysis into a complex generalized airload matrix in the frequency domain. Flutter calculations then proceeded in conventional fashion. Applied in this way, the interactive method imitated fairly closely the procedure of conventional flutter calculations, necessitating a considerable number of computation runs equalling the number of vibration modes (2) times the number of frequencies (3) times the number of flight Mach numbers to produce the generalized airload matrix. It should be mentioned in this context that it is not unusual to use 20 vibration modes to define the flutter properties of a wing alone. The interactive method applied in this way is therefore only useful as an occasional supplement to conventional methods, say, as a check on aerodynamic loads in the transonic regime.

To reduce the computational expense a more efficient way of applying the present interactive method was recently tested by us using the pulse excitation technique to determine the required airloads with a fraction of the computation runs used above. In this technique (Ref 27) the wing is excited by a pulse rather than by a sinusoidal motion, yielding a response with a rich harmonic content from which airloads for the entire spectrum of required frequencies can be extracted in just one run. It should be noted that for a successful implementation of this technique the computational grid must be about twice as fine in the z-direction to avoid internal numerical reflections.

In both of the techniques described above it is tacitly assumed that the non-linear variation of the airloads with motion amplitude is small enough to justify the use of linear methods. The time-accuracy of the viscous-inviscid interaction method under discussion, however, offers the possibility of determining the flutter speed in the time-domain where the aerodynamic non-linearities are preserved, and thus can have an effect on the flutter speed. This was done, in fact, for 2D flow in Ref 28 , and for 3D flow in Ref 29. The motion of the wing there was not prescribed, but determined by introducing the structural flexibility of the wing, and calculating the elastic deflection due to the airloads. The ensuing time record of the motion (in general not sinusoidal) was then analysed for positive or negative damping indicating whether the flight speed was higher or lower than the flutter speed. Usually three computation runs were necessary to determine the flutter speed with sufficient accuracy. Since all vibration modes relevant to flutter are included in each run, the advantage of this approach is of course that it is not necessary any more to perform a large number of computation runs for all combination of vibration modes and frequencies. Our results of this type of flutter simulation are discussed in Ref 25, where it is also shown that computation time was considerably shortened by exciting the wing in the flutter mode, thereby suppressing the production of unduly long transients. This flutter mode was determined by a conventional linear flutter calculation.

Besides flutter computations, further problem areas of unsteady aerodynamics are planned to be investigated in the near future. One such area is the efficiency of control surfaces used in active control technology. The applications range from flutter-margin augmentation systems to the alleviation of gust loads. For steady flow the lift reduction due to a spoiler deflection was discussed in Sect. 4.1. This work will be extended to unsteady transonic flow.

Another example is the computation of self-induced flow unsteadiness, in particular buffet onset and buffeting. It

THIS DOCUMENT PROVIDED BY THE ABBOTT AEROSPACE
TECHNICAL LIBRARY
ABBOTTAEROSPACE.COM

has been shown in Ref 30, that interactive computation methods have the potential to cope with this challenging task. Buffet onset has been computed for airfoils, e.g. NACA 0012, and compared with experimental data. We are currently following that work, since our method is both time-accurate and capable of handling separated flow.

6 CONCLUDING REMARKS

The paper's main theme is the validation of an integral boundary layer method, which ultimately is to be used within viscous-inviscid interaction computations of unsteady transonic flow around a wing.

First, a number of test calculations was performed in the direct mode, i.e. with prescribed outer-flow boundary conditions, and compared to experimental data as well as to the results of finite-difference field computations. In the case of 2D unsteady flows, the field calculations using a mixing length turbulence model simulated the unsteady boundary layer behaviour well, while a low-Reynolds-number k-ε model was shown to resolve the inner-layer velocity oscillation even better in comparison to the measurements. On the other hand, the integral method, though not based on an unsteady oscillatory velocity profile family, reproduced the integral boundary layer displacement thicknesses very well, with the computer cost advantageously being only about one percent of that of the field method. The same result was obtained when simulating 3D incompressible and compressible boundary layers, again by means of the k-ε and the integral methods. It was shown that the integral technique accurately produced displacement and momentum thicknesses in flows with moderate pressure gradients, and thus with moderate skewing of the flow. For treating severe three-dimensionality, several small-crossflow assumptions of the currently employed closure relations need to be improved.

In a second step, a 2D integral boundary layer version was applied within viscous-inviscid interaction calculations of transport aircraft sections and wings by means of a TSP method. The interactive procedure for coupling the boundary layer with the outer flow consisted of the simultaneous solution of the outer flow field and the boundary layer flow; this scheme has the advantage of being implicit and also time accurate. Several sample calculations for steady and unsteady transonic flows were performed, including the NLR 7301 and RAE 2822 profiles, the RA16SC1 profile with and without spoiler, and the wing of the "Aeroelastic Model Program". A comparison of computational results for inviscid and interactive flows with experimental data demonstrated the necessity of including the boundary layer in transonic flows for a proper prediction of shock strength and position, and also for a proper simulation of shock oscillation in case of excited unsteadiness.

The 3D-boundary layer code is not fully incorporated into the production method yet; but even a 2D boundary layer coupled stripwise to the TSP outer flow showed a marked improvement in the shock position and strength over the wing. The most important practical consequence to emerge from this calculation was that the inclusion of the boundary layer increased the computational time by only about ten percent. This may increase somewhat when the 3D method is used, but even so it may be said that the interactive method described here is, on the one hand, accurate enough to predict important features such as shock position and strength for an unsteady flow around a wing, and, on the other hand, inexpensive enough to be used in routine development work in industry.

7 References

1. Zimmermann,H.,"The Aeroelastic Challenge of the Airbus Family - Review and Perspectives", in"International Forum on Aeroelasticy and Structural Dynamics", Aachen, FRG,1991.

2. Henke,H.H.,Müller,U.R.and Schulze,B., "A Viscous-Inviscid Interaction Method for Use in Transonic Flutter Analysis", in"International Forum on Aeroelasticy and Structural Dynamics", Aachen, FRG,1991.

3. Mulak,P.,Meurzec,J.P.and Angelini,J.J., Extension and Use of a Numerical Procedure for Three Dimensional Unsteady Transonic Flows",in "Second International Symposium on Aeroelasticy and Structural Dynamics", Aachen, FRG, 1985, DGLR-Report 85-02, p. 62-70.

4. Chien,K.-Y.,"Predictions of Channel and Boundary Layer Flows with a Low-Reynolds-Number Turbulence Model", AIAA J.,20,1,January 1982,p.33.

5. Wu,J.,"Berechnung zwei- und dreidimensionaler turbulenter Grenzschichten", Doctoral Dissertation, Rheinisch-Westfälische Technische Hochschule, Aachen, FRG,1989.

THIS DOCUMENT PROVIDED BY THE ABBOTT AEROSPACE
TECHNICAL LIBRARY
ABBOTTAEROSPACE.COM

6. Swafford,T.W. and Whitfield,D.L., "Time-Dependent Solution of Three-Dimensional Compressible Integral Boundary-Layer Equations", AIAA J.,23,7,July 1985.

7. Whitfield,D.L.,Swafford,T.W.and Donegan,T.L.,"An Inverse Integral Computational Method for Compressible Turbulent Boundary Layers",in"Recent Contributions to Fluid Mechanics",W.Haase (ed.), Springer-Verlag, 1982.

8. Borland,C.J.,Rizetta,D.P.and Yoshihara, H.,"Numerical Solution of Three-Dimensional Unsteady Transonic Flow over Swept Wings",AIAA Journal,20,3, March 1982, pp 340-347.

9. Engquist,B.and Osher,S.,"Stable and Entropy Satisfying Approximations for Transonic Flow Calculations", Mathematics of Computations,34, No. 149,1980,pp. 45-75.

10. Batina, J.T., "Unsteady Transonic Small-Disturbance Theory Including Entropy and Vorticity Effects". AIAA Paper 88-2278.

11. Whitlow Jr.,W.and Seidel,D.A.,"Nonreflecting Boundary Conditions for The Complete Unsteady Transonic Small Disturbance Equation",AIAA Journal, 23,10,October 1985,pp. 315-317.

12. Houwink,R. and Veldman,A.E.,"Steady and Unsteady Separated Flow Computations for Transonic Airfoils", AIAA-84-1618, 1984

13. LeBalleur,J.C.and Girodroux-Lavigne, P.,"A Semi-Implicit and Unsteady Numerical Method of Viscous-Inviscid Interaction for Transonic Separated Flows",La Recherche Aerospatiale 1984-1,1984,p.15-37.

14. Dau,K.,Müller,U.R.and Henke,H.,"A Strong Viscous-Inviscid Interaction Method for Computing Unsteady Transonic Airloads for Use in Aeroelastics", in"European Forum on Aeroelasticy and Structural Dynamics",DGLR-Bericht 89-01,1989.

15. Cook,W.J.,"Experimental Investigation of Oscillating Flow Turbulent Boundary Layers", Iowa State University, Rep. ISU-ERI-Ames-88418,1988.

16. Menendez,A.N.and Ramaprian,B.R., "An Asymptotic Theory for the Periodic Turbulent Boundary Layer in Zero Mean-Pressure Gradient", Aeronaut. J., August/September, 93, (927),1989,p.95.

17. Cousteix,J.,Javelle,J.and Houdeville, R.,"Influence of Strouhal Number on the Structure of a Flat Plate Turbulent Boundary Layer",in"Third Symposium on Turbulent Shear Flows",1981,p.8.41.

18. Kebebe,W.,Launder,B.E.and Younis,B.A., "Large-Amplitude Periodic Pipe Flow : A Second-Moment Study",in "Turbulent Shear Flows 5", 1985, p.16.23.

19. Pironneau,O.,Rodi,W.,Rhyming,I.L., Savill,M.and Truong,T.V., "ERCOFTAC Workshop on Numerical Simulation of Unsteady Flows", to be published by Cambridge University Press, 1991.

20. Wu,J.,Müller,U.R.and Krause,E.,"Computation of the 3D Turbulent Boundary Layer in an S-Shaped Channel", in "ERCOFTAC Workshop on Numerical Simulation of Unsteady Flows", 1990.

21. Müller,U.R.,"Comparison of Three-Dimensional Turbulent Boundary-Layer Calculations with Experiment",in"Three-Dimensional Turbulent Boundary Layers" (IUTAM Symposium, Berlin), Eds.: H.H. Fernholz and E. Krause, Springer,1982.

22. ANON.,"Compendium of Unsteady Aerodynamic Measurements",AGARD-R-702, 1982.

23. Cook,P.H.,McDonald,M.A.and Firmin, M.C.P.,"Airfoil RAE 2822 -- Pressure Distributions, Boundary Layer and Wake Measurements", RAE, AGARD WG 04, 1977.

24. LeBalleur,J.C., "Numerical Flow Calculation and Viscous-Inviscid Interaction Techniques",in "Computational Methods in Viscous Flows, Recent Advances in Numerical Methods in Fluids", ed. W.G.Habashi, Pineridge, 1984.

25. Zimmermann,H.,Vogel,S.,Henke,H. and Schulze,B.,"Computation of Flutter Boundaries in the Time and Frequency Domain",in "AGARD Specialists' Meeting on Transonic Unsteady Aerodynamics and Aeroelasticity", San Diego, 1991.

26. Zingel,H.,"Measurement of Steady and Unsteady Airloads on a Stiffness Scaled Model of a Modern Transport Aircraft Wing", in"International Forum on Aeroelasticy and Structural Dynamics", Aachen, FRG,1991.

27. Mohr,R.W.,Batina,J.T.and Yang,H.T.Y., "Mach Number Effects on Transonic Aeroelastic Forces and Flutter Characteristics", J. Aircraft,26, 11,November 1986,pp.1038-1046.

28. Zimmermann,H.and Schulze,B.,"Comparison between 2D Transonic Flutter Calculations in the Time and Frequency Domain", in "Future Research on Transonic Unsteady Aerodynamics and its Aeroelastics Applications" AGARD-R-749, 1986.

29. Guruswamy,G.P.,"Unsteady Aerodynamic and Aeroelastic Calculations for Wings Using Euler Equations", AIAA Journal, 20,3,March 1990.

30. Girodroux-Lavigne,P.and LeBalleur,J.C., "Time Consistent Computation of Transonic Buffet over Airfoils", ICAS-88-5.5.2, 1988.

THIS DOCUMENT PROVIDED BY THE ABBOTT AEROSPACE
TECHNICAL LIBRARY
ABBOTTAEROSPACE.COM

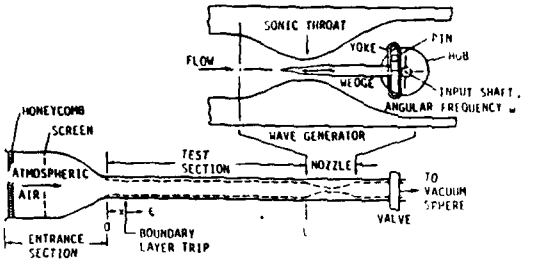


Fig 1. Unsteady boundary layer experiment, from Ref 15 .

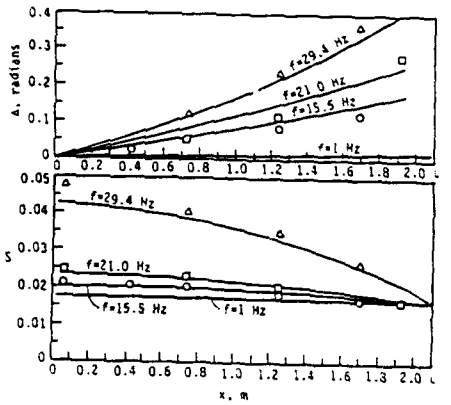


Fig 2. Comparison of measured and predicted variation of Mach number (S) and phase (Δ), from Ref 15 . —— prediction; experiment: O , □ , Δ , f=15.5,21.,29.4 Hz.

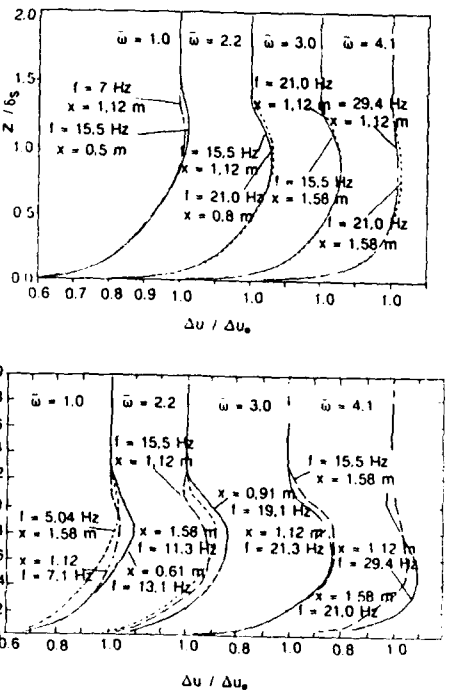


Fig 3. Comparison of measured and computed (l_{mix}) velocity amplitude ratio. top :computation, bottom : experiment.

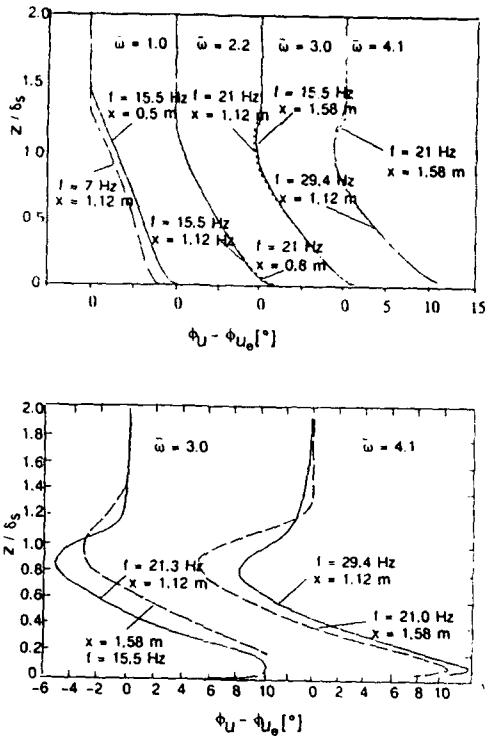


Fig 4. Comparison of measured and computed (l_{mix}) phase of velocity oscillation.
top :computation, bottom : experiment.

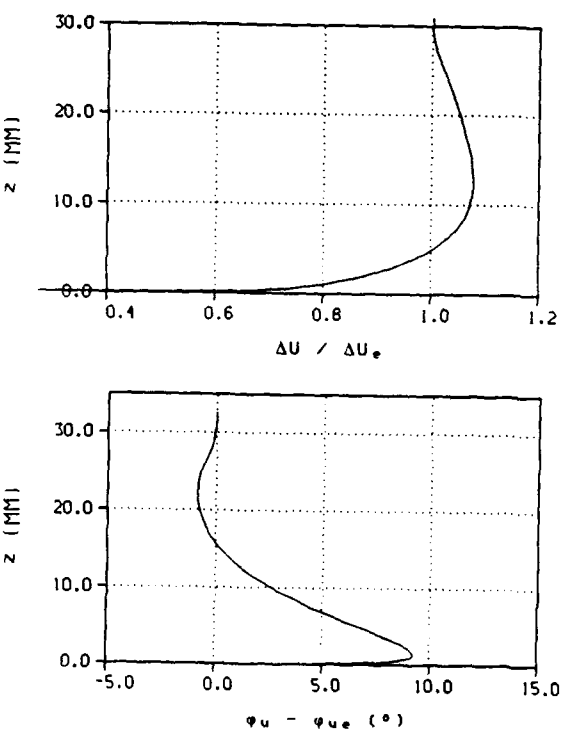


Fig 5. Velocity amplitude ratio and phase at x=1.58 m, computed by k-ε model. f=21 Hz, $\bar{\omega}$=4.1.

THIS DOCUMENT PROVIDED BY THE ABBOTT AEROSPACE
TECHNICAL LIBRARY
ABBOTTAEROSPACE.COM

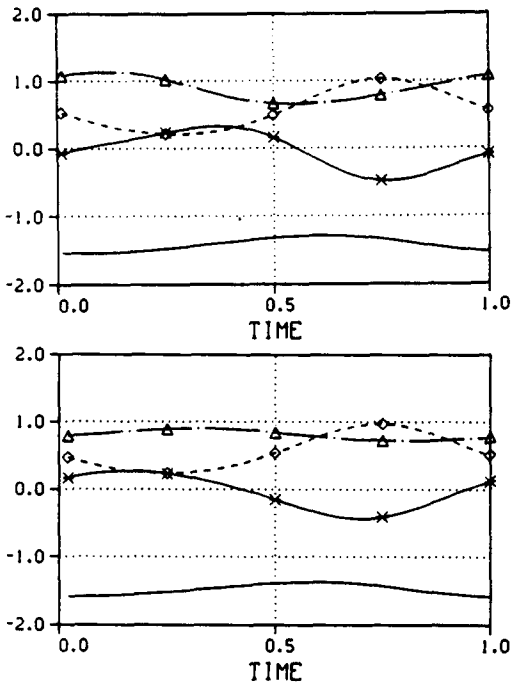


Fig 6. Comparison of computed momentum budgets for one cycle; x=1.58 m, f=21 Hz. top:integral, bottom:field method (l_{mix}).
– x unsteady, –.Δ inertia, --◇ pressure, —— skin friction terms.

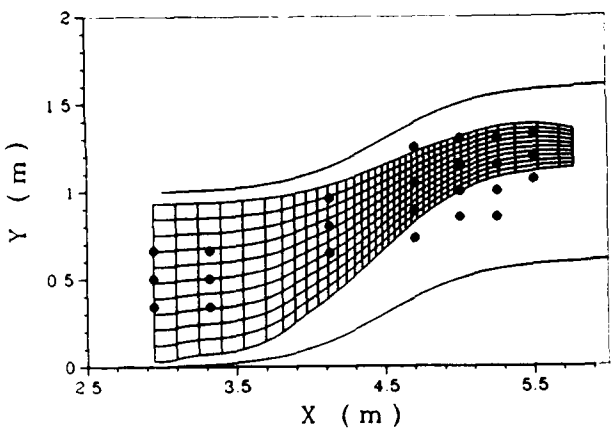


Fig 7. Downstream part of S-shaped duct (top view); included:measuring stations, computational domain.

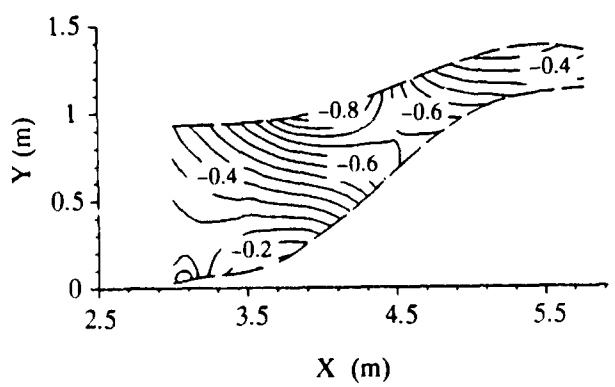
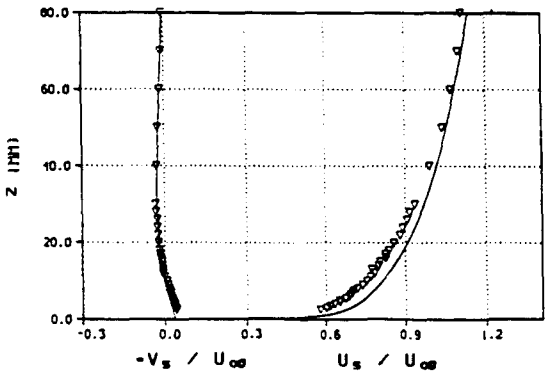
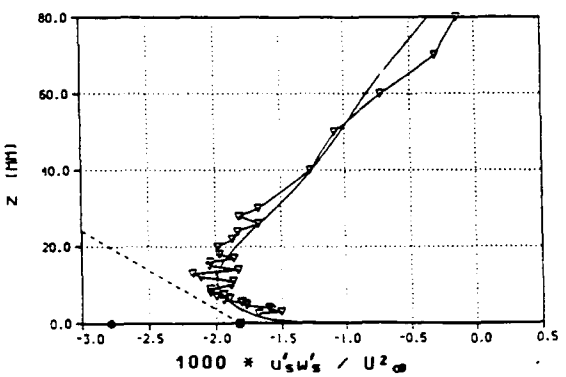


Fig 8. Isobars of measured c_p distribution of S-shaped duct.





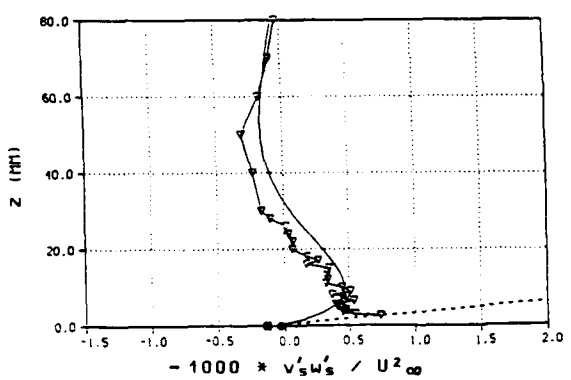


Fig 9. Comparison of measured and computed (k-ε) mean velocities and Reynolds shear stresses at x=5.225 m, y=1.3 m of S-duct.
●, ■ measured, computed wall shear stress
---- $\tau_i=\tau_{wi}+\partial p/\partial x_i * z$.

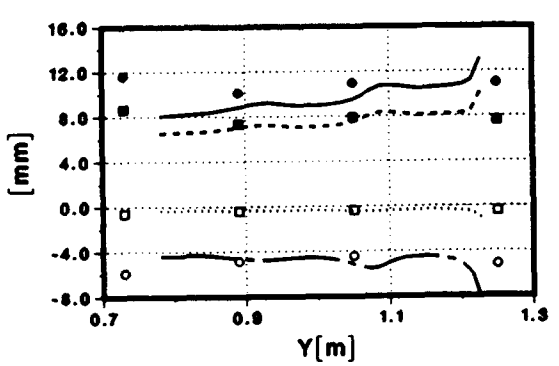


Fig 10. To be continued.

THIS DOCUMENT PROVIDED BY THE ABBOTT AEROSPACE
TECHNICAL LIBRARY
ABBOTTAEROSPACE.COM

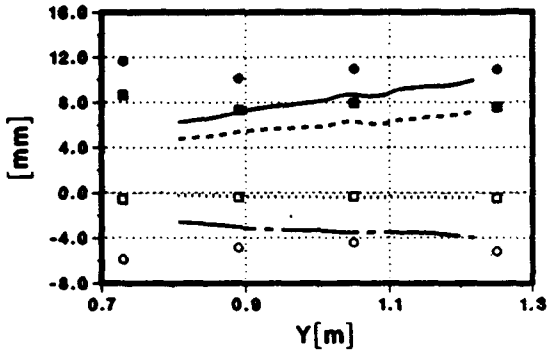


Fig 10. Comparison of measured and computed integral thicknesses at x= 4.7 m of S-duct. top:integral, bottom:field method (k-ε)
●,— δ_1; ■,-- θ_{11}; O, -. δ_2; □,.. θ_{22}

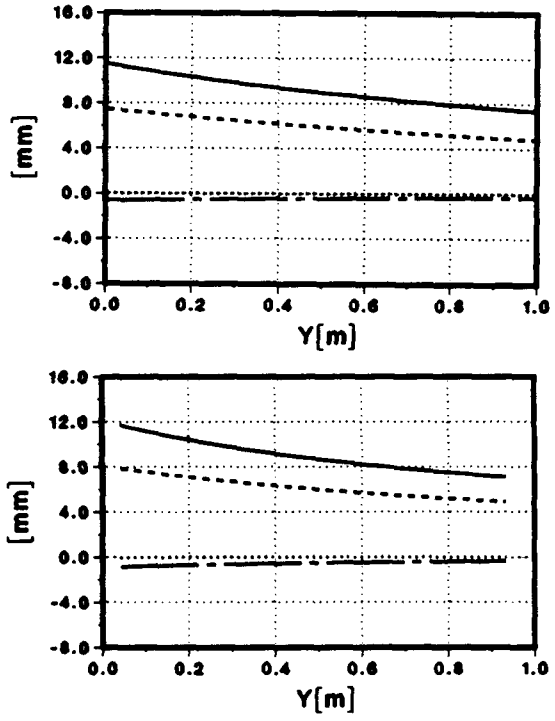


Fig 11. Comparison of integral and field computations of 3D flow at M=0.7; x=1.25 m. top:integral, bottom:field method (k-ε).
— δ_1; --- θ_{11}; -.- δ_2; ... θ_{22}

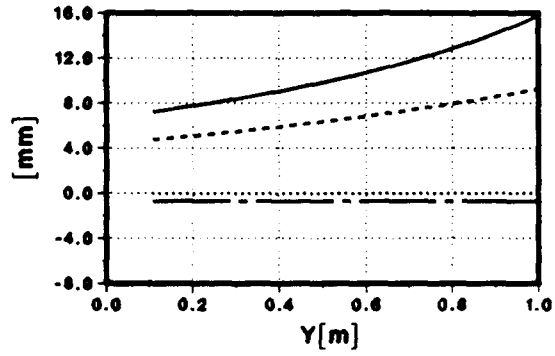


Fig 12. To be continued.

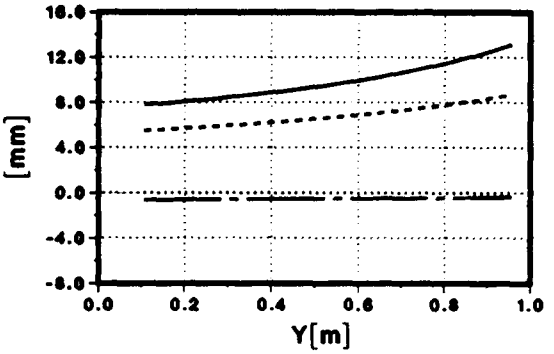


Fig 12. Comparison of integral and field computations of 3D flow at M=0.7; x=1.75 m.
top:integral, bottom:field method (k-ε)
— δ_1; --- θ_{11}; -.- δ_2; ... θ_{22}

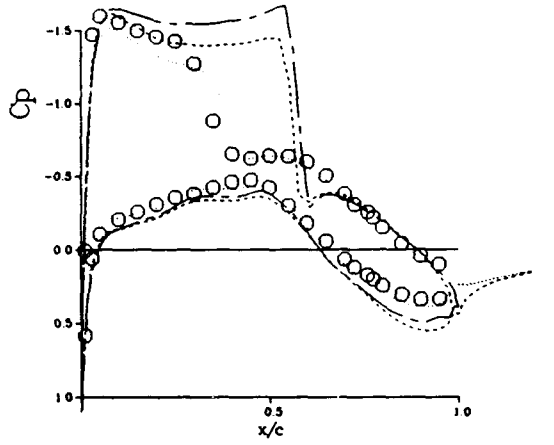


Fig 13. Steady pressure distribution, NLR 7301 profile,M=0.7,α=2°,Re=2.14 millions. O, experiment AGARD CT11; --- TSP; -.- Euler; ... interactive TSP.

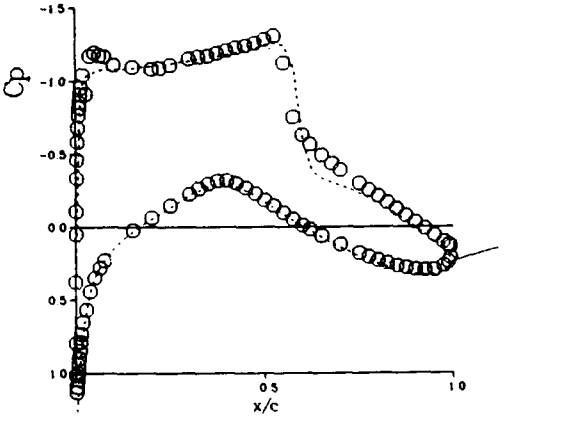


Fig 14. Steady pressure distribution, RAE 2822 profile,M=0.72,α=3.19°,Re=6.5 millions. O, experiment Ref(23), case 9.

THIS DOCUMENT PROVIDED BY THE ABBOTT AEROSPACE
TECHNICAL LIBRARY
ABBOTTAEROSPACE.COM

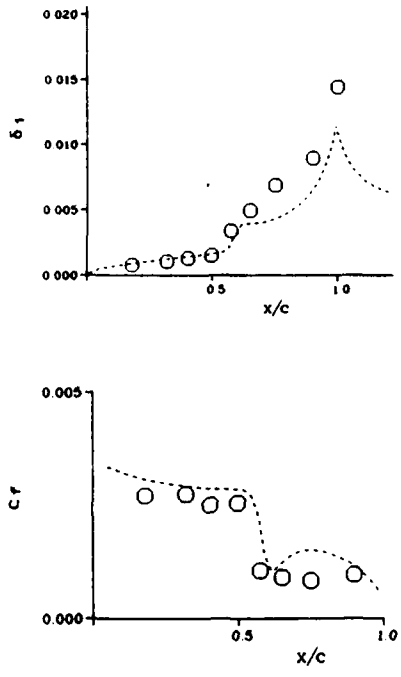
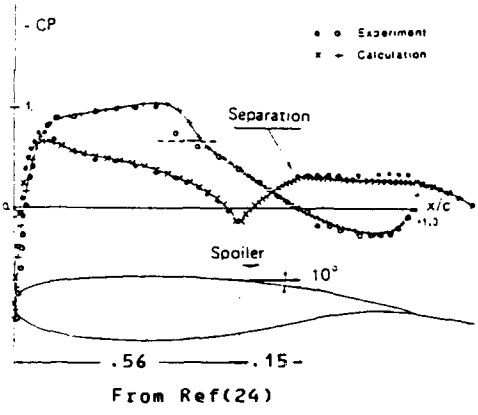


Fig 15. Displacement thickness and skin friction on RAE 2822 profile.
O, experiment Ref(23), case 9.



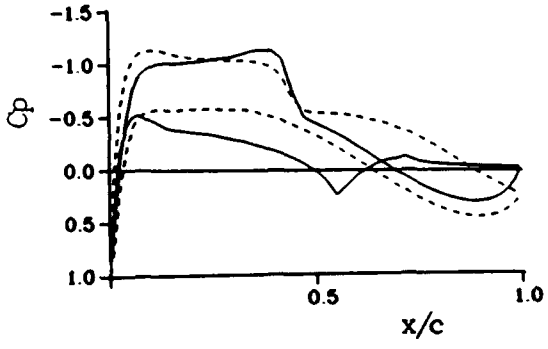


Fig 16. Steady pressure distribution on RA16SC1 profile, M=0.727, α=0°, Re=4.2*10^6, with and without spoiler deflection.
--- , δ_{sp} = 0° ; —— , δ_{sp} = 10°

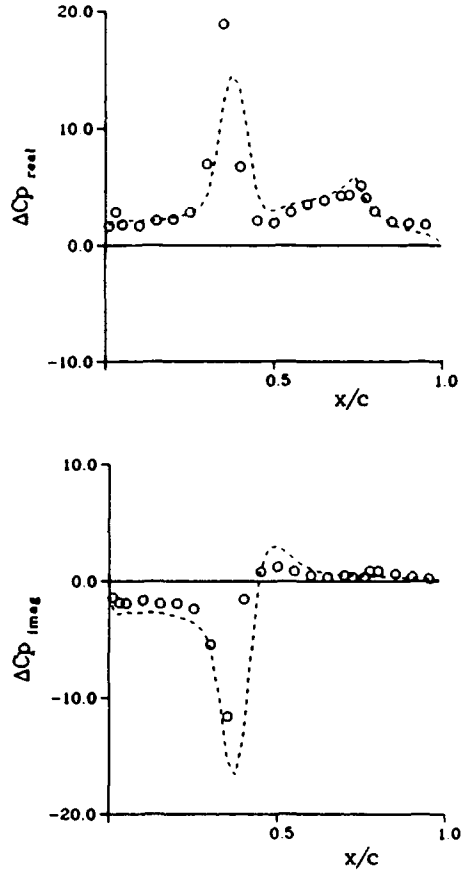


Fig 17. Unsteady pressure distribution for NLR 7301 with oscillating flap; δ_0=0.97°, k=0.142.

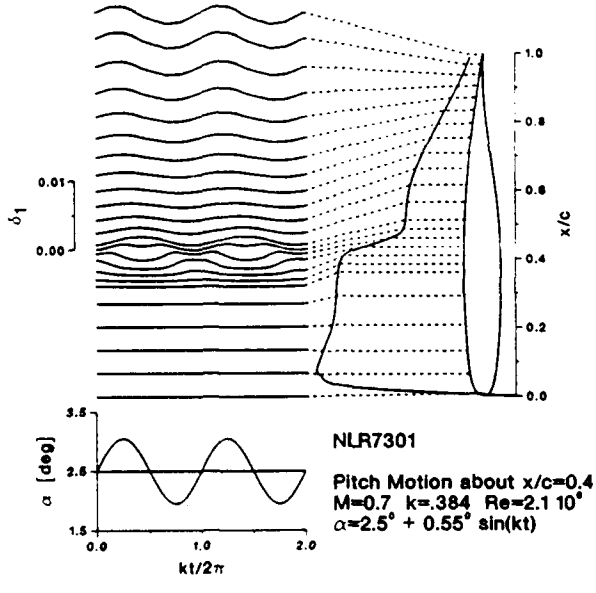


Fig 18. Oscillation of local displacement thickness for NLR 7301 profile.

THIS DOCUMENT PROVIDED BY THE ABBOTT AEROSPACE
TECHNICAL LIBRARY
ABBOTTAEROSPACE.COM

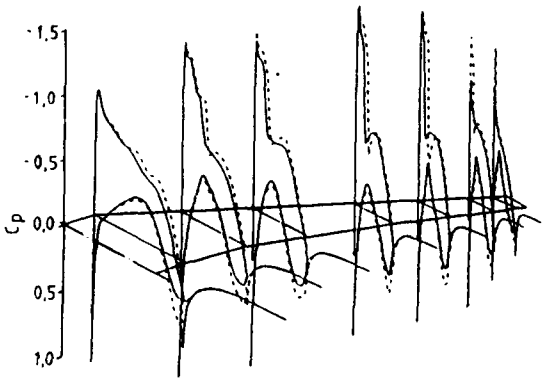


Fig 19. Steady pressure distribution for wing of Aeroelastic Model Program.
M =0.78, α=2.84°, Re=3*10⁶
- - - inviscid calculation
——— interactive calculation

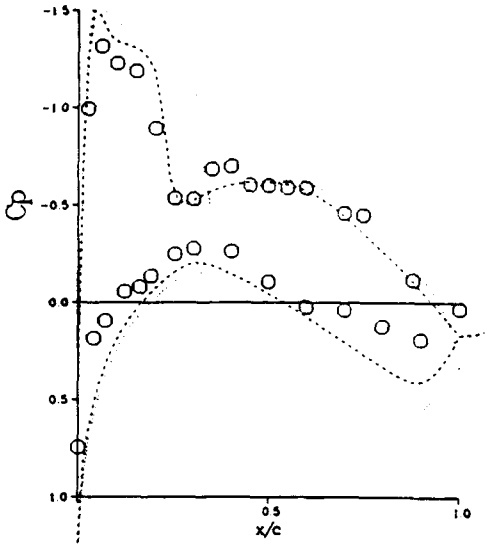


Fig 20. Steady pressure distribution for wing of Aeroelastic Model Program.
M =0.78, α=2.84°, Re=3*10⁶, y/s=.66
o o o experiment
..... inviscid calculation
- - - interactive calculation

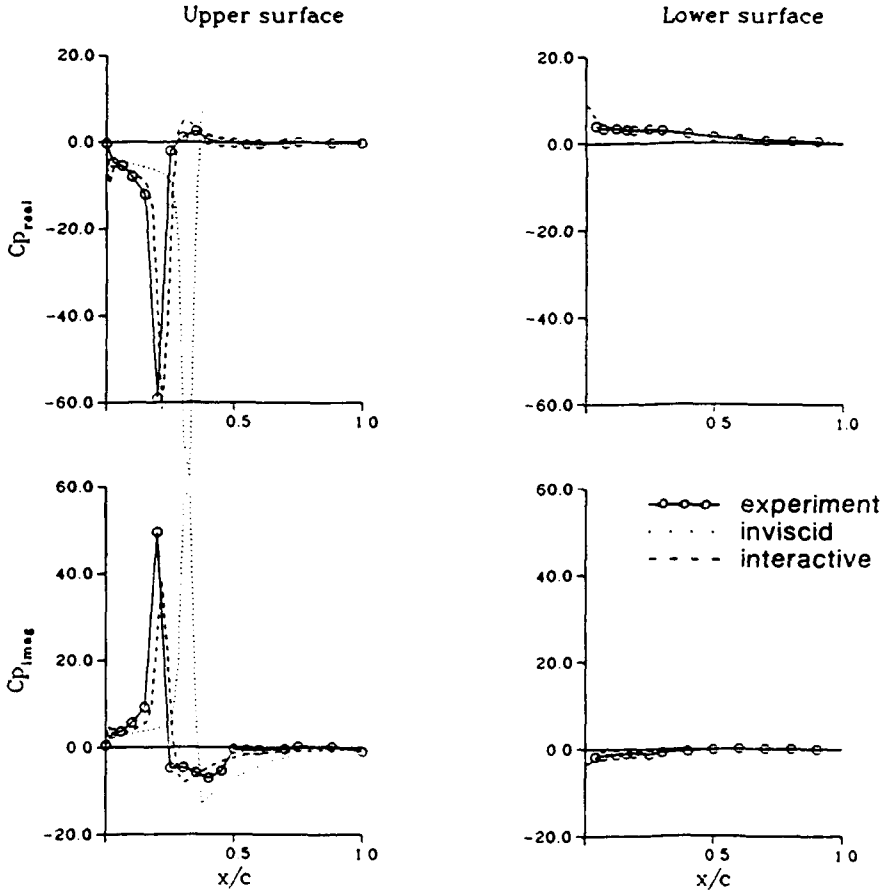


Fig 21. Unsteady pressure distribution for wing of Aeroelastic Model Program.
M =0.78, α=2.84°, Re=3*10⁶, y/s=.66
k=0.614, α_0=.223°.

THIS DOCUMENT PROVIDED BY THE ABBOTT AEROSPACE
TECHNICAL LIBRARY
ABBOTTAEROSPACE.COM

AD-P007 807

TRANSONIC AEROELASTIC CALCULATIONS IN BOTH THE TIME AND FREQUENCY DOMAINS

M.J. Knott
Senior Aerodynamicist
British Aerospace (Military Aircraft) Ltd
Kingston-Upon-Thames
Surrey KT2 5QS
UNITED KINGDOM

92-16045

SUMMARY

A method for exploring the flutter characteristics of wing-only configurations in the transonic flow regime is presented. At the heart of the method is the UTSP program, which solves the non-linear transonic small perturbation equation with or without the simultaneous integration of the structural equations of motion.

The UTSP program was obtained by British Aerospace from the Royal Aerospace Establishment and modified and fine-tuned to provide a tool suitable for use by Dynamics engineers.

The aim of the paper is to describe the functionality of the program, with a particular emphasis on its implementation within the existing aeroelastics analysis environment at the Kingston site of British Aerospace. Before demonstrating the use of the UTSP program on a production combat wing, results for the AGARD Taileron and wing 445.6 models are presented, with the aim of validating the method.

LIST OF SYMBOLS

M	Freestream Mach number.
ϕ	perturbation velocity potential.
c_0	Root chord.
s	Semi-span.
U	Freestream Velocity.
x	Physical streamwise coordinate.
y	Physical transverse coordinate.
z	Physical vertical coordinate.
t	Time (non-dimensional w.r.t. c_0/U_∞.
γ	Ratio of specific heats.
λ	$=(\gamma+1)M^4+3(1-M^2)M^2$.
X	Transformed streamwise coordinate.
Y	Transformed transverse coordinate.
Z	Transformed vertical coordinate.
u	perturbation velocity.
a^*	Speed of sound at the sonic point.
u^*	Sonic perturbation velocity.
Δs	Entropy jump across the shock wave.
C_v	Specific heat at constant volume.
U_1	Velocity immediately upstream of shock wave.
U_2	Velocity immediately downstream of shock wave.
U_s	Velocity of shock wave motion.
Φ	Steady state perturbation velocity potential.
ψ	Unsteady perturbation velocity potential.
δ	Amplitude factor.
A	Generalised structural inertia matrix.
D	Generalised structural damping matrix.
E	Generalised structural stiffness matrix.
B	Generalised aerodynamic damping matrix.
C	Generalised aerodynamic stiffness matrix.
q	Generalised displacement.

1. INTRODUCTION

For some time now British Aerospace has recognised the need for accurate flutter calculations in the transonic flow regime. In 1987 a Working Group was set up to oversee the development of unsteady aerodynamics' methods, both theoretical and experimental, across all of the sites and divisions - i.e. across both commercial and military organisations. This working group produced a programme of research to develop, amongst other things, the existing Royal Aerospace Establishment's (RAE) Unsteady Transonic Small Perturbation method into a tool that could be used by Dynamics engineers to perform flutter calculations in both the time- and frequency domains.

To this end, the programme was divided into two phases. The first phase was to develop the technology required, such as non-isentropic corrections for shock generated entropy and the simultaneous integration of the structural equations of motion and to release to the users a "Preliminary Design Tool". Such a tool would possess most of the required functionality, but may lack finesse. The second phase was to produce the so-called "Enhanced Design Tool" - which would be more user-friendly and which would fit into the Dynamics engineers' environment with ease. This product would also be subject to the Company's quality assurance procedures.

Such a program is now available, and ready for use on project work. In fact, the Commercial Aircraft side of British Aerospace has already been using the Preliminary Design Tool for project work on Airbus. Within the Military Aircraft company it is intended that UTSP will be used for "production calculations" on the European Fighter Aircraft.

The aim of this paper is firstly to describe the functionality of the UTSP Enhanced Design Tool, including a description of the underlying solution algorithm employed. Following that, some results are presented which seek to validate the program. To this end, steady and unsteady pressures for the AGARD taileron are presented and comparison made between UTSP and experiment. Next, results are presented for the AGARD standard configuration wing 445.6 where the variation of the flutter speed with Mach number is investigated. Finally, the implementation of the UTSP method within the Dynamics environment is discussed, and flutter speed loci presented for the wing of an actual combat aircraft. Following this, conclusions are presented along with a look into the future.

2. THE UTSP ENHANCED DESIGN TOOL

2.1 The Underlying TSP Algorithm

The basic algorithm at the heart of the UTSP Enhanced Design Tool is due to the work of Watson[1] at the RAE. The equation solved is,

$$M^2\phi_{tt} + 2M^2\phi_{xt} = F_x + \{(1 - M^2\phi_x)\phi_y\}_y + \phi_{zz} \quad (1)$$

THIS DOCUMENT PROVIDED BY THE ABBOTT AEROSPACE
TECHNICAL LIBRARY
ABBOTTAEROSPACE.COM

where F is the streamwise flux term, which in the original (classical tsp) formulation is

$$[(1 - M^2)\phi_x - \tfrac{1}{2}\lambda\phi_x^2 - \tfrac{1}{2}M^2\phi_y^2] \qquad (2)$$

An alternative flux can be used in order to take account of entropy generated across shock.waves. It was decided to incorporate such corrections when, on studying papers by Fuglsang and Williams[2] and Gibbon et al[3], it was evident that solutions could be obtained that were close to the Euler solutions without any significant increase in CPU time.

Thus, following their lead, eqn. (2) is replaced by

$$(\gamma + 1)M^2R(V^*V - \frac{V^2}{2}) - \tfrac{1}{2}M^2\phi_y^2 \qquad (3)$$

where
$$V = \frac{u}{1 + u/(1+R)} \qquad (4)$$

$$R = \frac{a^*}{U} \qquad (5)$$

$$V^* = V(u^*) = \frac{R^2 - 1}{2R} \qquad (6)$$

For the calculation of shock generated entropy, and its subsequent convection downstream of the trailing edge, the one-dimensional approach of Refs. 2 & 3 was adopted, where the 1-D Rankine-Hugoniot relation is used, along the wing surface only, to calculate the entropy rise across the shock at each spanwise station. The Rankine-Hugoniot relation is

$$\frac{\Delta s}{C_v} = \log \left| r^\gamma \frac{\gamma + 1 - r(\gamma - 1)}{(\gamma + 1)r - (\gamma - 1)} \right| \qquad (7)$$

with
$$r = U_2/U_1 = R^2/(1 + u_1 - U_s)^2 \qquad (8)$$

where u_1 is the perturbation velocity immediately in front of the shock. During the development of the above method, the author came across Batina's work[4], where he considers a two-dimensional approach and allows for shock generated vorticity as well. Unfortunately, time was too short to incorporate these additional corrections - it being more preferable to deliver a program to the users and then move onto the development of an unsteady Euler code.

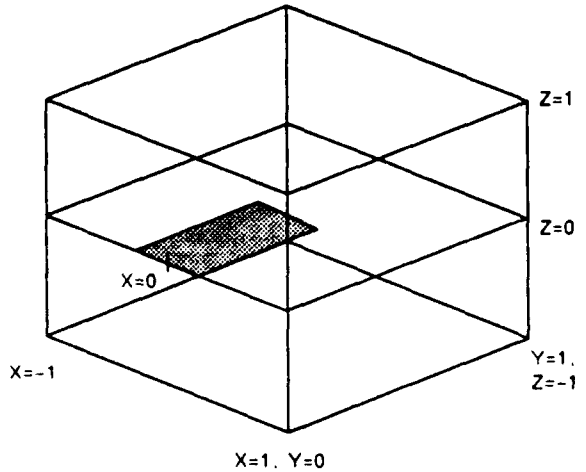


Fig. 1. The Computational Domain

Before differencing the unsteady tsp equation, eqn. (1), grid transformations are applied. These transformations are such as to map the whole of physical space on to a cube with sides of length 2. (e.g. the x-coordinates are transformed so that $x = -\infty$ maps to $X = -1$ and $x = +\infty$ maps to $X = +1$ as seen in figure 1). This computational domain is then discretised using uniform grid spacing in each of the coordinate directions, thus simplifying the finite difference formulation of eqn. (1). The transformation also ensures clustering of grid nodes at the leading and trailing edges and at the root and tip, as shown in figure 2.

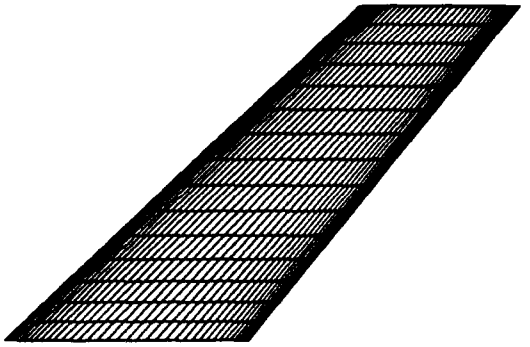


Fig. 2. The Computational Grid on the Wing Surface

The transformed unsteady tsp equation is solved using an Alternating Direction Implicit (ADI) scheme. The discretisation of the streamwise flux, eqn. (2) or (3) uses an Engquist-Osher switched difference operator to ensure that the correct domain of dependence is applied in regions of supersonic flow. Use of the operator results in central-differences in regions of subsonic flow and backward (upwind) differences in supersonic regions.

The wing surface boundary condition, of tangential flow, is applied in the classical manner, either side of a slit at $z = 0$, using a transpirational technique. Thus, if $f_x^{\pm}(x,y)$ represents the thickness distribution of the wing and $\zeta(x,y,t)$ represents the elastic deformation then the wing surface boundary conditon is

$$\phi_z = f_x^{\pm}(x,y) + \delta(\zeta_x + \zeta_t) \qquad (9)$$

where δ is an "amplitude" factor. The defintition of ζ is addressed in sections 2.2 and 2.3 when the various solution options are presented.

Recognising that the non-linear effects are manifest predominantly in the underlying mean static flow, Watson performed a linearisation of eqn. (1). He achieved this by replacing the velocity potential $\phi(x,y,z,t)$ in eqn. (1) by a linear combination of the static part $\Phi(x,y,z)$ and the unsteady part $\psi(x,y,z,t)$, so that

$$\phi(x,y,z,t) = \Phi(x,y,z) + \delta\psi(x,y,z,t) \qquad (10)$$

where the amplitude is assumed infinitesimally small. The resulting "steady" equation is of the same form as eqn. (1) and the unsteady equation becomes, for the isentropic formulation,

$$M^2\psi_{tt} + 2M^2\psi_{xt} = [(1 - M^2 - \lambda\Phi_x)\psi_x - M^2\Phi_y\psi_y]_x + [(1 - M^2\Phi_x)\psi_y - M^2\psi_x\Phi_y]_y + \psi_{zz} \qquad (11)$$

THIS DOCUMENT PROVIDED BY THE ABBOTT AEROSPACE
TECHNICAL LIBRARY
ABBOTTAEROSPACE.COM

with the wing surface boundary condition,

$$\psi_z = (\zeta_x + \zeta_t) \qquad (12)$$

2.2 Coupled Structural – Aerodynamic calculations
For the simulation of the full non-linear interaction of the airflow over a flexible wing, the unsteady tsp equation (1) is integrated simultaneously with the modal structural equations of motion.,

$$\mathbf{A}\ddot{q} + \mathbf{D}\dot{q} + \mathbf{E}q = \mathbf{Q}(q,\dot{q}) \; . \qquad (13)$$

where **Q** is the aerodynamic generalised force vector.

The structural equations of motion, eqn. (13), are integrated using a three-step Runge-Kutta algorithm which gives fourth order accuracy. This algorithm was taken from a dynamics simulation program in use at British Aerospace, and has proved to be very robust.

For the case where the modeshapes, ζ, are orthogonal eigenvectors, such that the structural inertia matrix, **A**, and stiffness matrix, **E**, are diagonal, the structural damping matrix, **D**, can be used, with great effect, to control the dominance of the aerodynamic damping contribution to the overall solution. Structural damping is often an unknown quantity and at British Aerospace, we tend to solve the aeroelastics equations using a nominal amount of structural damping which is one or two percent of the critical damping value for each mode. (The critical damping value is that value which just gives real eigenvalues).

Thus for small values of **D** the aerodynamic damping is predominant and decaying transient oscillations can be obtained for an impulse initial condition. However, if **D** is chosen to be about 20% critical then asymptotic static solutions can be obtained within 1000 to 2000 time steps. Such a static solution can then be used as a starting point for an uncoupled unsteady solution.

2.3 Modes of Operation of the UTSP Program
In this section the various options available to the User are discussed.

2.3.1 Static Solutions
The starting point of all unsteady calculations is the mean steady flow solution. Thus the UTSP program can calculate the steady flow solution by setting $\delta = 0$ in eqn. (9) and gradually introducing the thickness distribution over the first few time steps. To cut down on unnecessary computation a convergence checking mechanism is incorporated.

As mentioned in Section 2.2 a steady flow solution can also be obtained for a flexible wing by simultaneously integrating the structural equations of motion with **D** set to 20% critical.

2.3.2 Unsteady Uncoupled Solutions
Given the steady state solution, the UTSP program can then be used to calculate unsteady pressures and generalised forces in the frequency domain, for a prescribed sinusoidal modal oscillation about the mean "steady" position.

A number of cycles of forced oscillation are calculated, in the time-domain, and the pressures integrated over each cycle to produce the frequency domain values of real and imaginary unsteady pressure. These pressure values can then be integrated over the wing to obtain the generalised forces. The convergence of the generalised forces can be optionally checked after each cycle and the solution halted accordingly. The procedure is then repeated for further vibration modes and frequency parameters.

There are three options available for the calculation of the frequency-domain unsteady pressures:

NON-LINEAR HARMONIC
The first option is to integrate the full non-linear unsteady tsp equation, eqn. (1), using eqn. (9) as the wing boundary condition with the amplitude factor, δ, set to a user-defined value.

LINEARISED HARMONIC
The next option is to integrate the linearised tsp equation, eqn. (11), using eqn. (12) as the wing boundary condition. This option generally requires fewer time steps per cycle for stability and fewer cycles for convergence than the non-linear harmonic option.

Although this option is more approximate than the non-linear option, it can be used to great effect once an accurate static solution has been obtained.

LINEARISED INDICIAL
Both of the above options require the time integration to be peformed for each frequency parameter of interest. However, the UTSP program provides a means of extracting frequency domain pressures for a range of frequency parameters with only one time-integration. The wing boundary condition is defined only by the modeshape as an indicial pulse.

The length of the pulse is either based on a pulse frequency parameter of 0.5 or on a value derived from the frequencies of interest. The time-integration is progessed as before and the frequency domain pressures for each frequency parameter are recovered by Fourier transformations at intervals equal to the pulse length. Convergence can be checked as before.

2.3.3 Coupled Unsteady Solutions
The final option available is to perform coupled aeroelastic solutions to obtain a set of decaying (or otherwise) transients for the generalised displacements. As discussed earlier, this is achieved by setting the structural damping to something nominal.

With this option the UTSP program can optionally post-process the transients to extract the frequency and damping characteristics of each mode. This is achieved by a least-squares curve fitting approach.

The time histories of each mode are also written to disk to allow the user to perform his own post-processing externally of the UTSP program, should he not like any of the results.

2.4 Validation of the UTSP Enhanced Design Tool
The ability of the unsteady tsp program to produce physically reasonable solutions is discussed. To this end results for two wing configurations are presented. Firstly, the validity of the steady and unsteady pressures is established by comparing the UTSP results with experiment for the AGARD SMP Tailcron, figure 3. Secondly, the validity of the generalised aerodynamic matrices is established by comparing the UTSP results with the experimental results for the AGARD standard wing 445.6, figure 4.

THIS DOCUMENT PROVIDED BY THE ABBOTT AEROSPACE
TECHNICAL LIBRARY
ABBOTTAEROSPACE.COM

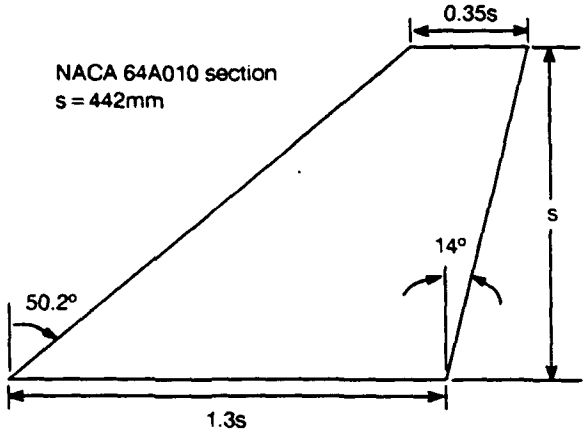


Fig. 3. The AGARD SMP Taileron

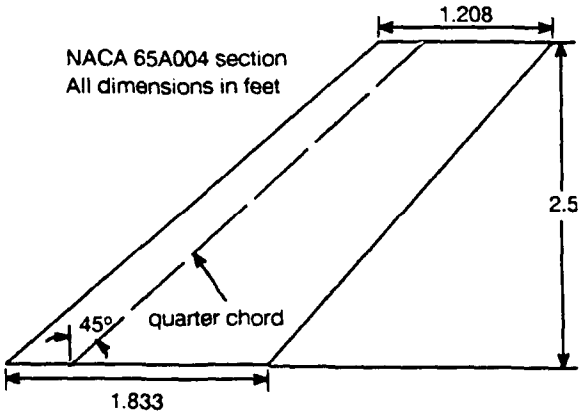


Fig. 4. The AGARD Wing 445.6 - Model 3

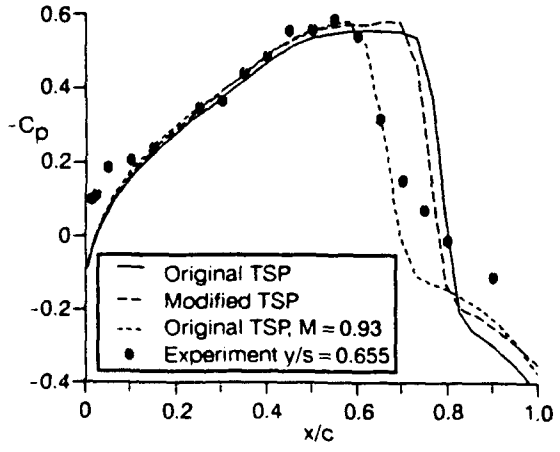


Fig. 5. Steady Lower Surface Pressures on AGARD Taileron, M = 0.95, α = 0.4 degrees, y/s = 0.688

2.4.1 Steady Pressures

In this section, and the next, validation of the UTSP program is sought by comparing the calculated results with experimental data. Figure 5 shows the comparison with experiment of the UTSP results, for the AGARD taileron set at an incidence of 0.4 degrees in an onset flow of free stream Mach number of 0.95.

Results are presented for both the original isentropic unsteady tsp formulation and the non-isentropic formulation. Whilst it is not expected that the M = 0.95 UTSP results should agree perfectly with experiment, the figure shows that the UTSP results are sensible. Furthermore, the figure shows that the non-isentropic corrections act to improve the comparison.

Remembering that the steady flow solution plays the dominant role in subsequent unsteady calculations, the Dynamics' Engineer seeks to make the best use of all available information to obtain as accurate a steady solution as possible. To this end, figure 5 shows the UTSP results, using the original formulation, for M = 0.93. The agreement with experiment is thus improved and hence the Dynamics' Engineer can place more confidence in the results of subsequent unsteady calculations.

For these calculations a time step of 0.05 was used and 1000 steps were required for the isentropic calculations to converge the sectional lift coefficient to a tolerance of 1 percent. The non-isentropic calculations required a further 500 time steps. The standard grid size of 60 by 20 by 40 was used. The calculations required approximately 0.24 seconds per time step on the Cray Y-MP (single processor) for the isentropic calculations and 0.26 seconds per step for the non-isentropic calculations.

2.4.2 Unsteady Pressures

The comparison of a variety of unsteady calculations with experiment, again for the AGARD taileron, is shown in figure 6, for a pure pitch oscillation of small amplitude.

The figure shows that, for small amplitudes, the results of the linear and non-linear harmonic options are very similar. The figure also shows the results of a non-linear harmonic calculation using the steady flow solution at M = 0.93. The agreement with experiment is greatly improved.

The calculations used 150 time-steps per period were used. Ten periods were required to converge the generalised forces to a tolerance of 3 percent for the non-linear option, whilst only five were required for the linearised calculations. The CPU time required per time step is again aproximately 0.25 seconds, with a premium of approximately 10 percent for the linearised calculations.

2.4.3 Generalised forces

The validity of the calculation of the generalised aerodynamic force matrices is established by examining the variation of the flutter speed index with the free-stream Mach number, for the standard AGARD aeroelastic configuration, wing 445.6. (see Ref. 5).

The first three modes of the "2.5 foot weakened model 3" were used for the calculations. The frequency of these modes were those given, in Ref. 5, for the calculated modes.

THIS DOCUMENT PROVIDED BY THE ABBOTT AEROSPACE
TECHNICAL LIBRARY
ABBOTTAEROSPACE.COM

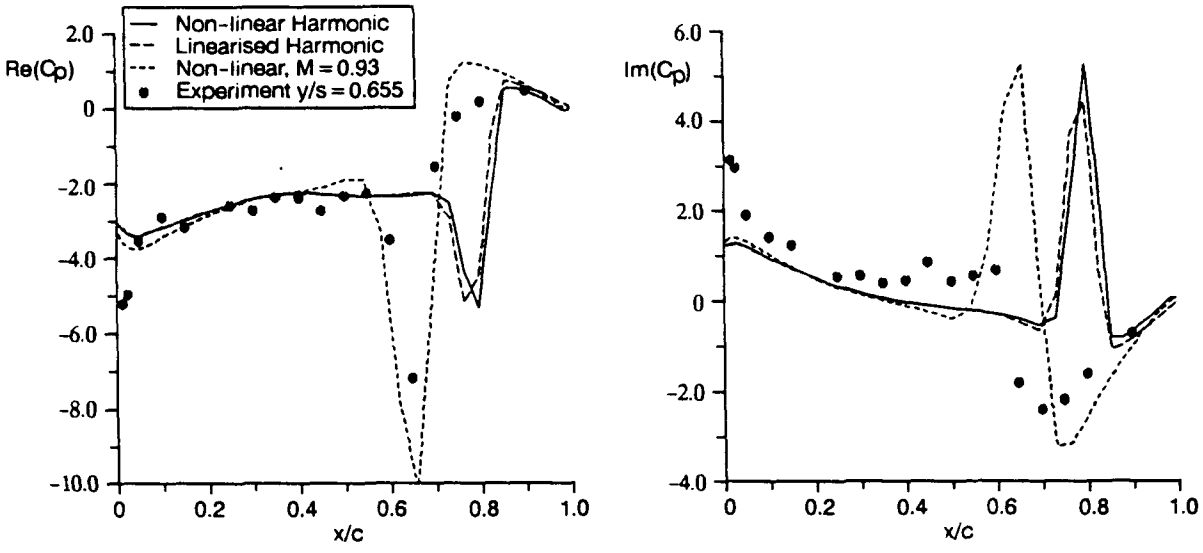


Fig. 6. Unsteady Lower Surface pressures on AGARD Taileron, M = 0.95, α = 0.4 degrees, ν = 0.583, y/s = 0.688

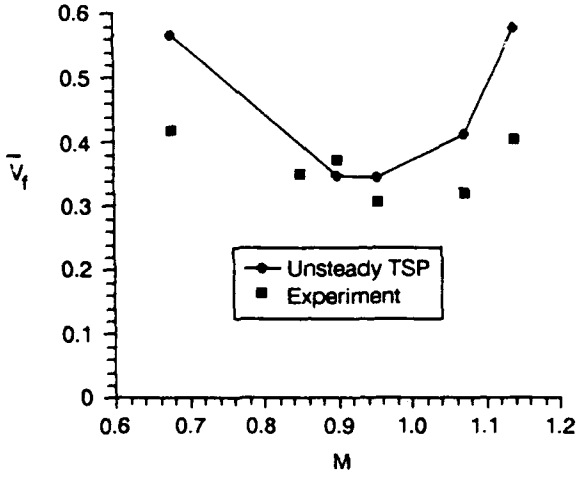


Fig. 7. Flutter Characteristics of AGARD Wing 445.6

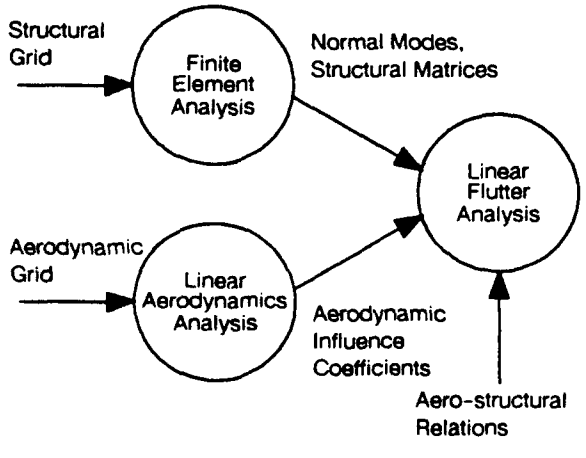


Fig. 8. The Existing Aeroelastics Analysis Environment

The flutter speeds for each Mach number were calculated using the in-house flutter package at British Aerospace. To this end a UTSP post-processor program was used to scale the matrices and output them in the required format. These flutter speeds were then factored using the experimental values of mass ratio, $\bar{\mu}$, and torsion frequency, ω_α, to give the results presented in figure 7, where

$$\bar{V}_f = 2V_f/(c_o\omega_\alpha\sqrt{\bar{\mu}})$$

This figure demonstrates the ability of the UTSP program to predict the transonic flutter dip.

The CPU times are the same as above. However, because of the low frequency parameter of the cases considered, all cases required some 800 time steps per cycle. Convergence to within 1 percent tolerance was obtained after between 3 periods for low subsonic and supersonic Mach numbers and 8 periods for high subsonic Mach numbers.

3. IMPLEMENTATION WITHIN THE DYNAMICS ENVIRONMENT

Before discussing in detail how the UTSP program fits into the current working environment of the Dynamics engineer at British Aerospace, Kingston, the existing environment will be described.

3.1 Existing Environment

Figure 8 shows that there are 3 processes involved:

a) The finite element structural analysis program. This program, NASTRAN™, is usually used to provide a set of normal modes, (i.e. eigenvectors normalised to give a generalised-mass matrix that is the identity matrix), and a generalised stiffness matrix, E. The mode shapes are defined at the nodes of the STRUCTURAL GRID.

b) The linear aerodynamics package, comprising a number of programs to produce Aerodynamic Influence Coefficients (AICs) for subsonic and supersonic Mach numbers. These AICs are defined at the nodes of the, so-called, AERODYNAMIC GRID. The geometry definition comprises the planform coordinates for several "lifting surfaces", including control surfaces.

THIS DOCUMENT PROVIDED BY THE ABBOTT AEROSPACE
TECHNICAL LIBRARY
ABBOTTAEROSPACE.COM

c) The linear aeroelastics analysis program. This program interpolates the normal modes between the structural and aerodynamic grids and then uses them to produce the generalised aerodynamic damping and stiffness matrices, B & C respectively. From here it solves the Flutter equation,

$$A\ddot{q} + (Bv + D)\dot{q} + (Cv^2 + E)q = 0 \qquad (14)$$

using a "mode-tracking" algorithm based on Inverse Iteration, over a velocity range $0 \leq v \leq 1$. (The density and reference airspeed are incorporated in the AICs).

The aerodynamic grid is an arbitrary set of points chosen by the user. It bears no relation to the underlying discretisation of the geometry by the aerodynamic prediction algorithm (which is a boundary-element method for subsonic flow and a finite difference method for supersonic flow). The nodes of this underlying grid are termed AEROPOINTS.

The interpolation between the structural and aerodynamic grids is accomplished by a semi-manual approach whereby a set of relationships are defined between the grid points of the two models. Forces and moments are defined at each structural grid node resulting from a unit force at each aerodynamic grid node. These relationships are termed the Aero-Structural Relations (ASR). The displacements, normal to the lifting surface, at each aerodynamic grid node can then be obtained from the displacements and rotations at the structural grid nodes.

Each element of the AIC matrices is calculated by prescribing modeshapes which have unit displacement at one node and zero displacement everywhere else. These modeshapes on the AERODYNAMIC GRID are interpolated on to the AEROPOINTS using a linear tile-interpolation, using triangular tiles. The complete interpolation process is shown schematically in figure 9.

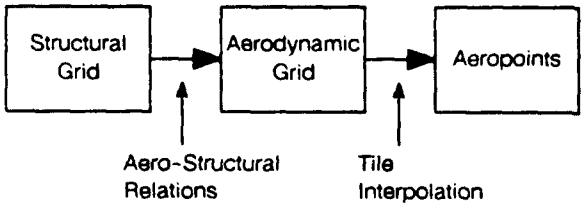


Fig. 9. Interpolation of Modeshapes between the Structural and Aerodynamic Models

3.2 How the Unsteady TSP program fits in

3.2.1 Pre-processing

As discussed earlier the UTSP program can be used either to investigate the aeroelastic behaviour of the flexible wing in the time-domain, or to produce generalised aerodynamic matrices for a prescribed set of modes. In either case the modeshapes need to be defined at the computational grid nodes of the unsteady tsp solution. These nodes are the aeropoints for the UTSP algorithm.

In order to interpolate between the structural grid and the aeropoints, use is made of the existing set of relationships between the structural and aerodynamic grids and the existing tile-interpolation routines. This interpolation is done externally to the UTSP program by means of a pre-processor program.

This pre-processor, which performs the interpolation process shown in figure 9, requires the coordinates of the aeropoints. These can be obtained from a previous run of the UTSP program, or the UTSP program can be run solely to process the geometry without performing any solution.

The implication of all this is that the UTSP Enhanced Design Tool can be used for an existing wing model, one for which linear aerodynamics have already been calculated, with minimal extra effort.

The only additional data required to run the UTSP program, other than control data, is the definition of the wing surface geometry. However, the layout of the geometry input data is compatible with that required for the steady flow wing-body Full-Potential and Euler codes in use at British Aerospace. Therefore, in most cases the Dynamics engineer can obtain a geometry deck off-the-shelf from the Fluid Dynamics section.

3.2.2 Post-Processing

There are two approaches to determining the flutter characteristics of a wing using the UTSP program. The first is to use the full non-linear coupled solution of the structural and aerodynamic equations of motion, to obtain generalised displacement transients. These transients can be analysed internally or externally of the program to obtain the frequency and damping characteristics of each mode.

The second way is to produce generalised force matrices, B & C, for each frequency parameter and Mach number of interest. These matrices can then be used as input to the flutter analysis program mentioned in Section 3.1 above. However, before they can be picked up by the flutter program, they need to be scaled and written in the required format. This process is achieved by a post-processor program.

It is not necessary that all modes are calculated in one UTSP run. The user can run subsets of the whole and then form the complete matrices using a combination of the post-processor and a text editor.

The overall implementation of the UTSP program is shown in figure 10, where the type of data required at each stage is identified.

3.3 The Flutter Analysis of a Combat Aircraft Wing

In this section the above methods are applied to a production combat aircraft wing. The planform is shown in figure 11, where the UTSP grid can also be seen. The wing is one for which linear unsteady aerodynamics have already been calculated for subcritical Mach numbers. The only additional information required was the wing surface geometry. In this case, a compatible geometry file was not available, but the relevant data was obtainable from the Fluid Dynamics section.

THIS DOCUMENT PROVIDED BY THE ABBOTT AEROSPACE
TECHNICAL LIBRARY
ABBOTTAEROSPACE.COM

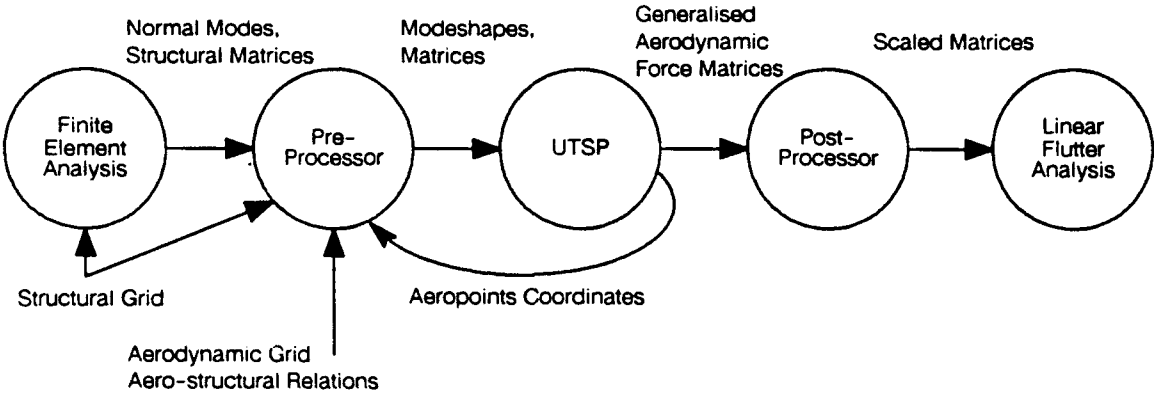


Fig. 10. Implementation of UTSP within the Aeroelastics Analysis Environment

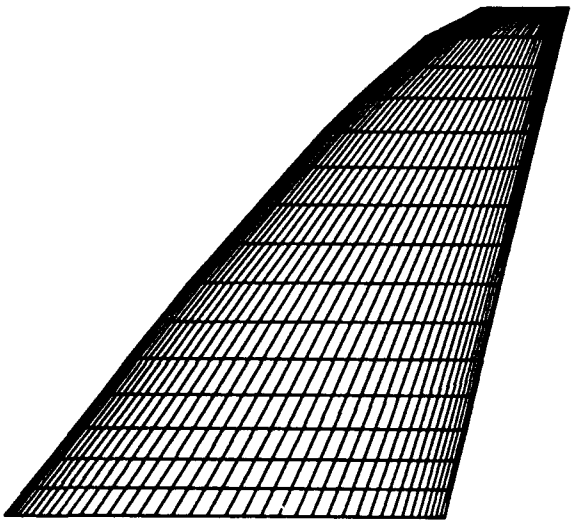


Fig. 11. A 'Production' Aircraft Wing

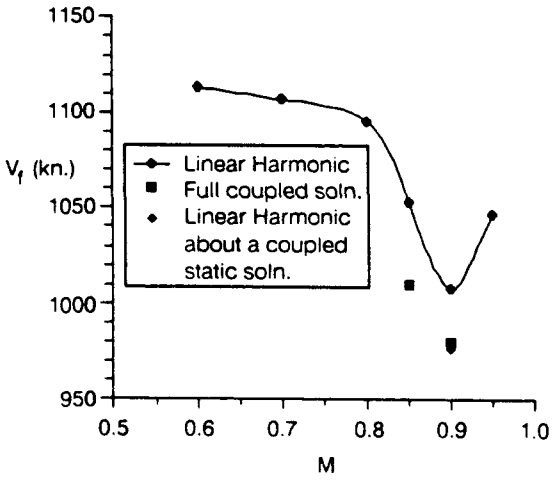


Fig. 12. Flutter Characteristics of a 'Production' Aircraft Wing

Figure 12 shows the calculated flutter speed variation with Mach number. Three solution methods are represented in this figure. Firstly, the bulk of the data presented was generated using the linearised harmonic option about a rigid wing at zero incidence. The other points, with lower flutter speeds, were calculated using non-linear coupled solutions.

The plot indicates that the flutter characteristics of this wing are more pessimistic when a full non-linear analysis is performed. The third solution method represented in the figure is that of a linear harmonic calculation using an asymptotic steady state solution. The results are almost exactly the same as for the full non-linear analysis, indicating that the non-linearities in the flow are predominantly due to the mean steady state flow.

As far as CPU time required for each point on the plot, there is not much difference between the methods. Six modes were used in the calculations and so the cost of each linear-harmonic analysis run was quite high; whilst the number of modes is virtually irrelevant to the full non-linear analysis, runs for several values of dynamic pressure are required in order to find the point of zero-damping.

4. CONCLUSIONS

The unsteady tsp program, UTSP, currently in use at British Aerospace has been described. Particular attention has been paid to the straight forward implementation of the program within the Dynamics engineers' environment at the Kingston site.

Steady and unsteady pressures calculated by the UTSP program for the AGARD SMP taileron have been presented which validate the basic solution algorithm, as well as the non-isentropic corrections.

The validity of the calculation of the generalised aerodynamic force matrices has been established by investigating the flutter characteristics of the standard AGARD aeroelastic configuration, wing 445.6.

Beyond UTSP, work is currently underway to produce an unsteady Euler solver. This work is in its initial stages and includes investigations by a number of different agencies into aspects such as moving meshes, implicit algorithms and complex geometries.

THIS DOCUMENT PROVIDED BY THE ABBOTT AEROSPACE
TECHNICAL LIBRARY
ABBOTTAEROSPACE.COM

5. ACKNOWLEDGEMENTS

The author is grateful to British Aerospace for permission to publish this paper. Any views expressed are those of the author and not necessarily those of British Aerospace.

6. REFERENCES

1. Watson, M., "Solution of the 3-D Unsteady Transonic Small Perturbation Equation", RAE Technical Report (in preparation).
2. Fuglsang, D.F. and Williams, M.H.,"Non-Isentropic Unsteady Transonic Small Disturbance Theory", AIAA paper 85-0600, 1985.
3. Gibbons, M.D., Whitlow, M. Jr. and Williams, M.H., "Non-Isentropic Unsteady Three Dimensional Small Disturbance Potential Theory", AIAA paper 86-0863, 1986.
4. Batina, J.T., "Unsteady Transonic Small Disturbance Theory including Entropy and Vorticity Effects", AIAA paper 88-2278, 1988.
6. Carson Yates, E., Jr., "AGARD Standard Aeroelastic Configurations for Dynamic Response: I - Wing 445.6", AGARD Report No. 765, July 1988.

THIS DOCUMENT PROVIDED BY THE ABBOTT AEROSPACE
TECHNICAL LIBRARY
ABBOTTAEROSPACE.COM

AD-P007 808

AEROELASTIC CALCULATIONS FOR FIGHTER AIRCRAFT USING THE TRANSONIC SMALL DISTURBANCE EQUATION

Dale M. Pitt
Dennis F. Fuglsang
McDonnell Aircraft Company
McDonnell Douglas Corporation
P.O. Box 516
St. Louis, Missouri 63136 USA

ABSTRACT

The Transonic Small Disturbance (TSD) equation provides a fast and efficient tool for calculating both static and dynamic nonlinear aerodynamic effects. To become an accepted part of the aircraft design process, time-accurate TSD equation solvers for aeroelastic calculations now need to be evaluated on realistic aircraft configurations that have complex geometry. This paper reports on the application of NASA Langley's Computational Aeroelastic Program - Transonic Small Disturbance (CAP-TSD) code for both static and dynamic transonic aeroelastic calculations for McDonnell Aircraft Company's F-15 and F/A-18 fighter aircraft. The results for flutter speed and aileron reversal speed are compared with results from standard linear aerodynamic analysis.

1. INTRODUCTION

In the transonic speed range, where shock waves affect lifting surfaces, the assumption of linear aerodynamics can introduce large errors into predictions of aircraft aeroelastic response. The transonic speed region is of primary interest since the flutter dynamic pressure is typically critical there. This is also the region of various static aeroelastic responses, such as aileron reversal and leading edge control surface divergence.

The equations governing transonic aerodynamics are inherently nonlinear and preclude analytic or numerical solutions by traditional methods. In the last few years, however, advances in computers and numerical algorithms have allowed aeroelastic calculations to be performed using computational fluid dynamic (CFD) techniques. One such CFD technique is the Transonic Small Disturbance (TSD) formulation of the unsteady aerodynamic problem. This paper describes the results of using the NASA-Langley developed TSD code, Computational Aeroelastic Program - Transonic Small Disturbance (CAP-TSD), for both static and dynamic aeroelastic analysis of fighter aircraft.

2. BACKGROUND/OBJECTIVE

As reported in Reference 1, McDonnell Aircraft Company started investigating the use of CFD for aeroelastic analysis in the early 1980s. The initial effort focused on the transonic flutter speed dip experienced by the AV-8B model during wind tunnel testing. Reference 1 reported on the results of using the 2-Dimensional TSD equation in the NASA AMES LTRAN2 computer program applied to the AV-8B supercritical airfoil. The 3-Dimensional TSD equation as formulated in the United States Air Force program XTRAN3S was also used to compare steady wing pressures with measured results.

Reference 2 reported on the NASA Langley 3-Dimensional TSD solver, CAP-TSD, and its use to model the F-15 wing, fuselage, and horizontal tail surfaces. Comparisons were presented for static measured wind tunnel pressure data with CAP-TSD calculated results. The results agreed both subsonically and supersonically over a moderate range of angles-of-attack. The inner wing pressures predicted by CAP-TSD correlated well with the test data, and verified the fuselage effect on the inner wing pressures. The calculated forward fuselage pressures also compared well with the measured data.

The work reported in Reference 3 used both the CAP-TSD and XTRAN3S codes to perform flutter analyses for the F-15 wing and the F-15 STOL Maneuvering Demonstrator aircraft. The F-15 STOL CAP-TSD analysis modeled the canard, wing, and horizontal tail. The wing was modeled as a flexible structure, but the canard and tail were assumed to be rigid. The objective of this model was to isolate the aerodynamic effects of these surfaces on the wing flutter speed. Reference 3 also reported on the F/A-18 fighter clean wing configuration and a configuration that considered the tip missile and launcher installed.

The calculations made in Reference 3 were significant in that realistic wing geometries were considered. The CFD grids had to adequately represent physical geometry such as multiple control surfaces, wing twist, and external stores such as the tip missile and launcher. The flutter calculations were made with 3 to 5 vibratory mode shapes for each configuration. This limited number was imposed by the time required to spline the structural mode shapes to the CFD grids.

Generally, to obtain accurate results from a modal aeroelastic calculation, a modal convergence study to determine the minimum number of required modes must be accomplished. Such studies for the F-15 and

92-16046

THIS DOCUMENT PROVIDED BY THE ABBOTT AEROSPACE
TECHNICAL LIBRARY
ABBOTTAEROSPACE.COM

F/A-18 has been conducted using the faster and cheaper linear aerodynamic theories rather than the more expensive CFD codes. The convergence study indicated that the Reference 3 CFD studies did not possess sufficient modes to quantitatively address the exact transonic flutter dip airspeed. However, they did qualitatively show the nonlinear aerodynamic effects on flutter speed.

The objective of this present study is to perform both static and dynamic CAP-TSD aeroelastic calculations on representative complex wings of the F-15 and F/A-18 aircraft. The study uses the number of structural modes required to obtain convergence based on linear theory.

3. DESCRIPTION OF CAP-TSD CODE

The CAP-TSD code is an unsteady TSD finite difference based code developed for transonic aeroelastic analysis of complete aircraft configurations. The code uses a time-accurate approximate factorization (AF) algorithm developed by Batina, Reference 4, for the efficient solution of the unsteady TSD equation. The AF algorithm consists of a Newton linearization procedure coupled with an internal iteration technigue. The CAP-TSD code is capable of treating combinations of lifting surfaces and bodies, and includes the following algorithm features:
(1) Engquist-Osher monotone differencing;
(2) Nonreflecting far field boundary conditions;
(3) Second-order accurate spatial differencing in supersonic regions of the flow; and
(4) Entropy and vorticity effects to treat cases with strong shock waves.

The aeroelastic computational procedure implemented within CAP-TSD includes the simultaneous integration of the structural equations of motion and the unsteady aerodynamic time-marching solution procedure. In the current version of CAP-TSD, the aeroelastic equations of motion are formulated in terms of generalized coordinates, i.e., modal solution, with lifting surface motion limited to the z-direction. The time-marching solution procedure uses a state equation formulation which is solved numerically using a modified state-transition matrix integrator. Further details of the algorithm development and solution procedures are reported in Reference 4, and a more detailed description of the CAP-TSD code is presented in Reference 5.

4. REQUIRED PRE-PROCESSING: TRANSFORMING VIBRATORY MODE SHAPES

Before a time accurate aeroelastic analysis using CAP-TSD can be performed, the wing vibratory mode shapes must first be transformed to the CAP-TSD grid. In CAP-TSD, these structural deformations are assumed to be described by a modal representation of the structure. For the present study, the NASTRAN finite element code of Reference 6 was used to develop the vibration model of the aircraft. The NASTRAN models used in these studies were beam rod models, but they need not be limited to this idealization of the structure. The stiffnesses of the elements were adjusted to correlate each model with ground vibration test data. A real eigenvalue solution of the NASTRAN model produces the natural modes of vibration and the natural frequencies needed for the modal representation of the structure.

The vibratory mode shapes for the wings studied are defined in terms of 3 translations and 3 rotations at each NASTRAN grid point. In order to approximate this mode shape in terms of vertical displacements and streamwise slopes at the CAP-TSD grid points, a surface transformation or mapping method is used. Normally, this method is a surface spline fit of the NASTRAN displacements and rotations over the wing surface. However, difficulties can be encountered when splining across rotational discontinuities such as control surface edges, where the slope changes are abrupt and should not be "smoothed" by a spline. In the method chosen for this study, only the NASTRAN displacement and rotation values at the grid points along the wing elastic axis and control surface hinge lines are used. Each aerodynamic grid point is rigidly translated and rotated in the streamwise direction about the elastic axis or hinge line, using the linearly interpolated NASTRAN values at that spanwise station. By modeling mode shapes in this manner we assume that both the wing chordwise bending and the chordwise camber induced by wing torsion were negligible. The advantage of the method is that a piecewise smooth representation of the mode shapes can easily be obtained while still retaining sharp breaks along the control surface discontinuities. This technique is similar to the "Rigid Spline" method used in the NASTRAN aeroelastic solution procedure, and is recommended for beam rod type structural models.

5. REQUIRED POST-PROCESSING: EXTRACTING DAMPING AND FREQUENCY VALUES

The dynamic solutions from the CAP-TSD code generate lift, moment, and individual modal coordinate information (displacements, velocities, and accelerations) at each time integration point. These modal time histories must be post-processed to identify modal damping and frequencies for the given Mach and dynamic pressure conditions. An interactive program has been developed at MCAIR to curve-fit a series of damped sine-waves to the transient response. The program performs a Fast Fourier Transformation of the transient response to give starting values for the damped sine curve-fits. An optimization gradient procedure is used to find the values of the curve-fit. The number of damped sine curves fitted, m, is increased until the level of desired accuracy is achieved. The damped sine equation is:

$$y = c\sum_{i=1}^{m}\left\{e^{-\zeta\omega_n t}\sin(\omega_d t+\theta)\right\}$$

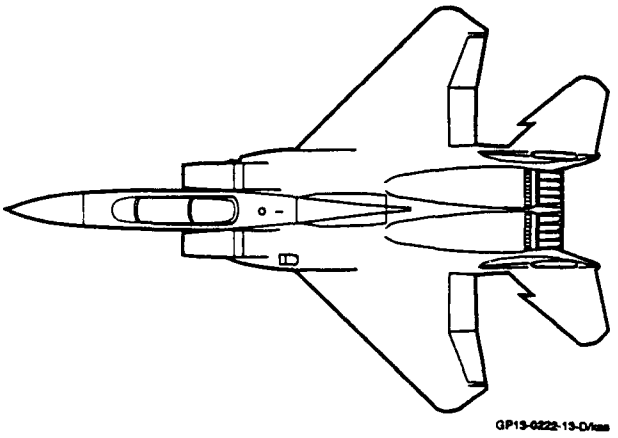
THIS DOCUMENT PROVIDED BY THE ABBOTT AEROSPACE
TECHNICAL LIBRARY
ABBOTTAEROSPACE.COM

where ζ represents the fraction of critical damping, $\zeta=c/c_c$ and is assumed to be one half the structural damping coefficient g, $g=-2\zeta$. The terms ω_n and ω_d are the natural and damped frequencies, respectively. The phase lag between the motion and the response of the system is θ.

When a large number of vibratory modes are used to represent the dynamics of the structure, the same large number of modal displacement time histories are produced. The rigorous method of stability analysis is the curve-fit decompositions of each generalized displacement. However, in this study, curve-fitting the wing lift and/or moment time histories was found to be a simpler and less tedious indicator of system stability, with little or no loss of accuracy in the extracted frequency and damping values.

6. CAP-TSD AEROELASTIC MODELING ASSUMPTIONS FOR THE F-15 WING

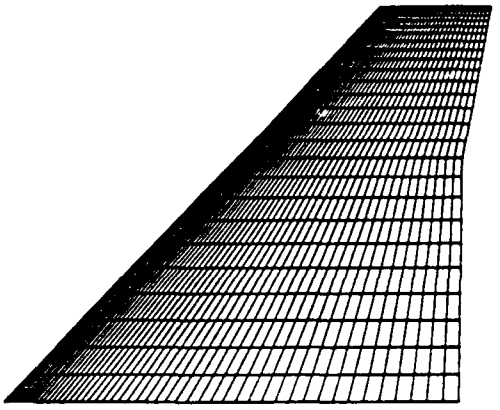
CAP-TSD was used to perform both static and dynamic aeroelastic calculations for the F-15 wing, because much data is available for this configuration. The F-15 wing, shown in planform in Figure 1, has an aspect ratio of 3.01, a leading edge sweep of 45 degrees, and a taper ratio of 0.25. The airfoil section is a modified NACA64A series that varies in thickness from 5.9 percent at the root to 3 percent at the wing tip. The wing clip tip was not modeled in these studies, because the wind tunnel data was measured on a wing with an unclipped tip.



GP13-0222-13-D/kss

Figure 1. Planform View of the F-15 Aircraft

The CAP-TSD grid for the F-15 wing, shown in Figure 2, is a more dense grid than the previous grid of the Reference 3 studies. The grid has 110 streamwise grid lines (with 51 per wing chord), 45 spanwise grid lines (with 26 on the wing), and 60 vertical grid lines. Before the aeroelastic analysis was performed, the accuracy of the CAP-TSD F-15 wing grid resolution was examined through steady-state aerodynamic calculations. Examining the wing steady pressures helps to assess the basic character of the flow field. The unsteady flow field, and hence generalized aerodynamic forces, depend strongly on the steady-state flow, especially in the transonic speed range. So the steady pressure distributions frequently can give physical insight into critical flow mechanisms which control aeroelastic phenomena.



GP13-0222-15/kss

Figure 2. Planform View of the F-15 CAP-TSD Grid

7. CAP-TSD AEROELASTIC ANALYSIS OF THE F-15 WING: STATIC RESULTS

Steady pressure distributions were obtained for the F-15 wing at M_∞=0.9, 0.95, and 1.2 for comparison with the experimental data of Reference 7. Steady pressure distributions at one span station along the wing for the M_∞=0.9, α=0.08 deg. and α=2.46 deg. cases are presented in Figure 3. Results for M_∞=0.9, α=0.08 deg. are shown in Figure 3(a); results for M_∞=0.9, α=2.46 deg. are shown in Figure 3(b). These pressure distributions indicate the presence of embedded supersonic regions along the lower surface for α=0.08 deg. and a very strong upper surface shock at the higher angle-of-attack, α=2.46 deg.

In general, the CAP-TSD pressures agree well with the experimental data and are typical of the agreement achieved at the other Mach numbers. The good agreement also indicates that the 110x45x60 grid size provides sufficient resolution of the transonic flow features. Although a finer grid point distribution would almost certainly improve the comparison, a compromise was made due to the computational resources required to perform the study.

A static aeroelastic analysis was performed using both linear and nonlinear CAP-TSD aerodynamics. The wing was modeled structurally using the first 23 natural vibration modes, excluding zero frequency (rigid body) modes. The free stream conditions were M_∞=0.9, α=2.46 deg., V_∞=881 knots, and q_∞=18.2 psi. The vibrating mode shapes were transferred to the CAP-TSD grid by the "rigid spline" method outlined above, with examples of the modal displacements of the CAP-TSD grid shown in Figure 4 for two modes.

THIS DOCUMENT PROVIDED BY THE ABBOTT AEROSPACE
TECHNICAL LIBRARY
ABBOTTAEROSPACE.COM

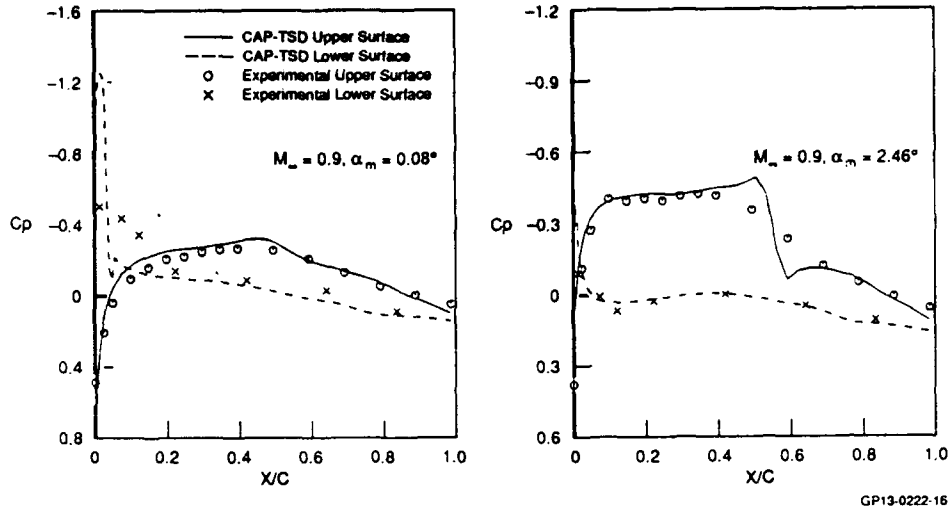


Figure 3. Comparison of CAP-TSD Predicted Static Cp With Measured Data, for M_∞ = 0.9, at Semi Span of 77.0%

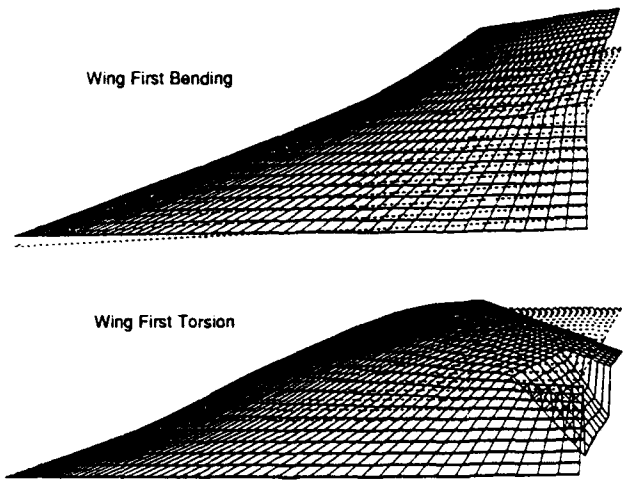


Figure 4. F-15 Vibratory Mode Shapes Transformed to the CAP-TSD Grid

Specifically, the modes shown in Figure 4 are the principal modes comprising the basic wing flutter mechanism.

Figure 5 shows static aeroelastic deflection contours for three different aerodynamic representations: linear TSD, nonlinear TSD, and nonlinear Euler. The Euler solution was computed using a specially modified version of CFL3D described in Reference 8. This version of CFL3D incorporates the same structural equations of motion and time-integration scheme used in CAP-TSD allowing the same mode shape representation of the structure between the two methods.

Two important observations can be made from Figure 5. First, the assumption of linear aerodynamics produces an erroneous "wing tip up" deformed shape for this transonic condition. Second, the nonlinear CAP-TSD aerodynamic model provides an accurate representation of the static wing deformation based on the good agreement with the Euler solution.

8. CAP-TSD AEROELASTIC ANALYSIS OF THE F-15 WING: DYNAMIC RESULTS

In the dynamic phase of the CAP-TSD analysis, aeroelastic stability and flutter at transonic speeds were investigated. Calculations were performed for several values of free stream Mach number, free stream velocity, and dynamic pressure. All solutions were performed at a mean wing angle-of-attack of α=0.0 deg. and utilize the same 23 vibration mode structural model as in the static aeroelastic calculations. Time step size and the number of iterations were selected to allow at least three cycles of the lowest frequency mode and at least four cycles of the flutter mode to be computed. A temporal accuracy study was performed to insure sufficient resolution of the aeroelastic response. In this accuracy study, successively smaller time steps were run, keeping all other conditions constant, until the maximum error between lift time histories was less than two percent.

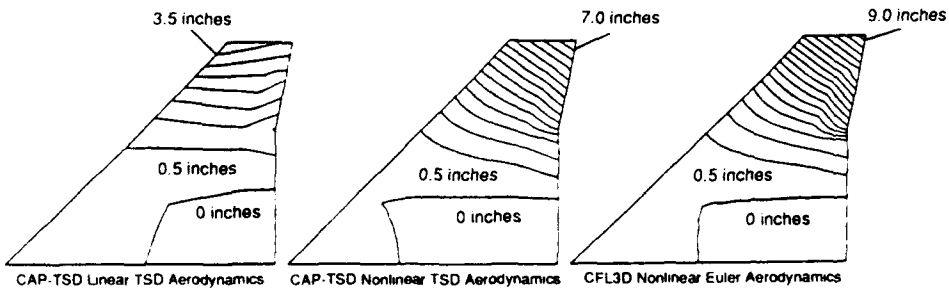


Figure 5. Comparison of F-15 Predicted Static Aeroelastic Deflections for 23 Vibratory Modes at M = 0.9, α = 2.46 °, q_∞ = 20 psi

THIS DOCUMENT PROVIDED BY THE ABBOTT AEROSPACE
TECHNICAL LIBRARY
ABBOTTAEROSPACE.COM

Results from the dynamic aeroelastic analysis at M_∞=0.9 are shown in Figure 6. The figure contains the lift time histories from four different CAP-TSD runs. Each run is for a different free stream velocity and dynamic pressure. These responses were curve-fit using the damped sine decomposition method outlined above to extract damping and frequency values and determine the stability of the system. For this Mach number, the V_∞=900 and V_∞=870 knot solutions bound the zero damping, neutral stability point. A flutter speed of 880 knots was found by linear interpolation of the damping between these points.

The F-15 wing lift coefficient time history for the M_∞=0.9 flutter point at V_∞=880 knots is presented in Figure 7. Three points on the time history are labeled as -90, 0, +90 degrees in the flutter cycle. Within Figure 7 are comparison plots of the wing upper and lower surface Cp distributions for the -90, 0, +90 points at the 50, 75, and 90 percent span locations along the wing. Important features of the figure are the emergence of a strong lower surface shock near the wing leading edge and the presence of a strong upper surface shock near mid-chord. Large variations in shock strength are observed through the -90, 0, +90 portion of the flutter cycle and when moving outboard along the wing. Very little activity is seen at the 50 percent span location or further inboard. The inboard portion of the wing has very little displacements during the flutter cycle. This reduced inboard motion results in relatively small unsteady pressures, and consequently the inboard unsteady forces are also small or negligible during the flutter cycle. These small forces justify not modeling the fuselage and neglecting the extra fuselage upwash effects on the inner wing. The outboard lower surface shock is due to the thin, highly cambered airfoil sections on the outer portion of the F-15 wing.

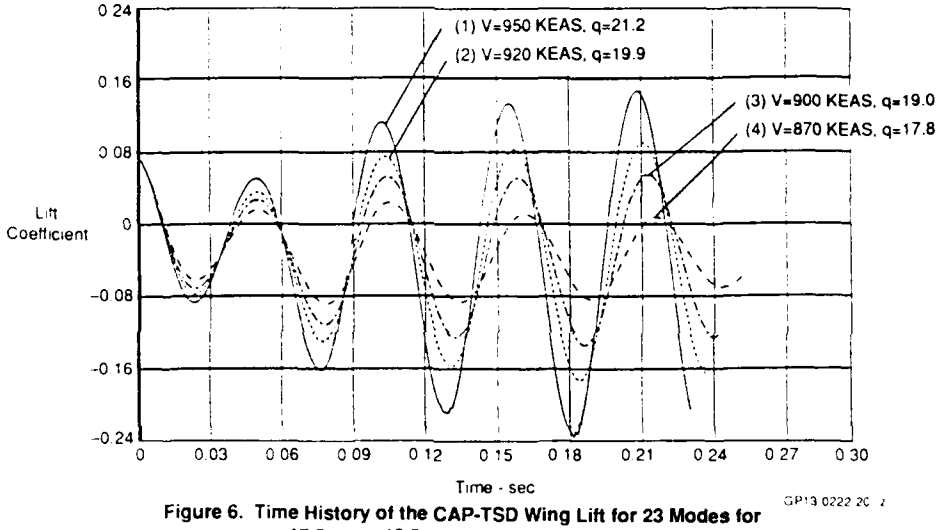


Figure 6. Time History of the CAP-TSD Wing Lift for 23 Modes for q_∞ = 17.8, q_∞ = 19.0, q_∞ = 19.9, and q_∞ = 21.2 psi

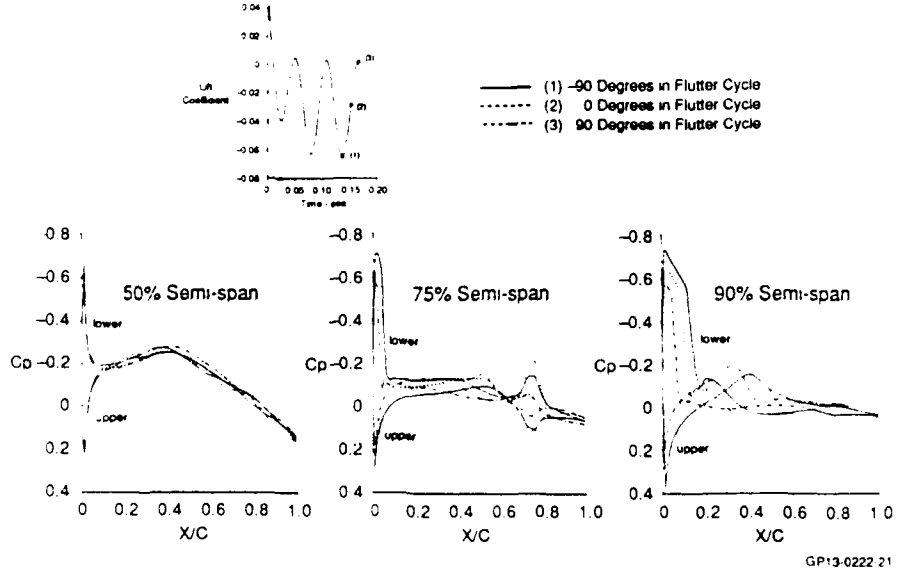


Figure 7. Comparison of CAP-TSD Instantaneous Cp for 3 Different Times During the Wing Flutter Cycle, 23 Modes, M_∞ = 0.9, α = 0, V_∞ = 880 KEAS

THIS DOCUMENT PROVIDED BY THE ABBOTT AEROSPACE
TECHNICAL LIBRARY
ABBOTTAEROSPACE.COM

The flutter mechanism in this figure is a classical outer wing bending-torsion. This conclusion is based on previous linear (V-g-ω) calculations, past experience, and by tracking the frequencies extracted from the lift time histories. Unfortunately, it would be very difficult to determine which modes contribute to a the flutter mechanism for a wing that was not as well understood as the F-15's. That is one of the drawbacks of time marching aeroelastic methods.

The final flutter boundary for the F-15 wing computed using CAP-TSD is shown in Figure 8. A very distinct dip in flutter speed is seen at M_∞=0.9 which clearly differs from the linear TSD results. Also plotted in this figure are the flutter speeds obtained using a more traditional V-g-w technique in conjunction with Doublet Lattice aerodynamics. The two linear aerodynamic based methods show excellent agreement at M_∞=0.5 and 0.7 with a difference in flutter velocity and frequency of 2 percent or less. As Mach number increases, the computed linear flutter speeds start to differ slightly, but qualitatively show very similar trends. The nonlinear CAP-TSD calculates the minimum flutter speed or transonic flutter dip at M_∞=0.9, with a difference of 60 knots between the traditional linear speed and the nonlinear speed. It is also interesting to note that the nonlinear aerodynamic results compare well with the linear aerodynamic solutions at M_∞=0.5 and 1.2. The M_∞=0.5 and 1.2 are points in which the flow over the wing is purely subsonic or supersonic, and their comparability reinforces how well linear aerodynamic based methods can do at these conditions. This comparability also documents that the TSD aeroelastic solution converges to the linear solution at flow conditions where the nonlinear aerodynamic terms are negligible.

9. CAP-TSD AEROELASTIC MODELING ASSUMPTIONS FOR THE F/A-18 WING

As with the F-15 wing, CAP-TSD was used to perform both static and dynamic aeroelastic analysis of the F/A-18 wing. The wing, shown in planform in Figure 9, has two leading edge flaps, a trailing edge flap, and a trailing edge aileron. It has an aspect ratio of 3.5, a leading edge sweep of 26.7 degrees, and a taper ratio of 0.348. The airfoil section is a modified NACA65A series which varies in thickness from 5 percent at the root to 3.5 percent at the wing tip. The wing has a 4 degree linear geometric twist starting at the wing fold mechanism, which is at a semi-span location of 65 percent, to the wing tip.

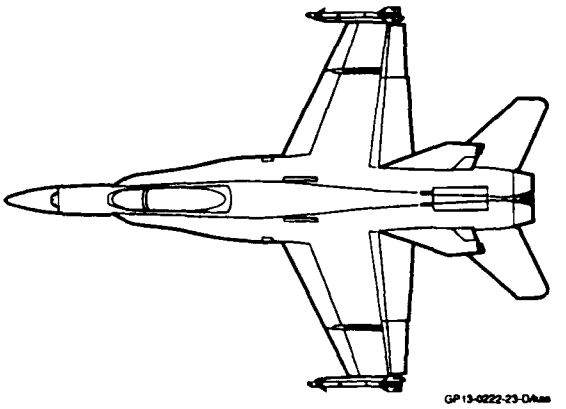


Figure 9. Planform View of the F/A-18 Aircraft

The CAP-TSD grid for the F/A-18 studies is shown in Figure 10. It is essentially the same grid as used in Reference 3 studies. The grid has 82 streamwise grid lines (with 39 on the wing in the chordwise direction), 37 spanwise grid lines (with 14 on the wing), and 52 vertical streamlines. To adequately model the tip missile, certain geometric simplifications had to be made to the aerodynamic model of the tip missile. First, the tip missile body was modeled as a lifting surface with airfoil ordinates representing the missile cross-sectional shape. This was necessary so that the unsteady missile body pressures could be integrated in the generalized force calculations. It was not

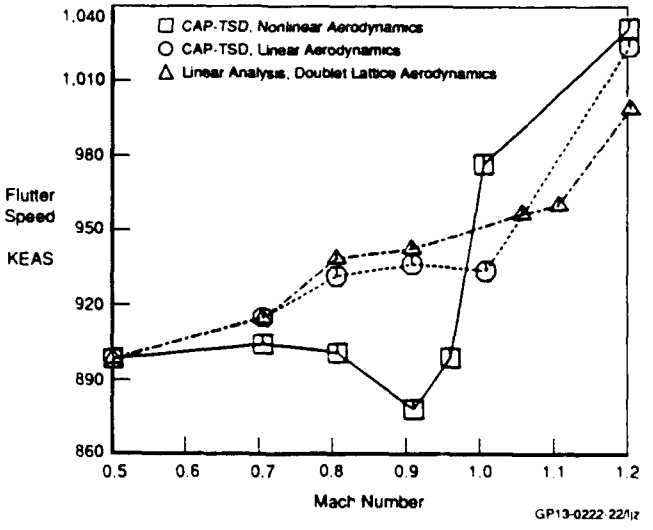
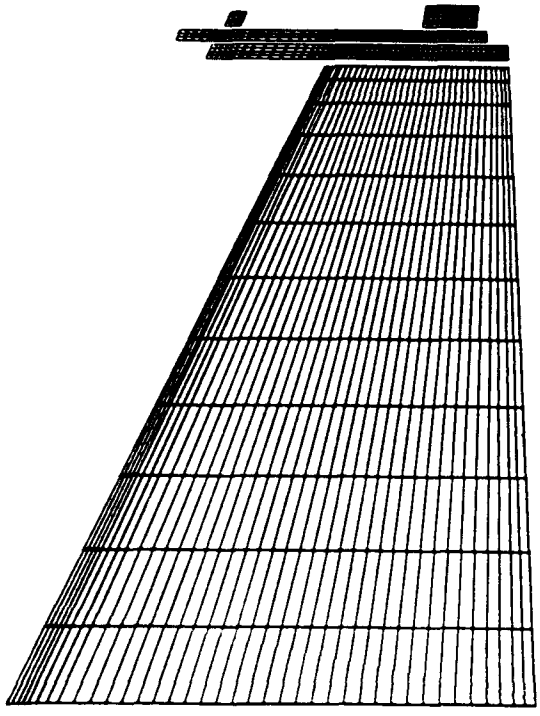


Figure 8. CAP-TSD Predicted Transonic Flutter Boundary for F-15 Wing With 23 Vibratory Modes

THIS DOCUMENT PROVIDED BY THE ABBOTT AEROSPACE
TECHNICAL LIBRARY
ABBOTTAEROSPACE.COM

possible to model the missile forward and aft fins at their normal 45 degree inclination (i.e. dihedral compared to the wing), so the fins were rotated into the horizontal and vertical planes. This resulted in four vertical fins and two horizontal fins on the missile. Slight compromises were made to fin planform shape.



GP13-0222-26-es

Figure 10. Planform View of CAP-TSD Grid for F/A-18 Wing, Launcher, Tip Missile, and Tip Missile Fins

As in the F-15 studies, the F/A-18 structure was modeled using the NASTRAN finite element model. The structure was supported at the aircraft center of gravity, and included a beam rod representation of the fuselage, wing torque box, and each control surface elastic axis. The first 40 NASTRAN flexible modes were transformed to the CAP-TSD grid using the "rigid spline" technique described previously. F/A-18 linear flutter calculations using the Doublet-Lattice Method aerodynamics verified the requirement for 40 vibratory modes for dynamic aeroelastic calculations. The high frequency modes are required to model the leading edge flaps which have a very high rotational natural frequency at zero airspeed; however, the addition of aerodynamics gives the leading edge control surface modes a tendency to diverge, in which case the modal frequencies decrease with increasing airspeed.

The initial study of Reference 3 used the first 5 vibratory modes. The linear Doublet-Lattice flutter calculations with 5 modes resulted in the same basic flutter mechanism as the linear Doublet-Lattice 40 mode case, with the flutter airspeed being considerably higher for the 5 mode case. Figure 11 presents the orthographic projection of mode 3 (outboard pylon pitch) and mode 4 (first wing bending) transformed to the CAP-TSD grid. These two modes combine for the basic bending-torsion flutter mechanism. The CFD grid lines for these modes are well behaved. Due to space limitations the remaining 38 modes are not presented, but they were equally smooth.

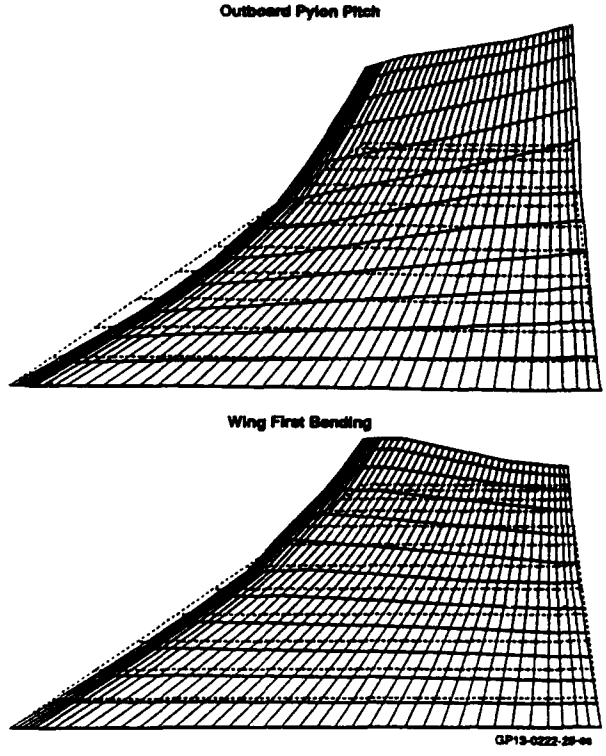


Figure 11. Example of F/A-18 Vibratory Mode Shapes Transformed to the CAP-TSD Grid

Flight testing of the F/A-18 showed that the dynamic aeroelastic response of the F/A-18 was significantly modified with different commanded leading and trailing edge control surface settings. With this in mind, the static aeroelastic effects of the control surfaces were determined before embarking on a flutter study. The 5 mode representation of Reference 3 was used first. Subsequently it was increased to the 40 mode idealization to determine if the modal convergence criteria for static aeroelasticity are the same as for dynamic aeroelasticity.

10. CAP-TSD AEROELASTIC ANALYSIS OF THE F/A-18 WING: STATIC RESULTS

CAP-TSD was used to calculate the aileron reversal dynamic pressure for the F/A-18 aircraft. The aileron was rigidly displaced 2 degrees down for these calculations. Figure 12 is a comparison of the chordwise static rigid pressure distribution at a semi span location of 97 percent for M_∞=0.9 and α=0.44 deg. The pressures for an aileron deflected case are compared to a nondeflected case. It is easy to see the change in pressure coefficient before and after the aileron hinge line. A strong shock wave is present on the lower wing surface close to the wing leading edge. This lower surface shock is one of the major nonlinear aerodynamic factors in the aeroelastic studies.

THIS DOCUMENT PROVIDED BY THE ABBOTT AEROSPACE
TECHNICAL LIBRARY
ABBOTTAEROSPACE.COM

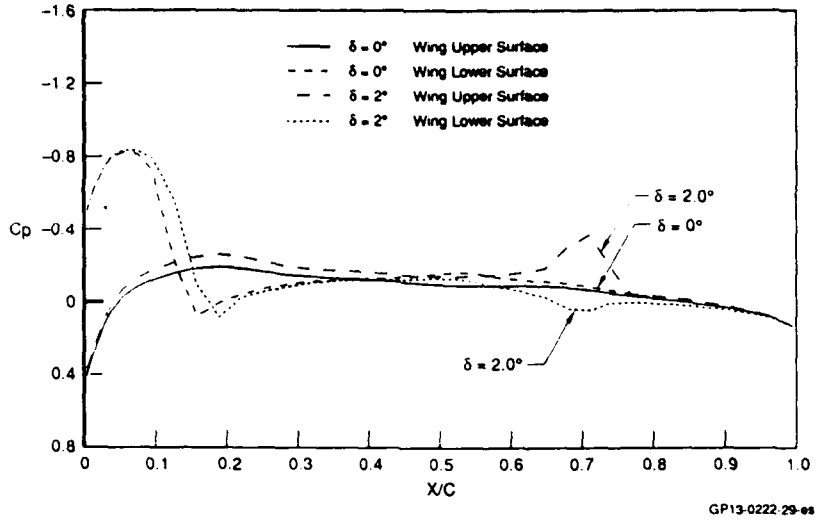


Figure 12. Comparison of CAP-TSD Predicted Cp for F/A-18 Wing With Aileron at δ = 0° and δ = 2°, M_∞ = 0.9, α = 0.44° and Wing Semi Location 97.0%

Aileron reversal was calculated by making incremental static aeroelastic runs for increasing free stream dynamic pressures, and monitoring the resultant change in flexible lift. All runs were made at M_∞=0.9 and α=0.44 deg. The first case considered was the five mode case. It should be noted that these modes do not contain any modes for control surface rotation per se, even thou there is some control surface motion in the five flexible modes. Figure 13 plots the rigid Cl and the flexible Cl for various dynamic pressures versus nondimensional time. The dynamic pressure that results in zero flexible lift is the dynamic pressure for aileron reversal. All cases were started from zero initial conditions, and modal damping was added to all 5 modes because the aileron reversal dynamic pressure is above the dynamic pressure for flutter for this heavy store case.

Figure 14 plots the rigid and flexible span wise lift coefficient versus semi span and the rigid and flexible pitching moment coefficient about the wing 1/4 chord. It is seen that the aileron reversal causes more outboard wing twist and decreases the lift greatly at the wing tip. Note the lift is also decreased at the root, because the structural vibratory modes were calculated for a supported wing, not a cantilevered wing. The wing tip, which has a geometric negative 4 degree twist compared to the root, is twisted downwards much more.

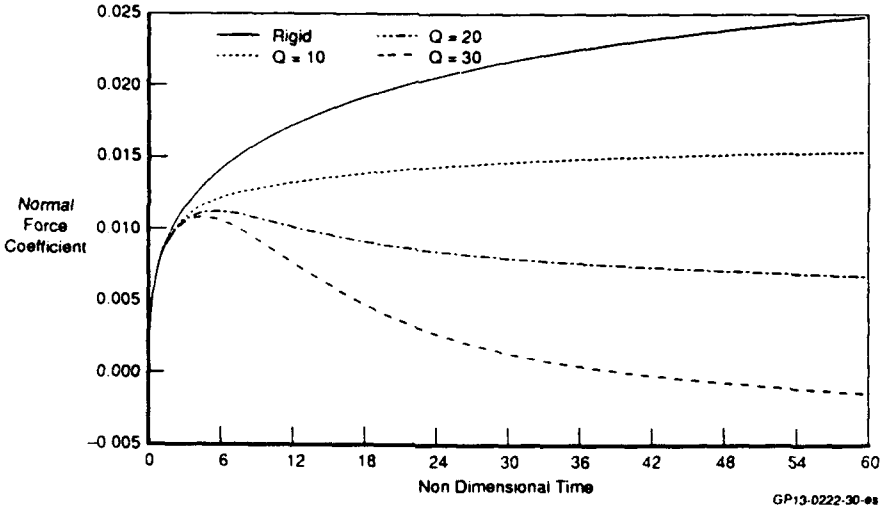


Figure 13. Comparison of CAP-TSD Predicted Wing Cn Time History for 5 Vibratory Mode Case, for Rigid Wing and q_∞ = 10, q_∞ = 2.0, and q_∞ = 30 psi

THIS DOCUMENT PROVIDED BY THE ABBOTT AEROSPACE
TECHNICAL LIBRARY
ABBOTTAEROSPACE.COM

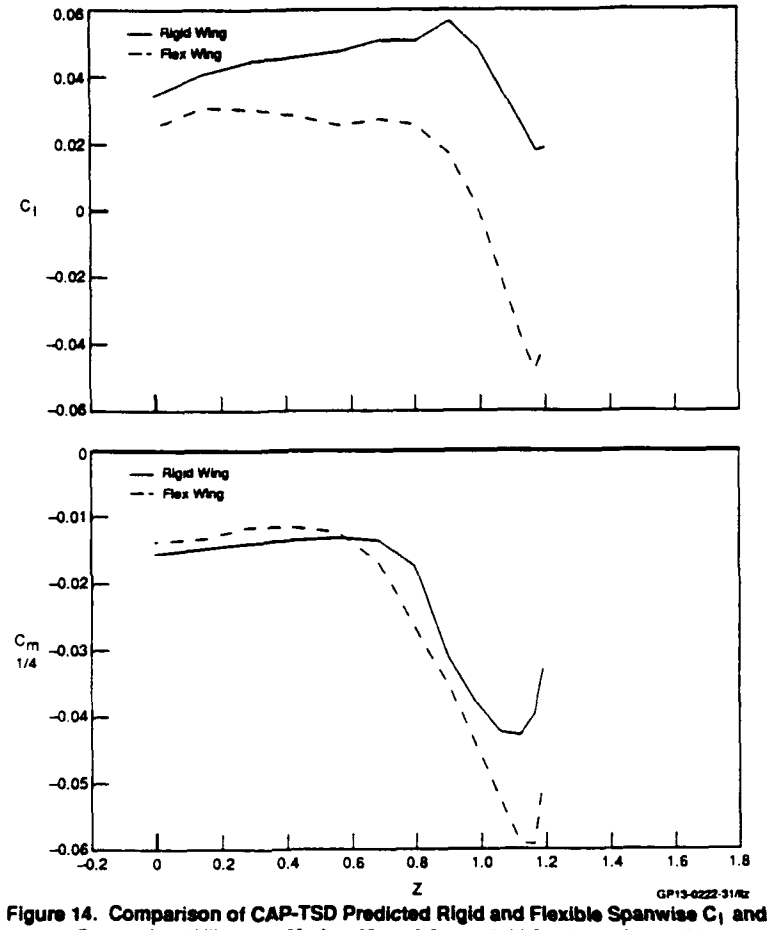


Figure 14. Comparison of CAP-TSD Predicted Rigid and Flexible Spanwise C_l and $C_{m\ 1/4}$ for 5 Vibratory Modes, $M_\infty = 0.9$, $\alpha = 0.44$, $\beta = 2°$ and $q_\infty = 30$

The local pressures at the wing tip are compared in Figure 15. A leading edge shock is seen on the lower surface for both the rigid and reversed case. However, the reversed case results in a much larger shock at a slightly more aft location, and there appears to be a second lower surface shock at x/c=25 percent for the flexible case.

A linear 5 mode aileron reversal study was also conducted. The linear aileron reversal dynamic pressure was q_∞=41.4 psi compared to q_∞=29.5 psi for the nonlinear. The dynamic pressure for aileron reversal based on linear aerodynamics is 40 percent higher than the value derived using nonlinear aerodynamics. The nonlinear dynamic pressure is lower due to the strong shock on the wing outboard lower surface. The 40 mode nonlinear aileron reversal study predicted a reversal dynamic pressure of q_∞=5.7 psi.

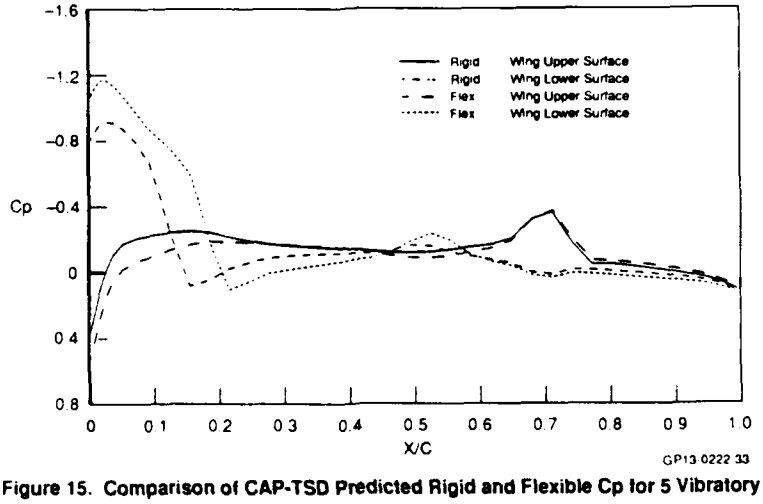


Figure 15. Comparison of CAP-TSD Predicted Rigid and Flexible Cp for 5 Vibratory Modes, $M_\infty = 0.9$, $\alpha = 0.44$, $\beta = 2°$ and $q_\infty = 30$ at Semi Span = 97%

THIS DOCUMENT PROVIDED BY THE ABBOTT AEROSPACE
TECHNICAL LIBRARY
ABBOTTAEROSPACE.COM

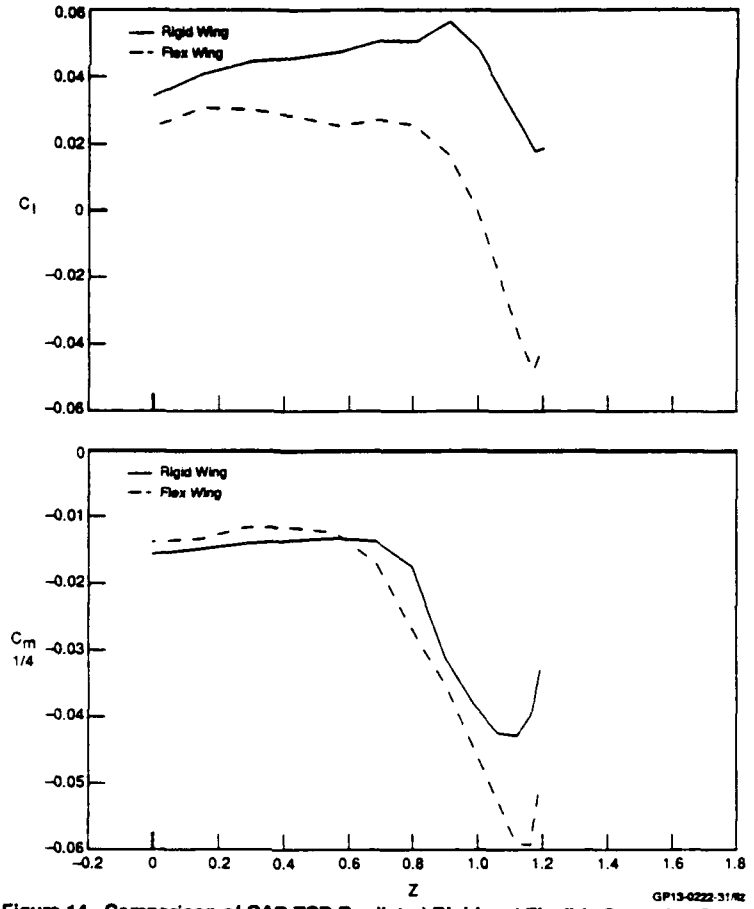


Figure 14. Comparison of CAP-TSD Predicted Rigid and Flexible Spanwise C_l and $C_{m\ 1/4}$ for 5 Vibratory Modes, $M_\infty = 0.9$, $\alpha = 0.44$, $\beta = 2°$ and $q_\infty = 30$

The local pressures at the wing tip are compared in Figure 15. A leading edge shock is seen on the lower surface for both the rigid and reversed case. However, the reversed case results in a much larger shock at a slightly more aft location, and there appears to be a second lower surface shock at x/c=25 percent for the flexible case.

A linear 5 mode aileron reversal study was also conducted. The linear aileron reversal dynamic pressure was q_∞=41.4 psi compared to q_∞=29.5 psi for the nonlinear. The dynamic pressure for aileron reversal based on linear aerodynamics is 40 percent higher than the value derived using nonlinear aerodynamics. The nonlinear dynamic pressure is lower due to the strong shock on the wing outboard lower surface. The 40 mode nonlinear aileron reversal study predicted a reversal dynamic pressure of q_∞=5.7 psi.

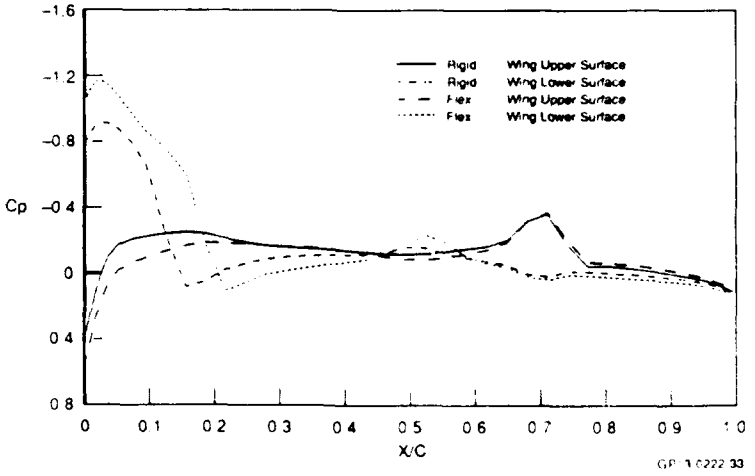


Figure 15. Comparison of CAP-TSD Predicted Rigid and Flexible Cp for 5 Vibratory Modes, $M_\infty = 0.9$, $\alpha = 0.44$, $\beta = 2°$ and $q_\infty = 30$ at Semi Span = 97%

THIS DOCUMENT PROVIDED BY THE ABBOTT AEROSPACE
TECHNICAL LIBRARY
ABBOTTAEROSPACE.COM

The CAP-TSD code was also used to calculate the aileron reversal speed for the F/A-18. The wing, tip missile launcher, tip missile and tip missile fins were included in both the aerodynamic and structural calculations. Static aeroelastic calculations were initially performed based on the first 5 vibratory modes, and later based on 40 vibratory modes. The inclusion of more vibratory modes lowered the aileron reversal speed and gave a reasonable comparison with flight measured values. Aileron reversal dynamic pressure calculations based on nonlinear aerodynamics gave a lower value than the corresponding linear aerodynamic cases. The addition of the tip missile and launcher aerodynamics in CAP-TSD was found to lower the aileron reversal dynamic pressure from the clean wing value.

Accurately predicting both static and dynamic transonic aeroelasticity effects requires nonlinear aerodynamics codes such as CAP-TSD. A sufficiently large number of modes is required for accurate static and dynamic aeroelastic calculations when using theories based on a modal structural approach. The "rigid spline" method of transforming the vibratory modes to the CAP-TSD grid worked well for both the F-15 and F/A-18 analyses. The F/A-18 aeroelastic effects are greatly influenced by the tip missile aerodynamics.

Nonlinear aeroelastic calculations are becoming more routine for complex aircraft such as the F-15 and F/A-18. The CAP-TSD code is no longer a research code, but is an engineering tool for the practicing aeroelastician. The use of well developed pre- and post-processing tools, as described in this paper, greatly reduces the man-hours involved in using the TSD equation for aeroelastic studies.

13. ACKNOWLEDGMENTS

The authors would like to gratefully acknowledge the support of Dr. John Mallone, Head of the Unsteady Aerodynamics Branch at NASA Langley Research Center, for providing the computer resources for this study. The fruitful discussions and thoughts of Dr. John Batina and Michael Gibbons of this same branch are also gratefully acknowledged.

REFERENCES

1. Pitt, D. M., MCAIR LTRAN2 and XTRAN3S Experiences, Presented at the NASA Langley "TRANSONIC UNSTEADY AERODYNAMICS AND AEROELASTICITY WORKSHOP," NASA Langley Research Center, Hampton, VA, Jun 22-23, 1983.

2. Pitt, D. M., CAP-TSD Analysis of the F-15 Aircraft, NASA Conference Publication 3022, Transonic Unsteady Aerodynamics and Aeroelasticity 1987, NASA Langley Research Center, Hampton, VA, May 20-22, 1987.

3. Pitt, D. M., Fuglsang, D. F., Drouin, D. V., Applications of XTRAN3S and CAP-TSD to Fighter Aircraft, AIAA Paper No. 99-1035, presented at the AIAA Structures and Dynamic Materials Conference. Long Beach, CA., Apr 2, 1990.

4. Batina, J. T., Unsteady Transonic Algorithm Improvements for Realistic Aircraft Applications, AIAA Paper No. 88-0105, Presented at the AIAA 26th Aerospace Sciences Meeting, Reno, NV, Jan 11-14, 1988.

5. Batina, J. T., Seidel, D. A., Bland, S. R., and Bennett, R. M., Unsteady Transonic Flow Calculations for Realistic Aircraft Configurations, AIAA Paper No. 87-0850, Presented at the AIAA/ASME/ASCE/AHS 28th Structural Dynamics and Materials Conference, Monterey, CA, Apr 2-4, 1990.

6. MacNeal, R. H., The NASTRAN Theoretical Manual, NASA SP-221(01), Apr 1971.

7. Anderson, R. M., Wind Tunnel Test on the 4.7 Percent Scale F-15 Model in the McDonnell Douglas Polysonic Wind Tunnel, Test PSWT 281 and 286, MDC Report No. A0974, Aug 1971.

8. Robinson, B. A., Batina, J. T., Yang, H. T. Y., Aeroelastic Analysis of Wings Using the Euler Equations With a Deforming Mesh, AIAA Paper No. 99-1032, presented at the AIAA Structures and Dynamic Materials Conference, Long Beach, CA., Apr 2, 1990.

AD-P007 809
THIS DOCUMENT PROVIDED BY THE ABBOTT AEROSPACE
TECHNICAL LIBRARY
ABBOTTAEROSPACE.COM

COMPUTATION OF FLUTTER BOUNDARIES IN THE TIME AND FREQUENCY DOMAIN

H. Zimmermann
S. Vogel
H. Henke
B. Schulze
Deutsche Airbus GmbH
Dept. Aeroelastics
Hünefeldstr. 1-5
D-2800 Bremen 1, FRG

92-16047

SUMMARY

Computations of flutter boundaries in the time and frequency domain are presented using an interactive 3D Transonic Small Perturbation code. Results of conventional flutter calculations in the frequency domain are opposed to those of flutter simulations integrating the aerodynamic and structural equations of motion simultaneously in the time domain.
The paper first highlights the basic properties of these two approaches and then presents results for a six and a two degrees-of-freedom model. A comparison of generalized airloads determined by harmonic and pulse excitation is presented additionally.

1 INTRODUCTION

In the transonic region flutter calculations based on linear unsteady aerodynamic theories such as Doublet Lattice may lead to nonconservative flutter results because of a phenomenon generally described as transonic dip. This is mainly important for aircraft equipped with supercritically profiled wings.

In order to improve the prediction of flutter in the transonic regime nonlinear unsteady aerodynamic codes have been developed during the last 15 years which are based on Transonic Small Perturbation- (TSP), Full-Potential-, Euler-and Navier-Stokes equations and their time-linearized approximations.

The application of these codes showed that the inviscid methods lead to predictions of insufficient accuracy for wings used on modern commercial aircraft. Therefore boundary layer methods have to be incorporated into inviscid flow solvers.

The flutter computations presented in this paper have been performed by such an interactive method. A 3D-TSP code is coupled with an unsteady integral boundary layer method in a stripwise fashion.

The paper first describes the interactive TSP method. Then fundamentals of the aeroelastic analysis in the time and frequency domain are discussed, and results of flutter computations for the AMP-wing (Aeroelastic Model Program) are presented.[1,2]

Emphasis is focussed on following topics:

- the comparison of time and frequency domain flutter results
- the comparison of frequency domain airloads calculated by harmonic and pulse excitation
- the evaluation of time histories by a curve fitting procedure
- the influence of the excitation on the time histories during a flutter simulation
- the estimation of the computation time for the different approaches.

2 INTERACTIVE TSP METHOD

In this section, a short description of the computational method for solving the aerodynamic equations are given. More details of this method are published in Ref. 3. Results of calculations will be given in comparison to experimental data of the AMP wing.

The inviscid transonic flow is described by the 3D TSP (*Transonic Small Perturbation*) equation. A computer code developed by ONERA[4] and based on the classical TSP equation was modified by introducing additional cross-flow terms.[5] These become important for treating swept shocks in the transonic flow regime. The numerical method for solving the TSP equation is the Alternating Direction Implicit (ADI) method.[6] The additional cross derivatives, which have been introduced, are not implemented fully implicitly, and therefore might result in a restriction of the computational time step. Special attention was focussed on numerical treatment of sonic and shock points. The Engquist-Osher switch was introduced, which gives stable and monotone solutions in transonic flow regions.[3]

In transonic flows viscous effects become significant and need to be modeled within the potential flow method. Because integral boundary layer methods are sufficiently accurate for many purposes and yield viscous displacements comparable to those evaluated by the more elaborate finite-difference field method, an integral boundary layer method was chosen for the present calculations. For the time being, a 2D boundary layer method was coupled stripwise with the potential method.
The integral boundary layer method used includes the dissipation integral closure assumption. Such a method, with a suitably chosen velocity profile family, is applicable to attached as well as separated flow regions. The budget equations for momentum and kinetic energy includes unsteady operators. The boundary layer equations are valid for laminar, transitional and turbulent flows. The corresponding closure assumptions used were those of Ref. 7. The integral boundary layer method can be used in direct or inverse computational mode.

The semi-inverse method for coupling boundary layer and potential flow is widely used for treating weak to moderate interaction. In the case of strong interaction, however, this method does not always yield converged solutions. In order to avoid this problem, a different approach was used, involving the simultaneous solution of the governing equations for inviscid and viscous flow [3]. At each streamwise station, the viscous displacement is incorporated into the normal z-sweep of the ADI technique. Thereby both the viscous and inviscid boundary conditions are implicitly accounted for and, are solved as part of the solution. This computationally strong interaction

THIS DOCUMENT PROVIDED BY THE ABBOTT AEROSPACE
TECHNICAL LIBRARY
ABBOTTAEROSPACE.COM

approach reflects the close physical interdependence of viscous and inviscid flow regions. Time accuracy of coupling is achieved by repeating the z-sweeps at a given time instant, closely following Ref. 9.

The recently developed 3D interaction method was extensively tested and validated by comparing it with experimental data.[8] The main emphases of the present wing calculations is focussed on comparisons with the experimental data of the AMP wing, in which transonic experiments were performed in considerable detail.[10] Transonic flow about the AMP wing was computed for Ma=0.78, α=2.84° and Re=3*10^6. In Fig. 1 calculated pressure distributions are compared with the experimental data at the section y/s=0.66. The figure shows the influence of the viscous displacement on the pressure distribution, which noticeable changes the shock position and strength. The upstream shift of the shock position was nearly 15 percent due to the boundary layer displacement. The interactive solution agrees fairly well with the measured data. In Fig. 2 a more detailed look at the time-dependent behaviour of the pressure at a number of selected locations is given for a pitch motion. The pressures show a typically harmonic variation outside the shock region. The foot of the shock, however, is followed by a slight reexpansion, and both produce higher harmonics in the oscillation.

3 AEROELASTIC EQUATIONS OF MOTION

In the flutter calculation the displacement of the aircraft structure is represented by a set of N natural modes.

$$h(x,y,t) = \sum_{i=1}^{N} \varphi_i(x,y) \cdot q_i(t) \qquad (1)$$

In matrix formulation, the final structural equation of motion then reads:

$$\mathbf{M} \cdot \ddot{\mathbf{q}}(t) + \mathbf{C} \cdot \dot{\mathbf{q}}(t) + \mathbf{K} \cdot \mathbf{q}(t) = \mathbf{A}(\mathbf{q}, \dot{\mathbf{q}}) \qquad (2)$$

where M, K and C denote the matrices of generalized masses, stiffnesses and dampings respectively and q denotes the vector of generalized coordinates. The right hand side of equation (2) is the vector of generalized aerodynamic forces A. The components of A are calculated by integrating the unsteady pressure difference Δc_p due to the actual movement of the lifting surface, weighted with the eigenmode φ_i :

$$A_i(q,\dot{q}) = \frac{1}{2}\varrho V^2 \int\int_S \varphi_i(x,y) \cdot \Delta C_p(x,y;h,\dot{h})\, dx\, dy \qquad (3)$$

In the classical flutter calculation method the unsteady airloads are calculated for pure harmonic motion $q(t) = \bar{q}\, e^{i\omega t}$, although the amplitude of motion is either decaying or growing. Therefore those flutter results are strictly valid only in the flutter point where pure harmonic motions occur.

If superposition of modes is admitted so that the generalized airloads may be expressed in terms of the generalized coordinates, i.e.
$A(q,\dot{q}) \Rightarrow \bar{A}(k)\, \bar{q}\, e^{i\omega t}$, equation (2) can be transformed into the frequency domain:

$$[\, \lambda \cdot \mathbf{M} + \mathbf{K}\,(1+ig) - \bar{\mathbf{A}}(k)\,]\, \bar{\mathbf{q}} = 0 \qquad (4)$$

with the assumption for the structural damping $\omega C = Kg$ and the introduction of $\lambda = -\omega^2$. The reduced frequency parameter is defined as $k = \omega C_{ref}/V$.

4 FLUTTER CALCULATION

In Equation (4) the flutter equation is transformed into a *nonlinear eigenvalue problem*. The implicit dependence of the airloads on the eigenvalue allows only an iterative solution.

This eigenvalue problem is determined by the number of degrees of freedom N, given by the number of natural vibration modes taken into account, and by the reduced frequency range, determined by the flight speed and eigenfrequency range of the modes. The solution process of the eigenvalue problem requires that the airloads have to be calculated for a sufficient large number M of reduced frequencies to get the airloads precisely interpolated in the defined frequency range for each natural mode. Then the eigenvalue problem can be solved e.g. by a pk-method.[7] The results are shown as modal frequency and damping versus flight speed.

With this representation of the results not only the flutter speed is indicated, but the entire frequency and damping behaviour of all degrees of freedom is given for a wide flight range. Aeroelasticians are used to think and work in this manner, and the flight vibration tests are adapted to it.

In principle this flutter solution method can be used in the transonic region with nonlinear airloads with the following prerequisites:

- superposition of modes is admitted
- the airload dependence on motion amplitude is negligible
- the higher harmonics of the airloads do not influence the flutter result significantly.

The first harmonic does not depend very much on the amplitude in our experience. In the first approximation the higher harmonics do not change the result because the higher harmonics of the airloads do not do any work in the first harmonic of motion.

A conventional flutter calculation requires the performance of a number of NxM computations of unsteady airloads. For every natural mode the airloads have to be calculated at M reduced frequencies, which requires a lot of CPU time.
The number of calculations can be reduced by using the pulse transfer technique.

Pulse Transfer Function Technique

The pulse transfer function technique is an alternative method for determining generalized airloads in classical flutter calculations. Instead of the usual harmonic excitation an exponentially shaped pulse motion is applied to each vibration mode.

The time histories of excitation and airload are Fourier transformed and the resulting transfer function yields the generalized airload in the frequency domain.

The main advantage of this procedure is that a wide range of reduced frequencies can be covered in a single calculation run.

THIS DOCUMENT PROVIDED BY THE ABBOTT AEROSPACE
TECHNICAL LIBRARY
ABBOTTAEROSPACE.COM

The calculation time using the pulse technique seems to be of the same order as for two reduced frequencies of a harmonic motion because accuracy problems require a grid about twice as fine in the z-direction for the pulse technique than for the harmonic calculation.

5 FLUTTER SIMULATION

Most of the methods for determining transonic airloads, with the exception of the time linearized ones, are time marching procedures, integrating from one time step to the next. The solution of the time domain flutter equation (2) by a similar procedure, i.e. simultaneous integration of the aerodynamic equation and the structural equation of motion takes into account

- the higher harmonics of the airloads
- the influence of decaying and growing amplitudes on the aerodynamics.

while in conventional flutter calculations the airloads have to be computed for each vibration mode separately, the flutter simulation takes account of the actual deformation of all modes involved. Such a time domain flutter procedure reduces the amount of aerodynamic calculations and so the CPU-time for a flutter computation.

The flutter equation (2) is solved by the method of Newmark.[7] With a constant-average-acceleration scheme the velocities and displacements at the end of a time interval can be written as:

$$\dot{\mathbf{q}}^{n+1} = \dot{\mathbf{q}}^n + [(1-\beta)\,\ddot{\mathbf{q}}^n + \beta\,\ddot{\mathbf{q}}^{n+1}]\,\Delta t$$
$$\mathbf{q}^{n+1} = \mathbf{q}^n + \dot{\mathbf{q}}^n \Delta t + \left[\left(\frac{1}{2}-\alpha\right)\ddot{\mathbf{q}}^n + \alpha\,\ddot{\mathbf{q}}^{n+1}\right]\Delta t^2 \qquad (5)$$

Newmark originally proposed an unconditionally stable scheme with $\alpha=1/4$ and $\beta=1/2$. With Eq. (5) the displacements, velocities and accelerations at the time step n+1 for the equation of motion (2) result in the algorithm

$$\mathbf{q}^{n+1} = [a_0\,\mathbf{M} + a_1\,\mathbf{C} + \mathbf{K}]^{-1} [\,A^{n+1} + \mathbf{M}(\,a_0\mathbf{q}^n + a_2\dot{\mathbf{q}}^n + a_3\ddot{\mathbf{q}}^n\,) + \mathbf{C}(\,a_1\mathbf{q}^n + a_4\dot{\mathbf{q}}^n + a_5\ddot{\mathbf{q}}^n\,)]$$

$$\dot{\mathbf{q}}^{n+1} = \dot{\mathbf{q}}^n + a_6\,\ddot{\mathbf{q}}^n + a_7\,\ddot{\mathbf{q}}^{n+1} \qquad (6)$$

$$\mathbf{q}^{n+1} = a_0\,(\mathbf{q}^{n+1} - \mathbf{q}^n) - a_2\,\mathbf{q}^n - a_3\,\mathbf{q}^n$$

The integration constants a_i depend on α, β and Δt.
Since the aerodynamic forces A^{n+1} are still unknown when solving equation (6), they are replaced by the forces A^n at time level n. This phase shift of one time step does not change the time response significantly. Fully time accurate calculations require time constant iterations.

Curve fitting procedure

The solution of equation (6) leads to decaying, growing or beat oscillations of the type:

$$q(t) = const + \sum_{i=1}^{N} e^{-\delta_i t}\,[\,a_i \cos\omega_i t + b_i \sin\omega_i t\,] \qquad (7)$$

given at a finite number of time steps. The frequency and damping are estimated by fitting the calculated time response to the function (7). A least squares curve fitting procedure is employed in combination with an optimization algorithm.[8] The damping parameter D which is given in comparison to flutter calculation results is defined as:

$$D = \delta / \sqrt{\delta^2 + \omega^2} \qquad (8)$$

6 RESULTS

Flutter investigations were carried out for the AMP wing.[9] Fig. 3 shows the measured natural modes of the flutter model.

First the typical procedure of the flutter simulation will be shown taking into account all six degrees of freedom (DOF's) while further investigations will be restricted to the first two modes which mainly determine the flutter behaviour.

A flutter calculation was performed with Doublet Lattice airloads. The flutter simulation was performed for two pressures in the vicinity of the critical flutter pressure predicted with Doublet Lattice airloads. The bending mode was excited with the frequency of the critical mode as predicted by the Doublet Lattice flutter calculation. Therefore the time histories in Fig. 4 show mainly single frequency responses in the first two modes, whereas the other modes are superimposed by several frequencies.

Fig. 5 shows the result of the curve fitting of the third mode. It is mainly superimposed by four natural modes of the flutter model.

These curve fitting results are marked in Fig. 6 which shows the result of the flutter calculation performed in the frequency domain with Doublet Lattice airloads. Instead of the velocity the stagnation pressure is varied. The frequencies of the degrees of freedom of the flutter simulation are in good agreement with the frequencies of the flutter calculation. For the damping values discrepancies are present.

That is the procedure in which flutter simulation can supplement flutter calculation with linear airloads.

For the aeroelastic coupling mechanism may be characterized as a classical bending-torsion flutter the following investigations are restricted to the first two modes.

Fig. 7 shows generalized airloads calculated for harmonic motion compared with the airloads calculated for pulse motion. Index 1 denotes the fundamental bending mode, and index 2 denotes the fundamental torsion mode of the model. The two results agree well.

The choice of the excitation has a large influence on the time histories of the flutter simulation results. In order to avoid coupled transients of all investigated modes, the system is excited with the flutter vector and frequency determined in a previous flutter calculation, e.g. with Doublet Lattice airloads. In this way the time histories mainly reflect the development of the flutter mode while transients of all other modes are almost completely suppressed.

THIS DOCUMENT PROVIDED BY THE ABBOTT AEROSPACE
TECHNICAL LIBRARY
ABBOTTAEROSPACE.COM

Fig. 8 shows the flutter responses for various excitations. Only a suitable excitation choice leads to a response type, which can be properly evaluated for frequency and damping when only a few periods of the function have been calculated. A correspondingly small CPU-time can be achieved only if not more than three to five periods have to be calculated for such an evaluation.

In Fig. 9 flutter calculation and flutter simulation results are compared which both use TSP airloads. Even in the subcritical region both the frequency and the damping values are in good agreement.

Fig. 10 shows the transonic dip calculated with the same degrees of freedom of the flutter model as in Fig. 9. The flutter results calculated in the frequency domain show the dip more pronounced than the flutter simulation results. The flutter boundary based on airloads calculated with the time-linearized TSP equation is shifted a little to smaller stagnation pressures. This effect reflects the discrepancies between the generalized airloads calculated with interactive TSP and time-linearized TSP.[14,15]

Computation time

Fig. 11 shows the computation time for the various flutter calculation methods, which is dominated by the computation time of the unsteady airloads. While the CPU-time for the flutter calculation in the frequency domain increases linearly with the number of modes, the CPU-time for the flutter simulation is determined largely by a skilful choice of the excitation. In any case the flutter calculation in the frequency domain based on harmonic airloads leads to the largest computation times.

The calculation amount using the pulse technique is assumed to be of the same order as for two reduced frequencies of a harmonic motion. Nevertheless the pulse technique saves considerably more CPU-time than the harmonic calculation.

7 CONCLUSIONS

- Flutter calculations with Doublet Lattice airloads cover the whole frequency-velocity range, and cannot at this time be replaced by those with nonlinear airloads for industrial applications. In the critical transonic speed and frequency range, however, supplementary flutter calculations applying nonlinear aerodynamics are necessary.

- For such a task the "flutter simulation method" is well suited, and the CPU-time necessary for performance is acceptable.

- The flutter simulation method overcomes the shortcomings in the representation of the airloads for flutter calculation in the frequency domain, such as neglecting higher harmonics, and the validity of the airloads for growing and decaying motion.

- The examples shown, however, give no indication of significant influence of either higher harmonics or a precise representation of the growing and decaying motion on the flutter behaviour. Also, in the tests chosen, the flutter simulation results do not significantly deviate from those of the pk-method.

- If and where the higher harmonics play a more practical role in flutter is a subject for future investigation.

- Methods for the evaluation of the time histories of flutter simulations should be further developed.

REFERENCES

1. Zingel, H.; "Measurement of Steady and Unsteady Airloads on a Stiffness Scaled Model of a Modern Transport Aircraft Wing". International Forum on Aeroelasticity and Structural Dynamics, Aachen 1991, DGLR-Report 91-069.

2. Zingel, H., Jajes, U., Vogel, S. "Aeroelastisches Modellprogramm - Windkanalversuche zur Unter stützung von Flatterrechnungen für moderne Verkehrsflugzeuge". Deutsche Airbus DA/BRE/91-111, Bremen, 1991.

3. Henke, H.H., Müller, U.R., Schulze, B., "A Viscous-Inviscid Interaction Method for Use in Transonic Flutter Analysis", in "International Forum on Aeroelasticity and Structural Dynamics", Aachen, FRG, 1991

4. Mulak, P., Meurzec, J.P., Angelini, J.J., "Extension and Use of a Numerical Procedure for Three Dimensional Unsteady Transonic Flows", DGLR-Report 85-02, p. 62-70 Second International Symposium on Aeroelasticity and Structural Dynamics, 1985, Aachen, FRG

5. Borland, C.J., Rizetta, D.P., Yoshihara, H., "Numerical Solution of Three-Dimensional Unsteady Transonic Flow over Swept Wings", AIAA Journal Vol. 20, No. 3, pp. 340-347, 1982

6. Engquist, B.,, Osher, S., "Stable and Entropy Satisfying Approximations for Transonic Flow Calculations", Mathematics of Computations, Vol. 34, No. 149, pp. 45-75

7. Drela, M. and Giles, M.B., "Viscous-Inviscid Analysis of Transonic and Low Reynolds Number Airfoils", AIAA Journal, Vol. 25, pp. 1347-1355, 1987.

8. Houwing, R. and Veldman, A.E., "Steady and Unsteady Separated Flow Computations for Transonic Airfoils", AIAA-84-1618, 1984

9. Girodroux-Lavigne, P. and LeBalleur, J.C., "Time Consistent Computation of Transonic Buffet over Airfoils", ICAS-88-5.5.2, 1988.

10. Vogel, S., "Ein Beitrag zur Lösung der Flattergleichung unter Berücksichtigung von Servosteuerung und Flugregler", ZFW Band 1, Heft 2, 1977.

11. Seidel, D.A, Bennett, R.M., and Whitlow, W. Jr., "An Exploratory Study of Finite-Difference Grids for Transonic Unsteady Aerodynamics", AIAA Paper, 83-0503, Jan. 1983

12. Bathe, K.-J., "Finite Element Procedures in Engineering Analysis", Prentice-Hall, Inc. Englewood Cliffs, New Jersey 07632, 1982

13. Jacob, H.G., "Rechnergestützte Optimierung statischer und dynamischer Systeme", Springer Verlag, Berlin, Heidelberg, New York, 1982

THIS DOCUMENT PROVIDED BY THE ABBOTT AEROSPACE
TECHNICAL LIBRARY
ABBOTTAEROSPACE.COM

14. Voss, R., "Calculation of 3-D Unsteady Transonic Potential Flows by a Field Panel Method". Second International Symposium on Aeroelasticity and Structural Dynamics, Aachen 1985, DGLR-Bericht 85-02, pp. 33-46

15. Schulze, B., Vogel, S., "Comparison of Two Potential Flow Methods for Transonic Flutter Analysis", European Forum on Aeroelasticity and Structural Dynamics 1989, Aachen 1989, FRG, DGLR-Bericht 89-01, pp. 43-48.

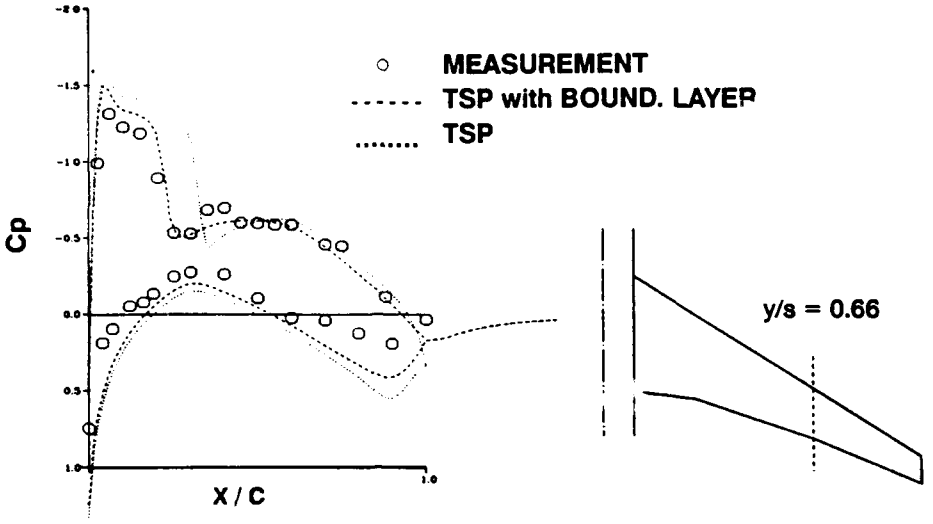


Fig. 1: Steady pressure distribution and planform of AMP wing $M=0.78, \alpha=2.84^{\circ}$, $Re=3.0 \cdot 10^{6}$, $y/s=0.66$

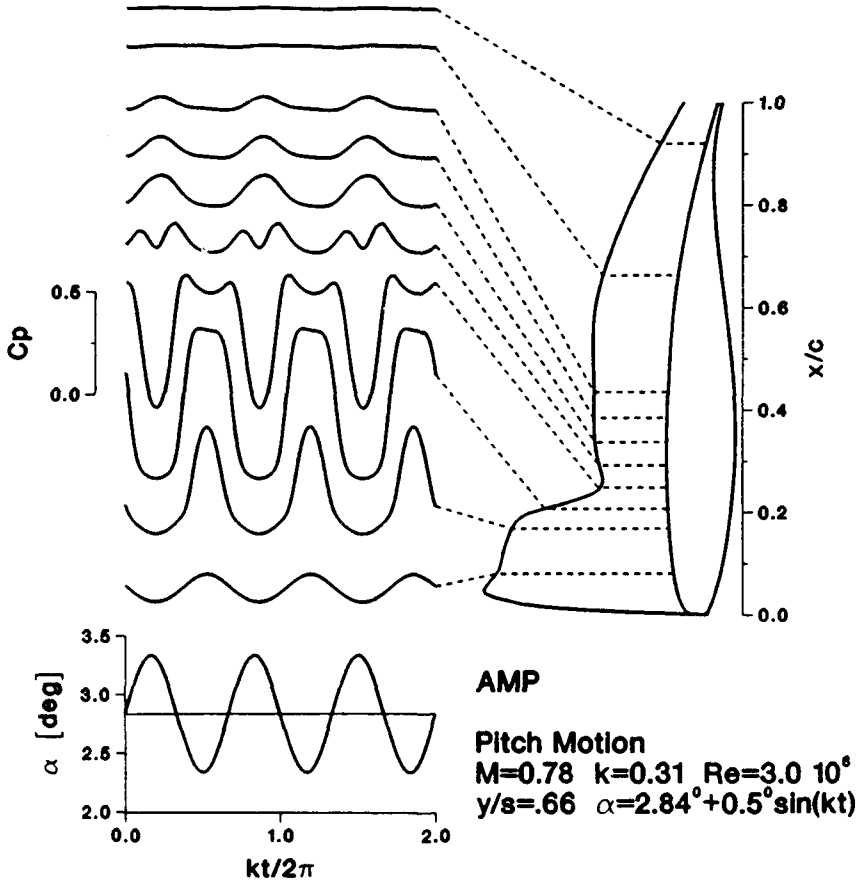


Fig. 2: Time histories of upper surface pressure coefficients

THIS DOCUMENT PROVIDED BY THE ABBOTT AEROSPACE
TECHNICAL LIBRARY
ABBOTTAEROSPACE.COM

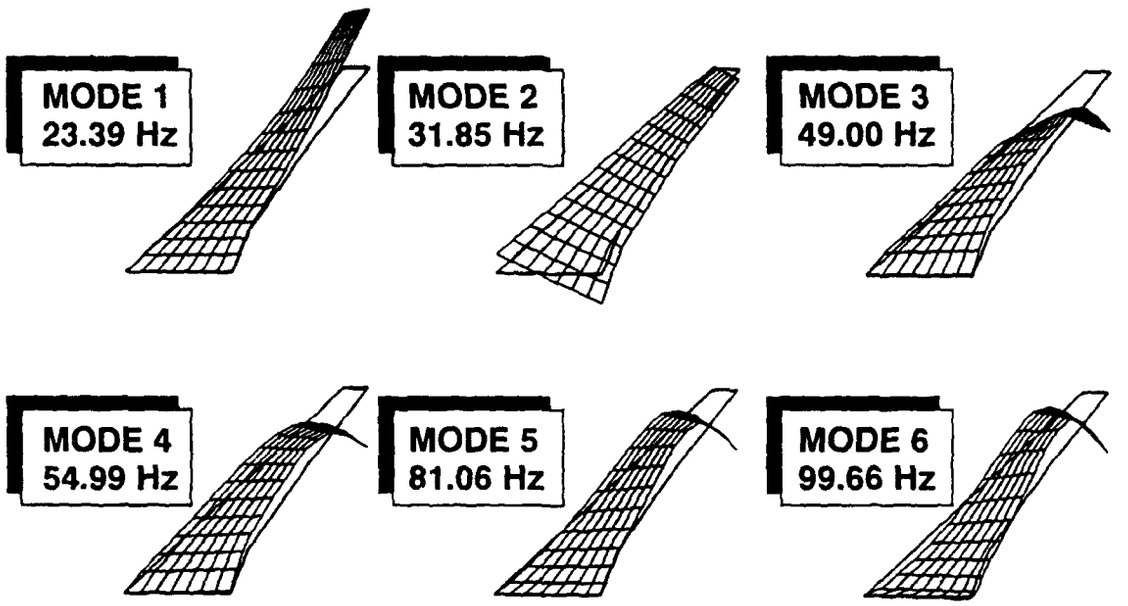


Fig. 3: Natural mode shapes of the AMP wing

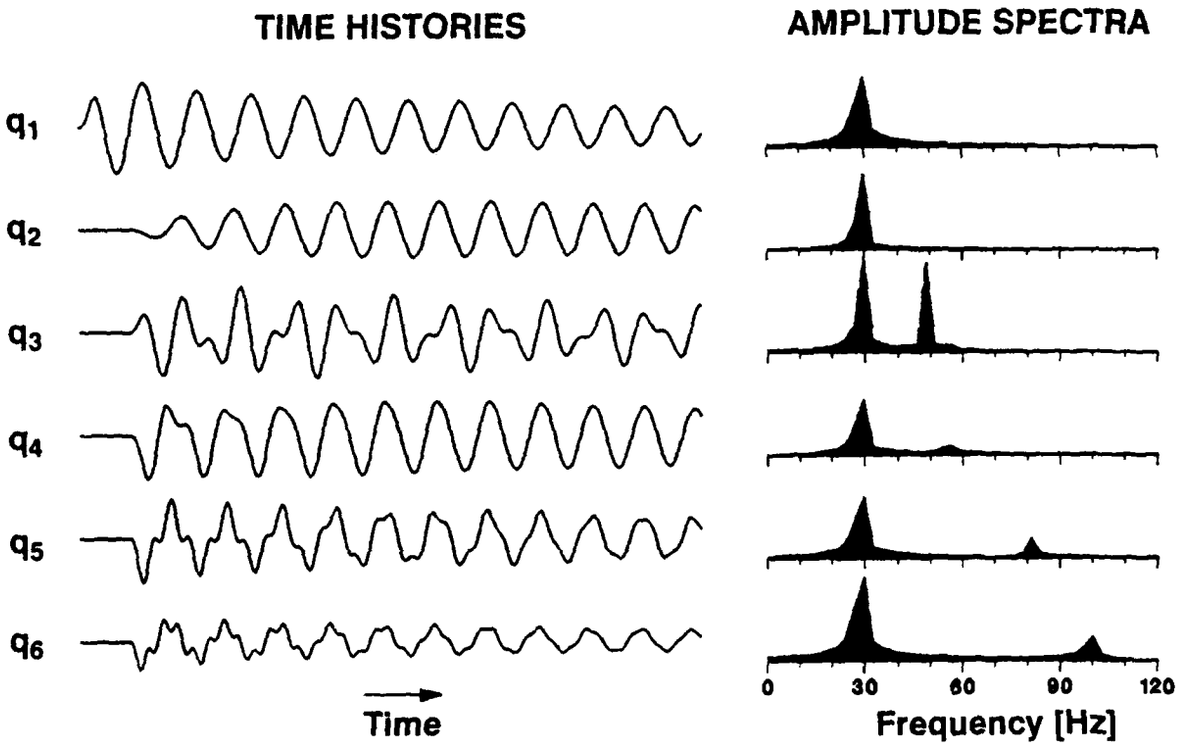


Fig. 4: Flutter simulation with 6 DOF's, AMP, $M = 0.78, \alpha = 2.84^{\circ}$, $Re = 3.0 \cdot 10^6$, $p_t = 1.1$ bar

THIS DOCUMENT PROVIDED BY THE ABBOTT AEROSPACE
TECHNICAL LIBRARY
ABBOTTAEROSPACE.COM

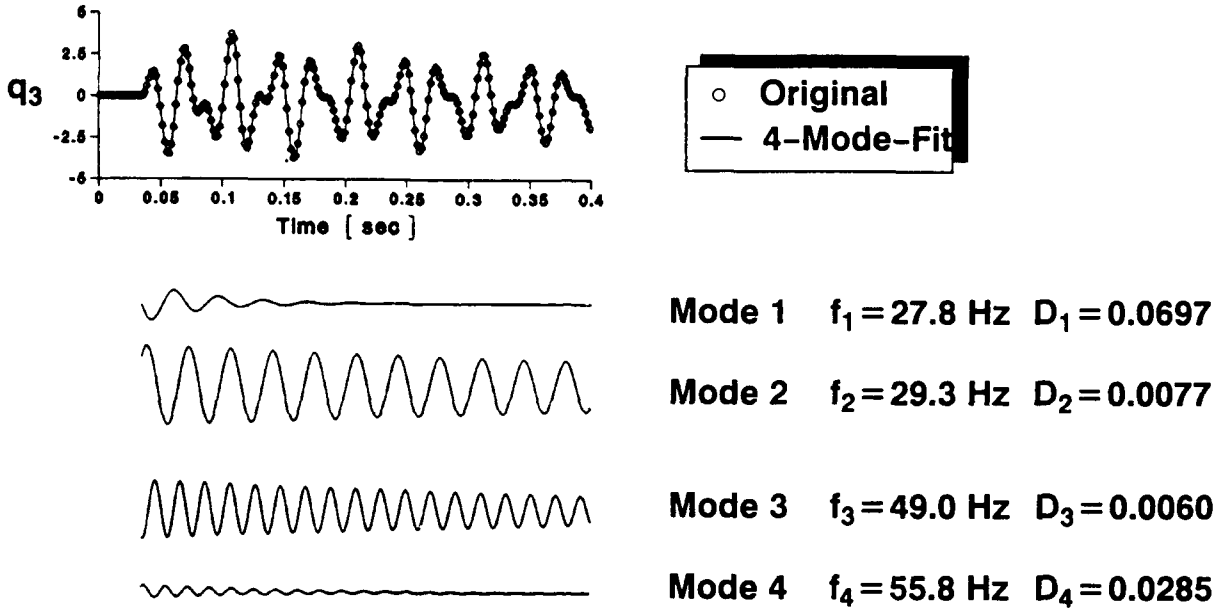


Fig. 5: Curve fitting result of coordinate q_3
6 DOF's, AMP, M = 0.78, $\alpha = 2.84^{\circ}$, Re = $3.0 \cdot 10^6$, p_t = 1.1 bar

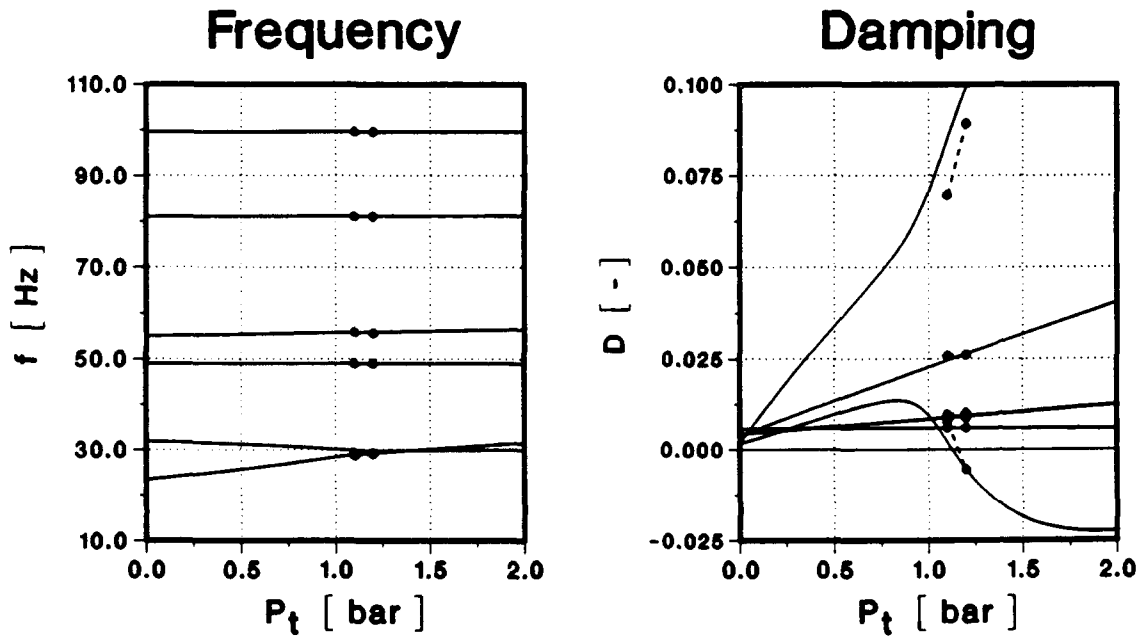


Fig. 6: Flutter results with 6 DOF's
AMP, M = 0.78, $\alpha = 2.84^{\circ}$, Re = $3.0 \cdot 10^6$
• TSP-Simulation
—Doublet Lattice

THIS DOCUMENT PROVIDED BY THE ABBOTT AEROSPACE
TECHNICAL LIBRARY
ABBOTTAEROSPACE.COM

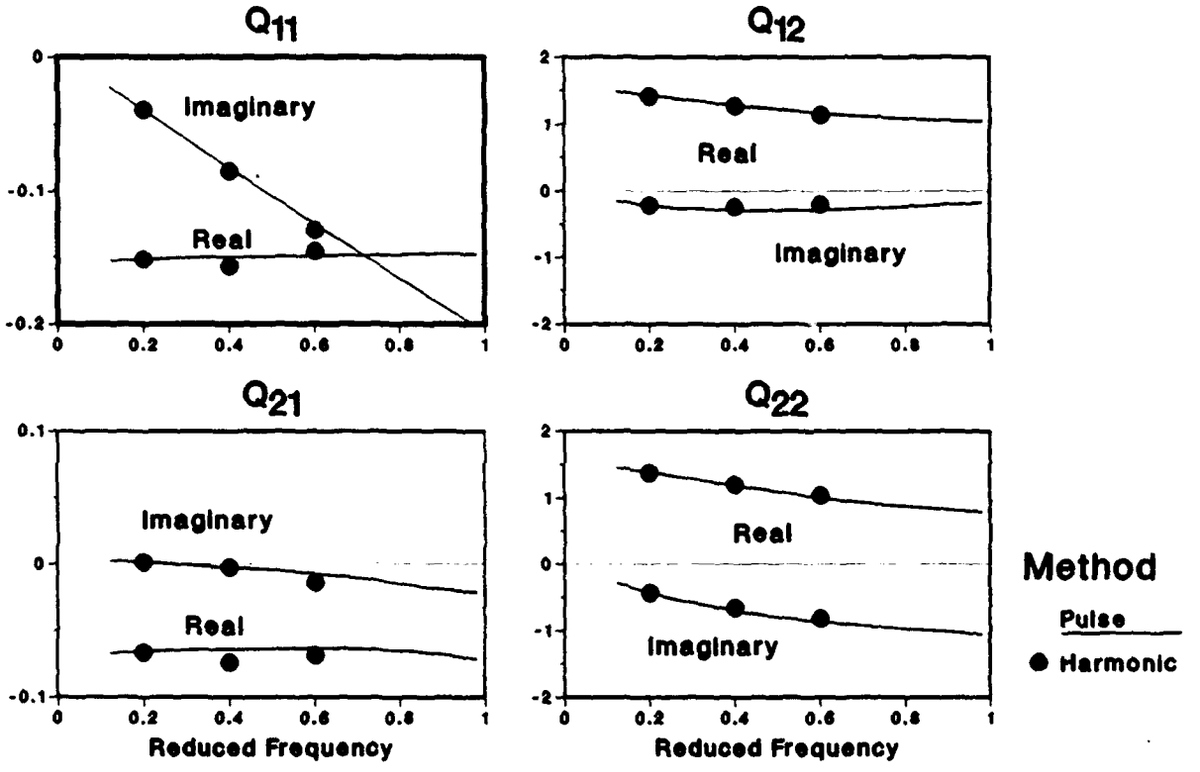


Fig. 7: Comparison of generalized aerodynamic forces
2 DOF's, AMP, M = 0.78, $\alpha = 2.84^{o}$, Re = $3.0 \cdot 10^{6}$

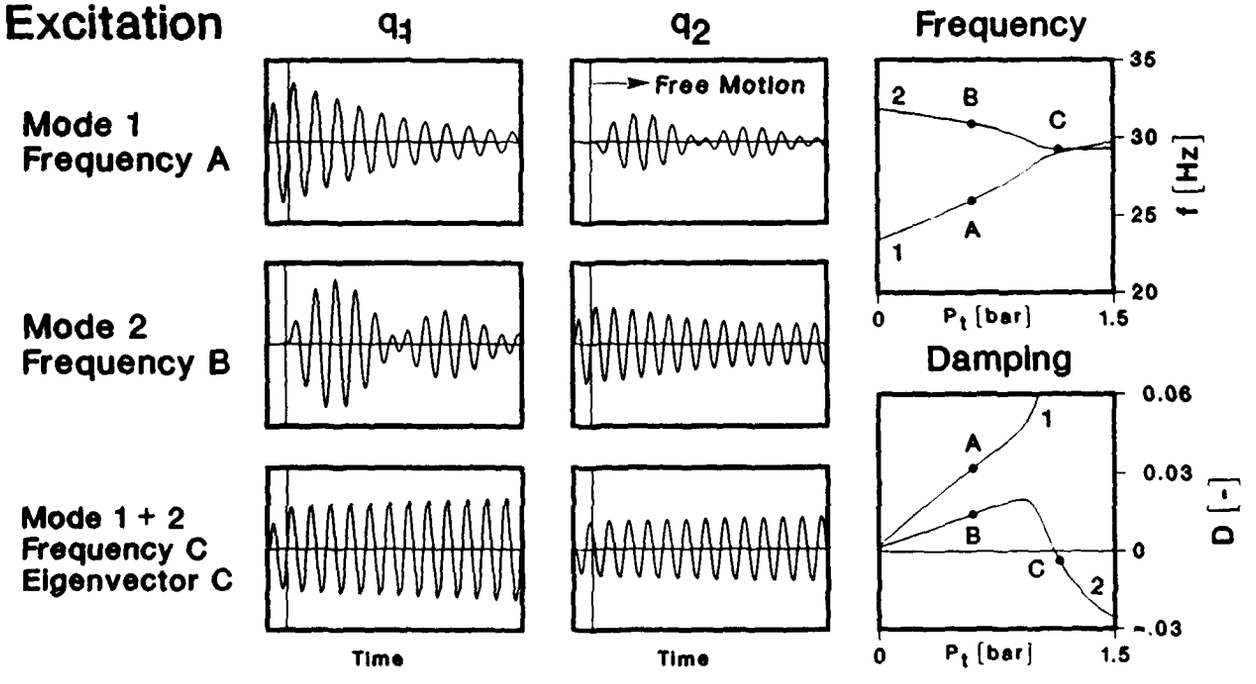


Fig. 8: Influence of excitation on time histories
2 DOF's, AMP, M = 0.78, $\alpha = 2.84^{o}$, Re = $3.0 \cdot 10^{6}$

THIS DOCUMENT PROVIDED BY THE ABBOTT AEROSPACE
TECHNICAL LIBRARY
ABBOTTAEROSPACE.COM

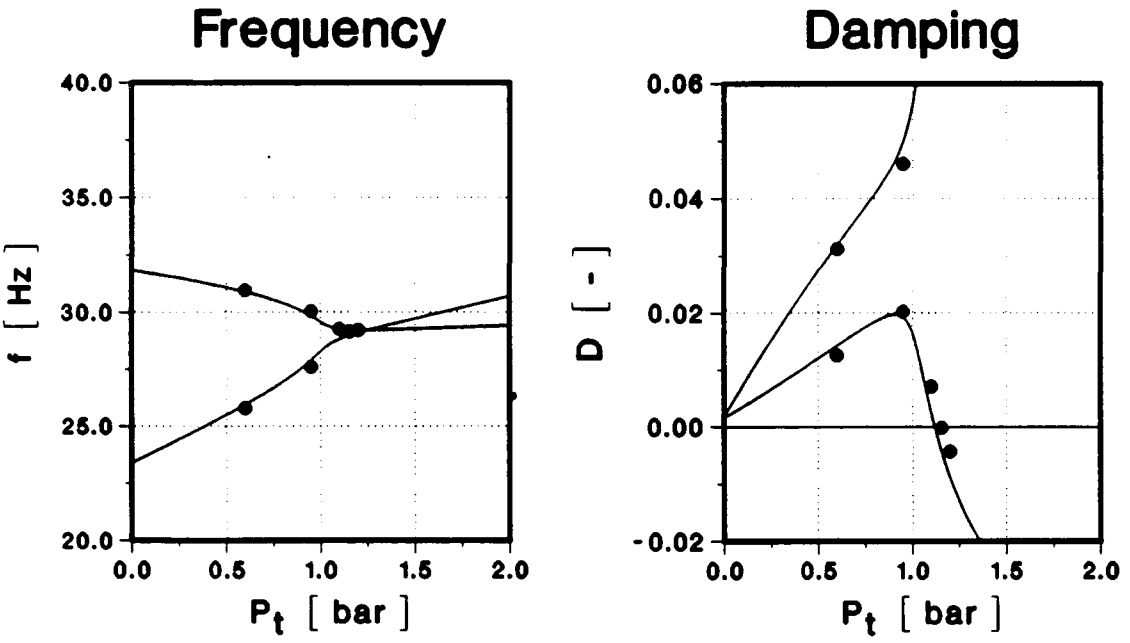


Fig. 9: Comparison of flutter calculation with flutter simulation
2 DOF's, AMP, M = 0.78, α = 2.84°, Re = 3.0·10^6
• TSP–Simulation
——TSP–Harmonic

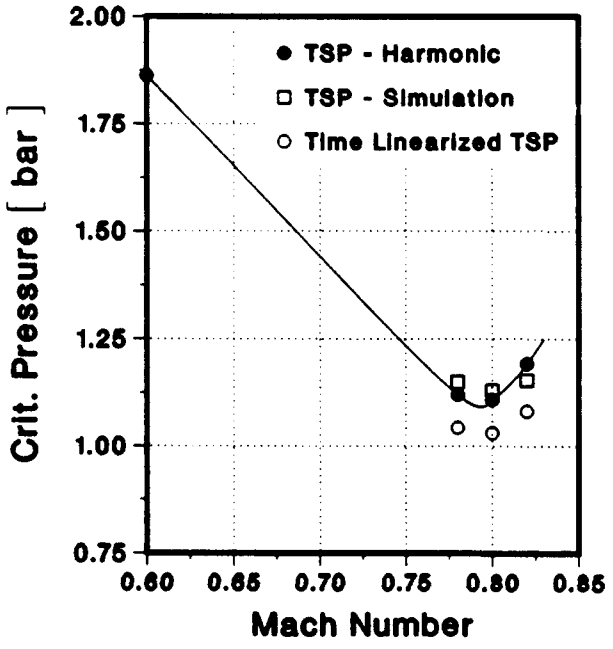


Fig.10: Calculated flutter boundary
AMP, 2 DOF's

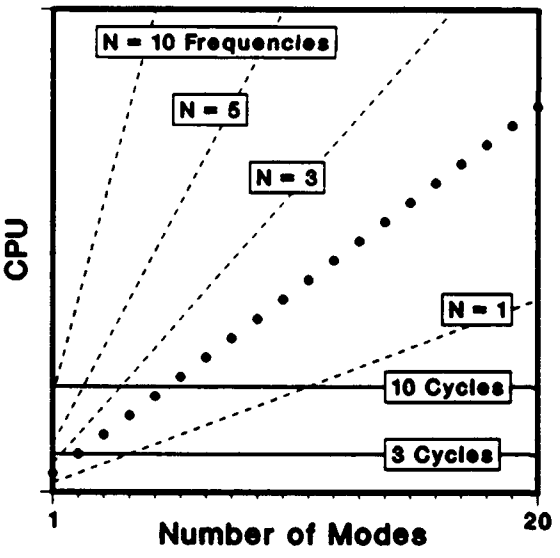


Fig.11: Computation time
per flutter point
----- Harmonic Exitation
• Pulse Exitation
——Simulation

THIS DOCUMENT PROVIDED BY THE ABBOTT AEROSPACE
TECHNICAL LIBRARY
ABBOTTAEROSPACE.COM

AD-P007 810

Analysis of Unsteady Aerodynamic and Flutter Characteristics of an Aeroelastic Model in Transonic Flow

G. SenGupta, C. J. Borland, F. T. Johnson, J. E. Bussoletti,
R. G. Melvin, D. P. Young, M. B. Bieterman, P. A. Palotas

P.O. Box 3707, M.S. 7H-91
The Boeing Company
Seattle, Wa. 98124, USA

Summary

Prediction of unsteady pressure distributions is an important step towards analyzing the flutter characteristics of an airplane. For this purpose, the TRANAIR code (Ref. [1], [2]), originally developed for predicting steady transonic flow past bodies of complex geometry, was extended to handle unsteady problems, in which the unsteady solution could be viewed as a harmonic perturbation to the steady transonic flow. The predicted unsteady flow effects were compared with linear solutions for subsonic flow problems. The predicted results were also compared with available experimental data on unsteady pressure distributions on an oscillating wing in transonic flow. In all these cases, excellent agreements were obtained. The unsteady TRANAIR code and a structural finite element code were then used to analyze the flutter characteristics of a three dimensional wing model. The predicted flutter speeds and frequencies including nonlinear flow effects were significantly different than those predicted by linear analysis. Further analyses including the effects of nacelles and fuselage bodies are in progress.

1 Introduction

Prediction of unsteady pressure distributions is an important step toward analyzing the aeroelastic response of an airplane. Past methods for predicting the unsteady aerodynamic characteristics were based either on linearized theory (Ref. [3]) or on small disturbance transonic flow theory (Ref. [4], [5]). Recently, we have completed development of an unsteady version of the TRANAIR code, which includes all steady nonlinear flow effects (in the context of the full potential theory) and then develops the unsteady solution as a harmonic perturbation to that steady flow. In this report, we present comparisons of the predicted results with available theoretical solutions, and experimental data. We also show the results of using the unsteady TRANAIR code and a structural finite element code to analyze the flutter characteristics of an aeroelastic model in transonic flow.

[1] Presented at the AGARD Specialists' Meeting on *Transonic Unsteady Aerodynamics and Aeroelasticity*, in San Diego, Ca., 9-11 October, 1991

2 Theory

The TRANAIR method is based on the observation that the equations for potential fluid flow may be derived from a variational principle. The Bateman Variational Principle provides a basis for a finite element discretization of the Euler equations. In essence it provides an equivalence between Euler equations and the minimization of the integral J:

$$J = \int_t \int_D p \, dD \, dt \tag{1}$$

Here D is the space domain, and p is pressure and is a function of total enthalpy, H, entropy, S, and velocity $\vec{V}$ of magnitude q.

Assuming an ideal gas, the pressure p and density ρ can be expressed as

$$p = A(S)\left[\frac{(\gamma-1)}{\gamma A(S)}(H - \frac{1}{2}q^2)\right]^{\gamma/(\gamma-1)} \tag{2}$$

$$\rho = \left[\frac{(\gamma-1)}{\gamma A(S)}(H - \frac{1}{2}q^2)\right]^{1/(\gamma-1)} \tag{3}$$

$$A(S) = A_0 e^{(S-S_0)/c_v} \tag{4}$$

With S, H, and $\vec{V}$ as independent variables, this

92-16048

Original contains color plates: All DTIC reproductions will be in black and white

THIS DOCUMENT PROVIDED BY THE ABBOTT AEROSPACE
TECHNICAL LIBRARY
ABBOTTAEROSPACE.COM

means:

$$\delta J = \int_t \int_D \left(\frac{\partial p}{\partial S} \delta S + \frac{\partial p}{\partial H} \delta H + \frac{\partial p}{\partial \vec{V}} \delta \vec{V} \right) dD\, dt \tag{5}$$

For potential flow, we take:

$$\begin{aligned} S &= S_0 \\ H &= H_0 - \Phi_t \\ \vec{V} &= \vec{\nabla}\Phi \end{aligned} \tag{6}$$

From the following differential relationships for pressure p:

$$\begin{aligned} \frac{\partial p}{\partial S} &= -\rho T \\ \frac{\partial p}{\partial H} &= \rho \\ \frac{\partial p}{\partial \vec{V}} &= -\rho \vec{V} \equiv -\vec{W} \end{aligned} \tag{7}$$

and for density ρ:

$$\begin{aligned} \frac{\partial \rho}{\partial S} &= -\rho \\ \frac{\partial \rho}{\partial H} &= \frac{\rho}{c^2} \\ \frac{\partial \rho}{\partial \vec{V}} &= -\frac{\rho}{c^2}\vec{V} \end{aligned} \tag{8}$$

where c is the speed of sound, we have, for flows periodic in time :

$$\delta J = -\int_t \int_D \left(\rho\, \delta\Phi_t + \vec{W} \cdot \delta \vec{V} \right) dD\, dt \tag{9}$$

Integrating by parts,

$$\delta J = \int_t \int_D \left(\rho_t + \vec{\nabla} \cdot \vec{W} \right) \delta\Phi\, dD\, dt - \int_\Sigma \vec{\nu} \cdot \left(\vec{W}, \rho \right) dD\, dt \tag{10}$$

where Σ is a boundary or discontinuity surface with unit normal

$$\vec{\nu} = \frac{(\vec{n}, -a)}{\sqrt{1 + a^2}} \tag{11}$$

Here a is the surface speed. The second equation on the right applies to both sides of Σ in the case of a discontinuity surface. If J is stationary with respect to arbitrary variations in Φ, the first integral on the right of equation (10) yields the mass conservation equation

$$\rho_t + \vec{\nabla} \cdot \vec{W} = 0 \tag{12}$$

The second integral on the right hand side of equation (10) yields conservation laws for discontinuity surfaces. For a shock surface across which Φ is continuous, it follows that

$$\Delta \vec{\nu} \cdot \left(\vec{W}, \rho \right) = 0 \tag{13}$$

where Δ denotes the difference of values on the two sides.

For a slip surface across which Φ may be discontinuous, $\vec{\nu} \cdot \left(\vec{W}, \rho \right)$ must vanish on both sides. The discontinuity in Φ is determined by the additional side constraint

$$\Delta p = 0 \tag{14}$$

For time harmonic unsteady flow all variables are expanded about their steady state values, i.e.

$$\begin{aligned} \Phi &= \Phi_0 + \Re\{\Phi_1 e^{\imath\omega t}\} \\ \rho &= \rho_0 + \Re\{\rho_1 e^{\imath\omega t}\} \end{aligned} \tag{15}$$

Here the subscript 0 denotes steady state values and the subscript 1 denotes the time independent part of the unsteady component (assumed to be small in magnitude).

Expanding the pressure to second order about steady state values results in

$$\begin{aligned} p = {} & p_0 - \vec{W}_0 \cdot (\vec{V} - \vec{V}_0) + \rho_0 (H - H_0) \\ & -(1/2)(\vec{V} - \vec{V}_0) \cdot B_0 \cdot (\vec{V} - \vec{V}_0) \\ & +(1/2)\frac{\rho_0}{c_0^2}(H - H_0)^2 - (H - H_0)\frac{\vec{W}_0}{c_0^2} \cdot (\vec{V} - \vec{V}_0) \end{aligned} \tag{16}$$

where $c_0^2 = \gamma p_0 / \rho_0$ and $B_0 = \rho_0 (I - \vec{V}_0 \vec{V}_0^{\,T} / c_0^2)$, c_0 being the local steady state speed of sound.

Substituting (15) and (16) into (1), integrating over one time period and taking a variation with respect to Φ_1 yields the expression

$$\delta J = \frac{\pi}{\omega} \Re\{ \int_D (-\rho_1 \imath\omega \delta\Phi^* - \vec{W_1} \cdot \delta \vec{V_1}^*) dD \} \tag{17}$$

where * denotes complex conjugate. Here

$$\rho_1 = -\frac{\rho_0}{c_0^2}[\imath\omega\Phi_1 + \vec{V_0} \cdot \vec{V_1}] \quad \text{and} \quad \vec{W_1} = \rho_0 \vec{V_1} + \rho_1 \vec{V_0} \tag{18}$$

Integrating the second term of (17) by parts results in

$$\delta J = \frac{\pi}{\omega} \Re\{ \int_D [\imath\omega\rho_1 + \vec{\nabla} \cdot \vec{W_1}] \delta\Phi^* dD - \int_\Sigma (\vec{W_1} \cdot \vec{n}) \delta\Phi^* d\Sigma \} \tag{19}$$

from which it follows that

$$\imath\omega\rho_1 + \vec{\nabla} \cdot \vec{W_1} = 0 \tag{20}$$

THIS DOCUMENT PROVIDED BY THE ABBOTT AEROSPACE
TECHNICAL LIBRARY
ABBOTTAEROSPACE.COM

in D. This is the standard time harmonic potential equation. It can also serve as an aeroacoustics equation.

Note that in the far field equation (20) reduces to the convected Helmholtz equation

$$\omega^2\Phi_1 - 2\imath\omega V_\infty \Phi_{1x} + \frac{C_\infty^2}{\rho_\infty}\vec{\nabla}\cdot(B_\infty\ \vec{\nabla}\Phi_1) = 0 \quad (21)$$

where

$$B_\infty = \rho_\infty(I - M_\infty^2 \vec{x}\vec{x}^T) \quad (22)$$

By a transformation of variables in x, equation (21) is equivalent to a standard constant coefficient Helmholtz equation.

The natural boundary conditions for (1) may be deduced from (10), i.e. either Φ is specified on Σ or else

$$\vec{\nu}\cdot(\vec{W},\rho) = 0 \quad (23)$$

Other boundary conditions may be imposed by adding boundary integrals to (1). As an example, for the inhomogeneous Neumann condition,

$$\vec{\nu}\cdot(\vec{W},\rho) = h \quad (24)$$

the following modification to J is made:

$$J = J + \int_\Sigma h\Phi d\Sigma \quad (25)$$

For the implicit homogeneous Dirichlet condition,

$$\Phi = g \quad (26)$$

the modification to J is

$$J = J + \int_\Sigma \vec{\nu}\cdot(\vec{W},\rho)(\Phi - g)d\Sigma \quad (27)$$

For a wake or slip surface where μ is specified so that $\Delta p = 0$,

$$\Delta\Phi = \mu\,\Delta\,\vec{\nu}\cdot(\vec{W},\rho) = 0 \quad (28)$$

the modification to J is

$$J = J + \int_\Sigma \alpha[\vec{\nu}\cdot(W,\rho)](\Delta\Phi - \mu)d\Sigma \quad (29)$$

where α denotes the average of values on each side of Σ.

2.1 Steady TRANAIR Operators

In the steady TRANAIR code, the finite element discretization of the mass flux term is approximated by:

$$-\int_D \vec{W}\cdot\delta\vec{V}\,dD \approx \sum_i (R_i + b_i)\,\delta\Phi_i \quad (30)$$

where R_i is defined by

$$R_i = \sum_{jl} \tilde{\rho}_j\,\mathtt{DIV}_{ijl}\,\Phi_l \quad (31)$$

with

$$\tilde{\rho}_j = \sum_k \alpha_{jk}\,\rho_k \quad (32)$$

and $\mathtt{DIV}_{ijl}$ represents the divergence of $\vec{V}$ operators as defined in the steady TRANAIR code and α_{jk} are the coefficients for the upwinded density $\tilde{\rho}_j$ in terms of the appropriate values of ρ_k (Ref. [1], [2]).

In addition,

$$b_i = \sum_j \tilde{\rho}_j\,\vec{\mathtt{D}}_{ij}\cdot\vec{V}_\infty + \sum_{jn} \mathtt{B}_{ijn}\,S_{jn} \quad (33)$$

where $\vec{\mathtt{D}}_{ij}$ are the coefficients of the dependence of the divergence of $\vec{W}$ on the freestream velocity $\vec{V}_\infty$, and $\mathtt{B}_{ijn}$ are the coefficients of dependence of $\vec{W}\cdot\hat{n}$ on other-than-natural boundary conditions, and S_{jn} are the boundary condition values imposed on those corner points (the n index) which lie with in region j.

2.2 Unsteady TRANAIR Operator

From the similarity in the variational principle integral, we can use the steady TRANAIR operator to provide us with a finite element approximation to the $\vec{W}\cdot\delta\vec{V}$ term. To do unsteady or time dependent potential flow modeling we need to provide a finite element discretization of the $\rho\Phi_t$ term in the integral. We choose to approximate the "mass matrix" term by evaluating ρ and $\delta\Phi$ at the centroid of each element, scaled by the volume of the element. Define

$$\Phi|_{D_j} = \sum_i \gamma_{ji}\,\Phi_i \quad (34)$$

is the potential evaluated at the centroid of region D_j, where γ_{ji} are the coefficients used to evaluate the trilinear basis functions at the centroid.

For time harmonic problems, integrating over one time period, we get

$$\int_t\int_D \rho\,\delta\Phi_t\,dD\,dt = \frac{\pi}{\omega}\Re\{\sum_j \rho_j\,\imath\omega\,\delta\Phi|_{D_j}\int_D dD\} \quad (35)$$

Then we have for the finite element discretization of the unsteady problem:

$$-\int_t\int_D \left(\rho\,\delta\Phi_t + \vec{W}\cdot\delta\vec{V}\right)dD\,dt = \frac{\pi}{\omega}\Re\{\sum_i (R_i^U + b_i^U)\,\delta\Phi\} \quad (36)$$

THIS DOCUMENT PROVIDED BY THE ABBOTT AEROSPACE
TECHNICAL LIBRARY
ABBOTTAEROSPACE.COM

where

$$R_i^U = \sum_j \tilde{\rho}_j \, \mathtt{DIV}_{ijl} \, \Phi_l + \iota\omega \, \rho_{\cdot\,\cdot ij} \, D_j \qquad (37)$$

D_j represents the volume of the finite element. If sum of R_i^U and b_i^U vanishes identically, the Bateman variational principle says this is a solution to the full potential flow equation.

2.3 Linearization of Discrete Equations

In steady TRANAIR we solve this system for $\omega = 0$. We solve the nonlinear system by a Newton iteration, successively linearizing R about interim approximations to the solution.

We linearize the operator R_i^U by differentiating with respect to some Φ_m, taking into account the proper dependence of density on the potential through its dependence on velocity and enthalpy. Thus

$$\frac{\partial \rho_j}{\partial \Phi_m} = \left.\frac{\partial \rho}{\partial H}\right|_j \frac{\partial H_j}{\partial \Phi_m} + \left.\frac{\partial \rho}{\partial \vec{V}}\right|_j \cdot \frac{\partial \vec{V}_j}{\partial \Phi_m} \qquad (38)$$

Defining the velocity in an element as

$$\vec{V}_j = \sum_l \vec{\mathcal{J}}_{jl} \, \Phi_l \qquad (39)$$

we have

$$\frac{\partial \rho_j}{\partial \Phi_m} = -\left(\frac{\rho_j}{c_j^2} \gamma_{jm} \frac{\partial}{\partial \Phi_m} \frac{\partial \Phi_m}{\partial t} + \frac{\rho_j}{c_j^2} \vec{V}_j \cdot \vec{\mathcal{J}}_{jm} \right) \qquad (40)$$

As before, we assume that Φ_m has the form of a steady solution plus a time harmonic perturbation

$$\Phi_m = \Phi_{0m} + \Re(\Phi_{1m} e^{\iota\omega t}) \qquad (41)$$

with the time derivatives becoming either zero or a simple factor of $\iota\omega$.

Defining the operator $\mathtt{EDIV}_{ij}$ by:

$$\mathtt{EDIV}_{ij} = \sum_l \mathtt{DIV}_{ijl} \, \Phi_{0l}, \qquad (42)$$

we have the steady Jacobian for linearization about a steady Φ_{0m}:

$$\begin{aligned} \left[\bar{L}_{\Phi_0}\right]_{im} &= \frac{\partial R_i^U}{\partial \Phi_{0m}} \\ &= \sum_{jk} \alpha_{jk} \, \rho_k \, \mathtt{DIV}_{ijm} \\ &\quad - \alpha_{jk} \frac{\rho_k}{c_k^2} \vec{V}_k \cdot \vec{\mathcal{J}}_{km} \, \mathtt{EDIV}_{ij} \end{aligned} \qquad (43)$$

and we have the harmonic Jacobian for linearization about a steady Φ_{0m}:

$$\begin{aligned} \left[L_{\Phi_0}\right]_{im} &= \frac{\partial R_i^U}{\partial \Phi_{1m}} \\ &= \sum_{jk} \alpha_{jk} \, \rho_k \, \mathtt{DIV}_{ijm} \\ &\quad - \alpha_{jk} \frac{\rho_k}{c_k^2} \vec{V}_k \cdot \vec{\mathcal{J}}_{km} \, \mathtt{EDIV}_{ij} \\ &\quad - \iota\omega \frac{\rho_k}{c_k^2} \gamma_{jk} \, \mathtt{EDIV}_{ij} \\ &\quad - \iota\omega \, \alpha_{jk} \, \vec{\mathcal{J}}_{km} \\ &= \sum_k \iota\omega \, \alpha_{jk} \, \rho_k \, D_k \end{aligned} \qquad (44)$$

In the above equation α_{jk} is zero unless $j = k$, in which case it equals 1. The first two terms of this equation are our steady Jacobian (the ones which do not depend on the frequency ω). The terms scaled by the frequency are associated with the unsteady problem. Note that we have neglected the fact that the α_{kj} coefficients depend on the velocity and hence the potential.

Note that although the $\bar{L}$ operators above have been linearized about Φ_0, the linearized operators would have the same functional form if the linearization were imposed about some other solution (e.g., one which has a finite amplitude, multiple harmonic time dependence), as long as the definitions of density and speed of sound were allowed to vary in time with the correct differential thermodynamic relationships. The linearized operator is "easy" to solve only when the coefficients are constant in time. For this reason we only consider linearizations about the steady solution at present.

The far field radiation condition is handled by using a discrete Green's function associated with the convected Helmholtz equation. This permits the computational mesh to be of finite size and quite close to the configuration as it needs only to contain the region where equation (20) differs significantly from equation (21) (Ref. [6]).

There remains the question of how the b_i^U terms enter into the equation. The boundary condition that occurs most commonly is specification of flow tangency on an impermeable surface. For our steady TRANAIR code this is equivalent to the condition:

$$\vec{W} \cdot \hat{n} = 0 \qquad (45)$$

This is the "natural" boundary condition which emerges from the Bateman variational integral. In the case of unsteady flow, this equation requires some modifications.

THIS DOCUMENT PROVIDED BY THE ABBOTT AEROSPACE
TECHNICAL LIBRARY
ABBOTTAEROSPACE.COM

TRANAIR modifies the Bateman integral by adding a variety of extra surface integrals in order to impose various boundary conditions. Examples of these include the $\Delta C_p = 0$ condition on wake surfaces, expressing that the pressure jump across wake surfaces vanishes. Each boundary condition surface integral needs to be examined under the more general harmonic solution conditions. First we consider the natural boundary conditions in this context.

3 Natural Boundary Conditions

A configuration geometry is defined by specifying the coordinates of selected points on the configuration surface in groups called networks. The points in a network are a rectangularly indexed set of **NM** by **NN** points. Each point in the configuration is assumed to be represented by:

$$\vec{P} = \vec{P}_0 + \Re(\vec{P}_1\, e^{\imath\omega t}) \tag{46}$$

This implies that the surface has a local velocity of the form:

$$\vec{V}_S = \Re(\imath\omega\, \vec{P}_1\, e^{\imath\omega t}) \tag{47}$$

Now, the most common boundary condition for an aircraft configuration is the velocity tangency condition (impermeable surface). In steady flow this is usually represented in terms of a zero normal mass flux condition, $\vec{W} \cdot \hat{n} = 0$, where $\vec{W} = \rho\vec{V}$ is the mass flux of the fluid and $\hat{n}$ reperesents the local surface normal. In its more general form (permitting transpiration through the surface), it is given as $\vec{W} \cdot \hat{n} = h$. For the case of a moving surface, this equation should be modified to the form:

$$\rho(\vec{V} - \vec{V}_S) \cdot \hat{n} = h \tag{48}$$

To evaluate this boundary condition in harmonic Unsteady TRANAIR, we need to compute the normal vector on a moving surface (projected onto a harmonic variation) and we need to linearize and project the mass flux terms as well.

3.1 Unit Normal Vector on Moving Surface

A point lying in any two dimensional surface can be parameterized in terms of two variables, say (r, s). Derivatives with respect to these parameters define tangent vectors to the surface. Then a vector normal to the surface at $\vec{P}$ is represented by the cross product of the tangent vectors:

$$\vec{n} = \frac{\partial \vec{P}}{\partial r} \times \frac{\partial \vec{P}}{\partial s} \tag{49}$$

Using the definition of $\vec{P}$ we have:

$$\vec{n} = \left[\frac{\partial \vec{P}_0}{\partial r} + \Re\left(\frac{\partial \vec{P}_1}{\partial r} e^{\imath\omega t}\right)\right] \times \left[\frac{\partial \vec{P}_0}{\partial s} + \Re\left(\frac{\partial \vec{P}_1}{\partial s} e^{\imath\omega t}\right)\right] \tag{50}$$

Expanding the product we have:

$$\begin{aligned} \vec{n} &= \frac{\partial \vec{P}_0}{\partial r} \times \frac{\partial \vec{P}_0}{\partial s} \\ &\quad + \Re\left[\left(\frac{\partial \vec{P}_1}{\partial r} \times \frac{\partial \vec{P}_0}{\partial s} + \frac{\partial \vec{P}_0}{\partial r} \times \frac{\partial \vec{P}_1}{\partial s}\right) e^{\imath\omega t}\right] \\ &\quad + \Re\left[\left(\frac{\partial \vec{P}_1}{\partial r} \times \frac{\partial \vec{P}_1}{\partial s}\right) e^{\imath 2\omega t}\right] \end{aligned} \tag{51}$$

Now define two vectors $\vec{n}_0$ and $\vec{n}_1$ by:

$$\vec{n}_0 = \frac{\partial \vec{P}_0}{\partial r} \times \frac{\partial \vec{P}_0}{\partial s} \tag{52}$$

$$\vec{n}_1 = \frac{\partial \vec{P}_1}{\partial r} \times \frac{\partial \vec{P}_0}{\partial s} + \frac{\partial \vec{P}_0}{\partial r} \times \frac{\partial \vec{P}_1}{\partial s} \tag{53}$$

Then the normal vector is approximately given by:

$$\vec{n} \approx \vec{n}_0 + \Re(\vec{n}_1 e^{\imath\omega t}) \tag{54}$$

assuming that the products of derivatives of $\vec{P}_1$ are sufficiently small that they can be ignored (small displacement assumption).

The unit vector in the $\vec{n}$ direction is obtained by normalizing the vector.

$$\hat{n} = \frac{\vec{n}}{|\vec{n}|} \approx \hat{n}_0 + \Re\left[e^{\imath\omega t}\left(\frac{\vec{n}_1}{|\vec{n}_0|} - \frac{\vec{n}_1 \cdot \hat{n}_0}{|\vec{n}_0|}\hat{n}_0\right)\right] \tag{55}$$

Then if we define the vector $\hat{n}_1$ by

$$\hat{n}_1 = \frac{\vec{n}_1}{|\vec{n}_0|} - \frac{\vec{n}_1 \cdot \hat{n}_0}{|\vec{n}_0|}\hat{n}_0 \tag{56}$$

we can define the (time dependent) unit vector at a surface point as:

$$\hat{n} = \hat{n}_0 + \Re(\hat{n}_1 e^{\imath\omega t}) \tag{57}$$

3.2 Unsteady Mass Flux Boundary Conditions

To evaluate the boundary conditions we first expand the fluid density, mass flux and specified transpiration into steady and harmonic perturbation terms.

$$\begin{aligned} \rho &= \rho_0 + \Re(\rho_1 e^{\imath\omega t}) \\ \vec{V} &= \vec{V}_0 + \Re(\vec{V}_1 e^{\imath\omega t}) \\ h &= h_0 + \Re(h_1 e^{\imath\omega t}) \end{aligned} \tag{58}$$

THIS DOCUMENT PROVIDED BY THE ABBOTT AEROSPACE
TECHNICAL LIBRARY
ABBOTTAEROSPACE.COM

Expanding the $\rho\hat{n}\cdot(\vec{V}-\vec{V}_S)$ product and keeping only the steady and first harmonic terms yields two boundary conditions, one for the steady flow and one for the unsteady perturbation. The steady flow boundary condition is

$$\hat{n}_0\cdot\vec{W}_0=\rho_0\hat{n}_0\cdot\vec{V}_0=h_0 \tag{59}$$

and the unsteady flow boundary condition is

$$\hat{n}_0\cdot\vec{W}_1=h_1+\iota\omega\rho_0\hat{n}_0\cdot\vec{P}_1-\hat{n}_1\cdot\vec{W}_0 \tag{60}$$

where

$$\hat{n}_0\cdot\vec{W}_1=\rho_0\hat{n}_0\cdot\vec{V}_1+\rho_1\hat{n}_0\cdot\vec{V}_0 \tag{61}$$

Under potential flow assumptions,

$$\rho_1=-\frac{\rho_0}{c_0^2}\left(\vec{V}_0\cdot\vec{\nabla}\Phi_1+\iota\omega\Phi_1\right) \tag{62}$$

and the unsteady boundary condition becomes:

$$\rho_0\hat{n}_0\cdot\vec{\nabla}\Phi_1+(\hat{n}_0\cdot\vec{V}_0)\left[-\frac{\rho_0}{c_0^2}\left(\vec{V}_0\cdot\vec{\nabla}\Phi_1+\iota\omega\Phi_1\right)\right]=h_1+\iota\omega\rho_0\hat{n}_0\cdot\vec{P}_1-\hat{n}_1\cdot\vec{W}_0 \tag{63}$$

In most applications, the input to unsteady TRANAIR defines the coordinate perturbations $\vec{P}_1$. From these definitions TRANAIR will compute a vector $\hat{n}_1$ consistent with TRANAIR's definition of the steady surface normal $\hat{n}_0$. The user may also specify a transpiration term h_1.

Under some conditions, the user may want to specify both coordinate perturbations $\vec{P}_1$ and normal perturbations $\hat{n}_1$. Unsteady TRANAIR allows this form of input as well. However in this case, it is the user's responsibility to assure that the specified $\hat{n}_1$ are consistently defined with respect to TRANAIR's definition of the normal vector at each point.

At this point we can define the b_i^U operator:

$$b_i^U=\sum_{jn}\mathbf{B}_{ijn}S_{jn} \tag{64}$$

where S_{jn} is given by

$$S_{jn}=\left(h_1+\iota\omega\rho_0\hat{n}_0\cdot\vec{P}_1-\hat{n}_1\cdot\vec{W}_0\right)|_{jn} \tag{65}$$

where the quantities are to be evaluated at the n-th panel corner point of the panel lying in the j-th region.

The $\mathbf{B}_{ijn}$ operators are linear. Thus they are identical to the $\mathbf{B}_{ijn}$ operators in the steady flow case.

4 Results

4.1 Comparison with Analytical Solutions

For initial verification of the unsteady results, we considered the simplest possible case, i.e., the unsteady pressure distribution on a sphere pulsating radially in a stationary medium. Comparing predicted results with analytical solutions at a given frequency allowed us to check the mass matrix that was being generated by the code and make sure that the boundary conditions on the sphere were being handled correctly.

The next problem considered was scattering of an acoustic plane wave by a sphere, since the analytical solution for this problem is well known (Ref. [8]). Fig. 1 shows the predicted unsteady C_p magnitudes on the surface of the sphere for $ka=\omega a/c=1$, where a is the radius of the sphere and c is the speed of sound in a stationary medium. The maximum and minimum analytical values are also shown in parenthesis. As can be seen, the numerical solutions are very close to the analytical values. To simulate a stationary medium in the TRANAIR code, the free stream velocity was set at .001 m/sec, which explains the unusually large C_p values shown in the figure!

4.2 Comparison With Linear Solutions for Subsonic Flow

A numerical solution for unsteady pressure distribution on an oscillating wing in linear subsonic flow is available in Ref. [3]. The specific configuration considered was a thin wing with a plan form similar to that of the F5 aircraft. In the case of thin lifting surfaces, when the boundary conditions are completely linearized, the steady mean flow consists of the undisturbed free stream. The linear solution presented in Ref. [3] was verified against doublet lattice theory. For this reason, we chose to compare our solution (linearized about the freestream) against the results presented in Ref. [3].

Fig. 2 shows the wing plan form. The wing was assumed to oscillate in pitch about the midpoint of the root chord with a reduced frequency ($k=\omega C_r/2U_\infty=.3577$, where C_r is the root chord length) in uniform flow with a Mach number of 0.6. Fig. 3 shows the grid generated by TRANAIR, and Fig. 4 shows the comparison of the real and imaginary parts of ΔC_p predicted by the two independent codes, where ΔC_p represents the difference between the C_p values on the upper and lower surfaces. As

THIS DOCUMENT PROVIDED BY THE ABBOTT AEROSPACE
TECHNICAL LIBRARY
ABBOTTAEROSPACE.COM

can be seen, an excellent agreement was obtained between the two sets of predictions.

4.3 Validation for Transonic Flow

For validation in the transonic flow regime, we compared the predicted levels against available experimental data. The experimental data available in Ref. [7] was used for this comparison. The details of the experimental program are given in the cited reference, and only the highlights are being summarized here. The aim of the investigation was to determine the unsteady pressure distribution on a fighter type wing in the transonic environment. The model chosen was the F-5 wing. The wing model was made to oscillate in a pitching motion about the center of the root chord axis at model scale frequencies up to 40 Hz. The Mach number ranged from 0.6 and 1.35. In addition to the unsteady pressures, the vibration modes of the model during the unsteady tests were also analyzed. The plan form of the wing along with the locations of the pressure transducers and accelerometers are shown in Figs. 5 and 6.

For comparison purposes, we chose the data at M = .9 with the reduced frequency ($k = \omega C_r/2U_\infty$) ranging from 0.137 to 0.276, and M = .95 with reduced frequencies of 0.132 and 0.264.

4.3.1 Comparison of Steady Pressure Data

Figs. 7a and 7b show the comparisons of the predicted and measured steady C_p on the wing at M = .9.

In general, the predicted results are seen to be in general agreement with the measured data. The data are somewhat overpredicted. One probable reason could be the influence of the tunnel boundary layer, which would be expected to influence the pressure distribution near the root section. On sections near the wing tip (Fig. 7b), the predicted and measured shock characteristics are in better agreement; however, the C_p levels are still somewhat higher. A part of this could be due to the fact that the effects of the wing boundary layer were not simulated in the TRANAIR predictions.

Figs. 8a and 8b show the comparisons of the predicted and measured steady C_p on the wing at M = .95. Once again, the pressure levels are somewhat higher than the measured data, and the differences in the shock characteristics become less pronounced near the wing tip. Fig. 9 shows cuts through the final grid, and comparison of the C_p levels obtained at the earlier level and the final level showed that the differences were not significant. We can therefore conclude that going to an even finer grid would not have brought the predicted levels any closer to the test data. It is planned to revisit this case in order to include the boundary layer simulation capability being incorporated in TRANAIR.

4.3.2 Comparison of Unsteady Pressure Data

Figs. 10a, b, c show the comparisons of the real and imaginary parts of the unsteady pressure at M = .9 and k = .137. The agreement appears to be excellent at all span stations. It is clear that the measured data did not have enough resolution near the shocks. It is interesting to note that the agreement is better for the unsteady pressure distribution than for the steady pressure distribution which tends to confirm the suspicion that a part of the discrepancy for the steady case is due to the lack of boundary layer simulation in our prediction. The boundary layer is expected to reduce the steady pressure levels. However, at frequencies where the acoustic wavelength is large compared to the boundary layer thickness, the unsteady pressures should be relatively unaffected by the presence of the boundary layer.

Figs. 11a, b, c show the comparisons at M = .95 and k = .264, and again trends are similar to the previous case.

5 Combination of Unsteady TRANAIR and a Structural Finite Element Code for Flutter Analysis

The unsteady TRANAIR code was used in conjunction with the ELFINI structural finite element (Ref. [9]) code to do flutter analysis of a three dimensional elastic wing. The *in-vacuo* mode shapes and natural frequencies of the wing were first generated using ELFINI. These mode shapes and frequencies were then input into the unsteady TRANAIR code to calculate the unsteady pressure distributions on the wing model at those frequencies. These unsteady pressure values were then fed into ELFINI to calculate the flutter speeds and frequencies of the wing model, as shown in Fig.12. Initially, the TRANAIR code was used in its linear mode so that the flutter frequencies and speeds predicted in the above manner could be compared with those predicted by using the ELFINI code alone, which carries out a lin-

THIS DOCUMENT PROVIDED BY THE ABBOTT AEROSPACE
TECHNICAL LIBRARY
ABBOTTAEROSPACE.COM

ear aerodynamic analysis based on the doublet lattice theory. After this consistency check, the steady TRANAIR code was used in its nonlinear mode, and the unsteady pressure distributions associated with the above mode shapes and frequencies were calculated and fed into ELFINI. The flutter frequencies and speeds were then re-calculated to determine the effect of the flow nonlinearities. In the particular case we have looked at, the flutter speed predicted by the linear analysis was found to be approximately 40that predicted by the nonlinear analysis. Further analyses including the effects of nacelles and fuselage bodies are in progress.

6 Conclusions

We have developed an unsteady version of the TRANAIR code and compared the predicted results with analytical solutions, numerical solutions and experimental data. In all these cases, excellent agreements were obtained. The TRANAIR method is particularly well-suited for handling steady transonic flow past complex bodies of arbitrary shapes, and the extension for unsteady flow in transonic environment represents attainment of a major goal. We have also used the TRANAIR code in conjunction with the ELFINI structural analysis code to calculate the flutter characteristics of an aeroelastic model in transonic flow with and without the steady nonlinear flow effects. In the particular case we have looked at, nonlinearities seemed to have a significant effect, and further check out for more complex configurations is in progress. It may also be noted that a significant spin-off of this work is in the area of simulation of acoustic scattering problems, and it has already proved useful for simulating problems in submarine acoustics (Ref. [10]).

7 Acknowledgment

The work was funded by the Integrated Airplane Design and Analysis Project which is a part of the Computing Development Program of the Boeing Company, and the cooperation received from Mr. Dave Jack throughout the entire project is gratefully acknowledged.

References

[1] Johnson, F. T., *et al*,"TRANAIR Computer code (Theory Document and Users' Manual)", Final Report, NASA Contract NAS2-12513, November 1989.

[2] Young, D. P., *et al*,"A Locally Refined Rectangular Grid Finite Element Method: Application to Computational Fluid Dynamics and Computational Physics", J. of Computational Physics, Vol. 92, No. 1, January 1991.

[3] Dusto, A. R. and Epton, M. A.,"An Advanced Panel Method for Analysis of Arbitrary Configurations in Unsteady Subsonic Flow", NASA CR-152323, February 1980.

[4] Borland, C. J., "XTRAN3 - Transonic Steady and Unsteady Aerodynamics for Aeroelastic Applications - Vol. 1", AFWAL-TR-85-3124, January, 1986.

[5] Bennet, R. M., Bland, S. R., Batina, J., Gibbons, M. D., Mabey, D. G., "Calculation of Steady and Unsteady Pressures on Wings at Supersonic Speeds with a Transonic Small-Disturbance Code", J. Aircraft, Vol. 28, No. 3, March 1991, pp.175-180

[6] Rubbert, P. E., *et al*,"A New Approach to the solution of Boundary Value Problems Involving Complex configurations", presented in the *Future Directions of Computational Mechanics*, ASME winter Annual Meeting, Anaheim, Ca., December, 1986.

[7] Tijdeman J., et al, "Transonic Wind Tunnel Tests on an Oscillating Wing with External Stores; Part II - The Clean Wing", AFFDL-TR-78-194, Part II, March 1979.

[8] Morse, P. M., "Vibration and Sound", McGraw-Hill Book Co., 1948.

[9] Avions Marcel Dassault-Breguet Aviation, "ELFINI Aeroelasticity General Introduction Manual", Document No. ELF-AER-1, version 6.3, January 1990.

[10] SenGupta, G., Bussoletti, J. E., Johnson, F. T., Melvin, R. G. , Young, D. P., Bieterman, M. B., "Numerical Simulation of Acoustic Scattering from Submarines", Paper presented at the Third IMACS Symposium on Computational Acoustics, Harvard University, Cambridge, Ma., June 26-28, 1991.

THIS DOCUMENT PROVIDED BY THE ABBOTT AEROSPACE
TECHNICAL LIBRARY
ABBOTTAEROSPACE.COM

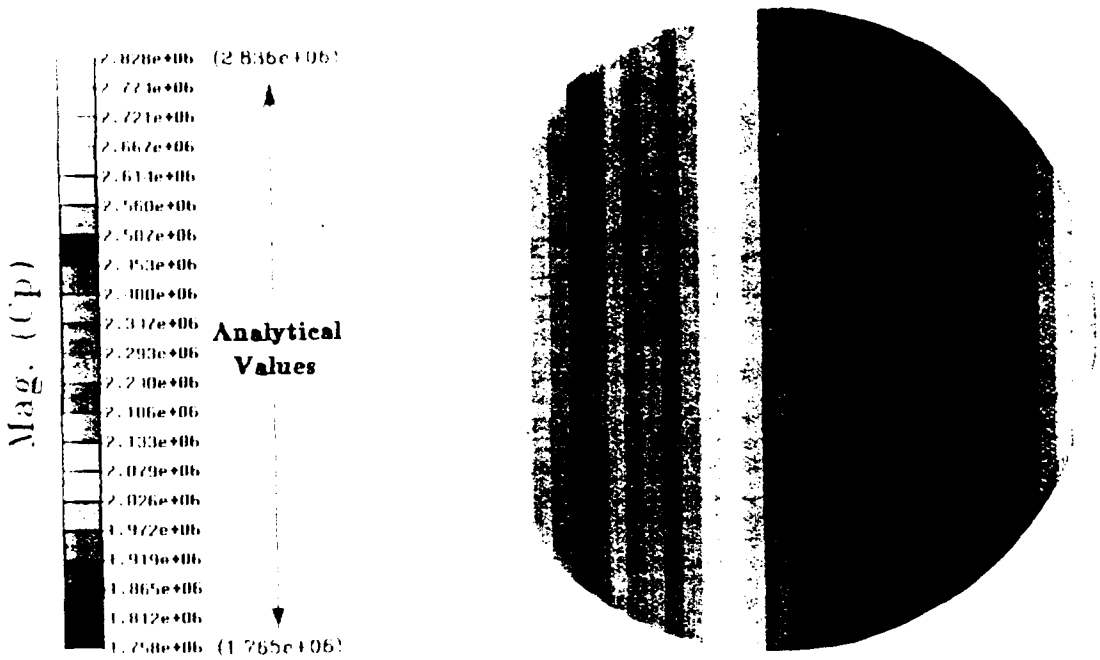


Fig. 1 Scattering of an acoustic plane wave by a sphere (ka = 1, V =.001 m/sec)

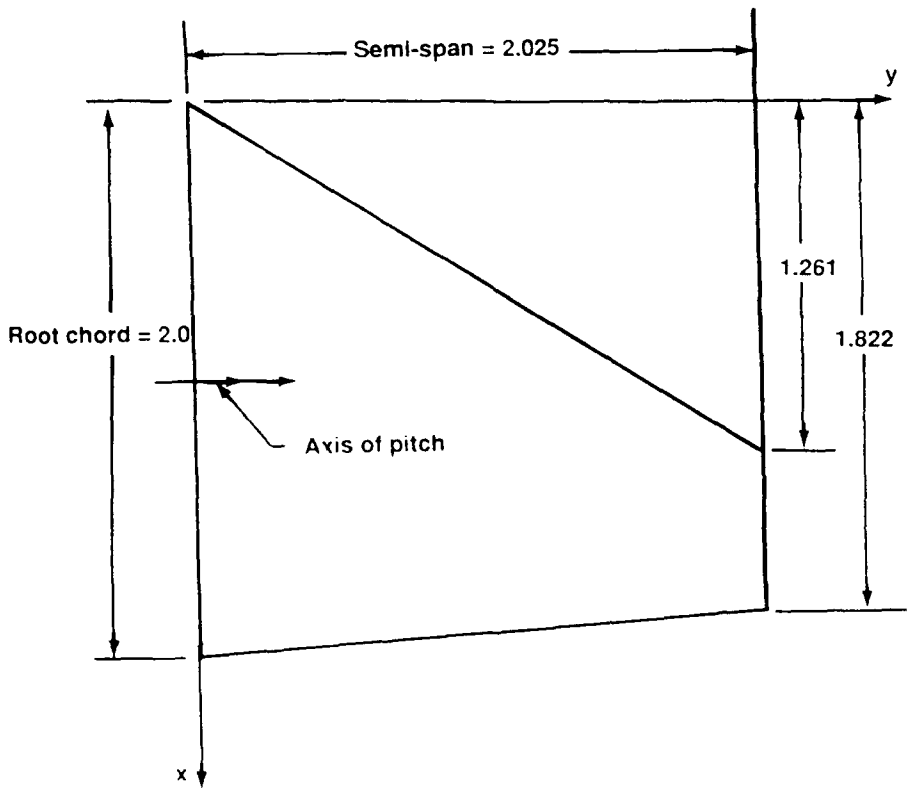


Figure 2. Planform of test wing
(Dimensions in meters)

This Document Provided by the ABBOTT AEROSPACE
TECHNICAL LIBRARY
ABBOTTAEROSPACE.COM

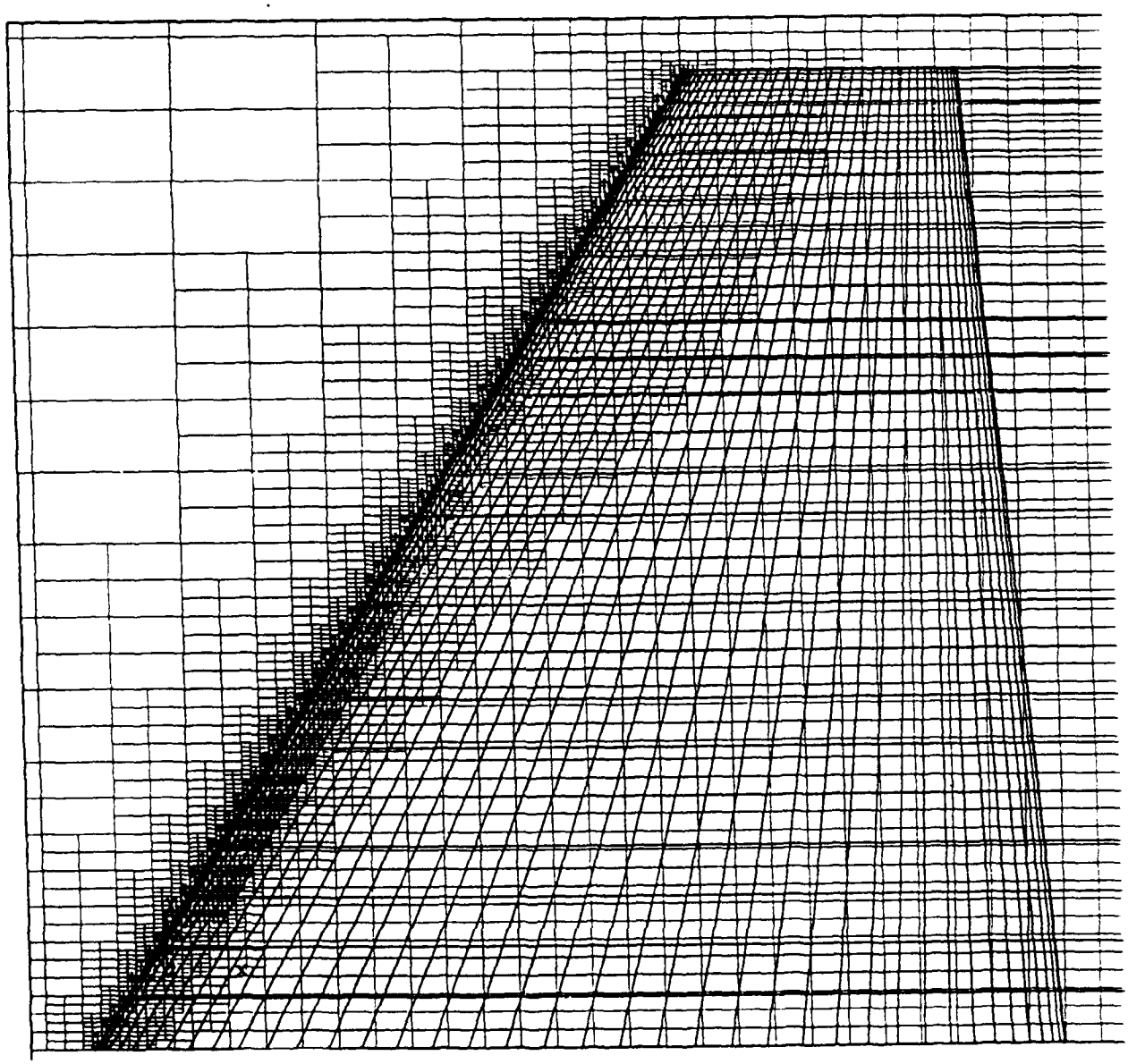


Figure 3. An example of grid refinement in TRANAIR

THIS DOCUMENT PROVIDED BY THE ABBOTT AEROSPACE
TECHNICAL LIBRARY
ABBOTTAEROSPACE.COM

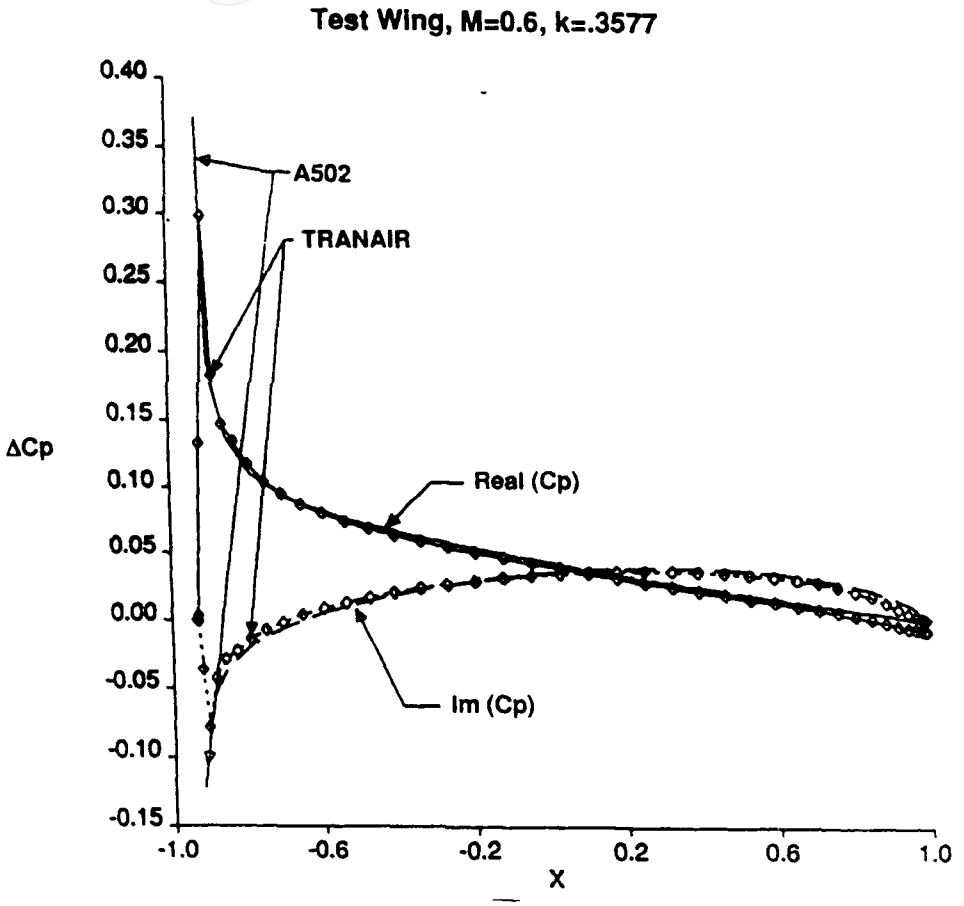


Figure 4. Comparison of unsteady TRANAIR predictions against a linear unsteady code (A502)

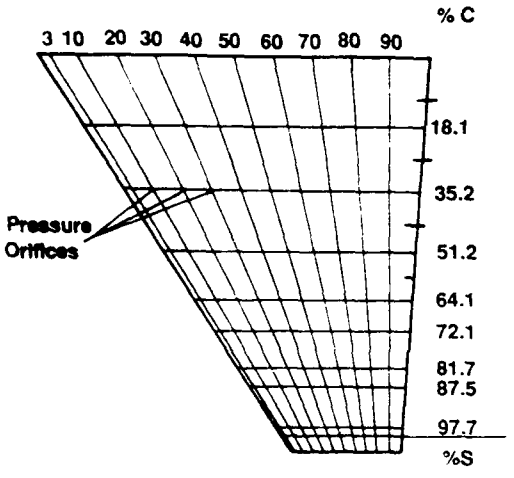


Figure 5. Locations of orifices for pressure measurement (Ref. 7)

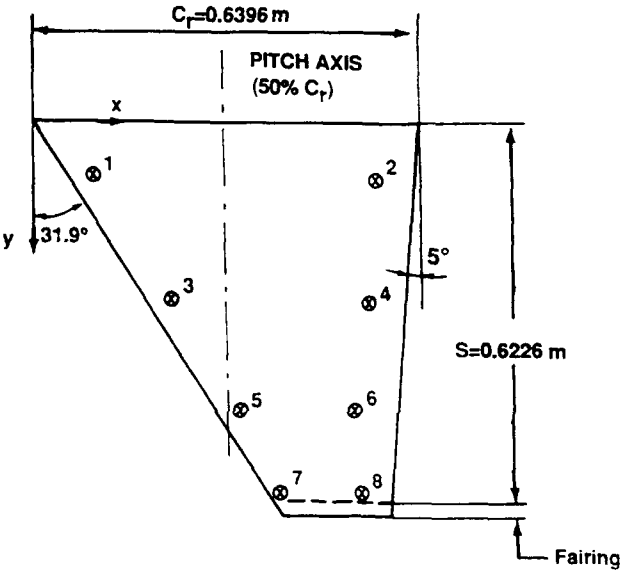


Figure 6. Locations of accelerometers used to determine the mode shapes (Ref. 7)

This Document Provided by the Abbott Aerospace
TECHNICAL LIBRARY
ABBOTTAEROSPACE.COM

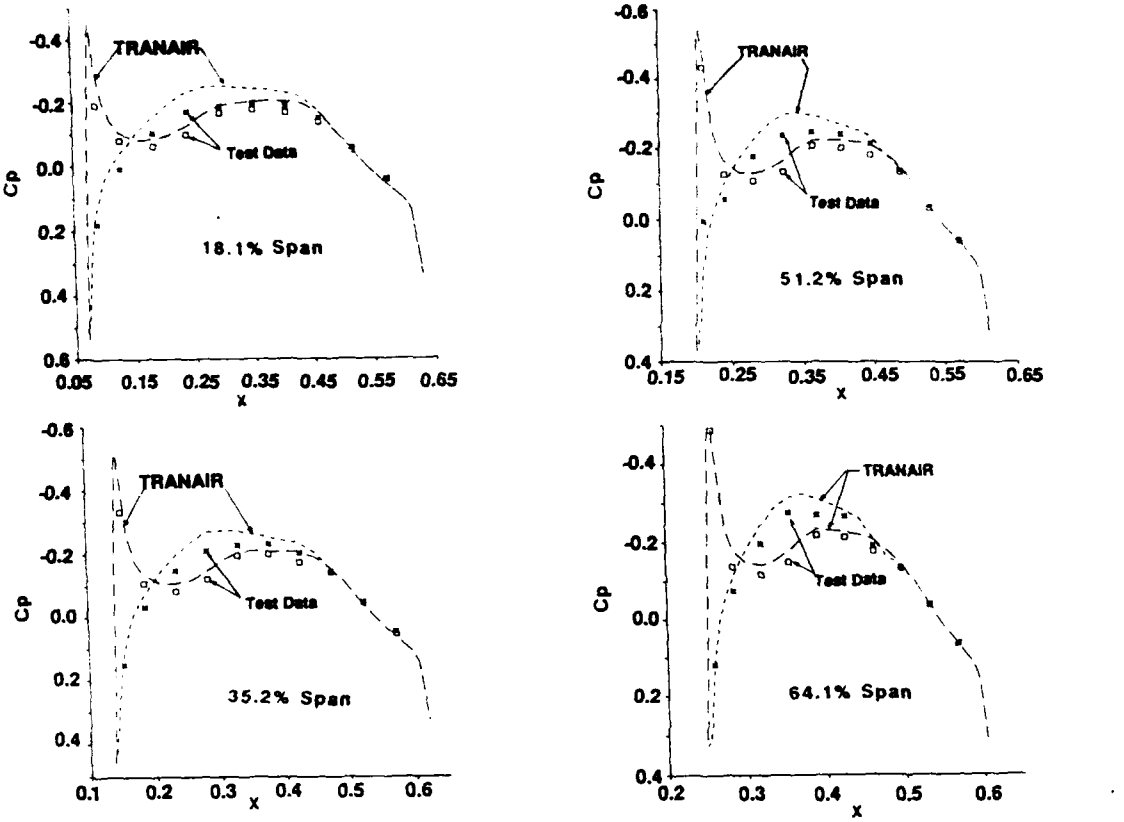


Figure 7a. Comparison of Steady Cp at M=.9, α=0 deg.

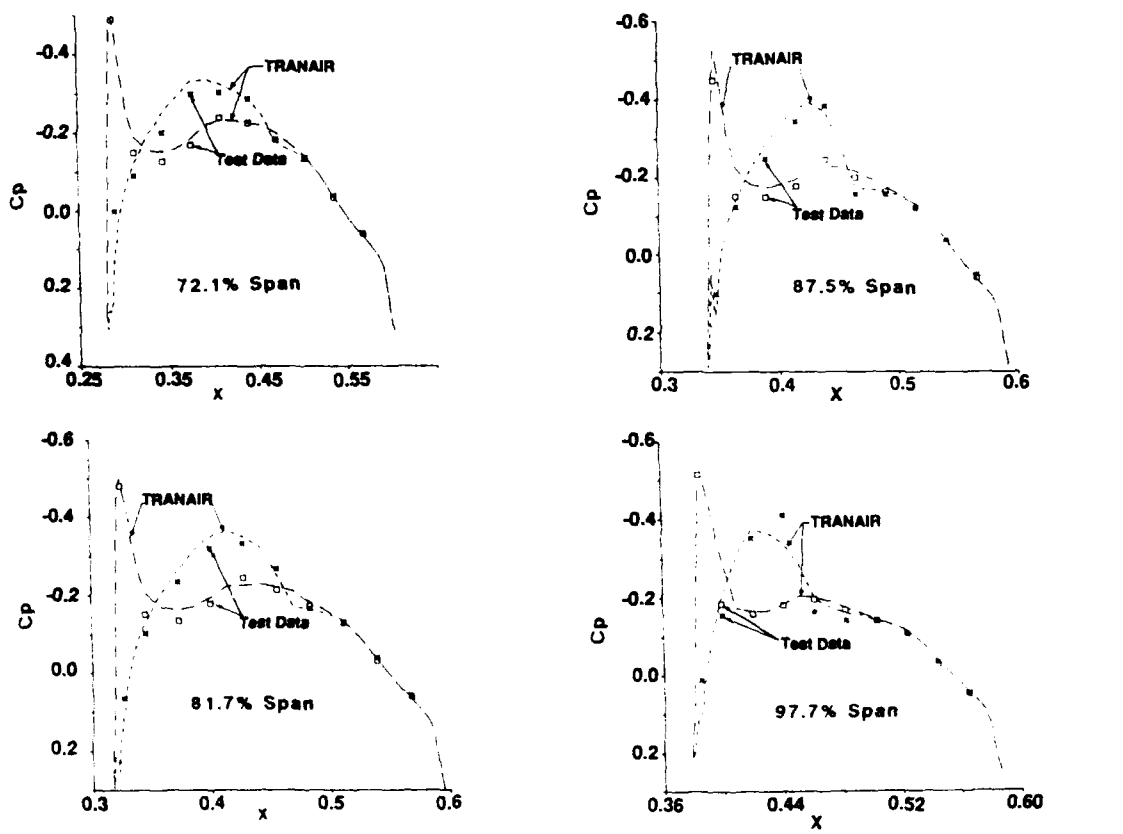


Figure 7b. Comparison of Steady Cp at M=.9, α=0 deg.

THIS DOCUMENT PROVIDED BY THE ABBOTT AEROSPACE
TECHNICAL LIBRARY
ABBOTTAEROSPACE.COM

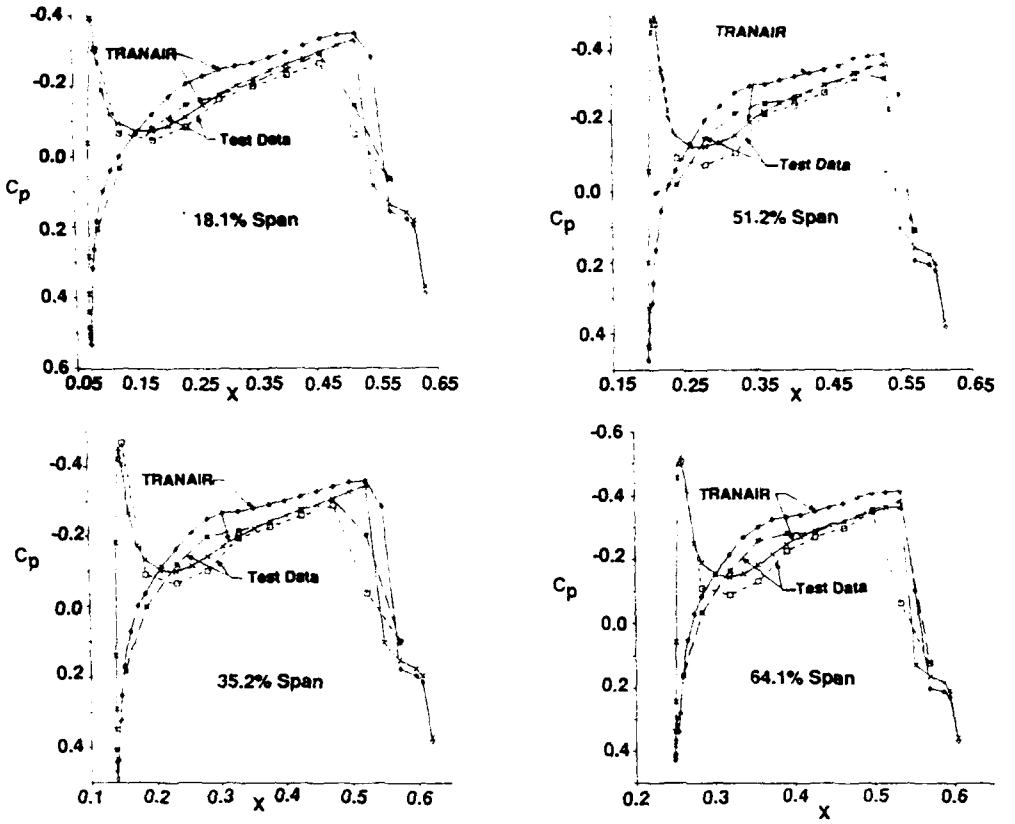


Figure 8a. Comparisons of steady Cp at M=.95, α=0 deg.

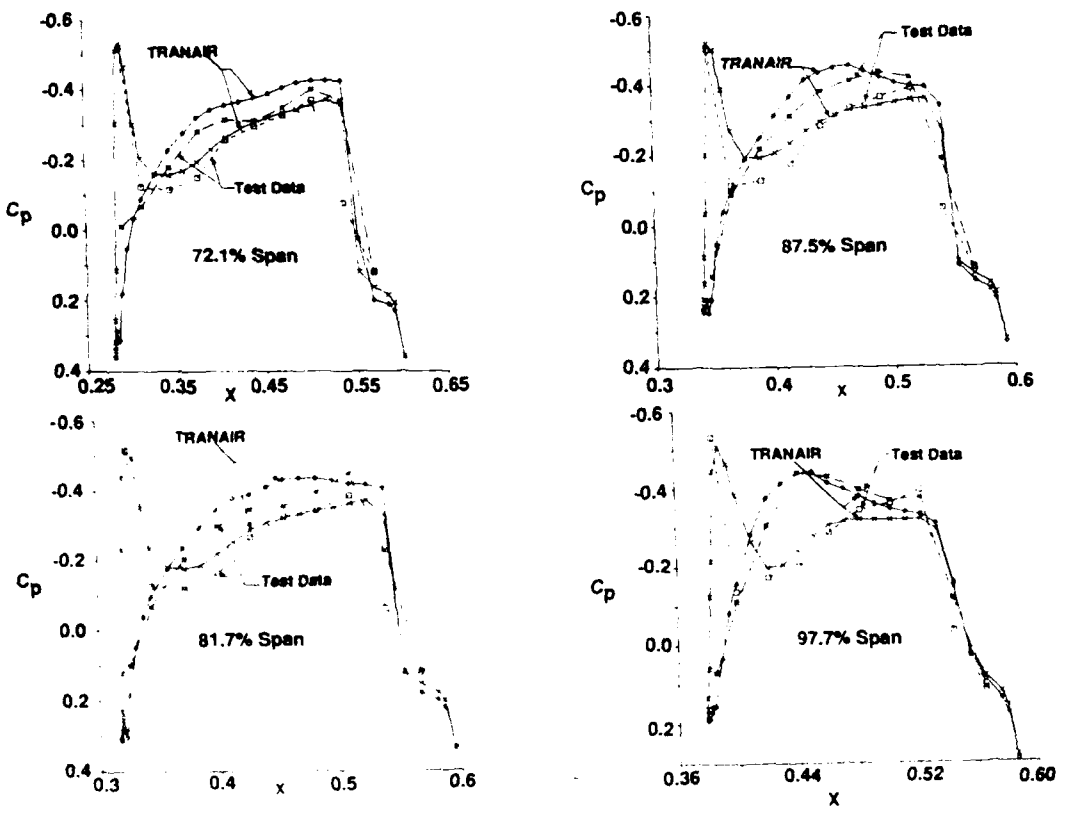


Figure 8b. Comparisons of steady Cp at M=.95, α=0 deg.

This Document Provided by the Abbott Aerospace
TECHNICAL LIBRARY
ABBOTTAEROSPACE.COM

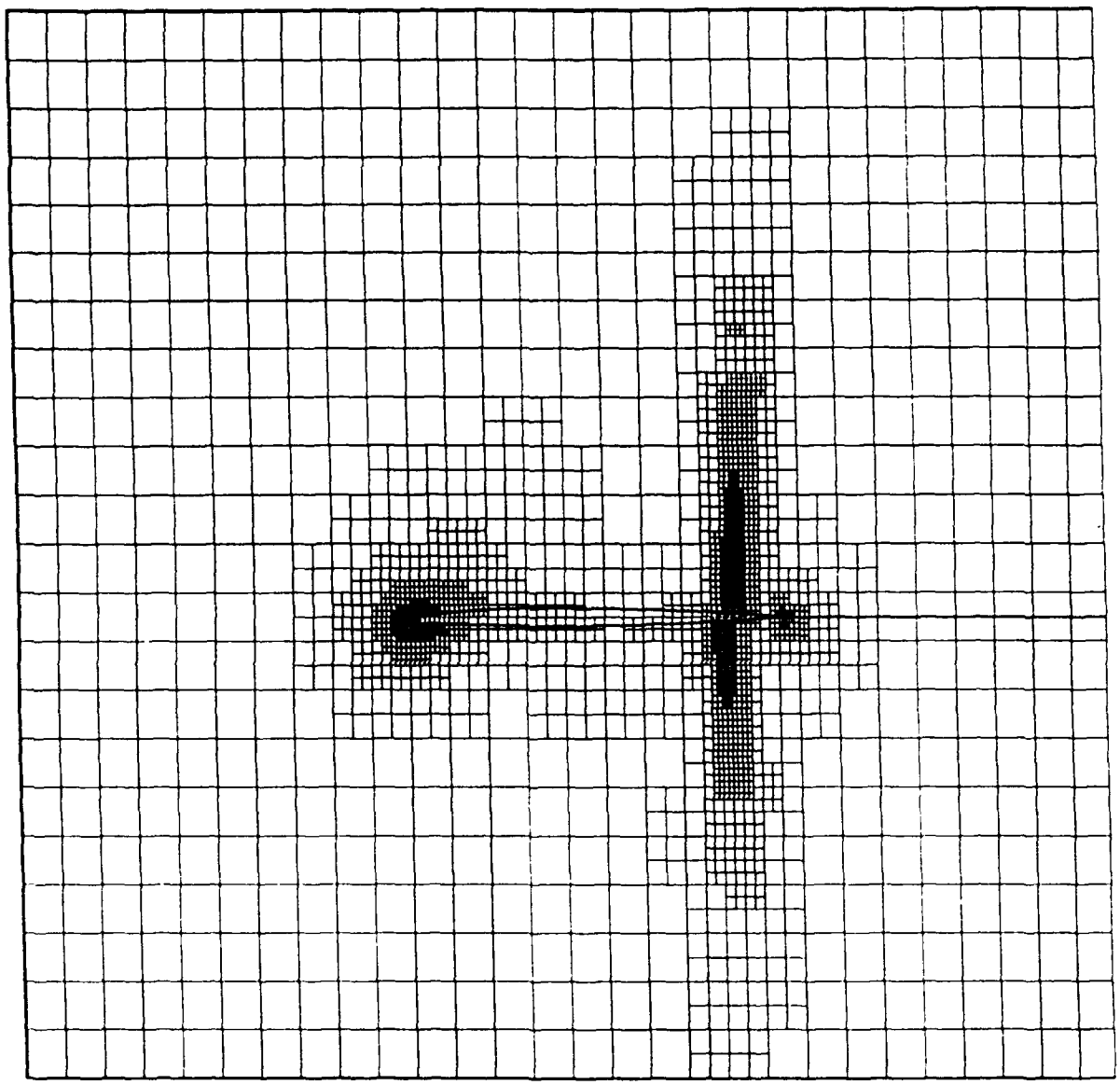


Figure 9. An example of the final grid generated in TRANAIR (M=.95, α=0 deg.)

THIS DOCUMENT PROVIDED BY THE ABBOTT AEROSPACE
TECHNICAL LIBRARY
ABBOTTAEROSPACE.COM

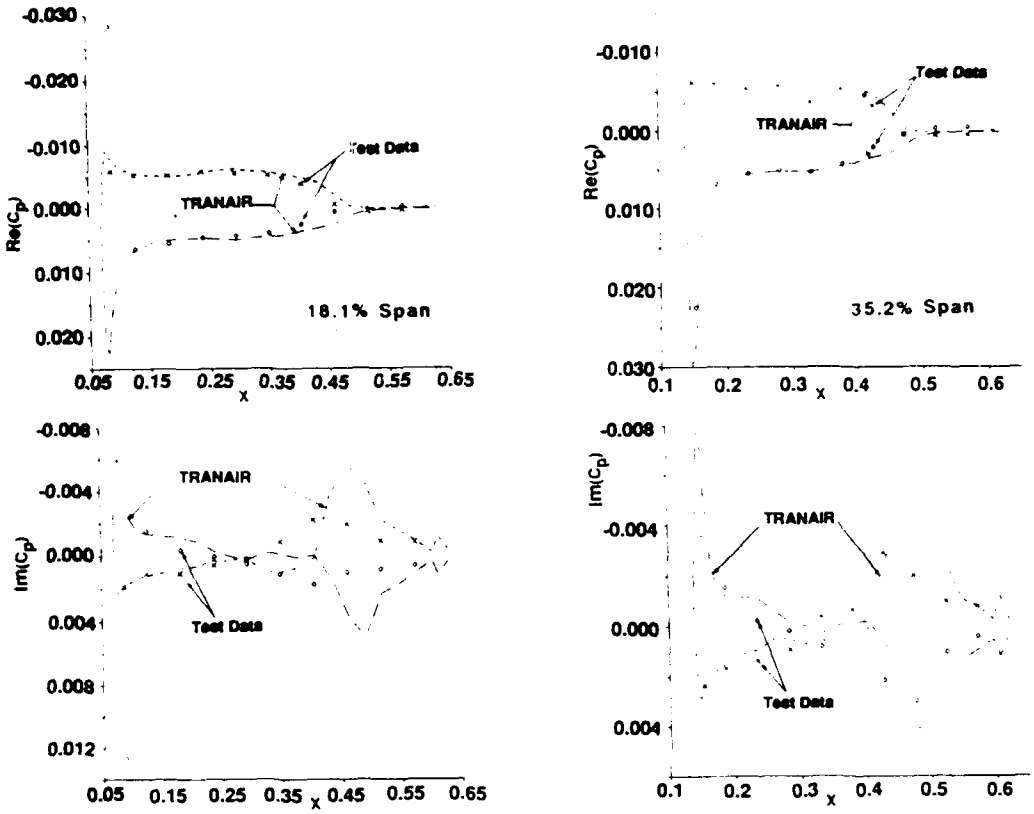


Figure 10a. Comparisons of unsteady C_p
(M=.9, α=0, k=.137, f=20Hz, Amplitude=.11 deg)

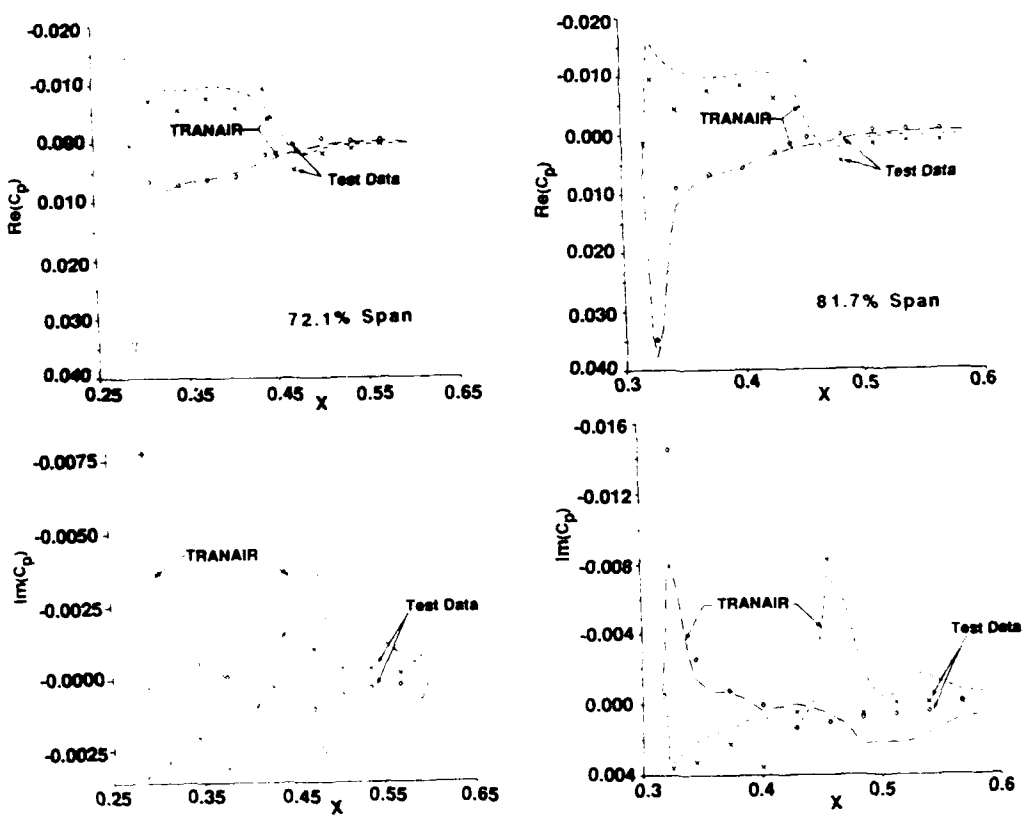


Figure 10b. Comparisons of unsteady C_p
(M=.9, α=0, k=.137, f=20Hz, Amplitude=.11 deg)

THIS DOCUMENT PROVIDED BY THE ABBOTT AEROSPACE
TECHNICAL LIBRARY
ABBOTTAEROSPACE.COM

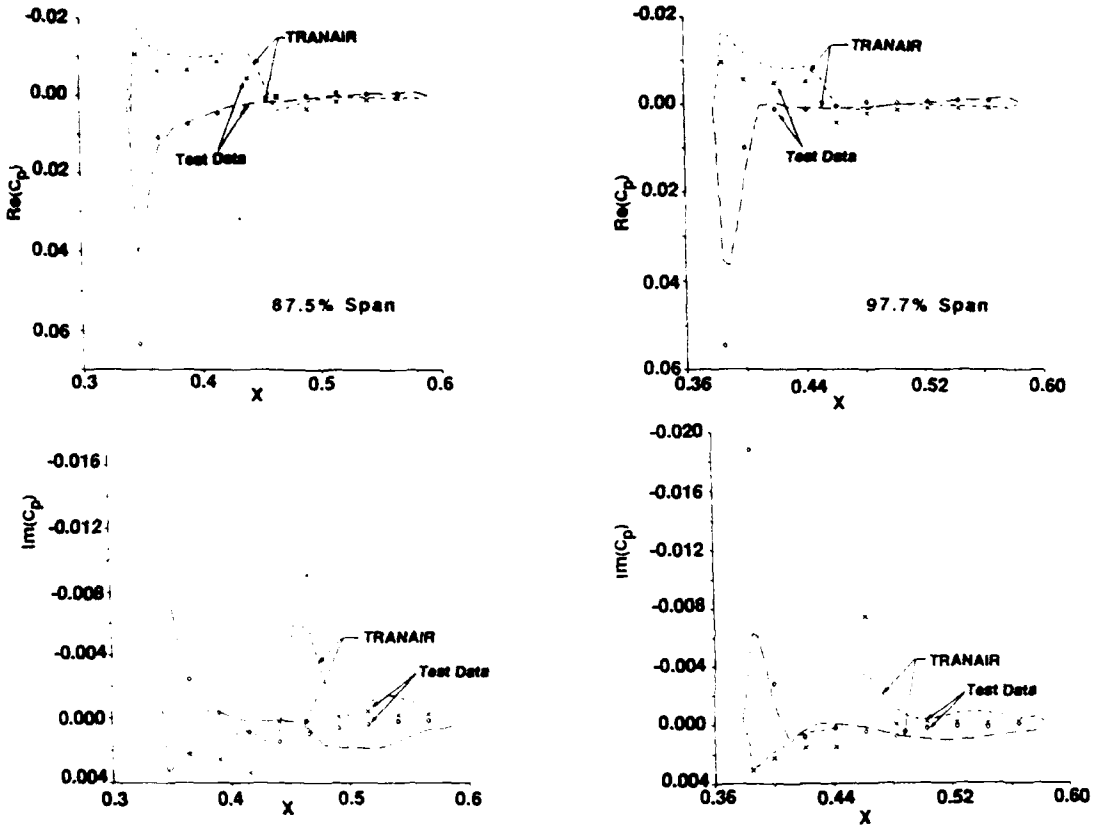


Figure 10c. Comparisons of unsteady C_p
(M=.9, α=0, k=.137, f=20Hz, Amplitude=.11 deg)

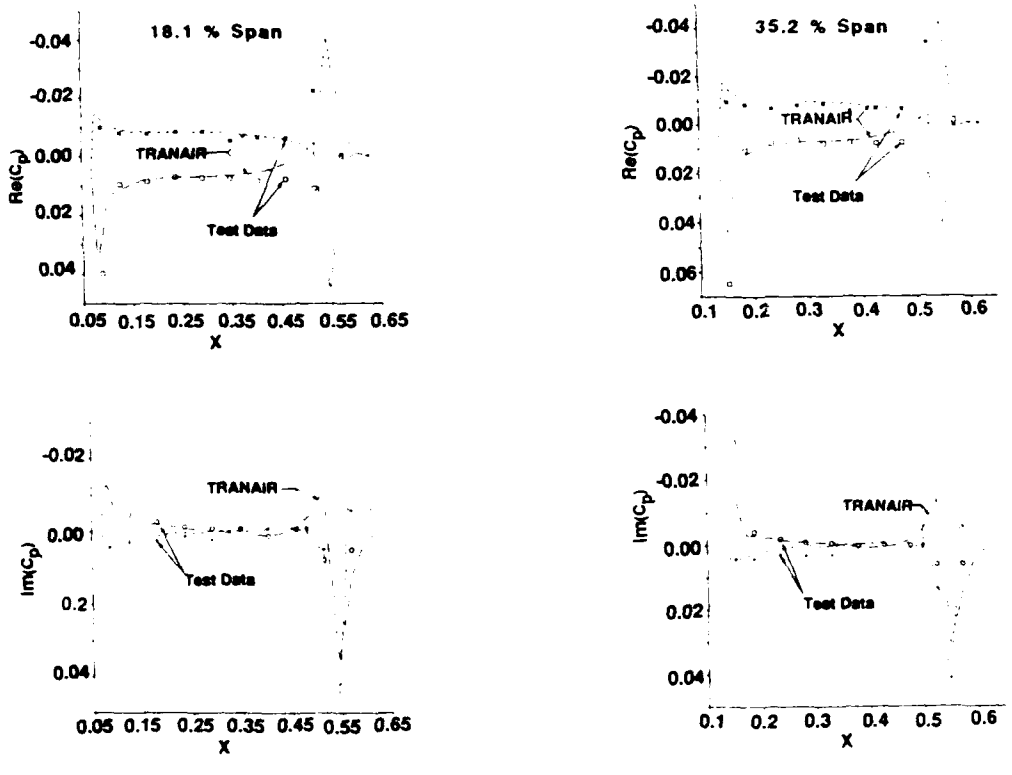


Figure 11a. Comparisons of unsteady C_p
(M=.95, α=0, k=.264, f=40Hz, Amplitude=.22 deg)

THIS DOCUMENT PROVIDED BY THE ABBOTT AEROSPACE
TECHNICAL LIBRARY
ABBOTTAEROSPACE.COM

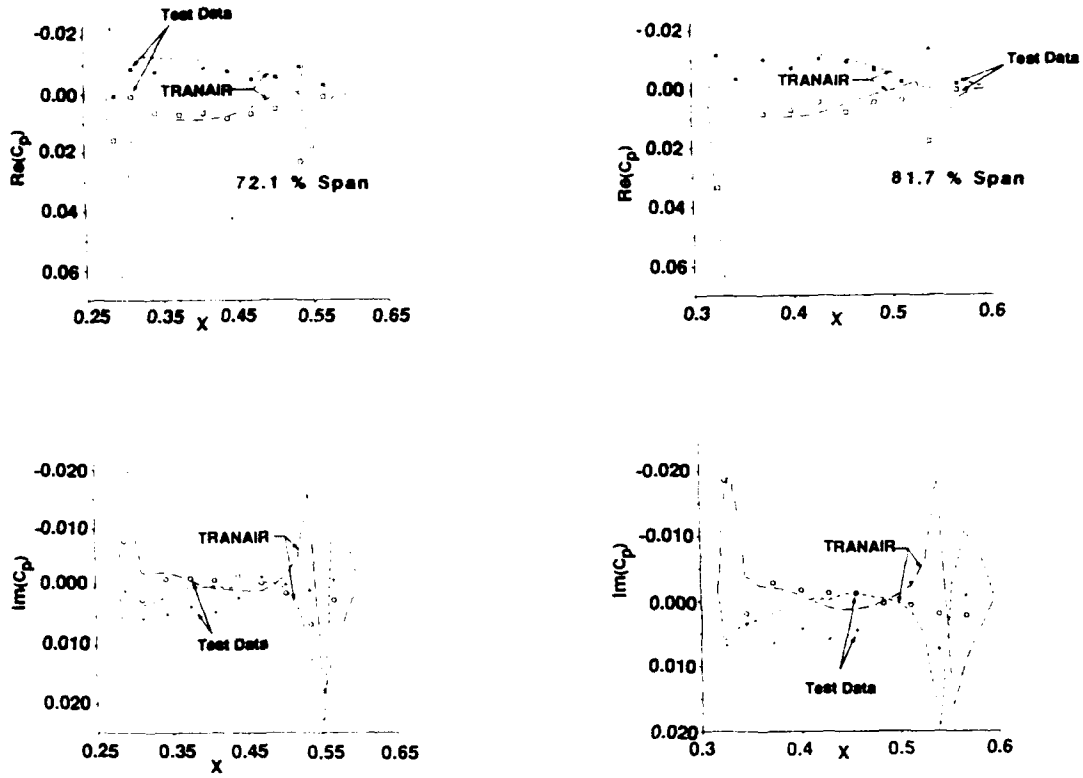


Figure 11b. Comparisons of unsteady C_p
(M=.95, α=0, k=.264, f=40Hz, Amplitude=.22 deg)

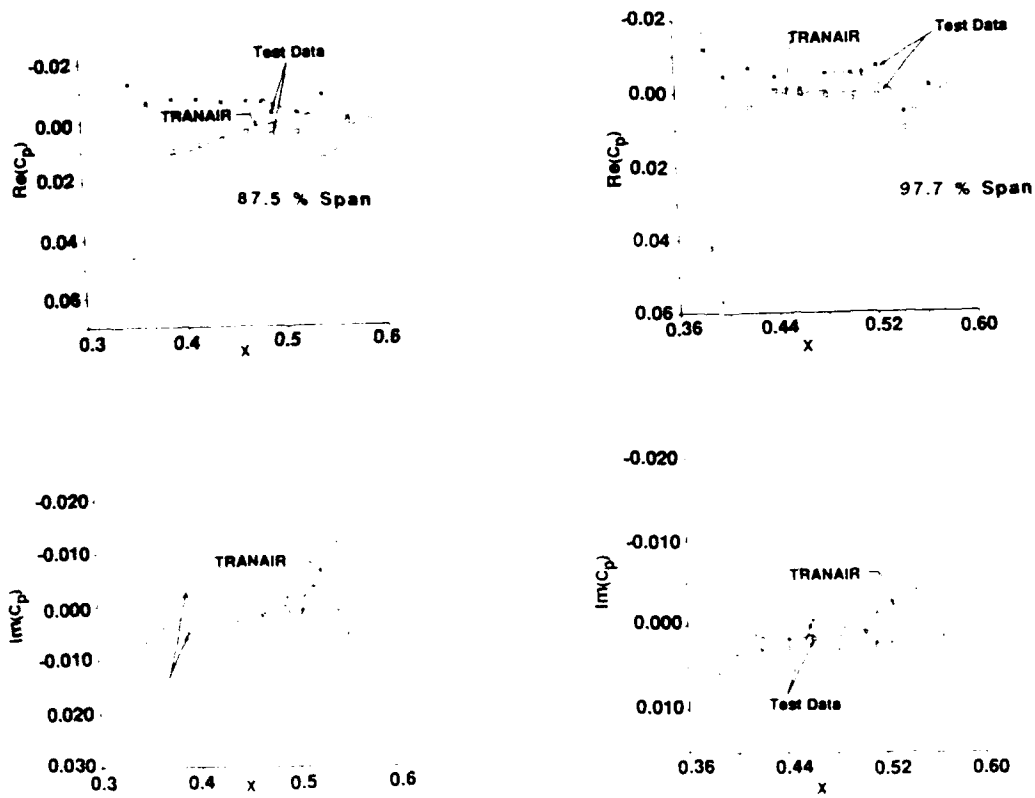


Figure 11c. Comparisons of unsteady C_p
(M=.95, α=0, k=.264, f=40Hz, Amplitude=.22 deg)

THIS DOCUMENT PROVIDED BY THE ABBOTT AEROSPACE
TECHNICAL LIBRARY
ABBOTTAEROSPACE.COM

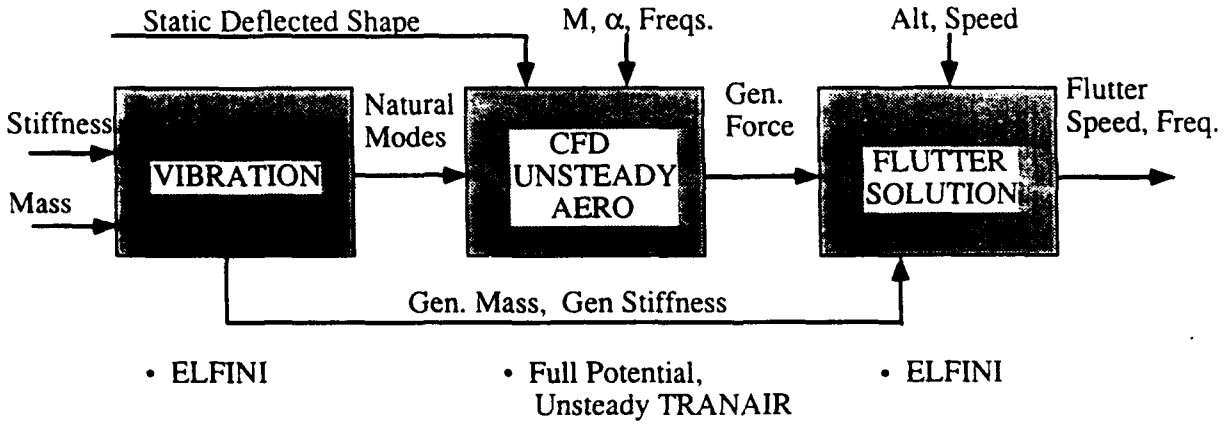


Figure 12. Flutter Prediction based on computational fluid and structural dynamics

THIS DOCUMENT PROVIDED BY THE ABBOTT AEROSPACE
TECHNICAL LIBRARY
ABBOTTAEROSPACE.COM

COUPLAGE DIRECT FLUIDE STRUCTURE EN AEROELASTICITE TRANSSONIQUE

J.P. GRISVAL et J.L. MEURZEC

OFFICE NATIONAL D'ETUDES ET

DE RECHERCHES AEROSPATIALES

29, avenue de la Division Leclerc

BP 72, 92322 Châtillon Cedex France

RESUME

Une méthode numérique appelée couplage direct est présentée pour l'étude de l'aéroélasticité transsonique.

Le couplage direct est réalisé entre les forces aérodynamiques et les déplacements calculés.

L'écoulement est modélisé par la méthode des petites pertubations transsoniques (PPT). La déformation statique de la structure est déterminée en stationnaire. Le couplage fort assure l'équilibre entre les forces aérodynamiques et les déformations statiques. En instationnaire, l'équilibre entre les forces aérodynamiques et élastiques est réalisé dans le domaine temporel.

L'analyse des déplacements donne l'évolution des modes structuraux et permet de déterminer le flottement.

Des résultats numériques sur un avion de transport civil sont présentés. Ils sont comparés à ceux obtenus par d'autres méthodes dans le domaine fréquentiel.

ABSTRACT

We present a numerical approach named direct coupling method for transonic aeroelasticy studies.

This direct coupling is realized between the computation of aerodynamic forces and the computation of displacements.

The flow is modeled by using the transonic small perturbation (TSP). In steady flow, we determine the static deformations of the structure. The strong coupling insure the equilibrium state between the aerodynamic forces and the static deformations and in unsteady flow between the aerodynamic and the aeroelastic forces in the time domain.

The analysis of the resulting displacements give the evolution of the structural modes and enable us to detect flutter.

Numerical results are presented for a civil aircraft and are compared whit other methods in frequential domain.

1. INTRODUCTION

Des méthodes numériques d'aérodynamiques linéaires sont largement utilisées pour la prévision de la stabilité aéroélastique des avions. Lorsque les effets visqueux sont négligeables, les méthodes basées sur la résolution des équations linéarisées du potentiel sont bien adaptées au problème en aérodynamique subsonique et supersonique. Ces méthodes ne nécessitent qu'un maillage des surfaces aérodynamiques et permettent l'évaluation des forces aérodynamiques généralisées instationnaire le plus généralement dans le domaine fréquentiel. Le système couplé aérodynamique-structure est lui aussi résolu dans le domaine fréquentiel dans le cas où la structure est elle même à comportement linéaire.

Dans le domaine transsonique, l'aérodynamique est non linéaire. L'existence des non-linéarités induit une interaction entre les états stationnaire et instationnaire et impose la détermination de l'état stationnaire. Celui-ci dépend de conditions aérodynamiques et géométriques. La prise en compte de la déformée statique représente une amélioration dans sa prévision.

Classiquement, à partir de la position d'équilibre stationnaire, une excitation harmonique est imposée à la structure (petits mouvements). Une analyse harmonique des forces aérodynamiques instationnaires obtenues dans le domaine temporel permet la résolution du système couplé fluide-structure dans le domaine fréquentiel. Cette approche nécessite de nombreux calculs instationnaires pour caractériser les instabilités aéroélastiques des avions du fait du balayage de nombreux paramètres : configurations, Mach, incidences, modes et fréquences. De plus, dans le cas d'une solution numérique construite dans le domaine temporel et d'une aérodynamique instationnaire non linéaire, la résolution du système couplé fluide-structure dans le domaine fréquentiel utilise seulement le premier harmonique des forces aérodynamiques instationnaires. C'est pourquoi, parallélement au développement de méthodes numériques de résolution des équations des écoulements transsoniques, il est nécessaire de développer des méthodes de couplage aérodynamique-structure et de les améliorer sur le plan algorithmique pour diminuer le volume des calculs d'aérodynamique. Ces méthodes sont à développer en stationnaire pour l'analyse aéroélastique statique des avions et en instationnaire pour la prédiction du flottement.

A la fin des années 70, des développements utilisant la réponse temporelle pour la prévision de la stabilité d'un système aéroélastique ont été menés. Les premières études concernaient un profil à un degré de liberté [1]. Des travaux ont été conduits pour résoudre simultanément les équations aérodynamiques et aéroelastiques du mouvement pour des profils bidimensionnels avec 2 ou 3 degrés de liberté [2,3,4,5]. Ces études ont montré l'influence des non linéarités aérodynamiques sur la stabilité aéroélastique.

Les extensions au tridimensionnel ont été réalisées pour des voilures isolées [6,8] et pour des voilures avec charges [7]. Dans le domaine de l'aéroélasticité transsonique, le solveur aérodynamique repose souvent sur la résolution de l'équation des petites perturbations transsoniques : code XTRAN2S [9] pour le bidimensionnel, code XTRAN3S, ATRAN3S et CAP-TSD pour le tridimensionnel. Des solveurs Euler 3D en maillage non structurés sont en développement pour traiter les problèmes d'aéroélasticité [12,13] et des solveurs Naviers-Stokes 3D ont déjà permis de traiter l'aéroélasticité statique d'un avion [14].

THIS DOCUMENT PROVIDED BY THE ABBOTT AEROSPACE
TECHNICAL LIBRARY
ABBOTTAEROSPACE.COM

La Direction des Structures de l'ONERA a développé pour les problèmes d'aéroélasticité transsonique la méthode des petites perturbations transsoniques à partir de 1978 en bidimensionnel [15]. Cette méthode fut étendue au cas de l'aile rectangulaire [16] puis au cas de l'aile de forme en plan quelconque [17]. Elle est utilisée classiquement en première approximation avec la méthode dite du 1er harmonique qui consiste à ne conserver que le premier terme dans le développement en série de Fourier des forces aérodynamiques généralisées instationnaires et à résoudre le problème couplé fluide-structure dans le domaine fréquentiel. Cette méthode permet des prévisions généralement correctes des F.A.G. à des coûts numériques très modestes dans la mesure où elle utilise un maillage structuré 3D et une méthode de résolution ADI bâtie sur un schéma de différences finies. Elle est la base des calculs d'aérodynamique dans la méthode de couplage direct présentée dans la suite.

Les hypothèses, les bases de la méthode aérodynamique, la modélisation statique et dynamique de la structure, la méthode de couplage statique et dynamique, les critères de convergence sont exposés. Le code de couplage, les techniques d'analyse des signaux instationnaires sont présentés au travers d'une application sur une configuration d'aile lisse d'avion de transport. Les performances du code et une comparaison des résultats numériques avec ceux obtenus par d'autres méthodes sont décrites.

2. DONNEES DU PROBLEME

On se donne une structure dans une configuration de référence (non déformée et non chargée). Celle-ci est un solide déformable occupant un domaine Ω ouvert borné de $\mathbb{R}^3$, de bord $\partial\Omega = S_0 \cup S_A$ où S_0 (respectivement S_A) sera la partie de $\partial\Omega$ sur laquelle il n'y aura pas (respectivement, il y aura) des forces aérodynamiques. Une approximation du comportement de la structure supposé être à comportement linéaire est donnée à partir de l'opérateur de souplesse statique dans une certaine base de représentation. Par ailleurs, un solveur aérodynamique permet de déterminer les forces aérodynamiques à partir de la forme extérieure de la structure et ceci sur une base de représentation différente de la précédente. Le but de la modélisation statique est la recherche d'un état d'équilibre entre les forces aérodynamiques stationnaires et les déformées statiques.

Pour la modélisation dynamique de la structure, on limite la représentation de la structure à un ensemble de modes propres de vibrations qui sont associés à la structure dans la configuration d'équilibre statique sous les charges aérodynamiques stationnaires. On suppose la dynamique de la structure linéaire autour de cette configuration de référence. Après la détermination de l'état d'équilibre stationnaire, l'énergie apportée à la structure sous forme de conditions initiales permet une prévision des instabilités aéroélastiques, but de la modélisation dynamique. Cette énergie induit des mouvements à la structure et l'analyse de ces mouvements en présence des forces aérodynamiques permet la détermination du domaine de stabilité. La dissipation structurale peut être prise en compte dans cette approche.

3. COUPLAGE DIRECT EN STATIONNAIRE

3.1 Modélisation statique de la structure

Le comportement statique de la structure est supposé être linéaire. Une approximation de ce dernier est donné par des modèles numériques basés, le plus souvent sur une méthode d'éléments finis relative à Ω. Le système discrétisé ayant r degrés de libertés (DDL), il est régi par l'équation matricielle :

$$\mathbf{K}\,X = F \qquad (1)$$

où $X \in \mathbb{R}^r$ représente les inconnues nodales du champ de déplacement, $\mathbf{F} \in \mathbb{R}^r$ les forces nodales équivalentes et $\mathbf{K} \in Mat_{\mathbb{R}}(r,r)$ la matrice de raideur.

Pour le calcul du couplage, les forces aérodynamiques n'étant appliquées que sur S_A, on peut condenser (1) pour ne conserver que les degrés de libertés qui interviendront. Pour simplifier, on utilise la décomposition par bloc de (1).

$$\begin{pmatrix} K_{11} & K_{12} \\ K_{21} & K_{22} \end{pmatrix} \begin{pmatrix} X_0 \\ X_A \end{pmatrix} = \begin{pmatrix} 0 \\ F_A \end{pmatrix} \qquad (2)$$

Pour diminuer le coût numérique pendant les itérations de couplage direct, la matrice est factorisée :

$$K = L\,D\,L^T \qquad (3)$$

avec D matrice diagonale et L matrice triangulaire inférieure. L'équation (2) s'écrit :

$$\begin{pmatrix} L_{11} & 0 \\ L_{21} & L_{22} \end{pmatrix} \begin{pmatrix} D_1 & 0 \\ 0 & D_2 \end{pmatrix} \begin{pmatrix} L_{11}^T & L_{21}^T \\ 0 & L_{22}^T \end{pmatrix} \begin{pmatrix} X_0 \\ X_A \end{pmatrix} = \begin{pmatrix} 0 \\ F_A \end{pmatrix} \qquad (4)$$

soit :

$$\begin{cases} K\,X_A = F_A \\ K = L_{22}\,D_2\,L22^T \end{cases} \qquad (5)$$

où

$$K \in Mat\,\mathbb{R}(r_A, r_A), \quad X \in \mathbb{R}^{r_A}, \quad F_A \in \mathbb{R}^{r_A}$$

r_A étant le nombre de degrés de liberté concernés par le couplage.

3.2 Champ de déplacement sur S_A et interpolation

Soit $\vec{W}(m_A)$ le champ de déplacement statique défini sur S_A à valeurs dans $\mathbb{R}^3$ dont une discrétisation est donnée par une connaissance de X relative au maillage structure. Pour les calculs d'aérodynamique et partant de la connaissance de X, il est nécessaire de construire une bonne représentation du champ $\vec{W}$ (ainsi que certaines dérivées). Pour l'interpolation évoquée ci-dessus, on introduit une base orthonormée $\{\psi_k, k \in \mathbb{N}\}$ de $L^2(S_A, \mathbb{R})$

$$(\psi_k, \psi_l) = \delta_{kl}$$

Cette base est construite à l'aide des polynomes de Legendre. Une interpolation d'ordre K de $\vec{W}$ est donné par:

$$\vec{W}(m_A) = \sum_{k=1}^{K} \psi_k(m_A)\,\vec{Q^k} \qquad (6)$$

avec $\vec{Q^k} \in \mathbb{R}^3$

Soit $M_A, j \quad , j \in \{1, \ldots, ns\}$, l'ensemble des bords sur S_A relatif à la discrétisation de la structure. On introduit les notations suivantes :

$$X = \begin{pmatrix} \vec{W}(m_A, 1) \\ \vdots \\ \vec{W}(m_A, ns) \end{pmatrix} ; Q = \begin{pmatrix} \vec{Q}^1 \\ \vdots \\ \vec{Q}^k \end{pmatrix}$$

avec $X \in \mathbb{R}^{3ns}$; $Q \in \mathbb{R}^{3k}$

Alors de la relation (6), on peut contruire la matrice $\mathbf{P}_s \in Mat\,\mathbb{R}(3k, 3ns)$ fonction des $\psi_k\,(m_A, j)$ telle que :

$$X = \mathbf{P}_s * Q \qquad (7)$$

THIS DOCUMENT PROVIDED BY THE ABBOTT AEROSPACE
TECHNICAL LIBRARY
ABBOTTAEROSPACE.COM

3.3 Champ de forces aérodynamiques et projection

Soit $\vec{f}(m_A)$ le champ de forces aérodynamiques défini sur S_A à valeurs $\mathbb{R}^3$. Soit $\delta\vec{W}$ une variation arbitraire cinématiquement admissible du champ de déplacement. Alors on a :

$$(\vec{f}, \delta\vec{W}) = -\int_{SA} \frac{1}{2}\rho V_\infty^2 C_p(m_A)\vec{n}(m_A)\delta\vec{W}(m_A)ds(m_A) \tag{8}$$

Une approximation d'ordre N de $\vec{f}$ est donnée par la projection :

$$\vec{f}(m_A) = \sum_{k=1}^{N} \psi_k(m_A)\,\vec{\mathcal{F}}^k \tag{9}$$

avec $\vec{\mathcal{F}}^k \in \mathbb{R}^3$ qui s'écrit pour $l \in \{1,2,3\}$

$$\mathcal{F}_l^k = (f_l, \psi_k)$$

$$= -\int_{SA} \frac{1}{2}\rho V_\infty^2 C_p(m_A) n_l(m_A)\psi_k(m_A)ds(m_A) \tag{10}$$

Le calcul des trois composantes de $\vec{\mathcal{F}}^k$ est fait en approchant l'intégration du membre de droite de (10) par une quadrature numérique qui utilise les noeuds du maillage aérodynamique où sont calculés les coefficients de pression. Vu l'interpolation de (6), le champ de pression est fonction de Q et en dépend non linéairement par l'aérodynamique transsonique. Il en est de même de $\mathcal{F}$ qui sera noté $\mathcal{F}(Q)$ pour indiquer la dépendance non linéaire.

3.4 Equation projetée pour le système couplé

Soit δQ une variation arbitraire de Q. Il lui correspond une variation $\delta\vec{w}$ et une variation δX données respectivement par (6) et (7). Vu (5), on a :

$$< KX, \delta X > = < F_A, \delta X > = (\vec{f}_A, \delta\vec{w}) \tag{11}$$

Les relations (6), (8), (10) permettent d'écrire le système projeté :

$$(f_A, \delta\vec{W}) = \sum_{k=1}^{N}\sum_{l=1}^{N} (\psi_k, \psi_l)\,\vec{\mathcal{F}}^k\,\delta\vec{Q}^l$$

$$= \sum_{k=1}^{N} \vec{\mathcal{F}}^k\,\delta\vec{Q}^l = < \mathcal{F}(Q), \delta Q >$$

Par substitution de (7) dans (11), on obtient finalement :

$$< \mathbb{P}_S^T K \mathbb{P}_S Q, \delta Q > = < \mathcal{F}(Q), \delta Q > \qquad \forall \delta Q$$

soit

$$\mathcal{K} Q = \mathcal{F}(Q)$$
$$\mathcal{K} = \mathbb{P}_S^T K \mathbb{P}_S \qquad \in Mat\,\mathbb{R}(3N, 3N) \tag{12}$$

Pour le calcul de $\mathcal{K}$,on profite de la factorisation (5). On a:

$$\begin{cases} \mathcal{K} = Z^T D Z \\ Z = L_{22}^T \mathbb{P}_S \end{cases} \tag{13}$$

3.5 Résolution

La recherche de l'état d'équilibre statique s'effectue par un procédé itératif dans le temps au moyen d'un calcul instationnaire. A l'instant t, l'équation (12) s'écrit:

$$\mathcal{K} Q(t) = \mathcal{F}(t, Q(t))$$

A l'équilibre la relation :

$$\mathcal{K} Q(t_{n+1}) = \mathcal{F}(t_{n+1}, Q(t_n)) \tag{14}$$

est vérifiée.

Pour $t = 0$, le champ de potentiel est nul, la surface aérodynamique est un plan sans épaisseur et sans incidence. Le processus itératif commence par un gonflement du profil, de l'incidence et par conséquent des déformées. Celles-ci sont superposées à la géométrie initiale par l'intermédiaire des conditions limites. Après la période de gonflement, le processus continue jusqu'à l'obtention de l'état convergé. Le test de convergence pourrait être :

$$\| Q(t_{n+1}) - Q(t_n) \| \leq \epsilon$$

En fait, le critère n'est pas assez sensible pour l'aérodynamique transsonique et on utilise un test portant sur la dérivée suivant la direction de l'écoulement du potentiel de vitesse.

$$\| \varphi_x(t_{n+1}) - \varphi_x(t_n) \| \leq \epsilon$$

Rien n'indique à priori que l'algorithme utilisé (14) soit toujours convergent, même s'il existe un état stationnaire stable. Pour étudier la stabilité du schéma, il faudrait avoir une information sur la matrice jacobienne de $\mathcal{F}$ par rapport à $Q(t)$ pour t fixé. Compte tenu de la formulation de l'aérodynamique transsonique, celà n'est pas possible. La validation de l'algorithme a donc été effectuée par des tests numériques. La convergence a toujours été rapide. Dans le cas de divergence, le pas de temps peut être modifié surtout dans la période de gonflement. D'autre part, une relaxation peut être introduite en remplaçant (14) par

$$\mathcal{K}(\lambda Q(t_{n+1}) + (1-\lambda)Q(t_n)) = \mathcal{F}(t_{n+1}, Q(t_n)) \tag{15}$$

avec $0. < \lambda \leq 1$.

4. COUPLAGE DIRECT EN INSTATIONNAIRE

4.1 Modélisation dynamique de la structure

On étudie la dynamique du système couplé aérodynamique-structure autour d'une configuration en équilibre statique sous les charges aérodynamiques stationnaires. La dynamique de la structure autour de cette configuration est linéaire et peut être décrite par un ensemble de modes rigides et souples. La base modale est donnée sous forme discrète sur S_A.

On note $m_j, \omega_j, a_j, \phi^j \in \mathbb{R}^{r_A}, j \in \{1,\ldots,m\}$ les m masses généralisées, fréquences propres, coefficients d'amortissement et déformées modales relatives au mode j. La dynamique de la structure est régie par le système suivant:

$$\begin{cases} \mu\,\ddot{q}(t) + \alpha\dot{q}(t) + \gamma\,q(t) = FAG(t) \\ q(0) = q_0 \\ \dot{q}(0) = q_1 \\ X(t) = \sum_{j=1}^{m} q_j(t)\,\phi^j \end{cases} \tag{16}$$

avec

$$[\mu]_{jk} = m_j\,\delta_{jk}$$
$$[\alpha]_{jk} = 2\,a_j\,\omega_j\,\mu_j\,\delta_{jk}$$
$$[\gamma]_{jk} = m_j\,\omega_j^2\,\delta_{jk}$$

$q_0(t)$ et $q_1(t) \in \mathbb{R}^m$ sont les coordonnées et vitesses généralisées. $FAG(t) \in \mathbb{R}^m$ sont les forces aérodynamiques instationnaires généralisées et $X(t) \in \mathbb{R}^{r_A}$ les degrés de liberté du système dynamique. On considère la base $\{\psi_k\}$ introduite au paragraphe 3.2. Le champ de déplacement instationnaire s'écrit:

$$\vec{W}(t, m_A) = \sum_{j=1}^{m} q_j(t)\,\vec{\phi^j}(m_A) \tag{17}$$

THIS DOCUMENT PROVIDED BY THE ABBOTT AEROSPACE
TECHNICAL LIBRARY
ABBOTTAEROSPACE.COM

où l'on utilise l'interpolation suivante pour les $\vec{\phi_j}$:

$$\vec{\phi^j}(m_A) = \sum_{k=1}^{K} \psi_k(m_A)\,\vec{\mathcal{A}}^k \qquad (18)$$

avec $\vec{\mathcal{A}}^k \in \mathbf{R}^3$

$$\mathcal{A}_l^k = (\phi_l^j, \psi_k) = \int_{SA} \phi_l^j(m_A)\,\psi_k(m_A)\,ds(m_A) \qquad (19)$$

Pour chaque mode j, l'intégrale (19) est calculée par une quadrature numérique qui utilise les points m_A de S_A. Compte tenu de (17) et (18), le champ de déplacement instationnaire s'écrit:

$$\vec{W}(t, m_A) = \sum_{j=1}^{m} q_j(t) \sum_{k=1}^{K} \psi_k(m_A)\vec{\mathcal{A}^k} \qquad (20)$$

On peut alors calculer explicitement les dérivées de $\vec{W}$ par rapport à l'espace pour le solveur aérodynamique.

4.2 Méthode de résolution pour le flottement

Les forces aérodynamiques instationnaires sont calculées suivant (10), où Cp représente la variation instationnaire du coefficient de pression autour du champ de Cp stationnaire à l'équilibre statique.

Le système (16) peut être réécrit :

$$\begin{cases} \mu\,\ddot{q}(t) + +\alpha\,\dot{q}(t) + \gamma\,q(t) = FAG(t\,,\,q(t)) \\ q(0) = q_0 \\ \dot{q}(0) = q_1 \end{cases}$$

L'objectif est la détermination du domaine de stabilité à travers l'analyse des $q(t)$ pour des conditions initiales données. Les conditions initiales correspondent à une équirépartition de l'énergie entre tous les modes. L'énergie communiquée au système ne doit pas entraîner des déplacements trop importants pour ne pas mettre en défaut le solveur aérodynamique. D'autre part, l'énergie ne doit pas être trop faible afin d'avoir des forces aérodynamiques significatives par rapport au bruit numérique. L'énergie initiale fournie au système est telle qu'elle induise en extrémité d'aile un déplacement vertical de l'ordre de 1/10 de la corde d'emplanture ou l'équivalent d'une torsion de 1 degré .

Pour la discrétisation temporelle, un schéma centré implicite (cas particulier des schémas de Newmark) est utilisé. En posant $q^n = q(t_n)$, $Q = \begin{pmatrix} q \\ \dot{q} \end{pmatrix}$,

$$A = \begin{pmatrix} 1 & 0 \\ 0 & \mu \end{pmatrix} \quad B = \begin{pmatrix} 0 & -1 \\ \gamma & \alpha \end{pmatrix} \quad F = \begin{pmatrix} 0 \\ F_A \end{pmatrix}$$

Le système (16) s'écrit :

$$A\,\dot{Q} + B\,Q = F \qquad (21)$$

La discrétisation de l'équation (21) à l'instant $t = (t_n + t_{n+1})/2$, s'écrit avec $\Delta t = t_{n+1} - t_n$,

$$A\frac{Q^{n+1} - Q^n}{\Delta t} + B\frac{Q^{n+1} + Q^n}{2} = F$$

soit

$$Q^{n+1} = (2 + A^{-1}B\Delta t)^{-1}[(2 - A^{-1}B\Delta t)Q^n + 2\Delta t A^{-1}F] \qquad (22)$$

La force F_A discrétisée à l'instant $(t_n + t_{n+1})/2$ s'écrit:

$$\frac{1}{2}\left[FAG(t_{n+1}\,,\,q^{n+1}) + FAG(t_n\,,\,q^n\right]$$

Le système (22) est non linéaire en Q^{n+1}. Pour trouver la solution Q^{n+1} connaissant Q^n, on utilise une méthode de point fixe. Le critère de convergence porte sur la variation absolue des forces aérodynamiques instationnaires c'est à dire :

$$\| FAG(t_{n+1}\,,\,q_{p+1}^{n+1}) - FAG(t_n + 1\,,\,q_p^{n+1}) \| \leq \epsilon$$

L'algorithme utilisé ne converge pas forcément malgré l'utilisation d'un schéma de Newmark inconditionnellement stable. Pour étudier la convergence, il faudrait avoir une information sur la matrice jacobienne de FAG par rapport à $Q(t)$. La validation de l'algorithme a été effectuée par des tests numériques. Les paramètres influant la convergence ou permettant de l'améliorer sont d'une part le pas de temps et d'autre part l'énergie initiale fournie au système.

4.3 Analyse des résultats instationnaires

Le problème consiste à analyser la réponse en un point d'un système linéaire qui est une combinaison linéaire des réponses modales. Deux techniques ont été utilisées pour l'analyse de la fonction discrète du temps $X(t)$ issue du système (16).

Dans la première, on choisit d'approximer cette fonction comme une somme d'exponentielles complexes dans le domaine temporel:

$$X(t) \simeq \sum_{p=1}^{m1} B_p\,e^{\beta_p t}$$

avec $m1 = 2m$, B_p et $\beta_p \in \mathbb{C}$. Les coefficients B_p et β_p sont obtenus par la méthode de Prony [19,20]. Les fréquences ω_k et les amortissements aérodynamiques α_k des modes sont obtenus à partir des coefficients β_p:

$$\beta_k = i\,\omega_k(1 + i\alpha_k)$$

Dans la seconde méthode, une transformée de Fourier $\widehat{q}_k(\omega)$ de la coordonnée généralisée $q_k(t)$ est réalisée. Le signal obtenu est ensuite analysé par une méthode de lissage des fonctions de transfert [21]. Le signal $\widehat{q}_k(\omega)$ est approximé par une fraction rationnelle de la forme:

$$\widehat{q}_k(\omega) \simeq \frac{P(i\omega)}{Q(i\omega)}$$

avec

$$P(i\omega) = \sum_{r=0}^{m} (i\omega)^r\,X_r$$

$$Q(i\omega) = \sum_{r=0}^{n} (i\omega)^r\,Y_r$$

Les degrés m du numérateur et n du dénominateur sont fixés par le nombre de modes que l'on veut représenter. Les pôles du dénominateur $Q(i\omega)$ fournissent les fréquences et les amortissements réduits.

THIS DOCUMENT PROVIDED BY THE ABBOTT AEROSPACE
TECHNICAL LIBRARY
ABBOTTAEROSPACE.COM

5. AERODYNAMIQUE TRANSSONIQUE

5.1 Principe

La méthode de calcul de l'écoulement transsonique instationnaire utilisée s'appuie sur la résolution de l'équation du potentiel de vitesse avec l'approche des petites perturbations transsoniques tridimensionnelles (PPT3D) [15,16,17]. La méthode de résolution est une méthode implicite de directions alternées: utilisation de 3 pas correspondant aux 3 directions et à la factorisation de l'équation.

5.2 Equations

Dans le repère orthonormé $OXYZ$, soit $\vec{V} = (U_\infty, 0, 0)$ la vitesse infini amont, $\hat{\varphi}$ le potentiel total et φ le potentiel de perturbation alors:

$$\hat{\phi}(X,Y,Z,T) = U_\infty X + \varphi(X,Y,Z,T)$$

Après adimensionnalisation des grandeurs physiques: grandeurs géométriques par une corde de référence C_0, grandeurs temporelles par $1/\omega$ avec ω fréquence et potentiels par $U_\infty C_0$, en notant $k = \omega C_0/U_\infty$ la fréquence réduite et $M_\infty = U_\infty/a$, le nombre de Mach de l'écoulement, la forme conservative de l'équation de conservation de la masse s'écrit en négligeant les termes non linéaires en $\partial/\partial y$ et $\partial/\partial z$:

$$div\,\vec{\mathbf{F}} = 0$$

avec

$$\vec{\mathbf{F}} = \begin{pmatrix} k(1-M_\infty^2\varphi_x) - k^2M_\infty^2\varphi_t \\ 1+(1-M_\infty^2)\varphi_x - kM_\infty^2\varphi_t - \frac{\lambda}{2}(\varphi_x)^2 \\ \varphi_y \\ \varphi_z \end{pmatrix} \qquad (23)$$

et

$$\lambda = [(\gamma+1)M_\infty^2 + 3(1-M_\infty^2)]M_\infty^2$$

où γ est l'indice adiabatique des gaz ($\gamma = 1.4$).

Soit $\vec{n} = (n_x, n_y, n_z)$ la normale temporelle à la surface aérodynamique, la condition limite sur le profil traduisant le fait que le débit à travers la paroi est nul s'écrit:

$$\vec{\mathbf{F}} \cdot \vec{n} = 0 \qquad (24)$$

Les conditions limites sur les frontières du domaine s'écrivent comme suit:

infini amont	:	$\varphi = 0$
infini aval	:	$\varphi_x = 0$
plancher-plafond	:	$\varphi_z = 0$
	ou	$\varphi_z + kM_\infty\varphi_t = 0$
emplanture	:	$\varphi_y = 0$
	ou	$\varphi = \varphi_0$ en instationnaire anti-symétrique
paroi latérale	:	$\varphi_y = 0$
sillage	:	$\varphi_z + k\varphi_t = 0$

Le coefficient de pression isentropique a pour expression :

$$-\frac{C_p}{2} = \frac{1-\rho^\gamma}{\gamma M_\infty^2}$$

L'expression retenue pour le coefficient de pression en fonction du potentiel de perturbation est :

$$-\frac{C_p}{2} = k\varphi_t + \varphi_x + \frac{(1-M_\infty^2)}{2}\varphi_x^2 + -kM_\infty^2\varphi_t\varphi_x - \frac{k^2M_\infty^2}{2}\varphi_t^2 - \frac{\lambda}{6}\varphi_x^3$$

5.3 Résolution

Après une transformation de cisaillement. $X = X(x,y), Y = y, Z = z$ telle que: $dx = CdX + fdY$, $dy = dY$, l'équation de conservation de la masse est discrétisée dans le temps à l'instant $(n+\frac{1}{2})\Delta t$. Elle peut se mettre sous la forme symbolique suivante après l'introduction de la fonction auxiliaire $\mathcal{Z} = k\frac{\partial\varphi}{\partial t}$:

$$\frac{2AC}{\Delta t^2}(\varphi^{n+1}-\varphi^n) + \frac{B}{\Delta t}\frac{\partial}{\partial X}(\varphi^{n+1}-\varphi^n) - D_{XX}(\frac{\varphi^{n+1}+\varphi^n}{2})$$

$$-A_{XY}(\frac{\varphi^{n+1}+\varphi^n}{2}) - C\frac{\partial^2}{\partial Z^2}(\frac{\varphi^{n+1}+\varphi^n}{2}) = \frac{BC}{\Delta t}\mathcal{Z}^n$$

avec $A = k^2M_\infty^2 \quad B = 2kM_\infty^2$

D_{XX} : opérateur transsonique non linéaire de dérivée en X

A_{XY} : opérateur linéaire de dérivée croisée en X et Y

Cet opérateur peut se scinder en deux parties :

A_1 contient uniquement les termes en $\frac{\partial}{\partial X}(\frac{f^2}{C}\frac{\partial}{\partial X})$ et A_2 contient le reste.

Une procédure numérique de directions alternées est utilisée pour résoudre cette équation en trois pas successifs.

Pas en X : calcul de la fonction intermédiaire $\tilde{\varphi}$

$$\frac{2AC}{\Delta t^2}(\tilde{\varphi}-\varphi^n) + \frac{B}{\Delta t}\frac{\partial}{\partial X}(\tilde{\varphi}-\varphi^n) - D_{XX}(\frac{\tilde{\varphi}+\varphi^n}{2})$$

$$-A_1(\frac{\tilde{\varphi}+\varphi^n}{2}) = \frac{B}{\Delta t}C\mathcal{Z}^n + A_2\varphi^n + C\frac{\partial^2\varphi^n}{\partial Z^2}$$

Pas en Y, Z qui se divise en deux pas:

Pas en Y calcul de ψ

$$\frac{2AC}{\Delta t^2}\psi + \frac{B}{\Delta t\Delta X}\psi - \frac{1}{2}A_2\psi = \frac{2AC}{\Delta t^2}(\tilde{\varphi}-\varphi^n) + \frac{B}{\Delta t}\frac{\partial\tilde{\varphi}}{\partial X} + \frac{B}{\Delta t\Delta X}(\varphi_{j-1}^{n+1}-\varphi_j^n)$$

Pas en Z calcul de φ^{n+1}

$$\frac{2AC}{\Delta t^2}(\varphi^{n+1}-\varphi^n) + \frac{B}{\Delta t\Delta X}(\varphi^{n+1}-\varphi^n)$$

$$-\frac{C}{2}\frac{\partial^2}{\partial Z^2}(\varphi^{n+1}-\varphi^n) = \frac{2AC}{\Delta t^2}\psi + \frac{B}{\Delta t\Delta X}\psi$$

Une fois ces trois pas d'espaces résolus, la fonction $\mathcal{Z}^n$ est réactualisée par:

$$\frac{\mathcal{Z}^{n+1}+\mathcal{Z}^n}{2} = \frac{k}{\Delta t}(\varphi^{n+1}-\varphi^n)$$

La condition aux limites sur l'aile est introduite dans le terme en $\partial/\partial Z^2$. Pour le couplage direct instationnaire, la détermination de l'état à l'instant $(n+1)$ par la méthode du point fixe décrite en 4-2 nécessite seulement un balayage en Y et Z sur le profil car la condition aux limites à l'instant $(n+1)$ n'apparait pas dans le pas en X.

THIS DOCUMENT PROVIDED BY THE ABBOTT AEROSPACE
TECHNICAL LIBRARY
ABBOTTAEROSPACE.COM

6. APPLICATIONS

6.1 Description

L'application porte sur un modèle de référence représentatif d'un avion de transport civil. Ce modèle est utilisé à l'ONERA en aéroélasticité pour tester les développements théoriques nouveaux ou étudier l'influence des modifications apportées à des méthodes numériques déjà existantes. Pour ce modèle, on dispose d'une matrice de flexibilité définie initialement sur une grille de points répartis sur l'aile, l'empennage, le fuselage et le réacteur. La base modale (masses généralisées, fréquences, déformées) a été déterminée numériquement et recalée par un essai de vibration au sol. Les différentes étapes de l'application présentée sont:

-détermination de la matrice de raideur.
-détermination de la base modale.
-couplage dans le domaine fréquentiel avec une méthode d'aérodynamique linéaire (doublets).
-couplage dans le domaine fréquentiel avec une méthode d'aérodynamique non linéaire (1^{er} harmonique PPT3D).
-couplage direct stationnaire.
-couplage direct instationnaire.

6.2 Couplage direct stationnaire

6.2.1 Modélisation statique de la structure

L'approximation statique de la voilure résulte d'un calcul par éléments finis. La matrice de flexibilité S est connue sur la grille schématisée figure 1. Elle vérifie la relation suivante:

$$S\,F = X \qquad (25)$$

où X est le champ de déplacements aux nœuds et F les forces correspondantes. Avant d'être introduite dans la séquence de couplage direct stationnaire, la matrice de flexibilité est transformée de la façon suivante:

-passage en matrice de raideur.
-condensation sur les noeuds situés sur l'aile où sont appliquées les forces aérodynamiques.
-projection sur une base de polynômes (polynômes de Legendre) permettant le passage de la grille aérodynamique à la grille structure.

La matrice de flexibilité n'est pas directement inversible. En effet le calcul de ses éléments caractéristiques fait apparaître une valeur propre nulle correspondant au point d'encastrement et un certain nombre de valeurs propres très petites traduisant des liaisons rigides entre certains points de la structure.

Soient λ_j une valeur propre de S et ϕ_j le vecteur propre associé, tel que $< \phi_i, \phi_j > = \delta_{ij}$, on peut écrire en notant $\bar{\phi}_j$ le vecteur transposé de ϕ_j:

$$S = \sum_{j=1}^{M} \lambda_j \phi_j \bar{\phi}_j + \sum_{j=M+1}^{N} \lambda_j \phi_j \bar{\phi}_j$$

où

M est le nombre de valeurs propres non nuls positives supérieures à une valeur μ,

N est le nombre total de valeurs propres correspondant au nombre de noeuds introduit.

L'expression $\mu = \lambda_{max}\,\varepsilon$ dans laquelle λ_{max} est la plus grande valeur propre et ε petit égal à 10^{-4} définit la borne inférieure des valeurs propres significatives.

On obtient alors une matrice de raideur K symétrique et définie positive par la relation:

$$K = \sum_{j=1}^{M} \frac{1}{\lambda_j} \phi_j \bar{\phi}_j + \sum_{j=M+1}^{N} \frac{1}{\mu} \phi_j \bar{\phi}_j \qquad (26)$$

On effectue alors les deux transformations suivantes:

- la condensation sur les points situés sur l'aile.
- la projection sur la base des polynômes de Legendre, le nombre de polynômes en corde étant égal à 2 et en envergure à 8.

On vérifie après ces transformations que, pour un champ de forces F donné, on obtient les mêmes champs de déplacements X par la relation (25) et la projection de (26).

6.2.2 Résultats

Le calcul du couplage direct stationnaire a été effectué pour 4 valeurs d'incidence i de l'aile: $i = -0,8;\ 0;\ 0,8;\ 1,5$ degré. Pour l'incidence de 1,5 degré, les déplacements du bord d'attaque et du bord de fuite et l'angle de dévrillage sont représentés en fonction de l'envergure figure 2. Pour une charge correspondant au poids de l'avion, à l'extrémité de l'aile le déplacement est de $0,80m$ et il apparait un dévrillage de 1.5 degrés.

Les coefficients de pressions stationnaires sont présentés figure 3 pour 4 sections situées à 30%, 50%, 70% et 90% de l'envergure avec et sans couplage fluide-structure. La prise en compte de la déformation statique se traduit par une diminution du ΔCp. Cet effet est plus sensible sur l'extrados surtout au niveau de la position du choc. L'influence est croissante lorsqu'on s'éloigne de l'emplanture, conséquence de la loi de dévrillage calculée.

Sur la figure 4, la portance par tranche est présentée en fonction de l'envergure avec et sans déformation statique. Sur cette même figure, la portance globale de l'aile pour ces deux cas de calcul est présentée en fonction de l'incidence. Il apparait une réduction de 13% de la portance globale de la voilure due à la prise en considération de la souplesse de celle-ci. Cependant, on peut constater des coefficients $C_{z\alpha}$ pratiquement constant.

6.3 Couplage direct instationnaire

6.3.1 Modélisation dynamique de la structure

La base modale retenue pour les calculs instationnaires de l'application présentée a été limitée aux 10 premiers modes symétriques de la structure dans la gamme de fréquences [1.6 Hz, 13. Hz]. Cette base modale est issue d'un calcul par éléments finis et recalée par un essai de vibration au sol.

6.3.2 Résultats méthode fréquentielle

Dans le but d'évaluer l'influence des non-linéarités aérodynamiques sur les résultats du flottement, les forces généralisées ont été calculées sur l'aile par:

- la méthode classique linéaire des doublets;
- la méthode des petites perturbations transsoniques.

La résolution de l'équation du flottement dans le domaine fréquentiel par la méthode du double balayage ou méthode "pk"[22] permet l'accès aux évolutions des fréquences et des amortissements aérodynamiques. Celles-ci sont présentées figure 7 en fonction de la masse volumique ρ. Dans le cas où les modes sont peu couplés (modes 3, 4, 5, 6, 10), les évolutions des fréquences et des amortissements sont comparables. L'influence des non-linéarités apparait nettement sur les autres modes et montre la nécessité de prendre en compte les effets aérodynamiques transsoniques. L'examen de ces planches révèle que les non-linéarités amplifient certains couplages (notamment couplage des modes 1 et 2, et couplage des modes 7, 8, 9).

THIS DOCUMENT PROVIDED BY THE ABBOTT AEROSPACE
TECHNICAL LIBRARY
ABBOTTAEROSPACE.COM

6.3.3 Résultats couplage direct

Les résultats numériques sont présentés pour un nombre de Mach de 0.82 et une incidence de 1.5 degrés. La fréquence d'échantillonnage correspond à $k = \frac{\omega}{V} = 0.045$, ce qui donne 100 points par période pour une fréquence de 2 Hz et 15 points pour le mode le plus élevé à 13 Hz. Les évolutions des coordonnées généralisées en fonction du temps (nombre de pas de temps) sont présentées figures 5 et 6 pour les 8 modes les plus représentatifs de l'avion et pour une condition de masse volumique. L'analyse visuelle de cette évolution montre un comportement régulier des modes 3 et 6 et l'absence de couplage de ces modes avec d'autres. Il n'en est pas de même pour les autres modes. A ce niveau, on peut également constater l'absence d'instabilité aéroélastique.

L'analyse des signaux temporels est réalisée par les deux méthodes décrites en 4.3.

L'analyse de la réponse en déplacement $z(P,t)$ sur un ensemble de points P de la structure par la méthode de Prony permet de définir les paramètres caractéristiques de stabilité c'est-à-dire la fréquence et l'amortissement réduit pour chaque mode (f_k, α_k). Les résultats obtenus sont présentés figure 8. Dans cette approche, le choix de la solution finale présente des difficultés du fait de la dispersion des résultats plus particulièrement dans le cas où les modes intervenant dans l'analyse sont nombreux. L'analyse de chaque composante du vecteur $q(t)$ pose également quelques problèmes. L'approximation par une seule exponentielle comme dans le cas du mode isolé ne met pas en évidence la contribution des autres modes et l'approximation par plusieurs exponentielles pour chaque coordonnée généralisée met en évidence le phénomène décrit précédemment c'est-à-dire la dispersion des solutions.

C'est pourquoi, une analyse de Fourier de la réponse temporelle et un lissage par fraction rationnelle de la réponse fréquentielle ont été mis en œuvre. Dans cette approche, une transformée de Fourier $\widehat{q}_k(\omega)$ de chaque coordonnée $q_k(t)$ est effectuée. Celle-ci permet de suivre coordonnée par coordonnée l'évolution des résonances et par conséquent elle permet de mettre en évidence les éventuels couplages. Le lissage des signaux obtenus en isolant ou en regroupant certaines coordonnées généralisées par des fractions rationnelles donne accès aux paramètres caractéristiques du flottement. L'évolution des fréquences propres et des amortissements aérodynamiques est présentée en fonction de la masse volumique figure 8. Un critère de continuité locale de la solution permet de suivre cette évolution et ceci même dans le cas de fréquence propre double avec amortissements distincts.

6.4 Temps de calcul

Le maillage aérodynamique pour cette application est le suivant:

en X : 78 points dont 36 sur la voilure.

en Y : 28 points dont 19 sur la voilure.

en Z : 53 points dont 26 de part et d'autre de la coupure.

La place mémoire requise pour cette application est de 800 000 mots.

Le calcul stationnaire avec couplage statique convergé (résidus quadratiques moyens sur les gradients de potentiels inférieurs à 10^{-6}) est obtenu en 285 itérations pour un temps de calcul de 129 secondes sur CRAY-XMP.

Le calcul instationnaire avec couplage direct nécessite en moyenne 4 tours de point fixe. Ceci représente un temps de calcul de 365 secondes pour une valeur de ρ et 500 itérations temporelles.

Le gain apportée au niveau du temps de calcul par la méthode de couplage direct en instationnaire est estimé à un facteur équivalent au nombre de modes divisé par deux.

7. CONCLUSION

La prise en compte des non-linéarités aérodynamiques dans le domaine transsonique est nécessaire. La prévision du flottement par la méthode du premier harmonique ne semble pas suffisante dans les cas où les non-linéarités sont importantes.

La méthode de couplage direct permet la prise en compte de la déformée statique en stationnaire et la résolution du système couplé fluide-structure dans le domaine temporel en instationnaire. Elle donne accès directement aux paramètres de la prévision de la stabilité aéroélastique et ceci avec des gains de temps de calculs très appréciables. La mise en œuvre de la méthode (algorithmes de résolution, conditions initiales, traitements numériques des signaux temporels de sorties) a été validée au travers d'applications en utilisant comme solveur aérodynamique la résolution de l'équation des petites perturbations transsoniques tridimensionnelles par une méthode implicite de directions alternées. Le couplage direct utilisant un solveur aérodynamique basé sur la résolution des équations d'Euler en maillage non structuré fait l'objet actuellement de travaux à l'ONERA.

THIS DOCUMENT PROVIDED BY THE ABBOTT AEROSPACE
TECHNICAL LIBRARY
ABBOTTAEROSPACE.COM

REFERENCES

[1] W.F. Ballhaus and P.M. Goorjian : "Computation of Unsteady Transonic Flows by the Indicial Method". AIAA Journal, Vol. 16, Feb. 1978, p. 117-124.

[2] D.P. Rizzeta : "Time-Dependant Responses of a Two-dimensional Transonic Airfoil in Transonic Flow". AIAA Journal, Vol. 17, Jan. 1979, p. 26-32.

[3] C. Caretta, M. Couston, and J.J. Angelini : "Simultaneous Resolution of Aerodynamic and Aeroelastic Equations of Motion for Transonic of Motion for Transonic Two-Dimensional Airfoils". International Conference on Numerical Methods for Coupled Problems, Swansea, U.K., Sept. 1981.

[4] P. Guruswamy and T.Y. Yang : "Aeroelastic Time Response Analysis of Thin Airfoils by Transonic Code LTRAN2". Computers and Fluids, Vol. 9, Dec. 1981, p. 409-425.

[5] T.Y. Yang and J.T. Batina : "Transonic Time-Response Analysis of 3-Degree-of-Freedom Conventional and Supercritical Airfoils". Journal of Aircraft, Vol. 20, No 8, Aug. 1983, p. 703-710.

[6] G.P. Guruswamy and P.M. Goorjian : "Computations and Aeroelastic Applications of Unsteady Transonic Aerodynamics about Wings ". Journal of Aircraft, Vol.21, No 1, Jan. 1984, p. 37-43.

[7] G.P. Guruswamy P.M. Goorjian and E.L. Tu : "Transonic Aeroelasticity of Wings with Tip Stores". Journal of Aircraft, Vol.24, No 10, Oct. 1987, p. 688-695 and AIAA Paper-86-1007.

[8] R.M. Bennet, J.T. Batina and H.J. Cunningham : "Wing Flutter Calculations with the CAP-TSD Unsteady Transonic Small-Disturbance Program". Journal of Aircraft, Vol.26, No 9, Sept. 1989, p. 876-882.

[9] W.F. Ballhaus, P.M. Goorjian : "Implicit Difference Computations of Unsteady Transonic about Airfoil in Transonic Flow". AIAA Paper 77-205, Jan. 1977.

[10] G.P. Guruswamy P.M. Goorjian and E.L. Tu : "Unsteady Transonics of a Wing with Tip Store ". Journal of Aircraft, Vol.23, No 8, Aug. 1986, p. 662-668 and AIAA Paper-86-0010.

[11] J.T. Batina : "Efficient algorithm for Solution of the Unsteady Transonic Small-Disturbance Equation". Journal of Aircraft, Vol.25, No 7, July 1988, p. 598-605.

[12] G.D. Mortchelewicz : "Résolution des équations d'-Euler instationnaire en maillage non structuré." La Recherche Aérospatiale 1989-6, p. 1-16.

[13] G.D. Mortchelewicz and A.S. Sens : "Solution of 3-D Euler Equations with Unstructured Meshes for Aeroelasticity Problems." International Symposium on Aeroelasticity and Structural Dynamics, Aachen (Germany), 3-6 June 1991 and TP Onera No 1991-62.

[14] D.M. Schuster, J. Vadyak and E. Atta : "Static Aeroelastic Analysis of Fighter Aircraft Using a Three Dimensional Navier-Stokes Algorithm ". Journal of Aircraft, Vol.27 No 9, Sep. 1990, p. 820-825.

[15] M. Couston and J.J. Angelini : "Solution of Nonsteady Two-dimensional Transonic Small Disturbances Potential Flow Equation". ASME Journal of Fluids Engineering, Vol. 101, No 3-1979, p. 431-437.

[16] P. Mulak, J.L. Meurzec and J.J. Angelini : "Extension of the Transonic Perturbation Approach to Three-Dimensional Problems". International Symposium on Aeroelasticity, Nuremberg 5-7 oct. 1981.

[17] P. Mulak, J.L. Meurzec and J.J. Angelini : "Extension and use of a Numerical Procedure for Three-Dimensional Unsteady Transonic Flows". Second International Symposium on Aeroelasticity and Structural Dynamics, Aachen (Germany), 1-3 Apr. 1985.

[18] J.P. Grisval et J.L. Meurzec : "Couplage Direct Fluide Structure en Aérodynamique Transsonique". 27e Colloque d'Aéodynamique Appliquée. Marseille (France), 15-17 Oct. 1990 and TP Onera No 1990-165.

[19] B. Darras : "Identification de système vibrant par la méthode du décrément aléatoire". Revue Française de Mécanique No 58-59, p. 21-27, 1976.

[20] C.L. Keller : "Determination of Complex Exponentials, Least Squares and Predictions Methods". Air Force Wright Aeronautical Laboratories. AFWAL-TR-88-3042, Febr. 1988.

[21] R. Dat : "Détermination des caractéristiques dynamiques d'une structure par analyse de ses fonctions de transfert". Revue Française de Mécanique No 58-59, 1976.

[22] R. Dat, J.L. Meurzec : "Sur les calculs de flottement par la méthode dite du 'balayage en fréquence réduite'". La Recherche Aérospatiale No 133, Nov. Dec. 1969.

THIS DOCUMENT PROVIDED BY THE ABBOTT AEROSPACE
TECHNICAL LIBRARY
ABBOTTAEROSPACE.COM

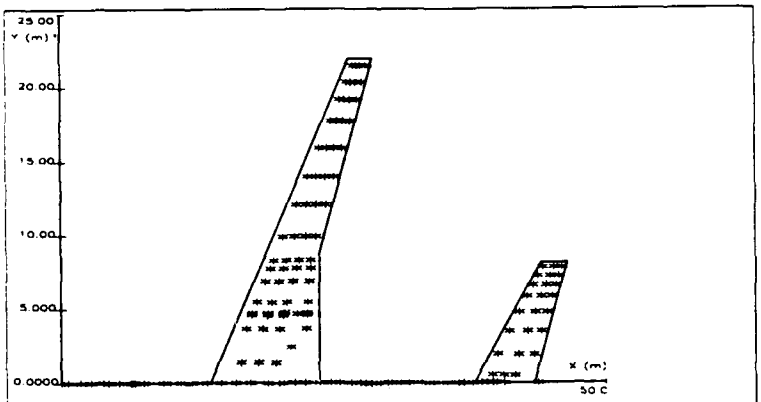


Fig. 1 — GRILLE MASSIQUE

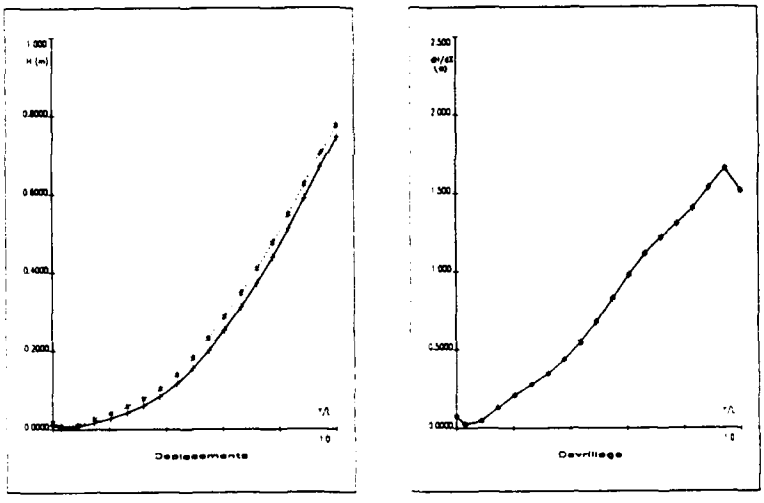
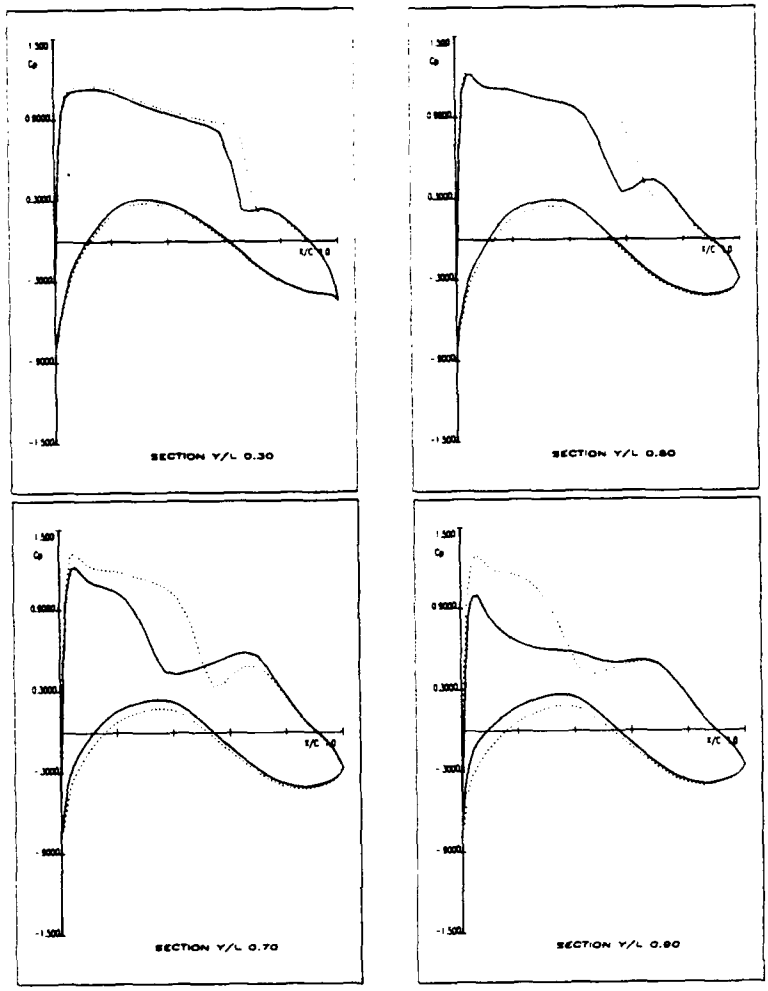


Fig. 2 — Deformation statique de la Voilure

Mach=.820 Alpha=+1.5 degre

THIS DOCUMENT PROVIDED BY THE ABBOTT AEROSPACE
TECHNICAL LIBRARY
ABBOTTAEROSPACE.COM

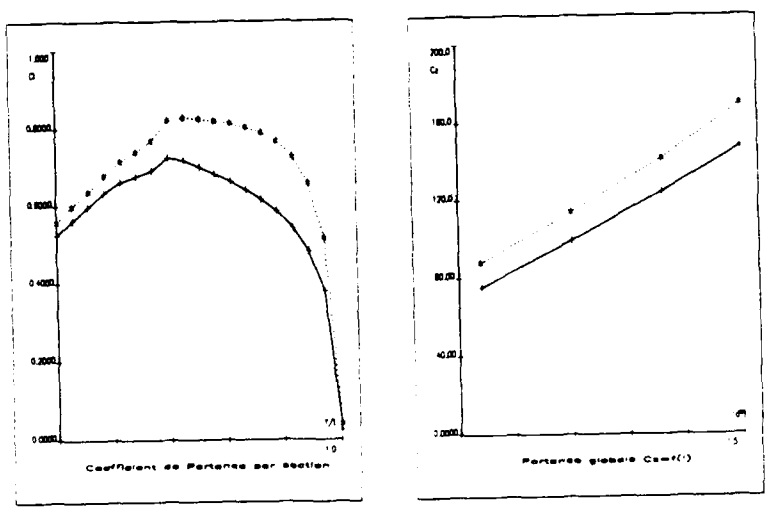


.. Sans déformation statique

— Avec déformation statique

Fig. 3 — Distribution des Pressions Stationnaires sur la Voilure

Mach = .82 Incidence 1.5 degre



✱ Sans déformation statique

+ Avec déformation statique

Fig. 4 — Portance de la Voilure

Mach=.820

THIS DOCUMENT PROVIDED BY THE ABBOTT AEROSPACE
TECHNICAL LIBRARY
ABBOTTAEROSPACE.COM

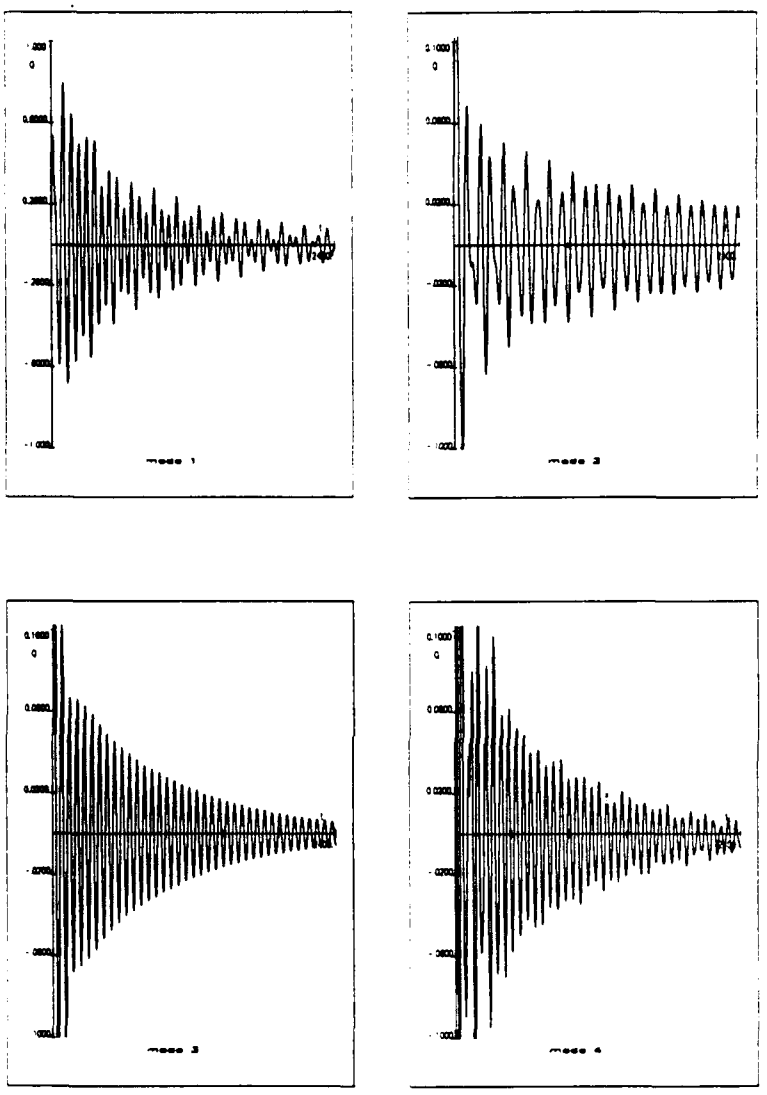


Fig. 5 — Evolution des coordonnees generalisees
en fonction du temps
Mach=.82 Incidence +1.5 degre
QO=47958. Ro=1.226

THIS DOCUMENT PROVIDED BY THE ABBOTT AEROSPACE
TECHNICAL LIBRARY
ABBOTTAEROSPACE.COM

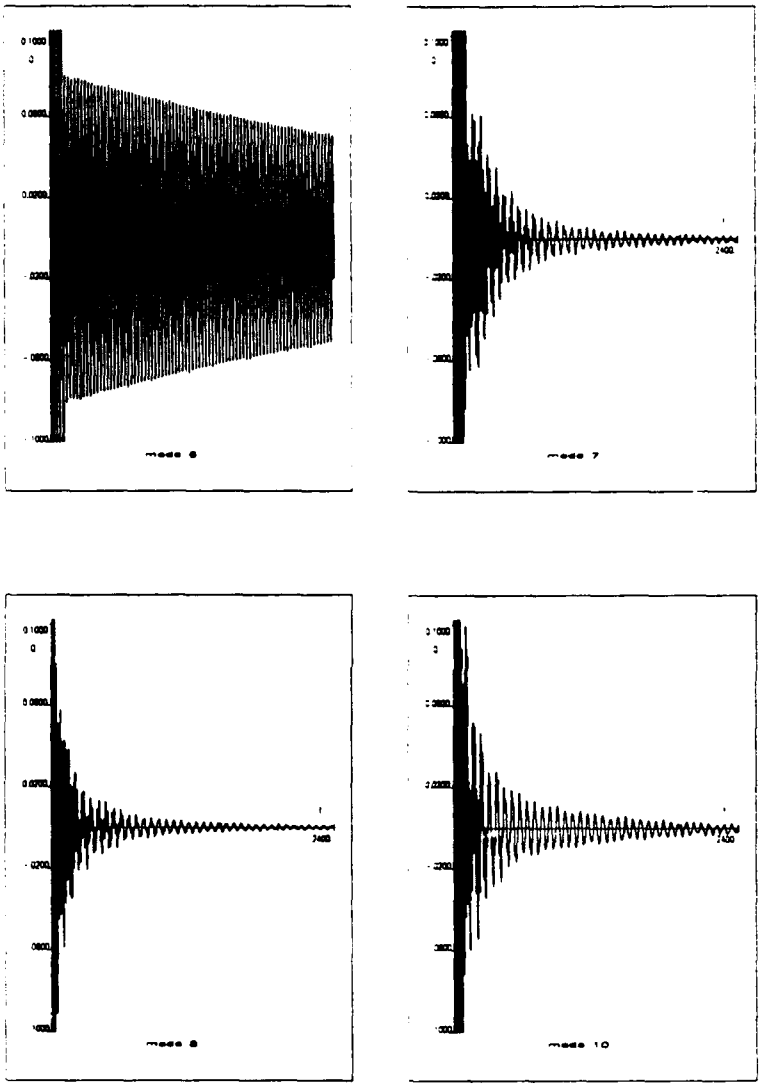


Fig. 6 — Evolution des coordonnees generalisees
en fonction du temps
Mach=.82 Incidence +1.5 degre
Q0=47958. Ro=1.226

THIS DOCUMENT PROVIDED BY THE ABBOTT AEROSPACE
TECHNICAL LIBRARY
ABBOTTAEROSPACE.COM

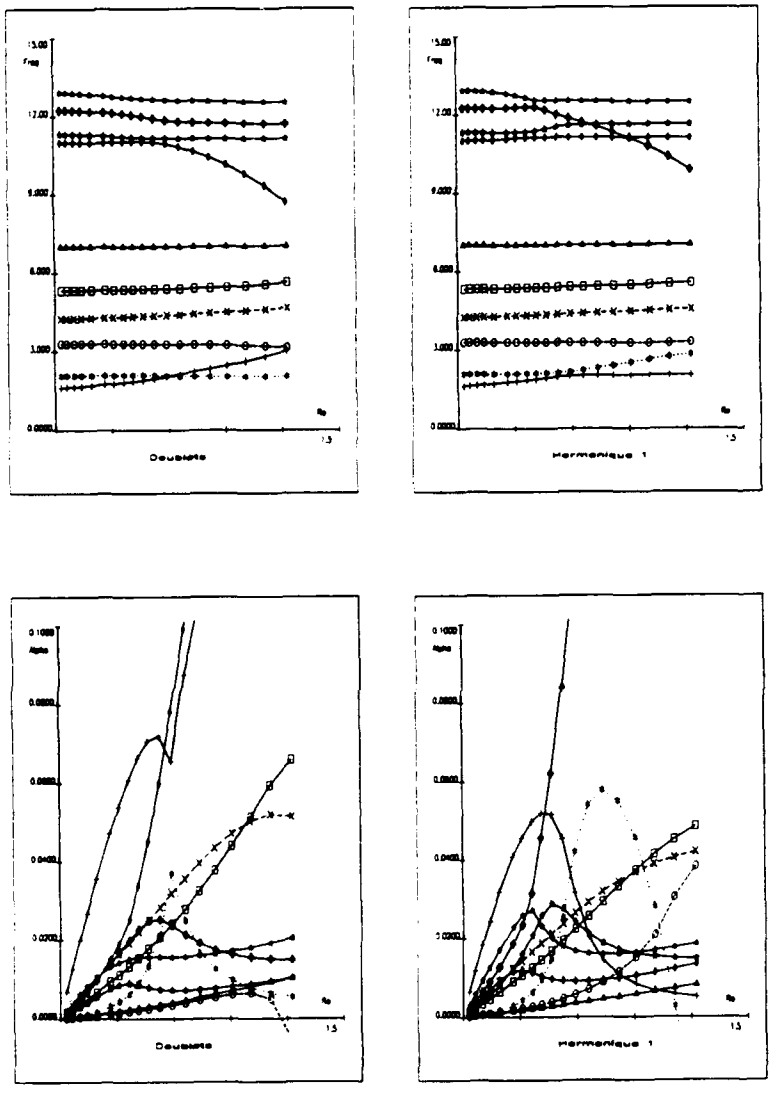


Fig. 7 – Evolution des frequences et des amortissements
par la methode frequentielle
en fonction de la masse volumique
Mach = .82 incidence 1.5 degre

THIS DOCUMENT PROVIDED BY THE ABBOTT AEROSPACE
TECHNICAL LIBRARY
ABBOTTAEROSPACE.COM

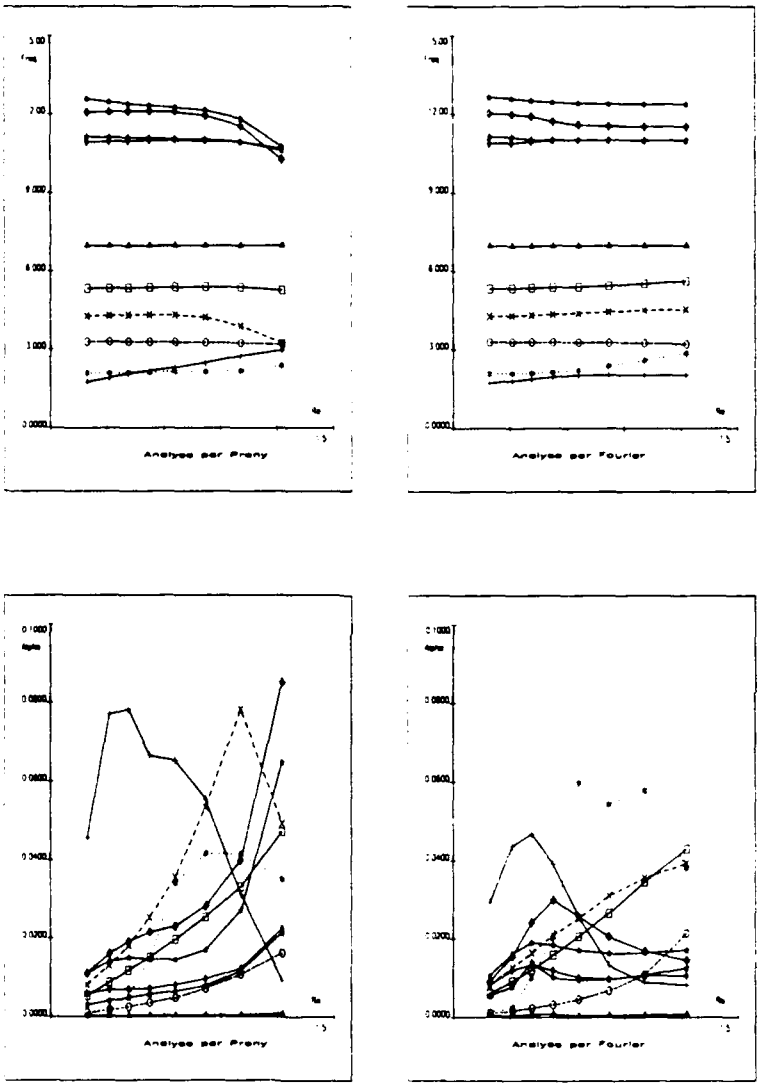


Fig. 8 — Evolution des fréquences et des amortissements
par COUPLAGE DIRECT
en fonction de la masse volumique
Mach = .82 incidence 1.5 degré

THIS DOCUMENT PROVIDED BY THE ABBOTT AEROSPACE
TECHNICAL LIBRARY
ABBOTTAEROSPACE.COM

AD-P007 811

INVESTIGATION OF THE AEROELASTIC STABILITY OF THE AFW WIND-TUNNEL MODEL USING CAP-TSD

Walter A. Silva and Robert M. Bennett
Unsteady Aerodynamics Branch
NASA Langley Research Center
Hampton, VA 23665-5225

1. SUMMARY

The CAP-TSD (Computational Aeroelasticity Program - Transonic Small Disturbance) code, developed at the NASA - Langley Research Center, is applied to the Active Flexible Wing (AFW) wind-tunnel model for prediction of the model's transonic aeroelastic behavior. A semi-span computational model is used for evaluation of symmetric motions and a full-span model is used for evaluation of antisymmetric motions. Static aeroelastic solutions using CAP-TSD are computed. Dynamic (flutter) analyses are then performed as perturbations about the static aeroelastic deformations and presented as flutter boundaries in terms of Mach number and dynamic pressure. Flutter boundaries that take into account modal refinements, vorticity and entropy corrections, antisymmetric motions and sensitivity to the modeling of the wing tip ballast stores are also presented and compared with experimental flutter results.

2. INTRODUCTION

An understanding of the aeroelastic behavior of flight vehicles in the transonic regime is of great importance for flight safety. For example, it is well known that aircraft flying into or through the transonic regime may encounter a region of reduced flutter speed known as the transonic flutter dip. Valuable insight into the nature of this transonic flutter dip phenomena is provided by Isogai[1] for a typical, two-dimensional streamwise section of an aft-swept wing, while comparison of aerodynamic theory with the experiments reported by Davis and Malcolm[2] reveals the limitations of linear theory when applied in the transonic regime. Linear aerodynamics, although highly successful in the subsonic and supersonic regimes, cannot normally be used to accurately predict transonic aeroelastic behavior. Transonic flow equations capable of modelling flow nonlinearities (shocks, boundary layer, separation and vorticity) and boundary condition nonlinearities (airfoil thickness and shape, and large deflections) must then be solved. The surveys by Edwards and Thomas[3] and Ballhaus and Bridgeman[4] review recent computational developments in the field of transonic aeroelasticity. Some of these developments include modelling of the Navier-Stokes equations[5] and the Euler equations[6] for flutter analysis. Application of these higher order formulations, however, has primarily been limited to two-dimensional configurations, due to the large computational costs incurred. Certain assumptions regarding the flow can be made to yield reduced order formulations such as the full-potential equation[7] and the computationally efficient transonic small-disturbance (TSD) equation. Research efforts involving the TSD formulation include the development of the XTRAN3S code[8], the work by Yang, Guruswamy, and Striz[9], and many others.

A transonic aerodynamics code known as CAP-TSD (Computational Aeroelasticity Program-Transonic Small Disturbance) has been developed at the NASA - Langley Research Center (LaRC). CAP-TSD is capable of handling multiple lifting surfaces with control surfaces, bodies (nacelles, pylons, stores), vertical surfaces, and a fuselage, and solves the TSD equation using an efficient approximate factorization scheme[10]. References 11-12 verified the code's ability to accurately predict steady and unsteady pressures for wings and configurations at subsonic, transonic, and supersonic Mach numbers. Flutter prediction using CAP-TSD for two thin, swept-and-tapered wings compared well with experimental flutter results[13].

The goal of the present study was to update the transonic aeroelastic analysis of the Active Flexible Wing (AFW) wind-tunnel model[14,15] that was reported in Ref. 16. The Active Flexible Wing (Fig. 1) model is a full-span, sting-mounted wind-tunnel model designed and built by the Rockwell International Corporation. The main goal of the AFW project was to design, implement and validate digital control laws for flutter suppression[14] with simultaneous roll maneuvers with load alleviation. Knowledge of possible regions of instability was, therefore, crucial.

This paper first presents the computational procedures incorporated in CAP-TSD. This includes a brief description of the TSD formulation and the coupled aerodynamic and structural equations of motion that are integrated in time. These equations are used for both static aeroelastic and dynamic analyses of the AFW. An important conclusion of the studies by Yates, Wynne, and Farmer[17] and Yates and Chu[18] was that the accuracy of the transonic flutter prediction is highly dependent on the

92-16049

THIS DOCUMENT PROVIDED BY THE ABBOTT AEROSPACE
TECHNICAL LIBRARY
ABBOTTAEROSPACE.COM



Figure 1 The AFW in NASA-LaRC's Transonic Dynamics Tunnel (TDT).

accuracy of the static aeroelastic state of the wing. As a result, a procedure for computing static aeroelastic deformations[16] is applied to the AFW computational model. The dynamic behavior is computed as a perturbation about previously computed static aeroelastic solutions. The resultant dynamic time histories of the generalized displacements are then analyzed using a modal identification technique to estimate the stability parameters (damping and frequency) of the system at a given Mach number and dynamic pressure. Dynamic results are presented in the form of flutter boundaries, in terms of Mach number and flutter dynamic pressure. Flutter boundaries that account for a corrected modeling of the wing tip ballast store of the AFW, an updated set of mode shapes and frequencies, vorticity and entropy corrections, and a subsonic antisymmetric flutter result are presented and compared with experimental flutter results.

3. COMPUTATIONAL PROCEDURES

In this section, an overview of the computational procedures is presented including a description of the CAP-TSD program, the aeroelastic equations of motion, the time-marching solution of these equations, and the modal identification of the resulting free decay transients.

3.1 CAP-TSD Program

The CAP-TSD program is a finite-difference program which solves the general-frequency modified transonic small-disturbance (TSD) equation. The TSD potential equation is defined by

$$M_\infty^2 (\phi_t + 2\phi_x)_t = [(1 - M_\infty^2)\phi_x + F\phi_x^2 + G\phi_y^2]_x + (\phi_y + H\phi_x\phi_y)_y + (\phi_z)_z \qquad (1)$$

where M_∞ is the freestream Mach number, ϕ is the disturbance velocity potential, and the subscripts of ϕ represent partial derivatives.

Several choices are available for the coefficients F, G, and H depending upon the assumptions used in deriving the TSD equation. For transonic applications, the coefficients are herein defined as

$$F = -\frac{1}{2}(\gamma + 1) M_\infty^2,$$

$$G = \frac{1}{2}(\gamma - 3) M_\infty^2,$$

$$H = -(\gamma - 1) M_\infty^2 \qquad (2)$$

where γ is the ratio of specific heats. The linear potential equation is recovered by simply setting F, G, and H equal to zero.

Equation (1) is solved within CAP-TSD by a time-accurate approximate factorization (AF) algorithm developed by Batina[10]. In Refs. 11 to 13, the AF algorithm was shown to be efficient for application to steady or unsteady transonic flow problems. It can provide accurate solutions in only several hundred time steps yielding a significant computational cost savings when compared to alternative methods. Several algorithm modifications have been made which improve the stability of the AF algorithm and the accuracy of the results[19,20]. One of these improvements is the option to include vorticity and entropy corrections[20] for improved shock modelling. The effect of these corrections on the transonic flutter boundary of the AFW model is investigated and presented in a subsequent section of this paper.

The CAP-TSD program can treat configurations with combinations of lifting surfaces and bodies including canard, wing, tail, control surfaces, tip launchers, pylons, fuselage, stores, and nacelles. The configuration capability of the current version of CAP-TSD permits the calculation of pressures on the fuselage and bodies. In the version of CAP-TSD used in this study, modal perturbations of the fuselage and bodies are not included in the boundary conditions and the integration of the pressures on the fuselage and bodies (for computation of the generalized aerodynamic forces) is not included in the aeroelastic solution. However, the aerodynamic influence of both the fuselage and wing tip body of the AFW model are included as interference effects upon the wing pressures.

3.2 Equations of Motion

The aeroelastic equations of motion are based on a right-hand orthogonal coordinate system with the x-direction defined as positive downstream, y-direction positive out the right wing, and the z-direction positive upward. The equations of motion may be written as

$$M\ddot{q} + C\dot{q} + Kq = Q \qquad (3)$$

THIS DOCUMENT PROVIDED BY THE ABBOTT AEROSPACE
TECHNICAL LIBRARY
ABBOTTAEROSPACE.COM

where q is a vector of generalized displacements, M is the generalized mass matrix, C is the generalized damping matrix, and K is the generalized stiffness matrix. Q is the vector of generalized forces where its elements are defined by

$$Q_i = \frac{\rho U^2}{2} c_r^2 \int_s \frac{\Delta p\, h_i}{\rho U^2/2} \frac{dS}{c_r^2}$$

and Δp is the lifting pressure, ρ is the fluid density, c_r is the root chord, U is the freestream velocity, S is the area of the lifting surface(s) and h_i is the vibration mode shape. Equation (3) is rewritten as

$$\ddot{q} = -M^{-1} Kq - M^{-1} C\dot{q} + M^{-1} Q \qquad (4)$$

to permit integration of the equation with respect to time.

3.3 Time-Marching Aeroelastic Solution

The aeroelastic solution procedure implemented within CAP-TSD for integrating Eq. (4) is similar to that described by Edwards, Bennett, Whitlow, and Seidel[21]. Equation (4) is composed of normal mode equations which may be expressed in linear, first-order state-space form as

$$\dot{x}_i = Ax_i + Bu_i \qquad (5)$$

where

$$x_i = [\, q_i \;\; \dot{q}_i \,]^T$$

and

$$A = \begin{bmatrix} 0 & 1 \\ -m_i^{-1} k_i & -m_i^{-1} c_i \end{bmatrix}$$

$$B = m_i^{-1} \frac{\rho U^2}{2} c_r^2 \begin{bmatrix} 0 \\ 1 \end{bmatrix}$$

$$u_i = \int_s \Delta C_p\, h_i\, dS/c_r^2$$

$$\Delta C_p = \frac{\Delta p}{\rho U^2/2}$$

In these definitions, m_i, c_i, and k_i are elements of the mass, damping, and stiffness matrices, respectively, corresponding to mode i. The analytical solution to Eq. (5) and a description of its numerical implementation in CAP-TSD is found in Refs. 13 and 21.

For aeroelastic analysis, two steps are generally required in performing the calculations. In the first step, the steady-state flow field is calculated to account for wing thickness, camber, mean angle of attack, and static aeroelastic deformation, thus providing the starting flow field for the dynamic aeroelastic analysis. Previously published CAP-TSD flutter studies analyzed only symmetric airfoils at zero angle of attack[13], thereby avoiding the problem of static aeroelastic deformations. For the AFW, the airfoil sections are not symmetric and are rigged at a non-zero angle of attack, so a procedure for computing static aeroelastic solutions had to be developed before an accurate dynamic analysis could be performed. The dynamic analysis would then be a perturbation about a converged static aeroelastic solution at each Mach number and dynamic pressure of interest.

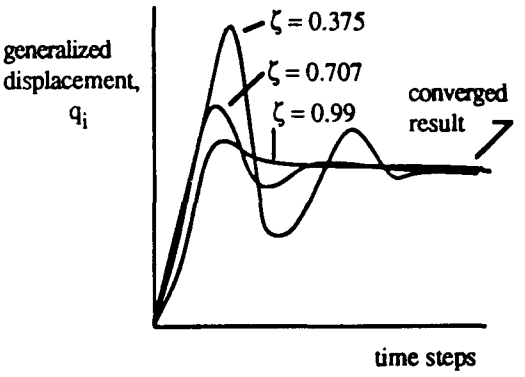
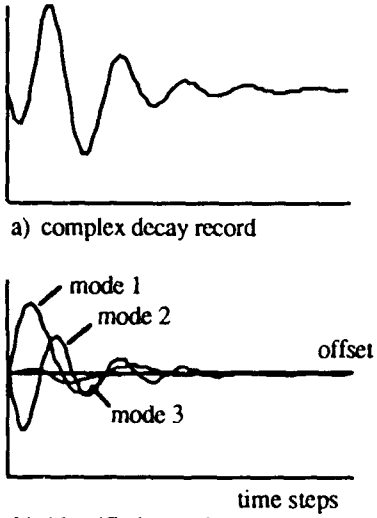


Fig. 2 Convergence of generalized displacements for different values of viscous damping.

The procedure developed[16] and applied in this study for computing static aeroelastic deformations is to allow the structure and aerodynamics to interact with no initial excitation (no initial deflection or velocity) and with a large value of viscous damping to prevent divergence of the solution. This method resulted in convergence of the generalized displacements. Static aeroelastic deformations should be independent of viscous damping and so different values of viscous damping (ζ=.375, .707, and .99) were evaluated. A typical result for this type of analysis is presented in Fig. 2, which shows a representative variation of a generalized displacement as a function of computational time steps for the three values of viscous damping. It is clear from Fig. 2 that the convergence is indeed independent of the value of viscous damping. Furthermore, the larger the value of viscous damping, the faster the convergence. Therefore, the highest value of viscous damping (ζ = 0.99) was used in order to accelerate the static aeroelastic solution. For the applications presented herein, 2000- 4000 time steps were used to converge the static aeroelastic solutions. An interesting result of this procedure was that it allowed the computation of static aeroelastic deformations at dynamic pressures above the flutter dynamic pressure for the AFW.

THIS DOCUMENT PROVIDED BY THE ABBOTT AEROSPACE
TECHNICAL LIBRARY
ABBOTTAEROSPACE.COM

Once converged static aeroelastic solutions were computed, the next step was to prescribe an initial disturbance to begin the dynamic structural integration. Disturbance (or modal) velocities in the first three modes were used as initial perturbations. About 7 cycles of the lowest frequency (first) mode were needed for accurate modal identification. For a constant, non-dimensional time step of .01, this required 8000 time steps. In determining a flutter point, the freestream Mach number, M_∞, and the associated freestream speed, U, were held fixed. A value of the dynamic pressure $\rho U^2/2$ is then used and free decay transients are computed. These resulting transients of the generalized coordinates are analyzed for their content of damped or growing sine-waves, with the rates of growth or decay indicating whether the dynamic pressure is above or below the flutter value. This analysis then indicates whether to increase or decrease the value of dynamic pressure in subsequent runs to determine a neutrally stable result.



a) complex decay record

b) identified modal components and offset

Fig. 3 Example of dynamic decay record and its modal components.

3.4 Modal Identification

As previously mentioned, CAP-TSD generates free decay transients that must be analyzed for the modal stability characteristics. A typical transient for the AFW model, calculated using CAP-TSD is shown in Fig. 3(a). The first three modes used in the analysis were excited by specifying an initial condition for each modal velocity to produce a complex decay record. This record is analyzed using a least-squares curve-fit of the response data with complex exponential functions. The program utilized is a derivative of the one described in Ref. 22. The components of the transient of Fig. 3(a) are plotted in Fig. 3(b) to the same scale. The free decay properties of each mode for this condition are readily apparent and the mean or offset value is the static aeroelastic deformation of the mode being analyzed. A sufficient range of dynamic pressure must be considered to determine all relevant flutter points.

4. ANALYSIS AND RESULTS

4.1 CAP-TSD Computational Model

The AFW geometry data was obtained from Rockwell International, including detailed airfoil shape information. From this geometry data two computational models of the AFW were generated. A half-span model, with symmetry specified at the centerline, was used for symmetric analyses and a full-span model was used for antisymmetric analyses. Both computational models consist of a fuselage, the addition of the region aft of the main wing and next to the fuselage referred to as the coat-tail, the main wing(s) with all four control surfaces per wing, and the wing tip ballast store(s). The grid dimensions for the half-span model are 134x51x62 in the x-, y-, and z-directions respectively for a total of 423,708 grid points. The grid extends 10 root chords upstream, 10 root chords downstream, 2 semi-span lengths in the y-direction, and 10 root chords in the positive and negative z-direction. The full-span grid is dimensioned 134x101x62 grid points in the x-, y-, and z-directions (839,108 grid points). The wind-tunnel sting mount is modeled by extending the computational fuselage aft to the downstream boundary of the grid. The grid density is increased in regions where large changes in the flow are expected, such as at the leading edge, trailing edge, wing tip, and control-surface sides and hinge lines. The four control surfaces per wing are the leading-edge inboard (LEI), leading-edge outboard (LEO), trailing-edge inboard (TEI), and trailing-edge outboard (TEO). Each control surface has a chord that is 25% of the local chord and a span that is 28% of the semi-span. The airfoil definition includes the control surface actuator bumps on the outboard half of the wing. There are slight surface discontinuities on the wind-tunnel model where the wing box and control surfaces meet (at the quarter- and three-quarter chord). These discontinuities

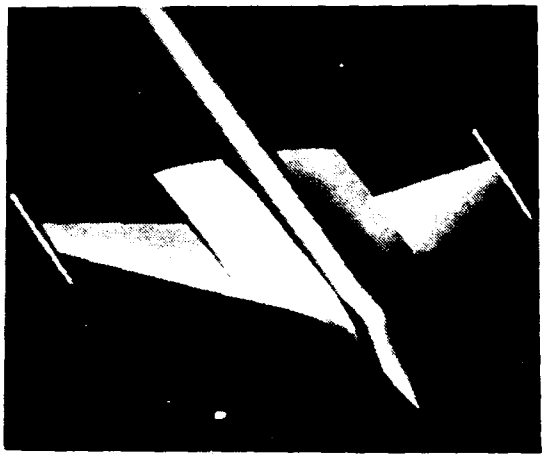


Fig. 4 CAP-TSD computational model of the AFW.

THIS DOCUMENT PROVIDED BY THE ABBOTT AEROSPACE
TECHNICAL LIBRARY
ABBOTTAEROSPACE.COM

are not included in the analytical model because of potential numerical difficulties. The effect of the actuator bumps and the control surface/wing box discontinuities on the measured and computed static pressure distributions will be presented in a subsequent section. A computer-generated picture of the CAP-TSD model of the AFW is shown in Fig. 4. Although not shown in the figure, a protrusion on the underside of the fuselage that houses the model's pitch actuator is also included in the analytical model.

Analytical modes and frequencies were obtained from a finite-element model, that includes the mass of the tip ballast store, and separated into symmetric and antisymmetric modal data sets. The flutter analyses of Ref. 16 were performed using analytical mode shapes with measured frequencies (ground vibration test). The symmetric data was shown by linear analysis[14] to be the most flutter critical in the higher, subsonic Mach number regime and so only symmetric motions were analyzed in Ref. 16 using the semi-span model. Since then, an updated set of symmetric and antisymmetric mode shapes have been generated based on experimental data. These updated mode shapes are defined at a denser set of structural node points for improved accuracy in the interpolation procedure. The interpolation of mode shape displacements and slopes at the computational grid points is done via a surface spline[23]. Each structural section was splined separately and then recombined to form the necessary input to CAP-TSD. The separate structural sections are the wing box, coat-tail, and the four control surfaces. Slender bodies such as the fuselage and tip ballast store are not given any modal definition in CAP-TSD, as was previously mentioned, therefore no modal data were needed for these components.

4.2 Static Aeroelastic Results

The accuracy of the static aeroelastic solution was investigated in Ref. 16 by comparing analytical results, using the original set of symmetric mode shapes, with existing experimental data. Two sets of experimental data from previous AFW tests in a heavy gas were used for this purpose. These data included : 1) pressure coefficient distributions and 2) control-surface effectiveness parameters. In Ref. 16, by comparing calculated and experimental pressure distributions at a chosen Mach number and dynamic pressure, it was concluded that the static aeroelastic procedure provided reasonable estimates of the static aeroelastic deformation of the AFW using the original set of mode shapes. It was also concluded that comparisons between the calculated and experimental control surface effectiveness parameters were qualitatively reasonable but were deficient quantitatively due to the lack of viscous effects in the CAP-TSD model. Therefore, in the present study, the accuracy of the static aeroelastic procedure is not reassessed, but instead only a comparison of calculated pressure distributions using the updated set of mode shapes and the experimental pressure distributions is presented. It should be mentioned that the AFW configuration for these previous tests did not include the tip ballast store used in the recent test so that in order for the CAP-TSD calculations to compare with the earlier experiments, the tip ballast store was deleted from the computational model and the tip fairing was added.

4.2.1 *Pressure distributions*

Figure 5 presents pressure coefficient distributions versus percent chord for CAP-TSD with the updated set of mode shapes and experiment at M = 0.9 and a dynamic pressure, q, of 150 psf (7.18 kPa) at the three spanwise stations shown.

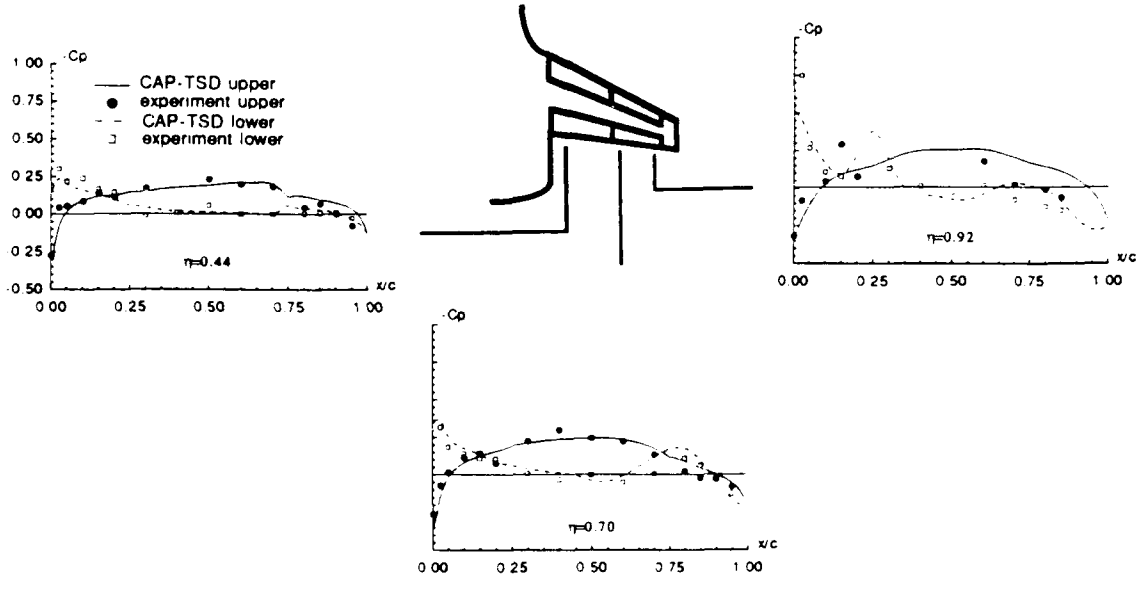


Fig. 5 Pressure distributions at M=0.9 and q=150 psf in a heavy gas.

THIS DOCUMENT PROVIDED BY THE ABBOTT AEROSPACE
TECHNICAL LIBRARY
ABBOTTAEROSPACE.COM

As with the original set of mode shapes, the overall agreement between the most recent analysis and experiment is good, with some discrepancies occurring near the trailing edge and wing tip. The first two span stations compare reasonably well from the leading edge up to about sixty percent of the local chord. Sudden changes in the experimental data can be seen near the quarter-chord at the second span station and near the three-quarter chord for all three span stations. These disruptions in the flow may be caused by the previously-mentioned physical discontinuities where wing box and control surfaces meet. At the second and third span stations, the effect of the actuator bumps on the lower surface pressures is evident. Agreement between analysis and experiment deteriorates at the third span station, possibly due to separated and/or tip vortex flow around the wing tip region.

Comparisons of the static aeroelastic results using the updated structural model with those of the previous model of Ref. 16 show essentially the same behavior. There exists a slight difference between the two results at the first span station near the three-quarter chord location where the updated structural model reveals the presence, or beginnings of, a shock that was not present with the original structural model. This appears to be a slight improvement in comparison with the test data. However, the exact cause of the sudden change in the experimental pressure distribution at this location is not clear as it may be due to a shock or to the geometric discontinuity that exists at the quarter-chord and three-quarter chord locations of the wing.

4.3 Dynamic Results

4.3.1 *Symmetric motions*

Flutter boundaries were computed at M=0.5, 0.9, 0.92, 0.93, 0.94, and 0.95. The analyses that included the vorticity and entropy corrections were computed at M=0.5, 0.9, 0.92, 0.93, and 0.95. Although the results for all of these Mach numbers are included in the figures, results are discussed primarily for the M=0.5, 0.9, 0.93, and 0.95 cases. All flutter analyses are for the AFW model in air at 1.5 degrees angle of attack and including a viscous damping of 0.015 (structural damping of 0.03).

4.3.1.1 Corrected tip store modeling

In Ref. 16, a rather severe transonic flutter dip was computed using the CAP-TSD code and the bottom of this computational transonic flutter dip did not agree well with the experimental transonic flutter dip. Figure 6, from Ref. 16, is a comparison of the CAP-TSD computed flutter boundary, the linear flutter boundary defined using the doublet lattice theory[24], and the experimental flutter results from the fall of 1989 and the spring of 1991 wind-tunnel tests. Accounting for nonlinearities in the flow, by the application of the CAP-TSD code, is a clear improvement over the linear flutter predictions. The no-flutter track, shown in the figure, is the path, in terms of Mach number and dynamic pressure, through which the wind tunnel proceeds for which no experimental flutter was encountered. This no-flutter track therefore defines a lower bound for the bottom of the experimental transonic flutter dip which disagrees with the CAP-TSD predicted bottom of the transonic flutter dip. As a result, one of the goals of the present study was to investigate some of the possible causes of this discrepancy by modifying and improving specific elements of the analysis.

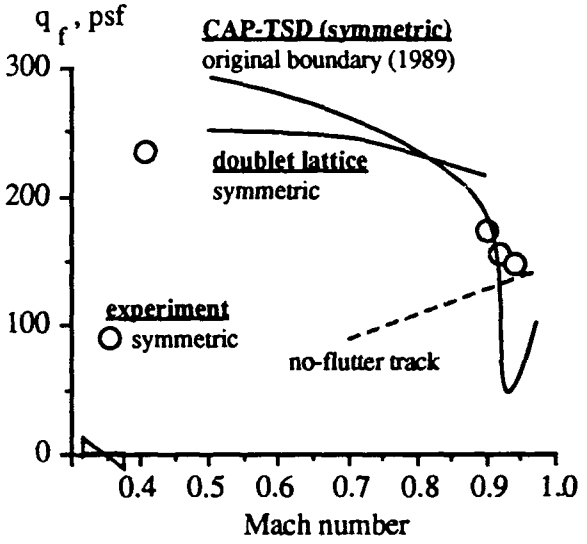


Fig. 6 Comparison of linear, nonlinear and experimental flutter boundaries for original mode shapes (Ref. 16).

The first improvement to the analysis was the correction of an error in the modeling of the wing tip ballast store. The error consisted of a sign change in a portion of the slopes that geometrically define the wing tip ballast store. The effect of this error was investigated and the resultant flutter boundary for the corrected wing tip ballast store model is presented in Fig. 7 along with the original, uncorrected flutter boundary presented in Fig. 6. At M = 0.5, the effect of the corrected tip store model was to reduce the flutter dynamic pressure from 290 psf (13.89 kPa) to 259 psf (12.40 kPa) with a change in flutter frequency from 10.70 Hz to 11.20 Hz. There was no change in the flutter mechanism at this Mach number from the mechanism reported in Ref. 16, which consisted of a classical coalescence of the first-bending mode and the first-torsion mode. The flutter dynamic pressure dropped only slightly at M=0.9 from 190 psf (9.10 kPa) to 182 psf (8.71 kPa) while at M=0.93 the flutter dynamic pressure increased from 52 psf (2.49 kPa) to 77 psf (3.69 kPa). The flutter dynamic pressure at M=0.95 increased significantly from 81 psf (3.88 kPa) to 133 psf (6.37 kPa). Again, the flutter mechanism for these three transonic Mach numbers was essentially the same as the mechanism reported in Ref. 16 for transonic Mach numbers, which consisted of a first-bending-dominated instability. The changes in flutter frequency at M=0.9, M=0.93, and M=0.95 were, respectively, from 9.50 Hz to

THIS DOCUMENT PROVIDED BY THE ABBOTT AEROSPACE
TECHNICAL LIBRARY
ABBOTTAEROSPACE.COM

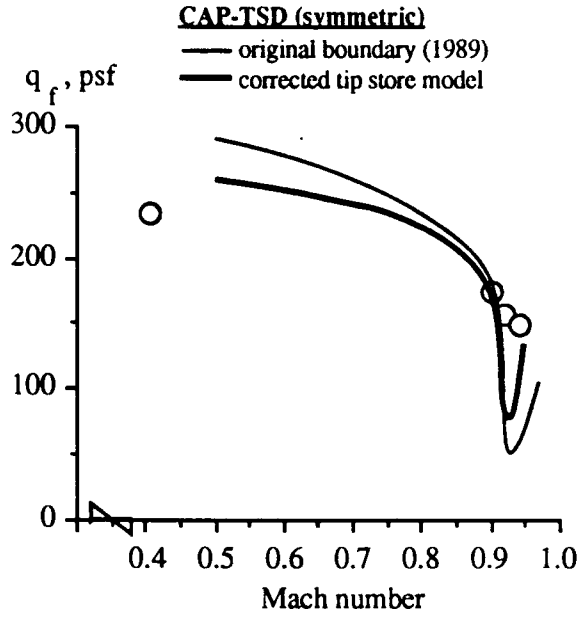


Fig. 7 The effect of the corrected tip store modeling using the original mode shapes.

9.36 Hz, from 7.78 Hz to 8.08 Hz, and from 8.07 Hz to 8.83 Hz.

The corrected modeling of the wing tip ballast store therefore improved the subsonic flutter boundary by lowering the flutter dynamic pressure in the direction of the experimental result while reducing the severity of the computational transonic flutter dip and thereby improving the correlation with the transonic experimental results. These results also indicate the sensitivity of the calculated flutter boundary to modeling of tip aerodynamics at both subsonic and transonic conditions. For all of the results that follow, the corrected modeling of the wing tip ballast store has, of course, been implemented.

4.3.1.2 Updated mode shapes and frequencies

An updated and improved set of mode shapes and frequencies were obtained after the wind-tunnel test of 1989. The improvements consisted of : a) refinements to the structural model based on experimental data and b) a denser set of structural node points for improved mode shape definition, in particular around the control surface regions and the wing tip regions of the AFW.

The flutter boundary due to the updated structural model is shown in Fig. 8 and compared to the flutter boundary due to the original structural model (corrected boundary from Fig. 7). There is an increase in flutter dynamic pressure at M=0.5 with the new structural model. The increase in flutter dynamic pressure is from 259 psf (12.40 kPa) to 281 psf (13.45 kPa) with a decrease in flutter frequency from 11.20 Hz to 10.86 Hz. At M=0.9, the flutter dynamic pressure increases from 182 psf (8.71 kPa) to 203 psf (9.72 kPa) with a slight change in flutter frequency from 9.36 Hz to 9.44 Hz. The flutter dynamic pressure at M=0.93 increases significantly from 77 psf (3.69 kPa) to 103 psf (4.93 kPa) with an increase in frequency from 8.08 Hz to 8.32 Hz. For M=0.95 the flutter dynamic pressure also increases significantly from 133 psf (6.37 kPa) to 183 psf (8.76 kPa) with an increase in flutter frequency from 8.83 Hz to 9.33 Hz.

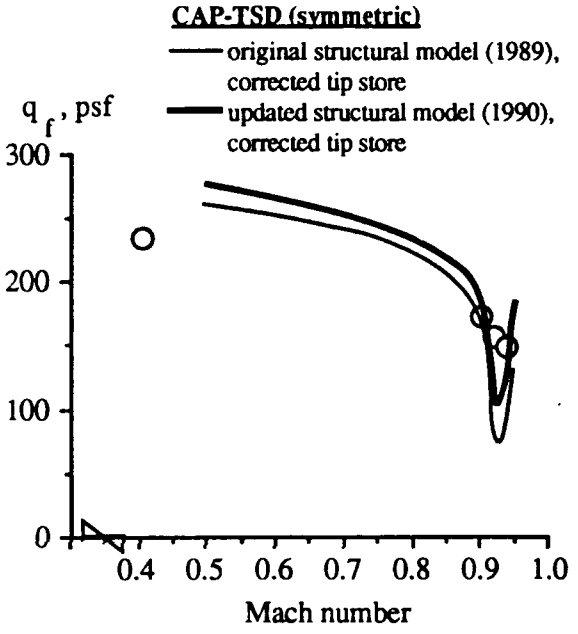


Fig. 8 Comparison of original (corrected) and updated structural models.

The effect of the updated structural model is therefore beneficial at transonic Mach numbers greater than M=0.9 since the correlation with the experimental transonic flutter results is improved, but at M=0.5 and M=0.9 the comparison with experiment is degraded. A possible reason for this deficiency in the CAP-TSD prediction is that the current version of the code treats bodies such as the wing tip ballast store and fuselage as aerodynamic influences with no modal definition. Although the effect of a modally-defined fuselage on the flutter boundary may be minimal, the effect of a modally-defined wing tip ballast store is probably significant as can be seen by the sensitivity to changes in the modeling of the wing tip ballast store in Fig. 7. These effects should be investigated when a version of the CAP-TSD code becomes available that accounts for modal deformations of the fuselage and bodies and thus the contribution of these components to the generalized aerodynamic forces. Viscous effects, not accounted for in the current inviscid version of the code, may also have a significant effect on both the subsonic and transonic flutter boundaries.

THIS DOCUMENT PROVIDED BY THE ABBOTT AEROSPACE
TECHNICAL LIBRARY
ABBOTTAEROSPACE.COM

4.3.1.3 Vorticity and entropy corrections

The vorticity and entropy corrections defined in Ref. 20 and incorporated in current versions of the CAP-TSD code were applied with updated mode shapes and frequencies at M=0.5, 0.9, 0.92, 0.93, and 0.95. These corrections typically reduce shock strength and shift the shock location forward. The resultant flutter boundary due to the implementation of these corrections is compared to the transonic portion of the flutter boundary for the updated structural model without vorticity and entropy corrections in Fig. 9. The effect of the corrections at M=0.9 is minimal, lowering the flutter dynamic pressure from 203 psf (9.72 kPa) to 200 psf (9.58 kPa) and reducing the flutter frequency from 9.44 Hz to 9.40 Hz. The effects of the corrections are significant at M=0.93 where the flutter dynamic pressure increased from 103 psf (4.93 kPa) to 126 psf (6.03 kPa) with an increase in flutter frequency from 8.32 Hz to 8.53 Hz. An interesting effect is noticed at M=0.95 where the flutter dynamic pressure is reduced from 183 psf (8.76 kPa) to 130 psf (6.22 kPa) and the flutter frequency drops from 9.33 Hz to 8.60 Hz. The effect of the vorticity and entropy corrections therefore is significant in that it improves the correlation with experiment at the transonic Mach numbers evaluated. The inclusion of vorticity and entropy also tends to widen the rather steep and narrow transonic flutter dip previously computed (Figs. 6, 7, and 8).

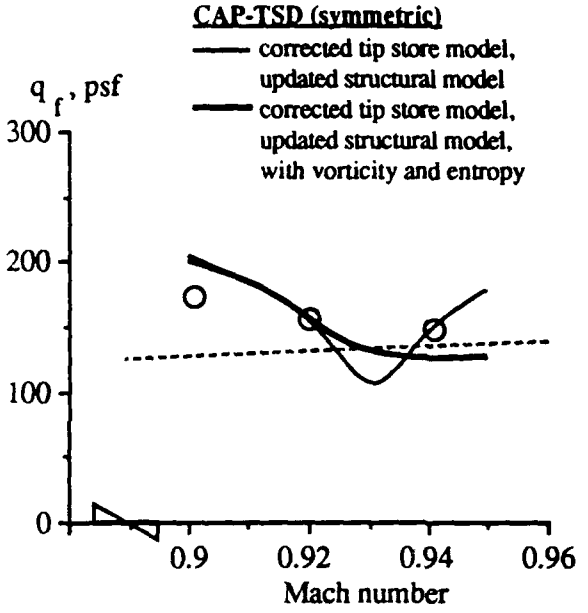


Fig. 9 Comparison of transonic computational and experimental flutter boundaries for updated structural model with and without vorticity and entropy corrections.

In general, for symmetric motions, the effects of improved and updated analyses results in excellent agreement with experiment at transonic conditions while resulting in some degradation of the comparisons at M=0.5 and M=0.9. It is possible that accounting for the modal definition of the wing tip ballast store will provide some insight into this discrepancy. It is also interesting to note that the computational result at M=0.92 is insensitive to the computational modifications and improvements described above and compares extremely well with experiment. At this Mach number, the calculated flutter dynamic pressure, for the vorticity and entropy case, for example, is 151 psf (7.23 kPa) which differs only slightly from the experimental flutter value of 156 psf (7.47 kPa).

4.3.2 *Antisymmetric motions*

In order to generate antisymmetric aeroelastic responses, a full-span model of the AFW was generated. A progressive verification of the full-span model and of the CAP-TSD code's capability for handling full-span aeroelastic analyses was deemed necessary before any antisymmetric flutter analyses were performed. This progressive verification proceeded as follows. First, a full-span, rigid and steady solution was compared to a semi-span, rigid and steady solution at the same Mach number. Lift and moment coefficients for both cases were identical, thereby verifying the aerodynamic modeling of the full-span model and the accurate implementation of the symmetric boundary condition for the semi-span model. Second, static aeroelastic solutions were computed for both models using symmetric modes at a chosen Mach number and dynamic pressure. Again, the resultant lift and moment coefficients including static aeroelastic deformation of both models were in exact agreement, verifying the modal definition of the full-span model. Finally, a full-span, symmetric dynamic analysis was compared to a semi-span, symmetric dynamic analysis resulting in identical transients, verifying the full-span model for dynamic analyses.

An important aspect of the antisymmetric flutter analyses is the necessary addition of symmetric mode shapes to the aeroelastic modeling along with the antisymmetric mode shapes. The reason for this is that since dynamic analyses are computed about converged static aeroelastic solutions and since static aeroelastic solutions are symmetric for a vehicle defined symmetrically about its centerline, antisymmetric dynamic analyses require the inclusion of symmetric modes as well. The computational model therefore consists of ten symmetric modes needed for static aeroelastic solutions and ten antisymmetric modes needed for the dynamic aeroelastic solutions. These additional modes do not increase the computer time significantly as the finite-difference aerodynamics dominate the CPU time.

An antisymmetric computational flutter point has been obtained for the M=0.5 case thus far. Figure 10 is a comparison of the linear symmetric and antisymmetric flutter boundaries computed using the doublet lattice unsteady aerodynamic theory for the updated set of mode

THIS DOCUMENT PROVIDED BY THE ABBOTT AEROSPACE
TECHNICAL LIBRARY
ABBOTTAEROSPACE.COM

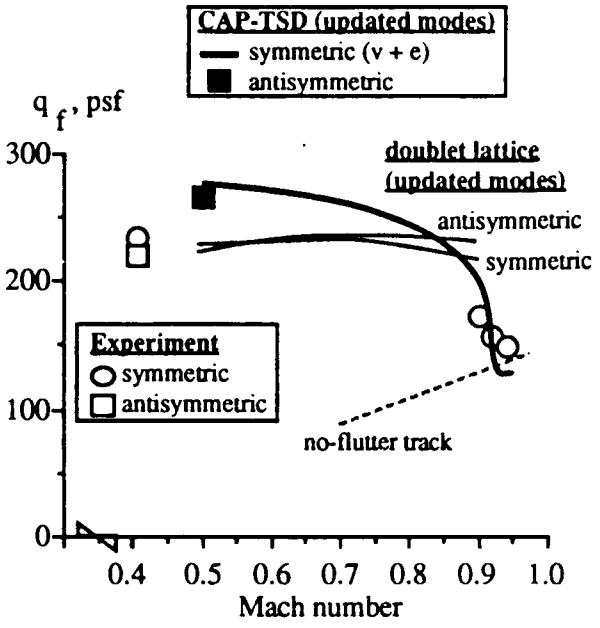


Fig. 10 Comparison of linear and nonlinear flutter boundaries for the updated symmetric (with vorticity and entropy) and antisymmetric structural model and experimental results.

shapes[24], the CAP-TSD symmetric flutter boundary for the updated set of mode shapes with vorticity and entropy (Fig. 9), the CAP-TSD antisymmetric flutter result at M=0.5, and the symmetric and antisymmetric experimental flutter points. Although the CAP-TSD predicted antisymmetric flutter dynamic pressure of 272 psf (13.02 kPa) is significantly higher than the experimental value of 219 psf (10.49 kPa), the CAP-TSD analyses indicate that the antisymmetric instability is lower in flutter dynamic pressure than the symmetric instability at M=0.5 (dynamic pressure of 281 psf (13.45 kPa)). This is consistent with the doublet lattice symmetric and antisymmetric results and the experimental symmetric and antisymmetric results. The discrepancy between the CAP-TSD results at M=0.5 and the subsonic experimental flutter results (and the doublet lattice results as well) may be due to the lack of modal definition of the wing tip ballast store and thus its contribution to the unsteady generalized forces in the CAP-TSD computations. The effect of a modally-defined wing tip ballast store on the subsonic and transonic CAP-TSD flutter boundaries still needs to be investigated. Furthermore, viscous effects have not been addressed by the analyses presented thus far and need to be investigated as well.

5. CONCLUDING REMARKS

The goals of this study were to update the calculated symmetric aeroelastic behavior of the AFW wind-tunnel model using the CAP-TSD code, to evaluate the full-span, antisymmetric aeroelastic capability of the code, and to compare the results with experimental flutter data.

A static aeroelastic procedure previously developed was applied to an updated structural model. Results compared favorably with experimental pressure data from a previous AFW wind tunnel test. Static aeroelastic solutions therefore provided reasonable estimates of the static aeroelastic deformation of the wing. Dynamic analyses were then performed as perturbations about converged static aeroelastic solutions.

The updated dynamic analyses consisted of modifications and improvements to key elements of the aeroelastic modelling. These modifications and improvements include a corrected aerodynamic modelling of the wing tip ballast store, an updated structural model, and the addition of vorticity and entropy corrections.

The corrected modelling of the wing tip ballast store resulted in improved correlation with subsonic and transonic symmetric experimental flutter points. The significant sensitivity of the aeroelastic analyses to changes in the modelling of the wing tip ballast store was revealed. The updated structural model improved the correlation with experiment at transonic Mach numbers but degraded the correlation with experiment at the subsonic condition. The addition of vorticity and entropy corrections provided further improvements in the correlation with experiment at transonic Mach numbers. This is an indication of the importance of including vorticity and entropy effects in the computations.

A full-span computational model of the AFW was generated and used for generating an antisymmetric flutter point at M=0.5. Deficiencies in the correlation with experiment at this Mach number may be due to the lack of modal definition in the aerodynamics of the wing tip ballast store, which might have a significant effect on the generalized aerodynamic forces of the vehicle. Viscous effects, not accounted for in this inviscid version of the CAP-TSD code, may also play an important role in both the subsonic and transonic regimes.

6. ACKNOWLEDGEMENT

The authors would like to thank B. Perry III of the Aeroservoelasticity Branch and S. R. Cole of the Configuration Aeroelasticity Branch for providing experimental flutter data.

7. REFERENCES

[1]Isogai, K. : On the Transonic-Dip Mechanism of Flutter of a Sweptback Wing. *AIAA Journal*, Volume 17, Number 7, July 1979, pp. 793-795.

[2]Davis, S. S.; and Malcolm, G. N. : Experiments in Unsteady Transonic Flow. AIAA Paper Number 79-0769, AIAA/ASME/ASCE/AHS 20th Structures, Structural Dynamics, and Materials Conference, St. Louis, MO, April 4-6, 1979.

THIS DOCUMENT PROVIDED BY THE ABBOTT AEROSPACE
TECHNICAL LIBRARY
ABBOTTAEROSPACE.COM

[3]Edwards, J. W.; and Thomas, J. L. : Computational Methods for Unsteady Transonic Flows, Chapter 5 in Unsteady Transonic Aerodynamics, Edited by David Nixon, Progress in Astronautics and Aeronautics, Volume 120, 1989.

[4]Ballhaus, W. F.; and Bridgeman, J. O. : Numerical Solution Techniques for Unsteady Transonic Problems. AGARD Report Number 679, Paper Number 16, March 1980.

[5]Wu, J. C. ; Kaza, K. R. V.; and Sankar, N. L. : A Technique for the Prediction of Airfoil Flutter Characteristics in Separated Flows. AIAA Paper Number 87-0910, Presented at the AIAA/ASME/ASCE/AHS 28th Structures, Structural Dynamics, and Materials Conference, Monterey, CA, April 6-8, 1987.

[6]Bendiksen, O. O.; and Kousen, K. : Transonic Flutter Analysis Using the Euler Equations. AIAA Paper Number 87-0911, Presented at the AIAA/ASME/ASCE/AHS 28th Structures, Structural Dynamics, and Materials Conference, Monterey, CA, April 6-8, 1987.

[7]Shankar, V.; and Ide, H. : Unsteady Full Potential Computations Including Aeroelastic Effects. *Proceedings of the 5th International Conference on Numerical Methods in Laminar and Turbulent Flow*, Volume 5, Part 2, Montreal, Canada, July 6-10, 1987.

[8]Borland, C. J.; and Rizzetta, D. P. : Nonlinear Transonic Flutter Analysis. *AIAA Journal*, Volume 20, November 1982, pp. 1606-1615.

[9]Yang, T. Y.; Guruswamy, P.; and Striz, A. G. : Application of Transonic Codes to Flutter Analysis of Conventional and Supercritical Airfoils. AIAA Paper Number 81-0603, Proceedings of AIAA Dynamics Specialist Conference, Atlanta, GA, April 9-10, 1981, pp. 332-342.

[10]Batina, J. T. : Efficient Algorithm for Solution of the Unsteady Transonic Small-Disturbance Equation. *Journal of Aircraft*, Volume 25, July 1988, pp. 598-605.

[11]Batina, J. T.; Seidel, D. A.; Bland, S. R.; and Bennett, R. M. : Unsteady Transonic Flow Calculations for Realistic Aircraft Configurations. *Journal of Aircraft*, Volume 26, January 1989, pp. 21-28.

[12]Bennett, R. M.; Bland, S. R.; Batina, J. T.; Gibbons, M. D.; and Mabey, D. G. : Calculation of Steady and Unsteady Pressures on Wings at Supersonic Speeds with a Transonic Small-Disturbance Code. AIAA Paper Number 87-0851, Presented at the AIAA/ASME/ASCE/AHS 28th Structures, Structural Dynamics, and Materials Conference, Monterey, CA, April 6-8, 1987.

[13]Bennett, R. M.;Batina, J. T.; and Cunningham,H. J. : Wing Flutter Calculations with the CAP-TSD Unsteady Transonic Small-Disturbance Program. *Journal of Aircraft*, Volume 26, Number 9, September 1989, pp. 876 - 882.

[14]Perry, B. III; Mukhopadhyay, V.; Hoadley, S. T.; Cole, S. R.; Buttrill, C. S.; and Houck, J. A. : Design, Implementation, Simulation, and Testing of Digital Flutter Suppression Systems for the Active Flexible Wing Wind-Tunnel Model. ICAS Paper Number 90-1.3.2, Presented at the 17th International Council of the Aeronautical Sciences, Stockholm, Sweden, September 9-14, 1990.

[15]Mukhopadhyay, V.; Perry, B. III; and Noll, T. E. : Flutter Suppression Control Law Synthesis for the Active Flexible Wing Model. Paper Number 89-059, Presented at the European Forum on Aeroelasticity and Structural Dynamics, Aachen, FRG, April 17-19, 1989.

[16]Silva, W. A. ; and Bennett, R. M. : Predicting the Aeroelastic Behavior of a Wind-Tunnel Model Using Transonic Small-Disturbance Theory, ICAS Paper Number 90-1.1.1, Presented at the 17th International Council of the Aeronautical Sciences, Stockholm, Sweden, September 9-14, 1990.

[17]Yates, E. C. Jr.; Wynne, E. C. ; and Farmer, M. G. : Measured and Calculated Effects of Angle of Attack on the Transonic Flutter of a Supercritical Wing. NASA TM 83276, August 1982.

[18]Yates, E. C. Jr.; and Chu, L. : Static Aeroelastic Effects on the Flutter of a Supercritical Wing. NASA TM 89132, March 1987.

[19]Batina, J. T. : Unsteady Transonic Algorithm Improvements for Realistic Aircraft Applications. *Journal of Aircraft*, Volume 26, February 1989, pp. 131-139.

[20]Batina, J. T. : Unsteady Transonic Small-Disturbance Theory Including Entropy and Vorticity Effects. *Journal of Aircraft*, Volume 26, Number 6, June 1989, pp. 531 - 538.

[21]Edwards, J. W.; Bennett, R. M.; Whitlow, W. Jr.; and Seidel, D. A. : Time-Marching Transonic Flutter Solutions Including Angle-of-Attack Effects. *Journal of Aircraft*, Volume 20, Number 11, November 1983, pp. 899-906.

[22]Bennett, R. M.; and Desmarais, R. N. : Curve Fitting of Aeroelastic Transient Response Data with Exponential Functions. *Flutter Testing Techniques*, NASA SP-415, pp. 43-58, May 1975.

[23]Harder, R. L.; and Desmarais, R. N. : Interpolation Using Surface Splines. *Journal of Aircraft*, Volume 9, February 1972, pp. 189-191.

THIS DOCUMENT PROVIDED BY THE ABBOTT AEROSPACE
TECHNICAL LIBRARY
ABBOTTAEROSPACE.COM

[24] Silva, W. A. ; Heeg, J. ; and Bennett, R. M. : Aeroelastic Modeling of the Active Flexible Wing Wind-Tunnel Model, In NASA CP 10065, Presented at the Fourth NASA Workshop on Computational Control of Flexible Aerospace Systems, Williamsburg, Virginia, July 11-13, 1990.

THIS DOCUMENT PROVIDED BY THE ABBOTT AEROSPACE
TECHNICAL LIBRARY
ABBOTTAEROSPACE.COM

AD-P007 812

NUMERICAL SIMULATION OF SHOCK-STALL FLUTTER OF AN AIRFOIL USING THE NAVIER-STOKES EQUATIONS

92-16050

K. Isogai

Structural Mechanics Division
National Aerospace Laboratory
7-44-1 Jindaiji-Higashi-Machi
Chofu Tokyo 182
Japan

SUMMARY

In order to confirm, qualitatively, the unusual flutter phenomenon, which has been observed experimentally for the high-aspect-ratio (non-tailored) forward swept wing model, as a shock-stall flutter, the aeroelastic response calculation of a two dimensional airfoil whose vibration characteristics are similar to those of the typical section of a forward swept wing, has been performed by using the compressible Navier-Stokes equations as a flow solver. By the examination of the flow pattern, pressure distribution and the behavior of the unsteady aerodynamic forces during the diverging oscillation of the airfoil, it is concluded that this is a shock-stall flutter, in which the large scale shock-induced flow separation is playing the dominant role and that there is a mechanism of putting energy into the elastic system of the airfoil, leading to nearly a single-degree-of-freedom flutter.

LIST OF SYMBOLS

a	distance of elastic axis behind midchord, percent semichord
b	semichord
C	chord length
C_L	lift coefficient ($L/(1/2\rho U^2C)$)
C_M	pitching moment coefficient ($M_y/(1/2\rho U^2C^2)$)
C_p	pressure coefficient ($(p-p_\infty)/(1/2\rho U^2)$)
$C_{p,\theta}$	first harmonic component (in complex form) of local pressure coefficient per unit θ
$f_e(x,t)$	elastic displacement of airfoil (nondimensionalized by semichord)
Im	imaginary part
k	reduced frequency ($b\omega/U$)
L	lift per unit span
M	free stream Mach number
My	pitching moment per unit span
m	mass per unit span
q	free stream dynamic pressure
q_i	generalized coordinate corresponding to i-th mode
$\tilde{q}_i$	q_i/b
R	Reynolds number based on chord
Re	real part
r_{cg}	dimensionless radius of gyration about center of gravity
T	time
t	dimensionless time $(U/b)T$
U	free stream velocity
x, y	Cartesian coordinates, nondimesionalized by semichord
x_{cg}	distance of center of gravity behind midchord, nondimensionalized by semichord
$x_{pv,i}$	distance of pivotal point (of ith mode) behind midchord, nondimesionalized by semichord
y^+_1	standard law of wall coordinate corresponding to one grid space off the wall
α	angle of attack
θ	amplitude of pitching oscillation, radians
θ_t	elastic twist angle about pivotal point, degrees
ρ	free stream density
ξ,η	curvilinear coordinates, nondemensionalized by semichord
ω	circular frequency
ω_h, ω_α	uncoupled circular frequency of airfoil in plunging and in pitch, respectively

1. INTRODUCTION

In the course of our experimental study (Ref 1) on the transonic flutter/divergence characteristics of the aeroelastically tailored and non-tailored high-aspect-ratio forward swept wings, the unusual flutter phenomenon was observed for the non-tailored wing. The planform and construction of the flutter model used in our experimental study is shown in Fig. 1 for completeness. And the results of the flutter test are also reproduced in Fig. 2. As seen in Fig. 2, the theoretical prediction using Doublet Lattice Method (Ref 2) says that this non-tailored wing should be divergence critical rather than flutter. However, what we observed in the experiment for this model was flutter rather than divergence in the entire transonic Mach number range tested.

As seen in Fig. 2, this flutter phenomenon has two unusual characteristics compared with the conventional (classical type) flutter. The first one is the flutter frequency. The flutter frequencies of this model are about 64 Hz - 75 Hz depending on Mach numbers, which are slightly lower than the first natural frequency of this model (80.7 Hz). The second characteristic is that the flutter boundary depends strongly on the mean angle of attack, that is, the flutter dynamic pressure decreases about 30% - 40% by changing the angle of attack from 0 degree to 2 degrees. From these characteristics it is

THIS DOCUMENT PROVIDED BY THE ABBOTT AEROSPACE
TECHNICAL LIBRARY
ABBOTTAEROSPACE.COM

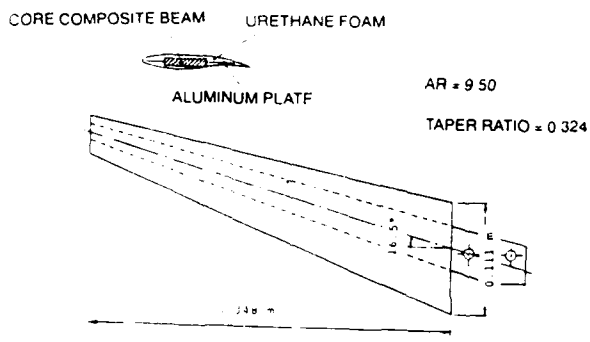


Fig. 1 Planform and construciton of aeroelastically simulated forward swept wing model

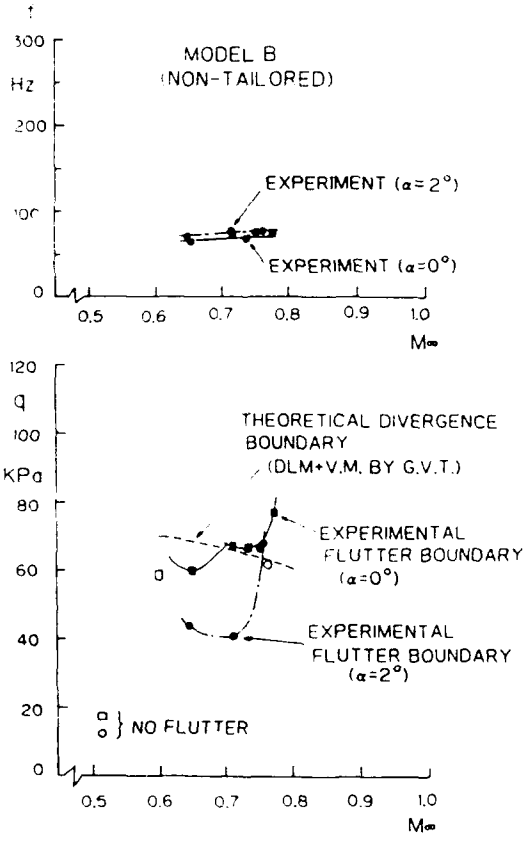


Fig. 2 Flutter dynamic pressure and frequency of non-tailored model

conjectured that the flutter experienced by this non-tailored model is "Shock-Stall Flutter", in which the shock induced flow separation is playing the dominant role. As will be discussed in the later section, it can easily be demonstrated that there is a mechanism of a single-degree-of-freedom flutter when the first natural mode shape of the wing has a wash-in tendency and the variation of the unsteady aerodynamic forces shows the hysteresis like that experienced for a low speed stall flutter. Although the low speed stall flutter only occures at high angles of attack, the shock-stall flutter can occur even at low angles of attack since the non-tailored forward swept wing has a strong divergence tendency and the local angle of attack induced by the static aeroelastic deformation easily reaches the shock-stall angle (which is the order of 5 - 6 degrees), leading to the shock-stall flutter. These conjectures should be validated by further investigations since no flow visualization nor unsteady pressure measurements was conducted for the flutter experiments reported in Ref 1.

In this report we have attempted to validate the above conjecture by the numerical simulation technique. Since the rigorous simulation of the flutter of a three-dimensional (3D) wing by using the 3D Navier-Stokes equations is far beyond the capability of the current super-computers, a qualitative simulation using a 2D model is attempted in this paper. Namely, the aeroelastic response of the 2D flexible wing whose vibration characteristics simulate those of the typical section of the non-tailored forward swept wing is calculated by employing the 2D (time averaged) compressible Navier-Stokes equations. And the unsteady flow patterns and the behavior of the unsteady aerodynamic forces during the shock-stall flutter are examined in detail. The numerical method and the results of the simulation are presented in the following sections.

2. NUMERICAL METHOD AND CODE VALIDATION

In order to simulate the shock-stall flutter, it is essential to solve the compressible Navier-Stokes equations time accurately, since the shock induced flow separation is playing the dominant role in the phenomenon. The finite differece technique we have employed is the linearized conservative implicit (LCI) form of the Yee-Harten (Ref 3) TVD (Total Variation Diminishing) scheme. Although this scheme is an upwind scheme, it is written in a symmetric form, that is, a central difference plus an appropriate numerical dissipation term. This means that one can modify a standard three-point central difference code, such as those based on the Beam-Warming algorithm (Ref 4), by simply changing the conventional numerical dissipation term into the one designed for the TVD scheme. Thus, our 2D Navier-Stokes code, which was originally based on the Beam-Warming scheme (Ref 4, Ref 5), has been modified into the Yee-Harten TVD scheme (Ref 3). Since the detailed procedure of the Beam-Warming scheme and its modification into Yee-Harten TVD scheme are well documented (Ref 5, Ref 3), they are not repeated here.

The grid used for the present calculation is a body fitted grid which moves with the airfoil motion. The technique we have employed for obtaining the moving grid is relatively simple. As shown in Fig. 3, we initially generate the grid system around the airfoil fixed at some mean position, which is defined by

$$x=x_0(\xi,\eta), \qquad y=y_0(\xi,\eta) \qquad (1)$$

THIS DOCUMENT PROVIDED BY THE ABBOTT AEROSPACE
TECHNICAL LIBRARY
ABBOTTAEROSPACE.COM

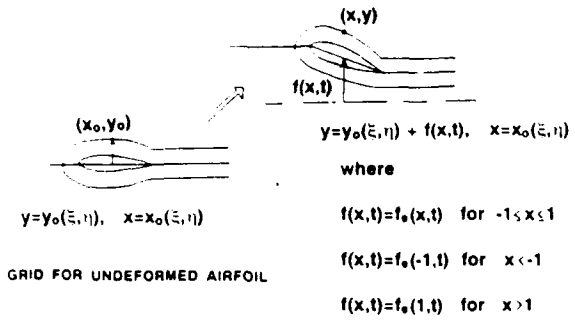


Fig. 3 Concept of moving grid generation

where (x,y) are the Cartesian coordinates in the physical space and (ξ,η) are the curvilinear coordinates in the computational space. If we denote the elastic displacement of the airfoil by

$$f_e(x,t) \qquad -1 \le x \le 1 \qquad (2)$$

the grid system around the deformed airfoil at time t is obtained by

$$y=y_o(\xi,\eta) + f(x,t), \quad x=x_o(\xi,\eta) \qquad (3)$$

where

$$\left.\begin{aligned} f(x,t)&=f_e(x,t) \quad \text{for} \quad -1\le x\le 1 \\ f(x,t)&=f_e(-1,t) \quad \text{for} \quad x<-1 \\ f(x,t)&=f_e(1,t) \quad \text{for} \quad x>1 \end{aligned}\right\} \quad (4)$$

The elastic deformation obtained at one time step before is used as $f_e(x,t)$ since the elastic displacement at the new time level is not known yet. The C type grid is generated by using the algebraic grid generation technique, and the grid points thus obtained are later redistributed so that the grid lines become orthogonal near the airfoil surfaces.

For all the calculations presented in this paper, the thin layer approximation is made. The Baldwin and Lomax (Ref 6) algebraic turbulence model is employed as a turbulence closure model.

In order to evaluate the present code, the steady and unsteady caluculations have been done for the standard airfoils for which the experimental data are available. The first exmple is the computation of the steady flow around the RAE 2822 airfoil, for which the experimental data obtained by Cook, et al. (Ref 7) are avilable. The computation has been performed to compare with the experimental data obtained at M=0.725, α=2.92 degrees, and R=6.5x10^6. The number of grid points used for the computation are 280x80, in ξ and η directions respectively. The law of the wall coordinate y^+_1 of the grid points next to the airfoil surface is about 1.0. In Fig. 4, the pressure distributions obtained by the present computation are compared with those of

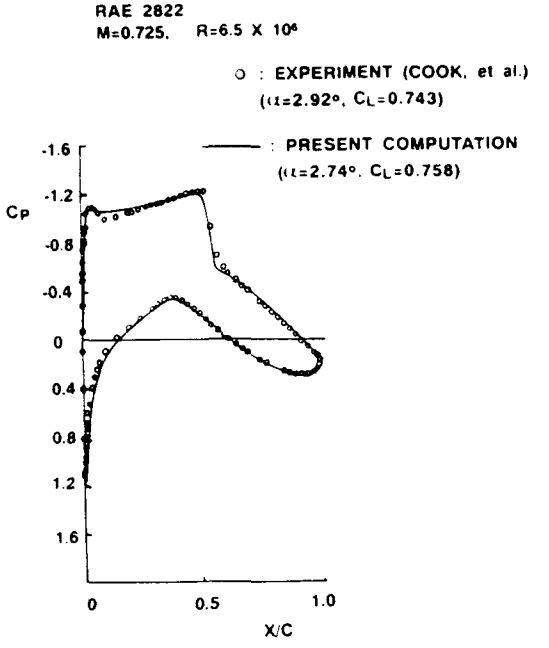


Fig. 4 Comparison of pressure distributions for the RAE2822 airfoil

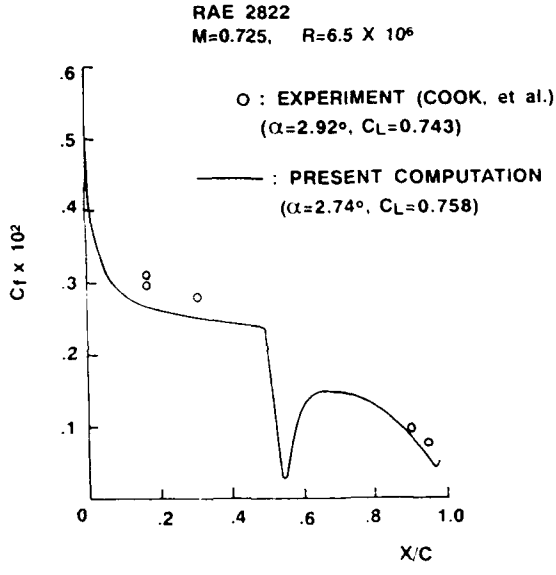


Fig. 5 Comparison of skin-friction coefficient ditributions from the RAE2822 airfoil upper surface

THIS DOCUMENT PROVIDED BY THE ABBOTT AEROSPACE
TECHNICAL LIBRARY
ABBOTTAEROSPACE.COM

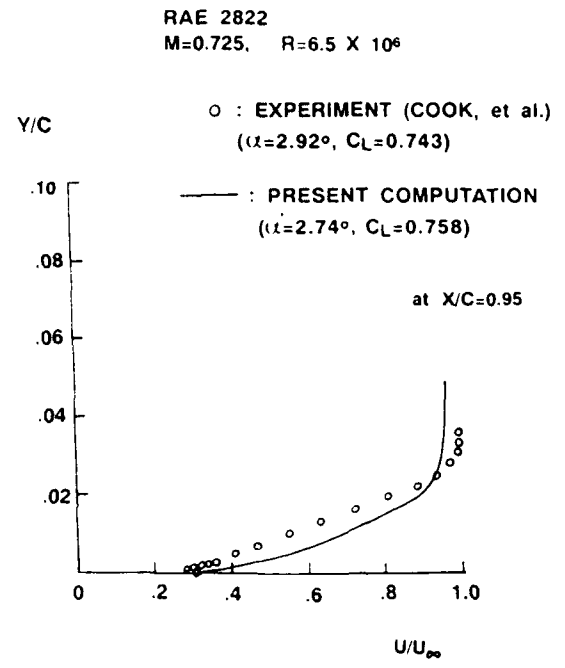


Fig. 6 Velocity profile comparison from the RAE2822 airfoil upper surface at X/C=0.95.

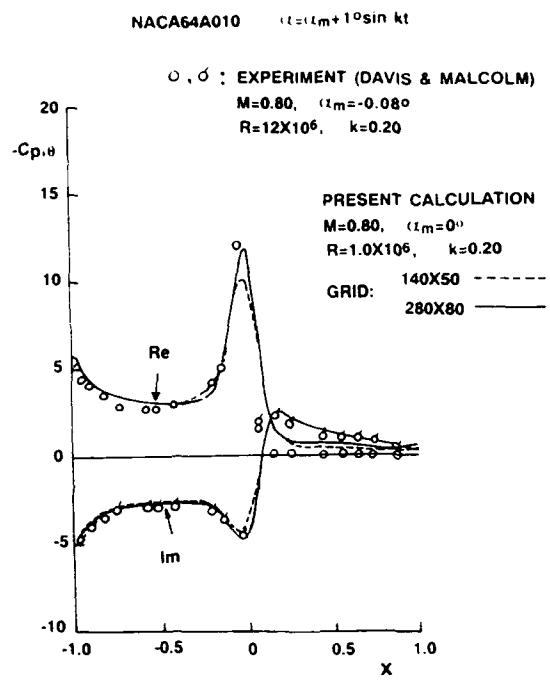


Fig. 7 Comparison of upper surface unsteady pressure distributions on NACA64A010 airfoil oscillating in pitch about quarter-chord

the experiment. The angle of attack 2.74 degrees used for the computation is selected to obtain the best fit of the pressure distribution to the experimental data. In Fig. 5, the computed skin friction distributions on the upper surface on RAE2822 for the same case are compared. The skin friction coefficient shown in the figure is refered to the boundary layer edge dynamic pressure. In Fig. 6, the computed boundary layer velocity profile on the upper surface at X/C=0.95 is compared with the experimental data. From these comparisons, the present code seems to give reliable results for the viscous transonic flow simulations as far as the boundary layer is attached.

In order to validate the capability of calculating the unsteady transonic viscous flow, the unsteady pressure distributions around NACA64A010 airfoil oscillating in pitch at M=0.80 and k=0.20 are computed, being compared with the experimental data obtained by Davis and Malcolm (Ref 8). The mean angle of attack is 0 degree and the amplitude of oscillation is 1 degree. The axis of pitch is the quarter chord position. The results are shown in Fig. 7. The results obtained with grid points of 140x50 and 280x80 are both shown in the same figure. For both the calculations, y^+_1 is about 2.0. Satisfactory agreement of the result with 140x50 grid points with that of 280x80 grid points suggests that 140x50 grid points seem to be enough for our present purpose, that is, the qualitative investigation of the mechanism of the shock-stall flutter phenomenon. (It should be noted here that the Reynolds number of Davis and Malcolm's experiment is 1.2×10^7 while present computation is performed at Reynolds number of 1.0×10^6. This is because the computation time becomes prohibitive amount for our present

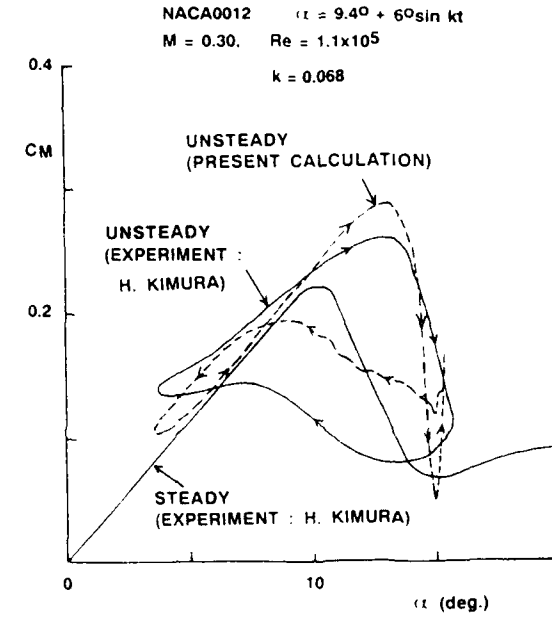


Fig. 8 Comparison of pitching moment (about midchord axis) during dynamic stall of NACA0012 airfoil

THIS DOCUMENT PROVIDED BY THE ABBOTT AEROSPACE
TECHNICAL LIBRARY
ABBOTTAEROSPACE.COM

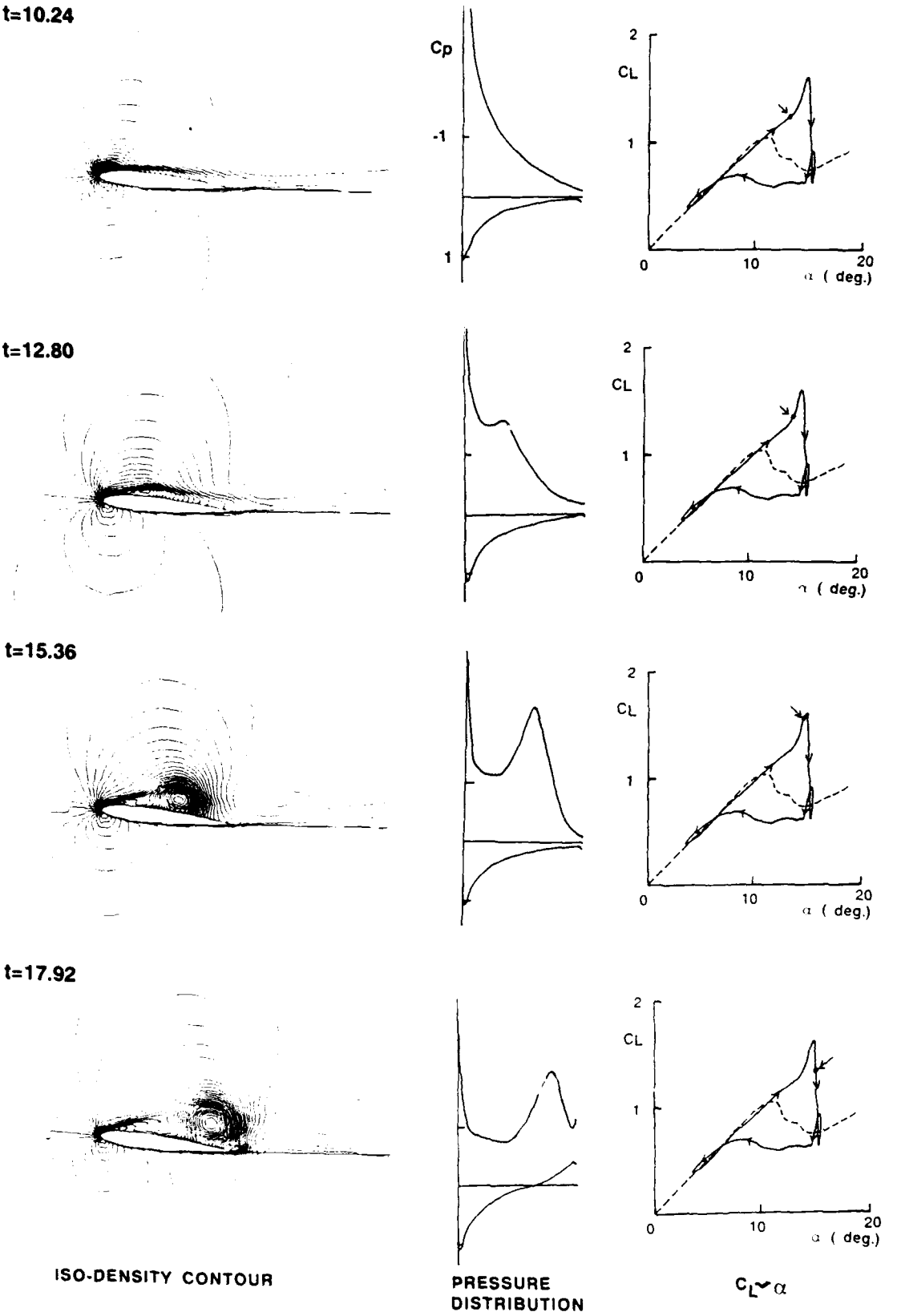


Fig. 9 Iso-density contour, pressure distribution and lift during dynamic-stall of NACA0012 airfoil ($M=0.30$, $R=1.1\times10^5$, $k=0.068$, $\alpha=9.4^o+6^o\sin kt$).

THIS DOCUMENT PROVIDED BY THE ABBOTT AEROSPACE
TECHNICAL LIBRARY
ABBOTTAEROSPACE.COM

code to do the computation at $R=1.2\times10^7$ by keeping the y^+_1 in the oder of 1.)

In order to evaluate the capability of the present code for simulating the large scale separated flow, the low speed dynamic stall phenomenon around NACA0012 airfoil oscillating in pitch near static stalling angle has been calculated, being compared with the experimental data obtained by Kimura (Ref 9). The flow condition is M=0.30 and $R=1.1\times10^5$. At this Reynolds number, the static stalling angle is about 10 degrees. The airfoil is oscillated in pitch with the amplitude of 6 degrees around the mean angle of attack of 9.4 degrees. The reduced frequency is k=0.068. The behavior of the pitching moment about the midchord axis is shown in Fig. 8, being compared with the experimental data obtained by Kimura (Ref 9). Although some quantitative discrepancy between the calculated and experimental results is observed, the qualitative behavior of the experimental pitching moment is well reproduced by the calculation. In Fig. 9, the iso-density contour, the instantaneous pressure distribution and the instantaneous value of the lift in C_L~α plane at some typical time steps during dynamic stall are shown. It can be seen that the formation of the leading edge separation vortex and its effect on the upper surface pressure distribution and the production of the "vortex lift" are well reproduced by the present calculation. Since further detailed descriptions of the numerical simulation of "low speed dynamic stall" phenomenon are beyond the scope of this paper, they will be published in the coming paper (Ref 10). In the above calculations, 140x50 grid points with $y^+_1\fallingdotseq1.0$ are used.

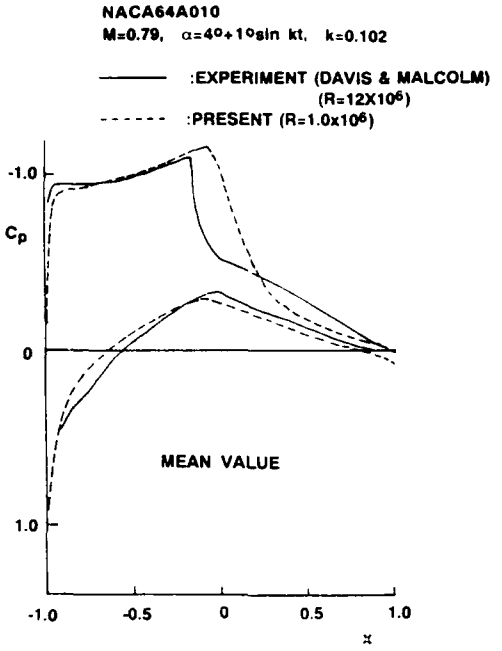


Fig. 10a Comparison of upper surface unsteady pressure distributions on NACA64A010 airfoil oscillating in pitch about quarter-chord

In order to evaluate the capability of the present code for simulating unsteady flow including severe shock-induced flow separation, computation is performed for the NACA64A010 airfoil oscillating in pitch about mean angle of attack 4 degrees at M=0.79 and k=0.102, for which Davis & Malcolm's experimental data (Ref. 8) are avilable. The axis of pitch is 25% chord position and the amplitude of oscillation is one degree. In Figs. 10a-10c, comparisons are made for the mean presssure distributions, the real and imaginary parts of unstaedy pressure distrubutions on the upper surface, respectively. As seen in Fig. 10a, the present computation predicts stronger and aft-positioned a shock wave compared with that of the experiment. It is well known that this phenomenon could be attributed to the use of the Baldwin & Lomax turbulence model (Ref. 11). This discrapancy of the shock position and shock strength between the experiment and computation seems also to be the possible cause of the quantitative discrepancies of the unsteady pressure distributions. Since the agreement of the unsteady pressure distributions between the experiment and the present computation is not too bad *in a qualitative sense*, the use of the Baldwin & Lomax turbulence model might be justified for the present purpose, that is, the verification of the *possibility* of the shock-stall flutter and the *qualitative understanding* of its mechanism.

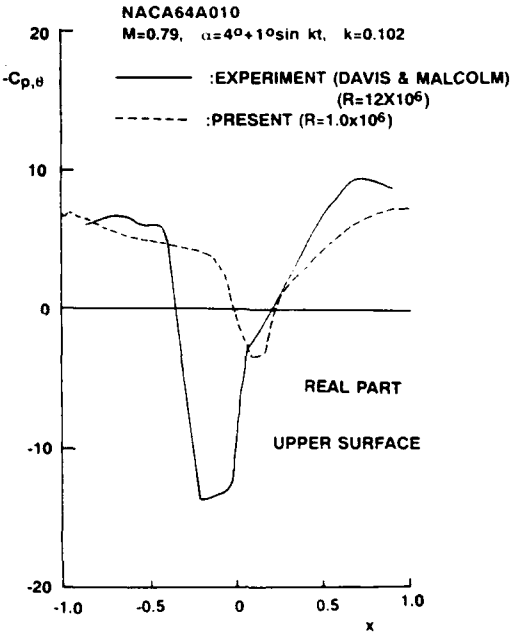


Fig. 10b -continued

THIS DOCUMENT PROVIDED BY THE ABBOTT AEROSPACE
TECHNICAL LIBRARY
ABBOTTAEROSPACE.COM

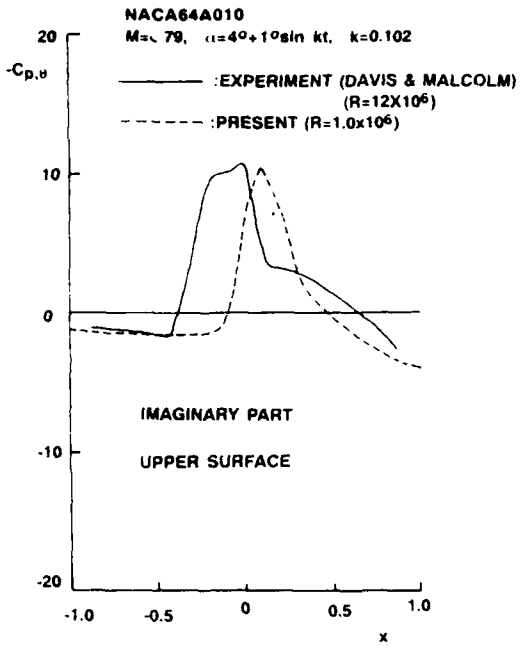


Fig. 10c -continued

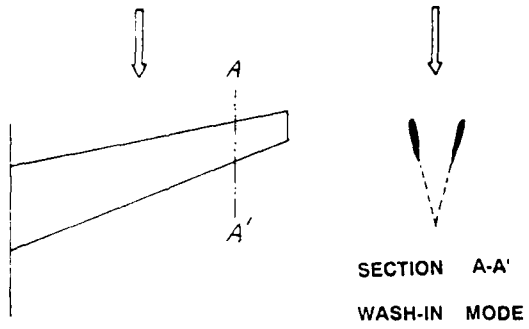


Fig. 11 Characteristics of the first bending mode of (non-tailored) forward swept wing

3. SIMULATION OF SHOCK-STALL FLUTTER

3.1 Binary System Simulating the Natural Vibration Mode of Typical Section of Forward Swept Wing

As already described in section 1, the non-tailored model of the high-aspect-ratio forward swept wing has experienced the flutter phenomenon which is conjectured as "Shock-Stall Fiutter" (Ref 1). The characteristic feature of the first natural vibration mode of the non-tailored forward swept wing is "wash-in mode" (pivotal point located downstream of the trailing edge) as shown in Fig. 11. In order to simulate the shock-stall flutter phenomenon by the binary system qualitatively, it is essential to give the wash-in mode to the system. The sketch of the binary system used for the present simulation is given in Fig. 12. It is easy to find the analytical forms of the natural frequency and mode shapes of this binary system. In order to give the wash-in mode to the first natural mode shape, we have selected the following values for the parameters to determine the mode shapes:

$$m=1.0\ \text{Kg},\quad b=0.05\ \text{m},\quad x_{cg}=-0.20$$

$$r_{cg}^2=0.24,\quad a=2.0,\quad \omega_h/\omega_\alpha=1.0 \qquad (5)$$

$$\omega_\alpha=794.5\ \text{rad.}\ (126.5\ \text{Hz})$$

With these values of parameters, we have obtained the natural mode shapes shown in Fig. 13. The first natural mode shape is wash-in with the pivotal point located at 4.25 semichord behind the midchord. The second mode represents the torsion mode with the pivotal point located at 0.254 semichord upstream of the midchord.

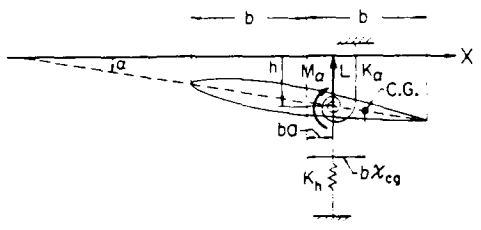


Fig. 12 Binary system of airfoil



f_1=90.0 Hz $\qquad$ f_2=818.2 Hz

x_{pv1}=4.25 $\qquad$ x_{pv2}=-0.254

Fig. 13 Natural vibration modes

THIS DOCUMENT PROVIDED BY THE ABBOTT AEROSPACE
TECHNICAL LIBRARY
ABBOTTAEROSPACE.COM

3.2 Aeroelastic Response Calculation

The aeroelastic response calculation has been performed by the modal approach using these natural mode shapes. The equations of motion of the binary system expressed in the generalized coordinates are solved by coupling with the Navier-Stokes equations. The airfoil section at 80 percent semispan station of our 3D forward swept wing model (Ref 1) is employed for the present 2D numerical simulation. The airfoil is a natural laminar flow type supercritical section of about 12 percent thick.

The flow condition used for the present aeroelastic response calculations is M=0.724, R=1.1x10^5, α=2 degrees and q=50 Kpa. For the solution of the Navier-Stokes equations, 140x50 grid points with $y^+_1 \doteq 1.0$ are employed. The time step size used is Δt=0.002.

In Fig. 14, the time responses of the generalized coordinates q_i (i=1,2) are shown. It can be seen that the magnitude of the response of the 2nd mode is the order of only about 1 percent of that of the 1st mode. Therefore, it can be concluded that this is essentially a single-degree-of-freedom flutter for which the first natural mode is predominant. From the response of the first mode, it can be identified that the flutter frequency is 76.9 Hz. It should be noted that the flutter frequency of 76.9 Hz is about 15 percent lower than the first natural frequency 90.0 Hz of this binary system. This seems to correspond, qualitatively, with our experimental results obtained for 3D non-tailored forward swept wing model, that is mentioned previously. That is, the experimental flutter frequencies of the 3D wing model are about 70.0 Hz, which is about 13 percent lower than its first natural frequency of 80.7 Hz (Ref 1). In Fig. 15, the time responses of the pitching moment (about the pivotal point of the first natural mode : x_{pv1}=4.25) and the twist angle θ_t are shown.

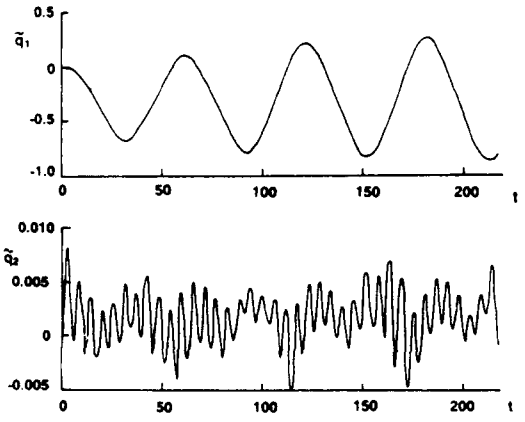


Fig. 14 Responses of Generalized coordinates (M=0.724, R=1.1x10^5, α=2^o, q=50 Kpa)

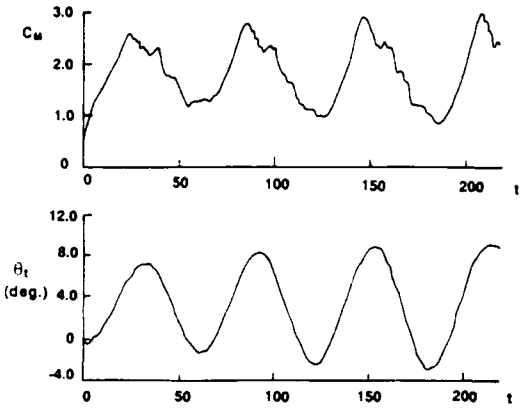


Fig. 15 Responses of pitching moment and twist angle (about pivotal point of the first natural mode) (M=0.724, R=1.1x10^5, α=2^o, q=50 Kpa)

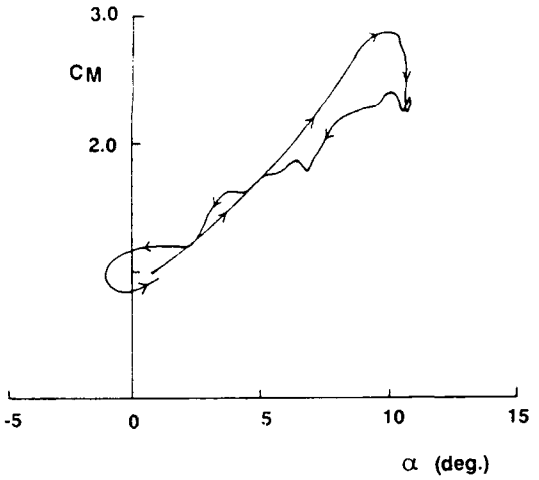


Fig. 16 Behavior of pitching moment (about pivotal point of the first natural mode) on C_M-α plane (M=0.724, R=1.1x10^5, α=2^o, q=50 Kpa)

THIS DOCUMENT PROVIDED BY THE ABBOTT AEROSPACE
TECHNICAL LIBRARY
ABBOTTAEROSPACE.COM

In order to see the mechanism of the single-degree-of-freedom flutter, it is better to plot the behavior of the pitching moment on C_M~α plane as shown in Fig. 16. In the figure, the variation of the pitching moment from t=120 to t=190 is plotted. This hysteresis loop of C_M~α curve clearly shows the mechanism of the single-degree-of-freedom flutter, in which the work done by the pitching moment to the airfoil motion becomes positive, leading to the diverging oscillation. In order to see the reason why this kind of hysteresis loop is produced, the instantaneous flow pattern (iso-density contour), pressure distrubution and the instantaneous value of the pitching moment in the C_M~α curve at the several typical time steps are plotted in Figs. 17. The flow patterns at t=142.0 - t=154.0 clearly show the process that the flow separation induced by the shock wave rapidly spreads toward the leading edge, leading to the shock-stall phenomenon. It is also interesting to see that the considerable portion of the flow on the upper surface is still separated during the pitch-down motion (t=158.8 - t=175.6). Thus, the flow patterns during the pitch-up motion and those during the pitch-down motion are completely different each other producing the hysteresis loop of C_M~α curve. Any way, these figures manifest themselves that the shock-stall phenomenon is the predominant feature of this flutter. It should be noted that this kind of single-degree-of-freedom flutter is always possible when the first natural mode shape is wash-in and the pitching moment about the pivotal point varies in advanced phase against the airfoil pitching motion about the pivotal point.

4. CONCULDING REMARKS

In order to confirm, qualitatively, the unusual flutter phenomenon, which has been observed experimentally for the high-aspect-ratio (non-tailored) forward swept wing model, as a shock-stall flutter, the aeroelastic response calculation of a two dimensional airfoil whose vibration characteristics are similar to those of the typical section of a forward swept wing, has been performed by using the compressible Navier-Stokes equations as a flow solver. By the examination of the flow pattern, pressure distribution and the behavior of the unsteady aerodynamic forces during the diverging oscillation of the airfoil, it is concluded that this is a shock-stall flutter, in which the large scale shock-induced flow separation is playing the dominant role and that there is a mechanism of putting energy into the elastic system of the airfoil, leading to nearly a single-degree-of-freedom flutter. It should be pointed out here that the numurical simulation technique using the Navier-Stokes code is a very usuful tool to investigate viscous dominated aeroelastic phenomena qualitatively such as those investigated here although ,for the rigorous quantitative simulation, further validation of the code, especially its capability for treating the unsteady large scale shock induced flow separation phenomenon is still needed.

REFERENCES

1. Isogai, K.,"Transonic Flutter/Divergence Characteristics of Aeroelastically Tailored and Non-Tailored High-Aspect-Ratio Forward Swept Wings", ICAS-90-1.1.2, Proceedings of ICAS 1990, Stockholm, Sweden, September 9-14, 1990, pp. 11-18.

2. Albano, E. and Rodden, W.P.,"A Doublet-Lattice Method for Calculating Lift Distributions on Oscillating Surfaces in Subsonic Flows", AIAA J., Vol. 7, Feb., pp. 279-285.

3. Yee, H.C. and Harten, A.,"Implicit Scheme for Hyperbolic Conservation Laws in Curvilinear Coordinates", AIAA Paper 85-1513, 1985.

4. Beam, R., and Warming, R.F.,"An Implicit Finite-Difference Algorithm for Hyperbolic Systems in Conservation Law Form", J. Comp. Phys. Vol.22, 1976, pp. 87-110.

5. Steger, J.L.,"Implicit Finite-Difference Simulation of Flow about Arbitrary Two-Dimensional Geometries", AIAA J., Vol. 16, No. 7, July 1978, pp. 679-685.

6. Baldwin, B.S. and Lomax, H.,"Thin Layer Approximation and Algebraic Model for Separated Turbulent Flows", AIAA Paper 78-257, AIAA 16th Aerospace Sciences Meeting, Huntsville, Alabama, January 16-18, 1978.

7. Cook, P.H., McDonald, M.A. and Firmin, M.C.P., "Aerofoil RAE2822-Pressure Distributions, and Boundary Layer and Wake Measurements", AGARD-AR-138, 1979.

8. Davis, S.S. and Malcolm, G.N.,"Transonic Shock-Wave/Boundary-Layer Interractions on an Oscillating Airfoil", AIAA J., Vol. 18, No.11, Nov. 1980, pp. 1306-1312.

9. Kimura, H., private communication or also see Isogai, K., "Semi-Empirical Theory to Estimate the Airforces Acting on the Harmonically Oscillating Two-Dimensional Wing at High Angle of Attack Where Separation Can Occur", (Japanese Text) NAL TR-122, Dec. 1966.

10. Isogai, K.,"Numerical Simulation of Dynamic Stall of NACA0012 Airfoil Oscillating near Static Stall Angle Using Navier-Stokes Equations", to be published.

11. Coakley, T.J.,"Numerical Simulation of Viscous Transonic Airfoil Flows", AIAA Paper No. 87-0416, Jan. 1987.

THIS DOCUMENT PROVIDED BY THE ABBOTT AEROSPACE
TECHNICAL LIBRARY
ABBOTTAEROSPACE.COM

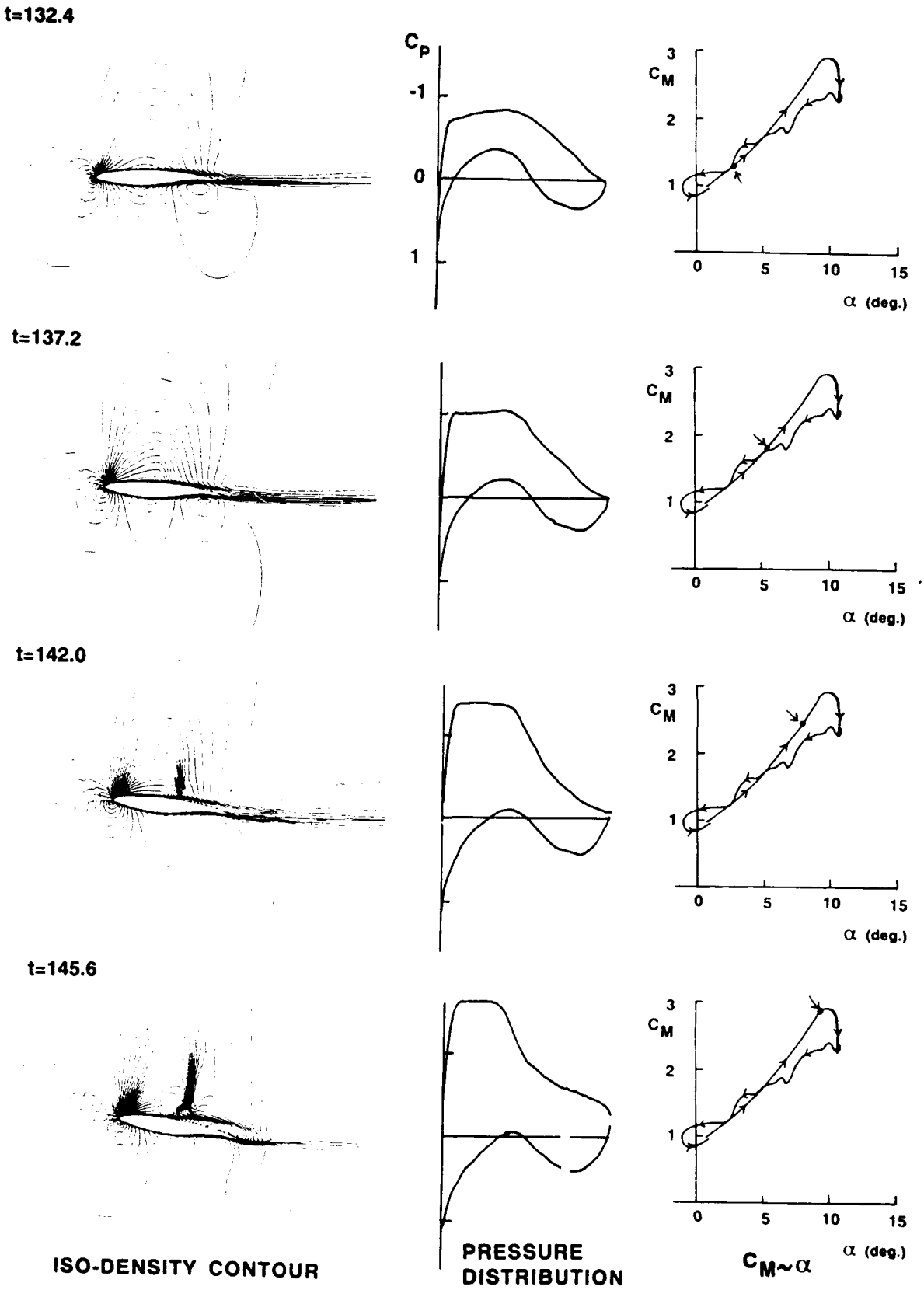


Fig. 17a Iso-density contour, pessure distribution and pitching moment
(M=0.724, R=1.1x10^5, α=2°, q=50 Kpa)

THIS DOCUMENT PROVIDED BY THE ABBOTT AEROSPACE
TECHNICAL LIBRARY
ABBOTTAEROSPACE.COM

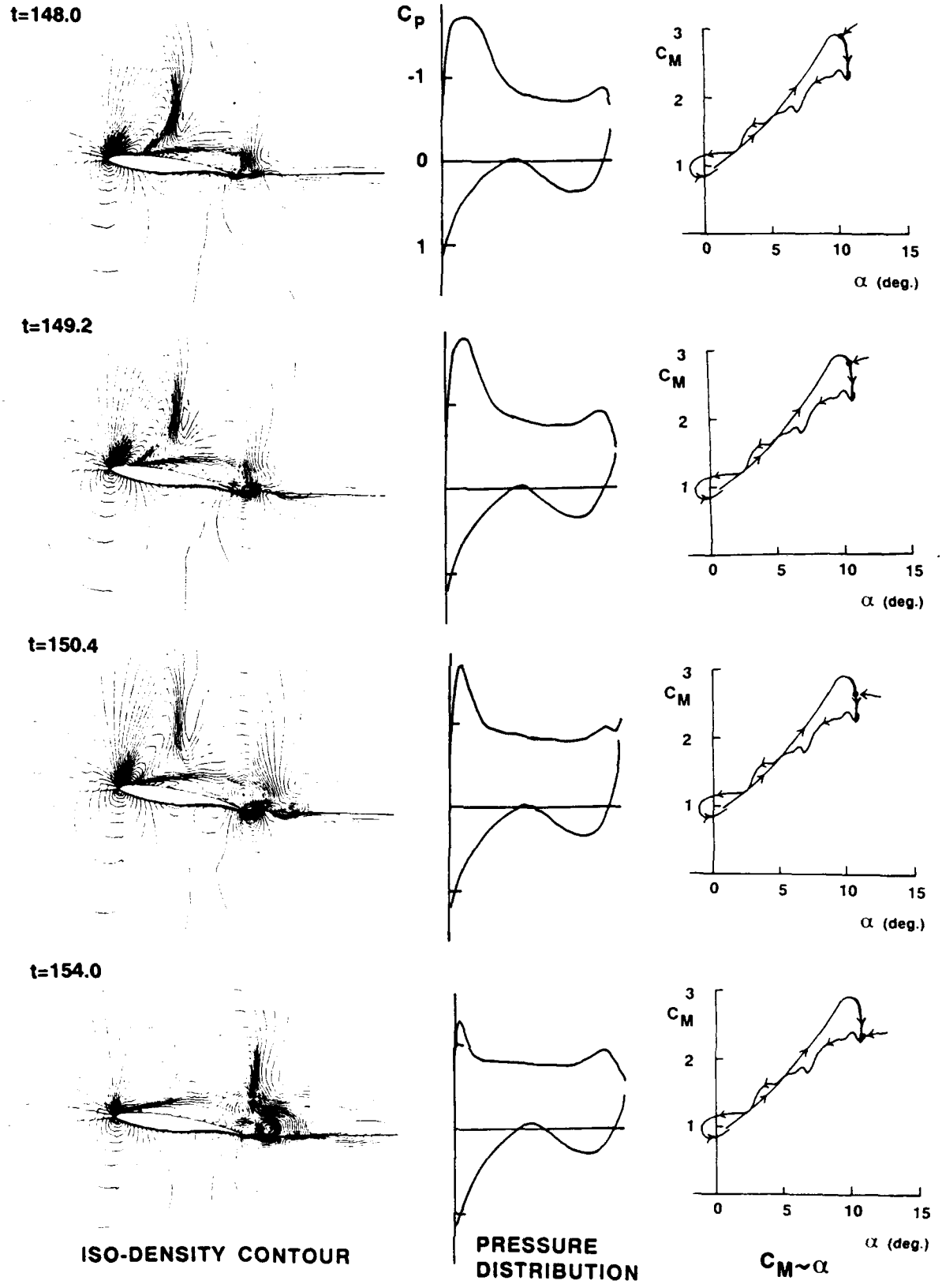


Fig. 17b - continued

This Document Provided by the Abbott Aerospace
TECHNICAL LIBRARY
ABBOTTAEROSPACE.COM

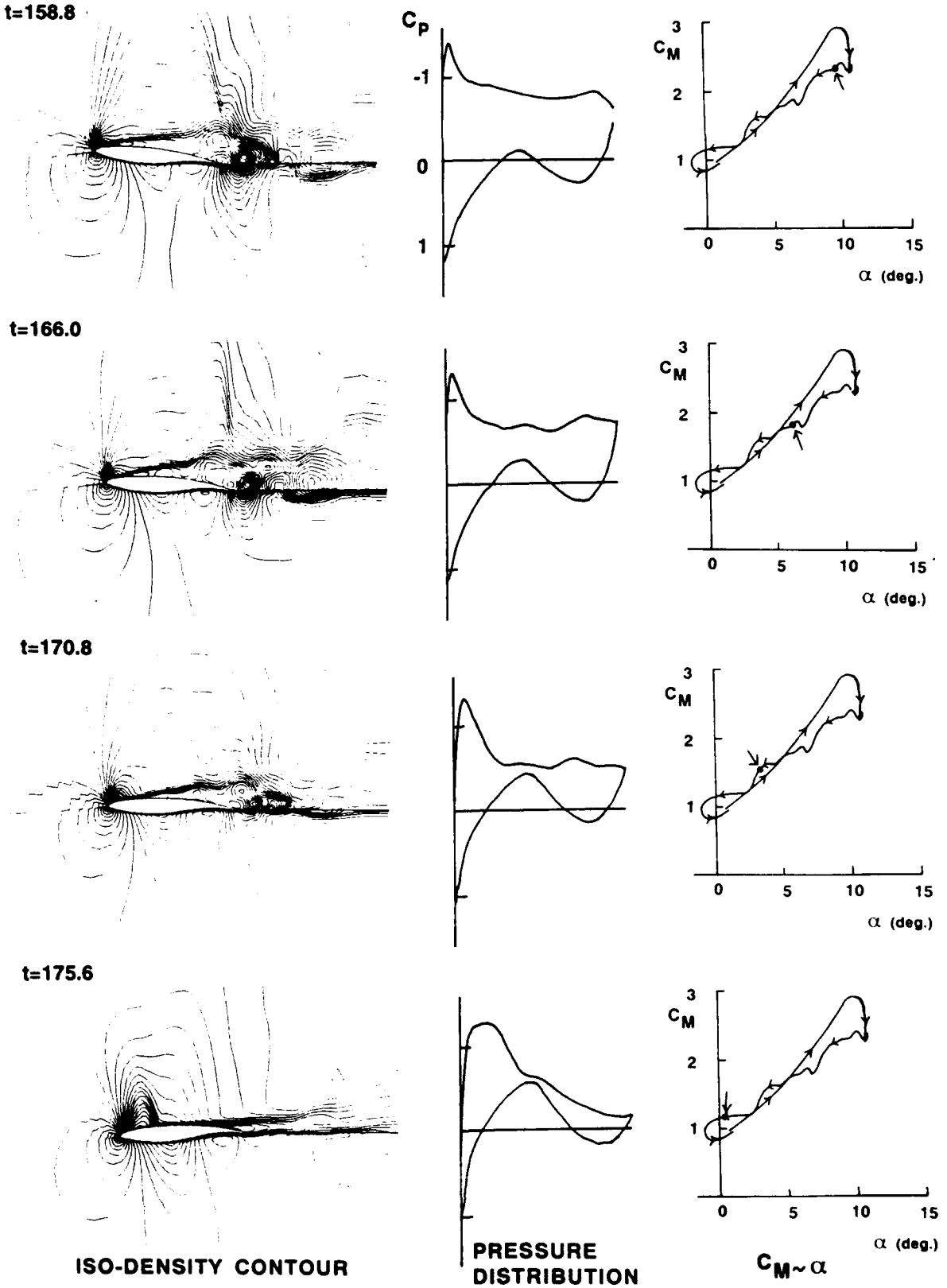


Fig. 17c - continued

THIS DOCUMENT PROVIDED BY THE ABBOTT AEROSPACE
TECHNICAL LIBRARY
ABBOTTAEROSPACE.COM

AD-P007 813

TRANSONIC AEROELASTIC COMPUTATIONS ON WINGS USING NAVIER-STOKES EQUATIONS

Guru P. Guruswamy and Shigeru Obayashi
NASA Ames Research Center, Moffett Field, California 94035.

SUMMARY

Aeroelastic computations are made on fighter-type wings in the transonic regime. The flow is modeled using the Navier-Stokes equations and is coupled with structural equations of motion. The flow equations are solved by a time accurate finite-difference scheme with moving grids. The coupled aeroelastic equations of motion are solved using the linear-acceleration method. The configuration-adaptive dynamic grids are time-accurately generated using the aeroelastically deformed shape of the wing. Computations are made for oscillating rigid wings with moving shock waves in the presence of leading edge vortices. The computed results compare well with the experiment. Unsteady computations are made to demonstrate the shock-vortex interaction phenomenon on wings in ramp motion. Effects of flexibility and pitch rate are demonstrated for flows with vortices.

SYMBOLS

A = pitch rate of ramp motion
a = speed of sound
b = full-span of the wing
C_p = coefficient of pressure
$\{d\}$ = displacement vector
E,F,G,S = flux vectors in Cartesian coordinates
M, D, K = modal mass, damping and stiffness matrices, respectively
$\{q\}$ = generalized displacement vector
Re_c = Reynolds number based on the root chord
U = flight velocity
u,v,w = Velocity components in x, y, and z directions, respectively
x,y,z = Cartesian coordinates
$\{Z\}$ = generalized force vector
α = angle of attack
γ = ratio of specific heats
Δ = difference between upper and lower surface pressures
∞ = subscript representing freestream quantities
ξ, η, ζ = general curvilinear coordinates
ρ = density
τ = nondimensional time
$[\phi]$ = modal displacement matrix
$\tilde{}$ = indicates quantities in generalized coordinate system
$\dot{}$ = represents first derivative with respect to time
$\ddot{}$ = represents second derivative with respect to time

1. INTRODUCTION

Understanding the nature of flows and their interactions with structures is becoming more important than ever for aircraft, particularly for fighters. High performance and maneuverability are playing major roles in the design of fighters. Because of extreme flight conditions, flows over fighters are quite often complex with vortices, shock waves and separation.

The formation of vortices changes the aerodynamic load distribution on a wing. Vortices formed on aircraft have caused several instabilities, such as wing rock (Ref. 1) for a rigid delta wing and aeroelastic oscillations for a highly swept flexible wing (Ref. 2). Such instabilities can severely impair the performance of an aircraft. On the other hand, there are possibilities of using the vortices to control the aircraft at high angles of attack when some of the conventional control techniques are not adequate. Also, vortical flows associated with rapid, unsteady motions has been claimed to be able to increase the unsteady lift, which can be used for maneuvering the aircraft (Ref. 3). The presence of shock waves on wings can reduce the flutter speed and considerably influence the role of active control surfaces (Ref. 4). For highly swept wings with sharp leading edges both vortices and shock-waves can be present at the same time even at moderate angles of attack in the transonic regime (see Fig. 1). Shock-induced flow separation can further complicate the above phenomena. All these phenomena are often dominated by viscous effects. For example, the aeroelastic oscillations reported for the highly swept wing in Ref. 2 is a result of the phase-lag effect of viscous dominated vortical flows involving separation. The Navier-Stokes equations are necessary to accurately model these cases dominated by viscous effects.

Unsteady computations using the Navier-Stokes equations for three-dimensional flows on flexible components have begun recently. For realistic configurations it is necessary to account for the flexibility in order to compute flows accurately. The aeroelastic deformation resulting from the flexibility of a wing can considerably change the nature of the flow. Strong

92-16051

This Document Provided by the ABBOTT AEROSPACE
TECHNICAL LIBRARY
ABBOTTAEROSPACE.COM

interactions between the vortical flows and the structures can lead to sustained aeroelastic oscillations for highly swept wings (Ref. 5). Also it is necessary to include the flexibility for proper correlations of computed data with experiments, particularly with those obtained from flight tests. In order to account for the flexibility of a wing, it is necessary to solve the aerodynamic and aeroelastic equations of motion simultaneously.

In this work, the flow is modeled using the Navier-Stokes equations and is coupled with the aeroelastic equations of motion. The computer code developed for computing the unsteady aerodynamics and aeroelasticity of aircraft using the Euler/Navier-Stokes equations is referred to as ENSAERO (Ref. 6). The flow is solved by time-accurate, finite-difference schemes based on the implicit algorithms. An algebraic model is used to compute the turbulent flows.

Results are demonstrated for typical fighter wings with moderate to high sweep angles. Computations are made at Mach numbers ranging from subsonic to transonic.

2. GOVERNING AERODYNAMIC EQUATIONS

The strong conservation-law form of the Navier-Stokes equations are used for shock capturing purposes. The thin-layer version of the equations in generalized coordinates can be written as (Ref. 7)

$$\partial_\tau \hat{Q} + \partial_\xi \hat{E} + \partial_\eta \hat{F} + \partial_\zeta \hat{G} = Re^{-1} \partial_\zeta \hat{S} \qquad (1)$$

where $\hat{Q}$, is the vector of conserved variables $\hat{E}, \hat{F}, \hat{G}$, and $\hat{S}$, are flux vectors in generalized coordinates. The following transformations are used in deriving Eq. (1).

$$\begin{aligned} \tau &= t \\ \xi &= \xi(x, y, z, t) \\ \eta &= \eta(x, y, z, t) \\ \zeta &= \zeta(x, y, z, t) \end{aligned} \qquad (2)$$

It should be emphasized that the thin-layer approximation is valid only for high Reynolds number flows and very large turbulent eddy viscosities invalidate the model.

ENSAERO utilizes two efficient numerical schemes based on central difference and upwind schemes to solve Eq. (1). The central difference scheme is based on the Pulliam-Chaussee diagonal form (Ref. 8) of the implicit, approximate-factorization algorithm of Beam and Warming (Ref. 9). The upwind scheme is based on a streamwise upwind scheme recently developed by Obayashi and Goorjian (Ref. 10). The diagonalized forms of the upwind and central difference schemes are used in the present computations.

The diagonal algorithm used both in central and upwind schemes are fully implicit for the Euler equations. For the Navier-Stokes equations the diagonal algorithm works as an explicit scheme since viscous terms in the right-hand side of Eq. (1) are treated explicitly. The diagonal algorithm is first-order accurate in time for both Euler and Navier-Stokes equations. Numerical exercises conducted during this work and in previous work reported in Ref. 6 showed that the time step size required to solve Eq. (1) is limited by accuracy rather than by stability considerations. Therefore the explicit treatment of viscous terms of the diagonal algorithm does not influence the computational accuracy when solving the Navier-Stokes equations.

For turbulent flow, the coefficient of viscosity appearing in Eq. (1) is modeled using the Baldwin-Lomax algebraic eddy-viscosity model (Ref. 11). This isotropic model is used primarily because it is computationally efficient. All viscous computations presented in this paper assume fully turbulent flow. This approximation is consistent with the high Reynolds-number assumption. It is noted that Baldwin-Lomax turbulence model may not be suitable for cases with strong shock waves. Most of the cases considered here have shock-waves with moderate strength. For vortex-dominated flow structures of swept wings, a modification to the original Baldwin-Lomax model is required. For this study, the Degani-Schiff modification (Ref. 12) to the original model for treating vortical flows is used.

3. AEROELASTIC EQUATIONS OF MOTION

The governing aeroelastic equations of motion of a flexible blended wing-body configuration are obtained using the Rayleigh-Ritz method. In this method, the resulting aeroelastic displacements at any time are expressed as a function of a finite set of assumed modes. The contribution of each assumed mode to the total motion is derived by the Lagrange's equation. Furthermore, it is assumed that the deformation of the continuous wing structure can be represented by deflections at a set of discrete points. This assumption is valid for linear structures and facilitates the use of discrete structural data, such as the modal vector, the modal stiffness matrix, and the modal mass matrix. The number of modes required is determined by the complexity of the structure. Four to six modes are adequate to accurately model a clean wing without control surfaces and external stores. The modal data can be generated from a finite-element analysis or from experimental influence coefficient measurements. In this study, the finite-element method is used to obtain the modal data.

It is assumed that the deformed shape of the wing can be represented by a set of discrete displacements at

THIS DOCUMENT PROVIDED BY THE ABBOTT AEROSPACE
TECHNICAL LIBRARY
ABBOTTAEROSPACE.COM

selected nodes. From the modal analysis, the displacement vector $\{d\}$ can be expressed as

$$\{d\} = [\phi]\{q\} \tag{3}$$

where $[\phi]$ is the modal matrix and $\{q\}$ is the generalized displacement vector. The final matrix form of the aeroelastic equations of motion is

$$[M]\{\ddot{q}\} + [G]\{\dot{q}\} + [K]\{q\} = \{Z\} \tag{4}$$

where [M], [G], and [K] are modal mass, damping, and stiffness matrices, respectively. $\{Z\}$ is the aerodynamic force vector defined as $(\frac{1}{2})\rho U_\infty^2[\phi]^T[A]\{\Delta C_p\}$ and $[A]$ is the diagonal area matrix of the aerodynamic control points.

The aeroelastic equation of motion, Eq. (4), is solved by a numerical integration technique based on the linear acceleration method (Ref. 13).

4. AEROELASTIC-CONFIGURATION-ADAPTIVE GRIDS

One of the major problems in computational aerodynamics using the Euler/ Navier-Stokes equations lies in the area of grid generation. For steady flow simulations, advanced techniques such as zonal grids are being used for full aircraft. Such grid-generation techniques for aeroelastic calculations that involve moving components are in an early stage of development (Ref. 14). The effects of the aeroelastic-configuration-adaptive dynamic grids on the stability and accuracy of the numerical schemes are yet to be studied in detail.

This work developed an algebraic grid-generation technique for aeroelastic applications. The scheme satisfies the general requirements of a grid required for finite-difference schemes used in the analysis. Some of the requirements are: 1) the grid lines intersect normal to the wing surface in the chordwise direction, 2) the grid cells are smoothly stretched away from the wing surface, 3) the outflow boundaries are located far from the wing to minimize the effect of boundary reflections, and 4) the grids adapt to the deformed wing position at each time step.

The computational grids used in this study have a C-H topology, as shown in Fig. 2 for a typical fighter wing. The grid deforms to remain coincident with the wing surface as it deflects, while the outer boundary of the grid is fixed in space. At the end of each time step, the deformed shape of the wing is computed using Eq. (4). The ξ and η grid distributions on the grid surface corresponding to the wing surface (ζ grid index = 1) are obtained from previously assumed distributions. These distributions are selected to satisfy the general requirements of a grid for accurate computations. In this work, the grid in the ξ direction is selected so that the grid spacing is small near the wing and stretches exponentially to the outer boundaries. The grid near the leading edge is made finer than the rest of the wing in order to model the geometry accurately. In the spanwise direction, a uniformly distributed grid spacing is used on most of the wing. To model the wing tip, a finer grid spacing is used. Away from the wing tip, the outboard η grid spacing stretches exponentially. The ζ grid spacing is computed at each time step using the deformed shape of the wing computed using Eq. (4). The ζ grid lines start normal to the surface in the chordwise direction and their spacing stretches exponentially to a fixed outer boundary. To prevent the outer boundaries from moving, the grid is sheared in the ζ direction. The shearing is accomplished so that the outer boundary remains stationary and inner point are re-distributed using an exponential stretching function. During this shearing, the number of ζ grid points are kept constant. The metrics required in the computational domain are computed using the following relations

$$\begin{aligned} \xi_t &= -x_\tau\xi_x - y_\tau\xi_y - z_\tau\xi_z \\ \eta_t &= -x_\tau\eta_x - y_\tau\eta_y - z_\tau\eta_z \\ \zeta_t &= -x_\tau\zeta_x - y_\tau\zeta_y - z_\tau\zeta_z \end{aligned} \tag{5}$$

The grid velocities x_τ, y_τ, and z_τ required in Eq. (5) are computed using the grids at new and old time levels. The ability of this scheme to compute accurate aeroelastic responses has been demonstrated in Ref. 15.

Computational efficiency and robustness of the solution method are important for computationally intensive aeroelastic calculations with configuration-adaptive grids. The diagonal algorithm used in the present study computes time accurate calculations in a geometrically nonconservative fashion. Geometric conservation in time can improve the accuracy of the results for moving grids. However, earlier studies have shown that satisfying geometric conservation has little effect on the solutions associated with the moving grids (Ref. 16). The time steps used for Navier-Stokes calculations are typically small enough that the temporal error from geometric nonconservation is negligible for most practical purposes. The validation of computed results with experiments reported in this paper further support the use of the diagonal scheme for computations associated with moving grids. In order to maintain the efficiency and robustness of the diagonal scheme, the present time accurate computations are made without geometric conservativeness in time.

5. RESULTS

In this work, computations are made for typical fighter-type wings. All computations are made using a C-H type grid shown in Fig. 2. The grid have 151, 25, and 34 points in the streamwise, spanwise, and normal directions, respectively. The grid spacing in the direction normal (ζ) to the surface of the wing is of the order 10^{-5} times the chord length. The minimum grid spacing in the ξ direction along the wing surface is of

THIS DOCUMENT PROVIDED BY THE ABBOTT AEROSPACE
TECHNICAL LIBRARY
ABBOTTAEROSPACE.COM

the order 10^{-3} of the chord length. The number of grid points on the wing in the chordwise and spanwise directions are 121 and 17, respectively. The distribution in the chordwise direction is selected such that the flow details near the leading and trailing edges and near the shock wave are adequately resolved. The distribution of the grid in the spanwise direction is selected such that the spacing is uniform over most of the wing and becomes finer as it approaches the tip. The main objective of this work is to capture most of the flow details in the streamwise and normal directions. Though the present grid is adequate to model the spanwise three-dimensional effects, it is not designed to capture details of the flow over the tip. From numerical experiments, it is found that this grid spacing is adequate to compute surface pressures associated with turbulent flows including shock waves and vortices on the wing. It is noted that the present grid has a smaller number of grid points than that normally used for computationally less intensive steady flow computations. In this work, the number of grid points are reduced so that the computational time is practical to make computationally expensive unsteady calculations on flexible wings.

All computations are made on CRAY-YMP832 computers available at Ames and NAS (Numerical Aerodynamic Simulation). The current version of ENSAERO runs at 160 MFLOPS (million floating point operations per second) with a single processor. The central processing unit (CPU) times per time step per grid point are 15 and 17 micro seconds for the central and upwind options, respectively.

5.1 Computations on Conventional-Type Fighter Wing

All these computations are made using the central difference option of the code.

5.1.1 Steady Flow

Steady-state computations are made on the F-5 wing of aspect ratio 2.98 and taper ratio 0.31 to validate the code. The leading-edge sweep angle is 32 deg. For this wing, wind tunnel data is available from an experiment conducted by Tijdeman et. al. (Ref. 17) at the National Aeronautical Laboratory of the Netherlands (NLR). Figure 3 shows the computed and measured steady pressures at $M_\infty = 0.90$, $\alpha = 0.0$ deg, and Re_c (Reynolds number based on the root chord) $= 12.0 \times 10^6$. The computed steady pressures compare well with the experimental data for all span stations. Slight discrepancies near the leading edge can be attributed to the grid resolution. It is noted that the F-5 wing has a nose that droops down and thus requires a very fine grid to capture complete details of the flow. Since the main objective of this work is to design a grid that is suitable for unsteady flows, it was beyond the scope of the current work to concentrate grid near the nose. This computation verifies the suitability of the grid to make computations on fighter-type wings.

5.1.2 Oscillating Rigid Wing

Time accuracy of the computed results is important for aeroelastic applications. One conclusive way of verifying the time accuracy is by computing flows over oscillating wings and comparing unsteady pressure results with the experiment. In this case, there is a definite reference motion of the wing to verify the time accuracy. This procedure is more exact than just comparing the time averaged pressures of arbitrary motions. In this section, computations are made on the F-5 wing oscillating in a pitching mode.

Figure 4 shows the modal motion used in the wind tunnel experiment (Ref 17). The wing is pitching about an axis located at the 50% root chord and the pitching axis is normal to the wing root. Computations were made for the transonic $M_\infty = 0.90$ at $Re_c = 12.0 \times 10^6$ and a mean angle attack of zero. Figure 5 shows plots of the upper surface unsteady pressures at four span stations computed by the Navier-Stokes equations and from the NLR experiments. These results of were obtained by harmonically oscillating the wing in a sinusoidal motion at a frequency of 40 Hz with an amplitude of 0.11 deg as was done in the experiment. Results from the code were obtained by forcing the wing to undergo a sinusoidal modal motion for three cycles with 1440 time steps per cycle, during which time the transients disappeared and a periodic response was obtained. From numerical experiments it was found that 1440 time steps per cycle was adequate to compute unsteady pressures accurately. The results for the third cycle are shown.

At $M_\infty = 0.90$, where the flow is transonic, the comparisons shown in Fig. 5 are good except near the root and tip. Discrepancies near the root may be due to the wall viscous effects which are not accounted for in this analysis. A greater number of spanwise stations than are currently used would further improve the solution near the tip. Some discrepancies found at other span stations can be attributed to the inconsistency in the measured data, particularly near shock waves. In general, the computed shock wave is slightly downstream of the measured one. These favorable comparisons with the experiment demonstrate the time-accuracy of the present computations. Additional computations of flow about the F-5 wing using the central and upwind methods are presented by the authors in Refs. 18 and 16, respectively.

5.1.3 Wings in Ramp Motion

In this section, the code is demonstrated to compute flow over a typical fighter-wing pitching from $\alpha =$ 0.0 to 30.0 deg in a ramp motion. The wing selected is

THIS DOCUMENT PROVIDED BY THE ABBOTT AEROSPACE
TECHNICAL LIBRARY
ABBOTTAEROSPACE.COM

of aspect ratio of 3.0, taper ratio of 0.30 and leading-edge sweep angle of 30 deg with NACA0015 sections. Computations are made on both rigid and flexible configurations. All computations for both the rigid and flexible wings are made for $M_\infty = 0.50$ and $Re_c = 2.0$ x 10^6, using a time-step size of 8.4×10^{-3}. From numerical experiments, it was found that the time-step size used is adequate to obtain a stable and accurate unsteady solution. This computation requires about 5 hours of CPU time on CRAY-YMP832 computer.

For the rigid wing, computations were made at three pitch rates (A) of 0.10, 0.050, and 0.025. The pitch rate, A, is defined as $\dot{\alpha}c/U_\infty$ where α is in radians. Figure 6 shows computed responses of upper surface unsteady pressures for the rigid wing undergoing a ramp motion from $\alpha = 0.0$ to 30 deg at a pitch rate of 0.1. For this pitch rate, the wing reaches $\alpha =$ 30 deg at a nondimensional time of 10.47 as indicated by the arrow in Fig. 6. Chordwise pressure histories for spanwise stations located at 2y/b = 0.0, 0.3, 0.60 and 0.90 are shown in Figs. 6a - 6d, respectively. The unsteady computations are started from a converged steady state solution at $\alpha = 0.0$ deg. Figure 6 shows the vortex/wing interaction due to initiation, development and convection of the leading-edge vortex by means of surface pressure histories plotted at four span stations. The results in Fig. 6 show the evaluation and dynamics of vortex development. As the wing is pitched toward the maximum angle of attack, a rapid pressure decrease (increasing suction peak) occurs over the leading edge which signals the formation of a leading-edge vortex. This vortex starts moving downstream rapidly after the wing has reached a certain angle of attack. The vortex motion is highly three dimensional. The vortex core starts moving downstream earlier for span stations closer to the tip. Also it is observed that the tip stall occurs before the root stall. A similar phenomenon has been observed in an experimental study for a rectangular wing at a low Mach number (Ref. 19).

One area where unsteady vortical flows play an important role is in increasing the dynamic lift. From earlier studies (Ref. 3) on airfoils, it has been observed that the dynamic lift can be increased by increasing the pitch rates. It is expected that such increases in the dynamic lift can be used in maneuvering an aircraft (Ref. 3) Because the dynamic lift is an unsteady phenomenon and is associated with the presence of vortices, it is important to model it accurately. The present computational tool was used to investigate dynamic lift over fighter wings, including the wing flexibility. Computations are made for the rigid fighter wing for pitch rates A = 0.05 and 0.025, and the results are compared with those obtained earlier for A = 0.10. The unsteady lift is plotted against time in degrees in Fig. 7. Thus the wing reaches the maximum value $\alpha = 30$ deg at t (in degrees) = 30. For all pitch rates, the stall occurs at the wing tip before it occurs at the root section. The increase in the dynamic lift at the higher pitch rates can be seen in Fig. 7.

5.2 Computations on Clipped-Delta Wing

To verify the accuracy of the present code for simulating the complicated flow field containing a leading-edge vortex and a shock wave, test cases are chosen from the experiment on a clipped delta wing undergoing prescribed pitching motion (Ref. 20). Since the experiment was conducted using a Freon test medium, the ratio of specific heats γ is set to 1.135 in the following computations. All the following computations are made by using the upwind option of the code.

5.2.1 Steady Flow

Steady-state calculations have been performed to examine the validity of the numerical procedure and the computational grid. The wing has a leading-edge sweep angle of 50.4 deg and a 6%-thick circular-arc airfoil section. The ξ, η, and ζ coordinates represent the chordwise, spanwise, and normal (to the wing surface) directions, respectively in the C-H topology. The grid contains $151 \times 25 \times 34$ points.

With the present grid, a typical unsteady case can be computed within 5 hr by using a Cray YMP computer with a single processor. (The code requires about 19 μsec per grid point per time step for a flexible-wing case.) Then, three different time-step sizes were tried for each case to check the dependency in time-step sizes. Thus, in total, it took about 17 hr to complete one unsteady pitching case including the corresponding steady-state computation.

The present grid was chosen from several candidate grids by comparing the pressure distributions computed using each grid with the experiment for a typical flow condition containing both a leading-edge separation and a shock wave at steady state. Among those grids, the H-O grid topology was also considered. However, the results showed that it did not have any advantage over the C-H grid topology either in capturing a leading-edge vortex (because of the moderate sweep angle of the present delta wing) or in capturing a shock wave (because of the relatively coarse grid distribution in the streamwise direction). The present grid is found to give a reasonable agreement with the experiment because the leading-edge vortex is formed at relatively low angles of attack due to the sharp leading edge.

Two steady-state cases are computed for flow conditions at $M_\infty = 0.90$ with angles of attack $\alpha = 3$ and 4 deg. The Reynolds number based on the root chord is about 17 million. Figures 8 and 9 show the comparisons of steady pressures between the computed and measured data at 34%, 54%, and 68% semispan sections for $\alpha = 3$ and 4 deg, respectively. The shock wave appears in the computed pressure distributions at $M_\infty = 0.9$. Suction peaks near the leading edge indicate the formation of the vortex along the leading edge.

THIS DOCUMENT PROVIDED BY THE ABBOTT AEROSPACE
TECHNICAL LIBRARY
ABBOTTAEROSPACE.COM

At $\alpha = 3$ deg, weak suction peaks are found only at the outboard sections. At $\alpha = 4$ deg, the suction peaks appear larger and develop from more inboard sections. This indicates that the leading-edge vortex develops as the angle of attack increases from 3 to 4 deg. Therefore, the computed results successfully represent the effects of the different angles of attack. At 4 deg angle of attack the leading edge vortex with a stronger suction peak is located further downstream than at 3 deg. It appears that the angle of attack has less influence on the shock wave structure than on the vortex structure.

For all cases, the computed results show good agreement with the experimental data at inboard sections. On the other hand, the comparisons at the outboard section show that the peaks near the leading edge in the computed profiles are located farther downstream than in the experimental data. In other words, the computed results predict the location of the leading-edge vortex more inboard than the experiment. (As a result of the discrepancy in the leading-edge region, the downstream upper-surface pressure shows a minor disagreement, too.) One of the sources of the discrepancy is the fact that the flow was probably transitional in the experiment. Even though the modified Baldwin-Lomax model is used here, the model still assumes a fully turbulent flow. Another source is from the slots at 57% and 83% semispan stations because of leading-edge and trailing edge control surfaces of the wind tunnel model.

5.2.2 Rigid Wing in Pitching Motion

The unsteady data are given for the case when the rigid wing is oscillating in the pitching mode, $\alpha(t) = \alpha_m - \bar{\alpha}\sin(\omega t)$, about an axis at 65.22% root chord, where ω is the pitching circular frequency in radians per second. Computations are made for flow conditions at $M_\infty = 0.90$ with mean angles of attack $\alpha_m = 3$ and 4 deg, a pitch amplitude $\bar{\alpha} = 0.5$ deg and a frequency of 8 Hz that corresponds to a reduced frequency of $k \simeq 0.6$ ($k = \omega c/U_\infty$ where c is the root chord).

Unsteady computations are started from the corresponding steady-state solutions. The number of time steps per cycle of 3600 was chosen from the numerical experiments to assure the time accuracy (the typical time-step size was about 3.2×10^{-3}). The convergence of the unsteady computations to a periodic flow is verified by comparing the results between cycles. The third-cycle results are shown in the following. The numerical transient is confirmed to disappear within two cycles.

Figures 10 and 11 show the comparisons of unsteady pressures between the computed and measured data at 34%, 54%, and 68% semispan sections for α_m = 3 and 4 deg. The plots show the comparison of real and imaginary parts of the first Fourier component between the computed and measured unsteady upper surface pressure coefficients of the wing. Consistent with the steady pressures, the peaks near the leading edge in the computed profiles are located farther downstream than the experimental data at the outboard sections. Although the experimental data at the 68% section in Fig. 10 shows no effect due to the leading-edge vortex, it is inconsistent with the other data. Overall, the numerical results show fairly good agreement with the experimental data. Again, the difference of shock motion due to the Mach numbers and the difference of the vortex motion due to the angles of attack are successfully captured.

5.2.3 Rigid and Flexible Wings in Ramp Motion

In maneuvering, aircraft often undergo rapid ramp motions. During such motions, flow unsteadiness and wing flexibility play important roles. In this section, the applicability of the present development to computing such flow fields is demonstrated.

Computations are performed for rigid and flexible wings in ramp motion. Structural properties of the wing were selected to represent a typical fighter wing. Figure 12 shows the mode shapes and the frequencies of the first four normal modes for the clipped delta wing used in the following computations. The dynamic pressure is set to be 1.0 psi. Test cases consider 10 deg ramp motions for both rigid and flexible wings.

The sectional lift responses for the 10 deg ramp motion at several spanwise sections are shown in Fig. 13. The computations are again started from the steady-state solution at 0 deg angle of attack. The flexible wing gives lower lift because of the deformation of the wing. The unsteady increase of the lift is observed more widely in both rigid and flexible cases. The sectional lift at the 90% section indicates a stall before reaching 10 deg angle of attack for both rigid and flexible wings. Instead, the plot does not have any significant perturbations. Figure 14 shows the deformation of the wing at 1600 time steps (the ramp motion ends at 1500 time steps: $t \simeq 0.10$ *sec*). The actual displacement of the leading edge at the wing tip is 1.7% of the root chord length.

Figures 15 and 16 show the corresponding pressure history plots of every 100 time steps for the rigid and flexible cases, respectively. The deformation of the wing does not affect the flow field strongly because the leading-edge vortex lifts off from the wing surface at the outboard sections. Since there is no significant difference in both plots, the flexible case (Fig. 16) is considered in the following discussion. At the most inboard section, the pressure distributions show no interaction of the leading-edge vortex with the shock wave. The flexibility does not play an important role here because the section is close to the wing root. At the 54% section, both vortex and shock wave develop, then both

THIS DOCUMENT PROVIDED BY THE ABBOTT AEROSPACE
TECHNICAL LIBRARY
ABBOTTAEROSPACE.COM

disappear. At the 68% section, a similar but more rapid change occurs. This rapid reduction of the lift indicates a vortex breakdown.

To see the interaction of the leading-edge vortex with the shock wave, the density contours at the 68% section are plotted every 200 time steps from 1200 to 2400 time steps ($0.08 < t < 0.16$) in Fig. 17. Initially there is no interaction between the vortex and the shock wave. As the vortex develops, it moves toward the trailing edge, that is, toward the shock wave. When the vortex starts to interact with the shock wave, the shock wave starts to ride on the shear layer and to form a lambda type shock wave. At this point, the shock wave disappears from the surface pressure plots. As the front shock grows, the flow separation grows and the vortex core bursts quickly. Simultaneously, the rear shock weakens. Finally, the fully separated flow is observed. However, computations with finer grids are required to make more definitive conclusions on the flow structure. Also unsteady computations should be preceded by the selection of an optimum grid. This can be done by conducting a systematic grid refinement study such as that reported in Ref. 21.

Figure 18 shows the corresponding contour plots of the negative u-component. The contours are plotted at intervals of 0.1 (bold line indicates $u = 0$). Up to 1800 time steps, no negative contours are observed. As the vortex is deformed by the strong front shock at 2000 time steps ($t \simeq 0.13$ *sec*), a negative u region appears. As the vortex core diffuses, a reverse flow region grows. The shock wave plays an essential role in the process of this breakdown. Figure 19 shows plots of the streamline pattern at 1500 and 2400 time steps ($t \simeq 0.10$, 0.16 *sec*, respectively). At 1500 time steps, when the ramp motion has just ended, a leading-edge separation is formed over the entire span. Although it is not clear from the plots, the vortex starts bursting near the tip as indicated in Fig. 16d. In contrast, at 2400 time steps, a bubble-type breakdown is clearly observed in the middle of the span. The breakdown grows toward the upstream slowly. Then the flow reaches the nearly steady state.

Although no corresponding experiment was performed for the present wing at this angle of attack, Ref. 22 reported a vortex breakdown about a similar wing at similar flow conditions, including a comparison with experiment. A further grid-refinement study will be required to assess the validity of the present observations.

Figure 20 shows the lift response of the flexible wing for a longer period plotted with the variation of the effective angle of attack. After the initial lift increase, the lift oscillates due to the structural oscillation. Figure 21 shows the corresponding first and second modal responses of the flexible wing. The first mode response is damping, but the second mode response stays oscillatory. More details about this case is given in Ref. 23.

6. CONCLUSIONS

The following conclusions can be made based on the present work.

1. Coupled solutions of the time-accurate three-dimensional Navier-Stokes equations and those of the modal structural equations of motion have been demonstrated for fighter-type wings.
2. The time-accurate Navier-Stokes solutions are valid for laminar and turbulent flows, and permit computation of aeroelasticity associated with shock/vortex interactions driven by viscous phenomena which cannot be predicted using either potential or Euler solutions.
3. Steady and unsteady computations for fighter wings show good general qualitative and also specific quantitative agreements with experiments.
4. The shock/vortex interaction for unsteady flows is successfully simulated for the clipped delta wing.
5. For the 10 deg ramp motion, a possible vortex breakdown is observed for the clipped delta wing. The interaction with the shock wave plays an essential role in the process of the breakdown observed in the present calculation.
6. Further studies are required using finer grids for more complete geometry using improved turbulence models.

7. REFERENCES

1. Nguyen, L. T., Yip, L. P., and Chambers, J. R., "Self-Induced Wing Rock Oscillations of Slender Delta Wings," AIAA Paper 81-1883, August 1981.
2. Dobbs, S. K. and Miller, G. D., "Self-Induced Oscillation Wind Tunnel Test of a Variable Sweep Wing," AIAA Paper 85-0739, April 1985.
3. Mabey, D. G., "On the Prospects for Increasing Dynamic Lift," *Aeronaut. J. Roy. Aeronaut. Soc.* Mar. 1988, pp. 95-105.
4. Guruswamy, G. P., Goorjian, P. M., Ide, H. and Miller, G. D. "Transonic Aeroelastic Analysis of the B-1 Wing," *J. of Aircraft* Vol. 23, No. 7, July 1986, pp. 547-553.
5. Guruswamy, G. P. "Integrated Approach for Active Coupling of Fluids and Structures, " *AIAA J.* Vol. 27, No. 6, June 1989, pp 788-793.
6. Guruswamy, G. P., "ENSAERO- A Multidisciplinary Program for Fluid/Structural Interaction Studies of Aerospace Vehicles , " *Computing Systems in Engineering* Vol. 1, Nos2-4, pp 237-256, 1990.
7. Peyret, R. and Viviand, H., "Computation of Viscous Compressible Flows Based on Navier-Stokes Equations," AGARD AG-212, 1975.

This Document Provided by the ABBOTT AEROSPACE
TECHNICAL LIBRARY
ABBOTTAEROSPACE.COM

8. Pulliam, T. H., and Chaussee, D. S., "A Diagonal Form of an Implicit Approximate Factorization Algorithm," *J.of Comp. Phys.*, Vol. 39, No. 2, Feb. 1981, pp. 347-363.
9. Beam, R. and Warming, R. F., "An Implicit Finite-Difference Algorithm for Hyperbolic Systems in Conservation Law Form," *J. of Comp. Phys.*, Vol. 22, No. 9, Sept. 1976, pp. 87-110.
10. Obayashi, S., Goorjian, P. M, and Guruswamy, G. P., "An Extension of a Streamwise Upwind Algorithm to a Moving Grid System," NASA TM-102800, April 1990.
11. Baldwin, B. S and Lomax, H.,"Thin-Layer Approximation and Algebraic Model for Separated Turbulent Flows, " AIAA Paper 78-257, 1978.
12. Degani, D. and Schiff, L. B., "Computations of Turbulence Supersonic Flows Around Pointed Bodies Having Crossflow Separation," *J. Computational Physics*, Vol. 66, No. 1, Sept. 1986, pp. 173-196.
13. Guruswamy, P. and Yang, T. Y., "Aeroelastic Time Response Analysis of Thin Airfoils by Transonic Code LTRAN2," *Computers and Fluids*, Vol. 9, No. 4, Dec. 1980, pp. 409-425.
14. Chaderjian, N., and Guruswamy, G. P. "Unsteady Transonic Navier-Stokes Computations for an Oscillating Wing Using Single and Multiple Zones," AIAA paper 90-0313, Jan. 1990.
15. Guruswamy, G. P., "Unsteady Aerodynamic and Aeroelastic Calculations for Wings Using Euler Equations," *AIAA J.*, Vol. 28, No. 3, March 1990, pp. 461-469.
16. Obayashi, S., Guruswamy, G. P., and Goorjian, P. M., "Application of a Streamwise Upwind Algorithm for Unsteady Transonic Computations over Oscillating Wings," AIAA Paper 90-3103,
17. Tijdeman, J. et al, "Transonic Wind Tunnel Tests on an Oscillating Wing with External Stores; Part II- The Clean Wing," AFFDL-TR-78-194, March, 1979.
18. Guruswamy, G. P., "Navier-Stokes Computations on Swept-Tapered Wings, Including Flexibility," AIAA-90-1152, April 1990.
19. Robinson, M. C. and Wissler, J. B., "Unsteady Surface Pressure Measurements on a Pitching Rectangular Wing," AIAA Paper 88-0328, Jan. 1988.
20. Hess, R. W., Cazier, F. W., Jr., and Wynne, E. C., "Steady and Unsteady Transonic Pressure Measurements on a Clipped Delta Wing for Pitching and Control-Surface Oscillations," NASA TP-2594, Oct. 1986.
21. Fujii, K., Gavali, S. and Holst T. L., "Evaluation of Navier-Stokes and Euler Solutions for Leading-Edge Separation Vortices, " *International Journal of Numerical Methods in Fluids*, Vol. 8, Oct. 1988, pp. 1319-1329.
22. Tu, E. L., "Navier-Stokes Simulations of a Close Coupled Canard-Wing-Body Configurations," AIAA Paper 91-0070, Jan. 1991.
23. Obayashi, S., and Guruswamy, G. P, "Unsteady Shock-Vortex Interaction on A Flexible Delta Wing," AIAA Paper 91-1109, April 1991.

THIS DOCUMENT PROVIDED BY THE ABBOTT AEROSPACE
TECHNICAL LIBRARY
ABBOTTAEROSPACE.COM

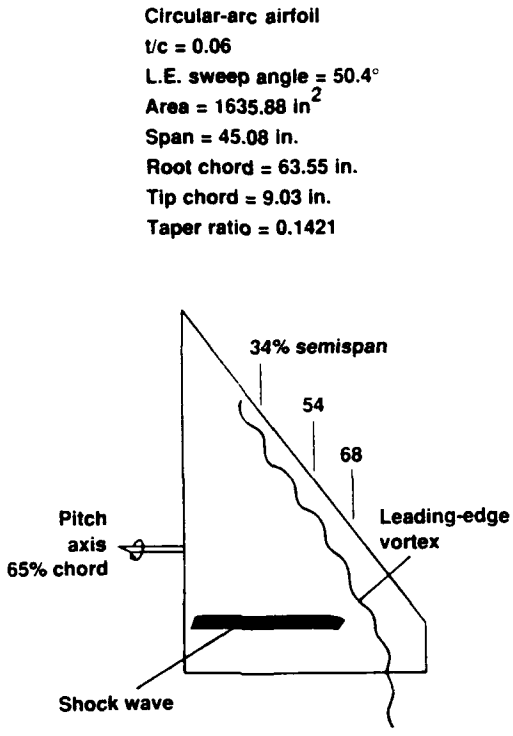


Fig. 1 Flow structure on a clipped delta wing.

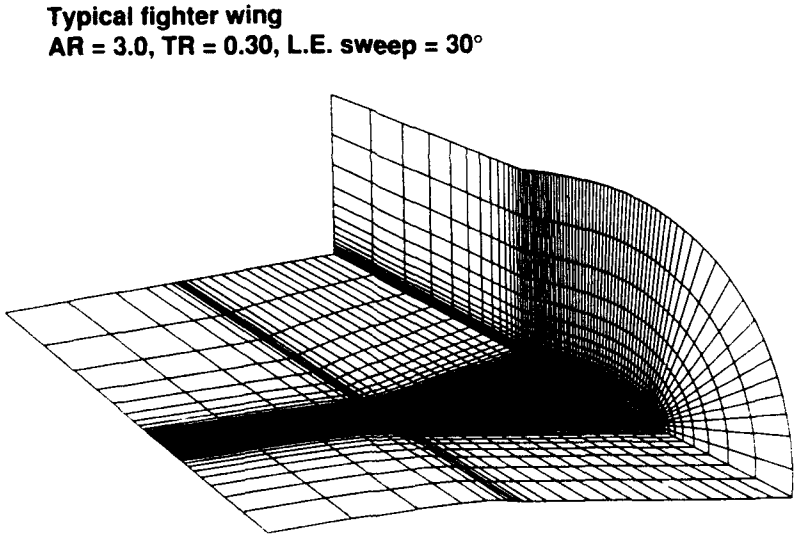


Fig. 2 C-H type grid topology on a typical fighter wing (151, 25 and 34 points in ξ, η, and ζ directions, respectively).

THIS DOCUMENT PROVIDED BY THE ABBOTT AEROSPACE
TECHNICAL LIBRARY
ABBOTTAEROSPACE.COM

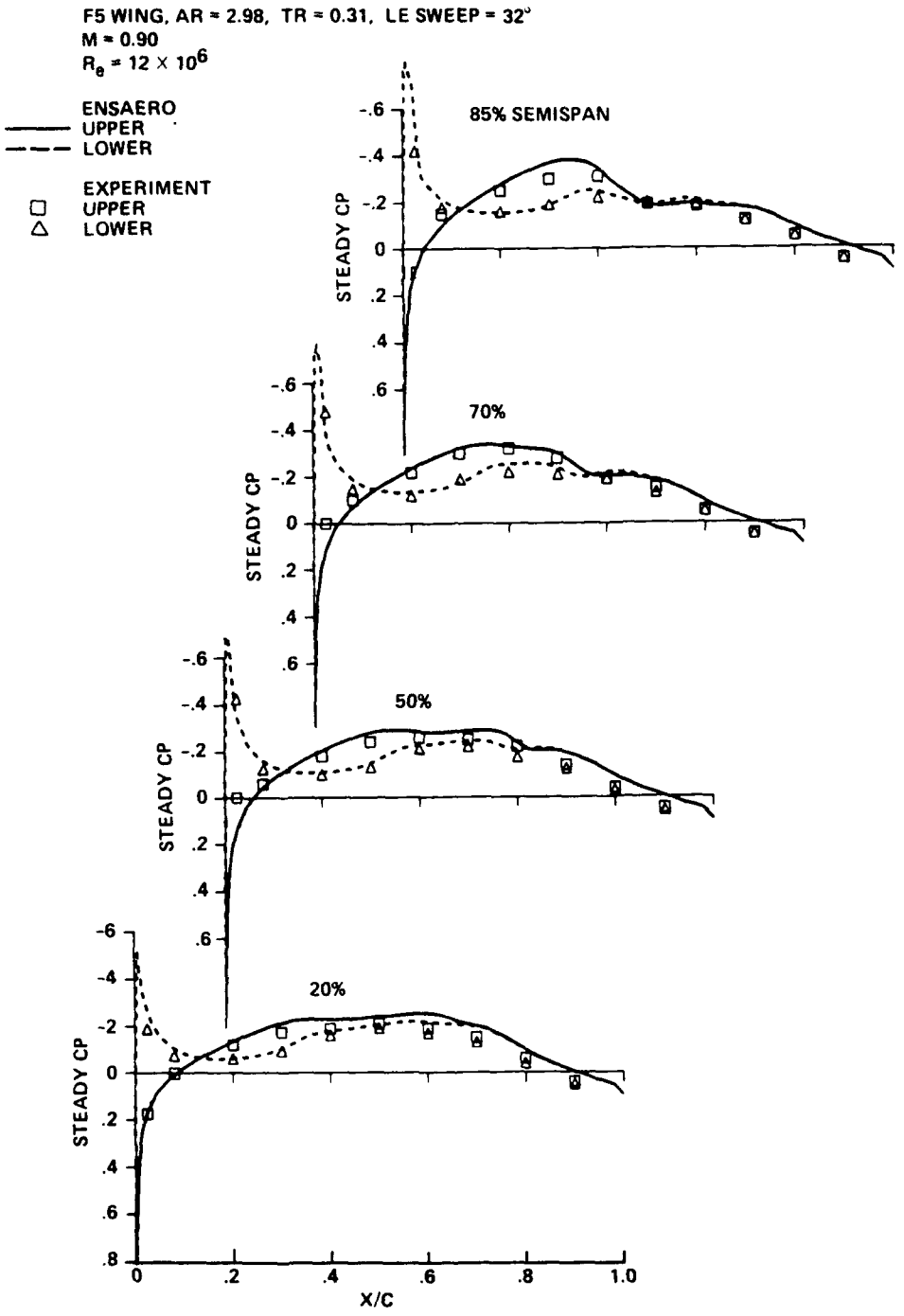


Fig. 3 Comparison of computed steady pressures with experiment for the F-5 wing.

THIS DOCUMENT PROVIDED BY THE ABBOTT AEROSPACE
TECHNICAL LIBRARY
ABBOTTAEROSPACE.COM

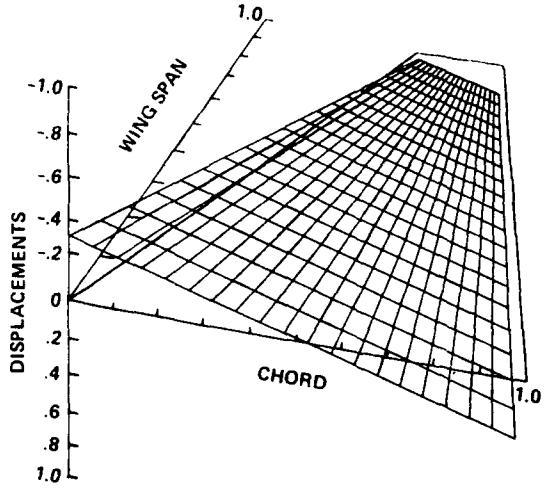


Fig. 4 Unsteady motion of the F-5 wing for unsteady computations.

THIS DOCUMENT PROVIDED BY THE ABBOTT AEROSPACE
TECHNICAL LIBRARY
ABBOTTAEROSPACE.COM

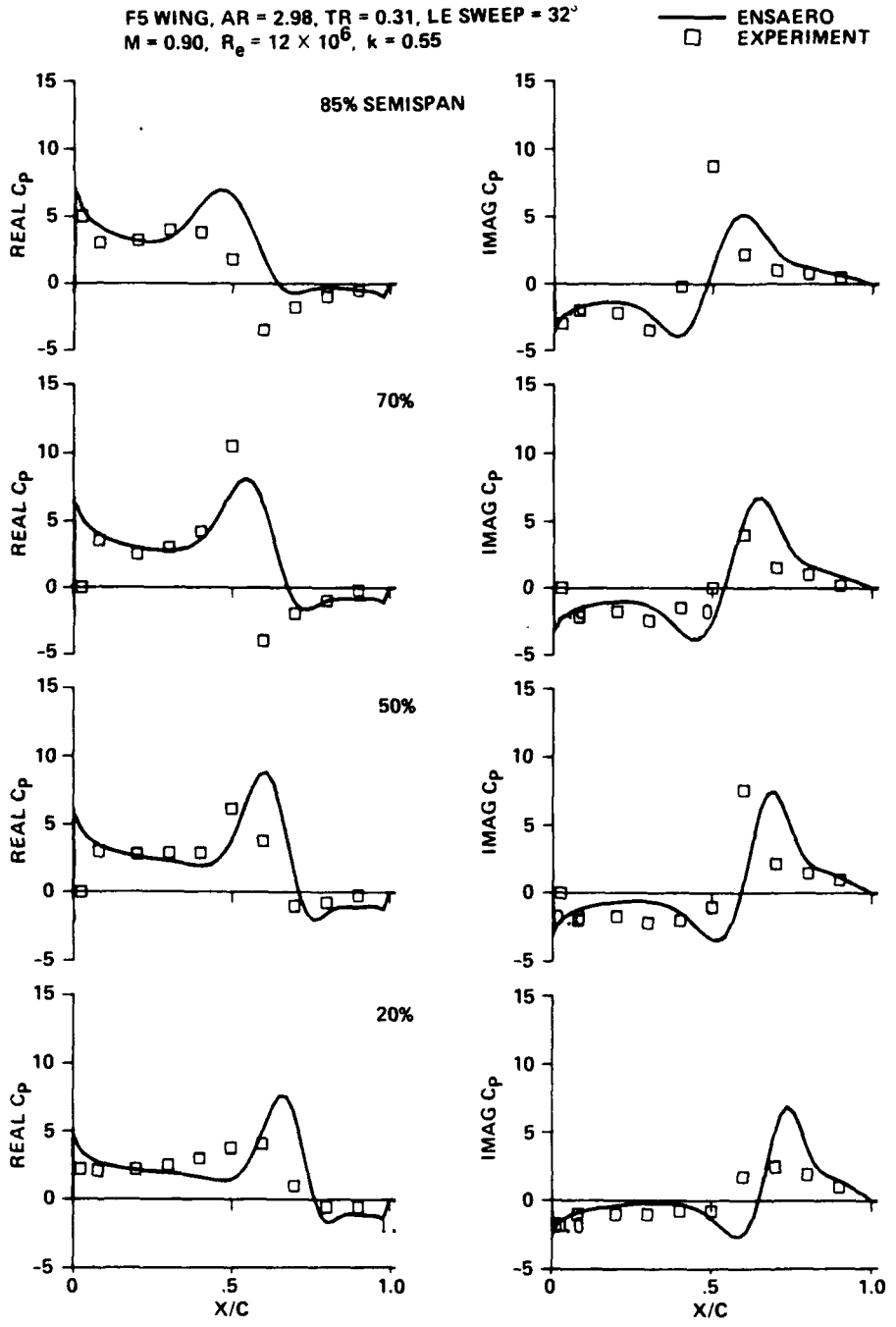


Fig. 5 Comparison of computed unsteady upper surface pressures with experiment for the F-5 wing at M = 0.90.

THIS DOCUMENT PROVIDED BY THE ABBOTT AEROSPACE
TECHNICAL LIBRARY
ABBOTTAEROSPACE.COM

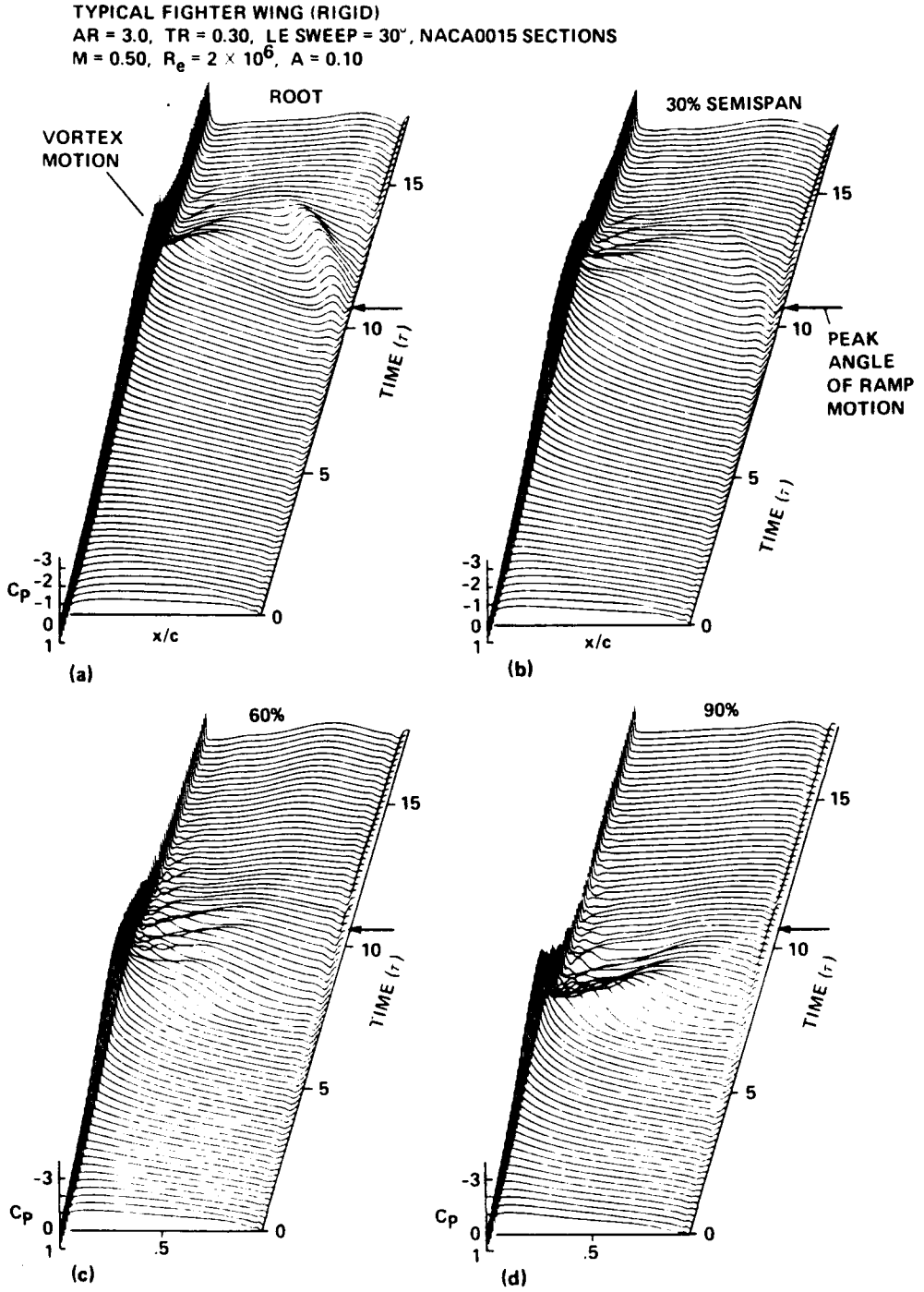


Fig. 6 Unsteady upper surface pressure responses of fighter wing in ramp motion. a) root , b) 30%, c) 60%, d) 90% sections.

THIS DOCUMENT PROVIDED BY THE ABBOTT AEROSPACE
TECHNICAL LIBRARY
ABBOTTAEROSPACE.COM

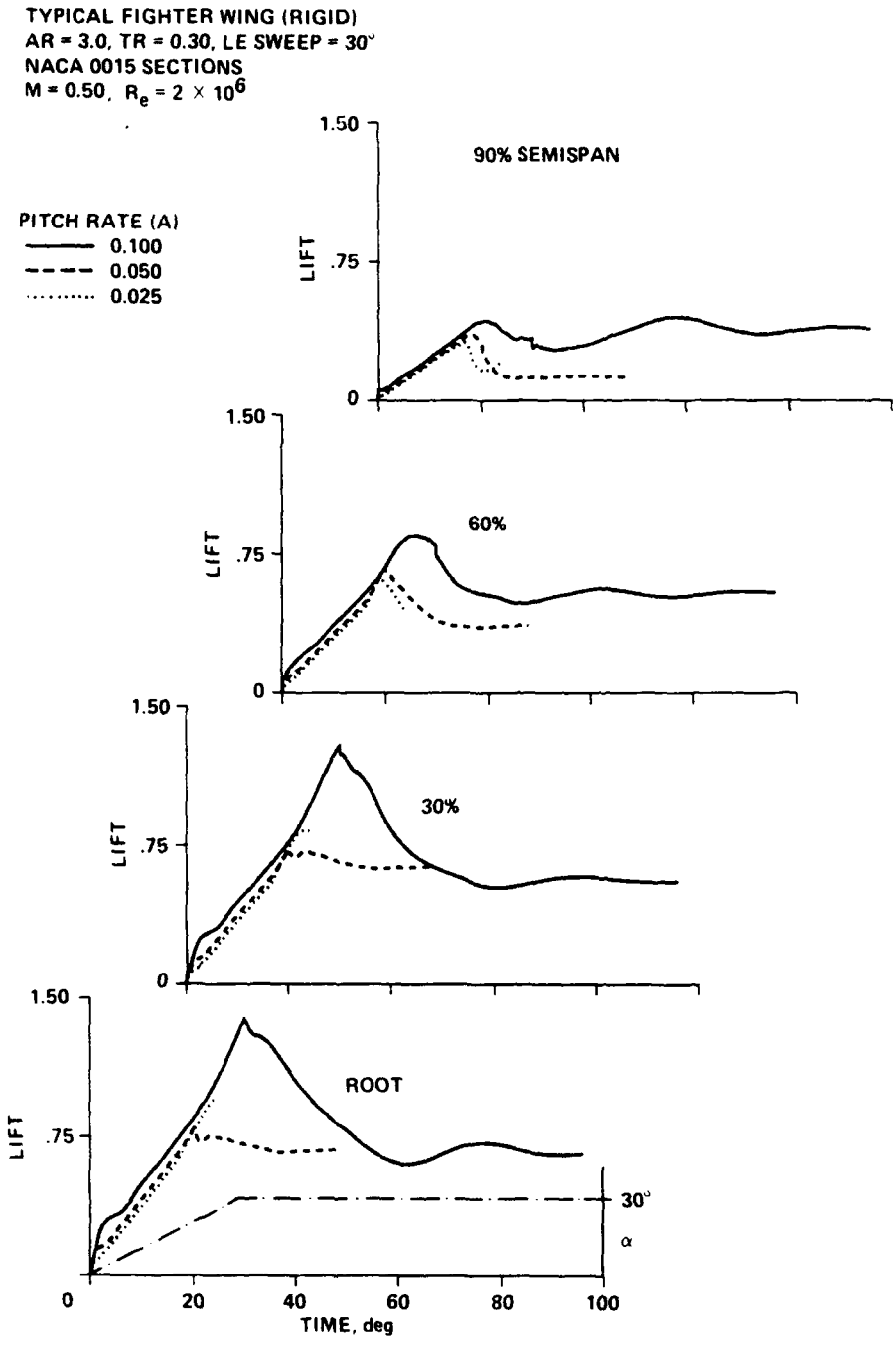


Fig. 7 Effect of pitch rates on lift responses of a fighter wing in ramp motion.

THIS DOCUMENT PROVIDED BY THE ABBOTT AEROSPACE
TECHNICAL LIBRARY
ABBOTTAEROSPACE.COM

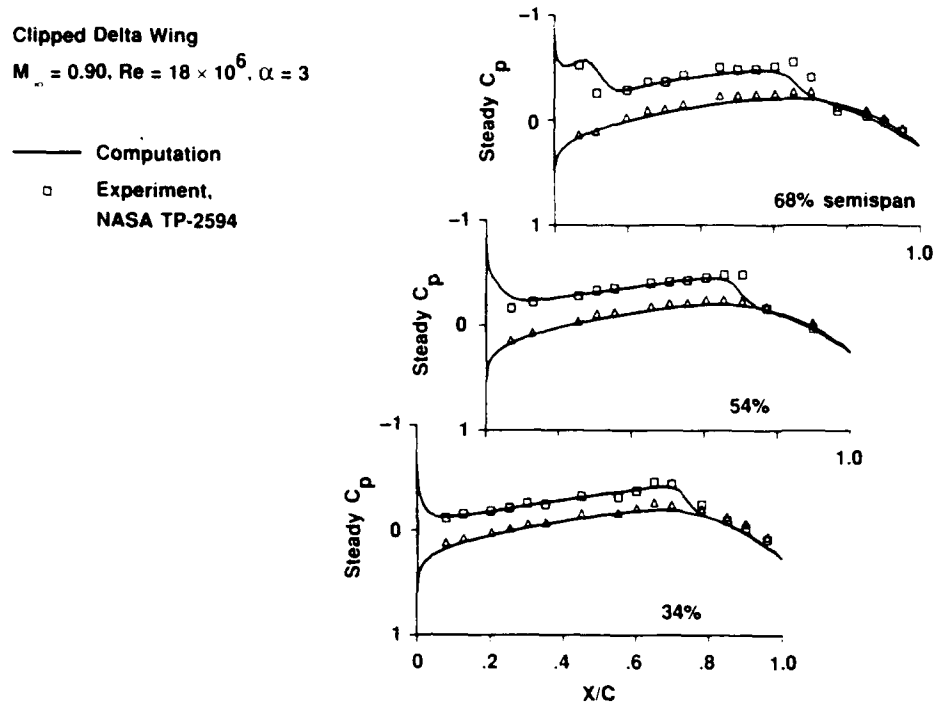


Fig. 8 Comparison of steady pressures with experiment. $M_\infty = 0.90$, $\alpha = 2.99$, $Re_c = 17.8 \times 10^6$.

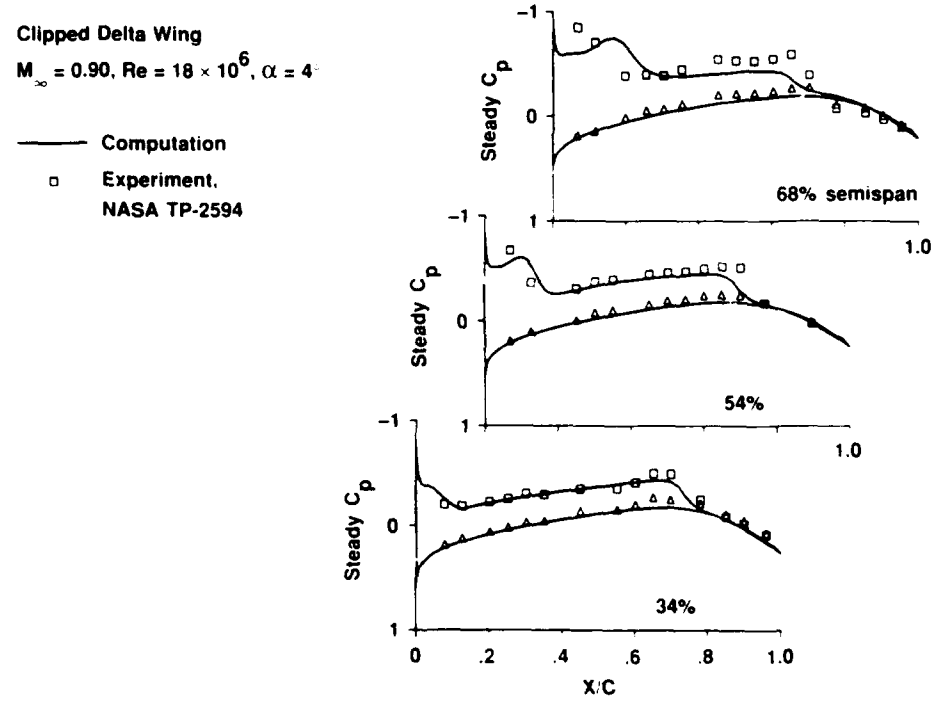


Fig. 9 Comparison of steady pressures with experiment. $M_\infty = 0.90$, $\alpha = 3.97$, $Re_c = 17.6 \times 10^6$.

THIS DOCUMENT PROVIDED BY THE ABBOTT AEROSPACE
TECHNICAL LIBRARY
ABBOTTAEROSPACE.COM

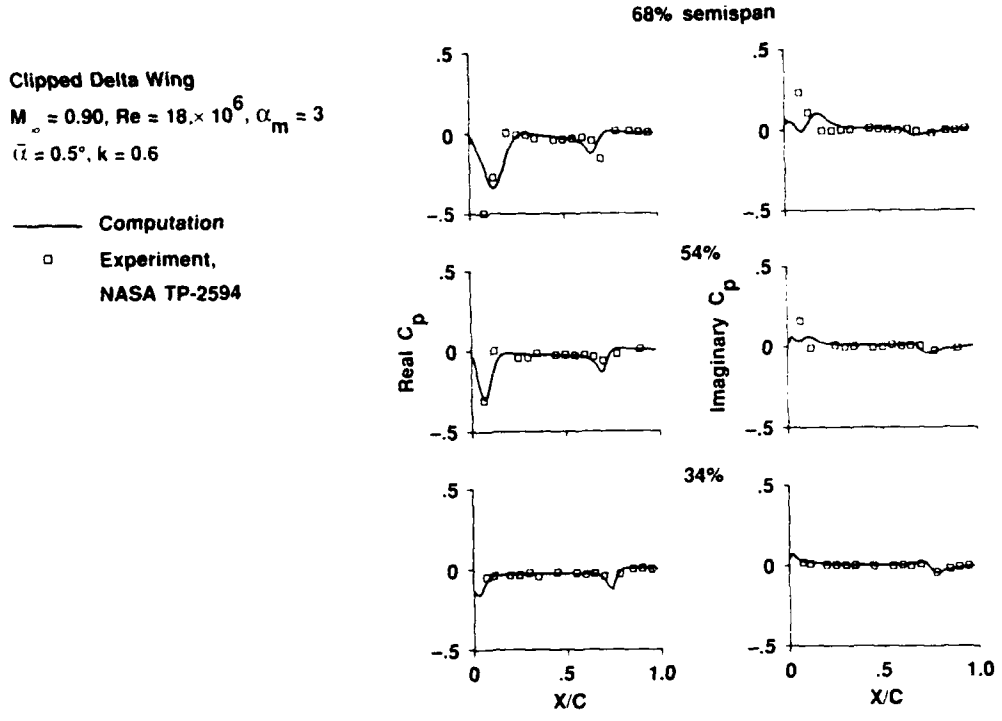


Fig. 10 Comparison of unsteady pressures with experiment, $M_\infty = 0.90$, $\alpha_m = 2.99$, $\bar{\alpha} = 0.47$, $Re_c = 17.8 \times 10^6$, k= 0.5989.

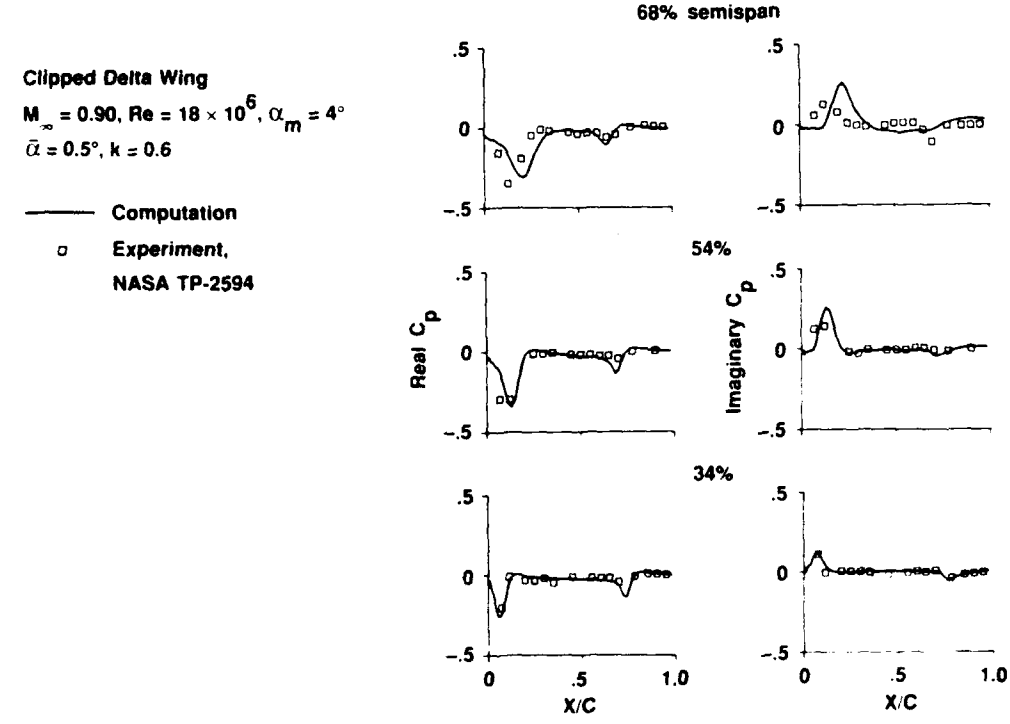


Fig. 11 Comparison of unsteady pressures with experiment, $M_\infty = 0.90$, $\alpha_m = 3.97$, $\bar{\alpha} = 0.46$, $Re_c = 17.6 \times 10^6$, k= 0.5919.

This Document Provided by the Abbott Aerospace
TECHNICAL LIBRARY
ABBOTTAEROSPACE.COM

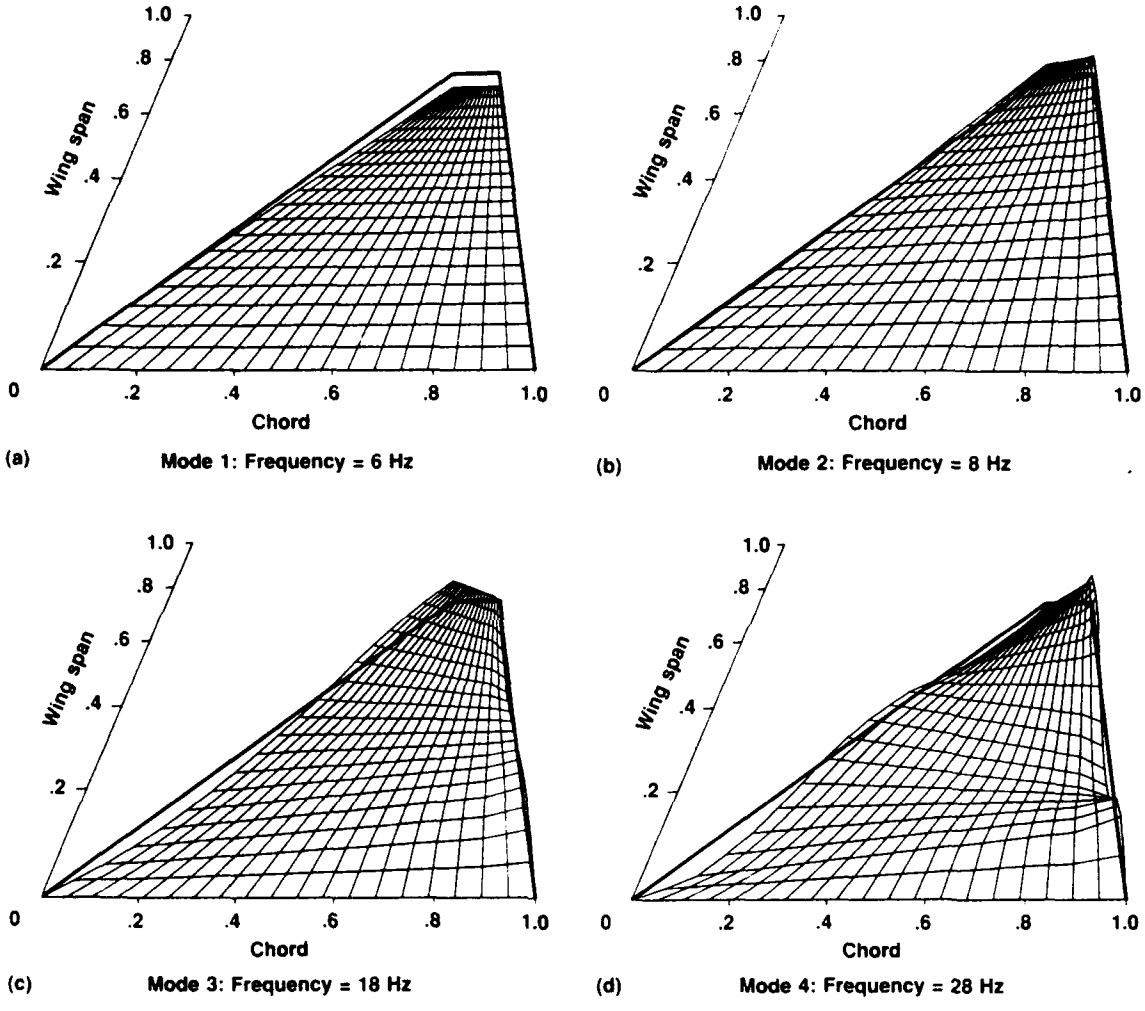


Fig. 12 Mode shapes and frequencies of clipped delta wing. a) First mode: 6 Hz; b) second mode: 8 Hz; c) third mode: 18 Hz; d) fourth mode: 28 Hz.

THIS DOCUMENT PROVIDED BY THE ABBOTT AEROSPACE
TECHNICAL LIBRARY
ABBOTTAEROSPACE.COM

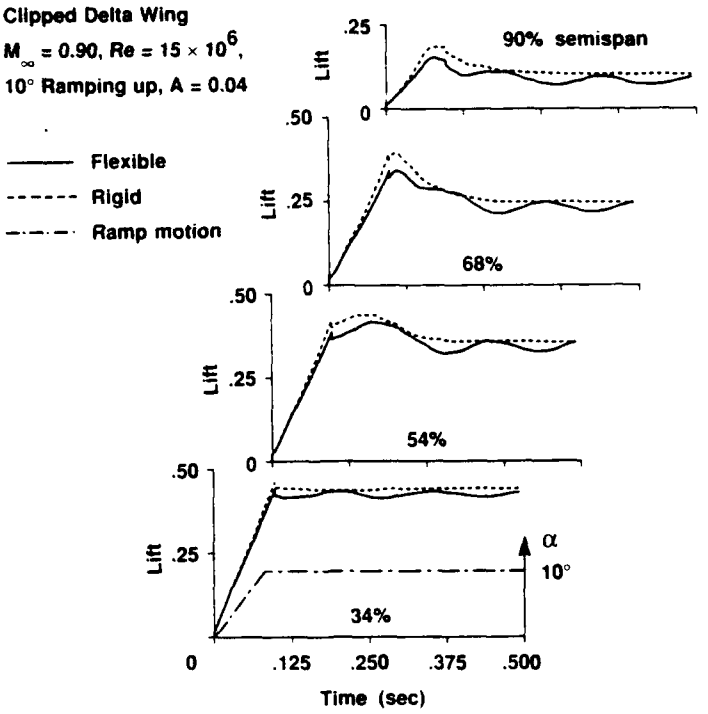


Fig. 13 Comparison of sectional lift responses between rigid and flexible wings, $M_\infty = 0.90$, 10 deg ramping up, $Re_c = 15.0 \times 10^6$, A= 0.04.

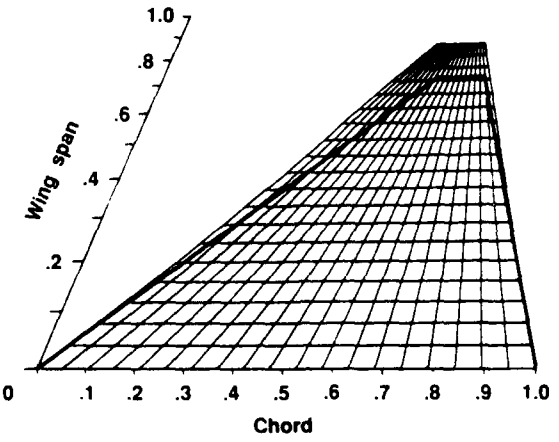


Fig. 14 Deformation of flexible wing in comparison to rigid wing at 1600 times steps, $M_\infty = 0.90$. 10 deg ramping up, $Re_c = 15.0 \times 10^6$, A= 0.04.

THIS DOCUMENT PROVIDED BY THE ABBOTT AEROSPACE
TECHNICAL LIBRARY
ABBOTTAEROSPACE.COM

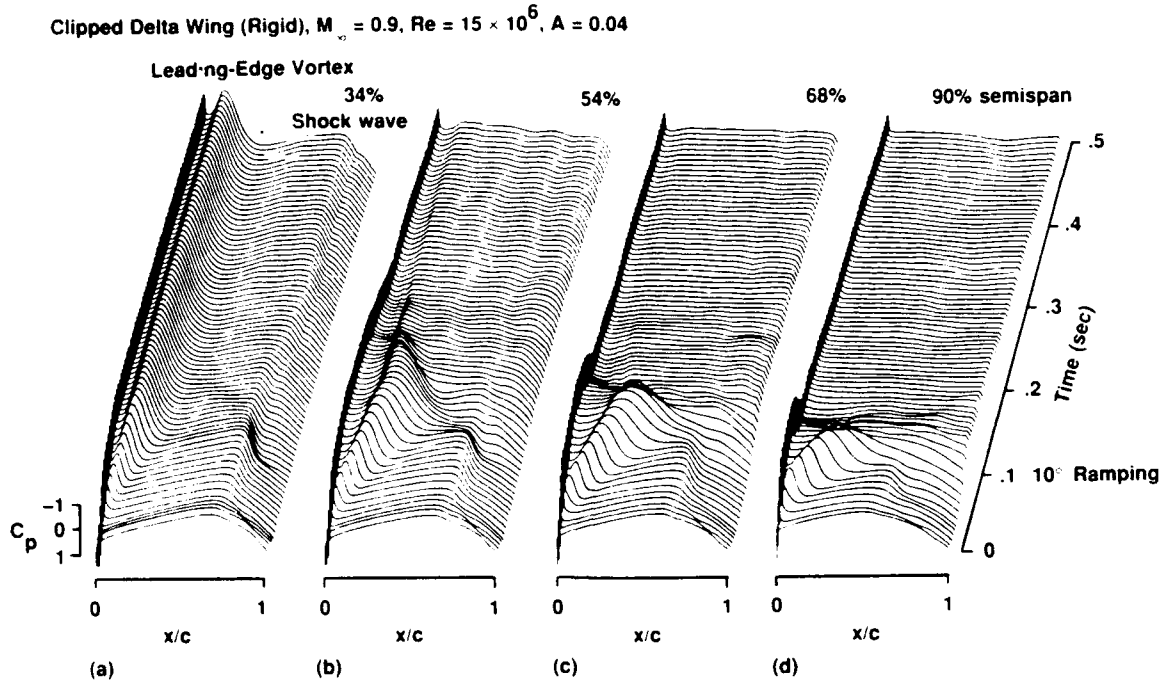


Fig. 15 Unsteady upper surface pressure responses of rigid wing, $M_\infty = 0.90$, 10 deg ramping up, $Re_c = 15.0 \times 10^6$, A= 0.04. a) 34% section; b) 54% section; c) 68% section; d) 90% section.

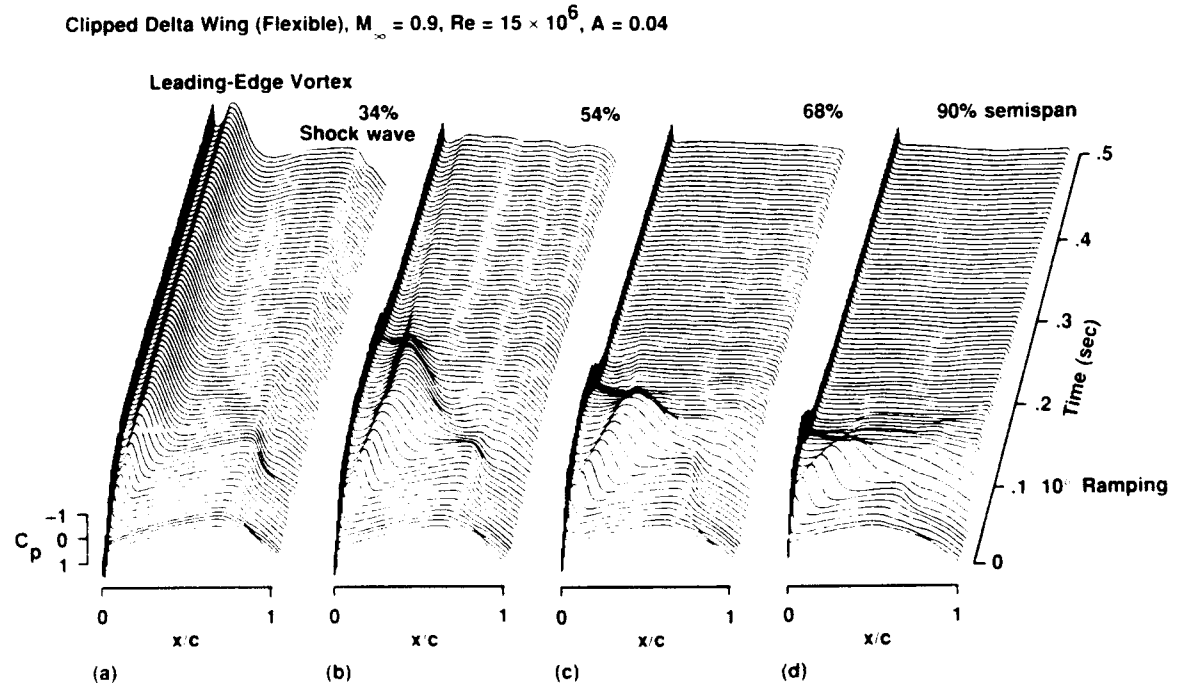


Fig. 16 Unsteady upper surface pressure responses of flexible wing, $M_\infty = 0.90$, 10 deg ramping up, $Re_c = 15.0 \times 10^6$, A= 0.04. a) 34% section; b) 54% section; c) 68% section; d) 90% section.

THIS DOCUMENT PROVIDED BY THE ABBOTT AEROSPACE
TECHNICAL LIBRARY
ABBOTTAEROSPACE.COM

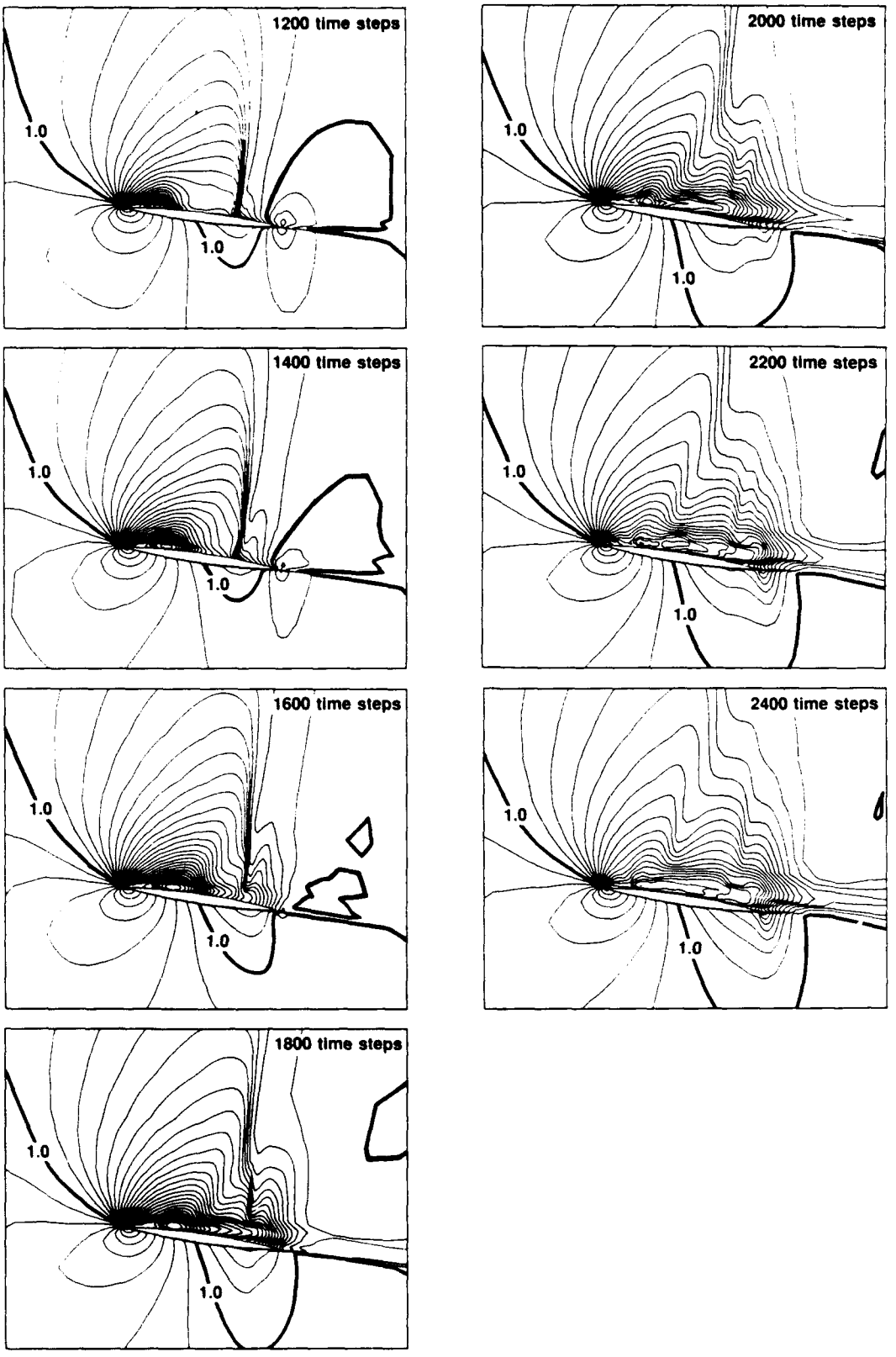


Fig. 17 Instantaneous density contour plots at 68% semispan section, $M_\infty = 0.90$, 10 deg ramping up, $Re_c = 15.0 \times 10^6$, A= 0.04.

THIS DOCUMENT PROVIDED BY THE ABBOTT AEROSPACE
TECHNICAL LIBRARY
ABBOTTAEROSPACE.COM

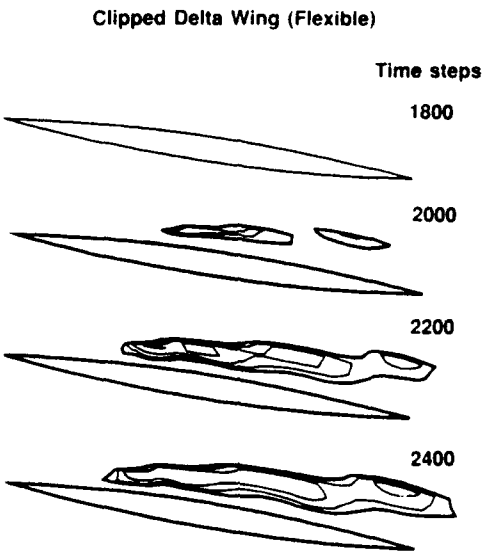


Fig. 18 Instantaneous negative-u-velocity contour plots at 68% semispan section. $M_\infty = 0.90$. 10 deg ramping up, $Re_c = 15.0 \times 10^6$, A= 0.04.

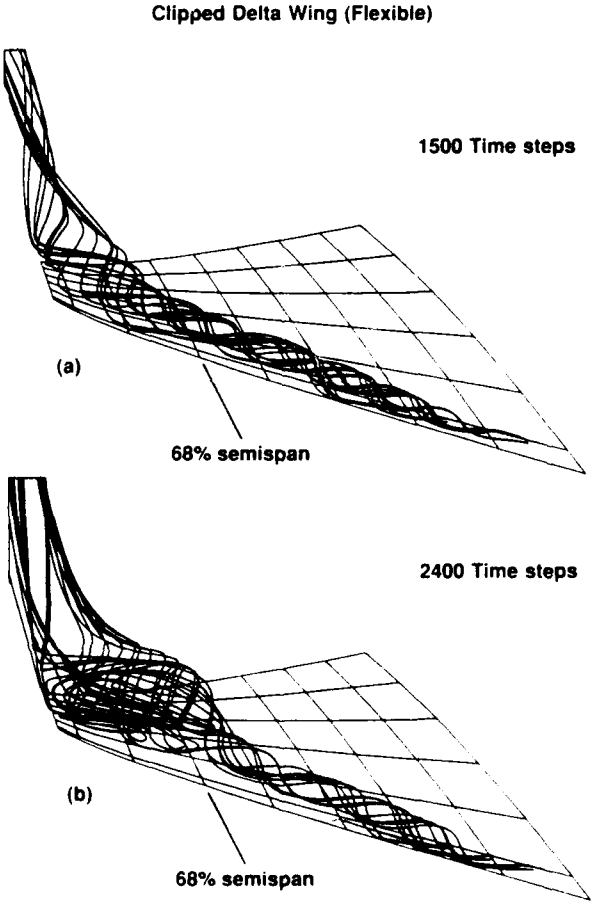


Fig. 19 Streamline pattern over the upper surface of flexible wing. $M_\infty = 0.90$. 10 deg ramping up, $Re_c = 15.0 \times 10^6$. A= 0.04. a) 1500 time steps; b) 2400 time steps.

THIS DOCUMENT PROVIDED BY THE ABBOTT AEROSPACE
TECHNICAL LIBRARY
ABBOTTAEROSPACE.COM

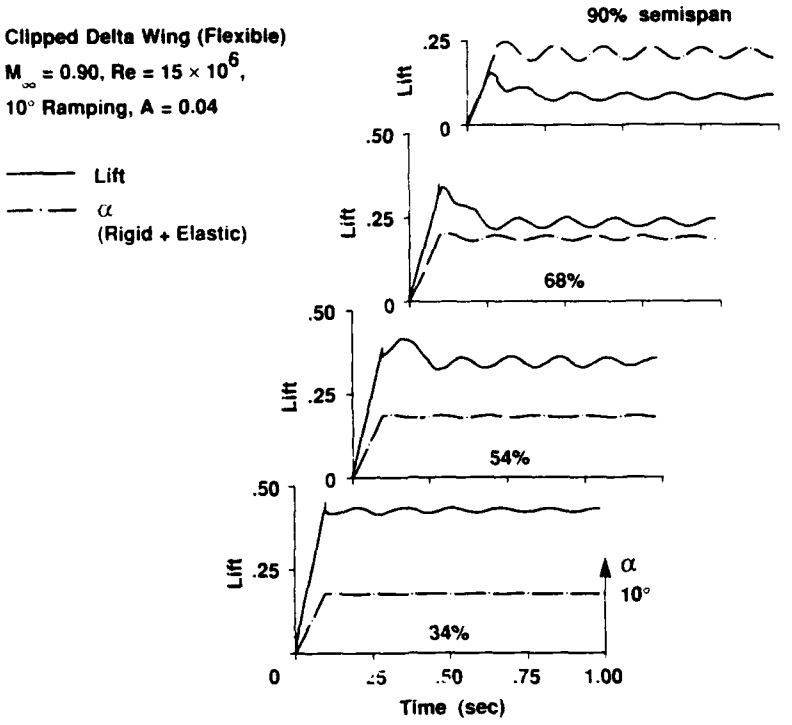


Fig. 20 Responses sectional lift and elastic angle of attack for flexible wing, $M_\infty = 0.90$, 10 deg ramp. $Re_c = 15.0 \times 10^6$, A= 0.04.

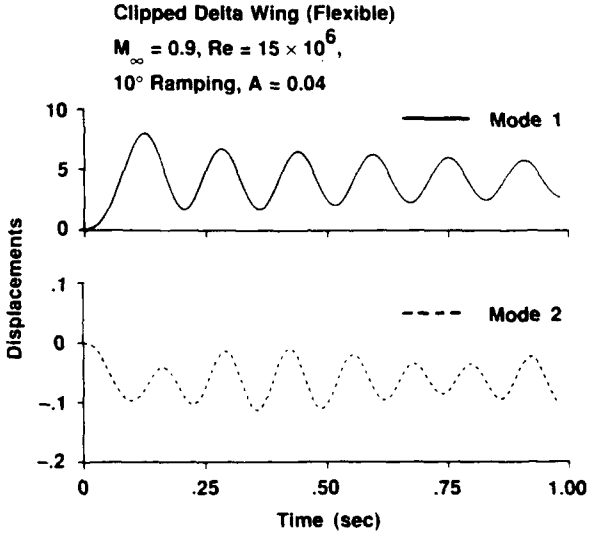


Fig. 21 First and second modal responses of flexible wing, $M_\infty = 0.90$, 10 deg ramping up, $Re_c = 15.0$ A= 0.04. a) Mode 1: 6 Hz; b) Mode 2 : 8 Hz.

THIS DOCUMENT PROVIDED BY THE ABBOTT AEROSPACE
TECHNICAL LIBRARY
ABBOTTAEROSPACE.COM

92-16052

AD-P007 814

Development of a Method to Predict Transonic Limit Cycle Oscillation Characteristics of Fighter Aircraft

J.J. Meijer

Senior Research Engineer
National Aerospace Laboratory (NLR)
1059 CM Amsterdam, The Netherlands

A.M. Cunningham, Jr.

Engineering Staff Specialist
General Dynamics Fort Worth Division
Fort Worth, Texas, U.S.A.

Abstract

An analysis of steady wind tunnel data, obtained for a fighter type aircraft, has indicated that shock-induced and trailing-edge separation plays a dominant role in the development of Limit Cycle Oscillations (LCO) at transonic speeds. On this basis, a semi-empirical LCO prediction method is being developed which makes use of such steady wind tunnel data. The preliminary method has been applied to several configurations and has correctly identified those which have encountered LCO. The method has the potential for application early in the design process of new aircraft to determine and understand these non-linear aeroelastic characteristics. The method is still being evaluated and upgrading and refinements are expected from unsteady wind tunnel force and pressure measurements to be obtained from oscillating models as part of an extensive investigation into the aerodynamic nature of LCO. The method will be described in its present form and results of the latest predictions will be compared with flight test trends and used to further assess various parametric effects.

1 Introduction

Requirements of fighter aircraft to operate with high maneuverability in the transonic speed regime increase the potential to encounter a transonic non-linear flutter, known as limit cycle oscillations (LCO). LCO is a limited amplitude self-sustaining oscillation produced by a structural/aerodynamic interaction. The phenomenon is related to buffet but has characteristics similar to classical flutter in that it usually occurs at a single frequency. From an operational point of view, LCO results in an undesirable airframe vibration that limits the pilot's functional abilities and produces extreme discomfort and anxiety. More importantly, targeting accuracy is degraded, e.g. wing mounted missiles cannot be fired because of high levels of wing motion that prevent target lock-on.

As an example a recording is shown in figure 1 of LCO of a fighter aircraft which was encountered during flight flutter tests (Ref. 1). In many cases, as in figure 1, the maximum amplitudes occur during aircraft deceleration. LCO is experienced by aircraft with highly swept wings as well as with high aspect ratio wings, although different flow mechanisms may be involved. In references 2 to 6 such cases were analyzed in relation to wing bending oscillations.

For fighter aircraft, LCO is characterized by an almost harmonic oscillation which appears at Mach numbers ranging from 0.8 to 1.1, and at moderate angles-of-attack depending on the Mach number, but usually less then 10 deg. The flow conditions during LCO are characterized by mixed attached/separated flow. Lowly damped vibration modes tend to respond provided they have the proper characteristics to couple with this type of flow. This coupling frequently occurs near flutter boundaries, which implies that classical flutter predictions with linear theory may be applied as a guide for identifying lowly damped modes in the transonic speed range that might be sensitive to LCO.

Several research programs on unsteady aerodynamics and flutter predictions were conducted by NLR and General Dynamics to improve the accuracy and reduce the time and costs of flutter clearance of the many store configurations of a fighter aircraft. Currently there are several aerodynamic computer codes available to predict the unsteady loading in subsonic, transonic, and supersonic inviscid flow. However, codes capable of dealing with the transonic speed range with regions of separated flow and shock-wave/boundary-layer interactions have not yet been developed to an acceptable level of reliability.

In response to the above needs, an investigation was started as a cooperative effort between NLR and General Dynamics to understand the nature of LCO experienced by fighter aircraft maneuvering at transonic speeds. This investigation is being funded by the US Air Force, The Netherlands Ministry of Defense, NLR, and General Dynamics. In addition to conducting an extensive wind tunnel investigation (Refs. 7 and 8), a major objective of this investigation is to develop a method for predicting LCO characteristics of full scale aircraft. The wind tunnel data from reference 8 will be used in some form for guidance in the development of the method.

THIS DOCUMENT PROVIDED BY THE ABBOTT AEROSPACE
TECHNICAL LIBRARY
ABBOTTAEROSPACE.COM

An analysis of steady wind tunnel data, obtained for a fighter type aircraft, has indicated that shock-induced and trailing-edge separation play a dominant role in the development of LCO at transonic speeds as first described in reference 9 and further discussed in reference 10. On this basis, a semi-empirical prediction method was developed which makes use of such steady wind tunnel data. A preliminary version of this method and some results were presented in reference 11 and further developments were discussed in reference 12. As described in these presentations, the method has been applied to several configurations and has correctly identified those which have encountered LCO.

This paper will present further developments of the method as well as additional parametric effects aimed at improving the understanding of the non-linear mechanisms involved with predicting transonic LCO. The basic method will first be reviewed including a summary of the conclusions reached in earlier presentations (Refs. 11 and 12). Next, the effects of time step size, time lag as applied to steady aerodynamic data and leading-edge flap settings will be described. Finally, a discussion will be presented on the role of damping in the prediction of total airframe response during LCO.

2 Basic LCO Prediction Method

A brief review of the method will be given in this section. The non-linear aerodynamics involved with transonic LCO will first be discussed followed by a description of the aeroelastic equations of motion and their solution using a time-marching approach. Next considerations for mode selections to obtain the best LCO modeling will be presented. Finally, previous results and conclusions will be summarized to bring the reader up-to-date.

2.1 Non-linear Aerodynamics for LCO

In order to identify the important non-linearities in the aerodynamic forces that could drive LCO, steady pressure data of a full-span wind tunnel model of a typical fighter aircraft were analyzed at NLR which were made available by the aircraft manufacturer (Ref. 13). The objective of that test was to obtain pressure data for investigating the role of shock-induced trailing-edge separation in LCO as suggested in reference 9. Pressure data were acquired on the wings, the horizontal tails and the fuselage for the following test conditions: Mach number ranging from 0.90 to 0.96, with increments of 0.01, and angle-of-attack ranging from 0 to 10 deg, with increments of 0.5 deg. During these tests different tip launchers and leading-edge flap settings were also included in the configuration matrix. The wing planform of the wind tunnel model provided with pressure orifices is shown in figure 2. Also shown is the panel distribution used in the chordwise and spanwise integration.

Results of the NLR analysis are presented for one type of tip launcher and one leading-edge flap setting. In figures 3 and 4 the steady normal force and moment coefficients are shown for stations 1 and 6 (most inboard and outboard, respectively) as function of angle-of-attack (0 to 10 deg) and Mach number (0.90 to 0.96). The coefficients for the intermediate stations show a gradual transition. It is immediately clear that the coefficients in station 1 do not show any irregular behavior, whereas in station 6 both lift and moment coefficients show rapid changes in short intervals of the angles-of-attack (centered on about 5 to 7 deg) in the greater part of the Mach number interval. These rapid changes are typical of those described in reference 9 that were shown to drive LCO.

To analyze the kind of pressure distributions which lead to the rapid changes in the aerodynamic coefficients, the pressure distributions on the upper and lower wing surface in stations 1 and 6 at Mach number 0.92 are presented in figures 5 and 6. The pressure distribution at the upper surface in station 1 shows a very gradual development with angle-of-attack, with a small upstream shift of the shock along with a slight trailing edge flow separation at the highest angle-of-attack. At station 6 a strong upstream shift of the shock starts at about 5 to 7 deg coupled with a rapidly developing flow separation at the trailing edge. This occurs after a merging of the weaker nose and aft shocks into a much stronger single shock that induces the extensive separation as is discussed in detail in reference 14. The shock motion also reverses at this point which coincides with breaks in the sectional lift and pitching moment coefficients. The pressure distributions on the lower side show only very gradual developments. For the other type of tip launcher and leading-edge flap settings the same kind of trends were observed.

2.2 Aeroelastic Equations of Motion

An adequate description of the displacements of the unrestrained aircraft structure is obtained by taking the symmetric and antisymmetric natural vibration modes as generalized coordinates, completed by adding the rigid body modes. The modes with the lowest natural frequencies are fully utilized, whereas the remaining higher modes may be treated with the concept of residualization. In the present study, however, the presence of these remaining modes is neglected altogether. The equations of motion are expressed then in matrix form as:

$$\begin{bmatrix} M_R & 0 \\ 0 & M_E \end{bmatrix} \begin{Bmatrix} \ddot{q}_R \\ \ddot{q}_E \end{Bmatrix} + \begin{bmatrix} 0 & 0 \\ 0 & 2\zeta_E M_E \omega_E \end{bmatrix} \begin{Bmatrix} \dot{q}_R \\ \dot{q}_E \end{Bmatrix} + \begin{bmatrix} 0 & 0 \\ 0 & M_E \omega_E^2 \end{bmatrix} \begin{Bmatrix} q_R \\ q_E \end{Bmatrix} = \begin{Bmatrix} L_R \\ L_E \end{Bmatrix}, \quad (1)$$

THIS DOCUMENT PROVIDED BY THE ABBOTT AEROSPACE
TECHNICAL LIBRARY
ABBOTTAEROSPACE.COM

where M is the generalized mass matrix and q is the vector of generalized coordinates. The indices R and E refer to the rigid body and elastic modes and their number is N_R and N_E , respectively. ζ and ω are the damping factor and natural frequency of each elastic mode. The generalized aerodynamic force for the i-th coordinate, L_i, is formulated as:

$$L_i = \frac{1}{2}\rho V^2 \int_S \phi_i\langle x,y\rangle \Delta C_p\langle x,y,\alpha\langle t\rangle\rangle dS, \qquad (2)$$

in which $\frac{1}{2}\rho V^2$ is the dynamic pressure, $\phi_i\langle x,y\rangle$ is the natural mode shape and $\Delta C_p\langle x,y,\alpha\langle t\rangle\rangle$ is the pressure difference distribution over the wing depending on the dynamic angle-of-attack distribution α. This distribution is expressed by:

$$\alpha = \alpha_m + \Delta\alpha, \quad \Delta\alpha = \Delta\alpha\langle x,y,t\rangle, \qquad (3)$$

$$\Delta\alpha = \sum_{N_R+N_E} \left(\frac{\partial}{\partial x} + \frac{1}{V}\frac{\partial}{\partial t}\right) \phi_j\langle x,y\rangle q_j\langle t\rangle. \qquad (4)$$

α_m is the mean angle-of-attack and $\Delta\alpha$ the time-dependent variation at point x, y. In the present approach, the pressure distribution ΔC_p in expression (2) is a time-independent non-linear function of α. It is this relation by which the aerodynamic peculiarities discussed in section 2.1 enter the equations of motion (1), weighted by an appropriate mode shape ϕ_i.

In the numerical solution of the equations of motion the aerodynamic forces L_i are discretized as follows:

$$L_i = \frac{1}{2}\rho V^2 \sum_k \left(\phi_i\langle x,y\rangle \Delta C_p\langle x,y,\alpha\langle t\rangle\rangle\right)_k \Delta S_k, \qquad (5)$$

in which ΔS_k is the k-th panel area, and the product $\langle\phi_i \Delta C_p\rangle$ is taken constant over the whole k-th panel, being evaluated at the $\langle x,y\rangle$ position of the k-th pressure orifice. Because of the non-linear aerodynamics, these forces have to be evaluated for both right and left wing and added at each time step of the time simulation. It should be noted that in the present study only aerodynamic forces on the wing have been taken into account and those on the wing stores, fuselage and empennage surfaces ignored.

Before solving, the equations of motion are brought into state space form. Writing equation (1) as:

$$[M]\{\ddot{q}\} + [C]\{\dot{q}\} + [K]\{q\} = \{L\langle q,\dot{q}\rangle\}, \qquad (6)$$

their state space form is:

$$\begin{aligned} \{\dot{s}\} &= [M]^{-1}\left(\{L\langle q,\dot{q}\rangle\} - [C]\{s\} - [K]\{q\}\right), \\ \{\dot{q}\} &= \{s\}, \end{aligned} \qquad (7)$$

and the working form is:

$$\{\dot{x}\} = [A]\{x\} + [B]\{u\}, \qquad (8)$$

where A and B are constant matrices that result from the change of the variables $x = [s,q]^T$ and u is the generalized force $L\langle q,\dot{q}\rangle$.

2.3 Time-Marching Aeroelastic Solution

The aeroelastic solution procedure implemented for integrating equation (8) is similar to that described by Edwards et al (Ref. 15). Since equation (8) is a finite-dimensional differential equation, its solution (Ref. 16) is given by:

$$x_i\langle t\rangle = \Phi\langle t\rangle x_i\langle 0\rangle + \int_0^t \exp\left[A\langle t-\tau\rangle\right] Bu\langle\tau\rangle d\tau. \qquad (9)$$

The state transition matrix, $\phi\langle t\rangle = exp[At]$ in general, can be calculated to any assigned accuracy by using a sufficient number of terms of the series expansion of the matrix exponential function. As explained in reference 16, the first term in equation (9) is the homogeneous response portion of equation (8), while the second term is a convolution integral giving the forced response. Numerically, the solution is advanced from any time step n to step n+1, by:

$$x_i\left[(n+1)\Delta t\right] = \Phi\langle\Delta t\rangle x_i\langle n\Delta t\rangle + \int_{n\Delta t}^{(n+1)\Delta t} \exp\left[A\langle(n+1)\Delta t-\tau\rangle\right] Bu\langle\tau\rangle d\tau, \qquad (10)$$

where Δt is the time step. Since $u\langle\tau\rangle$ is not known over the interval $n\Delta t < t < (n+1)\Delta t$, the integral in (10) must be approximated. The simplest approximation for the integral is to assume that $u\langle\tau\rangle$ is constant, i.e. $u\langle\tau\rangle = u\langle n\Delta t\rangle$ over the interval. A better approximation may be obtained by assuming u to vary linearly from $u\langle n\Delta t\rangle$ and $u\langle(n+1)\Delta t\rangle$:

$$u^{n+1} = u^n + \left(u^n - u^{n-1}\right). \qquad (11)$$

The resulting algorithm is:

$$x_i^{n+1} = \Phi x_i^n + \Theta B\left(3u^n - u^{n-1}\right)/2, \qquad (12)$$

where Θ is the integral of the state transition matrix Φ. The integration matrices Φ and Θ were calculated using the computational system described in reference 17. The final result of the time integration process is the variation of the generalized coordinates q and their time derivatives as functions of time.
They can easily be reduced to quantities of practical interest, like wing tip acceleration, pilot seat acceleration, etc.

2.4 Selection of Modes for LCO Predictions

In the investigation described in reference 9, it was possible to reduce the number of modes to a single degree of freedom (DOF) as a result of knowledge gained from flight test measured LCO characteristics. Also, since LCO did not occur near a flutter boundary, the natural modes were essentially unchanged and represented those of the full-scale aircraft at flight LCO conditions. This is not the general case, however, particularly where LCO occurs near the flutter boundary.

THIS DOCUMENT PROVIDED BY THE ABBOTT AEROSPACE
TECHNICAL LIBRARY
ABBOTTAEROSPACE.COM

In this case, the modified modes resulting from the flutter eigenvectors may be quite different from the natural modes. The concept of a single DOF response in LCO still applies, however, but it applies to a complex mode as prescribed by the eigenvectors.

Some guidance for mode selection may be derived from the results of routine linear flutter calculations for a complete multi-DOF system in attached flow. Modes that exhibit low aerodynamic damping values within the flight conditions of interest, are good candidates for producing LCO. Along with the damping values, the eigenvectors are also available for constructing the appropriate complex modes if they are significantly different from the natural modes. However, the LCO potential of each mode, real or complex, is governed by its shape and how this shape interacts with the non-linear flow fields. Such evaluation by visual inspection is a qualitative judgement process which requires a high level of aerodynamic expertise, and its outcome may not always be the right answer. Finally, if the LCO conditions are near a flutter boundary, it is also quite possible that the eigenvectors are significantly modified by non-linear aerodynamic forces. Thus, even with all of this information, the analyst would have to spend a significant amount of time making the mode selections but would have no guarantee that he made the right decisions and the results could be entirely misleading.

In spite of the additional computer costs, a better alternative is to use the full set of vibration modes within the frequency range of interest. This has the advantages that (1) the system can filter out the mode(s) that will respond in LCO, (2) the time requirement and uncertainty of the decision process for mode selection is eliminated, and (3) more modes are available to describe a possible shift in mean angle-of-attack due to static wing deflections. The mean angle-of-attack due to aircraft maneuvering and/or static aeroelastic effects has a major influence on the aerodynamic loads during LCO. Modes that contribute dynamically to LCO may differ from the modes that contribute to static deflections. The representation of the latter modes in the equations of motion may be simplified by the concept of modal residualization.

2.5 Previous Results

Many applications of the LCO prediction method were made in references 11 and 12 to both generic as well as realistic configurations. In addition to various parametric effects, the basic mechanism of coupling between flow fields and structural response was examined for the generic model. Predictions were also made for realistic configurations, some of which were known to exihibit LCO and others that did not.

2.5.1 Flow Characteristics during LCO

To demonstrate the potential role of shock-induced trailing-edge separation during LCO (Ref. 9) the wing motion and the pressure distributions on the upper surface were plotted as shown in figure 7, during one cycle of oscillation for an LCO calculation with the generic model. The cycle starts at 25.1 s and the time intervals are 0.005 s. These time steps were chosen to correspond to the extremes of angle-of-attack variation at wing tip station 6 about $\alpha = 6$ deg. These deflections are highlighted as a heavy line in figure 7 and represent the incremental angle-of-attack for (I) maximum nose down, (II) zero with positive pitch rate, (III) maximum nose up, and (IV) zero with negative pitch rate. The two important modes responding in the LCO are shown in figure 8.

The results in figure 7 along with the C_N and C_m trends for station 6 in figure 4, may be used to clearly demonstrate the relationship between shock-induced trailing-edge separation and LCO. At point I in figure 7, the wing tip is at a minimum total angle-of-attack (i.e. $\alpha = \alpha_m + \Delta\alpha$) of about $\alpha = 4.7$ deg and a large positive (up) deflection as indicated by the deflections (heavy line) at station 6. Two shocks (nose and aft shocks) are distinctly seen in the chordwise pressure distributions (heavy line) also at station 6. The flow is attached at the trailing edge as indicated by the nearly zero value of the pressure coefficient. In figure 4 at $\alpha = 4.7$ deg, C_N is at its lowest value during the cycle and C_m is at its highest value. Thus, attached flow with two shocks is providing a nose up pitching moment increment at the minimum angle and a downward acting normal force incremental at a large upward deflection.

Continuing on to point II in figure 7, the wing tip is at $\alpha = 6$ deg and a maximum downward deflection. The two shocks have merged into a single strong shock and the trailing edge pressures are indicating that separation has begun. In figure 4, C_N is higher but at a plateau that continues up to $\alpha = 8.5$ deg. C_m is lower (less nose up).

At point III in figure 7, the wing tip is at a maximum angle-of-attack of about $\alpha = 7.3$ deg. The single strong shock formed at point II has fully separated the flow to the trailing edge which in turn has driven the shock forward as shown in the pressures at station 6. In figure 4, the C_N is still about the same as it was at point II, however, C_m is now lower and more nose down.

Finally, at point IV in figure 7, the wing tip is at about $\alpha = 6$ deg but maximum upward deflection. The trailing edge pressures are indicating that re-attachment is occurring and a strong single aft shock is now present. In figure 4, C_N is the same as it was at $\alpha = 7.3$ deg at point III but C_m is higher giving less nose down pitching moment. From point IV, the cycle continues to point I where the two-shock system is re-formed.

The relationship just illustrated between shock-induced trailing-edge separation, pitching moment and

THIS DOCUMENT PROVIDED BY THE ABBOTT AEROSPACE
TECHNICAL LIBRARY
ABBOTTAEROSPACE.COM

torsion response at station 6, is identical to that described in reference 9 where it was concluded that a non-linear aerodynamic spring was the principal driving mechanism for LCO. For the current example, however, significant vertical translation in the LCO (or eigen) mode was opposed by C_N variations at point II. For angles-of-attack above $\alpha = 6$ deg , C_N was constant and did not affect the wing motion which would make it a neutral spring for half of the cycle. Thus, the existence of an additional non-linear spring for opposing translation for half of the cycle further substantiates the above conclusion of reference 9.

2.5.2 LCO Sensitive Parameters

An extensive investigation of the effects of various parameters on predicted LCO characteristics was described in reference 12. The effects of varying structural damping, altitude, Mach number and mean angle-of-attack were determined for the generic configuration. Because the generic configuration was very sensitive to LCO, the unrealistic amplitudes of normal acceleration obtained for that model cast some doubt on the quantitative relevance of observed trends. It was demonstrated, however, that the relationships between the various parameters are highly non-linear and, in some cases, seemingly erratic. The effect of altitude was very significant for structural damping values of g = 0.01 (g = 2 ζ) or less below 10,000 feet but was very small at that altitude or above. The boundaries for existence of LCO as function of angle-of-attack or Mach number also changed erratically depending on the value assumed for structural damping. As a result, it was concluded that these parameters are all very important and that their values must be accurately determined before reliable predictions can be obtained.

This is an easy task for all parameters with exception of total damping (i.e. sum of structural and aerodynamic damping). Since the method does not involve any aerodynamic damping due to the use of steady aerodynamic data, an equivalent structural damping must be assumed that accounts for the aerodynamic damping as well. This composite value would then be used in the basic equations of motion given in equation (1). Because each mode has different values of aerodynamic damping, which also depend on flight conditions, the importance of this parameter requires that modal variation also be accounted for. Results from the wind tunnel test summarized in reference 8 will be used to formulate an approach for estimating appropriate damping characteristics for the LCO prediction method.

2.5.3 Prediction of Configuration Effects

The LCO prediction method was applied to several configurations for which the LCO characteristics are known. Parameter selection was based on the experience gained with the generic model as described above, however, structural damping values were varied since their correct values were not known. All modes were used within the frequency range of interest.

Response calculations were carried out for configuration A for which classical flutter calculations showed an unstable antisymmetrical mode at a frequency of 7.6 Hz just above the desired maximum speed of 600 KEAS. The LCO calculations were made for a system with natural modes up to 15 Hz (12 DOF) and varying structural damping values of g = 0.01, 0.02 and 0.03. The frequency is about 7.6 Hz in the results shown in figure 9. It appears that for a mean angle-of-attack of 6 deg and structural damping values of g = 0.01 and 0.02 rapidly developing LCO was obtained, whereas for a structural damping of 0.03 the calculations had to be continued to 60 s to obtain sustained oscillations.

Flight test results for configuration A yielded LCO at M = 0.9 (during a wind-up turn) at an altitude of 5K ft. The frequency of the forward tip launcher acceleration was about 7.5 Hz and the amplitude 2 g. The conclusion is that the calculated LCO and the flight test data agree qualitatively.

Configuration B has the same loading conditions as configuration A, but with a different type of tip launcher which required changes in the structural representation. Classical flutter calculations show an unstable antisymmetrical mode at a frequency of 7.6 Hz, but well above the required maximum speed of 600 KEAS. Response calculations were carried out for the same conditions as for configuration A, including a system with natural modes up to 15 Hz (12 DOF) and varying structural damping values. Predicted accelerations at the forward tip launcher position for mean angle-of-attack of 6 deg, and varying structural damping are presented in figure 10. The frequency is about 7.7 Hz. After the calculations were continued to 40 s, sustained oscillations were found for g = 0.01. LCO was suppressed by increasing the structural damping to g = 0.02. Obviously the calculated responses of configuration B show a weaker sensitivity to LCO than was calculated for configuration A because at lower assumed structural damping values LCO disappears. This observation is confirmed by the results of flight tests.

Other configurations were analyzed with the LCO prediction method in reference 12. Results also agreed qualitatively with flight test trends, thus justifying the conclusion that the method is very promising and that the approach is fundamentally correct.

3 Additional Parametric Effects

As an important part of the continuing refinement of the LCO prediction method being developed between NLR and General Dynamics, other parametric effects have been recently investigated in addition to those re-

THIS DOCUMENT PROVIDED BY THE ABBOTT AEROSPACE
TECHNICAL LIBRARY
ABBOTTAEROSPACE.COM

ported in reference 12. These include the effects of the time step size of the integration technique, time lag in the aerodynamic force development, leading-edge flap settings and variation of mode dependent damping values. The first three effects will be discussed in the following paragraphs of this section. The last item of mode dependent damping will have an entire section devoted to its discussion following this section.

3.1 Time Step Size

The time step size used to integrate the aeroelastic equations of motion (see sections 2.2 and 2.3) has been held constant at 0.005 seconds for the previous developments summarized in references 11 and 12. This yielded about 25 time steps per cycle at the expected frequency of about 8 Hz. (In actuality, 26 time steps per cycle were obtained at the resulting frequency of 7.6 Hz.) Smaller time step sizes were not considered because of the very inefficient time-marching procedure used in the method as reported in reference 11. In contrast, the earlier calculations reported in reference 9 used about 100 time steps per cycle.

With the incorporation of a more efficient time-marching integration procedure as reported in reference 12, it was possible to examine easily the effect of smaller time steps. Calculations reported in reference 12 using a time size step of $\Delta t = 0.005$ seconds were repeated for $\Delta t = 0.002$ seconds. The results obtained with the smaller step size did show a slight reduction in LCO amplitudes of about 2 %. Thus, it was concluded that $\Delta t = 0.002$ seconds should provide solutions that are essentially converged for the problems currently being investigated. Since the time step is full scale time, the nondimensional step size, $\Delta\tau$, becomes:

$$\Delta\tau = \frac{2V\Delta t}{c} \approx 0.35$$

where c is the wing mean aerodynamic chord and V corresponds to a Mach number of 0.92 at an altitude of 5K ft. Unless otherwise noted, all calculations to be discussed in the remainder of this paper were performed with $\Delta t = 0.002$ seconds.

3.2 Aerodynamic Time Lag Effects

A finite time is required for signals to propagate through an aerodynamic flow field which results in a time lag for changes to occur in the flow. The effect of this "aerodynamic time lag" is different depending on the size of the disturbance and the dominant characteristics of the flow field. These characteristics may be classified by mostly attached, separated, or transitioning types of flows. A more complete discussion is given in reference 8 regarding these effects.

The LCO calculations performed in reference 9 showed that introducing time lag for the transition to shock-induced trailing-edge separation resulted in increased LCO amplitudes. The assumed damping value was g = 0.07 based on previous knowledge of the aircraft and the particular mode. This damping is considerably higher than those values used for the calculations discussed in section 2 where no transition time lag was used. Because a finite time is required for the flows to separate or reattach, a lag must be introduced into the quasi-steady analysis technique used in this paper.

In order to have an estimate of the time lag value for transitioning to shock-induced trailing-edge separation, appropriate data from several sources of unsteady flow information were examined to see if such a quantity could be determined. The results of this investigation, as also discussed in reference 8, showed that a "universal" parameter may exist which could quantify the desired transition time lag. The observed time delay was expressed in a non-dimensional form as:

$$\Delta\tau_{LAG} = \frac{2V\Delta t_{LAG}}{c_{SEP}} \approx 8.4$$

where c_{SEP} is the approximate chord length of the shock-induced trailing-edge separation zone (or the mean distance from the shock to the trailing edge). For the current LCO model, the estimated physical value was $\Delta t_{LAG} = 0.011$ seconds which corresponds to a phase lag of about 30 deg at 7.6 Hz.

The current LCO prediction method was modified to allow an input time lag parameter of arbitrary size. This time lag specified a previous point in time for which aerodynamic forces would be calculated for use in integrating the equations of motion at the current time. By increasing the time lag to an equivalent phase angle, greater than 180 deg, a time lead effect could also be investigated with the modified method.

The effect of varying the time lag parameter is illustrated in figures 11, 12, and 13. Figure 11 shows the baseline acceleration results for several points on the airplane as well as the time varying local angle-of-attack for the wing tip (pressure station 6). The conditions are $M = 0.92$, altitude = 5K ft and a mean angle-of-attack of 6 deg. Structural damping, g, is 0.01 and time lag is 0.0. Figure 12 shows the same items at the same conditions for a time lag phase angle of 30 deg. In this case damping has to be increased to g = 0.05 before a stable LCO was achieved. The tip launcher forward accelerations are about the same as shown in figure 11. However, all other items are considerably larger which indicates that a significant change has occurred in the LCO eigenmode. The higher damping values required to achieve stable LCO are more in agreement with the early LCO model described in reference 9.

Further increase of the the time lag to produce an effective lead angle of 45 deg was also investigated for which the results are shown in figure 13. Since phase lead introduces stability into the system in this case, damping was kept at g = 0.01. LCO growth is much

THIS DOCUMENT PROVIDED BY THE ABBOTT AEROSPACE
TECHNICAL LIBRARY
ABBOTTAEROSPACE.COM

slower in comparison with cases in figure 11 and 12. About 60 seconds are required to reach a converged limit. Comparison of figures 11 and 13, however, reveals that the LCO eigenmode is about the same.

A summary plot of variation of the tip launcher forward acceleration with increasing time lag is shown in figure 14. Time lag is expressed as phase lag at 7.6 Hz for ease of discussion. Total damping is maintained at g = 0.02 and angle-of-attack is constant at 6 deg. Up to 30 deg lag, the amplitude increases and diverges beyond the aerodynamic data base incidence limits at 30 deg lag. From 30 deg to 225 deg lag, the solution is diverged beyond the data base limits. After 225 deg lag, the amplitude is high but is rapidly decreasing with increasing lag. At 270 deg lag, the system is completely stabilized as might be expected and continues in this mode up to 315 deg lag, where LCO begins to appear again. From 330 up to 360 deg lag, the amplitude increases slightly and stabilizes between 345 deg and 360 deg.

The purpose of this investigation of time lag effects was to determine their importance in the non-linear modeling of transonic LCO. The approach used actually applied the same time lag to all parts of the wing, with either attached or separated flow, which is not correct. However, the smoothness of variation of the established attached or separated aerodynamic forces as compared to the flow transition forces (see figures 3 and 4) tends to weight the time lag effects toward the transitory conditions. Thus, it is concluded that the effects demonstrated here emphasize the importance of introducing some type of time lag parameter in the LCO prediction method. This parameter will be established on the basis of the wind tunnel test results (Ref. 8).

3.3 Effect of Leading-Edge Flap Settings

In addition to data for zero leading-edge flap deflection, data for two other positions of 5 deg and 10 deg (nose down) are available in the data base of reference 13. The effect of leading-edge flap settings was investigated with the LCO prediction method by substituting pressure data for the flap setting of interest and running the method in its normal mode. No account was made for different orientations of the aerodynamic forces on the deflected flaps, as this effect would introduce a maximum error of only about 1.5 % based on the cosine of 10 deg.

The prediction runs were made at $M = 0.92$ and altitude = 5K ft with angle-of-attack linearly increasing in time from 1 deg to 10 deg in 27 seconds (i.e. a pitch rate of 1/3 deg per second). Damping was held constant for all 12 modes at g = 0.01 (same as in figure 11) and time lag was set to zero. Three leading-edge flap settings of 0 deg, 5 deg, and 10 deg were analyzed. Results are shown in figure 15 for the tip launcher forward acceleration time histories at all three leading-edge flap settings along with the time history of mean angle-of-attack variation.

The results in figure 15 indicate that leading-edge flap settings have a significant effect on LCO development during a simulated maneuver. This is in contrast to the conclusions in reference 14 which stated that the effect of leading-edge flap setting was minimal on the development of shock-induced trailing-edge separation. However, these flap deflections effect the location of the critical aerodynamic forces and this is most likely the key influence that is responsible for the trends shown in figure 14.

The levels of LCO for leading-edge flaps at 0 deg and 5 deg are low at ±3 g's. Normal flying practice with optimized leading-edge flap scheduling, depending on Mach number and altitude, would use 0 deg flap up to about 5 deg angle-of-attack, 5 deg flap up to about 8 deg, and 10 deg flap up to about 13 deg. With such scheduling, the heavy LCO shown in figure 14 for 10 deg flap would not be encountered since this flap setting would not be used below about 7 or 8 deg angle-of-attack. Corresponding points for the other leading-edge flap settings of 0 deg and 5 deg would encounter the milder LCO shown for these points.

Based on the effects shown in figure 15, leading-edge flap scheduling must be included in LCO prediction models for transient maneuvers. In addition, the high sensitivity of LCO to Mach number as demonstrated in reference 12, suggests that Mach variations also need to be included in the transient models. Ideally, flight path modeling would be desirable and needs to be considered as part of the LCO prediction method refinements.

4 Role of Damping in Total Air Frame LCO Response

The prediction of aircraft LCO characteristics has the same requirements as other aircraft dynamic response predictions such as gust response and buffeting. These requirements include accurate predictions of the response of various parts of the aircraft as well as amplitudes and frequencies. Thus, the LCO eigenmode shape is as important as its amplitude and frequency. Since the LCO eigenmode may be composed of several natural modes (as in the cases discussed in this paper as compared with the one DOF case in reference 9), the correct total damping applicable to each natural mode must be included in the LCO model. Similar requirements and techniques for satisfying these needs were discussed extensively in reference 18 with regard to accurate buffet response predictions.

The importance of mode dependent damping effects were therefore investigated as part of the LCO prediction method refinements. Because the introduction of

THIS DOCUMENT PROVIDED BY THE ABBOTT AEROSPACE
TECHNICAL LIBRARY
ABBOTTAEROSPACE.COM

time lag (see section 3.2) seemed to require more realistic damping values, a time lag of 0.011 seconds was used throughout this investigation. The flight conditions were also constant at M = 0.92, altitude = 5K ft and mean angle-of-attack = 6 deg. Damping was first varied as a uniform value for all modes and then varied between the two important modes shown in figure 8.

4.1 Uniform Damping for All Modes

Since a higher damping value, g = 0.05, was needed to obtain a stable LCO, this was used as a starting point. LCO limit results are shown in figure 16 as function of uniform damping for all modes. The top part of this figure includes the predicted acceleration amplitudes for the tip launcher forward (circles) and aft (squares) as well as the pilot's seat (triangles). The amplitudes of the wing tip incidence (relative to the mean angle-of-attack) are shown in the bottom of figure 16. These parameters are the same as those presented in figures 11, 12, and 13.

The rapid change in response levels between g = 0.05 and 0.06 are in line with the diverged results obtained for g $\leq$ 0.04 with a time lag of 0.011 seconds. The similar amplitudes noted at all dampings for the forward and aft tip launcher accelerations indicate that the LCO eigenmode is not changing much as uniform damping is increased. This is further substantiated by similar relative changes in the other response items with increasing damping in figure 16.

Thus, returning to figures 11 and 12, it appears that the change in the LCO eigenmode is most likely caused by introduction of the time lag rather than the large increase in damping. If this is true, then the importance of correct determination of time lag characteristics is increased. Such a determination is possible with the unsteady aerodynamic data base discussed in reference 8.

4.2 Variable Damping for the Pitch Mode

Referring to figure 10, the pitch mode is similar to mode 1 at a frequency of 7.02 Hz but is actually mode 4 in the 12 mode simulation of the current modeling. The effect of varying pitch mode damping from g = 0.06 to 1.0 was investigated while holding damping of other modes constant. Damping for the bending mode (similar to mode 2 in figure 8, but actually mode 5 in the 12 mode simulation) was fixed at g = 0.02 and the damping of the remaining 7 structural modes was fixed uniformly at g = 0.01. Results for this investigation are shown in figure 17 in the same format as used in figure 16.

The most obvious and expected trend shown in figure 17 is the reduction of oscillatory wing tip incidence with increasing damping for the pitch mode. The reduction in pilot's seat acceleration also tracks with expected trends. The reduction in both launcher accelerations follows the same logic, although, the constant differential between the two seems contradictory. What is not shown in the figure is the phasing between the two tip launcher responses which is needed to define the oscillatory incidence. The phasing is more clearly illustrated by the mode deflections shown in figure 7 where the pitching motion appears to lead the translation motion at the wing tip by about 90 deg. (This relationship is similar to that of classical flutter for a simple pitch/plunge coupling.) Thus, because of the phasing, oscillatory wing tip incidence cannot be estimated purely on the basis of differential accelerations at the forward and aft ends of the tip launcher. However, reduction of the pitch mode amplitude (due to higher damping in that mode) will result in a reduction of the bending mode response since the former is providing the driving force which opposes the damping force for the latter mode.

4.3 Variable Damping for the Bending Mode

Damping for the bending mode (mode 2 in figure 8) was varied from g = 0.01 to 1.0 while fixing damping for the pitching mode at g = 0.07 and the remaining 7 structural modes at g = 0.01. Response results for this variation are shown in figure 18 in the same format as used in figures 16 and 17.

The effect of bending mode damping over such a wide range is minimal on both the pilot's seat acceleration and the wing tip incidence. Accelerations on the wing tip launcher show a very slight increase at the aft end but a substantial decrease at the front end. The final values for all items shown in figure 18 for g = 0.07 are about the same as those shown in figure 16 for g = 0.07. This might be expected since damping of the two important modes should be the dominant factor in driving the LCO amplitude. This also confirms that the LCO eigenmode is little affected by responses of the non-critical modes for which g = 0.07 in figure 16 and g = 0.01 in figure 18.

The important result illustrated in figure 18 is that mode dependent damping characteristics can significantly alter the LCO eigenmode. Although responses are similar for the pilot's seat and wing tip incidences with increased bending mode damping, the wing tip launcher motion is not the same. Such characteristics are important for determining the degradation of weapons platform capability as a result of LCO. Also, in other cases, the pilot's seat may be more affected than is shown in figure 18. (see figure 17 for example). Thus, in order to obtain representative LCO eigenmodes, individual total damping for each mode included in the LCO modeling must be estimated as accurately as possible through such techniques as presented in reference 18.

THIS DOCUMENT PROVIDED BY THE ABBOTT AEROSPACE
TECHNICAL LIBRARY
ABBOTTAEROSPACE.COM

4.4 Effect of Damping on Non-Critical Modes

As just discussed, correct damping characteristics are needed for the critical modes in order to accurately obtain the LCO eigenmode. It was implied that damping in the non-critical modes was not important for LCO limit conditions and this is further illustrated by the flagged symbols shown in figure 18. These symbols represent results obtained with g = 0.02 for the 7 non-critical structural modes as opposed to g = 0.01 for the non-flagged symbols. (In addition, g = 0.07 for the non-critical modes is illustrated in figure 16.)

One of the most critical conditions for LCO is close-in air combat in which rapid high-g maneuvers are highly transient. Under these conditions LCO can limit tracking, weapons launch windows, pilot functioning, aircraft handling qualities and so on. Thus, the transient nature of LCO must also be predictable.

A comparison is made for time history developments of LCO for the two cases of g = 0.01 in figure 19 and g = 0.02 in figure 20 for the non-critical modes with g = 0.07 for the pitching and bending modes. The transient characteristics are quite different although the final amplitudes are about the same. The unrealistically low total damping of g = 0.01 allows a beating transient to exist for a significant period beyond what is shown in figure 20 where g = 0.02 is a realistic value. Thus, it is also important for predicting transient LCO that accurate damping values for the non-critical modes be included in the modeling. And, since the critical modes may not be known beforehand, it is even more important that accurate damping data be used for all modes included in the LCO predictions.

5 Method Refinements

Various refinements to the LCO prediction method were discussed in reference 12 which reflected the evolutionary development of such an approach. One of the key ingredients in the developments listed were the results from an unsteady wind tunnel test that has just recently been conducted and is described in reference 8. The results discussed in section 3 and 4 in this current paper were obtained as part of the investigation to better understand more specifically what information is needed from the unsteady wind tunnel test. These requirements are discussed in reference 8 but are summarized below along with a summary of the refinements suggested in reference 12.

The wind tunnel data base (Ref. 8) is expected to provide information necessary to characterize the unsteady nature of three-dimensional transonic flows with extensive shock-induced separations that may also extend to the trailing edge. This information will provide the unsteady complement to that contained in reference 14. Such items of interest are flow transition lag times, effects of surface motion as well as the development of aerodynamic stiffness and damping forces. Information is also needed to determine if techniques such as those described in references 19, 20, and 21 are capable of providing the unsteady aerodynamic loads suitable for use in the simulation of LCO phenomena.

The trends demonstrated in section 3.2 for time lag effects and section 4 for the role of total damping in total airframe LCO response emphasize (1) the importance of accurately defining the unsteady aerodynamic characteristics in LCO flows and (2) the need for a generalized model of these characteristics that does not require condition dependent adjustments to match known results. This means that aerodynamic stiffness and damping forces in each natural mode used in the simulation must be known a priori through the use of some type of prediction technique which may be semi-empirical (Refs. 18, 19, 20, and 21) or theoretical (Ref. 22). Current thinking suggests that configuration and condition specific information can be obtained from steady pressure tests (as is done for the current LCO prediction method) and that unsteady information can be developed that is more generic (such as transition lag time, etc.).

Another item of great importance is the definition of static aeroelastic effects in the LCO model. Since the transonic shock-induced separated flows are highly sensitive to local static changes in mean angle-of-attack, it is important that these effects be accounted for. This aspect was discussed in reference 12 where the use of modal residualization was suggested as a means to account for higher frequency modes not included in the dynamic simulation but that could be important in the static aeroelastic effects.

Finally, the use of aerodynamic forces on the fuselage and tail surfaces has also been considered in reference 12. Although these are important in buffeting and gust response predictions (Ref. 18) they are probably not key ingredients to the LCO mechanism and may not be needed. However, this is still under consideration.

6 Conclusions

A semi-empirical method to predict LCO characteristics of fighter aircraft is being developed. The method has been described in its present form, and results of the latest predictions were compared with flight test trends and used to further assess various parametric effects. The important conclusions from reference 12 are summarized below.

1. Data from steady wind tunnel tests were sufficient for predicting qualitative LCO trends for the cases studied.

2. Altitude, mean angle-of-attack, Mach number and total damping were found to be sensitive parameters in transonic LCO.

THIS DOCUMENT PROVIDED BY THE ABBOTT AEROSPACE
TECHNICAL LIBRARY
ABBOTTAEROSPACE.COM

3. The effects of store configurations on LCO trends were qualitatively predicted in all cases using only the store mass effects in the natural modes.

4. It was clearly demonstrated that shock-induced trailing-edge separation plays a dominant role in the development of LCO at transonic speeds.

5. Running the method using all modes in the frequency range of interest and sweeping through the desired angle-of-attack range (to simulate a maneuver) provides a means for determining LCO trends without prior knowledge of important natural modes or angle-of-attack that are sensitive to LCO. Pitch rate effects can distort the picture, however, and miss points that could be seen only in a sustained maneuver.

Additional conclusions from the investigations discussed in the current paper are summarized below.

6. Non-dimensional time step sizes on the order of $\Delta\tau \approx 0.35$ are sufficient for converged time integration of the equations of motion for the cases studied.

7. Time lag associated with transition to and from shock-induced trailing-edge separation was shown to be destabilizing when set at realistic values. Higher but more realistic total damping was needed to prevent solution divergence.

8. Increasing time lag to provide an effective phase lead produced more stable solutions.

9. Leading-edge flap settings were found to affect the LCO solutions for an incidence sweep.

10. It appears that the introduction of time lag into the LCO calculations has significant effect on the LCO eigenmode. Thus, the importance of correct determination of time lag characteristics is increased. Such a determination is possible with the unsteady aerodynamic data base discussed in reference 8.

11. The separate variation of pitch and bending mode damping values showed that mode dependent total damping characteristics for the critical modes are very important for establishing the correct LCO eigenmodes, amplitude and frequency.

12. Modal total damping values for non-critical modes are important for transient developments of LCO.

13. It has been emphasized that unsteady effects are needed to properly quantify the aerodynamic driving and damping forces that are important for developing a consistent LCO model.

7 Acknowledgement

This investigation was funded by U.S. Air Force, General Dynamics, The Netherlands Ministry of Defense and National Aerospace Laboratory NLR, The Netherlands. The monitors for the USAF were: Messrs. Faustino Zapata and Larry Huttsell. The monitor for The Netherlands Ministry of Defense was the Netherlands Agency for Aerospace Programs (NIVR), contract number 07801N.

8 References

1. Meijer, J.J., *NLR Contributions to the Flutter Certification of Aircraft with External Stores*, 7th Aircraft/Stores Compatibility Symposium, Wright-Patterson AFB, Ohio, 8-10 April 1986 and at the 17th Annual Symposium of the Society of Flight Test Engineers, Washington, D.C., USA, 10-14 August 1986.

2. Ericsson, L.E., *Vortex-induced Bending Oscillation of a Swept Wing*, J. Aircraft, Vol. 24, No. 3, March 1987, pp. 195-202.

3. Dobbs, S.K., Miller, G.D., Stevenson, J.R., *Self Induced Oscillation Wind Tunnel Test of a Variable Sweep Wing*, AIAA-85-0739, August 1985.

4. Moss, G.F., Pierce, D., *The Dynamic Response of Wings in Torsion at High Subsonic Speeds*, AGARD-CP-226, 1977.

5. Seidel, D.A., Eckstrom, C.V., Sandford, M.C., *Investigation of Transonic Region of High Dynamic Response Encountered on an Elastic Supercritical Wing*, AIAA-87-0735-CP, April 1987. Also J. Aircraft, Vol. 26, No. 9, September 1989, pp. 870-875.

6. Eckstrom, C.V., Seidel, D.A., Sandford, M.C., *Unsteady pressure and structural Response Measurements on an Elastic Supercritical Wing*, AIAA-88-2277.

7. Boer, R.G. den, Cunningham, Jr., A.M., *Unsteady Transonic Wind Tunnel Testing of Fighter Type Wings*, 31st AIAA/ASME/ASCE/AHS/ ASC Structures, Structural Dynamics, and Materials Conference, Long Beach, California, April 2-4, 1990.

8. Cunningham, Jr., A.M., Boer, R.G. den, *Transonic Wind Tunnel Investigation of Limit Cycle Oscillations on Fighter Type Wings*, AGARD Structures and Materials Panel Specialist Meeting on Transonic Unsteady Aerodynamics and Aeroelasticity, San Diego, California, 9-11 October 1991.

9. Cunningham, Jr., A.M., *The Role of Shock-Induced Trailing-Edge Separation in Limit Cycle Oscillations*, NASA-CP-3022, 1987.

THIS DOCUMENT PROVIDED BY THE ABBOTT AEROSPACE
TECHNICAL LIBRARY
ABBOTTAEROSPACE.COM

10. Cunningham, Jr., A.M., *Practical Problems: Airplanes*, Chapter 3, Unsteady Transonic Aerodynamics, edited by D.L. Nixon, AIAA Progress in Astronautics and Aeronautics Series, 1989.

11. Meijer, J.J., Zwaan, R.J., *Investigation of a Semi-empirical Method to Predict Limit Cycle Oscillations of Modern Fighter Aircraft*, AGARD CP No. 483, April 1990.

12. Meijer, J.J., Cunningham, Jr., A.M., Zwaan, R.J., *A Semi-Empirical Approach to Predict Transonic Limit Cycle Oscillation Characteristics of Fighter Aircraft*, 8th Aircraft/Stores Compatibility Symposium, Fort Walton Beach, Florida, 23-25 October 1990.

13. Elbers, W.K., *Wind Tunnel Data Report 1/9-Scale F-16A Pressure Model Investigation of Shock-Induced Separation for Limit Cycle Oscillation Studies (AEDC PWT-16T Test TF-695)*, General Dynamics, Fort Worth Division Report 16PR4694, September 1985, (Contract No. F33657-84-C-2034).

14. Cunningham, Jr., A.M., Spragle, G.S., *A Study of the Effects of Reynolds Number and Mach Number on Constant Pressure Coefficient Jump for Shock-Induced Trailing-Edge Separation*, NASA-CR-4090, August 1987.

15. Edwards, J.W., Bennett, R.M., Whitlow, Jr., W., Seidel, D.A., *Time-marching Transonic Flutter Solutions including Angle-of-attack Effects*, J. Aircraft, Vol. 20, No. 11, Nov. 1983, pp. 899-906.

16. Brockett, R.W., *Finite Dimensional Linear Systems*, John-Wiley and Sons, Inc. 1970.

17. Armstrong, E.S., *ORACLS: A Design System for Linear Multivariable Control*, Control and Systems Theory, Vol. 10, 1980.

18. Cunningham, Jr., A.M., Coe, C.F., *Predictions of F-111 TACT Aircraft Buffet Response*, AGARD CP No. 483, April 1990.

19. Dat, R. *Development of the Basic Methods Needed to Predict the Aeroelastic Behavior of Helicopters*, Rech. Aerosp. 1983-1.

20. Petot, D., *Differential Equation Modeling for Dynamic Stall*, Rech. Aerosp. 1989-5.

21. Leishman, J.G., Crouse, Jr., G.L., *State-space Model for Unsteady Airfoil Behavior and Dynamic Stall*, AIAA-89-1319.

22. Reddy, T.S.R., Kaza, K.R.V., *A Comparitive Study of Some Dynamic Stall Models*, NASA TM 88917, 1987.

THIS DOCUMENT PROVIDED BY THE ABBOTT AEROSPACE
TECHNICAL LIBRARY
ABBOTTAEROSPACE.COM

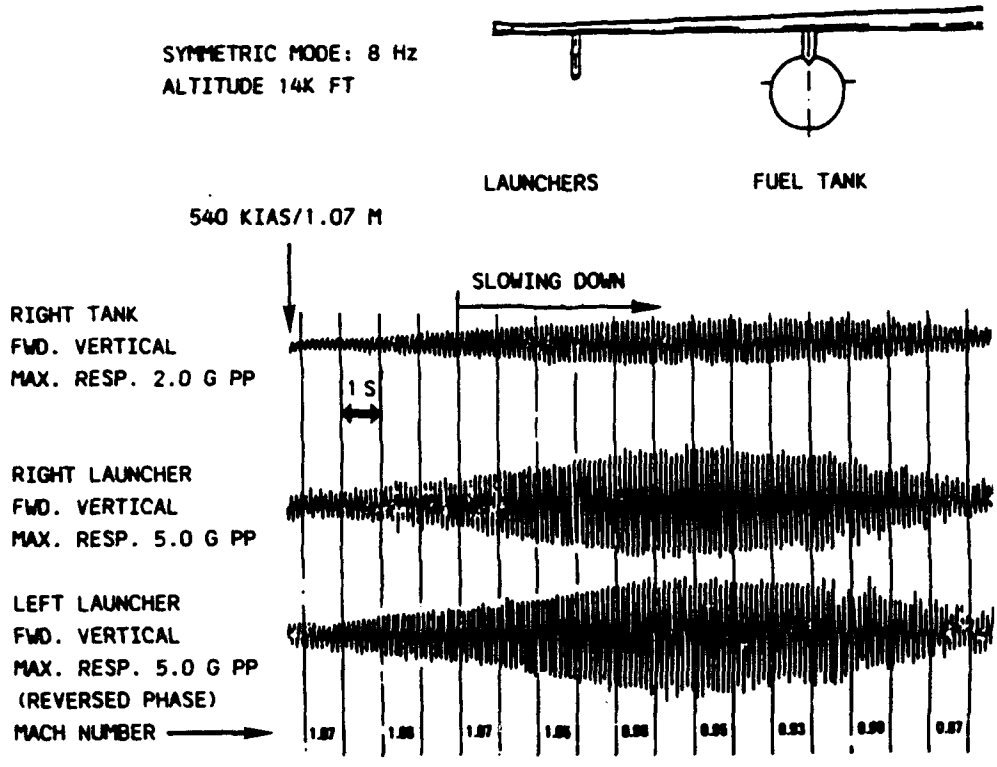


Fig. 1 Recordings of accelerometers during flight flutter testing of fighter-type aircraft.

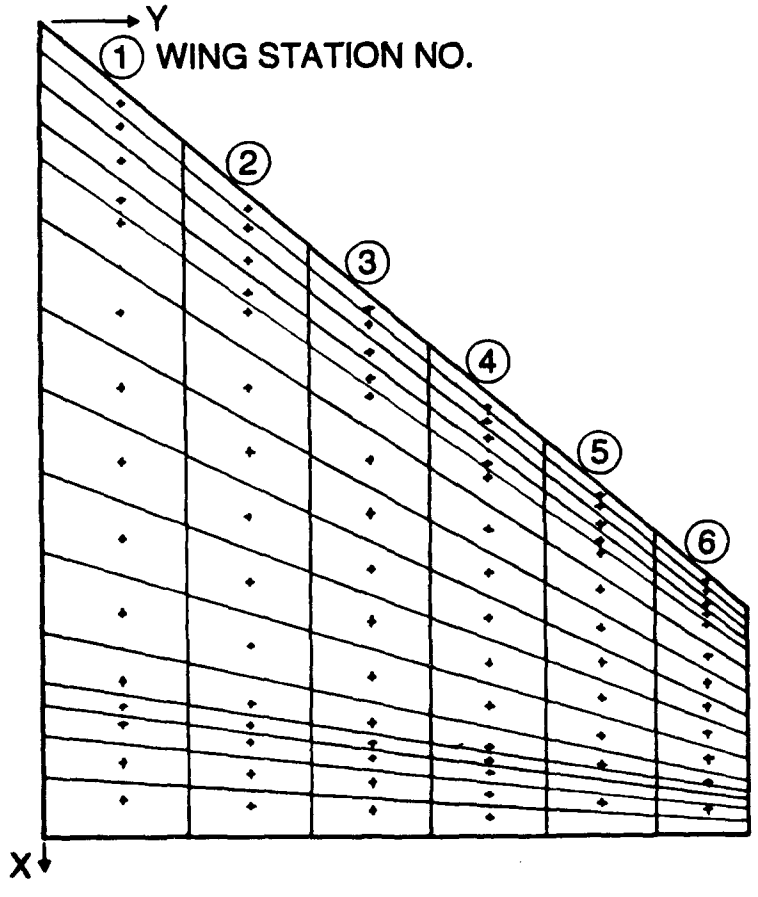


Fig. 2 Location of pressure orifices and corresponding panels on the model wing planform.

This Document Provided by the Abbott Aerospace
TECHNICAL LIBRARY
ABBOTTAEROSPACE.COM

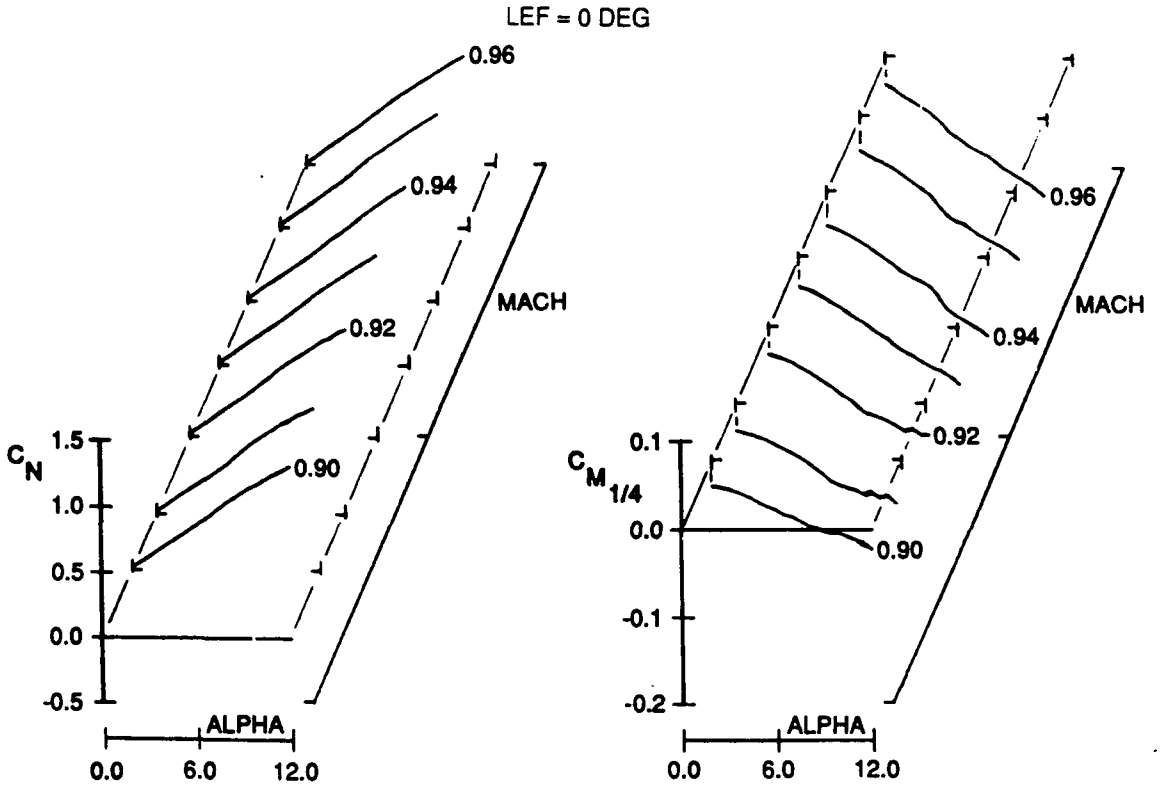


Fig. 3 Steady lift and moment coefficients in station 1 as function of Mach number and angle-of-attack.

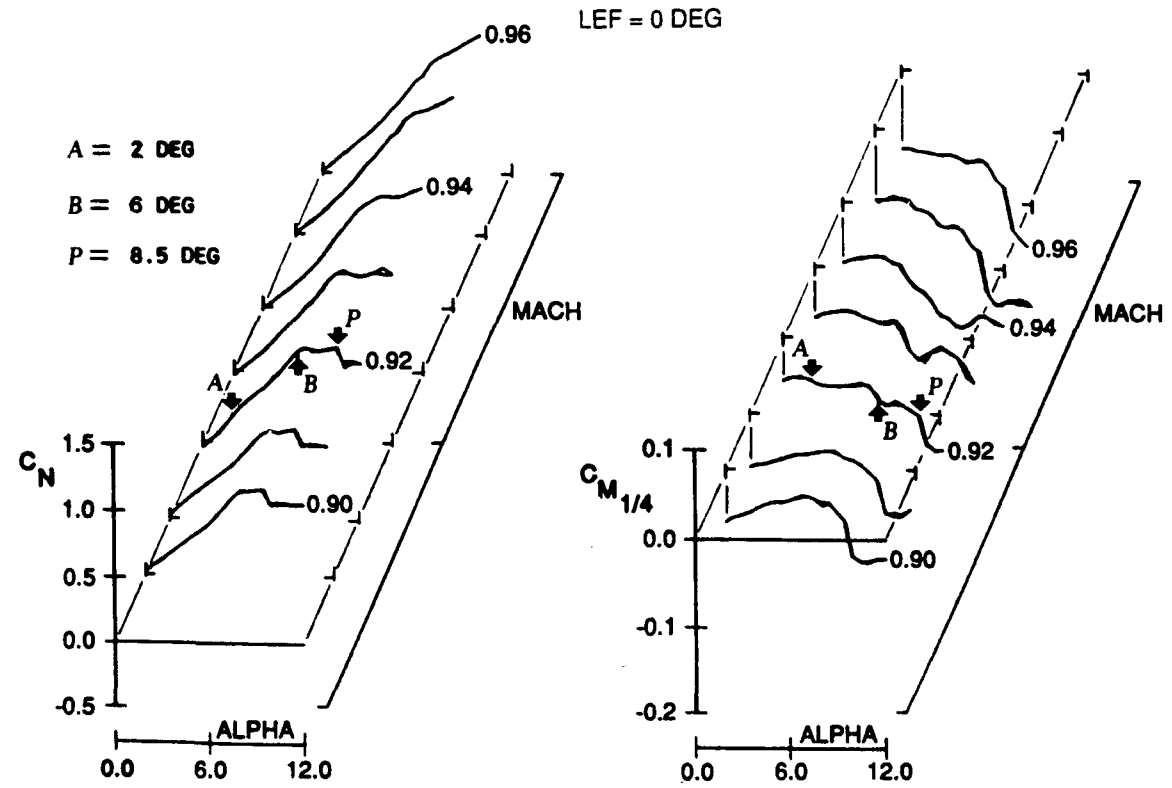


Fig. 4 Steady lift and moment coefficients in station 6 as function of Mach number and angle-of-attack.

THIS DOCUMENT PROVIDED BY THE ABBOTT AEROSPACE
TECHNICAL LIBRARY
ABBOTTAEROSPACE.COM

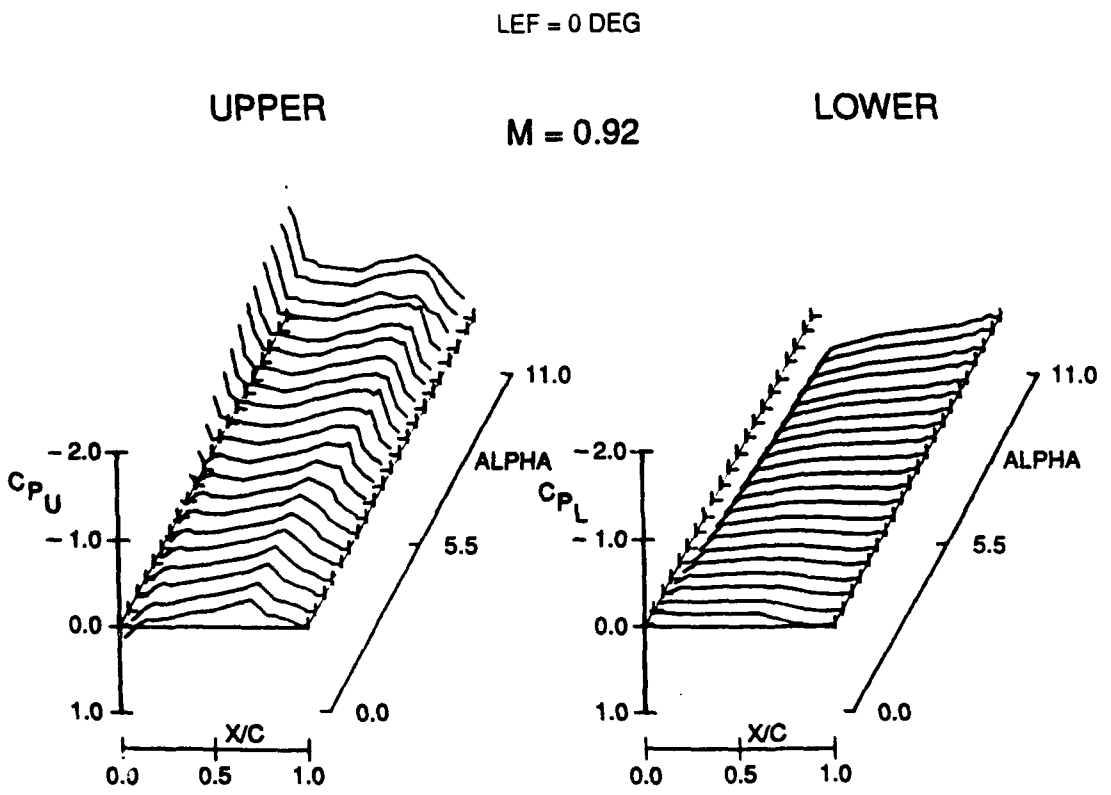


Fig. 5 Steady pressure distributions in station 1 as function of angle-of-attack and constant Mach number (M = 0.92).

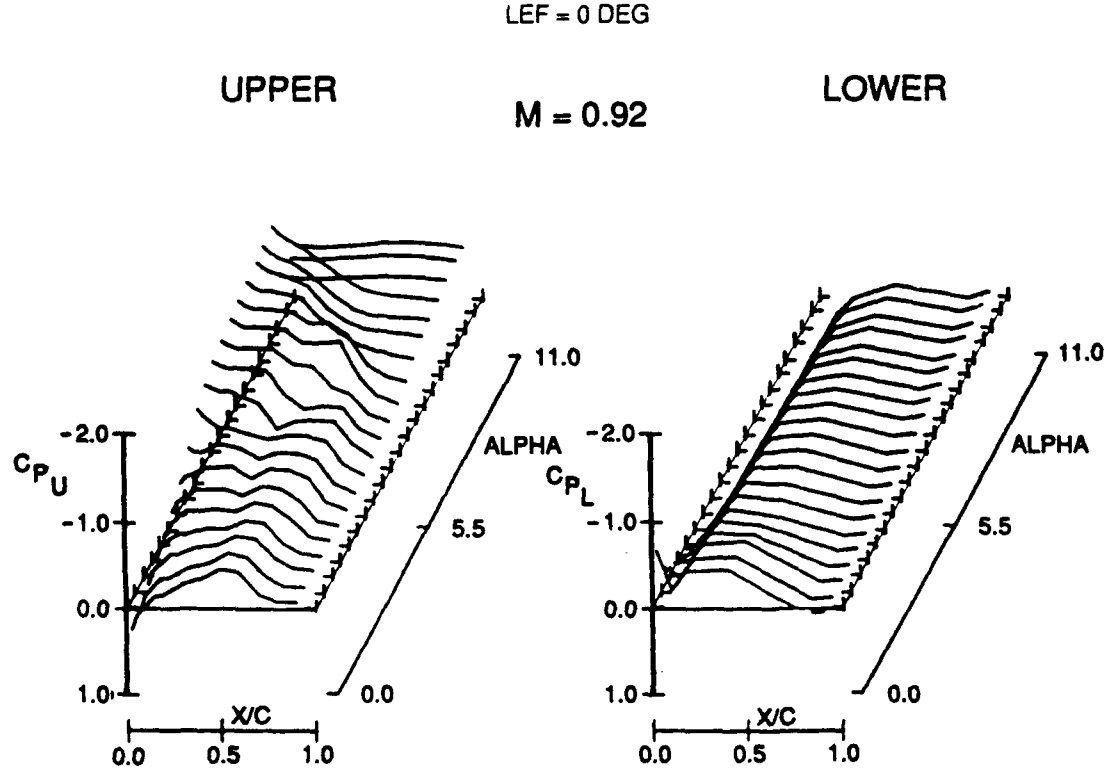


Fig. 6 Steady pressure distributions in station 6 as function of angle-of-attack and constant Mach number (M = 0.92).

THIS DOCUMENT PROVIDED BY THE ABBOTT AEROSPACE
TECHNICAL LIBRARY
ABBOTTAEROSPACE.COM

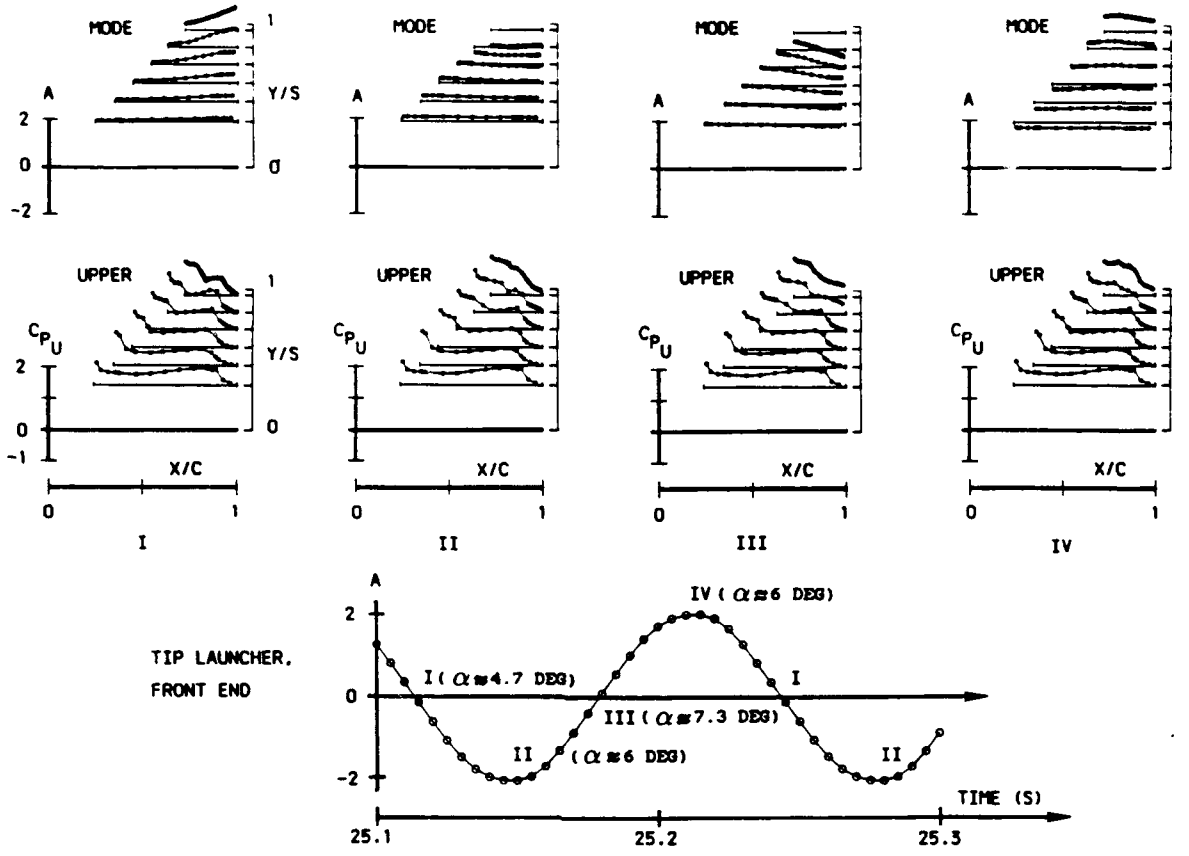


Fig. 7 Vibration mode and flow characteristics for generic model during LCO.

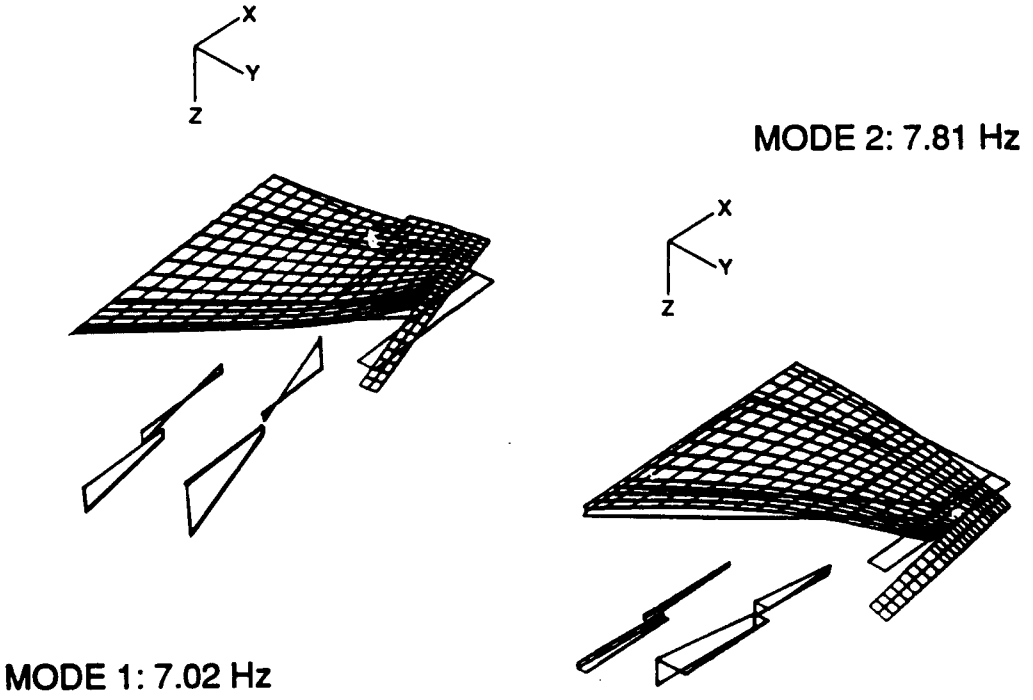


Fig. 8 First two unrestrained vibration modes of generic model.

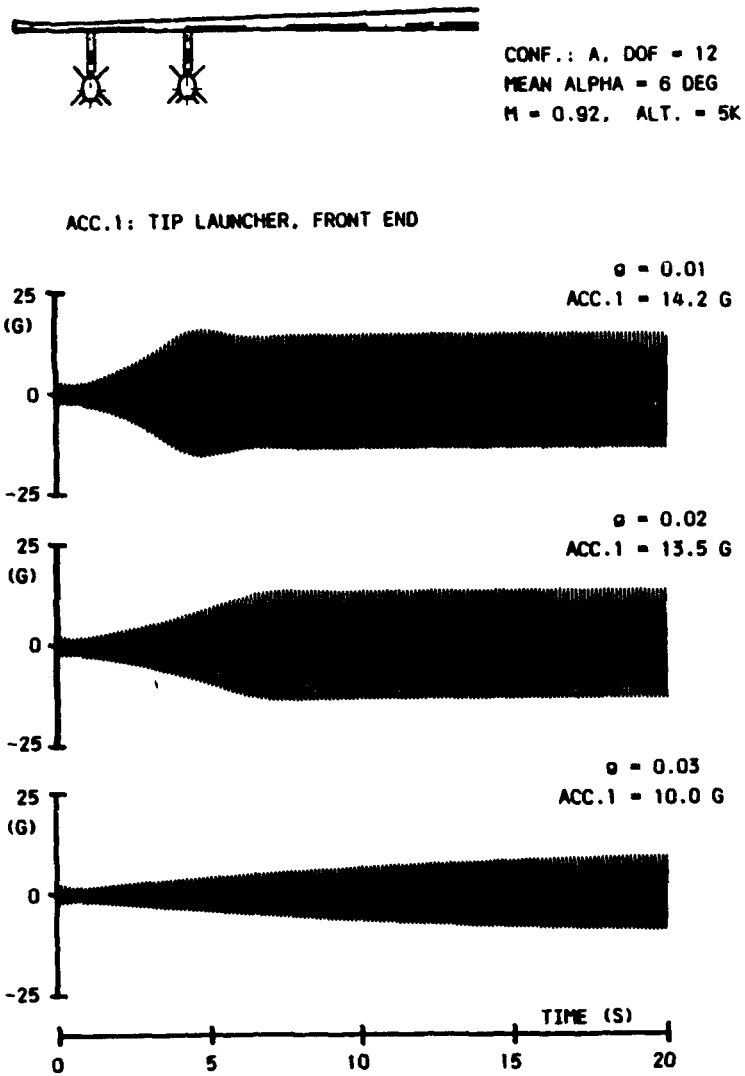


Fig. 9 Response calculations for configuration A; 12 DOF, M = 0.92, α_m = 6 deg, altitude = 5K ft, structural damping variable.

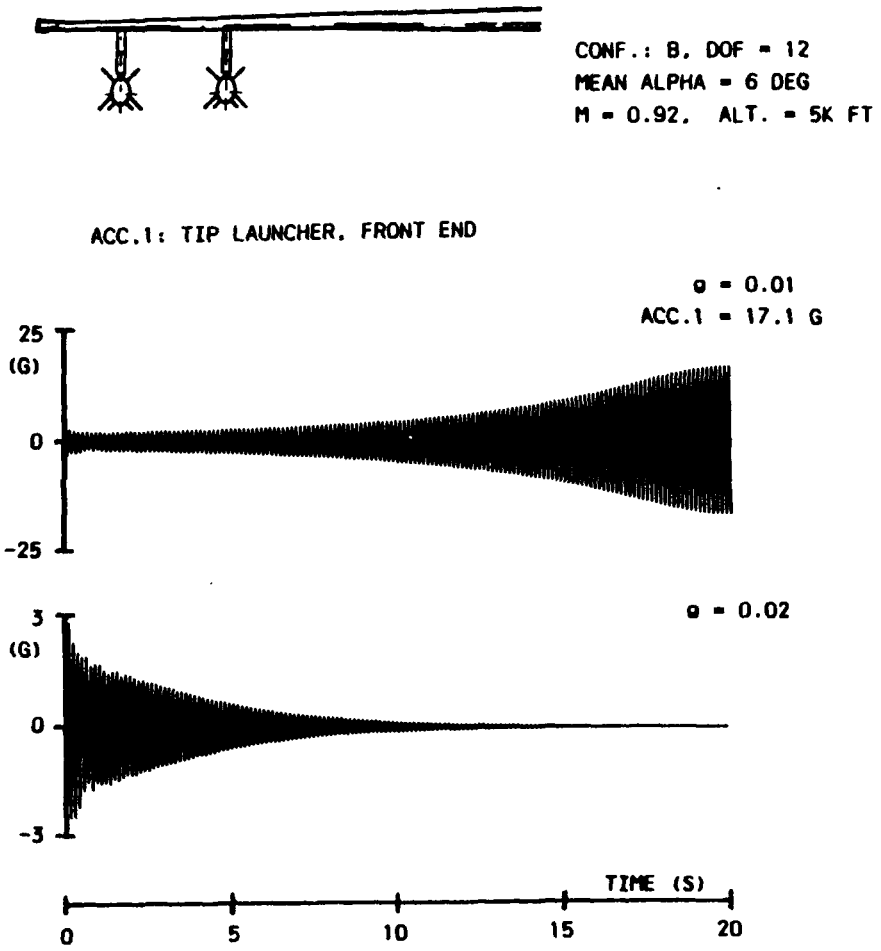


Fig. 10 Response calculations for configuration B; 12 DOF, M = 0.92, α_m = 6 deg, altitude = 5K ft, structural damping variable.

TECHNICAL LIBRARY
ABBOTTAEROSPACE.COM

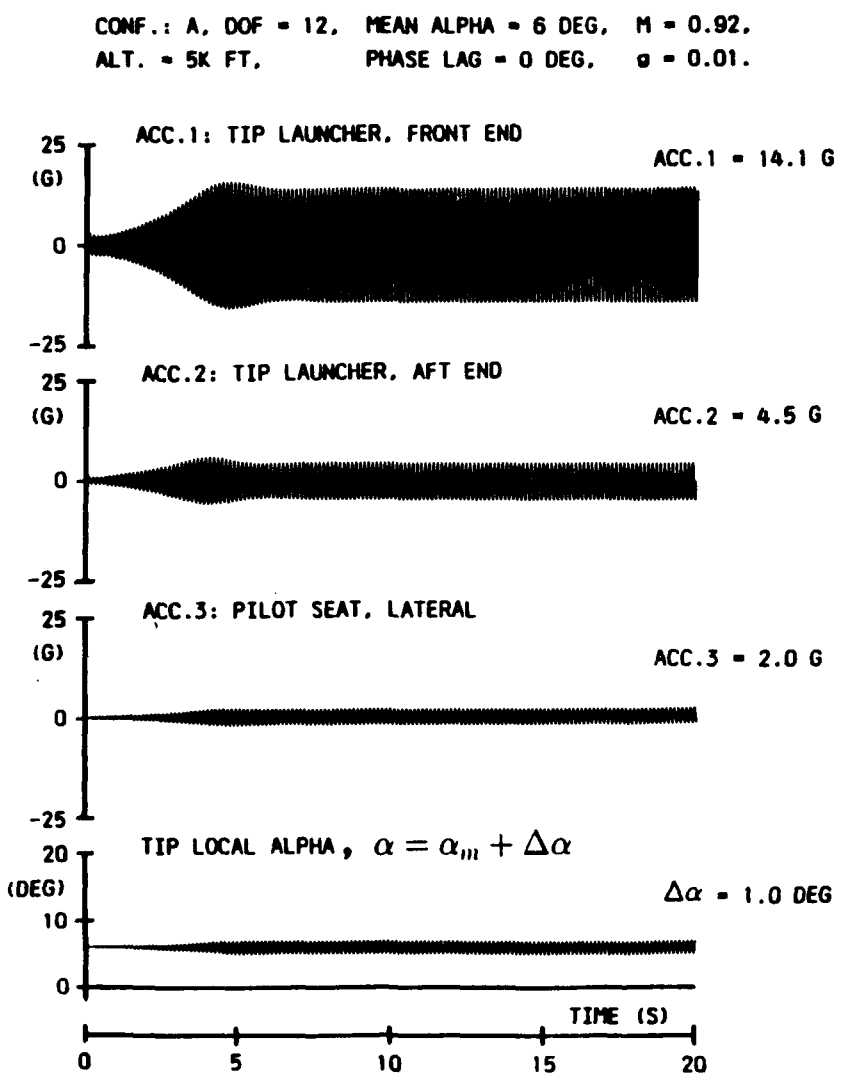


Fig. 11 Response calculations for config. A; 12 DOF, M = 0.92, α_m = 6 deg, alt. = 5K ft, structural damping: g = 0.01, phase lag = 0 deg.

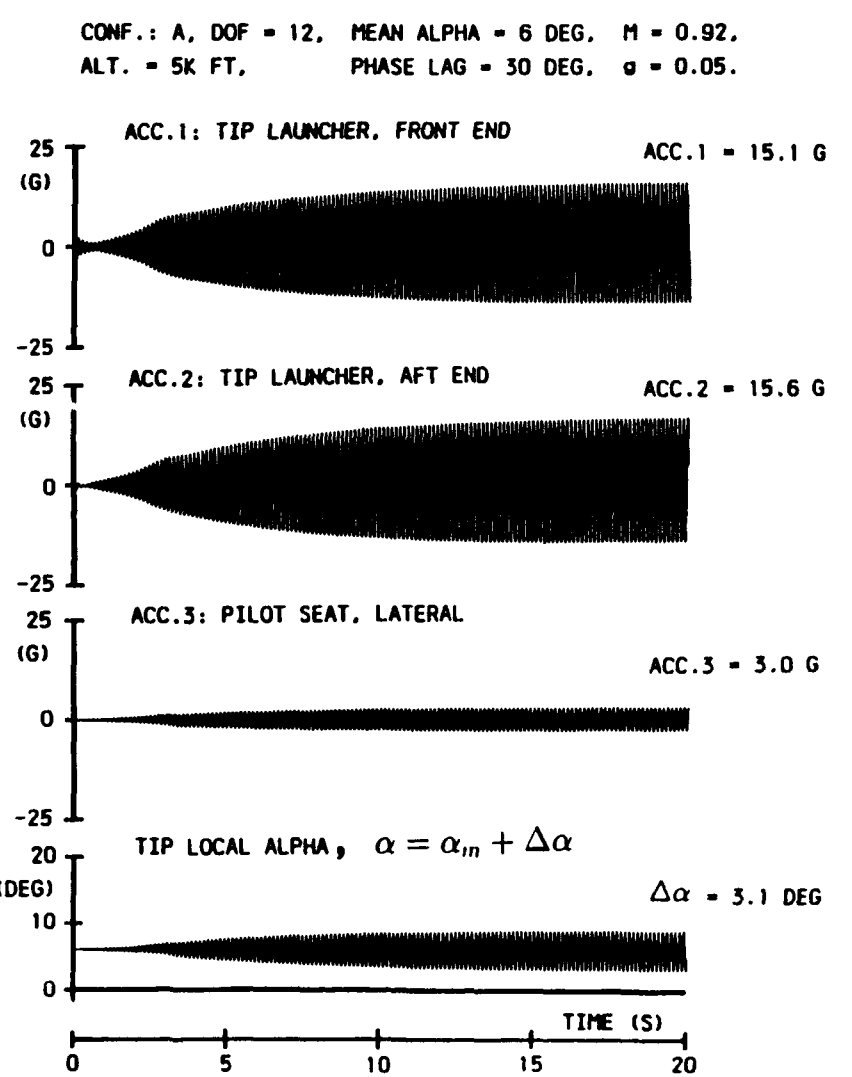


Fig. 12 Response calculations for config. A; 12 DOF, M = 0.92, α_m = 6 deg, alt. = 5K ft, structural damping: g = 0.05, phase lag = 30 deg.

THIS DOCUMENT PROVIDED BY THE ABBOTT AEROSPACE
TECHNICAL LIBRARY
ABBOTTAEROSPACE.COM

THIS DOCUMENT PROVIDED BY THE ABBOTT AEROSPACE
TECHNICAL LIBRARY
ABBOTTAEROSPACE.COM

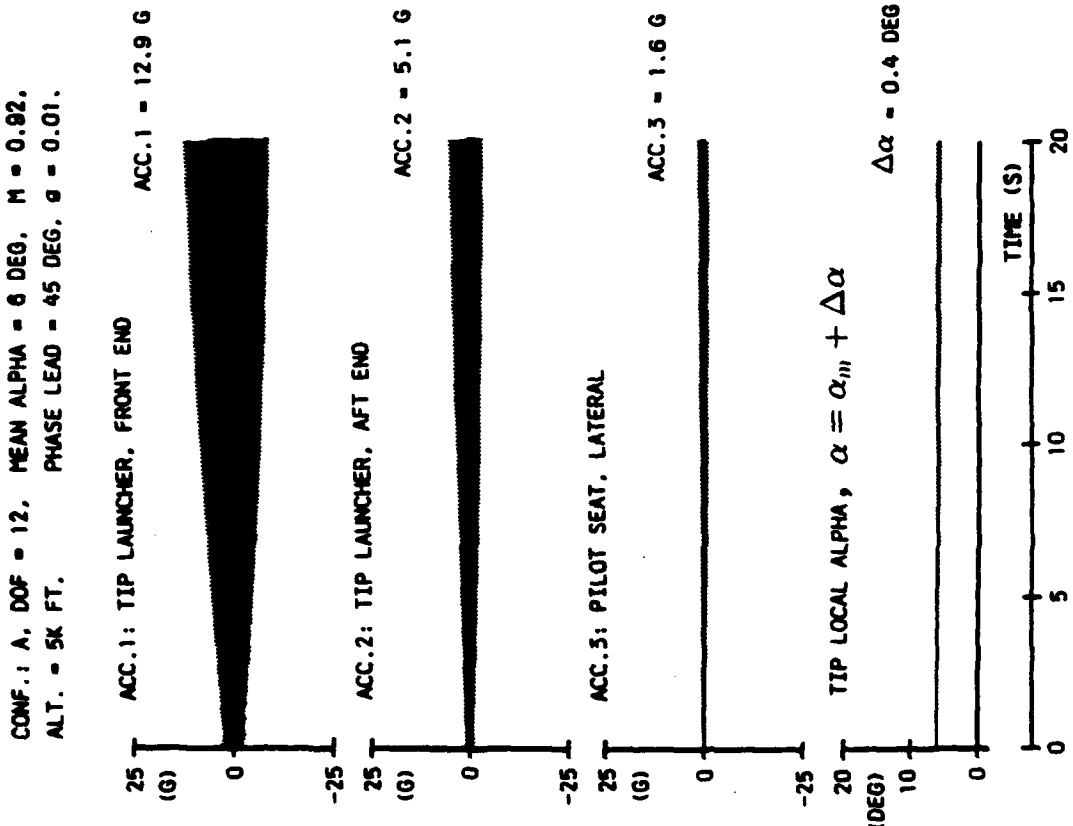


Fig. 13 Response calculations for config. A; 12 DOF, M = 0.92, α_m = 6 deg, alt. = 5K ft, structural damping: g = 0.01, phase lead = 45 deg.

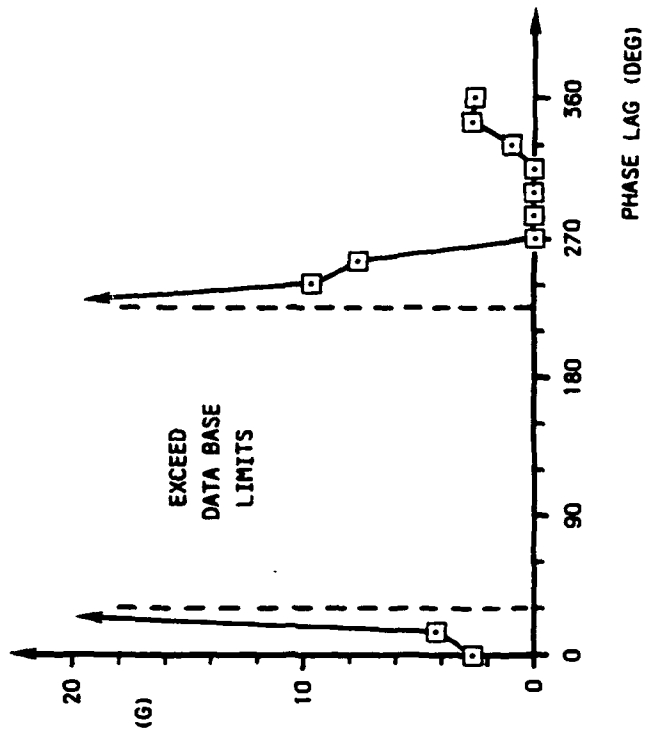


Fig. 14 Calculated response variation with time lag for config. A; 12 DOF, M = 0.92, α_m = 6 deg, alt. = 5K ft, structural damping: g = 0.02.

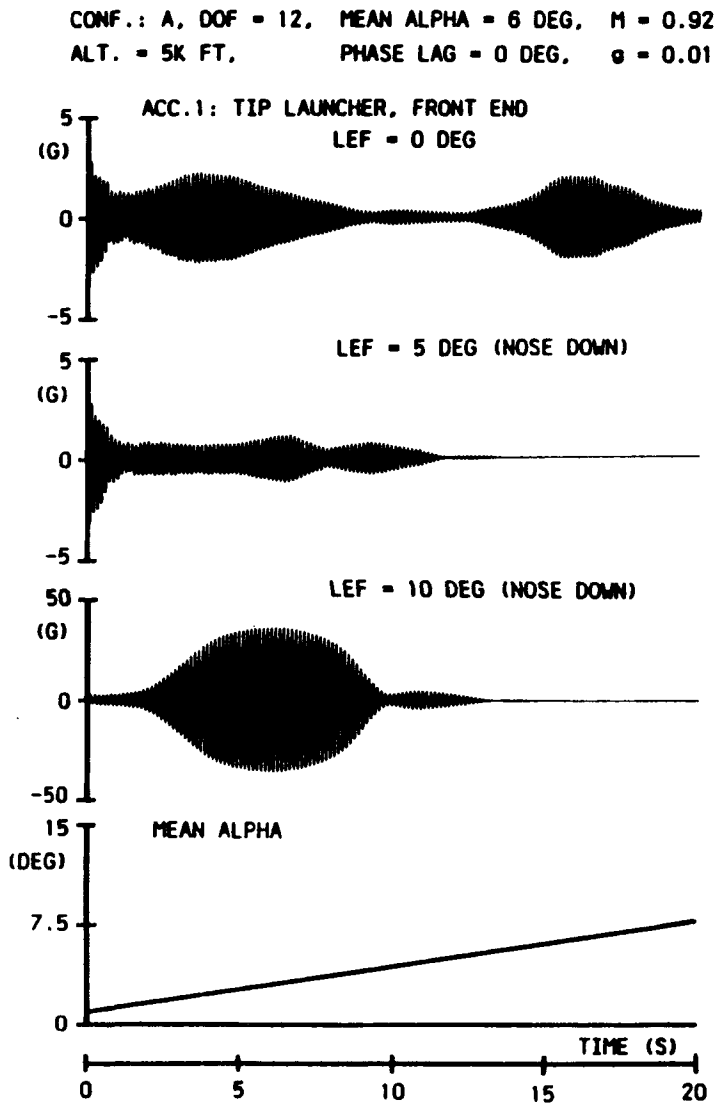


Fig. 15 Calculated response variation with leading edge flap deflections for config. A; 12 DOF, M = 0.92, α_m varaiable, alt. = 5K ft, structural damping: g = 0.01, phase lag = 0 deg.

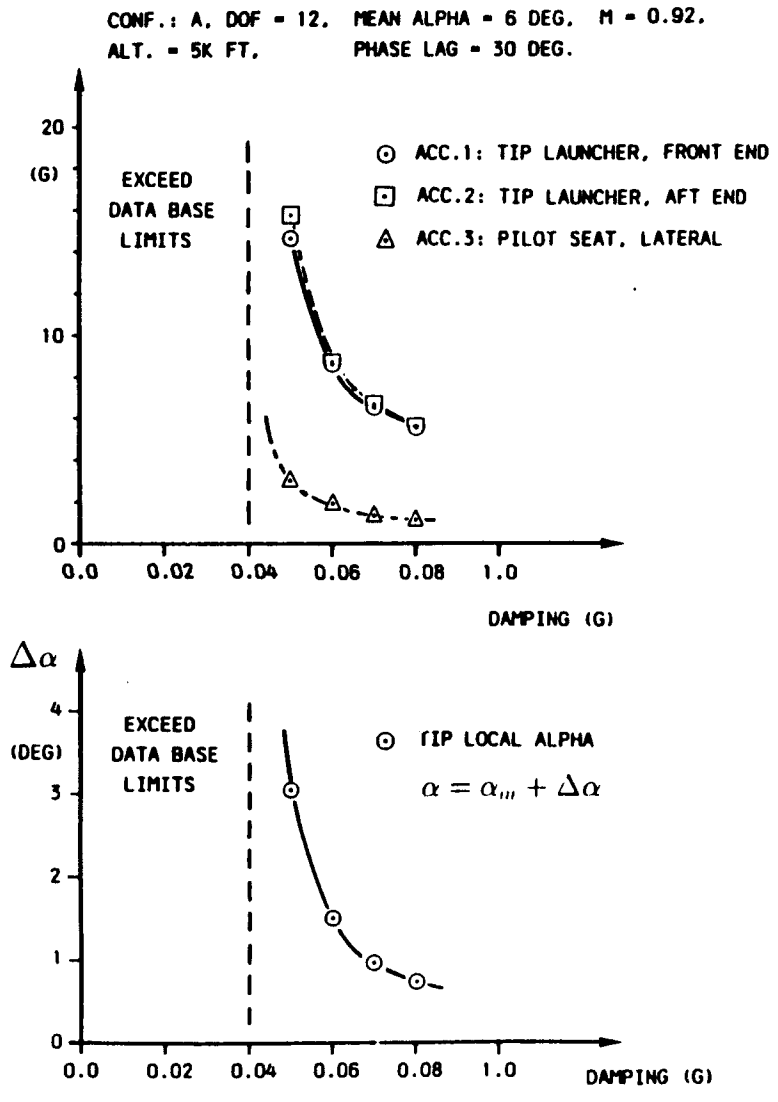


Fig. 16 Effect of uniform damping on calculated responses for config. A; 12 DOF, M = 0.92, α_m = 6 deg, alt. = 5K ft, phase lag = 30 deg.

THIS DOCUMENT PROVIDED BY THE ABBOTT AEROSPACE
TECHNICAL LIBRARY
ABBOTTAEROSPACE.COM

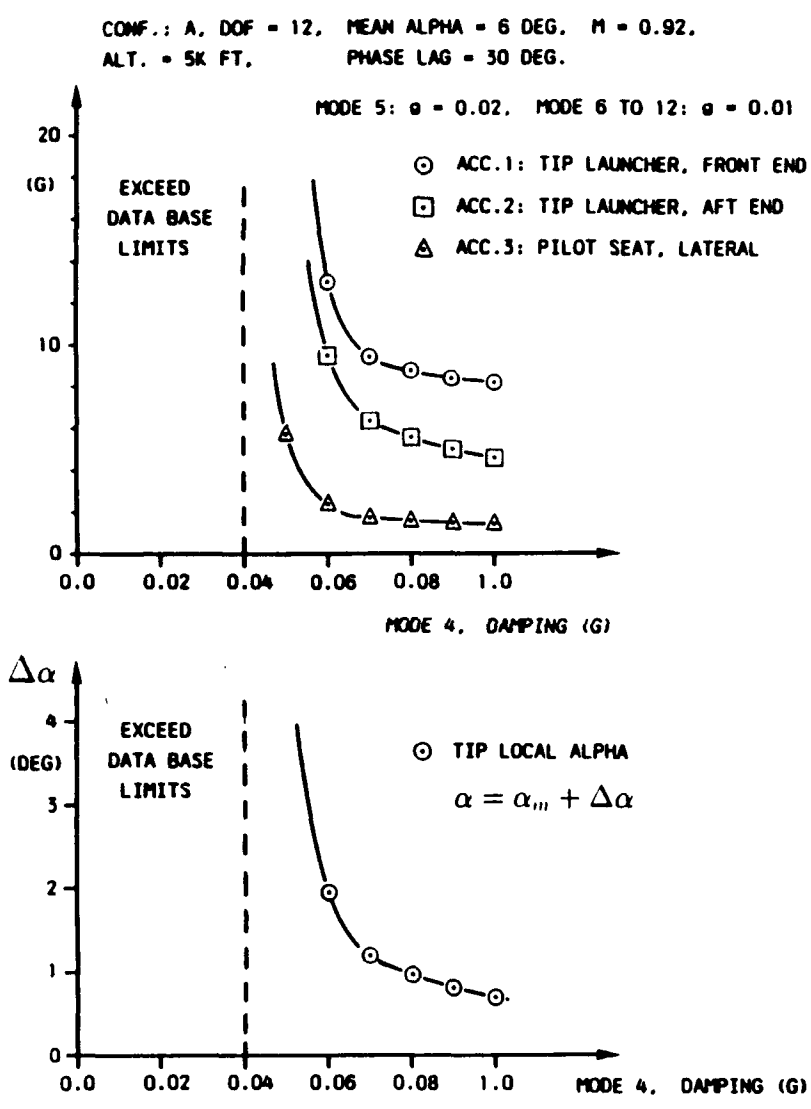


Fig. 17 Effect of pitch mode damping on calculated responses for config. A; 12 DOF, M = 0.92, α_m = 6 deg, alt. = 5K ft, phase lag = 30 deg.

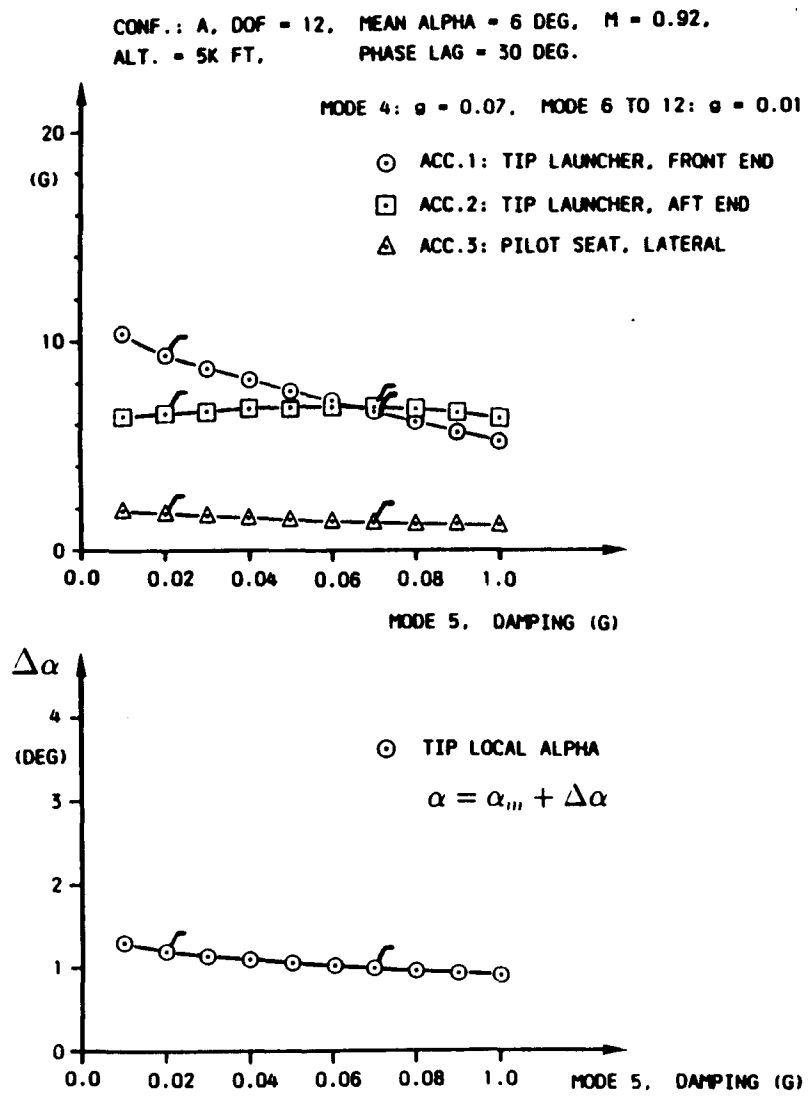


Fig. 18 Effect of bending mode damping on calculated responses for config. A; 12 DOF, M = 0.92, α_m = 6 deg, alt. = 5K ft, phase lag = 30 deg.

THIS DOCUMENT PROVIDED BY THE ABBOTT AEROSPACE
TECHNICAL LIBRARY
ABBOTTAEROSPACE.COM

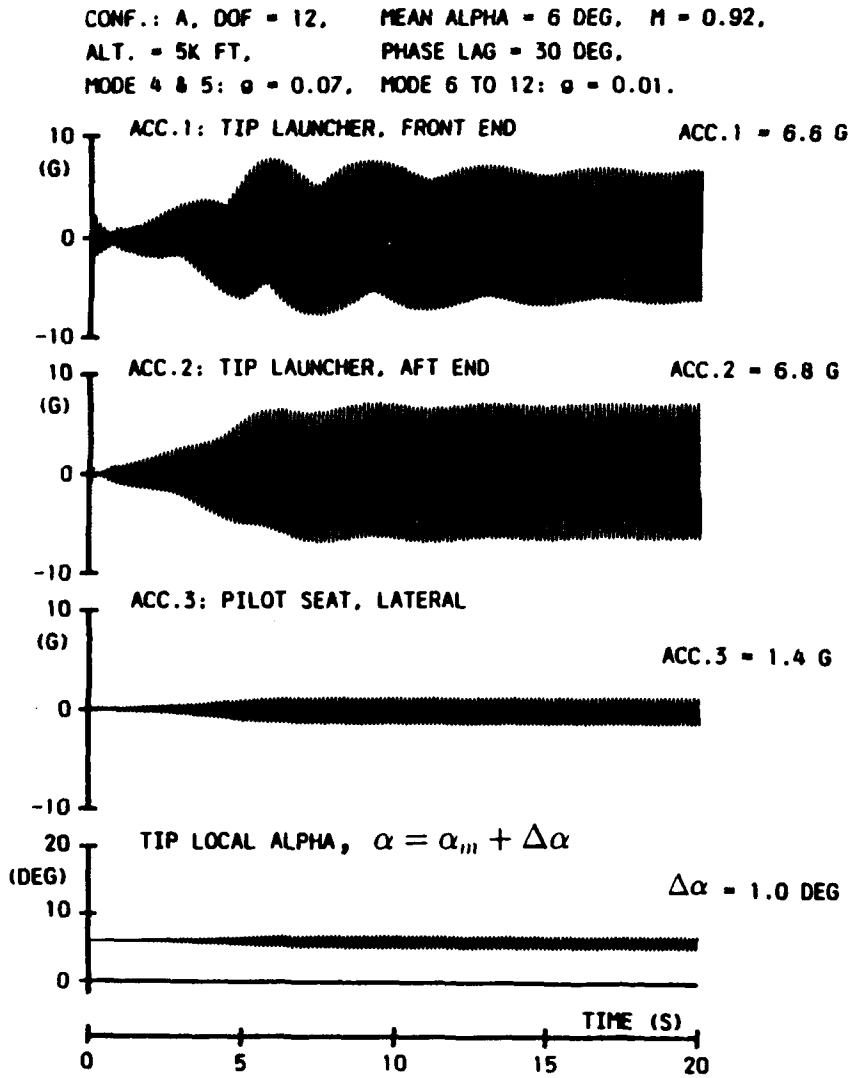


Fig. 19 Calculated transient response for config. A; 12 DOF, M = 0.92, α_m = 6 deg, alt. = 5K ft, phase lag = 30 deg, damping for mode 4 & 5: g = 0.07, for mode 6 to 12: g = 0.01.

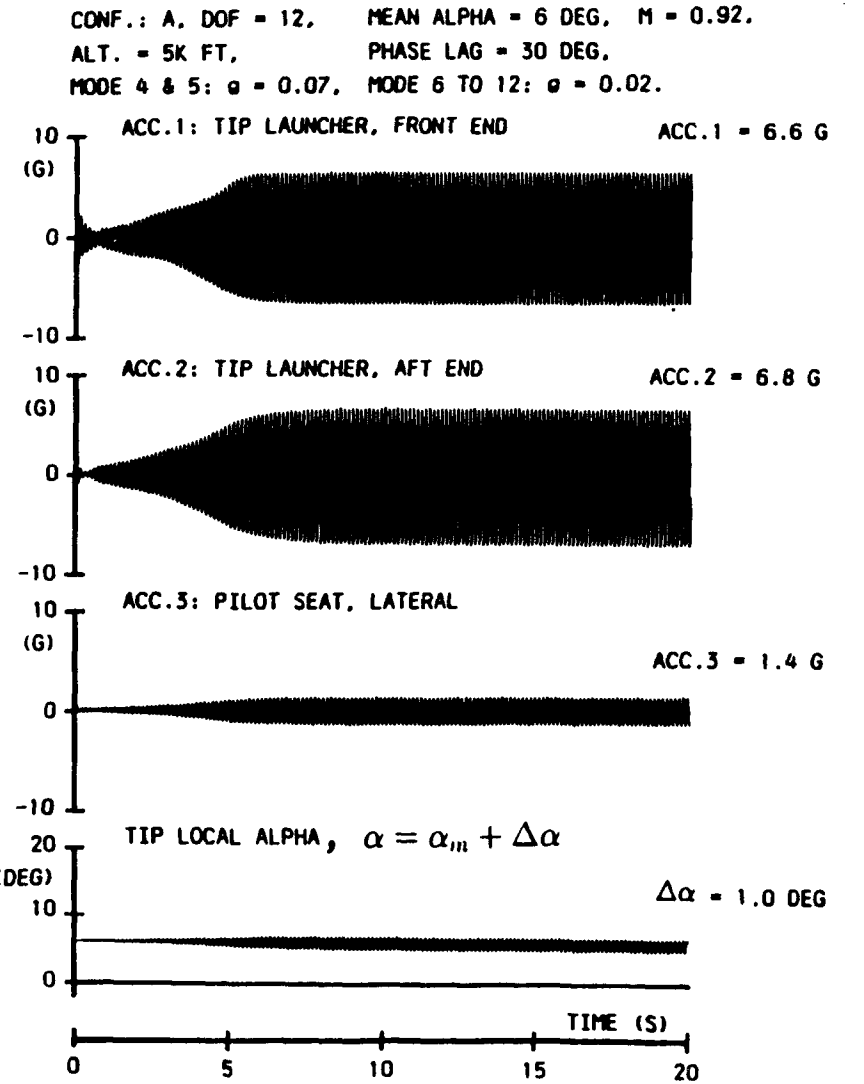


Fig. 20 Calculated transient response for config. A; 12 DOF, M = 0.92, α_m = 6 deg, alt. = 5K ft, phase lag = 30 deg, damping for mode 4 & 5: g = 0.07, for mode 6 to 12: g = 0.02.

THIS DOCUMENT PROVIDED BY THE ABBOTT AEROSPACE
TECHNICAL LIBRARY
ABBOTTAEROSPACE.COM

THIS DOCUMENT PROVIDED BY THE ABBOTT AEROSPACE
TECHNICAL LIBRARY
ABBOTTAEROSPACE.COM

AD-P007 815

92-16053

TRANSONIC WIND TUNNEL INVESTIGATION OF LIMIT CYCLE OSCILLATIONS ON FIGHTER TYPE WINGS

by

Atlee M. Cunningham, Jr.
General Dynamics, Fort Worth, Texas

Ruud G. den Boer
National Aerospace Laboratory (NLR), The Netherlands

ABSTRACT

A wind tunnel investigation was conducted to investigate the unsteady aerodynamic aspects of transonic Limit Cycle Oscillations (LCO) on fighter type aircraft wings. This investigation is a cooperative effort of General Dynamics (Fort Worth) and the National Aerospace Laboratory (NLR) of the Netherlands which is funded by the U.S. Air Force and the Dutch Ministry of Defense. Two tests were planned and the first test, conducted during September 1991, was concerned with a wing body configuration with wing stores and was restricted to incidences below 10 deg. The second test, planned for March 1992, will be for a simple wing-strake geometry and will cover incidences up to at least 30 deg. This paper presents results from the first test with the objective to obtain unsteady pressures and forces necessary for identifying the aerodynamic nature of transonic LCO which is currently encountered on many fighter configurations. The wing panel was oscillated in pitch at amplitudes and frequencies typical of LCO for flow conditions in which significant shock-induced separation is encountered. Unsteady pressure data were obtained for the wing panel in terms of both harmonic components and time-histories to highlight the nonlinearities. Unsteady forces and moments measured on the wing panel as well as on each wing store were also obtained to indicate the level of contribution of each element to the overall unsteady wing loads for pitching motions.

Nomenclature

b	= local wingspan, m
C_m	= wing pitching-moment coefficient, = m/QSc$_r$; reference axis shown in Figs. 2 and 3
C_N	= wing normal-force coefficient, N/QS
C_p	= pressure coefficient, = (p - p$_s$)/Q
$(C_p)_i$	= unsteady pressure coefficient, = p$_i$/QΔα = Re(C_p) + iIm(C_p)
$(C_p)_m$	= mean pressure coefficient
c	= local chord, m
c_r	= root chord, m
f, FREQ	= frequency, Hz
HARM	= harmonic component (HARM = 0,mean: = 1,first harmonic)
g	= structural damping as a fraction of critical damping
i	= SQRT(-1)
k	= see REDFR
l	= wing and store rolling moment, Nm, positive wing tip up
M, MACH	= freestream Mach number
m	= wing and store pitching moment, Nm, positive nose up
N	= wing and store normal force, N, positive up
n	= store yawing moment, Nm, positive nose left
p	= pressure at model surfaces, Pa
p$_s$	= freestream static pressure, Pa
Q	= dynamic pressure, Pa
REDFR	= reduced frequency, = πfc$_r$/V
S	= wing area, m^2
V	= freestream velocity, m/s
x	= chordwise coordinate, m, positive left
Y	= store side force in y direction, N, positive outboard (left)
y	= spanwise coordinate, m, positive outboard (left)
z	= coordinate normal to x-y plane, m
α,ALPHA	= angle of attack, deg
Δα,dα DALPHA	= amplitude of pitching motion, deg
δ	= control surface deflection, deg

Subscripts

i	= unsteady
LAU	= tip launcher
LEF	= leading edge flap
m	= mean
MAIN	= main wing
TIP	= wing tip

1.0 INTRODUCTION

Requirements for fighter aircraft to operate with high maneuverability in the transonic speed regime increase the potential to encounter a transonic non-linear flutter, known as limit cycle oscillations (LCO). LCO is a limited amplitude self-sustaining oscillation produced by a structural/aerodynamic interaction. The phenomenon is related to buffet but is similar to classical flutter in that it usually occurs at a single frequency. From an operational point of view, LCO results in an undesirable airframe vibration that limits the pilot's functional abilities and produces extreme discomfort and anxiety. More importantly, targeting accuracy is degraded, e.g., wing mounted missiles cannot be fired because of high levels of wing motion that prevent target lock-on.

THIS DOCUMENT PROVIDED BY THE ABBOTT AEROSPACE
TECHNICAL LIBRARY
ABBOTTAEROSPACE.COM

For fighter aircraft, transonic LCO is characterized by a nearly harmonic oscillation which appears at Mach numbers ranging from 0.8 to 1.1, and at moderate angles of attack depending on the Mach number, but usually less than 10 deg. The flow conditions during LCO are characterized by mixed attached/separated flow. Lowly damped vibration modes tend to respond provided they have the proper characteristics to couple with this type of flow. Thus, in order to predict LCO characteristics of fighter aircraft a better understanding of the important flow phenomena is needed for the development and refinement of a reliable prediction method.

In response to the above needs, an investigation was begun, as a cooperative effort between General Dynamics and NLR to understand the nature of LCO experienced by fighter aircraft maneuvering at transonic speeds. This investigation is being funded by the US Air Force, Dutch Ministry of Defense, NLR, and General Dynamics. In addition to conducting an extensive wind tunnel investigation (Reference 1), a major objective of this investigation is to develop a method for predicting LCO characteristics of full scale aircraft (References 2 and 3). Analyses of steady wind tunnel data in References 2 and 3 have indicated that shock-induced and trailing edge separation play a dominant role in the development of LCO at transonic speeds as first described in Reference 4 and further discussed in Reference 5. On this basis, a semi-empirical prediction method (References 2 and 3) is being developed which makes use of such data. Results from the current wind tunnel investigation of LCO will be used for guidance in development of this prediction method as well as to provide input to the method for defining the important unsteady aerodynamic effects.

This paper will present a description of the test objectives, the wind tunnel model test program and some preliminary test results. Background for the test will first be discussed followed by descriptions of the wind tunnel, models, model support, instrumentation, excitation, and data acquisition system. Next, test procedures for measuring overall loads and pressure distributions as well as the techniques used for incidence and blockage corrections will be discussed. Finally, the test program and some preliminary results will be presented followed by concluding remarks.

2.0 TEST OBJECTIVES

2.1 General Requirements

In support of the development of a method for predicting LCO characteristics of fighter aircraft, a wind tunnel test was conducted to investigate the unsteady aerodynamic aspects of transonic LCO. This test was concerned with a wing body configuration with wing stores and was restricted to incidences below 10 deg. General objectives of this test were: (1) to develop an understanding of the physics of unsteady transonic flows about a wing/store/fuselage configuration at conditions typical of full-scale LCO; and (2) to generate a steady and unsteady airloads data base for use in LCO/flutter calculations. The fundamental understanding of LCO type flows and the data base will be used in the development and refinement of an LCO prediction method.

A second related test is planned for 1992 in which a simple wing-strake geometry will be dynamically tested up to 30 deg incidence at transonic speeds in order to simulate unsteady transonic maneuvers. General objectives of this second test will be: (1) to develop a better understanding of the physics of unsteady transonic vortex flows about a simple straked wing geometry; and (2) to generate a steady and unsteady airloads data base for a simple straked wing suitable for use in the validation of computational fluid dynamic computer codes.

2.2 Specific Requirements

Analysis of steady wind tunnel data in References 2 and 3 have indicated that shock-induced and trailing edge separation plays a dominant role in the development of LCO at transonic speeds as first described in Reference 4 and further discussed in Reference 5. On this basis, a semi-empirical prediction method is being developed which makes use of such steady wind tunnel data. In the development of this prediction method, as described in References 2 and 3, specific needs have evolved which are deemed necessary for the achievement of reliable LCO predictions for fighter aircraft. These needs include detailed information on (1) lag time involved with transition to and from shock induced trailing edge separation, (2) aerodynamic damping for natural modes of vibration under flow conditions typical of transonic LCO, and (3) an adequate data base for developing an unsteady aerodynamic model as suggested in References 2 and 3. The following paragraphs will present discussions on each of these items.

2.2.1 Aerodynamic Time Lag

A finite time is required for signals to propagate through an aerodynamic flow field which results in a time lag for changes to occur in the flow. The effect of this "aerodynamic time lag" is different depending on the size of the disturbance and the dominant characteristics of the flow field. These characteristics may be classified by mostly attached, separated, or transitioning types of flows.

For attached flows over oscillating lifting surfaces, aerodynamic time lag effects are generally second order in terms of modifying overall flow field characteristics. This observation is justified by the well known success of small disturbance and perturbation methods in predicting unsteady aerodynamic effects on lifting surfaces. When coupled with lifting surface motion, however, aerodynamic lag has a first order effect on determining aerodynamic damping which likewise has a first order effect on structural response.

THIS DOCUMENT PROVIDED BY THE ABBOTT AEROSPACE
TECHNICAL LIBRARY
ABBOTTAEROSPACE.COM

For separated flows over oscillating lifting surfaces, little interaction takes place between the moving surface and the separated flow fields. Aerodynamic damping may be significantly reduced, however, aerodynamic stiffness may likewise be reduced. The structure is more likely to respond to the fluctuating pressure distributions imposed by the separated flows so that the resulting dynamic characteristics are more related to buffeting.

For flows that transition between attached and separated conditions, aerodynamic time lag effects on the flow fields become first order when they affect the point at which the transition occurs. As an example, for positive pitch rate, shock induced trailing edge separation will occur at an incidence higher than that at which it would occur for steady flow. This delay to a higher incidence is a direct result of the finite time required for the transition to be completed. Therefore, the time lag will cause a shift in the unsteady aerodynamic forces and will produce an out-of-phase (imaginary) component that may be stabilizing or destabilizing to the oscillatory motion that is driving the transition.

The LCO calculations performed in Reference 4 showed that introducing time lag for the transition to shock induced trailing edge separation resulted in increased LCO amplitudes. The assumed damping value was g = 0.07 based on previous knowledge of the airplane and the particular mode. This damping is considerably higher than those values used for the calculations discussed in Section 2.0 of Reference 3 where no transition time lag was used. Because a finite time is required for the flows to separate or reattach, a lag must be introduced into the quasi-steady analysis technique used in Reference 3.

In order to have an estimate of the time lag value for transitioning to shock induced trailing edge separation, appropriate data from several sources of unsteady flow information have been examined to see if such a quantity could be determined. The results of this investigation, have shown that a universal parameter may exist which could quantify the desired transition time lag. The observed time delay is expressed in a non-dimensional form as:

$$\Delta\tau_{LAG}=\frac{2V\Delta T_{LAG}}{C_{SEP}}=8.4$$

where C_{SEP} is the approximate chord length of the shock induced trailing edge separation zone (or the mean distance from the shock to the trailing edge).

The above value of 8.4 was derived from data presented in Reference 6 concerned with natural oscillations of shock-induced trailing edge separation on thick bi-convex airfoils in two-dimensional flow. It was observed that about 1/3 of a cycle was required for the separation to develop and that the separation occurred over the aft half of the airfoil. A reduced frequency of k = 0.5 for the oscillations was reported in Reference 6 which with the 1/3 factor for ΔT_{LAG} and the 1/2 factor for C_{SEP}, the $\Delta\tau_{LAG}$ becomes

$$\Delta\tau_{LAG}=\frac{1}{3}\frac{2\pi}{k/2}=\frac{1}{3}\frac{2\pi}{0.25}=8.37$$

For the LCO calculations in Reference 3 with time lag, the estimated physical value is Δt_{LAG} = 0.011 seconds which corresponds to a phase lag of about 30 deg at 7.6 Hz.

It has also been observed that massive stalling on simple delta wings pitching at large incidence amplitudes and low speeds is delayed in a similar manner where

$$\Delta\tau_{LAG}=8.3$$

This is the transition for vortex burst flows to completely stalled flows (Reference 7). It may seem coincidental that similar non-dimensional transition times are required for (1) shock induced trailing edge separation to develop at transonic speeds and (2) massive stalling of simple delta wings to develop at low speeds. However, indications are that both types of separations begin at the forward boundary, the shock for (1) above and the delta wing leading edge for (2) above. If this is the case then the propagations of the stall front would be similar and, hence, the transition times would also be similar.

The importance of aerodynamic time lag in the calculation of LCO characteristics places a specific requirement on the LCO wind tunnel test. This requirement is to obtain sufficient information to quantify the aerodynamic time lag characteristics for attached, separated, and transitioning flows that are involved in LCO. It must also be determined if a simple time lag concept as discussed above is sufficient for modeling first order unsteady aerodynamic characteristics using steady pressure distributions for LCO calculations as described in Reference 3.

2.2.2 Mode Dependent Aerodynamic Damping

Several parametric variations for assumed mode total damping values were made in Reference 3 to determine the sensitivity of LCO calculations to mode dependent damping. The results showed that variation of total damping for the critical modes involved in the LCO mechanism could significantly alter the LCO response characteristics in terms of both amplitudes and spatial distributions of aircraft response. This response "shape" was referred to as the "LCO eigenmode" which was a complex combination of the primary natural modes known to provide the proper coupling characteristics. The LCO eigenmode was quite different depending on whether damping was assumed uniform for the two primary modes or if each primary mode was assigned a damping value consistent with flutter analyses.

The effect of damping variation for non-critical modes with fixed damping for the critical modes was also investigated in

THIS DOCUMENT PROVIDED BY THE ABBOTT AEROSPACE
TECHNICAL LIBRARY
ABBOTTAEROSPACE.COM

Reference 3. It was shown that the limit amplitude was essentially unaffected after starting transients had died out. However, the transients included significant motions of the non-critical modes. Since one of the most critical conditions for LCO is close-in air combat in which highly transient high-g maneuvers are frequently performed, the transient nature of LCO must also be predictable. Thus, it is important that the correct aerodynamic damping characteristics for the non-critical modes be included in the LCO modeling. And, since the critical modes may not be known beforehand, it is even more important that accurate aerodynamic damping data be used for all modes included in the predictions.

Thus, another specific requirement of the LCO wind tunnel test is to provide sufficient information for developing an approach to accurately model aerodynamic damping. A possible approach is that which was used in the F-111 TACT buffet predictions (Reference 8) where combinations of measured wind tunnel damping data and predicted flutter results were used in a semi-empirical method to predict aerodynamic damping for individual natural modes. Such an approach would require aerodynamic damping measurements from the LCO wind tunnel test for appropriate modes of the model.

2.2.3 Unsteady Aerodynamic Data Base

In addition to providing sufficient information to establish aerodynamic time lag and damping characteristics appropriate for LCO calculations as discussed above, the unsteady aerodynamic data base should also contain results that can be used to develop a more general technique for determining the required unsteady aerodynamic characteristics. Several more general approaches were discussed in Reference 2 which use semi-empirical techniques to predict unsteady aerodynamic effects.

Specific requirements for the data base are to provide: (1) steady mean data for reference conditions unique to the LCO wind tunnel model geometry and test set-up; (2) harmonic unsteady data with sufficient incidence and Mach number resolution; and (3) time history recordings of unsteady data from which time lag and aerodynamic damping for model modes can be determined. The data types include steady and unsteady forces and moments for the model wing and all stores as well as steady and unsteady pressures on the model wing. Data from accelerometers located on the wing and from wing position instrumentation are also needed to accurately define wing and store motions during model oscillation.

3.0 TEST SETUP

3.1 Wind Tunnel

The LCO tests were conducted in the NLR 2.0 x 1.6 m^2 high-speed wind tunnel situated in Amsterdam. The tunnel has a closed circuit with a test section length of about 2.5 m. The test section can accommodate either sting or sidewall mounted models. Sidewall mounting was used for the semi-span model in the current test. The tunnel has a Mach range of 0.3 to 1.2 and a maximum Reynolds number of 22 x 10^6 per meter at M = 0.95. Variable pressure and temperature capability provides close control of Reynolds number as well as Mach number.

3.2 Model and Model Support

Since two tests of similar configurations are planned in this investigation, a common instrumented wing panel was designed to be used in the two tests. The wing panel with basic instrumentation is shown schematically in Figure 1. Support is provided through a semi-span balance beam which is in turn supported by bearings mounted on the sidewall turntable. The hydraulic actuator, also mounted on the turntable, provides the oscillatory pitching excitation of the wing panel. Model mean angle-of-attack is then controlled through positioning of the sidewall turntable independent of the nydraulic actuator position.

The wing panel is of a "clam-shell" design so that all instrumentation inside the wing is accessible. It was fabricated of high-strength aluminum alloy so as to minimize inertia loads and has instrumented leading and trailing edge flaps whose positions may be varied by changing the attachment brackets. Instrumentation is described in Section 3.3.

The LCO configuration is shown in Figure 2. In this case two underwing missiles and a tip launcher are attached to the basic wing panel. A suitable fuselage is rigidly attached to the sidewall turntable and is, therefore, held stationary at the model mean angle-of-attack. The balance support for the basic wing panel extends through an opening in the fuselage so that no contact exists between the moveable balance/wing panel and the fixed fuselage. Lybrinth seals are provided at the interface between the wing panel and fuselage except for the

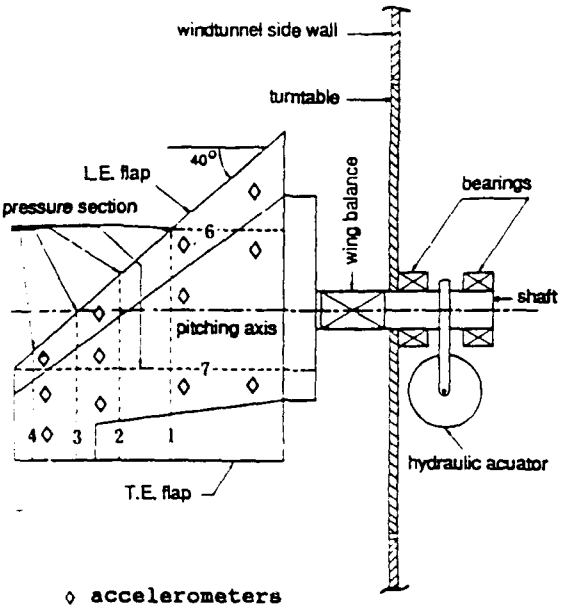


Figure 1 Outboard Wing Panel

THIS DOCUMENT PROVIDED BY THE ABBOTT AEROSPACE
TECHNICAL LIBRARY
ABBOTTAEROSPACE.COM

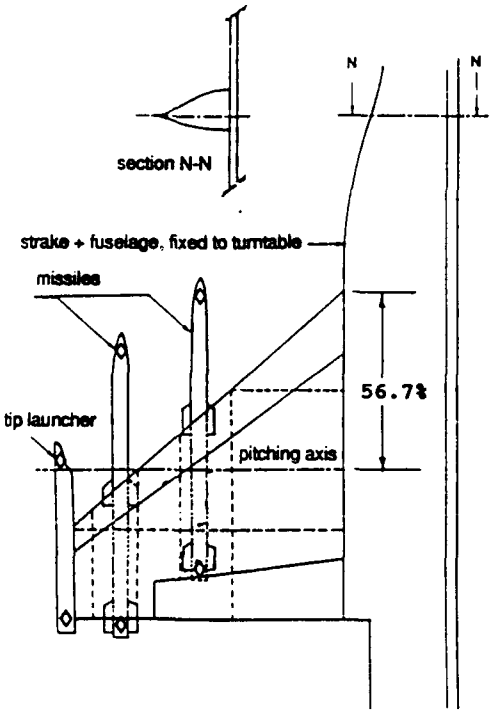


Figure 2 LCO Configuration (Oscillating Outboard Wing)

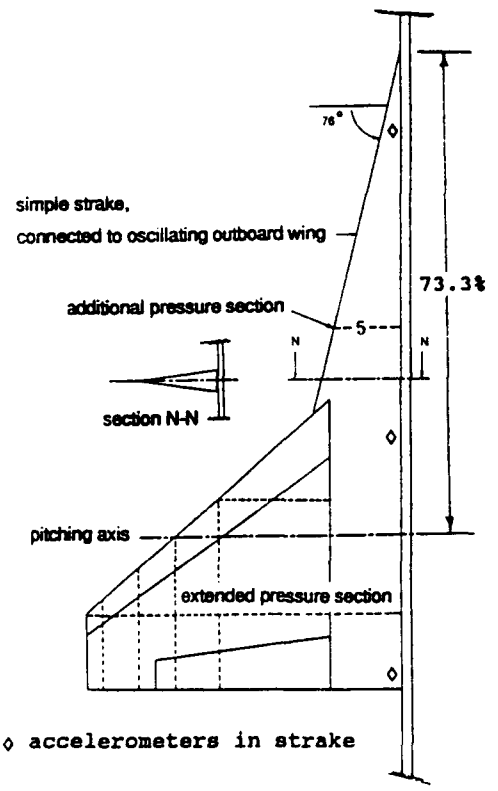


Figure 3 Simple Strake Configuration (Oscillating Semi-Span Model)

ends of the leading and trailing edge flaps. The purpose of this arrangement is to simulate wing motions representative of structural natural modes where the fuselage is essentially rigid.

The simple strake configuration, as shown in Figure 3, is to be tested in 1992. Since this test will be a transonic counterpart to the low speed test of a simple straked wing (Reference 9), the strake section must also move with the wing and is, therefore, attached to the basic wing panel. Loads from both the wing and strake are carried through the semi-span balance beam. The leading and trailing edge flaps cannot be deflected as in the case of the LCO model setup.

Figure 4 shows the relationship between the two test configurations relative to the rotation axis and the sidewall turntable. Two semi-span beam balances were provided: (1) a long beam for the LCO test and, (2) a short beam for the simple strake test. The pitch axis locations are also different at 56.7% of the outboarding panel root chord for the LCO configuration and 73.3% of the strake root chord for the simple strake configuration. Incidence and oscillatory amplitude ranges are also different for the two tests. For the LCO tests, a maximum mean (fuselage) angle-of-attack is 10 deg and maximum wing oscillatory amplitude is ±1.5 deg. Maximum mean angle-of-attack is 30 deg for the simple strake tests and ±15 deg for the oscillatory amplitude of both wing plus strake.

All model and support system parts were designed and fabricated by NLR at the Amsterdam and Noordoostpolder facilities. The instrumentation and calibration were also accomplished by NLR.

3.3 Model Instrumentation

The model instrumentation consisted of main wing semi-span balances, a dynamic incidence transducer, store balances, in situ pressure transducers, and accelerometers. In addition, temperature and reference pressure transducers were provided in the model. Locations of instrumentation are indicated in Figures 1, 2 and 3.

The three component main wing balances were designed to provide adequate stiffness and strength and yet retain sufficient sensitivity for accurate aerodynamic loads measurements. Specifically, those balances measured normal force, rolling (or bending) moment and pitching moment.

A linear variable differential transducer (LVDT) was mounted between the beam balance and the support to measure the oscillation amplitude input to the model. Mean incidence of the model was measured by a very sensitive accelerometer attached to the sidewall turntable.

All stores shown in Figure 2 were mounted on five component balances attached to the wing panel. As was required for the main wing balance, the store balances also had to have the optimum mixture of adequate

THIS DOCUMENT PROVIDED BY THE ABBOTT AEROSPACE
TECHNICAL LIBRARY
ABBOTTAEROSPACE.COM

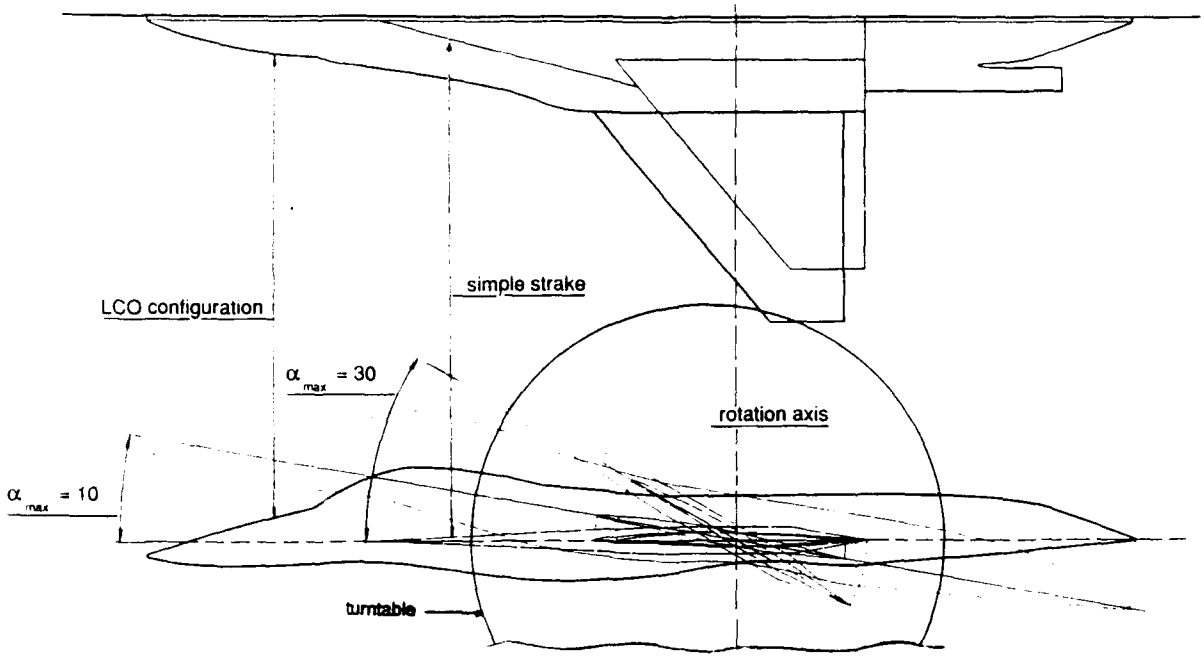


Figure 4 Two Wind Tunnel Tests

strength, stiffness, and sensitivity. Each balance could measure normal and side forces as well as yawing, rolling, and pitching moments.

The pressure transducers were mounted such that they were electrically isolated, free of local model deformations, and not influenced by model accelerations. Four chordwise and two spanwise rows were located as shown in Figure 1 for a total of 87 pressure transducers. The two inboard chordwise rows contained both upper and lower transducers with more on the upper surface. All pressure rows extended onto the leading and trailing edge flaps. Grouping toward the wing tip was done in order to concentrate instrumentation in the regions of known shock induced separation as well as leading edge separation at transonic speeds and low incidence. The sensitivity of the pressure transducers showed a small variation with temperature. By measuring the model temperature with a thermistor, the correct sensitivity of the pressure transducers could be selected for processing recorded electrical signals into pressure data.

Vertical accelerometers were also located at 12 positions on the wing as shown in Figure 1 and at 6 positions on the wing stores as shown in Figure 2. The capability to rotate the underwing stores accelerometers from vertical to lateral directions was also provided.

3.4 Model Excitation

Excitation was provided by an electro-hydraulic shaker system which consisted of a hydraulic power supply, a combined linear actuator and servo valve, and a feedback control unit (Reference 10). The hydraulic actuator was mounted on the sidewall turntable. The piston was connected to a crank on the balance beam (see Figure 1) to convert from linear to rotational motion. Design amplitude limitations for the LCO configuration were ±0.5 deg at 90 Hz. All motions during the LCO test were sinusoidal.

3.5 Data Acquisition System

The wind tunnel tests were performed using a computer controlled data acquisition system (see Figure 5) called PHARAO (Processor for HArmonic and Random Oscillations), which is capable of sampling 64 (time) signals simultaneously. Using a switch panel in the LCO test, the process was conducted twice to record a total of 128 channels.

The electrical signals of the instruments are first amplified in the Multi Channel Conditioning Units (MCCU's) and a separation is made between AC and DC. The AC signals are switched in two groups of 64, filtered (for anti-aliasing), sampled by the AD converter and stored on an optical disc. One oscillator is used to control both the hydraulic actuator (see Section 3.4) as well as the sampling of the electrical signals, to have perfect synchronization. Sample frequencies and filter settings are chosen proportional to the driving frequency of the mode. In most cases, 4096 samples were recorded for each channel with a frequency of 32 times the frequency of the model motion, so 128 full cycles of the first harmonic were recorded. For quick look presentation, the time traces were averaged using Phase Locked Time Domain Averaging (PLTDA) and Fourier transformed to harmonic components. The balance loads were corrected for inertial loads and the influence of temperature on pressure transducer sensitivity was accounted for.

For the measurements on the simple strake model (in 1992), the data acquisition system will be expanded up to 128 channels.

This Document Provided by the Abbott Aerospace
TECHNICAL LIBRARY
ABBOTTAEROSPACE.COM

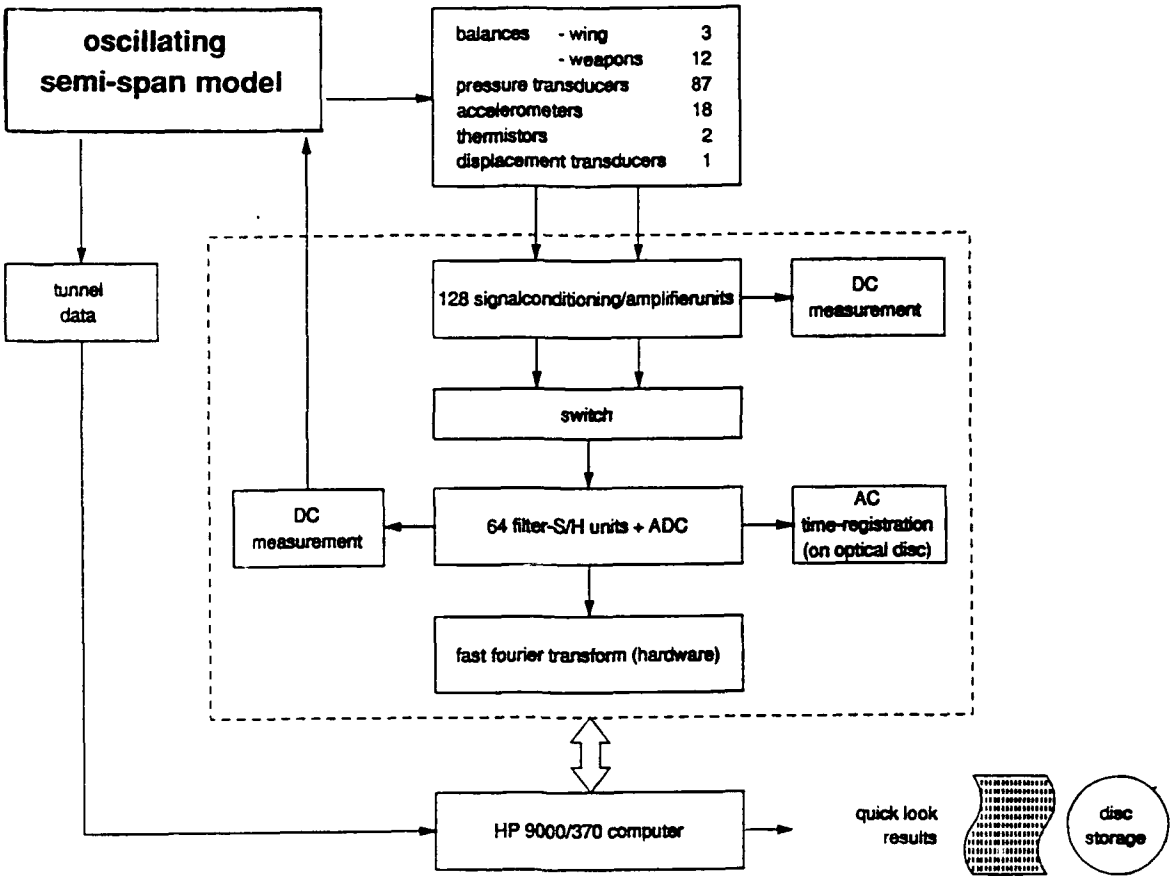


Figure 5 Data Acquisition System

This will provide faster data acquisition as well as the possibility for cross correlation of all the recorded signals.

4.0 PROCEDURES AND PREPARATORY TESTS

4.1 Measurement of Forces, Moments, and Pressure Distributions

The main objective of these measurements was to establish the relationship between the mechanical motion of the model as input and the pressures, forces, and moments as output. Using the data acquisition system (Section 3.5), the relationship was established through determination of the zeroth (mean) and the first eight harmonics of the measured output signals. All data quantities were normalized into standard coefficient form using model motion and wind tunnel aerodynamic quantities for the normalization terms. In most cases, about one minute was required per test point at a given mean angle, frequency, and amplitude. All data reduction was performed on the HP 9000/370 computer and all results including time histories were stored on disks for later analyses.

The data items obtained were as follows:

1.) Four chordwise and two spanwise rows (see Figure 1) of pressure distributions for mean pressures, $(C_p)_m$, and unsteady pressures, $Re(C_p)$ and $Im(C_p)$ for the first eight harmonics and time histories;

2.) Integrated section coefficients C_N and C_m for the four chordwise rows and coefficients C_N and C_l for the two spanwise rows;

3.) Mean values, the first eight harmonics and time histories of all force and moment coefficients for the main wing panel and all wing store balances; and

4.) Amplitudes and displacements derived from accelerometer signals.

With exception of the mean value quantities, all unsteady quantities were normalized with the model angular displacement.

4.2 Incidence and Blockage Corrections

Wing incidence was influenced by structural deformations of the balance and wing panel. The fuselage incidence needed no corrections since it was rigidly attached to the sidewall turntable. Thus, mean wing position was adjusted with the hydraulic actuator system for each mean angle-of-attack setting to align the wing with the fuselage. This correction was less than 0.1 deg for the maximum design aerodynamic pitching moment applied to the wing.

No additional incidence or blockage corrections due to wind tunnel wall presence were needed for this test because of model size and low maximum incidence.

THIS DOCUMENT PROVIDED BY THE ABBOTT AEROSPACE
TECHNICAL LIBRARY
ABBOTTAEROSPACE.COM

TABLE 1 MODEL MODE FREQUENCIES

MODE	CONFIGURATION, Hz		
	CLEAN	WITH TIP LAUNCHER	TIP LAUNCHER + 2 MISSILES
1st Wing Bending	99.93	83.96	72.58
1st Wing Torsion	144.15	138.17	138.35
2nd Wing Bending	174.5	167.07	164.69

TABLE 2 FREQUENCY/AMPLITUDE TEST MATRIX

dα, DEG	FREQUENCY/k			
	6 Hz/0.02	40 Hz/0.16	56 Hz/0.22	110 Hz/0.43
0.125	✓	✓	✓	✓
0.25		✓	✓	
0.5		✓		
1.0		✓		
1.5		✓		

4.3 Preparatory Tests

Model vibration modes, frequencies, and masses were needed for calculating inertia corrections to the various balance measurements. Thus, vibration test were conducted on the model for all possible wing store configurations. The wing was mounted on the semi-span balance and support system as normally installed on the sidewall turntable. Frequency ranges for the primary wing modes for all configurations are shown in Table 1. Underwing store frequencies were scattered at intermediate frequencies starting at about 90 Hz. Mode frequencies were also measured with the model mounted in the wind tunnel.

Flutter analyses were also performed with the measured model modes, frequencies, and generalized masses using linear theory (doublet lattice) unsteady aerodynamics. Results for the worst case indicated that flutter speeds were more than twice the testing speeds.

5.0 LCO MODEL TEST PROGRAM

The LCO test program was designed to investigate the effects of various parameters on the aerodynamic loads and pressures associated with a pitching wing with stores on a fixed fuselage at transonic conditions typical of full scale LCO. Mean angle-of-attack was varied from 0 deg up to 10 deg in 0.5 deg increments at selected Mach numbers within the range of M = 0.90 to 0.975. A frequency and amplitude matrix as shown in Table 2 was tested by first setting frequency and amplitude and then varying mean angle, all at a fixed Mach number. This approach permitted rapid testing of a large array of conditions since the time required for a mean angle change of 0.5 deg was very short in comparison to that required for changing frequency or amplitude.

Configuration effects were also investigated by varying the leading and trailing edge flap settings as well as removing or changing wing stores. These configurations included a completely clean wing with no stores.

6.0 TEST RESULTS

The LCO wind tunnel test began on 10 September 1991 and was completed on 19 September 1991. As a result, little time was available for analysis of the results, however, samples of the various data can be presented in this paper to give an impression of the scope and nature of the data base. All data discussed in the following two sections are processed results obtained during the test. The pressure data were reduced to standard coefficient form and the unsteady data were further normalized by the oscillatory pitch amplitude, dα, in radians. The force and moment data were processed in the same manner except that it was necessary to subtract inertial forces and moments from the measurements to obtain pure aerodynamic loads. All unsteady results presented in the following sections are for the first harmonic only and are given in terms of in-phase (real) and out-of-phase (imaginary) components relative to the forced oscillatory motion of the wing.

THIS DOCUMENT PROVIDED BY THE ABBOTT AEROSPACE
TECHNICAL LIBRARY
ABBOTTAEROSPACE.COM

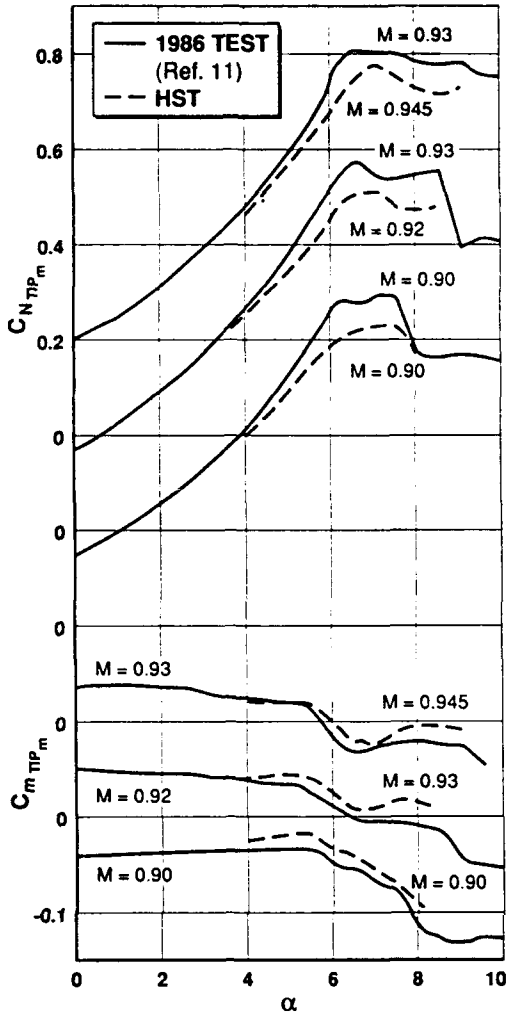


Figure 6 Comparison of Integrated Steady Pressures at the Wing-Tip Pressure Row for the HST Test and the 1986 Test (Reference 11)

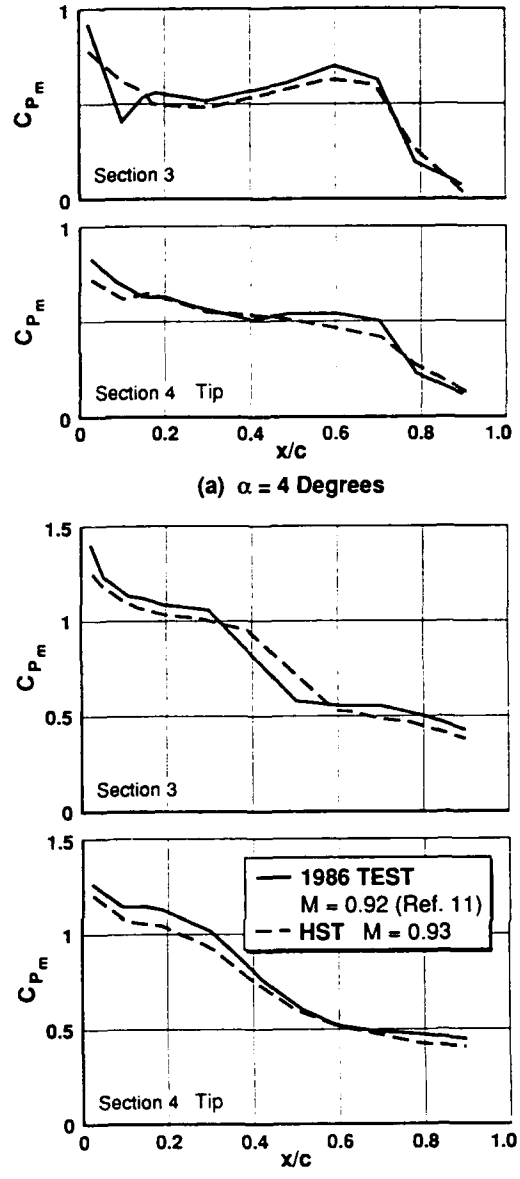


Figure 7 Comparison of Steady Pressure Distributions for the HST Test and the 1986 Test (Reference 11)

6.1 Steady and Unsteady Pressure Data

As part of the test procedure, correlations with the LCO test in 1986 (Reference 11) were made in order to establish the test conditions of interest. Analyses of the 1986 data base in References 2 and 3 indicated that M. = 0.90, 0.92, and 0.93 were important conditions in terms of understanding the LCO phenomena. Since most analyses in References 2 and 3 were performed at M = 0.92, this became the central point of study.

The correlation parameter was also chosen on the basis of the Reference 2 and 3 analyses. This was the chordwise integration of the upper surface steady or mean pressure data on the most outboard chordwise row of transducers which was shown to be a good indicator of LCO sensitivity. Results of this correlation are shown in Figure 6 for δ_{LEF} = 0 deg. The HST Mach numbers showing the best correlations with the 1986 test points of M = 0.9, 0.92, and 0.93 were M = 0.9, 0.93, and 0.945 in the HST respectively. Considering the differences in models, wind tunnels, and test objectives, these correlations are quite good both in character and magnitude. The reasons for slightly lower levels of C_{NTIP} for α above 4 deg are not yet fully understood and are the subject of continuing analysis.

A direct comparison of steady pressure distributions is shown in Figure 7 for two chordwise pressure rows (3 and 4 in Figure 1) and two angles of 4.0 deg and 7.5 deg at M = 0.93 in the HST but M = 0.92 in the 1986 test. The results at α = 4.0 deg reflect the good agreement shown in Figure 6 for the integrated results at α = 4.0 deg. Results at α = 7.5 deg show that the levels measured in the HST are slightly lower than those from the 1986 test but the difference are nearly uniform. Similarity of the distributions are indicative of the good agreement shown by C_{mTIP} trends in Figure 6.

THIS DOCUMENT PROVIDED BY THE ABBOTT AEROSPACE
TECHNICAL LIBRARY
ABBOTTAEROSPACE.COM

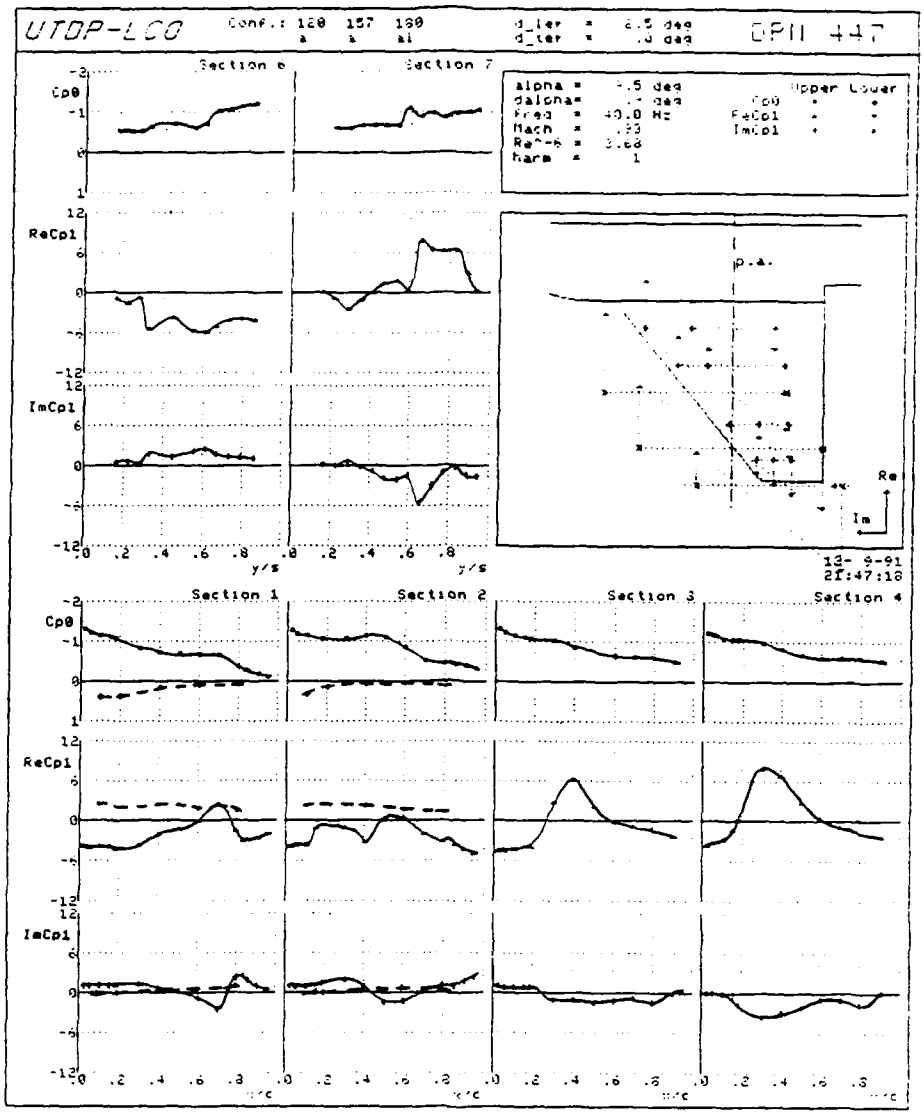


Figure 8 Sample Unsteady Results for HST Test, M = 0.93, α_m = 9.5 deg, f = 40 Hz, k = 0.16 dα = 1.0 deg, Mean and First Harmonic Results

An example of unsteady pressure distributions is shown in Figure 8 for M = 0.93, α_m = 9.5 deg, dα = 1.0 deg and f = 40 Hz (k = 0.16) with δ_{LEF} = 2.5 deg. All chordwise rows, 1, 2, 3, and 4, as well as the spanwise rows, 6 and 7, are represented. Upper surface mean, real and imaginary pressure coefficient distributions are shown for all rows. Lower surface data are also shown for rows 1 and 2. Because of a data processing error, however, all unsteady values are 11% high. The model wing and stores motions are shown in the small mode plot, which for the case of 40 Hz indicates a fairly clean pitching motion. Typical shock induced trailing edge separated flow characteristics are seen at rows 3 and 4.

The effects of leading edge flap setting, δ_{LEF}, oscillation amplitude, dα, and frequency, k, are shown in Figures 9, 10, and 11 respectively for M = 0.93. These effects are illustrated for the unsteady C_{NTIP} and C_{mTIP} quantities, both real and imaginary parts. The effect of δ_{LEF} = 0 deg and 2.5 deg, for k = 0.16 and dα = 0.5 deg in Figure 9 is a classic example which illustrates the displacement of major discontinuities by an incremental angle that is similar to the flap deflection angle. In both cases, the real parts track the slopes of the mean results shown in Figure 6 and the imaginary parts tend to mirror the real parts in the usual manner. The large discontinuities at 6.5 to 7.0 deg for δ_{LEF} = 0 deg are pushed up to about 9.0 and 9.5 for δ_{LEF} = 2.5 deg.

The effects of dα for δ_{LEF} = 2.5 deg at a fixed frequency of 40 Hz, k = 0.16, as illustrated in Figure 10 generally show a tendency to smooth out the variations of C_{NTIP} and C_{mTIP} with incidence as the amplitude is increased. Some anomalies occur in the imaginary parts, however, between α = 6.5 and 8.5 deg for both C_{NTIPi} and C_{mTIPi}. Again, with exception of these anomalies, the unsteady characteristics

THIS DOCUMENT PROVIDED BY THE ABBOTT AEROSPACE
TECHNICAL LIBRARY
ABBOTTAEROSPACE.COM

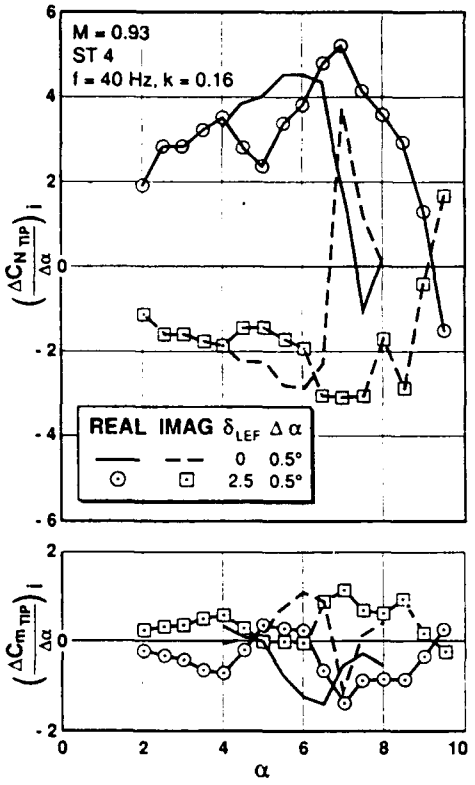


Figure 9 Integrated Unsteady Pressures at Section 4 Showing Effect of Leading Edge Flap Deflection at M = 0.93

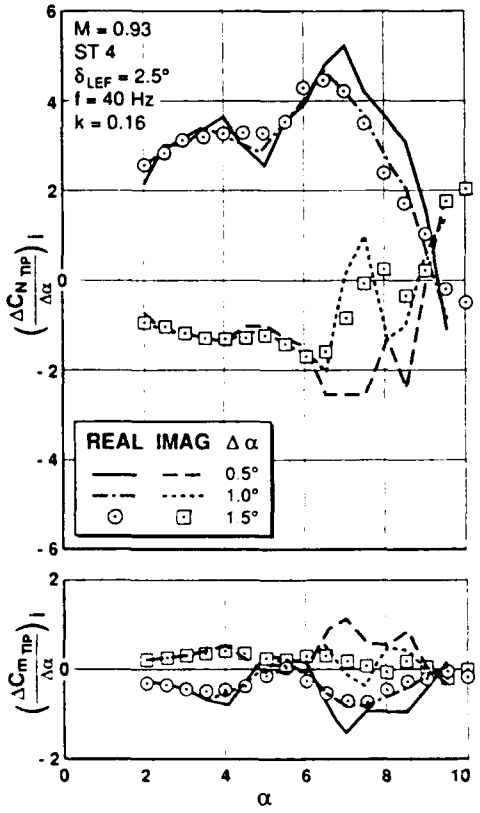


Figure 10 Integrated Unsteady Pressures at Section 4 Showing Effect of dα Amplitude at M = 0.93

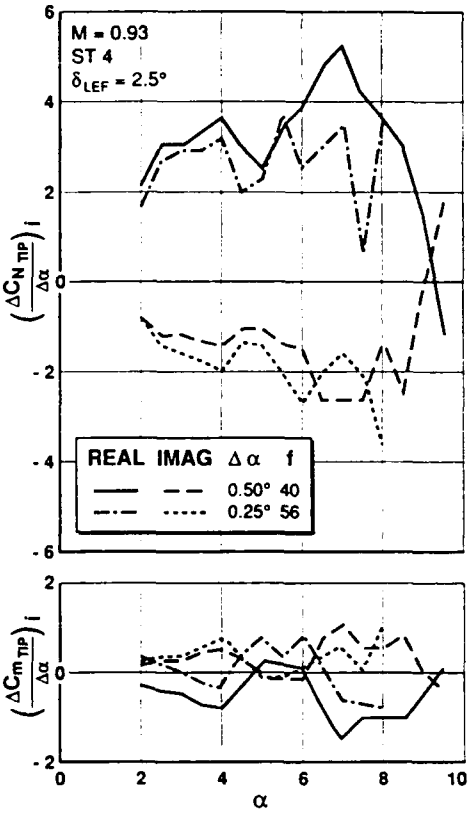


Figure 11 Integrated Unsteady Pressures at Section 4 Showing the Effect of Oscillation Frequency at M = 0.93

track as they might be expected to. The effect of frequency is shown in Figure 11 for δ_{LEF} = 2.5 deg with dα = 0.5 deg at 40 Hz, k = 0.16, and dα = 0.25 deg at 56 Hz, k = 0.22. There are some changes in the characteristics which show a general tendency to become more imaginary. The more erratic behavior at the higher frequency is attributed mostly to the smaller amplitude of dα = 0.25 deg.

6.2 Steady and Unsteady Balance Data

Balance measurements were made for the main wing panel as well as the tip and underwing stores. The subtraction of inertia forces and moments is part of the data processing so that aerodynamic forces and moments can be obtained. Some problems were suspected to exist in this step of the processing that was performed during the test. Since sufficient time was not available between the end of the test and the writing of this paper to investigate and correct the problem, all balance data to be presented below will be shown without vertical scales. The trends are, however, felt to be realistic and of great importance to this paper.

Main wing balance results are shown in Figure 12 for the mean C_{Nm} and C_{mm} quantities with δ_{LEF} = 2.5 deg and M = 0.93. The C_{Nm} data are quite smooth in variation with α where as the C_{mm} data become somewhat erratic above about 6 deg. Most of this erratic behavior is attributed to flow transitions in the wing tip region. Un-

THIS DOCUMENT PROVIDED BY THE ABBOTT AEROSPACE
TECHNICAL LIBRARY
ABBOTTAEROSPACE.COM

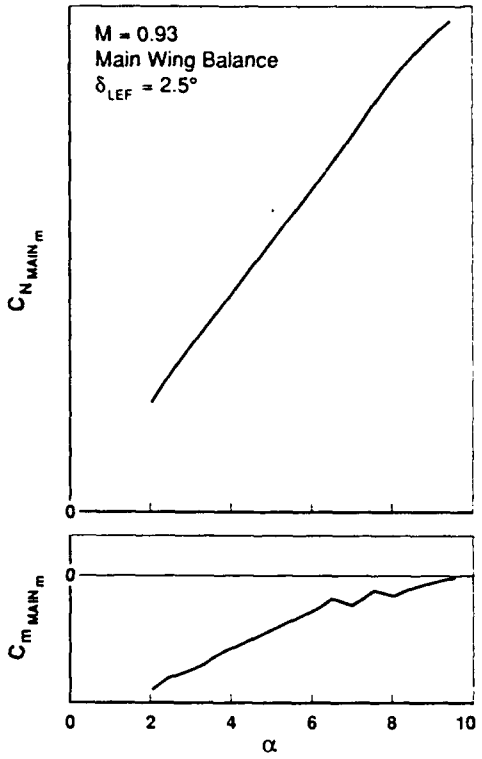


Figure 12 Main Wing Balance Steady Mean Results for M = 0.93

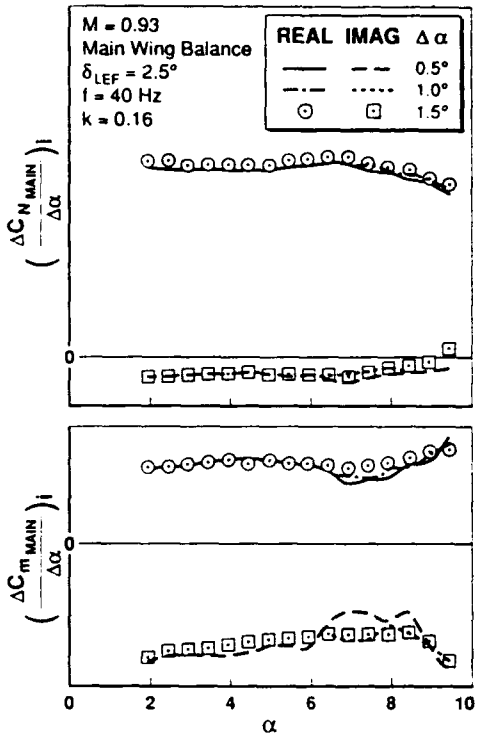


Figure 13 Main Wing Balance Unsteady Results for M = 0.93, Effect of dα Amplitude

steady results for the main wing balance at M = 0.93 are shown in Figure 13 for three amplitudes, dα = 0,5, 1.0 and 1.5 deg at k = 0.16. These trends also track the mean characteristics as expected and the primary effect of increasing amplitude is to further smooth the variations with α_m.

Balance data for the wing tip launcher with δ_{LEF} = 2.5 deg are shown in Figure 14 for the mean C_{NLAUm} and C_{mLAUm} quantities at M = 0.93. These results are similar in trend to those of the integrated pressure row 4 mean results in Figure 6. Unsteady data at M = 0.93 are shown in Figure 15 for δ_{LEF} = 2.5 deg and dα = 0.5, 1.0, and 1.5 deg at k = 0.16. These trends also seem to generally track the mean data in Figure 14. Again the primary effect of increasing amplitude is to smooth out the variations with incidence.

7.0 CONCLUDING REMARKS

A wind tunnel investigation was conducted to investigate the unsteady aerodynamic aspects of transonic LCO on fighter type aircraft wings. Test requirements were established based on extensive analyses of a steady wind tunnel test data base obtained in 1986 also for the purpose of investigating transonic LCO. A specialized semi-span wing-fuselage-stores model was designed and fabricated for the current unsteady test equipped with balances to measure wing and store loads, high response pressure transducers to measure unsteady pressures and accelerometers to monitor model motion. The model wing was sinusoidally oscillated in pitch at various amplitudes and frequencies for mean model incidences varying from 0 deg to 10 deg. The test was conducted in the NLR HST in the Mach range of 0.90 to 0.975. A follow-on test is to be conducted with a simpler configuration at higher incidences and oscillatory amplitudes in early 1992.

A significant data base was obtained which included Mach variations in 0.015 increments, mean incidence variations in 0.5 deg increments, amplitude variations from 0.125 to 1.5 deg and frequency variations from k = 0.02 to 0.43 (6 Hz to 110 Hz). Configuration effects were also covered for flap deflections and various store combinations which included a completely clean wing. The high resolution in Mach, incidence and amplitude was shown to be needed in order to identify the important features of transonic LCO type flow fields.

Correlations of steady pressure data from the current test with those of the 1986 test showed very good agreement in view of the model and test set-up differences. It was possible to reproduce the incidence and Mach sensitive characteristics in detail sufficient enough to conclude that a good match between the two tests was achieved.

Some steady and unsteady pressure results were presented to illustrate effects of various parameters. Loads data were presented for the main wing balance and tip launcher balance but vertical scales were not given due to some suspected problems that had not yet been corrected in the initial data processing. These problems were thought to affect amplitudes only and

THIS DOCUMENT PROVIDED BY THE ABBOTT AEROSPACE
TECHNICAL LIBRARY
ABBOTTAEROSPACE.COM

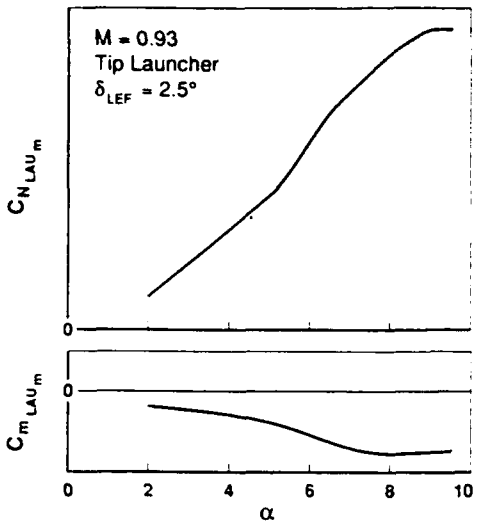


Figure 14 Wing Tip Launcher Balance Steady Results for M = 0.93

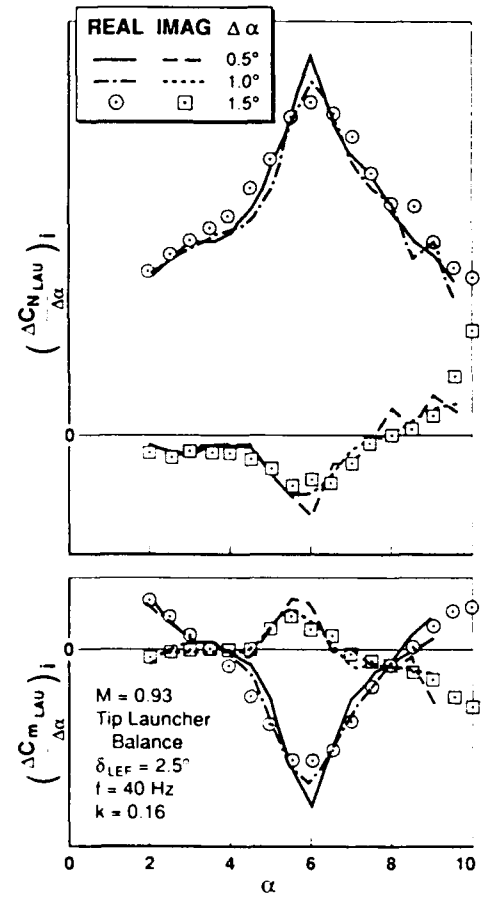


Figure 15 Wing Tip Launcher Balance Unsteady Results for M = 0.93, Effect of dα Amplitude

not trends. Variations of unsteady pressures and loads in the wing tip region were very sensitive to incidence where large changes occurred for incidence differences of 0.5 deg. Variations of the main wing balance loads were much less dramatic in steady and unsteady components but still noticeable.

The effects of oscillation amplitude increases were shown to primarily smooth out the trends with incidence, although some anomalous behavior was noted in regions of major transitions. The effect of frequency increases was to shift the pressures and loads in the imaginary (or out-of-phase) direction as expected. Isolated anomalies were also noted for frequency variations.

The next steps will be to complete the final data processing and build the data base. Analysis will begin to determine (1) aerodynamic time lag characteristics; (2) appropriate aerodynamic damping characteristics; and (3) development of a generalized unsteady aerodynamic model. These items will then be incorporated into the LCO prediction method also being developed as part of this investigation.

References

1. Boer, R. G. den, Cunningham, Jr., A. M., "Unsteady Transonic Wind Tunnel Testing of Fighter Type Wings", 31st AIAA/ASME/ ASCE/AHS/ASC Structures, Structural Dynamics, and Materials Conference, Long Beach, California, April 2-4, 1990.

2. Meijer, J. J., Cunningham, Jr., A. M., and Zwaan, R. J., "A Semi-Empirical Approach to Predict Transonic Limit Cycle Oscillation Characteristics of Fighter Aircraft", 8th Aircraft/Stores Compatibility Symposium, Fort Walton Beach, Florida, 23-25 October 1990.

3. Meijer, J. J. and Cunningham, Jr., A. M., "Development of a Method to Predict Transonic Limit Cycle Oscillation Characteristics of Fighter Aircraft", AGARD Specialists' Meeting on Transonic Unsteady Aerodynamics and Aeroelasticity, San Diego, California, 9-11 October 1991.

4. Cunningham, Jr., A. M., "The Role of Shock-Induced Trailing-Edge Separation in Limit Cycle Oscillations", NASA-CP-3022, 1987.

5. Cunningham, Jr., A. M., "Practical Problems: Airplanes", Chapter 3, Unsteady Transonic Aerodynamics, Edited by D. L. Nixon, AIAA Progress in Astronautics and Aeronautics Series, 1989.

6. McDevitt, J. B., Levy, Jr., L. L., and Deiwert, G. S., "Transonic Flow About a Thick Circular-Arc Airfoil", AIAA Journal, Vol. 14, pp. 606-613, May 1976.

THIS DOCUMENT PROVIDED BY THE ABBOTT AEROSPACE
TECHNICAL LIBRARY
ABBOTTAEROSPACE.COM

7. Cunningham, Jr., A. M., Unpublished Results for Analysis of Unsteady Aerodynamic Characteristics of Simple Delta Wing Models at High Angles-of-Attack, General Dynamics, Fort Worth Division, Fort Worth, Texas, USA.

8. Cunningham, Jr., A. M. And Coe, C. F., "Predictions of F-111 TACT Aircraft Buffet Response", AGARD CP No. 483, April 1990.

9. Boer, R. G. den and Cunningham, Jr., A. M., "Low-Speed Unsteady Aerodynamics of a Pitching Straked Wing at High Incidence - Part I: Test Program", AIAA Journal of Aircraft, Vol. 27, No. 1, pp. 23-30, January 1990.

10. Poestkoke, R., "Hydraulic Test Rig for Oscillating Wind Tunnel Model", National Aerospace Laboratory, Amsterdam, The Netherlands, NLR MP 76020 U, 1976.

11. Elbers, W. K., "Wind Tunnel Data Report 1/9-Scale F-16A Pressure Model Investigation of Shock-Induced Separation for Limit Cycle Oscillation Studies (AEDC PWT-16T Test TF-695)", General Dynamics, Fort Worth Division Report 16PR4694, September 1985, (Contract No. F33657-84-C-2034).

THIS DOCUMENT PROVIDED BY THE ABBOTT AEROSPACE
TECHNICAL LIBRARY
ABBOTTAEROSPACE.COM

AD-P007 816

THE BENCHMARK AEROELASTIC MODELS PROGRAM — DESCRIPTION AND HIGHLIGHTS OF INITIAL RESULTS

Robert M. Bennett
Clinton V. Eckstrom
Jose A. Rivera, Jr.
Bryan E. Dansberry
Moses G. Farmer
Michael H. Durham

NASA Langley Research Center
Unsteady Aerodynamics Branch
Configuration Aeroelasticity Branch
Structural Dynamics Division
Hampton, Virginia 23665-5225 USA

92-16054

1. SUMMARY

The Structural Dynamics Division of NASA Langley Research Center has implemented an experimental effort in aeroelasticity called the Benchmark Models Program. The primary purpose of this program is to provide the necessary data to evaluate CFD codes for aeroelastic analysis. It also focuses on increasing the understanding of the physics of unsteady flows and providing data for empirical design. This paper gives an overview of this program and highlights some results obtained in the initial tests. The tests that have been completed include measurement of unsteady pressures during flutter of a rigid wing with a NACA 0012 airfoil section, and dynamic response measurements of a flexible rectangular wing with a thick circular arc airfoil undergoing shock-boundary layer oscillations.

2. INTRODUCTION

A significant number of aircraft aeroelastic problems occur in the transonic speed range. Generally, minimum flutter speed is encountered at transonic Mach numbers. In addition, buffeting, control surface buzz, and other non-classical instabilities may be encountered. Computational fluid dynamic (CFD) computer codes are now maturing and hold promise for rational analysis of all these phenomena. The state of the art in this area is reviewed by Edwards and Malone.[1]

Currently, the assessment of the CFD codes even for the classical flutter problem is far from complete. For example it is not clear which equation level is required for a given configuration, Mach number, and angle of attack range. One reason for this situation is the level of resources required to apply the CFD codes for enough cases to establish trends. Typically these codes require enormous computer resources even to evaluate one flutter boundary, and also require significant expertise and effort by the users. However, an additional and very significant reason for the incomplete calibration of the CFD codes is the lack of well documented experimental data sets.

Although the flutter data available in the literature is quite extensive, much of it is not suitable for validation efforts. For example, after an extensive literature search, only one configuration was accepted as an AGARD standard configuration[2] and the calculation of mode shapes from a finite element model was required. Early experimenters were operating within a framework of linear theory which does not require airfoil shape, for example, and airfoil ordinates were not generally measured. Similarly, modal definitions or model structural and mass properties were given within a framework of beam theory. In addition, many of the investigations give only the flutter boundary defined in terms of the test conditions such as dynamic pressure and Mach number at flutter, sometimes even omitting the flutter frequency. Such data sets are useful as a guide for CFD validation, but they provide little insight in the event of discrepancies which are at times encountered. Reliance must then be placed on the experience and intuition of the investigator to resolve the problems encountered in applications. Such is particularly the case with CFD codes as it is very difficult to separate numerical short comings and the limitations of the treatment of the flow physics. It is very difficult to evaluate convergence in terms of the computational grid or time step within computer budgets, time, and memory constraints and questions concerning the numerical solutions are seldom answered. For example, premature rises in the flutter boundary versus Mach number are sometimes encountered. The premature rises may be related to an inadequate computational grid, but also may be related to the required equation level or other factors.

There are many significant data sets available for measured unsteady pressures on models undergoing forced oscillations. Such data are, of course, fundamental to the validation of CFD codes, but it is difficult to assess the implication of discrepancies between calculated and measured experimental pressures for flutter analyses.

The Structural Dynamics Division (SDyD) of the NASA Langley Research Center has been actively involved in the development and application of CFD codes for treating the flutter problem for nearly two decades. In view of the difficulty that has been experienced in evaluating such codes in comparison with current data sets, an experimental program in aeroelasticity has been developed and is called the Benchmark Models Program. The primary purpose of this program is to provide well documented data sets suitable for CFD code validation. Additional supplementary goals are to provide increased understanding of the physics of transonic unsteady flows, and where necessary provide data for empirical design. This paper gives an overview of the SDyD Benchmark Models Program, describes the models for the tests, and then gives highlights of some of the initial tests.

3. BENCHMARK MODELS PROGRAM OVERVIEW

The SDyD Benchmark Models Program is a joint effort of

THIS DOCUMENT PROVIDED BY THE ABBOTT AEROSPACE
TECHNICAL LIBRARY
ABBOTTAEROSPACE.COM



Figure 1. PAPA model with NACA 0012 Airfoil mounted in TDT.

the three aeroelasticity-related branches of SDyD, the Configuration Aeroelasticity Branch, the Unsteady Aerodynamics Branch, and the Aeroservoelasticity Branch. It consists both of simple models for concept exploration, and highly instrumented models for CFD validation studies. The test team consists of about six engineers, depending on the test, with varied backgrounds such as wind tunnel testing, CFD applications, and control systems. The testing is being conducted in the NASA Langley Transonic Dynamics Tunnel (TDT), and is scheduled for about two tests per year.

Goals for the benchmark models for CFD validation studies include:

- -Aerodynamically smooth surfaces
- -Complete description of geometry including static and dynamic deformation
- -Complete experimental definition of structural dynamics including modal frequencies, dampings, generalized masses, and mode shapes
- -Measured flutter boundary including flutter frequency and mode shapes
- -Measured unsteady pressures on at least two chords during flutter
- -At least qualitative indication of transition and separation
- -Flow visualization where possible

The testing program has been designed to start with simple models and then to evolve into more complex models and tests. This is advantageous from the test technique development point of view as well as for CFD validation. The initial tests are for rigid wings mounted on the pitch and plunge apparatus (PAPA). The wings are rectangular in planform and are of panel aspect ratio 2.0. The initial wing is shown in figure 1 as mounted in the Transonic Dynamics tunnel. Currently there are three wings with different airfoils in this series for conventional flutter testing. These three models are designed to be essentially plug-compatible for ease of testing, instrumentation, and data processing. In addition, a model similar to one of this series will be tested with a trailing edge control and upper and lower surface spoilers. Active flutter control systems will also be tested using this model. A flexible high speed civil transport (HSCT) model is also incorporated into the plan following several of the initial tests. Subsequent models will investigate other widely-varying planforms.

The test plan is illustrated in the tentative schedule shown in figure 2. At this time two models have been tested. One was a simple model to briefly investigate the dynamic response of a flexible wing with an 18% circular-arc airfoil undergoing periodic shock-boundary layer oscillations.[3] This model was tested in the spring and fall of 1990 as shown in figure 2. The first of the models on the PAPA mount system had a NACA 0012 airfoil[4] (fig. 1) and was tested in the summer of 1990 and winter of 1991. Some highlights of these tests will be subsequently presented after further description of the PAPA system, the wind tunnel, and the Benchmark Models.

4. THE PAPA MOUNT SYSTEM

As previously indicated, several of the Benchmark Models are to be tested on the Pitch and Plunge Apparatus (PAPA) of the Langley Transonic Dynamics Tunnel (TDT).[5,6] A photograph of the PAPA mount is shown in figure 3. It consists primarily of four steel rods attached to a turntable on the wall of the tunnel and attached to a moving steel plate at the other end (fig. 3). The rods permit vertical translation or plunge, and pitch or torsional motion. A central beam that is thin vertically, but wide horizontally, stiffens the system in the fore-and-aft direction. The turntable is remotely adjustable to permit changes in angle of attack. The rods have essentially fixed-fixed

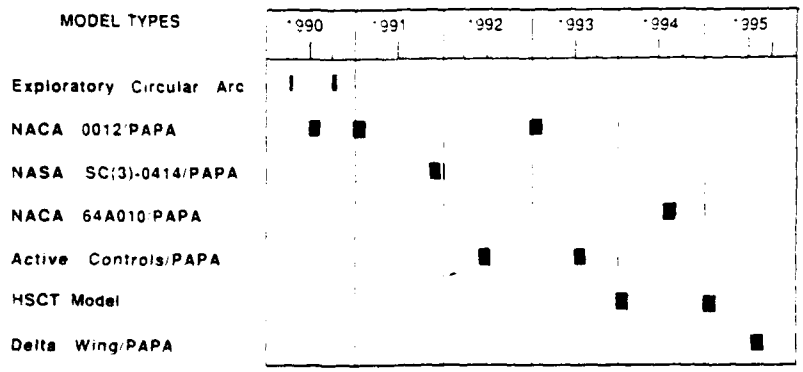


Figure 2. Benchmark Models test schedule.

THIS DOCUMENT PROVIDED BY THE ABBOTT AEROSPACE
TECHNICAL LIBRARY
ABBOTTAEROSPACE.COM

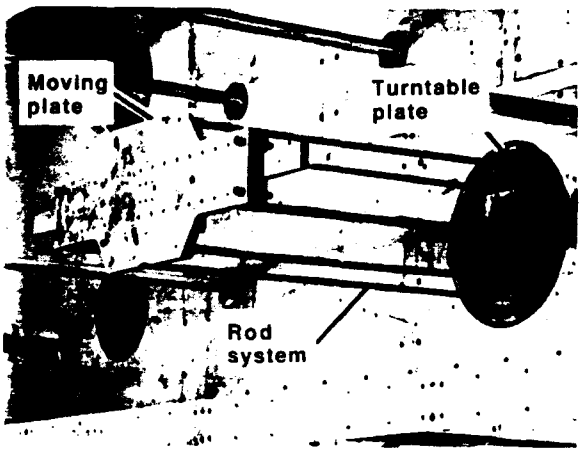


Figure 3. Photograph of pitch and plunge apparatus (PAPA) mounted in the TDT.

end conditions to provide linear pitch and plunge stiffnesses for elastic restraint. The PAPA mechanism is instrumented with strain gages to provide pitch and plunge position, and accelerometers to measure pitch and plunge accelerations. The root of the wing is attached to the moving plate in the wind tunnel.

As shown in figure 3, the PAPA system projects out into the wind tunnel. A splitter plate is used as an effective end plate or side wall. This splitter plate is 10 feet high (3.05 m) by 12 feet long (3.66 m) and is shown in figure 4. The center of the PAPA system is 7 feet (2.13 m) from the leading edge of the splitter plate. An end plate attached to the root of the model covers the hole through which the wing mounting pedestal extends. This circular end plate is one chord in diameter and is recessed into the splitter plate. The splitter plate is supported from the wall by struts that extend about 3.3 feet (1.0 m) from the wind tunnel wall. The PAPA mount system is surrounded by a steamlined fairing behind the splitter plate. For the Benchmark Model tests, splitter plate pressures are measured with 20 pressure transducers (fig. 4). A 0.42 foot (0.13 m) span boundary layer rake with ten pressure transducers is located above and aft of the wing. Studies are currently underway to examine the feasibility of locating the PAPA system behind the tunnel wall to simplify installation.

The PAPA system is quite rugged and robust thus permitting measurement of many flutter points with very low risk to the models. The strength of the system permits flutter testing at moderate angles of attack unlike the usual flutter models which are limited to small values by aerodynamic loads. Most models tested on PAPA have a somewhat mild flutter crossing which permits dwelling at nearly constant amplitude for even as long as one to two minutes so that many cycles of data can be used for averaging measured pressures. The natural frequencies of this system are usually around three to five Hertz which also permits easier flutter testing than for models with higher frequencies. The PAPA system contains no bearings, and the structural damping is very low, on the order of 0.0005 in fraction of critical damping. Overall the mount system can be well defined such that the effect of unsteady aerodynamics on flutter can be investigated in detail.

For static pressure measurements, the system can be rigidized readily with a simple fixture. For later tests, installation of a strain gage balance for steady state force measurements is being investigated. The development of an excitation system to permit dynamic measurements prior to flutter is also underway.

The moving plate and rods of the PAPA are relatively heavy. The models can therefore also be relatively heavy without significant further penalty. Thus it is practical to use machined metal models along the lines of an aerodynamic static test model. These models can be very smooth by usual aeroelastic model standards, and can be manufactured much less expensively than the usual flutter model. A smooth surface is considered vital for transonic benchmark aerodynamic data.

One consequence of the large mass of the PAPA/model system is that the flutter data is for high mass ratio, on the order of 1000 in air (or 250 in the heavy gas). This leads to an unusually low value of reduced frequency, k, of the order of 0.02 based on semichord (in air). Such a low reduced frequency would normally be expected to accentuate transonic aerodynamic effects.

5. WIND TUNNEL

The Benchmark Model tests are to be conducted in the Langley Transonic Dynamics Tunnel (TDT). This tunnel is a large facility with a test section 16–feet (4.88 m) square with cropped corners. All four walls are slotted. The TDT is a continuous flow, single return tunnel that can operate at Mach numbers up to 1.2, and for pressures from near vacuum to atmospheric. Either air or a heavy gas can be used as a test medium, but only air has been used for the initial Benchmark Model tests. This tunnel is used primarily for aeroelastic testing, and is equipped with four quick-opening bypass valves for rapidly reducing test section dynamic pressure and Mach number upon encountering an instability. The large tunnel size and the use of heavy gas as the test medium considerably facilitate aeroelastic model design and instrumentation.

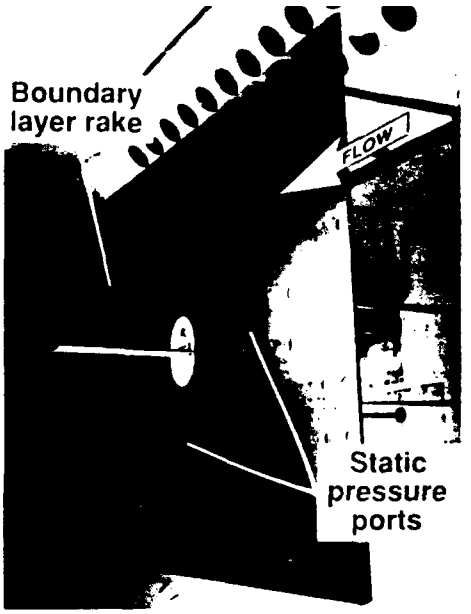


Figure 4. Splitter plate arrangement for PAPA tests.

THIS DOCUMENT PROVIDED BY THE ABBOTT AEROSPACE
TECHNICAL LIBRARY
ABBOTTAEROSPACE.COM

A key ingredient in the Benchmark Model tests is the data acquisition system of the TDT. The PAPA models are currently designed for 128 channels of data, with later models increasing to 192 and 256 channels. Software has been developed to permit nearly on-line display of first harmonic and static data. Typically 40 seconds of data are recorded at 100 samples/second for nearly-on-line analysis. For subsequent analyses, 20 seconds of the time history of each data channel is recorded at 1000 samples/second. These data become a massive set of data for a typical test and are recorded on tape. Transfer to central site supercomputers has been accomplished. Data gathering, handling, reduction, and analysis for tests of this type is a large effort and requires considerable specialized software development. This data processing system is still being developed and refined for the Benchmark Models program.

6. DESCRIPTION OF PAPA MODELS

6.1 Conventional Flutter Models

The first Benchmark Model for the PAPA system is shown in figure 1. As previously mentioned, there are three similar models in this series that differ only in airfoil section and are designed for basic flutter tests. The three airfoils are the NACA 0012, the NASA SC(2)-0414, and the NACA 64A010. The profiles of these airfoils are shown in figure 5. The NACA 0012 is an old design, twelve per cent thick airfoil that has been extensively tested. For example, reference 7 summarizes over forty steady wind tunnel tests for this airfoil. The NASA SC(2)-0414 is a typical modern supercritical airfoil and is described as one of a series of airfoils in reference 8. It has a design lift coefficient of 0.4, is fourteen percent thick, and is described as an airfoil for a business jet[8]. The NACA 64A010 is a symmetrical ten percent thick NACA design that has been used in an AGARD standard unsteady two dimensional pressure test,[9]and in a three dimensional test[10]. These three airfoils have very different types of transonic flow development. The NACA 0012 airfoil develops a shock wave forward of midchord as Mach number in increased into the transonic range. The SC(2)-0414 is an aft-loaded supercritical airfoil with significant aft camber and develops a shock further aft. The NACA 64A010 airfoil is somewhat intermediate. Although the PAPA models are of relatively low aspect ratio, this range of airfoils should give a good survey of the effects of widely differing airfoils on transonic flutter characteristics for CFD calibration studies.

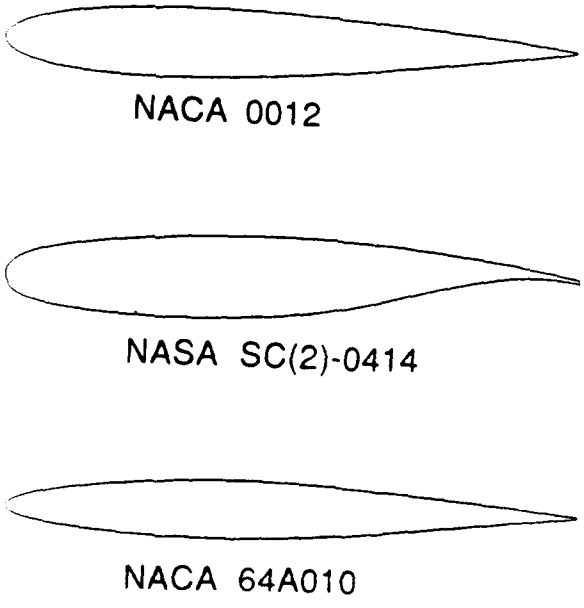


Figure 5. Airfoils for initial PAPA wings.

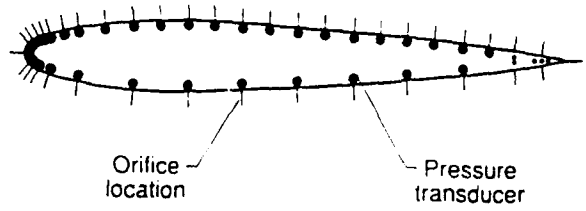


Figure 6. Orifice and pressure transducer locations for 0012/PAPA model.

As shown in figure 1, the PAPA models are rectangular in planform. They have a 16 inch (0.406 m) chord and a semispan of 32 inches (0.812 m) plus the tip of revolution. There are two rows of in-situ pressure transducers, each row containing 40 unsteady pressure transducers. One row is at 60 per cent span, and the other one at 95 percent span. The location of the pressure transducers for the 0012 model is illustrated in figure 6. The model is machined from aluminum and is constructed in three sections that are bolted together. A row of orifices is located about one inch (2.54 cm) outboard of each of the outer joints. The pressure transducers were bonded into brass tubes for protection during installation and removal, and the brass tubes were bonded into holes drilled into the wing section. The mounting holes, a bare transducer, and a transducer mounted in a brass tube are shown in the upper left portion of figure 7. Four accelerometers near the corners of the wing were installed in pockets as shown in the upper right portion of the figure.

During the initial test of the NACA 0012 model in July 1990, only the inboard row of transducers was installed, but both rows were operational during the January 1991 tunnel entry.

The model with the NASA SC(2)-0414 airfoil has been completed and is being prepared for testing during November and December 1991 (fig. 2). The model is constructed in essentially the same fashion as the 0012 model with only some minor improvements in detail. It is designed to be essentially plug compatible with the 0012 model. Some redistribution of

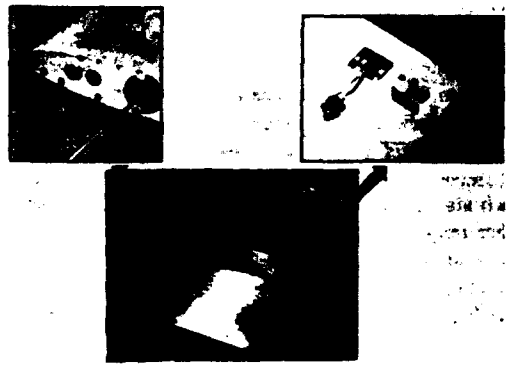


Figure 7. Details of 0012 model.

This Document Provided by the Abbott Aerospace
TECHNICAL LIBRARY
ABBOTTAEROSPACE.COM

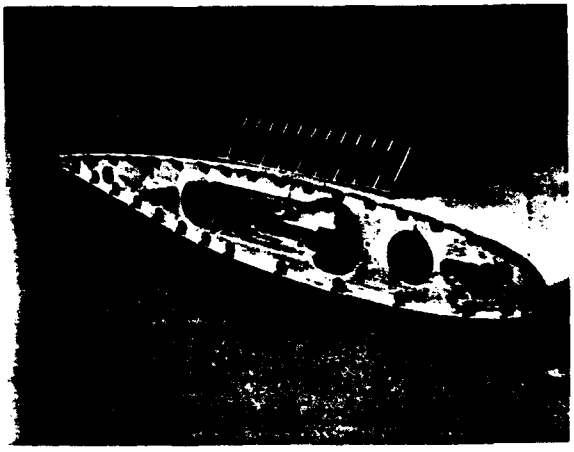


Figure 8. Cross section of SC(2)-0414 model showing transducer locations.

the pressure transducers has been made by moving some from the nose to the aft lower surface to improve the definition of pressures in the aft lower surface. A photograph of a section of this model is shown in figure 8. The holes near the surface are for mounting the pressure transducers.

The model with the NACA 64A010 airfoil has been designed and is being machined. It is scheduled for a later entry (fig. 2), but may serve as a backup for the other tests if mechanical or instrumentation problems are encountered with the other models.

6.2 Active Controls Model

An active controls model is under construction to investigate flutter suppression on the PAPA system.[11] This model will have a NACA 0012 airfoil and will be very similar to the other NACA 0012 flutter model in order to build on the experience and results of the earlier model. The planform and controls layout are shown in figure 9. The model will have a thirty per cent span trailing edge control of twenty five percent chord. Spoilers are located on the upper and lower surfaces of the wing upstream of the trailing edge control. The spoilers are fifteen per cent chord in length. The unsteady pressures will be measured at one full chord which is the same as for the earlier model but with a different distribution to define the pressures near the hinge lines of the control surface and spoilers. An additional partial row of pressure transducers is located at

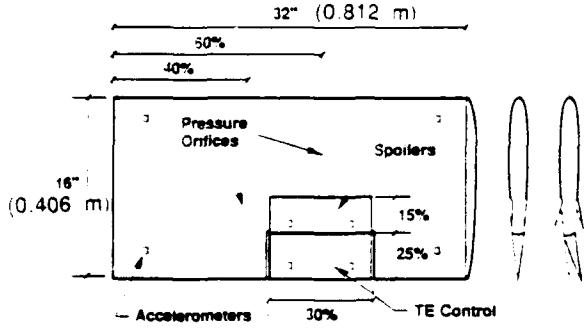


Figure 9. Drawing of active controls model.

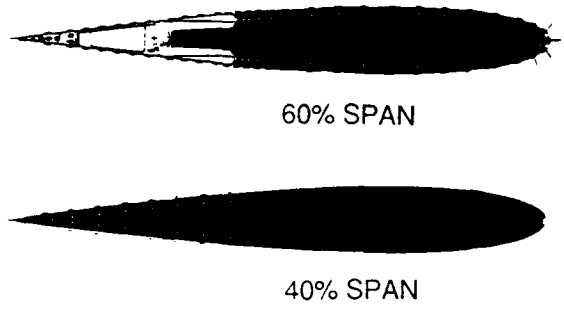


Figure 10. Orifice locations for active controls model.

forty per cent span (fig. 9). The planned orifice locations are presented in figure 10.

To meet the space and torque requirements for this model, a new hydraulic actuator is being designed. A prototype actuator has been built and is being tested. The breadboard test setup is shown in figure 11. Laboratory tests to determine the dynamic characteristics and load limits are underway.

Two tunnel entries are planned (fig. 2) for this model. The initial entry will measure the open-loop flutter boundaries for comparison with results from the earlier model. The model will also be mounted on a five component force balance which will permit measurement of the static and dynamic loads of the model with oscillating controls. The experimental data base will be used to design active flutter suppression control laws. The second entry will evaluate these control laws.

7. HIGHLIGHTS OF INITIAL 0012/PAPA TESTS

Some preliminary results from the July 1990 tests will be discussed. The data reduction for the 1991 tests is currently in progress. For these tests the plunge mode frequency was 3.40 Hz with a damping of 0.0017 (fraction of critical damping). The corresponding pitch frequency and damping were 5.18 Hz and 0.0008. The PAPA assembly was balanced such that the pitch axis and the center of gravity were both at midchord.

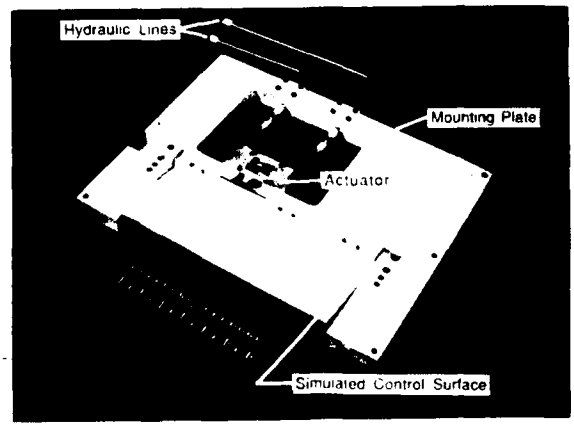


Figure 11. Miniature hydraulic actuator prototype in test fixture.

THIS DOCUMENT PROVIDED BY THE ABBOTT AEROSPACE
TECHNICAL LIBRARY
ABBOTTAEROSPACE.COM

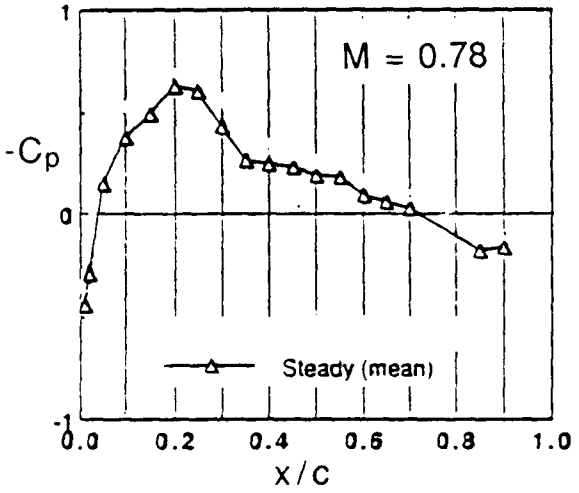


Figure 12. Steady pressure distributions for upper surface at 60 per cent span and zero angle of attack.

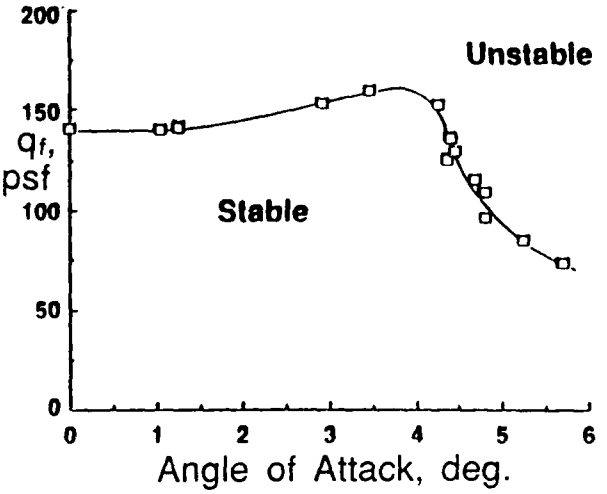


Figure 14. Flutter boundary variation with angle of attack for M = 0.78. (Note 100 psf = 4.79 kPa)

7.1 Steady Pressure Measurements

The test program included measuring pressures on the model with the PAPA rigidized to prevent pitch or plunge motion. A systematic schedule of Mach numbers and angles of attack up to 4° was run at a value of dynamic pressure near that of flutter, 140 psf (6.70 kPa). This technique should permit evaluation of the static pressure versus the mean pressure during flutter, and the basic unsteadiness of the flow over a stationary model. A sample upper surface pressure distribution is presented in figure 12 for M = 0.78 and for sixty percent span. For this Mach number a shock is evident near thirty per cent chord. Dynamic data analysis for such conditions should also give an indication of buffet conditions.

7.2 Flutter at Zero Angle of Attack

The flutter boundary measured at zero angle of attack is shown in figure 13. The conventional flutter boundary is given by the square symbols. An unusual trend of an increase in flutter dynamic pressure with Mach number is shown which is a result of the aeroelastic parameters of this system. There is a small dip near M = 0.78 and a rapid rise near M = 0.80. Note that the boundary is well defined with a large number of flutter points and relatively small scatter.

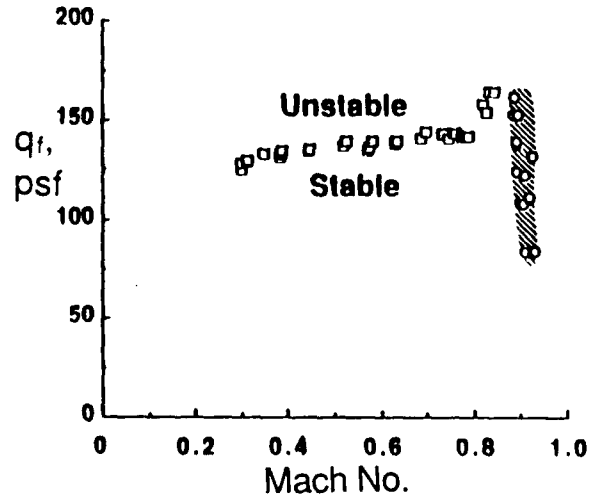


Figure 13. Measured flutter boundaries for 0012/PAPA model at zero angle of attack. (Note 100 psf = 4.79 kPa)

In addition to the conventional flutter boundary, a flutter instability involving a nearly pure plunging motion was encountered over a narrow Mach number range from about M = 0.88 to 0.92 as shown by the circular symbols and the cross hatched region (fig. 13). At low dynamic pressures, both the start and end of flutter could be defined, but at the higher dynamic pressures, the motion became so large that only the start of flutter could be determined. Strong shock-induced separation is encountered for this Mach number range. An instability of similar characteristics was also reported for a transport type wing in reference 12.

7.3 Flutter at Angle of Attack

The variation of the flutter boundary with angle of attack is shown in figure 14 for M = 0.78. The flutter dynamic pressure shows a small increase with angle of attack for angles up to four degrees. Above four degrees, a rapid decrease in flutter dynamic pressure occurs. Flutter near five degrees has been shown by tufts to involve shock induced separation and reattachment during the cycle of motion. This type of study is difficult to perform on the usual aeroelastic models without exceeding allowable load limitations.

7.4 Unsteady Pressures Measured During Flutter

A sample of a measured time history at a flutter point at M = 0.78 and zero angle of attack is given in figure 15. Pitch and plunge motions are shown along with the corresponding unsteady upper surface pressure measurements at x/c = 0.25. The flutter frequency is readily apparent in the pressure, and for this location appears to be nearly in phase with the plunge motion.

The range of unsteady pressure measurements can be visualized by plotting the mean, minimum, and maximum of the pressures as shown in figure 16. For this example, there appears to be only small changes in pressure near the trailing edge of the airfoil, but large changes in the forward portion.

THIS DOCUMENT PROVIDED BY THE ABBOTT AEROSPACE
TECHNICAL LIBRARY
ABBOTTAEROSPACE.COM

Harmonic or Fourier analysis of the unsteady pressures are performed to determine the amplitude and phase of the first harmonic of the pressure sensed by each transducer. Data of this type are shown in figure 17 for the sixty per cent span section at M = 0.39 and M = 0.78. The phase is referenced to plunge displacement. The magnitude of the pressures at M = 0.39 display a typical subsonic pressure distribution with a strong peak at the leading edge and decreasing rapidly near the trailing edge. The upper and lower surface pressures are essentially identical. The upper and lower surface phases differ by 180°, as expected, and vary only slightly from leading to trailing edge. At M = 0.78, (fig. 17b) the magnitude shows a strong forward loading ahead of the shock wave near x/c

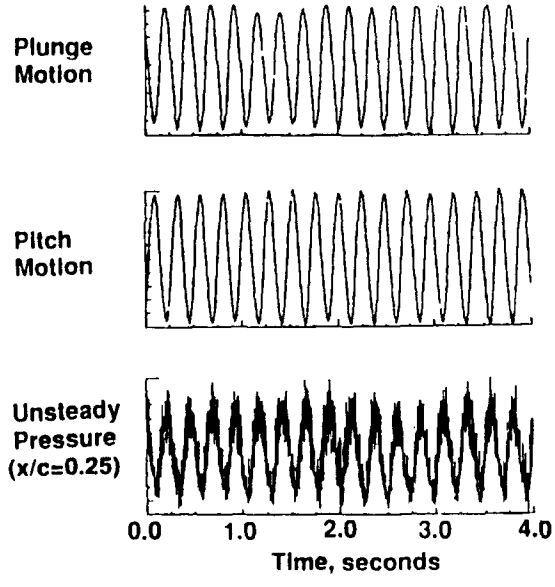


Figure 15. Sample time histories at flutter, M = 0.78, f = 4.15 Hz.

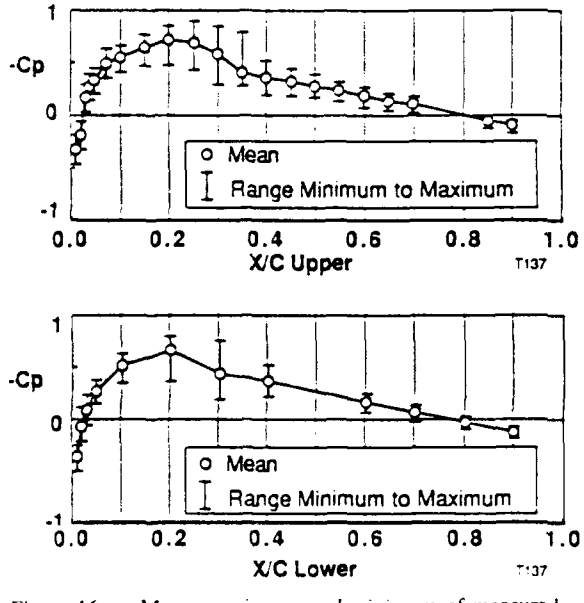
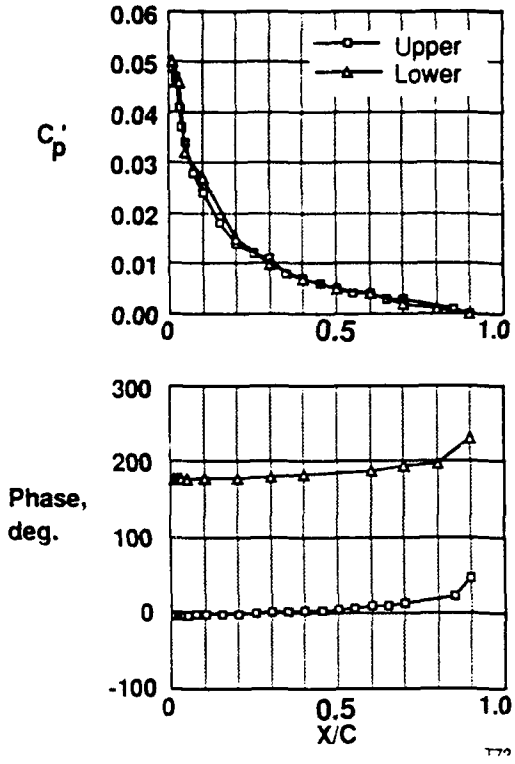
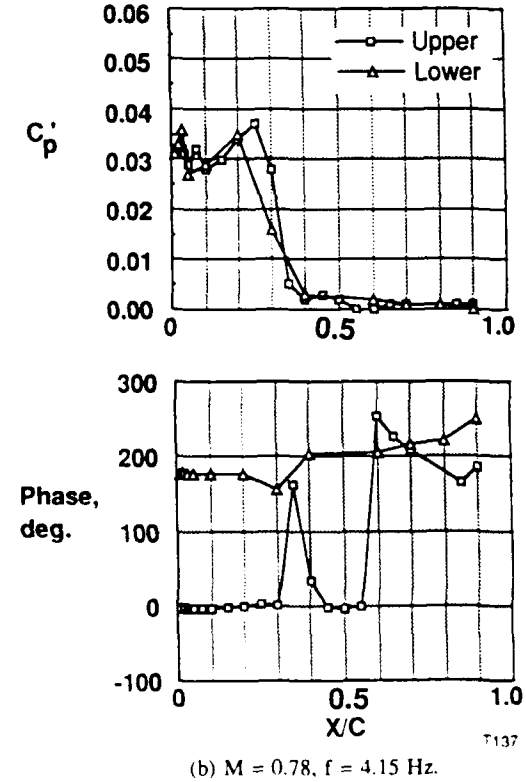


Figure 16. Mean, maximum, and minimum of measured pressures during flutter, M = 0.78 and zero angle of attack.



(a) M = 0.39, f = 4.50 Hz.



(b) M = 0.78, f = 4.15 Hz.

Figure 17. Magnitude and phase of measured pressures during flutter at zero angle of attack.

THIS DOCUMENT PROVIDED BY THE ABBOTT AEROSPACE
TECHNICAL LIBRARY
ABBOTTAEROSPACE.COM

= 0.30, and little loading aft of the shock. The phase (fig. 17b) also shows a rapid variation through the shock and some difference in trends near the trailing edge where the magnitude is small. Data of this type can be displayed by the TDT data acquisition system in nearly on-line fashion. Results such as these including the measured flutter modal amplitude and phase information should be valuable in CFD code calibration efforts.

7.5 Flow Visualization

Tufts and shear sensitive liquid crystals have been used to give some indication of surface flow features. White tufts have been used on a model painted flat black to indicate separated flow features. These features are recorded with a video camera for later analysis. The liquid crystals, which are normally used for transition detection, have been found to indicate surface features such as shock waves much like oil flow techniques. These techniques have been applied to the NACA 0012 wing on the PAPA and will serve as a qualitative guide in the CFD code calibration efforts.

8. OTHER BENCHMARK MODELS

8.1 HSCT Aeroelastic Model

As indicated in figure 2, the Benchmark Models program includes a high speed civil transport (HSCT) model scheduled to be tested in January 1994. This model is in the preliminary or conceptual design stage at this time. It is planned as a flexible model in contrast to the rigid PAPA models previously described. Currently, the design is a half model, wall mounted, and has a control for excitation of the aeroelastic modes prior to flutter. An extensive number of unsteady pressure transducers and accelerometers will be used. The total number of channels will be near the 256 channel limit of the facility.

8.2 Thick Circular-Arc Airfoil Model

The Benchmark Models Program involves both highly instrumented models for CFD calibration work and simple models for concept exploration or a brief look at interesting physical phenomena. One simple model that was built and tested was a flexible rectangular wing with an 18 percent circular-arc airfoil section.[3] The model was built to study the dynamic response of a flexible wing to transonic shock-boundary layer oscillations that occur on thick circular-arc airfoils over a small range of Mach numbers. The conditions for this oscillation are illustrated in the sketch of figure 18. As Mach number is increased subsonically, the strength of the shocks terminating the supersonic region on the fore part of the airfoil increases. Initially, a small separation zone occurs at the foot of the shock and at the trailing edge. As the Mach number is further increased, the flow over the airfoil becomes fully separated behind the shockwave. On the thick circular-arc airfoils, near the Mach numbers where the transition from partial to fully separated flows takes place, there is a Mach number range of about 0.04 where the flow alternates antisymmetrically from partially attached to fully separated flow. This occurs with large pressure changes yielding an alternating lift coefficient of about 0.10 at a high frequency ($k = \omega c/2V$) of about 0.50.

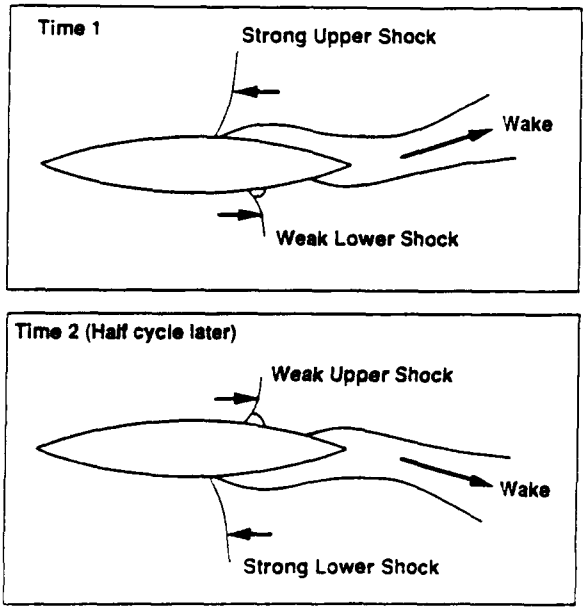


Figure 18. Sketch of transonic shock-boundary layer oscillation on circular-arc airfoil.

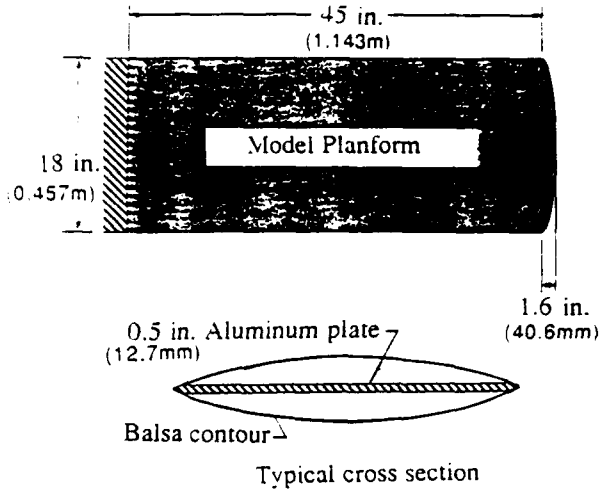


Figure 19. Sketch of wing with thick circular-arc airfoil.

The model planform and cross section are sketched in figure 19. The central portion was a 0.50 inch (12.7 mm) aluminum flat plate with bevelled edges. Balsa wood was glued to the plate

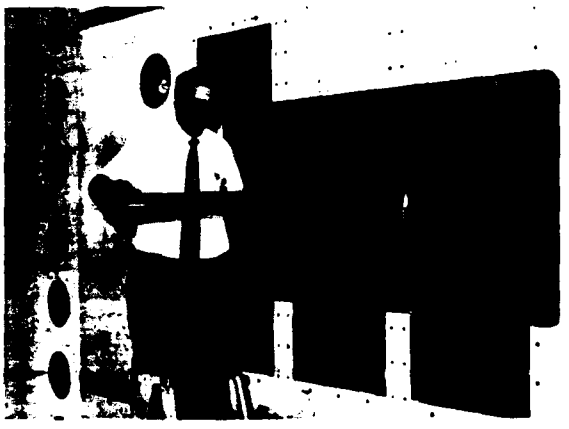


Figure 20. Wing with 18% circular-arc airfoil mounted in the TDT.

THIS DOCUMENT PROVIDED BY THE ABBOTT AEROSPACE
TECHNICAL LIBRARY
ABBOTTAEROSPACE.COM

with the grain running spanwise and formed to an 18 percent circular-arc section with sharp leading and trailing edges. The root of the plate of the model was clamped in a near cantilever fashion to a turntable in the wall of the tunnel. A small splitter plate of about 6 feet (1.83 m) in length and 3 feet (0.914 m) high was used to keep the root of the model outside the tunnel wall boundary layer. The model is shown mounted in the TDT in figure 20. Transition was fixed at ten percent chord.

For the configuration presented herein, the first bending frequency was 7.8 Hz, and a 3rd bending mode that involved splitter plate motion was at 92 Hz. The splitter plate was attached to the wing mounting bracket and coupled with the wing in this case for the higher frequency modes.

9. HIGHLIGHTS OF THE TESTS OF THE CIRCULAR ARC WING

9.1 Character of the Measured Results

The overall character of the results is illustrated in the short segment of time histories presented in figure 21. For low Mach numbers, the first bending mode responded at its frequency (7.8 Hz) with random beating or bursts of motion typical of a buffeting response (fig. 21, M = 0.751). As Mach number was increased, the buffeting of the first bending mode increased and nearly constant amplitude response in the third bending mode at approximately 90 Hz was also observed (fig. 21, M = 0.781). Further small increases in Mach number resulted in little change (fig. 21, M = 0.795), until slightly above a Mach number of 0.80 no further response of the third bending mode was apparent (fig. 21, M = 0.819). Bending response was obtained only in the 1st and 3rd bending modes and not in the 2nd bending mode.

The root-mean-square (RMS) responses were calculated after low-pass and high pass filtering and are shown in figure 22 in nondimensional form. The responses increase rapidly near M = 0.76 and decrease rapidly again near M = 0.80. This corresponds closely to the Mach number range of the shock-boundary layer oscillations for the 18% circular arc airfoil.[13]

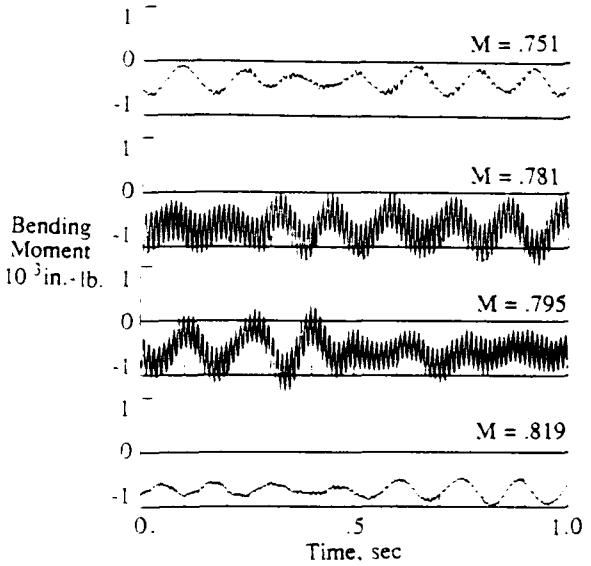
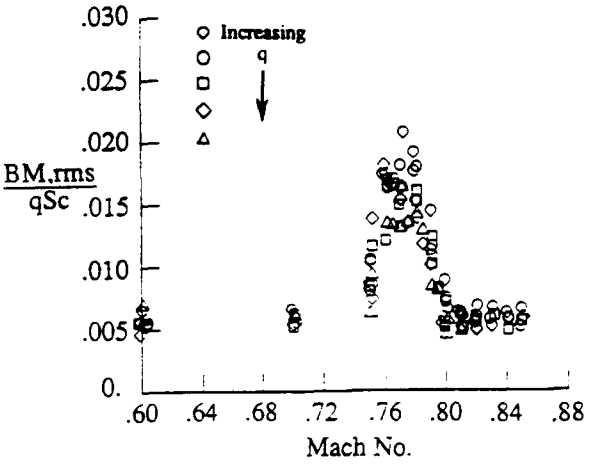
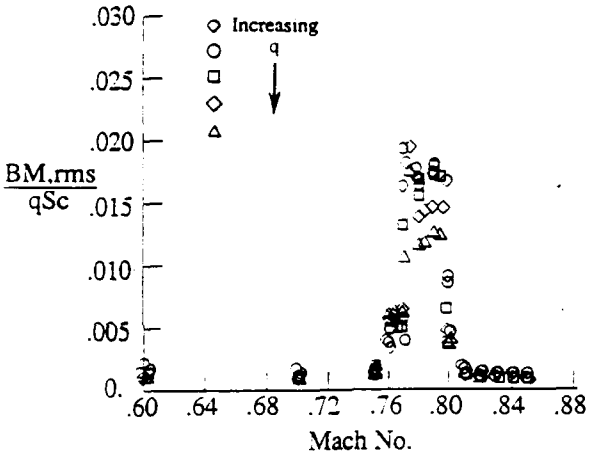


Figure 21. Sample of time histories of bending moment response.



(a) Filtered low frequency response (1st bending).



(b) Filtered high frequency response (3rd bending).

Figure 22. Bending moment response measurements for several wind tunnel pressures.

Similar levels of RMS response are obtained for both modes. These results indicate that the region of shock-boundary layer oscillations leads to a buffeting condition on this wing for the 1st bending mode which was well removed in frequency for the aerodynamic oscillations, and also leads to a limit-cycle oscillation for the 3rd bending-like mode. The dimensional frequency for the shock boundary layer oscillation is calculated to be 93 Hz, based on k = 0.5, which is quite near the 3rd bending frequency. Large effects of the transition strip and removal of the splitter plate were also found.[3]

9.1.1 *Liquid crystal pattern*

During this test, shear-senstive liquid crystals were used to visualize surface flow phenomena in the spirit of oil flows. A liquid crystal pattern for M = 0.82 is shown in figure 23. At this Mach number the flow behind the shock should be non-oscillatory and fully separated. The light line gives an indication of the shock location and shows a nearly constant chord location over much of the span. However a strong tip effect with a complex flow pattern is evident.

THIS DOCUMENT PROVIDED BY THE ABBOTT AEROSPACE
TECHNICAL LIBRARY
ABBOTTAEROSPACE.COM

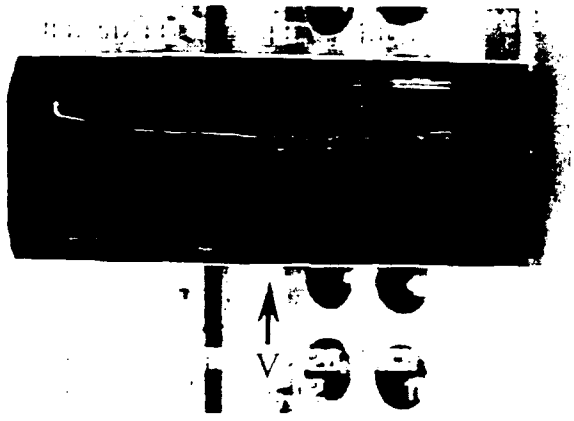


Figure 23. Liquid crystal pattern on wing with circular arc airfoil, M = 0.82.

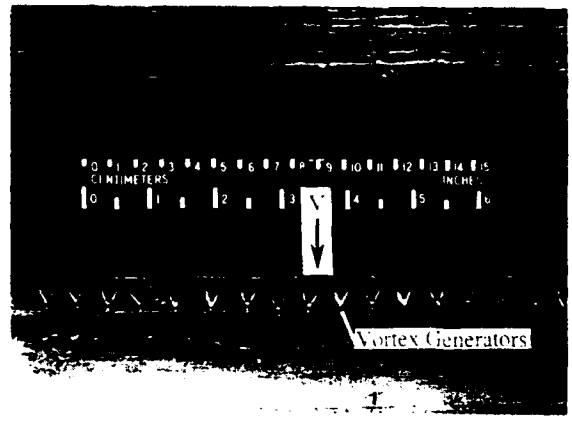


Figure 25. Photograph of wing with vortex generators, configuration 1.

9.1.2 *Effect of spanwise strip*

A spanwise wire located aft of the shockwave was shown to be a good fix or suppressor of the shock-boundary layer oscillations.[14] In the present study, a 0.25 inch (6.4 mm) square strip with rounded corners was taped to the surface at x/c = 0.75 on both upper and lower surfaces.[3] The low and high frequency results are shown in figure 24. The high frequency oscillations are effectively suppressed. However the trend for the low frequency buffeting shown (fig. 24) persisted at lower Mach numbers and a large increase in buffeting levels was obtained. A data point (not shown) at M = 0.43 gave a bending moment coefficient of 0.033 which is a pronounced increase in buffeting level. In summary, the spanwise strip eliminates the high frequency oscillation, but has the strong and undesirable side effect of increased subsonic buffeting response.

9.1.3 *Effect of vortex generators*

The Wheeler wishbone-type vortex generators were applied to the circular-arc model in an effort to suppress the aerodynamic oscillations as shown in figure 25. These vortex generators are normally used as sub-boundary layer devices, but here they were 0.100 inch (2.5 mm) and 0.96 inch (2.4 mm) high and were higher than would be considered sub-boundary layer devices. These were applied at 60% chord. The low and high freqency test results are shown in figure 26. The high frequency oscillations were effectively suppressed, but the low frequency buffeting grew in the transonic range. A large flutter-like response, with a frequency near the 1st bending frequency was encountered near M = 0.80 (fig. 26). Moving the vortex generators forward to 45% chord resulted in some reduction of the low frequency buffeting, but did not satisfactorily suppress the high frequency mode.[3] This type of vortex generator appears to have potential for alleviating the dynamic effects of shock boundary layer interaction, but must be carefully designed and further development is required.

Experience with these efforts to eliminate the shock boundary layer oscillations indicates that fixes derived on rigid models need to be tested on a dynamic model to verify that unsatisfactory side effects are not induced.

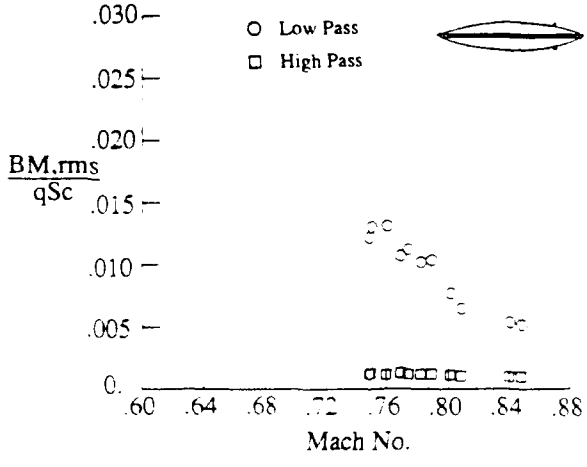


Figure 24. Filtered measured bending moment with spanwise strip.

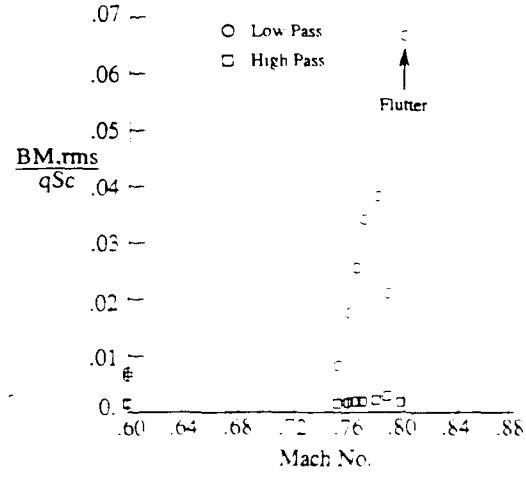


Figure 26. Filtered measured bending moment with vortex generators, configuration 1.

THIS DOCUMENT PROVIDED BY THE ABBOTT AEROSPACE
TECHNICAL LIBRARY
ABBOTTAEROSPACE.COM

10. CONCLUDING REMARKS

The NASA Langley Research Center Structural Dynamics Division Benchmark Models Program has been described. This program consists of about two tests per year over a five year period. The primary purpose is to obtain data for calibration or validation of modern CFD codes for aeroelastic analysis. In addition, the goals of increased understanding of the physics of unsteady flows, and the developing of a data base for empirical design are also included. The overall plan has been described and some of the highlights of the initial test presented including initial tests of flutter of a rigid wing on the flexible PAPA system, and tests of a simple wing with a thick circular arc airfoil have been carried out. Further tests are proceeding and it is hoped that in the very near future additional data suitable for CFD validation efforts will be available.

11. ACKNOWLEDGEMENTS

We wish to acknowledge the significant assistance of Clifford J. Obara of the Flight Research Branch of NASA Langley with the application of liquid crystals, and of John C. Lin of the Low Turbulence Pressure Tunnel Section of NASA Langley with vortex generator application.

12. REFERENCES

1. Edwards, J. W.; and Malone, J. B.: "Current Status of Computational Methods for Transonic Unsteady Aerodynamics and Aeroelastic Applications," Paper No. 1, AGARD Specialists Meeting on Aerodynamics and Aeroelasticity, San Diego, CA, October 9–11, 1991.

2. Yates, E. C., Jr.: "AGARD Standard Aeroelastic Configurations for Dynamic Response. I - Wing 445.6." AGARD Report-R-765, July 1988.

3. Bennett, R. M.; Dansberry, B. E.; Farmer, M. G.; Eckstrom, C. V.; Seidel, D. A.; and Bennett, R. M.: "Transonic Shock-Induced Dynamics of a Flexible Wing With a Thick Circular-Arc Airfoil." AIAA Paper No. 91–1107, 1991. Also NASA TM 104088, 1991.

4. Rivera, J. A., Jr.; Dansberry, B. E.; Farmer, M. G.; Eckstrom, C. V.; Seidel, D. A.; and Bennett, R. M.: "Experimental Flutter Boundaries with Unsteady Pressure Distribution for the NACA 0012 Benchmark Model." AIAA Paper No. 91–1010, 1991. Also NASA TM 104072, 1991.

5. Farmer, M. G.: "A Two-Degree-of-Freedom Flutter Mount System with Low Damping for Testing Rigid Wings at Different Angles of Attack," NASA TM-83302, 1982.

6. Farmer, M. G.: "Model Mount System for Testing Flutter," U. S. Patent Number 4,475,385, October 9, 1984.

7. McCroskey, W. J.: "A Critical Assessment of Wind Tunnel Results for the NACA 0012 Airfoil," NACA TM 100019, October 1987.

8. Harris, C. D.: "NASA Supercritical Airfoils." NASA TP 2969, March 1990.

9. Davis, S. S.: "Data Set 2–NACA 64A010 (NASA Ames Model) Oscillatory Pitching," Paper No. 2 in "Compendium of Unsteady Aerodynamic Measurements," AGARD Report No. 702, August 1982.

10. Mabey, D. G.; Welsh, B. L.; and Cripps, B. E.: "Measurement of Steady and Oscillatory Pressures on a Low Aspect Ratio Model at Subsonic and Supersonic Speeds," British Royal Aerospace Establishment, Bedford, England, TR-84095, September 1984.

11. Durham, M. H.; Keller, D. F.; Bennett, R. M.; and Wieseman, C. D.: "A Status Report on a Model for Benchmark Active Controls Testing," AIAA Paper No. 91–1011, April, 1991.

12. Eckstrom, C. V.; Seidel, D. A.; and Sandford, M. C.: "Unsteady Pressure and Structural Response Measurements on an Elastic Supercritical Wing," Journal of Aircraft, Vol. 27, No. 6, June 1990.

13. McDevitt, J. B.: "Supercritical Flow About a Thick Circular-Arc Airfoil," NASA TM-78549, 1979.

14. Gibb, J.: "The Cause and Cure of Periodic Flows at Transonic Speeds," ICAS, 1988, Paper 3.10.1.

THIS DOCUMENT PROVIDED BY THE ABBOTT AEROSPACE
TECHNICAL LIBRARY
ABBOTTAEROSPACE.COM

AD-P007 817

FURTHER INVESTIGATION OF THE EFFECT OF MODEL COOLING ON PERIODIC TRANSONIC FLOW

S. Raghunathan
F. Zarifi-Rad
Queen's University, Belfast, UK.

and

D.G. Mabey
Royal Aerospace Establishment,
Bedford, UK.

SUMMARY

Experimental investigation of the effect of model cooling on transonic periodic flows on biconvex aerofoils are reported. The test conditions included shock interactions with laminar and turbulent boundary layers at a Reynolds number 0.9 million and model wall temperature to tunnel total temperature ratios 0.5 to 1.0. The results show large effects of model cooling on transonic periodic flows. The effects observed are thought to correspond to what would happen at high Reynolds numbers at adiabatic wall conditions.

NOMENCLATURE

c	model chord length (mm)
C_p	pressure coefficient
C_{p_w}	pressure coefficient measured at x/c=0.95
M	free stream Mach number
M_1	Mach number just upstream of the shock
$\bar{p}$	RMS pressure fluctuation (N/M^2)
q	kinetic pressure (N/M^2)
R	Reynolds number based on model chord
T_w, T_{ad}	wall and adiabatic recovery temperature (K)
t	time(s)
x,y	co-ordinates from the leading edge of model
n	non dimensional frequency parameter ($2\pi fc/u$)
f	frequency (Hz)
$F(n)$	contribution of $\bar{p}^2/q^2$ in frequency band Δf
$\sqrt{nF(n)}$	rms buffet excitation parameter $\bar{p}/(q\epsilon^{1/4})$
u	free stream velocity (m/s)
δ	boundary layer thickness
ϵ	$\Delta f/f$

1 INTRODUCTION

Recent reviews (Refs. 1,2) by Mabey show the large effects of heat transfer on boundary-layer development, transition and separation. Therefore testing a model at non adiabatic wall temperature effects drag and buffet measurements in the wind tunnel and prediction of landing performance of reentry vehicles. Further the above reviews suggest that the flow sensitivity to Reynolds number can be identified by observing the effect of variation in temperature ratios T_w/T_{ad}. Preliminary experimental investigations (Ref. 3) on 14% and 18% thick biconvex aerofoils, at transonic speeds and with laminar boundary-layer on the models support such a hypothesis. This paper presents further investigations on 14% thick biconvex aerofoils at transonic speed involving periodic shock oscillations and at test conditions corresponding to the boundary-layer approaching the shock wave (a) fully laminar and (b) fully turbulent.

2 REVIEW OF TRANSONIC PERIODIC FLOWS FOR ADIABATIC WALL CONDITIONS (T_w/T_{ad}= 1)

Biconvex aerofoils in transonic flows have an unusual form of buffet excitation, due to periodic transonic flows (Refs. 4,5,6,7). The excitation is confined to a single frequency and occurs over a narrow range of Mach numbers (Fig. 1). Some significant features of these flows are now enumerated. (i) They are caused by the dynamic effect of a disturbance field interacting with a shock induced separation. (ii) The necessary, but

92-16055

THIS DOCUMENT PROVIDED BY THE ABBOTT AEROSPACE
TECHNICAL LIBRARY
ABBOTTAEROSPACE.COM

not sufficient, criteria for the periodic flow to occur are that the free stream Mach numbers correspond to a shock Mach number range of M_1 approximately $1.14 < M_1 < 1.24$ for low Reynolds number ($R \approx 0.6 \times 10^6$) boundary-layer interactions and $1.22 < M_1 < 1.34$ for turbulent boundary-layer interaction at higher Reynolds numbers. (iii) Shock waves move in antiphase on the upper and lower surfaces during shock oscillations. (iv) The periodic flows can be modified, or even disappear, if the shock interaction occurs in the vicinity of boundary-layer transition (cf Fig. 2 for a thickness chord ratio of 14% with free transition). With these unusual and well defined flow characteristics it was expected that cooling would have a large effect on the shock oscillations with laminar and turbulent boundary-layers, and this is demonstrated in the experiments.

3. EXPERIMENTS

Experiments were made in a 100 mm x 100 mm intermittent transonic wind tunnel with a running time of 15 s at atmospheric pressure. The tunnel had closed side walls and perforated top and bottom walls. The porosity of the perforated walls was 9.6% (Fig. 3).

The models were 14% and thick biconvex aerofoils of various chord length (Table 1). It was expected that without a transition fix, the 25 mm and 50 mm chord models would produce laminar boundary-layer shock wave interaction. The type of shock wave boundary-layer interaction was inferred from the mean pressure distributions.

The models were made of two aluminium halves with 14 static orifices (made of stainless steel tubes) on the upper surface, 5 orifices at 5.00 mm intervals and 9 at 2.5 mm intervals. The materials chosen for the models had low thermal expansion and contraction rates at low temperatures. Compared to ambient temperature the contraction of the model at 198K was less than 0.2%. Thermocouples were installed within the model, twenty close to the surface and one at the centre line at mid span (Fig. 4). The thermocouples were copper-constantan type T which had an operating temperature range of 73 K to 673 K. The thermocouples had exposed tips to reduce the response time to approximately 70μs. A length of 10-15 mm of insulated leads was placed in an isothermal region and at low temperatures within the model to reduce lead wire thermal conduction errors. The halves of the models were bonded together by ECCOBOND 286 which also had a very low expansion rate.

For experiments with turbulent boundary layers transition was fixed by a strip of carborundum power 3 mm wide, at x/c = 0.08 and on both surfaces of the aerofoil.

Time history of T_w/T_{ad} on the model surface at three locations 1, 2 and 3 showed that for the adiabatic model the changes in T_w/T_{ad} with t are negligible. For the cooled model, the temperature of the surface increases due to heat transfer from the airflow to the model. Both mean and dynamic pressures were sampled 3s after the start of the run. The rate of change of temperature at this point was typically 4 K/S which corresponds to a value of $1/T_w \; \delta T_w/\delta t \leq 0.02\%$. The sampling period itself was less than 1s, during which the change in model temperatures was negligible. The change in mean static pressures on the model (as observed by continuous sampling) over a period of 1s was negligible when compared to changes observed when the wall temperature was changed in steps of 25 K. Further, the differences in temperatures recorded by thermcouples at various locations on the model were less than 4 K. Hence the model was at nearly uniform temperature during a run and the flow could be analysed as quasi-steady. No frost formation on the model was noticed even during runs at temperatures as low as 173 K.

4. Results

4.1 Datum experiments, adiabatic all conditions ($T_w/T_{ad} \simeq 1.0$)

Figs. 5a,b show mean pressure distributions obtained at several transonic free stream Mach numbers for the models with c = 50 mm, transition free and transition fixed ($R = 0.9 \times 10^6$) respectively. The range of Mach numbers include conditions at which periodic shock oscillations occur (Figs. 6a,b). Pressure distribution on c = 50 mm, transition free model (Fig. 5a) is typical of laminar shock wave

THIS DOCUMENT PROVIDED BY THE ABBOTT AEROSPACE
TECHNICAL LIBRARY
ABBOTTAEROSPACE.COM

boundary-layer interaction in transonic flow with an extended region of interaction and gradual pressure gradients in the interaction region. The pressure coefficient at the trailing edge has diverged at M = 0.80 indicating a separated boundary-layer on the model. The pressure distribution on c = 50 mm, transition fixed model (Fig. 5b) is similar to transonic shock wave turbulent boundary-layer interaction with sharp pressure gradients. Significant divergence of the trailing edge pressure has occurred on this model at M = 0.80.

The corresponding dynamic pressure measurements are shown by plots of $\overline{p}/q$ vs M in Fig. 6. There exists a narrow range of free stream Mach numbers in which relatively high levels of pressure fluctuations occur, due to periodic shock oscillations. For the LBL interactions (Fig. 6a) this range is M = 0.76 - 0.84 and the peak levels of $\overline{p}/q$ = 10%. For TBL interaction (Fig. 6b) both the range of shock oscillations (M = 0.76 to 0.83) and the peak level of $\overline{p}/q$ (6%) are relatively smaller. These results are broadly in agreement with the results obtained with small scale models with a side wall pressure transducer (Ref. 5). The levels of $\overline{p}/q$ are smaller, as one would expect when compared with measured levels with a surface mounted transducer (Ref. 6). The second peak occurring for 14% thick aerofoil has been observed before (Ref. 8).

Transonic periodic flows have a fundamental frequency and various harmonics. Fig. 7 shows typical spectra of pressure fluctuations for both models and for three Mach numbers for each model. For each of the models two of the Mach numbers are outside the range of shock oscillations and the third Mach number corresponds to the peak level of $\overline{p}/q$. The spectra are plotted in the form $\sqrt{n}F(n)$ vs n. For the LBL interaction (Fig. 7a) the spectrum at M = 0.79 has a peak at n = 1.0 (f = 800 Hz). There are no peaks at M = 0.75 and 0.82 indicating random rather than strong periodic oscillations. For the TBL interaction (Fig. 7b) the spectrum at M = 0.8 has a peak of n = 0.8 (f = 687.5 Hz).

4.2 Experiments with cooled walls ($T_w/T_{sd} < 1.0$)

The effect of model cooling on the pressure distributions for both models is shown in Fig. 8. The free stream Mach numbers chosen for these cases M = 0.79 and 0.80 correspond to peak levels of $\overline{p}/q$. Although experiments were conducted at several temperature values, for clarity the pressure distributions at only three values of T_w/T_{sd} = 0.99, 0.68 and 0.58 are shown in these figures. For the LBL interaction (Fig. 8a) the effect of cooling on the pressure distribution in the interaction region is large. Reduction in T_w/T_{sd} values resulted in an increase in shock Mach numbers and the pressure gradients in the interaction region and decrease in the extent of interaction. The pressure distribution in the interaction region at low values of T_w/T_{sd} resembles that of a turbulent boundary-layer shock wave interaction. Cooling resulted in strong pressure gradients which could have triggered boundary-layer transition in the much thinner layer at the shock. For the TBL interaction (Fig. 8b) the effect of reducing T_w/T_{sd} values on pressure distribution is smaller when compared to LBL interaction but still significant.

The effects of cooling on shock boundary-layer interaction observed here are in general similar to those observed by Inger (Ref. 9) in a transonic turbulent boundary-layer interaction and by Frishett (Ref. 10) in a supersonic turbulent boundary-layer interaction. The model proposed by Elfstrom (Ref. 11) in supersonic flow also indicates similar effects.

The effects noticed here are a direct result due to the cooling of the reductions in boundary-layer thickness and sonic height in the boundary-layer approaching the shock wave. Cooling reduces the viscosity and increases the density near the model surface which increases the "effective" Reynolds number. This should result in larger velocities (smaller velocity defect) near the surface and reduced sonic height. The reduced sonic height reduces the communication of signals (upstream propagation) across the shock and therefore produces larger pressure gradients. Decrease in temperature should reduce the velocity of sound and hence increase Mach numbers near the surface.

At low Reynolds numbers and for a laminar boundary-layer (Fig. 8a) the

THIS DOCUMENT PROVIDED BY THE ABBOTT AEROSPACE
TECHNICAL LIBRARY
ABBOTTAEROSPACE.COM

viscous region is of the same thickness as the sonic layer and therefore cooling has a large effect in both dimensions. For a turbulent boundary-layer (Fig. 8b) the viscous layer is relatively small compared to the sonic height and the effect of cooling is primarily due to the change in sonic height. Further the heat transfer effects (region of large temperature gradients) due to cooling is felt over a smaller height in the case of turbulent boundary-layer when compared to laminar boundary-layer.

Fig. 8 also shows that in spite of the increase in shock strength associated with cooling, the pressure coefficients near the trailing edge have not changed significantly. This suggests that the reduction in T_w/T_{ad} has a favourable effect on the separated flow either indirectly as mentioned above or directly. Fig. 8 also implies that a reduction in T_w/T_{ad} increases M_1 with no appreciable change in the c_p near the trailing edge. The effect of cooling on the trailing edge pressure coefficient for a fixed value of M can be seen from Fig. 9 which shows plots of c_p near the trailing edge vs M_1 for T_w/T_{ad} = 0.99 and 0.7. For a given shock strength and for both laminar and turbulent boundary-layers the effect of cooling is to improve the trailing edge pressures. As shown (Fig. 12) the latter position of the peak Mach number on the aerofoil was not sensitive to the changes in T_w/T_{ad}. Although for a given M_1 the pressure gradients at the shock were not the same at different T_w/T_{ad} ratios, the Figs. 9 a and b indicate large effects due to cooling on the boundary-layer development downstream of the shock interaction.

Figs. 10 shows the important effect of cooling on the random and periodic buffet excitation. For a laminar boundary-layer interaction (Fig. 10a) the maximum values of p/q were reduced from 10% to 4% when T_w/T_{ad} was reduced from 0.99 to 0.59. This is a large reduction in pressure fluctuation levels. The corresponding reduction in p/q levels for a turbulent boundary-layer interaction (Fig. 10b) is 6% to 4% which is relatively smaller.

As seen from typical spectra of pressure fluctuations (Fig. 11) cooling reduces the levels of fundamental frequency and the harmonics on interactions with shock oscillations.

Fig. 12 based on typical Schlieren optical flow visualisation clearly shows the effect of cooling on the shock motion, its strength and the wake. At adiabatic wall conditions (Fig. 12a) the shock is relativley weak and its position is time dependent. The wake is relatively wide. At cooled wall conditions the shock is relatively stronger and its position is virtually independent of time. The wake is relatively thin.

Figs. 13 to 18 refer to typical test conditions both laminar and turbulent boundary-layer interactions at a fixed free stream Mach number and at several T_w/T_{ad} ratios in the range $0.5 < T_w/T_{ad} < 0.99$. The Mach numbers chosen were M = 0.79 for laminar boundary-layer interaction and 0.80 for turbulent boundary-layer interaction which gave large shock oscillations as mentioned earlier.

Cooling the models had only a weak influence on the position of the shock Mach number (Fig. 13). However for a laminar boundary-layer interaction, the pressure distribution upstream of the interaction to some extent and the interaction region to a large extent are affected by cooling. The correponding effects with turbulent boundary-layer interaction was smaller. The shock Mach number M_1 (Fig. 14), the interaction length L^*/c, (Fig. 15) calculated by the procedures suggested by Pearcy (Ref. 13) and Delery (Ref. 14) the dynamic pressures (Fig. 16) and trailing edge pressures (Fig. 17) and the reduced frequency (Fig. 18) are all affected by cooling. Some results from Ref. 6 at a higher Reynolds number of 7×10^6 and at adiabatic wall conditions are shown in Figs. 14, 15 and 18 for comparison. It is clear that at low values of T_w/T_{ad}, M_1, L^*/C and n approach values are correspondingly much higher Reynolds number flows at adiabatic wall conditions.

5. DISCUSSION

Figs. 5 to 18 show that model cooling has effects on the mean and dynamic flow field about biconvex aerofoils at transonic speeds. The effects on shock interaction involving laminar boundary-layer is larger when compared with shock interaction involving turbulent boundary-layer. It is likely that

THIS DOCUMENT PROVIDED BY THE ABBOTT AEROSPACE
TECHNICAL LIBRARY
ABBOTTAEROSPACE.COM

cooling has an effect on both the sonic height and boundary-layer thickness for laminar boundary-layers whereas the influence of cooling on the turbulent boundary-layer is primarily through the laminar sublayer.

The figures also suggest that cooling can change the nature of shock wave interaction from a laminar to turbulent boundary-layer due to pressure gradients or increase in effective roughness or to a combination of both. Increase in pressure gradients should increase boundary-layer to separation but the results indicate that cooling reduces separation.

For an adiabatic flow, reduced trailing-edge pressure divergence would normally be taken to indicate a reduction in the severity of separation effects. If we assume that the separation position is unchanged at the lower values of T_w/T_{aw} (shock position is unchanged), the length of the separation is manifestly unchanged. The change in the trailing-edge pressure divergence must be attributed then to a reduction in the thickness of the separation bubble and this is consistent with what was expected when these tests were planned[1,2]. Similar trends, albeit of reduced magnitude, are observed for comparable tests with fixed transition. Hence taken together the measurement with both free and fixed transition suggest that flows sensitive to large indirect scale effects can be identified by model cooling as suggested previously,[1,2].

With regard to the unsteady measurements, the reduction in the amplitude of periodic pressure fluctuations is consistent with greatly reduced shear layer thicknesses due to model cooling. Fig. 18 shows a reduction in n with the decrease in T_w/T_{aw}. It is interesting to consider how the reductions in shear layer thickness reduce the frequency parameter of the oscillations. The frequency of these oscillations is determined by the time taken for disturbances to convect downstream from the shock to the trailing-edge (through the shear layer) and also by the time taken for these reflected disturbances to pass upstream from the trailing-edge to the shock, (see discussion of Fig. 13 in Ref. 15). The convection velocity decreases as the parameters fc/u (Fig. 13c of Ref. 15) and $f\delta/u$ decrease. Hence the time taken for disturbances to propagate from the shock to the trailing edge will increase, lowering the frequency parameter. Hence cooling the model, which decreases δ, should decrease the convection velocity and hence lower the frequency parameter, just as observed. It should be noted that also there will be changes in the time taken for disturbances to propagate upstream from the trailing edge to the shock because of the changes in the mean pressure distribution. As the frequency parameter of the periodic flow falls, the aerodynamic resonance moves "off-tune" and the amplitude falls. The flow reverts to the normal type of buffet excitation. Hence it is reasonable that the level of random pressure fluctuations should increase. A similar increase in random pressure fluctuations is observed with fixed transition. Hence the decrease in periodic excitation and the increase in random excitation should be observed for high Reynolds number flows with adiabatic wall boundary conditions. This has yet to be confirmed.

Some limitations of these tests must be admitted. So far there has been no opportunity to attempt surface flow visualisation (such as oil flow) which were so successful for the adiabatic experiments,[4,5,6].

There has been no opportunity to monitor the state of the boundary-layer. Transition has been detected by surface hot films in cryogenic wind tunnels and hence they should work equally well on cooled models. Despite these limitations, Figs. 8 - 18 should be of interest to anyone considering the problem of simulating high Reynolds number flows at transonic speeds.

6. CONCLUSION

These preliminary tests on biconvex aerofoils with free and fixed transition show that periodic flows at transonic speeds can be modified strongly by cooling, as expected. The five main effects observed as the model is cooled are as follows.

1. A marked increase in the local Mach number at the shock, which remains in much the same position.

THIS DOCUMENT PROVIDED BY THE ABBOTT AEROSPACE
TECHNICAL LIBRARY
ABBOTTAEROSPACE.COM

2. A decrease in trailing-edge pressure divergence (indicative of a reduced length scale of the separation normal to the surface).

3. A decrease in the amplitude of the periodic pressure fluctuations consistent with a reduced shock amplitude.

4. A decrease in the frequency parameter of the periodic shock oscillations, due to the combined effects of increased downstream convection and upstream propagation times.

5. An increase in the random pressure fluctuations, associated with 3 and 4 above.

All of these observations are thought to correspond with what would happen to adiabatic flows at greatly increased Reynolds numbers.

7. REFERENCES

1. Mabey, D.G., "Effects of heat transfer in aerodynamics and possible implications for wind tunnel tests", Progress in Aerospace Sciences,Vol. 27, No. 4, pp 267-303, 1991.

2. Mabey, D.G., "Heat transfer effects on aerodynamics and implications for wind tunnel tests". To be published in AIAA J.Aircraft.

3. Raghunathan, S., Zarifi-Rad, F. and Mabey, D.G., "Effect of model cooling on periodic transonic flow", AIAA Paper 91-1714.

4. McDevitt, J.B., "Super-critical flow about a thick circular aerofoil", NASA TM 78549, 1979.

5. Mabey, D.G., "Oscillatory flow from shock induced separation on biconvex aero-foils of varying thickness in ventilated wind tunnels", AGARD CP 296, Paper 11, 1980.

6. Mabey, D.G. Welsh, B.L. and Cripps, B.E., "Periodic flow on a rigid 14% thick biconvex wing at transonic speeds", RAE TR 81-059, 1981.

7. Raghunathan, S., Hall, D.E. and Mabey, D.G., "Alleviation of shock oscillations in transonic flow by passive control", The Aeronautical J., Vol. 94, No. 937, pp 245-250, 1990.

8. Gibb, J., "The cause and cure of periodic flows at transonic speeds", ICAS, Paper 3.10.1, 1988.

9. Inger, G.R., Lynch, F.T. and Fancher, M.F., "A theoretical and experimental study of non-adiabatic wall effects on transonic shock/boundary-layer inter-action", AIAA Paper 83-1421, 1983.

10. Frishett, J.C., "Incipient separation of a supersonic turbulent boundary-layer including effects of heat transfer", PhD thesis, University of California, 1971.

11. Elfstrom, G.M., "Turbulent separation in hypersonic flow", Imperial College of Science and Technology, Aero Report 71-16, 1971.

12. Settles, G.S., "An experimental study of compressible turbulent boundary-layers at high Reynolds number", PhD thesis, Aerospace and Mechanical Sciences Dept., Princeton University, 1975.

13. Pearcy, H.H., "Shock induced separation and its prevention by design and boundary-layer control". In: Boundary Layer and Flow Control, Vol.2, (ed. G.V. Lachmann) Pergamon Press, 1961.

14. Delery, J.M. "Shock wave/ turbulent boundary-layer inter-action and its control", Prog. Aerospace Sci. Vol. 22, pp 209-280, 1985.

15. Mabey, D.G., "Physical phenomena associated with unsteady transonic flows". Progress in Astro. and Aero., V.120, 1989, pp 1-56.

THIS DOCUMENT PROVIDED BY THE ABBOTT AEROSPACE
TECHNICAL LIBRARY
ABBOTTAEROSPACE.COM

Aerofoil	**14% thick biconvex**
c	50 mm
R	0.9×10^6
M	0.75-0.88
T_w/T_{ad}	0.51-0.99
Transition	**Free and Fixed**

Table 1

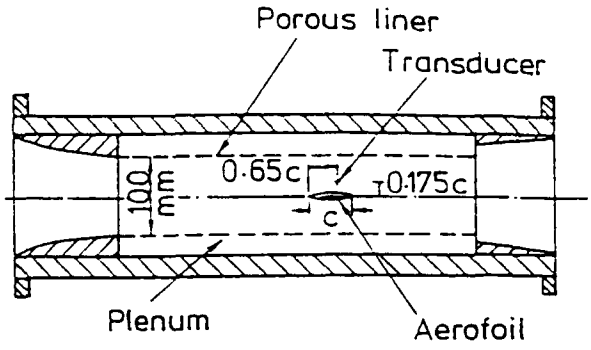


Fig. 3. Model in the transonic tunnel.

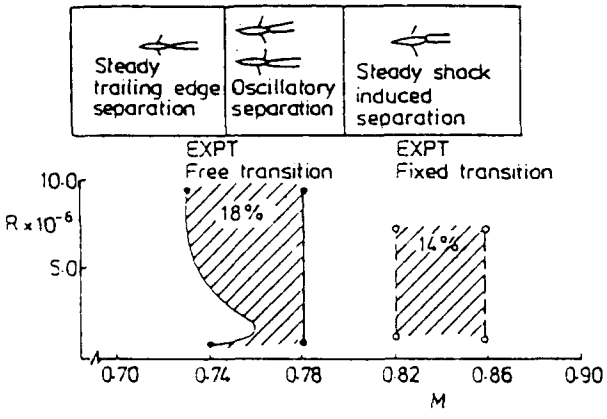
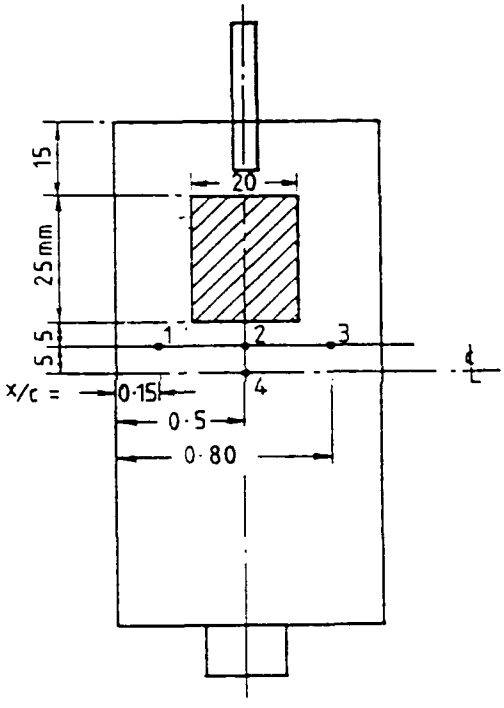


Fig. 1. Range of periodic flows.



Thermocouples (1,2,3,4) placed in 1mm dia.holes, 0·5mm below the surface.

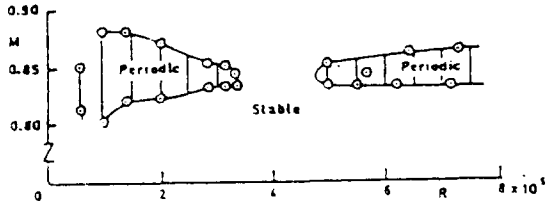


Fig. 2. Effect of Reynolds number on periodic flow range over a biconvex wing.

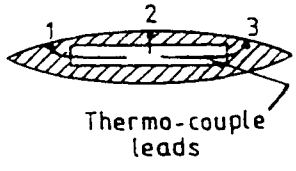
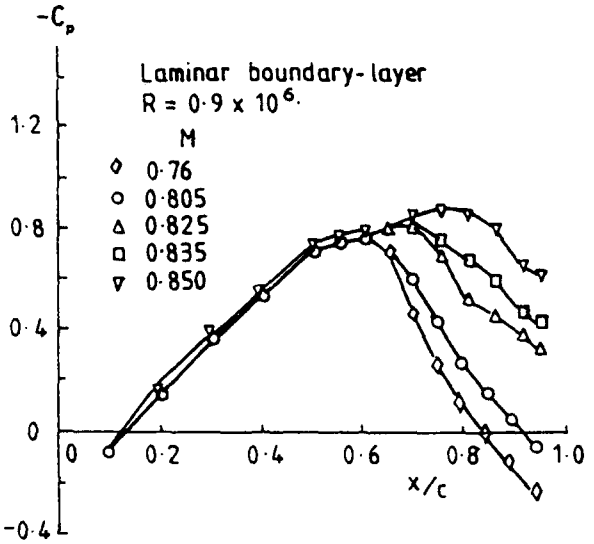
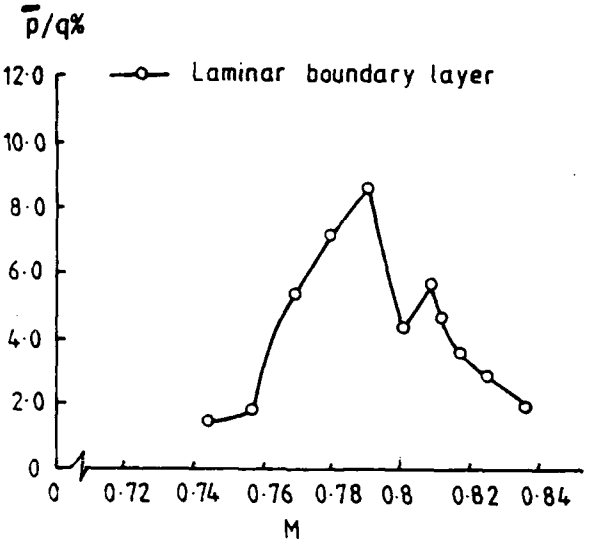
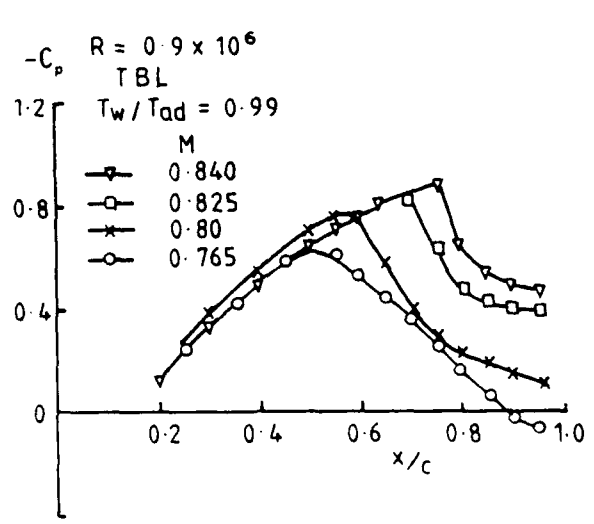


Fig. 4. Details of thermocouples.

THIS DOCUMENT PROVIDED BY THE ABBOTT AEROSPACE
TECHNICAL LIBRARY
ABBOTTAEROSPACE.COM







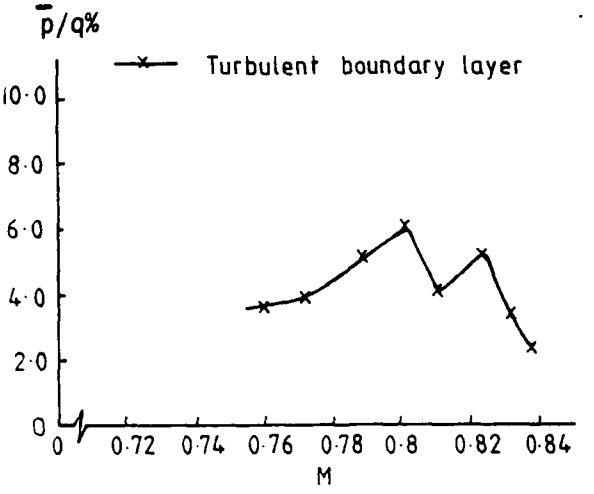


Fig. 5. Typical pressure distributions.
T_w/T_{ad} = 0.99

Fig. 6. Variation of unsteady pressures with Mach number.
T_w/T_{ad} = 0.99

This Document Provided by the ABBOTT AEROSPACE
TECHNICAL LIBRARY
ABBOTTAEROSPACE.COM

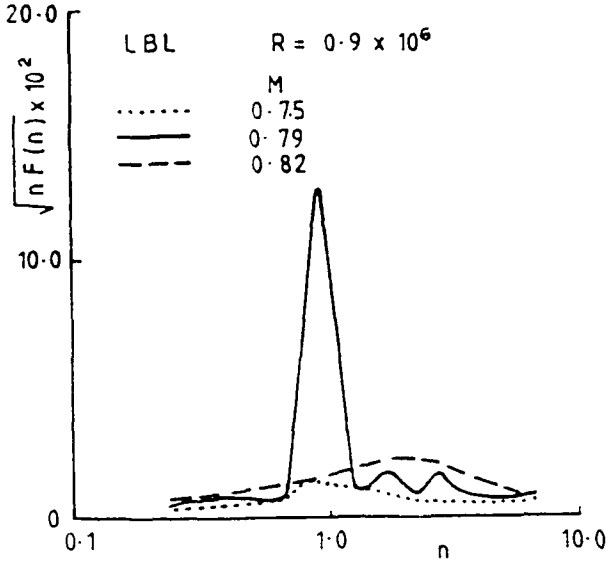


Fig. 7(a)

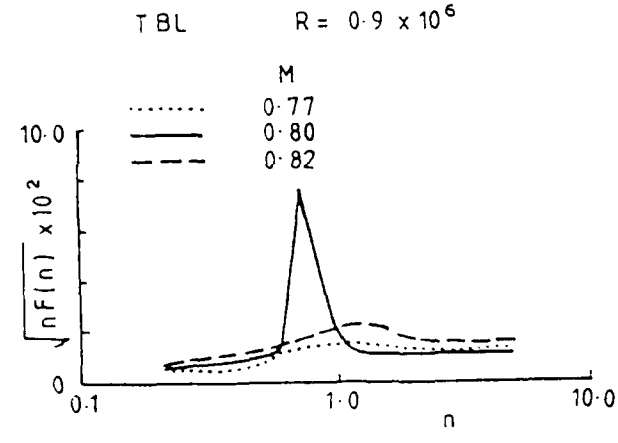


Fig. 7(b)

Fig. 7. Typical spectra.
T_w/T_{ad} = 0.99

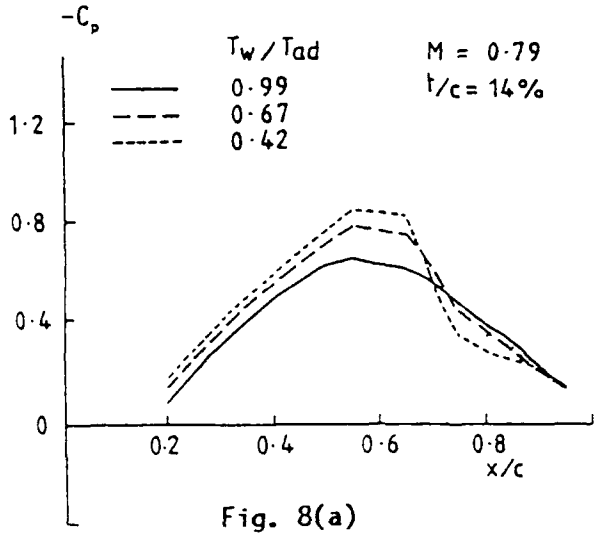


Fig. 8(a)

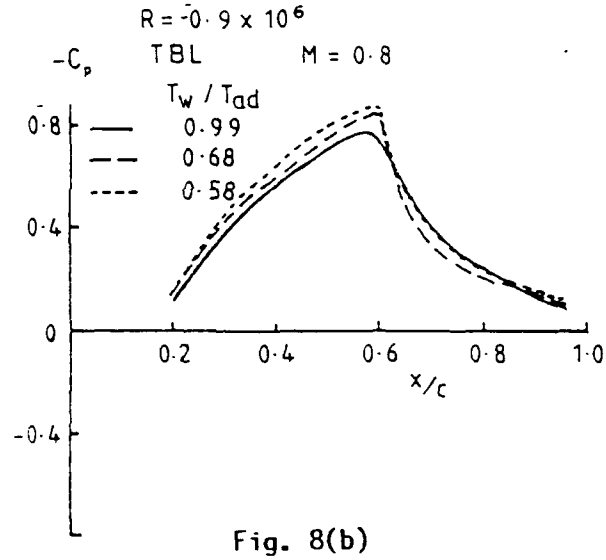
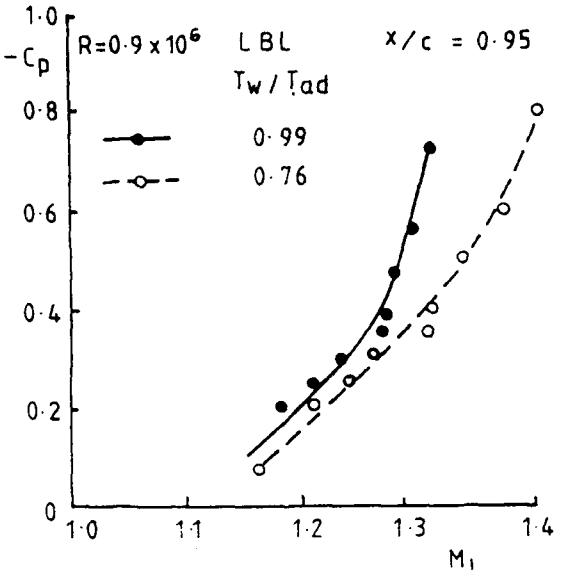


Fig. 8(b)

Fig. 8. Effect of wall temperature ratio on pressure distribution.

THIS DOCUMENT PROVIDED BY THE ABBOTT AEROSPACE
TECHNICAL LIBRARY
ABBOTTAEROSPACE.COM



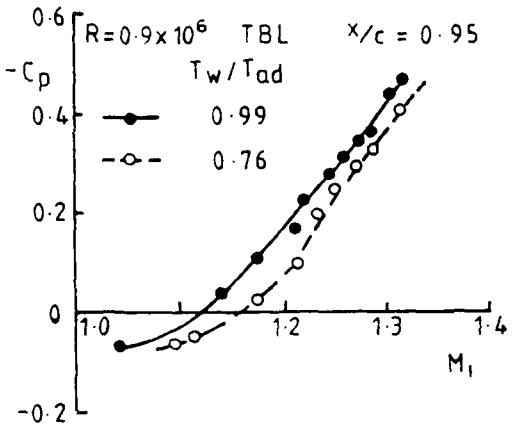
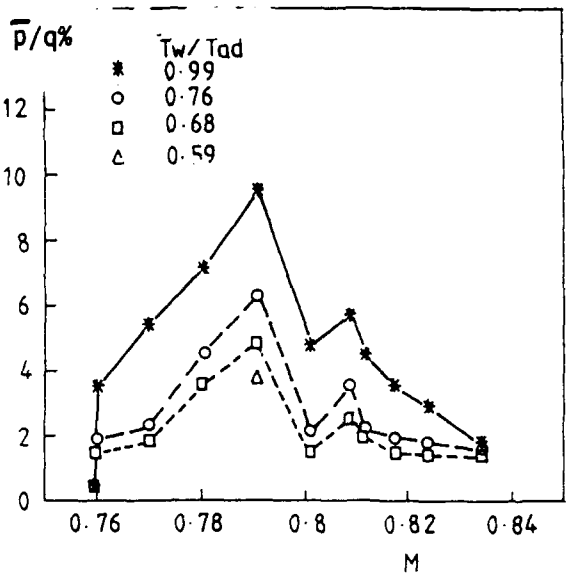


Fig. 9. Pressure coefficient at trailing edge as a function of shock Mach number.



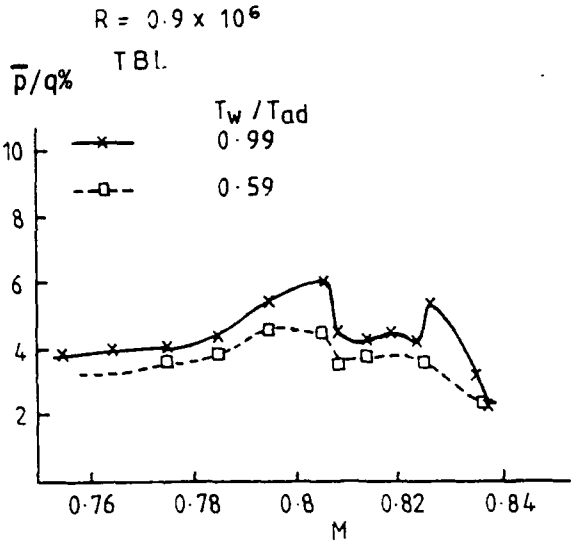


Fig. 10. Variation of pressure fluctuations with Mach number. Several temperature ratios.

THIS DOCUMENT PROVIDED BY THE ABBOTT AEROSPACE
TECHNICAL LIBRARY
ABBOTTAEROSPACE.COM

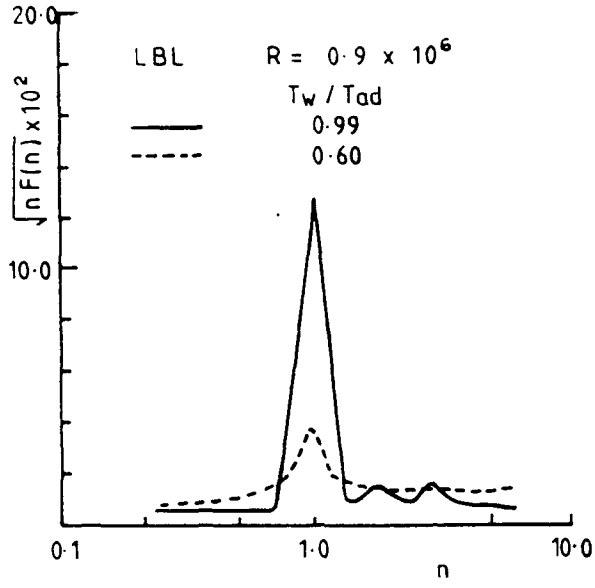


Fig. 11(a). Effect of wall temperature ratio on excitation spectra LBL.

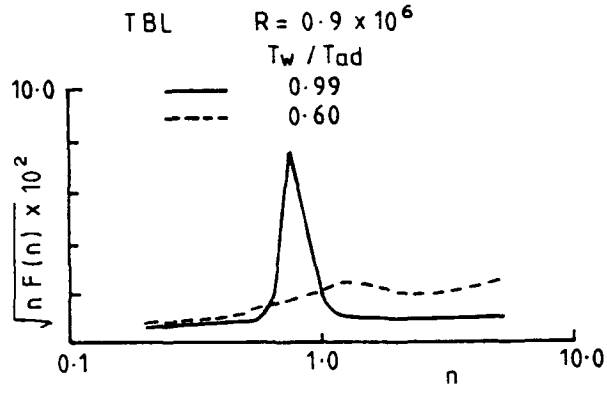


Fig. 11(b). Effect of wall temperature ratio on excitation spectra TBL.

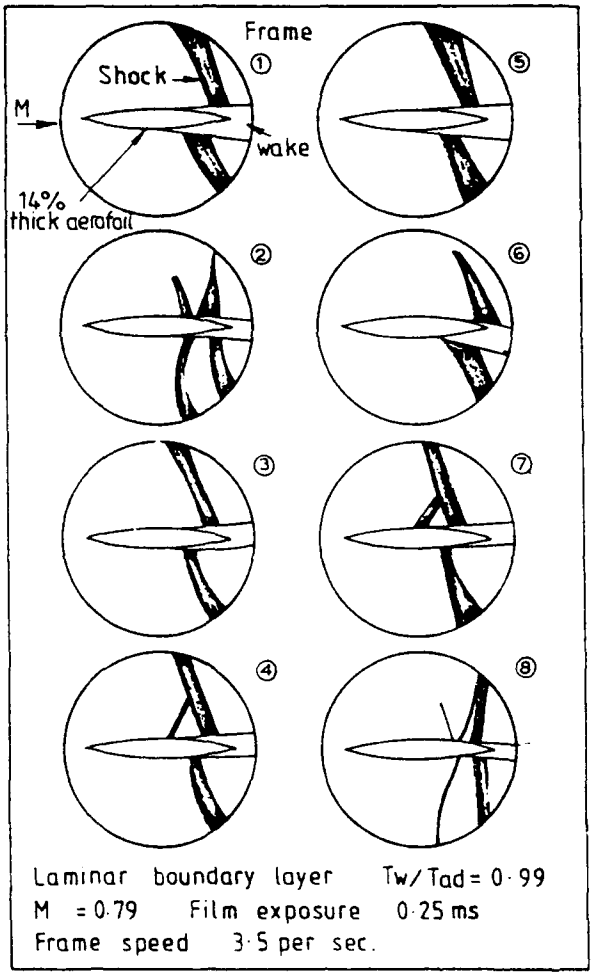


Fig. 12(a). Schlieren pictures: Laminar boundary layer M = 0.79. T_w/T_{ad} = 0.99. Film exposure = 0.2…s, frame speed 3.5 per sec. Film speed 1600.

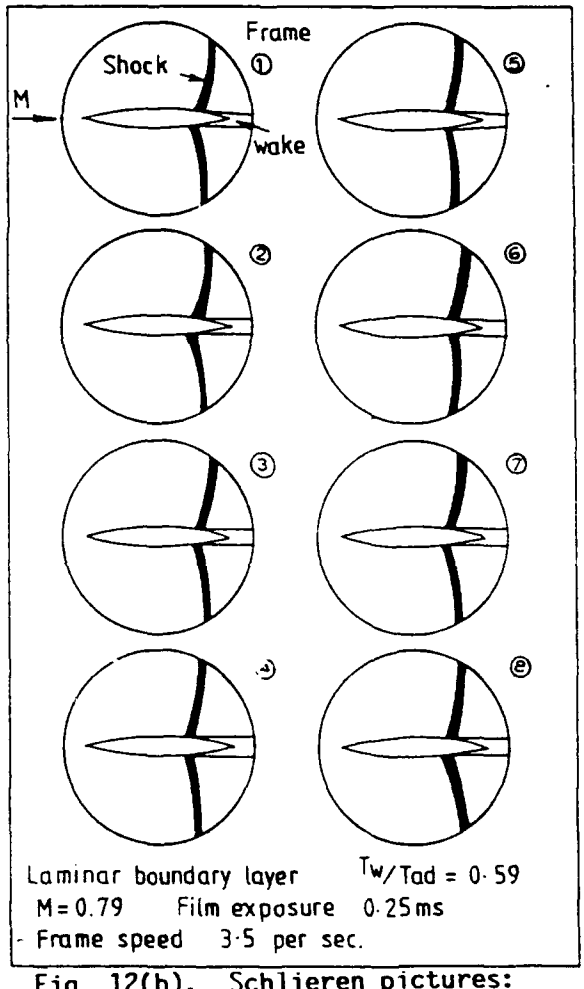


Fig. 12(b). Schlieren pictures: Laminary boundary layer M = 0.79, T_w/T_{ad} = 0.59. Film details are the same as in Fig. 12(a).

THIS DOCUMENT PROVIDED BY THE ABBOTT AEROSPACE
TECHNICAL LIBRARY
ABBOTTAEROSPACE.COM

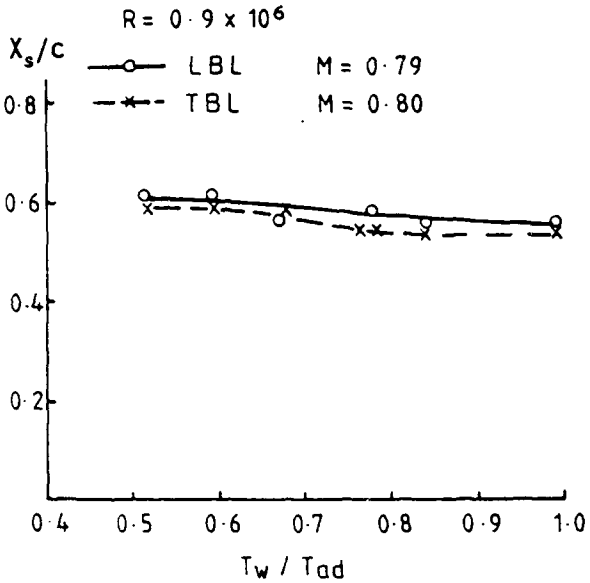


Fig. 13. Variation of shock position with wall temperature ratios.

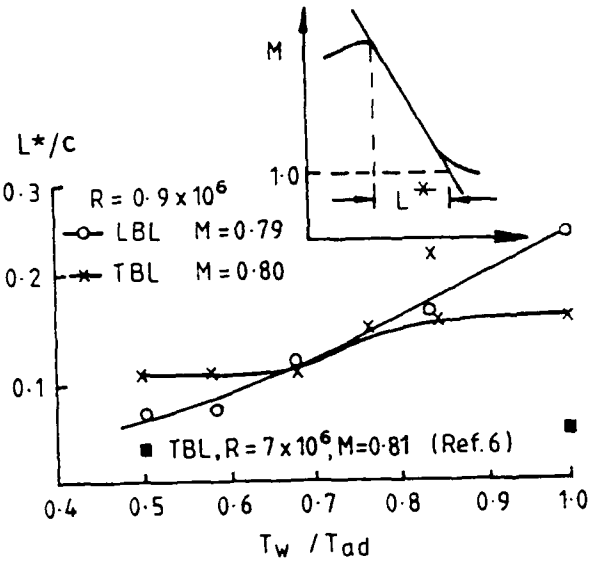


Fig. 15. Variation of interaction length with wall temperature ratios.

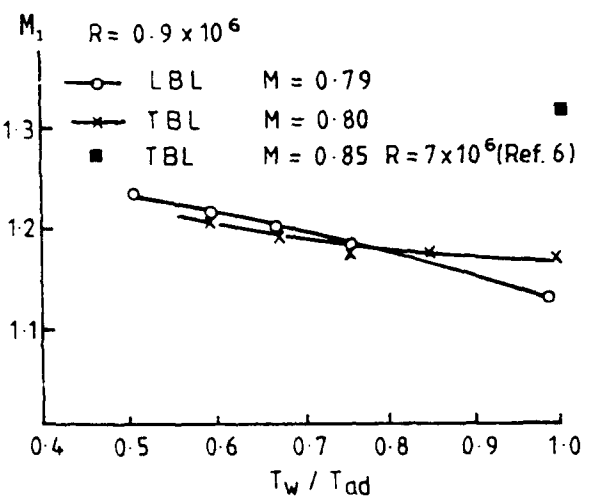


Fig. 14. Variation of shock Mach number with wall temperature ratios.

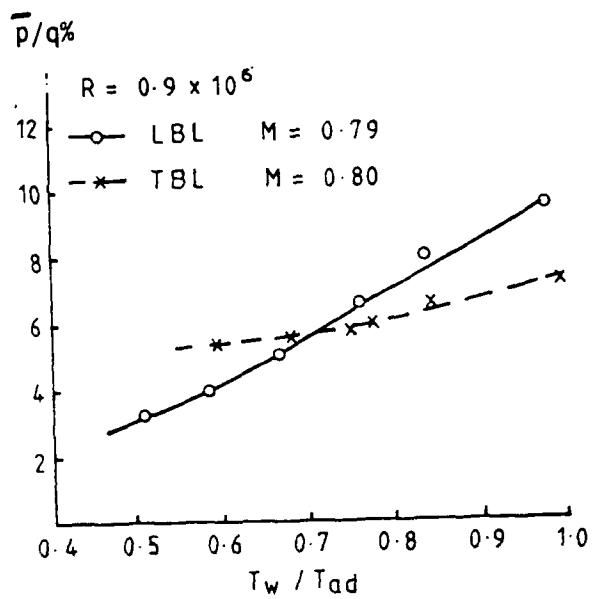


Fig. 16. Variation of dynamic pressures with wall temperature.

THIS DOCUMENT PROVIDED BY THE ABBOTT AEROSPACE
TECHNICAL LIBRARY
ABBOTTAEROSPACE.COM

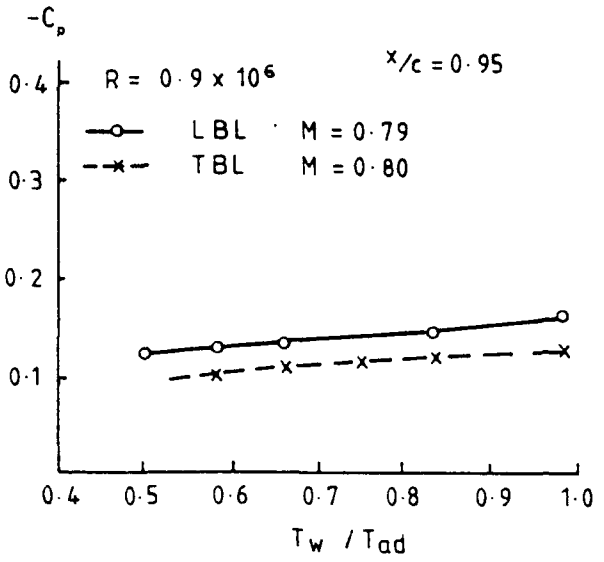


Fig. 17. Variation of trailing edge C_p with T_w/T_{ad}.

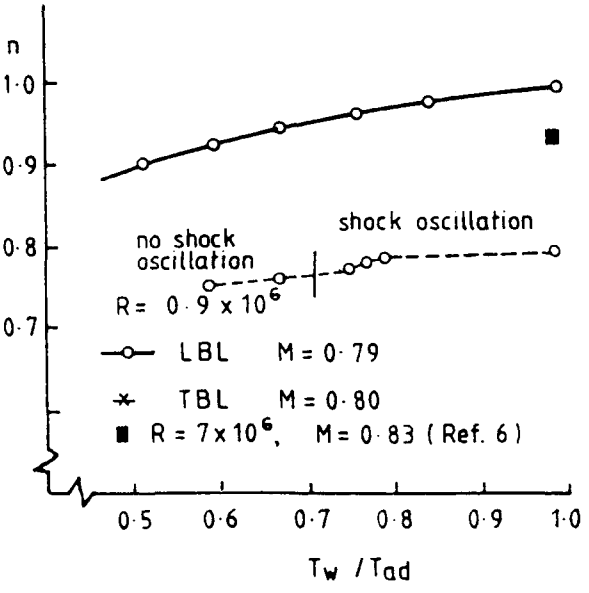


Fig. 18. Variation of reduced frequency with wall temperature ratios.

THIS DOCUMENT PROVIDED BY THE ABBOTT AEROSPACE
TECHNICAL LIBRARY
ABBOTTAEROSPACE.COM

AD-P007 818

A REVIEW OF SCALE EFFECTS ON SURFACES IN UNSTEADY MOTION

D. G. Mabey
Aerodynamics Department
Royal Aerospace Establishment
Bedford MK41 6AE, UK

92-16056

SUMMARY

The importance of scale effects is recognised generally in steady aerodynamics but is often ignored in unsteady aerodynamics. An attempt is made to remedy this situation by the compilation of a review of information on the influence of Reynolds number from a wide range of unsteady aerodynamic tests, with particular reference to wing flows. The unsteady tests considered here relate to surfaces in unsteady motion and include dynamic tests of aerofoils and wings, pressure measurements, oscillatory control surface derivatives, and stability derivatives.

The review suggests that for the recommended model conditions with fixed transition, scale effects are small for fully-attached or well-separated flows, but may be large close to incipient separation. With fixed transition extrapolation from model to full-scale Reynolds numbers is usually possible. In contrast, with free transition, scale effects can be large for both attached and separated flows, and extrapolation from model to full-scale Reynolds numbers is usually extremely difficult.

Much more research is needed into the magnitude of scale effects on unsteady flows at transonic speeds. Some test cases for the prediction of scale effects in unsteady aerodynamics are suggested. A review dealing with surfaces in steady motion was given at ICAS 1990, Stockholm.

LIST OF SYMBOLS

c , $\bar{c}$, $\bar{\bar{c}}$	local, mean and aerodynamic mean chords
c_o	root chord
C_L	lift coefficient
C_N	normal force coefficient
C_p	steady pressure coefficier
$R(C_p)$, $I(C_p)$	real and imaginary components of oscillatory pressure coefficient
C_m	pitching moment coefficien
f	frequency (Hz)
h_β , $h_{\dot\beta}$	hinge moment derivatives: stiffness and damping
M	free stream Mach number
p_t	tunnel total pressure
$q = \frac{1}{2}\rho U^2$	kinetic pressure
R	unit Reynolds number
s	wing semi-span
T	time for transient spoiler motion
t	time
t_a	time to achieve maximum adverse lift
t_f	time to achieve final lift
U	free stream velocity
x , y , z ,	co-ordinates (x streamwise)
x_t	boundary transition position (mean or onset)
α	incidence (°)
α_c	canard effective incidence
$\dot\alpha$	rate of change of incidence
δ_f , δ_s	flap and spoiler deflections
θ	boundary layer momentum thickness
η	semi-span ratio y/s
η_c	canard setting angle (°)
$\nu = \omega c/U$	frequency parameter based on local chord
$\omega = 2\pi f$	circular frequency (rad/s)

1 INTRODUCTION

A comprehensive review of the problems of boundary layer simulation and control in wind tunnels is now available (Ref 1). This includes a review of boundary layer simulation procedures, a simulation/extrapolation methodology and a discussion of the physical aspects of boundary layer separation and the associated research requirements. However, the emphasis is primarily on steady measurements, although there is some brief discussion of scale effects on buffet onset. Further evidence about scale effects on steady measurements is provided for combat aircraft by Peckham and Woodward (Ref 2) and for both combat and transport aircraft at transonic speeds by Haines (Ref 3).

The present paper provides a supplement to these references by reviewing the comparable evidence regarding scale effects on unsteady measurements, with particular reference to wing flows. This evidence is severely limited, but it is enumerated here both to stimulate discussion and to ensure that the possibility of significant scale effects is considered when planning wind tunnel and flight test programmes for unsteady measurements. In preparing this brief review some evidence has had to be discarded due to uncertain aeroelastic effects.

In order to provide an indication of the origin of scale effects, section 2 of the present paper inevitably involves some repetition and duplication of Ref 1 but this has been kept as small as possible. Section 3 is the heart of the paper and reviews scale effects on different types of unsteady experiment with surfaces in unsteady motion. Section 4 provides some conclusions and recommendations.

2 ORIGIN OF SCALE EFFECTS AND IMPLICATIONS FOR UNSTEADY AERODYNAMICS

Scale effects as between measurements on models and aircraft in flight may be attributed to two inter-related causes

THIS DOCUMENT PROVIDED BY THE ABBOTT AEROSPACE
TECHNICAL LIBRARY
ABBOTTAEROSPACE.COM

which are discussed. Then options for investigating scale effects, and the character of scale effects are considered.

2.1 Origin of scale effects

2.1.1 Failure to achieve full scale Reynolds number

The common and generally-recognised cause of scale effects is the inability of a wind tunnel test to reproduce the full-scale Reynolds number. The Reynolds number (based on an appropriate reference length) such as the aerodynamic mean chord $\bar{c}$, or a boundary layer momentum thickness, θ, represents the ratio of the inertia forces in the fluid to the viscous forces. Based on the aerodynamic mean chord of a wing, the Reynolds number is typically in the range of only 10^6 to 10^7 for a model in a conventional wind tunnel, compared to 10^7 to 10^8 for an aircraft in flight. [The corresponding Reynolds number for a helicopter blade in flight would be between 4×10^6 and 6×10^6.]

For fully-turbulent local flows, Reynolds number determines the thickness of attached boundary layers, the conditions for separation and the thickness of separated shear layers. Fig 1a shows an aerofoil at a high angle of incidence having a flow separation at about mid-chord for a low Reynolds number. The changes in boundary layer thickness as the Reynolds number is increased (Fig 1b) are large on the upper surface (with adverse pressure gradients) because of changes in separation position. The changes in boundary layer thickness with Reynolds number are much smaller on the lower surface (with favourable pressure gradients and attached boundary layers). In this example the changes in separation position on the upper surface affect the overall circulation about the aerofoil and the pressure distribution on both surfaces. Hence according to Elsenaar (Ref 4) there are two types of Reynolds number effects. The first type are direct effects, due to variations in boundary layer thickness with a fixed pressure distribution. The second type are indirect effects, due to changes in pressure distribution caused by changes in boundary layer displacement thickness and wake effects. Fig 1c illustrates how both types of Reynolds number effect might be identified from steady pressure distributions.

2.1.2 Failure to achieve full scale transition position

The less familiar cause of scale effects is the failure of a model test to reproduce the position of boundary layer transition, x_t, appropriate to full scale. This short-coming can create scale effects even when the Reynolds number of the tunnel test duplicates the full scale value. For this condition often the transition position on the model will be further forward, either because of surface roughness or because of flow unsteadiness, including noise, in the wind tunnel absent in flight. With the incorrect transition position, the attached boundary layer thickness will be incorrect, conditions at separation will be incorrect (separation may be advanced or delayed according to the details of the problem) and the thickness of the separated shear layers will be incorrect (Fig 2). With varying transition position, changes with Reynolds number are thus unlikely to be smooth and monotonic, particularly in the range from 10^6 to 10^7. Generally the failure to fix transition at the appropriate point on a wind tunnel model is probably more serious than the failure to reproduce the correct Reynolds number. [Some discussion of the most appropriate point is included in Ref 1.]

2.2 Possible methods for the investigation of scale effects

With two inter-related causes for scale effects (the incorrect transition position and the incorrect turbulent boundary layer thickness) model experiments might investigate the sensitivity of particular measurements by three possible methods. The objective is to be able to extrapolate from measurements on a model (at say $R\bar{c} = 3 \times 10^6$) to predict the performance of an aircraft (say at $R\bar{c} = 30 \times 10^6$). For transonic speeds boundary layer thicknesses and shock positions must be correctly represented.

The three methods are:

(1) Variations in transition position at constant Reynolds number.

(2) Variations in Reynolds number with fixed transition.

(3) Variations in transition position combined with variations in Reynolds number.

The Reynolds number may be increased by increasing the model scale, or by increasing the free stream density at constant Mach number (as in a conventional wind tunnel) or by lowering the total temperature (as in a cryogenic wind tunnel). Method (1) is generally inconvenient but is exploited in some investigations. Only the transition position is varied so that extrapolation to full scale is not difficult. In a conventional wind tunnel for Method (1), [unlike Methods (2) and (3)] the measurements have the same precision for every transition position. An example may be cited: it is fairly common practice at transonic speeds to vary the transition position (forced by roughness at constant Reynolds number) upstream of the shock, to provide a varying value of $R\theta$ there, as discussed by Haines (Ref 3). Although distributed roughness is usually used to fix transition, the air-injection technique can be used, as in Ashill's tests on a large swept panel model (Ref 5). Here transition could be controlled at constant Reynolds number by the injection of air near the leading-edge of a swept wing. [The unit Reynolds number was also varied for some tests.] The air-injection technique of fixing transition is attractive because lines of air-holes could be provided at a series of streamwise stations to give a range of different transition positions without stopping the tunnel. In addition, it allows useful control of the

THIS DOCUMENT PROVIDED BY THE ABBOTT AEROSPACE
TECHNICAL LIBRARY
ABBOTTAEROSPACE.COM

disturbance needed to fix transition thereby avoiding 'overfixing'. Overfixing transition can give misleading results, as discussed elsewhere for steady flows.

Method (2) is exploited widely in pressurised wind tunnels, such as the RAE 8ft x 8ft Tunnel, but hitherto has been little used in the low speed RAE 5m Tunnel (possibly due to the difficulties of fixing transition at high lift condition at low speeds) or in the new cryogenic facilities. With only one parameter varied (Reynolds number), extrapolation to full scale should be possible, even if the measurements are not always monotonic.

Method (3) is exercised whenever wind tunnel tests are made with free transition and varying Reynolds number. With two parameters varied simultaneously it is much more difficult to extrapolate to full scale and changes with Reynolds number are unlikely to be smooth and monotonic. [Morkovin once proposed the term 'uncontrolled transition' for this method.] It is unfortunate that many tests in unsteady aerodynamics are made with free transition. This is particularly unfortunate when tests are made on NACA 0012 aerofoils, for which the static aerodynamic characteristics are known to be sensitive to variations in Reynolds number (Ref 6). This practice has aroused concern (Ref 7). The overall suitability of these three methods for time-dependent experiments must now be considered.

A special requirement for unsteady experiments is that the free stream flow without model motion should be *as steady as* possible. In practice for model tests this means that the flow unsteadiness must be low (in accordance with the criteria specified originally in Ref 8) and that transition should be at a fixed point. Free transition is itself essentially an unsteady phenomenon, characterised by intermittency in both space and time. During a model test it is undesirable that the mean position of transition should vary during a motion cycle (due say to the oscillation of a control or the bending of a wing), if such variations do not occur at full scale.

Method (3) thus appears excluded a priori from most model experiments in unsteady aerodynamics (although it forms an important constituent of the methodology of boundary layer simulation recommended for steady aerodynamic measurements (Ref 1)). However, at full scale there may be situations where transition will vary during a motion cycle. An example occurs in the motion of a helicopter rotor blade. Full scale Reynolds numbers range from 4×10^6 to 6×10^6 and, as these can be reached on rotor blades with chords of say, 100 mm, in the ARA two-dimensional tunnel, most aerofoil tests there are made with free transition. When transition does vary during a cycle large dynamic effects may be caused, eg the amplitude - limited single degree of freedom flutter discussed in Ref 9, observed in Ashill's measurements on the swept panel model (Ref 5).

In contrast Methods (1) and (2) both effectively offer fixed transition positions during a motion cycle and might therefore be considered equally suited to unsteady experiments. Despite this conclusion other factors must be considered when comparing the advantages of Methods (1) and (2). Method (2) has a variation in Reynolds number which has intrinsic advantages for all kinds of unsteady experiments. Two examples may be cited. For buffeting measurements in a conventional wind tunnel, the variation in density (at constant velocity) allows a variation in aerodynamic damping at constant frequency parameter which is essential for valid extrapolation to full scale conditions (Ref 10). For the measurement of oscillatory pressures, the variation in density provides an indication of the accuracy of the measurements. Unfortunately Method (2) may give effects due to varying static aeroelastic distortion. Despite this difficulty Method (2) is preferred over both Methods (1) and (3) for experiments in time-dependent aerodynamics in conventional tunnels. In cryogenic wind tunnels Method (2) offers a direct indication of changes due to variations in Reynolds number (Ref 11). This is because when the Mach number and total pressure are held constant, Reynolds number may be increased by lowering the total temperature. Then the kinetic pressure, and thence the static aeroelastic distortion should remain constant.

2.3 General character of scale effects

If Method (2) is adopted (ie transition is fixed and Reynolds number varied), a tentative attempt may be made to infer the general character of scale effects. For simplicity this discussion assumes that the effects of static aeroelastic distortion are small, or negligible, compared to the scale effect and that there is no tunnel interference.

Fig 3a reproduces the sketch (Fig 1a) of the flow on a conventional aerofoil at low and high Reynolds numbers at Mach number M and a high angle of incidence α giving separations on the upper surface. Generally direct scale effects will be comparatively small on the lower surface, where the boundary layers are thin at both Reynolds numbers, due to the strong favourable pressure gradient. In contrast, direct scale effects will be larger on the upper surface, due to the rear separation, provoked by the strong adverse pressure gradient. In addition there will be indirect scale effects on both surfaces due to the change in circulation produced by the movement in the separation position. Note that the magnitude of indirect scale effects will depend on whether the comparisons are made at constant angle of incidence (as here) or at constant lift coefficient. If comparisons are made at constant lift coefficient indirect scale effects will be different, at least for aerofoils. This is illustrated by some recent measurements of trailing-edge pressure divergence indicative of trailing-edge separation (Ref 12). The changes with Reynolds number are much larger when comparisons are made at constant angles of incidence (Fig 3b) than they are when made at constant lift coefficient (Fig 3c). For the higher Reynolds

This Document Provided by the ABBOTT AEROSPACE
TECHNICAL LIBRARY
ABBOTTAEROSPACE.COM

numbers the plot against the angle of incidence (Fig 3b) has a gentle slope which meanders from α = 2-4° with appreciable scatter. In sharp contrast, the plot against the lift coefficient (Fig 3c) has a precipitous drop at C_L = 0.68 which is almost independent of Reynolds number and negligible scatter. The lift coefficient controls separation and a single, unique value is much to be preferred. For a wing there is the additional complication of variations in the spanwise lift distribution.

For a transonic flow with a shock induced separation, Green (Ref 13) suggested that if the local momentum thickness Reynolds number exceeds a certain critical value (somewhere between $R\theta = 10^3$ and 10^4) subsequent increases in Reynolds number should produce monotonic and favourable scale effects, such that the onset of flow separation should be further downstream. There is evidence that this hypothesis is correct (Ref 3).

As shown in Fig 3a, local scale effects would be comparatively small for attached flow regions, very large near separation and large for the area of separated flow (for this is appreciably different in size). These remarks relate to the local flow at a particular Mach number and angle of incidence, but can be generalised, as suggested below.

With regard to the wider issues of the overall effects of variations in Reynolds number on the aerodynamic performance of an aircraft wing, a sensitive indication should be given by contours (in the M-C_L domain) for onset, light, moderate and heavy buffeting. These are the dynamic wing buffeting criteria defined after the methods of Refs 14 and 15. As an illustration, Fig 4 shows such criteria for a 45° swept wing with fixed transition, taken from Ref 16, but corresponding contours could be drawn for all wings.

With regard to steady measurements (Fig 4a), say of the drag coefficient or lateral static derivatives, scale effects should be small for attached flow regions (below the buffet onset contour), very large for small separations between buffet onset and light buffeting) and small again when the flow is very well separated (heavy buffeting). This last would be consistent with Townsend's suggestion (Ref 17) that, owing to the large length scales of well-separated flow structures, changes due to variations in Reynolds number are unimportant. Between the heavy and moderate buffeting contours, it is plausible to suggest that scale effects for steady flows are medium, and from the moderate to light buffeting contours that scale effects are large.

Unsteady experiments of all types are more difficult and often inherently less accurate than steady measurements. Hence it is reasonable to expect that scale effects will generally be lost within the experimental scatter for attached flow regions (below buffet onset) and for well separated flow regions at or above heavy buffeting). Thus it is plausible to expect that observed scale effects will be medium between the buffet onset and moderate buffeting, and small between moderate buffeting and heavy buffeting (Fig 4b). Plainly the region near buffet onset will be sensitive to scale effects in unsteady aerodynamics.

The differences between steady and unsteady tests implied by Fig 4a&b take no account of effects of frequency parameter, which are known to be important for certain separated flows. However, the evidence available for the variation of scale effects with frequency parameter is limited and still awaits careful investigations. Hence no particular range of frequency parameter can be assigned to Fig 4b. This simplified and tentative view of the character of overall scale effects in unsteady experiments, inferred from the physics of scale effects in steady flow (Fig 3a) is generally consistent with the detailed review of the different types of experiments which follows.

The author has been unable to find any predictions for scale effects in unsteady flows for comparison with these experiments. Accordingly some special test cases are suggested in the Appendix.

3 REVIEW OF DIFFERENT TYPES OF UNSTEADY EXPERIMENTS

Comments are given on the magnitude of scale effects on the many different types of unsteady experiments with surfaces in unsteady motion, and how these results compare with the tentative classification suggested in Fig 4b.

3.1 Dynamic tests of aerofoils

Davis remarked (Ref 18) that for "unsteady transonic aerodynamics scale effect has hardly been considered seriously, either experimentally or analytically." His own aerofoil measurements with small amplitude motions covered the wide Reynolds number range from about Rc = 3 x 10^6 to 12 x 10^6 but were restricted to free transition. Despite this limitation, scale effects were small on the unsteady pressures for attached flows at subsonic speeds or at transonic speeds with weak shock waves. Scale effects were much larger and non-monotonic for flows that were just separated and on a supercritical aerofoil.

Dynamic stalling tests of aerofoils form an important class of unsteady experiments with large amplitude motions. Besides being of theoretical interest, dynamic measurements for different aerofoil sections are essential to predict the performance of helicopter rotors. These must operate at transonic speeds and moderate lift coefficients (for advancing blades) and at subsonic speeds and high lift coefficients (for retreating blades). Dynamic measurements on aerofoils are difficult, and even for steady measurements there are often significant differences on one model when tested at the same nominal conditions in different facilities. In view of differences of this type, the emphasis in most dynamic research has been placed on comparative tests of different aerofoils in a single facility (normally at a series

THIS DOCUMENT PROVIDED BY THE ABBOTT AEROSPACE
TECHNICAL LIBRARY
ABBOTTAEROSPACE.COM

of related Reynolds numbers and Mach numbers), rather than on evaluating aerofoil performance at a single Mach number over a range of Reynolds number. Accordingly there are few measurements available for the evaluation of scale effects on dynamic tests of aerofoils. Carr in his review paper (Ref 19) on the dynamic stall of aerofoils, concluded that "proper representation of the Reynolds number effect on dynamic stall remains an important and presently unsolved question". In an attempt to supply this deficiency, the author arranged some special pitching tests on an aerofoil typical of modern designs - an RAE 9615.

Measurements at M = 0.30

Fig 5 shows quasi-steady measurements with free transition at $Rc = 1.2 \times 10^6$ and 3.4×10^6. With the incidence increasing very slowly (Fig 5a) the lift and moment stalls occur significantly later at the higher Reynolds number which would be consistent with a large favourable scale effect. In contrast, with the incidence decreasing very slowly (Fig 5b), the lift and moment curves are not significantly different at the two Reynolds numbers.

Fig 6 shows corresponding rapid dynamic ramp measurements with free transition at $Rc = 1.1 \times 10^6$ and 3.5×10^6. With the incidence increasing (Fig 6a), the 'moment stalls' occur at the same incidence at both Reynolds number, consistent with negligible scale effects. [During this ramp the lift stall is not apparent at the highest incidence, only 17°.] In contrast, with the incidence decreasing (Fig 6b) the lift and moment curves are quite different from those of Fig 6a, and there are differences between the measurements at the two Reynolds numbers over the incidence range from about 17° to 12°. These differences illustrate that dynamic conditions controlling reattachment are very important. [It is interesting to observe that these differences are in the opposite sense to those observed with the incidence increasing slowly (Fig 5a) and occur over the same range of incidence. However, this could be fortuitous.] The important conclusion to be drawn from the comparison of Figs 6 and 5 is that, even with free transition, scale effects are smaller for rapid motion than for quasi-steady motion.

For the quasi-steady measurements (Fig 7), the effects of fixing transition are negligible both at $Rc = 1.1 \times 10^6$ (Fig 7a&b) and at $Rc = 3.4 \times 10^6$ (Fig 7c&d). (Perhaps with free transition the adverse pressure gradient makes the boundary layer turbulent before separation.) As would be expected, the effect of fixing transition is also small on the dynamic ramp measurements, even at the lower Reynolds number (Fig 8). The measurements at the higher Reynolds number were comparable and have been omitted for brevity.

Measurements at M = 0.60

Fig 9 shows the quasi-steady measurements with the incidence increasing. (There is no hysteresis at M = 0.60, in contrast to the quasi-steady measurements at M = 0.30 in Fig 5). The effects of fixing transition are negligible at the lower Reynolds number (Fig 9a) but somewhat larger at the higher Reynolds number (Fig 9b).

With regard to dynamic measurements, it is widely accepted that dynamic effects on aerofoil stall decrease as Mach number increases as illustrated by Fig 13 of Ref 19, Figs 32 and 34 of Ref 20 and in the more recent tests of Ref 21. However in the present tests the decrease observed is due to the combined effects of the increase in Mach number and the decrease in ramp rate parameter, $c\dot{\alpha}/U$, caused by measurements at fixed ramp rates. Here a fixed ramp rate $\dot{\alpha} = 1000°/s$ was adopted for both M = 0.60 and 0.30, so the ramp rate parameter was smaller at the higher speed. For M = 0.60 the rapid ramp measurements with free transition are radically different in character for increasing and decreasing incidence, but virtually independent of Reynolds number (Fig 10). Thus Fig 10, for M = 0.60, is quite different from Fig 6, for M = 0.30. This is consistent with the observation that where the dynamic effects are smaller (M =0.60), (due to the combined effects of the increase in Mach number and the decrease in ramp rate parameter) the scale effects are smaller. Consistent with the small scale effects at M = 0.60, Fig 11 shows that the effects of fixing transition on the ramp measurements are negligible, even at the lower Reynolds number.

The tentative conclusion drawn from the measurements at M = 0.30 and 0.60 is that even in the Reynolds number range from 1×10^6 to 3×10^6 scale effects can be important for dynamic aerofoil tests, particularly at low frequency parameters and ramp rates. It is a reasonable inference that measurements at even lower Reynolds numbers (typically less than 2×10^5 in water tunnels) are unlikely to be representative of full-scale conditions.

3.2 Dynamic tests of wings

Many dynamic stalling tests of wings are made in water tunnels and a critical review of the results from some of these experiments is given in Ref 22. Most of these tests are made at low Reynolds numbers (typically only 10^4 to 10^5) with free transition (Method (3)) and are concerned with the development of well separated flows, believed to generate significant dynamic lift. It is widely believed by the experimentalists that, for such large separations, scale effects are small, both on aerofoils and on swept wings with sharp leading-edges, which would be consistent with Fig 4b.

As an illustration, Reynolds number effects on the vortex positions above a 45° swept delta wing, oscillating in pitch with an amplitude of 10° about a mean angle (α_o) of 15° are small (Ref 23) (Fig 12). The vortex height for this oscillatory motion varies appreciably as

THIS DOCUMENT PROVIDED BY THE ABBOTT AEROSPACE
TECHNICAL LIBRARY
ABBOTTAEROSPACE.COM

the frequency parameter, $\nu = \omega c_o/U$, varies from 0.25 to 1 (at constant Reynolds number) and is significantly different from the steady state or quasi-steady position (Fig 12a). In contrast, if the frequency parameter is maintained constant at $\nu = 1$, no variation in vortex height is observed between Reynolds numbers of $Rc_o = 2.5 \times 10^4$ and 3.4×10^5 (Fig 12b).

The differences in vortex breakdown position observed above a 60° swept delta wing with a sharp leading-edge are small between a water tunnel test and a wind tunnel test (Ref 24). Although these small differences represent the combined effects of tunnel interference, different Mach numbers and different Reynolds numbers, it is reasonable to infer that Reynolds number effects between the water tunnel test at $Rc_o = 1 \times 10^5$ and the wind tunnel test at $Rc_o = 1.1 \times 10^6$ are small. Thus for the stationary wing the differences between the water tunnel and the wind tunnel are comparable with the differences observed between the smoke and schlieren techniques in the wind tunnel tests (Fig 13). When the wing is oscillating in pitch with an amplitude of 10° about a mean angle (α_o) of 20°, a small shift forward in the vortex burst position is observed in the wind tunnel as compared to the water tunnel (Fig 14), for both the quasi-steady and the oscillatory motion.

A forward displacement of the vortex burst position must be associated with an earlier initiation of heavy buffeting (Ref 25). Hence the measurements shown in Figs 13 and 14 apparently represent a small adverse scale effect in the region between light and heavy buffeting, ie in the region in which small effects would be expected according to Fig 4b. (Here comparative buffeting measurements in the water tunnel and the wind tunnel would have been of great value but no such comparisons are available.)

Many other comparisons of flow visualisation in water tunnels and wind tunnels are included in the special conference reported in Ref 26. For high angles of incidence and well separated flows most contributors are confident that scale effects are small on steady observations covering a wide range of configurations which include fighter aircraft and missiles. With regard to unsteady observations in Ref 26, in addition to Ref 24 (already discussed) there are measurements on moving parachute canopies and visualisation of unsteady flows at leading and trailing edges. However, neither of these papers comment on possible scale effects.

3.3 Unsteady pressure measurements

Pressure measurements due to model oscillation are discussed first because these are most common. Unfortunately, comparatively few of these measurements include a variation in Reynolds number at constant frequency parameter. However where such comparisons have been made, Reynolds number effects are negligible for attached boundary layers with fixed transition, consistent with Fig 4b. Two examples may be cited from RAE measurements.

In Refs 27 and 28, steady and oscillatory pressures due to pitching motion were reported on a low aspect ratio model at subsonic and supersonic speeds. For $M = 0.86$ and $\alpha = 0°$, with weak shocks on the outer wing sections, Reynolds number was increased from 3×10^6 to 4.5×10^6, without affecting either the steady or the oscillatory pressures.

In Refs 29 and 30, steady and oscillatory pressures due to pitching motion were reported on an unswept wing at subsonic speeds. For $M = 0.80$ and $\alpha = 0°$ (with transonic flow developing on the wing centre sections), Reynolds number effects were negligible from 2.4×10^6 to 3.5×10^6, except in the vicinity of the shock, where scale effects were small (Fig 15). In addition at subsonic speeds ($M = 0.2$ to 0.7) good agreement with Davies' inviscid linearised theory (Ref 31) for oscillatory flow was obtained over a wide range of frequency parameter, despite a Reynolds number variation 0.8×10^6 to 2.2×10^6 with Mach number.

Bublitz (Ref 32) and Zingel (Ref 33) have made detailed studies of the steady and time-dependent pressures and forces in an atmospheric low speed wind tunnel on a thin swept wing with a planform resembling the F 104 aircraft. Their measurements covered a wide incidence range (0 to 40°), which thus generated both attached and separated flows, and included oscillatory pressures due to pitching motion at the same frequency parameter at two different Mach numbers (about 0.09 and 0.18) giving Reynolds numbers ($R\bar{c} = 1.2 \times 10^6$ and 2.4×10^6). Although these Reynolds numbers were low and transition was not fixed, the thin wing section used (NACA 64A005) always gave a swept bubble type separation very close to the leading edge at low speeds. [It is difficult to fix transition on wings with such thin sections at low speeds.]

Buffet onset occurs at about $\alpha = 5°$ and the first local measurements presented relate to $\alpha = 7.5°$ for section 4 on the wing (Fig 16) where large scale effects would be expected according to both Fig 4b and the surface oil flows, which are now considered. According to Fig 16a, at the lower Reynolds number there is a small bubble at the leading edge at section 4. In contrast, according to Fig 16b, at the higher Reynolds number the bubble is smaller all along the leading edge and does not extend onto section 4. Hence section 4 would be sensitive to scale effects within the range from $R = 1.2 \times 10^6$ to 2.4×10^6. This is confirmed by the steady pressure distribution at both Reynolds numbers, which suggest that a swept bubble exists close to the leading-edge, quickly followed by reattachment (Fig 16c). The random pressure fluctuations confirm this; being high close to the leading-edge and falling rapidly (Fig 16d). On a flat plate the pressure fluctuations would peak just upstream of the reattachment point (Ref 34) and a comparable peak just upstream of reattachment has been observed on several swept wings (Ref 35). Hence the lower level of pressure fluctuations at $x/c = 0.11$ at the higher Reynolds

THIS DOCUMENT PROVIDED BY THE ABBOTT AEROSPACE
TECHNICAL LIBRARY
ABBOTTAEROSPACE.COM

number would be consistent with earlier reattachment upstream. Fig 16e compares the real and imaginary components of the pressure on the upper surface at $\alpha = 7.5°$ due to pitching oscillation at a frequency parameter of 0.25. The major change is that the peak in the real component of the pressure is further forward, at the higher Reynolds number, consistent with the elimination of the separation bubble. Thus these local measurements show that immediately after buffet onset scale effects are large in unsteady aerodynamics, consistent with the suggestion of Fig 4b. [The scale effects on the integrated forces will be much smaller.]

An important cause for concern is the magnitude of the scale effects on canard/wing configurations, particularly with separated flows. This problem is being addressed by a number of studies at low speeds on a large half-model of the High Incidence Research Model (HIRM 1) in the RAE 13ft x 9ft Tunnel. Following Method (2) of section 2.2, roughness bands are applied to fix transition and comparative measurements are made at speeds of U = 40 and 60 m/s. These measurements allow a rough assessment of Reynolds number effects in the range from $R\bar{c} = 2.5 \times 10^6$ to 3.7×10^6, if effects due to the change in Mach number are neglected. Subject to this assumption, within this Reynolds number range, Reynolds number effects on the steady lift and pitching moment characteristics are negligible, at least on all the configurations studied so far. However, there are significant Reynolds number effects on the wing local steady pressures and the wing oscillatory pressures, due to the oscillation of the canard.

Fig 17 shows the general arrangement of a typical configuration studied (Ref 35). A strake added to the HIRM 1 wing gives a wing planform resembling that of the Experimental Aircraft Project (EAP) and the canard represents that of the EAP. The canard can be oscillated at an amplitude of about 0.7° about the axis shown, with an appropriate mean setting ($\eta_c = -10°$ here).

Fig 18 shows measurements at the inboard section at $\eta = 0.4$ for an incidence $\alpha = 5°$, where the wing flow is fully attached. The canard effective incidence, α_c, (due to canard setting, incidence and wing/body upwash) is only -2.8°, so that the canard flow is fully attached throughout the motion cycle. For this condition, with attached flows on both surfaces, Reynolds number effects should be small. There are some changes in the steady pressures (Fig 18a) but the small oscillatory pressures (Fig 18b), show no significant variation with Reynolds number.

In contrast, Fig 19 shows measurements for an incidence of $\alpha = 12°$, where the wing flow is about to separate (ie $\alpha = 12°$ is buffet onset). The effective mean incidence, α_c, is now 7.2°, ie just below buffet onset. The canard amplitude thus ensures that the canard flow approaches separation ($\alpha_c = 8°$) during the motion. For this condition, with flows about to separate on both interacting surfaces, Reynolds effects would be expected to be larger than for the attached flow. This inference is confirmed by both the somewhat larger differences between the two speeds in the steady pressures (Fig 19a) and by the corresponding difference between the oscillatory pressures (Fig 19b), which are larger than those in Fig 18b.

It would be interesting to see how these local Reynolds number effects change when the wing flow is separated. However, the random pressures on the wing then become of the same magnitude as the induced oscillatory pressures, so that the induced pressure cannot be measured accurately. Hence no statement can be made about scale effects with well separated flows from the oscillatory pressure measurements on the HIRM 1 model.

While on the subject of unsteady pressure measurements on canard/wing configurations, a special warning should be added about the fluctuating pressures observed on nominally rigid models. There is mounting evidence that at high angles of incidence the frequency spectrum of the buffet excitation is not flat (as for moderate separation) but contains sharp peaks (Ref 32). The existence of these peaks has serious implications with respect to the prediction of buffeting on such configurations, and invalidates any attempt to deduce a sensitivity to Reynolds number by changing velocity.

Scale effects on transient pressures are now considered. Some measurements are available of the dynamic lift and pitching moment on a model wing due to the rapid extension and retraction of a spoiler (Ref 36). For these tests the main objective was to confirm that rapidly extending spoilers can decrease lift quickly (due to the rapid development of the larger scale flow separation behind the spoiler) and that rapidly retracting spoilers can increase lift quickly (due to the rapid collapse of the separated flow region). The large size of the separation behind the spoiler suggests that according to Fig 4b scale effects should be small, and this is confirmed by the measurements.

Within the tests of Ref 36 the dimensionless rate of spoiler motion ($UT/c = 5$) was the same at $M = 0.25$ and 0.50, corresponding with Reynolds numbers of $Rc = 1 \times 10^6$ and 2×10^6, with fixed transition at $x/c = 0.075$. Fig 20 shows typical transient measurements, expressed in terms of the non-dimensional time Ut/c. The spoiler displacement-time curves are virtually the same at both Reynolds numbers, for extensions and retractions, despite differences in Mach number and kinetic pressure (which could have altered aeroelastic distortion). The lift variation with Ut/c (inferred from the integration of the pressures) is the same form at the two Reynolds numbers although quite different for extension and retraction. However, there are larger variations with Reynolds number in the pitching moment, particularly for spoiler retraction (cf Fig 20a&b). Hence from this single transient comparison for a spoiler, Reynolds number effects appear

THIS DOCUMENT PROVIDED BY THE ABBOTT AEROSPACE
TECHNICAL LIBRARY
ABBOTTAEROSPACE.COM

insignificant on lift, and larger on pitching moment, if the possible Mach number effect is ignored.

With regard to the lift variation for spoiler extension, two parameters (defined in Fig 20) are of particular importance for a transient time history at a fixed value of UT/c . The first is the time delay, t_a/T , for the maximum adverse lift. The second is the time delay, t_f/T , to achieve the final lift. For subsonic speeds both of these parameters are correlated in terms of UT/c , despite variations in Mach number, kinetic pressure and Reynolds number (Fig 21). It is unlikely that separate effects due to these variations would mutually cancel and hence it is reasonable to infer that for the lift transients, Reynolds effects are small at subsonic speeds, as suggested in Fig 4b.

This finding is consistent with low speed tests (Ref 37) on a large model of a lifting rectangular supercritical wing at $\alpha = 2°$, fitted with both an oscillating spoiler (hinge line at $x/c = 0.67$) and a flap (hinge line at $x/c = 0.88$). The test Mach number was only $M = 0.2$ but the Reynolds number was high and varied from $Rc = 4 \times 10^6$ to $Rc = 16 \times 10^6$. Transition was not fixed, but was observed for $Rc = 4 \times 10^6$ at $x/c = 0.09$ and 0.53 on the upper and lower surface respectively. For $Rc = 16 \times 10^6$ no flow visualisation was available, but calculations suggested (Ref 38) that the transition position would be just upstream of those at $Rc = 4 \times 10^6$. [This is because transition was controlled primarily by the strong pressure gradients round the lifting wing.] Hence for all test conditions transition should have been well upstream of the hinge lines of both controls. Flap amplitudes were about 1°.

Fig 22 shows the measured steady spoiler characteristics for zero flap angle ($\delta_f = 0°$) and with the flap deflected ($\delta_f = 5°$). The wing steady normal force coefficient, C_N , is a non-linear function of spoiler deflection, δ_s , particularly for $\delta_s \leq 7°$ (Fig 22a). This is a limitation typical of many spoiler configurations. However, the variation of this non-linear characteristic from $Rc = 4 \times 10^6$ to 16×10^6 is very small for $\delta_f = 0°$ and small for $\delta_f = 5°$. The modulus of the wing unsteady normal force coefficient due to spoiler oscillation, C_{N_δ} , is also non-linear and has a significant phase lag, but neither the magnitude nor the phase lag vary significantly with Reynolds number (Fig 22b).

Fig 23 shows the measured flap characteristics for zero spoiler deflection. The wing steady normal force is an almost linear function of flap deflection, δ_f , and increases a little at the higher Reynolds number due to the reduction in boundary layer thickness (Fig 23a). The magnitude of the wing unsteady normal force due to flap oscillation is shown only for $\delta_f = 10°$. The lift from the flap has only a very small phase lag, (Fig 23b), and is thus different in character from that due to the spoiler. For the flap neither the magnitude nor the phase lag vary significantly with Reynolds number.

3.4 Oscillatory control surface derivatives

In Ref 39, Moore presented a comprehensive review of scale effects on oscillatory derivatives for the measurements available in 1969. Subsequently, relatively few additional measurements have become available, and hence it is reasonable to recapitulate his findings and offer some comments. Moore recognized that virtually all the measurements then available related to tests at zero incidence with attached flow and relatively thin boundary layers. Thus local scale effects on a control (invariably a trailing-edge flap) would be small according to Figs 3 and 4b. This inference is consistent with Moore's observations. Thus in two-dimensional tests, increases in Reynolds number reduce the boundary layer thickness a little and "tend to increase the magnitude of the important hinge moment derivatives (h_β for stiffness, $h_{\dot\beta}$ for damping). Artificially thickening the boundary layer by fixing transition tends to reduce the magnitude of these derivatives". In three-dimensional tests, comparable effects were present but were generally smaller.

Figs 24 to 26 show some typical results illustrating these effects. Fig 24 shows some hinge moment measurements on an outboard flap on a swept back tapered wing at transonic speeds (Ref 40). Considering first the stiffness derivative (Fig 24a), at $p_t = 1$ bar with free transition this is appreciably higher than with fixed transition. Then with free transition an increase in total pressure to $p_t = 1.8$ bar lowers the stiffness derivative because of the thicker boundary layer caused by the forward movement of transition. In contrast, with fixed transition the stiffness derivative is almost independent of total pressure and a little lower, due to the thicker boundary layers. Considering the damping derivative (Fig 24b), at $p_t = 1$ bar with free transition this is somewhat higher than with fixed transition. With free transition an increase in total pressure to $p_t = 1.8$ bar produces a further increase. In contrast, with fixed transition the damping derivative is independent of total pressure. Hence a much more consistent set of measurements was achieved with fixed transition although all these measurements differ significantly from the predictions of inviscid theory (Ref 41).

Fig 25 shows some RAE unpublished low speed hinge moment measurements made with free transition on a rectangular wing. Fig 25b shows that the stiffness derivative falls rapidly as the Reynolds number increases from $Rc = 0.25 \times 10^6$ to 0.50×10^6 , and then remains in good agreement with the inviscid value (Ref 41). This agreement is in marked contrast with most other measurements (eg those in Figs 24 and 26). One hypothesis is that the initial decrease may be attributed to the thickening of the turbulent boundary layer close to the control

THIS DOCUMENT PROVIDED BY THE ABBOTT AEROSPACE
TECHNICAL LIBRARY
ABBOTTAEROSPACE.COM

caused by the forward movement of transition. Fig 25c shows that the smaller damping derivative is constant, in good agreement with the inviscid theory, which is unusual.

Fig 26 shows some hinge moment measurements on an inboard flap on another swept back tapered wing at transonic speeds (Ref 42). Roughness sized to fix transition at about p_t = 0.5 bar was applied close to the leading edge of the model. This roughness would have been inadequate at the lower Mach numbers for p_t = 0.23 bar , and may explain the higher values of the stiffness derivative there, shown linked with a dotted line in Fig 26a. This is the same trend as shown in Fig 25 above and as observed in the review of Moore (Ref 39). For this control, both the stiffness and damping derivative were only about half the theoretical value. This difference is consistent with many previous measurements and does not appear to be a scale effect.

Thus we can see why Moore recommended that with attached flow oscillatory control tests should be made with free transition at model Reynolds numbers, to obtain results closer to full scale. However this recommendation has disadvantages, as discussed in section 2.2. For tests with separated flows Moore thought it would be important to exclude laminar separations at low Reynolds numbers. Hence he recommended tests with a range of fixed transition positions. Moore emphasized that "these were tentative conclusions based on limited evidence" and was unable to show how these small scale effects varied with frequency parameter.

Some brief comment about the current situation with respect to scale effects on control surface derivatives seems appropriate. For transport aircraft without power controls, which usually operate in attached flow regions, there is still some interest in oscillatory control surface derivatives. With fully attached flow, scale effects should be small and inviscid theoretical methods will generally overestimate the derivatives. In contrast, for aircraft with power controls, which may operate with attached or separated flows with the help of Active Control Technology (ACT), oscillatory control surface derivatives h_β , $h_{\dot\beta}$ may be of less importance. However, interest has been expressed in the measurement of the lift and pitching moment derivatives due to control surface oscillation on models of combat aircraft at high angles of incidence with well separated flows. For such well separated flows, Reynolds number effects should be small because of the large size of the separation, but theoretical methods are not available.

It is interesting to note that in one investigation of control surface buzz on an aerofoil (a special case of single degree of freedom flutter) at transonic speeds with fixed transition, a Reynolds number variation from $Rc = 1.6 \times 10^6$ to 3.2×10^6 had more effect at lower frequencies than at higher frequencies (Ref 43). This effect was noticeable on both the stiffness and damping derivatives (Fig 27) and recalls the much larger Reynolds number effects on aerofoils in quasi-steady motion as compared to rapid motion (cf section 3.1 above).

3.5 Single degree of freedom flutter

Single degree of freedom flutter, fully described in Ref 44, may be caused immediately after incipient separation. This makes the phenomenon very sensitive to variations in Reynolds number even with fully turbulent boundary layers. A typical example, related to control surface buzz, was discussed above; cf Fig 27.

Another example of single degree of flutter due to flow separation is the stall flutter of aerofoils. Stall flutter depends on the boundaries in the C_L - M plane defining regions of negative aerodynamic damping, as discussed in Ref 45. This investigation showed that the stall flutter boundaries were sensitive to the condition of the leading edge and in particular to the roughness bands used to fix transition. The roughness bands used were formed of irregular grains of carborundum extending from the leading edge to x/c = 0.02 on both surfaces. More recent practice would recommend spherical roughness particles (ballotini) extending from, say, x/c = 0.05 to 0.07 on both surfaces. Thus the authors of Ref 45 (who were concerned with the problem of helicopter blades) concluded that "any deterioration in the surface condition might lead to stall flutter under conditions where it did not previously occur". This observation suggests that great care should be taken if roughness bands are used in investigations of stall flutter. The investigation reported in Ref 45 compared two different aerofoils with both fixed and free transition but included no variation in Reynolds number. [The test Reynolds number was about half that of the full scale helicopter blade.]

Even in the absence of separation a transitional boundary layer can excite single degree of freedom flutter. One example has been cited already - the wing bending oscillations on an ordinary wind tunnel model (Ref 9).

Other examples are:

a. On a flutter model of a supercritical wing (Ref 46), anomalous flutter instability at the first bending frequency was observed at low Equivalent Air Speeds (EAS). It was attributed to "the transition trip becoming ineffective at low total pressure, leading to a variable transition location and a deviation in unsteady airloads".

b. In a transonic test (Ref 47), a low-aspect ratio flutter model was destroyed by an aeroelastic oscillation at low EAS.

c. Anomalies were observed at transonic speeds when making tests with free transition on a flutter model of the highly swept fin of the Concorde Aircraft (Ref 48). These phenomena were eliminated when the tests were made with fixed

THIS DOCUMENT PROVIDED BY THE ABBOTT AEROSPACE
TECHNICAL LIBRARY
ABBOTTAEROSPACE.COM

transition. Thus for any single degree of freedom flutter very careful attention must be paid to the state of the shear layers and the magnitude of any variations due to variations in Reynolds number.

3.6 Classical flutter

Consideration of classical flutter is normally restricted to attached flows. Hence, with fully-turbulent boundary layers, Reynolds number effects should be small. In principle, it should be possible to infer the magnitude of such small effects from information (measured or predicted) about the oscillatory aerodynamics. It is interesting to recall that AGARD has specified a set of classical flutter measurements on a model of a swept back wing at transonic speeds (Ref 49). The flutter boundary includes a pronounced transonic dip. The measurements were made with free transition, but display no obvious anomalies. Presumably, spanwise contamination, spreading from the sidewall boundary layer, ensures fully turbulent flow fairly close to the leading edge. This well defined configuration appears ideally suited for an assessment of viscous effects on classical flutter.

3.7 Stability derivatives

The static and dynamic stability derivatives of combat aircraft and missiles must be known with good accuracy to enable their handling characteristics to be predicted. Hence it is important for model measurements to be made and to know the scale effects on these measured derivatives.

In h initial summing up of the AGARD Conf nce on Unsteady Aerodynamics (Ref 6), Chambers referred to "our ability to examine very important Mach and Reynolds number effects which were heretofore not possible". However, within the papers presented at the Conference there was little evidence for any effects of Reynolds number apart from the following.

Malcolm has provided a comprehensive review of recent measurements of yawing moment with rotary balances on a 1/20 model of the F 15 aircraft (Ref 50). (These tests were made with free transition although this was not stated in the paper.) Malcolm concluded that Reynolds number effects in the range from 1.5×10^6 to 4.0×10^6 were generally small. However, when there were cross flow separations on the forebody and fuselage at high angles of incidence (say $\alpha \geq 40°$), scale effects were large, both with the nose boom off and the nose boom on (Fig 28). [It should be recalled that rotary balance measurements are made for flows that are nominally steady. However, with large areas of separated flow at high angles of incidence, such measurements are unsteady, at least in the sense that they are made in the presence of large random fluctuating pressures.]

Schmidt (Ref 51) has provided some oscillatory balance measurements on a standard dynamics model. This was tested with a roughness band round the ogival nose to maintain a turbulent boundary layer, while Reynolds number was generally varied only from about 1×10^6 to 2×10^6. Schmidt concluded that scale effects on the stiffness and damping derivatives were small.

O'Leary and Rowthorn also have made a number of oscillatory balance measurements on a large number of different configurations. Although most of these tests have been made with free transition, Reynolds number effects are small generally, within the wind tunnel experiment. Scale effects were small in the Reynolds number range from $Rc = 2.4 \times 10^6$ to 5.1×10^6 at $M = 0.2$ in their measurements on a model of the RAE HIRM 1 model in the RAE 8ft x 8ft Tunnel (Ref 52). Here no difference was observed between the character of the derivatives for attached flows, flows with incipient separation or well separated flows.

Boundary layer transition is known to affect the dynamic stability in pitch of full-scale re-entry bodies at high supersonic speeds (Ref 53). When the boundary layer is either completely laminar or turbulent, the effects of changes in the boundary layer thickness are small. However, when transition occurs, the boundary layer effects become appreciable. They can cause large reductions in pitch damping for bluff bodies and increases in pitch damping for slender bodies.

Finally, it should be noted that a recent review shows that wing rock oscillations at high angles of incidence are controlled by the static and dynamic aerodynamic derivatives (Ref 54). Significant scale effects between wind tunnels and flight have been observed in the conditions for the onset of wing rock (close to the onset of flow separations); in contrast, for large amplitude wing rock (with large scale separations), scale effects are small. This distinction is consistent with the suggestions made about scale effects on both static and dynamic derivatives when discussing Fig 4.

4 CONCLUSIONS AND RECOMMENDATIONS

The unsteady experiments reviewed in section 3 confirm the four principal suggestions advanced tentatively in section 2.

(1) With free transition, scale effects can be very large and non-monotonic.

(2) With fixed transition, scale effects are more likely to be monotonic and large effects are generally confined to the region close to the onset of flow separation. This conclusion has important implications with respect to the prediction of any unsteady phenomenon involving separation, such as buffet onset or dynamic stall tests. It is recommended that unsteady tests should always be made with fixed transition.

(3) Scale effects in unsteady transonic flow are of great importance and have been considered only briefly here because of the shortage of useful data. Much more research (both theoretical and

THIS DOCUMENT PROVIDED BY THE ABBOTT AEROSPACE
TECHNICAL LIBRARY
ABBOTTAEROSPACE.COM

experimental) is essential, particularly with respect to the buffet onset boundaries of transport aircraft.

(4) A careful assessment must be made between the magnitude of direct and indirect scale effects. If comparisons are made at constant lift coefficient, indirect scale effects may be smaller, at least for aerofoils.

Overall, the review reveals an unsatisfactory situation with regard to scale effects in both experimental and theoretical unsteady aerodynamics. It is recommended that unsteady experiments should be made with fixed transition and varying Reynolds number and/or with various fixed transition positions as recommended for steady experiments in Ref 1. A similar recommendation is made with respect to theoretical studies. For the few problems in time-dependent aerodynamics where Computational Fluid Dynamics (CFD) does provide predictions, such predictions are presented generally for a comparison with a model experiment at a single, low Reynolds number (say 10^6). For such problems it is recommended that, in addition, predictions should be made always either with fully turbulent boundary layers at much lower and much higher Reynolds numbers (say 10^4, 10^5, 10^7, and 10^8) or at fixed Reynolds number with varying transition. Such theoretical studies might prove helpful in resolving many anomalies observed in experiments in time-dependent aerodynamics. Three important test cases, which might be studied theoretically are suggested in the Appendix. [These test cases have been considered already for a few limited Reynolds numbers and restricted transition positions.]

No discussion has been given of possible misleading effects of 'overfixing' transition on unsteady flows. In addition this review has been directed primarily towards aircraft wings so that no attempt has been made to summarise the complicated scale effects on the unsteady flow about other shapes, eg circular cylinders, a subject of great importance in industrial aerodynamics.

APPENDIX

SUGGESTED TEST CASES FOR THE PREDICTION OF SCALE EFFECTS IN UNSTEADY AERODYNAMICS

The two-dimensional and unsteady flows selected for prediction with varying Reynolds numbers and transition positions have already been calculated for a few limited conditions. All three flows selected are of great intrinsic interest.

1 Periodic flow at transonic speeds on a rigid 14% thick biconvex aerofoil at $\alpha = 0°$

This is one of the two test cases (Ref 55) for the AGARD SMP/FDP meeting on "Aircraft Dynamic Loads due to Flow Separation".

Calculations should be made of the dynamic lift and pitching moment with transition fixed (Mach number range for periodic flow in tests is $0.81 \lesssim M \lesssim 0.86$) for $Rc = 10^6,\ 7 \times 10^6,\ 70 \times 10^6$.

In addition, calculations should be attempted with transition free (the Mach number range for periodic flow in tests is $0.81 \lesssim M \lesssim 0.88$). Note that, in experiments the frequency parameter is the same with turbulent and laminar boundary layers for biconvex aerofoils from 14 to 20% thickness.

2 Light stall of NACA 0012 aerofoil (cf Fig 4 of Ref 56)

Preferably calculations should be made with fixed and free transition for

$$Rc = 10^6,\ 3 \times 10^6 \text{ and } 10^7 \ .$$

$$\alpha = 15° + 6° \sin(\nu t) \ .$$

3 Light stall of AMES AOI aerofoil (cf Fig 7 of Ref 56)

As (2) above.

The large effect of transition location shown by this review of the experiments should be illustrated by the predictions of (2) and (3). However the measurements made in air on these aerofoils involve transonic flow at high angles of incidence and this may create computational difficulties.

All three test cases have the advantage that there is no interaction between structural distortion and the flow. Thus there can be no buffeting or flutter motion of the rigid aerofoil in case (1). Similarly, there is no aerodynamic damping due to aeroelastic distortion of the aerofoil for cases (2) and (3), although there will, of course, be aerodynamic damping due to the hysteresis loops in the pitching moment curves.

REFERENCES

1 AGARD Fluid Dynamics Panel, "Boundary layer simulation and control in wind tunnels", AGARD AR 224 (1988).

2 Peckham, D.H., and Woodward, D.S., "The importance of high Reynolds number in low-speed wind tunnel tests of canard delta combat aircraft", RAE Technical Memorandum Aero 2095 (1987).

3 Haines, A.B., "Scale effects in transonic flow", 27 Lanchester Memorial Lecture (1987), Aeronautical Journal 91, Part 907, 291-313 (1987).

4 Elsenaar, A., "On Reynolds number effects and simulation", AGARD CPP 429, Paper 429 (1987).

5 Ashill, P.R., Fulker, J.L., and Weeks, D.J., "The air-injection method of fixing boundary-layer transition and investigating scale effects", Aeronautical Journal of Royal Aeronautical Society, 214-224 (1987).

6 Anon, "Unsteady aerodynamics - fundamentals and applications to aircraft dynamics", AGARD CP 386 (1985).

THIS DOCUMENT PROVIDED BY THE ABBOTT AEROSPACE
TECHNICAL LIBRARY
ABBOTTAEROSPACE.COM

7 Mabey, D.G., and Chambers, J.R., "Technical evaluation report on unsteady-aerodynamics and applications to aircraft dynamics", AGARD AR 22 (1986).

8 Mabey, D.G., "Flow unsteadiness and model vibrations in wind tunnels at subsonic and transonic speeds", ARC CP 1155 (1971).

9 Mabey, D.G., Ashill, P.R., and Welsh, B.L., "Aeroelastic oscillations caused by transitional boundary layers and their attenuation", AIAA Journal Aircraft (1987).

10 Jones , J.G., "A survey of the dynamic analysis of buffeting and related phenomena", RAE Technical Report 72197 (1972).

11 Kilgore, R.A., Adcock, J.B., and Ray, E.J., "Flight simulation characteristics of the Langley high Reynolds number cryogenic transonic tunnel", AIAA 74-80 (1974).

12 Chan, Y.Y., "Analysis of experimental data for cast 10-2/DOA2 supercritical aerofoil at high Reynolds numbers", NAE-AN-49 (1988).

13 Green, J.E., "Some aspects of viscous-inviscid interactions at transonic speeds and their dependence on Reynolds number", AGARD CP 83, Paper 2 (1971).

14 Mabey, D.G., and Cripps, B.E., "Some measurement of buffeting on a flutter model of a typical strike aircraft", AGARD CP 339, Paper 13 (1982).

15 Mabey, D.G., "An hypothesis for the prediction of flight penetration of wing buffeting from dynamic tests of a wind tunnel model", ARC CP 1171 (1971).

16 Mabey, D.G., "Buffeting criteria for a systematic series of wings", AIAA Journal Aircraft 26, Part 6, 576-582 (1989).

17 Townsend, A.A., "The structure of turbulent shear flow", 2nd Edition, Cambridge University Press (1976).

18 Davis, S.S., "Experimental studies of scale effects on oscillating aerofoils at transonic speeds", AGARD CP 296, Paper 9, "Boundary layer effects on unsteady airloads" (1980).

19 Carr, L.W., "Progress in analysis and prediction of dynamic stall", AIAA Journal Aircraft 25, Part 1, 6-17.

20 Carr, L.W., McCloskey, W.J., McAlister, K.W., and Pucci, S.L., "An experimental study of dynamic stall on advanced aerofoil sections", NASA Technical Memorandum 84245 (1982).

21 Lorber, P.F., and Carta, F.O., "Unsteady stall penetration experiments at high Reynolds number", AFOSR Technical Report 87-1202 (1987).

22 Mabey, D.G., "On the prospects for increasing dynamic lift", RAE Technical Memorandum Aero 2068 (1986), also Aeronautical Journal, 95-106 (1988).

23 Gad-el-Hak, M., "The pitching delta wing", AIAA Journal 23, Part 11, 1660-1665 (1985).

24 Woffelt, K.W., and Peterson, L., "Investigation of vortex burst position with hydrodynamically changing angle of attack for a schematic delta wing in a water tunnel with correlation to similar studies in a wind tunnel", AGARD CP 413, Paper 27 (1986).

25 Mabey, D.G., "Measurements of buffeting on slender wing models", ARC CP 917 (1967).

26 Anon, "Aerodynamic and related hydrodynamic studies using water facilities", AGARD CP 413 (1986).

27 Mabey, D.G., Welsh, B.L., and Cripps, B.E., "Measurements of steady and oscillatory pressures on a low aspect ratio model at subsonic and supersonic speeds", RAE Technical Report 84-095 (1984).

28 Mabey, D.G., and Welsh, B.L., "Measurements and calculations of steady and oscillatory pressures on a low aspect ratio model at subsonic and transonic speeds", Journal of Fluids and Structures 1, 445-468 (1987).

29 Mabey, D.G., Welsh, B.L., and Pyne, C.R., "Measurements of steady and oscillatory pressures on a rectangular wing", RAE Technical Report 86-040 (1986).

30 Mabey, D.G., Welsh, B.L., and Pyne, C.R., "A summary of measurements of steady and oscillatory pressures on a rectangular wing", Journal Royal Aeronautical Society 10-27 (1988).

31 Davies, D.E., "Theoretical determination of subsonic oscillatory air-force coefficients", RAE Technical Report 76-059 (1976), R & M 3804.

32 Bublitz, P., "Unsteady airloads on oscillatory wings in post stall conditions", Paper in VKI lecture series on "Unsteady airloads and aeroelastic problems in separated and transonic flow" (1981).

33 Zingel, H., "Zur bestimmung des aeroelastischen Verhaltens von Auftriebsystemen infolge von Strömungsablösung", DFVLR-FB-86-35 (1986).

34 Mabey, D.G., "Analysis and correlation of data on pressure fluctuations in separated flow", AIAA Journal (1972).

35 Mabey, D.G., Welsh, B.L., and Pyne, C.R., RAE (unpublished data).

THIS DOCUMENT PROVIDED BY THE ABBOTT AEROSPACE
TECHNICAL LIBRARY
ABBOTTAEROSPACE.COM

36 Mabey, D.G., Welsh, B.L., Stott, G., and Cripps, B.E., "The dynamic characteristics of rapidly moving spoilers at subsonic and transonic speeds", RAE Technical Report 82-109 (1982).

37 Costes, M., Gravelle, A., and Philippe, J.J., "Investigation of unsteady subsonic spoiler and flap aerodynamics", AIAA Journal Aircraft 24, Part 9, 629-637 (1987).

38 Costes, M., Private communication, 27 November 1987.

39 Moore, A.A., "Scale effects on oscillatory control - surface derivatives", ARC CP 1151 (1971).

40 Lambourne, N.C., Wright, K.C., and Welsh, B.L., "Measurements of control-surface oscillatory derivatives on a swept back tapered model wing in two transonic tunnels", R & M 3806 (1976).

41 Davies, D.E., "Calculation of unsteady generalised airforces on a thin wing oscillating harmonically in subsonic flow", R & M 3409 (1963).

42 Jones, R.T., "An experimental determination of transonic hinge moment derivatives", RAE Technical Report 83-067 (1983).

43 Nakarmura, Y., and Woodgate, L., "Effect of Reynolds number and frequency parameter on control surface buzz at high subsonic speeds", NPL Aero Report 1312 (1970).

44 Lambourne, N.C., "Flutter in one degree of freedom", Chapter 5, Part 5, AGARD Manual of Aerolasticity.

45 Moore, A.W., Lambourne, N.C., and Woodgate, L., "Comparison between dynamic stability boundaries for NPL 9615 and NASA 0012 aerofoils pitching about quarter-chord", ARC CP 1279 (1971).

46 Houwink, R., Kraan, A.N., and Zwaan, R.J., "Wind tunnel study of the flutter characteristics of a supercritical wing", AIAA Journal of Aircraft 19, 400-405 (1984).

47 Erickson, L.L., "Transonic single-mode flutter and buffet of a low aspect ratio wing having a subsonic aerofoil shape", NASA IND 7346 (1974).

48 Martin, L., BAe unpublished tests.

49 Yates, E.C., "AGARD standard aeroelastic configuration for dynamic response. 1 - Wing 445.6", AGARD Report No 765 (1988).

50 Malcolm, G.N., and Schiff, L.B., "Recent developments in rotary balance testing of fighter aircraft configurations at NASA Ames Research Centre", AGARD CP 386, Paper 18 (1985).

51 Schmidt, E., "Standard dynamics model experiments with the DFVLR/AVA transonic derivative balance", AGARD CP 386, Paper 21 (1985).

52 O'Leary, C., and Rowthorne, E.N., "Measurements of the oscillatory lateral derivatives of a high incidence research model (HIRM I) at speeds up to M = 0.8 ", RAE Technical Report 87-018 (1987).

53 Erickson, L.E., " Effect of boundary layer transition on vehicle dynamics", AIAA Journal of Spacecraft and Rockets 6, 1404-1409 (1969).

54 Ross, A.J., and Nguyen, L.T., "Some observations regarding wing rock oscillations at high angles of attack", AIAA Atmospheric Flight Mechanics Conference (1988).

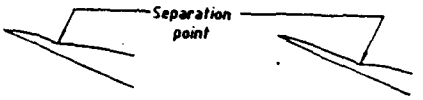
55 Mabey, D.G., "Some aspects of aircraft dynamic loads due to flow separation", AGARD R750 (1988), also Prog Aerospace Sci, Vol 26, 115-151 (1989).

56 Geisler, W., "Unsteady boundary layer separation on aerofoils performing large amplitude oscillations - dynamic stall", AGARD CP 386, Paper 7 (1985).

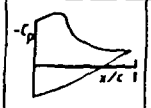
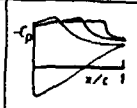
Copyright © controller HMSO London 1991

THIS DOCUMENT PROVIDED BY THE ABBOTT AEROSPACE
TECHNICAL LIBRARY
ABBOTTAEROSPACE.COM

Pressure gradient - upper surface adverse
- lower surface favourable

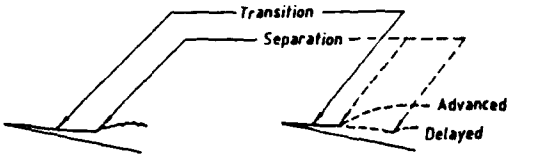


(a) Low Reynolds number (b) High Reynolds number

	DIRECT	INDIRECT
Pressure distributions	 Constant	 Variable
Circulation	Constant	Variable
Magnitude of scale effects on lift	Often small and predictable	Large and may be unpredictable

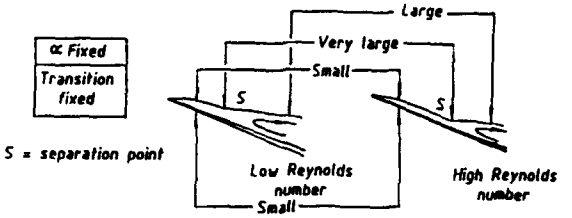
(c) Differences between direct and indirect effects

Fig.1 Origin and nature of scale effects



(a) Correct (b) Premature (due to roughness or free-stream flow unsteadiness)

Fig.2 Influence of transition position at full scale Reynolds number on aerofoil separation



(a) Local effects

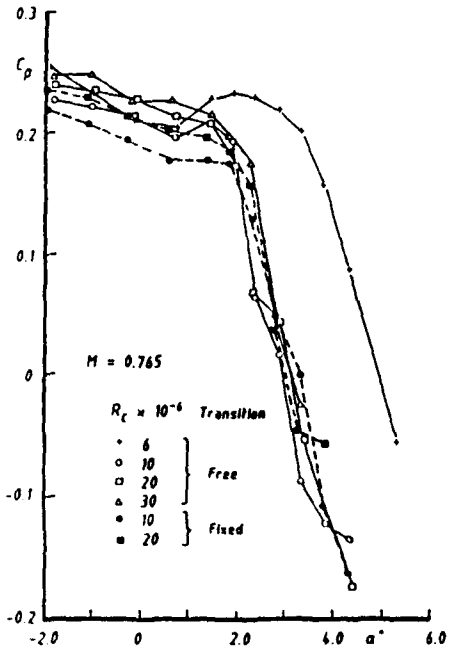


Fig.3 (b) Scale effects on trailing-edge pressure coefficient at constant α (after Ref. 12)

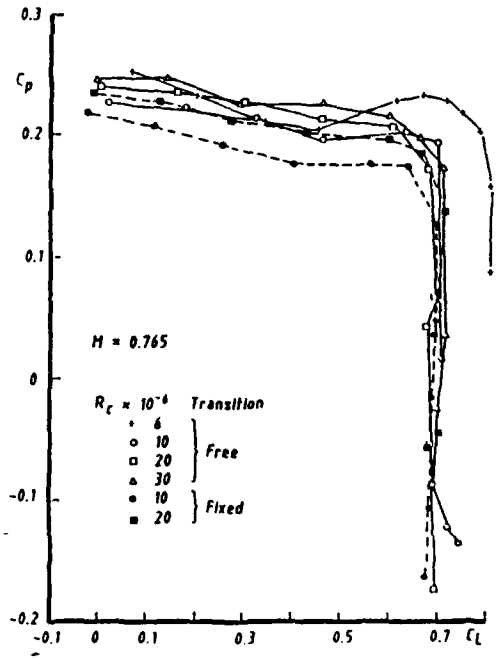


Fig.3 (c) Scale effects on trailing-edge pressure coefficient at constant C_L (after Ref. 12)

Fig.3 Scale effects on an aerofoil with separated flow (M, α, or C_L fixed)

THIS DOCUMENT PROVIDED BY THE ABBOTT AEROSPACE
TECHNICAL LIBRARY
ABBOTTAEROSPACE.COM

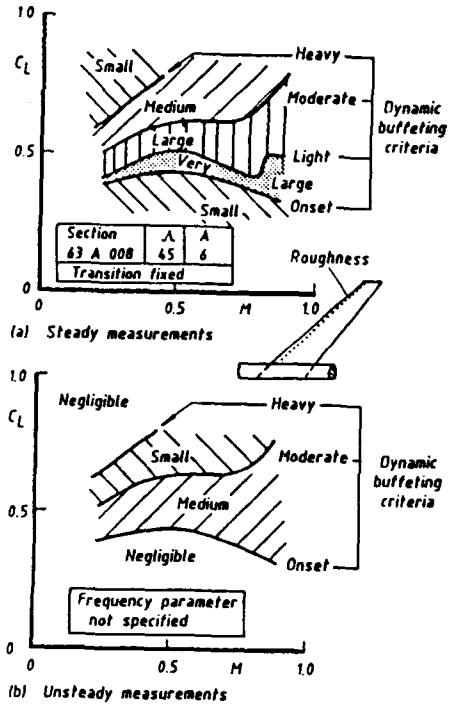


Fig. 4 *Tentative assessment on overall scale effects on a typical swept wing (after Ref.16)*

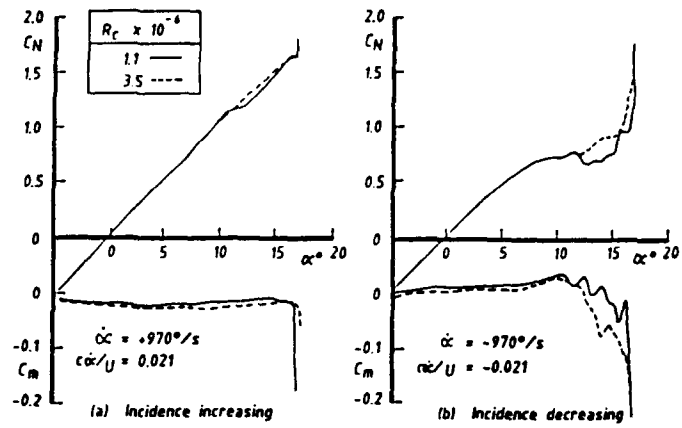


Fig 6 ***RAE9615 aerofoil, Scale effect on ramp measurements with free transition M = 0.3***

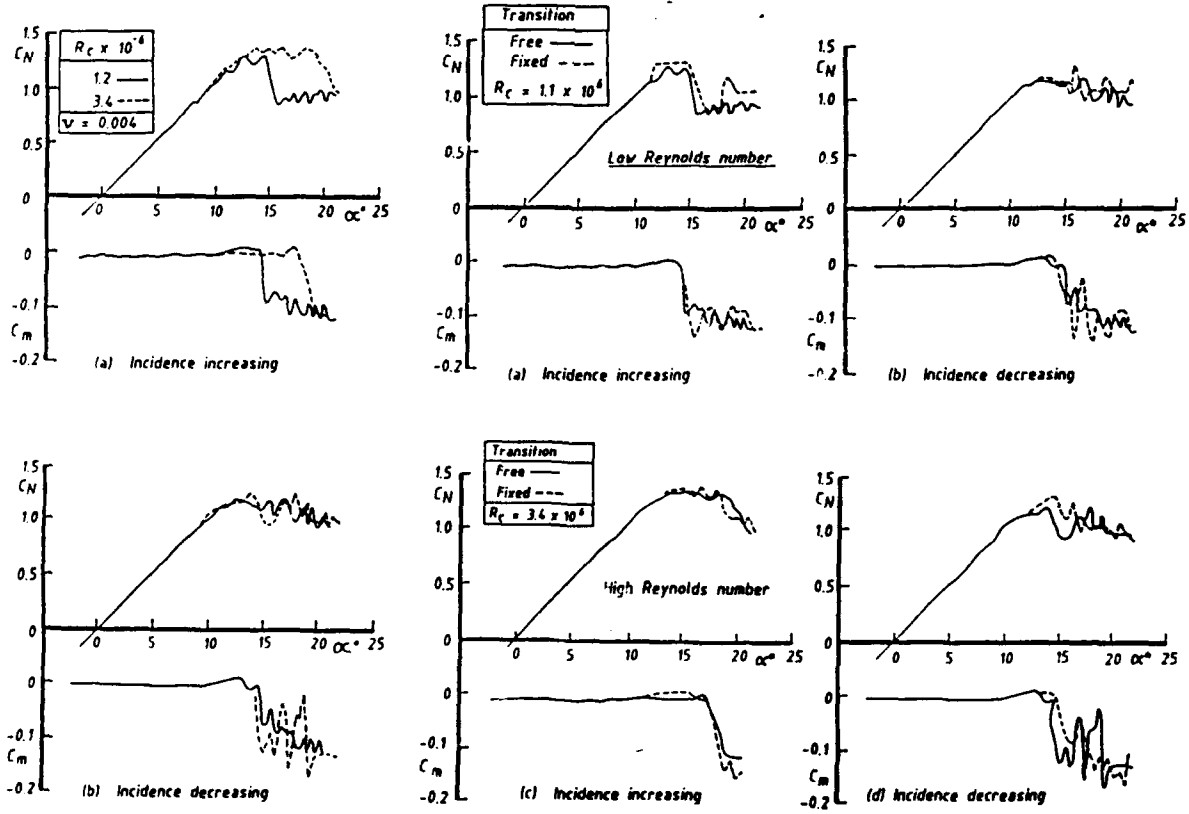
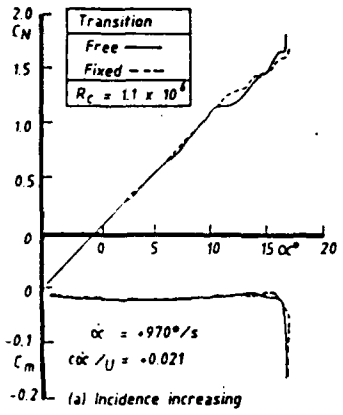


Fig 5 ***RAE9615 Scale effects on quasi-steady measurements with free transition M = 0.3***

Fig 7 ***RAE9615 aerofoil, Effect of fixing transition on quasi-steady measurements at M = 0.3***

THIS DOCUMENT PROVIDED BY THE ABBOTT AEROSPACE
TECHNICAL LIBRARY
ABBOTTAEROSPACE.COM



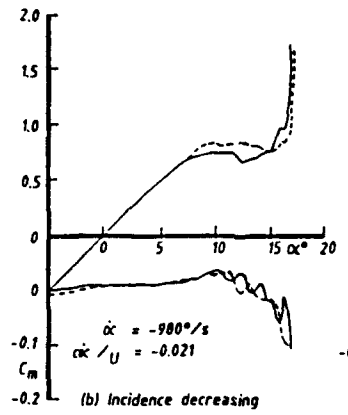
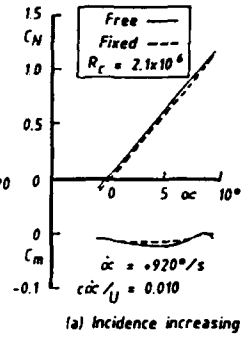


Fig 8 **RAE9615 aerofoil, Effect of fixing transition on ramp measurements at M = 0.3**



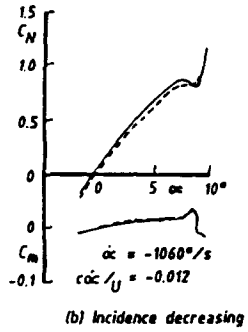
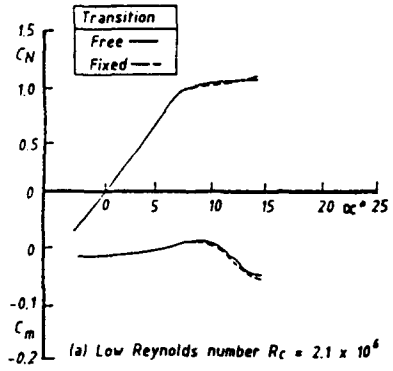


Fig 11 **RAE 9615 aerofoil, effect of fixing transition on ramp measurements at M = 0.6**



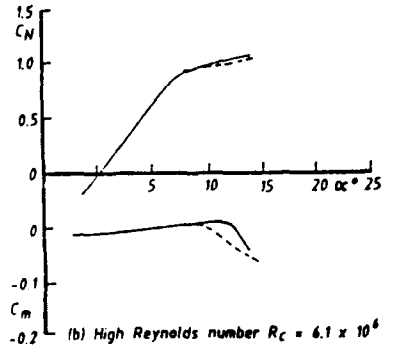


Fig 9 **RAE9615 aerofoil, Effect of fixing transition on quasi- steady measurements at M = 0.6**

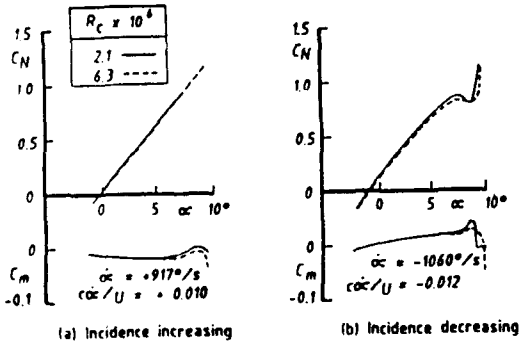
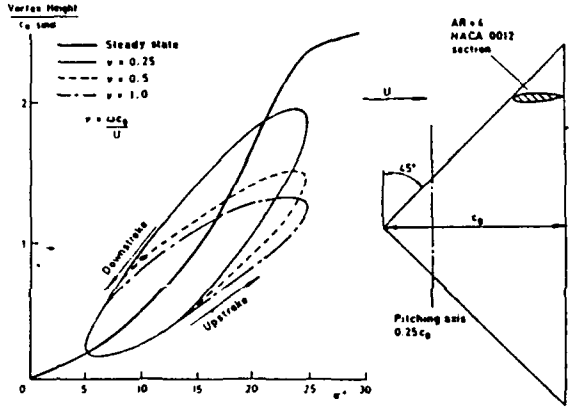


Fig 10 **RAE 9615 aerofoil, Scale effect on ramp measurements with free transition, M = 0.6**



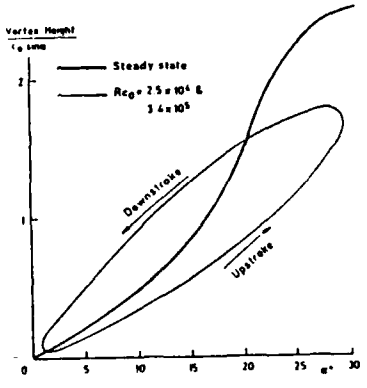


Fig 12 Hysteresis loop on delta wing (after Ref 23)

THIS DOCUMENT PROVIDED BY THE ABBOTT AEROSPACE
TECHNICAL LIBRARY
ABBOTTAEROSPACE.COM

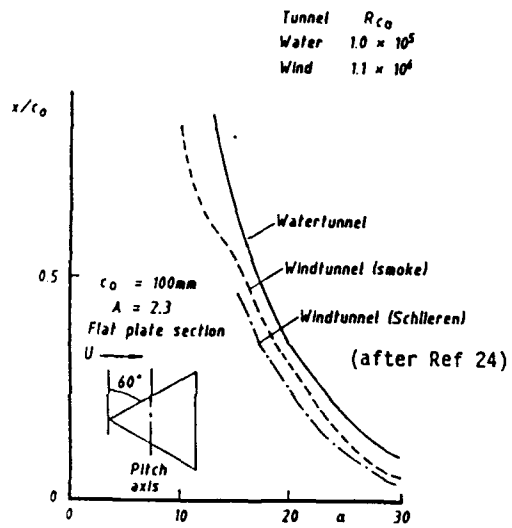


Fig 13 **Stationary vortex burst position – comparison watertunnel and windtunnel**

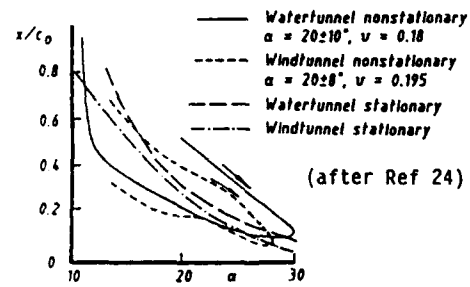


Fig 14 **Comparison between watertunnel and windtunnel of stationary and nonstationary vortex burst positions**

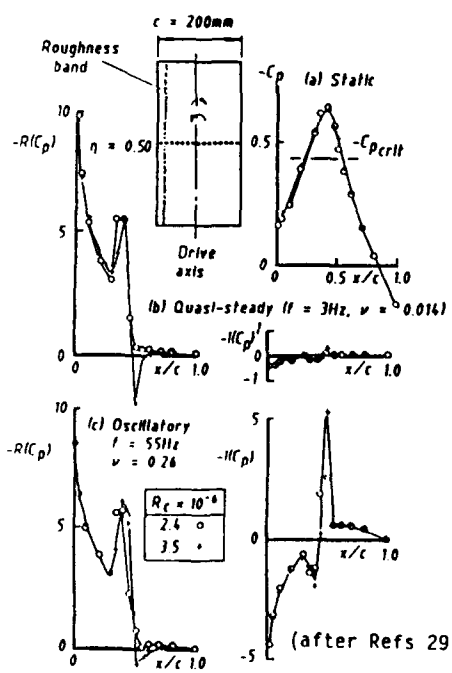
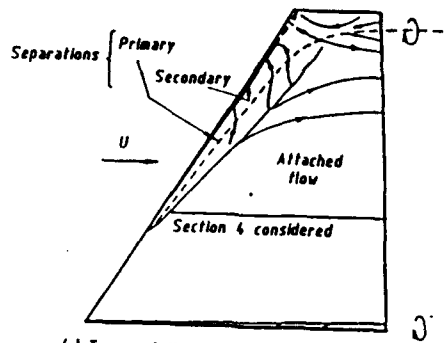
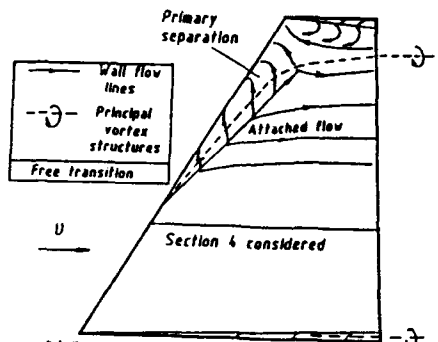


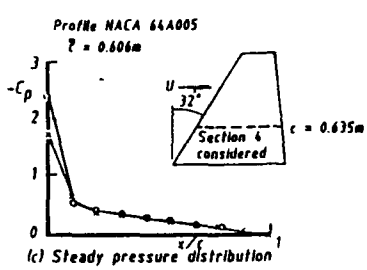
Fig 15 **Small influence of Reynolds number on pressure due to oscillation in pitch, M = 0.80, α = 0°, η = 0.50 (after Refs. 49 & 50)**



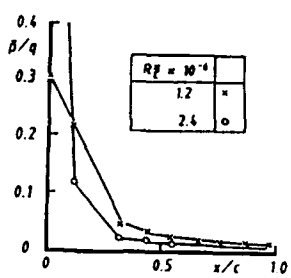
(a) Types of flow $R = 1.2 \times 10^6$



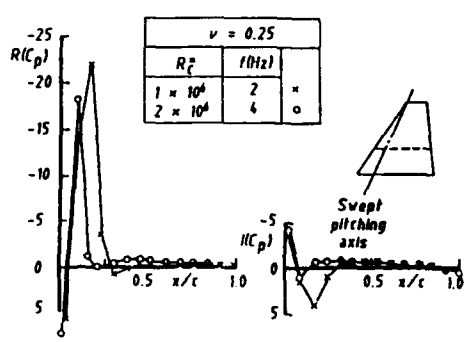
(b) Types of flow $R_{\bar{c}} = 2.4 \times 10^6$



(c) Steady pressure distribution



(d) Random pressure distribution



(e) Real and imaginary components of oscillatory pressure distributions due to pitching oscillation

Fig 16 **Reynolds number effect on a thin swept wing just after buffet onset, α = 7.5°,**

(after Refs 32 and 33)

THIS DOCUMENT PROVIDED BY THE ABBOTT AEROSPACE
TECHNICAL LIBRARY
ABBOTTAEROSPACE.COM

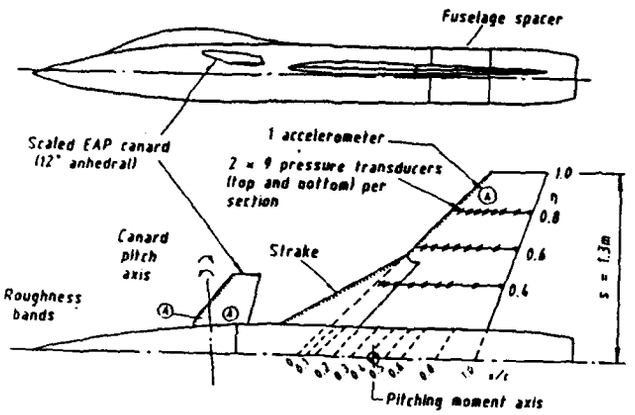


Fig 17 **Details of canard/wing model**

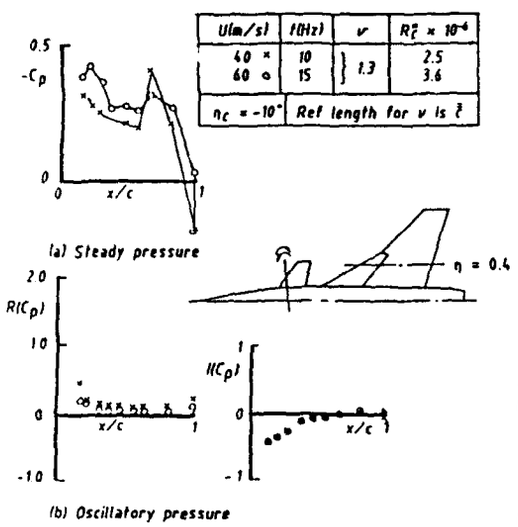


Fig 18 **EAP configuration, wing pressures at two speeds, α = 5° (α_c = -2.8°)**

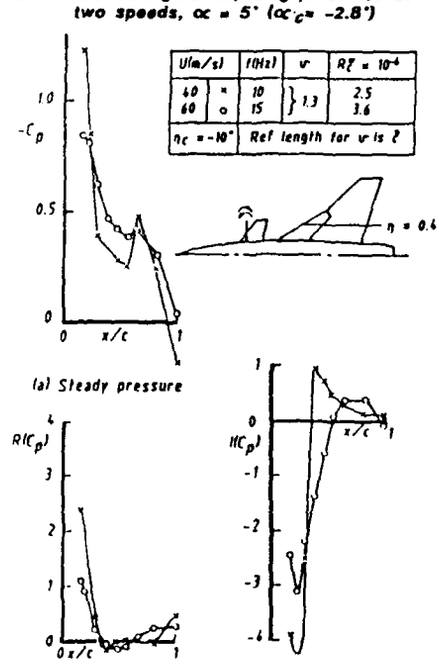


Fig 19 **EAP configuration, wing pressures at two speeds, α = 12° (α_c = 7.2°)**

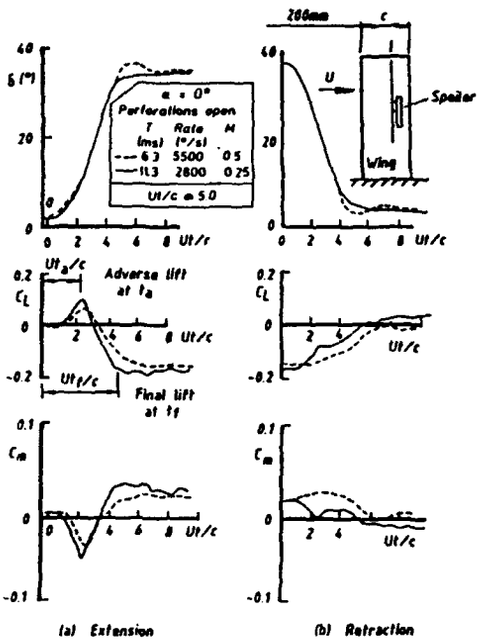


Fig 20 **Correlation of subsonic time histories for spoiler motion** (after Ref 36)

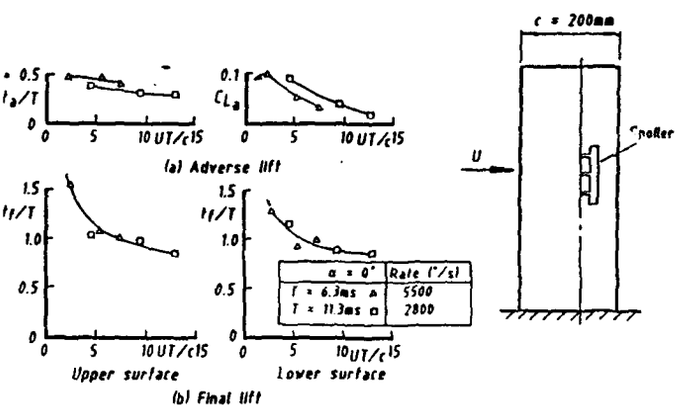


Fig 21 **Correlation of subsonic delay times for spoiler extension** (after Ref 36)

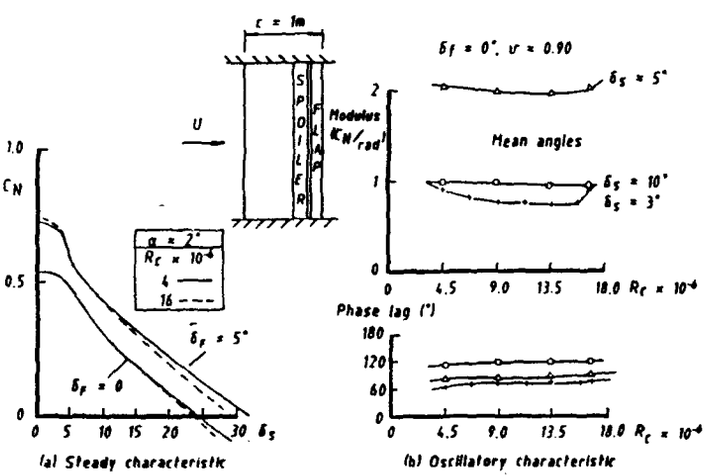


Fig 22 **Reynolds number effect due to spoiler oscillation** (after Ref 37)

THIS DOCUMENT PROVIDED BY THE ABBOTT AEROSPACE
TECHNICAL LIBRARY
ABBOTTAEROSPACE.COM

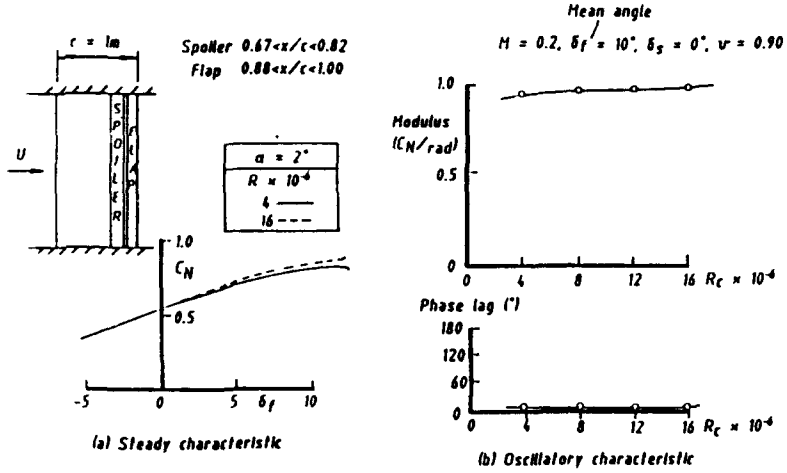


Fig 23 **Reynolds number effect due to flap oscillation** (after Ref 37)

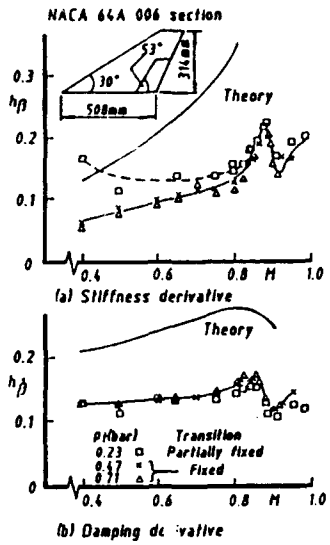


Fig 26 **Measurements of oscillatory control hinge moments** (after Ref 42)

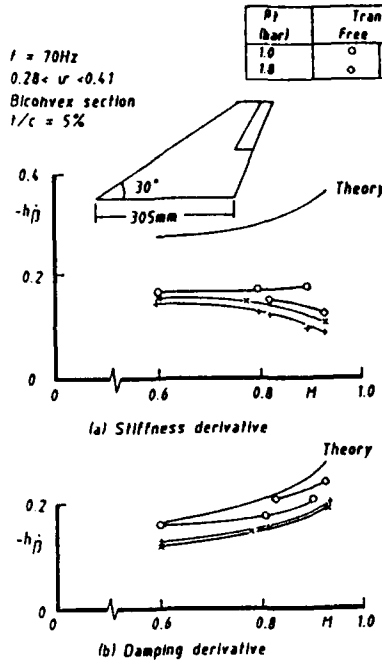
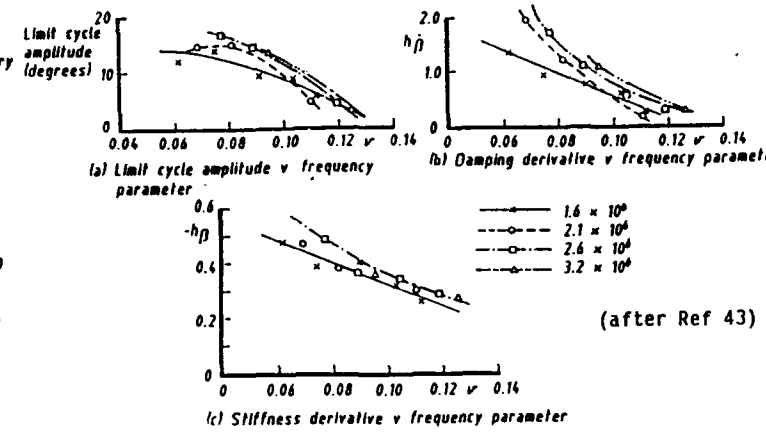


Fig 24 **Hinge moment due to oscillating flap v Mach number**



(after Ref 43)

Fig 27 **Influence of Reynolds number and frequency on parameters influencing control limit cycle at M = 0.78**

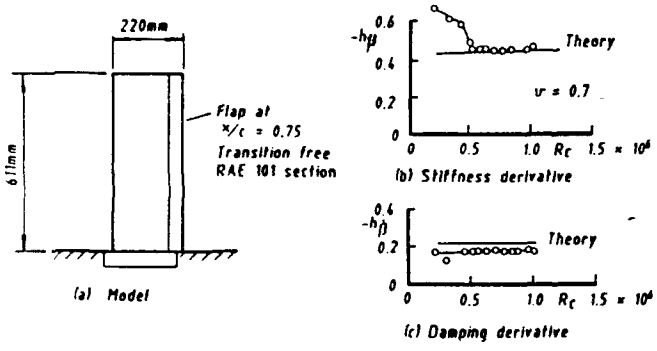


Fig 25 **Measurements of oscillatory control hinge moments**

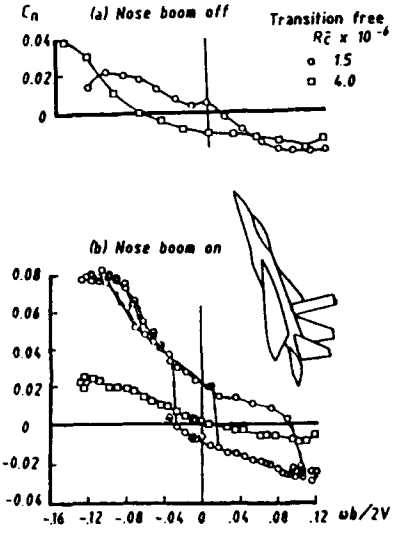


Fig 28 **Effects of rotation rate on the yawing-moment coefficient for the F-15 at α = 70°**

THIS DOCUMENT PROVIDED BY THE ABBOTT AEROSPACE
TECHNICAL LIBRARY
ABBOTTAEROSPACE.COM

REPORT DOCUMENTATION PAGE

1. Recipient's Reference	2. Originator's Reference	3. Further Reference	4. Security Classification of Document
	AGARD-CP-507	ISBN 92-835-0660-X	UNCLASSIFIED

5. Originator Advisory Group for Aerospace Research and Development
North Atlantic Treaty Organization
7 rue Ancelle, 92200 Neuilly sur Seine, France

6. Title TRANSONIC UNSTEADY AERODYNAMICS AND AEROELASTICITY

7. Presented at the 73rd Meeting of the AGARD Structures and Materials Panel, held in San Diego, CA, United States from 7th—11th October 1991.

8. Author(s)/Editor(s)	9. Date
Various	March 1992
10. Author's/Editor's Address	**11. Pages**
Various	406

12. Distribution Statement This document is distributed in accordance with AGARD policies and regulations, which are outlined on the back covers of all AGARD publications.

13. Keywords/Descriptors

Transonic flow	Flow distribution
Unsteady flow	Aerodynamics
Aeroelasticity	Computation
Flutter	Experimentation

14. Abstract

This publication reports the papers presented to a Specialists' Meeting organized by the Structures and Materials Panel of AGARD and held at its Fall 1991 Meeting.

The Specialists' Meeting provided a forum for the exchange of experiences between the NATO nations with an aim to demonstrate and discuss the present state of knowledge in the field of transonic unsteady aerodynamics and aeroelasticity; to evaluate the various methods of calculation and to highlight straightforward engineering-level aeroelastic prediction techniques.

AGARD Conference Proceedings 507 Advisory Group for Aerospace Research and Development, NATO TRANSONIC UNSTEADY AERODYNAMICS AND AEROELASTICITY Published March 1992 406 pages This publication reports the papers presented to a Specialists' Meeting organized by the Structures and Materials Panel of AGARD and held at its Fall 1991 Meeting. The Specialists' Meeting provided a forum for the exchange of experiences between the NATO nations with an aim to demonstrate and discuss the present state of knowledge in the field of transonic unsteady aerodynamics P.T.O.	AGARD-CP-507 Transonic flow Unsteady flow Aeroelasticity Flutter Flow distribution Aerodynamics Computation Experimentation	AGARD Conference Proceedings 507 Advisory Group for Aerospace Research and Development, NATO TRANSONIC UNSTEADY AERODYNAMICS AND AEROELASTICITY Published March 1992 406 pages This publication reports the papers presented to a Specialists' Meeting organized by the Structures and Materials Panel of AGARD and held at its Fall 1991 Meeting. The Specialists' Meeting provided a forum for the exchange of experiences between the NATO nations with an aim to demonstrate and discuss the present state of knowledge in the field of transonic unsteady aerodynamics P.T.O.	AGARD-CP-507 Transonic flow Unsteady flow Aeroelasticity Flutter Flow distribution Aerodynamics Computation Experimentation
AGARD Conference Proceedings 507 Advisory Group for Aerospace Research and Development, NATO TRANSONIC UNSTEADY AERODYNAMICS AND AEROELASTICITY Published March 1992 406 pages This publication reports the papers presented to a Specialists' Meeting organized by the Structures and Materials Panel of AGARD and held at its Fall 1991 Meeting. The Specialists' Meeting provided a forum for the exchange of experiences between the NATO nations with an aim to demonstrate and discuss the present state of knowledge in the field of transonic unsteady aerodynamics P.T.O.	AGARD-CP-507 Transonic flow Unsteady flow Aeroelasticity Flutter Flow distribution Aerodynamics Computation Experimentation	AGARD Conference Proceedings 507 Advisory Group for Aerospace Research and Development, NATO TRANSONIC UNSTEADY AERODYNAMICS AND AEROELASTICITY Published March 1992 406 pages This publication reports the papers presented to a Specialists' Meeting organized by the Structures and Materials Panel of AGARD and held at its Fall 1991 Meeting. The Specialists' Meeting provided a forum for the exchange of experiences between the NATO nations with an aim to demonstrate and discuss the present state of knowledge in the field of transonic unsteady aerodynamics P.T.O.	AGARD-CP-507 Transonic flow Unsteady flow Aeroelasticity Flutter Flow distribution Aerodynamics Computation Experimentation

THIS DOCUMENT PROVIDED BY THE ABBOTT AEROSPACE
TECHNICAL LIBRARY
ABBOTTAEROSPACE.COM

and aeroelasticity; to evaluate the various methods of calculation and to highlight straightforward engineering-level aeroelastic prediction techniques.

Papers presented at the 73rd Meeting of the AGARD Structures and Materials Panel, held in San Diego, CA, United States from 7th–11th October 1991.

ISBN 92-835-0660-X

and aeroelasticity; to evaluate the various methods of calculation and to highlight straightforward engineering-level aeroelastic prediction techniques.

Papers presented at the 73rd Meeting of the AGARD Structures and Materials Panel, held in San Diego, CA, United States from 7th–11th October 1991.

ISBN 92-835-0660-X

and aeroelasticity; to evaluate the various methods of calculation and to highlight straightforward engineering-level aeroelastic prediction techniques.

Papers presented at the 73rd Meeting of the AGARD Structures and Materials Panel, held in San Diego, CA, United States from 7th–11th October 1991.

ISBN 92-835-0660-X

and aeroelasticity; to evaluate the various methods of calculation and to highlight straightforward engineering-level aeroelastic prediction techniques.

Papers presented at the 73rd Meeting of the AGARD Structures and Materials Panel, held in San Diego, CA, United States from 7th–11th October 1991.

ISBN 92-835-0660-X

THIS DOCUMENT PROVIDED BY THE ABBOTT AEROSPACE
TECHNICAL LIBRARY
ABBOTTAEROSPACE.COM

THIS DOCUMENT PROVIDED BY THE ABBOTT AEROSPACE
TECHNICAL LIBRARY
ABBOTTAEROSPACE.COM

AGARD

NATO OTAN

7 RUE ANCELLE · 92200 NEUILLY-SUR-SEINE

FRANCE

Téléphone (1)47.38.57.00 · Télex 610 176
Télécopie (1)47.38.57.99

DIFFUSION DES PUBLICATIONS
AGARD NON CLASSIFIEES

L'AGARD ne détient pas de stocks de ses publications, dans un but de distribution générale à l'adresse ci-dessus. La diffusion initiale des publications de l'AGARD est effectuée auprès des pays membres de cette organisation par l'intermédiaire des Centres Nationaux de Distribution suivants. A l'exception des Etats-Unis, ces centres disposent parfois d'exemplaires additionnels; dans les cas contraire, on peut se procurer ces exemplaires sous forme de microfiches ou de microcopies auprès des Agences de Vente dont la liste suite.

CENTRES DE DIFFUSION NATIONAUX

ALLEMAGNE
Fachinformationszentrum,
Karlsruhe
D-7514 Eggenstein-Leopoldshafen 2

BELGIQUE
Coordonnateur AGARD-VSL
Etat-Major de la Force Aérienne
Quartier Reine Elisabeth
Rue d'Evere, 1140 Bruxelles

CANADA
Directeur du Service des Renseignements Scientifiques
Ministère de la Défense Nationale
Ottawa, Ontario K1A 0K2

DANEMARK
Danish Defence Research Board
Ved Idraetsparken 4
2100 Copenhagen Ø

ESPAGNE
INTA (AGARD Publications)
Pintor Rosales 34
28008 Madrid

ETATS-UNIS
National Aeronautics and Space Administration
Langley Research Center
M/S 180
Hampton, Virginia 23665

FRANCE
O.N.E.R.A. (Direction)
29, Avenue de la Division Leclerc
92320, Châtillon sous Bagneux

GRECE
Hellenic Air Force
Air War College
Scientific and Technical Library
Dekelia Air Force Base
Dekelia, Athens TGA 1010

ISLANDE
Director of Aviation
c/o Flugrad
Reykjavik

ITALIE
Aeronautica Militare
Ufficio del Delegato Nazionale all'AGARD
Aeroporto Pratica di Mare
00040 Pomezia (Roma)

LUXEMBOURG
Voir Belgique

NORVEGE
Norwegian Defence Research Establishment
Attn: Biblioteket
P.O. Box 25
N-2007 Kjeller

PAYS-BAS
Netherlands Delegation to AGARD
National Aerospace Laboratory NLR
Kluyverweg 1
2629 HS Delft

PORTUGAL
Portuguese National Coordinator to AGARD
Gabinete de Estudos e Programas
CLAFA
Base de Alfragide
Alfragide
2700 Amadora

ROYAUME UNI
Defence Research Information Centre
Kentigern House
65 Brown Street
Glasgow G2 8EX

TURQUIE
Milli Savunma Başkanlığı (MSB)
ARGE Daire Başkanlığı (ARGE)
Ankara

LE CENTRE NATIONAL DE DISTRIBUTION DES ETATS-UNIS (NASA) NE DETIENT PAS DE STOCKS DES PUBLICATIONS AGARD ET LES DEMANDES D'EXEMPLAIRES DOIVENT ETRE ADRESSEES DIRECTEMENT AU SERVICE NATIONAL TECHNIQUE DE L'INFORMATION (NTIS) DONT L'ADRESSE SUIT.

AGENCES DE VENTE

National Technical Information Service
(NTIS)
5285 Port Royal Road
Springfield, Virginia 22161
Etats-Unis

ESA/Information Retrieval Service
European Space Agency
10, rue Mario Nikis
75015 Paris
France

The British Library
Document Supply Division
Boston Spa, Wetherby
West Yorkshire LS23 7BQ
Royaume Uni

Les demandes de microfiches ou de photocopies de documents AGARD (y compris les demandes faites auprès du NTIS) doivent comporter la dénomination AGARD, ainsi que le numero de série de l'AGARD (par exemple AGARD-AG-315). Des informations analogues, telles que le titre et la date de publication sont souhaitables. Veuiller noter qu'il y a lieu de spécifier AGARD-R-nnn et AGARD-AR-nnn lors de la commande de rapports AGARD et des rapports consultatifs AGARD respectivement. Des références bibliographiques complètes ainsi que des résumés des publications AGARD figurent dans les journaux suivants:

Scientifique and Technical Aerospace Reports (STAR)
publié par la NASA Scientific and Technical
Information Division
NASA Headquarters (NTT)
Washington D.C. 20546
Etats-Unis

Government Reports Announcements and Index (GRA&I)
publié par le National Technical Information Service
Springfield
Virginia 22161
Etats-Unis

(accessible également en mode interactif dans la base de données bibliographiques en ligne du NTIS, et sur CD-ROM)

Imprimé par Specialised Printing Services Limited
40 Chigwell Lane, Loughton, Essex IG10 3TZ

THIS DOCUMENT PROVIDED BY THE ABBOTT AEROSPACE
TECHNICAL LIBRARY
ABBOTTAEROSPACE.COM

AGARD

NATO OTAN

7 RUE ANCELLE · 92200 NEUILLY-SUR-SEINE

FRANCE

Telephone (1)47.38.57.00 · Telex 610 176
Telefax (1)47.38.57.99

DISTRIBUTION OF UNCLASSIFIED AGARD PUBLICATIONS

AGARD does NOT hold stocks of AGARD publications at the above address for general distribution. Initial distribution of AGARD publications is made to AGARD Member Nations through the following National Distribution Centres. Further copies are sometimes available from these Centres (except in the United States), but if not may be purchased in Microfiche or Photocopy form from the Sales Agencies listed below.

NATIONAL DISTRIBUTION CENTRES

BELGIUM
Coordonnateur AGARD — VSL
Etat-Major de la Force Aérienne
Quartier Reine Elisabeth
Rue d'Evere, 1140 Bruxelles

CANADA
Director Scientific Information Services
Dept of National Defence
Ottawa, Ontario K1A 0K2

DENMARK
Danish Defence Research Board
Ved Idraetsparken 4
2100 Copenhagen Ø

FRANCE
O.N.E.R.A. (Direction)
29 Avenue de la Division Leclerc
92320 Châtillon

GERMANY
Fachinformationszentrum
Karlsruhe
D-7514 Eggenstein-Leopoldshafen 2

GREECE
Hellenic Air Force
Air War College
Scientific and Technical Library
Dekelia Air Force Base
Dekelia, Athens TGA 1010

ICELAND
Director of Aviation
c/o Flugrad
Reykjavik

ITALY
Aeronautica Militare
Ufficio del Delegato Nazionale all'AGARD
Aeroporto Pratica di Mare
00040 Pomezia (Roma)

LUXEMBOURG
See Belgium

NETHERLANDS
Netherlands Delegation to AGARD
National Aerospace Laboratory, NLR
Kluyverweg 1
2629 HS Delft

NORWAY
Norwegian Defence Research Establishment
Attn: Biblioteket
P.O. Box 25
N-2007 Kjeller

PORTUGAL
Portuguese National Coordinator to AGARD
Gabinete de Estudos e Programas
CLAFA
Base de Alfragide
Alfragide
2700 Amadora

SPAIN
INTA (AGARD Publications)
Pintor Rosales 34
28008 Madrid

TURKEY
Milli Savunma Başkanlığı (MSB)
ARGE Daire Başkanlığı (ARGE)
Ankara

UNITED KINGDOM
Defence Research Information Centre
Kentigern House
65 Brown Street
Glasgow G2 8EX

UNITED STATES
National Aeronautics and Space Administration (NASA)
Langley Research Center
M/S 180
Hampton, Virginia 23665

THE UNITED STATES NATIONAL DISTRIBUTION CENTRE (NASA) DOES NOT HOLD STOCKS OF AGARD PUBLICATIONS, AND APPLICATIONS FOR COPIES SHOULD BE MADE DIRECT TO THE NATIONAL TECHNICAL INFORMATION SERVICE (NTIS) AT THE ADDRESS BELOW.

SALES AGENCIES

National Technical
Information Service (NTIS)
5285 Port Royal Road
Springfield, Virginia 22161
United States

ESA/Information Retrieval Service
European Space Agency
10, rue Mario Nikis
75015 Paris
France

The British Library
Document Supply Centre
Boston Spa, Wetherby
West Yorkshire LS23 7BQ
United Kingdom

Requests for microfiches or photocopies of AGARD documents (including requests to NTIS) should include the word 'AGARD' and the AGARD serial number (for example AGARD-AG-315). Collateral information such as title and publication date is desirable. Note that AGARD Reports and Advisory Reports should be specified as AGARD-R-nnn and AGARD-AR-nnn, respectively. Full bibliographical references and abstracts of AGARD publications are given in the following journals:

Scientific and Technical Aerospace Reports (STAR)
published by NASA Scientific and Technical
Information Division
NASA Headquarters (NTT)
Washington D.C. 20546
United States

Government Reports Announcements and Index (GRA&I)
published by the National Technical Information Service
Springfield
Virginia 22161
United States

(also available online in the NTIS Bibliographic Database or on CD-ROM)

Printed by Specialised Printing Services Limited
40 Chigwell Lane, Loughton, Essex IG10 3TZ

ISBN 92-835-0660-X